Evolution of the continental crust and significance of the zircon record, a case study from the French Massif Central

Simon Couzinié

N° d'ordre NNT : 2017LYSES035

THESE de DOCTORAT DE L'UNIVERSITE DE LYON
opérée au sein de
l'Université Jean Monnet, Saint-Etienne

Ecole Doctorale N° SIS 488
Sciences, Ingénierie, Santé

Spécialité de doctorat : Sciences de la Terre
Discipline : Pétrologie-Géochimie

Simon Gwenaël Couzinié

Evolution of the continental crust and significance of the zircon record, a case study from the French Massif Central

---

Soutenue le 03 novembre 2017

Jury composé de :

Storey, Craig	Professeur, University of Portsmouth	Rapporteur
Teyssier, Christian	Professeur, University of Minnesota	Rapporteur
Gardien, Véronique	Maitre de Conférences, Université de Lyon	Examinatrice
Roger, Françoise	Chargée de Recherche, CNRS Montpellier	Examinatrice
Moyen, Jean-François	Professeur, Université de Saint-Etienne	Directeur de thèse
Stevens, Gary	Professeur, Stellenbosch University	Co-directeur de thèse
Laurent, Oscar	Chercheur post-doctoral, ETH Zürich	Invité
Bouilhol, Pierre	Maitre de Conférences, Université de Nancy	Invité

Abstract

The formation of the continental crust is a major consequence of Earth differentiation. Understanding how the crust formed and evolved through time is paramount to locate the vast mineral deposits hosted therein and address its influence on the global climate, ultimately affecting the development of terrestrial life. Recent advances on the topic of continental crust evolution benefited from improvements of analytical techniques enabling *in situ* measurements of U–Pb–Hf–O isotope compositions in zircon, a widespread accessory mineral of continental igneous rocks. The time constrains derived from the U–Pb chronometer coupled with the petrogenetic information retrieved from Hf–O isotope signatures are currently used to unravel the diversity and succession of magmatic events affecting the continental crust at the regional and global scales.

This study reconstructs the evolutionary path followed by the crust segment today exposed in the eastern part of the French Massif Central (FMC), a portion of the Variscan belt of Western Europe, with the aim to investigate the potential flaws of the zircon record of crust evolution. In this scope, the origin and geodynamic significance of the constituent FMC lithological units are tackled by combining conventional petrological observations with zircon U–Pb–Hf–O isotope data. The results obtained following this integrated approach are then confronted to the conclusions that would have been drawn solely from zircon isotopic signatures, taken out of their petrological context, as is commonly performed in studies investigating crust evolution.

The oldest rocks of the FMC correspond to Ediacaran (590–550 Ma) meta-sediments deposited in back-arc basins along the northern Gondwana margin. Such basins were fed by a mixed detritus originating from the adjacent Cadomian magmatic arc and a distal Gondwana source, presumably the Sahara Metacraton. Partial melting of these meta-sediments at the Ediacaran/Cambrian boundary led to voluminous S-type granitic magmatism, pinpointing a first major crust reworking event in the FMC. The origin of anatexis likely stems from the transient thickening of the hot, back-arc crust caused by the flattening of the Cadomian subduction. Subordinate melting of the depleted back-arc mantle at that time is also documented. During the Lower Paleozoic, rifting of the northern Gondwana provoked coeval crust and (limited) mantle melting. Mantle-derived igneous rocks show markedly diverse trace element and isotopic signatures, consistent with a very heterogeneous mantle source pervasively modified by the Cadomian subduction. Finally, the Variscan collision resulted in crustal melting as evidenced by the emplacement of S-type granites and the formation of migmatite domes, the spatial distribution of which being partly controlled by the crustal architecture inherited from pre-orogenic events. Synchronous intrusion of mafic mantle-derived magmas and their differentiates testify for Variscan post-collisional new continental crust production in the FMC.

Two major inconsistencies exist between these results and the zircon record. First, zircon Hf model ages would point to substantial Mesoproterozoic crust formation in the FMC whereas more than 60% of the crust is actually Neoproterozoic in age. Second, new additions to the continental crust volume during the Variscan orogeny are not recorded even though 5 to 10% of the exposed crust formed at that time. The origin of both discrepancies inherently lies in the mixed isotopic signature carried by many zircon grains. Such equivocal information can only be detected when additional petrological constrains on the zircon host rocks are available and provide guidance in interpreting the zircon record of crust evolution.

Keywords: crust evolution, zircon U–Pb–Hf isotopes, Cadomian orogeny, Variscan orogeny, collisional magmatism, French Massif Central.

Acknowledgements

Here comes the time to write the acknowledgement section, trickier than I would have thought at first glance. Dare not forget anyone! If so, my apologies... This section will be full of french language interludes, depending on the person(s) considered.

I will start first with the members of the committee. Thanks for having accepted to evaluate this work and, for some of you, having travelled quite a distance for the defence.

Mes remerciements vont ensuite à Jean-François Moyen. Tellement de choses se sont passées depuis notre première rencontre un soir d'orage fin aout 2011 à la Part-Dieu (ce n'est pas l'accroche d'un film de série B, le lecteur pourra s'assurer de la véracité de ces faits auprès des intéressés). Six ans plus tard, je tiens à te remercier pour la grande liberté que tu m'as laissé dans l'accomplissement de mes travaux, ton soutien/confiance quand je me suis engagé dans tous ces (multiples) projets et pour avoir partagé ton expertise sur le magmatisme granitique. J'ai particulièrement apprécié toutes nos discussions de synthèse (à tendances agrégatives) sur la typologie des granites.

My sincere gratitude goes to Gary Stevens. Thanks for your patience and the time you spent sharing your knowledge on experimental and granite petrology. It was a great experience to interact with you on these topics and I have learnt a lot through this.

I also wish to express my gratitude to the Stellies group. Thanks Sara for having shared with me the experimental despair and scientific excitement that goes along with this peculiar activity (I did not find any alternative way of saying it). It was a pleasure to work with you at the lab and solve some thermodynamics. Andrew "Toodle-oo" thanks so much for having improved my understanding and wording of english so well! Telling kak with you was delighting, especially at lunch time or with a good craft at ... Craft. To the artists and computer scientists: thanks to Nora, Rentzia, Nicola, Pieter and Albert for all the everlasting discussions about life and so many topics (special thanks to the guys for having kindly accommodated me). Shawn merci beaucoup! for your kindness and good mood. Francesco the Italian Stallion is greatly acknowledged for having saved me while I was locked inside the geology building along with a potential fugitive. I very much enjoyed our chats they helped a lot to unwind! un grand merci à Cynthia pour tous les moments passés à Lombardi, Cassis, sur la N1 ("Turn around! Turn around!"), Dorp Street Deli ou sur le Rooiplein. Tu as grandement contribué à mon acclimatation sud-africaine et malgré tous les petits troubles au labo, on aura quand même bien rigolé. J'en profite pour remercier Sylvain pour nous avoir envoyé du rêve pendant 15 jours avec deux loustics que j'évoquerai un peu plus tard...(et pour avoir créé THE nickname le plus utilisé durant ma thèse). My thanks also go to the CAF and Geology managers, whose help and encouragements during my stays were greatly appreciated (Madelaine, Herschel, Angelique, Mareli, Rianna, George, Loxie, Jeanne). Dorothy is thanked for making the admin tasks so easy. Thanks to Thomas for being such a pleasant tennis challenger and for the fun we had at quizznight (this includes Valby). I must say a massive merci! to Matthew/Matt/Matiou for all the great moments we have spent together since january 2014 when we first met in Grahamstown. Thanks so much for having organized so many things while I was in South Africa: hiking, playing cricket with Ben (gasp...), snorkeling, quizznighting, listening to crazy bands (including at ParkOff), maintaining a scientific thrill with all the Rcrust and S-type discussions, having Whiskey parties at your parents' (thanks to them and Corbin for their kindness... but don't tell me kak!). It was basically

awesome! Finally, thanks for sharing your views on so many topics, it is really inspiring.

Un retour en France maintenant. Tout d'abord, un grand merci aux amis castrais (Flo, Sophie, Bobi)! Nos escapades plus ou moins lointaines (Sivens, Verdon, Réunion, etc...) m'ont à chaque fois fait le plus grand bien. Merci aussi de m'avoir fait (re)rencontrer des personnes vraiment sympas (qui se reconnaitront). Le temps est venu, ma foi, de châtier un temps soit peu mon language s'agissant d'aborder la situation dudit Docteur Arnaud J. You know how much I owe you buddy! Ainsi, je vous prie d'agréer, monsieur, l'expression de mes remerciements les plus sincères. Nos discussions, des plus raffinées, égayent mon quotidien depuis fort longtemps déjà, puissent le druide de Cubservies, le Marshall de Stellies et le mazout de la Salvetat en témoigner. J'en profite pour remercier Emelyne, Marie et Amaury pour ces agréables moments passés en sud-afriquie, à Paris ou dans la Montagne Noire (berceau de la civilisation)!

Au tour des Lyonnais d'y passer. Mes remerciements vont tout d'abord au Docteur Alexandre A. dont la justesse de raisonnement n'a que peu d'égal. Ce fut un plaisir d'échanger sur tant de sujets. J'ai aussi énormément appris et clarifié de concepts à travers nos discussion. Merci à toi. Un grand merci aussi à Jean-Loup qui, depuis 7 ans déjà, partage une grande variété de moments/pensées/émotions avec moi. Un petit mot pour la promo ENS 2010 (Hélène, Gaelle Number 4, Amo, Fatma et al.) que j'ai pu revoir au compte-gouttes pendant ces 3 ans. Merci au Docteur (lui aussi!) Paul Anto. from Ariège (je te mets dans les Lyonnais car je t'ai rencontré à cette époque) pour cette mémorable conférence à Florianopolis. On se sera vraiment bien marré! Mes remerciements vont également au Professeur Olivier "of the letter" et à Clara pour leur bonne humeur, leur accueil toujours chaleureux et nos longues discussions introspectives qui sont une source d'enrichissement personnel certain. Pour terminer l'étape lyonnaise, je tiens à remercier les locataires du R6 (Véro, Gwelt, Manu, Maxime, Arnaud, Ivan, David, Marianne, Hervé...) et de la prépa agreg pour leur accueil et leur patience. Récupérer un Simon qui sort de 5 mois d'écriture c'est pas de la tarte !

J'enchaine ainsi avec les Stéphaniens (bah oui fallait bien que je la fasse, Juan Miguel Moulin-style!). Je remercie en premier lieu toutes les personnes de la FST qui, par leur bonne humeur, professionalisme et bienveillance, ont rendu mon expérience au labo agréable. Pour citer quelques coupables je pense entre autres au duo Anne-Marie/Pascal, à Colette, Anne-Sab, Anne-Mag, Damien, Bertrand, Marie, Véronique, Peter, Adélie, Lucile et al. Parmi les étudiants qui se sont succédés merci à Pierre (PyPy) et Théo qui m'ont bien aidé sur le terrain et en magnétisme. Je vais faire des "special thanks" à Jérôme qui a partagé "l'expérience Chasseradès" avec moi. Merci pour ta patience sur le terrain, tes conseils et ta gentillesse. Special thanks aussi pour June qui a été d'un grand soutien pendant ces 3 ans. Merci pour tout mate!

Je fais un paragraphe pour les "historiques", ceux qui ont hanté le bureau des thésards (certains le canapé) pendant si longtemps. J'ai nommé Gaëlle ("On va manger"), Gautier et Boguie. Merci pour ces moments passés un peu partout (au bureau, sur le terrain, en conf, à Stellies). Merci au nouvel arrivant Antonin "Justinho" qui a pour notre plus grand bonheur élevé le niveau d'humour parmi nous! Et enfin le champion en titre, qui franchit tous les cols hors catégorie (y compris les voies blanches à bloc à brac), sans qui ces 3 ans de thèse n'auraient pas été ce qu'ils ont été, j'ai nommé l'illustre Dotorre Adrien Vezinete (prononcer vézinété). Je voulais faire une phrase stylée en mode "Si son fromage se rapporte à son plumage..." mais je n'ai pas réussi à la finir. Je resterais donc correct et me contenterais de te remercier sincèrement pour tous ces moments passés ensemble.

C'est le tour des papys flingueurs ! La génération 79-86 qui m'a accompagné durant ce périple que fût la thèse (et pour certains déjà bien avant). Merci à Arnaud Vill. "l'homme qui voit tout fondre plus vite que son ombre" pour ta bonne humeur, ton soutien quand des oiseaux de mauvaise augure tournaient autour de moi et pour toutes les discussions qu'on a pu avoir sur la complexité extrême de la nature. Merci à Cyril Che.-Mich. avec

qui on se sera bien éclaté à refaire le monde... Néoproterozoique! Merci à Luc-SD pour sa prise en charge sociale du Simon "en rédaction" (broyer du caillou y a que ça de vrai pour se détendre). On aura bien rigolé à Gambon et dans le Velay Han Solo! Les Special Thanks sont de retour pour Pierre lo bouiol (lieu-dit commune de Prévenchères). Merci pour tout ce que tu m'as appris, ta gentillesse et ton soutien/disponibilité lors de la rédaction. Ce fut un plaisir de travailler avec toi. Un autre Special pour Oscar LauLau. Tu as plus qu'intensément contribué à l'accomplissement de ce travail. Merci d'avoir ainsi partagé ton savoir et de m'avoir apporté ton soutien permanent et inconditionnel. Merci également pour ton accueil à Frankfurt/Zuerich et pour les discussions multiples (sérieuses comme imitatoires) qu'on a pu avoir ces 4 dernières années.

Looks like the French interlude was quite long. One last drop of English though for Vojtěch Janoušek, for his kindness and the tremendous job he and his colleagues have done with GCDkit, this way I shall say that he substantially contributed to the achievement of my PhD! Thank you.

Il est certains de mes professeurs qui, par leurs enseignements et conseils, m'ont particulièrement inspiré et, de fait, ont indirectement contribué à la réalisation de ce travail. Je voudrais ainsi sincèrement remercier mes enseignants de classe préparatoire Christine V., Olivier L. et Olivier A. ainsi que Hervé B. de l'ENS de Lyon.

Last but not least, merci à toute ma famille pour leur soutien ainsi qu'à Marine pour son infinie patience, son aide sur le terrain (notamment sa perception redoutable des linéations) et son soutien au quotidien durant la rédaction. Un grand Merci!

Contents

Chapter 1

Introduction

1.1 The continental crust

1.1.1 Structure and composition

By definition, the continental crust is the section of the continental lithosphere lying above the Moho seismic discontinuity and laterally bounded by the continental slope, at the transition zone with the low-lying oceanic crust (Davidson and Arculus, 2006; Rudnick and Gao, 2003). The continental crust has an average thickness of $\sim$ 35–40 km (Mooney et al., 1998) and multi-methods studies based on surface heat flow measurements, seismic profiles and large-scale geochemical surveys concluded that it has a bulk andesite/diorite composition (Christensen and Mooney, 1995; Gao et al., 1998; Holbrook et al., 1992; Rudnick and Fountain, 1995; Rudnick and Gao, 2003; Wedepohl, 1995). A similar conclusion was drawn by Taylor (1977) and Taylor and McLennan (1985; 1995) but these authors' estimates relied on a partisan mode of new crust formation and not uniquely on quantifiable geological observations.

Based on seismic data, the continental crust may be subdivided into three layers of contrasted P-wave velocities and chemical compositions (see Fig. 1.1): the upper and middle crusts (each corresponding to c. 30% of the bulk section, sometimes grouped together) are granodioritic while the lower crust (the remaining 40%) has a gabbroic composition (Christensen and Mooney, 1995; Gao et al., 1998; Rudnick and Fountain, 1995; Rudnick and Gao, 2003; Wedepohl, 1995). The boundary between these crustal domains is sometimes underlined by the so-called Conrad seismic discontinuity (Fig. 1.1). The upper crust typically features volcanic, plutonic and sedimentary lithologies which metamorphosed equivalents (up to the amphibolite-facies) are common in the middle crust. The lower crust is built up by granulite-facies meta-igneous (mostly gabbroic) and metasedimentary rocks (Rudnick and Gao, 2003). Coupled to its lithospheric mantle root, the silica-rich continental crust forms thick, buoyant and poorly subductable masses at the surface of the Earth.

1.1.2 From mantle to continental crust...

The continental crust has been extracted from the Earth mantle for more than 4 billion years (Bowring and Williams, 1999; Iizuka et al., 2006). Importantly, rocks of granodiorite compositions are not in equilibrium with the mantle, meaning that the upper and middle crusts must originate from the *differentiation* of a basaltic precursor (the most common magma type formed by mantle melting). Such process may occur through: (i) fractionation of primary basaltic magmas, (ii) melting of pre-existing mafic lithologies or/and (iii) weathering and erosion of similar rocks (Anderson, 1982; Rudnick and Fountain, 1995; Taylor and McLennan, 1995), even though the latter effect has proven less significant than magmatic processes (Hawkesworth and Kemp, 2006a). In this manuscript, the term *crustal differentiation*, generally taken as the whole set of phenomena that leads

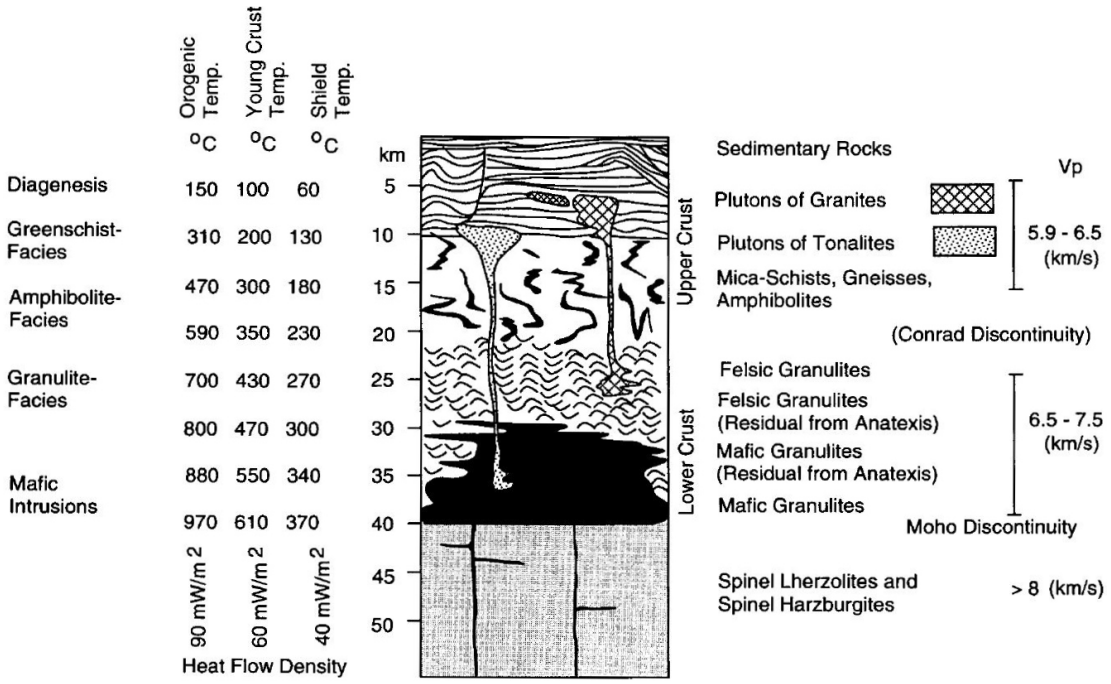

Figure 1.1: Sketch column diagram showing the structure, composition and seismic properties of standard continental crust. Temperatures prevailing at different crustal levels are those calculated by Chapman (1986). The "Upper Crust" gathers both the upper and middle crusts described in text. Figure from Wedepohl (1995).

to a stratified crust section, is strictly used in a crust evolution perspective and will refer to the conversion of basaltic precursors into upper/middle crustal intermediate/felsic lithologies via the above-mentioned processes.

Clearly, the *basaltic* flux from the mantle contrasts with the bulk crust *andesite* composition and entails that formation of new crust necessarily requires a mafic component to return back to the mantle, most probably via the foundering of dense cumulates and/or residues left after upper/middle crust extraction (Arndt and Goldstein, 1989; Davidson and Arculus, 2006; Kay and Mahlburg-Kay, 1991; Rudnick, 1995; Rudnick and Gao, 2003; Taylor, 1977; Taylor and McLennan, 1985; Zandt et al., 2004). This would also account for the fact that the lower crust composition is not complementary to that of the upper/middle crust (Hawkesworth and Kemp, 2006a).

1.1.3 ...in a one- or two-stage process?

Production of new continental crust necessitates: (i) addition of mantle-derived magmas to a pre-existing crustal volume; (ii) differentiation of the basaltic precursor; (iii) foundering of mafic residual materials in the mantle. These successive steps may occur concurrently or be temporally decoupled leading to two contrasted views on how new crust is formed.

A first model taken as "one-stage" or "island-arc" argues that accretionary orogens (in the sense of Scholl and Von Huene, 2009) are the main locus of new crust production, at least in Phanerozoic times (Arculus, 1999; Hawkesworth and Kemp, 2006a; Vogel et al., 2004). There, melting of the mantle wedge supplies large volumes of basaltic magma which evolve by fractional crystallization (and possible assimilation) in the arc crust towards granodiorite compositions meanwhile the mafic dense cumulates are delaminated in the mantle (see Kelemen et al., 2003, and references therein). In other words, new, differentiated crust forms in a short time span, in a single geodynamic setting. This model is supported by the fact that some trace element ratios displayed the bulk continental crust markedly resemble that of island arc basalts (IAB, see Arculus, 1999). Besides, estimates of the magma volumes erupted in different settings indicate that convergent

margins host the largest input of mantle-derived magmas, thus most likely to generate substantial amounts of new crust.

Alternatively, a "two-stage" model postulates that the processes at stake in the generation of new continental crust do not operate synchronously (at geological time scale). A first mantle melting event would supply basaltic magmas to the continental crust (Downes, 1993) or a transient reservoir such as oceanic plateaux (Albarede, 1998) and the MOR oceanic crust (Niu et al., 2013). After a period of geological quiescence, changes in the magmatic/tectonic regime e.g. continent–continent collision or oceanic plateau accretion would provoke melting and associated differentiation of the basaltic precursor (Niu et al., 2013), forming new continental crust. Delamination of dense mafic residua would take place synchronously (Arndt and Goldstein, 1989). This way, the model temporally separates the mantle extraction stage from the differentiation stage (melting plus foundering of the most mafic components).

1.1.4 Crust recycling, growth and reworking

The inherent dynamics of subduction zones promote the foundering of upper-crustal, intermediate to acid lithologies in the mantle by sediment subduction and subduction erosion (Clift, 2004; Stern, 2011; Von Huene and Lallemand, 1990). Such phenomenon clearly destroys continental crust materials and is referred to as *crust recycling*. The latter do not encompass the loss in the mantle of mafic cumulates/residues left after crustal differentiation, independently necessary to account for the bulk crust composition.

The extent of crust recycling would be as high that the net gain to the crust volume (the difference between crust formation and destruction) would currently be null (Clift et al., 2009; Scholl and Von Huene, 2009; Stern and Scholl, 2010). In the following, *crustal growth* will be regarded as the positive imbalance between new crust production and crust destruction, after subtraction of the baseline mafic cumulates/residues foundering.

Lastly, *crust reworking* is taken as the magmatic processes that re-shape pre-existing, differentiated crustal lithologies, i.e. sediments and intermediate/felsic igneous rocks. Reworking does not participate to crust differentiation from a crust evolution perspective (see previous section). Nevertheless, the upwards transport of crust-derived magmas certainly reinforces the continental crust chemical layering and contributes to its stabilisation by concentrating the incompatible, heat-producing elements in its uppermost part (Michaut and Jaupart, 2007). Weathering and sedimentation are not included in this definition of crust reworking because erosion of basaltic rocks do participate to the differentiation of the crust.

How to track crustal growth If the continental crust is not currently growing, the present-day 7.2×10^9 km^3 of crustal materials provide unambiguous evidence for past crustal growth. Challenging questions are: when was the continental crust extracted from the mantle and at which pace? Was crustal growth a continuous or discrete process? Addressing them converts into estimating the crustal residence time of each fragment of the present-day crust, i.e. when was it first incorporated to the crustal volume, before being potentially reworked during subsequent geological events? If the very first seed of newborn crust is a mantle-derived basaltic magma, new additions to the continental crust are best pinpointed by the crystallization of intermediate to acid magmatic rocks originating from such basaltic precursors (Hawkesworth and Kemp, 2006a;b), i.e. by the crust differentiation stage. On these grounds, recent advances on the topic of crustal growth benefited from the study of zircon $ZrSiO_4$, primarily encountered as an accessory mineral of intermediate to acid igneous rocks (Hoskin et al., 2000). Such advances are summarized in the next section.

1.2 The zircon record of crust evolution

The reader can found detailed discussions on this topic in the excellent reviews of Hawkesworth et al. (2010); Cawood et al. (2013) and Roberts and Spencer (2014).

1.2.1 Zircon U–Pb–Hf–O isotope compositions

U–Pb geochronology

When zircon crystallizes, it incorporates U but virtually no Pb and thus can be dated via the U–Pb geochronometer. This mineral is extremely resilient to weathering, erosion, transport, and high-grade metamorphism (see discussion in Mezger and Krogstad, 1997) so that it preserves the record of the earliest events on Earth (Amelin et al., 1999). In the past 20 years, the improvement of laser ablation techniques enabled to routinely date *in situ* portions of zircon crystals (Jackson et al., 2004; Hirata and Nesbitt, 1995). Such strong spatial control coupled to high quality cathodoluminescence imaging of the grain interiors allows to unravel complex zircon crystallization histories (e.g. Vavra et al., 1999).

Hf–O isotopes

Zircon accommodates noticeable amounts of Hf in its lattice (up to the %) but few Lu (Fujimaki, 1986), such that *in situ* measurements of the Yb–Lu–Hf isotope compositions allows to retrieve the zircon $^{176}Hf/^{177}Hf$ ratio which is close to that of the melt/fluid from which the zircon crystallized (Fisher et al., 2014; Griffin et al., 2002; Hawkesworth and Kemp, 2006a; Woodhead et al., 2004). As Lu/Hf ratios are fractionated during mantle melting (Lu is more compatible than Hf), extracted crustal materials and mantle residues develop contrasted time-integrated Hf isotope signatures (reported as ε_{Hf} normalized to the CHUR, Bouvier et al., 2008; Patchett et al., 1981) with the crust becoming less radiogenic and the mantle more radiogenic than the CHUR. This way, the $^{176}Hf/^{177}Hf$ ratio of a magmatic zircon grain recalculated at the time its crystallization is a first-order indicator of the crust- vs. mantle-origin of the local magma batch surrounding the newly formed mineral (Fig. 1.2).

Furthermore, the zircon oxygen isotope composition, notably the $^{18}O/^{16}O$ (expressed as $\delta^{18}O$ normalized to the SMOW, see Valley, 2003) can also be measured by laser fluorination or ion microprobe and allows to retrieve the $\delta^{18}O$ of the host magma (King et al., 1998; Valley, 2003; Valley et al., 2005). The mantle is fairly homogeneous in terms of O isotopes (Eiler, 2001) and shows a value of $+5.3 \pm 0.6$ (2σ, Valley et al., 1998). Materials that experienced low-T supra-crustal weathering show higher $\delta^{18}O$ than the mantle while interaction with high-T fluids yields lower $\delta^{18}O$ (see Fig. 1.3).

A window onto the source of granitic magmas

Altogether, zircon Hf(–O) isotope compositions yielded new constraints on the petrogenesis of intermediate to acid igneous rocks, pinpointing the respective contributions of the crust and the mantle in the evolution of several magma types (Appleby et al., 2009; Belousova et al., 2006; Goodge and Vervoort, 2006; Griffin et al., 2002; Hawkesworth and Kemp, 2006a; Kemp et al., 2005; 2007; Murgulov et al., 2007; Pietranik et al., 2013). These studies interpreted the spread of $^{176}Hf/^{177}Hf$ ratios displayed by magmatic zircons at the time of crystallization as reflecting the mixing, at source or during emplacement, between crust- and mantle-derived materials, even though such views have been challenged (e.g. Farina et al., 2014; Villaros et al., 2012).

From there emerged the idea that zircon grains preserve the best record of the origins of magmatic rocks as they allow to track processes otherwise undepictable by "traditional" whole-rock geochemical studies. On these grounds, many workers attempted to

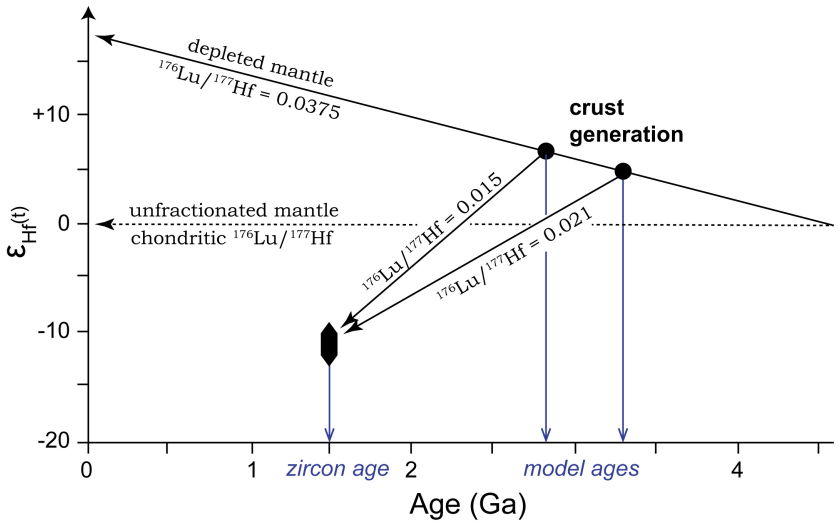

Figure 1.2: Zircon Hf isotope systematics and calculation of "depleted mantle model ages" for a zircon grain crystallized at 1.5 Ga. Several values are used for the $^{176}Lu/^{177}Hf$ ratio of the host material. A $^{176}Lu/^{177}Hf$ of 0.021 is rather typical of a mafic igneous rock and 0.015 of upper crustal lithologies. Inspired from Roberts and Spencer (2014).

decipher the evolution of the continental crust by considering the Hf(–O) systematics of detrital and magmatic zircon grains out of their rock matrix (Belousova et al., 2009; 2010; Condie et al., 2005; 2011; Dhuime et al., 2012; Hawkesworth and Kemp, 2006; Iizuka et al., 2010; Kemp et al., 2006; 2015; Kirkland et al., 2013; Naeraa et al., 2012; Pietranik et al., 2008; Roberts, 2012; Spencer et al., 2013; Wang et al., 2011; Zeh and Gerdes, 2010; Zeh et al., 2014). The methodology and main results are summarized hereafter.

1.2.2 Timing of crustal growth from zircon U–Pb–Hf(–O) data

The present-day age distribution of crustal materials at the surface of the Earth (Fig. 1.4) reflects the time-integrated end-product of the crustal growth process. That being said, part of the today-exposed continental crust is built up from materials that have been reworked, i.e. their geological age does not reflect that of extraction from the mantle. This is the case for (meta-)sediments, which encompass crustal materials formed before erosion and deposition, and also for crust-derived granitoids that typically re-shape pre-existing crustal lithologies.

U–Pb age distributions

The original idea behind this approach is that zircon being mostly encountered in intermediate to felsic igneous rocks (Hoskin et al., 2000), the distribution of crystallization ages would record periods of marked crustal differentiation and new additions to the continental crust volume. Many workers built up databases of U–Pb crystallizations ages for zircon grains extracted from both today-exposed magmatic rocks and detrital (meta-)sediments in an attempt to be as representative as possible of the Earth geological record. Detrital zircons are regarded as repositories of the pre-erosive magmatic history of the detritus they are hosted by.

Rino et al. (2004) proposed to filter the signal of crust recycling out by: (i) discarding metamorphic zircon grains and, (ii) only focusing on the core of grains showing evidence for multiple crystallization events. The age retrieved from the core is taken as representative of that of the genuine crustal material before reworking. A first-order criterion to discriminate between metamorphic and magmatic zircon grains is given by the zircon Th/U ratios measured concomitantly on the same U–Pb spot (Rubatto et al.,

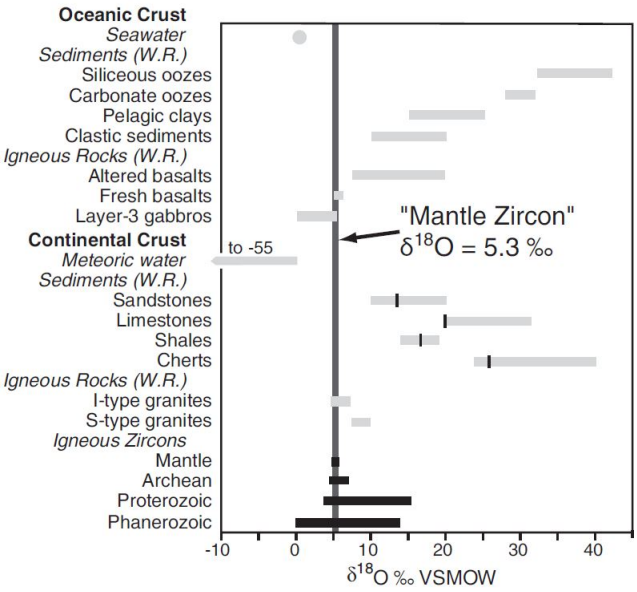

Figure 1.3: Ranges of $\delta^{18}O$ observed in different crustal and mantle reservoirs. Figure from Roberts and Spencer (2014).

2001; Rubatto, 2002).

The resulting distribution shows marked peaks at *c.* 0.3, 0.6, 1.0, 1.9 and 2.7 Ga (Rino et al., 2004) and converts into a step-like crustal growth curve with periods of significant and short-lived additions to the crustal volume (Fig. 1.4). Importantly, statistical analyses of the U–Pb databases of Condie and Aster (2010) and Voice et al. (2011) yielded identical results than Rino et al. (2004)'s, even though the formers did not apply any filter to minimize the impact of crust reworking ages. It comes from this that either Rino et al. (2004)'s procedure is inefficient or crust recycling is a second-order feature within zircon U–Pb age databases. The latter possibility has not been fully investigated but petrological evidence for voluminous silica-rich magmas originating from melting of pre-existing, differentiated crustal lithologies (typically intermediate to acid igneous and metasedimentary protoliths, e.g. Chappell and White, 1974; 2001) strongly suggests that a substantial proportion of the U–Pb dates attests to crust reworking and not new crust formation.

An alternative approach consisted in focusing only on grains extracted from today-exposed igneous rocks as conclusions on the magma origin could be drawn from whole-rock major, trace element and Sr–Nd-Hf isotope data. This way, Condie (1998) and Condie and Aster (2010) showed that the age distributions of (putatively) mantle-derived granitoids does feature the same peaks observed by Rino et al. (2004). Yet, limitations of such method are of two types: (i) there is still an ongoing debate around the source of some magma types (see for instance the case of I-type granites, Clemens et al., 2011 and references therein); (ii) sampling of igneous rocks is in essence biased (Condie and Aster, 2010) and the contribution of rocks which have been eroded and their detritus mixed in sedimentary basins cannot be accounted for, even though such detritus still takes part of the continental crust.

Following the puzzling results of U–Pb database analyses, several studies relied on another potential indicator of the genuine signal of new crust formation: the Hf model ages.

Hf model ages

The $^{176}Hf/^{177}Hf(t)$ ratio of each zircon grain can be converted into a crustal residence "model" age corresponding to the time at which the crustal source of the zircon-hosting

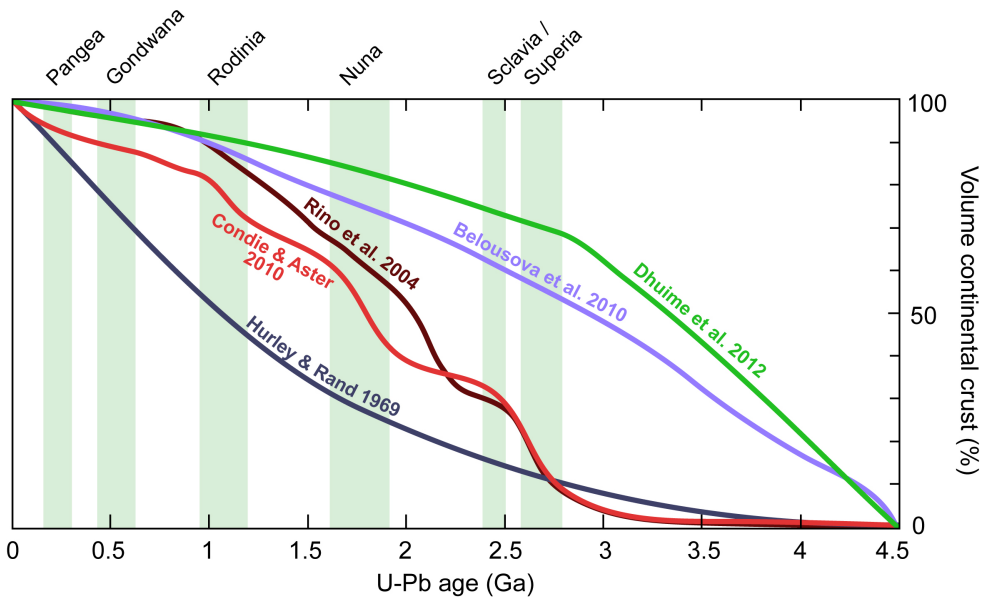

Figure 1.4: Selected crustal growth curves obtained by step-wise integration of the volume of new crust formed and preserved at each time period. Curves based on zircon U–Pb data from Rino et al. (2004) and Condie and Aster (2010), on Hf model ages from Belousova et al. (2010) and Dhuime et al. (2012), on the age of present-day continental areas from Hurley and Rand (1969). Are also depicted the main periods of supercontinent amalgamation (from Campbell and Allen, 2008). Figure inspired from Roberts and Spencer (2014).

magma would have been extracted from the mantle. Such calculations assume that a precursor crustal material was formed at time T with a given $^{176}Lu/^{177}Hf$ ratio. Radioactive decay led to a time-dependent increase of its bulk $^{176}Hf/^{177}Hf$. Reworking of the precursor material at time t produced silica-rich melts that crystallized zircon, encapsulating its $^{176}Hf/^{177}Hf(t)$. Provided an assumption on the value of the precursor $^{176}Lu/^{177}Hf$ ratio, it becomes possible to retrieve the time T at which the precursor and a reference mantle were at isotopic equilibrium, thus bracketing the timing of new crust formation (Fig. 1.2). The reference mantle most often considered is the Depleted Mantle, for which a range of compositions have been described (Griffin et al., 2000; Naeraa et al., 2012). Resulting model ages are accordingly termed "depleted mantle model ages" (T_{DM}).

However, petrogenetic studies conducted on several granite types and mentioned above revealed that the zircon Hf–O systematics may record the sampling of reservoirs with contrasted isotope compositions. When this is the case, the Hf model age retrieved from each zircon grain is arguably of mixed origin and thus meaningless from a crust evolution perspective (Arndt and Goldstein, 1987). Besides, mixing trends cannot be identified when looking at detrital zircon populations. Consequently, Hawkesworth and Kemp (2006a) and Kemp et al. (2006) suggested to use the $\delta^{18}O$ of the zircon domain analysed for U–Pb–Hf isotopes as a tool to identify the presence of mixed components in the magma from which the grain crystallized. This way, excluding analyses with $\delta^{18}O$ >6.5, presumably reflecting the reworking of supra-crustal sedimentary materials in the magma, retrieved model ages would selectively indicate the time at which new crust was formed and hitherto preserved, thus contributing to crustal growth.

Many studies interrogated the ever-growing zircon U–Pb–Hf(–O) isotope databases and observed that the distributions of Hf model ages (with or without screening out high $\delta^{18}O$ grains) differ from that of U–Pb crystallization ages (Belousova et al., 2010; Dhuime et al., 2012; 2017; Hawkesworth and Kemp, 2006; Iizuka et al., 2010; Kemp et al., 2006; Wang et al., 2011). Clearly, crustal growth curves derived from Hf model ages rather point to a continuous increase of the crust volume with a potential inflexion at 3 Ga expressing a slowdown in the rate of crustal growth (Fig. 1.4).

ε_{Hf}-time relationships

An alternative approach to decipher the timing and mechanisms of crust evolution consists in estimating the age and evolutionary path of a given crust segment. The associated methodology relies on the regional temporal evolution of the ε_{Hf}(t) displayed by detrital and/or magmatic zircon grains from a set of crustal lithologies. For instance, episodic oscillations of the ε_{Hf}(t) has been linked to variations of the mantle-derived magma supply and new crust production, in line with the regional geodynamic evolution (Boekhout et al., 2015; Kemp et al., 2009). A similar interpretation has been proposed at the global scale by Roberts (2012).

Besides, identification ε_{Hf}-time arrays is regarded as reflecting inner-crustal reworking processes, the age of the original crustal precursor corresponding to the array intercept with the evolutionary trend of the Depleted Mantle reservoir (Block et al., 2016; Eglinger et al., 2017; Kemp et al., 2009; Marschall et al., 2010; Petersson et al., 2015; Zeh et al., 2011). Furthermore, a spread in ε_{Hf}(t) at a given age between the evolutionary trends of two crustal reservoirs is taken as: (i) evidence for mixing between both end-members (Linnemann et al., 2014; Orejana et al., 2015; Petersson et al., 2016; 2017); or, (ii) a genuine record of continuous crust production with reworking at the given time t and preservation of the original model age range (Lancaster et al., 2011).

1.2.3 Enhanced crust production or preservation bias

In the following, a controversial aspect of the zircon U–Pb–H(–O) record of crust evolution is addressed through the prism of the Ying–Yang conceptualization developed by Stern and Scholl (2010), i.e. net crustal growth occurs when there is a positive imbalance between new crust formation and crust destruction.

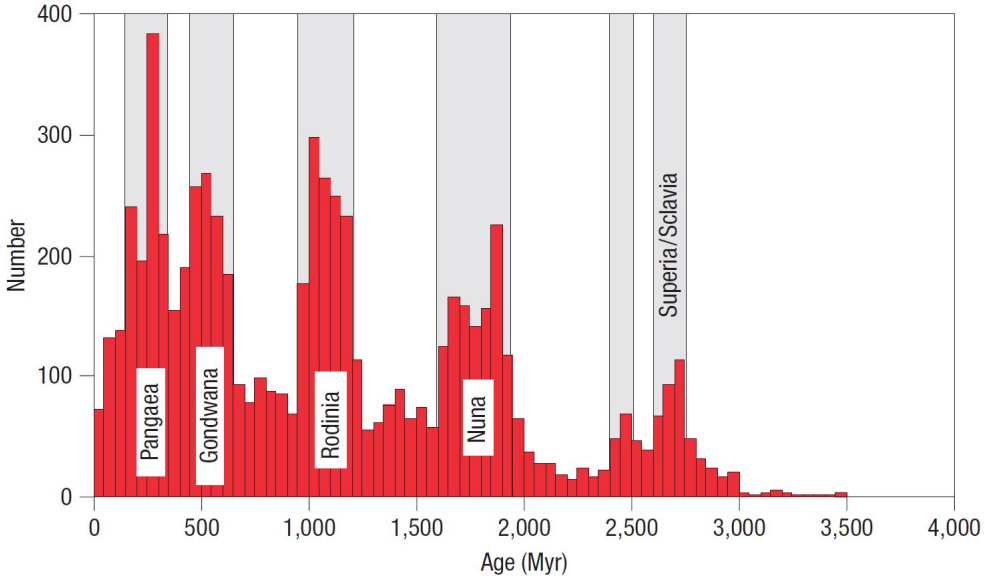

Figure 1.5: Supercontinent ages compared to the distribution of U–Pb ages of *c.* 8,000 concordant detrital zircon grains from 40 majors rivers, Australian dunes and Antarctic Paleozoic sediments. Figure from Campbell and Allen (2008).

A first range of models consider that U–Pb age peaks reflect periods of enhanced crust production to such an extent that it substantially outweighed crustal losses (Condie, 1998; 2004; Iizuka et al., 2010; Rino et al., 2004). This view is supported by the coeval peak of mantle-derived magma additions (Condie, 1998; Condie and Aster, 2010). As a matter of fact, such periods of juvenile magmatic flare-ups would match those of supercontinent amalgamation (Campbell and Allen, 2008), suggesting causality (Fig. 1.5).

At the other side of the spectrum, several studies consider that there was no substantial burst of crust production during supercontinent assembly (Condie and Aster,

2010; Condie et al., 2011; Condie, 2014; Hawkesworth et al., 2009; Lancaster et al., 2011; Spencer et al., 2015). These workers advocate that the age peaks rather reflect the high preservation potential of igneous rocks formed during continent collision episodes and would thus be of little significance in unravelling the timing of crustal growth. This viewpoint relies on the examination of the relative magma productivity and preservation potential of materials formed at each step of the supercontinent cycle (e.g. Hawkesworth et al., 2009). From this, magmatic rocks generated at the end of the subduction stage and during the main collision would be best preserved due to their location in the core of newly formed continental masses (Hawkesworth et al., 2010).

Such conclusion has been challenged by Stern and Scholl (2010) who argued that collisional episodes result in a marked loss of the continental crust volume, incompatible with an over-representation of collisional events in the geological record. In support to this interpretation would be the systematic negative excursion of the average ε_{Hf}(t) during periods of super-continent assembly (Gardiner et al., 2016; Roberts, 2012; Voice et al., 2011).

The discussion on the relative balance between crust production and its recycling back to the mantle throughout Earth history is extremely challenging to conduct, both at the regional and global scale for several reasons summarized below.

1.2.4 Some complications

The detrital zircon age distribution is often taken as representative of the timing of intermediate to acid magmatism, arguably related to crust production and differentiation. Yet, eroded igneous rocks do not contribute evenly to the detrital record as they do not have the same amount of zircon to deliver (Dickinson, 2008; Moecher and Samson, 2006) clearly introducing a bias in the detrital record. Besides, results retrieved from the model age approach are severely conditioned by (see discussion in Payne et al., 2016; Roberts and Spencer, 2014): (i) the $^{176}Lu/^{177}Hf$ ratio considered for the zircon crustal host; (ii) the reference model mantle composition retained; (iii) the premise that zircon Hf(–O) isotope composition considered alone is a good repository of the petrogenesis of its host magma (Fig. 1.6, see also Nebel et al., 2011; Roberts et al., 2013). The effect of such uncertainties are very difficult to monitor at the global scale even though Dhuime et al. (2017) recently advocated that the two former are negligible.

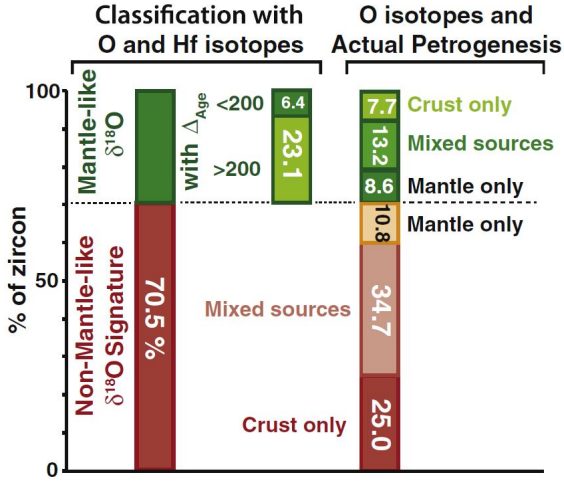

Figure 1.6: Illustration of one caveat of the zircon Hf–O approach. Compilation of 2586 magmatic rocks for which both zircon Hf–O isotopes and a petrogenetic model are available. Taken out of their context, zircon Hf–O isotopes fail to unravel the mantle vs. crust (or mixed) origin of the magma from which the zircon crystallized. Figure from Payne et al. (2016).

1.3 Rationale

As demonstrated in the previous section, unravelling regional to global crust evolution from zircon U–Pb–Hf–O isotope compositions is a promising approach. Yet, its design is quite recent as most studies have been conducted in the past 10 years. Consequently, some aspects of the methodology still require evaluation (see section 1.2.4). As a matter of fact, the approach has proven most efficient and the uncertainties best accounted for when additional petrological constraints were available on the zircon host rocks (Block et al., 2016; Eglinger et al., 2017; Kemp et al., 2009; Laurent and Zeh, 2015; Nebel et al., 2011; Roberts et al., 2013; Zeh et al., 2007).

The work presented in this manuscript focuses on a c. 30,000 km^2 area located in the eastern part of the Massif Central (France), one of the largest exposure of the Variscan belt in Europe. A critical feature of this geological region is that it would have been sequentially shaped by both the Neoproterozoic *Cadomian* accretionary and the Paleozoic *Variscan* collisional orogenies thus offering the opportunity to investigate the relative extent of crust production/reworking in both geodynamic settings.

A new set of zircon U–Pb (N=2,715), Hf (N=347) and O (N=131) isotope compositions in close conjunction with geochemical, structural and monazite geochronological data from regional magmatic et metamorphic lithologies is used to: (i) reconstruct the history and evolution of this crust segment; (ii) address the nature and potential flaws of the zircon record of crust evolution.

1.4 Geological background

1.4.1 The Variscan belt of Western Europe

General overview

The Variscan belt of Western Europe is part of the Paleozoic Peri-Atlantic collisional orogenic system extending over 5000 km from the Ouachitas in the USA to the Caucasus (Matte, 1986a;b; 1991). It developed as a result of the convergence between Gondwana and Laurentia–Baltica (Franke, 1989; 2000; Kroner and Romer, 2013; Matte, 1986a) leading to the assembly of Pangea, the latest supercontinent on Earth (Rogers and Santosh, 2003).

N–S shortening would have been accommodated by the closure of at least two oceanic domains (Fig. 1.7) (i) the Galicia–Massif Central, between Gondwana and the microcontinent Armorica; and (ii) the Rheic ocean, between Armorica and Avalonia, another continental ribbon docked to the Laurentia–Baltica landmass during the Caledonian orogeny (Franke, 2000; Matte, 1991; 2001; Rey et al., 1997). Diachronic and assymetric subductions (towards the North for the GMC, South for the Rheic, see Fig. 1.7) resulted in the Variscan belt showing a "fan-like" shape (Fig. 1.8) with north-verging and south-verging thrusts on each side of the sandwiched Armorica block (Matte, 2001). Large and coeval lateral displacements are also evidenced by crustal-scale strike-slip dextral shear zones (Arthaud and Matte, 1975; 1977; Kroner and Romer, 2013).

Since the 70's, the Variscan belt has been recognized as an ancient analogue of the Himalayan orogen (Burg, 1983; Dewey and Burke, 1973; Girardeau, 1986; Mattauer et al., 1988; Matte et al., 1990; Ménard and Molnar, 1988) with the Variscan high-grade rocks being regarded as the eroded roots of an orogenic plateau, a structure not accessible for sampling in Tibet where it can only be probed through geophysical methods. This way, our knowledge on mountain belt dynamics clearly benefited from the inter-comparisons between both orogens (see Maierová et al., 2016 and references therein).

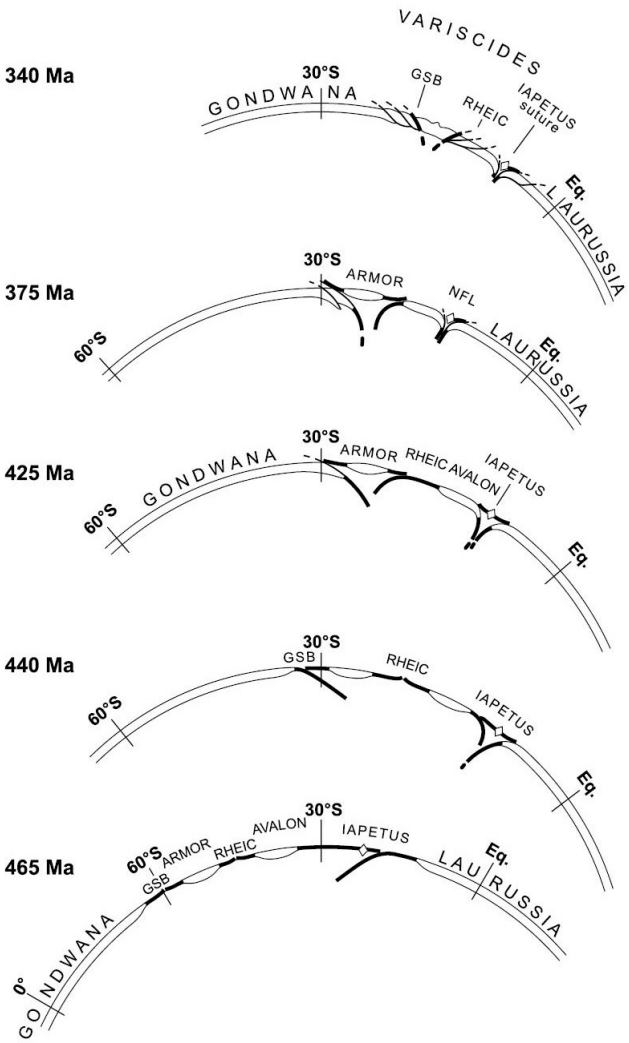

Figure 1.7: Simplified plate tectonic sketch showing the absolute motions of continental and oceanic plates (only the crustal parts are displayed) from the Ordovician to the Carboniferous. The closure of the Iapetus ocean ended up in the Caledonian orogeny, that of the Rheic and Galicia–Massif Central in the Variscan orogeny ("Variscides"). Abbreviations: ARMOR, Armorica; AVALON, Avalonia; NFL, Newfoundland; GSB, Galicia–Massif Central ocean. Figure from Matte (2001).

Main subdivisions and terrain affiliations

Figure 1.9 depicts the inferred crustal origin of the blocks involved in the Variscan orogeny. Terrains exposed in the northern domain of the belt belonged to the Avalonia micro-continent (Henderson et al., 2016; Linnemann et al., 2012). Sandwiched between the Galicia–Massif Central and Rheic suture zones lies the Armorica micro-continent. Both crustal blocks were originally part of the northern margin of Gondwana, from which they presumably got rifted apart in the Cambrian–Ordovician (Ballèvre et al., 2012; Nance and Murphy, 1994; Nance et al., 2010) forming the so-called peri-Gondwana terranes. The southern domain is ascribed to be derived from the Gondwana mainland or other smaller peri-Gondwana terranes (Ballèvre et al., 2014). Importantly, as the constituents of the Variscan belt belonged to the northern margin of Gondwana, they would have been affected, at varied extent, by the *Cadomian* accretionary orogen (see Garfunkel, 2015 and references therein).

Within the crustal blocks, regional "zones" have been delineated based on both metamorphic grade and location with respect to the sutures (Franke, 1989). For instance, the Moldanubian Zone of the Gondwana crustal block is regarded as an allochtonous unit as it features ophiolites and high-pressure metamorphic rocks (see Lardeaux et al., 2014

and references therein).

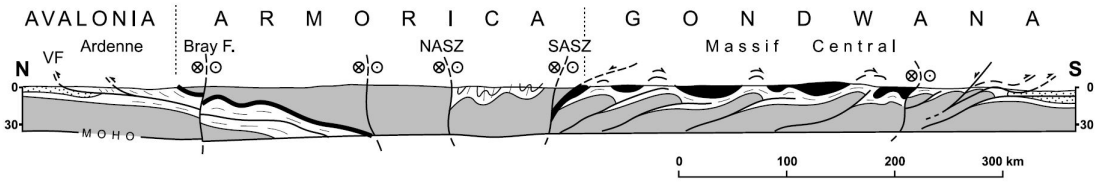

Figure 1.8: Simplified cross-sections at crustal scale through the Variscan belt in France, without granites. Grey, pre-Paleozoic (essentially Upper Proterozoic) low-grade basement; white, Lower Paleozoic sediments; black, ophiolitic nappes and sutures; dots, Carboniferous foredeeps; Bray SZ, NASZ and SASZ: Bray, North Armorican and South Armorican dextral shear zones; VF, Variscan Front. Figure and legend from Matte (2001).

The Armorica dispute

It must be stressed that many debates still surround the number of micro-continents and associated suture zones together with their respective locations (Ballèvre et al., 2009; 2014; Faryad et al., 2013; Faryad and Kachlík, 2013; Lardeaux et al., 2014; Linnemann et al., 2004; Martínez Catalán et al., 2007; 2009; Schulmann et al., 2014; Sláma and Žák, 2017). One of the most elusive aspect of the paleogeography and geodynamic evolution of the Variscan belt lies in the existence/absence of true Galicia–Massif Central oceanic domains (with a c. 4000 m deep oceanic floor). Indeed, palaeoclimatic and paleobiogeographical data argue against the existence of a wide oceanic domain and rather support a close connection between Armorica and Gondwana (Paris and Robardet, 1990; Robardet, 2003). Similarly, examination of the detrital zircon record of Cambrian to Devonian sediments indicate that the same sources were available throughout this period, inconsistent with opening of a true oceanic domain (Linnemann et al., 2004; Sláma and Žák, 2017). Even though recent models for the evolution of the belt (e.g. Kroner and Romer, 2013) consider Armorica as the attenuated Gondwana continental margin (referred to as "Armorican Spur" therein), there is still no consensus on this topic.

1.4.2 The French Massif Central

The study area is part of the French Massif Central which best exposes the Moldanubian Zone of the Variscan belt, i.e. a crustal domain where both allochtonous and (para)authochonous units have been described. The first historical map emphasizing the existence of metamorphic nappes is depicted Fig. 1.10 along with the regional names attributed to each geological region (Ledru et al., 1989). The main contours of this map remain valid almost 30 yrs after, for updated versions, the reader is referred to Chantraine et al. (1996) and Faure et al. (2009).

The nappe stack

The French Massif Central displays a dominantly south-verging stack of metamorphic nappes built up from the early Devonian to the early Carboniferous (Faure et al., 2009; Ledru et al., 1989) and composed of (see Fig. 1.10 for the regional denominations, Fig. 1.11 and Fig. 1.12):

- amphibolite- to greenschist-facies upper allochthonous units (UAU), e.g. the Thiviers-Payzac, Leyme, Gartempe, Génis, Brévenne formations (Leloix et al., 1999; Duguet et al., 2007);
- the Upper Gneiss Unit (UGU) which comprises amphibolite- to granulite-facies ortho- and paragneisses (Dufour, 1985; Forestier, 1961; 1969; Gardien et al., 1990;

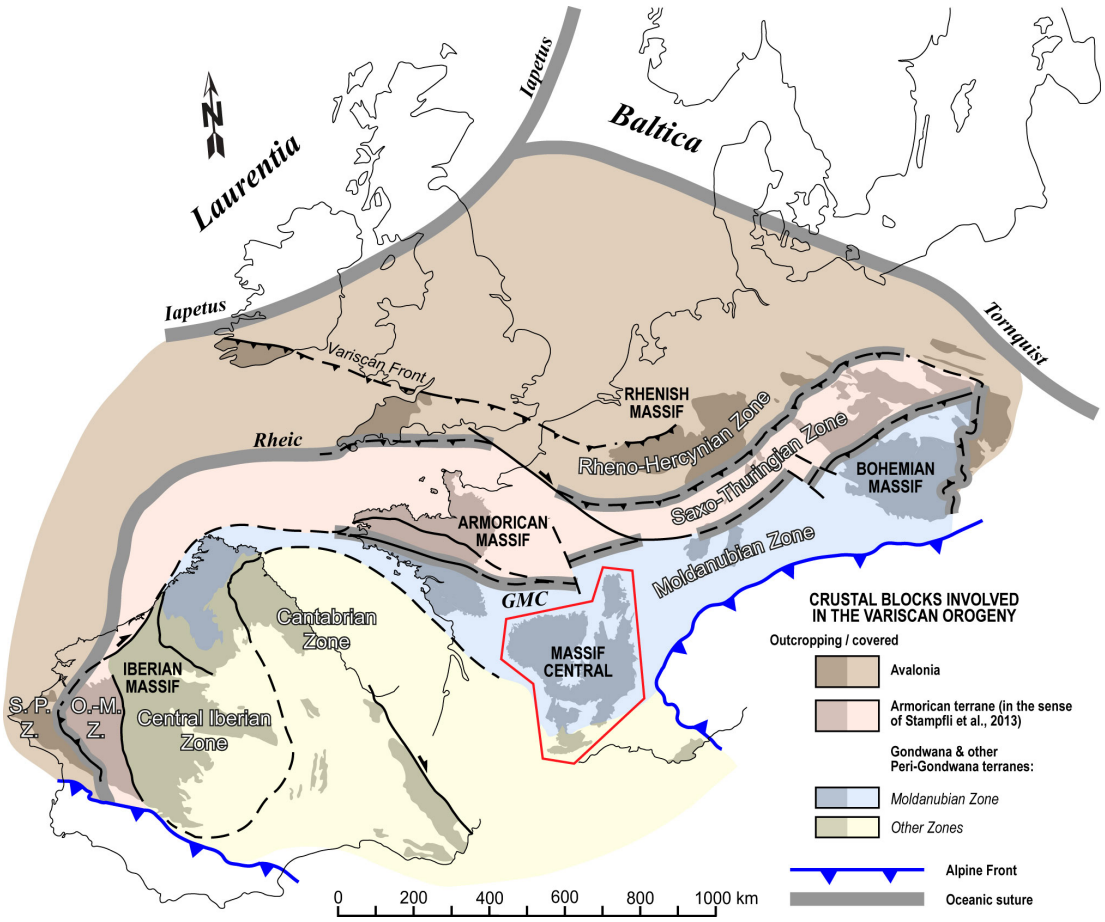

Figure 1.9: Simplified map of the Variscan belt of Europe, are depicted the main lithotectonic subdivisions (after Franke, 1989), the location of suture zones and origin of the crustal blocks (after Ballèvre et al., 2014 and Henderson et al., 2016). Abbreviations: O.-M.Z.: Ossa-Morena Zone; S.P.Z.: South-Portuguese Zone; GMC: Galicia–Massif Central suture. Adapted from Ballèvre et al. (2014).

Lardeaux et al., 1989; 2001; Schulz, 2014) and typically shows at its base a bimodal meta-igneous association referred to as *Leptynite-Amphibolite Complex* or LAC (Briand et al., 1995; Downes et al., 1989; Forestier, 1961; Giraud et al., 1984; Santallier et al., 1988) that contains relicts of eclogite-facies metamorphism (Bellot and Roig, 2007; Berger et al., 2010a;b; Bouchardon, 1987; 1989; Delor et al., 1986; 1987; Gardien and Lardeaux, 1991; Gardien, 1993; Godard, 1990; Lardeaux et al., 2001; Lasnier, 1968; Mercier et al., 1989);

- the Lower Gneiss Unit (LGU), an assemblage of amphibolite-facies micaschists, ortho- and paragneisses together with scarce amphibolites (Briand et al., 1992; Ledru et al., 2001);
- the lower-grade Parautochthonous Unit (PAU) made up largely of greenschist- to amphibolite-facies metasediments, e.g. the Cévennes schists and the Montagne Noire northern flank (Burg et al., 1989; Duguet and Faure, 2004; Rakib, 1996);
- a Fold-and-Thrust Belt of very low metamorphic grade, e.g. the Montagne Noire southern flank and the Vigan schists (Alabouvette et al., 1988; Doublier et al., 2006; 2015; Guérangé-Lozes and Burg, 1990; Wiederer et al., 2002)

The relationships between each unit may differ from a domain to another (Fig. 1.12).

Tectonic–metamorphic–magmatic evolution

The evolution of the FMC has been deciphered through the examination of the tectonic relationships between the different nappes and their P–T conditions attained at peak

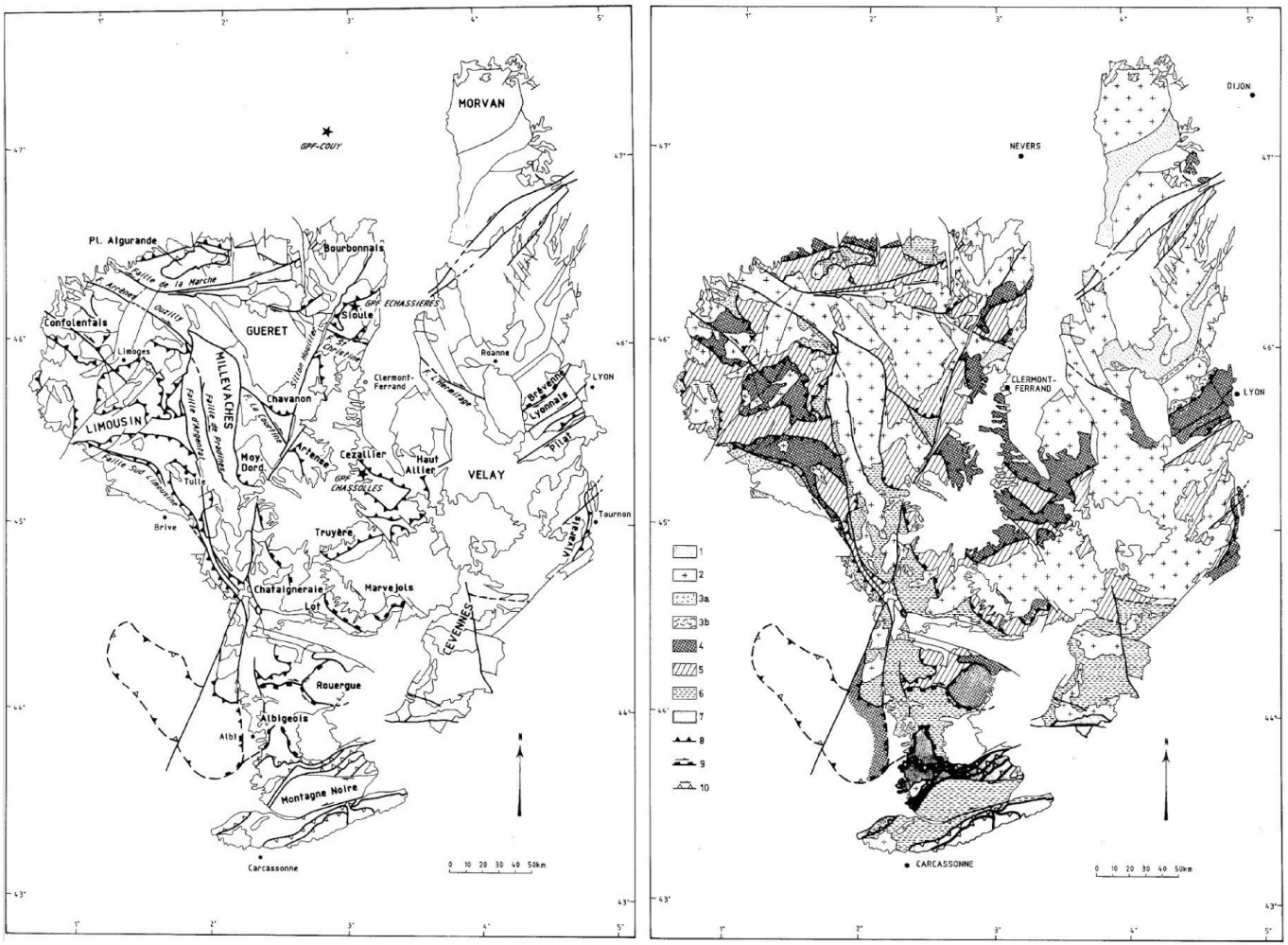

Figure 1.10: Geographic location of the main geological regions and sketch map of the main nappes in the French Massif Central. Figure and caption taken (and adapted) from Ledru et al. (1989). 1: Visean sediments; 2: undifferentiated granite bodies; 3: epizonal upper units (a) Thiviers-Payzac and Génis, (b) Brévenne; 4: Upper Gneiss Unit; 5: Lower Gneiss Unit; 6: Parautochtonous Unit; 7: Fold-and-Thrust-Belt; 8: thrusts (370–390 Ma); 9: thrusts and transcurrent shear zones (360–340 Ma); 10: thrusts and transcurrent shear zones (340–320 Ma).

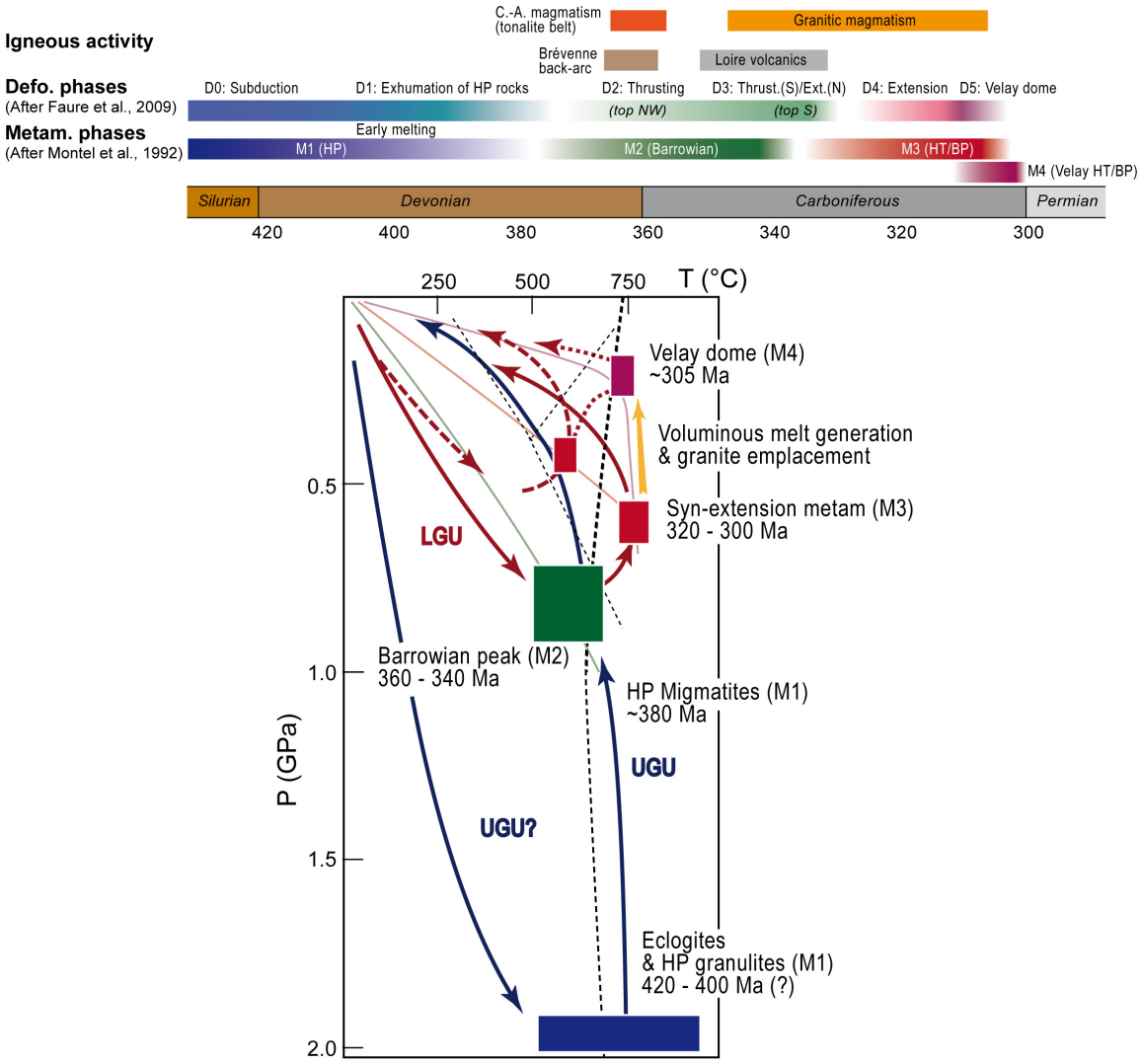

Figure 1.11: Summary of main metamorphic (after Montel et al., 1992) and deformation phases (after Faure et al., 2009) recognized in the French Massif Central. Further descriptions of the inverted Barrowian sequence can be found in Burg et al. (1984; 1989) and Schulz et al. (1996; 2001); Schulz (2009). Figure courtesy of J.-F. Moyen.

metamorphism. Six main deformational phases have been retained (see Faure et al., 1997; 2009 and references therein):

- an early stage D_0 of oceanic and continental subduction took place at 420–400 Ma, presumably related to the closure of the Galicia–Massif Central Ocean and recorded by the eclogites of the *Leptynite–Amphibolite Complex*.
- exhumation of the HP rocks was associated with top-to-the S D_1 thrusting of the Upper Gneiss Unit over the Lower Gneiss Unit (and Parautochtonous Unit in the Limousin and Sioule areas), developing an inverted Barrowian metamorphic sequence (Fig. 1.11). Deformation and MP–M(H)T metamorphism have been dated between 380–360 Ma. Following Montel et al. (1992), HP metamorphism and subsequent decompression-related anatexis experienced by the Upper Gneiss Unit during D_0 and D_1 are termed "M1" (see Fig. 1.11). The earliest dramatic magmatic event observed in the Massif Central correspond to the *c.* 360 Ma "Tonalite Belt" (Fig. 1.11) featuring gabbro-tonalite-granodiorite, amphibole-bearing calc-alkaline plutons (Bernard-Griffiths et al., 1985; Peiffer, 1985; Shaw et al., 1993). Coeval volcanics are observed in the Brévenne (Pin and Paquette, 1997; 2002) and Somme formations (Delfour, 1989).
- a pervasive top-to-the NW D_2 deformation reworked the early nappe stack and

transported the Upper Allochtonous Units and in some cases the Parautochtonous Unit above the Upper Gneiss Unit, still under MP–MT metamorphic conditions (Fig. 1.12 and 1.11). D_2 would have occurred at 360–345 Ma.

- D_3 is a dual event typified by syn-orogenic crustal extension and acid volcanism in the northern FMC (Binon and Pin, 1989) meanwhile top-to-the S thrusts developed to the South in the Parautochtonous Units. D_3 has been dated at 345–325 Ma and marks the onset of voluminous granitic magmatism in the Massif Central (with granites representing more than a third of the today-exposed lithologies).
- D_4 and D_5 events are characterized by general extension and localized transpression coeval to LP–HT metamorphism ("M3" of Montel et al., 1992) and granite intrusions. Activation of strike-slip to normal shear zones controlled the exhumation of migmatite domes (Montagne Noire, Velay) representing extruded portions of partially molten middle crust (Ledru et al., 2001; Whitney et al., 2015). The evolution of the Velay dome is typified by isobaric heating corresponding to the low-pressure granulite-facies "M4" metamorphic event (Fig. 1.11).

Geodynamic interpretations

According to Faure et al. (2009), the D_0 and D_1 events would reflect the closure of the Galicia–Massif Central ocean and docking of the Armorica micro-continent to the Gondwana mainland, generating major top-to-the S thrusts. Such interpretation is supported by the existence of an ophiolitic association in the Limousin area (Dubuisson et al., 1989) and (U)HP metabasic eclogites throughout the Massif Central (Berger et al., 2010a;b; Lardeaux et al., 2001; Matte, 2001; Mercier et al., 1989; Paquette et al., 1995). Yet, Silurian magmatic rocks that would testify for the existence of a subduction arc are lacking and the absence of Silurian zircon grains in the detrital record of the Devonian to Permian sediments suggests a period of magmatic quiescence (Lin et al., 2016; Pfeifer et al., 2016). Consequently, at our present state of knowledge, the significance of D_0 and D_1 remains elusive.

The D_2 top-to-the NW shearing event is attributed to the collision between Laurentia–Baltica–Avalonia (forming Laurussia) to the North and Gondwana–Armorica to the South, in line with the closure of the Rheic ocean (Faure et al., 2009; 2017). The "Tonalite Belt" and calc-alkaline volcanics in the Morvan would represent the remnants of a magmatic arc developed on Gondwana–Armorica in response to the south-directed subduction of the Rheic ocean (Faure et al., 2009; Lardeaux et al., 2014). A back-arc setting is preferred for the coeval bimodal volcanics of the Brévenne formation (Pin and Paquette, 1997; 2002).

D_3 coeval extension and compression in the northern and southern FMC, respectively, may be attributed to the growth and southwards lateral expansion of an orogenic plateau (Vanderhaeghe, Gardien, Moyen, Gébelin, Laurent, Couzinié, Chelle-Michou, and Villaros, Vanderhaeghe et al.) which existence is besides supported by paleontological and sedimentological data (Becq-Giraudon et al., 1996). D_4 and D_5 events would correspond to syn- to post-orogenic collapse of the belt in line with general extension and widespread magmatism (Burg et al., 1994).

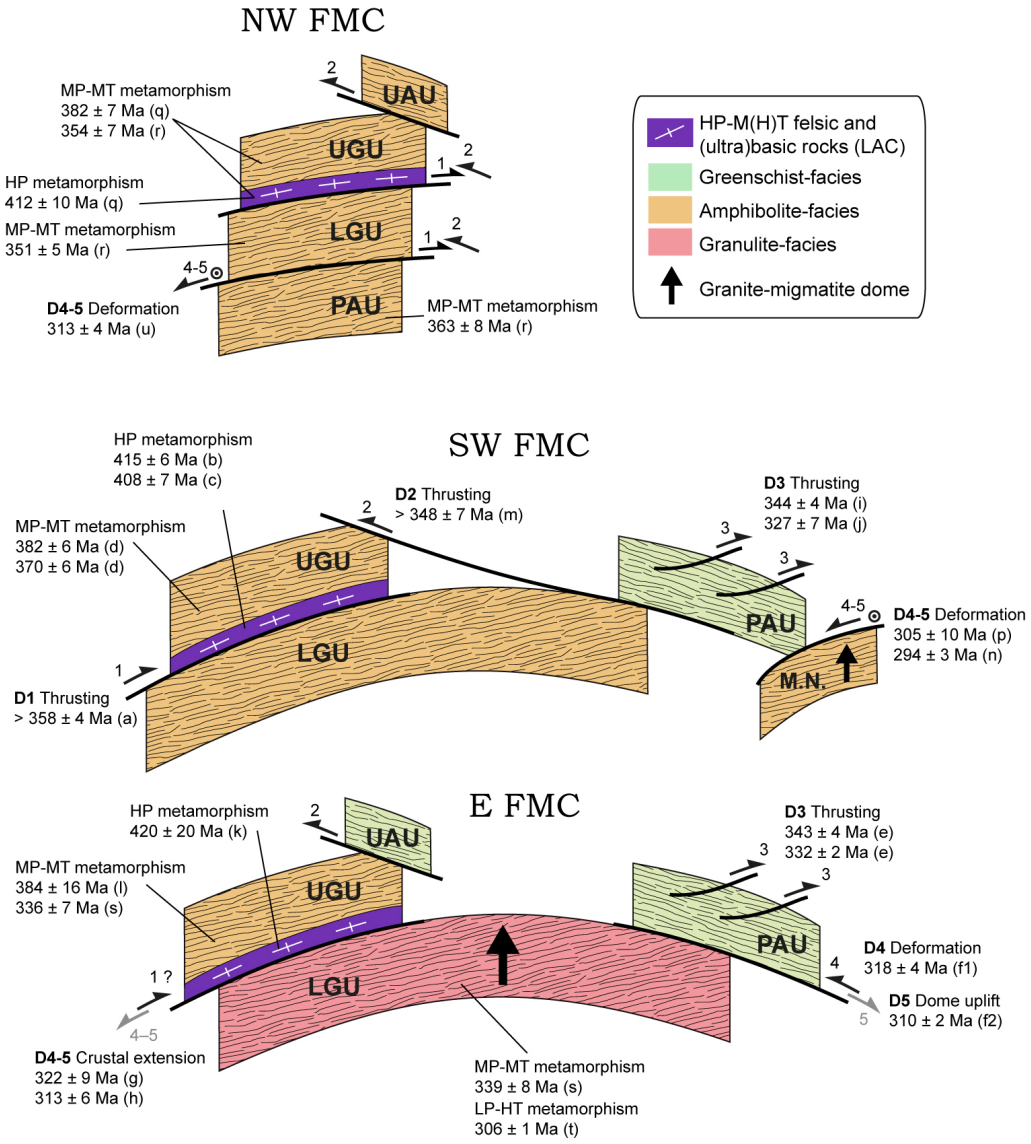

Figure 1.12: Simplified sketch showing the general metamorphic grade and structural relationships between the mains nappes in three domains of the French Massif Central. A selection of critical geochronological constraints are also depicted. NW FMC: Limousin, Sioule; SW FMC: Truyère, Lot, Marvejols, Rouergue, Albigeois, Montagne Noire (M.N.); E FMC: Brévenne, Lyonnais, Haut Allier, Vivarais, Velay, Cévennes; names of the geological regions after Ledru et al. (1989). UAU: Upper Allochtonous Units. UGU: the Upper Gneiss Unit. LGU: the Lower Gneiss Unit. PAU: Parautochtonous Unit. References and techniques for ages, mineral abbreviations from Whitney and Evans (2009): (a) Costa (1989), bt Ar–Ar; (b) Pin and Lancelot (1982), zrc U–Pb ID–TIMS; (c) Paquette et al. (1995) whole-rock/minerals Sm–Nd; (d) Legendre et al. (2009), mnz U–Th–Pb EPMA; (e) Caron (1994), bt–ms–amp Ar–Ar; (f) Bouilhol et al. (2006), ms Ar–Ar (f1), mnz U–Th–Pb EPMA (f2); (g) Caen-Vachette et al. (1984), whole-rock Rb–Sr; (h) Malavielle et al. (1990) bt Ar–Ar; (i) Costa (1990), ms Ar–Ar; (j) Doublier et al. (2006) ms Ar–Ar; (k) Ducrot et al. (1983) zrc U–Pb ID–TIMS; (l) Duthou et al. (1994), whole-rock Rb–Sr; (m) Maluski and Monié (1988), bt Ar–Ar; (n) Poilvet et al. (2011), zrc U–Pb LA–ICP–MS; (p) Faure et al. (2010) recalculated by Roger et al. (2015), zrc U–Pb SIMS; (q) Berger et al. (2010a); zrc U–Pb LA–ICP–MS; (r) Schulz (2009), mnz U–Th–Pb EPMA; (s) Schulz (2014), mnz U–Th–Pb EPMA; (t) Couzinié et al. (2014), mnz U–Th–Pb EPMA; (u) Gébelin et al. (2009), mnz U–Pb ID–TIMS.

1.5 Some analytical considerations

1.5.1 Error estimation associated with U–Pb dating

An adequate estimation of the error associated to an U–Pb age is critical to correctly address its geological significance. Errors are of two types. First, the *internal* error accounts for the intrinsic dispersion of the measured value during the analytical run. It is solely based on counting statistics and often corresponds to a standard error, i.e. the standard deviation of the measured value divided by the square root of the number of measurements. Such internal errors affect each individual analysis and monitor the *precision* of each of those.

Second, systematic errors refer to the uncertainties in a set of external parameters considered in the U–Pb data processing that may generate a bias in the results (Paton et al., 2010). Those are indicators of the *accuracy* of the analyses. They notably include the uncertainties on (Gehrels et al., 2008): (i) the decay constants for ^{238}U and ^{235}U; (ii) the isotope ratios of the primary standard (GJ–1 in all the analytical sessions conducted in this thesis); (iii) the overall validity of the applied corrections (notably the monitoring of the downhole U/Pb fractionation).

The uncertainties on the decay constants are 0.107% and 0.136% for ^{238}U and ^{235}U, respectively (Jaffey et al., 1971). Uncertainties on GJ–1 were set at 0.5% in the following. The average uncertainty of the corrections was estimated based on the obtained isotope ratios/ages for the secondary standards. For each of those, the average age obtained in the course of our analyses departs from the recommended ID–TIMS value by less than 1% ($<$ 0.6% for BB-16).

Systematic errors must be propagated to any U–Pb date calculation based on several individual analyses (Concordia date, weighted average date, Concordia intercept), yielding an estimate of both precision and accuracy and allowing to compare dates obtained during different analytical sessions. Error propagation has been conducted by quadratic addition of the internal error and the systematic errors listed above.

The add-on Isoplot/Ex v.4.15 (Ludwig, 2008) for MS Excel® calculates an uncertainty on dates based solely on the individual errors of the measurements, accordingly retained as an estimate of the internal error. The uncertainties on the decay constants can also be propagated automatically by Isoplot, which has been done in this work. Consequently, the *internal error* displayed in the Wetherill and Tera-Wasserburg diagrams does actually encompass a systematic error component. To calculate a Variscan date, the uncertainty on the corrections was estimated based on Plešovice (1% uncertainty). For Cadomian dates, the uncertainty on BB-16 was considered (0.6 %). Resulting systematic errors range between 0.8 and 1.12 %. Such systematic error propagation has not been conducted in the published articles (sections 2.1 and 6.3) but is followed in unpublished data.

1.5.2 Inter-comparison of data from different laboratories

The data presented in this thesis have been obtained in the course of several analytical sessions, in different laboratories using specific equipment (e.g. sector-field vs. quadrupole ICP–MS) and contrasted data processing schemes. For instance, U–Pb data acquired in Frankfürt-am-Main (GUF) and Stellenbosch (SUN) were processed using an in-house Excel spreadsheet (Gerdes and Zeh, 2006). In contrast, data reduction in Rennes relies on GLITTER® (Van Achterbergh et al., 2001). Finally, data obtained at ETH Zurich were processed with the Igor Pro Iolite v2.5 software (Hellstrom et al., 2008), using the VizualAge data reduction scheme (Petrus and Kamber, 2012). A similar situation is encountered for Lu–Hf analyses, between GUF and Clermont-Ferrand (with specific in-house spreadsheets). Despite the different specifications and data reduction procedures, the accuracy of each generated dataset can be monitored by examining the results obtained on secondary reference materials (Fig. 1.13 and 1.14).

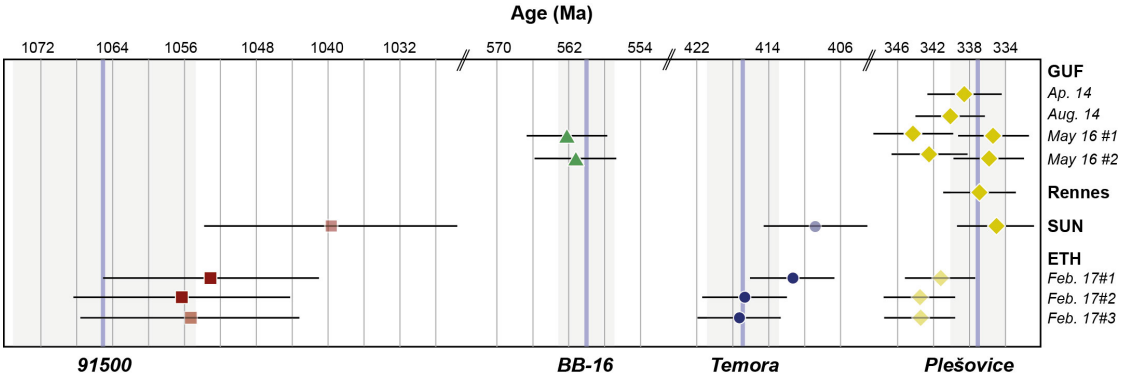

Figure 1.13: U–Pb Concordia ages obtained for secondary reference materials in the course of each analytical session. Plotted uncertainties are the quadratic additions of internal (at 2σ or 95% confidence, in which case the symbol is shaded) and systematic errors. The purple bars depict the ID–TIMS ages and associated errors for Plešovice (Sláma et al., 2008a), Temora (Black et al., 2003; 2004), BB-16 (Santos et al., in press) and 91500 (Wiedenbeck et al., 1995; 2004). Note the age scale breaks.

U–Pb data First, all but one analyses yielded U–Pb ages identical within error to the ID–TIMS value ± 1%. In each analytical session, at least one secondary standard shows the expected U–Pb age, within uncertainties. Consequently, the 9 datasets are considered as equivalent and inter-comparable. During the 2016 sessions conducted at GUF, two statistically different Concordia dates were calculated from the measurements conducted on the Plešovice reference material, at *c.* 335 and 344 Ma. Standard BB-16 analysed in the same sessions yielded reproducible and accurate results meaning that the two Plešovice dates are unlikely to be analytical artefacts. This may suggest the presence of older domains in the Plešovice grains but has not been investigated further.

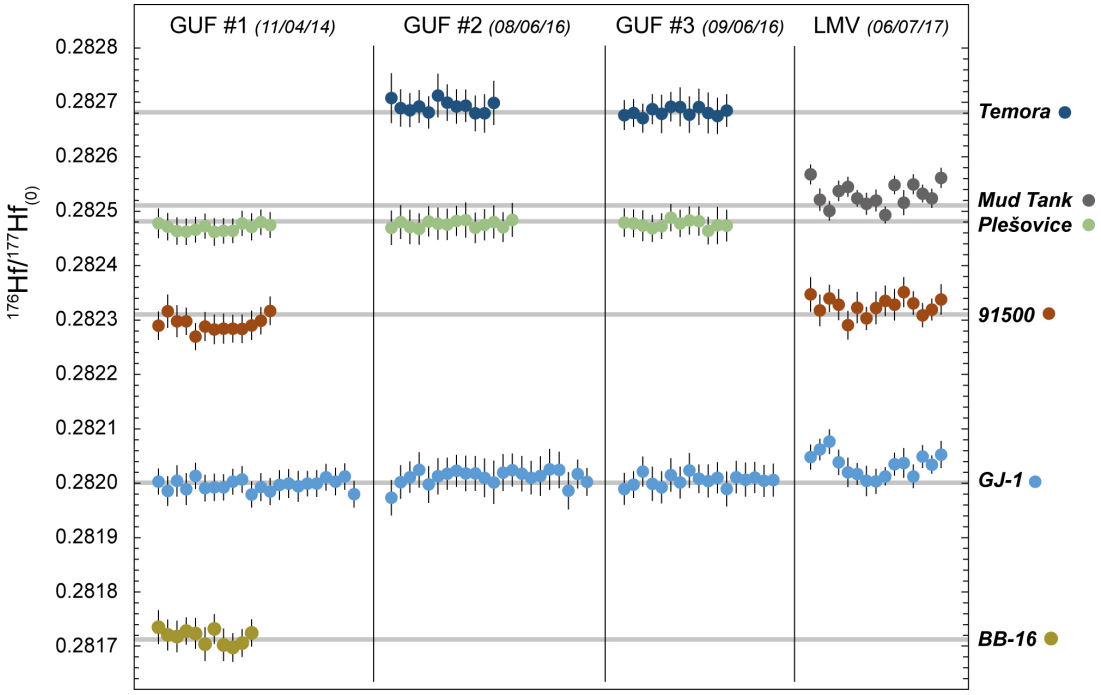

Figure 1.14: $^{176}Hf/^{177}Hf$ ratios obtained for secondary reference materials in the course of each analytical session. The grey bands depict the reference values for Plešovice (Sláma et al., 2008a), 91500 (Blichert-Toft, 2008), Temora (Woodhead et al., 2004), Mud Tank (Woodhead and Hergt, 2005), BB-16 (Santos et al., in press) and GJ-1 (Morel et al., 2008).

Lu–Hf data Measurements performed on secondary standards at GUF yielded identical results throughout both sessions. Analyses from Clermont-Ferrand (LMV) are less consistent as periodic oscillations in the measured ratios can be observed during the run. Such dispersion has been taken into account while processing the sample data by propagating the reproducibility of GJ-1, the least reproducible reference material, to the internal errors of each individual measurement. At first glance, the GUF data would seem more accurate but this is due to the instrumental offset correction developed at GUF but not at LMV. Overall, the observed offset would result in an overestimation of the ε_{Hf}(t) by 0.7 to 1.3 ε-unit, depending on the reference material considered. I believe that this offset will not alter the validity of the reasoning developed in this thesis because: (i) the associated error is of the same order of magnitude than the analytical uncertainties for individual measurements; and (ii) analyses have been performed on a large number of detrital zircon grains with the aim to draw general conclusions on the origin and nature of the detritus, insensitive to such limited offset.

This manuscript is divided in three main parts.

Part I focuses on the pre-Variscan evolution of the French Massif Central. Chapter 2 and 3 present comprehensive petrogenetic studies of the constituent rocks from the Lower and Upper Gneiss Units, respectively. Chapter 4 is a review of the pre-Variscan magmatic record in the French Massif Central with a particular emphasis on the disputed Cambrian–Ordovician geodynamic scenario.

Part II is a characterization of the timing, source and structural framework of Variscan post-collisional magmatism in the Massif Central. Chapter 5 describes the diversity of post-collisional magmas and provides chronological and petrological constraints. Chapter 6 is a structural and geochronological study conducted on a migmatite dome.

Part III has been written as a general discussion. Chapter 7 addresses the formation and differentiation of the continental crust in the French Massif Central seen through the prism of the zircon record.

Part I

Pre-Variscan evolution of the eastern French Massif Central

Chapter 2

Composition of the Lower Gneiss Unit in the Velay Dome

2.1 Article #1: The Velay Orthogneiss Formation

This article published to Lithos focuses on a constituent lithology of the Lower Gneiss Unit: the Velay Orthogneiss Formation. New whole-rock geochemical data together with zircon U–Pb–Hf determinations constrain the petrogenesis of the orthogneiss protoliths and their geodynamic significance is discussed.

The work presented hereafter was conducted in collaboration with several researchers. Part of it was undertaken during the 4th year internship of Michaël Mintrone, former student of Clermont-Ferrand University, co-supervised by Jean-François Moyen and myself.

I sampled all rocks investigated in the course of this study during two field campaigns (fall 2014 and spring 2015) with significant help from Adrien Vézinet, Jean-François Moyen and Michaël Mintrone. Adrien Vézinet and I conducted the sample preparation procedure for whole-rock geochemical determinations (that were subsequently carried out by the ALS firm). Zircon extraction, preparation and imaging were performed by Michaël Mintrone assisted by Adrien Vézinet and myself. U–Pb dating (data acquisition and processing) was conducted by Michaël Mintrone, Marc Poujol and myself. Hf isotope determinations were carried out by Oscar Laurent and Linda Marko. I wrote the whole manuscript with input and pieces of advice from Oscar Laurent, Cyril Chelle-Michou, Jean-François Moyen and Pierre Bouilhol.

Lithos 286–287 (2017) 16–34

Contents lists available at ScienceDirect

Lithos

journal homepage: www.elsevier.com/locate/lithos

Cadomian S-type granites as basement rocks of the Variscan belt (Massif Central, France): Implications for the crustal evolution of the north Gondwana margin

Simon Couzinié [a,b,*], Oscar Laurent [c,1], Marc Poujol [d], Michaël Mintrone [a,1], Cyril Chelle-Michou [a,2], Jean-François Moyen [a], Pierre Bouilhol [e,3], Adrien Vezinet [a,b], Linda Marko [f]

[a] Université de Lyon, Laboratoire Magmas et Volcans, UJM-UCA-CNRS-IRD, 23 rue du Dr. Paul Michelon, 42023 Saint-Etienne, France
[b] University of Stellenbosch, Department of Earth Sciences, Private Bag X1, 7602 Matieland, South Africa
[c] Université de Liège, Département de Géologie B20, Quartier Agora, allée du six Août 12, B-4000 Liège, Belgium
[d] Géosciences Rennes, UMR-CNRS 6118, Université de Rennes I, 35042 Rennes Cedex, France
[e] Department of Earth Sciences, Durham University, Science Labs, Durham DH13LE, United Kingdom
[f] Institut für Geowissenschaften, J.W. Goethe Universität, Altenhöferallee 1, 60438 Frankfurt Am Main, Germany

ARTICLE INFO

Article history:
Received 2 March 2017
Accepted 1 June 2017
Available online xxxx

Keywords:
North Gondwana margin
Cadomian orogeny
Variscan orogeny
S-type granites
Lu-Hf isotopes
French Massif Central

ABSTRACT

From the Neoproterozoic to the early Paleozoic, the northern Gondwana margin was sequentially shaped by the *Cadomian* accretionary and the *Variscan* collisional orogens which offers the opportunity to investigate the relative extent of crust production/reworking in both geodynamic settings. In the eastern part of the Variscan French Massif Central (FMC), the Velay Orthogneiss Formation (VOF) represents a consistent lithological unit of the pre-Variscan basement and comprises augen gneisses and leucogneisses. Such rocks constitute a unique record of the pre-Variscan magmatic history and bear critical information on the crustal evolution of the northern Gondwana margin.

Here, we present whole–rock major and trace element compositions indicating that: (i) the VOF shows a remarkable geochemical homogeneity; (ii) the protolith of the augen gneisses corresponds to strongly peraluminous, "S-type" porphyritic granites originating from partial melting of an Ediacaran sedimentary sequence; (iii) the leucogneisses are former leucogranites generated by fractionation of the magma at the origin of the porphyritic granites; and (iv) the whole suite emplaced at shallow crustal levels (<7 km). U–Pb LA–(MC–)ICP–MS analyses on zircon yielded similar emplacement ages of c. 542 Ma and a narrow range of $\varepsilon_{Hf}(t)$ clustering around 0 for the protoliths of both augen and leucogneisses. This homogeneous Hf isotope signature, notably uncommon for S-type granites, would originate from a sequential process of: (i) inherited zircon dissolution during melting and ascent in the crust due to Zr-undersaturated conditions, (ii) isotopic homogenization of the melt by advection and elemental/isotopic diffusion, followed by (iii) early saturation upon emplacement owing to rapid cooling at shallow crustal levels.

We propose that partial melting of Ediacaran sediments occurred during inversion of a Cadomian back-arc basin and was promoted by the high thermal gradient typical of thinned crust domains. Therefore, the VOF and other Cadomian S-type granitoids from the northern Gondwana margin are indicative of substantial crust reworking away from any proper continental collision zone.

1. Introduction

Accretionary orogens develop along oceanic and continental active margins, feature volumetrically abundant mantle-derived magmatism and are accordingly considered as the main locus of continental crust production (Cawood et al., 2009; Jagoutz and Kelemen, 2015; Reymer and Schubert, 1984; Taylor and McLennan, 1985). Conversely, collisional orogens juxtapose stable portions of continental lithospheric blocks and are rather seen as domains of extensive crust reworking through partial melting of pre-existing crustal rocks (Dewey et al., 1986; Harris

* Corresponding author at: Université de Lyon, Laboratoire Magmas et Volcans, UJM-UCA-CNRS-IRD, 23 rue du Dr. Paul Michelon, 42023 Saint-Etienne, France.
E-mail addresses: simon.couzinie@univ-st-etienne.fr, simon.couzinie@ens-lyon.org (S. Couzinié).
[1] Now at Institute for Geochemistry and Petrology, ETH Zürich, Zurich, Switzerland.
[2] Now at School of Earth Sciences, University of Bristol, Bristol BS8 1RJ, UK.
[3] Now at Laboratoire Magmas et Volcans, Université Clermont Auvergne-CNRS-IRD, OPGC, Campus Universitaire des Cézeaux, 6 Avenue Blaise Pascal, 63178 Aubière Cedex, France.

http://dx.doi.org/10.1016/j.lithos.2017.06.001
0024-4937/

et al., 1986; Hawkesworth et al., 2009, 2010). However, recent studies have refined and nuanced these end-member scenarios by pointing out that new crust may also be produced at the end of continental collision (Couzinié et al., 2016; Moyen et al., 2017; Niu et al., 2013) and likewise, that crust reworking also takes place in arc systems (Collins and Richards, 2008; Zurbriggen, 2015). Therefore, assessing the relative importance of each phenomenon in both geodynamic settings is paramount to understand the modes of continental crust formation and evolution through time.

Terranes formerly belonging to the northern Gondwana margin (Fig. 1, see review in Stampfli et al., 2013) are ideal targets to address this issue because they have sequentially been affected by: (i) the *Cadomian* Western Pacific-type marginal orogenic system, of Cryogenian–Ediacaran age (Chelle-Michou et al., 2017; Garfunkel, 2015; Linnemann et al., 2014; Nance et al., 1991); followed by, (ii) the *Variscan* orogeny, a major late Paleozoic continental collision episode resulting from the convergence between Laurussia and Gondwana (Kroner and Romer, 2013; Matte, 1986) and culminating with the assembly of Pangea, the latest supercontinent of Earth's history (Rogers and Santosh, 2003).

The French Massif Central (FMC) shows one of the largest exposures of the inner part of the Variscan orogen (Lardeaux et al., 2014) and isotopic evidence from the voluminous Variscan crust-derived granitoids demonstrate that such magmatism extensively reworked a continental crust of Neoproterozoic to early Paleozoic ancestry (Melleton et al., 2010; Moyen et al., 2017; Pin and Duthou, 1990; Turpin et al., 1990). However, the nature of this pre-Variscan crust as well as the geodynamic setting in which it formed is still a matter of debate. For instance, it remains unclear to what extent the crust segment today exposed in the FMC was impacted by the Cadomian orogeny (see discussion in Garfunkel (2015)). From this perspective, a better knowledge of the age, structure, lithological composition and configuration of the pre-Variscan crust in the FMC would: (i) provide new constraints on the late Ediacaran/early Paleozoic paleogeography and geodynamics of the northern Gondwana margin; (ii) improve our understanding of the rate and timing of crustal growth in Western Europe.

In the eastern part of the FMC, the Variscan nappes feature high-grade gneisses and, in particular, large amounts of meta-igneous rocks, which have likely witnessed one or several pre-Variscan magmatic episodes. Somewhat outdated radiometric dating from these orthogneisses (Caen-Vachette, 1979; R'Kha Chaham et al., 1990) as well as detrital and inherited zircon data from metasedimentary rocks (Chelle-Michou et al., 2017) and Variscan granitoids (Laurent et al., 2017) respectively, suggest that they emplaced close to the Proterozoic-Paleozoic boundary at ca. 545 Ma. Yet, these meta-igneous rocks lack modern and/or direct geochronological data, in contrast to the western FMC where such work has been undertaken (Alexandre, 2007; Alexandrov et al., 2001; Melleton et al., 2010). Similarly, the nature, petrogenesis and geodynamic

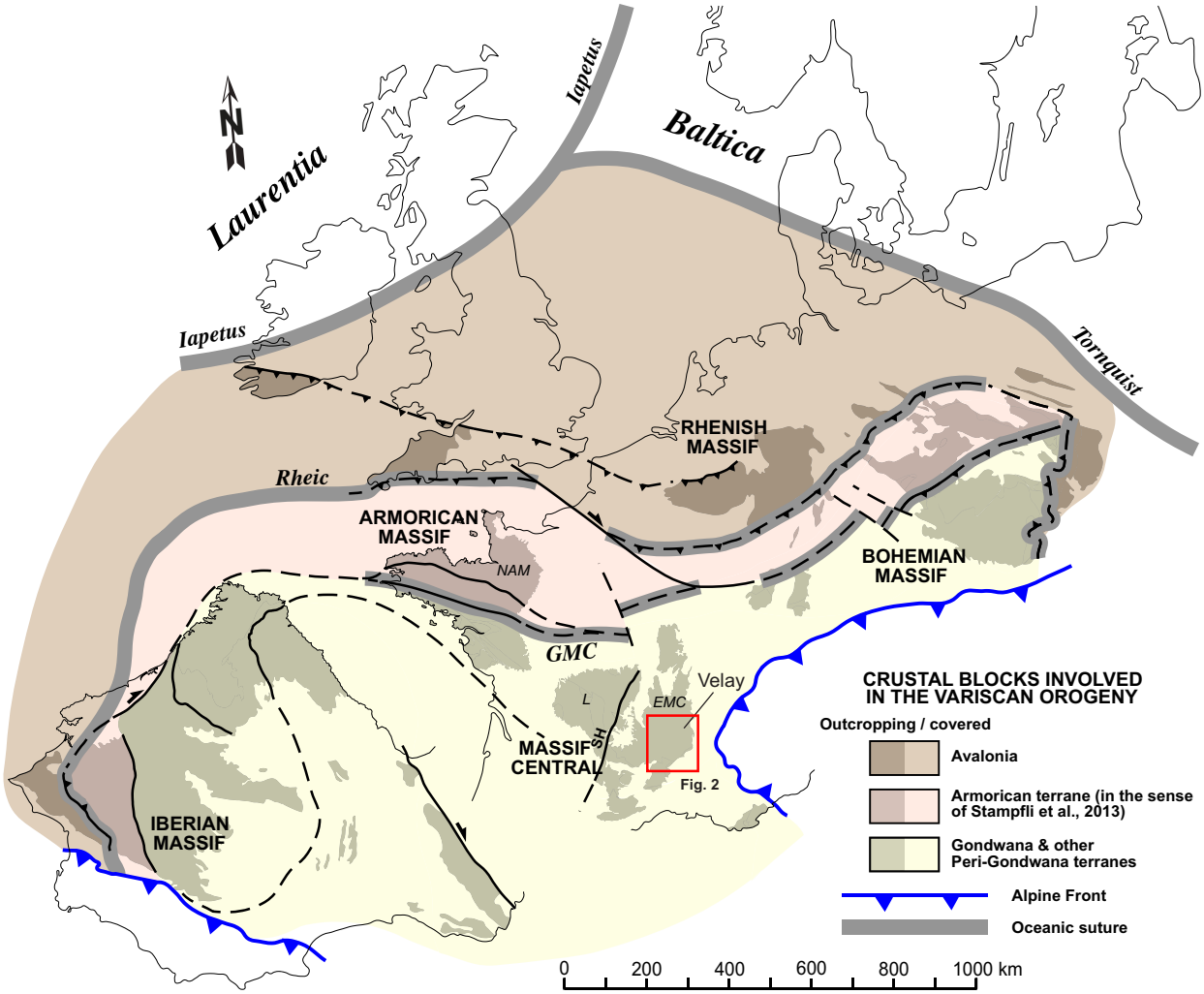

Fig. 1. Sketch map of the crustal blocks involved in the Variscan orogeny, adapted from Ballèvre et al. (2014). Yellow star highlights the location of the study area. Oceanic sutures: GMC, Galicia-Massif-Central Ocean. Regional subdivisions: NAM, North Armorican Massif; L, Limousin (Western Massif Central); EMC, Eastern Massif Central. Shear zones: SH, Sillon Houiller (coal line).

significance of the FMC orthogneisses are poorly constrained. The aim of this contribution is therefore to decipher the age and origin of the pre-Variscan orthogneiss units in the Velay area using field observations, whole–rock geochemistry, LA–ICP–MS zircon U–Pb dating and LA–MC–ICP–MS zircon Lu–Hf isotope measurements. This new dataset demonstrates that the pre-orogenic evolution of this part of the FMC is dominated by late Ediacaran events and features the emplacement at shallow crustal levels of a large (~1800 km^2) S-type granite batholith, most likely formed by melting of an Ediacaran back-arc supracrustal sequence at the end of the Cadomian orogeny. This pinpoints the importance of crust reworking in accretionary orogens, even in domains lacking significant volumes of ancient basement.

2. Geological setting

2.1. The French Massif Central and its pre-Variscan evolution

The French Massif Central displays a south-verging stack of metamorphic nappes built up from the early Devonian to the early Carboniferous and composed from top to bottom of (Faure et al., 2009b, Ledru et al., 1989, and references therein): (i) amphibolite- to greenschist-facies upper allochthonous units (UAU: Thiviers-Payzac, Leyme, Gartempe, S^t-Sernin-sur-Rance, Génis, Brévenne); (ii) the Upper Gneiss Unit (UGU) which comprises amphibolite- to granulite-facies ortho- and paragneisses and typically shows at its base a bimodal meta-igneous association ("Leptynite-Amphibolite Complex" or LAC) that contains relicts of eclogite-facies metamorphism; (iii) the Lower Gneiss Unit (LGU), an assemblage of amphibolite-facies micaschists, ortho- and paragneisses together with scarce amphibolites; (iv) the lower-grade Parautochthonous Unit (PAU) made up largely of greenschist- to amphibolite-facies meta-sediments (e.g. Cévennes schists); and (v) a Fold-and-Thrust Belt of very low metamorphic grade (Montagne Noire nappes, Vigan schists). The Variscan tectonic-metamorphic evolution encompasses (Burg et al., 1994; Faure et al., 2009b): (i) an early (late Silurian to early Devonian) event corresponding to the closure of several oceanic domains and coeval HP metamorphism; (ii) late Devonian nappe stacking and crustal thickening ending up in the growth and lateral flow of an orogenic plateau during the early Carboniferous; (iii) gravitational collapse via the activation of low-angle detachment faults marked by the development of migmatite domes in the late Carboniferous.

The pre-Variscan sedimentary materials that build up the low-grade nappes (UAU, PAU and Fold-and-Thrust Belt) are mostly late Ediacaran to early Ordovician in age as shown by paleontological data (Fournier-Vinas and Debat, 1970; Guérangé-Lozes and Burg, 1990; Reitz and Wickert, 1988) and dating of interlayered volcanics (Faure et al., 2009a; Lescuyer and Cocherie, 1992). In higher-grade, gneissic units (UGU and LGU), detrital zircon studies (Chelle-Michou et al., 2017; Melleton et al., 2010) together with field relationships between meta-sediments and adjacent dated orthogneisses suggest maximum depositional ages ranging from the early Ediacaran to the Cambrian (Ledru et al., 1994; Melleton et al., 2010). The conspicuous presence of volcanic rocks (meta-tuffs, meta-lavas) throughout the stratigraphic pile exposed in low-grade units (Alvaro et al., 2014; Marini, 1987; Pouclet et al., 2017) and the existence of several orthogneiss massifs of similar ages within the high-grade domains (Alexandre, 2007; Duthou et al., 1984; Melleton et al., 2010; Roger et al., 2015) testify for a protracted magmatic activity from the late Ediacaran to the late Ordovician. Petrogenetic studies attest to the tapping of two contrasting reservoirs throughout this period: (i) the asthenospheric/lithospheric mantle, source of the metabasites from the low-grade units and the LAC (Briand et al., 1992; Marini, 1987; Pin and Marini, 1993; Pouclet et al., 2017); (ii) preexisting crustal lithologies (Alexandre, 2007; Melleton et al., 2010) as a source of felsic magmas. Coeval sedimentation, crust- and mantle-derived magmatism have been attributed to long-lived continental extension ending up in the formation of a hyperextended margin during the Ordovician (Lardeaux et al., 2014). Collectively, these data suggest that the pre-Variscan crust of the FMC is not older than Neoproterozoic in age (Chelle-Michou et al., 2017).

2.2. The Velay dome

In the eastern Massif Central, the Variscan nappe stack (and notably the LGU; Fig. 3) is reworked by the formation of a 120 × 80 km granite-migmatite complex, referred to as the Velay dome. It corresponds to partially molten middle crust which exhumation was controlled on its northern edge by the Pilat low-angle detachment shear zone, typically showing top-to-the-NE sense of shear dated at 313 ± 6 Ma by ^{39}Ar/^{40}Ar on syntectonic biotite (Gardien et al., 1997; Malavielle et al., 1990). On its southern edge, the dome is overturned to the south (Lagarde and Dallain, 1994) onto the PAU, from which it is separated by a top-to-the south normal shear zone dated at 310 ± 5 Ma (Bouilhol et al., 2006). The Velay Dome consists of several lithologies including (Fig. 1): (i) ortho- and paragneisses ranging from unmolten to diatexitic (Montel et al., 1992) together with very scarce amphibolites (Briand et al., 1992); (ii) a set of peraluminous granitoids comprising early laccoliths (Ledru et al., 2001) and the heterogeneous biotite-cordierite-bearing "Velay" granite (Williamson et al., 1992). The migmatites and associated granites result from several successive melting events (Montel et al., 1992) over a period of 35 Ma, from c. 335 to 300 Ma (Couzinié et al., 2014; Laurent et al., 2017).

Here we define the **Velay Orthogneiss Formation** (VOF) as a consistent lithological unit gathering all pre-Variscan meta-igneous felsic rocks that crop out in the dome. The VOF can be divided into three main geographic sub-domains (Fig. 2): (i) the Pilat orthogneisses, exposed along the northeastern part of the dome; (ii) the Vivarais area, where meta-igneous rocks and paragneisses represent the weakly molten roof of the dome (Lagarde and Dallain, 1994); (iii) the "Arc-de-Fix" orthogneisses (R'Kha Chaham et al., 1990), which form a crescent outlining the western and southern parts of the dome. Collectively, the VOF covers an exposed area of ~1800 km^2. Field observations show that the VOF is intrusive within the adjacent paragneisses (Ledru et al., 1994, Fig. 3).

Typical lithologies of the VOF are (based on our field survey and unpublished French PhD theses from the 70s–80s, referenced in Supplementary text): (i) a volumetrically dominant biotite ± muscovite ± sillimanite augen gneiss (Fig. 4a) featuring pluricentimetric K–feldspar porphyroblasts and accessory garnet, allanite, ilmenite, apatite and zircon; (ii) a muscovite ± biotite ± garnet fine-grained leucogneiss (locally called "leptynite") with similar accessory minerals; (iii) a volumetrically subordinate biotite ± cordierite/garnet medium-grained banded orthogneiss. The leucogneisses occasionally occur as plurimetric enclaves or boudins within the augen gneiss (Fig. 4b), but most often form concordant bodies embedded within it (Fig. 4c,d). The contact between both lithologies can be sharp and locally underlined by a thin biotite selvage (Fig. 4c), or gradational, in which case leucogneisses appear as counterparts of the augen gneisses lacking biotite and K-feldspar porphyroclasts. All rock types are deformed by the Variscan tectonics, especially the augen gneiss that shows a well-developed foliation locally up to mylonitic grade (Fig. 4d), and locally display evidence for partial melting such as disruption of the foliation associated with segregation of leucosomes (especially close to the margins and at the roof of the Velay dome). The Vivarais gneisses tend to be more migmatitic (metatexite to diatexite) than the Arc-de-Fix (typically unmolten to metatexitic).

Studies on the VOF have concluded that augen gneisses in the Arc de Fix, Vivarais and Pilat domains correspond to former porphyritic granitoids (Ledru et al., 2001). Previous geochronological investigations suggest that those granitoids were emplaced in the early Cambrian as the Arc-de-Fix gneisses yielded a zircon Pb evaporation age of 533 ± 23 Ma (Mougeot et al., 1997) and a whole–rock Rb–Sr age of 528 ±

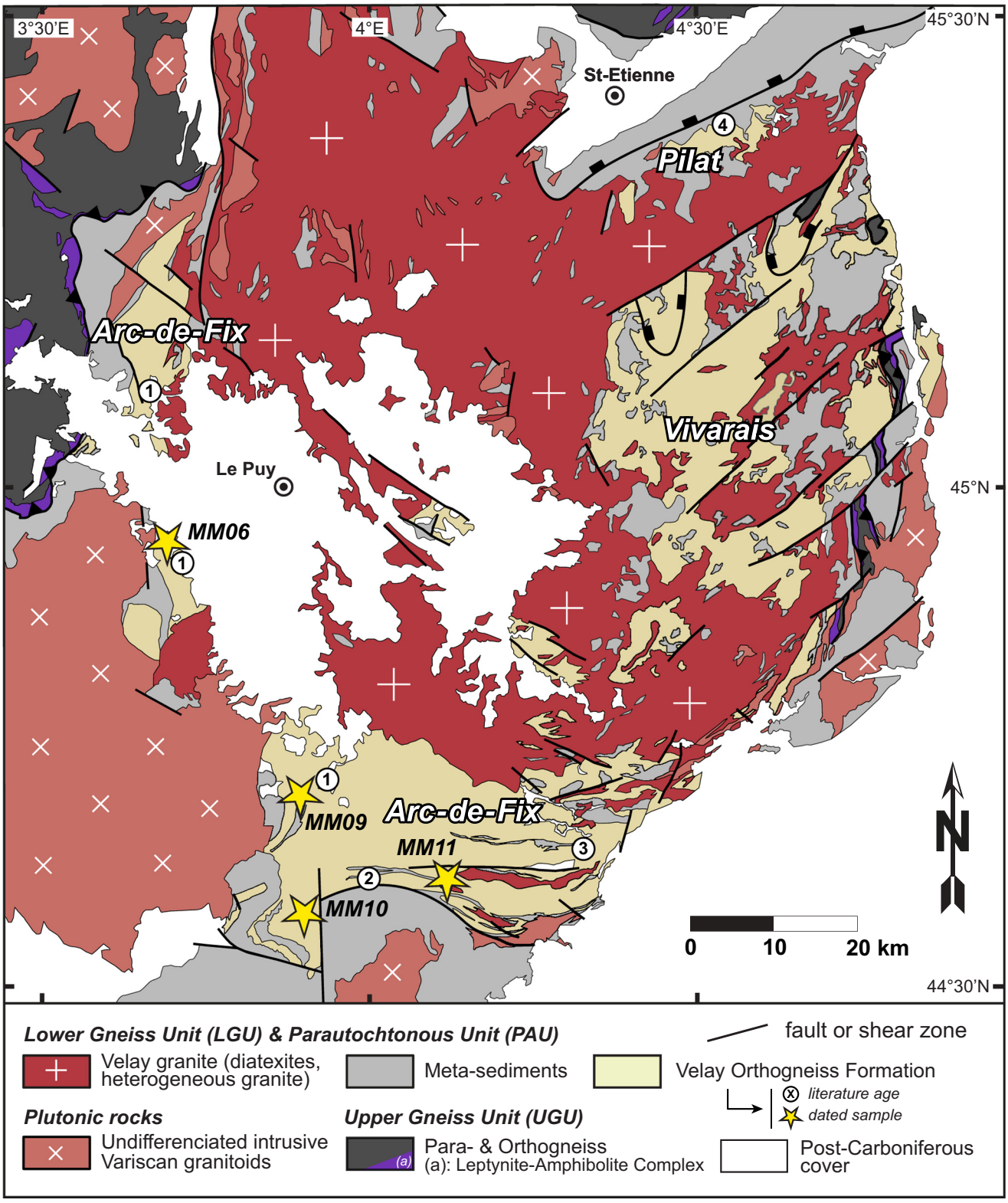

Fig. 2. Geological map of the Velay dome area. The extent of Variscan partial melting of the metamorphic lithologies is not shown for sake of clarity. Redrawn after Ledru et al. (2001) and regional geological maps of France at scale 1/50000. Literature geochronological data: 1, 528 ± 9 Ma, Rb–Sr whole-rock (R'Kha Chaham et al., 1990); 2, 543 ± 25 Ma, U–Th–Pb monazite (Be Mezeme et al., 2006); 3, 533 ± 23 Ma, zircon Pb evaporation (Mougeot et al., 1997); 4, 545 ± 14 Ma, Rb–Sr whole-rock (Caen-Vachette, 1979).

9 Ma (R'Kha Chaham et al., 1990). EPMA dating of inherited monazites in a migmatitic augen gneiss yielded similar results (543 ± 25 Ma; Be Mezeme et al. (2006)). The origin and age of leucogneisses are still disputed. In the Arc-de-Fix domain, they are thought to be part of the same magmatic suite of the augen gneiss protolith and would thus correspond to early Cambrian meta-leucogranites (R'Kha Chaham et al., 1990). In the Vivarais area, Chenevoy et al. (1986) also proposed a leucogranite protolith. In the Pilat domains, leucogneisses are rather regarded as former rhyolites or rhyolitic tuffs of late Ediacaran age (545 ± 14 Ma; Caen-Vachette (1979)).

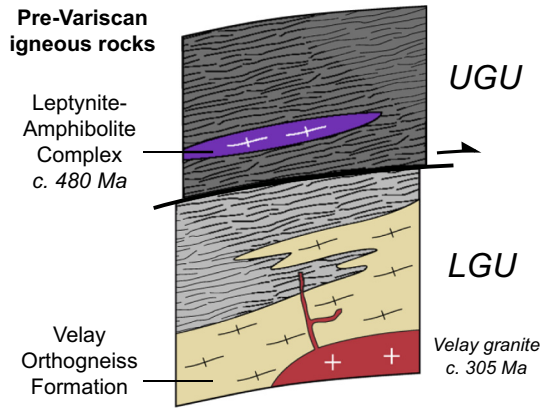

Fig. 3. Schematic diagram showing the field relationships and ages of the main lithological components within the two high-grade units (Upper and Lower Gneiss Units) of the eastern French Massif Central. See text for discussion.

3. Materials and methods

3.1. Whole–rock geochemistry

We collected 35 samples of unmolten augen gneisses, banded gneisses and leucogneisses from the three domains mentioned above. Location, GPS coordinates and description of investigated samples are presented Table S1. Whole–rock major and trace element contents were obtained from the ALS Global firm (details on the procedure and accuracy/reproducibility in Supplementary text). A database of VOF samples was compiled using this new dataset and analyses from the literature (see Table S2), carefully filtering out: (i) migmatitic samples, based on petrographic descriptions; and (ii) samples that experienced alteration and/or LILE (Large Ion Lithophile Elements) mobility during Variscan metamorphism, by calculating the weathering index (W) of Ohta and Arai (2007) and considering a cut-off value of W = 30% (see Supplementary text and Fig. S1). A total of 270 major element analyses were retained accordingly (including the newly obtained data). We will further consider that the retained VOF samples experienced nearly closed-system metamorphism during the Variscan orogeny, such that their chemical compositions reflect those of their igneous protoliths. This assumption is supported by (i) their position close to, or overlapping with the "igneous trend" in the MFW diagram of Ohta and Arai (2007), suggesting limited element mobility (Fig. S1); and (ii) the fact that 22 samples from the VOF analyzed for Rb–Sr isotopes (Caen-Vachette, 1979, and R'Kha Chaham et al., 1990) define a whole–rock isochron clearly yielding a pre-Variscan (Cambrian) date (see Supplementary text and Fig. S2), specifically identical (within uncertainties) to our zircon U–Pb dating results (see Section 4.2).

3.2. U–Pb geochronology

We selected four samples from the VOF for U–Pb dating, to constrain the age(s) of the igneous protolith(s). In this perspective, we focused the sampling in the Arc de Fix domain (Fig. 2) that is the least affected by the Variscan anatexis. Dated samples correspond to two augen gneisses (MM06 and MM11) and two leucogneisses (MM09 and MM10)

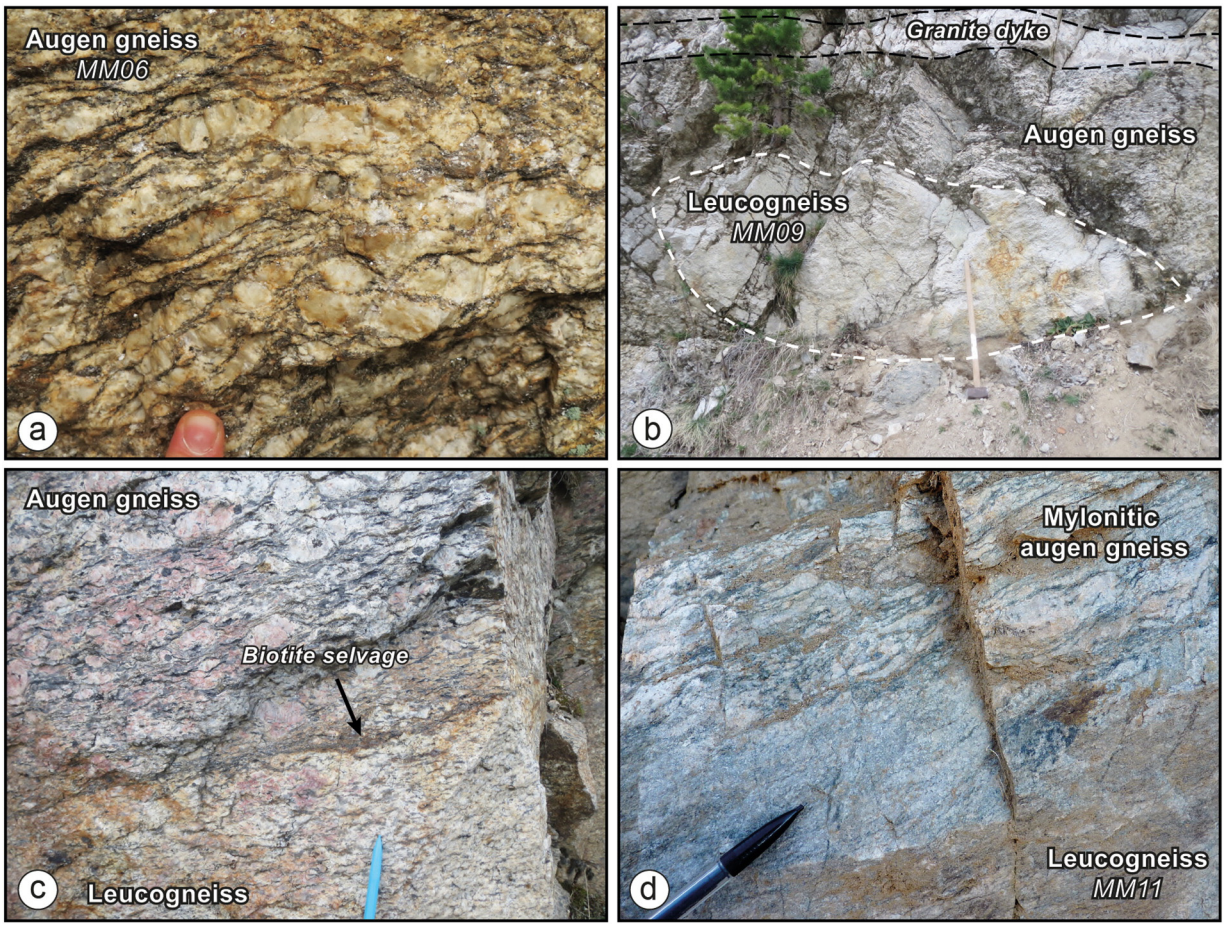

Fig. 4. Outcrop photographs showing: (a) a typical biotite + muscovite augen gneiss (dated sample MM06), St Privat-d'Allier; (b) a leucogneiss boudin (dated sample MM09) elongated within the augen gneiss facies, D906 Langogne; (c) sharp contact between the two facies underlined by a biotite-rich layer, D906 Langogne; (d) 10 cm-thick laminated layers of mylonitic augen gneiss embedded within strongly deformed leucogneiss, contact is intricate and gradational, Pont-du-Bon-Dieu, Labastide-Puylaurent.

Table 1
Nature, mineralogy and sampling localities of the investigated samples of the Velay Orthogneiss Formation together with results of zircon U–Pb dating performed in this study.

Sample	Velay domain	Locality	Lat. N	Long. E	Type	Mineralogy[a]	U-Pb age[b]	±2σ	N_{U-Pb}[c]	$MSWD_{C+E}$[d]	εHf(t)[e]	±2σ	N_{Lu-Hf}[f]
MM06	Arc de Fix	St Privat d'Allier	44.98811	3.68093	Augen gneiss	Qz + Kfs + Pl + Bt + Ms	541.8	3.1	16	0.34	−0.2	2.9	13
MM09	Arc de Fix	Langogne	44.69490	3.88376	Leucogneiss	Qz + Kfs + Pl + Bt + Ms + Gt	545.9	4.3	9	1.05			
MM10	Arc de Fix	Labastide-Puylaurent	44.56838	3.87095	Leucogneiss	Qz + Kfs + Pl + Ms	541.4	2.3	26	0.38			
MM11	Arc de Fix	Col de Meyrand	44.60534	4.07040	Augen gneiss	Qz + Kfs + Pl + Bt + Ms	542.5	3.1	17	0.43	−0.2	1.2	14

[a] Main mineral phases.
[b] U–Pb Concordia age obtained in the course of this study, in Ma.
[c] Number of analyses used to calculate the Concordia age.
[d] MSWD of concordance + equivalence for the displayed Concordia age.
[e] εHf(t) measured on magmatic zircons, calculated at the emplacement age of the sample.
[f] Number of Lu-Hf analyses.

representative of the main facies observed in the VOF. Their textures range from granoblastic to grano-lepidoblastic and porphyroclastic (for the augen gneisses, see Fig. 4a and c). Mineralogical assemblages are described Table 1 and representative annotated thin section photomicrographs can be found in the Supplementary text (Fig. S3).

Rock samples were crushed using standard procedures (jaw crusher, ring mill) and sieved to <500 μm. Zircons were concentrated using conventional techniques (panning, heavy liquids, magnetic separation) and hand-picked under a binocular microscope. Selected grains were subsequently cast in epoxy resin and polished to expose their interiors. The internal structures were characterized by back-scattered electron (BSE) and cathodoluminescence (CL) imaging using (i) a Jeol JSM-6400 SEM at the Ecole des Mines de St-Etienne for BSE and (ii) a Jeol JSM-5910 SEM at the Laboratoire Magmas et Volcans (Clermont-Ferrand) for CL.

U–Pb geochronology was conducted by in-situ laser ablation inductively coupled plasma mass spectrometry (LA–ICP–MS) at Géosciences Rennes using a ESI NWR193UC Excimer laser coupled to a quadrupole Agilent 7700x ICP-MS equipped with a dual pumping system to enhance sensitivity. The instrumental conditions are reported in Table S3.

The ablated material was carried into helium, and then admixed with nitrogen (Paquette et al., 2014) and argon, before injection into the plasma source. The alignment of the instrument and mass calibration was performed before each analytical session using the NIST SRM 612 reference glass, by inspecting the ^{238}U signal and by minimizing the ThO^+/Th^+ ratio (<0.5%). During the course of an analysis, the signals of ^{204}(Pb + Hg), ^{206}Pb, ^{207}Pb, ^{208}Pb and ^{238}U masses are acquired. The occurrence of common Pb in the sample can be monitored by the evolution of the ^{204}(Pb + Hg) signal intensity, but no common Pb correction was applied owing to the large isobaric interference with Hg. The ^{235}U signal is calculated from ^{238}U on the basis of the ratio $^{238}U/^{235}U = 137.88$. Single analyses consisted of 20s of background integration followed by 60s integration with the laser firing and then a 10 s wash-out delay. Ablation spot diameters of 20–35 μm with repetition rates of 3 Hz were used depending on the grain size. Data were corrected for U–Pb and Th–Pb fractionation and for mass bias by standard bracketing with repeated measurements of the GJ-1 zircon standard (Jackson et al., 2004). Along with the unknowns, the zircon standard Plešovice (337.13 ± 0.37 Ma, Sláma et al. (2008)) was measured to monitor accuracy of the analyses and produced a Concordia age of 337.0 ± 1.8 Ma (N = 20, $MSWD_{C+E} = 0.21$). Data reduction was carried out with the GLITTER® software package developed by the Macquarie Research Ltd. (Van Achterbergh et al., 2001). Concordia ages and diagrams were generated using Isoplot/Ex (Ludwig, 2008). Further information on the protocol can be found in Ballouard et al. (2015). The full set of results is available as Supplementary material (Tables S4 for standards and S5 for samples).

3.3. Zircon Lu–Hf isotope determination

Measurements were performed on magmatic zircons previously analyzed for U–Pb dating at GUF, using a Thermo-Finnigan Neptune multicollector ICP-MS attached to a Resolution M-50193 nm Ar–F excimer laser ablation system, equipped with a two-volume Laurin Technic ablation cell. Laser spots with diameters of 40 or 60 μm were drilled "on top" of the existing spots already analyzed for U–Pb dating or in the same domain as identified on the basis of CL images (Fig. 5), with repetition rates of 4 Hz and an energy density of 5 to 6 $J \cdot cm^{-2}$. He was used as a carrier gas (~0.6 $L \cdot min^{-1}$) and make-up gas consisting of high-purity Ar (~0.75 $L \cdot min^{-1}$) and N_2 (~0.07 $L \cdot min^{-1}$) was admixed to the carrier gas to improve sensitivity. Post-ablation homogenization is performed by fluxing the gases through a Resolution Instruments Squid® tubing. Data were acquired using multi-collector static mode, during 58 s of measurement characterized by 1.052 s integration time (55 baseline-corrected ratios). ^{172}Yb, ^{173}Yb and ^{175}Lu masses were monitored to allow the correction of isobaric interferences (^{176}Yb and ^{176}Lu on ^{176}Hf). Instrumental mass bias for Yb isotopes (calculation of β^{Yb}) was monitored for each measurement using an exponential law, and corrected to the natural ratio $^{172}Yb/^{173}Yb = 1.35351$. Mass fractionation of Lu isotopes was assumed identical to that of Yb isotopes ($\beta^{Lu} = \beta^{Yb}$). The isobaric interferences were subsequently corrected to mass bias-corrected $^{176}Yb/^{173}Yb = 0.79502$ and $^{176}Lu/^{175}Lu = 0.02656$ (see Gerdes and Zeh, 2006). Mass bias for Hf isotopes (β^{Hf}) was determined using an exponential law and normalized to $^{179}Hf/^{177}Hf = 0.7325$. Accuracy and external reproducibility of the method were controlled by repeated analyses of reference zircon standards GJ-1 (Jackson et al., 2004; Morel et al., 2008), Plešovice (Sláma et al., 2008), and Temora (Woodhead et al., 2004) (see Table S6 for results on the standards). The quoted uncertainties on $^{176}Hf/^{177}Hf$ ratios and εHf(t) are quadratic additions of within-run precision of each measurement with the external reproducibility (2 S.D.) of the reference zircon standard GJ-1 (~70 ppm). Data reduction was carried out using an in-house MS Excel© spreadsheet (Gerdes and Zeh, 2006, 2009).

Calculation of initial $^{176}Hf/^{177}Hf$ ratios was performed using the individual $^{176}Lu/^{177}Hf$ ratio of each measurement, a decay constant of $\lambda^{176}Lu = 1.867 \times 10^{-11}$ (Scherer et al., 2001; Söderlund et al., 2004) and the emplacement age obtained by U–Pb zircon dating. For the calculation of the εHf(t), parameters of the chondritic uniform reservoir (CHUR) recommended by Bouvier et al. (2008) were used ($^{176}Lu/^{177}Hf = 0.0336$; $^{176}Hf/^{177}Hf = 0.282785$). Two-step depleted mantle (DM) Hf model ages (T^C_{DM2}) were calculated using a DM model considering linear regression from present-day depleted mantle as recommended by Griffin et al. (2002), i.e. $^{176}Lu/^{177}Hf = 0.0384$ and $^{176}Hf/^{177}Hf = 0.28325$, and an average $^{176}Lu/^{177}Hf$ of 0.0113 for the crustal reservoir.

4. Results

4.1. Geochemistry

Regardless of the rock type, samples from the VOF are all very silicic (SiO_2 > 68 wt%) and have a granitic (s.s.) composition (Fig. 6a). More specifically, they show high A/CNK (1.05 to 1.4) and A/NK (1.1 to 1.6) implying that their protoliths are peraluminous granites (Fig. 6b). The very high values displayed by some samples (A/CNK in the range 1.4

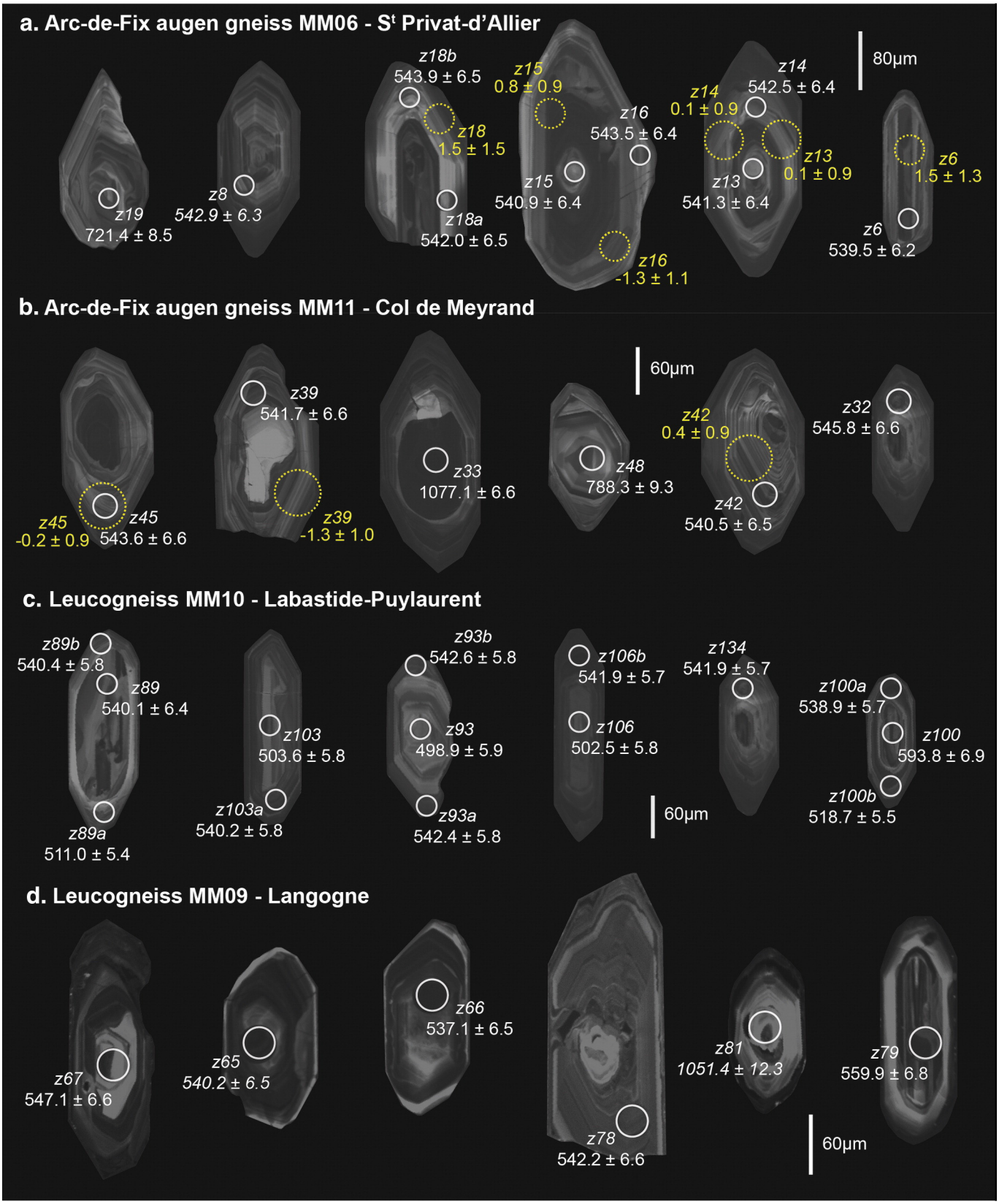

Fig. 5. Representative cathodoluminescence images of zircon grains from samples of the Velay Orthogneiss Formation. The locations of laser spots (white and yellow circles for U–Pb and Lu-Hf analyses respectively) are indicated along with the spot name (zXX). The corresponding $^{206}Pb/^{238}U$ dates are quoted with ±2σ uncertainty, in Ma. All displayed analyses are concordant at >98% (except those in italic). Hf isotope data are reported using the εHf calculated at the emplacement age of the corresponding sample, quoted with ±2σ uncertainty.

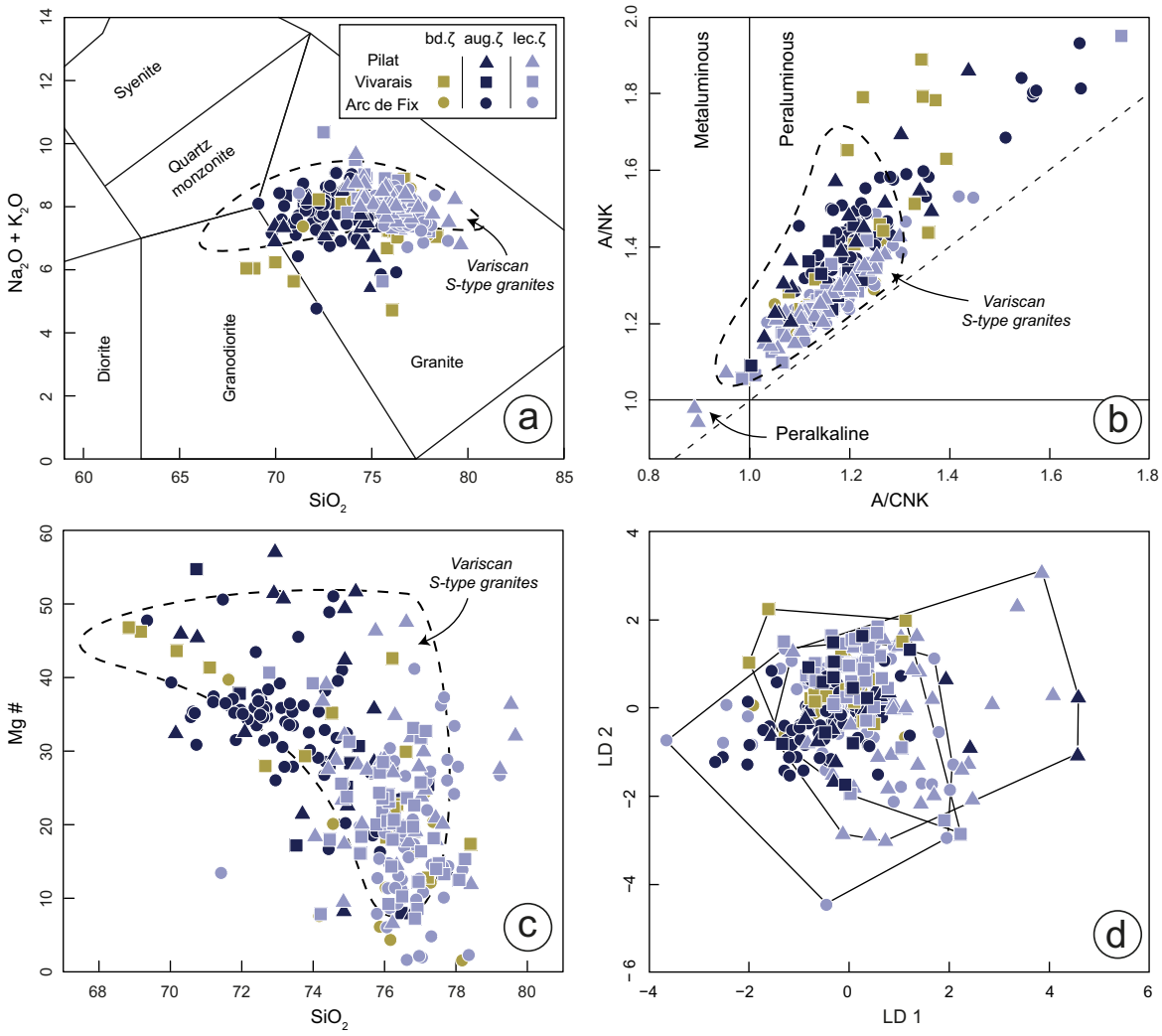

Fig. 6. Major elements compositions of samples from the Velay Orthogneiss Formation: (a) $Na_2O + K_2O$ vs. SiO_2 Middlemost's classification diagram (Middlemost, 1994); (b) A/CNK vs. A/NK Shand's diagram (Shand, 1943); (c) Mg# vs. SiO_2. All diagrams were plotted using the GCDkit software (Janoušek et al., 2006); (d) Results of linear discrimination analysis (LDA). More than 80% of the data are indistinguishable from one another. Data for Variscan S-type granites are from Moyen et al. (2017).

to 1.8) probably reflect alkali losses during amphibolite-facies metamorphism (not identified by the abovementioned filtering procedure, see Section 3.1). Mg# is highly scattered (2 to 60, Fig. 6c). Leucogneisses are SiO_2 richer (>74 wt%) and have lower and variable Mg# (<30) compared to augen gneisses (SiO_2 = 69–75 wt.%; Mg# = 30–55). Banded gneisses span in composition between those two endmembers. As a whole, VOF compositions remarkably mimic that of Variscan S-type granites from the eastern Massif Central (Fig. 6a,b,c). We investigated possible systematic differences between the three domains (Pilat, Arc-de-Fix and Vivarais) of the VOF. We used linear discrimination analysis (LDA) on major elements, a statistical tool calculating the linear combination of variables that maximizes the difference between three previously defined sets of data (Fig. 6d). LDA was computed using the open-source R language (Ihaka and Gentleman, 1996) and the package MASS (Venables and Ripley, 2002). We followed the method of Aitchison (1986) and implemented the compositional variables X (Al_2O_3, MgO, FeO_t, TiO_2, CaO, Na_2O, K_2O) as $\log(X/SiO_2)$ ratios. No systematic difference is observed and samples from all three regions have statistically similar major elements compositions.

Like for major oxides, trace element compositions of VOF samples are very homogeneous between the three domains (Fig. 7). Augen gneisses show a slight enrichment in Light Rare Earth Elements (La/Yb: mostly 6–14), flat Heavy Rare Earth Elements patterns (Dy/Yb: 1.3–3) together with a negative Eu anomaly (Fig. 7a). Leucogneisses are less enriched in LREE (La/Yb: mostly 2–6), have similar HREE patterns and a more pronounced Eu anomaly (Fig. 7a). Banded gneisses seem significantly depleted in HREE compared to the other lithologies (La/Yb: 25 to 50), but this difference may not be statistically significant given that trace elements are only available for two samples. All rock types have multi-element patterns characterized by significant negative Ba–Sr, Nb–Ta and Ti anomalies and positive Pb and U anomalies (Fig. 7b). As a whole leucogneisses are depleted in all incompatible elements compared to augen gneisses with the exception of Nb–Ta (constant) and Rb–U (enriched in the leucogneisses).

4.2. U–Pb dating

4.2.1. Zircon textures

Fig. 5 shows representative CL images of zircon crystals from the investigated VOF samples. Zircon grains are idiomorphic to sub-idiomorphic, display aspect ratios between 1.5 and 3.5 and show well-developed pyramidal tips (Fig. 5a,b). Grains range in size from 200 to 350 μm in augen gneisses and are notably smaller in leucogneisses (150–250 μm). Core–rim relationships are commonly observed (Fig. 5). They often consist of CL-dark or bright sub-idiomorphic to rounded cores, mantled by a rim showing typical oscillatory zoning. A careful examination of CL images reveals the existence of small textural discontinuities in such oscillatory zoning, with truncations and irregular

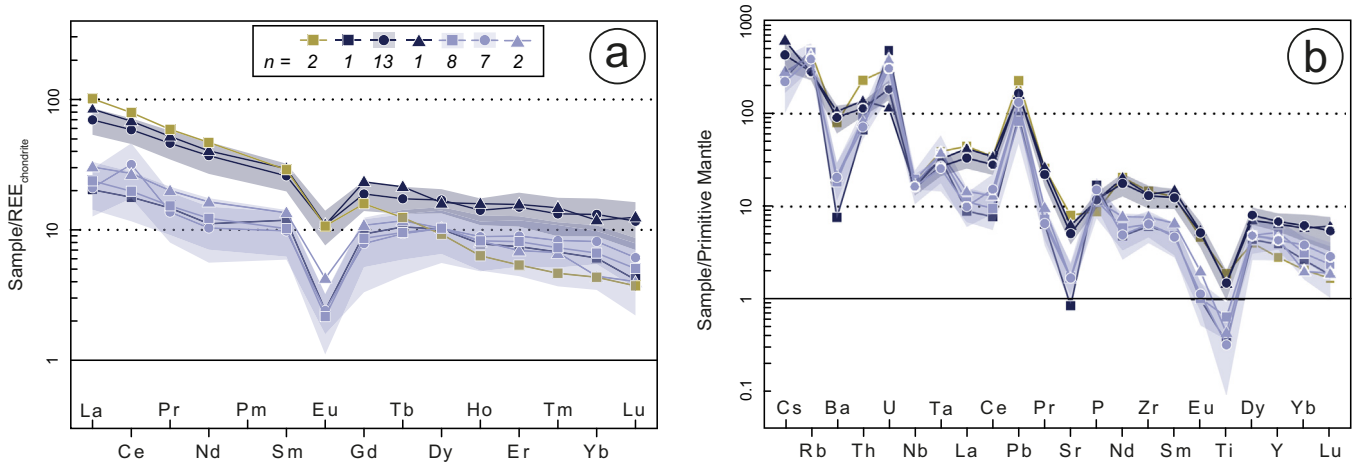

Fig. 7. Average trace-elements compositions of rocks from the Velay Orthogneiss Formation: (a) Rare Earth Elements patterns normalized to the chondrite (Boynton, 1984); (b) Coryell-Masuda diagram normalized to the Primitive Mantle (McDonough and Sun, 1995). Same legend as Fig. 4. The shaded areas correspond to 1 S.D. (standard deviation).

surfaces being common. Finally, few grains display very CL-bright narrow (<10 μm) rims (see Fig. 5d).

4.2.2. Sample MM06

This sample is a typical "Arc-de-Fix" augen gneiss collected from the cliff along the RD40 road below the village of S^{t}-Privat-d'Allier (Figs. 2 and 4a). Twenty-six analyses were performed on 24 zircon grains. Three cores yield concordant Neoproterozoic $^{238}U/^{206}Pb$ dates at 559.7 ± 13.4, 660.3 ± 15.2 and 721.4 ± 16.9 Ma respectively (errors quoted at 2σ, Table S5). Plotted in the Tera-Wasserburg diagram, 21 analyses from rims or grains devoid of any core trend along a mixing line between radiogenic and common Pb compositions. This trend has a lower intercept at 540.5 ± 3.2 Ma (MSWD = 0.26) and an identical Concordia date of 541.8 ± 3.1 Ma ($MSWD_{C+E}$ = 0.34, Fig. 8a) is calculated out of the 16 statistically equivalent concordant analyses. Two spots (z10 and z20) have $^{206}Pb/^{238}U$ dates of *c.* 510 Ma that are statistically different from those of the main population, and were therefore not included in the calculation. There is no systematic relationship between $^{238}U/^{206}Pb$ dates and Th/U ratios which range between 0.02 and 0.64. This observation is also valid for the three other samples.

4.2.3. Sample MM11

Sample MM11 is an augen gneiss collected at the "Col de Meyrand" (Fig. 4a). Out of 28 analyses, 7 correspond to zircon cores. Five yielded concordant Neoproterozoic $^{206}Pb/^{238}U$ dates ranging from 580.7 ± 14.1 Ma (z30) to 1077.1 ± 25.0 Ma (z33) and two discordant $^{207}Pb/^{206}Pb$ dates of 860 Ma and 2100 Ma (Fig. 8b). In the Tera-Wasserburg diagram, a total of 18 spots from zircon rims and core-free grains define a trend with a lower intercept at 541.2 ± 3.6 Ma (MSWD = 0.34), which slope is mostly controlled by discordant spot z38. Excluding the latter and the slightly discordant spot z44, an identical Concordia date of 542.5 ± 3.1 Ma ($MSWD_{C+E}$ = 0.43, Fig. 8b) can be calculated out of 16 analyses. Three spots yielded significantly younger $^{206}Pb/^{238}U$ dates (two are discordant and one concordant with a $^{206}Pb/^{238}U$ date of 502.6 ± 12.1 Ma) that were thus not included in the calculations.

4.2.4. Sample MM10

MM10 is a leucogneiss collected at the "Pont-du-Bon-Dieu" along the RD6 road south of Labastide-Puylaurent. It features an intricate association with mylonitic augen gneiss (see Fig. 4d). Sixty-five analyses were performed, out of which 12 spots on zircon cores gave concordant Neoproterozoic $^{206}Pb/^{238}U$ dates ranging from 560.3 ± 13.2 Ma (z88) to 657.8 ± 14.5 Ma (z136) and 805.8 ± 17.5 Ma (z137) to 921.7 ± 20.6 Ma (z130, Table S5). Three discordant analyses, also from zircon cores, yielded older Paleoproterozoic $^{207}Pb/^{206}Pb$ dates of 1600, 1900 and 2400 Ma. Twenty-eight spots from zircon rims or grains without cores trend along a mixing line between radiogenic and common Pb with a lower intercept at 540.7 ± 2.7 Ma (MSWD = 0.11). Considering the concordant analyses only (n = 26), a Concordia date of 541.4 ± 2.3 Ma ($MSWD_{C+E}$ = 0.38, Fig. 8c) can be calculated. Thirteen concordant spots have $^{206}Pb/^{238}U$ dates ranging between 523.4 ± 11.1 Ma and 482.4 ± 11.1 Ma. Those were not included in the calculations because as argued below (see Section 5.1), they would correspond to radiogenic Pb loss from the main population at c. 541 Ma.

4.2.5. Sample MM09

Sample MM09 is a leucogneiss boudin stretched within an augen gneiss matrix and exposed along the D906 road south of Langogne (Fig. 4b). Out of 25 analyses, 3 correspond to zircon cores: one displays a concordant $^{206}Pb/^{238}U$ date of 686.7 ± 16.3 Ma and two show similar discordant Paleoproterozoic $^{207}Pb/^{206}Pb$ dates of 1700 Ma (Table S5). From the remaining data obtained on rims and core-free zircons, nine concordant spots define a Concordia date of 545.9 ± 4.3 Ma ($MSWD_{C+E}$ = 1.05, Fig. 8d); the rest of the data show younger $^{206}Pb/^{238}U$ dates and are notably discordant, with the exception of two concordant spots having $^{206}Pb/^{238}U$ dates of 509.9 ± 12.2 Ma and 516.7 ± 12.4 Ma respectively.

4.3. Lu – Hf isotope data

Zircon Lu-Hf analyses obtained for augen gneisses MM06 and MM11 are displayed in Table S6. Only magmatic zircon grains and rims were analyzed. Therefore, initial Hf isotope compositions were calculated using the intrusion age determined for each sample (see Section 4.2). The $^{176}Hf/^{177}Hf(t)$ ratios of magmatic zircons from augen gneiss MM06 range from 0.282376 ± 0.000023 to 0.282487 ± 0.000036 (2 S.E. – standard error), corresponding to εHf(t) of –2.4 to 1.6 with a chondritic average value of −0.2 ± 2.9 (2 S.D. – standard deviation; Fig. 9a and Table 1). Augen gneiss sample MM11 shows a tighter range of zircon $^{176}Hf/^{177}Hf(t)$, from 0.282407 ± 0.000027 to 0.282462 ± 0.000025 (2 S.E. – standard error) equivalent to εHf(t) of –1.3 to 0.7 (Fig. 9a) and yielding an identical average εHf(t) at −0.2 ± 1.2 (2 S.D. – standard deviation; Table 1).

5. Discussion

5.1. Interpretation of the U–Pb data and orthogneisses emplacement ages

All investigated samples are characterized by a largely dominant population of zircon grains having statistically equivalent and concordant

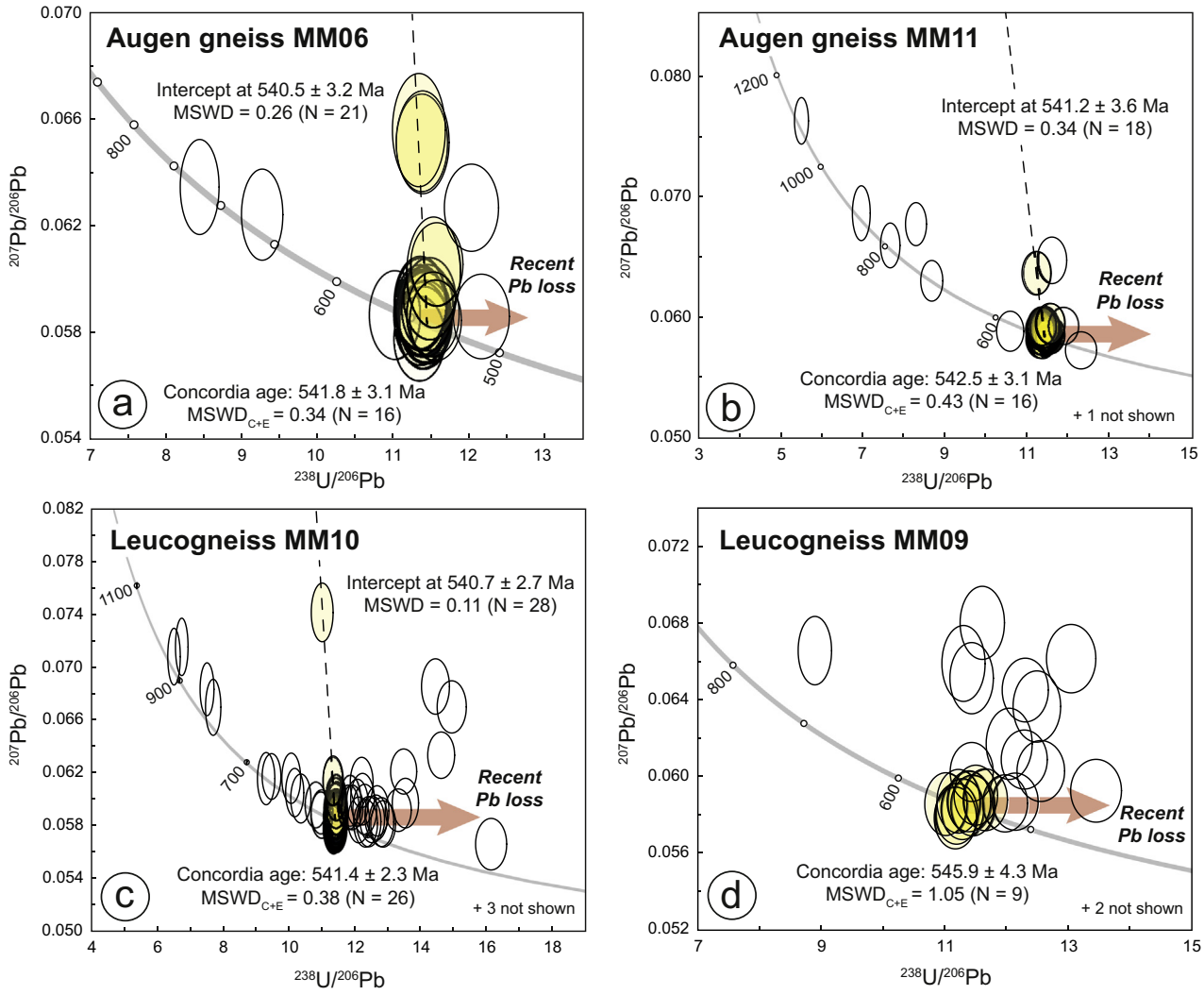

Fig. 8. Tera-Wasserburg diagrams (^{238}U/^{206}Pb vs. ^{207}Pb/^{206}Pb) showing zircon data from the Velay Orthogneiss Formation samples investigated in this study. Error ellipses and ages are displayed/quoted at 2σ level of uncertainty. Yellowish ellipses are those included in age calculations.

^{206}Pb/^{238}U dates between 550–540 Ma, which we interpret as the crystallization ages of the VOF granitic protoliths. This interpretation is supported by (i) the fact that these data were obtained on zircon rims or grains devoid of any core; (ii) the typical magmatic oscillatory zoning showed by the analyzed domains (Fig. 7); and (iii) the well-developed {211} pyramids of these crystals, which are characteristic of zircon grown in peraluminous granitic magmas (Belousova et al., 2006; Pupin, 1980), in line with whole–rock geochemistry of the investigated samples (Fig. 5b).

From this perspective, we interpret the 28 analyses obtained from zircon cores, showing notably older ^{238}U/^{206}Pb dates (from 560 Ma up to 1100 Ma, 75% of which being >95% concordant), as reflecting zircon inheritance from the source of these (meta)granites or xenocrysts sampled from the country-rocks during magma ascent and emplacement. The presence of these inherited cores and xenocrysts is significant because they occur in all of the four investigated samples (Fig. 8) and represent a non-negligible proportion of the dataset (ca. 19%). In addition, CL images hint the presence of more small, strongly resorbed or irregular cores (see Fig. 7c close to z134 or 7d close to z78) that could not be analyzed by LA-ICP-MS.

A significant amount of zircon analyses (including 17 concordant ones) show ^{206}Pb/^{238}U dates younger than the 550–540 Ma crystallization age, in the range 523 to 482 Ma. These are well represented in the leucogneiss samples (Fig. 8), particularly MM10 (Fig. 8c). We argue that these dates do not correspond to any geological event but rather result from recent radiogenic Pb loss affecting the main, 545–540 Ma-old zircon population. Firstly, these dates are often associated with incoherent core–rim relationships (cores having younger ^{238}U/^{206}Pb dates than their associated rims, see for instance zircons 93, 103 and 106, Fig. 7c). Second, recent Pb loss is represented by horizontal lines in the Tera-Wasserburg diagram because it does not affect ^{207}Pb/^{206}Pb ratios (Fig. 8c). The weak curvature of the Concordia at Paleozoic times implies that the Discordia and Concordia curves are nearly parallel so that any *c.* 540 Ma-old zircon having experienced a limited Pb loss would still be sub-concordant within uncertainty.

Following the abovementioned interpretations, the igneous protoliths of all the investigated VOF samples show overlapping emplacement ages of c. 542 Ma, at the Ediacaran/Cambrian boundary (541 ± 1 Ma, Finney et al., 2013). This age is close to, yet significantly older than the Cambrian Rb/Sr date of 528 ± 9 Ma obtained by R'Kha Chaham et al. (1990) on Arc de Fix augen gneisses. It complies with the zircon Pb evaporation age of 533 ± 22 Ma (Mougeot et al., 1997) and the chemical U–Th–Pb monazite date of 543 ± 25 Ma (Be Mezeme et al., 2006) both obtained on unmolten to anatectic Arc de Fix augen gneisses. It is also identical to the whole-rock Rb–Sr age of 545 ± 14 Ma determined by Caen-Vachette (1979) for the Pilat leucogneisses.

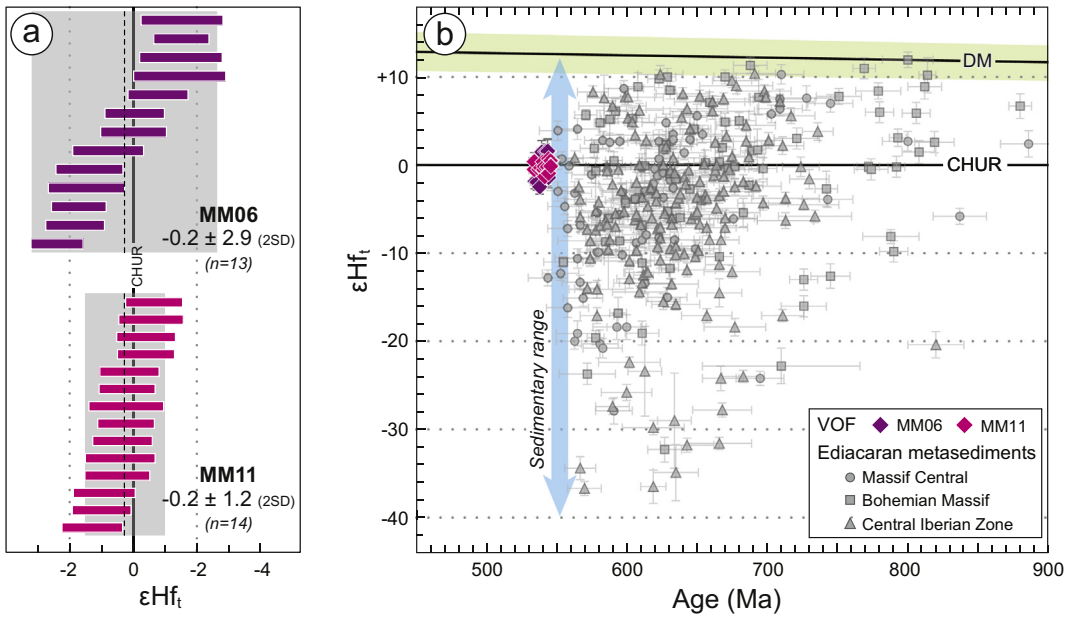

Fig. 9. (a) Measured εHf(t) on magmatic zircon grains and rims from the two investigated samples of augen gneisses of the Velay Orthogneiss Formation (VOF). (b) Zircon εHf(t) vs. age diagram for the two VOF samples and a compilation of data from detrital zircon in regional Ediacaran metasediments (n = 371), regarded as the potential source of the peraluminous magmas from which the VOF protoliths derive. Data from the French Massif Central (Chelle-Michou et al., 2017), the Bohemian Massif (Linnemann et al., 2014) and the Iberian Massif (Orejana et al., 2015; Teixeira et al., 2011). The εHf(t) range for the depleted mantle reservoir is bracketed by the models of Naeraa et al. (2012) (lowermost value) and Griffin et al. (2002) (uppermost value).

5.2. Petrogenesis of the magmatic suite

The VOF samples display remarkable geochemical homogeneity, regardless of their geographic provenance. Their composition is consistent with the chemistry of peraluminous S-type granites (see Fig. 6). Moreover, zircon grains from augen- and leucogneisses have similar, low aspect ratios which comply with a plutonic origin for the protoliths of both rocks (Corfu et al., 2003), and morphologies typical of crystals formed in S-type granitic magmas (Belousova et al., 2006; Pupin, 1980) (Fig. 5). Furthermore, the obtained emplacement ages for the four samples (545–540 Ma) are overlapping within analytical uncertainties. All these lines of evidence indicate that the VOF represents a former, large S-type granitic batholith emplaced at the Ediacaran/Cambrian boundary that was subsequently deformed and dismembered by Variscan tectonics. The aim of this section is to characterize its petrogenesis.

Given the narrow range of silica contents (mostly 70–76 wt%) and the apparent similar chemical composition of investigated samples, we plotted the geochemical data using the principal component approach. This procedure helps pinpointing petrogenetic trends (Buccianti and Peccerillo, 1999; Janoušek et al., 2004). Principal components were calculated using the internal routine of the GCDkit software (Janoušek et al., 2006) after recasting the chemical compositions to 100% in the system SiO_2–Al_2O_3–MgO–FeO–TiO_2–CaO–Na_2O–K_2O. The first three principal components account for 86% of the cumulative variance of the system. As principal component 1 (P.Comp$_1$) mostly opposes silica vs. compatible elements contents (MgO, FeO, TiO_2, CaO), the most silicic rocks (i.e., the leucogneisses) feature high P.Comp$_1$ values (Fig. 10). Similar to trends observed in major elements diagrams, the banded gneisses' compositions spread between an augen gneiss and a leucogneiss endmember.

5.2.1. Source of the magmatic suite

The complete absence of mafic or even intermediate meta-igneous rocks in the VOF together with the observation of inherited zircon cores in the dated samples precludes the formation of the magmatic suite by fractionation of mantle-derived magmas. This absence rather suggests that the granitic magmas originated from melting of pre-existing crustal lithologies. The low CaO contents (0.2–1.5 wt%) displayed by samples from the VOF discard amphibole-rich mafic rocks as a potential source material (Coldwell et al., 2011; Sisson et al., 2004), such that meta-sediments and meta-intermediate to felsic igneous rocks are most adequate as potential sources.

Fig. 11 compares the composition of VOF samples to primary liquids formed by melting of a range of meta-sedimentary and meta-igneous crustal lithologies. Relevant melting conditions correspond to a range of crustal pressures from 3 to 15 kbar and temperatures <900 °C in agreement with (i) the absence of magmatic orthopyroxene in the investigated suite (Frost and Frost, 2008); (ii) first-order estimates given by zircon saturation thermometry, the persistence of inherited zircon cores in the dated samples indicating *maximum* magma temperatures of 780 ± 15 °C upon emplacement (calculated with the equation of Boehnke et al. (2013)) and therefore, melting temperatures that cannot have been in excess of 840–885 °C considering a maximum melting pressure of 15 kbar and reasonable adiabats (i.e. between 4 and 7 °C/kbar; Annen et al., 2006; Clemens et al., 1997; Holtz and Johannes, 1994). Experimental melt compositions are projected on the principal component framework determined from statistical analysis of the VOF samples (Fig. 10). The considered experimental studies together with respective starting materials and P–T conditions are summarized in Table 2.

Clearly, tonalites and metaluminous granodiorites are inappropriate source rocks because melts derived from those lithologies have respectively lower Mg# (Fig. 11f) and/or lower K_2O/Na_2O (Fig. 11h) than natural samples. Peraluminous granodiorite melts display more adequate compositions but can only account for a small part of the natural samples variability centered on P.Comp$_1$ ~ 0 (Fig. 11). By contrast, melting of quartz-rich to quartz-poor pelites, greywackes and volcanoclastic rocks generates a range of primary melt compositions that fairly reproduce the compositional scatter of the augen- and part of the banded gneisses, i.e. samples with $-4 <$ P.Comp$_1$ < 0.5. This is in line with the VOF samples displaying a geochemical affinity to S-type granites (see Fig. 6) that derive from melting of such lithologies (Chappell and White, 2001). Therefore, it is reasonable to consider that the granitic protoliths of augen- and banded gneisses from the VOF represent liquids which originated from melting of a heterogeneous sedimentary

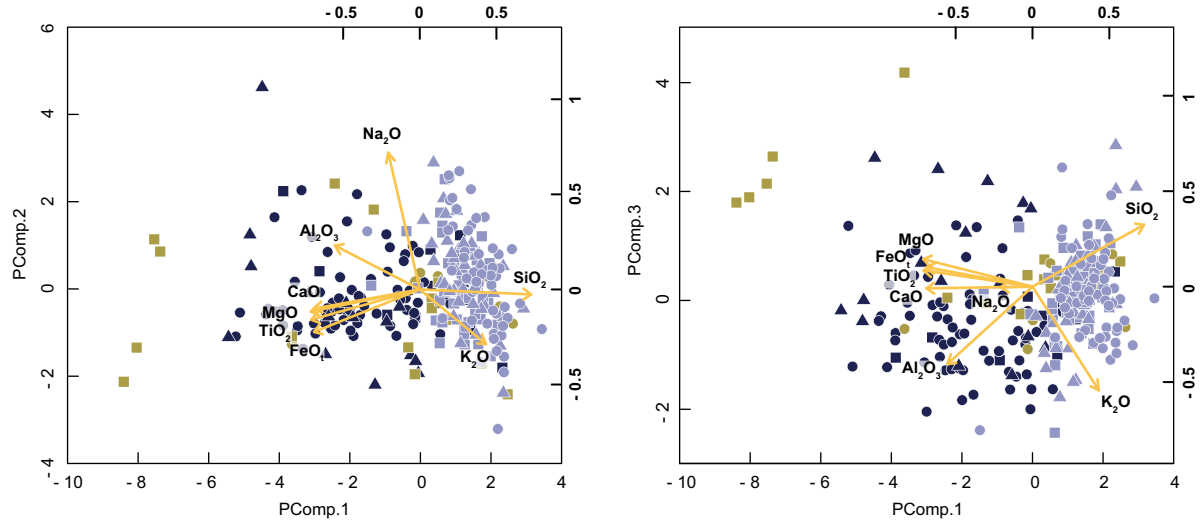

Fig. 10. Binary diagrams of the first three principal components calculated for the VOF samples. Scaled correlation matrix is displayed in bold. Same legend as Fig. 4. PComp.1 = 0.418 SiO_2 – 0.408 TiO_2 – 0.319 Al_2O_3 – 0.397 FeO_t – 0.409 MgO – 0.397 CaO – 0.118 Na_2O + 0.248 K_2O. PComp.2 = –0.183 TiO_2 + 0.266 Al_2O_3 – 0.258 FeO_t – 0.134 MgO – 0.116 CaO + 0.829 Na_2O – 0.332 K_2O. PComp.3 = 0.417 SiO_2 + 0.11 TiO_2 – 0.523 Al_2O_3 + 0.131 FeO_t + 0.185 MgO – 0.699 K_2O.

sequence at 750 < T < 900 °C and 3 < P < 15 kbars. This is consistent with the wide range of inherited zircon ages, scattering from 560 to 1100 Ma (Fig. 8), which points to an Ediacaran depositional age for the source sediments.

Importantly, leucogneiss samples (with $P.Comp_1 > 0.5$) clearly differ from any investigated experimental melt composition. Two non-exclusive scenarios may account for their origin: (i) leucogneisses derive from source materials and/or at P–T conditions not represented in our database; or (ii) they result from fractionation of the granitic magmas at the origin of augen- and banded gneisses with $P.Comp_1 < 0.5$. The first hypothesis is unlikely, since the range of investigated source materials (Table 2) is fairly representative of the most common felsic sources in the crust, and the investigated temperature range (680–900 °C) encompasses a wide domain of melting conditions, from water-present melting (c. 650–700 °C) to muscovite dehydration melting (c. 720–750 °C) and biotite dehydration melting (c. 850–875 °C). The feasibility of the fractionation hypothesis is tested hereafter.

5.2.2. Leucogneiss petrogenesis

In this section, we investigate whether leucogneisses could be derived from fractionation of the magma at the origin of the augen gneisses. Fig. 12a and b depicts the chemical evolution of a magma fractionating minerals typically found in peraluminous S-type granites: K-feldspar, oligoclase, biotite, muscovite, cordierite, garnet (Bea et al., 1994; Tartèse and Boulvais, 2010). Fractionation vectors are calculated using mass balance for major elements, and Rayleigh-type fractionation together with partition coefficients for traces (cordierite could not be modeled for traces due to the lack of available partitioning data). In terms of major elements, fractionation of an augen gneiss-like liquid to a leucogneiss composition cannot be driven by muscovite, nor K-feldspar, as both result in too high values for PComp.3 (Fig. 12b). Leucogneisses are better reproduced by concomitant fractionation of plagioclase and a ferromagnesian phase (biotite, garnet and/or cordierite, Fig. 12a,b). The low Ba-Sr contents displayed by leucogneisses can result from fractionation of either a K-feldspar dominated assemblage (however, this is ruled out by major elements), or a polymineralic assemblage comprising 40% biotite and 60% plagioclase (Fig. 12c). Fractionation of plagioclase is also in agreement with the more pronounced Eu anomaly displayed by leucogneisses (Fig. 6). The decrease in HREE and Y contents from augen gneisses to leucogneisses could result from fractionation of a small amount of garnet, zircon or xenotime (Bea, 1996). The same observation for LREE could originate from minor fractionation of apatite and/or monazite (Bea, 1996). As a result, fractionation of a Pl + Bt (+accessory phases) assemblage from an augen gneiss-like magma satisfactorily accounts for the composition of leucogneisses.

5.2.3. Emplacement depth

Leucogneisses are highly silicic (SiO_2 generally ranging between 74 and 77 wt.%), mostly contain quartz + feldspar, and, as demonstrated above, correspond to residual melts after fractionation of a Pl + Bt assemblage out of a magma similar to augen gneisses. Therefore, the leucogneisses compositions should be very close to that of the minimum or eutectic in the haplogranitic system. The position of this minimum/eutectic in the ternary Qz-Ab-Or diagram is a function of the water activity and the pressure of crystallization (Johannes and Holtz, 1996). At a given pressure, decreasing water activity (corresponding to H_2O-undersaturated melts) shifts the position of the minimum/eutectic towards the Qz-Or join keeping the normative Qz proportion constant (Johannes and Holtz, 1996). The latter is therefore strictly pressure-dependent and is an indicator of the pressure of magma crystallization. In this section, we aim at retrieving the depth of emplacement/crystallization of the batholith by comparing the compositions of leucogneisses to that of the haplogranitic minimum/eutectic as predicted by experimental data.

Experimental data on the Qz-Ab-Or-H_2O system have been compiled by Blundy and Cashman (2001). We projected natural leucogneiss compositions following the recommendations of the same authors by: (i) calculating the CIPW norm; (ii) correcting the effect of the normative component on the position of the natural melt in the ternary diagram. Only samples with measured Fe_2O_3/FeO ratios were retained (total of 66 analyses) to ensure calculation of accurate normative values. Leucogneisses from the VOF cluster around the minimal melt compositions expected at pressures of 0.5–2 kbars and water-saturated conditions ($a_{H2O} = 1$, Fig. 13). Few samples show higher Qz modal values which could result from limited sub-solidus chemical modifications or the presence of quartz veinlets.

Since leucogneisses and augen gneisses are intimately associated in the field (see Section 2.2), a pressure of crystallization for the whole batholith of 0.5–2 kbars can be inferred. This corresponds to depths of ~2 to 7 km and suggests that the VOF S-type granites emplaced at shallow crustal levels.

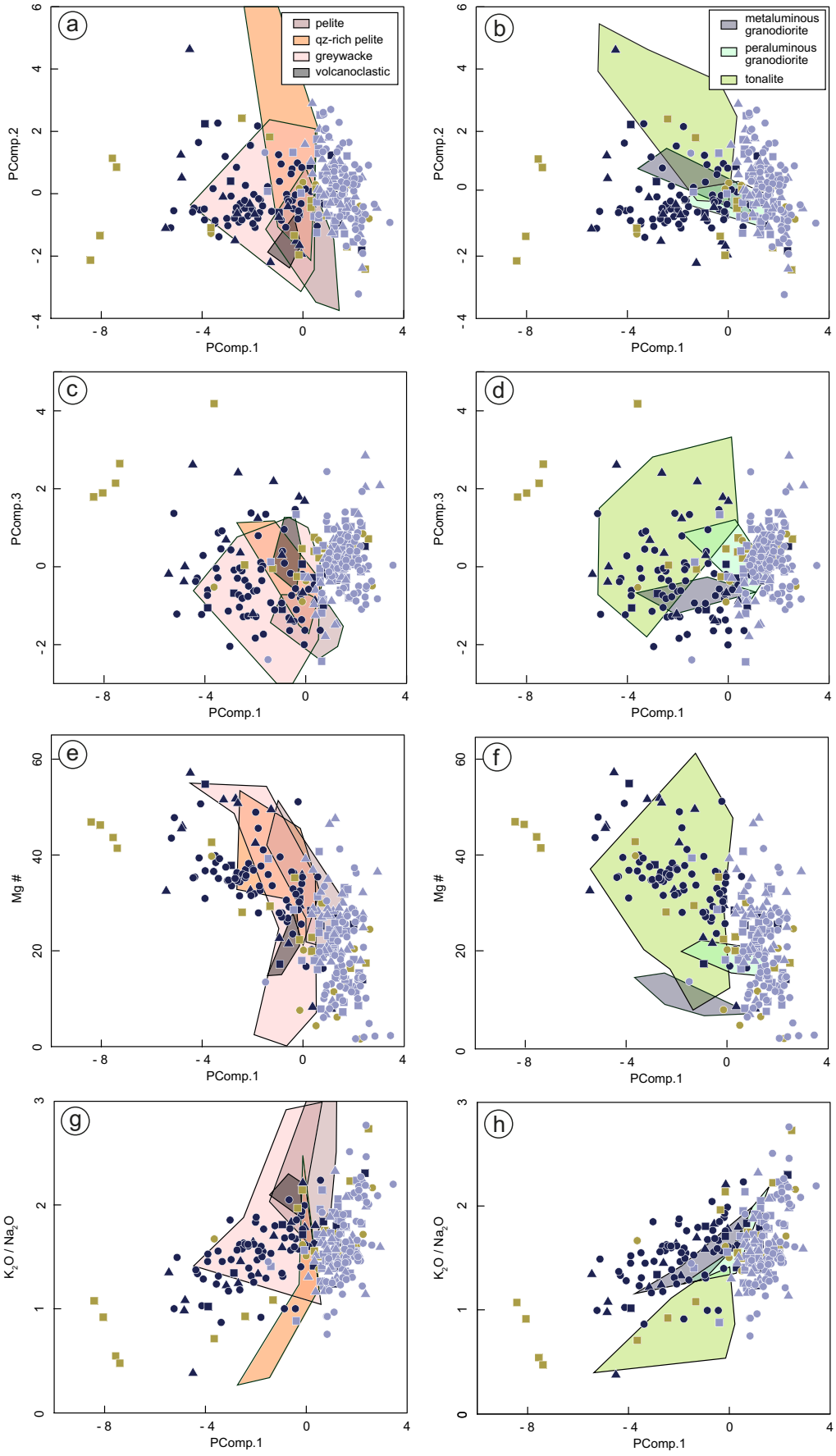

Fig. 11. Comparison between VOF samples and experimental melt compositions for a range of crustal sources (see Table 2). Experimental data are projected on the principal component framework. Same legend as Fig. 4.

Table 2
Experimental melts database used in this study. List of starting materials, pressures and temperatures of melting and associated references (available as Supplementary text).

Source rock	Reference	P (kbar)	T (°C)
Qz-rich pelite	Pickering and Johnson (1998), Patino-Douce and Harris (1998)	6–10	750–900
Pelite	Stevens (1995), Patino-Douce and Johnston (1991), Vielzeuf and Holloway (1988)	5–10	825–900
Greywacke	Patino-Douce and Harris (1998), Stevens (1995), Patino-Douce and Beard (1996), Montel and Vielzeuf (1997)	3–10	800–900
Metaluminous granodiorite	Bogaerts et al. (2006)	3.7–4.1	775–900
Peraluminous granodiorite	Holtz and Johannes (1991)	3–5	700–800
Tonalite	Watkins et al. (2007)	6–12	680–900
Metavolcanoclastic rock	Skjerlie and Johnson (1996)	10–15	850–900

5.3. Interpretation of Lu – Hf data

The εHf(t) variability within a given sample is small (<4 and even <2 εHf-units in MM11) and of the same order of magnitude than the analytical uncertainties (i.e. ± 1.1εHf-units), indicating that zircons crystallized from a magma with relatively homogeneous Hf isotope composition. Both samples reveal identical average εHf(t) clustering around the chondritic value, taken as representative of that of the magma at the time of crystallization.

Clearly, a chondritic mantle source for the magmas at the origin of the VOF must be discarded because geochemical data are rather in line with a sedimentary source (see Section 5.2.1). Accordingly, the chondritic value could originate from the melting of an isotopically homogeneous sedimentary reservoir that would itself rework continental crust extracted from the Depleted Mantle (DM) at ~1.3 Ga (calculated model age with a crustal $^{176}Lu/^{177}Hf$ of 0.0113, from Taylor and McLennan (1985)). However, there is no crust of that specific age in the north Gondwana margin, where crust production occurred

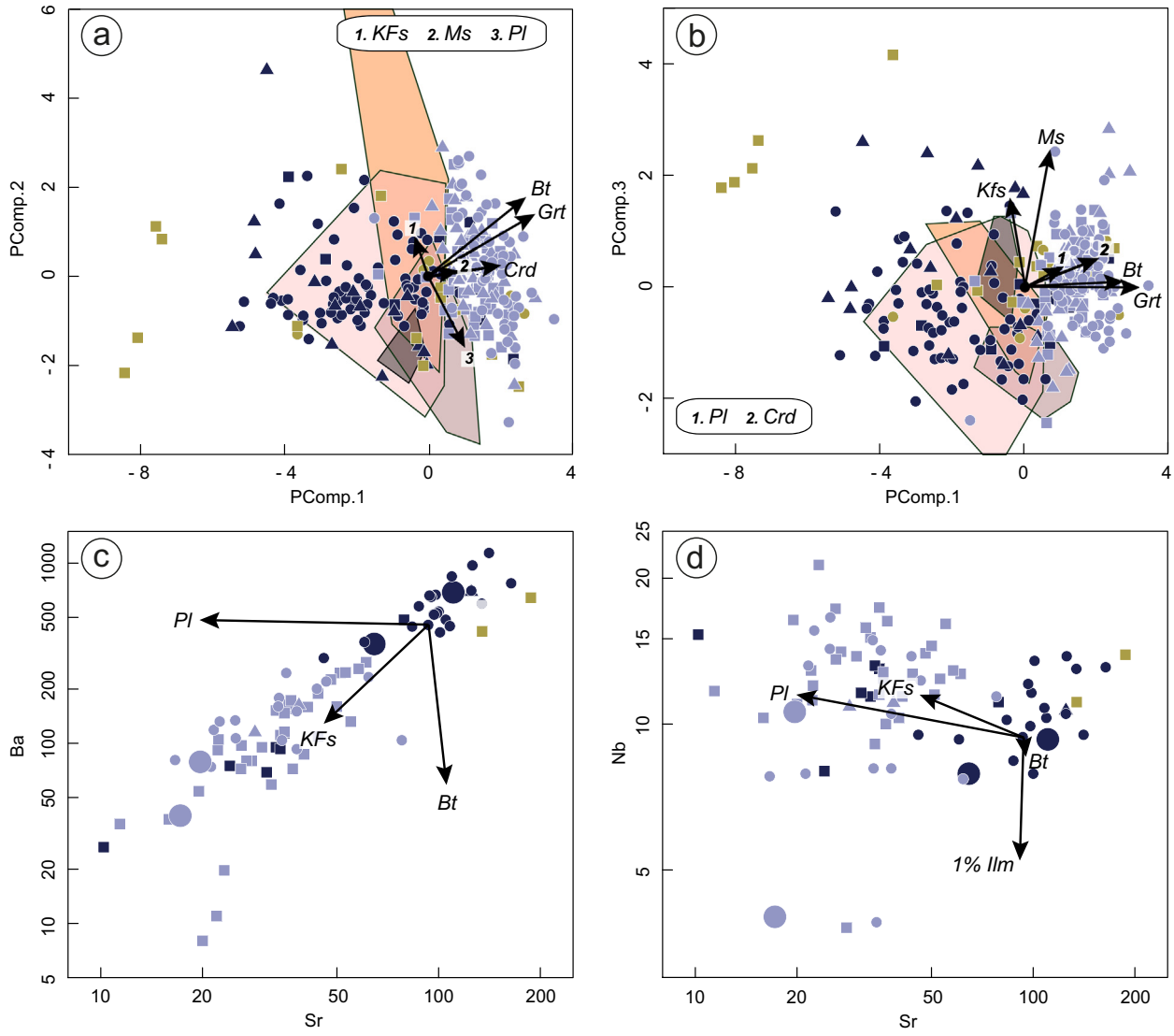

Fig. 12. (a) and (b) Major element compositions of fractionated melts. Each arrow shows the composition of a centroid melt ($P.Comp_1 = 0$) after 10% fractionation of the mentioned mineral phase. The melt composition in case of a poly-mineral fractionating assemblage can be graphically estimated by a linear combination of each vector. Generic mineral compositions are from Stevens et al. (2007). (c) and (d) Trace element compositions of fractionated melts. Each arrow depicts the composition of the melt after 20% (except mentioned value) fractionation of the mineral phase. The list of considered partition coefficients is available as Supp. Material (Table S8). Same legend as Fig. 4. Larger symbols correspond to dated samples.

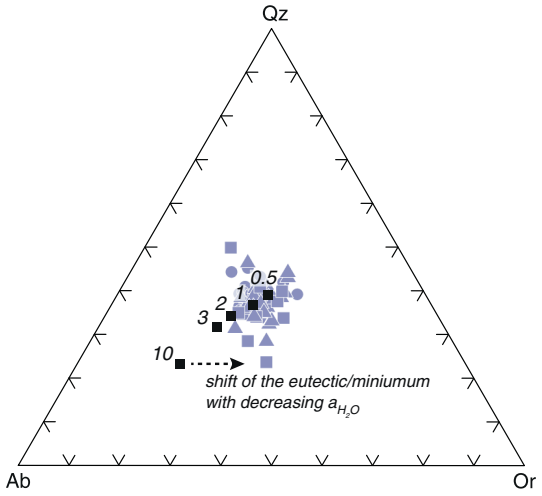

Fig. 13. Comparison of leucogneisses corrected normative compositions and experimental data on the H_2O-saturated Qz – Ab – Or system at different pressures (numbers in kbars). Minima/eutectics (black squares) as compiled by Blundy and Cashman (2001). Shift of minima/eutectic positions with decreasing water activity from Johannes and Holtz (1996).

in the Archean (2.5–3.3 Ga), Paleoproterozoic (1.8–2.2 Ga) and Neoproterozoic (0.6–0.7 Ga) (Gerdes and Zeh, 2006; Linnemann et al., 2014; Nance et al., 1991). As a result, the chondritic signature of the VOF parental magmas most probably stems from the melting of a sedimentary source composed of a mixture of the three above-mentioned reservoirs, including at least 50% of Neoproterozoic juvenile crust (as proposed for Variscan S-type granites from the same area (Moyen et al., 2017; Turpin et al., 1990). Ediacaran metasediments throughout the Variscan belt of Western Europe are characterized by a very large spread of detrital zircon εHf(t), specifically ranging from *c.* +10 down to *c.* −40 at 600 Ma (Fig. 9b), interpreted as reflecting the contribution of terrigenous material from both juvenile Neoproterozoic crust (such as the Arabian-Nubian Shield) and ancient, Paleoproterozoic to Archean crust from Gondwana (Chelle-Michou et al., 2017; Linnemann et al., 2014; Orejana et al., 2015). Therefore, the Ediacaran metasediments represent adequate sources for the VOF granites. The U–Pb dates of inherited zircons in the VOF samples strongly support this interpretation, since those are dominantly in the range 560–900 Ma (20 analyses out of 28, i.e. 71%) that is typical for detrital zircons in Ediacarian metasediments of the northern Gondwana margin (Chelle-Michou et al., 2017; Linnemann et al., 2014; Orejana et al., 2015; Teixeira et al., 2011; see also Fig. 8).

The Hf isotope homogeneity displayed by the parental magmas of the VOF (Fig. 9b) is rather uncommon for S-type granites, which magmatic zircons commonly show larger variations of εHf(t), most often of ~10 epsilon-units (Appleby et al., 2009; Farina et al., 2014; Teixeira et al., 2011; Villaros et al., 2012). Based on the natural case of the Cape Granite Suite in South Africa, Villaros et al. (2012) proposed that the Hf isotope scatter observed in S-type granites results from the dissolution at emplacement level of inherited detrital zircons in the melt phase. Such grains being isotopically disparate, their dissolution creates small-scale Hf isotopic heterogeneities captured by newly formed zircon when the melt crystallizes. However, Farina et al. (2014) showed that the cooling history of the magmatic body exerts a strong control on this process, with fast cooling rates (≥0.0125 °C/yr) leading to rapid zircon saturation. In that case, especially if some zircon has already been dissolved during melting and/or transport and the Hf isotopic composition was homogenized thereby, igneous zircons crystallized at the emplacement level would not show strong Hf isotope heterogeneities (i.e. about 1 εHf unit even though the initial inherited zircons showed compositional variation in excess of 10 εHf units; Farina et al., 2014). It is therefore likely that the parental magmas of the VOF experienced such a process, i.e. (i) inherited zircon dissolution during melting and/or ascent in the crust; (ii) coeval homogenization of Hf isotopic compositions in the melt; and (iii) limited further dissolution at the emplacement level (if any).

Liquids formed by melting of sedimentary lithologies at 750–850 °C can dissolve up to 115–390 ppm Zr (calculated using the equation of Boehnke et al., 2013 and the composition of experimental melts from the compilation presented in Table 2), which corresponds to 14 to 48% dissolution of detrital zircons present in the sedimentary source lithology, assuming a source composition of ca. 200 ppm Zr (close to the average composition of the upper crust, Rudnick and Gao, 2003), that all Zr is hosted in detrital zircons and an average melt fraction of ca. 25% (derived from experimental data listed in Table 2). Consistently, Zr concentrations in augen and banded gneisses from the VOF range mostly from ca. 50 to 180 ppm, indicating that they would have left the source in a Zr-undersaturated state after dissolution of maximum 6–23% detrital zircon (and probably much less, given the presence of inherited zircons in the VOF samples) using the same parameters as above. Close to their liquidus, the resulting melts would have readily undergone homogenization through advection and elemental/isotopic diffusion. Conversely, zircon saturation temperatures of the VOF samples are around 780 °C (see Section 5.2.1), meaning that they would have very rapidly reached saturation upon emplacement and cooling, especially considering that they emplaced at relatively shallow crustal levels (≤7 km, see Section 5.2.3). This would have indeed promoted fast cooling rates and in turn, limited dissolution (if any) of the remaining inherited zircon cores (Farina et al., 2014). All lines of evidence therefore suggest that the unusually homogeneous zircon Hf isotopic composition of the S-type VOF granites result from a combination of Zr-undersaturated conditions during melting and transport in the crust followed by early saturation upon emplacement owing to rapid cooling at shallow crustal levels.

5.4. Geodynamic setting of late Ediacaran magmatism in the French Massif Central

A compilation of available geochronological data (n = 74 dated samples) shows that pre-Variscan magmatism in the French Massif Central spanned over 150 Ma from the Ediacaran (c. 600 Ma) to the late Ordovician (c. 450 Ma) and possibly the Early Silurian (Fig. 14). The age pattern shows a bimodal distribution reflecting the existence of two pulses of magmatic activity at c. 475 Ma (Ordovician) and c. 540 Ma (Ediacaran/Cambrian boundary). As outlined before, Ordovician magmatic activity in the FMC is interpreted as reflecting long-lived extension of the Northern Gondwana margin that culminated in rifting and the opening of small-scale oceanic basins (Lardeaux et al., 2014). However, at the scale of the Variscan belt, the significance of this Ordovician event is much discussed and contrasted geodynamic settings have been proposed such as an active margin environment with a fore-arc accretionary complex (Zurbriggen, 2015) and continental subduction (Villaseca et al., 2016).

The existence of the Ediacaran/Cambrian peak together with its origin and significance has not been addressed in the FMC. By that time, the crust segment today exposed in the FMC was located along the northern margin of Gondwana (Stampfli et al., 2013) and was therefore likely affected by the Cadomian orogeny, a Cryogenian–Ediacaran Western Pacific-type marginal orogenic system (Nance et al., 1991). Accordingly, remnants of Cadomian granitoid rocks have been described in several parts of the Variscan belt (see review in Garfunkel (2015)). In the following, we compare the Cadomian magmatic record of the eastern FMC to that of the closest crustal block shaped by the Cadomian orogeny but nearly devoid of Variscan imprint: the Mancellian Domain of the North Armorican Massif (Fig. 1). Today located 500 km NW of the Velay Dome, it preserves an excellent record of the Cadomian orogenic evolution (Ballèvre et al., 2001; Chantraine et al., 2001) and the

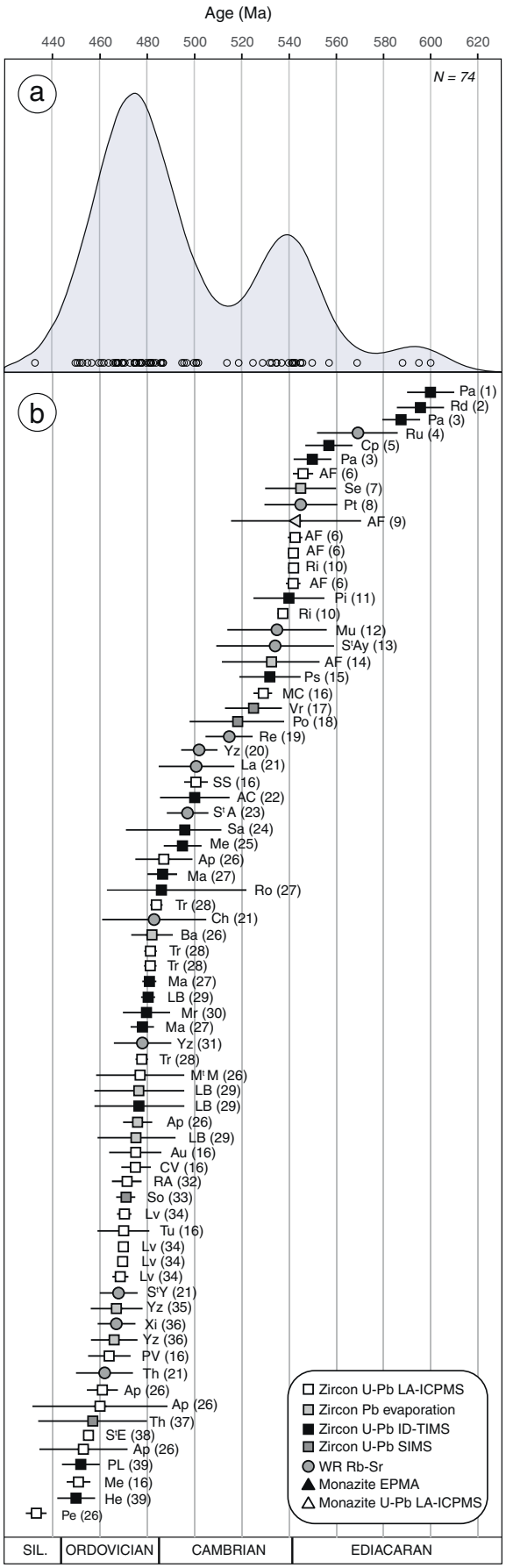

developed comparison would better constrain the origin and geodynamic setting of late Ediacaran magmatism in the FMC.

The Mancellian Domain comprises two main lithological units: (i) a terrigenous sedimentary sequence of Ediacaran ("*Brioverian*") age, interpreted as a turbidite-type back-arc to retro-arc basin (Ballèvre et al., 2001; Linnemann et al., 2014); (ii) a range of granitoids which intrude the sediments and develop thermal aureoles that suggest emplacement depths lower than 6 km (Ballèvre et al., 2001). Available ages on this magmatism range between 550 and 540 Ma (Egal et al., 1996, 2011; Peucat, 1986). This configuration clearly resembles that observed in the LGU of the eastern FMC (Ledru et al., 2001). As demonstrated above, orthogneisses correspond to a late Ediacaran S-type granitic suite emplaced at shallow crustal levels (2–7 km). Field observations clearly indicate that the VOF is intrusive within the regional paragneisses (Ledru et al., 1994). Consequently, our dating results on the VOF importantly constrain a minimum deposition age of 545 Ma for the sedimentary protoliths of the paragneisses, besides consistent with constraints based on the age of the youngest detrital zircons in these rocks (Chelle-Michou et al., 2017). We thus propose that Velay paragneisses are akin to the *Brioverian* sediments and that the VOF is the counterpart of the Mancellian granitoids.

However, when compared to the VOF, Mancellian plutonic rocks show a larger petrographic diversity as they include mafic to intermediate rocks which are not observed in the VOF. Accordingly, the Mancellian suite displays a larger scatter in SiO_2 contents (49–78 wt%) than the VOF (69–79 wt%) (Fig. 15a). Moreover, the dominant phase of the Mancellian suite is a granodiorite as opposed to a granite and leucogranites only form subordinate massifs. The Mancellian granodiorites trend between two endmembers in the ternary CaO – K_2O/Na_2O – $Al_2O_3/(FeO_t + MgO)$ diagram (Laurent et al., 2014) (Fig. 15b). This observation suggests a dual origin by: (i) melting of sedimentary materials in agreement with petrographic (Brown, 1995) and isotopic data (D'Lemos and Brown, 1993); (ii) involvement of K-rich mantle-derived magmas (Fig. 15b), either as a component of the source (remelting of underplated mafic rocks) and/or via magma mixing/mingling as suggested by the occurrence of mafic microgranular enclaves (Jonin, 1981) and the presence of mafic/intermediate calc-alkaline rocks as part of the suite (Le Gall and Barrat, 1987). Leucogranites have been interpreted as sediment-derived melts produced under high $a_{(H2O)}$ conditions and are not genetically linked to the granodiorites (Brown, 1995). As a result, the respective petrogenesis of Mancellian and VOF granitoid suites contrast by the extent of mantle contribution (respectively significant vs. lacking) and the relative role played by fractionation in accounting for the most felsic compositions.

The proposed geodynamic setting for Mancellian magmatism corresponds to the *post*-570 Ma inversion of a back-arc basin (the *Brioverian* sequence) in a transpressional regime coeval with collision between the Cadomian arc and the Gondwana continent (Chantraine et al., 2001; Dallmeyer et al., 1991; Linnemann et al., 2014). Given the evidence for limited thickening (maximum crustal thickness of ~40 km according to Ballèvre et al., 2001) and the presence of a mantle component in the Mancellian suite, crustal melting is considered to have been triggered by the underplating of mafic magmas (Ballèvre et al., 2001; Dissler et al., 1988; Linnemann et al., 2014). In contrast, the lack of substantial evidence for mantle-derived magmatism in the VOF despite its large surface (~1800 km^2), especially the invariably (leuco)granitic character and high SiO_2 content (>68 wt.%) of the samples (see Fig. 6), rules out mafic magma underplating as a potential heat source. The Cadomian back-arc basin corresponded to stretched and thinned continental crust (Brown and D'Lemos, 1991; Chantraine et al., 2001;

Fig. 14. Compilation of available intrusion ages for pre-Variscan volcanic and plutonic rocks in the French Massif Central. (a) Age distribution represented as Kernel Density Estimate, calculated using the DensityPlotter program of Vermeesch (2012); the bandwidth considered is the average 2σ error on emplacement ages (12 Ma). (b) Details on available intrusion ages. Abbreviations and references available in Supplementary text.

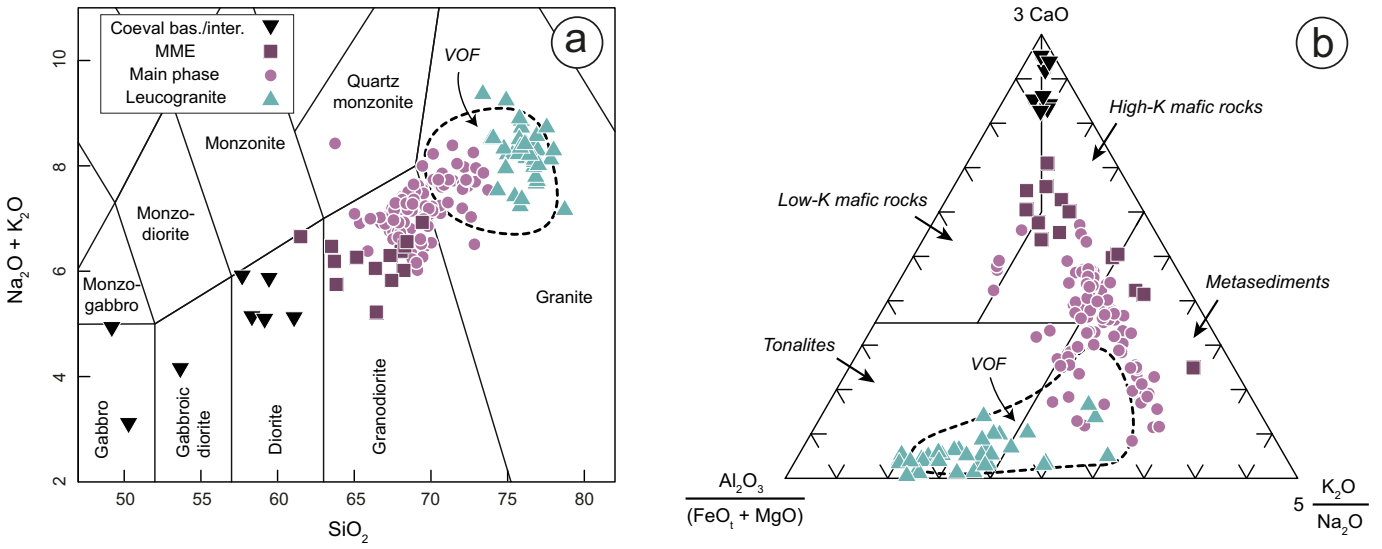

Fig. 15. Geochemical comparison between Cadomian granitoids from the Mancellian domain and the VOF (>95% of the samples in the gray field). (a) $Na_2O + K_2O$ vs. SiO_2 Middlemost's classification diagram (Middlemost, 1994); (b) ternary CaO – K_2O/Na_2O – $Al_2O_3/(FeO_t + MgO)$ diagram (Laurent et al., 2014). The fields represent the composition of melts derived from a range of potential sources. MME: mafic microgranular enclaves.

Linnemann et al., 2014) and by analogy with modern back-arc settings, high mantle heat flow was expected in this crust segment (Currie and Hyndman, 2006). As demonstrated by Clark et al. (2011), thermal relaxation following stacking of back-arc units generates temperatures in the middle crust in excess of 750 °C, compatible with extensive melting of sedimentary lithologies and with the conditions of formation inferred for the VOF parental magmas based on experimental constraints and zircon saturation (see above). Therefore, limited thickening of anomalously warm Cadomian back-arc basins would have triggered significant crustal melting (Brown and D'Lemos, 1991). As a result, we propose that the VOF is a lateral equivalent of the Mancellian batholith in an area unaffected by mantle melting during the Cadomian back-arc basin inversion. Several reasons can explain the apparent lack of coeval mantle-derived magmatism including: (i) previous depletion of the underlying mantle during back-arc spreading as evidenced by the 590–570 Ma tholeiitic to calc-alkaline mafic magmatism observed in parts of the Northern Armorican Massif (Chantraine et al., 2001; Linnemann et al., 2014); or (ii) lateral variations in the Cadomian subducting slab dynamics with localized break-off that strongly affected the thermal regime of the back-arc mantle (Nance et al., 2010).

6. Conclusion

Remnants of a Cadomian basement are described in the Velay area (eastern French Massif Central) where an S-type granitic suite intruded Ediacaran sediments at c. 542 Ma. The main phase of this large (~1800 km^2) batholith corresponded to a porphyritic granite (transformed into an augen gneiss during the Variscan orogeny) while some magmas evolved by fractional crystallization towards leucogranitic compositions (corresponding to the present-day leucogneisses). Such voluminous magmatism was likely caused by the inversion of a back-arc basin domain at the end of the Cadomian orogeny, leading to limited stacking of supracrustal sequences in a high thermal regime that favored significant melting. This is supported by the homogeneous εHf(t) of the VOF zircons compared with their inferred protoliths (sediments derived from various Gondwana-related reservoirs with extremely contrasted isotopic signatures) which points to dissolution of detrital zircons in the source and rapid cooling upon emplacement. From a crust evolution perspective, the Cadomian magmatism in the Velay area was strictly crust-derived and thus attests to substantial reworking of older crust away from a proper continent-continent collision zone. Conversely, there is currently no compelling evidence for Cadomian crust production in the FMC.

Supplementary data to this article can be found online at http://dx.doi.org/10.1016/j.lithos.2017.06.001.

Acknowledgements

We acknowledge funding from the European Commission, together with the UJM through the Campus France PRESTIGE program to C.C.-M.; and with Université de Liège through the Marie-Curie Actions Be-IPD-COFUND program to O.L. PB acknowledges support from ERC Starting Grant (MASE; 279828), and his Auvergne Fellowship (French Government Laboratory of Excellence initiative no. ANR-10-LABX-0006, ClerVolc contribution no. 255). We thank C. Guilbaud for making the thin sections, S. Sao-Joao and J.-L. Devidal for assistance during SEM imaging and B. Moine for help during zircon separation. We are indebted to M. Ballèvre who provided the file of Fig. 1. M. J. Mayne, G. Nicoli, A. Aubray, V. Gardien and A. Villaros are thanked for assistance on the field and fruitful discussions. Constructive reviews from P. Barbey and J. Melleton on an early draft were very much appreciated.

S. Gürsu and an anonymous reviewer are thanked for their comments on the present manuscript. We are grateful to N. Eby for editorial handling.

References

Aitchison, J., 1986. The Statistical Analysis of Compositional Data. Chapman and Hall, London, UK.

Alexandre, P., 2007. U–Pb zircon SIMS ages from the French Massif Central and implication for the pre-Variscan tectonic evolution in Western Europe. Comptes Rendus Geoscience 339, 613–621.

Alexandrov, P., Floc'h, J.-P., Cuney, M., Cheilletz, A., 2001. Ion microprobe dating of zircons from the upper gneiss unit (South Limousin, Massif Central, France). Comptes Rendus de l'Académie des Sciences, Paris 332, 625–632.

Alvaro, J.J., Bauluz, B., Clausen, S., Devaere, L., Gil Imaz, A., Monceret, E., Vizcaïno, D., 2014. Stratigraphic review of the Cambrian-Lower Ordovician volcano-sedimentary complexes from the northern Montagne Noire. Stratigraphy 11, 83–96.

Annen, C., Blundy, J.D., Sparks, R.S.J., 2006. The genesis of intermediate and silicic magmas in deep crustal hot zones. Journal of Petrology 47, 505–539.

Appleby, S.K., Gillespie, M.R., Graham, C.M., Hinton, R.W., Oliver, G.J.H., Kelly, N.M., 2009. Do S-type granites commonly sample infracrustal sources? New results from an integrated O, U–Pb and Hf isotope study of zircon. Contributions to Mineralogy and Petrology 160, 115–132.

Ballèvre, M., Le Goff, E., Hébert, R., 2001. The tectonothermal evolution of the Cadomian belt of northern Brittany, France: a Neoproterozoic volcanic arc. Tectonophysics 331, 19–43.

Ballèvre, M., Martinez Catalan, J.R., Lopez-Carmona, A., Pitra, P., Abati, J., Fernandez, R.D., Ducassou, C., Arenas, R., Bosse, V., Castineiras, P., Fernandez-Suarez, J., Gomez Barreiro, J., Paquette, J.L., Peucat, J.J., Poujol, M., Ruffet, G., Sanchez Martinez, S., 2014. Correlation of the nappe stack in the Ibero-Armorican arc across the Bay of Biscay: a joint French-Spanish project. Geological Society, London, Special Publications 405, 77–113.
Ballouard, C., Boulvais, P., Poujol, M., Gapais, D., Yamato, P., Tartèse, R., Cuney, M., 2015. Tectonic record, magmatic history and hydrothermal alteration in the Hercynian Guérande leucogranite, Armorican Massif, France. Lithos 220-223, 1–22.
Be Mezeme, E., Cocherie, A., Faure, M., Legendre, O., Rossi, P., 2006. Electron microprobe monazite geochronology of magmatic events: examples from Variscan migmatites and granitoids, Massif Central, France. Lithos 87, 276–288.
Bea, F., 1996. Residence of REE, Y, Th and U in granites and crustal protoliths; implications for the chemistry of crustal melts. Journal of Petrology 37, 521–552.
Bea, F., Pereira, M.D., Corretgé, L.G., Fershtater, G.B., 1994. Differentiation of strongly peraluminous, phosphorus granites: the Pedrobernardo pluton, central Spain. Geochimica et Cosmochimica Acta 58, 2609–2627.
Belousova, E.A., Griffin, W.L., O'Reilly, S.Y., 2006. Zircon Crystal Morphology, Trace Element Signatures and Hf Isotope Composition as a Tool for Petrogenetic Modelling: Examples From Eastern Australian Granitoids. Journal of Petrology 47, 329–353.
Blundy, J., Cashman, K., 2001. Ascent-driven crystallisation of dacite magmas at Mount St Helens, 1980-1986. Contributions to Mineralogy and Petrology 140, 631–650.
Boehnke, P., Watson, E.B., Trail, D., Harrison, T.M., Schmitt, A.K., 2013. Zircon saturation re-revisited. Chemical Geology 351, 324–334.
Bouilhol, P., Leyreloup, A.F., Delor, C., Vauchez, A., Monié, P., 2006. Relationships between lower and upper crust tectonic during doming: the mylonitic southern edge of the Velay metamorphic core complex (Cévennes-French Massif Central). Geodinamica Acta 19, 137–153.
Bouvier, A., Vervoort, J.D., Patchett, P.J., 2008. The Lu–Hf and Sm–Nd isotopic composition of CHUR: constraints from unequilibrated chondrites and implications for the bulk composition of terrestrial planets. Earth and Planetary Science Letters 273, 48–57.
Boynton, W.V., 1984. Cosmochemistry of the rare earth elements: meteorite studies. In: Henderson, P. (Ed.), Rare Earth Element Geochemistry. Elsevier, Amsterdam, pp. 63–114.
Briand, B., Bouchardon, J.-L., Santallier, D., Piboule, M., Ouali, H., Capiez, P., 1992. Alkaline affinity of the metabasites in the gneissic series surrounding the Velay migmatitic domain. Géologie de la France 2, 9–15.
Brown, M., 1995. The late-Precambrian geodynamic evolution of the Armorica segment of the Cadomian belt (France): distortion of an active continental margin during southwest directed convergence and subduction of a bathymetric high. Géologie de la France 3, 3–22.
Brown, M., D'Lemos, R.S., 1991. The Cadomian granites of Mancellia, northeast Armorican Massif of France: relationship to the St. Malo migmatite belt, petrogenesis and tectonic setting. Precambrian Research 51, 393–427.
Buccianti, A., Peccerillo, A., 1999. The complex nature of potassic and ultrapotassic magmatism in Central–Southern Italy: a multivariate analysis of major element data. In: Lippard, S.J., Naess, A., Sinding-Larsen, R. (Eds.), 5th Annual Conference of the International Association for Mathematical Geology Trondheim, Tapir, pp. 145–150.
Burg, J.-P., Van Den Driessche, J., Brun, J.P., 1994. Syn- to post-thickening extension in the Variscan Belt of Western Europe: modes and structural consequences. Géologie de la France 3, 33–51.
Caen-Vachette, M., 1979. Age cambrien des rhyolites transformées en leptynites dans la série métamorphique du Pilat (Massif Central français). Comptes Rendus de l'Académie des Sciences, Paris 289, 997–1000.
Cawood, P.A., Kröner, A., Collins, W.J., Kusky, T.M., Mooney, W.D., Windley, B.F., 2009. Accretionary orogens through Earth history. Geological Society, London, Special Publications 318, 1–36.
Chantraine, J., Egal, E., Thiéblemont, D., Le Goff, E., Guerrot, C., Ballèvre, M., Guennoc, P., 2001. The Cadomian active margin (Northern Armorican Massif, France): a segment of the North Atlantic Panafrican belt. Tectonophysics 331, 1–18.
Chappell, B.W., White, A.J.R., 2001. Two contrasting granite types: 25 years later. Australian Journal of Earth Sciences 48, 489–499.
Chelle-Michou, C., Laurent, O., Moyen, J.-F., Block, S., Paquette, J.-L., Couzinié, S., Gardien, V., Vanderhaeghe, O., Villaros, A., Zeh, A., 2017. Pre-Cadomian to late-Variscan odyssey of the eastern Massif Central, France: formation of the West European crust in a nutshell. Gondwana Research 46, 170–190.
Chenevoy, M., Gay, M., Lochon, P., 1986. Metamorphic alkali-basalts and leucogranites in the Western Vivarais series (French Central Massif): a record of two major tectonic events in paleozoic time. Comptes Rendus de l'Académie des Sciences, Paris 303, 725–730.
Clark, C., Fitzsimons, I.C.W., Healy, D., Harley, S.L., 2011. How does the continental crust get really hot? Elements 7, 235–240.
Clemens, J.D., Petford, N., Mawer, C.K., 1997. Ascent mechanisms of granitic magmas: causes and consequences. In: Holness, M.B. (Ed.), Deformation-Enhanced Fluid Transport in the Earth's Crust and Mantle. Mineralogical Society Series, pp. 145–172.
Coldwell, B., Clemens, J., Petford, N., 2011. Deep crustal melting in the Peruvian Andes: felsic magma generation during delamination and uplift. Lithos 125, 272–286.
Collins, W.J., Richards, S.W., 2008. Geodynamic significance of S-type granites in circum-Pacific orogens. Geology 36, 559.
Corfu, F., Hanchar, J.M., Hoskin, P.W.O., Kinny, P.D., 2003. Atlas of zircon textures. Reviews in Mineralogy and Geochemistry 53, 469–500.
Couzinié, S., Moyen, J.F., Villaros, A., Paquette, J.L., Scarrow, J.H., Marignac, C., 2014. Temporal relationships between Mg-K mafic magmatism and catastrophic melting of the Variscan crust in the southern part of Velay complex (Massif Central, France). Journal of Geosciences 69–86.
Couzinié, S., Laurent, O., Moyen, J.F., Zeh, A., Bouilhol, P., Villaros, A., 2016. Post-collisional magmatism: crustal growth not identified by zircon Hf-O isotopes. Earth and Planetary Science Letters 456, 182–195.
Currie, C.A., Hyndman, R.D., 2006. The thermal structure of subduction zone back arcs. Journal of Geophysical Research 111.
Dallmeyer, R.-D., Strachan, R.A., D'Lemos, R.S., 1991. Chronology of Cadomian tectonothermal activity in the baie de Saint-Brieux (North Brittany), France: evidence from $^{40}Ar/^{39}Ar$ mineral ages. Canadian Journal of Earth Sciences 28, 762–773.
Dewey, J.F., Hempton, M.R., Kidd, W.S.F., Saroglu, F., Şengör, A.M.C., 1986. Shortening of continental lithosphere: the neotectonics of Eastern Anatolia – a young collision zone. In: Coward, M.P., Ries, A.C. (Eds.), Collision Tectonics. Geological Society, London, Special Publications, pp. 3–36.
Dissler, E., Doré, F., Dupret, L., Gresselin, F., Le Gall, J., 1988. Cadomian geodynamical evolution in the northeastern Armorican massif. Bulletin de la Société Géologique de France 8, 801–814.
D'Lemos, R.S., Brown, M., 1993. Sm–Nd isotope characteristics of late Cadomian granite magmatism in northern France and the Channel Islands. Geological Magazine 130, 797–804.
Duthou, J.-L., Cantagrel, J.-M., Didier, J., Vialette, Y., 1984. Palaeozoic granitoids from the French Massif Central: age and origin studied by ^{87}Rb-^{87}Sr system. Physics of the Earth and Planetary Interiors 35, 131–144.
Egal, E., Guennoc, P., Le Goff, E., Thiéblemont, D., Lebret, P., Hallégouet, B., 1996. The Cadomian orogeny revisited in northern Brittany, Avalonian and related Peri-Gondwanan terranes of the Circum-North Atlantic. Geological Society of America, Special Publication 218–318.
Egal, E., Hallegouët, B., Le Goff, E., Schroetter, J.-M., Mougin, B., Cocherie, A., Langouët, L., Monnier, J.-L., Théveniaut, H., Thiéblemont, D., Thomas, E., 2011. Notice explicative, Carte géol. France (1/50 000), feuille Dinan (245). BRGM, Orléans, p. 196.
Farina, F., Stevens, G., Gerdes, A., Frei, D., 2014. Small-scale Hf isotopic variability in the Peninsula pluton (South Africa): the processes that control inheritance of source $^{176}Hf/^{177}Hf$ diversity in S-type granites. Contributions to Mineralogy and Petrology 168.
Faure, M., Brouder, P., Thierry, J., Alabouvette, B., Cocherie, A., Bouchot, V., 2009a. Notice explicative, Carte géol. France (1/50 000), feuille Saint-André-de-Valborgne (911). BRGM, Orléans, p. 138.
Faure, M., Lardeaux, J.-M., Ledru, P., 2009b. A review of the pre-Permian geology of the Variscan French Massif Central. Comptes Rendus Geoscience 341, 202–213.
Finney, S.C., Gibbard, P.L., Fan, J.X., 2013. The ICS international chronostratigraphic chart. Episodes 36, 199–204.
Fournier-Vinas, C., Debat, P., 1970. Présence de micro-organismes dans les terrains métamorphiques précambriens (schistes X) de l'Ouest de la Montagne Noire. Bulletin de la Société Géologique de France 7, 351–355.
Frost, B.R., Frost, C.D., 2008. On charnockites. Gondwana Research 13, 30–44.
Gardien, V., Lardeaux, J.M., Ledru, P., Allemand, P., Guillot, S., 1997. Metamorphism during late orogenic extension:insights from the French Variscan belt. Bulletin de la Société Géologique de France 168, 271–286.
Garfunkel, Z., 2015. The relations between Gondwana and the adjacent peripheral Cadomian domain—constrains on the origin, history, and paleogeography of the peripheral domain. Gondwana Research 28, 1257–1281.
Gerdes, A., Zeh, A., 2006. Combined U–Pb and Hf isotope LA– (MC–)ICP–MS analyses of detrital zircons: comparison with SHRIMP and new constraints for the provenance and age of an Armorican metasediment in Central Germany. Earth and Planetary Science Letters 249, 47–61.
Gerdes, A., Zeh, A., 2009. Zircon formation versus zircon alteration — new insights from combined U–Pb and Lu–Hf in-situ LA–ICP–MS analyses, and consequences for the interpretation of Archean zircon from the central zone of the Limpopo Belt. Chemical Geology 261, 230–243.
Griffin, W.L., Wang, X., Jackson, S.E., Pearson, N.J., O'Reilly, S.Y., Xu, X.-S., Zhou, X., 2002. Zircon chemistry and magma mixing, SE China: in-situ analysis of Hf isotopes, Tonglu and Pingtan igneous complexes. Lithos 61, 237–269.
Guérangé-Lozes, J., Burg, J.-P., 1990. Variscan nappes in the southwest of the Massif Central (1:250 000 geological and structural maps of Montpellier and Aurillac). Géologie de la France 3-4, 71–106.
Harris, N.B.W., Pearce, J.A., Tindle, A.G., 1986. Geochemical characteristics of collision-zone magmatism. In: Coward, M.P., Ries, A.C. (Eds.), Collision Tectonics. Geological Society, London, Special Publications, pp. 67–81.
Hawkesworth, C., Cawood, P., Kemp, T., Storey, C., Dhuime, B., 2009. A matter of preservation. Science 323, 49–50.
Hawkesworth, C.J., Dhuime, B., Pietranik, A.B., Cawood, P.A., Kemp, A.I.S., Storey, C.D., 2010. The generation and evolution of the continental crust. Journal of the Geological Society 167, 229–248.
Holtz, F., Johannes, W., 1994. Maximum and minimum water content of granitic melts—implications for chemical and physical properties of ascending magmas. Lithos 32, 149–159.
Ihaka, R., Gentleman, R., 1996. R: a language for data analysis and graphics. Journal of Computational and Graphical Statistics 5, 299–344.
Jackson, S.E., Pearson, N.J., Griffin, W.L., Belousova, E.A., 2004. The application of laser ablation-inductively coupled plasma-mass spectrometry to in situ U–Pb zircon geochronology. Chemical Geology 211, 47–69.
Jagoutz, O., Kelemen, P.B., 2015. Role of arc processes in the formation of continental crust. Annual Review of Earth and Planetary Sciences 43, 363–404.
Janoušek, V., Braithwaite, C.J.R., Bowes, D.R., Gerdes, A., 2004. Magma-mixing in the genesis of Hercynian calc-alkaline granitoids: an integrated petrographic and geochemical study of the Sázava intrusion, Central Bohemian Pluton, Czech Republic. Lithos 78, 67–99.
Janoušek, V., Farrow, C.M., Erban, V., 2006. Interpretation of whole–rock geochemical data in igneous geochemistry: introducing geochemical data toolkit (GCDkit). Journal of Petrology 47, 1255–1259.
Johannes, W., Holtz, F., 1996. Petrogenesis and Experimental Petrology of Granitic Rocks. Springer, Berlin Heidelberg New York.

Jonin, M., 1981. Un batholite fini-précambrien : le batholite mancellien (Massif armoricain, France). Thèse de Doctorat d'Etat, Université de Brest 319p.
Kroner, U., Romer, R.L., 2013. Two plates — many subduction zones: the Variscan orogeny reconsidered. Gondwana Research 24, 298–329.
Lagarde, J.-L., Dallain, C., 1994. Strain patterns within the late Variscan granitic dome of Velay, French Massif Central. Journal of Structural Geology 16, 839–852.
Lardeaux, J.M., Schulmann, K., Faure, M., Janou ek, V., Lexa, O., Skrzypek, E., Edel, J.B., tipska, P., 2014. The Moldanubian zone in the French Massif Central, Vosges/Schwarzwald and Bohemian Massif revisited: differences and similarities. Geological Society, London, Special Publications 405, 7–44.
Laurent, O., Martin, H., Moyen, J.F., Doucelance, R., 2014. The diversity and evolution of late-Archean granitoids: evidence for the onset of "modern-style" plate tectonics between 3.0 and 2.5 Ga. Lithos 205, 208–235.
Laurent, O., Couzinié, S., Zeh, A., Vanderhaeghe, O., Moyen, J.-F., Villaros, A., Gardien, V., Chelle-Michou, C., 2017. Protracted, coeval crust and mantle melting during Variscan late-orogenic evolution: U–Pb dating in the eastern French Massif Central. International Journal of Earth Sciences 106, 421–451.
Le Gall, J., Barrat, J.A., 1987. Petrology of late Cadomian magmatism in the northern Armorican Massif; the Ernee and Tregomar mafic and ultramafic complexes. Géologie de la France 1, 3–22.
Ledru, P., Lardeaux, J.M., Santallier, D., Autran, A., Quenardel, J.-M., Floc'h, J.-P., Lerouge, G., Maillet, N., Marchand, J., Ploquin, A., 1989. Where are the nappes in the French Massif central? Bulletin de la Société Géologique de France 8, 605–618.
Ledru, P., Vitel, G., Marchand, J., Maurin, G., Mercier, F., Turland, M., Etlicher, B., Dautria, J.M., Liotard, J.M., 1994. Notice explicative, Carte géol. France (1/50 000), feuille Craponne-sur-Arzon (767). BRGM, Orléans, p. 74.
Ledru, P., Courrioux, G., Dallain, C., Lardeaux, J.M., Montel, J.M., Vanderhaeghe, O., Vitel, G., 2001. The Velay dome (French Massif Central): melt generation and granite emplacement during orogenic evolution. Tectonophysics 342, 207–237.
Lescuyer, J.-L., Cocherie, A., 1992. Single-zircon dating of the Sériès meta-dacites: evidence for a late Proterozoic age of the "X Schists" from Montagne Noire (Southern French Massif Central). Comptes Rendus de l'Académie des Sciences, Paris 314, 1071–1077.
Linnemann, U., Gerdes, A., Hofmann, M., Marko, L., 2014. The Cadomian Orogen: Neoproterozoic to Early Cambrian crustal growth and orogenic zoning along the periphery of the West African Craton—constraints from U–Pb zircon ages and Hf isotopes (Schwarzburg Antiform, Germany). Precambrian Research 244, 236–278.
Ludwig, K.R., 2008. A Geochronological Toolkit for Microsoft Excel. Berkeley Geochronology Central Special Publication, p. 76.
Malavielle, J., Guihot, P., Costa, S., Lardeaux, J.M., Gardien, V., 1990. Collapse of the thickened Variscan crust in the French Massif Central: Mont Pilat extensional shear zone and St. Etienne Late Carboniferous basin. Tectonophysics 177, 139–149.
Marini, F., 1987. Relictual clinopyroxenes in paleozoic metabasites from Albigeois: tracers of a distensive transitional-to-tholeiitic volcanism ("Schistes et Roches Vertes" formation, Tarn, probable ordovician age). Comptes Rendus de l'Académie des Sciences, Paris 304, 29–34.
Matte, P., 1986. Tectonics and plate tectonics model for the Variscan belt of Europe. Tectonophysics 126, 329–374.
McDonough, W.F., Sun, S.-s., 1995. The composition of the Earth. Chemical Geology 120, 223–253.
Melleton, J., Cocherie, A., Faure, M., Rossi, P., 2010. Precambrian protoliths and Early Paleozoic magmatism in the French Massif Central: U–Pb data and the North Gondwana connection in the west European Variscan belt. Gondwana Research 17, 13–25.
Middlemost, E.A.K., 1994. Naming materials in the magma/igneous rock system. Earth Science Reviews 37, 215–224.
Montel, J.M., Marignac, C., Barbey, P., Pichavant, M., 1992. Thermobarometry and granite genesis: the Hercynian low-P, high-T Velay anatectic dome (French Massif Central). Journal of Metamorphic Geology 10, 1–15.
Morel, M.L.A., Nebel, O., Nebel-Jacobsen, Y.J., Miller, J.S., Vroon, P.Z., 2008. Hafnium isotope characterization of the GJ-1 zircon reference material by solution and laser-ablation MC-ICPMS. Chemical Geology 255, 231–235.
Mougeot, R., Respaut, J.P., Ledru, P., Marignac, C., 1997. U–Pb chronology on accessory minerals of the Velay anatectic dome (French Massif Central). European Journal of Mineralogy 9, 141–156.
Moyen, J.F., Laurent, O., Chelle-Michou, C., Couzinié, S., Vanderhaeghe, O., Zeh, A., Villaros, A., Gardien, V., 2017. Collision vs. subduction-related magmatism: two contrasting ways of granite formation and implications for crustal growth. Lithos 277, 154–177.
Naeraa, T., Schersten, A., Rosing, M.T., Kemp, A.I., Hoffmann, J.E., Kokfelt, T.F., Whitehouse, M.J., 2012. Hafnium isotope evidence for a transition in the dynamics of continental growth 3.2 Gyr ago. Nature 485, 627–630.
Nance, R.D., Murphy, J.B., Strachan, R.A., D'Lemos, R.S., Taylor, G.K., 1991. Late Proterozoic tectonostratigraphic evolution of the Avalonian and Cadomian terranes. Precambrian Research 53, 41–78.
Nance, R.D., Gutiérrez-Alonso, G., Keppie, J.D., Linnemann, U., Murphy, J.B., Quesada, C., Strachan, R.A., Woodcock, N.H., 2010. Evolution of the Rheic Ocean. Gondwana Research 17, 194–222.
Niu, Y., Zhao, Z., Zhu, D.-C., Mo, X., 2013. Continental collision zones are primary sites for net continental crust growth — a testable hypothesis. Earth-Science Reviews 127, 96–110.
Ohta, T., Arai, H., 2007. Statistical empirical index of chemical weathering in igneous rocks: a new tool for evaluating the degree of weathering. Chemical Geology 240, 280–297.
Orejana, D., Merino Martínez, E., Villaseca, C., Andersen, T., 2015. Ediacaran–Cambrian paleogeography and geodynamic setting of the Central Iberian Zone: constraints from coupled U–Pb–Hf isotopes of detrital zircons. Precambrian Research 261, 234–251.
Paquette, J.-L., Piro, J.-L., Devidal, J.-L., Bosse, V., Didier, A., Sanac, S., Abdelnour, Y., 2014. Sensitivity enhancement in LA–ICP–MS by N_2 addition to carrier gas: application to radiometric dating of U–Th–bearing minerals. Agilent ICP-MS Journal 58, 1–5.
Peucat, J.J., 1986. Behaviour of Rb–Sr whole–rock and U–Pb zircon systems during partial melting as shown in migmatitic gneisses from the Saint-Malo Massif, NE Brittany, France. Journal of the Geological Society, London 143, 875–886.
Pin, C., Duthou, J.-L., 1990. Source of Hercynian granitoids from the French Massif Central: inferences from Nd isotopes and consequences for crustal evolution. Chemical Geology 83, 281–296.
Pin, C., Marini, F., 1993. Early Ordovician continental break-up in Variscan Europe: Nd-Sr isotope and trace element evidence from bimodal igneous associations of the Southern Massif Central, France. Lithos 29, 177–196.
Pouclet, A., Álvaro, J.J., Bardintzeff, J.-M., Imaz, A.G., Monceret, E., Vizcaïno, D., 2017. Cambrian–early Ordovician volcanism across the South Armorican and Occitan domains of the Variscan Belt in France: continental break-up and rifting of the northern Gondwana margin. Geoscience Frontiers 8, 25–64.
Pupin, J.P., 1980. Zircon and granite petrology. Contributions to Mineralogy and Petrology 73, 207–220.
Reitz, E., Wickert, F., 1988. Upper Proterozoic microfossils in low-grade phyllites of the Brévenne-unit, NE Massif Central (France). Comptes Rendus de l'Académie des Sciences, Paris 307, 1717–1721.
Reymer, A., Schubert, G., 1984. Phanerozoic addition rates to the continental crust and crustal growth. Tectonics 3, 63–77.
R'Kha Chaham, K., Couturié, J.-P., Duthou, J.-L., Fernandez, A., Vittel, G., 1990. The fix augen gneiss (French Massif Central): new evidence for the lower Cambrian peraluminous magmatism. Comptes Rendus de l'Académie des Sciences, Paris 311, 845–850.
Roger, F., Teyssier, C., Respaut, J.-P., Rey, P.F., Jolivet, M., Whitney, D.L., Paquette, J.-L., Brunel, M., 2015. Timing of formation and exhumation of the Montagne Noire double dome, French Massif Central. Tectonophysics 640-641, 53–69.
Rogers, J.J.W., Santosh, M., 2003. Supercontinents in Earth history. Gondwana Research 6, 357–368.
Rudnick, R.L., Gao, S., 2003. Composition of the continental crust. In: Rudnick, R.L. (Ed.), The Crust. Elsevier-Pergamon, Oxford, pp. 1–64.
Scherer, E.E., Münker, C., Mezger, K., 2001. Calibration of the Lutetium-Hafnium clock. Science 293, 683–687.
Shand, 1943. Eruptive Rocks. John Wiley & Sons.
Sisson, T.W., Ratajeski, K., Hankins, W.B., Glazner, A.F., 2004. Voluminous granitic magmas from common basaltic sources. Contributions to Mineralogy and Petrology 148, 635–661.
Sláma, J., Košler, J., Condon, D.J., Crowley, J.L., Gerdes, A., Hanchar, J.M., Horstwood, M.S.A., Morris, G.A., Nasdala, L., Norberg, N., Schaltegger, U., Schoene, B., Tubrett, M.N., Whitehouse, M.J., 2008. Plešovice zircon — a new natural reference material for U–Pb and Hf isotopic microanalysis. Chemical Geology 249, 1–35.
Söderlund, U., Patchett, P.J., Vervoort, J.D., Isachsen, C.E., 2004. The 176Lu decay constant determined by Lu–Hf and U–Pb isotope systematics of Precambrian mafic intrusions. Earth and Planetary Science Letters 219, 311–324.
Stampfli, G.M., Hochard, C., Vérard, C., Wilhem, C., von Raumer, J., 2013. The formation of Pangea. Tectonophysics 593, 1–19.
Stevens, G., Villaros, A., Moyen, J.-F., 2007. Selective peritectic garnet entrainment as the origin of geochemical diversity in S-type granites. Geology 35, 9–12.
Tartèse, R., Boulvais, P., 2010. Differentiation of peraluminous leucogranites "en route" to the surface. Lithos 114, 353–368.
Taylor, S.R., McLennan, S.M., 1985. The Continental Crust: Its Composition and Evolution. Blackwell, Oxford.
Teixeira, R.J.S., Neiva, A.M.R., Silva, P.B., Gomes, M.E.P., Andersen, T., Ramos, J.M.F., 2011. Combined U–Pb geochronology and Lu–Hf isotope systematics by LAM–ICPMS of zircons from granites and metasedimentary rocks of Carrazeda de Ansiães and Sabugal areas, Portugal, to constrain granite sources. Lithos 125, 321–334.
Turpin, L., Cuney, M., Friedrich, M., Bouchez, J.L., Aubertin, M., 1990. Meta-igneous origin of Hercynian peraluminous granites in N.W. French Massif Central: implications for crustal history reconstructions. Contributions to Mineralogy and Petrology 104, 163–172.
Van Achterbergh, E., Ryan, C.G., Jackson, S.E., Griffin, W.L., 2001. Data reduction software for LA–ICP–MS: appendix. In: Sylvester, P.J. (Ed.), Laser Ablation-ICP-Mass Spectrometry in the Earth Sciences: Principles and Applications. Mineralog Assoc Canada (MAC), Ottawa, Ontario, Canada, pp. 239–243.
Venables, W.N., Ripley, B.D., 2002. Modern Applied Statistics with S. 4th ed. Springer.
Vermeesch, P., 2012. On the visualisation of detrital age distributions. Chemical Geology 312-313, 190–194.
Villaros, A., Buick, I.S., Stevens, G., 2012. Isotopic variations in S-type granites: an inheritance from a heterogeneous source? Contributions to Mineralogy and Petrology 163, 243–257.
Villaseca, C., Merino Martínez, E., Orejana, D., Andersen, T., Belousova, E., 2016. Zircon Hf signatures from granitic orthogneisses of the Spanish central system: significance and sources of the Cambro-Ordovician magmatism in the Iberian Variscan Belt. Gondwana Research 34, 60–83.
Williamson, B.J., Downes, H., Thirlwall, M.F., 1992. The relationship between crustal magmatic underplating and granite genesis: an example from the Velay granite complex, Massif Central, France. Transactions of the Royal Society of Edinburgh 83, 235–245.
Woodhead, J., Hergt, J., Shelley, M., Eggins, S., Kemp, R., 2004. Zircon Hf-isotope analysis with an excimer laser, depth profiling, ablation of complex geometries, and concomitant age estimation. Chemical Geology 209, 121–135.
Zurbriggen, R., 2015. Ordovician orogeny in the Alps: a reappraisal. International Journal of Earth Sciences 104, 335–350.

2.2 Metasediments in and around the Velay dome

2.2.1 Introduction

The French Massif Central crust segment typically lacks any remnant of old Precambrian rocks, neither at surface level (Melleton et al., 2010; Roques et al., 1995) nor in the lower crustal xenoliths sampled by Cenozoic volcanoes (Féménias et al., 2003; Rossi et al., 2006; Supply, 1981). Excluding geochronological results obtained by the multi-grain zircon U–Pb ID–TIMS method, likely to yield mixed ages, the oldest igneous rocks from the FMC correspond to the c. 540 Ma-old meta-granites from the Velay Orthogneiss Formation (see above). In the Velay dome, metasediments constitute the country-rocks within which the VOF (meta)granites emplaced (Ledru et al., 1994). The age pattern of inherited grains/xenocrysts in the VOF and younger Variscan granitoids suggests that the Velay metasediments were deposited in the Ediacaran (Couzinié et al., 2014; Chelle-Michou et al., 2017; Laurent et al., 2017). Therefore, such lithologies would correspond to the most ancient autochtonous rocks of the eastern FMC and would have recorded the earliest events that formed the FMC crust.

This section provides a new set of U–Pb–Hf measurements performed on detrital zircon grains extracted from four Velay metasediments. It aims at providing further constraints on: (i) the maximum depositional ages of the protoliths; (ii) the origin and nature of the detritus that fed the sedimentary basins and ultimately built up the first continental crust of the FMC.

2.2.2 Investigated samples

The sampling strategy was designed to cover the most typical metasedimentary formations in and around the Velay dome. Data are already available for the eastern flank of the dome (Chelle-Michou et al., 2017) which has accordingly not been re-sampled. Geochemical data for the investigated samples are available in the Appendix Table B1.

PIL-16-01 This sample was collected along the N82 road, at the southern exit of Saint–Etienne (GPS coordinates: 45.40051, 4.4165). It belongs to a 40 cm-thick meta-sandstone (quartzite) body interbedded within amphibolite-facies meta-pelites. The latter are generally referred to as "Pilat micaschists" (Chenevoy, 1971; Gardien, 1990) and form a constituent lithology of the Lower Gneiss Unit in the northern part of the Velay dome. PIL-16-01 is very silicic ($SiO_2 > 87\%$) and dominantly composed of quartz and muscovite with subordinate amounts of feldspar, Fe–Ti oxides and zircon (Fig. 2.2a).

SEN-16-01 This specimen was sampled along the D51 road, between the villages of Chavaniac–Lafayette and Jax (45.16402, 3.60390). It corresponds to a meter-thick quartz-rich layer within the "Senouire" amphibolite-facies micaschists, a typical metasedimentary unit of the western flank of the dome (Ledru et al., 1994). The rock is mostly composed of quartz and biotite with minor amounts of muscovite, garnet, plagioclase, Fe–Ti oxides and zircon (Fig. 2.2b).

CHA-16-02 Collected in the southwestern part of the dome, near the village of Chasseradès, this sample arguably corresponds to a meta-arkose because of: (i) its moderate SiO_2/Al_2O_3 and Fe_2O_3/K_2O ratios (< 6 and 0.7 respectively; Herron, 1988); (ii) the high modal proportion of feldspar which, together with quartz, builds up most of the rock. Other minerals include garnet, muscovite, Fe–Ti oxides and zircon (Fig. 2.2c). The 20 cm-thick meta-arkose layer is closely associated with amphibolite-facies micaschists (Briand et al., 1993; Négron, 1979; Rakib, 1996).

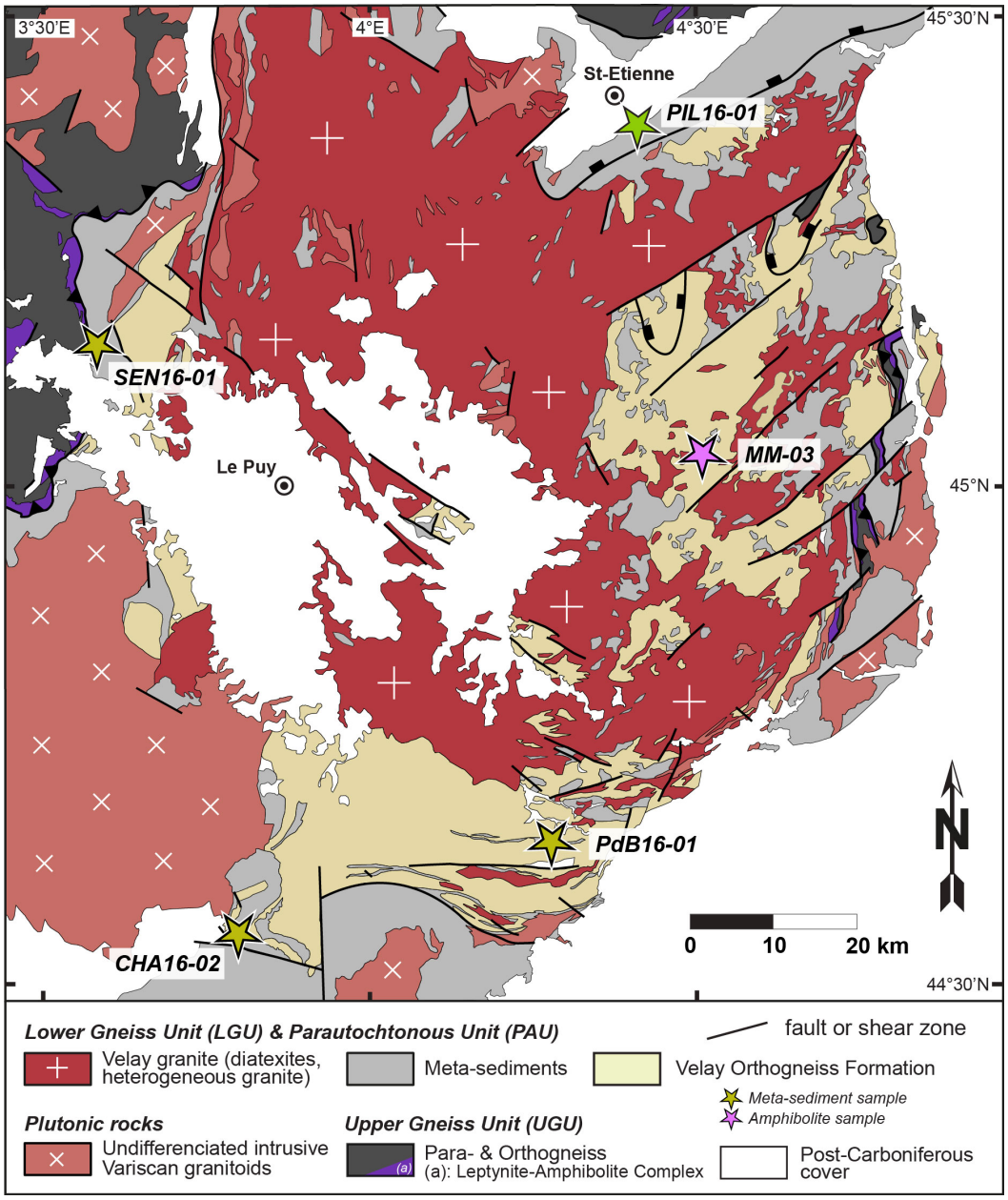

Figure 2.1: Geological map of the Velay dome area showing the location of analysed metasediment and amphibolite samples. The extent of Variscan partial melting of the metamorphic lithologies is not shown for sake of clarity. Redrawn after Ledru et al. (2001), Mintrone (2016) and regional geological maps of France at scale 1/50,000.

PdB-16-01 This sample was taken from a regionally famous outcrop known as "Pont-de-Bayzan" in the bed of the Ardèche river, west of the Lalevade-d'Ardèche village (described in Barraud et al., 2004; Be Mezeme et al., 2005a and Montel et al., 1992). PdB-16-01 is an anatectic paragneiss similar to those encountered in the southern part of the dome (Barbey et al., 2015). Only the melanocratic part of the sample, presumably corresponding to paleosome or residuum in the sense of Sawyer (2008), was selected for detrital zircon analysis. The mineral assemblage consists of quartz, plagioclase, alkali-felspar and biotite with accessory zircon, monazite and apatite (Fig. 2.2d).

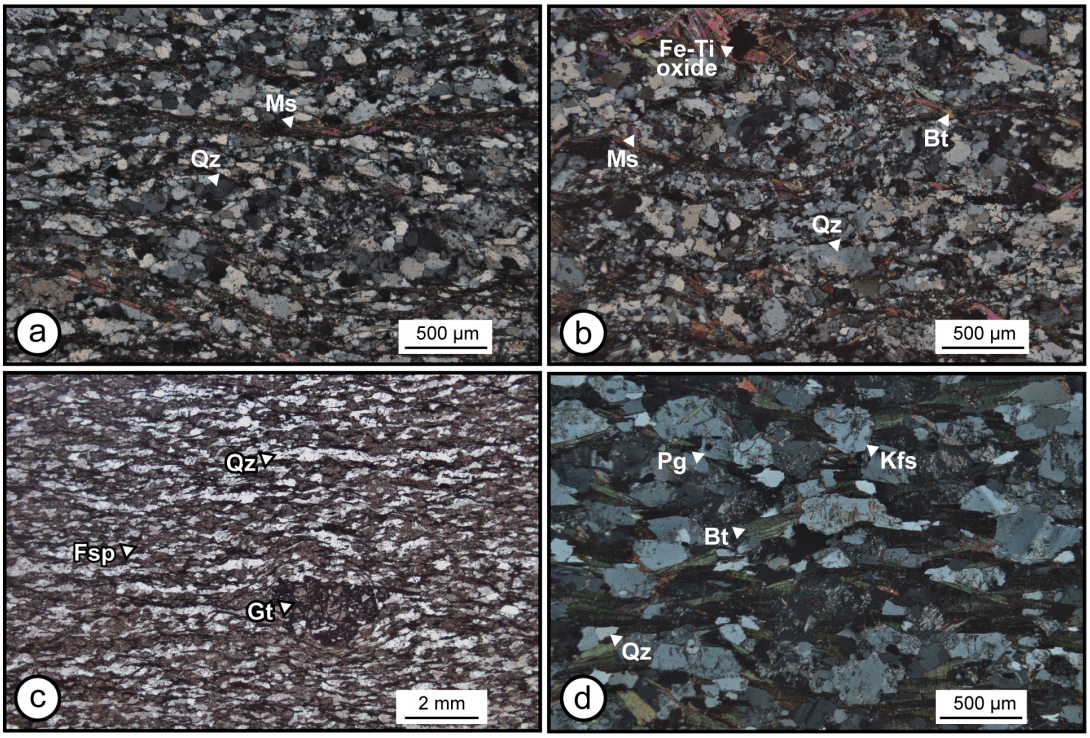

Figure 2.2: Cross- (a,b,d) and plane-polarized-light (c) photomicrographs of metasediments out of which detrital zircon grains were extracted to determine their U–Pb–Hf isotope compositions. (a) Pilat quartzite PIL-16-01; (b) Senouire quartzite SEN-16-01; (c) Cévennes meta-arkose CHA-16-02; (d) Pont-de-Bayzan paragneiss PdB-16-01. Mineral abbreviations from Whitney and Evans (2009).

2.2.3 Analytical techniques

Zircon grains were separated from the powdered rock samples at Saint-Etienne University using conventional techniques described section 2.1, subsequently cast into epoxy mounts and polished down to an equatorial grain section. CL-imaging was performed at the Laboratoire Magmas et Volcans in Clermont-Ferrand (France) using a Jeol JSM-5910 SEM. Selected grains were dated by LA–ICP–MS at ETH Zürich (see Appendix B.3.3 for analytical notes and Tables B6 and B9 for standards and samples results). In situ Hf isotope measurements were also performed at the Laboratoire Magmas et Volcans. The analytical procedure is reported Appendix B.4.2 and Table B10. The full set of results (standards and samples) is available Tables B13 and B14.

2.2.4 Zircon description

Zircon grains in the four investigated samples are mostly colorless, some being pinkish or yellowish. Their shapes vary from rounded (notably in sample PIL-16-01) to

sub-idiomorphic (sample PdB-16-01) with aspect ratios between 1:1 (rounded) and 1:3. Grains range in size from 50 to 160 µm, the shortest being encountered in SEN-16-01, and are often broken (particularly in samples PIL-16-01 and SEN-16-01). Cathodoluminescence images reveal very diverse internal structures (Fig. 2.3). Oscillatory or patchy, broad zoning is common in many grains (see for instance in PdB-16-01, Fig. 2.3d) even though some appear homogeneous (e.g. PIL-16-01, Fig. 2.3a). Importantly, core-rim relationships are typically lacking, with very few crystals showing narrow CL-bright or dark rims ($<$ 10 µm-large, see zircon 2 and 3, Fig. 2.3a, or zircon 2, Fig. 2.3b). Secondary textures include healed cracks and fractures (e.g. zircon 3, Fig. 2.3a) and zones of blurred oscillatory zoning (e.g. zircon 7, Fig. 2.3c). We did not specifically target any zircon population in the course of the U–Pb dating sessions in an attempt to be representative of the overall diversity. Apart from two exceptions, all analysed zircon yielded Th/U ratios $>$ 0.08 which supports a magmatic origin for those grains (Rubatto, 2002; Rubatto et al., 2001).

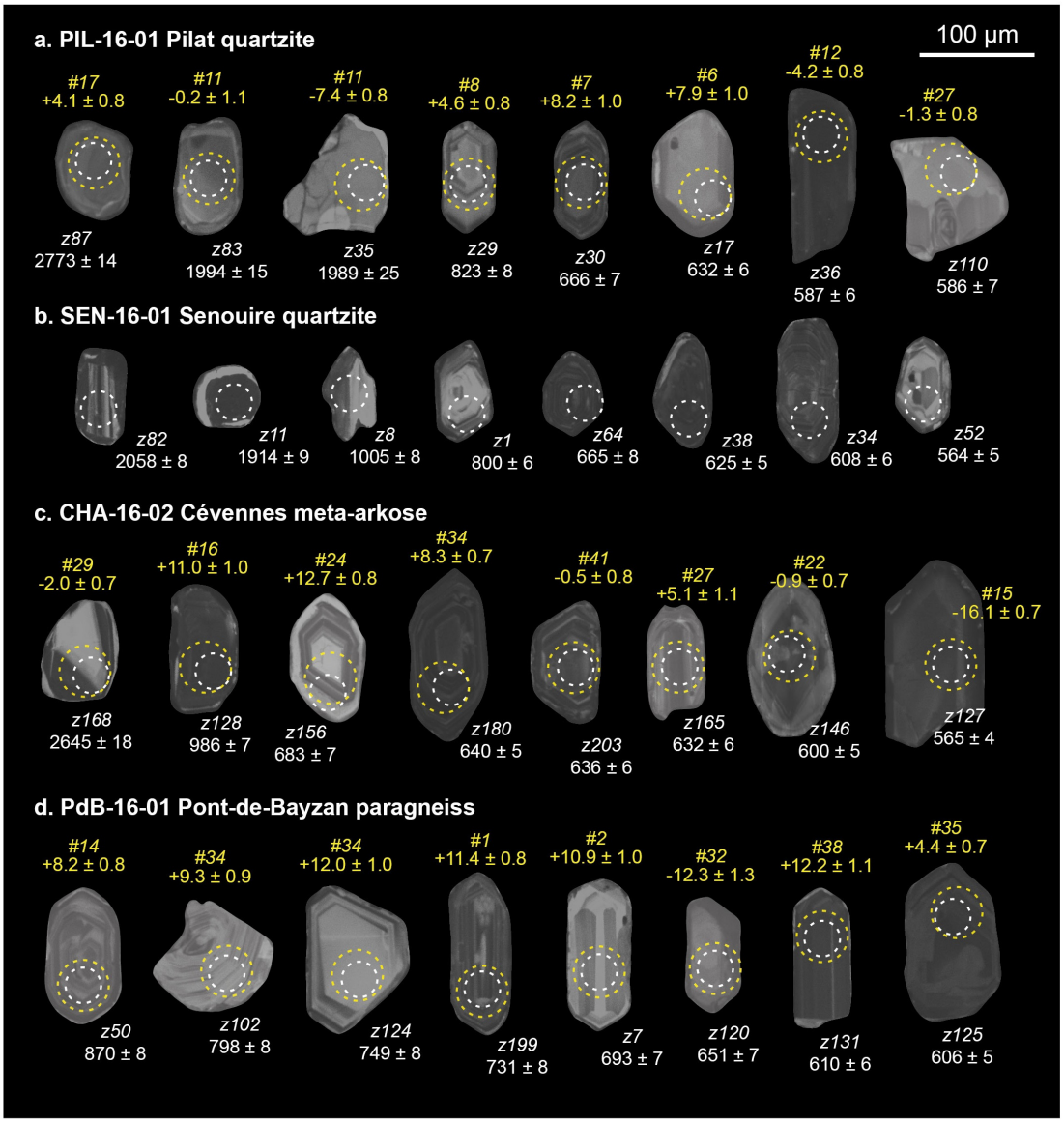

Figure 2.3: Representative cathodoluminescence images of zircon grains from Lower Gneiss Unit metasediments. The locations of laser spots (white and yellow circles for U–Pb and Lu–Hf analyses respectively) are indicated along with the spot name (zXX or #YY). The corresponding $^{206}Pb/^{238}U$ dates are quoted with $\pm$ 2σ uncertainty, in Ma. All displayed analyses are concordant at $>$ 95%. Hf isotope data are reported using the ε_{Hf} calculated at the $^{206}Pb/^{238}U$ date obtained on the same zircon domain, quoted with 2σ uncertainty.

2.2.5 U–Pb geochronology

PIL-16-01, SEN-16-01 and CHA-16-02 These samples are grouped together because they show similar detrital zircon age distribution. Only 53% of the grains analysed in sample PIL-16-01 yielded U–Pb results concordant at 95–105% (112/212 measurements). This proportion increases to 67% in CHA-16-02 (137/204) and reaches 85% in SEN-16-01 (53/62). The date spectra of all three samples reveal a dominant Ediacaran to late Cryogenian population in the range 550–680 Ma (Fig. 2.5a,b,c) with a prominent peak at c. 640 Ma (two sub peaks in SEN-16-01 at 620 and 660 Ma, probably in line with the lower number of measurements). The remaining analyses are mostly distributed over three main time periods: 760–1050 Ma (Tonian to late Stenian), 1.7–2.1 Ga (Paleoproterozoic) and 2.6–2.7 Ga (Neoarchean) in which they may cluster and form marginal peaks.

PdB-16-01 Out of 200 analyses, 143 are concordant at 95–105% (representing 72% of the dataset). The zircon U–Pb date spectrum markedly contrasts with that of the three other samples. Almost all dates (97%) range between 590 and 1050 Ma with Paleoproterozoic and Neoarchean dates being very scarce (only 3% of the record). The Neoproterozoic date distribution features a clear continuum with subordinate peaks at 640, 700 and 750 Ma (Fig. 2.5d).

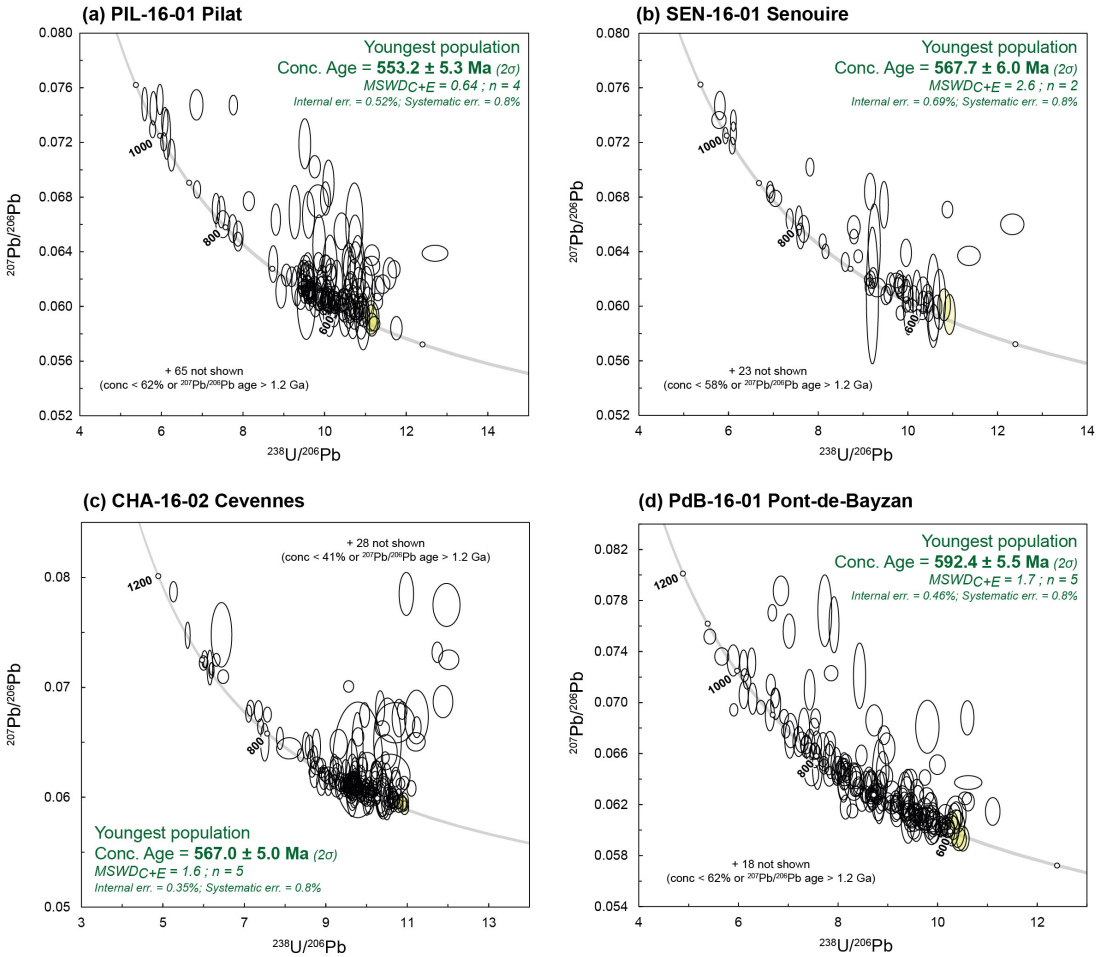

Figure 2.4: Tera–Wasserburg diagrams ($^{238}U/^{206}Pb$ vs. $^{207}Pb/^{206}Pb$) showing Neoproterozoic zircon data for the Lower Gneiss Unit metasediments. Error ellipses/ages are quoted at 2σ level of uncertainty. Yellowish ellipses are those included in age calculations.

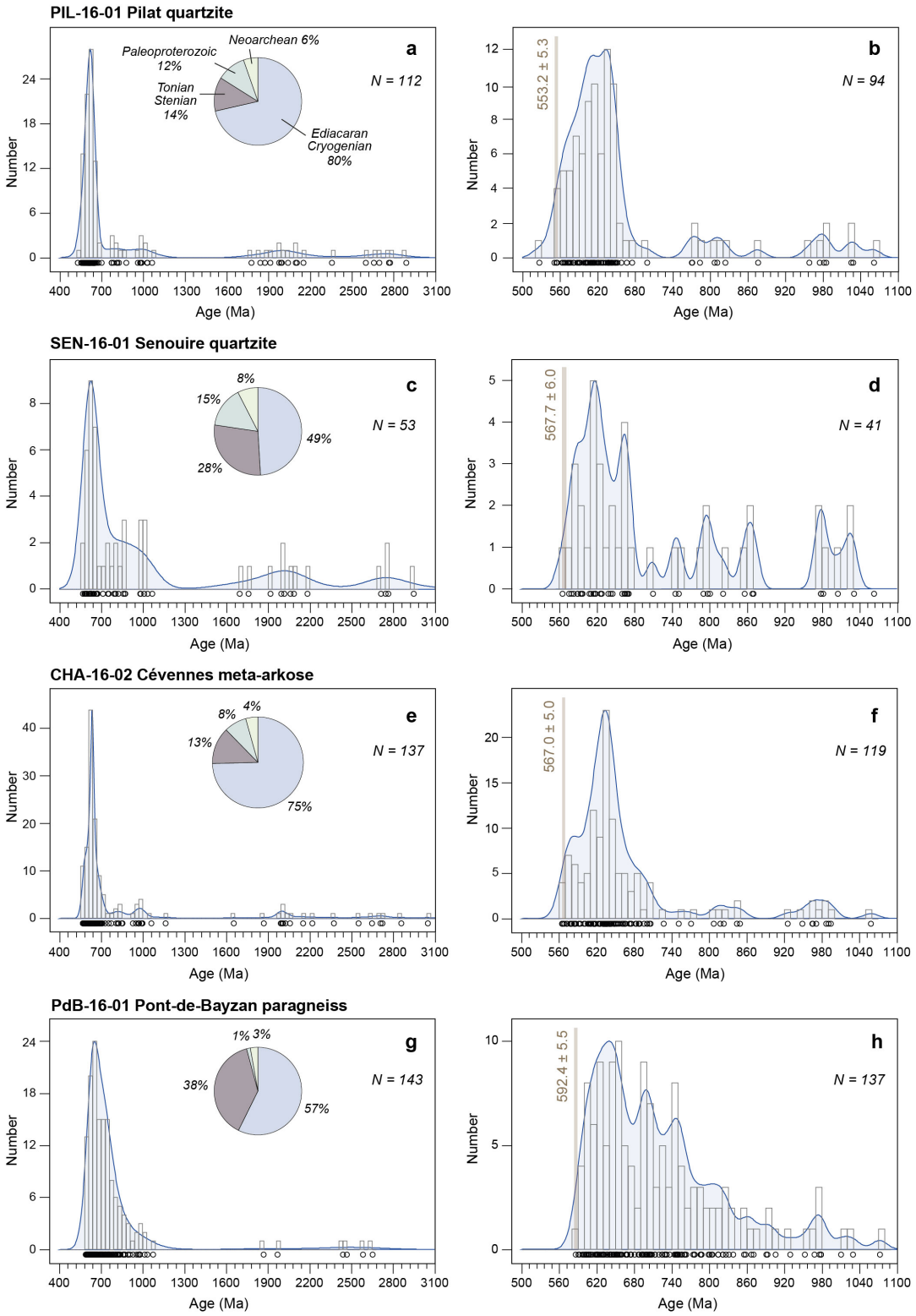

Figure 2.5: Zircon U–Pb date distribution of investigated metasediments from the Lower Gneiss Unit represented as Kernel Density Estimates (KDE). Only 95–105% concordant $^{206}Pb/^{238}U$ (for dates < 1.2 Ga) and $^{207}Pb/^{206}Pb$ dates (for dates > 1.2 Ga) were considered. Circles below the x-axis are the central value of individual data points. Plotted with the DensityPlotter program of Vermeesch (2012). The bandwidth was set to adaptative mode for the 400–3100 Ma diagram and 12 Ma (the average 2σ error of individual analyses) for the 500–1100 Ma plot.

2.2.6 Zircon Hf isotope compositions

The zircon grains analysed for Lu–Hf isotopes were selected based on the date distribution, trying to capture the diversity of each zircon population. The results are depicted Fig 2.6.

PIL-16-01 Twenty-two 550–665 Ma zircon grains show very diverse ε_{Hf}(t), from +8.7 (#3) down to -10.5 (#15). One late Tonian grain has a radiogenic ε_{Hf}(t) of +4.6 (#8). Early Tonian to late Stenian zircons have also variable Hf isotope signatures with 3 grains displaying ε_{Hf}(t) of -11.9, +1.6 and +10.8 ε-unit (#29, #20 and #22, respectively). Five Paleoproterozoic zircons range between -7.4 (#11) and +4.0 (#19) ε-unit. Three Neoarchean grains are chondritic to suprachondritic, with ε_{Hf}(t) ranging from -0.4 (#2) up to +4.1 (#17).

CHA-16-02 The Hf isotope signature of 32 Ediacaran–Cryogenian zircons (565–720 Ma) is highly scattered with ε_{Hf}(t) ranging from -16.9 (#18) up to +12.7 (#24). Seven Tonian–Stenian (n=6) and Paleoproterozoic grains (n=1) display chondritic to supra-chondritic ε_{Hf}(t) (between +0.5 and +12.3, #33 and #6, respectively). Three Neoarchean zircons are nearly chondritic with ε_{Hf}(t) ranging between -2.0 (#29) and +1.2 (#21).

PdB-16-01 Zircon with U–Pb dates in the range 590–980 Ma have dominantly very radiogenic Hf isotope signatures: 84% of the data yield ε_{Hf}(t) > +4.4, 47% Depleted Mantle-like values (up to +13.7, #41). Besides, 8% are nearly chondritic (between -1.8 and 1.2, #21 and #19 respectively) and the remaining 8% subchondritic (between -12.1 and -18.7, #8 and #31, respectively). Paleoproterozoic zircon grains show slightly non-radiogenic signature (of c. -2 ε-unit). Two Neoarchean zircon yielded sub and supra-chondritic values of -5.6 (#22) and +2.6 (#42).

General pattern The ε_{Hf}(t) measured on Paleoproterozoic and Neoarchean zircon are scattered and both sub and suprachondritic. Detrital zircon crystallized at the Tonian–Stenian boundary have even more diverse signatures with ε_{Hf}(t) ranging from -19 up to +11 (in the field of composition expected for the Depleted Mantle reservoir). A large majority of Cryogenian–Tonian zircons (mostly represented by sample Pdb-16-01) have radiogenic Hf isotope signatures. Ediacaran zircon grains are typified by their highly variable ε_{Hf}(t), from -16.9 to +12.2. This pattern differs from that observed by Chelle-Michou et al. (2017) in LGU metasediments from the eastern Velay for two reasons: (i) their measured Cryogenian–Tonian zircons tend to show subchondritic signatures, and (ii) the Ediacaran–Cryogenian highly radiogenic record (ε_{Hf}(t)>+6) documented in this study is lacking in theirs.

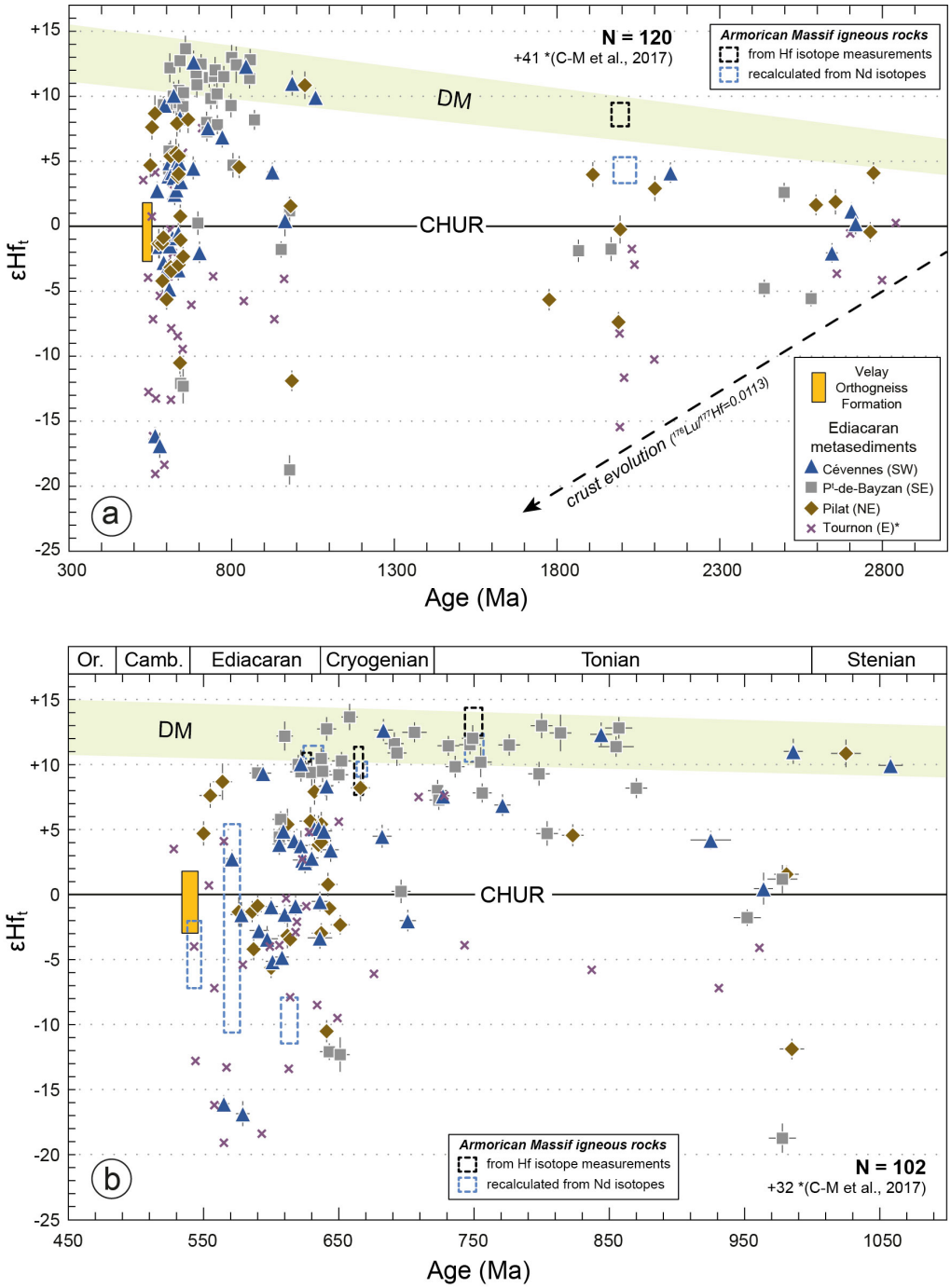

Figure 2.6: Combined U-Pb and Lu-Hf isotopic data for zircons from Ediacaran metasediments, constituent rocks of the Lower Gneiss Unit in the Velay area. Additional data for the eastern Velay are from Chelle-Michou et al. (2017). The yellow field depicts the composition of intruding meta-granites from the Velay Orthogneiss Formation (see above). The ε_{Hf}(t) range for the Depleted Mantle reservoir is bracketed by the models of Naeraa et al. (2012) and Griffin et al. (2002). The dotted arrow represent the isotopic evolution of continental crust (calculated using an average crustal $^{176}Lu/^{177}Hf$ ratio of 0.0113). Data for the northern Armorican Massif are from D'Lemos and Brown (1993); Samson and D'Lemos (1998) and Samson et al. (2003).

2.2.7 Depositional ages

Field relationships indicate that (meta)granites from the Velay Orthogneiss Formation (VOF) are intrusive within the (meta)sediments (Ledru et al., 1994). The oldest emplacement age determined for the VOF samples (545.9 ± 4.3 Ma, leucogneiss MM09) entails that the *minimum* depositional age of the sediments is at least Ediacaran. As a direct consequence of this, metasediment zircon grains with concordant $^{206}Pb/^{238}U$ dates younger than 546 Ma likely experienced limited recent Pb loss. Those analyses would have remained concordant because of the weak curvature of the Concordia at Neoproterozoic/Paleozoic times. This situation is observed in sample PIL-16-01 where spot #116 shows a concordant $^{206}Pb/^{238}U$ date of 526 ± 5 Ma.

Excluding those grains, the *maximum* depositional age is given by that of the youngest zircon population in each sample. The latter has been estimated via the following procedure. First, the youngest (and older than c. 545 Ma) concordant analysis is identified. A Concordia date is then calculated out of it and the closest older analysis. If the MSWD of concordance and equivalence is acceptable (close to 1, meaning that the two zircon grains likely belong to a single population), the next older analysis is added to this pool and a new Concordia date calculated. This procedure is repeated until the MSWD markedly departs from 1, indicating that two different populations are sampled. All investigated metasediments yielded late Ediacaran ages (Fig. 2.4), ranging from 592.4 ± 5.5 Ma for sample PdB-16-01 down to 553.2 ± 5.3 Ma for PIL-16-01. Samples SEN-16-01 and CHA-16-02 show identical *maximum* sedimentation ages of 567.7 ± 6.0 and 567.0 ± 5.0 Ma respectively. These results are consistent with the presence of inherited zircon grains/xenocrysts of that age in *c.* 540 Ma-old (meta)granites from the VOF.

2.2.8 Zircon sources

Comparison with other Cadomian terrains The zircon age distribution of all four samples is consistent with the pattern displayed by other Ediacaran (meta)sediments from the northern margin of Gondwana. Indeed, detrital zircon studies on the western Massif Central (Chelle-Michou et al., 2017; Melleton et al., 2010) together with Iberian (Díez Fernández et al., 2010; Fernández-Suárez et al., 2000; Fernandez-Suarez et al., 2002; Henderson et al., 2016; Linnemann et al., 2008; Orejana et al., 2015; Pereira et al., 2012), Northern Armorican (Ballouard, 2016; Fernandez-Suarez et al., 2002; Gougeon et al., 2017; Miller et al., 2001; Samson et al., 2005) and Bohemian (Drost et al., 2011; Gerdes and Zeh, 2006; Hajná et al., 2017; Linnemann et al., 2004; 2008; 2014; Sláma et al., 2008b; Sláma and Žák, 2017) massifs documented the predominance of Ediacaran–Cryogenian grains with additional populations of Tonian–Stenian (720–1100 Ma), Paleoproterozoic (1.8–2.1 Ga) and Archean (2.4-2.7, sometimes up to 3.45 Ga) age. Typical is the absence of Mesoproterozoic detrital record with a clear gap between 1.2 and 1.6 Ga.

Mixed origin of the detritus Multi-methods studies (encompassing geochemistry, petrography, sedimentology, geochronology) have demonstrated that Ediacaran sediments deposited along the northern margin of Gondwana were of mixed origin: a fraction of the detritus originated from the erosion of the Avalonian–Cadomian magmatic arc and the rest was supplied by an old Gondwana-derived source (Dabard et al., 1996; Denis and Dabard, 1988; Drost et al., 2011; Linnemann et al., 2000; 2008; 2014; Nance and Murphy, 1994; Orejana et al., 2015; Pereira et al., 2012; Rabu et al., 1990).

The proximal source The inferred proximal source, the Avalonian–Cadomian magmatic arc, crops out in the northern Armorican Massif (France and British Channel Islands, see Ballèvre et al., 2001; Brown, 1995; Chantraine et al., 2001; D'Lemos et al., 1990; Dissler et al., 1988; Dupret et al., 1990 and Strachan et al., 1996). Even though the rocks today exposed are unlikely to correspond to those eroded at Ediacaran times,

they can still provide constraints on the nature, age pattern and isotopic signature of the proximal detritus. In this crust segment, igneous rocks include: (i) late Cryogenian to early Ediacaran calc-alkaline suites comprising basic, intermediate and acid components with radiogenic Nd–Hf isotope signature, taken as evidence for arc–back-arc magmatism (Auvray et al., 1992; Brown et al., 1990; D'Lemos and Brown, 1993; Dallmeyer et al., 1991; Egal et al., 1996; Graviou and Auvray, 1990; Guerrot and Peucat, 1990; Miller et al., 2001; Nagy et al., 2002; Power et al., 1990; Samson et al., 2003); (ii) late Ediacaran migmatites and peraluminous granitoids (the Mancellian batholith), thought to have been generated during inversion of the back-arc and coeval arc–continent collision (Brown et al., 1990; Brown and D'Lemos, 1991; D'Lemos and Brown, 1993; Egal et al., 1996; 2011; Peucat, 1986). Paleoproterozoic and Tonian crustal rocks (Icartian and Port Morvan gneisses, respectively) are also documented (Calvez and Vidal, 1978; Egal et al., 1996; Inglis et al., 2004; Samson and D'Lemos, 1998; Samson et al., 2003). They are regarded either as the constituent autochtonous crust on which the Cadomian arc–back-arc was formed (Chantraine et al., 2001; Dissler et al., 1988) or as exotic blocks accreted to the arc in the early Ediacaran (Linnemann et al., 2014; Samson et al., 2003).

The ε_{Hf}(t) of various Cadomian intrusions are depicted Fig. 2.6 (from Hf isotope studies or recalculated from Nd isotopes based on the relation $\varepsilon_{Hf}(t) = 1.36\ \varepsilon_{Nd}(t) + 3$ determined by Vervoort et al., 1999). Magmas emplaced in the time period 750–625 Ma have supra-chondritic, DM-like Hf isotope signatures. A clear shift towards less radiogenic source compositions occurred in the Ediacaran as magmas younger than 625 Ma show a broad range of inferred ε_{Hf}(t) from +5 down to sub-chondritic values of -11. This pattern is similar to that observed in the detrital zircon record of the Velay metasediments (Fig. 2.6). As a direct consequence of this, the 750–555 Ma zircon population encountered in Ediacaran metasediments from the FMC could adequately originate from a proximal Cadomian arc source akin to the northern Armorican Massif.

The case of early Tonian–Stenian and Archean zircons is more problematic. Indeed, there is no rock of that age in the Armorican Massif. Besides, in this area, Paleoproterozoic granitoids have suprachondritic, DM-like, ε_{Hf}(t) which are more elevated than those observed in detrital zircons from the FMC Ediacaran (meta)sediments. These observations require the existence of a different, more distal source i.e. the main Gondwana land (Drost et al., 2011; Linnemann et al., 2008; 2014; Orejana et al., 2015; Pereira et al., 2012).

The distal source In the following, we address the nature and origin of the distal source based on the zircon age pattern and isotope signature of both Neoproterozoic detritus (Abati et al., 2010; 2012; Avigad et al., 2015; Meinhold et al., 2011; Morag et al., 2012) and today-exposed igneous rocks (Block et al., 2016; Eglinger et al., 2017; Küster et al., 2008; Morag et al., 2011b; Stern et al., 2010) from several segments of the Gondwana (West African Craton, Saharan Metacraton and Arabian Nubian Shield). We selectively reason on the early Tonian–Stenian, Paleoproterozoic and Neoarchean zircon populations (U–Pb date > 800 Ma) since those are the only ones for which a distal origin is ensured. Importantly, there is no rock older than Tonian in the Arabian Nubian Shield (Morag et al., 2011b; Stern, 2002) and older–than–800 Ma zircon grains are very scarce (Avigad et al., 2015; Morag et al., 2012; Stern et al., 2010) which discards this area as a potential source region. The West African craton (WAC) exposes Paleoproterozoic and Neoarchean rocks which zircon U–Pb–Hf isotope compositions match that of detrital grains from our samples (Block et al., 2016; Eglinger et al., 2017 and unpublished data from O. Laurent). However, there is no evidence for early Tonian–Stenian magmatic activity in the WAC (Ennih and Liégeois, 2008). Similarly, Ediacaran metasediments deposited in the vicinity of the WAC do feature Paleoproterozoic and Neoarchean zircon populations of adequate Hf isotope signature but lack any early Tonian–Stenian grain (Abati et al., 2010; 2012). This entails that the WAC alone cannot be the distal source

of late Ediacaran sediments from the eastern FMC. Little is known about the Saharan Metacraton. Early Tonian igneous rocks with both supra and subchondritic Nd isotope signatures are documented by Küster et al. (2008). Meinhold et al. (2011) report the existence of early Tonian–Stenian, Paleoproterozoic and Neoarchean zircon populations in a Neoproterozoic metasediment indicating that this area could have contributed to the detritus that fed the late Ediacaran basins of the FMC. Yet, the lack of Hf isotope data hinders further conclusions. Finally, involvement of crustal materials transported from very distant sources (central and southern Gondwana) may have been possible, as advocated for Cambrian–Ordovician sediments from northern Gondwana (Avigad et al., 2003; 2012; Altumi et al., 2013; Kolodner et al., 2006; Linnemann et al., 2011; Meinhold et al., 2011; 2013; Morag et al., 2011a).

Relative proportions of proximal vs. distal sources A total of 31% of detrital zircon U–Pb dates are older than 800 Ma (161/519 including the data of Chelle-Michou et al., 2017). Assuming that each eroded rock had a similar zircon content (same "fertility" in the sense of Dickinson, 2008), this yields a minimum estimate of the proportion of detritus derived from the Gondwana mainland, presumably the Saharan Metacraton. The compilation of Abdelsalam et al. (2002) demonstrate that Cryogenian–Ediacaran rocks with DM-like Nd isotope signatures today crop out in this crust segment. Yet, the youngest igneous rock emplacement age obtained by modern dating techniques (U–Pb on accessory minerals) are 578 ± 15 (Sultan et al., 1990) and even 591 ± 5 Ma when measurements performed by dissolution of multi-grain fractions are excluded. Therefore, metasediments zircon grains younger than 591 Ma most probably originate from the proximal Cadomian arc source. Such grains represent 13% of the dataset (68/519 including the data of Chelle-Michou et al., 2017). As a result, the proportion of detritus originating from distal Gondwana-land sources is bracketed between 31–87%. Refinement of this first-order estimate is hampered by our current knowledge of the structure and composition of both the Cadomian arc and the Saharan Metacraton.

Additional observations suggest that the actual value should be closer to 31 than 87%. Indeed, sample PdB-16-01 displays markedly different zircon U–Pb date pattern and Hf isotope signatures compared to other metasediments from the Lower Gneiss Unit, even though their protoliths were presumably deposited in the same basin and time period. This is indicative of brutal changes in the nature of the detritus sources through time. Such feature is consistent with a detritus originating from catchments submitted to high denudations rates, as would be the case of a continental arc. Consequently, it is very likely that the proximal Cadomian arc did supply an important fraction of the detritus that fed the late Ediacaran basins of Lower Gneiss Unit in the FMC.

2.2.9 Geodynamic inferences

Evolution of the Ediacaran back-arc basin

Several authors argued that late Ediacaran sediments from the north Gondwana margin were deposited in back-arc basins located at the rear of the Cadomian subduction (Fernández-Suárez et al., 2000; Linnemann et al., 2004; 2008; 2014; Orejana et al., 2015; Pereira et al., 2012). This conclusion is based on reconstructed plate motions since the Ediacaran (Stampfli et al., 2013), the present-day location of the Cadomian magmatic arc and the mixed nature of the detritus pinpointing the existence of both a nearby active margin and an evolved mature source by that time (Fig. 2.7).

In the French Massif Central, the pre-Variscan history of the Lower Gneiss Unit features the deposition of detrital sediments in the time period 550–590 Ma, i.e the late Ediacaran. The actual thickness of the sedimentary pile is difficult to estimate due to Variscan tectonics but was likely pluri-kilometric. Sediments were intruded by S-type granitic magmas at c. 540–545 Ma (see previous section). As a matter of fact, the oldest

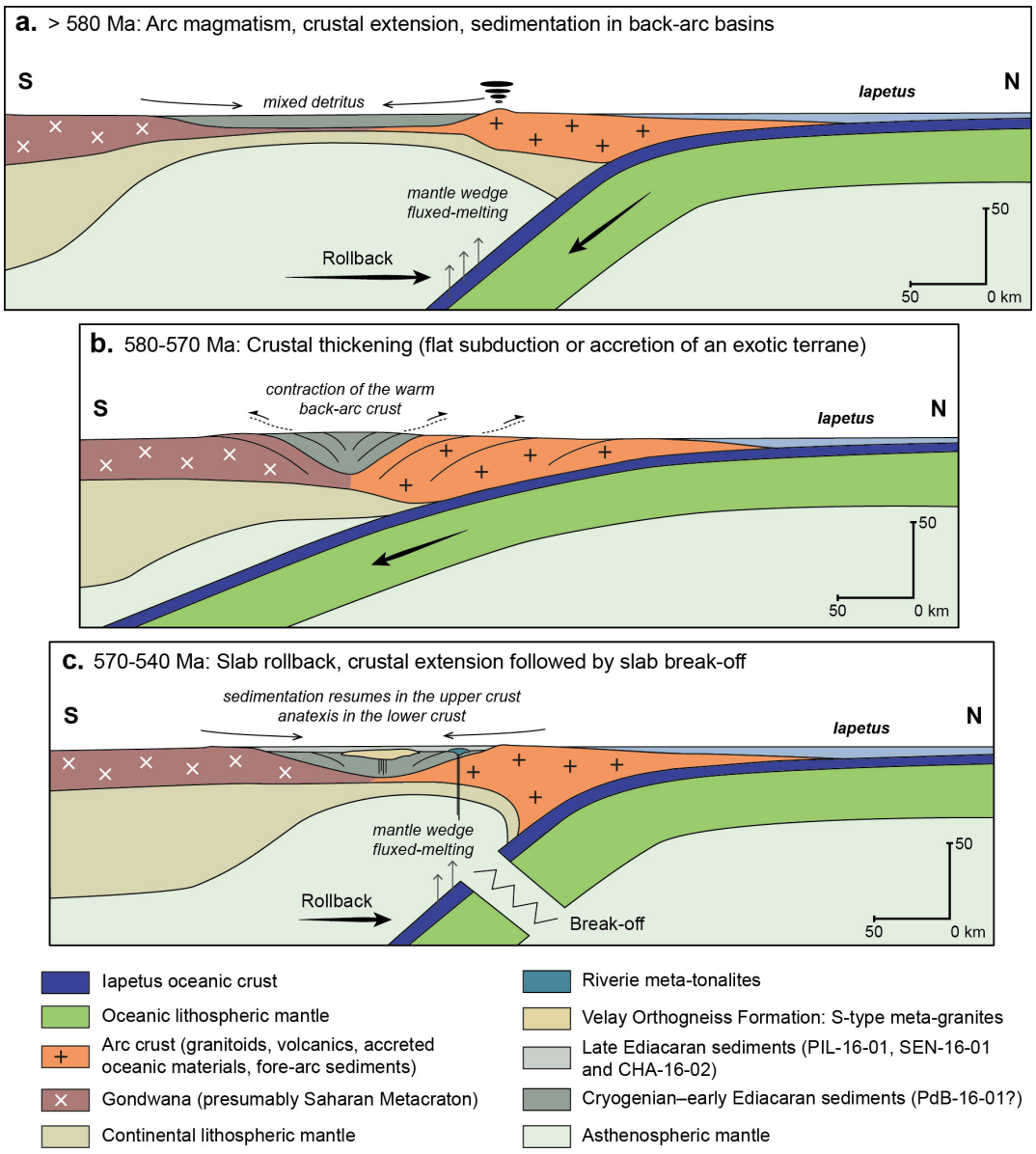

Figure 2.7: Interpretative geodynamic sketches illustrating the Ediacaran evolution of the crust segment to which the French Massif Central belongs. Inspired from Collins and Richards (2008). See text for discussion. The Riverie meta-tonalites are introduced section 3.5.

emplacement age determined for the VOF meta-granites and the age of the youngest zircon population encountered in metasediments are identical within errors (545.9 ± 4.3 and 553.2 ± 5.3 Ma, respectively). This points to a very short time span between sedimentation and crust-derived magmatism. Such situation is typically observed in accretionary orogenic settings where protracted periods of lithospheric extension and associated sedimentation (Fig. 2.7a) are punctuated by contractional events (Fig. 2.7b) leading to crust thickening and followed by anatexis (Barker et al., 1992; Cawood et al., 2009; Collins, 2002; Collins and Richards, 2008; Crook, 1980; Kemp et al., 2009; Zurbriggen, 2015). Therefore, geochronological constraints further support a late Ediacaran back-arc location for the crust segment today exposed in the Lower Gneiss Unit of the FMC.

S-type granites from the VOF emplaced *c.* 30 Ma after a thickening episode that affected the northern margin of Gondwana (see section 2.1), dated at 580–570 Ma in the North Armorican massif (Ballèvre et al., 2001; Strachan et al., 1996). Contraction in the upper plate would have been promoted by the shallowing of the Cadomian subduction angle (Collins, 2002; Strachan et al., 1996). The inferred time span (30 Ma) between thickening and magmatism is consistent with that predicted by numerical models (Clark

et al., 2011). In this frame, metasediments would have been deposited during the post-contraction relaxation period, between 570 and 550 Ma. Sample PdB-16-01 lacks any detrital zircon younger than c. 590 Ma and its deposition may pre-date the thickening event.

A glimpse of the Cadomian arc evolution?

Detrital zircon grains from the Velay metasediments record a marked change in their Hf isotope composition at *c.* 640 Ma with a drift towards less radiogenic ε_{Hf}(t). Assuming that a significant proportion of the Cryogenian–Ediacaran detritus originates from the proximal Cadomian arc (see section 2.2.8), such drift could be explained by the sudden incorporation of an isotopically evolved, old crustal component in younger–than–640 Ma arc magmas. Mixing would have occurred in the source, by addition of crust-derived material in the mantle (Nebel et al., 2011; Plank, 2005; Roberts et al., 2013), or during magma ascent (Laumonier et al., 2014b;a).

A similar pattern has been described in the Kohistan-Ladakh Batholith of the Himalayan belt by Bouilhol et al. (2013). In this oceanic arc developed above the Tethyan ocean, early granitoids show suprachondritic Nd–Hf isotope signatures which abruptly become subchondritic at 50–40 Ma. According to these authors, such change would reflect the collision of the India plate with the arc and resulting tapping of a continental crust-derived Indian source in addition to the mantle wedge. Following this, the *c.* 640 Ma drift observed in the detrital zircon record may be correlated to the accretion of an outboard-sitting exotic crustal terrane to the early Cadomian arc. The *c.* 2.0 Ga Icartian gneisses of the North Armorican Massif are good candidates because they are today located in the fore-arc region (Linnemann et al., 2014). Besides, those gneisses experienced amphibolite-facies metamorphism and were intruded by a set of leucogranites by 620–605 Ma (Samson and D'Lemos, 1998), consistent with an late Cryogenian–early Ediacaran accretion to the arc.

2.3 Amphibolites

2.3.1 Introduction

Investigating the origin of meta-igneous rocks is of primary importance in order to decipher the pre-orogenic history of the French Massif Central. In the Lower Gneiss Unit, the presence of igneous metabasites clearly testifies for the existence of mantle melting episode(s) before the onset of the Variscan orogeny. Such rocks constitute very scarce massifs with a maximal thickness of 60 m and lateral extension of 2–3 km (Chenevoy et al., 1995). They are intercalated within meta-greywackes (see Weisbrod, 1970 and Négron, 1979, for the Arc de Fix domain; Yousif, 1980, for the Vivarais and Pilat domains) or enclaved within the Velay granites (e.g. Vitel, 1985).

The metabasites were deformed and equilibrated in the amphibolite- to granulite-facies during the Variscan orogeny (Vitel, 1985). Most rocks are layered and relic gabbroic textures have been described locally (Lochon, 1985; Yousif, 1980). That being said, identifying the nature of the protolith has proven impossible in most cases. Previous geochemical studies have concluded that the amphibolites have major and trace elements compositions akin to alkali basalts (Briand et al., 1992; Chenevoy et al., 1986; Ouali, 1993; Pin and Marini, 1993).

The age of the melting event is unknown and all authors considered the meta-greywacke host as indicative of an intra-continental setting for basic magmatism (Briand et al., 1992; Pin and Marini, 1993). They postulated that the LGU amphibolites are Cambrian–Ordovician in age by analogy with the stratigraphically well-dated volcano-sedimentary successions of the lower-grade Parautochtonous Unit and Fold-and-Thrust Belt. There, metabasites transitional between enriched tholeiites and alkali basalts have

been described in the Lower Paleozoic strata (Alsac et al., 1987; Lépine et al., 1988; Marini, 1987; 1988; Pouclet et al., in press).

In order to put further constraints on the geochemical signature of the LGU metabasites and ascertain the validity of the Cambrian–Ordovician age, additional samples have been collected for whole-rock major and trace element determinations and zircon U–Pb dating. One layered metabasite (MM01) was sampled near the village of Rochepaule and three others (MM02 to 04) at the nearby Fromentoux farm (Fig. 2.1). The outcrops and mineralogy of the metabasites are described in Yousif (1980).

2.3.2 Geochemistry and petrogenesis

The whole-rock major and trace element compositions of the four samples were obtained from the *ALS Global* firm. A geochemical database was built up from this new dataset and the literature (Briand et al., 1992; Molina, 1973; Ouali, 1993; Pin and Marini, 1993; Weisbrod, 1970; Yousif, 1980). After screening out altered samples (high LOI and high W index of Ohta and Arai, 2007), a total of 113 analyses were retained (14 of which include trace element compositions).

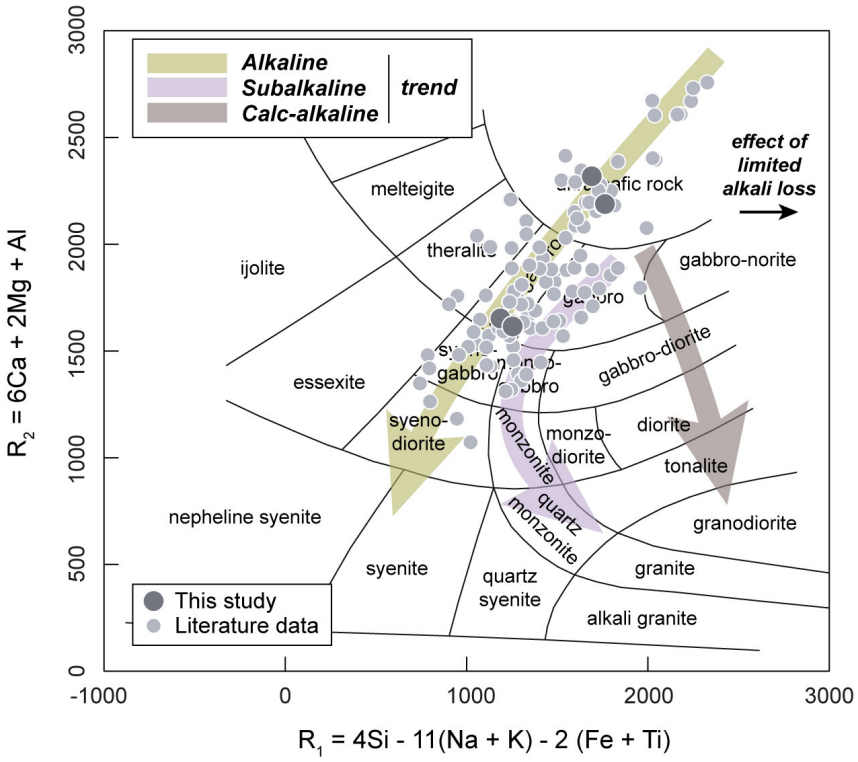

Figure 2.8: Composition of the Lower Gneiss Unit metabasites plotted in the R_1–R_2 diagram of De La Roche et al. (1980). The fractionation trends for each series are from Debon and Lemmet (1999).

In the R_1–R_2 diagram of De La Roche et al. (1980), metabasites plot in a variety of fields, mostly those of ultramafic rocks, alkali gabbros, gabbros, monzogabbros and syenogabbros (Fig. 2.8). They dominantly define an alkalic trend and subordinately a subalkaline trend (Debon and Lemmet, 1999). All rocks are enriched in Th, LREE, Zr but depleted in HREE with respect to N–MORBs and lack any negative Nb anomaly (Fig. 2.9). In the Th–Nb proxy diagram (Pearce, 2008), they accordingly plot in the mantle array and dominantly cluster around the OIB endmember (Fig. 2.10a). In the Ti–Nb proxy diagram (Fig. 2.10b), LGU metabasites plot within the OIB array and define a trend between a high Nb/Yb and Th/Yb endmember (Nb/Yb = 10; Th/Yb = 1) and a very high Nb/Yb and Th/Yb endmember (Nb/Yb = 30; Th/Yb = 2.5). The two remaining samples have ratios akin to OIBs (Sun and McDonough, 1989).

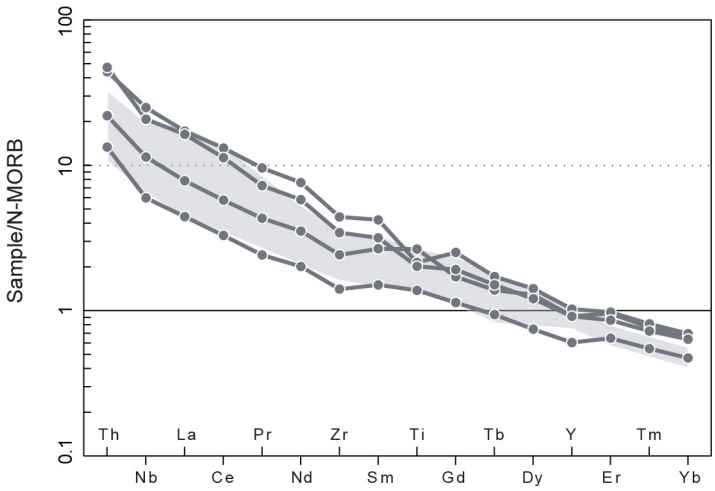

Figure 2.9: Incompatible, immobile element patterns normalized to the composition of N-MORBs (Sun and McDonough, 1989) for the metabasites of the Lower Gneiss Unit. The grey field depicts the composition of samples from the litterature.

These observations confirm that the LGU metabasites mostly define an alkaline series as already advocated by Briand et al. (1992). The existence of the subalkaline series is questionable. Indeed, in the R_1–R_2 diagram, alkali loss during metamorphism would displace sample compositions towards higher R_1 values at constant R_2. Therefore, samples from the main alkaline population experiencing limited alkali loss unidentified by our screening technique would create an artefactual subalkaline series. Such interpretation is supported by the fact that one sample from the literature (THUE, south of the Velay dome, reported by Pin and Marini, 1993) shows trace element compositions akin to alkali basalts yet is part of the subalkaline trend in the R_1–R_2 diagram.

The enrichment in LREE and more generally HFSE compared to N–MORBs is indicative of low melting degrees and/or an enriched mantle source (Pearce, 1996; 2014). The depletion in HREE, evidenced by the high TiO_2/Yb ratios, most likely originates from melting of a mantle source containing residual garnet and hence melting depths in excess of 50–70 km (Ziberna et al., 2013). The trend in the Nb–Ti proxy diagram could attest to a range of melting degrees at constant pressure (Pearce, 2008). Altogether, these geochemical proxies support an origin of the LGU metabasite protoliths by melting of a deep asthenospheric source or, alternatively, a lithospheric mantle source that did not previously interact with slab-derived fluids.

2.3.3 Zircon U–Pb dating

In order to constrain the emplacement age of the LGU metabasite protoliths, one sample (MM03) was selected for zircon U–Pb dating. Zircon grains were separated from the powdered rock at Saint-Etienne University using conventional techniques described section 2.1, subsequently cast into epoxy mounts and polished down to an equatorial grain section. CL-imaging were performed at the Laboratoire Magmas et Volcans in Clermont-Ferrand (France) using a Jeol JSM-5910 SEM. Selected grains were dated by LA–ICP–MS at ETH Zürich (see Appendix B.3.3 for analytical notes and Tables B6 and B9 for standards and samples results).

Zircon textures

Zircon grains from sample MM03 are xenomorphic with rounded to oval shapes and low aspect ratios (between 1 and 2). The grain edges are almost always corroded and irregular (Fig. 2.11). CL-dark cores (see zircon grains 3,5 and 6) are surrounded by poorly luminescent rims displaying sector zoning. Such zoning is locally blurred in domains of

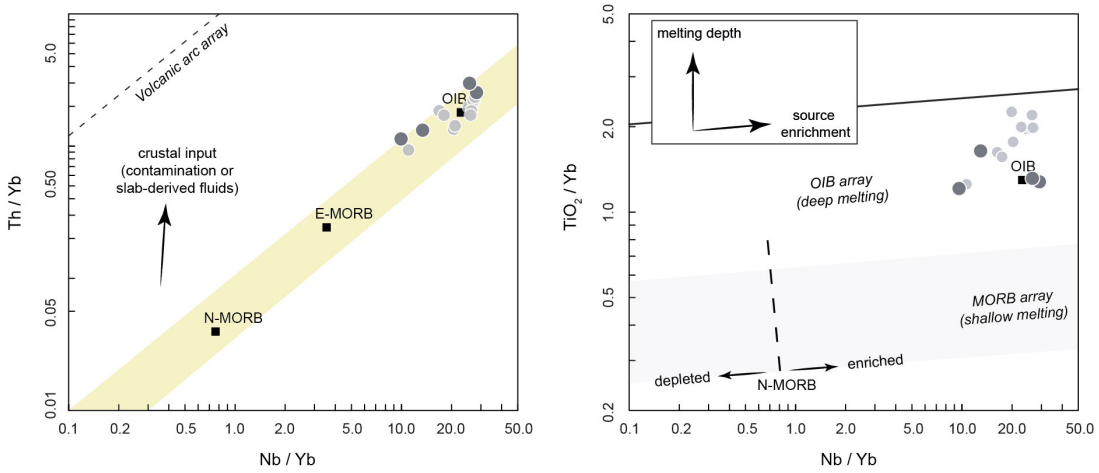

Figure 2.10: Proxy element diagrams for metabasites from the Lower Gneiss Unit. (a) Th–Nb proxy diagram of Pearce (2008). Oceanic basalts plot within the MORB–OIB array. Magmas contaminated by the continental crust during ascent or which mantle source interacted with slab-derived fluids plot in the volcanic arc array. (b) Ti–Nb proxy diagram of Pearce (2008). The TiO_2/Yb ratio strongly depends on the presence of residual garnet in the mantle source. Magmas formed at great depth feature high TiO_2/Yb ratio provided that garnet is not exhausted in the residua. Such samples plot in the OIB array. If the magmas result from melting of spinel peridotites, or if garnet has been exhausted in the residua, they plot in the MORB array. Same legend as Fig. 2.8

higher luminescence (see bottom of zircon 6 for instance). Fractures propagating from the grain cores have been subsequently healed and are thus visible on CL images (e.g. zircon 4).

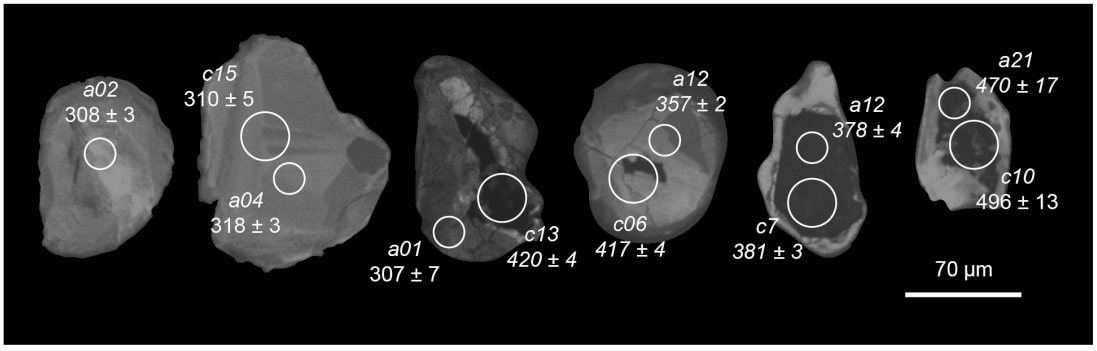

Figure 2.11: Representative cathodoluminescence images of zircon grains from amphibolite sample MM03. The locations of laser spots are indicated along with the spot name (aXX and cYY for measurements performed in the first and third sequence, respectively). The corresponding $^{206}Pb/^{238}U$ dates are quoted with $\pm 2\sigma$ uncertainty, in Ma. All displayed analyses are concordant (except those in italic). Spot diameters are 20 and 30 μm.

Results

Thirty-eight spots were drilled on 23 grains. Nine analyses are markedly discordant (concordance: 14–55%) and will not be discussed further. Eleven measurements performed on zircon domains displaying sector zoning and faint luminescence yielded $^{206}Pb/^{238}U$ dates between 318 ± 3 and 304 ± 4 Ma (Fig. 2.12a). A Concordia date of 307.8 ± 3.7 Ma (with a $MSWD_{C+E}$ of 1.5) can be calculated out of the seven youngest, equivalent and concordant analyses. All eleven have markedly low Th/U ratios, always <0.1 and often <0.06 (Fig. 2.12b). Fourteen spots drilled on CL-dark cores, on rims displaying sector zoning and on mixed domains gave a range of discordant $^{206}Pb/^{238}U$ dates ranging from 475 ± 8 down to 347 ± 3 Ma (Fig. 2.12a). One analysis performed on a CL-dark core

yielded a concordant $^{206}Pb/^{238}U$ date of 496 ± 13 Ma (Fig. 2.11 and 2.12a). Finally, one measurement conducted on an other CL-dark core gave a discordant $^{206}Pb/^{238}U$ date of 538 ± 10 Ma. Analyses with $^{206}Pb/^{238}U$ dates older than 320 Ma show elevated Th/U ratios (>0.48 and up to 2.5, see Fig. 2.12b).

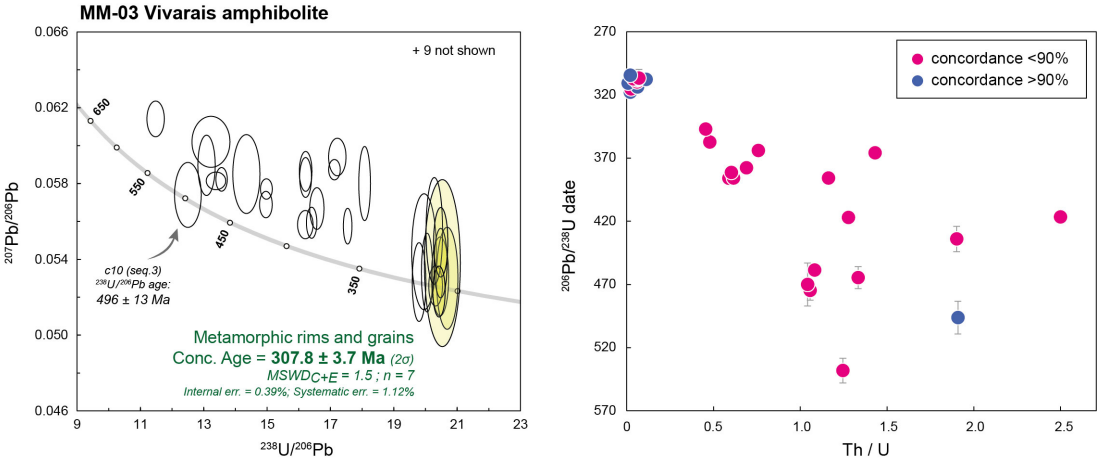

Figure 2.12: (a): Tera–Wasserburg diagram ($^{238}U/^{206}Pb$ vs. $^{207}Pb/^{206}Pb$) for zircon from the Vivarais amphibolite sample MM03. Error ellipses and ages are displayed at 2σ level of uncertainty. Yellowish ellipses are those considered for Concordia age calculations. (b) $^{206}Pb/^{238}U$ date as a function of zircon Th/U ratio for each measurement showing concordance >63%.

Interpretation

Zircon grains and rims showing U–Pb dates younger than 318 Ma are poorly luminescent, display sector zoning and have low Th/U. Such features are typically observed in metamorphic zircon (re)crystallized at subsolidus conditions (Corfu et al., 2003; Hoskin and Black, 2000; Vavra et al., 1999). Therefore, I interpret the Concordia date of 307.8 ± 3.7 Ma as the age of peak metamorphic conditions. At the regional scale, this age is very well documented and corresponds to: (i) the anatexis of surrounding paragneisses from the Lower Gneiss Unit, dated at 307.4 ± 2.3 Ma (Chelle-Michou et al., 2017); (ii) intrusion of mantle mantle-derived magmas ("vaugnerites") at 307.8 ± 1.6 and 307.3 Ma ± 1.3 Ma (Laurent et al., 2017); (iii) emplacement of the Velay granite at 307.5 Ma ± 2.0 Ma (Chelle-Michou et al., 2017).

Figure 2.12b illustrates the existence of a trend between a set of spots with low Th/U (<0.11) and late Carboniferous $^{206}Pb/^{238}U$ date (<318 Ma), corresponding to (re)crystallized metamorphic zircon, and an endmember with high Th/U and Cambrian–Ordovician $^{206}Pb/^{238}U$ dates. This observation suggests that the scattered $^{206}Pb/^{238}U$ ranging from 475 ± 8 down to 347 ± 3 Ma reflects the sampling of mixed zircon domains comprising: (i) (re)crystallized metamorphic sectors and (ii) old zircon cores. From this perspective, the discordance displayed by most analyses would be a direct consequence of such mixing.

Yet, mixing trends in the Tera-Wasserburg diagram (Fig. 2.12a) or in the $^{206}Pb/^{238}U$ date vs. Th/U plot (Fig. 2.12b) yield a non-unique solution. I interpret this feature as a consequence of common Pb incorporation, which is independently supported by the observation of healed micro-fractures in CL images. Consequently, the actual age of the zircon cores is most probably given by the single concordant $^{206}Pb/^{238}U$ date of 496 ± 13 Ma. Younger discordant dates would reflect both core/rim mixed analyses and common Pb incorporation. The significance of the discordant $^{206}Pb/^{238}U$ date of 538 ± 10 Ma remains unclear.

The CL-dark cores can have two different origins. First, they would have crystallized during the emplacement of the igneous protolith. Alternatively, they could correspond

to xenocrysts entrained within the basaltic parental magma during emplacement in the continental crust and not fully dissolved. In the first case, 496 ± 13 Ma would represent the intrusion age of the mafic magmatic protolith. Such result is consistent with other studies that reported the existence of similar tholeitic transitional to alkaline basic magmatic rocks of similar age in the low-grade units of the FMC (Alsac et al., 1987; Béziat et al., 1992; Lépine et al., 1988; Marini, 1987; 1988; Pouclet et al., in press).

2.4 Conclusion

The pre-Variscan rocks of the Lower Gneiss Unit mostly record Neoproterozoic events. Metasediments were deposited between 590 and 545 Ma in a back-arc basin supplied by a detritus originating from both a (present-day)north-sitting magmatic arc and the main Gondwana-land, presumably the Saharan Metacraton. Contractional events probably related to the shallowing of the Cadomian subduction angle resulted in burial and thickening of the thin, anomalously warm back-arc crust, itself dominated by sedimentary lithologies. This resulted in a voluminous magmatic event marked by the c. 540 Ma intrusion of a set of S-type porphyritic and leucogranites, protoliths of the Velay Orthogneiss Formation. Some amphibolite bodies from the LGU may represent Cambrian gabbros/basalts but their scarcity strikingly contrasts with the voluminous Cambrian–Ordovician magmatism observed in the LGU of the western FMC Melleton et al. (2010).

Chapter 3

Meta-igneous rocks of the Upper Gneiss Unit in the Monts-du-Lyonnais area

3.1 Introduction

In the eastern Massif Central, one of the largest and best exposure of the Upper Gneiss Unit is found in the *Monts-du-Lyonnais* area, North of the Velay dome. Such domain was thus specifically targeted in order to: (i) better characterize the pre-Variscan history of this metamorphic nappe, and ultimately (ii) get insights on the crustal evolution of the terrains today exposed in the Variscan belt.

The Upper Gneiss Unit mostly equilibrated in the amphibolite-facies (Dufour, 1982; Feybesse et al., 1995; Gardien et al., 1990). The volumetrically dominant lithological component corresponds to a set of orthogneisses, referred to as Lyonnais Orthogneiss Formation in the following, but garnet–biotite–sillimanite paragneisses are particularly abundant in the southern and western parts of the *Monts-du-Lyonnais* (Fig. 3.1). Following the studies of Peterlongo (1958) and Forestier (1961), I recognize hereafter the Leptynite–Amphibolite Complex (LAC) as its southern domain (i) comprising a large variety of metamorphic lithologies including leucocratic fine-grained orthogneisses of the Lyonnais Orthogneiss Formation, paragneisses, metabasic rocks, amphibole-bearing gneisses, marbles, garnet-bearing peridotites and (ii) featuring petrological relics of an early high-pressure metamorphic event (Blanc, 1981; Dufour et al., 1985; Dufour, 1985; Gardien et al., 1990; 1988; Lardeaux et al., 1989; Lasnier, 1968). Such definition is also that retained by Lasnier (1968); Blanc (1981) and Briand et al. (1995). The LAC would correspond to a Franciscan-type "subduction mélange" zone created during the northwards subduction of the Galicia–Massif Central ocean (Lardeaux et al., 2014).

In this chapter are typified the nature and origin of the meta-igneous rocks from the Upper Gneiss Unit based on a literature review (mostly unpublished PhD theses from the 80's) and a new set of samples on which were conducted geochemical (major and trace element together with zircon Hf isotope compositions) and geochronological investigations. A geochemical database for metamorphic lithologies was built up from the literature (Blanc, 1981; Davoine, 1971; Dufour, 1982; Ouali, 1993), unpublished analyses (courtesy of J.-F. Moyen, A.-C. Ganzhorn and V. Gardien) and a new dataset from rocks I sampled during my field survey (n=7). The total number of analyses is 430.

First, the geochemical database was screened to discard metasedimentary lithologies and altered samples. This has been done by a careful consideration of petrological descriptions and by calculation of the W index of Ohta and Arai (2007). The MFW plot of these authors clearly outlines the lithologies that experienced surface weathering (Fig. 3.2). They accordingly departs from the igneous trend defined by unaltered meta-igneous rocks. A total of 393 analyses was thus retained for further interpretations.

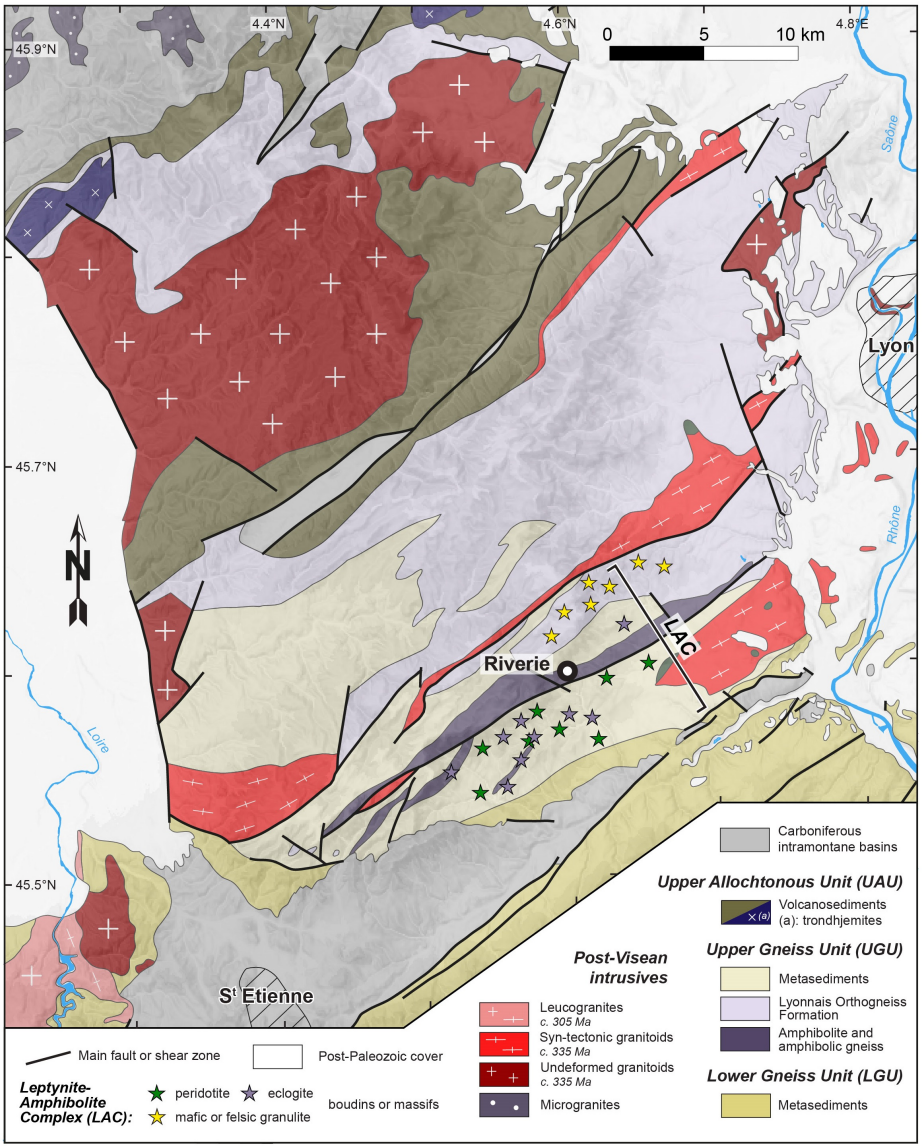

Figure 3.1: Geological map of the *Monts-du-Lyonnais* area. Redrawn after the maps of Chiron and Kerrien (1979), Dufour (1982) and Feybesse et al. (1995).

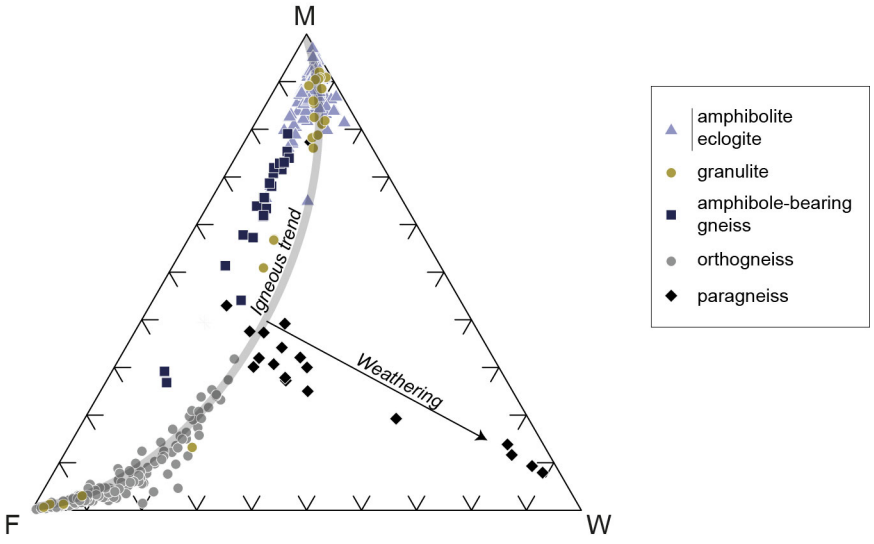

Figure 3.2: MFW plot (Ohta and Arai, 2007) for the *Monts-du-Lyonnais* metamorphic rocks. The distinction between metasedimentary and meta-igneous lithologies, based on petrological descriptions, is confirmed thereby. Overall, meta-igneous rocks experienced limited weathering.

3.2 The Lyonnais Orthogneiss Formation

3.2.1 Petrography

The orthogneisses correspond to amphibolite-facies meta-felsic rocks with the mineralogy Qz + Pg + Kf + Bt ± Grt ± Sill ± Ms + Ap + Ilm + Zrc ± All (mineral abbreviations from Whitney and Evans, 2009). Besides, hornblende and titanite have been locally described by Dufour (1982). Several facies coexist from a poorly deformed coarse-grained augen gneiss with microcline porphyroblasts to a strongly deformed medium-grained banded gneiss. A fine-grained leucocratic facies (locally called *leptynite*) is particularly abundant in the Leptynite–Amphibolite Complex. There, the orthogneisses feature meter to decameter-scale boudins of mafic to felsic granulite-facies meta-igneous rocks (Dufour, 1982; Duthou et al., 1981).

In some cases (especially for the felsic rocks), it has proven difficult to classify the analysed sample as amphibolite- or granulite-facies for lack of comprehensive petrological description. When this problem occurred, the rock was arbitrarily attributed to the main "orthogneiss" group. Therefore, our database for the main amphibolite-facies orthogneiss unit may still contain a few mislabelled granulite-facies igneous rocks.

3.2.2 Volcanic vs. plutonic origin

Previous investigations on igneous textures and zircon typology have concluded that the augen, banded and at least part of the leucogneisses are former plutonic rocks (Dufour, 1982). Based on faint chemical differences, Dufour (1982) regarded some leucogneisses from the Leptynite–Amphibolite Complex (the "ortholeptynites") as former volcanites. Given the petrographic continuity, similar chemistry and whole-rock Rb–Sr ages (see below) of all orthogneisses in the UGU, we will further consider them as meta-plutonic rocks.

The presence of few metasedimentary enclaves within the orthogneisses has been reported by Dufour (1982). At the "Crêt de Py Froid" locality, melanocratic enclaves with igneous textures that strongly recall mafic microgranular enclaves (MME) can be observed. Yet, they have never been studied or even mentioned in the literature.

3.2.3 Geochemistry

All orthogneisses (n=157) plot in or very close to the field of granites in the Na_2O+K_2O vs. SiO_2 classification diagram (Middlemost, 1994, Fig. 3.3a). Consistently, most analyses plot in the field of rhyolite and dacite in the diagram of Winchester and Floyd (1977), modified by Pearce (1996) (Fig. 3.3b). The consistency between major and trace element-based classifications, together with the low W index (<25) and the fact that orthogneisses still define pre-Variscan whole-rock Rb–Sr ages (see next section) collectively suggest that the meta-igneous rocks experienced closed-system metamorphism with limited alkali loss. As a result, they do correspond to meta-granites.

Apart from very few outliers, the meta-granites are potassic (K_2O: 4–6 wt.%) and plot in the high-K calc-alkaline to shoshonite fields in the K_2O vs. SiO_2 diagram (Pecerillo and Taylor, 1976, Fig. 3.3c). They are metaluminous (A/CNK: 0.9 to 1, 10% of the dataset) to mildly peraluminous (A/CNK: 1 to 1.2). In the B–A diagram (Debon and Le Fort, 1983; Villaseca et al., 1998), a large number of samples plot in the felsic-peraluminous field and define a trend towards low–peraluminous compositions (Figure 3.3d). The normative feldspar diagram (O'Connor, 1965) reassesses the meta-granitic nature of the orthogneisses, highlighting their low normative anorthite contents.

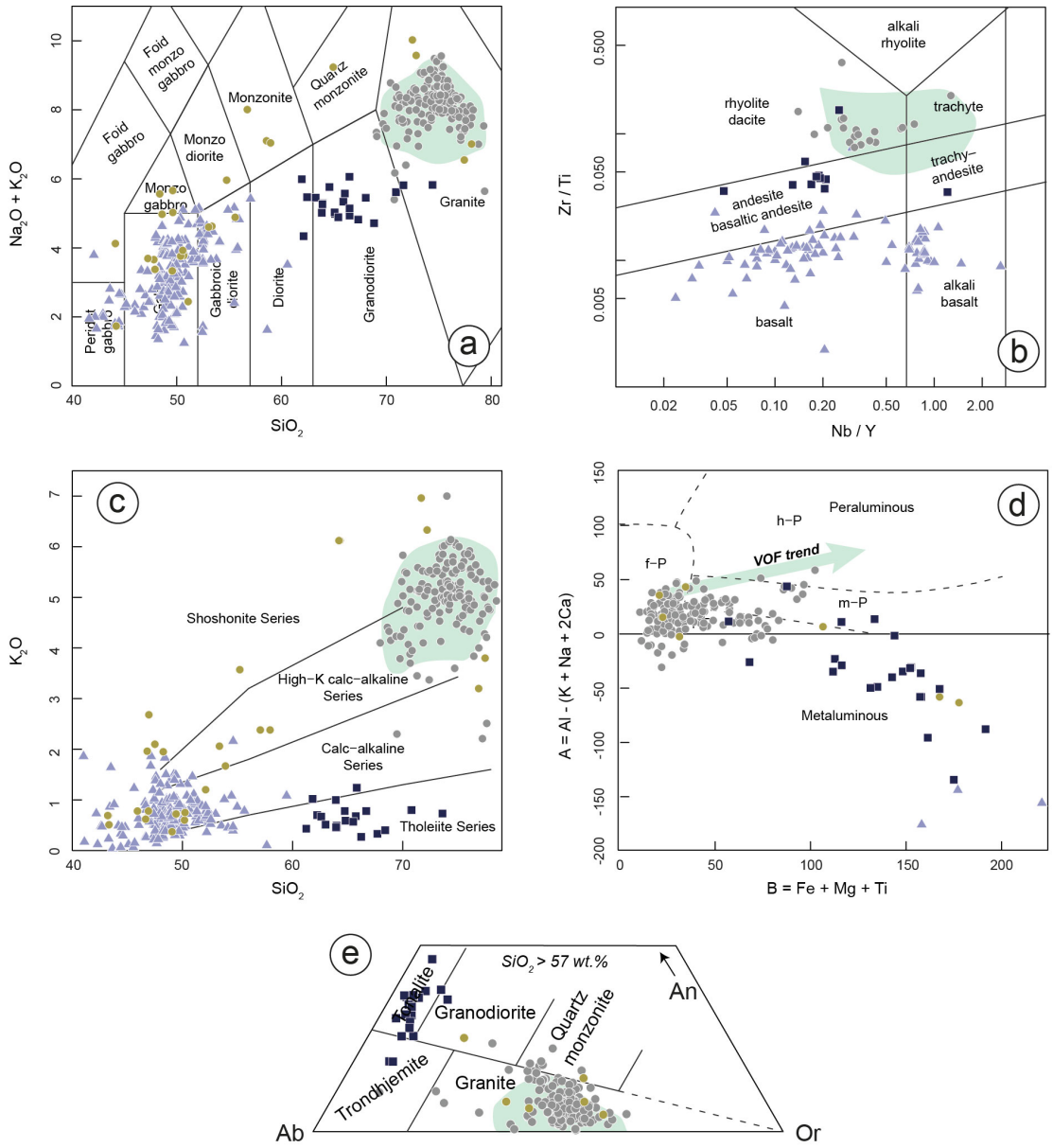

Figure 3.3: Geochemical diagrams outlining the main characteristics of the meta-igneous lithologies from the Upper Gneiss Unit of the Monts-du-Lyonnais area. (a) Total Alkali vs. Silica (TAS) classification diagram (Middlemost, 1994); (b) Zr/Ti vs. Nb/Y classification diagram of Winchester and Floyd (1977) modified by Pearce (1996); (c) K_2O vs. SiO_2 diagram of Pecerillo and Taylor (1976); (d) B–A diagram of Debon and Le Fort (1983) modified by Villaseca et al. (1998); (e) normative feldspar classification diagram of O'Connor (1965).

3.2.4 Age

The *Monts-du-Lyonnais* orthogneisses have been the subject of several geochronological investigations summarized Table 3.1. The three youngest dates are equivalent and yield a weighted average emplacement age for the igneous protolith of 469.6 ± 5.7 Ma (2σ, MSWD = 1.6). The significance of the older date of c. 500 Ma remains uncertain. The analysed rocks were sampled at the Yzeron quarry which features a great variety of orthogneiss facies which could include older and non-cogenetic rocks.

Location	Age	Method	Reference
Yzeron	502 ± 7	WR Rb–Sr isochron	Duthou et al., 1984
Chaussan	478 ± 11	WR Rb–Sr isochron	Dufour, 1982
Duerne	467 ± 10	Pb evaporation	Feybesse et al., 1995
Maringes	466 ± 9	Pb evaporation	Feybesse et al., 1995

Table 3.1: Summary of available geochronological data on the *Monts-du-Lyonnais* orthogneisses.

Moreover, a zircon extracted from the Duerne orthogneiss and analysed with the Pb evaporation method by Feybesse et al. (1995) yielded an Ediacaran date of 567 ± 12 Ma interpreted as an inherited age.

3.2.5 Isotope geochemistry

As evidenced above, the whole rock Rb–Sr isotope data from Dufour (1982) and the zircon Pb evaporation measurements of Feybesse et al. (1995) yield consistent and identical emplacement ages for the protoliths of the orthogneisses. This is indicative of limited disturbance of the Rb–Sr isotopic system by hydrothermal and/or weathering processes. As a result, the initial $^{87}Sr/^{86}Sr$ (I_{Sr}) ratio of each sample was recalculated at the emplacement age of 470 Ma.

Figure 3.4 shows the variability of I_{Sr} in the Monts du Lyonnais orthogneisses (data from Dufour, 1982). Most of the data plot along a mixing line between a high-Sr, low I_{Sr} (0.706) endmember and a low-Sr, high I_{Sr} (0.712) endmember.

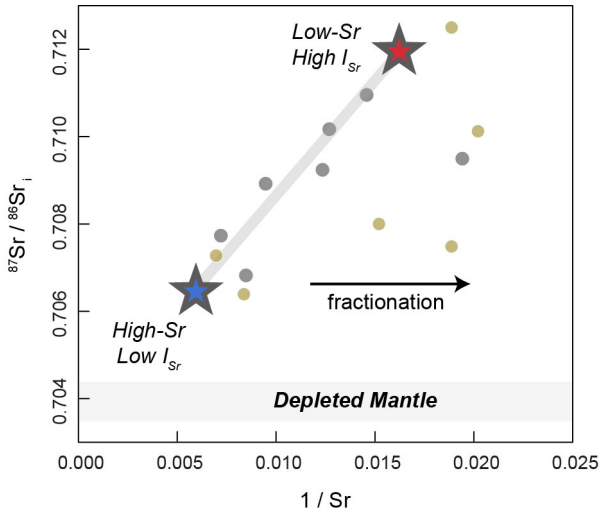

Figure 3.4: Initial $^{87}Sr/^{86}Sr$ (I_{Sr}) as a function of 1/Sr (in ppm) for the Lyonnais Orthogneiss Formation samples (in grey) and embedded felsic granulite boudins and massifs (in green). Data from Dufour (1982) and Duthou et al. (1981). Fractionation of plagioclase decreases the Sr content of the melt but keeps the I_{Sr} constant.

3.2.6 Petrogenesis

In this section, I attempt to characterize the petrogenesis of the Lyonnais Orthogneiss Formation (LOF) via a comparison with its well-characterized Lower Gneiss Unit counterpart: the Velay Orthogneiss Formation (section 2.1).

Figure 3.3 highlights their overall similar chemical compositions. Both are dominantly composed of K-rich granites including high-SiO_2 (>75%) components. Some subtle differences can be pinpointed. The LOF granites are statistically less peraluminous than the VOF (average A/CNK of 1.07 against 1.18 for the VOF, Fig. 3.5a). Accordingly, they feature rare amphibole-bearing facies and define a low-peraluminous trend in the B–A diagram while the VOF trends towards high-peraluminous compositions. Moreover, the LOF granites tend to be poorer in P (average of 0.14 vs. 0.24 wt.%, Fig. 3.5b). In the ternary CaO–K_2O/Na_2O–Al_2O_3/(FeO_t+MgO) diagram (Laurent et al., 2014), the compositions of 85% of the LOF samples overlap with the VOF's and spread within the fields of sediment- and tonalite-derived melts. The remaining 15% depart from the VOF and trend towards the compositions of melts derived from high-K mafic lithologies (Fig. 3.5c). Trace-elements data are available for only four leucogneisses from the LOF. In Whalen's discrimination diagrams (Whalen et al., 1987), two samples clearly plot in the field of fractionated I- & S-type granites, within the trend defined by the VOF samples, while two others plot close to the field of A-type granites (Fig. 3.5d). Lastly, it must be stressed that the LOF likely contains MME whereas such enclaves have never been observed within the VOF.

Collectively, the above-mentioned observations suggest that the petrogenesis of LOF and VOF igneous protoliths slightly differs. Of importance are the negative slope displayed by the LOF in the B–A diagram (Fig. 3.3d) together with its lower A/CNK values and P_2O_5 contents, features generally observed in I-type granitic suites (Villaseca et al., 1998). There is no clear consensus on the origin of such suites as they may form by: (i) mixing between crust- and mantle-derived magmas (Metcalfe et al., 1995; Zorpi et al., 1989); (ii) fractionation of mantle-derived magmas (Sisson et al., 2005); (iii) melting of mafic rocks (Ratajeski et al., 2005); (iv) melting of crustal lithologies such as meta-volcanic rocks of intermediate composition (andesite to dacite) and immature clastic sediments derived from them (Clemens et al., 2011).

The fact that the LOF granites share some characteristics with I-type granites can be interpreted in the light of our current knowledge of the eastern FMC pre-Variscan evolution. Following the conclusions drawn in Chapter 1, this crust segment originally consisted in a Ediacaran back-arc basin fed by detritus originating from a distal mature source (the Gondwana-land) and a proximal immature source (the Cadomian arc). I therefore propose that the LOF magmas formed by melting of a heterogeneous sedimentary sequence containing a significant proportion of immature volcaniclastic sediments, in contrast to the VOF which source would encompass more mature detritus. This model accounts for all the differences between the LOF and VOF and is besides supported by the spread in the LOF initial Sr isotope compositions which would attest to melting of a variety of source materials, from clasts of mantle-derived intermediate igneous rocks with low I_{Sr} and high Sr contents to isotopically evolved and Sr-depleted distal sediments (Fig. 3.4).

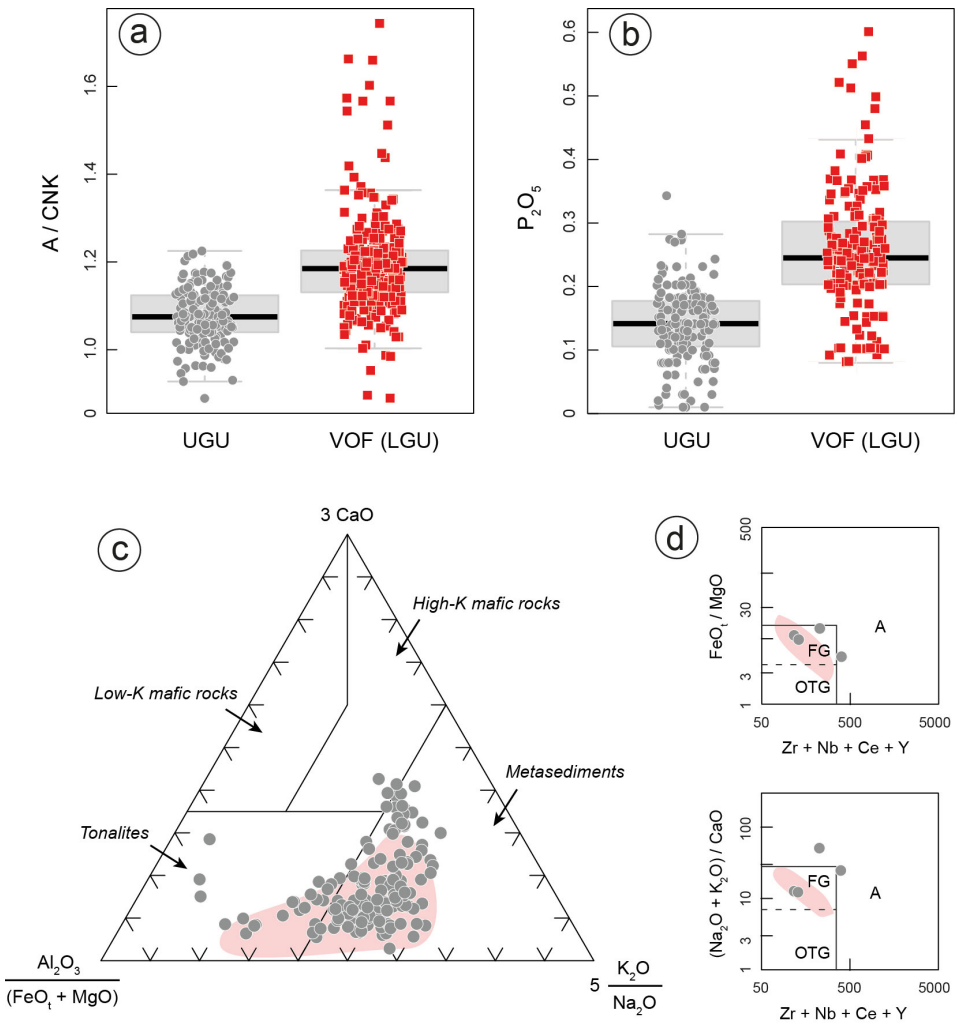

Figure 3.5: Geochemical comparison between the Lyonnais Orthogneiss Formation (grey circles) and the Velay Orthogneiss Formation (VOF, red squares). (a) and (b): boxplots of the A/CNK and P_2O_5 (in wt.%) values; (c) ternary CaO–K_2O/Na_2O–Al_2O_3/(FeO_t+MgO) diagram (Laurent et al., 2014), the fields represent the composition of melts derived from a range of potential sources; (d) discrimination diagrams of Whalen et al. (1987). *A* stands for A-type granites, *OTG* for ordinary-type granites (I-, S- and M-types) and *FG* for fractionated granites. The red field depicts the compositional range of >95% of the VOF samples.

3.3 The amphibolites/eclogites

3.3.1 Field occurrences

Metabasic igneous rocks in the *Monts-du-Lyonnais* UGU have been studied by Lasnier (1968), Coffrant and Piboule (1971), Blanc (1981), Costa et al. (1993), Dufour (1982), Briand et al. (1995) and Lardeaux et al. (2001). They crop out in the Leptynite–Amphibolite Complex in two different settings:

- intimately associated with amphibole-bearing gneisses in a 1.5x30 km consistent massif referred to as the "Riverie band". There, metabasites bear amphibolite-facies mineral assemblages and no eclogite-facies rock, even as relic, has ever been described.
- as small massifs or boudins stretched within the foliation of garnet and sillimanite-bearing paragneisses. Because of poor outcropping conditions, the contact between metabasites and surrounding gneisses is seldom exposed. Zones where abundant metabasite bodies crop out (often as loose blocks in the fields) are labelled "bands" in the literature (i.e. La Gachet, Saint-Joseph, Chagnon bands) even though their

petrographic continuity is not ascertained. Unlike the Riverie band, those bodies rather correspond to swarms of boudins than a single massif. There, amphibolite-facies rocks often correspond to retrogressed eclogites.

3.3.2 Geochemical data

Most studies have dealt with the metamorphic evolution of the metabasites and only Coffrant and Piboule (1971), Blanc (1981), Ouali (1993) and Briand et al. (1995) investigated their origin and geodynamic significance. Among them, Briand et al. (1995) and Ouali (1993) provided (a partial set of) trace element analyses. Here, we present a new dataset including full trace element determinations. Five amphibolites were sampled by myself in the Riverie band and thirteen analyses from small bodies were kindly provided by Anne-Céline Ganzhorn, Jean–François Moyen and Véronique Gardien. Chemical analyses were performed by the *ALS* firm (see Appendix A.3).

In the TAS diagram (Middlemost, 1994), metabasic rocks show chemical compositions akin to troctolites, gabbros and gabbroic diorites (Fig. 3.3). In the classification diagram of Winchester and Floyd (1977) modified by Pearce (1996), originally designed to classify rocks without relying on fluid mobile major elements, they plot within the fields of basalts, andesites/basaltic andesites and alkali basalts. K_2O contents are variable and range from 0.05 to 1.2 wt.% and sometimes up to 2 wt% (Fig.). Therefore, they mainly plot in the tholeite and calc-alkaline series fields in Pecerillo's diagram (Pecerillo and Taylor, 1976).

3.3.3 Variability between and within the different massifs

The aim of this section is to identify different magmatic suites and their potential geographic repartition within the Monts-du-Lyonnais metabasites. We address this point using a set of 61 specimens for which the sampling location is known (from our new dataset and literature data). In the following, all samples are assumed to be close to melt compositions as major and trace element contents are not consistent with a cumulative origin: Al_2O_3 <18 wt.%, Sc <60 ppm, Mg# between 40 and 70, Ni <150 ppm, Eu/Eu* between 0.8 and 1.4 (see Pearce, 1996). We also considered that fluid immobile trace element compositions were not substantially modified by high-grade metamorphism. Overall, the dataset can be divided into four subgroups based on the incompatible, immobile element patterns.

Group I Metabasites from Group I are found in both the small bodies (N=7) and the Riverie band (N=4). They are slightly to markedly enriched in LREE with respect to N–MORBs and display a negative Nb anomaly (coupled with negative Zr–Ti anomalies in some cases, Fig. 3.6a and c). Such metabasites are similar to the "LREE-enriched tholeiites" of Briand et al. (1995) but the magnitude of the LREE enrichment can be higher than observed by these authors (notably in the small bodies). In the Th–Nb proxy diagram (Fig. 3.7a), Group I metabasites plot within the volcanic arc array. In the Ti–Nb proxy diagram (Fig. 3.7b), they scatter in the MORB array between N– and E–MORBs compositions. In the V–Ti proxy diagram of Shervais (1982), most samples feature high Ti/V ratios (between 20 and 50) apart from two specimens bearing a strongly negative Ti anomaly (LY01a and LY02).

Group II Samples from Group II are typified by their flat to LREE-enriched patterns devoid of negative Nb anomaly. Among them, sample CHG (from a small body) is enriched in HREE, very enriched in LREE, displays a slight negative Ti anomaly and a positive Zr anomaly (Fig. 3.6b). Sample (LY22) is close to Group I metabasites from the Riverie band but has a weaker Nb anomaly. Group II specimens plot within the MORB–OIB and MORB arrays in the Th–Nb and Ti–Nb proxy diagrams, respectively

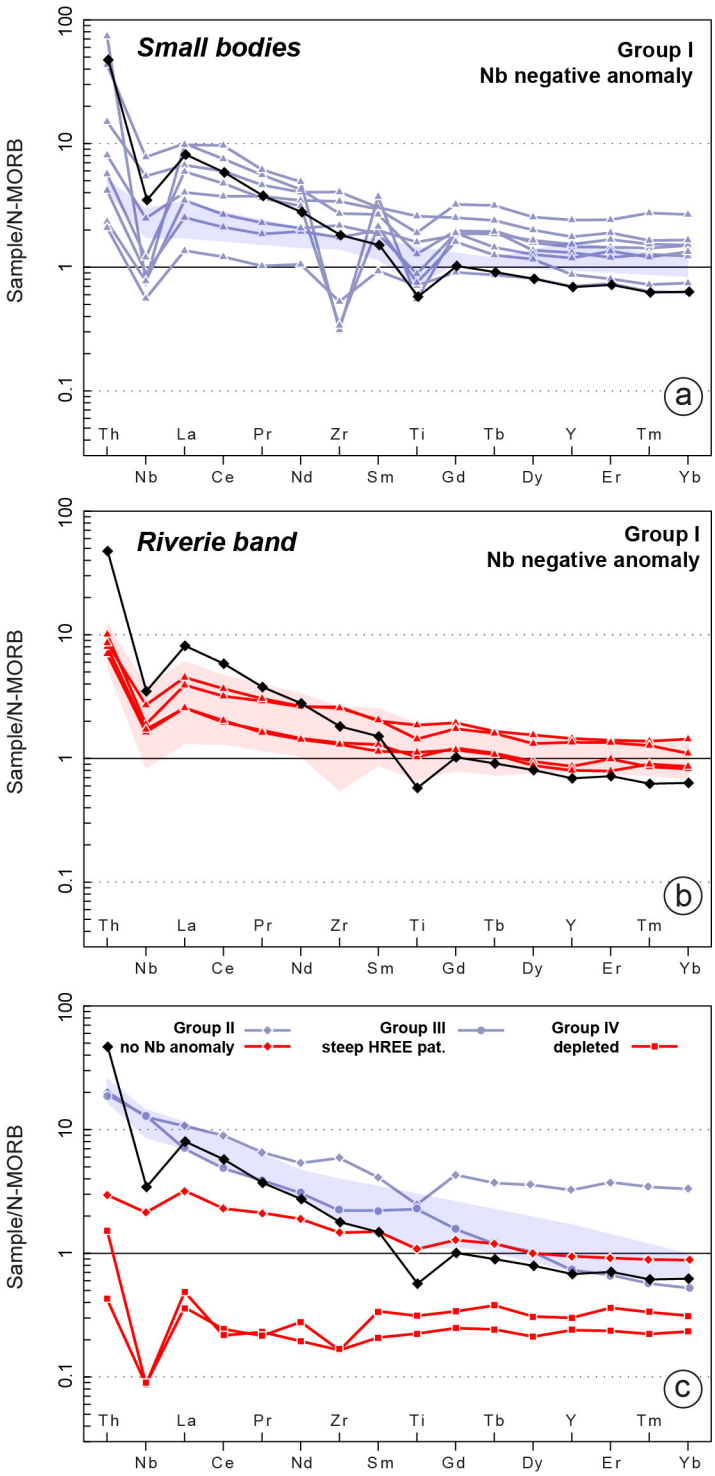

Figure 3.6: Incompatible, immobile element patterns normalized to the composition of N-MORBs (Sun and McDonough, 1989) for the metabasites of the Upper Gneiss Unit in the *Monts-du-Lyonnais* area. See text for a discussion on the differences between each group. The blue fields depict the compositional range of LREE-enriched tholeiites (in a) and "transitional" alkali basalts (in c) identified by Briand et al. (1995) and Ouali (1993) among the small bodies. The red field shows the compositional range of LREE-enriched tholeiites from the Riverie band (Ouali, 1993; Briand et al., 1995). Black line is the composition of the bulk continental crust (Rudnick and Gao, 2003).

(Fig. 3.7a and b). As for Group I rocks, their trace element ratios span between those of N– and E–MORBs.

Group III Group III gathers specimens showing a steep pattern with enrichment in LREE, depletion in HREE and no Nb anomaly (represented in our new dataset by sample LY08). Rocks from Group III are akin to the "transitional basalts" of Briand et al. (1995). In the Th–Nb proxy diagram (Fig. 3.7a), they plot close to the OIB endmember. In the Ti–Nb proxy diagram (Fig. 3.7b), they define a trend between the MORB array and an OIB-like endmember with elevated TiO_2/Yb ratio.

Group IV Two samples (MG1 and MG4) are markedly different as they display flat patterns, apart from a prominent Nb anomaly, and are strongly depleted in all incompatible elements compared to N–MORBs. They plot in the volcanic arc array in the Th–Nb diagram and in the MORB array in the Ti–Nb diagram (Fig. 3.7a and b). These two samples typically show low Ti/V ratios, close to 10 (Fig. 3.7c).

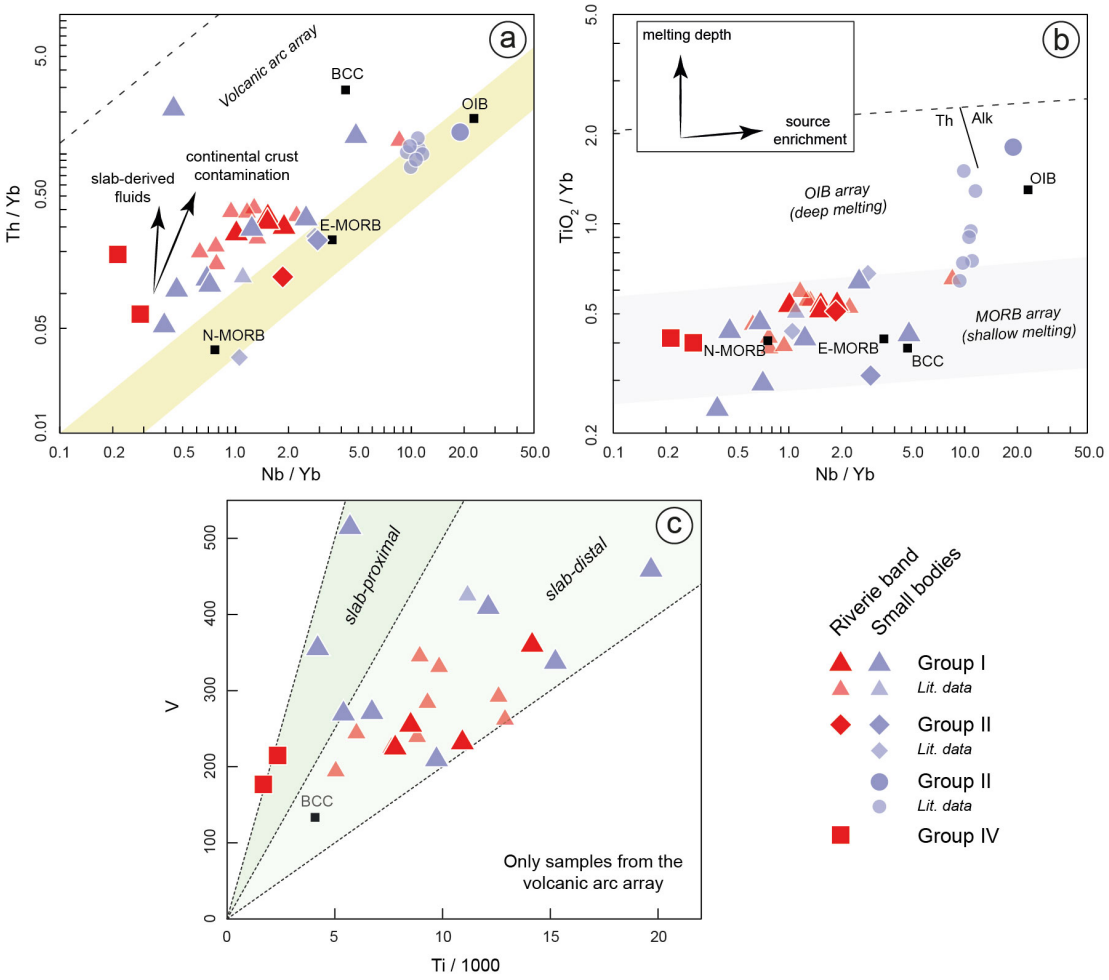

Figure 3.7: Proxy element diagrams for metabasites from the *Monts-du-Lyonnais* area. (a) Th–Nb proxy diagram of Pearce (2008). Oceanic basalts plot within the MORB–OIB array. Magmas contaminated by the continental crust during ascent or which mantle source interacted with slab-derived fluids plot in the volcanic arc array. (b) Ti–Nb proxy diagram of Pearce (2008). The TiO_2/Yb ratio strongly depends on the presence of residual garnet in the mantle source. Magmas formed at great depth feature high TiO_2/Yb ratio provided that garnet is not exhausted in the residua. Such samples plot in the OIB array. If the magmas result from melting of spinel peridotites, or if garnet has been exhausted in the residua, they plot in the MORB array. (c) V–Ti proxy diagram of Shervais (1982) applied to samples plotting in the volcanic arc array of the Th–Nb proxy diagram and assumed to have formed in an environment influenced by subduction. This diagram is based on the change in V redox state when the mantle is fluxed by slab-derived fluids. V becomes more incompatible and resulting magmas have characteristic high V/Ti ratios. Lower V/Ti ratios would be symptomatic of a more distal position with respect to the slab. Bulk continental crust from Rudnick and Gao (2003).

Table 3.2 summarizes the characteristics of each group and the inferred number of specimen in both the small bodies and the Riverie band. Overall, examination of our new dataset together with available literature data indicates that: (i) the "LREE-tholeiite" type of Briand et al. (1995) is the most abundant within the Leptynite–Amphibolite Complex; (ii) the small bodies and Riverie band are typified by the presence of Group III and IV samples, respectively.

3.3.4 Interpretation and origin of the metabasites

Samples bearing a negative Nb anomaly: Group I and IV

Origin of Th–Nb decoupling Those samples plot within the volcanic arc array in the Th-Nb proxy diagram (Fig. 3.7a). Nb being conservative and Th non conservative during subduction, selective addition of Th and LREE to the source of the magmas can account for their Th enrichment compared to MORB–OIB basalts (Pearce, 2008). This would require that the mantle source interacted at some point of its history with slab-derived fluids as those are selectively depleted in Nb and Zr (Ayers and Watson, 1991; Hermann and Rubatto, 2009; Spandler et al., 2007; Tatsumi et al., 1986). Alternatively, contamination of a MORB magma by incompatible element-rich materials bearing a negative Nb anomaly would result in a similar selective Th enrichment. This way, the samples would plot in the volcanic arc array even if they erupted far away from a active margin. The continental crust would constitute an adequate contaminant (Taylor and McLennan, 1985) especially for basalts erupted in attenuated continental settings such as a continent-ocean transitions (Pearce, 1996; 2014).

Melting depth and significance of varied Nb/Yb All samples with a negative Nb anomaly bear low TiO_2/Yb ratios (<0.6) and plot within the MORB array in the Ti–Nb proxy diagram (Fig. 3.7b). This suggests shallow melting depths or high melting degrees (so that garnet would have been exhausted if initially present in the source). The large scatter in Nb/Yb and TiO_2/Yb ratios can be interpreted in two contrasted ways. The incompatible elements Nb, Zr, Ti and Yb being markedly conservative during subduction, ratios of these elements would be diagnostic of the composition of the mantle source before addition of the slab-derived component (Escuder Viruete et al., 2006; Pearce and Peate, 1995; Pearce, 1996; 2008). Accordingly, the large scatter observed would indicate that the mantle was intrinsically heterogeneous before metasomatism and melting. Alternatively, considering that the Nb anomaly results from magma contamination, the wide range of Nb/Yb ratios would rather indicate the existence of a variety of contaminants and/or diverse rates of contamination.

Group I The moderate V/Ti ratios (between 20 and 50) displayed by most Group I samples bearing a Nb anomaly (Fig. 3.7c) do not provide self-consistent evidence for fluid-assisted mantle melting. Indeed MORB magmas show an identical range of V/Ti ratios (Shervais, 1982) that would keep unaffected by crustal contamination because the continental crust has: (i) V/Ti ratios similar to that of the MORBs; (ii) lower V and Ti contents than MORB magmas (Rudnick and Gao, 2003; Taylor and McLennan, 1985). Consequently, discriminating (at least partly) between source enrichment (driven by slab-derived fluids) and magma contamination is impossible from trace element compositions alone and would require radiogenic isotope data (Sm–Nd and/or Lu–Hf).

Group IV Given the very low HFSE contents of Group IV samples (one order of magnitude lower than N-MORBs for Nb), it is very unlikely that trace element compositions were substantially modified by assimilation of crustal rocks during ascent and emplacement. This way, trace element ratios would correspond to those of the mantle source. Elevated Th/Nb (Fig. 3.7a) point to the presence of a slab-derived component in the

mantle source, consistent with high Ti/V ratios (Fig. 3.7c) symptomatic of oxidizing, fluid-assisted melting conditions (Shervais, 1982). Importantly, samples from Group IV show lower Nb/Yb than N-MORB which would attest to strong depletion of their mantle source, probably due to high melting degrees, before re-enrichment by slab-derived fluids (Berger et al., 2010a; Escuder Viruete et al., 2006; Marchesi et al., 2009). Such signature is typically encountered in fore-arc and back-arc basalts (Pearce, 2014). An intrusion age of 545 Ma is proposed based on the petrological study of the presumably affiliated amphibole-bearing gneisses (see section 3.5).

Samples devoid of Nb anomaly: Group II and III

Group II and III samples plot in the MORB–OIB array of the Th–Nb proxy diagram and lack evidence for interaction with a crustal component, either at source level (addition of slab-derived fluids) or during ascent and emplacement (via contamination by crustal country-rocks). Therefore, they can be interpreted as pristine mantle melts.

Group II specimens have low TiO_2/Yb ratios (Fig. 3.7b) diagnostic of shallow melting (Pearce, 2008). Besides, they span in composition between the N– and E–MORBs endmembers. MORB-like magmas are generally produced via melting of depleted to enriched asthenospheric mantle domains in the spinel peridotite facies (Pearce, 2008). Such situation is observed in oceanic ridges and continental rifts (provided that crustal contamination during magma ascent is marginal). The age of this magmatism remains unknown.

In contrast Group III rocks display elevated Nb/Yb and Th/Yb ratios and plot close to the OIB reservoir. Such an observation attests to higher melting depths with garnet being present in the residue (Briand et al., 1995; Pearce, 2008). Therefore, Group III magmas probably originate from melting of a deeper, enriched mantle domain. It may correspond to asthenosphere or lithosphere if the latter has not interacted at any time with slab-derived fluids. Group III samples are chemically close to the alkali metabasites of the Lower Gneiss Unit (see section 2.3). If both rocks are part of the same magmatic suite, the geochronological constraints acquired in the Lower Gneiss Unit would suggest a *c.* 500 Ma intrusion age.

Table 3.2 summarizes the conclusions of this study, specifying the typology, potential source and age of the different series.

A comment on the potential usefulness of radiogenic isotope data

Metasomatized mantle domains are particularly prone to melting due to their lower solidus temperature than normal peridotites (Condamine and Médard, 2014; Gaetani and Grove, 1998; Hirose and Kawamoto, 1995; Hirose, 1997; Hirschmann et al., 2009; Mallik et al., 2015). Therefore, the time lapse between enrichment and melting is generally too short to generate a substantial deviation in radiogenic isotope compositions in the mantle source, despite the change in Sm/Nd and Lu/Hf ratios caused by the slab-derived fluids.

As a result, if the metasomatizing fluid dominantly originates from the igneous part of the oceanic crust, the subduction-zone mantle-derived magmas would bear radiogenic isotope compositions akin to that of the oceanic crust (namely ε_{Nd} and $\varepsilon_{Hf} \gg 0$). Highly radiogenic Nd and Hf signatures of the metabasites bearing a negative Nb anomaly would thus typify melting of a mantle domain that interacted with slab-derived fluids shortly prior to melting.

Conversely, a non-radiogenic signature would be non-specific and could stem from two contrasted scenarios: (i) melting of a mantle metasomatized by slab-derived fluids including a substantial contribution from non-radiogenic subducted sediments (Hidalgo et al., 2012; Nebel et al., 2011; Roberts et al., 2013); (ii) contamination of a primitive highly radiogenic magma by non-radiogenic continental crust (see for instance Pin and Marini, 1993).

Typology	Small bodies N(lit.)	Riverie N(lit.)	Source/processes	Age
Group I: flat to LREE-enriched patterns, <0 Nb anomaly	8+(1)	4+(22)	enriched mantle source or magma contaminated by continental crust	unk.
Group II: flat to LREE-enriched, no Nb anomaly	1+(2)	1+(0)	asthenospheric mantle	unk.
Group III: LREE-enriched, steep HREE pattern, no Nb anomaly	1+(19)	0+(0)	grt-bearing asthenospheric mantle	496 Ma?
Group IV: depleted to flat pattern, <0 Nb anomaly	0+(0)	2+(0)	depleted mantle subsequently enriched by slab-derived fluids	545 Ma?

Table 3.2: Characteristics of the different metabasite groups identified in the Upper Gneiss Unit from the *Monts-du-Lyonnais* area

3.4 The granulite-facies igneous rocks

Granulite-facies rocks crop out exclusively in the Leptynite–Amphibolite Complex as meter-scale boudins or decameter-scale massifs stretched within the foliation of the LOF leucogneisses (Dufour, 1982; Duthou et al., 1981). They bear typical granulite-facies assemblages (Dufour, 1985; Lardeaux et al., 1989):

- Gt + Cpx + Opx + Pg + Rt + Qz for mafic rocks.
- Qz + Pg + Gt + Kf ± Als ± Opx ± Krn for felsic rocks.

Thermobarometry estimates bracketed the P–T conditions of peak metamorphism at 830 ± 30 °C for 9 ± 1 kbar (Dufour, 1985).

Whole-rock major element analyses were obtained by Blanc (1981), Dufour (1982) and Downes and Duthou (1988). Granulites span over a wide range of compositions (Fig. 3.3a) from gabbro (N=13) to gabbroic/monzo-diorite (N=4), (qz-) monzonite (N=4) and granite (N=4). Yet, they do not clearly define a magmatic series in the K_2O vs. SiO_2 diagram as gabbros plot either in the calc-alkaline or the shoshonite field and intermediate rocks in the high-K calc-alkaline field (Fig. 3.3c). Granitic rocks are moderately to very rich in K_2O (3–4 or 6–7 wt.% respectively). In the B–A diagram of Debon and Le Fort (1983) modified by Villaseca et al. (1998), granitic rocks plot in the field of felsic-peraluminous rocks while intermediate samples trend towards metaluminous compositions (Fig. 3.3d).

The felsic granulites have been dated by Duthou et al. (1981) and yielded a whole-rock Rb–Sr isochron age of 497 ± 8 Ma. This age is close to that of the host amphibolite-facies orthogneisses. Initial $^{87}Sr/^{86}Sr$ (I_{Sr}) ratios were accordingly recalculated at the emplacement age of the LOF. With the exception of one sample with very high I_{Sr}, the felsic granulites show a spread in I_{Sr} values similar to that of the host orthogneisses (see Fig. 3.4). Nd isotope compositions were also obtained on two samples by Downes and Duthou (1988). Recalculated ε_{Nd} at 470 Ma yield non-radiogenic values of −2 and −5.2, respectively. Altogether, isotopic data suggest that the granitic protoliths of the felsic granulites originated from melting of pre-existing crustal lithologies. Since the felsic granulites display similar age, chemical compositions and isotopic signatures than their host orthogneisses, they probably represent a higher-grade equivalent of the LOF.

As a result, this suggests that the bulk of the orthogneisses from the LAC experienced an early granulite-facies metamorphic event and was subsequently re-equilibrated in the amphibolite facies. Relics of the early metamorphic stage would have only been preserved in low-strain or fluid-absent domains (Austrheim, 1986 1987; Barrientos and Selverstone, 1993).

Such reasoning holds true for the basic granulites as well. Their major element compositions are akin to the amphibolites/eclogites from the LAC. Dufour et al. (1985) described relict Na-rich augite in equilibrium with garnet within a basic granulite. According to these authors, this would testify for early equilibration in the eclogite-facies. Therefore, the P–T path of the basic rocks would feature an early eclogite-facies stage followed by an increase of temperature leading to equilibration in the granulite-facies and ultimately retromorphosis in the amphibolite-facies. Thus, the basic granulites embedded in the LAC orthogneisses would share the same origin than the amphibolites/eclogites but differ by their equilibration at higher T during peak metamorphism.

The origin of intermediate granulite samples remains uncertain. They may represent metasedimentary residues or differentiates of the K-rich gabbros which is in better agreement with their low W indexes (Ohta and Arai, 2007). Additional geochemical and geochronological data are needed to constrain their origin and significance.

3.5 The amphibole-bearing gneisses

3.5.1 Field description

The amphibole-bearing gneisses are mostly found within the "Riverie band" of the LAC and are intimately associated with the above-mentioned amphibolites (Feybesse et al., 1995). They are best exposed in the former Riverie quarry at the place known as "Les Roches", today a climbing spot (Fig. 3.1). There, amphibole-bearing gneisses display a conspicuous vertical foliation and embed several 20 cm to 3 m-large boudins of amphibolites (Fig. 3.8). Segregation of plagioclase–quartz–amphibole leucocratic layers or patches with characteristic igneous textures is attributed to limited anatexis of both protoliths. Deformation and partial melting are assumed to be Variscan in age and would result from burial, metamorphism and subsequent exhumation of the LAC rocks. The origin, age and significance of amphibole-bearing gneisses from the *Monts-du-Lyonnais* LAC have never been investigated.

3.5.2 Petrography

The amphibole-bearing gneisses feature a primary mineral assemblage consisting of Pg + Qz + Amp ± Bt ± Kfs + Mag + Ap + Zrc + Fe sulphides (Fig. 3.10, abbreviations from Whitney and Evans, 2009). Plagioclase is andesine or oligoclase (An_{25}, representative mineral analyses are presented Table 3.3, see also Appendix Table B2). Amphibole has a magnesio-hornblende composition (Tab. 3.3, Fig. 3.9). Some amphibole grains are altered and converted into a Chl + Cal + Rt assemblage (Fig. 3.10b). Biotite is also frequently chloritized.

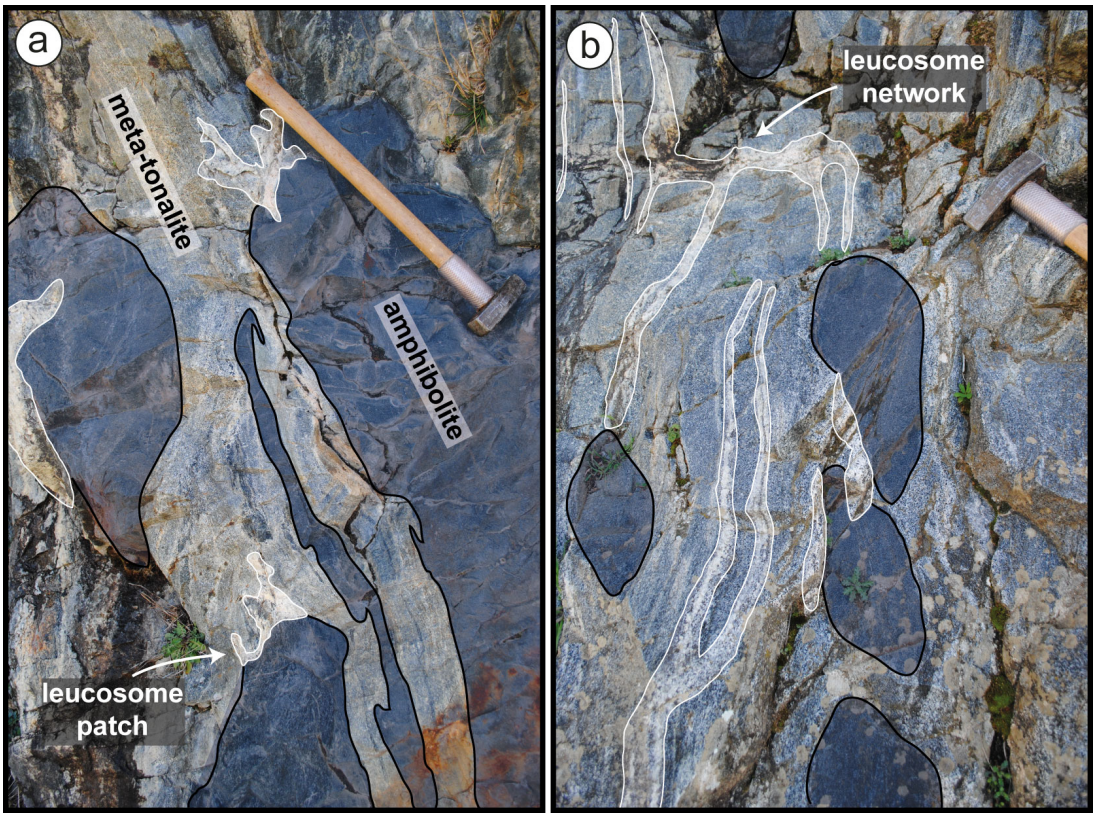

Figure 3.8: Outcrop photograph from Riverie showing the meta-tonalites and their embedded amphibolite boudins. Migmatitic neosomes appear as leucocratic patches (a) or a layered network cutting across the local foliation (b). Hammer for scale.

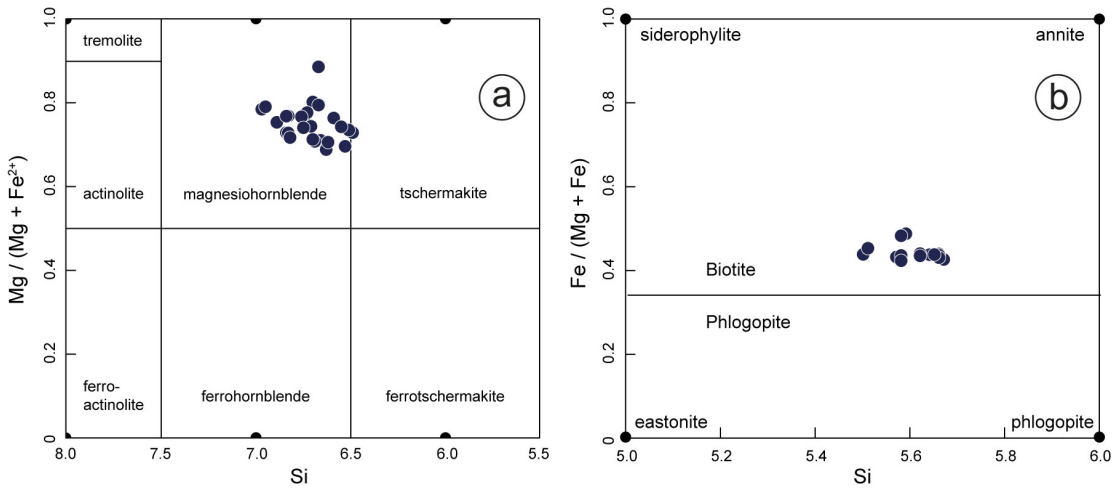

Figure 3.9: Mineral chemistry classification diagrams for (a) amphibole, with $Ca_B \geq 1.50$, $(Na + K)_A < 0.50$ and $Ca_A < 0.50$ (Leake et al., 1997), and (b) mica.

Spot	RV1-8	RV2-1	RV2-6	RV1-9	RV1-16	RV1-2	RV1-8	RV2-5
Min.	Amp	Amp	Amp	Bt	Bt	Pg	Pg	Pg
SiO_2	44.03	46.04	45.68	36.36	37.09	62.43	62.12	62.00
TiO_2	1.10	0.76	0.70	3.06	3.09	–	–	–
Al_2O_3	9.68	9.49	9.48	14.47	14.62	23.75	23.71	24.25
FeO	15.64	16.35	16.47	18.18	17.26	0.00	0.14	0.16
MnO	0.49	0.50	0.39	0.13	0.00	–	–	–
MgO	12.23	12.04	12.22	13.37	12.96	–	–	–
CaO	11.10	11.39	11.68	0.13	0.00	5.38	5.18	5.96
Na_2O	1.74	1.34	1.33	0.00	0.00	8.44	8.78	8.59
K_2O	0.43	0.38	0.47	8.03	9.13	0.23	0.19	0.18
Sum	96.44	98.29	98.42	93.72	94.16	100.23	100.13	101.14
Si	6.51	6.66	6.62	5.58	5.66	2.76	2.75	2.73
Al^{iv}	1.49	1.34	1.38	2.42	2.34	–	–	–
Al^{vi} vi	0.19	0.28	0.24	0.19	0.29	–	–	–
Al_{tot}	1.69	1.62	1.62	2.62	2.63	1.24	1.24	1.26
Ti	0.12	0.08	0.08	0.35	0.35	–	–	–
Fe^{3+}	0.97	0.91	0.90	0.00	0.00	–	–	–
Fe^{2+}	0.97	1.06	1.10	2.33	2.20	0.00	0.01	0.01
Mn	0.06	0.06	0.05	0.02	0.00	–	–	–
Mg	2.69	2.60	2.64	3.06	2.95	–	–	–
Ca	1.76	1.77	1.81	0.02	0.00	0.25	0.25	0.28
Na	0.50	0.38	0.37	0.00	0.00	0.72	0.75	0.73
K	0.08	0.07	0.09	1.57	1.78	0.01	0.01	0.01
OH	2.00	2.00	2.00	2.00	2.00	–	–	–
Sum	17.34	17.21	17.28	19.55	19.56	4.99	5.01	5.01
An	–	–	–	–	–	25.71	24.33	27.43
Ab	–	–	–	–	–	72.99	74.61	71.59
Or	–	–	–	–	–	1.29	1.06	0.97

Table 3.3: Representative mineral analyses of the main phases from samples RV-1 and RV-2. Calculation of the structural formula for calcic amphiboles was based on 23 oxygens and Fe^{2+}/Fe^{3+} estimated assuming a total of 13 cations. Biotite formula were calculated on a 22 oxygen basis, assuming all iron is ferrous.

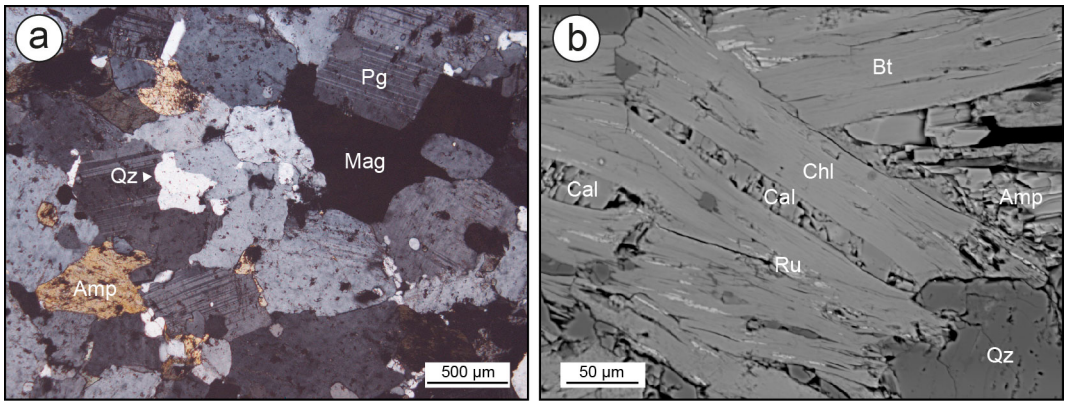

Figure 3.10: (a) Photomicrograph showing the Pg + Qz + Amp + Mag assemblage of the amphibole-bearing gneiss RV-1. (b) SEM image highlighting the Ca + Chl + Rt products of amphibole alteration (sample RV-2).

3.5.3 Geochemistry

In the TAS diagram (Middlemost, 1994), amphibole-bearing gneisses range in composition between diorites and granites (Fig. 3.3a). Importantly, they tend to define a tholeiite series in the SiO_2–K_2O diagram (Pecerillo and Taylor, 1976) and are metaluminous to slightly peraluminous (Fig. 3.3c and d). In line with their low K_2O contents, the amphibole-bearing gneisses plot in the field of tonalites in the normative felsdpar diagram (O'Connor, 1965, Fig. 3.3e). Therefore, they will be referred to as meta-tonalites in the following.

Immobile trace elements patterns normalized to N-MORB basalts shed light on the overall low trace element contents of the meta-tonalites. They are depleted in HREE and slightly enriched in Th, LREE and Zr with respect to N-MORBs (Fig. 3.14a). Of importance are the strongly pronounced Nb an Ti negative anomalies. The sample with the highest SiO_2 content shows a stronger enrichment in the most incompatible elements and features a steep HREE patterns that differs from the flat "MORB-like" pattern displayed by the other meta-tonalites.

3.5.4 Analytical techniques

3.5.5 Zircon U–Pb dating

Two meta-tonalite samples were selected for zircon U–Pb–Hf determinations. Both were collected at the Riverie quarry ("Les Roches" locality). Zircon grains were separated from the powdered rock samples at Saint-Etienne University using conventional techniques described section 2.1, subsequently cast into epoxy mounts and polished down to an equatorial grain section. BSE and CL-imaging were performed at the Central Analytical Facility of Stellenbosch University (SUN, South Africa) using a Zeiss MERLIN SEM. Selected grains were dated by LA–ICP–MS at Frankfurt-am-Main (Germany). Information on the analytical methods are presented Appendix B.3.1. The full datasets are reported in the Appendix Tables B4 (for standards) and B7 (for samples).

Zircon textures

Representative CL-images of zircon grains from both samples are displayed Fig. 3.11. Zircon grains are idiomorphic to sub-idiomorphic, range in lengths between 70 and 200 μm and often show aspect ratios higher than 2 with well-developed pyramidal tips. Few grains have lower aspect ratios (down to 1.1, see zircons 5 and 6, Fig. 3.11a, or zircon 1, Fig. 3.11b). CL-images reveal regular and concentric oscillatory zoning locally grading to sector zoning (see for instance zircons 1 and 2, Fig. 3.11a). Small textural discontinuities in such zoning can be observed (zircon 1, Fig. 3.11b) but are not common in both samples, most grains being devoid of core-rim relationships. Very narrow CL-bright rims (<5µm) are also observed on some grains. There, oscillatory zoning is clearly cut by newly grown mineral (zircons 1, 4 and 5, Fig. 3.11a; zircon 1, Fig. 3.11b).

U–Pb results

RV–1 Forty spots were drilled on 32 grains, all within zones displaying clear oscillatory zoning. Seven spots show moderate common Pb contents (up to 3%) and are markedly discordant (concordance <63%). They will not be discussed further. A total of 16 concordant spots are statistically equivalent and a Concordia date of 545.9 ± 4.7 Ma can be calculated out of them (with a MSWD of concordance and equivalence equal to 1.07). Besides, 6 analyses yielded similar $^{206}Pb/^{238}U$ dates but are discordant (concordance <94%). Nine analyses show discordant $^{206}Pb/^{238}U$ dates ranging between 535 ± 6 and 509 ± 9 Ma. Two spots (a20 and a30) gave concordant $^{206}Pb/^{238}U$ dates of 536 ± 10 and 515 ± 6 Ma respectively.

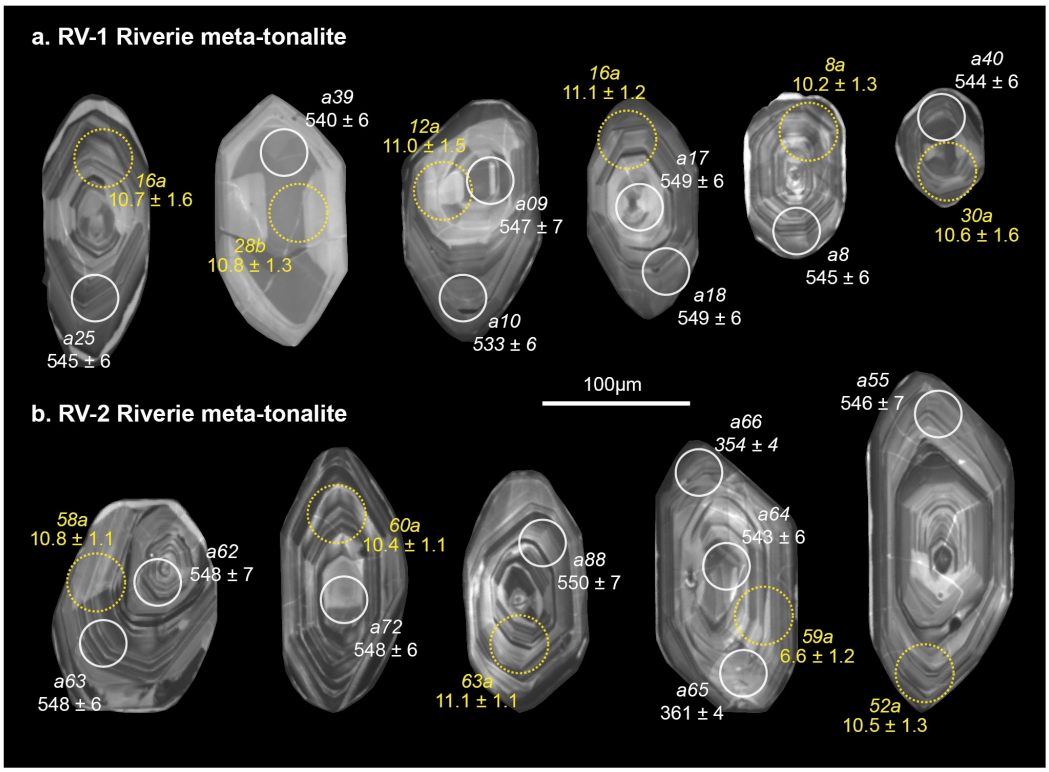

Figure 3.11: Representative cathodoluminescence images of zircon grains from samples of the Riverie meta-tonalites. The locations of laser spots (white and yellow circles for U–Pb and Lu–Hf analyses respectively) are indicated along with the spot name (aXX or YYa/b). The corresponding $^{206}Pb/^{238}U$ dates are quoted with $\pm$ 2σ uncertainty, in Ma. All displayed analyses are concordant at >98% (except those in italic). Hf isotope data are reported using the ε_{Hf} calculated at the $^{206}Pb/^{238}U$ date obtained on the same zircon domain, quoted with 2σ uncertainty.

RV–2 Thirty-three analyses were performed on 25 grains. A Concordia date of 543.9 ± 4.6 Ma can be calculated out of 19 statistically equivalent concordant analyses (with a MSWD of concordance and equivalence equal to 1.4). Spot a58 yielded an identical $^{206}Pb/^{238}U$ date but is discordant (concordance of 87%). Nine measurements devoid of common Pb yielded concordant to moderately discordant $^{206}Pb/^{238}U$ dates (concordance>91%) ranging from 536 ± 6 down to 520 ± 6 Ma. Two analyses (a50 and a60) with low to moderate common Pb contents (0.3–0.8%) show discordant (conc.: 58–67%) and younger $^{206}Pb/^{238}U$ dates of 484 ± 5 and 438 ± 7 Ma respectively. Two measurements performed on both tips of a single zircon yielded a concordant $^{206}Pb/^{238}U$ date of 361 ± 4 Ma and a discordant $^{206}Pb/^{238}U$ date of 354 ± 4 Ma (estimated common Pb content: 0.4%), respectively. Both also feature markedly lower Th/U ratios (0.02 and 0.04 respectively) than grains yielding $^{206}Pb/^{238}U$ dates of c. 545 Ma (always >0.15).

3.5.6 Zircon Lu–Hf isotope signature

In situ zircon Lu-Hf isotope measurements were performed at Frankfurt-am-Main (Germany) following the analytical procedure reported Appendix B.4.1. The full set of results (standards and samples) is available in Tables B11 and B12.

Twenty-eight spots were drilled on grain domains that previously yielded concordant $^{206}Pb/^{238}U$ dates and three on undated grains texturally identical to the main zircon population. Initial Hf isotope compositions were calculated using the intrusion age determined for each sample except for spot 59a which features a younger $^{206}Pb/^{238}U$ date of 361 Ma. The $^{176}Hf/^{177}Hf(t)$ ratios of RV-1 zircons range from 0.282709 ± 0.000042 to 0.282752 ± 0.000035 (2 S.E. – standard error), corresponding to $\varepsilon_{Hf}(t)$ of 9.5 to 11.0

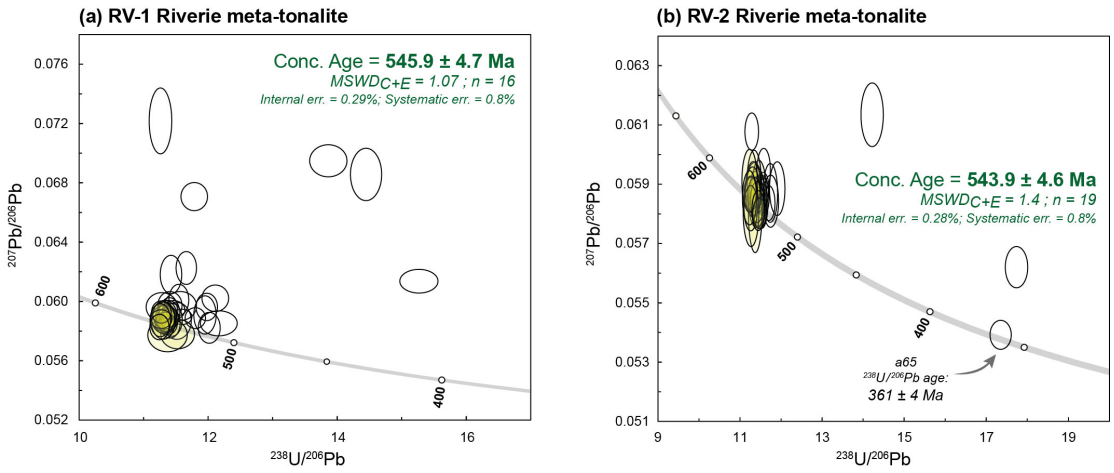

Figure 3.12: Tera-Wasserburg diagrams ($^{238}U/^{206}Pb$ vs. $^{207}Pb/^{206}Pb$) for zircon from the Riverie meta-tonalite samples. Error ellipses and ages are displayed at 2σ level of uncertainty. Yellowish ellipses are those considered for Concordia age calculations.

with an average value of 10.5 ± 0.9 (2 S.D. – standard deviation; Fig. 3.13). Zircons from sample RV-2 (excluding analysis 59a) show a similar range of $^{176}Hf/^{177}Hf(t)$ ratios, from 0.282717 ± 0.000033 to 0.282787 ± 0.000044 (2 S.E. – standard error) equivalent to $\varepsilon_{Hf}(t)$ of 9.7 to 12.2 (Fig. 3.13) and yielding an identical average $\varepsilon_{Hf}(t)$ at 10.7 ± 1.2 (2 S.D. – standard deviation). Spot 59a was performed on a zircon rim with a younger $^{206}Pb/^{238}U$ date of 361 ± 4 Ma. A $^{176}Hf/^{177}Hf(t)$ ratio of 0.282744 ± 0.000034 (2 S.E. – standard error) was accordingly recalculated at that date and corresponds to an $\varepsilon_{Hf}(t)$ of 6.6 ± 1.2 (Fig. 3.13).

3.5.7 Interpretation of U-Pb-Hf data

Protolith emplacement ages Both samples show a largely dominant population of grains having statistically equivalent and concordant $^{206}Pb/^{238}U$ dates of c. 545 Ma. As these zircons feature typical magmatic oscillatory zoning (Corfu et al., 2003), we interpret the Concordia dates of 545.9 ± 4.7 and 543.9 ± 4.6 Ma as the emplacement ages of the tonalite protoliths of samples RV-1 and RV-2, respectively. The zircon cores identified by CL-imaging yielded $^{206}Pb/^{238}U$ dates of c. 545 Ma (see for instance zircon 1, Fig. 3.11b). As a result, those cores likely reflect stepwise mineral growth with periods of dissolution followed by new zircon crystallization within the magma. This would generate textural discontinuities as observed when new magmatic zircon crystallizes around older, source-inherited grains. U–Pb evidence clearly suggests that the (meta)tonalite magma did not contain inherited grain or, if so, that they were fully dissolved prior to new magmatic zircon crystallization. Discordant zircons showing $^{206}Pb/^{238}U$ dates around 545 Ma are texturally similar to the concordant ones and their discordance would stem from the incorporation of common Pb as evidenced in some cases by the high signal on mass 204, reflecting elevated ^{204}Pb content. Similarly, discordant zircons with $^{206}Pb/^{238}U$ dates younger than 545 Ma likely experienced a combination of common Pb incorporation and Pb loss, which respective contributions cannot be retrieved. Two spots show younger concordant $^{206}Pb/^{238}U$ dates of 536 ± 10 and 515 ± 6 Ma respectively (a20 and a30). I argue that these dates do not correspond to any geological event because the weak curvature of the Concordia for the 600-400 Ma period entails that any c. 545 Ma-old zircon having experienced limited Pb loss would still be sub-concordant within uncertainty.

Significance of younger dates Of interest are analyses a65 and a66, both performed on the tips of the same zircon grain. They show younger $^{238}U/^{206}Pb$ dates that cannot be attributed to Pb loss from the main c. 545 Ma-old population. Indeed, a65 is concordant

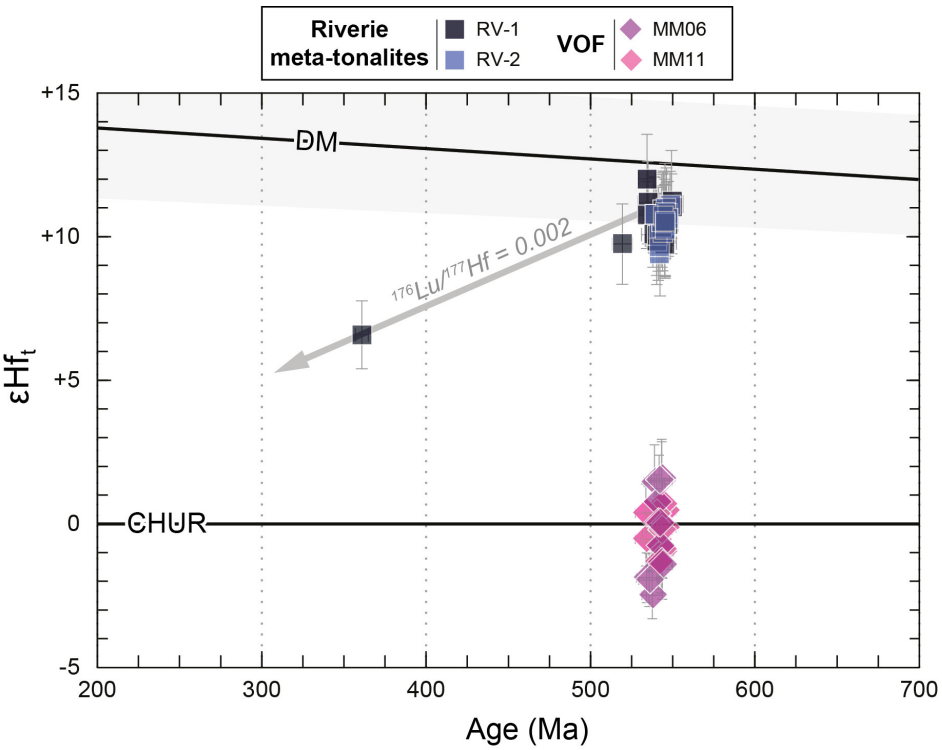

Figure 3.13: Measured ε_{Hf}(t) on magmatic zircon grains from the two investigated meta-tonalite samples of the Riverie band. The ε_{Hf}(t) are recalculated and plotted at the ^{206}Pb/^{238}U age of each analysed zircon domain (ensuring a better graphical representation). When such value was not available, the intrusion age determined for the sample was used. The range for the Depleted Mantle reservoir is bracketed by the models of Naeraa et al. (2012) for the lowermost value and Griffin et al. (2002) for the uppermost value. Data from the Velay Orthogneiss Formation (see section 1.1) are also plotted for sake of comparison.

at c. 360 Ma and a66 yielded a ^{207}Pb/^{206}Pb date of 460 ± 22 Ma, regarded as the maximal zircon crystallization age. CL images do not provide clear evidence for: (i) the existence of textural discontinuities associated with new zircon growth; (ii) extensive zircon recrystallization (zircon 4, Fig. 3.11b). Yet, both analyses show very low Th/U ratios as typically observed in recrystallized metamorphic zircon (Hoskin and Black, 2000; Vavra et al., 1999). Moreover, the zircon rim on which analyses a65 and a66 were performed yielded a ε_{Hf} at 361 Ma of 6.6 ± 1.2. This value connects with the main zircon population at c. 545 Ma along an evolutionary trend characterized by a ^{176}Lu/^{177}Hf ratio of 0.002 (Fig. 3.13), characteristic of zircon grains. Such observation is consistent with a closed-system evolution of the ^{176}Hf/^{177}Hf ratio. All these lines of evidence support a resetting of the U–Pb chronometer at c. 360 Ma in this zircon domain, leaving the Hf isotope signature unaffected because Hf is a constituent chemical element in zircon (Hoskin and Black, 2000). Discordance of analysis a66 likely originates from coeval common Pb incorporation and subsequent limited Pb loss. Resetting of the U–Pb chronometer would have been provoked by the metamorphic event developed during the thrusting of the UGU above the LGU, dated in the Lot area at c. 355 Ma (Ar–Ar on biotite, see Costa, 1989).

Hf isotope composition of the parental magma The ε_{Hf}(t) variability exhibited by magmatic zircon within a given sample is small (<2 ε_{Hf}-units) and of the same order of magnitude than analytical uncertainties (i.e. ± 1.4 ε_{Hf}-units). This indicate that zircon crystallized from a magma with homogeneous Hf isotope composition. Both samples reveal identical average ε_{Hf}(t) of c. 10.6, taken as representative of that of the magma at the time of crystallization, that falls in the range of expected values for the Depleted Mantle reservoir (Griffin et al., 2002; Naeraa et al., 2012).

3.5.8 Petrogenesis

Source of the magmatic suite The low K_2O (0.1–1.1 wt.%) and intermediate SiO_2 (61–64 wt.%) contents displayed by the meta-tonalites (see Fig. 3.3) indicate that their parental magmas cannot derive from melting of the continental crust which is notably enriched in both these incompatible elements. Similarly, the presence of magnetite suggests that the parental magmas were relatively oxidized which is at odds with an origin by melting of the continental crust as the latter generally produces melts evolving at low f_{O_2} (Ishihara, 1977). The Depleted Mantle-like Hf isotope signature of the parental magma entails that (meta)tonalites could represent: (i) differentiates of a basaltic magma; or (ii) primary melts of a mafic K-poor igneous source extracted from the DM shortly prior to melting. Both hypotheses are in line with the lack of inherited zircon core within both samples. In any case, the radiogenic Hf isotope signature together with the low K_2O and trace element contents demonstrate that crustal contamination during magma ascent and emplacement was unsignificant.

The Riverie meta-tonalites show major element compositions akin to the Archean TTG (tonalite-trondhjemite-granodiorite) suites for which an origin by melting of mafic rocks is proposed (Martin et al., 2005). Whatever the geodynamic setting in which it takes place, melting basic rocks to produce tonalites requires very high temperatures (>920°C, Beard and Lofgren, 1991; Rapp and Watson, 1995; Rushmer, 1991; Sen and Dunn, 1994) or elevated H_2O concentrations in the source (> 2 wt%, Sisson et al., 2005). Such UHT conditions are unusual in the Phanerozoic and never reported elsewhere in the basement rocks of the FMC. For instance, in the LGU, the voluminous VOF meta-granites originated from melting of pre-existing crustal lithologies at T < 850°C. Besides, field exposures of the LAC indicate that metabasic rocks are intimately associated with the tonalites and, if genetically related, would more likely represent coeval magmatic products than the source rocks of the tonalite suite. Therefore, the fractionation hypothesis is preferred and further discussed hereafter.

A genetic link between metabasites and tonalites from the LAC? As mentioned above, meta-tonalites have similar LREE, Th and Nb contents than Group I and II amphibolites and are even depleted in HREE (Fig. 3.14). It entails that the latter cannot correspond to the parental basic magmas from which the tonalites were differentiated because tonalites would have been way more enriched in incompatible trace elements if fractional crystallization had proceeded. Group IV metabasite (samples MG01 and MG04, see section 3.3) are markedly poorer in most incompatible elements than the tonalites and may correspond to the parental magmas. Forward geochemical modelling has been performed to evaluate the feasibility of this hypothesis. First, a set of crystallization experiments for a primary melt which composition matches that of MG1 and MG4 was selected. Was retained the study of Blatter et al. (2013) who investigated the phase relationships and residual melt compositions of 01SB-872, a natural basalt from the Cascades magmatic arc. This starting material features SiO_2, Al_2O_3, K_2O and MgO contents identical to metabasites MG01 and 04 but is lower in CaO and higher in Na_2O, FeO_t and TiO_2 (Table 3.4).

Equilibration of a 01SB-872 magma at c. 950–1000°C and 9–4 kbar yields melts which compositions adequately match that of the Riverie meta-tonalites even though the experimental melts tend to have overall higher Al_2O_3 and K_2O contents. At these P–T conditions, melt fractions range from 0.12 to 0.2 (Blatter et al., 2013). The phase proportions retrieved by Blatter et al. (2013) and a set of partition coefficients were used to calculate the trace element composition of the tonalite melts. Ti behaviour was not modelled because fractionation of magnetite can easily account for the negative Ti anomaly of the tonalites as is commonly observed during the differentiation of basaltic magmas (Grove et al., 2003). We only considered clinopyroxene, orthopyroxene, amphibole and plagioclase as trace element hosting phases. We used the minimal and maximal partition

	MG01	MG04	01SB-872
SiO_2	49.30	48.60	49.90
Al_2O_3	17.30	17.10	17.00
FeO_t	6.86	6.79	9.19
MnO	0.13	0.13	0.16
MgO	8.49	9.55	8.67
CaO	14.05	12.65	10.1
Na_2O	2.19	2.06	3.02
K_2O	0.30	0.62	0.50
TiO_2	0.39	0.28	1.26
P_2O_5	0.02	0.02	0.19

Table 3.4: Major-element compositions of: (i) the two metabasite samples from the Riverie band regarded as potential primary magmas from which the meta-tonalites differentiated; (ii) natural starting material 01SB-872 used by Blatter et al. (2013) in their crystallization experiments.

coefficients from Laurent et al. (2013) for clinopyroxene, orthopyroxene and plagioclase. For amphibole, we chose the self-consistent dataset of Sisson (1994). Nb is from Adam et al. (1993) and Th was set at 0.1. Gd and Tb were not modelled for lack of available partitioning data in the relevant chemical system. Experiments 2364, 2381, 2370 and 2376 from Blatter et al. (2013) were selected and yield a range of potential trace element compositions for the differentiates. The latter match the composition of the tonalites for HREE but fail to reproduce the enrichment in LREE and Th relative to N-MORBs (Fig. 3.14b).

Nature of the parental melt Reverse modelling has been performed to estimate the trace element composition of the parental basaltic magma which fractionation would produce the Riverie meta-tonalites. In each of the four experiments of Blatter et al. (2013), the trace element content of the tonalite melt is set to that of the average of the natural samples. The composition of the parental basaltic magma is then retrieved by least-square regression using the observed phase proportions and the above-mentioned set of partition coefficients. The four experiments and varied partitioning data yield a range of possible trace element contents for the primary melt. Figure 3.14c shows that the calculated primary basaltic melt would have been depleted relative to N-MORBs in all incompatible elements except for Th. Its immobile trace element pattern normalized to N-MORBS would have featured negative Nb and Zr negative anomalies and a slight enrichment in LREE with respect to HREE. This pattern clearly resembles that of samples MG01 and MG04 but the mantle source of the parental melt would have been less depleted with respect to N-MORBs.

Conclusion Given the uncertainties of the developed approach (values of partition coefficients, internal errors on trace element concentrations, melt proportions constrained based on a starting material with slightly different major element compositions than the investigated samples), it is reasonable to consider that, at first order, the Riverie meta-tonalites formed by fractionation of basaltic magmas akin to those at the origin of Group IV metabasites.

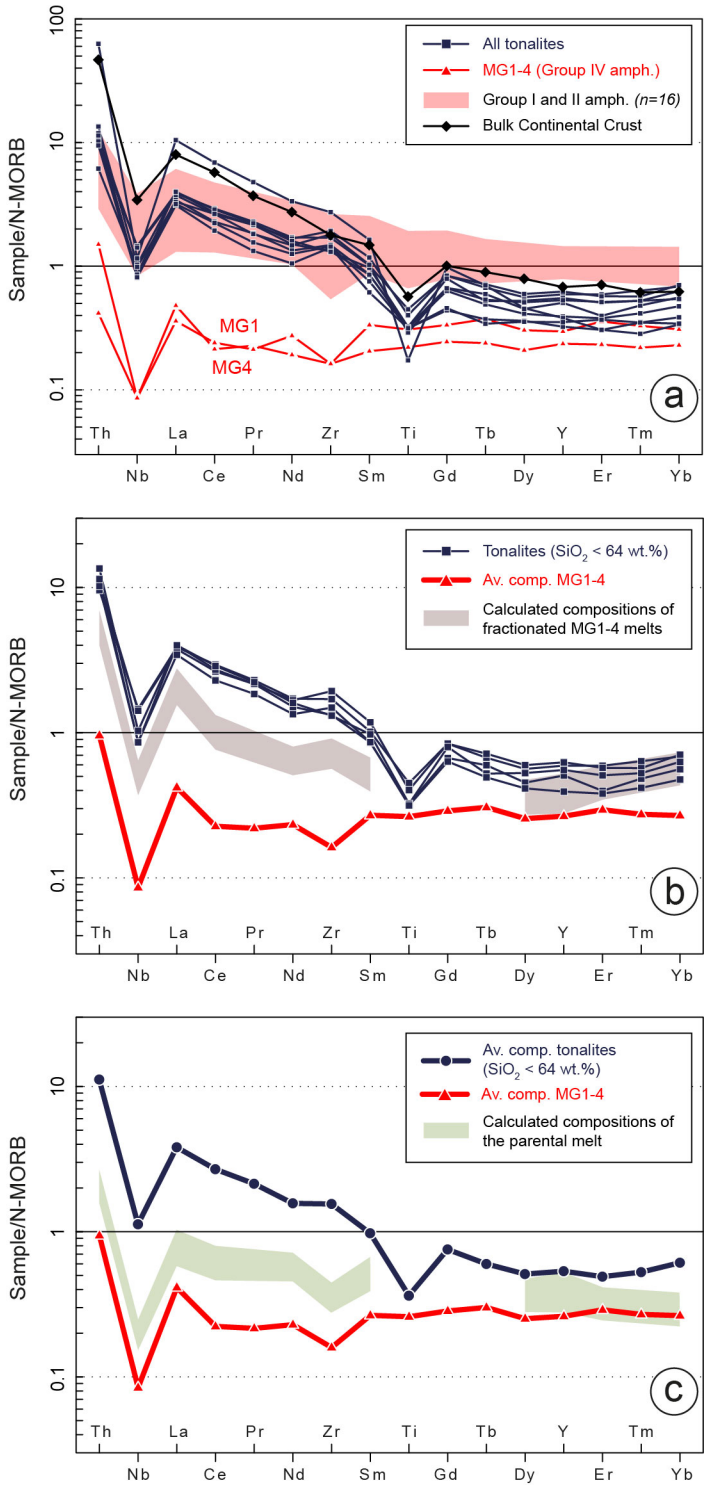

Figure 3.14: (a) Incompatible, immobile element patterns normalized to the composition of N-MORBs (Sun and McDonough, 1989) for the Riverie meta-tonalites and associated amphibolites. (b–c) Geochemical models questioning the genetic link between meta-tonalites and amphibolites: (b) Results of forward batch crystallization models showing the virtual trace element composition of a tonalite melt differentiated from a parental mafic magma of MG01–04 composition; (c) Results of reverse batch crystallization models yielding the trace element composition of the parental melt from which the tonalites would have been differentiated.

3.5.9 Geodynamic setting and other occurrences within the Variscan belt

As discussed in section 3.3, Group IV metabasites show geochemical characteristics typically observed in fore-arc and back-arc basalts (Escuder Viruete et al., 2006; Marchesi et al., 2009; Pearce, 2014). Reconstructed plate motions since the Ediacaran (Stampfli et al., 2013) and the today-location of the Cadomian magmatic arc (to the North of the FMC) support a back-arc rather than a fore-arc setting for the FMC crust segment in the late Ediacaran/early Cambrian (see discussion in Chapter 2). Therefore, both Group IV metabasites and their affiliated meta-tonalites from the *Monts-du-Lyonnais* Upper Gneiss Unit would testify for a *c.* 545 Ma mantle melting event in the Cadomian back-arc (Fig. 2.7c).

This situation markedly contrasts with that observed in the Lower Gneiss Unit where late Cadomian magmatism was strictly crust-derived and entails that the Upper and Lower Gneiss Units had different geographical locations by that time. The UGU may have had an outboard position with respect to the LGU in which case the thermal regime of its underlying mantle would have been more strongly affected by the Cadomian slab break-off (Nance et al., 2010), up to partial melting (Fig. 2.7c).

Low K_2O, amphibole-bearing meta-granitoids such as the Riverie meta-tonalites are very scarce within the Variscan belt. Seyler (1986) reports the existence of biotite- and amphibole-bearing gneisses in the LAC of the Maures Massif, south-east of the FMC, and referred to as "*mixed formation*". Their major and trace element contents (Innocent, 1993) clearly resemble that of Riverie meta-tonalites. Besides, isotope dilution U–Pb dating of zircon fractions yielded an upper intercept date of 548 $+15/-7$ Ma interpreted as the emplacement age of the igneous protolith (Innocent et al., 2003), identical to the ones obtained for the Riverie meta-tonalites. However, the Maures tonalites feature non-radiogenic whole-rock Nd isotope compositions which markedly contrasts with the highly radiogenic Hf isotope signature of their Riverie counterparts. Such observation entails that both rock groups did not derive from melting of a similar mantle source and hinders any attempt to correlate the Maures massif with the eastern part of the FMC.

3.6 Conclusion

The geochemical investigations conducted on the meta-igneous units of the *Monts-du-Lyonnais* UGU highlight the existence of three main magmatic suites: (i) basaltic magmas and their tonalitic differentiates emplaced at c. 545 Ma in a back-arc setting; (ii) basaltic magmas with very varied trace element compositions likely originated from melting of a heterogeneous mantle source, presumably between 500–475 Ma by analogy with other domains of the FMC; (iii) metaluminous to mildly peraluminous granites were generated at c. 470 Ma through melting of an immature sedimentary sequence containing a prominent volcaniclastic component.

Chapter 4

Pre-Variscan magmatic record in the Massif Central: a review

4.1 Lateral correlations within the Variscan nappe stack

Rationale In the French Massif Central, the main metamorphic nappes (the Upper Gneiss Unit, the Lower Gneiss Unit and the Parautochtonous Unit, see section 2.1) have originally been identified based on their contrasted tectonic-metamorphic evolutions during the Variscan orogeny (Ledru et al., 1989). These include the existence/absence of an early high-pressure event (recorded by eclogite-facies rocks) and varied temperatures/pressures reached at peak metamorphism. As outlined in the introductory section, examination of the three largest and best studied exposures of the French Massif Central (the Velay, Lot/Rouergue and Limousin areas) reveal that the structural relationships between the UGU, LGU and PAU units differ from a domain to another. In this section, we review the lithological composition and pre-orogenic magmatic histories of each nappe from the three domains in order to evaluate: (i) their lateral continuity in terms of pre-Variscan history; (ii) the potential role played by inherited, pre-orogenic features on the Variscan evolution.

Data compilation All metamorphic units from the FMC are typically composed of both metasedimentary and meta-igneous lithologies. Figure 4.1 is a compilation of emplacement ages obtained on meta-igneous rocks from the different nappes. The UGU and PAU from the Limousin are not considered because the available geochronological dataset is very limited and hampers to draw any large-scale picture. The depositional age of the (meta)sediments for each unit is estimated based on (i) paleontological data (Fournier-Vinas and Debat, 1970; Guérangé-Lozes and Burg, 1990) ; (ii) field relationships, when already dated (meta)plutonic bodies clearly feature intrusive contacts with adjacent (meta)sediments; (iii) dating of interlayered volcanics (Faure et al., 2009; Lescuyer and Cocherie, 1992); (iv) detrital zircon studies (Melleton et al., 2010). Results of this compilation are summarized on a structural sketch for each of the three investigated domains (Fig. 4.2).

Upper vs. Lower Gneiss Units East of the Sillon Houiller fault, examination of the pre-Variscan magmatic record (Fig. 4.1) reveals contrasting age patterns between the UGU and the LGU. Indeed, the LGU was almost exclusively affected by Cadomian magmatism and lacks any major Ordovician imprint (Fig. 4.3). The opposite situation is displayed by the UGU which dominantly records the Ordovician magmatic event (Fig. 4.3). Therefore, in this part of the FMC, a direct linkage exists between the pre-Variscan history of the crust segment and its evolution during the Variscan orogeny. Such conclusion might only been altered in the Rouergue area where most igneous rocks from the LGU have been dated with the U–Pb isotope dilution method on zircon multi-grain

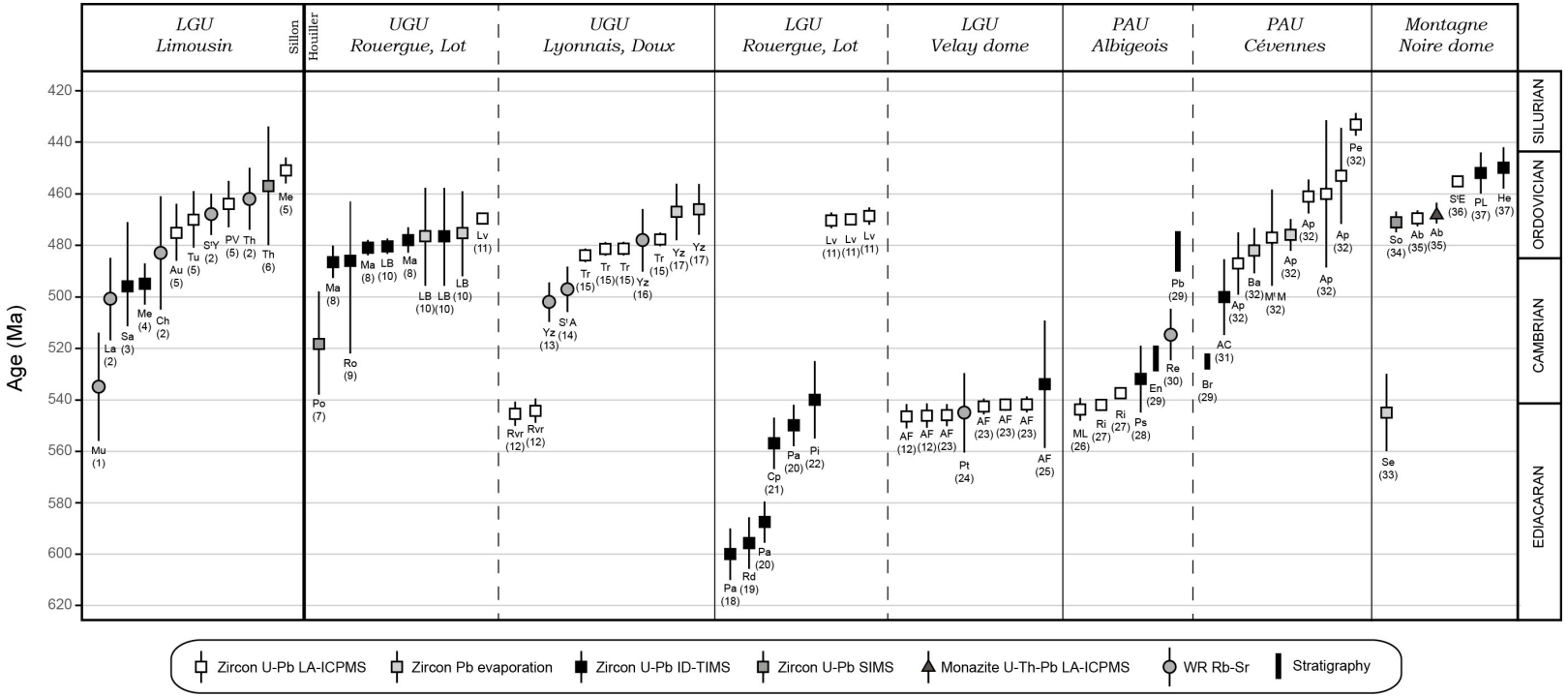

Figure 4.1: Compilation of available intrusion ages for pre-Variscan plutonic and volcanic rocks in the French Massif Central. In this compilation, the PAU of the Rouergue, Lot and Velay areas also includes the low-grade "Fold-and-Thrust Belt" and the Saint-Sernin-sur-Rance nappe of Faure et al. (2009) and thus refers to all low-grade metamorphic units a similar structural position. 1: Bernard-Griffiths (1975); 2: Duthou (1977); 3: Gebauer et al. (1981);4: Lafon (1986); 5: Melleton et al. (2010); 6: Alexandre (2007); 7: Maurel et al. (2003); 8: Pin and Lancelot (1982); 9: Pin (1979); 10: Paquette et al. (1995); 11: Lotout et al. (2017); 12: this work; 13: Duthou et al. (1984); 14: Duthou et al. (1981); 15: Chelle-Michou et al. (2017); 16: Dufour (1982); 17: Feybesse et al. (1995); 18: Lévêque (1985); 19: Alabouvette et al. (1989); 20: Defaut et al. (1990); 21: Lafon (1984); 22: Pin and Lancelot (1978); 23: this study; 24: Caen-Vachette (1979); 25: Mougeot et al. (1997); 26: Laurent O. personnal communication; 27: Padel et al. (2017); 28: Ducrot et al. (1979); 29: Pouclet et al. (in press); 30: Delbos et al. (1964 1965); 31: Caron (1994); 32: Faure et al. (2009); 33: Lescuyer and Cocherie (1992); 34: Cocherie et al. (2005); 35: TrapIJES2017; 36: Pitra et al. (2012); 37: Roger et al. (2015). Ab, Albine; AC, Aire de Côte; AF, Arc de Fix; Ap, Apié; Au, Aubazine; Ba, Bassurels; Br, Saint-Bresson; Ch, Chateauneuf; Cp, Caplongue; En, Ensièges; He, Héric; La, Lanneau; LB, La Bessenoits; Lv, Lévézou; Ma, Marvejols; Me, Meuzac; ML, Montredon-Labessonié; Mt M, Mont Mars; Mu, Mulatet; Pa, Palanges; Pb, Peyrebrune; Pe, Peyrolles; Pi, Picades; Ps, Plaisance: PL, Pont de Larn; Pt, Pilat; Pm, Pomayrols; Rd, Rodez; Re, Réquista; Ro, Rouergue; Rvr, Riverie; Se, Sériès; StE, St Eutrope; So, Somail; StA, St André-la-Côte; StY, St Yrieix; Th, Thaurion; Tr, Tournon; Tu, Tulle; Yz, Yzeron

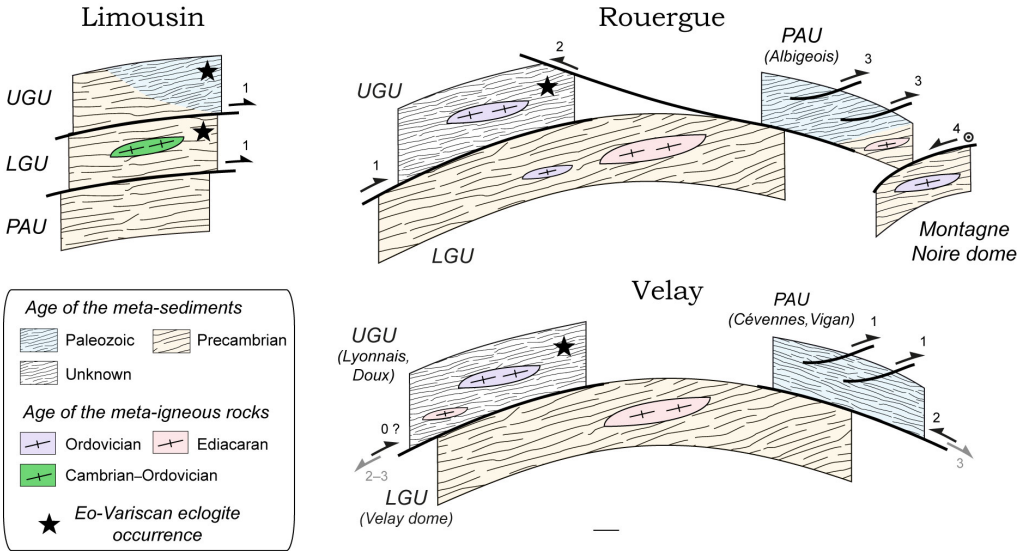

Figure 4.2: Summary of the lithological composition of each tectono-metamorphic unit recognized in the three largest and best studied exposures of the French Massif Central. Upper Allochtonous Units are not considered. See text and Fig. 4.1 for data sources and methodology. See introduction for a discussion on the overall architecture and the age of the contacts. The PAU of the Rouergue, Lot and Velay areas also includes the low-grade "Fold-and-Thrust Belt" and the Saint-Sernin-sur-Rance nappe of Faure et al. (2009) and thus refers to all low-grade metamorphic units a similar structural position. The Limousin sketch is inspired from Melleton et al. (2010).

fractions (Fig. 4.1). In this case, dissolution of grains with inherited cores may yield erroneous older emplacement ages. That being said, based on the well-documented case of the Velay dome, it is very likely that the contrasted age patterns of the UGU and LGU reflect their different paleogeographical positions by the Ordovician. Accordingly, both units experienced contrasted metamorphic evolutions at Variscan times. This also supports an allochtonous origin for the UGU, independently postulated based on its metamorphic record (Burg and Matte, 1978; Burg et al., 1984).

The Sillon Houiller East/West dichotomy The LGU in the Limousin area records a protracted Cambrian–Ordovician magmatic event (Fig. 4.1) which age pattern does not match that of its counterpart East of the Sillon Houiller but rather resembles the UGU from the same area (Fig. 4.3). This entails that the LGUs experienced contrasted pre-Variscan evolutions on both sides of the Sillon Houiller. Such structure is often described as a transfer fault nucleated during Variscan orogenic collapse in response to variable extension rates (Burg et al., 1994; Lapierre et al., 2008). Yet, it may also correspond to a lithospheric-scale structure that demarcates two crust segments having contrasted pre-Variscan histories. Alternatively, the discrepancy in the LGUs pre-Variscan magmatic record may stem from the existence of a distinct stack of nappes on both sides of the Sillon Houiller. Such hypothesis is backed up by the fact that the relics of eclogite-facies metamorphism are observed in the LGU only West of the Sillon Houiller (see introductory section). Dubuisson et al. (1988) and Berger et al. (2010b) provide further constraints to this point by highlighting that the Limousin LGU features additional lithological components including an ophiolitic unit, underlying micaschists and HP-UHP metabasites. They even propose a different nappe subdivision scheme, based on that observed in the Armorican Massif (Ballèvre et al., 2009). As a result, the age compilation presented in this study together with recent metamorphic investigations suggest that the nappes cannot be correlated on both sides of the Sillon Houiller.

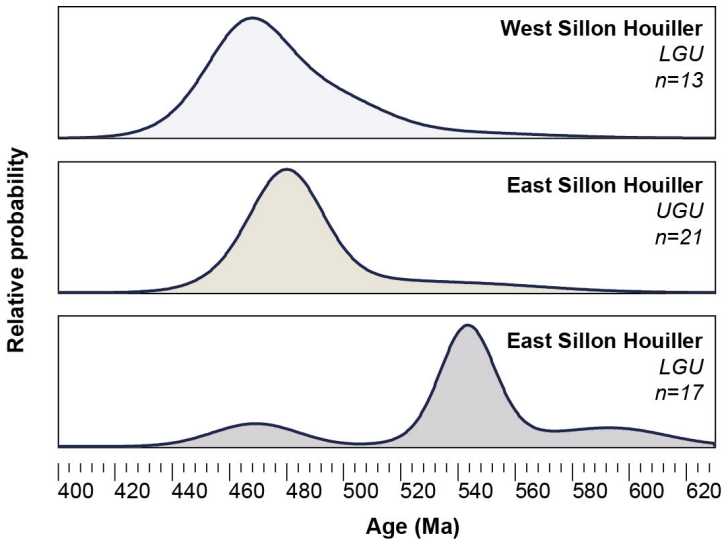

Figure 4.3: Comparison between the available intrusion ages for pre-Variscan igneous rocks represented as Kernel Density Estimates, calculated using the DensityPlotter program of Vermeesch (2012); optimal bandwidths were determined by the program (adaptive mode).

Significance of the Parautochtonous Units In the easternmost part of the FMC (Velay area), the PAU corresponds to the so-called "Cévennes" and "Vigan" schists, a former Paleozoic sedimentary sequence (see for instance Faure et al., 2009, Fig. 4.1). Consequently, the PAU (meta)sediments likely represent the (paleo)cover of the LGU Precambrian lithologies (Velay Orthogneiss Formation and associated metasediments, see Chapter 1) because of their: (i) structural position overlying the LGU (Bouilhol et al., 2006; Faure et al., 2001), (ii) low metamorphic grade symptomatic of limited burial and transport (Rakib, 1996).

A different situation is observed in the PAU from the Rouergue area which does exhibit Precambrian rocks below the Lower Paleozoic (meta)sedimentary sequence. Indeed, the lower part of the "Albigeois" schists is intruded by a c. 545 Ma-old granite turned into the Montredon-Labessonié orthogneiss at Variscan times (personal communications from O. Laurent, D. Béziat and J.-L. Séverac). Besides, in the "Monts-de-Lacaune" area, interlayered rhyolites and rhyolitic tuffs (locally called *blaviérites*) have recently yielded zircon LA–ICP–MS U–Pb ages of c. 540 Ma demonstrating the existence of Ediacaran (meta)sediments within the PAU (Padel et al., 2017). These observations suggest that in the Rouergue domain, the PAU corresponds to a constituent basement unit with Neoproterozoic sediments intruded by late Ediacaran granites (as observed in the LGU) and capped by Lower Paleozoic strata.

Lastly, in the Limousin domain, detrital zircon studies favour an Ediacaran depositional age for the (meta)sediments (Melleton et al., 2010). The latter would have been intruded by: (i) the Cambrian Moulin du Chambon orthogneiss which yielded a zircon U–Pb LA–ICP–MS emplacement age for the igneous protolith at 529 ± 4 Ma; (ii) the Ordovician Xaintrie augen gneiss which emplaced at 467 ± 8 Ma (whole-rock Rb–Sr, Monier, 1980). Consequently, there is no evidence for the presence of reworked Lower Paleozoic strata in the Limousin PAU which strongly contrasts with its presumed lateral equivalents East of the Sillon Houiller. Once again, it appears that, based on their pre-Variscan hisotry, the main metamorphic nappes do not easily correlate on both sides of the Sillon Houiller.

Origin of protoliths in the Montagne Noire dome The pre-Variscan lithologies of the Montagne Noire dome consist in an intricate association of meta-plutonic and meta-(volcano)sedimentary units (review in Demange, 2014). Recent geochronological investigations (see Fig. 4.1) confirmed the interpretations of Bard and Loueyit (1978): the meta-plutonic rocks do correspond to Ordovician granites which intruded an Ediacaran

sedimentary sequence. Importantly, such lithological composition and pre-Variscan evolution do not match with any other nappe identified in the FMC. As a direct consequence of this, the Montagne Noire dome cannot be regarded as a lateral equivalent of the LGU nappe that would have been exhumed below the PAU (Fig. 4.2).

4.2 Geodynamic scenario for the Cambrian–Ordovician period

4.2.1 State of the art

General overview

The geodynamic evolution of the North Gondwana margin at Cambrian–Ordovician times has been very much debated in the past 20 years and contrasted scenarios have been proposed:

- the pre-Mesozoic basement of the eastern Alps would feature relics of an Ordovician accretionary orogen (Zurbriggen, 2015). Conversely, in the western Alps, the coeval Chamrousse ophiolite (Ménot et al., 1988; Pin and Carme, 1987) would correspond to an oceanic domain formed in a back-arc setting above the SE-directed subduction of the Iapetus ocean (Guillot and Ménot, 2009).
- In the Iberian massif, a continental arc setting has been proposed by Valverde-Vaquero and Dunning (2000) and would have been followed by back-arc rifting (Abati et al., 2009; Díez Fernández et al., 2010). Similarly, Villaseca et al. (2016) argue for a flat subduction and thickening on a still ongoing Cadomian belt followed by passive margin development. On the other hand, Nance and Linnemann (2008), Murphy et al. (2008) and Díez Montes et al. (2010) advocate a continental rifting event away from any subduction zone influence.
- in the Armorican Massif, a similar opposition between continental arc (Jégouzo et al., 1986) and subduction-unrelated continental rifting (Ballèvre et al., 2012) is observed.
- in the Maures massif, rifting would have been provoked by a mantle plume (Briand et al., 2002).

Geological information from the Massif Central

Sedimentology The Variscan low-grade metamorphic units (Parautochtonous Units and Fold-and-Thrust Belt) preserve an excellent sedimentological record throughout the Lower Paleozoic. In the northern and southern flanks of the Montagne Noire, the carbonate-bearing early Cambrian to early Ordovician strata would correspond to inner shelf sediments (Álvaro et al., 1998; 2003; 2014; Guérangé-Lozes and Burg, 1990; Lescuyer and Giot, 1986). Of importance are the stratigraphic gap between the Lower and Upper Ordovician and associated Sardic unconformity presumed to reflect uplift and subsequent erosion (Javier Álvaro et al., 2016). Infilling of the negative paleo-reliefs would have started in the Upper Ordovician (Javier Álvaro et al., 2016). The sedimentological record together with the lack of folding and limited uplift (<2 km) during the Sardic event collectively point to an extensional setting in the Cambrian–Ordovician period (Javier Álvaro et al., 2016; Guérangé-Lozes and Burg, 1990).

Magmatic activity Continuous magmatic activity is recorded throughout the Lower Paleozoic as evidenced by: (i) volcanic complexes in the low-grade Variscan parautochton units (Alsac et al., 1987; Álvaro et al., 2014; Béziat et al., 1992; 1993; Lépine et al., 1988; Marini, 1987; 1988; Pouclet et al., in press); (ii) orthogneisses in the high-grade Variscan units (see Alexandre, 2007, Melleton et al., 2010 and the previous chapters);

(iii) magmatic zircon grains of that age present as detritus in younger Devonian to Permian sedimentary formations (Lin et al., 2016; Pfeifer et al., 2016). Magmatic products encompass basic to felsic rocks.

Geotectonic discrimination Metabasic rocks cropping out in high-grade metamorphic units of the French Massif Central have been the subject of numerous geochemical investigations in order to (i) characterize their mantle source(s) and (ii) reconstruct the geodynamic setting in which magmatism took place (Berger et al., 2010a; Bodinier, 1983; Bodinier et al., 1988; Briand and Piboule, 1979; Briand et al., 1988; 1991; 1992; 1995; Downes et al., 1989; Giraud et al., 1984; Piboule, 1977; 1979; Piboule and Briand, 1985; Pin and Marini, 1993). Those studies yielded contrasting results and point to melting of a range of sources from a deep/enriched to shallow/depleted asthenospheric mantle, sometimes bearing a strong "subduction component" (Berger et al., 2010a; Briand et al., 1995; Downes et al., 1989; Pin and Marini, 1993). Similarly, a varied set of Cambrian–Ordovician geodynamic scenarios has been inferred from them and include:

- the existence of an intra-oceanic supra-subduction zone, the metabasites being produced in a island-arc or back-arc setting (Berger et al., 2010a).
- a back-arc basin (Downes et al., 1989; Giraud et al., 1984), probably developed on stretched continental crust (Briand and Piboule, 1979; Briand et al., 1991; 1995; Piboule and Briand, 1985).
- a continental rift away from the influence of a subduction zone (Chèvremont et al., 1996; Pin and Marini, 1993).

4.2.2 Inferences from the metabasite geochemistry

Rationale All geochemical studies of the metabasites cropping out in high-grade units have been conducted at a regional scale, focusing on a specific domain or formation. In this section, I put further constraints on their mantle source(s) and their geodynamic significance based on the examination of the metabasite geochemical record at a larger scale, that of the whole FMC.

Material and methods In this scope, a geochemical database was built based on a literature survey and the newly obtained results presented sections 2.3 and 3.3. It gathers amphibolite-, eclogite- and granulite-facies basic rocks for which the full set of major and trace element compositions is available. In order to discard fractionates, cumulates and altered samples, the same procedure as explained section 2.3 and 3.3 was applied. We retained 21 samples from the Haut-Allier area (Giraud et al., 1984), 41 from the *Monts-du-Lyonnais* (data from Briand et al., 1995; Ouali, 1993 and this study), 36 from the *Lot* area (Briand et al., 1991; Downes et al., 1989; Pin and Marini, 1993) and 16 from the Velay dome (data from Briand et al., 1992; Pin and Marini, 1993 and this study). We also selected 17 samples from several massifs of the Limousin domain, in the western Massif Central (Berger et al., 2010a; Chèvremont et al., 1996), which yields a total of 131 metabasites. Isotopic data are available for 21 of them. A selected set of geochemical diagrams based on immobile trace element ratios is used to discuss the petrogenesis of the metabasic rocks, assumed to represent basaltic melt compositions. This diagrams are those of Pearce (2008) and Shervais (1982) and have already been presented sections 2.3 and 3.3.

Summary of geochronological results Few geochronological investigations have been performed on the metabasites from our database. In the *Lot* area, zircon fractions extracted from a meta-gabbro yielded a TIMS U–Pb age of 484 ± 7 Ma (Pin and Lancelot, 1982) interpreted as the emplacement age of the magmatic protolith. In the *Rouergue* area, a norite and an eclogite (not represented in our database) have been

dated by stepwise Pb-evaporation of single zircon grains and isotope dilution of zircon fractions (Paquette et al., 1995). Both methods yielded identical results and an emplacement age of c. 480 Ma is inferred for the protolith of both rocks. In the *Limousin* area, Berger et al. (2010a) obtained an emplacement age of 473 ± 6 Ma for the protolith of an eclogite by LA–ICP–MS dating of zircon cores. Identical ages obtained by the same method are reported by Chelle-Michou et al. (2017) for amphibolite-facies metabasic to intermediate rocks from the Doux massif (also not represented in our database). Finally, few samples from the *Monts-du-Lyonnais* area are probably as old as 545 Ma (see discussion section 3.5). All these lines of evidence suggest that the metabasites correspond to magmatic rocks formed during a late Ediacaran to early Ordovician magmatic episode (Berger et al., 2010a; Chelle-Michou et al., 2017; Paquette et al., 1995; Pin, 1979; Pin and Lancelot, 1982).

Trace element geochemistry

Figure 4.4a shows that 1/4 of the data plot within the MORB–OIB array and the remaining in the volcanic arc array. The compositions of samples from all massifs are evenly scattered apart for amphibolites from the Velay dome and a selection of samples from the *Monts-du-Lyonnais* area which characteristically plot in the MORB–OIB array close to the OIB reservoir. As explained section 3.3, metabasites plotting in the volcanic arc field were either contaminated by the continental crust during ascent/emplacement or originated from melting of a mantle that interacted with slab-derived fluids. Samples plotting in the MORB–OIB array show a wide range of Nb/Yb, indicative of contrasted melting degrees and/or variously enriched mantle sources. For instance, samples with high Nb/Yb would have formed by limited melting of a (potentially) enriched asthenospheric to lithospheric mantle source (Pearce, 2008).

In the Ti–Nb proxy diagram (Fig. 4.4b), 1/4 of the samples show high TiO_2 ratios and consistently plot in the OIB array. They trend from N–/E–MORB towards OIB compositions which attest to increasing amounts of residual garnet and hence melting of a deeper mantle source (see discussion in Pearce, 2008).

Samples with high Th/Nb ratios and suspected to have originated from a mantle source that interacted with slab-derived fluids are plotted in the V–Ti proxy diagram (Fig. 4.4c). Some display low Ti/V ratios (close to 10) which are indicative of melting under notably oxidizing conditions (Shervais, 1982). Such low ratios cannot originate from contamination of the magmas by the continental crust during ascent because the latter has higher Ti/V (between 20 and 50, see Taylor and McLennan, 1985). If the fluid-enriched mantle source hypothesis is correct, then the wide range of Ti/V ratios (from 10 to 60) attests to melting under varied oxygen fugacities conditions. In supra-subduction zone ophiolites, such range is interpreted in terms of distance to the subducting slab (the main fluid source) with low Ti/V magmas being produced in the arc and those with moderate to high Ti/V in a back-arc setting (Pearce, 2014).

Nd isotope data

Figure 4.4d highlights that samples plotting in the MORB–OIB array of figure 4.4a show radiogenic whole-rock ε_{Nd} (recalculated at 480 Ma) clustering around the value of +6. They will be referred to as subset A. Conversely, samples plotting in the volcanic arc array show a larger range of ε_{Nd}(t) from DM-like values of +9 down to slightly non-radiogenic values of -2.5. Two groups of samples can be identified. The first group (subset B) displays ε_{Nd}(t) similar to that of the DM and to samples plotting in the MORB–OIB array. The second group (subset C) gathers samples with ε_{Nd}(t) clustering around the chondritic value (± 3 ε units).

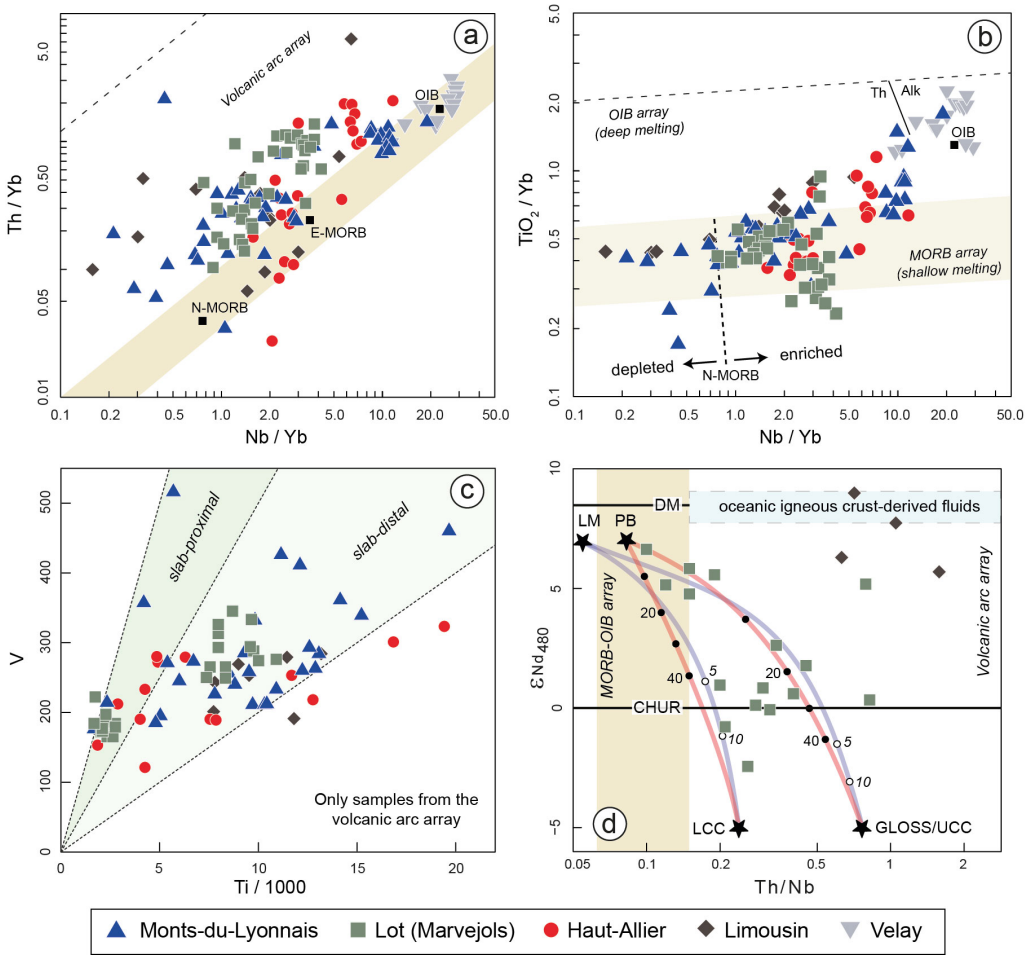

Figure 4.4: (a–c) Proxy element diagrams for metabasites from high-grade metamorphic units of the French Massif Central: (a) Th–Nb proxy diagram of Pearce (2008); (b) Ti–Nb proxy diagram of Pearce (2008); (c) V–Ti proxy diagram of Shervais (1982) applied to samples plotting in the volcanic array in the Th–Nb proxy diagram and assumed to have formed in an environment influenced by subduction. See caption of Fig. 3.7 for the interpretation of those proxies. (d) Whole-rock ε_{Nd} calculated at 480 Ma vs. Th/Nb ratio. The MORB–OIB and volcanic array are bracketed by the values of Pearce (2008). The isotopic composition of metasomatizing fluids derived from the oceanic igneous crust is assumed to be close to that of the Depleted Mantle (value from Liew and Hofmann, 1988). Red curve: results of binary mixing model of a basaltic melt PB (Nd, Th and Nb contents set as average of N– and E–MORBs, from Sun and McDonough, 1989; ε_{Nd}(t) of +7) assimilating upper and lower continental crust (UCC and LCC, Nd, Th and Nb contents from Rudnick and Gao, 2003; ε_{Nd}(t) of -5, average of the FMC crust, from Turpin et al., 1990; Simien et al., 1999; Downes and Duthou, 1988; Pin and Duthou, 1990 and Williamson et al., 1992). Blue curve: results of mass-balance, binary mixing models between the local mantle LM (ε_{Nd}(t)=+7, corresponding to that of the most radiogenic metabasite; Nd, Th and Nb contents from Workman and Hart, 2005) and (i) the GLOSS (Global Subducting Sediment, Plank and Langmuir, 1998), (ii) the LCC (Rudnick and Gao, 2003), both assumed to show an average ε_{Nd}(t) of -5 (see above). Percentages represent the proportion of UCC/LCC/GLOSS in the respective mixtures.

Samples from subset A have low Th/Nb ratios and originated from melting of a mantle source that did not interact at any time with slab-derived fluids (Pearce, 2008). As a result, the ε_{Nd}(t) of c. +6 can be taken as representative of that of the regional mantle devoid of slab-derived component. On the other hand, samples from subset B and C display high Th/Nb ratios which would result from: (i) the presence of a slab-derived component in the mantle source; or (ii) contamination by the continental crust during ascent. In the case of subset B samples, the highly radiogenic (between +6 and +9) ε_{Nd}(t) discards the continental crust as a contaminant since this would have driven the ε_{Nd}(t) towards non-radiogenic values. Therefore, the mantle source of samples from subset B did interact with slab-derived fluids shortly prior to melting. A similar conclusion was drawn by Berger et al. (2010a) using the Limousin dataset.

Deciphering the case of subset C samples has proven more difficult. Pin and Marini (1993) interpreted their slightly radiogenic to non-radiogenic Nd isotope composition as reflecting crustal contamination during magma ascent/emplacement. Yet, binary mixing models of continental crust assimilation indicate that incorporation of more than 20% (and probably 40%) of crustal material is required to account for the non-radiogenic values of subset C metabasites (Fig. 4.4d). Such substantial contamination is hampered by thermodynamic considerations (Glazner, 2007) and the fact that resulting contaminated magmas would certainly not be mafic anymore.

As samples from subset B provide unequivocal evidence for interaction of the mantle with slab-derived fluids, an alternative to the model of Pin and Marini (1993) would be to consider that rocks from subset C originated from melting of a mantle metasomatized by sediment-derived fluids (or melts). Such situation is observed in arc settings where the Nd isotope composition of subducting sediments is transferred to the overlying mantle Hidalgo et al. (2012). Similar conclusions have been drawn for Hf isotopes (see Nebel et al., 2011; Roberts et al., 2013 and section 5.3). In this case, binary mixing models show that the signature of subset C samples could accordingly stem from the incorporation of 5% percent of crustal material in their mantle source (Fig. 4.4d).

Discussion

The set of geochemical proxies and isotopic data presented above unambiguously points to markedly varied melting degrees, redox conditions, depths of melting (presence of residual garnet) and source compositions (including the existence of mantle domains that interacted with slab-derived fluids) for the magmatism at the origin of the metabasite protoliths. Such diversity is observed at the scale of the whole Massif Central and to a lesser extent within each massif (see Downes et al., 1989; Briand et al., 1991; 1995 and section 2.3).

The variable trace element ratios and isotope compositions are best explained by melting of a very heterogeneous mantle source that would readily correspond to the subcontinental lithospheric mantle present beneath the FMC crust segment during the Cambrian–Ordovician. Today inaccessible, the chemical properties of this reservoir can only be inferred from the regional geological context and the study of mantle xenoliths sampled by the Cenozoic volcanoes of the eastern FMC (Downes et al., 2003; Hutchison et al., 1975; Lenoir et al., 2000). Such peridotites provide critical information on the origin and evolution of the SCLM. First, clinopyroxene Nd isotope data show that the SCLM do not record any geological event older than 0.6 Ma (Wittig et al., 2007). Second, sulfide Re/Os geochronology demonstrates that the oldest melt depletion event experienced by the SCLM would be c. 0.9 Ga-old (Harvey et al., 2010). Altogether, these results indicate that the SCLM of the FMC likely formed during the Cadomian orogeny.

Given the back-arc setting retained for the FMC by the late Ediacaran (e.g. Chelle-Michou et al., 2017 and Chapter 2), the newly formed SCLM would have featured a range of chemical compositions reflecting the variable extent of (i) mantle depletion through melt extraction, and (ii) incorporation of a "subduction component" (corresponding to

igneous oceanic crust- and/or sediment-derived fluids). Melting of such a "patchy" mantle in the Cambrian–Ordovician adequately explains the wide range of Nb/Yb and Ti/V ratios and the prevalence of samples with high Th/Nb. Variations of the TiO_2/Yb ratios would result from low melting degrees of the deeper parts of this source (at pressures >3 GPa). As rocks with the highest TiO_2/Yb also display low MORB–OIB-like Th/Nb, the base of this lithospheric mantle may have been less altered by Cadomian slab-derived fluids. Alternatively the source of these rocks may correspond to the uppermost part of the asthenosphere. Finally, the radiogenic Nd isotope compositions at 480 Ma displayed by high Th/Nb samples (subset B) would stem from the short time span between mantle enrichment and mantle melting (c. 100 Ma).

Chemical inheritance of the Cadomian subduction in the lithospheric mantle, yet mentioned by Briand et al. (1995), has never been taken into account while interpreting the chemistry of Cambrian–Ordovician metabasites. Such model provides an alternative to the back-arc setting advocated by most studies (Berger et al., 2010a; Briand and Piboule, 1979; Briand et al., 1991; Downes et al., 1989; Giraud et al., 1984; Piboule and Briand, 1985). Importantly, it resolves the problem of the yet unlocated Cambrian–Ordovician subduction zone, which existence is critical in the "back-arc" model. As a result, a lithospheric thinning and associated melting event, coeval with the extensional setting recorded in the overlying crust, would adequately explain the chemistry of the Cambrian–Ordovician metabasites of the FMC. Therefore, such magmatic activity most probably results from rifting of the North Gondwana margin away from a subduction zone influence, as proposed by Pin and Marini (1993) and Chèvremont et al. (1996) in the FMC and Ballèvre et al. (2012); Díez Montes et al. (2010); Murphy et al. (2008) and Nance and Linnemann (2008) in western Europe.

4.2.3 Widespread crustal melting: the heat source problem

Origin of the Cambrian–Ordovician orthogneisses

Several lines of evidence strongly suggest that Cambrian-Ordovician orthogneisses from the FMC are continental crust-derived magmatic rocks. First, their whole-rock geochemistry and Sr–Nd isotope compositions are in line with melting of pre-existing crustal lithologies (see Demange, 2014; Downes and Duthou, 1988; Lotout et al., 2017; Turpin et al., 1990, and section 3.2). Second, geochronological studies have highlighted the systematic occurrence of inherited zircon grains in dated samples (Chelle-Michou et al., 2017; Lotout et al., 2017; Melleton et al., 2010; Pitra et al., 2012; Roger et al., 2004; 2015; Trap et al., 2017). Third, coeval basic enclaves or associated igneous rocks are scarce in the orthogneiss massifs (Demange, 2014; Lotout et al., 2017) which again points to a crustal source for the felsic magmas (Didier et al., 1982).

What triggered partial melting of the crust?

A striking feature of the Cambrian–Ordovician bimodal magmatism lies in the fact that mafic rocks are very subordinate in volume with respect to the felsic massifs. As a direct consequence of this, melting of the continental crust by basaltic magma underplating and associated heat advection must be disregarded. Indeed, numerical models indicate that in such scenario the relative proportions of crust- vs. mantle-derived magmas should be 1:9 (Annen and Sparks, 2002; Annen et al., 2006; Petford and Gallagher, 2001). Similarly, melting of a thickened continental crust has to be rejected because the sedimentological record rather indicates an extensional, shallow marine environment and does not provide any evidence for significant crustal thickening (Javier Álvaro et al., 2016; Guérangé-Lozes and Burg, 1990). Therefore, question is how to sustain high heat regimes in the crust throughout the Cambrian–Ordovician. The solution to this issue might dwell in the intrinsic nature of the Cambrian–Ordovician crust.

Thermal resilience The crust segment exposed in the FMC comprises a thick sedimentary succession deposited during the late-Ediacaran (see section 2.2) in a back-arc basin. High geothermal gradients are observed in such setting because of strong convection in the back-arc mantle (Currie and Hyndman, 2006). When subduction and thus convection cease, the lithosphere cools down by conduction and the geotherm becomes similar to that observed in inactive tectonic domains. Numerical models yield constraints on the duration of the transient cooling state and demonstrate that the crust and lithospheric mantle are still notably warm c. 100 Ma after subduction has ceased and the slab broke off (Currie and Hyndman, 2006). As a result, the Cambrian–Ordovician crust of the FMC would have still exhibited a thermal imprint of the Cadomian activity, meaning that it likely displayed a steep thermal gradient by that time.

Radioactive heat production As illustrated section 2.2, the Ediacaran detritus originated from: (i) arc crust extracted from the mantle in the Cryogenian–Ediacaran; (ii) Proterozoic to Archean continental rocks from the Gondwana mainland. Erosion of the latter likely produced a detritus rich in K, Th and U, the main heat producing elements in the continental crust (Birch, 1954). Accordingly, a compilation of whole-rock chemical compositions (N=24) of low- to medium-grade Ediacaran metasediments from the eastern Massif Central (data courtesy of J.-F. Moyen and D. Garcia) highlights that those rocks have elevated average K_2O (3.4 wt.%), U (5.9 ppm) and Th (14.4 ppm) contents. A heat production of 3043 $\mu W/m^3$ was calculated for such average crustal composition at 500 Ma based on these concentrations, the equation of Kramers et al. (2001), the constants of Rybach (1976) and an average density of 2700 kg/m^3. Such value is c. 40% higher than those derived from average upper crustal compositions, calculated using the same procedure, which yield 1789 $\mu W/m^3$ (based on Rudnick and Gao, 2003), 1795 $\mu W/m^3$ (based on Wedepohl, 1995) and 1888 $\mu W/m^3$ (based on Taylor and McLennan, 1985). Consequently, the Ediacaran sediments constituted layers or horizons of notably high radioactive heat production.

Synergetic effects The Cambrian–Ordovician crust of the FMC would have thus featured: (i) a rather steep geotherm, vestige of the high thermal regime of the late Cadomian period; (ii) sedimentary layers with anomalously high radioactive heat production. Therefore, thermal subsidence and burial of radioactive element-rich layers in such a warm crust segment would have generated thermal anomalies and triggered local anatexis of metasediments at *c.* 480 Ma, some 50 Ma after the Cadomian subduction ceased. Such model is adapted from that of Sandiford et al. (1998), initially designed to account for high geothermal gradients observed in high-temperature, low-pressure metamorphic terranes. It readily explains the scarcity of coeval mantle-derived magmas because the thermal trigger of crustal melting lies in the crust itself.

4.2.4 Conclusion

Contrasted Cambrian–Ordovician geodynamic models have been proposed for the crust segment today exposed in the FMC. Among them, the back-arc setting model has proven very popular (Berger et al., 2010a; Briand et al., 1995; Downes et al., 1989; Pin and Marini, 1993). Yet, a careful examination of the literature together with new geochemical data on basic igneous rocks discards any Cambrian–Ordovician subduction zone influence in the FMC for several reasons:

- there is no compelling evidence for the presence of an active subduction zone nearby the FMC by the Ordovician;
- the "subduction component" present in the mantle source of basic rocks would have been inherited from the pre-dating Cadomian subduction;

– anatexis leading to voluminous crust-derived granitic magmas was neither triggered by mafic magmas underplating nor the consequence of a thickening episode, as generally observed in back-arc basins (Collins and Richards, 2008).

In contrast, the extensional continental rift setting readily complies with a large set of geological observations and is in notable agreement with the sedimentary, tectonic and magmatic records which are summarized Figure 4.5.

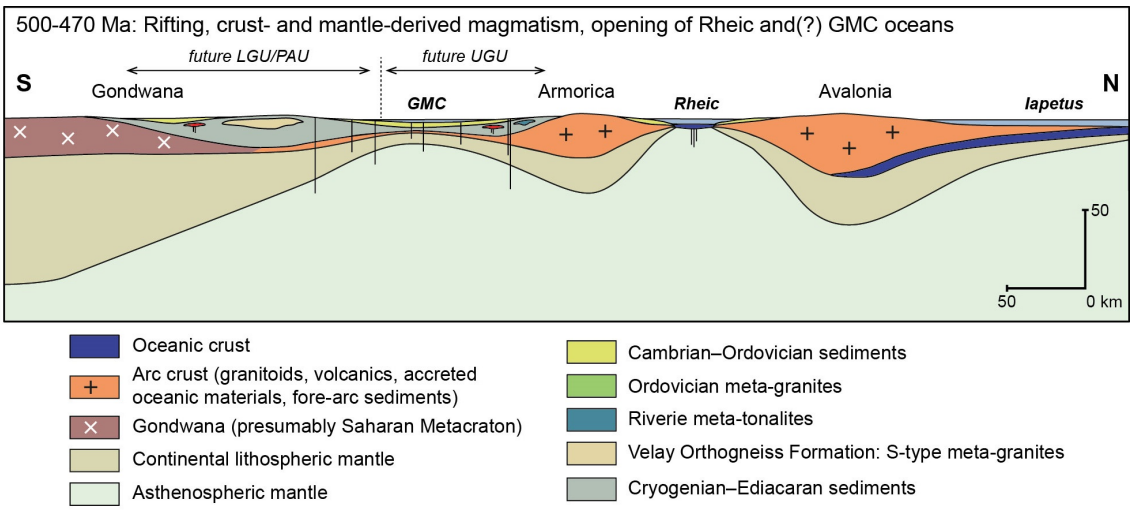

Figure 4.5: Interpretative geodynamic sketch illustrating the Cambrian–Ordovician evolution of the crust segment to which the French Massif Central belongs. See text for discussion.

Part II

Timescale and sources of Variscan post-collisional magmatism in the eastern French Massif Central

Chapter 5

Coeval crust and mantle melting during orogenic collapse

5.1 Article #2: U–Pb geochronology and granite typology

This contribution has been published in the International Journal of Earth Sciences. In the course of my M.Sc., I sampled 25 of the 33 investigated igneous rocks presented in this study with the help of Jean-François Moyen and Adrien Vezinet and prepared them for whole-rock geochemical determinations. I extracted the zircon grains and performed the U–Pb dating session for the vaugnerite samples at GUF under the supervision of Oscar Laurent and Armin Zeh. During my Ph.D., I processed the raw data with the help of Oscar Laurent. I compiled geochronological and geochemical data available from the literature (see Tab. 1 and Fig. 2 for instance), wrote part of the "Geological setting" and the "Results" sections together with the Supplementary text, participated to the writing of the rest of the manuscript and significantly contributed to the ideas presented in this article.

Int J Earth Sci (Geol Rundsch) (2017) 106:421–451
DOI 10.1007/s00531-016-1434-9

ORIGINAL PAPER

Protracted, coeval crust and mantle melting during Variscan late-orogenic evolution: U–Pb dating in the eastern French Massif Central

Oscar Laurent[1,2,12] · Simon Couzinié[3,4] · Armin Zeh[1,5] · Olivier Vanderhaeghe[6] · Jean-François Moyen[3] · Arnaud Villaros[7,8,9] · Véronique Gardien[10] · Cyril Chelle-Michou[3,11]

Received: 29 January 2016 / Accepted: 7 December 2016 / Published online: 6 January 2017

Abstract The late stages of the Variscan orogeny are characterized by middle to lower crustal melting and intrusion of voluminous granitoids throughout the belt, which makes it akin to "hot" orogens. These processes resulted in the development of large granite–migmatite complexes, the largest of which being the 305–300-Ma-old Velay dome in the eastern French Massif Central (FMC). This area also hosts a wide range of late-Variscan plutonic rocks that can be subdivided into four groups: (i) cordierite-bearing peraluminous granites (CPG); (ii) muscovite-bearing peraluminous granites (MPG); (iii) K-feldspar porphyritic, calc-alkaline granitoids (KCG) and (iv) Mg–K-rich (monzo) diorites and lamprophyres ("vaugnerites"). New results of LA-SF-ICP-MS U–Pb zircon and monazite dating on 33 samples from all groups indicate that both granites and mafic rocks emplaced together over a long period of ~40 million years throughout the Carboniferous, as shown by intrusion ages between 337.4 ± 1.0 and 298.9 ± 1.8 Ma for the granitoids, and between 335.7 ± 2.1 and 299.1 ± 1.3 Ma for the vaugnerites. Low zircon saturation temperatures and abundant inherited zircons with predominant late Ediacaran to early Cambrian ages indicate that the CPG and MPG formed through muscovite or biotite dehydration melting of ortho- and paragneisses from the Lower Gneiss Unit. The KCG and vaugnerites contain very few inherited zircons, if any, suggesting higher magma temperatures and consistent with a metasomatized lithospheric mantle source for the vaugnerites. The KCG can be explained by interactions between the CPG/MPG and the vaugnerites, or extensive differentiation of the latter. The new dataset provides clear evidence that the eastern FMC was affected by a long-lived magmatic episode characterized by coeval melting of both crustal and mantle sources. This feature is suggested here to result from

Electronic supplementary material The online version of this article (doi:10.1007/s00531-016-1434-9) contains supplementary material, which is available to authorized users.

✉ Oscar Laurent
oscarlaurent86@gmail.com

[1] Institut für Geowissenschaften, J.W. Goethe Universität, Altenhöferallee 1, 60438 Frankfurt Am Main, Germany

[2] Département de Géologie B20, Université de Liège, Quartier Agora, Allée du six Août 12, 4000 Liège, Belgium

[3] Département de Géologie, Université Jean Monnet, UMR6524-CNRS-IRD 23 rue du Dr. Paul Michelon, 42023 Saint-Étienne, France

[4] Department of Earth Sciences, University of Stellenbosch, Private Bag X1, Matieland 7602, South Africa

[5] Abteilung Mineralogie und Petrologie, Institut für Angewandte Geowissenschaften, Karlsruher Institut für Technologie, Campus Süd, Kaiserstrasse 12, 76131 Karlsruhe, Germany

[6] Géosciences Environnement Toulouse, Université Paul Sabatier, Observatoire Midi-Pyrénées 14 avenue E. Belin, 31400 Toulouse, France

[7] Université d'Orléans, ISTO, UMR 7327, 45071 Orléans, France

[8] CNRS, ISTO, UMR 7327, 45071 Orléans, France

[9] BRGM, ISTO, UMR 7327, BP 36009, 45060 Orléans, France

[10] LGL, TPE UMR5276, Université Lyon 1, Lyon, France

[11] Department of Earth Sciences, University of Geneva, Rue des Maraîchers 13, Geneva 1205, Switzerland

[12] Present Address: Institute for Geochemistry and Petrology, ETH Zürich, Zurich, Switzerland

a lithospheric-scale thermal anomaly, triggered by the removal of the lithospheric mantle root. The spatial distribution of the dated samples points to a progressive southward delamination of the lithospheric mantle, perhaps in response to rollback following continental subduction, or to "retro-delamination" owing to the retreat of a south-verging subduction zone.

Keywords U–Pb dating · Zircon · French Massif Central · Granitoids · Vaugnerites · Variscan orogeny

Introduction

Following crustal thickening, the final stages of continental collision, associated with lateral extension or orogenic collapse, are periods of intense magmatic activity characterized by emplacement of granitoids derived from both crustal and mantle sources (Liégeois et al. 1998; Bonin 2004; Clemens et al. 2009; Vanderhaeghe 2012; Laurent et al. 2014a). Granitoid magmas represent major heat and mass transfers from the lower to the upper crust, contributing to crustal differentiation, thermal maturation and ore deposits (Petford et al. 2000; Kemp and Hawkesworth 2003; Hou and Cook 2009). Voluminous layers of partially molten rocks at mid to lower crustal levels, as evidenced in modern orogens by geophysical investigations (Nelson et al. 1996; Schilling and Partzsch 2001), influence the thermomechanical behavior of the orogenic crust and its coupling to the lithospheric mantle (Brown 2001; Vanderhaeghe and Teyssier 2001; Schulmann et al. 2008; Vanderhaeghe 2009; Barbey et al. 2015). In addition, the mafic magmas emplaced during these periods and their derivatives may represent significant additions to the preexisting continental volume (Laurent et al. 2013; Couzinié et al. 2016; Moyen et al. in press). Therefore, late- to post-collisional magmatism is of primary interest to understand (i) the mechanisms of heat and mass transfer in the lithosphere; (ii) the geodynamic evolution at convergent plate boundaries; and (iii) continental crust formation and differentiation.

The Paleozoic Variscan belt of western Europe is often referred to as a "hot" orogen (Schulmann et al. 2008) characterized by the emplacement of abundant and diverse granitoid magmas, especially at the end of the continental collision sensu stricto and throughout late-orogenic collapse (Pin and Duthou 1990; Finger et al. 1997; Gardien et al. 1997; Fernández-Suárez et al. 2000; Janoušek et al. 2000; Rossi and Pin 2008). In the French Massif Central (FMC), the late-Variscan collapse led to the formation of the 305–300 Ma Velay granite–migmatite complex (Montel et al. 1992; Mougeot et al. 1997; Couzinié et al. 2014), a roughly circular dome of >100 km diameter and >6000 km^2 (Fig. 1), consisting of migmatites cored by a heterogeneous cordierite-bearing granite (Ledru et al. 2001; Barbey et al. 2015). It is suggested that the Velay dome was formed in response to a long-lived (>40 Ma) period of HT metamorphism and partial melting of the orogenic crust (Vanderhaeghe et al. 1999; Ledru et al. 2001; Vanderhaeghe and Teyssier 2001; Rossi and Pin 2008), first through limited low-temperature, possibly water-present melting between ca. 340 and 314 Ma; and second through high-temperature, extensive biotite breakdown melting at 310–300 Ma (Montel et al. 1992; Mougeot et al. 1997; Barbey et al. 1999, 2015; Couzinié et al. 2014).

Field relationships indicate that voluminous granitoid plutons and batholiths were emplaced before, during and after its formation (Ledru et al. 2001; Faure et al. 2009). Indeed, available geochronological data hint that granite formation lasted for several tens of million years between the early Carboniferous (340 ± 20 Ma) and early Permian (295 ± 15 Ma) (Duthou et al. 1984; Montel et al. 1992; Briand et al. 2002; Bé Mézème et al. 2006; Table 1). Moreover, granitoids are associated with volumetrically minor, but spatially ubiquitous mafic magmas, i.e., potassic to ultrapotassic diorites, gabbros and/or lamprophyres, locally referred to as "vaugnerites" (Sabatier 1991; Solgadi et al. 2007; Scarrow et al. 2008; von Raumer et al. 2013; Couzinié et al. 2014, 2016). Several questions arise from those observations. First, the genesis of large volumes of granite throughout the Carboniferous apparently contradicts the model proposed by some authors for the formation of the Velay dome, which implies that crustal anatexis was limited prior to 310 Ma and only produced significant amounts of granitic magmas at 310–300 Ma (Montel et al. 1992; Ledru et al. 2001). It has also been proposed that the formation of these granites and their ascent through the crust explains the temperature increase associated with the formation of the Velay dome at 310–300 Ma (Barbey et al. 2015), but then the problem translates to the origin of the heat source responsible for the genesis of the granites (Rossi and Pin 2008). Second, the role played by mafic magmas in the late-orogenic evolution is poorly understood; in particular, it is not yet clear whether the mafic magmas are responsible for crustal melting, or whether they represent a side effect of the processes at the origin of crustal anatexis.

To be addressed, those problems require a reliable geochronological framework for both granitic and mafic magmatism. Such a dataset is still lacking in the eastern FMC, where most available ages are either imprecise and possibly inaccurate radiometric dates based on whole-rock isochrons (Rb–Sr or Sm–Nd) or recent U–Pb dates but focused on small areas or specific plutons. This prevents a large-scale and systematic understanding of the magmatic evolution and questions the existence of long-lived granitic emplacement prior to the formation of the Velay complex, since this may only be an artifact of the large uncertainties

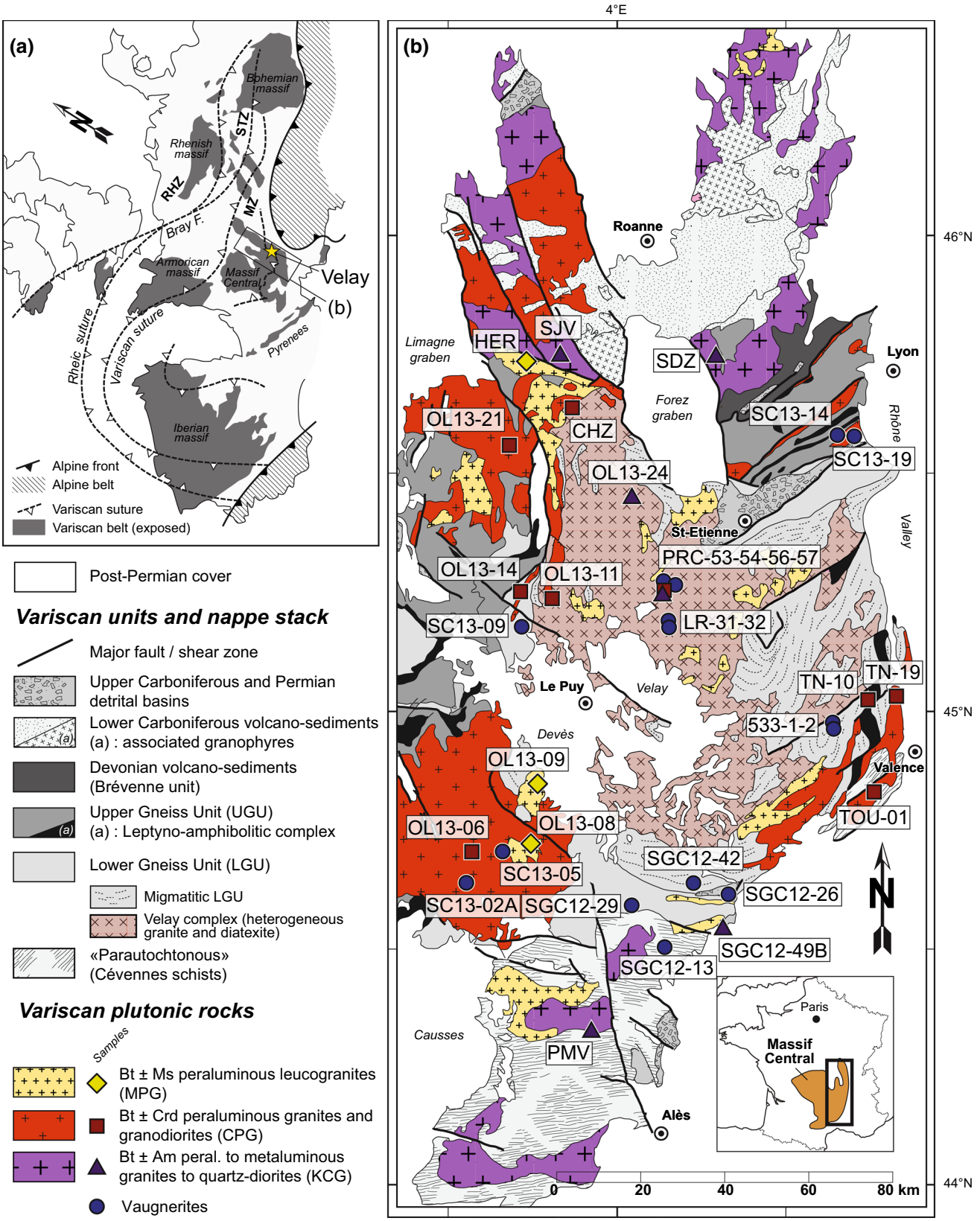

Fig. 1 **a** Sketch map showing the repartition of exposed Variscan domains in Western Europe, as well as the salient structural features of the Variscan belt (*MZ* moldanubian zone, *RHZ* Rheno-Hercynian zone, *STZ* Saxo-Thuringian zone). **b** Geological map of the eastern French Massif Central (after the 1:1000000[e] BRGM map of France) with particular emphasis on the late-Variscan plutonic rocks associated with the Velay Complex. Positions of the studied samples are also indicated

Table 1 List, nature and sampling localities of the investigated samples of Variscan igneous plutonic rocks from the eastern FMC, together with existing age data and results of zircon and monazite U–Pb dating performed in this study

Sample	Nature	Type[a]	Pluton/locality	Encl.[b]	Lat. N	Long. E	Literature age (Ma)[c]	Ref.[d]	Method[d]	Group[e]	Age (Ma)[f]	±2σ	MSWD[g]	Prob[g]	C^h	M^h	I^h	N^h	Z^h
CHZ	Porph. Bt granite	CPG	Chalmazel	y	45°42′15″	3°52′07″				3	**332.0**	**2.0**	0.58	0.87	7	17	5	22	19
HER	Bt-Ms leucogranite	MPG	Hermitage	n	45°45′50″	3°46′23″	329 ± 14	1	Rb/Sr WR	3	**325.7**	**1.3**	0.62	0.78	5	20	8	28	25
OL-13-06	Porph. Bt-Crd granite	CPG	Margeride	n	44°40′28″	3°26′01″	334 ± 9	2	U/Pb Zrn (TIMS)	2	**312.9**	**2.0**	0.39	0.98	8	33	–	33	28
							323 ± 12	3	Rb/Sr WR										
							314 ± 4	4	U/Pb Mnz (TIMS)										
OL-13-08	Bt-Ms leucogranite	MPG	Grandrieu	n	44°43′42″	3°40′26″	305 ± 4	5	U/Pb Mnz (TIMS)	3	**311.0**	**1.1**	1.12	0.34	6	13	25	38	35
											309.3[i]	1.2	1.10	0.36	6				
OL-13-09	Bt-Ms leucogranite	MPG	St-Christophe-d'Allier	n	44°49′07″	3°42′43″	305 ± 14	6	U/Pb Mnz (TIMS)	3	**312.7**	**2.3**	0.61	0.82	6	6	19	25	19
OL-13-11	Bt granite	CPG	Almance	n	45°18′16″	3°46′44″				3	**314.5**	**1.7**	0.25	0.99	5	15	15	30	28
											315.4[i]	0.9	0.86	0.60	8				
OL-13-14	Porph. Bt-Crd granite	CPG	Chaise-Dieu	n	45°19′37″	3°41′20″				3	**318.3**	**2.6**	0.44	0.88	4	18	31	49	39
											317.8[i]	1.3	1.60	0.10	5				
OL-13-21	Bt granite	CPG	St-Dier-d'Auvergne	n	45°40′18″	3°38′45″	330 ± 26	7	Rb/Sr WR	3	**336.9**	**1.8**	0.99	0.47	11	19	7	26	26
OL-13-24	Bt-Am Qz-diorite	KCG	Gumières	y	45°31′48″	3°59′09″	313 ± 2	8	U/Pb Zrn (LA)	1	**321.2**	**1.2**	1.40	0.03	27	32	–	32	30
PMV	Porph. Bt-Am granite	KCG	Pont-de-Montvert	n	44°20′06″	3°52′30″				2	**302.5**	**0.9**	1.06	0.38	13	24	2	26	24
PRC-56	Bt-Am granodiorite	KCG	Pont-Rouge quarry	y	45°19′44″	4°06′08″				1	**332.1**	**0.7**	1.40	0.03	26	31	–	31	30
PRC-57	Bt-Crd granite	CPG	Pont-Rouge quarry	n	45°19′44″	4°06′08″	305.9 ± 1.4	9	U/Pb Mnz (LA)	3	**302.8**[i]	**1.3**	1.50	0.09	10	11	21	32	32
											334.9[j]	*1.5*	*1.50*	*0.10*	7				
SDZ	Bt granite	KCG	Salt-en-Donzy	n	45°47′02″	4°18′25″				2	**337.4**	**1.0**	1.50	0.03	16	29	2	31	23

Table 1 continued

Sample	Nature	Type[a]	Pluton/locality	Encl.[b]	Lat. N	Long. E	Literature age (Ma)[c]	Ref.[d]	Method[d]	Group[e]	Age (Ma)[f]	±2σ	MSWD[g]	Prob[g]	C^h	M^h	I^h	N^h	Z^h
SGC-12-49B	Porph. Bt-granite	KCG	Largentière	n	44°33′17″	4°17′15″	304.1 ± 6.3	9	U/Pb Zrn (LA)	2	**298.9**	**1.8**	0.61	0.90	10	18	2	20	18
SJV	Bt-Am granodiorite	KCG	St-Julien-la-Vêtre	n	45°48′32″	3°50′07″	340 ± 20	10	Rb/Sr WR	2	**330.1**	**1.3**	1.11	0.28	14	28	–	28	26
TN-10	Poph. Bt-granodiorite	CPG	Colombier-le-Vieux	y	45°03′31″	4°43′57″				3	**321.9**	**1.3**	1.60	0.11	5	27	7	34	30
TN-19	Porph. Bt granite	CPG	Tournon	n	45°04′10″	4°49′35″	337 ± 13	11	Rb/Sr WR	3	**321.1**	**1.1**	1.17	0.07	6	14	17	31	31
TOU-01	Porph. Bt granite	CPG	Dunières-sur-Eyrieux	n	44°49′45″	4°39′08″				3	**322.2**	**1.5**	0.47	0.98	10	22	8	30	24
533-1	Vaugnerite		Lamastre	n	44°58′24″	4°37′41″				1	**307.8**	**1.6**	1.05	0.40	12	16	–	16	5
533-2	Vaugnerite		Lamastre	n	44°58′24″	4°37′41″				2	**307.3**	**1.3**	0.73	0.87	18	27	–	27	26
LR-31	Vaugnerite		La Roche	n	45°17′05″	4°06′50″				1	**299.1**	**1.3**	0.75	0.85	17	20	–	20	20
LR-32	Vaugnerite		La Roche	n	45°17′05″	4°06′50″				1	**301.5**	**1.4**	0.71	0.88	17	19	–	19	17
PRC-53	Vaugnerite		Pont-Rouge quarry	y	45°19′47″	4°06′05″				2	**318.9**	**1.8**	0.48	0.98	11	22	–	22	22
PRC-54	Vaugnerite		Pont-Rouge quarry	y	45°19′47″	4°06′05″				2	**320.5**	**1.8**	0.42	0.99	11	17	–	17	17
SC-13-02A	Vaugnerite		Moulin de Linas	n	44°41′14″	3°28′25″				1	**313.2**	**2.5**	0.53	0.85	5	7	–	7	5
SC-13-05	Vaugnerite		L'Aldeyres	n	44°45′53″	3°37′53″				2	**309.4**	**1.5**	1.40	0.09	12	18	–	18	17
SC-13-09	Vaugnerite		Pubellier	n	45°13′29″	3°39′33″				1	**309.7**	**1.2**	1.19	0.19	21	26	1	27	27
SC-13-14	Vaugnerite		Marcenod	n	45°35′04″	4°29′32″				2	**335.7**	**2.1**	0.34	0.99	9	18	*4*	22	20
SC-13-19	Vaugnerite		Chassagny	n	45°36′14″	4°42′60″				1	**333.9**	**1.4**	0.92	0.60	17	26	–	26	24
SGC-12-13	Vaugnerite		Borne	n	44°29′48″	4°05′19″				1	**306.6**	**2.4**	0.59	0.84	6	9	–	9	8
SGC-12-26	Vaugnerite		Pont-de-Bayzan	n	44°39′28″	4°18′24″				1	**306.1**	**1.3**	1.04	0.39	20	24	–	24	24

Table 1 continued

Sample	Nature	Type[a]	Pluton/locality	Encl.[b]	Lat. N	Long. E	Literature age (Ma)[c]	Ref.[d]	Method[d]	Group[e]	Age (Ma)[f]	±2σ	MSWD[g]	Prob[g]	C^h	M^h	I^h	N^h	Z^h
SGC-12-39	Vaugnerite		Loubaresse	n	44°36′02″	4°04′14″	307.4 ± 1.8	9	U/Pb Zrn (LA)	1	**306.6**	**1.6**	0.66	0.88	12	14	–	14	14
							313 ± 3	12	U/Pb Zrn (TIMS)										
SGC-12-42	Vaugnerite		Meyras	n	44°40′21″	4°16′26″	305.8 ± 2.3	9	U/Pb Zrn (LA)	1	**305.9**	**1.7**	0.56	0.95	11	16	–	16	16
							314 ± 3	12	U/Pb Zrn (TIMS)										

[a] For granitoids, classification according to Barbarin (1999)

[b] Occurrence as enclave in the Velay granite (yes/no)

[c] Existing age for the corresponding pluton or magmatic body

[d] Reference, dating system and technique for the age displayed in (c). 1 = Pin and Barbarin (unpublished); 2 = Respaut (1984); 3 = Couturié and Caen-Vachette (1979); 4 = Pin (1979b); 5 = Lafon and Respaut (1988); 6 = Isnard (1996); 7 = Saint-Joanis (1975); 8 = Barbarin et al. (2012); 9 = Couzinié et al. (2014); 10 = Pin (unpublished); 11 = Batias and Duthou (1979); 12 = Aït Malek (1997). *WR* whole-rock isochron, *Zrn* zircon, *Mnz* monazite, *LA* LA-ICP-MS

[e] Classification of the samples according to the distribution of U–Pb dates and zircon textures (see text for details)

[f] U–Pb Concordia age obtained in the course of this study, in Ma

[g] MSWD and Probability of concordance + equivalence for the displayed Concordia age

[h] C = number of analyses used to calculate the Concordia age; M = number of analyses corresponding to the "magmatic" age; I = number of analyses corresponding to zircon inheritance; N = total number of analyses for this sample (=$M + I$); Z = number of zircon grains analyzed in this sample (all for zircon data only)

[i] U–Pb Concordia age on monazite

[j] U–Pb Concordia age provided by zircons in sample PRC-57, probably reflecting inheritance (see "Discussion")

on the existing ages. In fact, the most recent U–Pb ages obtained on igneous rocks in the eastern FMC are almost exclusively in the range 310–300 Ma (Brichau et al. 2008; François 2009; Gardien et al. 2011; Barbarin et al. 2012; Didier et al. 2013; Couzinié et al. 2014), i.e., coeval with the migmatites and granites of the Velay dome. Furthermore, only a handful of ages are available so far on the mafic rocks (Aït-Malek 1997; Couzinié et al. 2014).

The aim of this study is therefore to provide a self-consistent geochronological dataset on both granites and mafic rocks in the eastern FMC. For this purpose, we sampled a total of 18 granitoids and 15 vaugnerites, representative of the lithological diversity observed at the regional scale, and performed U–Pb dating on individual zircons (and monazites for some samples) by laser ablation, sector field inductively coupled plasma mass spectrometry (LA-SF-ICP-MS). The results are used to discuss (i) the petrogenesis of the magmas; (ii) the nature of the heat source at the origin of late-Variscan magmatism in the eastern FMC; and (iii) its significance for the geological and tectonic evolution of the orogen.

Geological setting

The French Massif Central (FMC)

The Variscan belt of Western Europe (Fig. 1a) belongs to a Paleozoic orogenic system that results from convergence between Laurussia, Gondwana and several intervening microcontinents (Matte 1986; Kroner and Romer 2013; Stampfli et al. 2013), which ended up with the assembly of Pangea. The FMC is part of the inner domain of this belt (Lardeaux et al. 2014), referred to as the "Moldanubian" zone, and represents a reworked crustal domain that was previously formed along the northern margin of Gondwana (Faure et al. 2009; Melleton et al. 2010).

The FMC hosts a south-verging Devonian to early Carboniferous nappe pile (Ledru et al. 1989; Faure et al. 2009) that became dismembered by late Carboniferous ductile and brittle strike-slip shear zones and detachments accommodating late-orogenic extension and collapse (Malavieille et al. 1990; Faure 1995; Gardien et al. 1997). In the eastern FMC (Fig. 1b), this pile is made up from top to bottom (north to south) by:

1. The Brévenne unit, a greenschist-facies volcano-sedimentary basin (Feybesse et al. 1988) of late Devonian age (366 ± 5 Ma; Pin and Paquette 1997), presumably a back-arc system formed as a result of the southwards subduction of the Rheic Ocean (Lardeaux et al. 2014).
2. The Upper Gneiss Unit (UGU) consists of high-grade, migmatitic ortho- and paragneisses whose protoliths are early Ordovician in age (Duthou et al. 1984; Melleton et al. 2010; Chelle-Michou et al. 2015; Lotout et al. in press). The base of the UGU is characterized by the presence of (i) the leptynite–amphibolite complex (LAC), a bimodal Ordovician (487–478 Ma) magmatic association (Pin and Lancelot 1982; Briand et al. 1991) proposed to represent an ocean–continent transition zone (Lardeaux et al. 2014); and (ii) relics of (U)HP metamorphic rocks (Gardien et al. 1990; Mercier et al. 1991; Gardien 1993; Lardeaux et al. 2001).
3. The Lower Gneiss Unit (LGU) also made up of migmatitic ortho- and paragneisses with dominantly late Ediacaran to early Cambrian protolith age (Caen-Vachette 1979; Duthou et al. 1984; R'Kha Chaham et al. 1990; Couzinié et al. 2014; Chelle-Michou et al. 2015; Mintrone 2015) and minor amphibolites. The migmatites are cored by the heterogeneous Velay granite (Dupraz and Didier 1988; Ledru et al. 2001).
4. The Para-autochthonous Unit (PAU), dominantly made up of greenschist- to lower amphibolite-facies metasediments (Cévennes schists; Faure et al. 1999) deposited between the Neoproterozoic and the early Cambrian (Caron 1994; Melleton et al. 2010).

The tectono-metamorphic evolution of the eastern FMC can be summarized as follows. An early (D–M_0) (U)HP metamorphic event attributed to northward subduction was dated between 432 and 408 Ma (Pin and Lancelot 1982; Ducrot et al. 1983; Paquette et al. 1995; Do Couto et al. 2015) and recorded by the eclogitic relics (at the base of the UGU and in the LAC). The UGU experienced anatexis (M_1) coeval with exhumation of the (U)HP units and top-to-the-SW shearing (D_1) (Faure et al. 2008, 2009) between 384 ± 16 Ma (Duthou et al. 1994) and 360 ± 4 Ma (Gardien et al. 2011). The UGU was subsequently juxtaposed to the north to the Brévenne unit during top-to-the-NW (D–M_2) thrusting (Leloix et al. 1999) at ~360–350 Ma (Faure et al. 2002). This episode is also recorded in the western part of the FMC (Limousin area) by 360 ± 4 Ma top-to-the-NW thrusting (Melleton et al. 2009) and corresponds to the main event of nappe stacking (Faure et al. 2009). The early Carboniferous D_3 event corresponds to the onset of syn-orogenic extension in the northern part of the FMC, as recorded by 340–330-Ma-old volcano-sedimentary sequences (Bruguier et al. 1998), while crustal thickening was still ongoing in the southern domain, especially the PAU which experienced top-to-the-S thrusting (Arnaud and Burg 1993; Caron 1994). Subsequently, the nappe pile, specifically the LGU, was extensively reworked by a pervasive Carboniferous LP–HT event that culminated with the rise of the Velay dome (Ledru et al. 2001). This reworking process was proposed to happen in two steps (Montel et al. 1992; Barbey et al. 2015): (i) limited anatexis in the LGU with biotite remaining stable

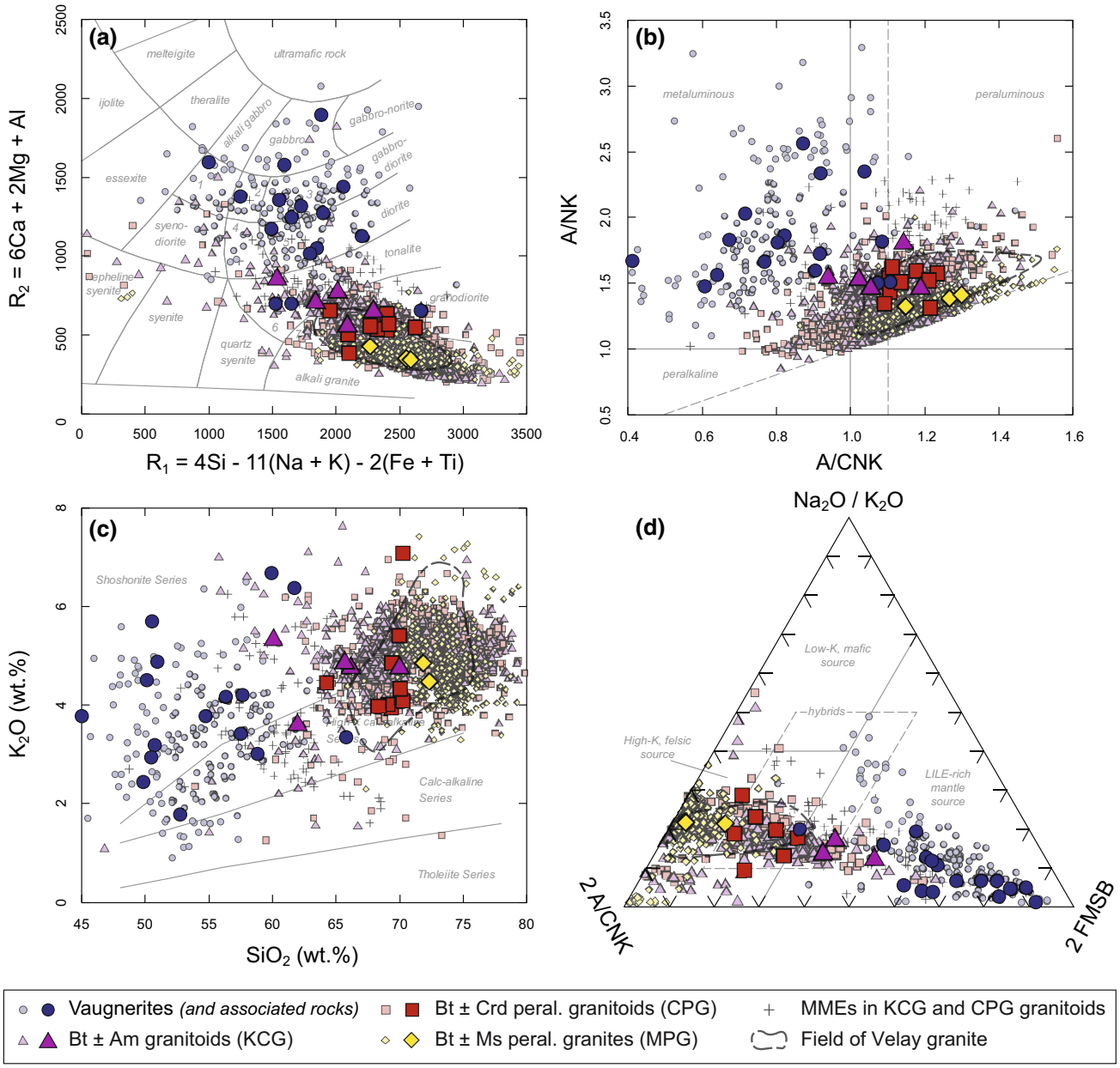

Fig. 2 Some geochemical characteristics of late-Variscan plutonic rocks in the eastern French Massif Central. The larger symbols correspond to samples investigated in the present study for which whole-rock geochemical data are available (unpublished data from S. Couzinié). **a** R_1–R_2 plot of De la Roche et al. (1980) (1 = syenogabbro; 2 = monzogabbro; 3 = monzonite; 4 = monzodiorite; 5 = quartz–monzonite; 6 = granite); **b** molar $Al_2O_3/(Na_2O + K_2O)$ (A/NK) vs. $Al_2O_3/(CaO + Na_2O + K_2O)$ (A/CNK) plot; **c** K_2O vs. SiO_2 plot (fields are from Peccerillo and Taylor 1976); and **d** ternary discrimination plot of Laurent et al. (2014a, b) proposed on the basis of late-Archean granitoid typology (FMSB = $[FeOt + MgO]_{wt\%} \times [Sr + Ba]_{wt\%}$)

(T < 750 °C), at ages between 329 ± 5 Ma (Bé Mézème et al. 2006) and 314 ± 5 Ma (Mougeot et al. 1997); and (ii) widespread biotite dehydration melting (760 < T < 850 °C) that affected the whole middle crust and gave rise to the formation of the Velay dome proper at 301–305 Ma (Couzinié et al. 2014). Those late Carboniferous events are attributed to N(W)–S(E)-directed late-orogenic extension (D_{4-5}) associated with large-scale crustal detachments and formation of detrital coal-bearing basins (Malavieille et al. 1990; Faure et al. 2009).

Petrographic-geochemical characteristics of late-Variscan igneous rocks in the eastern FMC

Exposure in the eastern FMC is largely dominated by Carboniferous plutonic rocks intruding the metamorphic

lithologies described earlier (Fig. 1b). Based on existing petrographic descriptions and classifications (Didier and Lameyre 1969; Didier et al. 1982; Barbarin 1983, 1992, 1999; Stussi and De la Roche 1984; Rossi and Pin 2008; Moyen et al. in press), four types of plutonic rocks can be distinguished (Fig. 1b) (nomenclature after Barbarin 1999):

1. Peraluminous to slightly metaluminous, biotite- and sometimes cordierite-bearing granitoids ("**CPG**") are the most abundant (Fig. 1b). They can be separated in two subgroups: (i) K-feldspar porphyritic, cordierite-poor plutons and batholiths (Margeride, Chaise-Dieu, Tournon) characterized by the presence of microgranular mafic enclaves (MMEs; Didier et al. 1982) and (ii) the cordierite-rich, heterogeneous Velay granite, which is closely associated with LGU migmatites and frequently contains large enclaves of the previous, cordierite-poorer type (Barbey et al. 2015; Ledru et al. 2001; Williamson et al. 1997). CPG are granites and granodiorites (Fig. 2a) with a peraluminous character (Fig. 2b) and elevated contents in SiO_2 (>65 wt%) and K_2O (3–7 wt%) (Fig. 2c). Those characteristics, together with Sr–Nd isotopic data, reflect that the CPG result from partial melting of the local crust (Duthou et al. 1984; Pin and Duthou 1990; Downes et al. 1997; Williamson et al. 1997).
2. Peraluminous, two-mica or muscovite-bearing (leuco-) granites ("**MPG**"), generally occurring as dykes and small laccoliths intrusive in the Velay complex (Ledru et al. 2001; Didier et al. 2013) as well as rare plutons (L'Hermitage, Saint-Christophe-d'Allier). The MPG show a tighter compositional range than the CPG. They

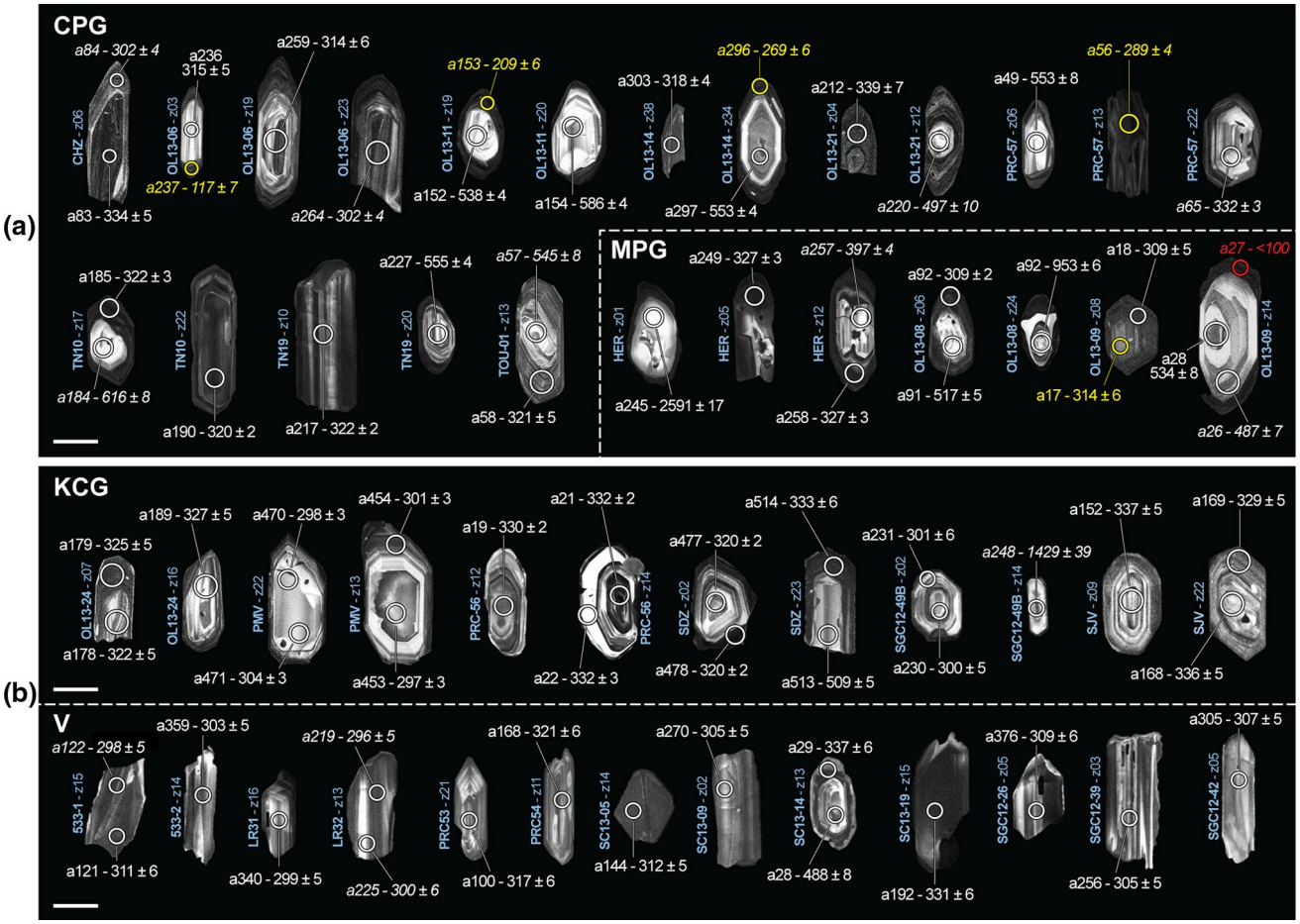

Fig. 3 Representative cathodoluminescence images of zircon grains from samples of late-Variscan plutonics rocks investigated in this study: **a** cordierite- and muscovite-bearing peraluminous granites (CPG and MPG); **b** K-feldspar porphyritic calc-alkaline granites and granodiorites (KCG) and vaugnerites (V). The position of the laser spots used for U–Pb dating (*circles*) is also indicated, along with the spot name (aXXX) and the corresponding $^{238}U/^{206}Pb$ age (with ±2σ uncertainty, in Ma). Each zircon grain is labeled with the sample it was extracted from and its number in this sample (zXX). Values with an *asterisk* indicate $^{207}Pb/^{206}Pb$ ages; labels in italics indicate >5% discordance. The *yellow circles* and font highlight analyses with large amounts of common ^{204}Pb (>5%); the *red circle* and font indicate an analysis (a27) from which no reliable age could be obtained because of high discordance and common Pb contents, and that was therefore discarded. The *scale bar* is 100 µm

are granites sensu stricto (Fig. 2a) with a clearer peraluminous character (Fig. 2b) and restricted to SiO_2 contents >70 wt% (Fig. 2b–c), pointing to a crustal source (Pin and Duthou 1990; Barbarin 1999) (Fig. 2d).

3. Weakly peraluminous to metaluminous, K-feldspar porphyritic, biotite- ± amphibole-bearing granites, granodiorites and quartz–diorites ("**KCG**"). They either form large plutons (Saint-Julien-la-Vêtre, Pont-de-Montvert, Aigoual) or enclaves within the Velay complex, of various sizes (a few cm across to pluri-kilometric screens like the Gumières enclave; Barbarin et al. 2012). The composition of the KCG largely overlaps that of the CPG, yet they are on average slightly more "mafic" than the latter (average SiO_2 and $FeO_t + MgO$ of KCG are ~69 and ~4.0 wt%, respectively, against ~72 and ~2.5 wt% for CPG) (Fig. 2). This makes KCG chemically intermediate between vaugnerites and MPG–CPG (Fig. 2) and led several authors to propose that they result from magma mixing between vaugnerites and crustal melts (Downes et al. 1997; Solgadi et al. 2007).
4. A suite of metaluminous, biotite-, amphibole- ± clinopyroxene-bearing intermediate to mafic rocks locally called "**vaugnerites**", which are akin to Mg–K magmatic rocks such as appinites, durbachites and lamprophyres (Sabatier 1991; Rossi and Pin 2008; Scarrow et al. 2008; von Raumer et al. 2013; Couzinié et al. 2014, 2016). Although they do not form mappable bodies at the scale of Fig. 1b, they are regionally ubiquitous and occur as enclaves (0.1–100 m in size) in the granitoids (Didier et al. 1982; Ledru et al. 2001), kilometric stocks and lamprophyric dykes. They form a compositionally heterogeneous group of gabbroic to dioritic rocks (Fig. 2a), yet all characterized by metaluminous affinities (Fig. 2b), lower SiO_2 (45–65 wt%) and higher $FeO_t + MgO$ (up to 25 wt%) than coexisting granitoids, together with high-K to shoshonitic affinities (K_2O = 1.5–6.0 wt%) and richness in incompatible trace elements (Sr + Ba, but also REE and HFSE) (Fig. 2c, d). This dual geochemical character clearly points to an enriched (metasomatized) lithospheric mantle source (Sabatier 1991; Solgadi et al. 2007; von Raumer et al. 2013; Couzinié et al. 2014, 2016).

Analytical methods

We selected 33 samples for U–Pb dating, collected throughout the eastern MCF (Fig. 1b) and representative of the geochemical diversity reported earlier (Table 1; Fig. 1b). Samples weighing 5–10 kg were reduced using jaw and disk mills and sieved to <500 µm. Heavy minerals were extracted by using conventional concentration techniques (shaking table, magnetic separator, heavy liquids). Between 50 and 100 zircon grains per sample, but also monazite wherever available, were handpicked, set in 1-inch epoxy mounts and polished to expose their interiors. The internal structures of these grains were characterized by cathodoluminescence (CL) and back-scattered electron (BSE) imaging prior to LA-SF-ICP-MS dating using (i) a Jeol JSM-6490 scanning electron microscope (SEM) equipped with a Gatan MiniCL at Goethe University Frankfurt (GUF) for the granite samples and (ii) a ZEISS EVO-150 SEM at University of Granada (Spain) for the vaugnerite samples.

U–Pb isotopic analyses were carried out at GUF by laser ablation using a Resolution M-50 (Resonetics) 193-nm ArF excimer laser system attached to Thermo Finnigan Element 2 sector field ICP-MS. A detailed description of the analytical techniques is available in the Supplementary Material. The data were corrected offline for background signal, common Pb, instrumental mass discrimination and downhole Pb/U fractionation using an in-house MS Excel© spreadsheet (Gerdes and Zeh 2006, 2009). For both zircon and monazite analyses, the corrections and determination of U, Th and Pb compositions were performed using normalization to standard zircon GJ-1. Reference materials Plešovice, OG-1 and BB (for zircon sessions) and Moacir, Manangoutry and in-house WM (for monazite sessions) were used as secondary standards to check the accuracy of the corrections, and all provide ages in good agreement with the reference values (see supplementary material Table S1). Age calculations and data plotting were performed using the Isoplot toolkit (Ludwig 2008) v.4.15 for MS Excel©. The complete dataset is available as supplementary material (Table S2).

Results

Zircon textures

Figure 3 shows representative CL and BSE images of zircons from igneous plutonic rocks of the eastern FMC. Zircon characteristics depend on the rock type considered. The MPG and CPG show heterogeneous zircon populations, having a range of sizes (from 50 up to 500 µm) and shapes (aspect ratios between 1.5 and 8), some of them being obvious xenocrysts (broken or irregular edges crosscutting the internal zoning). Grains with clear core–rim relationships are very common in both granitoid types: they show rounded or sub-idiomorphic CL-bright cores with oscillatory zoning, wrapped by CL-darker rims (Fig. 3a). The rims often show irregular or very fine oscillatory zoning, occasionally with porous textures and/or inclusions, and are generally wider (>50 µm) in CPG than in MPG (<50 µm) (Fig. 3a). The CPG and MPG also contain core-free,

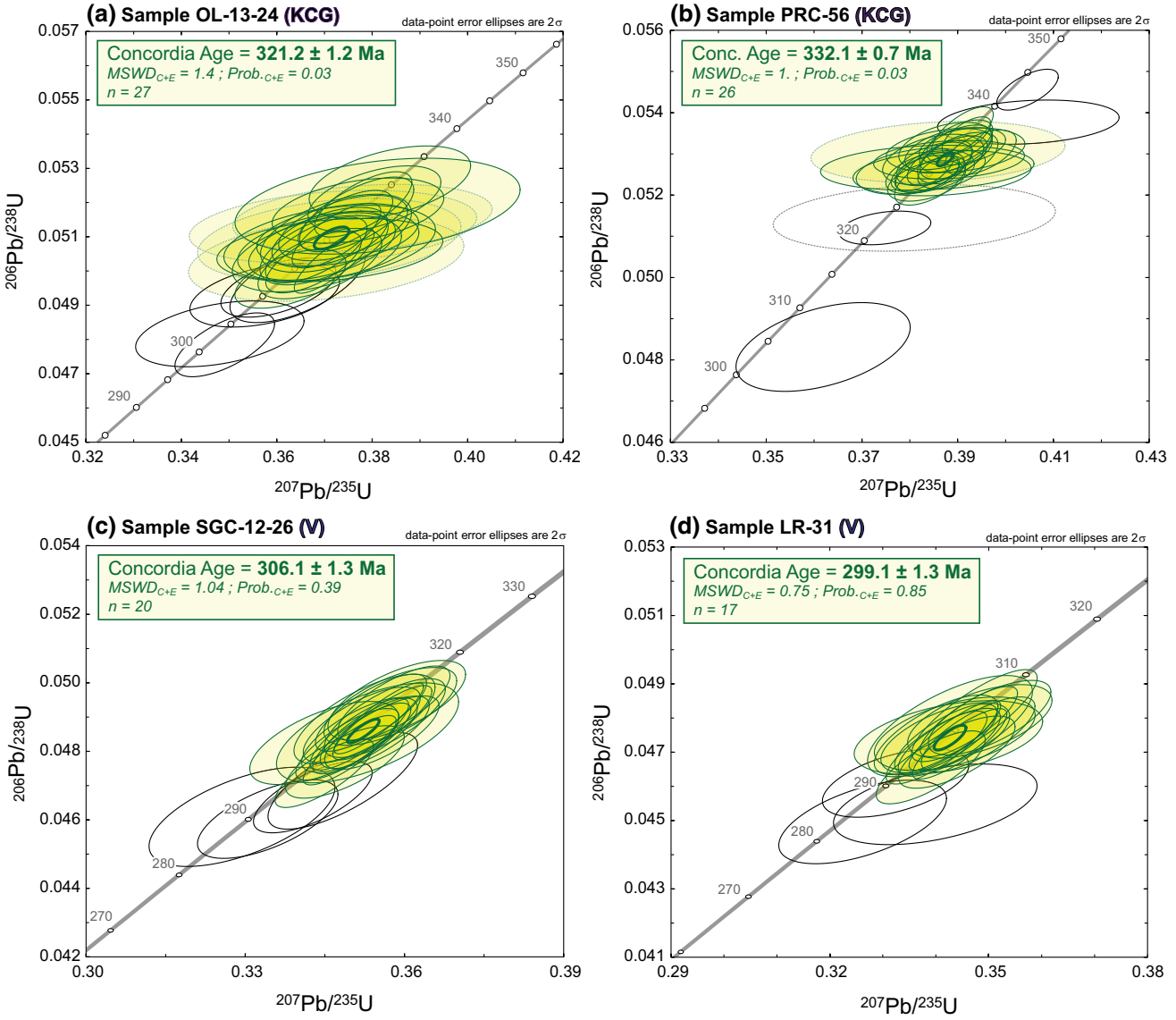

Fig. 4 Representative U–Pb Concordia diagrams (^{206}Pb/^{238}U vs. ^{207}Pb/^{235}U) showing examples of zircon analyses from samples of "group 1" (V = vaugnerite), i.e., showing a single generation of zircon dates with mostly identical ^{206}Pb/^{238}U ratios within uncertainties (see "Discussion"). Green ellipses are the oldest, equivalent concordant analyses from zircon rims or crystals devoid of any core (excluding outliers), used for the calculation of the Concordia Age. The *dashed ellipses* represent analyses with >5% of common ^{204}Pb. All ages are quoted to 2σ level of uncertainty

idiomorphic to xenomorphic crystals (scarce in MPG but dominant in CPG). These are relatively CL-dark, and show irregular or banded zoning patterns (Fig. 3a). A notable exception among the CPG is sample OL-13-06 (Margeride granite), of which zircons are relatively CL-bright, and display a well-developed oscillatory zoning and distinct aspect ratios (Fig. 3a).

Zircon grains in the KCGs are less diverse than in the CPG and MPG, and seldom show core–rim relationships (if any). Resorbed cores occasionally occur in samples SDZ (Fig. 3b) and PMV, and a single xenocryst was found in sample SGC-12-49B (Fig. 3b). The crystals are usually 100–350 µm long, form idiomorphic prisms with aspect ratios between 1.5 and 3, and reveal a concentric oscillatory zoning. They are CL-brighter than the zircons from the CPG and MPG (Fig. 3b). Zircon populations in vaugnerites are very homogeneous within a given sample, without any core–rim relationships (except sample SC13-14; Fig. 3b). The crystals range in size from 70 to 500 µm and display various shapes, from short prismatic to needle-shaped (aspect ratios between 1.5 and 6). In most samples, the grains appear CL-dark and display striped or sector zoning, but in two SiO_2-richer samples (quartz–syenites PRC-53 and PRC-54), oscillatory zoning is predominant (Fig. 3b).

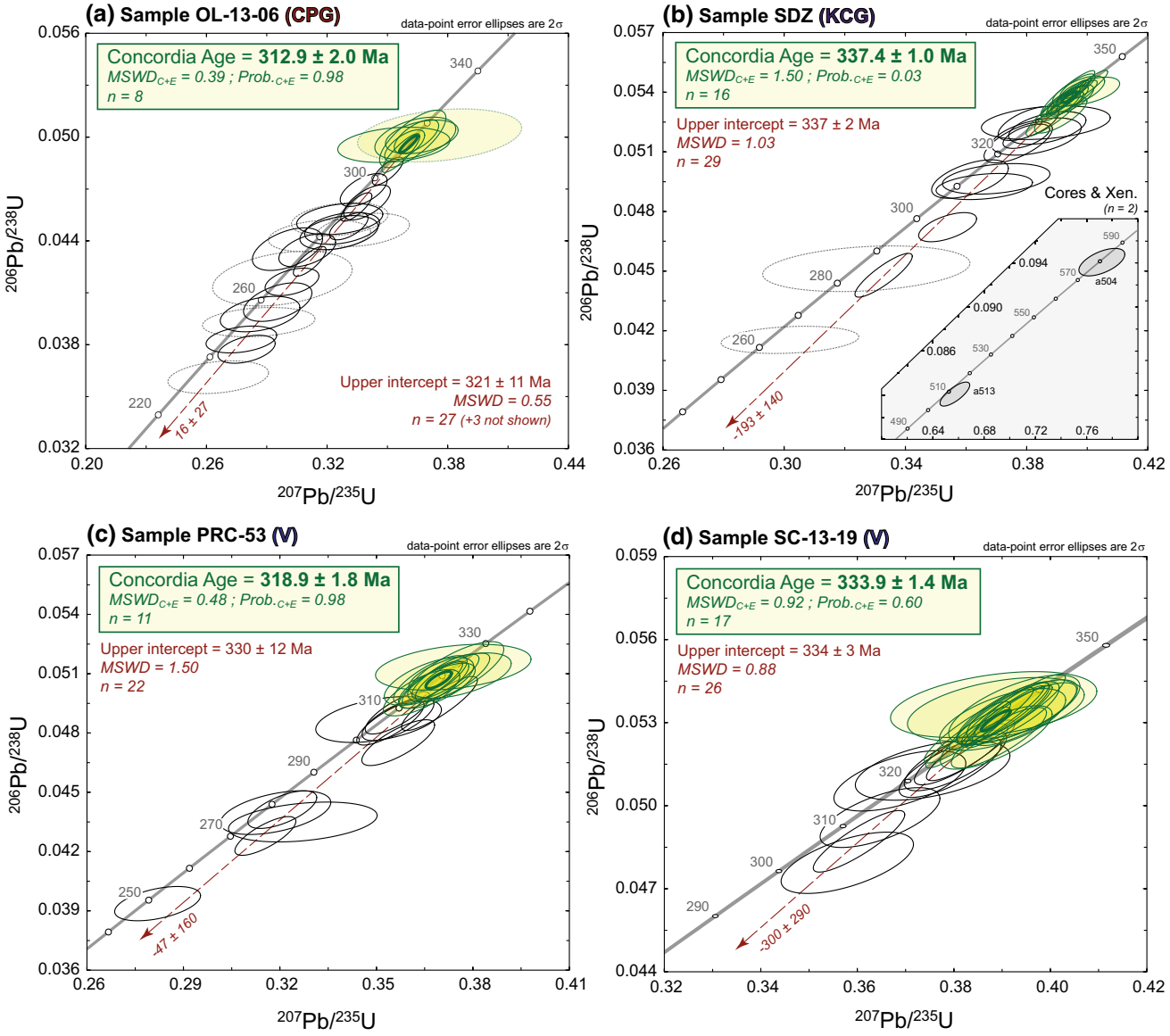

Fig. 5 Representative U–Pb Concordia diagrams ($^{206}Pb/^{238}U$ vs. $^{207}Pb/^{235}U$) showing examples of zircon analyses from samples of "group 2" (V = vaugnerite), i.e., showing a single generation of zircon (i.e., scarce or no core–rim relationships) but scattered $^{206}Pb/^{238}U$ dates with a Carboniferous upper intercept age, and a lower intercept at or close to zero within uncertainty. The *inset* in the bottom right of **b** represents a close-up to the analyses from two zircon cores, reported as shaded ellipses. *Green ellipses* are the oldest, equivalent concordant analyses from zircon rims or crystals devoid of any core (excluding outliers), used for the calculation of the Concordia Age. The *dashed ellipses* represent analyses with >5% of common ^{204}Pb. The *dashed red lines* are regressions through all the data from zircon rims or crystals devoid of any core; the arrow and numbers in italics point to the lower intercept. All ages are quoted to 2σ level of uncertainty

Back-scattered electron (BSE) images of monazite grains from the four samples in which this mineral was investigated are reported in the Supplementary Material.

U–Pb dates

Zircon populations were dated in 33 samples and monazite grains in four of them (OL-13-08, OL-13-11, OL-13-14, PRC-57). A detailed description of the data, statistics, as well as the complete set of Concordia diagrams, is available in the Supplementary Material. The most important points arising from this description, together with representative Concordia diagrams, are reported hereafter.

Based on the combination of U–Pb dating results and zircon textures, the investigated samples can be subdivided into three major groups (Table 1):

- *Group 1* (Fig. 4) samples are characterized by (i) zircons with the absence of any core–rim relationship; and (ii) zircon U–Pb analyses yielding a single generation of Carboniferous (to early Permian) U–Pb dates, the majority of which (>65% and commonly up to 85%) being identical within uncertainties and concordant. This includes most vaugnerite samples as well as two KCG (OL-13-24 and PRC-56).
- *Group 2* (Fig. 5) includes samples containing very few or no zircon cores, and a dominant population of zircons showing scattered $^{206}Pb/^{238}U$ dates younger than 340 Ma, specifically defining trends with a Carboniferous upper intercept and a lower intercept at or around zero within uncertainty. This group comprises most KCG samples, a few vaugnerites and one single CPG sample (OL-13-06).
- *Group 3* (Fig. 6) samples are characterized by two clear populations of zircon textures and dates, roughly equivalent regarding the number of analyses: (i) abundant zircon cores with U–Pb dates ranging from early Carboniferous (~340 Ma) to late-Archean (~2600 Ma) (those problems require a reliable geochronological 98; 42%) and (ii) zircon rims or grains devoid of any core, having U–Pb data repartition similar to that observed for group 2 samples, i.e., scattered U–Pb dates defining a Carboniferous upper intercept and a lower intercept close to zero ($n = 134$; 58%). This group encompasses all MPG and CPG samples, except sample OL-13-06.

Figure 7 compiles the data obtained from zircon cores in samples of groups 2 and 3. Out of 170 analyses, 106 are >90% concordant, with only few of them having dates >800 Ma ($n = 12$). The others reveal a nearly continuous date spectrum between 740 and 340 Ma, with a major peak at 540 ± 20 Ma ($n = 45$; 42% of all concordant data), and minor peaks at 475 ± 20 Ma ($n = 12$); 625 ± 10 Ma ($n = 6$); 375 ± 10 Ma ($n = 8$); and 340 ± 10 Ma ($n = 5$). There are additional minor peaks at 850 ± 15 Ma ($n = 3$) and ~955 Ma ($n = 2$), and a few grains reveal (mostly discordant) dates between ~1025 and ~2600 Ma.

Discussion

From date to age: interpretation of U–Pb data

In the following, the signification of zircon U–Pb dates obtained in each group of samples presented in the previous section is discussed, on the basis of zircon textures and U–Pb data. These interpretations are summarized in Table 1, where the deduced emplacement ages are reported.

- Samples from *group 1* contain no zircon cores and are characterized by a population of concordant U–Pb dates that, with the exception of few outliers, are identical within uncertainties (Fig. 4). Therefore, the Concordia dates calculated from such data can be considered as representative of the emplacement age for samples of this group. This includes the KCG samples OL-13-24 (321.2 ± 1.4 Ma) and PRC-56 (332.1 ± 0.7 Ma) as well as vaugnerite samples 533-1 (307.8 ± 1.6 Ma), LR-31 (299.1 ± 1.3 Ma), LR-32 (301.5 ± 1.4 Ma), SC-13-02A (313.2 ± 2.5 Ma), SC-13-09 (309.7 ± 1.2 Ma), SC-13-19 (333.9 ± 1.4 Ma), SGC-12-13 (306.6 ± 2.4 Ma), SGC12-26 (306.1 ± 1.3 Ma), SGC-12-39 (306.6 ± 1.6 Ma) and SGC-12-42 (305.9 ± 1.7 Ma). Zircons from these samples can be considered as essentially undisturbed by any post-magmatic event.
- Zircon analyses in samples from *group 2* yield Carboniferous dates that are generally concordant within uncertainty, but cannot be combined into a single date, as they show a wide range in $^{206}Pb/^{238}U$ ratios (Fig. 5). Such zircons, or at least part of them, most probably underwent post-magmatic disturbance of the U–Pb isotopic system. This likely took place through diffusion, fluid-driven dissolution–recrystallization or diffusion–reaction processes (Gerdes and Zeh 2009) such that the resulting scatter in $^{206}Pb/^{238}U$ dates can be explained by variable extent of radiogenic Pb loss (Fig. 5). This assumption is supported by (i) the fact that most samples have lower intercept ages at about zero within uncertainty; and (ii) the observation that the analyses with the youngest $^{206}Pb/^{238}U$ dates often correspond to U-rich, metamict domains and/or porous zones rich in common Pb (Figs. 3, 5; see also Supplementary Material) that are particularly prone to Pb loss (Mezger and Krogstad 1997; Geisler et al. 2001). Following this interpretation, the upper intercepts of these "Discordia" trends should represent the crystallization age of the samples. This upper intercept date is always identical within uncertainties to the (more precise) Concordia date calculated by using the equivalent analyses with the highest $^{206}Pb/^{238}U$ ratios (Figs. 5, 6). The latter is thus considered as the best estimate for the crystallization age of the samples. This interpretation applies to the CPG sample OL-13-06 (312.9 ± 2.0 Ma), the KCG samples PMV (302.5 ± 0.9 Ma), SDZ (337.4 ± 1.0 Ma) and SGC-12-49B (298.9 ± 1.8 Ma) as well as the vaugnerite samples 533-2 (307.3 ± 1.3 Ma), PRC-53 (318.9 ± 1.8 Ma), PRC-54 (320.5 ± 1.8 Ma), SC-13-05 (309.4 ± 1.5 Ma) and SC-13-14 (335.7 ± 2.1 Ma).
- Finally, samples from *group 3* clearly contain complex zircon populations, in which the grains were formed by several, distinct crystallization events. This is well illustrated by core–rim relationships, with cores and rims having significantly different ages (Figs. 3a, 6). The most straightforward interpretation is that (i) zircon

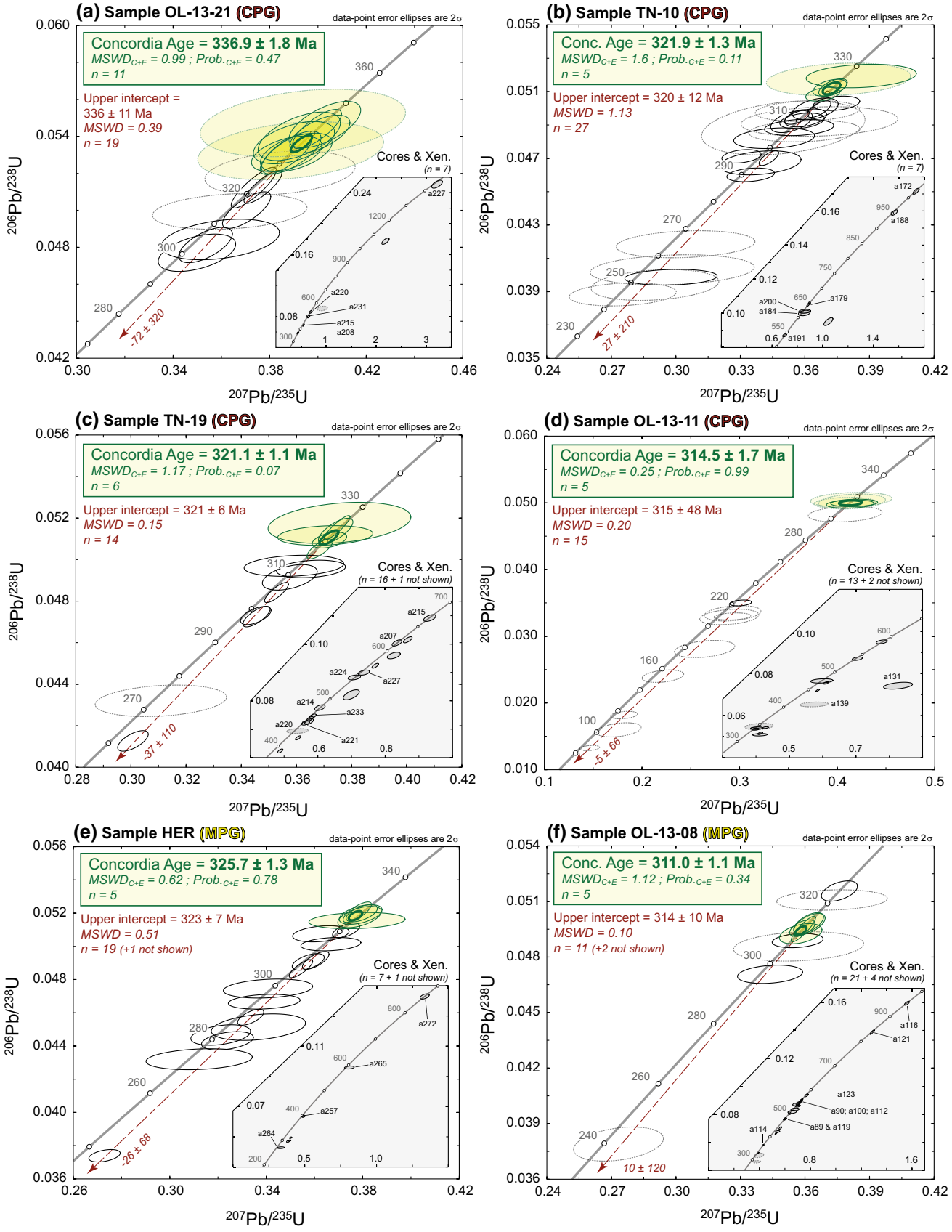
(a) Sample OL-13-21 (CPG)
data-point error ellipses are 2σ
Concordia Age = 336.9 ± 1.8 Ma
MSWD$_{C+E}$ = 0.99 ; Prob.$_{C+E}$ = 0.47
n = 11
Upper intercept = 336 ± 11 Ma
MSWD = 0.39
n = 19
Cores & Xen. (n = 7)
-72 ± 320
(b) Sample TN-10 (CPG)
data-point error ellipses are 2σ
Conc. Age = 321.9 ± 1.3 Ma
MSWD$_{C+E}$ = 1.6 ; Prob.$_{C+E}$ = 0.11
n = 5
Upper intercept = 320 ± 12 Ma
MSWD = 1.13
n = 27
Cores & Xen. (n = 7)
-27 ± 210
(c) Sample TN-19 (CPG)
data-point error ellipses are 2σ
Concordia Age = 321.1 ± 1.1 Ma
MSWD$_{C+E}$ = 1.17 ; Prob.$_{C+E}$ = 0.07
n = 6
Upper intercept = 321 ± 6 Ma
MSWD = 0.15
n = 14
Cores & Xen. (n = 16 + 1 not shown)
-37 ± 110
(d) Sample OL-13-11 (CPG)
data-point error ellipses are 2σ
Concordia Age = 314.5 ± 1.7 Ma
MSWD$_{C+E}$ = 0.25 ; Prob.$_{C+E}$ = 0.99
n = 5
Upper intercept = 315 ± 48 Ma
MSWD = 0.20
n = 15
Cores & Xen. (n = 13 + 2 not shown)
-5 ± 66
(e) Sample HER (MPG)
data-point error ellipses are 2σ
Concordia Age = 325.7 ± 1.3 Ma
MSWD$_{C+E}$ = 0.62 ; Prob.$_{C+E}$ = 0.78
n = 5
Upper intercept = 323 ± 7 Ma
MSWD = 0.51
n = 19 (+1 not shown)
Cores & Xen. (n = 7 + 1 not shown)
-26 ± 68
(f) Sample OL-13-08 (MPG)
data-point error ellipses are 2σ
Conc. Age = 311.0 ± 1.1 Ma
MSWD$_{C+E}$ = 1.12 ; Prob.$_{C+E}$ = 0.34
n = 5
Upper intercept = 314 ± 10 Ma
MSWD = 0.10
n = 11 (+2 not shown)
Cores & Xen. (n = 21 + 4 not shown)
10 ± 120
^{206}Pb/^{238}U
^{207}Pb/^{235}U

◂**Fig. 6** Representative U–Pb Concordia diagrams ($^{206}Pb/^{238}U$ vs. $^{207}Pb/^{235}U$) showing examples of zircon analyses from samples of "group 3", i.e., showing several generations of zircon crystallization (core–rim relationships) and scattered $^{206}Pb/^{238}U$ dates with a Carboniferous upper intercept age, and a lower intercept at or close to zero within uncertainty. Insets in the bottom right represent the close-up to the analyses from zircon cores or xenocrysts ("Xen."), reported as *shaded ellipses*. *Green ellipses* are the oldest, equivalent concordant analyses from zircon rims or crystals devoid of any core (excluding outliers), used for the calculation of the Concordia Age. The *dashed ellipses* represent analyses with >5% of common ^{204}Pb. The *dashed red lines* are regressions through all the data from zircon rims or crystals devoid of any core; the *arrow* and numbers in italics point to the lower intercept of the Discordia. All ages are quoted to 2σ level of uncertainty

cores represent either xenocrysts or crystals inherited from a zircon-bearing source material; and (ii) zircon rims, or grains devoid of any core, crystallized from the magma. The latter generally show the same distribution of U–Pb dates as zircon from samples of group 2, i.e., a range of apparent $^{206}Pb/^{238}U$ dates from a Carboniferous upper intercept and a lower intercept around zero. We thus apply the same interpretation as for group 2 samples, i.e., that such trends reflect the crystallization of zircon during emplacement of the host granitic magma, followed by recent loss of radiogenic Pb. This group includes all the MPG samples: HER (325.7 ± 1.3 Ma), OL-13-08 (311.0 ± 1.1 Ma) and OL-13-09 (312.7 ± 2.3 Ma); and most CPG samples: CHZ (332.0 ± 2.0 Ma), OL-13-11 (314.5 ± 1.7 Ma), OL-13-14 (318.3 ± 2.6 Ma), OL-13-21 (336.9 ± 1.8 Ma), TN-10 (321.9 ± 1.3 Ma), TN-19 (321.1 ± 1.1 Ma) and TOU-01 (322.2 ± 1.5 Ma).

- In three out of four investigated samples, monazite grains yielded Concordia dates that are identical within uncertainties to those deduced from zircon (sample OL-13-08: 309.3 ± 1.2 Ma; sample OL-13-11: 315.4 ± 0.9 Ma and sample OL-13-14: 317.8 ± 1.3 Ma; see Supplementary Material), which put further constraints on crystallization ages for these samples and supports our interpretation of the zircon U–Pb data. However, a notable exception is sample PRC-57, for which the monazite Concordia date is significantly younger (302.8 ± 1.3 Ma) than that of zircon (334.9 ± 1.5 Ma) (see Supplementary Material). This discrepancy might be explained by an inherited origin of all dated zircon grains, whereas monazite crystallized from the magma, as observed by Mougeot et al. (1997) and Couzinié et al. (2014) for other samples of the Velay granite. This interpretation is supported by (i) the fact that the ~335-Ma-old zircons of sample PRC-57 have identical ages, internal structures (bright CL luminescence, well-developed oscillatory zoning), and U–Th–Pb chemical compositions (150–500 ppm U, Th/U = 0.5–1.0, no common Pb) as zircons of sample PRC-56, which forms an amphibole-bearing granodiorite (KCG) enclave within the same granite (few meters away of sample PRC-57), representing a plausible, nearby source for those zircons in the Velay granite; (ii) existing geochronological data on the Velay granite, clustering around 305–300 Ma (Caen-Vachette et al. 1982; Mougeot et al. 1997; Couzinié et al. 2014); and (iii) the fact that vaugnerite enclaves in the Velay granite at the same locality (PRC-53 and PRC-54) show significantly younger and robust U–Pb zircon ages (~320 Ma) than that obtained from PRC-57 (~335 Ma), showing that the latter cannot reflect the age of the Velay granite. The monazite Concordia age of 302.8 ± 1.3 Ma is thus interpreted as reflecting the crystallization of sample PRC-57.

Emplacement ages: comparison with published data

1. *CPG* The age of 332 Ma obtained for the Chalmazel granite (sample CHZ) is identical within uncertainties to that of the neighboring Bois-Noirs CPG pluton (341 ± 15 Ma, U–Pb ID-TIMS on zircon; Kosztolanyi 1971). In the same area, our age of 337 Ma for the Saint-Dier granite (sample OL-13-21) is consistent with the existing, but imprecise Rb–Sr whole-rock isochron age of 330 ± 26 Ma for this pluton (Saint-Joanis 1975).

   Further south, the ages of 315 and 318 Ma, respectively, obtained for the (undated so far) Almance and Chaise-Dieu laccoliths (samples OL-13-11 and OL-13-14) are within uncertainties of the ages obtained on intrusive pophyritic monzogranite and leucogranite in the nearby Livradois area (U–Pb LA-ICP-MS zircon ages of 315 ± 4 and 311 ± 18 Ma, respectively; Gardien et al. 2011).

   The age of the Margeride granite (OL-13-06; ~313 Ma) is identical within uncertainties to existing monazite ID-TIMS ages for the same granite (314 ± 3 Ma; Pin Pin 1979b), the associated Chambon-le-Château pluton (311 ± 6 Ma; Isnard 1996) and a whole-rock Rb–Sr isochron age of 323 ± 12 Ma (Couturié and Caen-Vachette 1979). It is, however, significantly younger than the U–Pb zircon age of 334 ± 9 Ma (ID-TIMS) obtained by Respaut (1984) on the Margeride granite.

   The ages of ~320 Ma obtained on laccoliths from the eastern flank of the Velay dome (Tournon granite and associated intrusions; samples TN-10, TN-19 and TOU-01) are slightly younger than the Rb–Sr whole-rock isochron age of 337 ± 13 Ma obtained by Batias and Duthou (1979), but their data also include samples from the Vienne pluton further north, for which no zircon age is available.

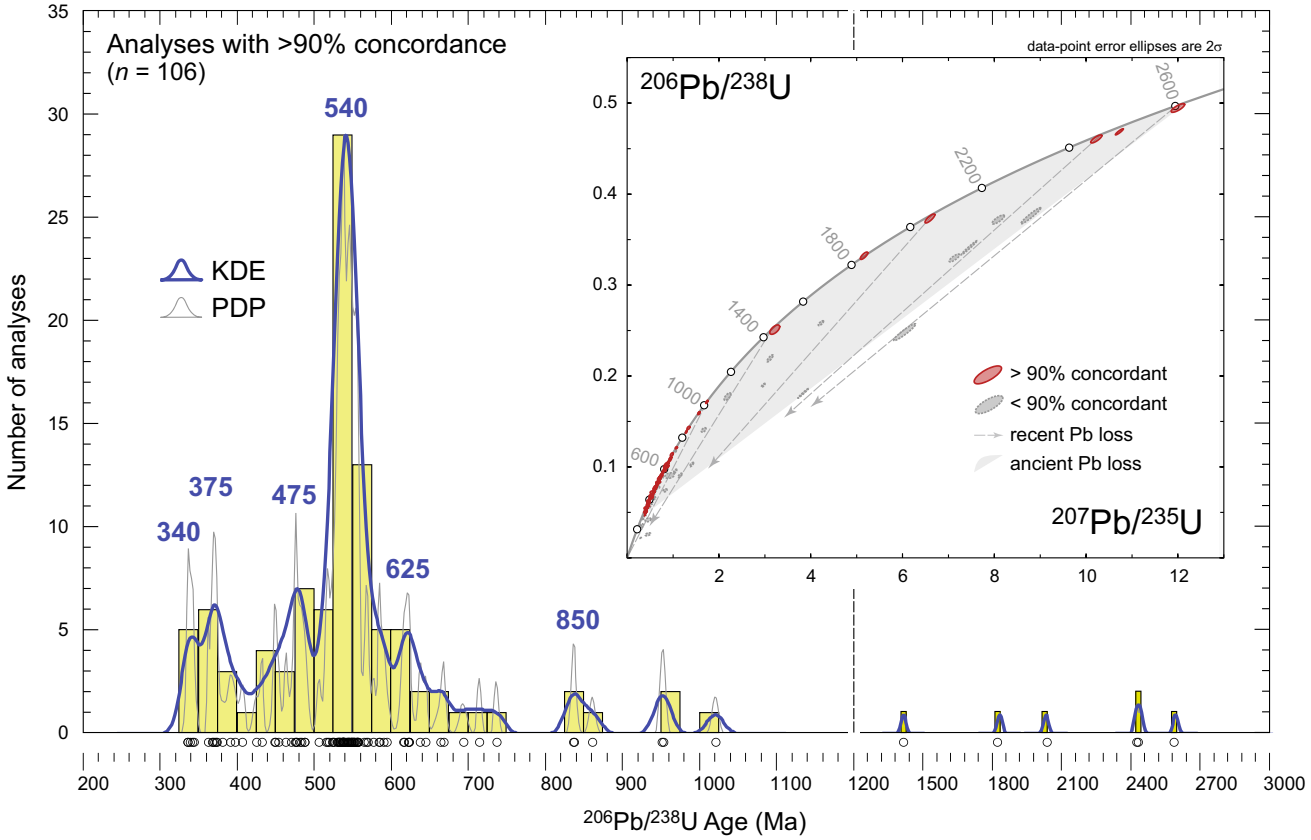

Fig. 7 Histogram (25 Ma bins), probability density plot (PDP) and Kernel Density Estimate (KDE) of $^{206}Pb/^{238}U$ ages for >90% concordant analyses of zircon cores from the eastern FMC granites (obtained using the density plotter program of Vermeesch 2012). The main peaks are identified using the KDE curve and labeled according to their average age. *Inset* Concordia diagram ($^{206}Pb/^{238}U$ vs. $^{207}Pb/^{235}U$) for all analyses from inherited zircon cores, including discordant ones

Finally, the monazite age of 302.8 ± 1.3 Ma obtained from the Velay granite at the Pont-Rouge quarry (sample PRC-57) is in line with the existing data obtained by different methods, including whole-rock Rb–Sr (Caen-Vachette et al. 1982) and monazite U–Th–Pb dating by ID-TIMS (Mougeot et al. 1997) or LA-ICP-MS (Couzinié et al. 2014), all pointing to crystallization ages in the range 305–300 Ma.

2. *MPG* In the northern part of the study area, the age of 327 Ma obtained for the Hermitage granite (sample HER) is identical to a whole-rock Rb–Sr isochron age of 329 ± 14 Ma (C. Pin, unpublished data mentioned in Didier et al. 1989). This age also complies with structural observations, since the Hermitage granite is a syn-kinematic intrusion emplaced along a WNW–ESE-trending dextral, strike-slip shear zone attributed to the D_3 deformation event (Barbarin 1983) that was most likely active at ~327 Ma, in agreement with a general NW–SW-directed stretching recorded throughout the FMC at that time (Faure et al. 2009).

In the Margeride area, the U–Pb ages of 311–309 and 313 Ma obtained for the Grandrieu leucogranite (sample OL-13-08) and Saint-Christophe-d'Allier pluton (sample OL-13-09), respectively, overlap with existing U–Pb ID-TIMS monazite ages of 305 ± 14 (Isnard 1996) and 305 ± 9 Ma (Lafon and Respaut 1988) for those two intrusions. Our ages are also identical within uncertainties to that of the Margeride granite (Table 1), which is crosscut by the Grandrieu granite in the field. This means that the two magmatic events were close enough in time such that they cannot be distinguished with respect to analytical uncertainties.

3. *KCG* The age of 337.4 ± 1.0 Ma obtained for the Salt-en-Donzy pluton (sample SDZ) is the first to document the absolute age of this intrusion. It is identical to whole-rock Rb–Sr isochron ages of 339 ± 8 and 322 ± 32 Ma obtained from granites flanking NE–SW-trending dextral shear zones in the Lyonnais mountains (Gay et al. 1981) and close to the ages of vaugnerite samples obtained from the same area (336–334 Ma;

see below). For the Saint-Julien-la-Vêtre pluton (sample SJV), the obtained age of 330.1 ± 1.3 Ma is consistent with an early Rb–Sr whole-rock isochron age of 340 ± 20 Ma (C. Pin, unpublished data quoted in Didier et al. 1989) and field relationships, since the pluton is intruded by the significantly younger (325.7 ± 1.3 Ma-old) Hermitage granite (Barbarin 1983; Didier et al. 1989).

The age of ~321 Ma obtained for the Gumières quartz–diorite (sample OL-13-24) is notably older than that obtained by Cocherie (2007) using the same technique (313 ± 2 Ma; U–Pb LA-ICP-MS on zircon). Excluding dating problems, this discrepancy might result from sampling of different lithologies in the composite Gumières Massif, which consists of porphyritic granodiorite associated with minor quartz–diorite, equigranular granite and dikes of the surrounding Velay granite (Barbarin et al. 2012). The sample dated by Cocherie (2007) may derive from the dominant biotite-bearing porphyritic granodiorite, whereas our sample is clearly more mafic (amphibole-bearing) and would thus derive from a dioritic enclave within this granodiorite, which are common yet not easy to identify given the scarcity of exposed contacts (Barbarin et al. 2012).

Another enclave within the Velay granite, sample PRC-56, yielded an age of 332.1 ± 0.7 Ma that is roughly equivalent to that of a suite of orthoclase-rich granites cropping out along the eastern margin of the Velay complex in the Vivarais area, dated at 353 ± 21 Ma (Rb–Sr whole-rock isochron) and 341 +8/–5 (U–Pb ID-TIMS on zircon, upper intercept age with two subconcordant spots at ~335 Ma) (Briand et al. 2002).

To the south of the Velay complex, in the Cévennes area, the age of 299 Ma obtained on sample SGC-12-49B from the Largentière granite is identical within uncertainties to that obtained by Couzinié et al. (2014) for the same granite (304.1 ± 6.3 Ma; U–Pb LA-ICP-MS on zircon) and also close to that of sample PMV from the Pont-de-Montvert pluton (302.5 ± 0.9 Ma). Both ages are identical within uncertainties to ages of 301 ± 4 and 307 ± 11 Ma (zircon and monazite U–Pb ID-TIMS) in the Mont-Lozère and Aigoual granitic complexes (Brichau et al. 2008; François 2009). Moreover, they overlap with Ar–Ar ages of 306–301 Ma obtained from aplitic–pegmatitic dykes and Au-mineralized quartz veins in the vicinity of the Mont-Lozère complex (Chauvet et al. 2011).

4. *Vaugnerites* Our new age data suggest that the vaugnerites in the eastern FMC intruded over >35 Ma, between 335.7 ± 2.1 Ma (SC-13-14) and 299.1 ± 1.3 Ma (LR-31). This period is much longer than previously suggested (Aït-Malek 1997; Couzinié et al. 2014). In the northern part of the study area, the new emplacement ages of ~335 Ma for the syn-kinematic vaugnerite dikes/bodies in the Lyonnais area (SC-13-14 and SC-13-19) are consistent with existing Rb–Sr data of 339 ± 8 and 322 ± 32 Ma obtained from nearby (and, as shown by magma mixing relationships, coeval) granites (Gay et al. 1981).

In the western and central parts of the Velay complex, no absolute ages were available so far for vaugnerite intrusions. Our results from samples in this area show emplacement ages scattered over more than 20 Ma, and specifically clustered at 321–319 Ma (age of the two quartz–syenite enclaves within the Velay granite at Pont-Rouge (PRC-53 and PRC-54), 310 Ma (Pubellier syenodiorite, SC-13-09) and 302–299 Ma (diorite enclaves in the Velay granite; LR-31 and LR-32).

Two vaugnerite enclaves within the Margeride batholith (SC-13-02a and SC-13-05) yielded ages (313–309 Ma) that are identical within uncertainties to the emplacement age of the surrounding Margeride granite (312.9 ± 2.0 Ma; sample OL-13-06), supporting field observations indicating that the vaugnerites are coeval with the granite.

Finally, to the south of the Velay complex, vaugnerite samples from Loubaresse (SGC-12-39) and Meyras (SGC-12-42) yield ages of 306.6 ± 1.6 and 305.9 ± 1.7 Ma, respectively, which are identical to those of Couzinié et al. (2014) for the same vaugnerite bodies (307.4 ± 1.8 and −305.8 ± 2.3 Ma, respectively; U–Pb zircon by LA-ICP-MS). The age obtained on the Meyras vaugnerite is also identical to that of Aït Malek (1997) (308 ± 6 Ma; U–Pb zircon by ID-TIMS), but this author obtained a significantly older age for the Loubaresse vaugnerite (313 ± 3 Ma; see Couzinié et al. 2014 for discussion). The Pont-de-Bayzan vaugnerite gave an emplacement age of 306.1 ± 1.3 Ma (SGC-12-26). This age is significantly older than the age of 294.4 ± 3.9 Ma published by Couzinié et al. (2014) from the same outcrop, but from a different vaugnerite body. The latter, Permian age would not reflect the crystallization age, due to perturbation of the zircon U–Pb isotopic system by fluid–rock interactions (Couzinié et al. 2014).

Significance of inherited zircon ages

Zircon xenocrysts from CPG and MPG reveal an age spectrum characterized by abundant early Paleozoic to Neoproterozoic ages between ~450 and ~740 Ma (with more prominent peaks at ~475, ~540 and ~625 Ma), together with very minor Grenville (955–1025 Ma) and Paleoproterozoic to early Archean ages (1800–2600 Ma) (Fig. 7). Such an age spectrum is similar to that of zircons from ortho- and paragneisses of the UGU and LGU in the FMC

(Melleton et al. 2010; Chelle-Michou et al. 2015), which are the country rocks and, most likely, the sources of CPG and MPG (Williamson et al. 1996, 1997; Downes et al. 1997; Barbey et al. 1999, 2015). Thus, it is clear that these zircons were inherited from the regional nappe units, either during melting or emplacement.

The observed age spectrum is very similar to the age distribution of detrital zircons from many Paleozoic (Cambrian to Devonian) sedimentary rocks throughout western Europe (Zeh et al. 2001; Kober et al. 2004; Linnemann et al. 2004, 2007, 2014; Gerdes and Zeh 2006) and has also been reported in inherited zircons from Variscan granites of the Iberian Massif (Castiñeiras et al. 2008; Fernández-Suárez et al. 2011). This age distribution is generally interpreted to reflect zircon derived from the Avalonian-Cadomian belt (and its cratonic hinterland), forming a ca. 10,000-km-long cordillera at the northern margin of Gondwana during Neoproterozoic to Cambrian times (see Nance et al. 1991; Nance and Murphy 1994; Fernández-Suárez et al. 2000; Zeh et al. 2001; Linnemann et al. 2014; and references therein). During the early Ordovician (490–470 Ma), this cordillera became dispersed, with individual microterranes (e.g., Avalonia, Amorica, Alpine terranes, etc.) drifting to the north and re-assembled subsequently during the Variscan orogeny at 360–320 Ma (Nance et al. 2002; von Raumer et al. 2002; Linnemann et al. 2007; Faure et al. 2009; Stampfli et al. 2013). The age peaks of the inherited zircons from the eastern FMC granitoids can be ascribed to several well-known events throughout this evolution, notably the formation of an arc-back-arc system at ca. 660–560 Ma; its evolution into an Andean-type continental margin at 550–530 Ma and its subsequent breakup at 530–480 Ma, resulting in the opening of the Rheic Ocean (see Ballèvre et al. 2001; Nance et al. 2002, 2010; Linnemann et al. 2004, 2007 and references therein). The two youngest peaks at middle Devonian (390–370 Ma) and early Carboniferous ages (360–340 Ma) correspond respectively to subduction processes related to the closure of the Rheic Ocean (Zeh and Gerdes 2010) and to the Variscan collision (Faure et al. 2009). The latter period is characterized by important crustal melting, granulite-facies metamorphism (Duthou et al. 1994; Gardien et al. 2011) and emplacement of arc-like, calc-alkaline gabbros and granitoids in the Morvan and Limousin areas (Bernard-Griffiths et al. 1985; Pin and Paquette 2002).

Zircon constraints on granitoid petrogenesis

Zircon constraints on CPG and MPG petrogenesis

These granitoids contain abundant, rounded to subhedral zircon cores with pre-Variscan ages, commonly wrapped by rims formed during the Variscan magmatic episode (Figs. 3, 6 and 7). These characteristics are in good agreement with previous interpretation that the MPG and CPG are of crustal origin (Williamson et al. 1996, 1997; Downes et al. 1997; Barbey et al. 1999) and formed at relatively low temperatures, specifically below magmatic Zr saturation. Considering that the pre-Variscan zircons in CPG and MPG were inherited from the source rock during melting, Zr saturation temperatures would provide a first-order estimate of *maximum* magma temperatures. These temperatures, calculated using the Zr saturation thermometer of Watson and Harrison (1983), are in the range 720–787 °C for the MPG and 761–842 °C for CPG (Fig. 8). Such values are consistent with results of previous melting experiments carried on metasedimentary rocks at mid-crustal pressures (Vielzeuf and Holloway 1988; Patiño-Douce and Johnston 1991; Gardien et al. 1995; Patiño-Douce and Harris 1998; Pickering and Johnston 1998), which produced granitic liquids that match the compositions of CPG and MPG at 700–850 °C (Fig. 8). The generally lower Zr saturation

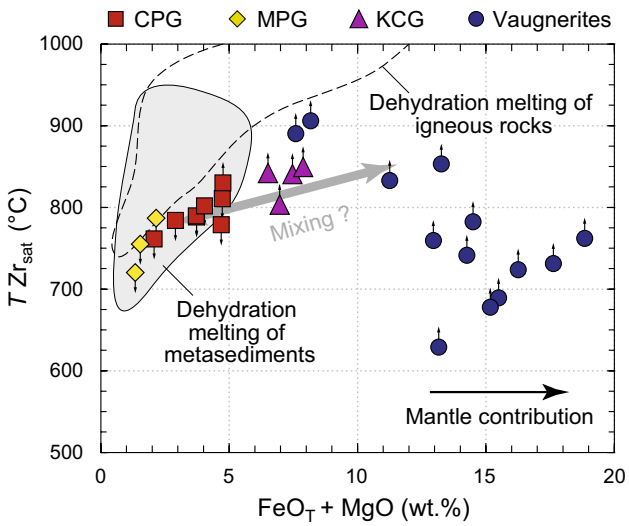

Fig. 8 Plot of the zircon saturation temperature (*T* Zr_{sat}, in °C) obtained from the whole-rock compositions of the dated samples of Variscan igneous rocks from the eastern FMC (using the equation of Watson and Harrison 1983), as a function of their "mafic" oxides contents (FeO_t + MgO). The fields correspond to the temperature and compositions of experimental melts of Gardien et al. (1995), Patiño-Douce and Harris (1998), Patiño-Douce and Beard (1995, 1996), Patiño-Douce and Johnston (1991), Pickering and Johnston (1998), Vielzeuf and Holloway (1988) and Vielzeuf and Montel (1994) for metasediments; Beard and Lofgren (1991), Bogaerts et al. (2006), Patiño-Douce and Beard (1995), Rapp and Watson (1995), Rapp et al. (1991), Singh and Johannes (1996), Sisson et al. (2005), Skjerlie and Johnston (1996); Tatsumi and Suzuki (2009), Watkins et al. (2007) and Wolf and Wyllie (1994) for igneous rocks. The arrows associated with the symbols indicate whether the calculated *T* Zr_{sat} represents maximum magma temperatures (*arrow down*, if source-inherited zircons are present) or minimum ones (*arrow up*, few or no inherited zircons)

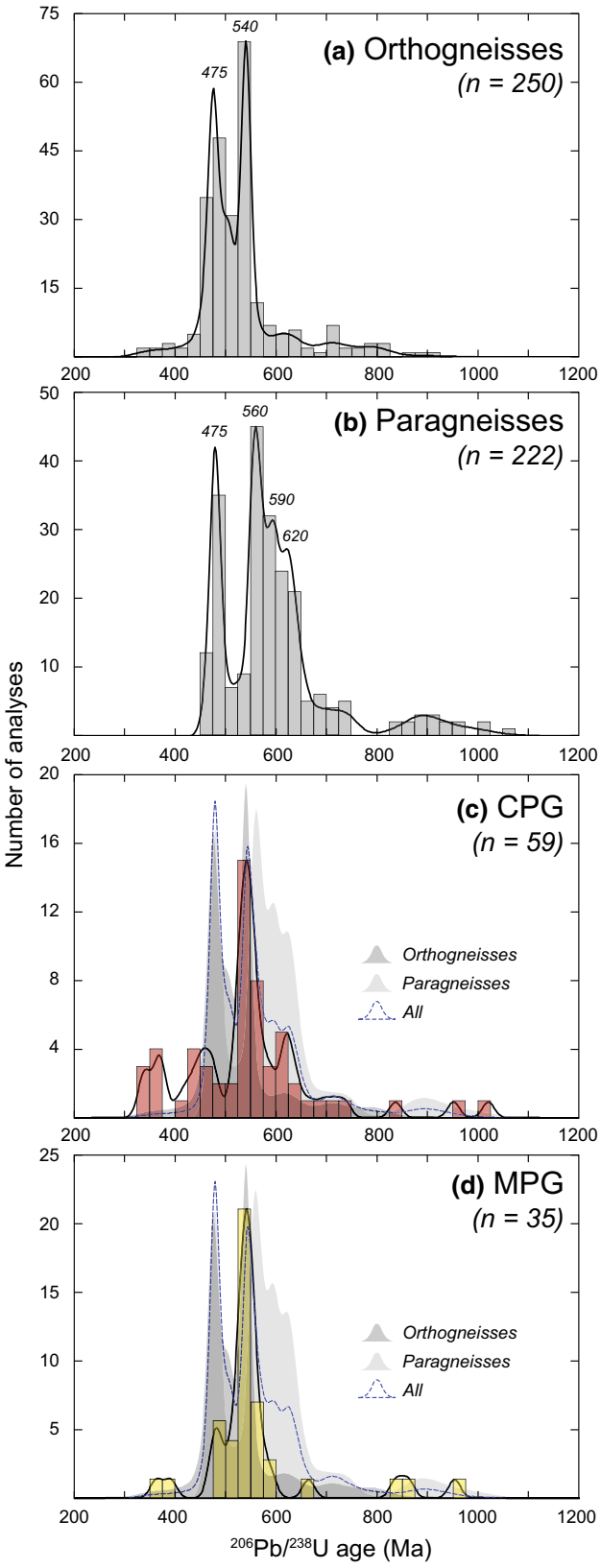

Fig. 9 Histograms and Kernel Density Estimates (KDE) (obtained using the DensityPlotter program of Vermeesch 2012) of $^{206}Pb/^{238}U$ ages of zircons from **a** orthogneisses and **b** paragneisses of the FMC (data from Melleton et al. 2010; Chelle-Michou et al. 2015; Mintrone 2015); compared to inherited zircons from (**c**) CPG and (**d**) MPG investigated in this study. Only analyses with >90% concordance and with $^{206}Pb/^{238}U$ ages <1200 Ma are considered. The gray fields in **c** and **d** are the KDE of age distributions for zircons of ortho- and paragneisses presented in (**a**) and (**b**); the *dashed blue curve* represent the KDE obtained with all zircons from both ortho- and paragneisses together

temperatures obtained for the MPG could be explained either by water-present melting (Williamson et al. 1996) or muscovite breakdown melting (720–770 °C at 7 kbar; Patiño-Douce and Harris 1998). In contrast, the higher temperatures obtained for the CPG exceed that of muscovite dehydration melting and thus require biotite dehydration melting (800–870 °C; Vielzeuf and Montel 1994; Patiño-Douce and Beard 1995, 1996), in good agreement with the previous interpretations of Barbey et al. (1999, 2015) and Moyen et al. (in press).

On the other hand, the respective contribution of pre-Variscan ortho- and paragneisses of the FMC in the source of MPG and CPG is the matter of several discussions (Turpin et al. 1990; Williamson et al. 1996, 1997; Downes et al. 1997; Moyen et al. in press). It is worthwhile noting that ortho- and paragneisses of the FMC reveal important differences in their age spectra. Zircon grains from the orthogneisses show two prominent age peaks at ~475 Ma (early Ordovician) and ~540 Ma (early Cambrian) (Fig. 9a), corresponding to the magmatic ages of their respective protoliths (Caen-Vachette 1979; Pin and Lancelot 1982; Duthou et al. 1984; Lafon 1986; R'Kha Chaham et al. 1990; Alexandrov et al. 2001; Alexandre 2007; Melleton et al. 2010; Chelle-Michou et al. 2015; Mintrone 2015), whereas detrital zircons from the paragneisses show the same peak at 475 Ma, in addition to a wide Neoproterozoic age cluster between 560 and 650 Ma, with a distinctive "tail" until 1000 Ma (Fig. 9b) (Melleton et al. 2010; Chelle-Michou et al. 2015). The inherited zircon age spectra of both CPG and MPG (Fig. 9c, d) are intermediate between those two end-members, with a prominent age peak at ~540 Ma like in orthogneisses together with a significant number of Neoproterozoic zircon grains (mostly at 560–650 and up to 1000 Ma), typical of paragneisses (Fig. 9c, d).

A striking difference, though, is the limited number of Ordovician (~475 Ma) inherited zircons in the CPG and MPG, as already noted in the case of the Velay granite (Couzinié et al. 2014; Chelle-Michou et al. 2015). It must be

emphasized that the age spectra presented in Fig. 9 for the MCF ortho- and paragneisses result from the compilation of data from all lithostratigraphic units (PAU, UGU, LGU) and both the eastern and western parts of the FMC. In fact, there are clear differences in the zircon age distributions between the UGU and LGU in the eastern FMC, the most relevant one being that Ordovician ages are restricted to the UGU and LAC (Pin 1979a; Pin and Lancelot 1982; Chelle-Michou et al. 2015) whereas in the LGU, both the youngest detrital zircon grains in paragneisses and the magmatic protoliths of orthogneisses have Cambrian ages at 545–520 Ma (Caen-Vachette 1979; Duthou et al. 1984; R'Kha Chaham et al. 1990; Chelle-Michou et al. 2015; Mintrone 2015). We therefore interpret the limited number of Ordovician inherited zircons from the CPG and MPG to reflect a source region rooted in the LGU, where zircons younger than 520 Ma are scarce.

All lines of evidence suggest that the source of both CPG and MPG consists of a mixed assemblage of para- and orthogneisses from the LGU. The CPG (including the Velay granite) formed by biotite dehydration melting at high temperature (≥800 °C), whereas MPG formed at lower temperature (<800 °C) through muscovite breakdown or water-present melting.

Zircon constraints on KCG and vaugnerite petrogenesis

Xenocrysts in KCGs and vaugnerites are very scarce ($n = 9$, among 21 samples). The estimated Zr saturation temperatures for these rocks are ≤850 °C (Fig. 8), i.e., much lower than presumed magma temperature for vaugnerites (>1000 °C; Montel and Weisbrod 1986), which may indicate that potential zircon xenocrysts in the magma were dissolved because of Zr undersaturation. These potential xenocrysts were probably assimilated from the wallrock in which the mafic magma percolated (e.g., in sample SC-13-14), rather than inherited from a crustal source. These magmas indeed have "crust-like" trace element and Nd–Hf isotopic compositions, yet their very high $FeO_t + MgO$ (most often >10 wt%; Fig. 8) and low SiO_2 contents preclude either a crustal origin or crustal contamination of a basaltic melt (Turpin et al. 1988; Couzinié et al. 2016). Instead, vaugnerites are more likely to be derived from an "enriched" mantle source metasomatized by 10–25% of crust-derived materials (see Couzinié et al. 2016 for a more detailed discussion about the origin of these rocks).

A crust-dominated origin for the KCGs is precluded by their high $FeO_t + MgO$ contents (>6 wt%) that would require an igneous mafic source (amphibolites, which are scare in the LGU) and melting temperatures ≥950 °C (Fig. 8) that are unrealistically high (Moyen et al. in press). These observations could indicate that KCG derive from interactions (mixing, mingling) between Zr-saturated crustal melts (similar to CPG and MPG) and a hot, mantle-derived, Zr-undersaturated vaugnerite magma (Downes et al. 1997; Solgadi et al. 2007), thereby triggering the partial to total dissolution of inherited zircons. Such mixing between vaugnerites and CPG/MPG is supported by the intermediate composition of KCG between the two end-members (Figs. 2, 8). Alternatively, the high SiO_2 content of the KCG (~69 wt%) could be explained also by a high degree of fractionation of vaugnerite magma, in agreement with the close spatial and petrographic relationships between these rocks (Barbarin 1988) and geochemical constraints (Moyen et al. in press). In either case, the involvement of mantle-derived, vaugnerite magma is required to explain the composition of the KCG.

The Carboniferous thermal anomaly in the eastern FMC: evidence for lithospheric mantle delamination

Our new geochronological data indicate that the late-Variscan plutonic rocks of the eastern FMC emplaced between ~339 and ~298 Ma (when uncertainties are considered) (Fig. 10). This dataset thus represents the first, self-consistent and unambiguous evidence that magmatic activity lasted throughout the entire late Carboniferous for ~40 Ma, as proposed by earlier studies (Vanderhaeghe et al. 1999; Vanderhaeghe and Teyssier 2001; Ledru et al. 2001; Rossi and Pin 2008; Faure et al. 2009). The estimated timescales for the magmatism in the FMC are much longer than those assessed for the evolution of magma from source to emplacement (production, segregation, ascent and crystallization) that commonly lasts no more than 5 Ma (Harris et al. 2000; Petford et al. 2000; Annen et al. 2006; Walker et al. 2007; de Saint-Blanquat et al. 2011). Thus, the ~40-Ma-long magmatism necessarily implies the existence of a long-lived thermal anomaly, to sustain a high heat flux and crustal anatexis throughout the Carboniferous (Rossi and Pin 2008; Vanderhaeghe 2012).

In fact, such a protracted Carboniferous thermal anomaly in the eastern FMC was already suggested on the basis of studies on metamorphic rocks, indicating an early, M_3-metamorphic episode characterized by incipient partial melting of the metamorphic nappe pile at *P–T* conditions of 5–6 kbar and 720–750 °C between ~330 and ~310 Ma (Montel et al. 1992; Mougeot et al. 1997; Barbey et al. 1999, 2015; Cocherie et al. 2005; Bé Mézème et al. 2006; Bouilhol et al. 2006), followed by biotite dehydration melting at *P–T* conditions of 4–5 kbar and 750–850 °C at 305–301 Ma (M_4-metamoprhic episode; Caen-Vachette et al. 1982; Montel et al. 1992; Mougeot et al. 1997; Barbey et al. 1999, 2015; Couzinié et al. 2014). The M_4 event required a higher apparent geothermal gradient than the M_3 episode and corresponds to the formation of the Velay granite–migmatite dome. In the past, limited partial melting during the M_3 episode

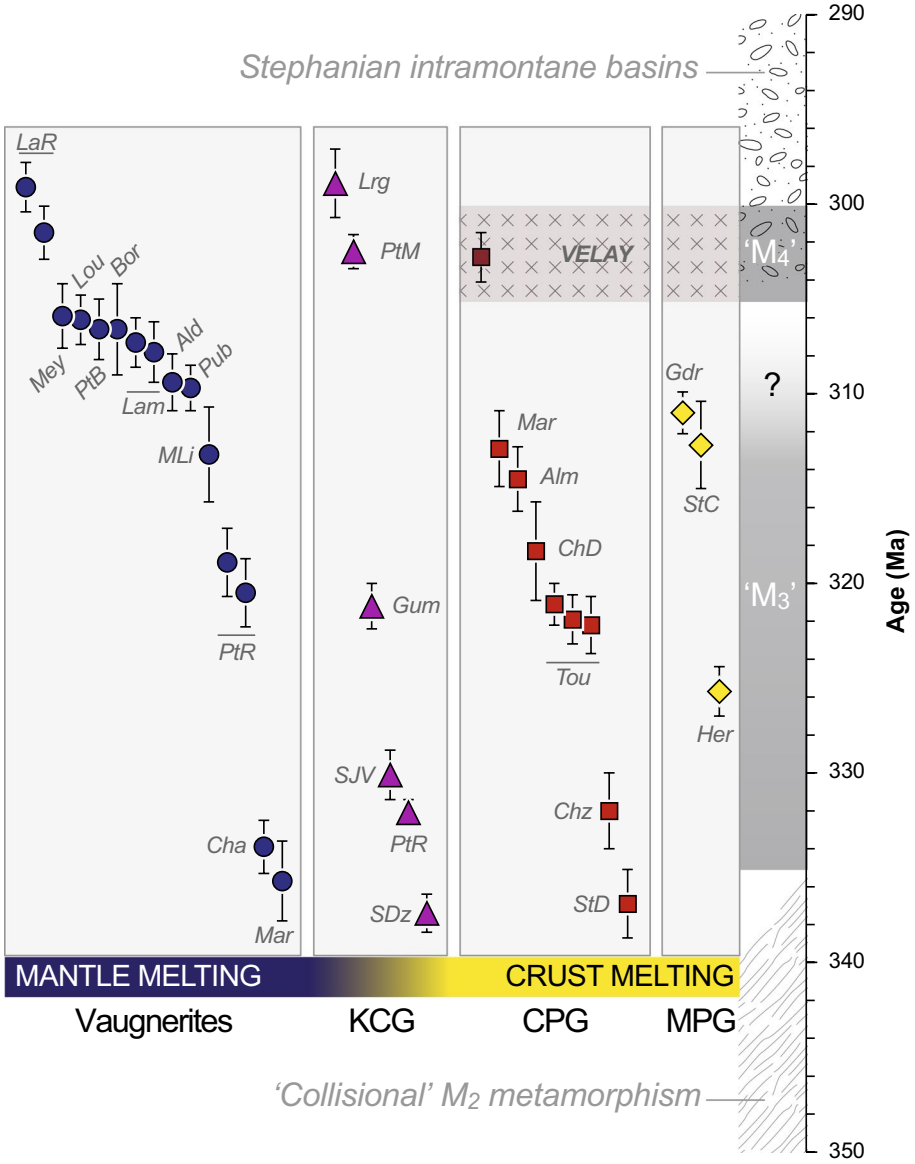

Fig. 10 Timeline summarizing all the intrusion ages obtained for Variscan igneous plutonic rocks from the eastern FMC in the course of this study (symbols are as in Figs. 2, 8). The groups of samples (CPG, MPG, KCG and vaugnerites) are sorted according to the respective contribution of crustal and mantle sources to their petrogenesis (see "Discussion"). On the right-hand side are represented major time markers in the Variscan evolution of the eastern FMC, including collision-related M_2 metamorphism (Gardien 1990; Caron 1994; Faure et al. 2009; Melleton et al. 2009; Schulz 2014), the two anatectic episodes M_3 and M_4—the latter being related to the development of the Velay dome (Montel et al. 1992; Barbey et al. 1999, 2015; Couzinié et al. 2014) and development of "Stephanian" (upper Pennsylvanian), intramontane coal-bearing basins (Malavieille et al. 1990; Faure et al. 2009). Abbreviations are for the names of the dated intrusions: *Ald* L'Aldeyrès, *Alm* Almance, *Bor* Borne, *Cha* Chassagny, *ChD* Chaise-Dieu, *Chz* Chalmazel, *Gdr* Grandrieu, *Gum* Gumières, *Her* Hermitage, *Lam* Lamastre, *LaR* La Roche, *Lou* Loubaresse, *Lrg* Largentière, *Mar* Margeride, *Mey* Meyras, *MLi* Moulin de Linas, *Mrc* Marcenod, *PtB* Pont-de-Bayzan, *PtM* Pont-de-Montvert, *PtR* Pont-Rouge quarry, *Pub* Pubellier, *SDz* Salt-en-Donzy, *SJV* Saint-Julien-la-Vêtre, *StC* Saint-Christophe-d'Allier, *StD* Saint-Dier-d'Auvergne, *Tou* Tournon and associated intrusions

has been attributed mainly to enhanced radioactive heat production, due to accumulation of radioactive elements in the over-thickened orogenic crust (e.g., Vanderhaeghe et al. 1999; Rossi and Pin 2008), possibly coupled to limited heat advection from the intrusion of vaugnerites. The higher, apparent geothermal gradient during the M_4 episode was assumed to result from two factors: first, the transfer of magmas from lower/middle to upper crustal levels during the formation of the Velay dome (Barbey et al. 2015), and second, the emplacement of mantle-derived (vaugnerite) melts (Williamson et al. 1992, 1997; Ledru et al. 2001; Rossi and Pin 2008).

Three problems, however, rise from these hypotheses:

1. As pointed out by Barbey et al. (2015), M_3 melting was necessarily more intense in the lower crust than it is recorded at the present level of exposure, in order to explain the formation and emplacement of the widespread 337–312-Ma-old CPG plutons (Fig. 10) for the origin of which biotite dehydration melting ($T > 800$ °C) is required.
2. The geochronological data obtained in this study show that vaugnerites ± KCG (338–298 Ma) and CPG + MPG (339–302 Ma) emplaced synchronously throughout the Carboniferous (Fig. 10), rather than successively, as would be expected if crustal melt production was caused by mafic magmatic underplating (first vaugnerites ± KCG, second CPG + MPG ± KCG).
3. Thermal modeling indicates that crustal melt productivity induced by heat advection from the intrusion or underplating of mantle-derived basalt rarely exceeds 10% of the whole volume of mafic magma (Petford and Gallagher 2001; Annen and Sparks 2002; Annen et al. 2006). This entails that the volume of basalt must have been nine times larger than the final volume of crust-derived granites. In the case of the eastern FMC, such a high ratio appears unrealistic because vaugnerites are largely subordinate in volume relative to the granites (Couzinié et al. 2016). There is evidence from lower crustal xenoliths brought up by Cenozoic volcanoes that mafic igneous rocks are present in the lower crust of the eastern FMC (Dostal et al. 1980; Downes et al. 1990). However, available age constraints on these rocks suggest that they would represent a Permian (300–250 Ma-old) underplating event (Supply 1981; Costa and Rey 1995; Féménias et al. 2003) and could therefore not be responsible for the heat anomaly at the origin of Carboniferous magmatism.

Thus, mantle-derived magmas unlikely represent the main heat source for crustal melting and the genesis of the voluminous CPG and MPG, during neither M_3, nor M_4, and an alternative hypothesis must be sought. The close association in both space and time of crust-derived granites and vaugnerites in the eastern FMC suggests that they are all the "byproducts" of one-and-the-same, lithospheric-scale geodynamic process. This process would be ideally represented by lithospheric mantle delamination, accompanied by the ascent of hot (>1200 °C) asthenospheric mantle up to the crust–mantle boundary (Moho). Thermo-mechanical modeling (van Hunen and Allen 2011; Duretz and Gerya 2013; Magni et al. 2013) and geological observations from other orogenic systems (Black and Liégeois 1993; Coulon et al. 2002; Guo et al. 2013; Laurent et al. 2014b) show that this process is common at the final stages of continental collision. Lithospheric mantle delamination was also suggested to explain the Carboniferous record in other parts of the Variscan belt (Henk et al. 2000; von Raumer et al. 2013; Denèle et al. 2014) and is backed by geophysical data, since the mantle underneath the eastern FMC is characterized by low P-wave velocities interpreted as reflecting the removal of the Variscan orogenic roots (Averbuch and Piromallo 2012). Thermal modeling demonstrated that an anomalously high heat flux through the Moho (equivalent to that of the convective mantle) triggers widespread lower crustal melting and magma transfer to the middle crust, accounting for high geothermal gradients and granulite-facies metamorphism (apparent geotherm of >50 °C km^{-1}) within 25–35 Ma (Depine et al. 2008). The increase in temperature is maximum in the case of conjunct crustal thickening enhancing radioactive heating and thinning of the lithospheric mantle causing an increase of the heat flux at the base of the crust (Vanderhaeghe and Duchêne 2010). This scenario is very consistent with geological and geochronological data from the eastern FMC showing the same incubation time between the intrusion of the first vaugnerites and granites at about 337 Ma and the rise of the Velay granite–migmatite dome at 310–300 Ma (Fig. 10) associated with the apparently higher-temperature "M_4" episode.

Consequences for the Variscan tectonic evolution of the eastern FMC

The magmatic rocks in the eastern FMC reveal a clear temporal vs. spatial evolution (Fig. 11). All magma types (CPG, MPG, KCG and vaugnerites) can indeed be found throughout the entire FMC, but their emplacement ages decrease systematically from north to south between 340 and 305 Ma (Fig. 11). The CPGs, KCGs and vaugnerites in the northernmost part of the FMC (Forez, Livradois and Lyonnais mountains) emplaced at 337 to 330 Ma; the youngest intrusion is represented by the Hermitage MPG pluton at ~326 Ma (Fig. 11). Further south, the CPG laccoliths that flank both the eastern (Tournon, Dunières) and western (Chaise-Dieu, Almance) sides of the Velay dome, as well as the large enclaves of CPG, KCG and vaugnerites in the latter, emplaced between 332 and 315 Ma, mostly at 320 Ma (Fig. 11). The Margeride batholith at the SW end of the Velay dome (the Margeride granite itself plus associated MPG and vaugnerites) intruded at 313–309 Ma; and finally, emplacement of the KCG plutons and abundant vaugnerites in the southernmost Cévennes domain took place at even younger ages of 307–298 Ma (Fig. 11).

We propose that the observed zonal pattern results from the progressive, southward migration of the thermal anomaly, which was responsible for coeval and protracted crust- and mantle-derived magmatism. This migrating thermal anomaly can be explained by asymmetric delamination of

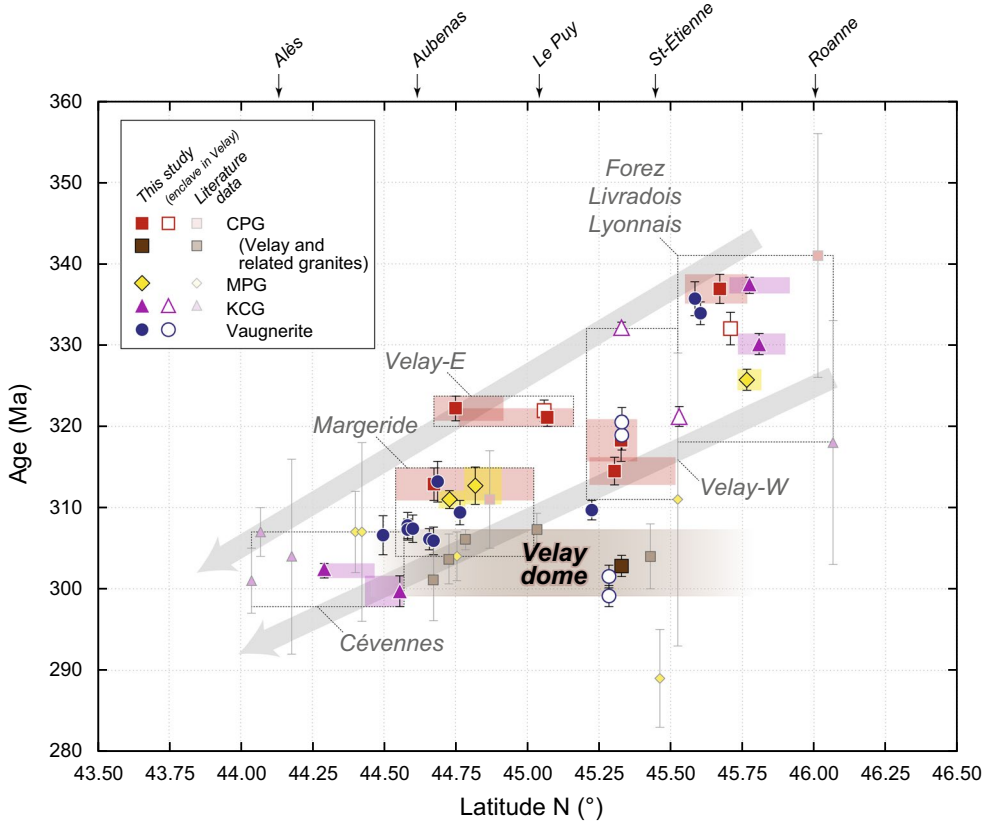

Fig. 11 Plot of the intrusion ages obtained for Variscan igneous rocks from the eastern FMC, as a function of the latitude (in decimal degrees) at which the samples were collected. The *colored boxes* represent individual plutons or batholiths (including the Velay dome); their horizontal extension is constrained by the geographic limits of the pluton, and their vertical extension by the age uncertainties obtained on dated samples from this pluton. The *dashed boxes* represent a group of plutons or intrusions that belong to the same geographic domain. The *light gray arrow* qualitatively highlights that the age of the oldest pluton/magmatic body in a given geographic area decreases southward (see "Discussion"), excluding the Velay dome which shows a relatively homogeneous age record across its entire surface. References are as in Table 1 with additional data from Barbarin et al. (2012) and Chelle-Michou et al. (2015) for the Velay granite and associated bodies

the subcontinental lithospheric mantle beneath the FMC, starting to the north and propagating southwards. Heat conduction from the inflowing asthenosphere triggered the partial melting of the lithospheric mantle enriched in incompatible elements during previous subduction (Couzinié et al. 2016; von Raumer et al. 2013) and caused formation of modest volumes of vaugnerite magmas. Such lithospheric mantle source could have either been part of the delaminating slab or represented by slivers that remained mechanically coupled to the lower crust during delamination. Concurrently, enhanced mantle heat flux through the Moho caused widespread lower crustal melting and the formation of granitic magmas (CPG + MPG). Interactions between those two magmatic end-members, and/or differentiation of vaugnerite magmas, led to the formation of KCG.

On the other hand, the granites and migmatites forming the core of the Velay complex span nearly the entire area covered by the other intrusions, but in contrast to the latter reveal no age zoning. These rocks rather crystallized within a short period of time at 305–300 Ma, regardless the latitude (Fig. 11). Our new age of 302.8 ± 1.3 Ma from the Pont-Rouge quarry, in the central-northern part of the dome, is indeed within uncertainties of, or very close to, the monazite U–Pb ages of 301 ± 5 (Mougeot et al. 1997), 303.7 ± 3.1 and 305.9 ± 1.4 Ma (Couzinié et al. 2014) from its southern part; and the zircon U–Pb ages of 307.5 ± 2.0 Ma (Chelle-Michou et al. 2015) and 304 ± 4 Ma (Cocherie 2007) obtained in the eastern and northern edges of the complex, respectively. The lack of "age zoning" in the Velay dome at the temporal resolution of existing data suggests that it represents a partially molten, middle to lower crustal layer rapidly exhumed during the late Carboniferous (Vanderhaeghe et al. 1999). Prolonged lower to middle crust melting started above the widening "asthenospheric window," which was formed during progressive southward lithospheric mantle delamination. This caused a rheologic weakening of the lower crust,

which eventually led to lateral crustal flow, thinning and collapse of the orogenic crust, and the exhumation of the partially molten crust in the core of domes like the Velay complex (Vanderhaeghe and Teyssier 2001; Vanderhaeghe 2012). In this perspective, the 305–300 Ma age cluster obtained in the Velay granite and migmatites does not necessarily correspond to a "catastrophic" melting event (Couzinié et al. 2014). Instead, it simply reflects the final exhumation and cooling of these rocks below their solidus, as a natural outcome of the whole delamination process.

The occurrence of southward lithospheric mantle delamination in the eastern FMC during the Carboniferous can be considered in the scope of existing geodynamic scenarios for this part of the Variscan belt. Faure et al. (2009) stressed out that there are two possible, competing models that may explain the present-day structure of the FMC:

1. A "monocyclic" model (e.g., Lardeaux et al. 2001) considering a single, northward-directed subduction from the Silurian to the late Devonian. In this context, the suggested southwards lithospheric delamination witnessed by the Carboniferous magmatic evolution could simply reflect the rollback of the lithospheric mantle (Fig. 12a), in response to decoupling with the overlying continental crust while convergence was still active (Vanderhaeghe and Duchêne 2010; Duretz and Gerya 2013; Magni et al. 2013).
2. A "polycyclic" model (e.g., Faure et al. 2005) in which northward-directed subduction during the Ordovician and early Silurian ("Eo-Variscan" cycle, Armorica–Gondwana collision) was followed by Devonian, southward-directed subduction that accommodated the closure of the Rheic Ocean ("Variscan" cycle, Laurussia-[Armorica + Gondwana] collision). In this case, thermo-mechanical models of mature continental collision suggest that if the lithospheric mantle of the lower (i.e., subducting) plate is retreating, it causes a "retro-delamination" of the lithosphere underneath the overriding plate and asthenospheric upwelling (Gray and Pysklywec 2012), equally accounting for southward lithosphere delamination under the eastern FMC (Fig. 12b).

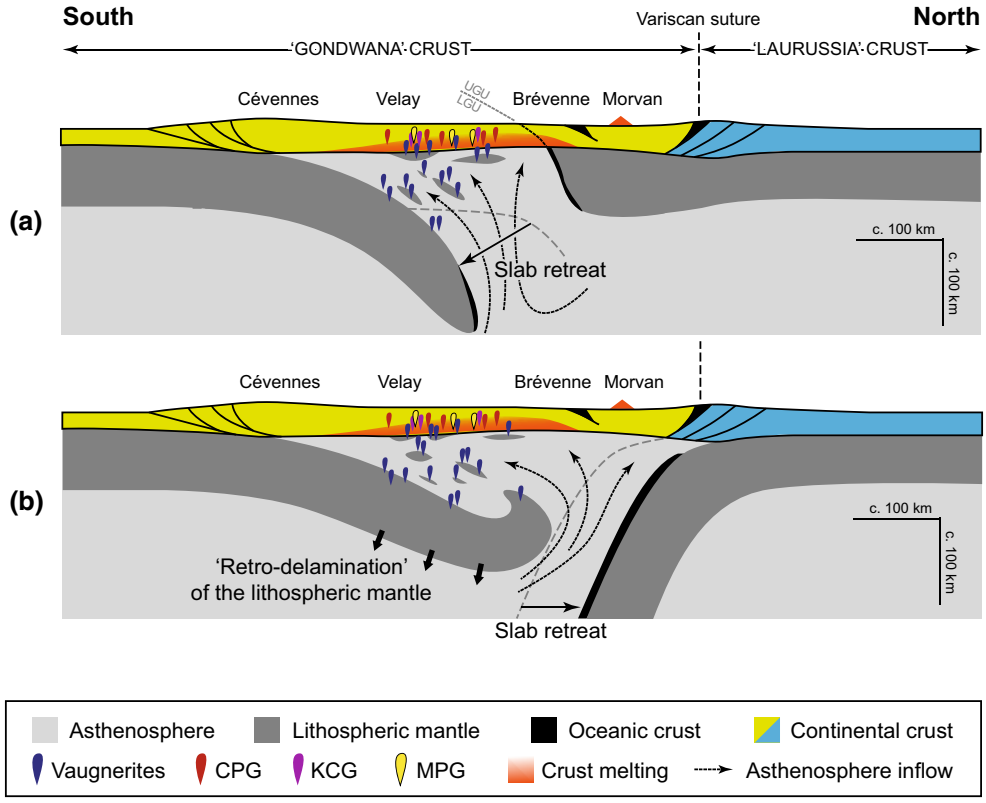

Fig. 12 Two possible, schematic geodynamic models that may account for the spatial and temporal distribution of Variscan igneous plutonic rocks in the eastern FMC during the Carboniferous (c. 340–300 Ma): **a** southward retreat of a lithospheric mantle slab, after middle Devonian (>360 Ma-old) subduction of continental crust now exhumed at the UGU/LGU boundary (highlighted by the *dashed line*); or **b** "retro-delamination" of the lithospheric mantle in response to slab retreat of the lower plate (i.e., the "Laurussia" plate) following collision (redrawn after Fig. 2c of Gray and Pysklywec 2012)

The two models have their strengths and weaknesses. The "monocyclic" model (Fig. 12a) is supported by the presence of (U)HP rocks at the base of the UGU (late Devonian migmatites with embedded eclogite boudins) that would represent remnants of the northward-subducted oceanic and continental crust (Lardeaux et al. 2001). Moreover, the rheological weakening and buoyancy of partially molten, subducted continental crust strongly enhances its decoupling with the lithospheric mantle and subsequent exhumation, as typically observed in numerical models (Duretz and Gerya 2013) and natural case studies (Labrousse et al. 2011). This would have readily triggered southward delamination of the lithospheric mantle in the context of ongoing convergence, which is supported by the fact that the orogenic front propagated southwards during the Carboniferous (Faure et al. 2009). However, the timing of exhumation of the (U)HP rocks at the base of the UGU is poorly constrained and could be as early as 360 Ma (Lardeaux et al. 2001). Thus, if this hypothesis was correct, there is a time lapse of $\geq$20 Ma between the end of continental subduction and the beginning of magmatism related to delamination (~340 Ma in the eastern FMC), which is difficult to explain since the response time between delamination and melting of the crust through asthenospheric heat advection would be much shorter, i.e., $\leq$10 Ma (Arnold et al. 2001; Depine et al. 2008).

On the other hand, the "polycyclic" model involving southward subduction during the Devonian (Fig. 12b) is consistent with arc magmatism in the Morvan and Limousin areas at 360–350 Ma and the development of the Brévenne trough as a back-arc basin (Pin and Paquette 1997; Faure et al. 2009; Lardeaux et al. 2014). It also avoids the problem of a too long time lapse between the onsets of delamination and magmatism: "retro-delamination" starting at ~350 Ma (the youngest documented subduction-related magmas being dated at 355 $\pm$ 2 Ma; Bernard-Griffiths et al. 1985) more realistically accounts for the onset of widespread magmatism at ~340 Ma in the eastern FMC. Nevertheless, this scenario implies that the asthenosphere window underneath the crust would have been much larger than in the previous one, specifically extending further north beyond the Brévenne basin, up to the Morvan area (Fig. 12b). This is problematic because in these domains, there is so far no evidence for any sequential emplacement of igneous rocks like that documented here, or even for any magmatic event younger than ~330 Ma.

More detailed investigations are therefore required to decipher between these two scenarios; at present we consider that both are equally likely to explain the observed southward lithosphere delamination and associated magmatism in the eastern FMC during the Carboniferous.

Conclusions

Variscan plutonic rocks from the eastern FMC were derived from two end-member sources: (i) a mixture of felsic lithologies (ortho- and paragneisses) from the local nappe pile (especially the Lower Gneiss Unit, in line with the predominance of late Ediacaran to early Cambrian ages in inherited zircon patterns), resulting in the formation of cordierite- and muscovite-bearing peraluminous granites (CPG and MPG); and (ii) an enriched (metasomatized) lithospheric mantle, source of the vaugnerites. The K-feldspar porphyritic, calc-alkaline granites and granodiorites (KCG) result from either interactions between these two end-members or fractionation from vaugnerite magmas.

Zircon and monazite U–Pb ages from these rocks testify for a long-lasting (~40 Ma) period of crust- and mantle-derived magmatism in the eastern FMC, as is reflected by the coeval emplacement of granites between 337.4 $\pm$ 1.0 and 298.9 $\pm$ 1.8 Ma, and vaugnerites between 335.7 $\pm$ 2.1 and 299.1 $\pm$ 1.3 Ma. Coeval and protracted crust- and mantle-derived magmatism points to the existence of a long-lived lithospheric-scale thermal anomaly, which probably formed in response to the delamination of the lithospheric mantle and asthenosphere upwelling beneath the eastern FMC during the late Carboniferous. Moreover, the spatial distribution of the dated samples indicates that delamination started at about 340 Ma in the northern part of the area and propagated southwards until 300 Ma. This may be explained either by (i) the progressive "retreat" of a lithospheric mantle slab following northward-directed subduction or (ii) "retro-delamination" of the lithosphere associated with southward-directed subduction.

Acknowledgements Financial support from CNRS-INSU (project SYSTER to J.F.M.) and the Deutscher Akademischer Austauschdienst (DAAD research grant nr. A/13/70682 to O.L.) are greatly acknowledged. We are grateful to E. Bruand, A. Gerdes, L. Marko and A. Vézinet for help during sample preparation and measurements. B. Barbarin and P. Bouilhol are thanked for discussions and assistance during fieldwork and sampling. We are grateful to the detailed and insightful comments provided by an anonymous reviewer, and thank W.C. Dullo, P. Pitra and M. Ballèvre for editorial handling and remarks on the manuscript.

References

Aït-Malek H (1997) Petrology, geochemistry and U/Pb geochronology of acid–basic associations: examples from SE Velay (French Massif Central) and western anti-Atlas (Morocco). Ph.D. thesis, University of Nancy

Alexandre P (2007) U–Pb SIMS ages from the French Massif Central and implication for the pre-Variscan tectonic evolution in Western Europe. C R Geosci 339:613–621

Alexandrov P, Floc'h JP, Cuney M, Cheilletz A (2001) Datation U–Pb à la microsonde ionique des zircons de l'unité supérieure de gneiss dans le Sud Limousin, Massif Central. C R Acad Sci Paris 332:625–632

Annen C, Sparks RSJ (2002) Effects of repetitive emplacement of basaltic intrusions on thermal evolution and melt generation in the crust. Earth Planet Sci Lett 203:937–955

Annen C, Blundy JD, Sparks RSJ (2006) The genesis of intermediate and silicic magmas in deep crust hot zones. J Petrol 47(3):505–539

Arnaud F, Burg JP (1993) Microstructures des mylonites schisteuses: cartographie des chevauchements varisques dans les Cévennes et détermination de leur cinématique. C R Acad Sci Paris 11:1441–1447

Arnold J, Jacoby WR, Schmeling H, Schott B (2001) Continental collision and the dynamic and thermal evolution of the Variscan orogenic crustal root—numerical models. J Geodynamics 31:273–291

Averbuch O, Piromallo C (2012) Is there a remnant Variscan subducted slab in the mantle beneath the Paris basin? Implications for the late Variscan lithospheric delamination process and the Paris basin formation. Tectonophysics 558–559:70–83

Ballèvre M, Le Goff E, Hébert R (2001) The tectonothermal evolution of the Cadomian belt of northern Brittany, France: a Neoproterozoic volcanic arc. Tectonophysics 331:19–43

Barbarin B (1983) Les granites carbonifères du Forez septentrional (Massif Central Français). Typologie et relations entre les différents massifs. Thèse 3e cycle, Université Clermont-Ferrand 199 p

Barbarin B (1988) Mise en évidence des différentes étapes d'un processus global de mélange de magmas acides et basiques: les interactions entre la diorite de Piolard et le monzogranite de Saint-Julien-la-Vêtre (Monts du Forez, Massif Central, France). C R Acad Sci Paris 306:129–134

Barbarin B (1992) Les granites crustaux hercyniens d'Europe Occidentale. Comparaison avec les granites S du Lachlan Fold Belt, Australie. Dualité d'origine. C R Acad Sci Paris 314:593–601

Barbarin B (1999) A review of the relationships between granitoid types, their origins and their geodynamic environments. Lithos 46(3):605–626

Barbarin B, Gerbe MC, Vitel G, Gonord H, Couette F, Lebret P (2012) Notice explicative, Carte géologique de la France (1/50,000^{e}), feuille Firminy (nr. 744). Orléans, Bureau de Recherches Géologiques et Minières

Barbey P, Marignac C, Montel JM, Macaudière J, Gasquet D, Jabbori J (1999) Cordierite growth textures and the conditions of genesis and emplacement of crustal granitic magmas: the Velay granite (Massif Central, France). J Petrol 40(9):1425–1441

Barbey P, Villaros A, Marignac C, Montel JM (2015) Multiphase melting, magma emplacement and P-T-time path in late-collisional context: the Velay example (Massif Central, France). Bull Soc Geol Fr 186(2–3):93–116

Batias P, Duthou JL (1979) Age Viséen supérieur du granite porphyroïde de Vienne-Tournon (Massif Central français). In: Proceedings 7ème Réunion Annuelle des Sciences de la Terre, Lyon

Bé Mézème E, Cocherie A, Faure M, Legendre O, Rossi P (2006) Electron microprobe monazite geochronology of magmatic events: examples from Variscan migmatites and granitoids, Massif Central, France. Lithos 87(3–4):276–288

Beard JS, Lofgren GE (1991) Dehydration melting and water-saturated melting of basaltic and andesitic greenstones and amphibolites at 1, 3 and 6.9 kbar. J Petrol 32(2):365–401

Bernard-Griffiths J, Gebauer D, Grünenfelder M, Piboule M (1985) The tonalite belt of Limousin (French Central Massif): U–Pb zircon ages and tectonic implications. Bull Soc Geol Fr 1(4):523–529

Black R, Liégeois JP (1993) Cratons, mobile belts, alkaline rocks and continental lithospheric mantle: the Pan-African testimony. J Geol Soc Lond 150:89–98

Bogaerts M, Scaillet B, Vander Auwera J (2006) Phase equilibria of the Lyngdal granodiorite (Norway): implications for the origin of metaluminous ferroan granitoids. J Petrol 47(12):2405–2431

Bonin B (2004) Do coeval mafic and felsic magmas in post-collisional to within-plate regimes necessarily imply two contrasting, mantle and crustal, sources? A review. Lithos 78:1–24

Bouilhol P, Leyreloup AF, Delor C, Vauchez A, Monié P (2006) Relationships between lower and upper crust tectonic during doming: the mylonitic southern edge of the Velay metamorphic core complex (Cévennes-French Massif Central). Geodin Acta 19(3–4):137–153

Briand B, Piboule M, Santallier D, Bouchardon JL (1991) Geochemistry and tectonic implications of two Ordovician bimodal igneous complexes, southern French Massif Central. J Geol Soc Lond 148:959–971

Briand B, Duthou JL, Guerrot C, Chenevoy M (2002) The orthoclase lath-rich granites from Vivarais, products of a Dinantian post-tectonic magmatism; identification of a NW-Vivarais geological unit. C R Geoscience 334:741–747

Brichau S, Respaut JP, Monié P (2008) New age constraints on emplacement of the Cévenol granitoids, South French Massif Central. Int J Earth Sci 97:725–738

Brown M (2001) Crustal melting and granite magmatism: key issues. Phys Chem Earth 26(4–5):201–212

Bruguier O, Becq-Giraudon JF, Bosch D, Lancelot J (1998) Late Visean hidden basins in the internal zones of the Variscan belt: U–Pb zircon evidence from the French Massif Central. Geology 26(7):627–630

Caen-Vachette M (1979) Age cambrien des rhyolites transformées en leptynites dans la série métamorphique du Pilat (Massif Central français). C R Acad Sci Paris 289:997–1000

Caen-Vachette M, Couturié JP, Didier J (1982) Ages radiométriques des granites anatectiques et tardimigmatitique du Velay (Massif Central français). C R Acad Sci Paris 294:135–138

Caron C (1994) Les minéralisations Pb-Zn associées au Paléozoique inférieur d'Europe méridionale. Traçage isotropique Pb-Pb des gites de l'Iglesiente (SW Sardaigne) et des Cévennes et évolution du socle encaissant par la géochronologie U–Pb, 40Ar-39Ar et K-Ar. Ph.D. thesis, University of Montpellier 288 pp

Castiñeiras P, Villaseca C, Barbero L, Romera CM (2008) SHRIMP U–Pb zircon dating of anatexis in high-grade migmatite complexes of Central Spain: implications in the Hercynian evolution of Central Iberia. Int J Earth Sci 97:35–50

Chauvet A, Volland-Tuduri N, Lerouge C, Bouchot V, Monié P, Charonnat X, Faure M (2011) Geochronological and geochemical characterization of magmatic-hydrothermal events within the Southern Variscan external domain (Cévennes area, France). Int J Earth Sci 101(1):69–86

Chelle-Michou C, Laurent O, Moyen JF, Block S, Gardien V, Paquette JL, Couzinié S (2015) New U–Pb and Hf zircon data from the eastern Massif Central: from Gondwana to Pangea in a nutshell. Géol Fr 1:37–38

Clemens JD, Darbyshire DPF, Flinders J (2009) Sources of post-orogenic calcalkaline magmas: the Arrochar and Garabal Hill-Glen Fyne complexes, Scotland. Lithos 112:524–542

Cocherie A (2007) Datations U–Pb (laser-ICPMS-MC) sur zircons et U-Th-Pb sur monazites de granitoïdes du Massif central (carte de Firminy). Rapport BRGM MMA/ISO-2007/279

Cocherie A, Be Mézème E, Legendre O, Fanning CM, Faure M, Rossi P (2005) Electron-microprobe dating as a tool for determining the closure of Th–U–Pb systems in migmatitic monazites. Am Mineral 90:607–618

Costa S, Rey P (1995) Lower crustal rejuvenation and growth during post-thickening collapse: insights from a crustal cross section through a Variscan metamorphic core complex. Geology 23(10):90–908

Coulon C, Megartsi M, Fourcade S, Maury RC, Bellon H, Louni-Hacini A, Cotten J, Coutelle A, Hermitte D (2002) Post-collisional transition from calc-alkaline to alkaline volcanism during the Neogene in Oranie (Algeria): magmatic expression of a slab breakoff. Lithos 62(3–4):87–110

Couturié JP, Caen-Vachette M (1979) Age Namurien d'un laccolite granitique différencié par gravité: le granite de la Margeride (Massif Central français). C R Acad Sci Paris 289:449–452

Couzinié S, Moyen JF, Villaros A, Paquette JL, Scarrow JH, Marignac C (2014) Temporal relationships between Mg-K mafic magmatism and catastrophic melting of the Variscan crust in the southern part of Velay Complex (Massif Central, France). J Geosci 59:69–86

Couzinié S, Laurent O, Moyen JF, Zeh A, Bouilhol P, Villaros A (2016) Post-collisional magmatism: crustal growth not identified by zircon Hf–O isotopes. Earth Planet Sci Lett 456:182–195

De la Roche H, Leterrier L, Grandclaude P, Marchal M (1980) A classification of volcanic and plutonic rocks using R1–R2 diagram and major element analyses—its relationship with current nomenclature. Chem Geol 29:183–210

De Saint-Blanquat M, Horsman E, Habert G, Morgan S, Vanderhaeghe O, Law R, Tikoff B (2011) Multiscale magmatic cyclicity, duration of pluton construction, and the paradoxical relationship between tectonism and plutonism in continental arcs. Tectonophysics 500:20–33

Denèle Y, Laumonier B, Paquette JL, Olivier P, Gleizes G, Barbey P (2014) Timing of granite emplacement, crustal flow and gneiss dome formation in the Variscan segment of the Pyrenees. In: Schulmann K, Martínez Catalán JR, Lardeaux JM, Janoušek V and Oggiano G (eds) *The Variscan Orogeny: Extent, Timescale and the Formation of the European Crust.* Geol Soc London Special Publications 405: 265–287

Depine GV, Andronicos CL, Phipps-Morgan J (2008) Near-isothermal conditions in the middle and lower crust induced by melt migration. Nature 452:80–83

Didier J, Lameyre J (1969) Les granites du Massif Central Français. Etude comparée des leucogranites et des granodiorites. Contrib Mineral Petrol 24:219–238

Didier J, Duthou JL, Lameyre J (1982) Mantle and crustal granites: genetic classification of orogenic granites and the nature of their enclaves. J Volc Geothermal Res 14:125–132

Didier J, Barbarin B, Gagny C, Leistel JM, Kerrien Y (1989) Notice explicative, Carte géologique de la France (1/50 000^{e}), feuille Noirétable (nr. 695). Orléans, Bureau de Recherches Géologiques et Minières, p 72

Didier A, Bosse V, Boulvais P, Bouloton J, Paquette JL, Montel JM, Devidal JL (2013) Disturbance versus preservation of U–Th–Pb ages in monazite during fluid–rock interaction: textural, chemical and isotopic in situ study in microgranites (Velay Dome, France). Contrib Mineral Petrol 165(6):1051–1072

Do Couto D, Faure M, Augier R, Cocherie A, Rossi P, Li XH, Lin W (2015) Monazite U-Th–Pb EPMA and zircon U–Pb SIMS chronological constraints on the tectonic, metamorphic and thermal events in the inner part of the Variscan orogen, example from the Sioule series. Int J Earth Sci, French Massif Central. doi:10.1007/s00531-015-1184-0

Dostal J, Dupuy C, Leyreloup A (1980) Geochemistry and petrology of meta-igneous granulitic xenoliths in Neogene volcanic rocks of the Massif Central, France—implications for the lower crust. Earth Planet Sci Lette 50(1):31–40

Downes H, Dupuy C, Leyreloup A (1990) Crustal evolution of the Hercynian belt of Western Europe: evidence from lower-crustal granulitic xenoliths (French Massif Central). Chem Geol 83(3–4):209–231

Downes H, Shaw A, Williamson BJ, Thirlwall MF (1997) Sr, Nd and Pb isotope geochemistry of the Hercynian granodiorites and monzogranites, Massif Central, France. Chem Geol 136:99–122

Ducrot J, Lancelot J, Marchand J (1983) Datation U–Pb sur zircons de l'éclogite de la Borie (Haut-Allier, France) et conséquences sur l'évolution ante-hercynienne de l'Europe occidentale. Earth Planet Sci Lett 62:385–394

Dupraz J, Didier J (1988) Le complexe anatectique du Velay (Massif Central français): structure d'ensemble et évolution géologique. Geol Fr 4:73–88

Duretz T, Gerya TV (2013) Slab detachment during continental collision: influence of crustal rheology and interactions with lithospheric delamination. Tectonophysics 602:124–140

Duthou JL, Cantagrel JM, Didier J, Vialette Y (1984) Palaeozoic granitoids from the French Massif Central: age and origin studied by ^{87}Rb–^{87}Sr system. Phys Earth Planet Interiors 35:131–144

Duthou JL, Chenevoy M, Gay M (1994) Rb-Sr middle Devonian age of cordierite bearing migmatites from Lyonnais area (French Massif Central). C R Acad Sci Paris 319:791–796

Faure M (1995) Late orogenic carboniferous extensions in the Variscan French Massif Central. Tectonics 14(1):132–153

Faure M, Charonnat X, Chauvet A (1999) Structural map and tectonic evolution of the Cévennes para-autochtonous domain of the Hercynian belt (French Massif Central). C R Acad Sci Paris 328:401–407

Faure M, Monié P, Pin C, Maluski H, Leloix C (2002) Late Visean thermal event in the northern part of the French Massif Central: new ^{40}Ar/^{39}Ar and Rb-Sr isotopic constraints on the Hercynian syn-orogenic extension. Int J Earth Sci 91:53–75

Faure M, Bé Mézème E, Duguet M, Cartier C, Talbot JY (2005) Paleozoic tectonic evolution of medio-Europa from the example of the French Massif Central and Massif Armoricain. In: Carosi R, Dias R, Iacopini D, Rosenbaum G (eds.), The southern Variscan belt. J Virtual Explorer 19, paper 5

Faure M, Bé Mézème E, Cocherie A, Rossi P, Chemenda A, Boutelier D (2008) Devonian geodynamic evolution of the Variscan belt, insights from the French Massif Central and Massif Armoricain. Tectonics. doi:10.1029/2007TC002115

Faure M, Lardeaux JM, Ledru P (2009) A review of the pre-Permian geology of the Variscan French Massif Central. C R Geoscience 341(2–3):202–213

Féménias O, Coussaert N, Bingen B, Whitehouse M, Mercier JC, Demaiffe D (2003) A Permian underplating event in late- to post-orogenic tectonic setting. Evidence from the mafic–ultramafic layered xenoliths from Beaunit (French Massif Central). Chem Geol 199:293–315

Fernández-Suárez J, Dunning GR, Jenner GA, Gutiérrez-Alonzo G (2000) Variscan collisional magmatism and deformation in NW Iberia: constraints from U–Pb geochronology of granitoids. J Geol Soc Lond 157:565–576

Fernández-Suárez J, Gutierrez-Alonso G, Johnston ST, Jeffries TE, Pastor-Galán D, Jenner GA, Murphy JB (2011) Iberian late-Variscan granitoids: some considerations on crustal sources and the significance of "mantle extraction ages". Lithos 123:121–132

Feybesse JL, Lardeaux JM, Johan V, Tegyey M, Dufour E, Lumière B, Delfour J (1988) La série de la Brévenne (Massif Central français): une unité dévonienne charriée sur le complexe métamorphique des Monts du Lyonnais à la fin de la collision varisque. C R Acad Sci Paris 307:991–996

Finger F, Roberts MP, Haunschmid B, Schermaier A, Steyrer HP (1997) Variscan granitoids of central Europe: their typology, potential sources and tectonothermal relations. Mineral Petrol 61:67–96

François T (2009) Geochemical and geochronological constraints on the origin and emplacement of Mont-Lozère granites. M.Sc. thesis, University of Montpellier

Gardien V (1990) Reliques de grenat et de staurotide dans la série métamorphique de basse pression du Mont Pilat (Massif Central français): témonis d'une évolution tectonométamorphique polyphasée. C R Acad Sci Paris 310:233–240

Gardien V (1993) Les reliques pétrologiques de haute à moyenne pression des séries du Vivarais oriental (Est du Massif Central français). Comptes rendus de l'Académie des sciences. Série 2, Mécanique, Physique, Chimie, Sciences de l'univers. Sciences de la Terre 316:1247–1254

Gardien V, Teygey M, Lardeaux JM, Misseri M, Dufour E (1990) Crust mantle relationships in the French Variscan Belt: the example of Monts du Lyonnais unit (Eastern French Massif central). J Metam Geol 8(5):477–492

Gardien V, Thompson AB, Grujic D, Ulmer P (1995) Experimental melting of biotite + plagioclase + quartz ± muscovite assemblages and implications for crustal melting. J Geophys Res 100:15581–15591

Gardien V, Lardeaux JM, Ledru P, Allemand P, Guillot S (1997) Metamorphism during late orogenic extension; insights from the French Variscan belt. Bull Soc Geol Fr 168(3):271–286

Gardien V, Vanderhaeghe O, Arnaud N, Cocherie A, Grange M, Lécuyer C (2011) Thermal maturation and exhumation of a middle orogenic crust in the Livradois area (French Massif Central). Bull Soc Geol Fr 182(1):5–24

Gay M, Peterlongo JM, Caen-Vachette M (1981) Age radiométrique des granites en massifs allongés et en feuillets minces, syntectoniques dans les Monts du Lyonais (Massif Central français). C R Acad Sci Paris 293:993–996

Geisler T, Ulonska M, Schleicher H, Pidgeon RT, van Bronswijk W (2001) Leaching and differential recrystallization of metamict zircon under experimental conditions. Contrib Mineral Petrol 141:53–65

Gerdes A, Zeh A (2006) Combined U–Pb and Hf isotope LA-(MC) ICP-MS analyses of detrital zircons: comparison with SHRIMP and new constraints for the provenance and age of an Armorican metasediment in Central Germany. Earth Planet Sci Lett 249:47–61

Gerdes A, Zeh A (2009) Zircon formation versus zircon alteration–new insights from combined U–Pb and Lu–Hf in situ LA-ICP-MS analyses, and consequences for the interpretation of Archean zircon from the Central Zone of the Limpopo Belt. Chem Geol 261:230–243

Gray R, Pysklywec RN (2012) Geodynamic models of mature continental collision: evolution of an orogen from lithospheric subduction to continental retreat/delamination. J Geophysical Res 117(B3):B03408

Guo Z, Wilson M, Zhang M, Cheng Z, Zhang L (2013) Post-collisional, K-rich mafic magmatism in south Tibet: constraints on Indian slab-to-wedge transport processes and plateau uplift. Contrib Mineral Petrol 165:1311–1340

Harris NBW, Vance D, Ayres M (2000) From sediment to granite: timescales of anatexis in the upper crust. Chem Geol 162:155–167

Henk A, Von Blankenburg F, Finger F, Schaltegger U, Zulauf G (2000) Syn-convergent high temperature metamorphism and magmatism in the Variscides: a discussion of potential heat sources. In: Franke W, Haak V, Oncken O, Tanner D (eds) Orogenic processes: quantification and modelling in the variscan belt. Geol Soc Lond Spec Publ 179:387–399

Hou Z, Cook NJ (2009) Metallogenesis of the Tibetan collisional orogen: a review and introduction to the special issue. Ore Geol Rev 36:2–24

Isnard H (1996) Datation par la méthode U–Pb sur monazites des granites du Mont Lozère et de l'Est de la Margeride (laccolites de Chambon-le- Château et de St-Christophe d'Allier): contribution à l'histoire post-tectonique du Massif Central Français. M.Sc. thesis, University of Montpellier, 55 pp

Janoušek V, Bowes DR, Rogers G, Farrow CM, Jelínek E (2000) Modelling diverse processes in the petrogenesis of a composite Batholith: the Central Bohemian Pluton, Central European Hercynides. J Petrol 41(4):511–543

Kemp AIS, Hawkesworth CJ (2003) Granitic perspectives on the generation and secular evolution of the continental crust. In: Rudnick RL (ed) The crust. Treatise on geochemistry. Elsevier-Pergamon, Oxford, pp 349–410

Kober B, Kalt A, Hanel M, Pidgeon RT (2004) SHRIMP dating of zircons from high-grade metasediments of the Schwarzwald/SW-Germany and implications for the evolution of the Moldanubian basement. Contrib Mineral Petrol 147:330–345

Kosztolanyi C (1971) Géochronologie des gisements uranifères français par la méthode uranium-plomb. Influence du déséquilibre radioactif sur les résultats. Ph.D. thesis, University of Nancy 279 pp

Kroner U, Romer RL (2013) Two plates—many subduction zones: the Variscan orogeny reconsidered. Gondwana Res 24(1):298–329

Labrousse L, Prouteau G, Ganzhorn AC (2011) Continental exhumation triggered by partial melting at high pressure. Geology 39(12):1171–1174

Lafon JM (1986) Géochronologie U-Pb appliquée à deux segments du massif central français, le Rouergue oriental et le Limousin central. Thèse de l'Université de Montpellier, p 152

Lafon JM, Respaut JP (1988) Géochronologie U–Pb et leucogranites varisques : cas des massifs de Grandrieu (Lozère) et de la Porcherie (Limousin), Massif Central français. Bull Minér 111:225–237

Lardeaux JM, Ledru P, Daniel I, Duchène S (2001) The Variscan French Massif Central—a new addition to the ultra-high pressure metamorphic "club": exhumation processes and geodynamic consequences. Tectonophysics 332:143–168

Lardeaux JM, Schulmann K, Faure M, Janoušek V, Lexa O, Skrzypek E, Edel JB, Tipska P (2014) The moldanubian zone in the French Massif Central, Vosges/Schwarzwald and Bohemian Massif revisited: differences and similarities. Geol Soc Lond Spec Publ 405(1):7–44

Laurent O, Doucelance R, Martin H, Moyen JF (2013) Differentiation of the late-Archaean sanukitoid series and some implications for crustal growth: insights from geochemical modelling on the Bulai pluton, Central Limpopo Belt, South Africa. Precambrian Res 227:186–203

Laurent O, Martin H, Moyen JF, Doucelance R (2014a) The diversity and evolution of late-Archean granitoids: evidence for the onset of modern-style plate tectonics between 3.0 and 2.5 Ga. Lithos 205:208–235

Laurent O, Rapopo M, Stevens G, Moyen JF, Martin H, Doucelance R, Bosq C (2014b) Contrasting petrogenesis of Mg–K and Fe–K granitoids and implications for post-collisional magmatism: case study from the Late-Archean Matok pluton (Pietersburg block, South Africa). Lithos 196–197:131–149

Ledru P, Lardeaux JM, Santallier D, Autran A, Quenardel JM, Floch JP, Lerouge G, Maillet N, Marchand J, Ploquin A (1989) Où sont les nappes dans le Massif central français ? Bulletin de la Société Geologique de France 8:605–618

Ledru P, Courrioux G, Dallain C, Lardeaux JM, Montel JM, Vanderhaeghe O, Vitel G (2001) The Velay dome (French Massif Central): melt generation and granite emplacement during orogenic evolution. Tectonophysics 342:207–237

Leloix C, Faure M, Feybesse JL (1999) Hercynian polyphase tectonics in the northeast French Massif Central: the closure of the Brévenne Devonian-Dinantian rift. Int J Earth Sci 88:409–421

Liégeois JP, Navez J, Hertogen J, Black R (1998) Contrasting origin of post-collisional high-K calc-alkaline and shoshonitic versus alkaline and peralkaline granitoids. The use of sliding normalization. Lithos 45:1–28

Linnemann U, McNaughton NJ, Romer RL, Gehmlich M, Drost K, Tonk C (2004) West African provenance for Saxo-Thuringia (Bohemian Massif): did Armorica ever leave pre-Pangean Gondwana? U/Pb-SHRIMP zircon evidence and the Nd isotopic record. Int J Earth Sci 93:683–705

Linnemann U, Gerdes A, Drost K, Buschmann B (2007) The continuum between Cadomian orogenesis and opening of the Rheic Ocean: Constraints from LA-ICP-MS U–Pb zircon dating and analysis of plate-tectonic setting (Saxo-Thuringian zone, northeastern Bohemian Massif, Germany). In: Linnemann U, Nance RD, Kraft P, Zulauf G (eds) the evolution of the Rheic Ocean: From Avalonian-Cadomian active margin to Alleghenian-Variscan collision. Geological Society of America Special Paper vol 423, pp 61–96

Linnemann U, Gerdes A, Hofmann M, Marko L (2014) The Cadomian Orogen: neoproterozoic to Early Cambrian crustal growth and orogenic zoning along the periphery of the West African Craton—Constraints from U–Pb zircon ages and Hf isotopes (Schwarzburg Antiform, Germany). Precambrian Res 244:236–278

Lotout C, Pitra P, Poujol M, van den Driessche J (in press) Ordovician magmatism in the Lévézou massif (French Massif Central): tectonic and geodynamic implications. Int J Earth Sci. doi:10.1007/s00531-016-1387-z

Ludwig KR (2008) Isoplot 3.70, a geochronological toolkit for microsoft excel. Berkeley Geochronology Central Special Publication No. 4

Magni V, Faccenna C, van Hunen J, Funiciello F (2013) Delamination versus break-off: the fate of continental collision. Geophys Res Lett 40:285–289

Malavieille J, Guilhot P, Costa S, Lardeaux JM, Gardien V (1990) Collapse of the thickened Variscan crust in the French Massif Central: Mont Pilat extensional shear zone and St. Etienne Late Carboniferous basin. Tectonophysics 177(1–3):139–149

Matte P (1986) Tectonics and plate tectonics model for the Variscan belt of Europe. Tectonophysics 126:329–374

Melleton J, Faure M, Cocherie A (2009) Monazite U–Th/Pb chemical dating of the Early Carboniferous syn-kinematic MP/MT metamorphism in the Variscan French Massif Central. Bull Soc Geol Fr 180(3):283–292

Melleton J, Cocherie A, Faure M, Rossi P (2010) Precambrian protoliths and Early Paleozoic magmatism in the French Massif Central: U–Pb data and the North Gondwana connection in the west European Variscan belt. Gondwana Res 17(1):13–25

Mercier L, Lardeaux JM, Davy P (1991) On the tectonic significance of retrograde P–T–t paths in eclogites of the French Massif Central. Tectonics 10(1):131–140

Mezger K, Krogstad EJ (1997) Interpretation of discordant U–Pb zircon ages—an evaluation. J Metamorphic Geol 15:127–140

Mintrone M (2015) Le Massif Central avant la chaîne Varisque: caractérisation des orthogneiss du début du Primaire. Travail d'Étude et de Recherche, University of Clermont-Ferrand, France, p 31

Montel JM, Weisbrod A (1986) Characteristics and evolution of "vaugneritic magmas": an analytical and experimental approach, on the example of the Cévennes Médianes (French Massif Central). Bull Minéral 109:575–587

Montel JM, Marignac C, Barbey P, Pichavant M (1992) Thermobarometry and granite genesis: the Hercynian low-P, high-T Velay anatectic dome (French Massif Central). J Metamorph Geol 10:1–15

Mougeot R, Respaut JP, Ledru P, Marignac C (1997) U–Pb chronology on accessory minerals of the Velay anatectic dome (French Massif Central). Eur J Mineral 9:141–156

Moyen JF, Laurent O, Chelle-Michou C, Couzinié S, Vanderhaeghe O, Zeh A, Villaros A, Gardien G (in press) Collision versus subduction-related magmatism: two contrasting ways of granite formation and implications for crustal growth. Lithos doi:10.1016/j.lithos.2016.09.018

Nance DR, Murphy BJ (1994) Contrasting basement isotopic signatures and the palinspastic restoration of peripheral orogens: examples from the Neoproterozoic Avalonian-Cadomian Belt. Geology 22:617–620

Nance DR, Murphy BJ, Strachan RA, D'Lemos RS, Taylor GK (1991) Late Proterozoic tectonostratigraphic evolution of the Avalonian and Cadomian terranes. Precambrian Res 53:41–78

Nance RD, Murphy JB, Keppie JD (2002) A Cordilleran model for the evolution of Avalonia. Tectonophysics 352:11–31

Nance RD, Gutierrez-Alonso G, Keppie JD, Linnemann U, Murphy JB, Quesada C, Strachan RA, Woodcock NH (2010) Evolution of the Rheic Ocean. Gondwana Res 17:194–222

Nelson KD et al (1996) Partially molten middle crust beneath southern Tibet: synthesis of project INDEPTH results. Science 274:1684–1688

Paquette LD, Monchoux P, Couturier M (1995) Geochemical and isotopic study of a norite-eclogite transition in the European Variscan belt: implications for U–Pb zircon systematics in metabasic rocks. Geochim Cosmochim Acta 59(8):1611–1622

Patiño-Douce AE, Beard JS (1995) Dehydration-melting of biotite gneiss and quartz amphibolite from 3 to 15 kbar. J Petrol 36:707–738

Patiño-Douce AE, Beard JS (1996) Effects of P, $f(O_2)$ and Mg/Fe ratio on dehydration-melting of model metagreywackes. J Petrol 37:999–1024

Patiño-Douce AE, Harris N (1998) Experimental constraints on Himalayan anatexis. J Petrol 39(4):689–710

Patiño-Douce AE, Johnston AD (1991) Phase equilibria and melt productivity in the pelitic system: implications for the origin of peraluminous granitoids and aluminous granulites. Contrib Mineral Petrol 107:202–218

Peccerillo A, Taylor SR (1976) Geochemistry of Eocene calc-alkaline volcanic rocks from the Kastamonu area, northern Turkey. Contrib Mineral Petrol 58:63–81

Petford N, Gallagher K (2001) Partial melting of mafic (amphibolitic) lower crust by periodic influx of basaltic magma. Earth Planet Sci Lett 193:483–489

Petford N, Cruden AR, McCaffrey KJW, Vigneresse JL (2000) Granite magma formation, transport and emplacement in the Earth's crust. Nature 408:669–673

Pickering JM, Johnston AD (1998) Fluid-absent melting behavior of a two-mica metapelite: experimental constraints on the origin of black hills granite. J Petrol 39(10):1787–1804

Pin C (1979a) Âge de 482 Ma des roches orthodérivées du groupe leptyno-amphibolique de Marvejols (Lozère, Massif central français) déterminé par la méthode U–Pb sur zircons. C R Acad Sci Paris Ser II 288:291–294

Pin C (1979b) Géochronologie U–Pb et microtectonique des séries métamorphiques anté-stéphaniennes de l'Aubrac et de la région de Marvejols (Massif Central). Ph.D. thesis, University of Montpellier, p 205

Pin C, Duthou J (1990) Sources of Hercynian granitoids from the French Massif Central: inferences from Nd isotopes and consequences for crustal evolution. Chem Geol 83:281–296

Pin C, Lancelot J (1982) U–Pb dating of an early paleozoic bimodal magmatism in the French Massif Central and of its further metamorphic evolution. Contrib Mineral Petrol 79:1–12

Pin C, Paquette JL (1997) A mantle-derived bimodal suite in the Hercynian Belt: Nd isotope and trace element evidence for a subduction-related rift origin of the Late Devonian Brévenne metavolcanics, Massif Central (France). Contrib Mineral Petrol 129:222–238

Pin C, Paquette JL (2002) Sr-Nd isotope and trace element evidence for a Late Devonian active margin in northern Massif Central (France). Geodin Acta 15:63–77

Pin C, Binon M, Belin JM, Barbarin B, Clemens JD (1990) Origin of microgranular enclaves in granitoids: Equivocal Sr-Nd Evidence From Hercynian Rocks in the Massif Central (France). J Geophysical Res 95(B11):17821

Rapp RP, Watson EB (1995) Dehydration melting of metabasalt at 8–32 kbar: implications for continental growth and crust–mantle recycling. J Petrol 36(4):891–931

Rapp RP, Watson EB, Miller CF (1991) Partial melting of amphibolite/eclogite and the origin of Archaean trondhjemites and tonalites. Precambrian Res 51:1–25

Respaut JP (1984) Géochronologie et géochimie isotopique U–Pb de la minéralisation uranifère de la mine des Pierres Plantées (Lozère) et de son encaissant: le massif granitique de la Margeride. Ph.D. thesis, University of Montpellier

R'Kha Chaham K, Couturié JP, Duthou JL, Fernandez A, Vitel G (1990) L'orthogneiss œillé de l'Arc de Fic : un nouveau témoin d'âge cambrien d'un magmatisme hyper alumineux dans le Massif Central français. C R Acad Sci Paris 311:845–850

Rossi P, Pin C (2008) Les magmatismes paléozoïques. La chaîne Varisque, Géochroniques 105:53–56

Sabatier H (1991) Vaugnerites: special lamprophyre-derived mafic enclaves in some Hercynian granites from Western and Central Europe. In: Didier J, Barbarin B (eds) Enclaves and granite petrology. Elsevier, Amsterdam, pp 63–81

Saint-Joanis R (1975) Étude géologique du socle cristallin du Bas-Livradois (Massif central français) dans le périmètre de la feuille d'Issoire. Ph.D. thesis, Université Blaise Pascal, Clermont-Ferrand

Scarrow JH, Bea F, Monter PG, Molina JF (2008) Shoshonites, vaugnerites and potassic lamprophyres: similarities and differences between 'ultra'-high-K rocks. Trans R Soc Edimburgh 99:159–175

Schilling FR, Partzsch GM (2001) Quantifying partial melt fraction in the crust beneath the central Andes and the Tibetan Plateau. Phys Chem Earth 26:239–246

Schulmann K, Lexa O, Štípská P, Racek M, Tajčmanová L, Konopásek J, Edel JB, Pescler A, Lehmann J (2008) Vertical extrusion and horizontal channel flow of orogenic lower crust: key exhumation mechanisms in large hot orogens? J Metamorph Geol 26:273–297

Schulz B (2014) Early Carboniferous P-T path from the Upper Gneiss Unit of Haut-Allier (French Massif Central)–reconstructed by geothermobarometry and EMP-Th–U–Pb monazite dating. J Geosci, pp 327–349

Singh J, Johannes W (1996) Dehydration melting of tonalites. 2. Compositions of melts and solids. Contrib Mineral Petrol 125:26–44

Sisson T, Ratajeski K, Hankins W, Glazner A (2005) Voluminous granitic magmas from common basaltic sources. Contrib Mineral Petrol 148:635–661

Skjerlie KP, Johnston AD (1996) Vapour-absentmelting from 10 to 20 kbar of crustal rocks that containmultiple hydrous phases: implications for anatexis in the deep to very deep continental crust and active continental margins. J Petrol 37:661–691

Solgadi F, Moyen JF, Vanderhaeghe O, Sawyer EW, Reisberg L (2007) The relative roles of crustal anatexis and mantle-derived magmas: generation of Synorogenic, Hercynian granites in the Livradois area, French Massif Central. Can Mineral 45:581–606

Stampfli GM, Hochard C, Vérard C, Wilhem C, von Raumer J (2013) The formation of Pangea. Tectonophysics 593:1–19

Stussi JM, De la Roche A (1984) Le magmatisme orogénique granitique de la chaîne varisque française. Typologie chimique et répartition spatiale. C R Acad Sci Paris (Série 2) 298:43–48

Supply P (1981) Géochronologie U–Pb et pétrologie des enclaves granulitiques de Bournac (Massif Central), M.Sc. thesis, University of Montpellier

Tatsumi Y, Suzuki T (2009) Tholeiitic versus calc-alkalic differentiation and evolution of arc crust: constraints from melting experiments on a basalt from the Izu–Bonin–Mariana Arc. J Petrol 50(8):1575–1603

Turpin L, Velde D, Pinte G (1988) Geochemical comparison between minettes and kersantites from the Western European Hercynian orogen: trace element and Pb–Sr–Nd isotope constraints on their origin. Earth Planet Sci Lett 87:73–86

Turpin L, Cuney M, Friedrich M, Bouchez JL, Aubertin M (1990) Meta-igneous origin of Hercynian peraluminous granites in N.W. French Massif Central: implications for crustal history reconstructions. Contrib Mineral Petrol 104:163–172

van Hunen J, Allen MB (2011) Continental collision and slab breakoff: a comparison of 3-D numerical models with observations. Earth Planet Sci Lett 302(1–2):27–37

Vanderhaeghe O (2009) Migmatites, granites and orogeny: flow modes of partially molten rocks and magmas associated with melt/solid segregation in orogenic belts. Tectonophysics 477:119–134

Vanderhaeghe O (2012) The thermal–mechanical evolution of crustal orogenic belts at convergent plate boundaries: a reappraisal of the orogenic cycle. J Geodynamics 56–57:124–145

Vanderhaeghe O, Duchêne S (2010) Crustal-scale mass transfer, geotherm and topography at convergent plate boundaries. Terra Nova 22:315–323

Vanderhaeghe O, Teyssier C (2001) Partial melting and flow of orogens. Tectonophysics 342:451–472

Vanderhaeghe O, Burg JP, Teyssier C (1999) Exhumation of migmatites in two collapsed orogens: Canadian cordillera and French Variscides. In: Ring U, Brandon MT, Lister GS, Willett SD (eds) Exhumation processes: normal faulting, ductile flow and erosion. Geological Society of London Special Publication vol 154, pp 181–204

Vermeesch P (2012) On the visualisation of detrital age distributions. Chem Geol 312–313:190–194

Vielzeuf D, Holloway JR (1988) Experimental determination of the fluid-absent melting relations in the pelitic system. Contrib Mineral Petrol 98:257–276

Vielzeuf D, Montel JM (1994) Partial melting of metagreywackes. 1. Fluid-absent experiments and phase relationships. Contrib Mineral Petrol 117:375–393

von Raumer JF, Stampfli GM, Borel G, Bussy F (2002) Organization of pre-Variscan basement areas at the north-Gondwanan margin. Int J Earth Sci 91:35–52

von Raumer JF, Finger F, Veselá P, Stampfli GM (2013) Durbachites-Vaugnerites—a geodynamic marker in the central European Variscan orogen. Terra Nova. doi:10.1111/ter.12071

Walker BA, Miller CF, Claiborne LL, Wooden JL, Miller JS (2007) Geology and geochronology of the Spirit Mountain batholith, southern Nevada: implications for timescales and physical processes of batholith construction. J Volcanol Geothermal Res 167(1–4):239–262

Watkins JM, Clemens JD, Treloar PJ (2007) Archaean TTGs as sources of younger granitic magmas: melting of sodic metatonalites at 0.6–1.2 GPa. Contrib Mineral Petrol 154:91–110

Watson EB, Harrison TM (1983) Zircon saturation revisited—temperature and composition effects in a variety of crustal magma types. Earth Planet Sci Lett 64:295–304

Williamson BJ, Downes H, Thirlwall MF (1992) The relationship between crustal magmatic underplating and granite genesis: an example from the Velay granite complex, Massif Central, France. Trans R Soc Edinb Earth Sci 83:235–245

Williamson BJ, Shaw A, Downes H, Thirlwall MF (1996) Geochemical constraints on the genesis of Hercynian two-mica leucogranites from the Massif Central, France. Chem Geol 127:25–42

Williamson B, Downes H, Thirlwall M, Beard A (1997) Geochemical constraints on restite composition and unmixing in the Velay anatectic granite, French Massif Central. Lithos 40(2–4):295–319

Wolf MB, Wyllie PJ (1994) Dehydration-melting of amphibolite at 10 kbar: the effects of temperature and time. Contrib Mineral Petrol 115:369–383

Zeh A, Gerdes A (2010) Baltica- and Gondwana-derived sediments in the Mid-German Crystalline Rise (Central Europe): implications for the closure of the Rheic ocean. Gondwana Res 17:254–263

Zeh A, Brätz H, Millar IL, Williams IS (2001) A combined zircon SHRIMP and Sm-Nd isotope study on high-grade paragneisses from the Mid-German Crystalline Rise: evidence for northern Gondwanan and Grenvillian provenance. J Geol Soc Lond 158:983–994

5.2 Additional data: zircon U–Pb dating of the Monts-du-Lyonnais synkinematic granitoids

5.2.1 Regional context and investigated sample

In the southern part of the Monts–du–Lyonnais area (see Fig. 3.1), the metamorphic lithologies of the Upper Gneiss Unit are intruded by the synkinematic Montagny, Saint-Héand, Soucieu and Grand-Chemin (or Civrieux-d'Azergues) granitoids emplaced along N45 dextral strike-slip shear zones (Feybesse et al., 1995; Gay et al., 1981). Those granitoids are of primary interest as they mark the latest stage of regional polyphase ductile deformation, thought to have occured at T < 600°C, and thus post-date eclogite-, granulite- and amphibolite-facies metamorphism (Costa et al., 1993; Feybesse et al., 1995; Gardien et al., 1990; Lardeaux et al., 1989; 2001).

Therefore, determination of their emplacement age would provide critical constrains on the P-T-t paths experienced by the Upper Gneiss Unit in the Monts-du-Lyonnais area. Ar–Ar dating of biotite and muscovite yielded cooling ages in the range 345–340 Ma (Costa et al., 1993) slightly older than the age obtained via the whole-rock Rb–Sr geochronometer (332 ± 10 Ma, Gay et al., 1981). Section 5.1 presents new geochronological data from vaugnerites closely associated with the synkinematic granitoids and regarded as coeval by Michon (1979) and Sabatier (1984). The inferred zircon U–Pb emplacement ages of 335.7 ± 2.1 and 333.9 ± 1.4 are in better agreement with the Rb–Sr results. To clarify the actual age of synkinematic magmatism, an additional granitoid sample was collected for zircon U–Pb age determination. Sample RV-3 was taken from in the former Riverie quarry at the place known as "Les Roches" (see Part I). It corresponds to a 10-cm thick biotite-bearing granite vein concordant in the foliation of amphibole-bearing gneisses. Constituent minerals are Qz, Pg (An_25, see Appendix Table B3), Kfs and Bt. Amphibole is typically lacking.

Polished 150 µm-thick sections were made and zircon identified by making automated Zr maps using a Merlin SEM at SUN. U–Pb dating was conducted *in situ* on the thick sections after BSE–CL imaging of the previously located grains (using the same SEM). Zircon grains are very small, often < 60 µm in length, and show a broad range of aspect ratios, from 1:2 to 1:9. Inherited cores are extremely scarce and, when observed, CL-brighter than the rims. The latter often display typical oscillatory zoning even though a few grains appear homogeneous.

5.2.2 U–Pb results and emplacement age

LA–ICP–MS U–Pb dating was conducted at SUN with a spot diameter of 20 µm (26th of October 2016, with the assistance of Riana Rossouw, see Appendix B.3.2 for analytical procedures and Tables B5 and B8 for the comprehensive dataset). Out of 53 analyses, only four are concordant with $^{206}Pb/^{238}U$ dates clustering between 334 ± 6 and 339 ± 6 Ma (spots b194 and b191, respectively, Fig. 5.1b). Thirteen analyses yielded discordant $^{206}Pb/^{238}U$ dates in the same range. These spots trend along a mixing line between common and radiogenic (anchored by the concordant population) Pb compositions at 335 Ma (Fig. 5.1b). Four discordant measurements show older $^{206}Pb/^{238}U$ dates, up to 452 ± 7 Ma (b185). The 32 remaining analyses have younger $^{206}Pb/^{238}U$ dates, from 331 ± 6 (b179) down to 261 ± 5 Ma (b177).

Given the scarcity of inherited cores and the typical magmatic oscillatory zoning evidenced by CL-images, I interpret the concordant zircon population as having crystallized from the melt phase. The best estimate of the crystallization age is given by the lower intercept of the mixing trend: 335.8 ± 4.4 Ma (including systematic errors). Spots yielding older $^{206}Pb/^{238}U$ dates would have sampled inherited zircon domains unidentified during CL imaging. Younger dates would result from a combination of Pb loss and common Pb incorporation, which respective contributions cannot be retrieved.

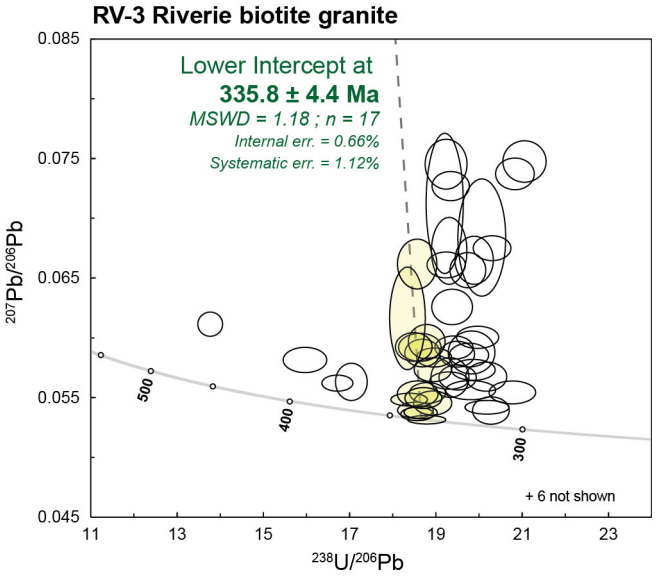

Figure 5.1: Tera–Wasserburg diagrams ($^{238}U/^{206}Pb$ vs. $^{207}Pb/^{206}Pb$) showing zircon data for the RV-3 synkinematic granite from the Monts–du–Lyonnais area. Error ellipses/ages are quoted at 2σ level of uncertainty. Yellowish ellipses are those included in age calculations.

5.2.3 Conclusion

This newly obtained emplacement age confirms that: (i) vaugnerites and granites from the southern Monts-du-Lyonnais area are coeval; (ii) the late increment of deformation, probably at the origin of the N45-trending regional foliation, is as young as c. 335 Ma and post-dates peak metamorphism which age has been independently estimated in this same outcrop at c. 360 Ma (see Part I).

5.3 Article #3: The mantle source of "vaugnerites" and other post-collisional mafic magmas

This contribution has been published in Earth and Planetary Science Letters. In the course of my M.Sc., I sampled all but two of the igneous rocks presented in this study with the help of Jean-François Moyen, Arnaud Villaros and Adrien Vezinet and prepared them for whole-rock geochemical determinations. I extracted the zircon grains and performed the Lu–Hf isotope measurements at GUF under the supervision of Oscar Laurent and Armin Zeh. Pilar Montero analysed the grains for O isotopes. During my Ph.D., I compiled geochronological and geochemical data available from the literature and wrote the manuscript with significant help from Oscar Laurent, Jean-François Moyen and Pierre Bouilhol.

Earth and Planetary Science Letters 456 (2016) 182–195

Contents lists available at ScienceDirect

Earth and Planetary Science Letters

www.elsevier.com/locate/epsl

Post-collisional magmatism: Crustal growth not identified by zircon Hf–O isotopes

Simon Couzinié [a,b,*], Oscar Laurent [c,d], Jean-François Moyen [a], Armin Zeh [c,e], Pierre Bouilhol [f], Arnaud Villaros [g,h,i]

[a] Univ. Lyon, UJM-Saint-Etienne, UBP, CNRS, IRD, Laboratoire Magmas et Volcans UMR 6524, F-42023 Saint Etienne, France
[b] University of Stellenbosch, Department of Earth Sciences, Private Bag X1, 7602 Matieland, South Africa
[c] J.W. Goethe Universität, Institut für Geowissenschaften, Altenhöferallee 1, D-60438 Frankfurt am Main, Germany
[d] Université de Liège, Département de Géologie B20, Quartier Agora, allée du six Août 12, B-4000 Liège, Belgium
[e] Karlsruher Institut für Technologie, Campus Süd, Institut für Angewandte Geowissenschaften, Abteilung Mineralogie und Petrologie, Kaiserstrasse 12, D-76131 Karlsruhe, Germany
[f] Department of Earth Sciences, Durham University, Science Labs, Durham DH13LE, United Kingdom
[g] Université d'Orléans, ISTO, UMR 7327, 45071, Orléans, France
[h] CNRS, ISTO, UMR 7327, F-45071 Orléans, France
[i] BRGM, ISTO, UMR 7327, BP 36009, 45060 Orléans, France

ARTICLE INFO

Article history:
Received 9 March 2016
Received in revised form 19 September 2016
Accepted 21 September 2016
Available online 20 October 2016
Editor: A. Yin

Keywords:
post-collisional mafic magmas
crustal growth
zircon
Lu–Hf isotopes
O isotopes
metasomatized mantle

ABSTRACT

The combination of U–Pb, Lu–Hf and O isotopic analyses in global zircon databases has recently been used to constrain continental crustal growth and evolution. To identify crust-forming events, these studies rely on the assumption that new crust is formed from depleted mantle sources. In contrast, this work suggests that post-collisional mafic magmas and their derivatives represent a non-negligible contribution to crustal growth, despite having zircons with "crust-like" Hf–O isotopic characteristics. We address this paradox and its implications for crustal evolution on the basis of a case study from the Variscan French Massif Central (FMC). The late stages of continental collisions are systematically marked by the emplacement of peculiar mafic magmas, rich in both compatible (Fe, Mg, Ni, Cr) and incompatible elements (K_2O, HFSE, LREE) and displaying crust-like trace element patterns. This dual signature is best explained by melting of phlogopite- (and/or amphibole-) bearing peridotite, formed by contamination of the mantle by limited amounts (10–20%) of crustal material during continental subduction shortly preceding collision. Mass balance constraints show that in melts derived from such a hybrid source, 62–85% of the bulk mass is provided by the mantle component, whereas incompatible trace elements are dominantly crustal in origin. Thereby, post-collisional mafic magmas represent significant additions to the crust, whilst their zircons have "crustal" isotope signatures (e.g. $-2 < \varepsilon Hf_t < -9$ and $+6.4 < \delta^{18}O < +10‰$ in the FMC). Because post-collisional mafic magmas are (i) ubiquitous since the late Archean; (ii) the parental magmas of voluminous granitoid suites; and (iii) selectively preserved in the geological record, zircons crystallized from such magmas (and any material derived from their differentiation or reworking) bias the crustal growth record of global zircon Hf–O isotopic datasets towards ancient crust formation and, specifically, may lead to an under-estimation of crustal growth rates since the late Archean.

1. Introduction

The formation of the continental crust is a major consequence of planetary differentiation and played a key role in the evolution of climate and life (Campbell and Allen, 2008; Lowe and Tice, 2004). The mechanisms and rates of continental formation are therefore fundamental parameters to be addressed and have long been a matter of controversy (Arndt, 2013; Hawkesworth et al., 2010). The formation of new continental crust requires two fundamental conditions to be fulfilled, regardless of the tectonic setting in which it takes place: (1) genesis (and differentiation) of mantle-derived igneous material; and (2) long-term incorporation and preservation of this material into the pre-existing continen-

* Corresponding author at: Univ. Lyon, UJM-Saint-Etienne, UBP, CNRS, IRD, Laboratoire Magmas et Volcans UMR 6524, F-42023 Saint Etienne, France.
E-mail addresses: simon.couzinie@univ-st-etienne.fr, simon.couzinie@ens-lyon.org (S. Couzinié).

http://dx.doi.org/10.1016/j.epsl.2016.09.033
0012-821X/

Table 1
Summary of the main documented occurrences of PCMM in the geological record.

Orogen	Age of PCMM	Specific nomenclature	Differentiates	Proposed references
Late Archean terranes	2950 to 2500 Ma	Sanukitoid	Sanukitoid suite	Laurent et al. (2014a)
Svecofennian (Scandinavia)	1800 Ma	Ladogite, Nevoite	Post-kinematic granitoids	Rutanen et al. (2011)
Pan-African	620–560 Ma	Sanukitoid	High-K calc-alkaline (HKCA) granitoids	Liégeois et al. (1998)
Ross (Antarctica)	515–500 Ma	*No specific name given*	*No specific name given*	Hagen-Peter et al. (2015)
East Kunlun (China)	c. 450 Ma	Appinite	*Not described*	Xiong et al. (2015)
Caledonian	425–410 Ma	Appinite	High Ba–Sr granites	Fowler and Rollinson (2012)
Central Asian Orogenic Belt	425 to 300 Ma (several pulses)	Sanukitoid	*Not described*	Yin et al. (2015)
Variscan	335–300 Ma	Vaugnerite, Durbachite, Redwitzite, Appinite	Felsic durbachites; K-rich calc-alkaline granitoids (KCG)	Moyen et al. (in press); Holub (1997); von Raumer et al. (2014)
North China Block assembly (Dabie-Sulu orogen…)	320 to 115 Ma (several pulses)	Appinite	Post-collisional granitoids	Zhao et al. (2013)
Himalaya	20 to 3 Ma	Post-collisional (ultra)potassic magmas	(Ultra)potassic silicic magmas	Williams et al. (2004)

tal volume (Condie et al., 2011; Hawkesworth et al., 2009; Stern and Scholl, 2010). Radiogenic isotope systems like Rb/Sr, Sm/Nd and Lu/Hf are extensively used to track crust-forming events, and it is consensually assumed that the radiogenic isotope composition of newly-formed crust is identical to that of the depleted mantle (DM) (McCulloch and Wasserburg, 1978; Patchett et al., 1982; Vervoort and Blichert-Toft, 1999).

In this respect, the study of continental growth recently benefited from advances in analytical techniques enabling *in situ* isotopic measurements in zircon, a widespread accessory mineral of continental igneous rocks. Because zircon is able to survive several metamorphic, igneous and sedimentary cycles and contains a wealth of isotopic information (U–Pb, Lu–Hf, O isotopes), it represents an outstanding archive of crust formation and evolution (Bouilhol et al., 2013; Bouilhol et al., 2011; Condie et al., 2011; Roberts and Spencer, 2015). The analyses of U–Pb and Lu–Hf isotope compositions within the same zircon give access to both the age and the Hf isotopic signature of the magma in which it crystallized (Griffin et al., 2002; Woodhead et al., 2004). The latter is converted into a crustal residence ("model") age corresponding to the time at which the crustal source of the zircon-hosting magma would have been extracted from the DM (Kemp et al., 2006). The coupled analysis of O isotopes has been proposed to discriminate between zircons crystallized from magmas having a sedimentary source ($\delta^{18}O > 6.5‰$; Kemp et al., 2006; Valley et al., 1998) and thus, meaningless "mixed" model ages (Arndt and Goldstein, 1987), from those having an ultimately mantle-derived source ($\delta^{18}O \sim 5.5 \pm 1.0‰$) and supposed to yield reliable model ages (Hawkesworth and Kemp, 2006). Accordingly, statistical analyses of U–Pb–Hf(–O) isotopic databases from both igneous and detrital zircons were extensively used to quantify the timing, amount and mechanisms of continental crust formation through time (Belousova et al., 2010; Dhuime et al., 2012; Hawkesworth and Kemp, 2006; Lancaster et al., 2011).

Nevertheless, the reliability of this approach has recently been questioned, especially because incorporation in the mantle of continental crust-derived materials (subducted supracrustal lithologies and/or any fluid/melt generated from them) may significantly blur the zircon Hf–O isotope signatures, a problem that has not been thoroughly taken into account in crustal evolution models (Payne et al., 2016; Roberts et al., 2012; Roberts and Spencer, 2015). Mafic magmas emplaced shortly after continental collision represent a typical, yet poorly considered case: although of unambiguous mantle origin (Bonin, 2004), they display "crustal" whole-rock radiogenic isotopes compositions (Nelson, 1992; Turpin et al., 1988) and zircon Hf isotopic signatures (e.g. Heilimo et al., 2013; Laurent and Zeh, 2015; Liu et al., 2014; Siebel and Chen, 2009; Zhao et al., 2013). Although such mafic magmas are ubiquitous amongst orogenic systems since the late Archean and may be the parent of volumetrically important granite suites (Fowler and Henney, 1996; Laurent et al., 2013), little attention has been paid so far to their role in the formation of new crust, as well as the impact of their ambiguous isotopic signatures on continental evolution models.

This study aims to review the characteristics and petrogenesis of post-collisional mafic magmas; propose a unified model to explain their origin; quantify to what extent they contribute to the formation of new crust; and address the potential biases introduced by their zircon Hf–O isotopic signature in global, zircon-based crustal evolution models. We address these issues using: (i) a new, comprehensive geochemical and zircon Hf–O isotopic dataset of post-collisional mafic magmas from the Variscan French Massif Central, and (ii) a global compilation of geochemical data from similar rocks over geological time.

2. Post-Collisional Mafic Magmas (PCMM)

2.1. Geological setting

Hereafter, the post-collisional period is referred to as the stage of the orogenic cycle immediately following the docking of two continental masses. Voluminous magmatism, often referred to as "syn- to post-collisional" (Bonin, 2004), takes place at that stage. The corresponding volcanic/plutonic rocks belong to two contrasting suites: (i) a peraluminous silicic suite, originating from melting of the local crust; and (ii) a mafic-felsic high-K calc-alkaline association in which the felsic material is generally regarded as the result of differentiation of the mafic parental melt, with varying contributions (assimilation/mixing) from the older crust (Bonin, 2004; Küster and Harms, 1998; Laurent et al., 2013; Liégeois et al., 1998; Moyen et al., in press). In this contribution, we focus on the genesis of the mafic parents of the high-K calc-alkaline suite that will be referred to as Post-Collisional Mafic Magmas (PCMM) hereafter. PCMM have been recognized in most orogenic systems since the late Archean, especially those corresponding to the amalgamation of the main supercontinents in Earth history (Table 1; see also Murphy, 2013). Because of their peculiar characteristics, they are often mentioned using local, non-IUGS nomenclature (Table 1) that hampers a comprehensive view of their global significance.

2.2. Case study: the Variscan French Massif Central

The Variscan belt of western Europe (Fig. 1a) was formed during the assembly of Pangea, as a result of the convergence between Laurussia and Gondwana from 420 to 295 Ma. In the eastern French Massif Central (FMC), continental collision took place

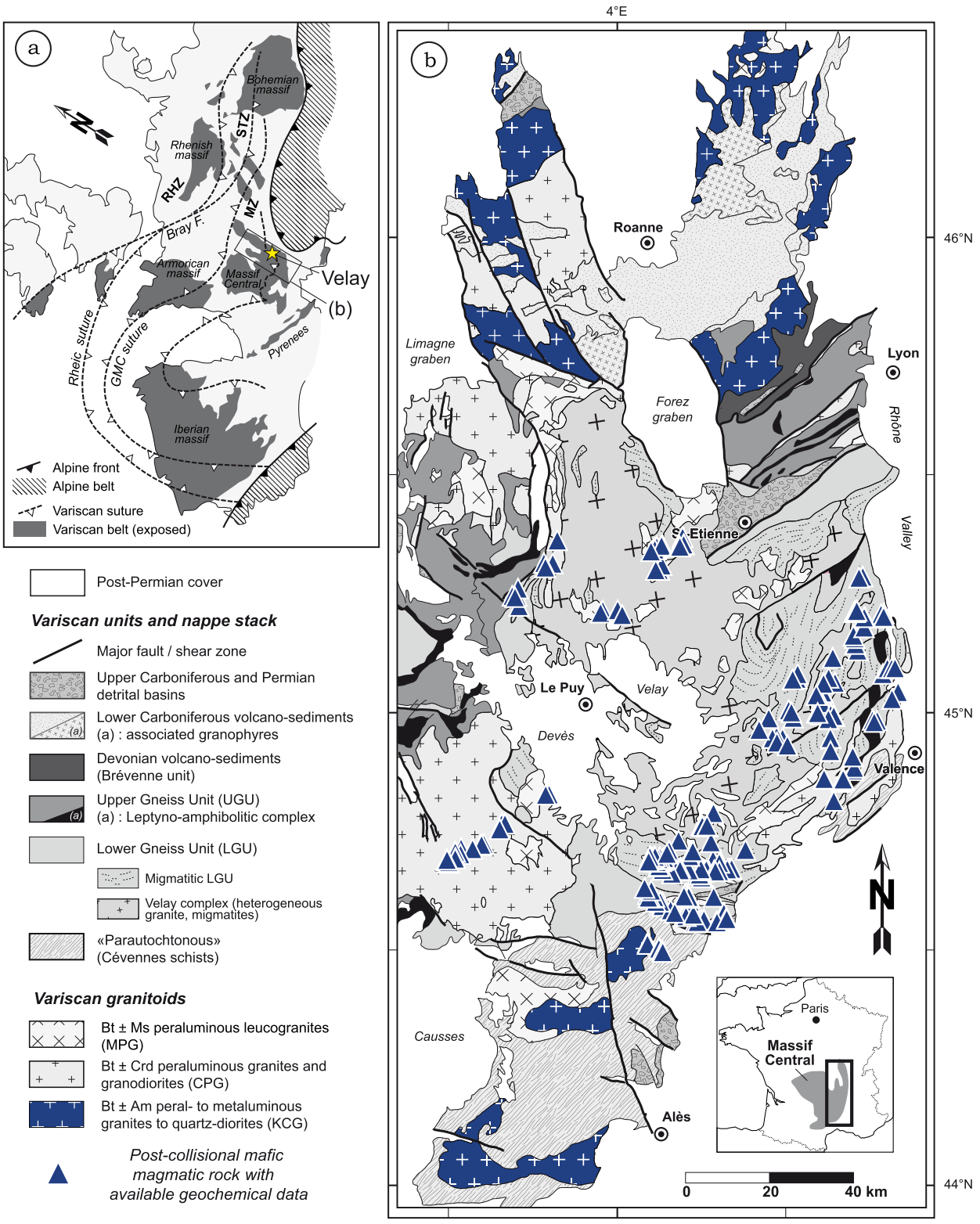

Fig. 1. (a) General location of the Variscan belt of Europe and inferred suture zones. Abbreviations: GMC Galicia-Massif Central, STZ Saxo-Thurigian Zone, RHZ Rhenohercynian Zone, MZ Moldanubian Zone. The yellow star highlights the location of the Velay Complex. (b) Geological map of the eastern French Massif Central (Velay area) redrawn after Chantraine et al. (1996). Post-collisional mafic magmas (triangles) and their derivatives (granite bodies in blue) are highlighted. The inset shows the location of the study area within the Massif Central. (For interpretation of the references to color in this figure legend, the reader is referred to the web version of this article.)

at c. 360–340 Ma and was followed by orogenic extension and collapse. The latter stage was associated with significant crustal melting resulting in widespread granite magmatism and the formation of granite–migmatite domes (e.g. Velay Complex) (Ledru et al., 2001 and references therein). PCMM are present throughout the Variscan belt (von Raumer et al., 2014). In the eastern FMC, they intruded the crust from c. 335 to 300 Ma (Couzinié et al., 2014; Laurent et al., 2015), forming meter- to hectometer-sized (monzo)diorite to monzonite bodies in granites/migmatites; and dykes at shallower crustal levels (Couzinié et al., 2014). These rocks

consist of an assemblage of plagioclase, amphibole, biotite and clinopyroxene; with orthopyroxene, K-feldspar and quartz in subordinate and various proportions (Sabatier, 1991). Accessory minerals include apatite, allanite, titanite and zircon. Like in other PCMM occurrences worldwide (e.g. Laurent et al., 2014a; Murphy, 2013), the predominance of biotite and/or amphibole as main mafic minerals points to high H_2O contents in the original magma. In the FMC, a suite of K-rich calc-alkaline granitoids demonstrably results from differentiation of PCCM with little or no input from the older crust (Moyen et al., in press). In this area, PCMM and their derivatives represent ≈10% of the exposed surface (Moyen et al., in press).

2.3. Samples, methods and data compilation

In this study, we present new whole-rock geochemical data and a new zircon Lu–Hf and O isotope dataset on PCMM from the eastern FMC (Fig. 1b). The whole-rock major and trace element compositions of 27 samples are reported in the Supplementary Material (Table S1). The Hf isotopic composition of zircons from 12 samples was measured by laser ablation – multicollector – inductively coupled plasma – mass spectrometry (LA-MC-ICP-MS) at Goethe Universität Frankfurt, Germany, after imaging of internal zircon structures (cathodoluminescence and back-scattered electron images) by scanning electron microscopy. The zircons were previously analyzed for U–Pb isotopes by LA-ICP-MS for age determination (Laurent et al., 2015). Out of the 12 samples investigated for Hf isotopes, zircons from 8 samples were also analyzed for O isotopes by SHRIMP at the University of Granada, Spain. The nature and ages of the investigated samples are detailed in Table 2; the Supplementary Material contains details about analytical methods, results of standard measurements (Table S2 for Hf and S4 for O) and the complete datasets (Table S3 for Hf, Table S5 for O).

We also present a compilation of data from PCMM worldwide, available in the Supplementary Materials and including whole-rock geochemistry ($N_{samples} = 1647$; Table S6) and zircon Hf ($N_{spots} = 2425$; Table S7) and O ($N_{spots} = 633$; Table S8) isotopes.

3. Whole-rock geochemistry and Hf–O isotope composition of PCMM

3.1. Whole-rock geochemistry

PCMM all share similar geochemical features (Fig. 2). They are mafic to intermediate (44 to 63 wt.% SiO_2) and dominantly plot in the high-K calc-alkaline to shoshonite fields (Fig. 2a). PCMM typically show a dual geochemical signature characterized by richness in both compatible and incompatible elements (Fowler and Rollinson, 2012; Holub, 1997; Laurent et al., 2014b). In PCMM from the FMC, this is best illustrated by high contents in both K_2O (1.0–7.5 wt.%) and $FeO_t + MgO$ (7–25 wt.%) (Fig. 2b). Likewise, both Ba + Sr (0.1–0.6 wt.%) and Ni + Cr contents (50–1000 ppm) are very high (Fig. 2c). Notably, there is no correlation whatsoever between compatible and incompatible elements (Fig. 2b, c). PCMM display high LREE and HFSE contents (Fig. 2d), together with crust-like incompatible trace element patterns systematically characterized by negative Nb–Ta and Ti anomalies (Fig. 2e). Strikingly, these rocks are markedly enriched in most incompatible elements (LILE, LREE, HFSE) relative to the bulk continental crust (Fig. 2e).

3.2. Hf isotopes

A compilation of available zircon Hf isotopic data from PCMM in various orogenic systems is presented in Fig. 3a. Apart from a few exceptions, such zircons display (sub-)chondritic $\varepsilon Hf_{(t)}$, clearly

Table 2
Summary of zircon Lu–Hf–O isotope data from post-collisional mafic magmatic rocks of the French Massif Central obtained in the course of this study.

Sample	Rock type (TAS, Middlemost, 1994)	Locality	Lat. N	Long. E	U–Pb age (Ma)[a]	±2σ	$^{176}Hf/^{177}Hf_{avg.}$[b]	±2 S.D.	Subset[c]	eHf(t)[d]	±2σ	T_{DM2} (Ga)[e]	N_{Lu-Hf}[f]	$\delta^{18}O$[g]	±2 S.D.	N_o[h]
PRC-53	Quartz Syenite	Pont-Rouge quarry	45°19'47''	4°06'05''	**318.9**	**1.8**	0.282413	0.000093	A	−6.1	3.3	1.58	18	8.21	0.87	20
PRC-54	Quartz Monzonite	Pont-Rouge quarry	45°19'47''	4°06'05''	**320.5**	**1.8**	0.282395	0.000070	A	−6.7	2.5	1.62	15	8.26	1.75	17
SC-13-02A	Quartz Monzodiorite	Moulin de Linas	44°41'14''	3°28'25''	**313.2**	**2.5**	0.282414	0.000088	A	−6.2	3.1	1.58	6	–	–	–
SC-13-05	Monzodiorite	L'Aldeyres	44°45'53''	3°37'53''	**309.4**	**1.5**	0.282410	0.000077	A	−6.3	2.7	1.59	14	–	–	–
SC-13-09	Quartz Monzodiorite	Pubellier	45°13'29''	3°39'33''	**309.7**	**1.2**	0.282483	0.000034	B	−3.8	1.2	1.45	16	8.10	0.58	15
533-1	Quartz Monzodiorite	Lamastre	44°58'24''	4°37'41''	**307.8**	**1.6**	0.282476	0.000045	B	−4.1	1.6	1.46	11	7.84	1.19	13
533-2	Diorite	Lamastre	44°58'24''	4°37'41''	**307.3**	**1.3**	0.282516	0.000041	B	−2.7	1.4	1.39	15	7.85	1.00	16
LR-31	Quartz Diorite	La Roche	45°17'05''	4°06'50''	**299.1**	**1.3**	0.282521	0.000041	B	−2.7	1.4	1.38	16	7.81	0.80	11
LR-32	Diorite	La Roche	45°17'05''	4°06'50''	**301.5**	**1.4**	0.282506	0.000051	B	−3.2	1.8	1.41	15	–	–	–
SGC-12-26	Monzodiorite	Pont-de-Bayzan	44°39'28''	4°18'24''	**306.1**	**1.3**	0.282502	0.000034	B	−3.2	1.2	1.41	15	7.32	0.92	23
SGC-12-39	Quartz Monzodiorite	Loubaresse	44°36'02''	4°04'14''	**306.6**	**1.6**	0.282485	0.000042	B	−3.8	1.5	1.45	16	–	–	–
SGC-12-42	Monzodiorite	Meyras	44°40'21''	4°16'26''	**305.9**	**1.7**	0.282461	0.000034	B	−4.7	1.2	1.49	14	7.43	1.15	16

[a] U–Pb intrusion age obtained by Laurent et al. (2015).
[b] Average $^{176}Hf/^{177}Hf$ ratio at the time of intrusion, calculated using the U–Pb intrusion age of the sample.
[c] Subset determined from Hf isotopes (see text).
[d] Calculated at the time of intrusion using the parameters of the Chondrite Uniform Reservoir (CHUR) recommended by Bouvier et al. (2008), i.e. present-day values of $^{176}Hf/^{177}Hf = 0.282785$ and $^{176}Lu/^{177}Hf = 0.0336$.
[e] Two stage model age in billion years using the measured $^{176}Lu/^{177}Hf$ of each spot (first stage = age of zircon), $^{176}Lu/^{177}Hf$ of 0.0113 for the average continental crust (second stage) (Taylor and McLennan, 1985), and $^{176}Lu/^{177}Hf$ and $^{176}Hf/^{177}Hf$ of 0.0384 and 0.28325, respectively, for evolution of the depleted mantle source.
[f] Number of individual Lu–Hf spots used in the calculation of the initial Hf isotope composition.
[g] Average $\delta^{18}O$ of the sample.
[h] Number of individual O spots used in the calculation of the O isotope composition.

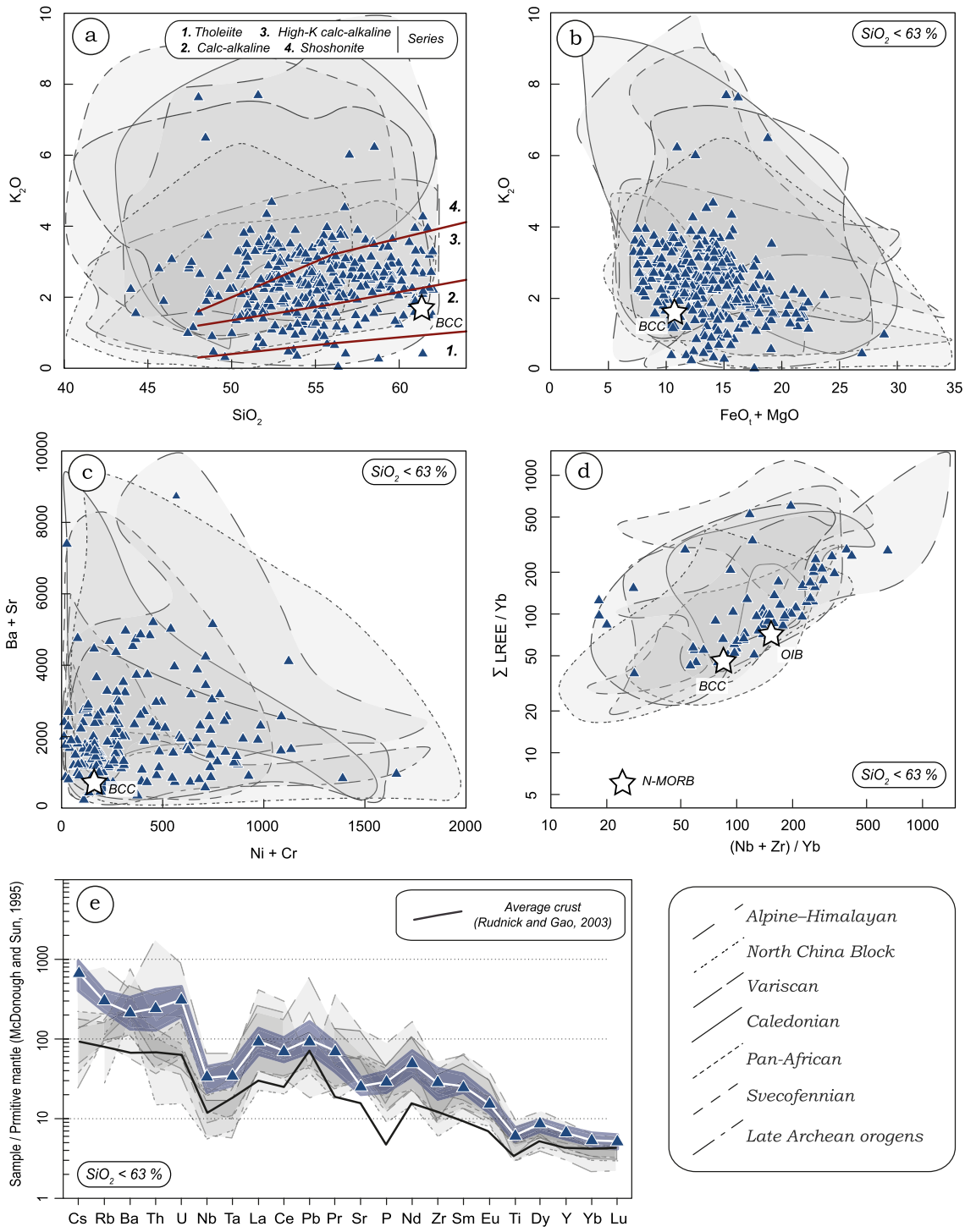

Fig. 2. Main geochemical features of post-collisional mafic magmatic rocks with special emphasis on the eastern FMC example (blue triangles). Each grey field illustrates the range of composition for similar rocks from other orogenic systems (data from Table S6). Plots of (a) K_2O vs. SiO_2 concentrations (the different series are after Peccerillo and Taylor, 1976); (b) K_2O vs. $MgO + FeO_t$ concentrations; (c) Large Ion Lithophile Elements ($Ba + Sr$) vs. transition element ($Ni + Cr$) concentrations and (d) sum of LREE ($La + Nd + Ce$) vs. HFSE ($Zr + Nb$) normalized to Yb; (e) Multi-element diagram normalized to the Primitive mantle (McDonough and Sun, 1995); the fields correspond to the 1st to 3rd quartile range of samples from the eastern FMC (in blue) and each other orogenic system (in grey), respectively. BCC stands for the Bulk Continental Crust (values from Rudnick and Gao, 2003), OIB for Ocean Island Basalts (values from Sun and McDonough, 1989), N-MORB for Normal-type Ocean Ridge Basalts (values from Sun and McDonough, 1989). (For interpretation of the references to color in this figure legend, the reader is referred to the web version of this article.)

differing from that of DM at the time of magma formation. This typical feature of PCMM is well reflected by rocks from the eastern FMC (Fig. 3b and Table 2). Zircon grains from such rocks show simple internal structures, without core–rim relationships and yield a single population of concordant U–Pb ages (Couzinié et al., 2014; Laurent et al., 2015). This argues for a single event of zircon formation during magma crystallization and limited or no host-rock assimilation. Hence, the initial Hf isotopic composition ($^{176}Hf/^{177}Hf_t$), can reliably be considered as representative of that of the magma at the time of zircon crystallization.

The newly-obtained zircon Hf dataset for PCMM from the FMC can be divided into two subsets (Table 1). **Subset A** comprises

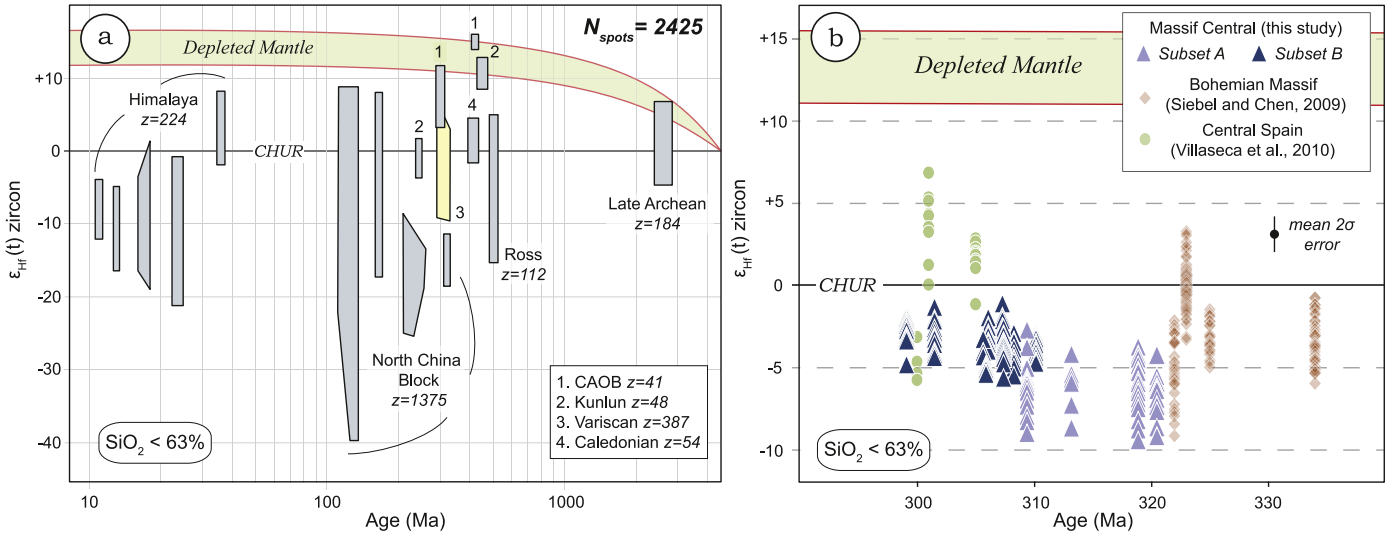

Fig. 3. (a) Compilation of available *in-situ* Hf isotope data for zircons from PCMM worldwide as a function of their intrusion age (note that the time-scale is logarithmic). Total number of zircon Hf measurements = 2425. The Variscan zircons (box 3) are shown in detail Fig. 3b. The $\varepsilon Hf_{(t)}$ range for the depleted mantle reservoir is bracketed by the models of Naeraa et al. (2012) (lowermost value) and Griffin et al. (2002) (uppermost value). Data from Table S7. (b) Measured zircon $\varepsilon Hf_{(t)}$ in post-collisional mafic rocks from the Variscan belt of Europe as a function of intrusion age. Additional data from Siebel and Chen (2009) and Villaseca et al. (2010).

the four oldest samples of the investigated dataset (309–320 Ma). The zircon $^{176}Hf/^{177}Hf_t$ ratios of samples from subset A range from 0.282319 ± 0.000032 to 0.282480 ± 0.000028 (2 S.E. – standard error), corresponding to subchondritic $\varepsilon Hf_{(t)}$ of −3.7 to −9.4 (Fig. 3b). **Subset B** includes the younger samples, all having ages in the range 299–310 Ma. Their zircons have $^{176}Hf/^{177}Hf_t$ ranging between 0.282441 ± 0.000026 and 0.282562 ± 0.000026 (2 S.E.) corresponding to subchondritic εHf_t of −1.1 to −5.0 (Fig. 3b). The εHf_t variability within a given sample is small (always <3 εHf-units) and in most cases close to the analytical uncertainties (i.e. ±1.1 εHf-units), indicating that zircons crystallized from a magma with homogeneous Hf isotope composition. Although some overlap occurs between the two groups, zircons from samples of subset A have more variable (the scatter is always >4 εHf-units for a given sample) and generally less radiogenic $^{176}Hf/^{177}Hf_t$ than samples from subset B, with most grains having εHf_t lower than −5 and down to −9.4 (Fig. 3b). Because of this large dispersion, the average εHf_t calculated for each sample of subset A is probably of little geological significance and the scatter may rather correspond to heterogeneous Hf isotope composition of the original magma.

3.3. Oxygen isotopes

Fig. 4a summarizes available *in situ* O isotopes measurements on PCMM zircons. The $\delta^{18}O_{SMOW}$ of zircons from PCMM are highly variable and range from +2.5 to +10‰. They are often out of the range of $\delta^{18}O_{SMOW}$ expected for zircons crystallizing from mantle-derived magmas, especially in the most recent (Himalayan, Variscan and Caledonian) orogens (Fig. 4a).

All zircon data from PCMM of the eastern FMC show high $\delta^{18}O_{SMOW}$ values (Fig. 4b), mostly between 6.39 ± 0.32 and 8.92 ± 0.26‰ (2 S.E. – standard error) with a few spots with even higher $\delta^{18}O_{SMOW}$ up to 9.97 ± 0.24. The variability per sample is typically large, >0.6‰ (2 S.D.), i.e. well above the range of analytical uncertainties (<0.3‰; see Table S5). This argues for heterogeneous O isotope compositions of the magmas at the time of zircon crystallization.

4. Discussion

4.1. Petrogenesis of PCMM in the FMC

4.1.1. Source vs. emplacement processes

The most mafic components of the PCMM suite in the FMC display low SiO_2 (<53%), with high $MgO + FeO_t$ (>12%) and transition element (Cr > 250 ppm. Ni > 120 ppm) contents. This demonstrates that the parental melt cannot be derived from crustal lithologies, but rather equilibrated with a(n) (ultra)mafic residue (i.e. peridotite/pyroxenite) (Holub, 1997; Sabatier, 1991). From that perspective, the high incompatible element contents and "crust-like" Hf–O isotopic signatures of PCMM could result from two distinct processes: (i) evolution of an incompatible element-poor, mantle-derived basaltic melt by fractionation and/or assimilation of crustal lithologies (i.e. AFC processes); or (ii) partial melting of a mantle source already enriched in K_2O, H_2O and LILE.

Several lines of evidence indicate that AFC cannot explain the geochemical signature of PCMM:

(1) Even starting from an "enriched" basaltic composition (i.e. OIB-like), considerable amounts of crystallization (>50%) are required to drive the incompatible element contents to the elevated concentrations observed in PCMM, such that the final melt would certainly not be mafic any more (Fig. 5a).
(2) Assimilation of continental crust during magma emplacement is precluded by the lower incompatible element contents of the most widespread crustal lithologies compared with PCMM, which holds true for both the FMC case and the global perspective (inset Fig. 5a).
(3) Even assuming that a crustal contaminant with the adequate trace element composition exists in the FMC and that only limited fractionation (≤20%) took place so that the final magma remained mafic, AFC calculations show that driving the Hf isotopic composition of a DM-derived basalt to that of the PCMM would require a crustal contaminant with $\varepsilon Hf_{310\,Ma}$ of −50 (Fig. 6a), corresponding to an early Archean crustal component (model age >3.6 Ga). This is extremely unlikely in the case of the FMC where the oldest crust is early Paleozoic to Neoproterozoic in age (Melleton et al., 2010).

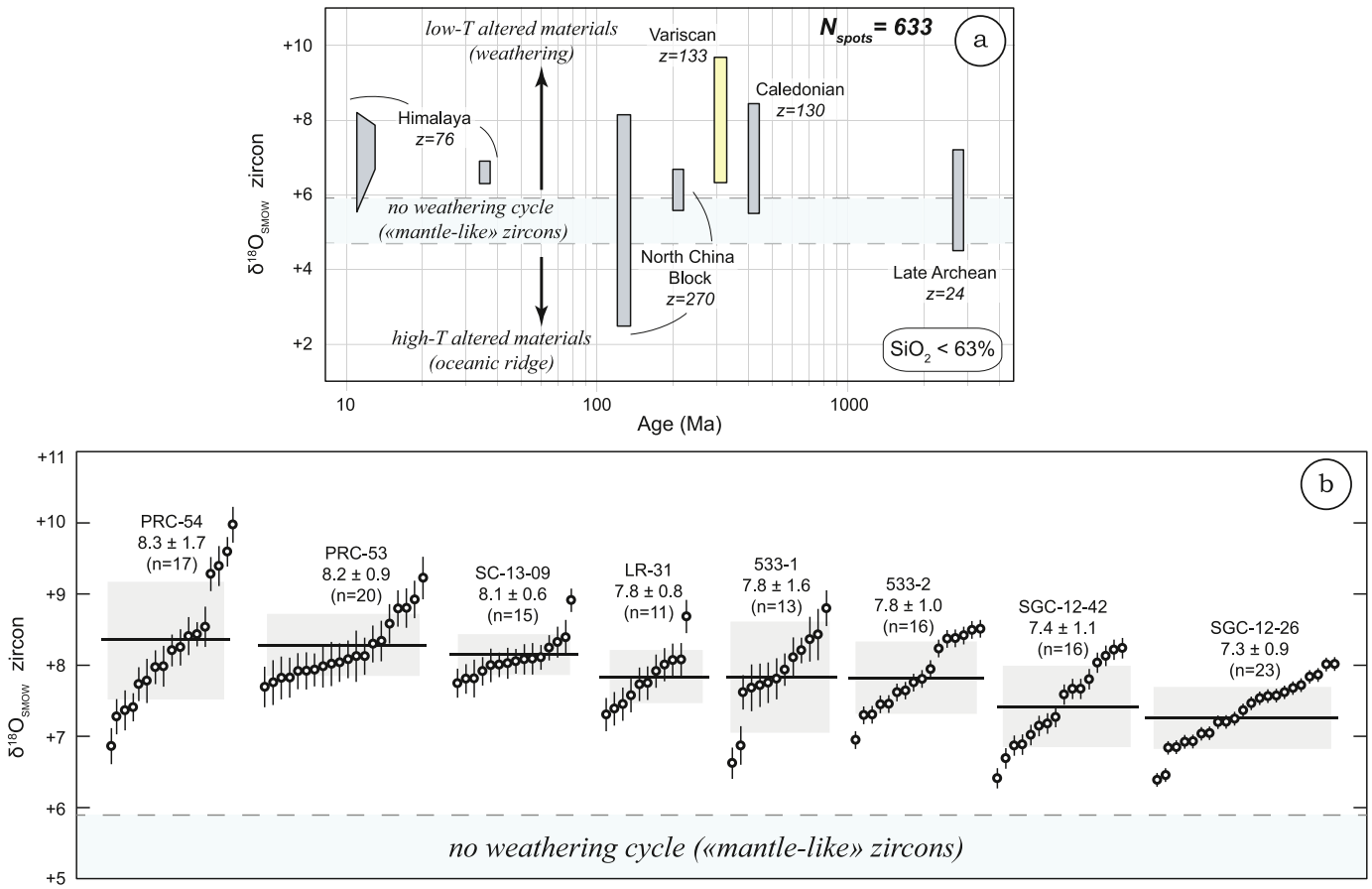

Fig. 4. (a) Compilation of *in-situ* O isotope data for zircons of post-collisional mafic rocks from worldwide occurrences. Total number of zircon measurements = 633. Data from Table S8. The $\delta^{18}O$ for the mantle is from Valley et al. (1998). Arrows for supra-crustal weathered materials and ridge-altered materials according to Bindeman (2008). (b) Zircon oxygen isotope composition of PCMM from the eastern French Massif Central. For each sample are displayed the mean and 2 S.D. confidence level. Error bars are the analytical standard errors of each measurement plotted at 2σ.

In contrast, PCMM plausibly represent primary melts derived from an anomalously K_2O-, LILE- and H_2O-rich mantle. Indeed, experimental melting of phlogopite- and/or amphibole-bearing (i.e. K-rich) peridotites, particularly spinel-lherzolites, yields melts with major element compositions matching those of PCMM from the FMC (Fig. 5b) (Conceição and Green, 2004; Condamine and Médard, 2014; Green, 2015; Mengel and Green, 1989; Thibault et al., 1992). Importantly, experiments conducted with mixed peridotite + felsic (granitoid) starting materials produce melts of similar compositions (Mallik et al., 2015; Prouteau et al., 2001; Rapp et al., 2010). The two sets of experiments are equivalent from a petro-geochemical point of view because, in the second approach, the mixture yields a phlogopite- and/or amphibole-bearing peridotite/pyroxenite in equilibrium with a mafic K-rich melt. Therefore, experimental evidence unequivocally shows that hybridization between peridotite and a felsic component is required to explain the major-element composition of PCMM (irrespective of the hybridization mechanism and the exact nature of the felsic component, which are discussed in §4.1.2).

The same conclusion can be drawn for trace elements. We calculated the REE contents of a melt generated from a hybrid source consisting of 75–90% DM and 10–25% of a LREE-rich component (having the composition of the bulk continental crust). Fig. 5c shows that the resulting melts (for 5 to 20% melting) match the composition of PCMM from the FMC, again with a better fit for a spinel-facies source.

Therefore, we propose that PCMM in the FMC result from partial melting, at <2 GPa, of a phlogopite-/amphibole-bearing peridotite (or pyroxenite) corresponding to mantle domains enriched in K_2O, H_2O and other incompatible elements.

4.1.2. Mechanism of mantle enrichment and nature of the metasomatic agent

Considering that they reflect the composition of the hybrid mantle source, the observed negative εHf_t signatures in PCMM zircons can be explained by two distinct scenarios: (i) contamination of the mantle (with $\varepsilon Hf_t >> 0$) by crustal material with strongly negative Hf isotope composition ($\varepsilon Hf_t << 0$) shortly prior to PCMM formation; or (ii) a long time span between mantle contamination (by any material having low $^{176}Lu/^{177}Hf$) and PCMM formation, whereby the initial decrease of the mantle $^{176}Lu/^{177}Hf$ ratio leads to a time-integrated, non-radiogenic Hf isotope composition.

Several lines of evidence clearly favor the first hypothesis. Firstly, the mantle beneath the FMC (sampled as xenoliths in Cenozoic volcanoes) do not show evidence for any geological event older than ca. 0.6 Ga (Wittig et al., 2007), which is also the age of the oldest autochtonous crust (Melleton et al., 2010). In contrast, the strongly negative εHf_t of PCMM zircons in the FMC would require the involvement of much older mantle, of at least Mesoproterozoic age (>1.1 Ga, considering an unlikely $^{176}Lu/^{177}Hf = 0$ for the source). Secondly, prior to the emplacement of PCMM in the late Carboniferous (330–300 Ma), other mafic magmas were emplaced throughout the FMC during the late Devonian and early Carboniferous (380–360 Ma) and contrastingly show positive bulk-rock εNd_t (+1 to +5, up to +8) (Pin and Paquette, 1997, 2002), indicative of a depleted mantle origin. If any long-term enriched mantle could have survived underneath the

FMC, it is difficult to envisage that it would have been sampled by magmatism at ca. 330–300 Ma, but not at 380–360 Ma, especially since "enriched" upper mantle domains are particularly prone to melting (solidus temperatures as low as 1025–1075 °C at 1 GPa; Conceição and Green, 2004; Condamine and Médard, 2014). Thirdly, PCMM of the FMC only post-date by 50–100 Ma an episode of Silurian–Devonian tectonic accretion and subduction of continental/oceanic units belonging to the northern margin of Gondwana (Faure et al., 2008; Melleton et al., 2010). Such units, now exposed as migmatitic ortho- and paragneisses containing eclogitic relics, were buried at depths >100 km and underwent HP partial melting (Faure et al., 2008; Lardeaux et al., 2001; Pin and Lancelot, 1982), thereby providing a straightforward way to metasomatize the mantle with crustal-derived K-, H_2O- and LILE-rich material. The same model was proposed to explain the occurrence of PCMM in the Variscan Bohemian Massif (Janoušek and Holub, 2007), the Himalayas (Campbell et al., 2014; Guo et al., 2014) and the Dabie-Sulu orogen (Zhao et al., 2013).

Importantly, mass balance calculations show that binary mixing between (i) 80–90% DM and (ii) 10–20% of a crustal component with $\varepsilon Hf_t = -10$ and $\delta^{18}O = +20‰$ readily explains the Hf–O isotopic composition of PCMM zircons in the FMC (Fig. 6b). High $\delta^{18}O$ is typically observed in subducted continental sedimentary materials having experienced a low-T weathering cycle, e.g. the East Indonesian ($\delta^{18}O = +15$ to $+24$; Vroon et al., 2001) or Lesser Antilles ($\delta^{18}O = +19$ to $+21$; Davidson, 1987) sediments. Moreover, the pre-Variscan crust of the FMC is dominated by paragneisses (and meta-granitoids derived from melting of the latter) corresponding to former sediments of the north Gondwana margin, which are characterized by Archean (2.5–3.3 Ga), Paleoproterozoic (1.8–2.2 Ga) and Neoproterozoic (0.5–0.7 Ga) detritus, as indicated by age patterns of detrital zircon grains (Albert et al., 2015; Linnemann et al., 2014). Fig. 7a shows that a mixture of these three crustal components, including at least 45–85% of Paleoproterozoic–Archean crust, would readily account for the inferred Hf isotopic signature ($\varepsilon Hf_{310\,Ma} = -10$; $T_{DM} = 1.8$ Ga) of the crustal material in the hybrid mantle source. In fact, the bulk Hf budget carried by detrital zircons in the pre-Variscan crust of the FMC is consistently characterized by an average εHf_{310Ma} of ca. −10 (Fig. 7b). This observation clearly supports that the hybrid source of PCMM in the FMC results from interactions between mantle peridotite and subducted pre-Variscan continental shelf sediments of the former north Gondwana margin.

Further constraints on the nature of the crust-derived materials and how they were incorporated in the mantle can be placed by considering bulk rock Th/La ratios, which are not significantly fractionated during mantle melting (Plank, 2005). Indeed, the source of PCMM samples with the highest Th/La and $\delta^{18}O$ and lowest εHf_t (Subset A) was likely metasomatized by felsic melts derived

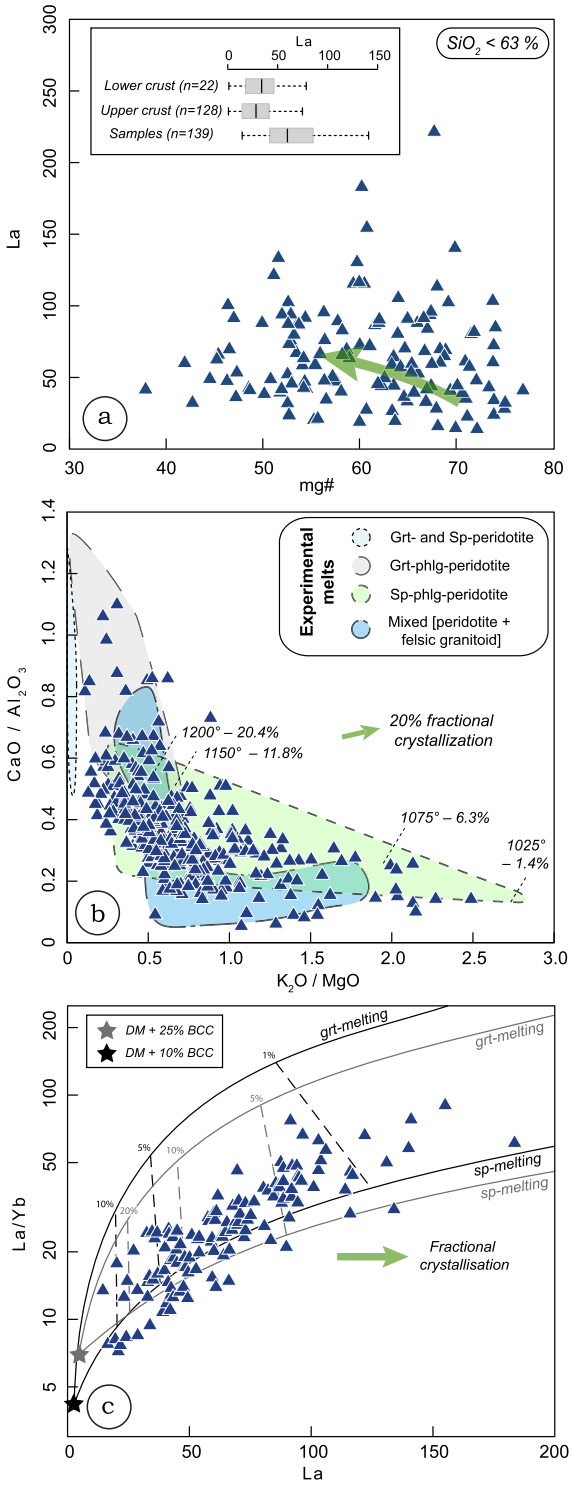

Fig. 5. Plots of major and trace element characteristics of PCMM from the eastern French Massif Central (only samples with $SiO_2 < 63\%$) highlighting important features of their petrogenesis. (a) Plot of La concentrations vs. Mg# (100*MgO/(FeO_t + MgO) [mol]) showing no particular correlation, precluding any significant role played by fractionation or crustal assimilation/contamination. The green arrow shows the evolution of a primary melt (La = 37 ppm, similar to OIB, Sun and McDonough (1989); Mg# = 70) for 50% fractional crystallization of a 25% clinopyroxene + 10% plagioclase + 60% biotite + 5% olivine assemblage (Mg# = 77), supposedly controlling the liquid line of descent of PCMM (mineral proportions and compositions from Parat et al., 2009). Partition coefficients are from Lee et al. (2007) for olivine and clinopyroxene, from Grégoire et al. (2000) for phlogopite, from McKenzie and O'Nions (1991) for garnet and plagioclase. Inset: La contents of FMC samples compared with those of the local upper (Moyen et al., in press) and lower (Downes et al., 1990) crust. (b) Major element ratios of PCMM and comparison with experimental liquids obtained by (i) melting of metasomatized, phlogopite- and/or amphibole-bearing peridotites (Conceição and Green, 2004; Condamine and Médard, 2014; Green, 2015; Mengel and Green, 1989; Thibault et al., 1992); (ii) melting of phlogopite-free peridotites (Gaetani and Grove, 1998; Tenner et al., 2012); and (iii) mixed peridotite + felsic granitoid sources (Mallik et al., 2015; Prouteau et al., 2001; Rapp et al., 2010). The temperatures (in °C) and melt fractions (in %) indicated in the field of spinel phlogopite peridotite correspond to the experimental conditions and results of Condamine and Médard (2014). The arrow shows the variation of elemental ratios for 20% fractional crystallization of the assemblage mentioned above. (c) La/Yb vs. La plot with batch melting models (curves) of spinel and garnet phlogopite peridotite. Source compositions correspond to the Depleted Mantle (Workman and Hart, 2005) mixed with 10% to 25% Bulk Continental Crust (Rudnick and Gao, 2003) (black and gray stars, respectively). Partition coefficients for olivine, clinopyroxene and phlogopite as mentioned above, orthopyroxene from Lee et al. (2007). Modal proportions in the residue are recalculated from Condamine and Médard (2014) for spinel peridotite (olivine 0.69, orthopyroxene 0.15, clinopyroxene 0.08, phlogopite 0.07, spinel 0.01) and Thibault et al. (1992) for garnet peridotite (olivine 0.25, orthopyroxene 0.5, clinopyroxene 0.15, phlogopite 0.03, garnet 0.07). (For interpretation of the references to color in this figure legend, the reader is referred to the web version of this article.)

from terrigenous sediments (Fig. 6c, d), which is consistent with the fact that subducted rocks in the FMC underwent melting at HP (Faure et al., 2008; Pin and Lancelot, 1982). The other samples (Subset B) are better explained by mixing between DM and a bulk continental crust composition (Fig. 6c, d), possibly resulting from mechanical mélanges during the subduction of the continental units. Importantly, compositions corresponding to average, bulk lower crust (low Th/La) cannot account for the observed compositions, even if we consider that such material had high $\delta^{18}O$ and low εHf_t (Fig. 6c, d), showing that subduction of supracrustal material is required.

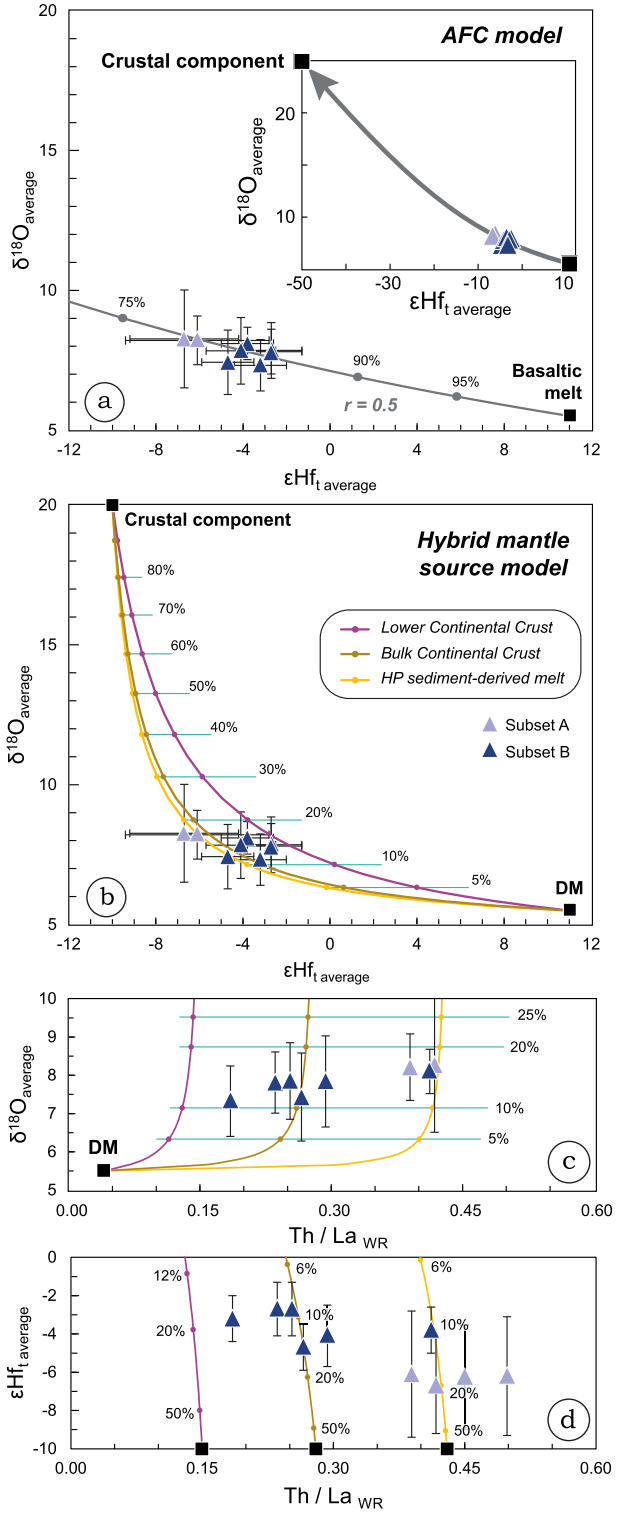

4.2. A unified model for PCMM petrogenesis

As outlined earlier, PCMM worldwide share a common geotectonic, petrographic identity and similar geochemical and Hf–O isotopic characteristics, which argues for a common origin. The fact that our samples from the FMC are chemically representative of the diversity of PCMM worldwide (Fig. 3) suggests that the general features of the petrogenetic model proposed above can be reasonably extended to all PCMM suites.

Consistently, many workers advocated that the particular geochemistry of PCMM necessarily requires an enriched mantle source (Fowler and Rollinson, 2012; Guo et al., 2014; Laurent et al., 2011; Laurent et al., 2014a; Laurent et al., 2014b; Liégeois et al., 1998; Murphy, 2013; Prelevic et al., 2012; von Raumer et al., 2014; Williams et al., 2004). Moreover, the presence of continental crust-derived material in such a source has often been proposed to explain the non-DM and "crustal" isotopic signatures of these rocks (Guo et al., 2014; Laurent et al., 2014b; Nelson, 1992; Prelevic et al., 2012). Given the generally higher $\delta^{18}O$ of PCMM zircons compared with mantle material (Fig. 4a), it is likely that these crustal materials are most often represented by supracrustal rocks. Finally, mantle enrichment shortly prior to PCMM genesis seems to be the rule because, like in the FMC, PCMM emplacement systematically post-dates by <50 Ma an oceanic and/or continental subduction stage, for instance in the late Archean terranes (Laurent et al., 2014a) and in the Himalayan (Chung et al., 2005), Caledonian (Atherton and Ghani, 2002) and Svecofennian (Andersson et al., 2006) orogens.

Therefore, we propose that PCMM are derived from: (i) interactions between subducted continental material (most often of supracrustal origin), or melts/fluids generated from them, and mantle peridotite; and (ii) subsequent melting of the resulting hybrid source shortly thereafter. Mantle enrichment through the subduction of continental units at the onset of collision (Campbell et al., 2014; Guo et al., 2014; Janoušek and Holub, 2007; Zhao et al., 2013) would be the most appropriate scenario to account for the short time lapse between the two steps; the systematic occurrence of PCMM in collision belts; and the more evolved isotopic composition and greater incompatible element contents of PCMM compared with classical arc magmas (related to oceanic subduction).

4.3. Quantifying crust and mantle contributions in post-collisional mafic magmas

The aim of this section is to quantify the respective mass fraction of mantle- vs. crust-derived elements in the "hybrid" mantle source of PCMM. This will be used in turn to determine the mass

Fig. 6. (a) Results of assimilation/fractional crystallization (AFC) model of a basaltic melt (Hf content of 2.03 ppm, from Sun and McDonough, 1989; DM-like isotopic composition with $\varepsilon Hf_{(t)} = +11$ calculated from Naeraa et al., 2012, and $\delta^{18}O = +5.3$ from Valley et al., 1998) assimilating bulk continental crust (Hf content of 3.7 ppm, from Rudnick and Gao (2003); $\varepsilon Hf_{(t)} = -50$ and $\delta^{18}O = +25$ adjusted to fit the data for a maximum fractionation rate of ca. 20%); grey dots indicate the fraction of remaining liquid and r the mass ratio between assimilated and crystallized material. (b), (c) and (d) Results of mass-balance, binary mixing models between DM ($\varepsilon Hf_{(t)} = +11$; $\delta^{18}O = +5.3$; Hf contents [0.2 ppm] and Th/La [0.04] from Workman and Hart (2005)) and three different crustal materials, all characterized by $\varepsilon Hf_{(t)} = -10$ and $\delta^{18}O = +20$ (adjusted to fit the data for a maximum mantle contamination rate of ca. 20%): (i) a melt derived from HP melting of terrigenous sediment (Hf contents [4.3 ppm] and Th/La [0.43] from Plank and Langmuir, 1998, corrected from HP melting using average partition coefficients of Hermann and Rubatto (2009)); (ii) Lower and (iii) Bulk Continental Crust (Rudnick and Gao, 2003). O contents are from Roberts et al. (2012). Light blue lines denote the percentage of crustal component in the mixture. Errors bars for samples are 2 S.D. All εHf_t are calculated at 310 Ma (average age of PCMM in the eastern FMC). (For interpretation of the references to color in this figure legend, the reader is referred to the web version of this article.)

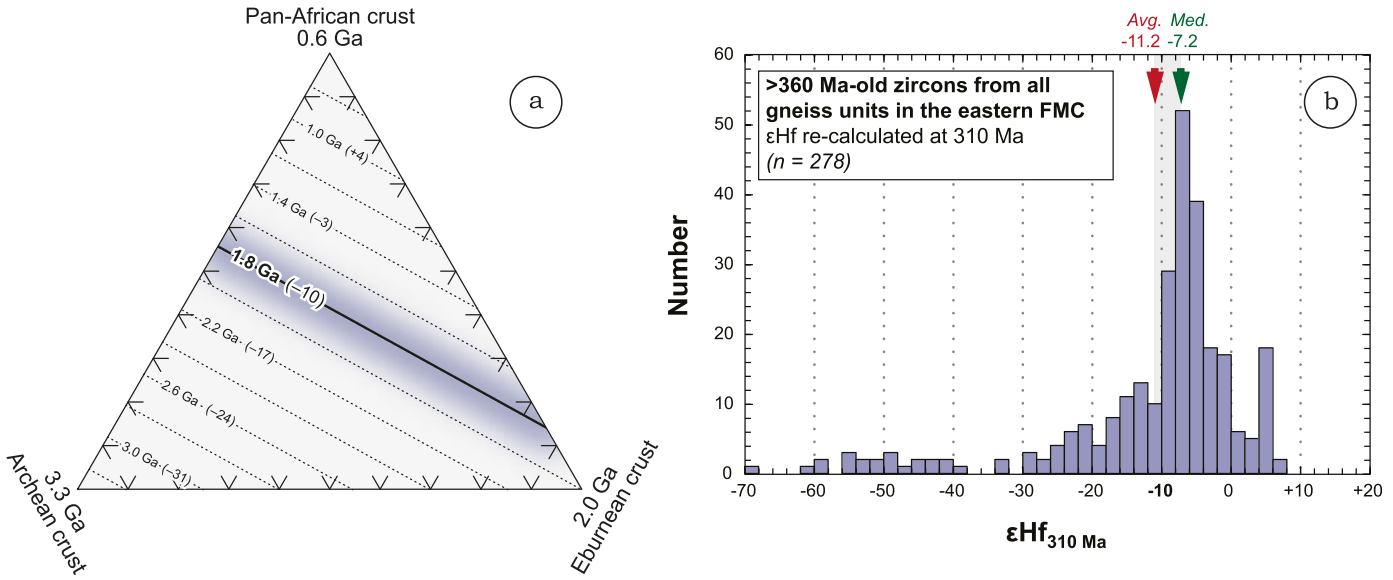

Fig. 7. (a) Triangular diagram showing the model age and $\varepsilon Hf_{310\,Ma}$ (in brackets) of a virtual sedimentary crustal material as a function of the relative proportion of Archean, Eburnean (Paleoproterozoic) and Pan-African (Neoproterozoic–Early Paleozoic) crust in the latter, assuming identical Hf concentrations in the three end-members. The highlighted model age of 1.8 Ga corresponds to the composition of the crustal material required to explain the zircon Hf isotopic compositions of PCMM in the FMC ($\varepsilon Hf_{310\,Ma}$ of ca. −10; see Fig. 6 and text for discussion). (b) Histogram showing the distribution of zircon $\varepsilon Hf_{310\,Ma}$ for >360 Ma-old grains from all gneiss units in the eastern FMC, taken as representative of the isotopic distribution of Hf in the pre-Variscan crust at the time of PCMM formation. The $\varepsilon Hf_{310\,Ma}$ are calculated using the measured $^{176}Hf/^{177}Hf$ and $^{176}Lu/^{177}Hf$ ratios of each zircon grain. Data from Chelle-Michou et al. (2015).

fraction of PCMM that derives from the mantle, which is a critical parameter to unravel their contribution to crustal growth.

As demonstrated above, the hybrid mantle source of PCMM is formed by interactions between mantle peridotite and crustal materials (fluid, melt or solid). These interactions may result in different cases in nature, e.g. a mechanical mixture of peridotite and meta-sedimentary/meta-igneous crustal rocks; a peridotite containing veins formed by reaction with percolating liquids; or a metasomatized rock where the added material is distributed in newly-crystallized phases (pyroxenes, amphibole, phlogopite). Irrespective of the nature of the metasomatic agent, the finite mass of each chemical element within any of these "hybrid" sources will be partitioned between the fraction that was already present in the original mantle prior to the interactions and that supplied by the added crust-derived material. The dual geochemistry of PCMM shows that they sampled both groups of elements, regardless the exact physical nature of the source and melting process. Therefore, for each chemical element, the mass fraction of "crust" vs. "mantle" atoms in the source of PCMM can be approximated using a simple binary mixing model based on mass-balance, assuming reasonable compositions for the two components (respectively Bulk Continental Crust and DM). Although simplistic, this calculation has the advantage of relying on few parameters, i.e. the mass fractions of the two end-members and their compositions, which in the case of crust–mantle mixing are not so critical given the huge concentration contrast between the two for most elements.

For each chemical element, we define x_{crust} as the mass fraction of atoms that originates from crust-derived materials. Fig. 8 shows that in a hybrid mantle containing 10 to 25% crustal component, x_{crust} varies for each element, incompatible elements being dominantly controlled by the crustal component (x_{crust} being as high as 99% for Rb, Ba, Th, U as the initial mantle contains very little of these) whilst compatible elements mostly come from the mantle (e.g. 97% of the MgO, Cr and Ni is of mantle origin). Importantly, the five most abundant major oxides in the source (SiO_2, Al_2O_3, MgO, FeO, CaO; ca. 95% of the bulk mass) are dominantly of mantle origin (x_{crust} is generally <30%) because of the limited concentration contrast (less than one order of magnitude) between mantle and crust and the low mass fraction of the crustal component in the hybrid source (Fig. 8). As a direct and critical consequence of this, assuming that the proportion of "crust" vs. "mantle" atoms for each element does not change during melting of the hybrid source, the bulk mass fraction of PCMM that derives from the crustal component is low. Typically, for three representative PCMM samples (from a Late-Archean terrane and the Variscan and Himalayan orogens), it lies between 15–21% and 31–38%, for respectively 10% and 25% of crustal materials in the hybrid source (see Fig. 8), meaning that >62% of the bulk mass of these samples are of mantle origin and thus represent new additions to the crust.

This first-order calculation implicitly presumes that "crust" and "mantle" atoms of each element are equally distributed over mineral phases in the hybrid source so that x_{crust} keeps constant during melting. This is likely over-simplistic for trace elements, especially the dominantly crust-derived elements that would be preferentially partitioned into the phases formed via metasomatic reactions such as pyroxenes, amphibole and phlogopite (Prouteau et al., 2001; Rapp et al., 2010), which in turn preferentially contribute to melting reactions (Condamine and Médard, 2014; Mallik et al., 2015). However, for major oxides, x_{crust} likely remains constant throughout the process. Indeed, metasomatic reactions would randomly use both "crust" and "mantle" elements to form new minerals and, even if not, solid-state diffusion, phase recrystallization and mixing enhanced by high-temperature deformation (Linckens et al., 2014) would smooth any significant difference of x_{crust} from a mineral to another. Moreover, even considering an artificial two-fold increase in the proportion of "crustal" SiO_2 and Al_2O_3 between a highly-enriched mantle composition (25% crustal component) and the melt owing to their potential concentration in newly formed phlogopite, amphibole and pyroxene, the mass fraction of crust-derived elements in the three PCMM samples used for calculation would not exceed 50–63%. These are definitely maximum values since this scenario is somewhat extreme. Therefore, it is reasonable to conclude that the proportion of reworked crustal materials in PCMM does not exceed 63% and is most often, as calculated earlier, between 15 and 38%.

Paradoxically, most PCMM (especially the three specimens used in the calculations) display markedly negative zircon εHf_t. Then, from an Hf isotope perspective alone, those rocks apparently cor-

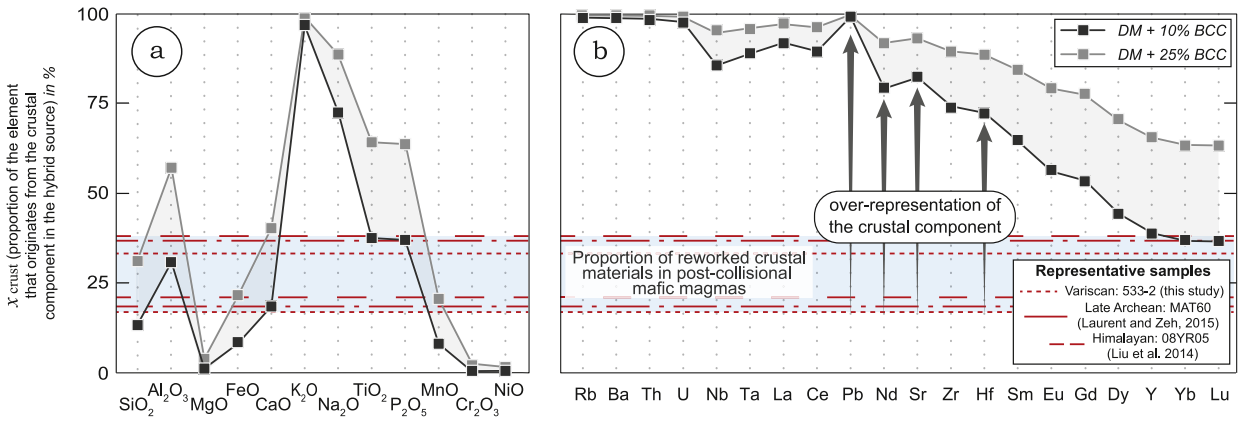

Fig. 8. Plot of the "x_{crust}" parameter for major oxides (panel (a), sorted as a function of their abundance in PCMM) and trace elements (panel (b), reported by increasing compatibility). x_{crust} is defined as the mass fraction of any element i controlled by the crustal component in a hybrid mantle source consisting of Depleted Mantle (Workman and Hart, 2005) +10 (black line) to 25% (grey line) crustal material (Bulk Continental Crust, Rudnick and Gao, 2003), calculated as follows: $x^i_{crust} = f_{crust}[i]_{crust}/(f_{crust}[i]_{crust} + (1 - f_{crust})[i]_{DM})$ where $[i]$ depicts the concentration of element i and f_{crust} the proportion of crustal component in the hybrid source. The blue field represents the bulk fraction of crust-derived elements (X_{crust}) in mafic magmas derived from such a source, calculated for three representative samples of PCMM suites: 533-2 (this study); MAT-60 (Laurent et al., 2014b); and 08YR05 (Liu et al., 2014). The calculation has been performed by (i) weighting the concentrations of all elements in each sample by the corresponding values of x_{crust}, and (ii) summing up the resulting values. See text for discussion. $X_{crust} = \sum_{i=1}^{n} (x^i_{crust} \cdot [i]_{PCMM})$.

respond to pure reworking of former crustal lithologies. This discrepancy simply results from the large dominance of the crustal component on the incompatible trace element budget (including the radiogenic tracers Sr, Nd, Hf, Pb) in the hybrid source (Fig. 8). Typically, the Hf budget in the source of PCMM consists of 72–89% non-radiogenic "crustal" Hf and only 11–28% radiogenic "mantle" Hf. Therefore, as long as incompatible element tracers are considered, PCMM would bear a "crustal" signature and the mantle contribution to their origin, although dominant in terms of mass, would be invisible.

4.4. Consequences for crustal growth

As demonstrated earlier (Table 1), PCMM have been emplaced during or at the end of continental collision since the late Archean (Bonin, 2004; Fowler and Rollinson, 2012; Laurent et al., 2014a), specifically at each stage of supercontinent amalgamation. They are therefore a systematic magmatic feature of the orogenic cycle, just as MORB, arc magmas or collisional granites are, and their significance for global crustal evolution must be addressed.

Although the surface expression of PCMM is limited, it has been demonstrated in several settings that they would actually represent the parental magmas of much more voluminous granitoid suites via fractionation (Fowler and Henney, 1996; Küster and Harms, 1998; Laurent et al., 2013; Moyen et al., in press) and/or limited interaction with coeval crustal melts (Clemens et al., 2009; Janoušek et al., 2004; Laurent et al., 2014a; Parat et al., 2009). In terms of mass balance, these two processes are antagonists: silicic liquids will represent only a fraction of the initial mass of mafic magma in the case of fractionation, whereas interaction with crustal material represents a mass addition to PCMM to form granitoids. Hence, it is reasonable to consider that in a given orogenic system, the initial volume of PCMM was roughly equivalent to that of their genetically related granitoids. According to Moyen et al. (in press), PCMM-derived granitoids represent ca. 10% of exposed rocks in the Variscan belt; given that 62 to 85% of the bulk mass of PCMM consist of elements extracted from the mantle (see section 4.3), and assuming that surface exposure reflects the repartition of lithologies at depth, then 6.2 to 8.5% of the bulk mass of the Variscan crust represents new additions from the mantle by PCMM.

At first glance, this estimate appears modest in comparison with arc settings, in which the large majority of the bulk crustal volume is derived from the differentiation of mantle-derived mafic magmas (Jagoutz and Kelemen, 2015). However, mantle-derived magmatic rocks only become long-term additions to the continental volume if they are subsequently preserved: while a small fraction of arc granitoids may be captured in collisional orogens (Condie et al., 2011), the majority of them are readily recycled into the mantle shortly after their formation owing to sediment subduction and/or subduction erosion (Stern and Scholl, 2010). In contrast, PCMM and derivatives represent small volumes of only partly mantle-derived magmas, but because they are shielded in the core of newly formed continental masses, they have a much greater preservation potential in the geological record (Hawkesworth et al., 2010). As a result, they may represent significant contributors to long-term crustal growth.

Recently, the problem of crustal growth through time has been extensively addressed via the statistical analysis of global zircon Hf (Belousova et al., 2010; Condie et al., 2011) or coupled Hf–O (Dhuime et al., 2012) isotopic databases: Hf model ages are used to determine the timing of crust formation, and O isotopes to distinguish zircons formed in granitoids reworking a "juvenile" source ($\delta^{18}O = 5.5 \pm 1.0‰$) or a "mixed" sedimentary source ($\delta^{18}O > 6.5‰$) (e.g. Hawkesworth and Kemp, 2006). The reliability of this approach has been questioned recently, especially because Hf and O isotopes in zircon reflect in most cases the contribution of multiple components in the origin of their host magma (magma mixing, heterogeneous sources, crustal contamination) (Payne et al., 2016; Roberts and Spencer, 2015). The case of PCMM raises an even more problematic issue, showing that igneous material representing a non-negligible contribution to long-term crustal growth may not have DM-like Hf isotope compositions and "pristine mantle" O isotope compositions because of the small proportions of crustal (possibly sedimentary) material in their hybrid mantle source.

Several lines of evidence suggest that, despite their limited volume, zircons from PCMM and derivatives represent a sizeable proportion of global detrital zircon databases. First, because of their selective preservation (Hawkesworth et al., 2010), zircons from collision-related igneous rocks dominate the detrital populations in sedimentary rocks wherever recent or ancient orogenic crust is present in the catchment area (Spencer et al., 2015). Second, because of their high Zr contents (370 ppm in average in the eastern FMC), rocks from the PCMM suite have a higher zircon fertility factor ("ZFF" of Dickinson, 2008) than other collisional granites (150 ppm Zr in the eastern FMC; Moyen et al., in press).

Third, magmatic zircons from these rocks show a greater proportion (~80%) of concordant U–Pb ages compared to those of purely crust-derived ("S-type") granites (~50%) (Couzinié et al., 2014; Laurent et al., 2015), such that in a detrital zircon population, the probability to discard zircons from PCMM and derivatives because of U–Pb discordance (Nemchin and Cawood, 2005) is smaller than for S-type granites. To illustrate the two latter issues, the erosion of the Variscan crust, assuming that the latter consists of 10% PCMM-derived granitoids (ZFF = 2.5; 80% U–Pb concordance); 30% crust-derived granites (ZFF = 1; 50% U–Pb concordance); and 60% of metamorphic and sedimentary rocks (ZFF = 1; 67% U–Pb concordance), would yield a detrital zircon population in which the final, U–Pb concordant dataset contains a minimum of 27% data from PCMM-derived material – notwithstanding the likely possibility that metamorphic and sedimentary rocks may contain zircons from reworked, earlier PCMM and related granites, exactly for the same reasons.

Therefore, zircons derived from PCMM, their differentiated products and any igneous and sedimentary material derived from them, would significantly bias the crustal growth signal of global detrital zircon databases, in two distinct ways:

(1) Zircons from any PCMM crystallized at time t would have been either discarded (non-mantle $\delta^{18}O$ resulting from the involvement of sedimentary components) or attributed to ancient events of crust formation because of non-radiogenic Hf isotope compositions (and old Hf model ages). Although the latter feature certainly reflects reworking of older crust to some extent, this reworking is over-estimated because the mantle contribution at time t cannot be resolved by Hf isotopes alone (see section 4.3).
(2) If PCMM-derived crustal material is reworked by later magmatic events, then the calculation of model ages based on DM for zircons formed in these younger magmas is inappropriate since their crustal source had a non-DM Hf isotopic composition.

Both would have the same global effect, i.e. skewing crustal growth models towards an over-estimation of ancient crustal growth with respect to younger crust formation. Specifically, because PCMM are present on Earth since the late Archean (Table 1), post-Archean crustal growth rates may be significantly under-estimated.

5. Conclusions

1. PCMM are ubiquitous in all continental collision settings since the late Archean and are characterized by a dual geochemistry, with high contents in both compatible, "mantle-hosted" elements ($FeO_t + MgO$, Ni, Cr) and incompatible, "crust-hosted" elements (LILE, REE, HFSE).
2. As illustrated by the case study from the eastern FMC, PCMM originated from low-degree partial melting of a phlogopite-(and/or amphibole-) bearing peridotite/pyroxenite. In the FMC, the non-radiogenic $\varepsilon Hf_{(t)}$ (−2 to −9) and elevated $\delta^{18}O_{SMOW}$ (+6 to +10‰) of PCMM zircons suggest that this mantle source was contaminated by 10 to 25% of subducted continental shelf sediments derived from Precambrian crust, shortly prior to melting.
3. Mass balance calculations indicate that the incompatible trace element budget (including radiogenic isotope tracers Sr, Nd, Hf, Pb) of the PCMM source is mainly controlled by the crustal component. Therefore, resulting magmas display "crust-like" non-radiogenic isotope compositions even though 62 to 85% of their bulk mass originates from the mantle component and represents new addition to the crust.
4. PCMM have contributed to crustal growth since the late Archean because they are the parent of voluminous granitoid suites and have a high preservation potential in the geological record. Owing to their peculiar hybrid origin, this contribution cannot be resolved in global crustal growth models based only on zircon Hf and O isotopes, such that post-Archean crustal growth may be significantly under-estimated.

Acknowledgements

We acknowledge financial support from an ERC grant (StG 279828, project MASE to J. van Hunen), two PNP grants from French CNRS ("Différentiation et évolution de la croûte tardi orogénique", 2014 and "Quantification de la durée d'un épisode de fusion partielle en contexte de désépaississement tardi-orogénique", 2016), the Deutsche Forschungsgemeinschaft (grant Zeh424/11-2 to A.Z.) and the Deutscher Akademischer Austauschdienst (grant A/13/70682 to O.L.). A.V. acknowledges funding by the Labex VOLTAIRE (ANR-10-LABX-100-01). V. Gardien provided two samples for this study. D. Garcia kindly supplied his database and guided us in the field. A. Vézinet, M. Benoit and E. Bruand assisted during zircon separation procedures. Helpful discussions with V. Janoušek and G. Stevens were much appreciated. A. Gerdes assisted during Hf analytical sessions and P. Montero performed zircon imaging and SHRIMP measurements. This contribution is IBERSIMS publication N° 35. We are grateful to A. Yin for editorial handling. C.L. Farmer and S. Wilde provided thorough and constructive reviews; R. Rudnick, P. Cawood and an anonymous reviewer provided insightful comments on an earlier version of this manuscript – may they all be thanked.

Appendix A. Supplementary material

Supplementary material related to this article can be found online at http://dx.doi.org/10.1016/j.epsl.2016.09.033.

References

Albert, R., Arenas, R., Gerdes, A., Sanchez Martinez, S., Marko, L., 2015. Provenance of the HP–HT subducted margin in the Variscan belt (Cabo Ortegal Complex, NW Iberian Massif). J. Metamorph. Geol. 33, 959–979.
Andersson, U.B., Eklund, O., Fröjdö, S., Konopelko, D., 2006. 1.8 Ga magmatism in the Fennoscandian Shield; lateral variations in subcontinental mantle enrichment. Lithos 86, 110–136.
Arndt, N.T., 2013. Formation and evolution of the continental crust. Geochem. Perspect. 2 (3), 405–533.
Arndt, N.T., Goldstein, S.L., 1987. Use and abuse of crust-formation ages. Geology 15, 893–895.
Atherton, M.P., Ghani, A.A., 2002. Slab breakoff: a model for Caledonian, Late Granite syn-collisional magmatism in the orthotectonic (metamorphic) zone of Scotland and Donegal, Ireland. Lithos 62.
Belousova, E.A., Kostitsyn, Y.A., Griffin, W.L., Begg, G.C., O'Reilly, S.Y., Pearson, N.J., 2010. The growth of the continental crust: constraints from zircon Hf-isotope data. Lithos 119, 457–466.
Bindeman, I., 2008. Oxygen isotopes in mantle and crustal magmas as revealed by single crystal analysis. Rev. Mineral. Geochem. 69, 445–478.
Bonin, B., 2004. Do coeval mafic and felsic magmas in post-collisional to within-plate regimes necessarily imply two contrasting, mantle and crustal, sources? A review. Lithos 78, 1–24.
Bouilhol, P., Jagoutz, O., Hanchar, J.M., Dudas, F.O., 2013. Dating the India–Eurasia collision through arc magmatic records. Earth Planet. Sci. Lett. 366, 163–175.
Bouilhol, P., Schaltegger, U., Chiaradia, M., Ovtcharova, M., Stracke, A., Burg, J.-P., Dawood, H., 2011. Timing of juvenile arc crust formation and evolution in the Sapat Complex (Kohistan–Pakistan). Chem. Geol. 280, 243–256.
Bouvier, A., Vervoort, J.D., Patchett, P.J., 2008. The Lu–Hf and Sm–Nd isotopic composition of CHUR: constraints from unequilibrated chondrites and implications for the bulk composition of terrestrial planets. Earth Planet. Sci. Lett. 273 (1–2), 48–57.
Campbell, I.H., Allen, C., 2008. Formation of supercontinents linked to increases in atmospheric oxygen. Nat. Geosci. 1, 554–558.
Campbell, I.H., Stepanov, A.S., Liang, H.-Y., Allen, C.M., Norman, M.D., Zhang, Y.-Q., Xie, Y.-W., 2014. The origin of shoshonites: new insights from the Tertiary high-potassium intrusions of eastern Tibet. Contrib. Mineral. Petrol. 167 (3), 1–22.

Chantraine, J., Autran, A., Cavelier, C., 1996. Carte géologique de la France à l'échelle du millionième, 6ème édition. BRGM, Orléans.
Chelle-Michou, C., Laurent, O., Moyen, J.F., Block, S., Gardien, V., Paquette, J.L., Couzinié, S., 2015. New U–Pb and Hf zircon data from the eastern Massif Central: from Gondwana to Pangea in a nutshell. Géol. Fr. 1, 37–38.
Chung, S.-L., Chu, M.-F., Zhang, Y., Xie, Y., Lo, C.-H., Lee, T.-Y., Lan, C.-Y., Li, X., Zhang, Q., Wang, Y., 2005. Tibetan tectonic evolution inferred from spatial and temporal variations in post-collisional magmatism. Earth-Sci. Rev. 68, 173–196.
Clemens, J.D., Darbyshire, D.P.F., Flinders, J., 2009. Sources of post-orogenic calc-alkaline magmas: the Arrochar and Garabal Hill–Glen Fyne complexes, Scotland. Lithos 112, 524–542.
Conceição, R., Green, D.H., 2004. Derivation of potassic (shoshonitic) magmas by decompression melting of phlogopite + pargasite lherzolite. Lithos 72, 209–229.
Condamine, P., Médard, E., 2014. Experimental melting of phlogopite-bearing mantle at 1 GPa: implications for potassic magmatism. Earth Planet. Sci. Lett. 397, 80–92.
Condie, K.C., Bickford, M.E., Aster, R.C., Belousova, E., Scholl, D.W., 2011. Episodic zircon ages, Hf isotopic composition, and the preservation rate of continental crust. Geol. Soc. Am. Bull. 123, 951–957.
Couzinié, S., Moyen, J.F., Villaros, A., Paquette, J.L., Scarrow, J.H., Marignac, C., 2014. Temporal relationships between Mg–K mafic magmatism and catastrophic melting of the Variscan crust in the southern part of Velay Complex (Massif Central, France). J. Geosci., 69–86.
Davidson, J., 1987. Crustal contamination versus subduction zone enrichment: examples from the Lesser Antilles and implications for mantle source compositions of island arc volcanic rocks. Geochim. Cosmochim. Acta 51, 2185–2198.
Dhuime, B., Hawkesworth, C.J., Cawood, P.A., Storey, C.D., 2012. A change in the geodynamics of continental growth 3 billion years ago. Science 335, 1334–1336.
Dickinson, W.R., 2008. Impact of differential zircon fertility of granitoid basement rocks in North America on age populations of detrital zircons and implications for granite petrogenesis. Earth Planet. Sci. Lett. 275, 80–92.
Downes, H., Dupuy, C., Leyreloup, A.F., 1990. Crustal evolution of the Hercynian belt of Western Europe: evidence from lower-crustal granulitic xenoliths (French Massif Central). Chem. Geol. 83, 209–231.
Faure, M., Bé Mézème, E., Cocherie, A., Rossi, P., Chemenda, A., Boutelier, D., 2008. Devonian geodynamic evolution of the Variscan Belt, insights from the French Massif Central and Massif Armoricain. Tectonics 27, TC2005.
Fowler, M., Henney, P.J., 1996. Mixed Caledonian appinite magmas: implications for lamprophyre fractionation and high Ba–Sr granite genesis. Contrib. Mineral. Petrol. 126, 199–215.
Fowler, M., Rollinson, H., 2012. Phanerozoic sanukitoids from Caledonian Scotland: implications for Archean subduction. Geology 40, 1079–1082.
Gaetani, G.A., Grove, T.L., 1998. The influence of water on melting of mantle peridotite. Contrib. Mineral. Petrol. 131, 323–346.
Green, D.H., 2015. Experimental petrology of peridotites, including effects of water and carbon on melting in the Earth's upper mantle. Phys. Chem. Miner. 42, 95–122.
Grégoire, M., Moine, B.N., O'Reilly, S.Y., Cottin, J.-Y., Giret, A., 2000. Trace element residence and partitioning in mantle xenoliths metasomatized by highly alkaline, silicate- and carbonate-rich melts (Kerguelen Islands, Indian Ocean). J. Petrol. 41, 477–509.
Griffin, W.L., Wang, X., Jackson, S.E., Pearson, N.J., O'Reilly, S.Y., Xu, X.-S., Zhou, X., 2002. Zircon chemistry and magma mixing, SE China: in-situ analysis of Hf isotopes, Tonglu and Pingtan igneous complexes. Lithos 61, 237–269.
Guo, Z., Wilson, M., Zhang, L., Zhang, M., Cheng, Z., Liu, J., 2014. The role of subduction channel mélanges and convergent subduction systems in the petrogenesis of post-collisional K-rich mafic magmatism in NW Tibet. Lithos 198–199, 184–201.
Hagen-Peter, G., Cottle, J.M., Tulloch, A.J., Cox, S.C., 2015. Mixing between enriched lithospheric mantle and crustal components in a short-lived subduction-related magma system, Dry Valleys area, Anatarctica: insights from U–Pb geochronology, Hf isotopes and whole-rock geochemistry. Lithosphere 7 (2), 174–188.
Hawkesworth, C., Cawood, P., Kemp, T., Storey, C., Dhuime, B., 2009. A matter of preservation. Science 323, 49–50.
Hawkesworth, C.J., Dhuime, B., Pietranik, A.B., Cawood, P.A., Kemp, A.I.S., Storey, C.D., 2010. The generation and evolution of the continental crust. J. Geol. Soc. (Lond.) 167, 229–248.
Hawkesworth, C.J., Kemp, A.I.S., 2006. Using hafnium and oxygen isotopes in zircons to unravel the record of crustal evolution. Chem. Geol. 226, 144–162.
Heilimo, E., Halla, J., Andersen, T., Huhma, H., 2013. Neoarchean crustal recycling and mantle metasomatism: Hf–Nd–Pb–O isotope evidence from sanukitoids of the Fennoscandian shield. Precambrian Res. 228, 250–266.
Hermann, J., Rubatto, D., 2009. Accessory phase control on the trace element signature of sediment melts in subduction zones. Chem. Geol. 265, 512–526.
Holub, F.V., 1997. Ultrapotassic plutonic rocks of the durbachite series in the Bohemian Massif: petrology, geochemistry and petrogenetic interpretation. Sb. Geol. Věd, Ložisk. Geol. Mineral. 31, 5–26.
Jagoutz, O., Kelemen, P.B., 2015. Role of arc processes in the formation of continental crust. Annu. Rev. Earth Planet. Sci. 43, 363–404.
Janoušek, V., Braithwaite, C.J.R., Bowes, D.R., Gerdes, A., 2004. Magma-mixing in the genesis of Hercynian calc-alkaline granitoids: an integrated petrographic and geochemical study of the Sázava intrusion, Central Bohemian Pluton, Czech Republic. Lithos 78, 67–99.
Janoušek, V., Holub, F.V., 2007. The causal link between HP–HT metamorphism and ultrapotassic magmatism in collisional orogens: case study from the Moldanubian Zone of the Bohemian Massif. Proc. Geol. Assoc. 118, 75–86.
Kemp, A.I., Hawkesworth, C.J., Paterson, B.A., Kinny, P.D., 2006. Episodic growth of the Gondwana supercontinent from hafnium and oxygen isotopes in zircon. Nature 439, 580–583.
Küster, D., Harms, U., 1998. Post-collisional potassic granitoids from the southern and northwestern parts of the Late Neoproterozoic East African Orogen: a review. Lithos 45, 177–195.
Lancaster, P.J., Storey, C.D., Hawkesworth, C.J., Dhuime, B., 2011. Understanding the roles of crustal growth and preservation in the detrital zircon record. Earth Planet. Sci. Lett. 305, 405–412.
Lardeaux, J.M., Ledru, P., Daniel, I., Duchene, S., 2001. The Variscan French Massif Central – a new addition to the ultra-high pressure metamorphic "club": exhumation processes and geodynamic consequences. Tectonophysics 332, 143–167.
Laurent, O., Couzinié, S., Vanderhaeghe, O., Zeh, A., Moyen, J.F., Villaros, A., Gardien, V., 2015. U–Pb dating of Variscan igneous rocks from the eastern French Massif Central: southward migration of coeval crust- and mantle-melting witnesses late-orogenic slab retreat. Géol. Fr. 1, 82–83.
Laurent, O., Doucelance, R., Martin, H., Moyen, J.-F., 2013. Differentiation of the late-Archaean sanukitoid series and some implications for crustal growth: insights from geochemical modelling on the Bulai pluton, Central Limpopo Belt, South Africa. Precambrian Res. 227, 186–203.
Laurent, O., Martin, H., Doucelance, R., Moyen, J.F., Paquette, J.L., 2011. Geochemistry and petrogenesis of high-K "sanukitoids" from the Bulai pluton, Central Limpopo Belt, South Africa: implications for geodynamic changes at the Archaean–Proterozoic boundary. Lithos 123, 73–91.
Laurent, O., Martin, H., Moyen, J.F., Doucelance, R., 2014a. The diversity and evolution of late-Archean granitoids: evidence for the onset of "modern-style" plate tectonics between 3.0 and 2.5 Ga. Lithos 205, 208–235.
Laurent, O., Rapopo, M., Stevens, G., Moyen, J.F., Martin, H., Doucelance, R., Bosq, C., 2014b. Contrasting petrogenesis of Mg–K and Fe–K granitoids and implications for post-collisional magmatism: case study from the Late-Archean Matok pluton (Pietersburg block, South Africa). Lithos 196–197, 131–149.
Laurent, O., Zeh, A., 2015. A linear Hf isotope-age array despite different granitoid sources and complex Archean geodynamics: example from the Pietersburg block (South Africa). Earth Planet. Sci. Lett. 430, 326–338.
Ledru, P., Courrioux, G., Dallain, C., Lardeaux, J.M., Montel, J.M., Vanderhaeghe, O., Vitel, G., 2001. The Velay dome (French Massif Central): melt generation and granite emplacement during orogenic evolution. Tectonophysics 342, 207–237.
Lee, C.-T.A., Harbert, A., Leeman, W.P., 2007. Extension of lattice strain theory to mineral/mineral rare-earth element partitioning: an approach for assessing disequilibrium and developing internally consistent partition coefficients between olivine, orthopyroxene, clinopyroxene and basaltic melt. Geochim. Cosmochim. Acta 71, 481–496.
Liégeois, J.-P., Navez, J., Hertogen, J., Black, R., 1998. Contrasting origin of post-collisional high-K calc-alkaline and shoshonitic versus alkaline and peralkaline granitoids. The use of sliding normalization. Lithos 45, 1–28.
Linckens, J., Bruijn, R.H.C., Skemer, P., 2014. Dynamic recrystallization and phase mixing in experimentally deformed peridotite. Earth Planet. Sci. Lett. 388, 134–142.
Linnemann, U., Gerdes, A., Hofmann, M., Marko, L., 2014. The Cadomian Orogen: Neoproterozoic to Early Cambrian crustal growth and orogenic zoning along the periphery of the West African Craton—constraints from U–Pb zircon ages and Hf isotopes (Schwarzburg Antiform, Germany). Precambrian Res. 244, 236–278.
Liu, D., Zhao, Z., Zhu, D.-C., Niu, Y., DePaolo, D.J., Harrison, T.M., Mo, X., Dong, G., Zhou, S., Sun, C., Zhang, Z., Liu, J., 2014. Postcollisional potassic and ultrapotassic rocks in southern Tibet: mantle and crustal origins in response to India–Asia collision and convergence. Geochim. Cosmochim. Acta 143, 207–231.
Lowe, D.R., Tice, M.M., 2004. Geologic evidence for Archean atmospheric and climatic evolution: fluctuating levels of CO_2, CH_4, and O_2 with an overriding tectonic control. Geology 32, 493–496.
Mallik, A., Nelson, J., Dasgupta, R., 2015. Partial melting of fertile peridotite fluxed by hydrous rhyolitic melt at 2–3 GPa: implications for mantle wedge hybridization by sediment melt and generation of ultrapotassic magmas in convergent margins. Contrib. Mineral. Petrol. 169 (5), 1–24.
McCulloch, M.T., Wasserburg, G.J., 1978. Sm–Nd and Rb–Sr chronology of continental crust formation. Science 200, 1003–1011.
McDonough, W.F., Sun, S.-s., 1995. The composition of the Earth. Chem. Geol. 120, 223–253.
McKenzie, D., O'Nions, R.K., 1991. Partial melt distributions from inversion of rare Earth element concentrations. J. Petrol. 32 (5), 1021–1091.
Melleton, J., Cocherie, A., Faure, M., Rossi, P., 2010. Precambrian protoliths and Early Paleozoic magmatism in the French Massif Central: U–Pb data and the North Gondwana connection in the West European Variscan belt. Gondwana Res. 17, 13–25.
Mengel, K., Green, D.H., 1989. Stability of amphibole and phlogopite in metasomatized peridotite under water-saturated and water-undersaturated conditions. In:

Ross, J. (Ed.), Kimberlites and Related Rocks, vol. 1, Their Composition, Occurrence, Origin and Emplacement. Blackwell, Melbourne, pp. 571–581.
Middlemost, E.A.K., 1994. Naming materials in the magma/igneous rock system. Earth-Sci. Rev. 37, 215–224.
Moyen, J.F., Laurent, O., Chelle-Michou, C., Couzinié, S., Vanderhaeghe, O., Zeh, A., Villaros, A., Gardien, V., in press. Collision vs. subduction-related magmatism: two contrasting sites of granite formation and implications for crustal growth. Lithos. http://dx.doi.org/10.1016/j.lithos.2016.09.018.
Murphy, J.B., 2013. Appinite suites: a record of the role of water in the genesis, transport, emplacement and crystallization of magma. Earth-Sci. Rev. 119, 35–59.
Naeraa, T., Schersten, A., Rosing, M.T., Kemp, A.I., Hoffmann, J.E., Kokfelt, T.F., Whitehouse, M.J., 2012. Hafnium isotope evidence for a transition in the dynamics of continental growth 3.2 Gyr ago. Nature 485, 627–630.
Nelson, D.R., 1992. Isotopic characteristics of potassic rocks: evidence for the involvement of subducted sediments in magma genesis. Lithos 28, 403–420.
Nemchin, A.A., Cawood, P.A., 2005. Discordance of the U–Pb system in detrital zircons: implication for provenance studies of sedimentary rocks. Sediment. Geol. 182, 143–162.
Parat, F., Holtz, F., René, M., Almeev, R., 2009. Experimental constraints on ultrapotassic magmatism from the Bohemian Massif (durbachite series, Czech Republic). Contrib. Mineral. Petrol. 159, 331–347.
Patchett, P.J., Kouvo, O., Hedge, C.E., Tatsumoto, M., 1982. Evolution of continental crust and mantle heterogeneity: evidence from Hf isotopes. Contrib. Mineral. Petrol. 78, 279–297.
Payne, J.L., McInerney, D.J., Barovich, K.M., Kirkland, C.L., Pearson, N.J., Hand, M., 2016. Strengths and limitations of zircon Lu–Hf and O isotopes in modelling crustal growth. Lithos 248–251, 175–192.
Peccerillo, A., Taylor, S.R., 1976. Geochemistry of Eocene calc-alkaline volcanic rocks from the Kastamonu area, Northern Turkey. Contrib. Mineral. Petrol. 58, 63–81.
Pin, C., Lancelot, J., 1982. U–Pb dating of an early paleozoic bimodal magmatism in the French Massif Central and of its further metamorphic evolution. Contrib. Mineral. Petrol. 79, 1–12.
Pin, C., Paquette, J.L., 1997. A mantle-derived bimodal suite in the Hercynian Belt: Nd isotope and trace element evidence for a subduction-related rift origin of the Late Devonian Brévenne metavolcanics, Massif Central (France). Contrib. Mineral. Petrol. 129, 222–238.
Pin, C., Paquette, J.L., 2002. Sr–Nd isotope and trace element evidence for a Late Devonian active margin in northern Massif Central (France). Geodin. Acta 15, 63–77.
Plank, T., 2005. Constraints from thorium/lanthanum on sediment recycling at subduction zones and the evolution of the continents. J. Petrol. 46, 921–944.
Plank, T., Langmuir, C.H., 1998. The chemical composition of subducting sediment and its conseqiences for the crust and mantle. Chem. Geol. 145, 325–394.
Prelevic, D., Akal, C., Foley, S.F., Romer, R.L., Stracke, A., Van Den Bogaard, P., 2012. Ultrapotassic mafic rocks as geochemical proxies for post-collisional dynamics of orogenic lithospheric mantle: the case of Southwestern Anatolia, Turkey. J. Petrol. 53, 1019–1055.
Prouteau, G., Scaillet, B., Pichavant, M., Maury, R., 2001. Evidence for mantle metasomatism by hydrous silicic melts derived from subducted oceanic crust. Nature 410, 197–200.
Rapp, R.P., Norman, M.D., Laporte, D., Yaxley, G.M., Martin, H., Foley, S.F., 2010. Continent formation in the Archean and chemical evolution of the cratonic lithosphere: melt–rock reaction experiments at 3–4 GPa and petrogenesis of Archean Mg-diorites (sanukitoids). J. Petrol. 51, 1237–1266.
Roberts, N.M.W., Slagstad, T., Parrish, R.R., Norry, M.J., Marker, M., Horstwood, M.S.A., 2012. Sedimentary recycling in arc magmas: geochemical and U–Pb–Hf–O constraints on the Mesoproterozoic Suldal Arc, SW Norway. Contrib. Mineral. Petrol. 165, 507–523.
Roberts, N.M.W., Spencer, C.J., 2015. The zircon archive of continent formation through time. In: Special Publications, London Geological Society, vol. 389, pp. 197–225.
Rudnick, R.L., Gao, S., 2003. Composition of the continental crust. In: Rudnick, R.L. (Ed.), The Crust. Elsevier–Pergamon, Oxford, pp. 1–64.
Rutanen, H., Andersson, U.B., Väisänen, M., Johansson, Å., Fröjdö, S., Lahaye, Y., Eklund, O., 2011. 1.8 Ga magmatism in southern Finland: strongly enriched mantle and juvenile crustal sources in a post-collisional setting. Int. Geol. Rev. 53, 1622–1683.
Sabatier, H., 1991. Vaugnerites: special lamprophyre derived mafic enclaves in some Hercynian granites from Western and Central Europe. In: Didier, J., Barbarin, B. (Eds.), Enclaves and Grantie Petrology. Elsevier, Amsterdam, pp. 63–81.
Siebel, W., Chen, F., 2009. Zircon Hf isotope perspective on the origin of granitic rocks from eastern Bavaria, SW Bohemian Massif. Int. J. Earth Sci. 99, 993–1005.
Spencer, C.J., Cawood, P.A., Hawkesworth, C.J., Prave, A.R., Roberts, N.M.W., Horstwood, M.S.A., Whitehouse, M.J., 2015. Generation and preservation of continental crust in the Grenville Orogeny. Geosci. Front. 6, 357–372.
Stern, R.J., Scholl, D.W., 2010. Yin and Yang of continental crust creation and destruction by plate tectonic processes. Int. Geol. Rev. 52, 1–31.
Sun, S.s., McDonough, W.F., 1989. Chemical and isotopic systematics of oceanic basalts: implications for mantle composition and processes. In: Saunders, A.D., Norry, M.J. (Eds.), Magmatism in the Ocean Basins. Geological Society, London, pp. 313–345.
Taylor, S.R., McLennan, S.M., 1985. The Continental Crust: Its Composition and Evolution. Blackwell, Oxford, 312 pp.
Tenner, T.J., Hirschmann, M.M., Humayun, M., 2012. The effect of H_2O on partial melting of garnet peridotite at 3.5 GPa. Geochem. Geophys. Geosyst. 13 (3).
Thibault, Y., Edgar, A.D., Lloyd, F.E., 1992. Experimental investigation of melts from a carbonated phlogopite lherzolite: implications for metasomatism in the continental lithospheric mantle. Am. Mineral. 77, 784–794.
Turpin, L., Velde, D., Pinte, G., 1988. Geochemical comparison between minettes and kersantites from the Western European Hercynian orogen: trace element and Pb–Sr–Nd isotope constraints on their origin. Earth Planet. Sci. Lett. 87, 73–86.
Valley, J., Graham, C.M., Harte, B., Eiler, J.M., Kinny, P.D., 1998. Ion microprobe analysis of oxygen, carbon, and hydrogen isotope ratios. In: Applications of Microanalytical Techniques to Understanding Mineralizing Processes. Society of Economic Geologists, Littleton, pp. 73–98.
Vervoort, J., Blichert-Toft, J., 1999. Evolution of the depleted mantle: Hf isotope evidence from juvenile rocks through time. Geochim. Cosmochim. Acta 63, 533–556.
Villaseca, C., Orejana, D., Belousova, E., Armstrong, R.A., Pérez-Soba, C., Jeffries, T.E., 2010. U–Pb isotopic ages and Hf isotope composition of zircons in Variscan gabbros from central Spain: evidence of variable crustal contamination. Mineral. Petrol. 101 (3–4), 151–167.
von Raumer, J.F., Finger, F., Veselá, P., Stampfli, G.M., 2014. Durbachites–Vaugnerites – a geodynamic marker in the central European Variscan orogen. Terra Nova 26, 85–95.
Vroon, P.Z., Lowry, D., Van Bergen, M.J., Boyce, A.J., Mattey, D.P., 2001. Oxygen isotope systematics of the Banda Arc: low $\delta^{18}O$ despite involvement of subducted continental material in magma genesis. Geochim. Cosmochim. Acta 65, 589–609.
Williams, H.M., Turner, S., Pearce, J.A., Kelley, S., Harris, N.B.W., 2004. Nature of the source regions for post-collisional, potassic magmatism in southern and northern Tibet from geochemical variations and inverse trace element modelling. J. Petrol. 45, 555–607.
Wittig, N., Baker, J.A., Downes, H., 2007. U–Th–Pb and Lu–Hf isotopic constraints on the evolution of sub-continental lithospheric mantle, French Massif Central. Geochim. Cosmochim. Acta 71, 1290–1311.
Woodhead, J., Hergt, J., Shelley, M., Eggins, S., Kemp, R., 2004. Zircon Hf-isotope analysis with an excimer laser, depth profiling, ablation of complex geometries, and concomitant age estimation. Chem. Geol. 209, 121–135.
Workman, R.K., Hart, S.R., 2005. Major and trace element composition of the depleted MORB mantle (DMM). Earth Planet. Sci. Lett. 231, 53–72.
Xiong, F., Ma, C., Wu, L., Jiang, H.a., Liu, B., 2015. Geochemistry, zircon U–Pb ages and Sr–Nd–Hf isotopes of an Ordovician appinitic pluton in the East Kunlun orogen: new evidence for Proto-Tethyan subduction. J. Asian Earth Sci. 111, 681–697.
Yin, J., Chen, W., Xiao, W., Yuan, C., Sun, M., Tang, G., Yu, S., Long, X., Cai, K., Geng, H., Zhang, Y., Liu, X., 2015. Petrogenesis of Early-Permian sanukitoids from West Junggar, Northwest China: implications for Late Paleozoic crustal growth in Central Asia. Tectonophysics 662, 385–397.
Zhao, Z.F., Dai, L.Q., Zheng, Y.F., 2013. Postcollisional mafic igneous rocks record crust–mantle interaction during continental deep subduction. Sci. Rep. 3, 3413.

5.4 Additional discussion on the source of crust-derived granites

5.4.1 Rationale

Moyen et al. (2017a) argued that the chemical differences between MPG and CPG granites result from both: (i) contrasted sources and (ii) different T–X_{H_2O} melting conditions and thus melting reactions. The MPG would have formed by water-present melting or muscovite-dehydration melting of metasediments while the CPG would correspond to higher-T magmas, generated by biotite-dehydration melting of a quartzo-feldspathic (orthogneiss) source. However, CPG and MPG share the same inherited zircon age pattern (Laurent et al., 2017) which is inconsistent with different magma sources. It rather suggests that chemical variations arose solely from petrogenetic processes i.e. contrasted melting temperatures/reactions, variable extent of peritectic assemblage entrainment, restite unmixing (see Clemens and Stevens, 2012).

Laurent et al. (2017) attempt to identify the source material of MPG/CPG granites by comparing their inherited zircon age distribution to the respective patterns of meta-igneous and metasedimentary rocks from the FMC. At the time the paper was written, such approach suffered from the scarcity of available zircon ages on the eastern FMC basement. This led the authors to use a (limited) dataset from the western FMC which pre-Variscan evolution markedly contrasts with that inferred for the eastern FMC (see Chapter 4). A better knowledge of the nature, zircon age distribution and Hf isotope composition of the eastern FMC constituent lithologies has been gained over the past two years and allows to put further constraints on the nature of the reworked materials during the Variscan orogeny.

In the following, we consider that inherited zircon grains in MPG/CPG are dominantly restitic and were incorporated in the magma at source level (Clemens, 2003) thus providing a faithful record of the source age pattern.

5.4.2 Meta-igneous vs. metasedimentary source

Figure 5.2 compares the age distribution of inherited zircon grains in MPG/CPG with that of the main lithologies of (a) the Lower Gneiss Unit (b) and the Upper Gneiss Unit. Clearly, the dominant *c.* 545 Ma inherited population matches the emplacement age of meta-granites from the Velay Orthogneiss Formation. Besides, the Hf isotope composition of these inherited grains remarkably mimicks that of VOF zircons (Fig. 5.3a) providing further evidence for extensive melting of the VOF meta-granites at Variscan times. Involvement of meta-igneous rocks akin to the Riverie tonalites, also of adequate age (Fig. 5.2b) is excluded by their highly radiogenic isotope signature (Fig. 5.3b) not encountered in the *c.* 545 Ma-old inherited grains. The "tail" of inherited zircon ages running from 560 to 1100 Ma (besides subordinate c. 2 Ga and 2.7 Ga components, not shown) could be explained by the coeval subordinate melting of LGU metasediments and incorporation of detrital zircon grains in the resulting magmas. Such detrital grains do have suitable Hf isotope compositions as they show a similar scatter than the one observed in inherited zircons (Fig. 5.3a). Finally, the age distribution of inherited zircons also displays a peak at *c.* 470 Ma which does not correspond to any LGU lithology, in our present state of knowledge (Fig. 5.2a). Alternatively, it could be explained by the presence in the granite source region of UGU gneisses and amphibolites (Fig. 5.2b). Apart for one grain, *c.* 470 Ma-old inherited zircons have Hf isotope compositions closer to UGU gneisses than amphibolites favouring a gneissic source, in line with the chemistry of MPG/CPG granites (Moyen et al., 2017a).

Overall, these comparisons suggest that the source of MPG/CPG is mixed and composed of: (i) meta-granites of the VOF; (ii) metasediments of the LGU; (iii) a metamorphic lithology which zircon age pattern resembles that of UGU gneisses. It is unlikely

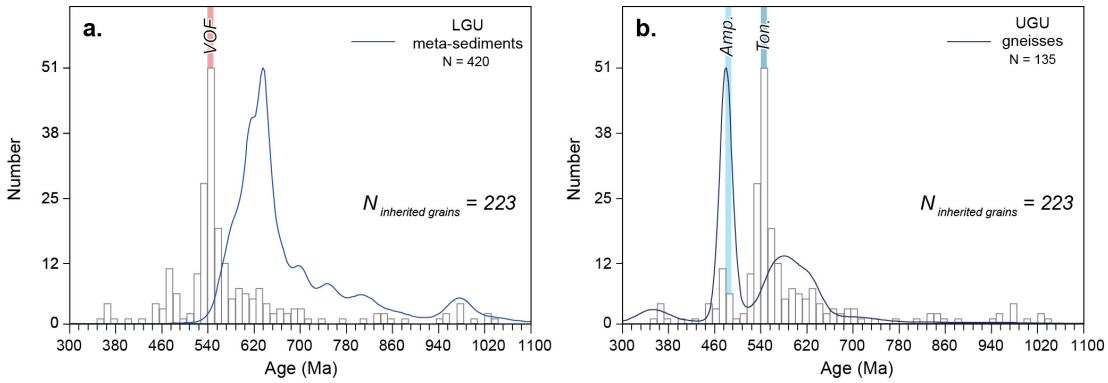

Figure 5.2: Inherited zircon U–Pb date distribution for MPG/CPG granites from the eastern French Massif Central. Only 95–105% concordant $^{206}Pb/^{238}U$ dates were considered. Data from Couzinié et al. (2014); Laurent et al. (2017) and Chelle-Michou et al. (2017). Are shown for comparison: (a) the distribution of U–Pb dates in metasediments from the Lower Gneiss Unit represented as Kernel Density Estimate (KDE), together with the range of emplacement ages of meta-granites from the Velay Orthogneiss Formation (data from Chelle-Michou et al., 2017; Couzinié et al., 2017 and Chapter 6); (b) the distribution of U–Pb dates in gneisses from the Upper Gneiss Unit represented as Kernel Density Estimate (KDE), together with the range of emplacement ages of meta-basites and meta-tonalites from the Upper Gneiss Unit (data from Chelle-Michou et al., 2017 and Chapter 3). Plotted with the DensityPlotter program of Vermeesch (2012). The bandwidth of the KDEs was set to 12 Ma (the average 2σ error of individual analyses).

that the UGU itself is present in the source region of MPG/CPG. Indeed, metamorphic and structural investigations clearly support an allochtonous origin of the nappe which would have been rooted further north with respect to the Velay dome (Burg et al., 1984; 1989). An alternative would be to consider that early Variscan thrusting resulted in the imbrication of crust slices with contrasted pre-Variscan histories so that a crust segment having recorded Ordovician magmatic events would lie structurally below the LGU. Such possibility is supported by U–Pb dating conducted on metasedimentary lower crustal xenoliths scavenged by Cenozoic volcanoes (Rossi et al., 2006). In addition to grains showing "Variscan" dates, these authors report the presence of older zircons with concordant $^{206}Pb/^{238}U$ dates ranging from 629 ± 56 Ma down to 436 ± 12 Ma. Such material would adequately correspond to the UGU-alike component. Yet, limited available data do not allow to further test this hypothesis.

Rough estimates of the proportion of the three above-mentioned components may be retrieved via the following procedure. The set of inherited zircon grains is divided into three subsets: late Cambrian–Ordovician (445–530 Ma), Ediacaran–early Cambrian (530–560) and older dates (> 560 Ma). Each subset is assumed to exclusively originate from one of the three inferred source components, respectively the "UGU-alike" material, the VOF meta-granites and the LGU metasediments. A zircon "fertility" factor (ZFF of Dickinson, 2008) is attributed to each source based on their average Zr content, provided that all Zr is hosted in zircon. Our chemical survey (see Chapter 2 and Appendix Table B1) indicate that the VOF meta-granites and LGU metasediments have average Zr concentrations of 104 and 260 ppm resulting in ZFF of 1 and 2.5, respectively. The ZFF of the "UGU-alike" material was set free to vary between these two values. Resulting proportions in the source of MPG/CPG are 10–22 % for the "UGU-alike" component, 55–65 % for the VOF and 22–26 % for the LGU metasediments. Such first-order calculation implicitly requires that all three sources melt synchronously and produce magmatic liquids of similar compositions so that each zircon grain, no matter its origin, has the same probability to survive dissolution. Of course, such assumption is highly simplistic and entails that the results are only crude estimates.

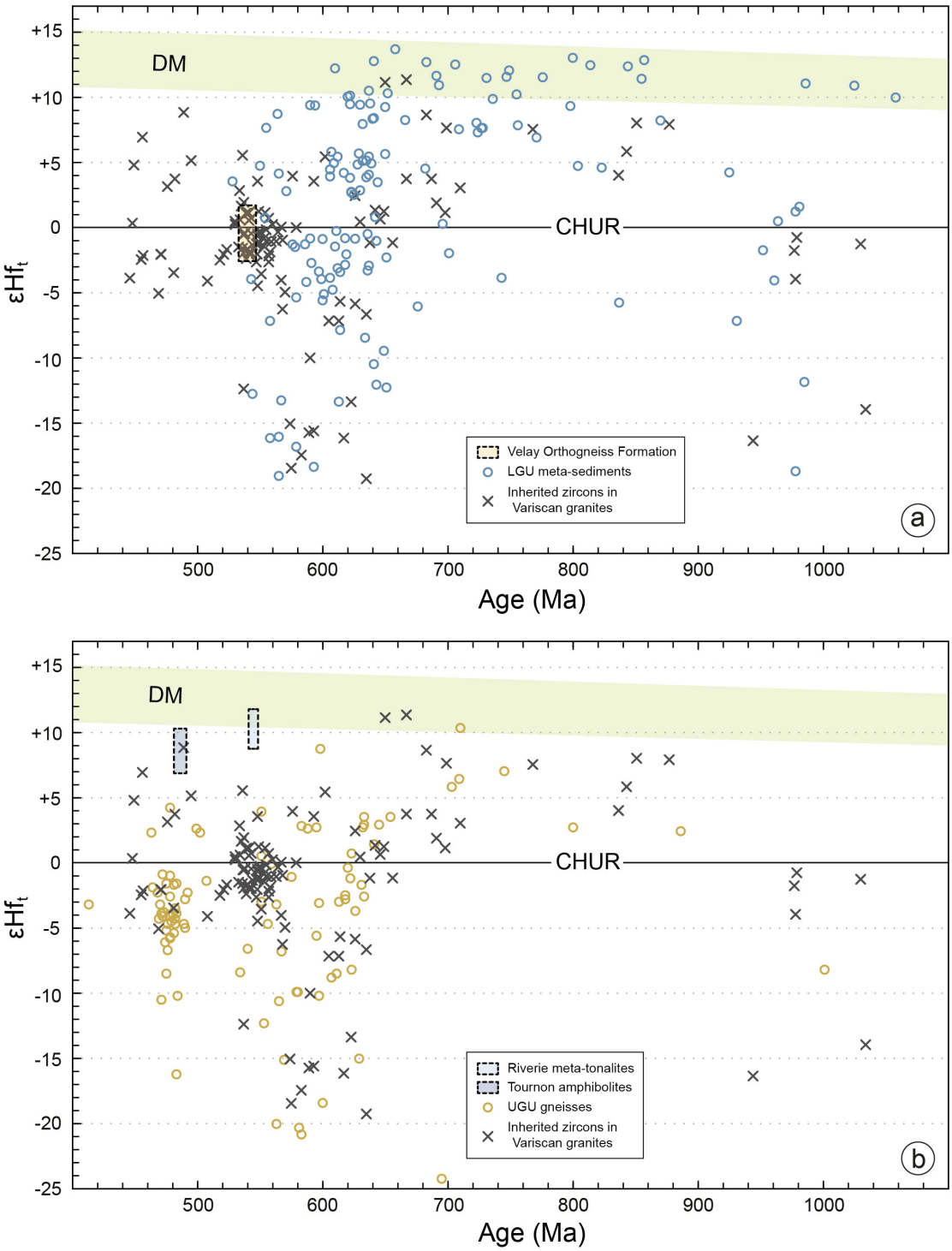

Figure 5.3: Combined U-Pb and Lu-Hf isotopic data for inherited zircons in Variscan crust-derived granites (CPG/MPG) compared to the signature of constituent lithologies from the Lower (a) and Upper (b) Gneiss Units. Data for the Velay Orthogneiss Formation from Couzinié et al. (2017), for the Riverie meta-tonalites from this work, for LGU metasediments from Chelle-Michou et al. (2017) and this work, for Variscan granites from Moyen et al. (2017a); Chelle-Michou et al. (2017), for UGU gneisses from Chelle-Michou et al. (2017). The ε_{Hf}(t) range for the Depleted Mantle reservoir is bracketed by the models of Naeraa et al. (2012) and Griffin et al. (2002).

5.4.3 Conclusion

Examination of the inherited zircon record in Variscan peraluminous granites suggests that one of the constituent lithology of the FMC crust segment (the Velay Orthogneiss Formation) was selectively reworked during the post-collisional magmatic episode. Several hypotheses can be formulated to account for this. First, this may reflect the mass distribution of each crustal component at depth, the VOF being volumetrically dominant as observed at present-day outcropping level. Alternatively, such apparent pattern may arise from contrasted zircon behaviour in metasedimentary vs. meta-igneous derived magma batches. These hypotheses can be tested by further examining the root zone of granite magmas i.e. migmatite terrains. This is further discussed in the next Chapter which provides a comprehensive case study of a migmatite dome from the southern part of the Velay Complex.

Chapter 6

Post-collisional exhumation of the partially molten crust: a case study from the Masméjean migmatite dome

Partial melting of the continental crust generates incompatible element-rich, mobile and buoyant melts that rise upwards to the surface and ultimately lead to the chemical layering of the crust (Sawyer, 1994; Sawyer et al., 2011; Vielzeuf et al., 1990). Migmatites are crustal rocks that preserve evidence for the concomitant presence of a melt and a residual solid phase in their framework and are thus regarded as the source of crust-derived magmas (Brown, 1994; Clemens, 1990). Such rocks are abundant in orogenic domains where they often crop out in gneiss domes. Those are typically composed of a core built up by high-grade, commonly anatectic, metamorphic lithologies (plus granites) featuring a domal foliation and are mantled by rocks of lower metamorphic grade (Teyssier and Whitney, 2002; Whitney et al., 2004a). The concurrence of dome formation and anatexis has been interpreted as reflecting the vertical flow of partially molten middle to lower crustal layers (Tirel et al., 2004; Whitney et al., 2004b) and suggests that doming is intimately linked with the process of continental crust reworking.

Anatectic gneiss domes are generated in a range of regional strain conditions, from extensional (in metamorphic core complexes, where dome formation is controlled by localized extension in the upper crust, e.g. Brun and Van Den Driessche, 1994; Chen et al., 1990; Escuder Viruete et al., 2000) to compressional (buckle folds, e.g. Burg et al., 1997; 2004; Štípská et al., 2000; Zeitler et al., 1993). In both cases, diapirism, which refers to the buoyancy-driven ascending flow that counteracts inverted density gradients (Biot and Odé, 1965; Weinberg and Schmeling, 1992), would proceed during doming since partially molten rocks are less dense than their overlying roof units (Bouhallier et al., 1995; Burg and Vanderhaeghe, 1993; Calvert et al., 1999; Kruckenberg et al., 2011; Soula et al., 2001; Weinberg and Podladchikov, 1994; Whitney et al., 2004b).

Diapirism may strongly shape migmatite domes as it generates a set of positive feedback scenarios (Whitney et al., 2004b). Vertical transfer of anatectic rocks during doming provokes near-isothermal decompression which enhances melting (Rey et al., 2009; Whitney et al., 2004a). At increasing melt fractions, the viscosity drop and rheological transitions towards a magma behavior (Vanderhaeghe and Teyssier, 2001; Vanderhaeghe, 2009; Vigneresse et al., 1996) would ease the *en-masse* vertical flow of the partially molten crust and establish it as a self-sustained process. Numerical models show that buoyancy-driven flow does control the structure of extensional domes submitted to slow free-boundary extension (Rey et al., 2011), a setting observed in the collapse of orogenic plateaux associated with divergence (Rey et al., 2001). Yet, such models do not investigate the case where dome formation is related to collapse at fixed-boundary conditions.

This situation features substantial potential energy transfer between adjacent crustal domains (Rey et al., 2001) partly accommodated by strike-slip tectonics which role during doming remains unclear (Lagarde and Dallain, 1994).

In this chapter, I attempt to: (i) evaluate the respective contributions of the regional strain field vs. buoyancy-driven partially molten crust dynamics in determining the shape of migmatite domes formed during orogenic collapse; (ii) identify the parameters that control their regional distribution; (iii) characterize the petrogenesis of exhumed migmatites and associated granites; and (iv) investigate the behaviour of the zircon U–Pb chronometer in anatectic settings. This study is based on a natural example from the Variscan eastern French Massif Central: the Masméjean dome, on which new structural observations, Anisotropy of Magnetic Susceptibility (AMS) mapping and zircon/monazite U–Pb geochronological investigations were performed.

Field work was conducted with Pierre Bouilhol (now at CRPG, Nancy) who significantly contributed to all the ideas presented hereafter. The AMS study was performed in collaboration with Jérôme Bascou (Saint-Etienne University). U–Pb data was acquired with the assistance and under the supervision of Oscar Laurent (ETH Zürich, for zircon) and Jean-Louis Paquette (Laboratoire Magma et Volcans, Clermont–Ferrand, for monazite).

6.1 Geological setting

The Masméjean dome is located at the intersection between three main Variscan lithotectonic units from the eastern French Massif Central (Fig. 6.1 and 6.2). To the North-East, it flanks the southern part of the Velay Complex, a 120x80 km granite–migmatite poly-diapiric dome that nucleated during orogenic collapse and is attributed to the Lower Gneiss Unit of Ledru et al. (1989) (see review in Ledru et al., 2001). The Margeride granite crops out to the West and corresponds to the largest intrusive batholith of the French Massif Central (Chantraine et al., 1996). To the South, lies one of the peripheral parautochton complexes (PAU) defined by Ledru et al. (1989).

6.1.1 The Velay Complex

General architecture The Velay Complex is an asymmetric granite–migmatite dome bounded to the North by a ductile extensional shear zone showing top-to-the N sense of shear (Malavielle et al., 1990) and referred hereafter as "Pilat Shear Zone" (Fig. 6.1). The timing of its activity and associated dome exhumation is bracketed by the intrusion of the syntectonic "Gouffre d'Enfer" granite (Vitel, 1988) dated at 322 ± 9 (Rb–Sr on whole-rock, Caen-Vachette et al., 1984) and 301.8 ± 3.1 Ma (U–Pb on zircon, C. Chelle-Michou, personal communication). To the East, flat-lying migmatites represent the dome roof, which is seen intruding the overlying Upper Gneiss Unit (Anthonioz, 1987; Lagarde et al., 1990; Lagarde and Dallain, 1994; Ledru et al., 2001). The western and southern margins are steeply dipping with the dome being locally overturned to the South (Burg and Vanderhaeghe, 1993; Lagarde and Dallain, 1994; Ledru et al., 2001). The strain pattern in the dome core features: (i) concentric structures regarded as intrusive, diapiric effects; (ii) vertical wrench ductile N–S sinistral and NE–SW dextral shear zones (Dupraz and Didier, 1988; Lagarde et al., 1990; Lagarde and Dallain, 1994; Ledru et al., 2001).

Tectonic–metamorphic evolution of its southern margin Recent river incision resulted in the southern margin being the best-exposed part of the dome (Fig. 6.2) and this area has accordingly been the subject of numerous studies reviewed in Barbey et al. (2015). The southernmost part of the Velay Complex, separated from the main granite–migmatite mass by the La Souche fault, corresponds to an E–W trending sub-dome referred to as "Tanargue" dome in the following (Fig. 6.2).

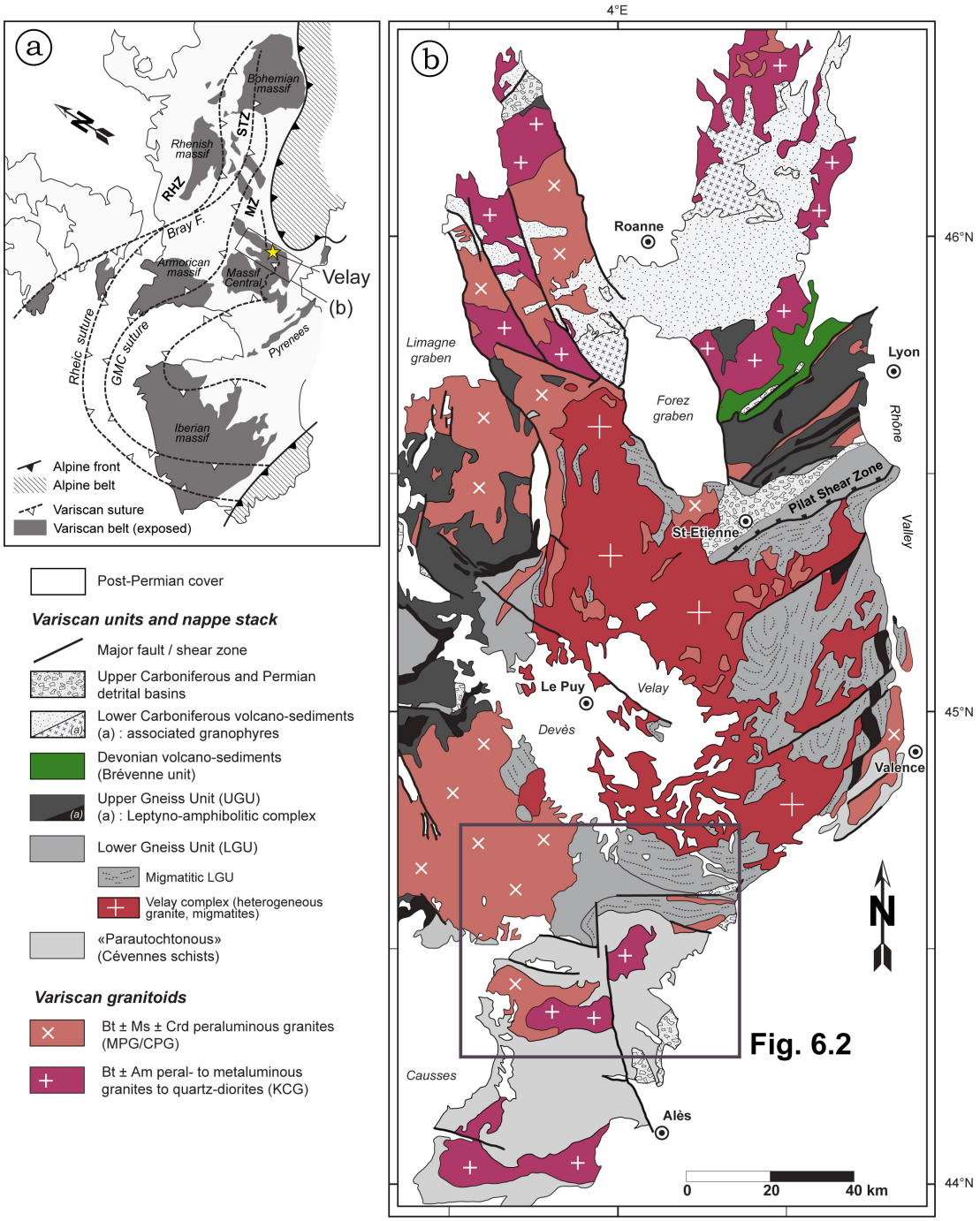

Figure 6.1: (a) General location of the Variscan belt of Europe and inferred suture zones. Abbreviations: GMC Galicia-Massif Central, STZ Saxo-Thurigian Zone, RHZ Rhenohercynian Zone, MZ Moldanubian Zone. The yellow star highlights the location of the Velay Complex. (b) Geological map of the eastern French Massif Central (Velay area) redrawn after Chantraine et al. (1996).

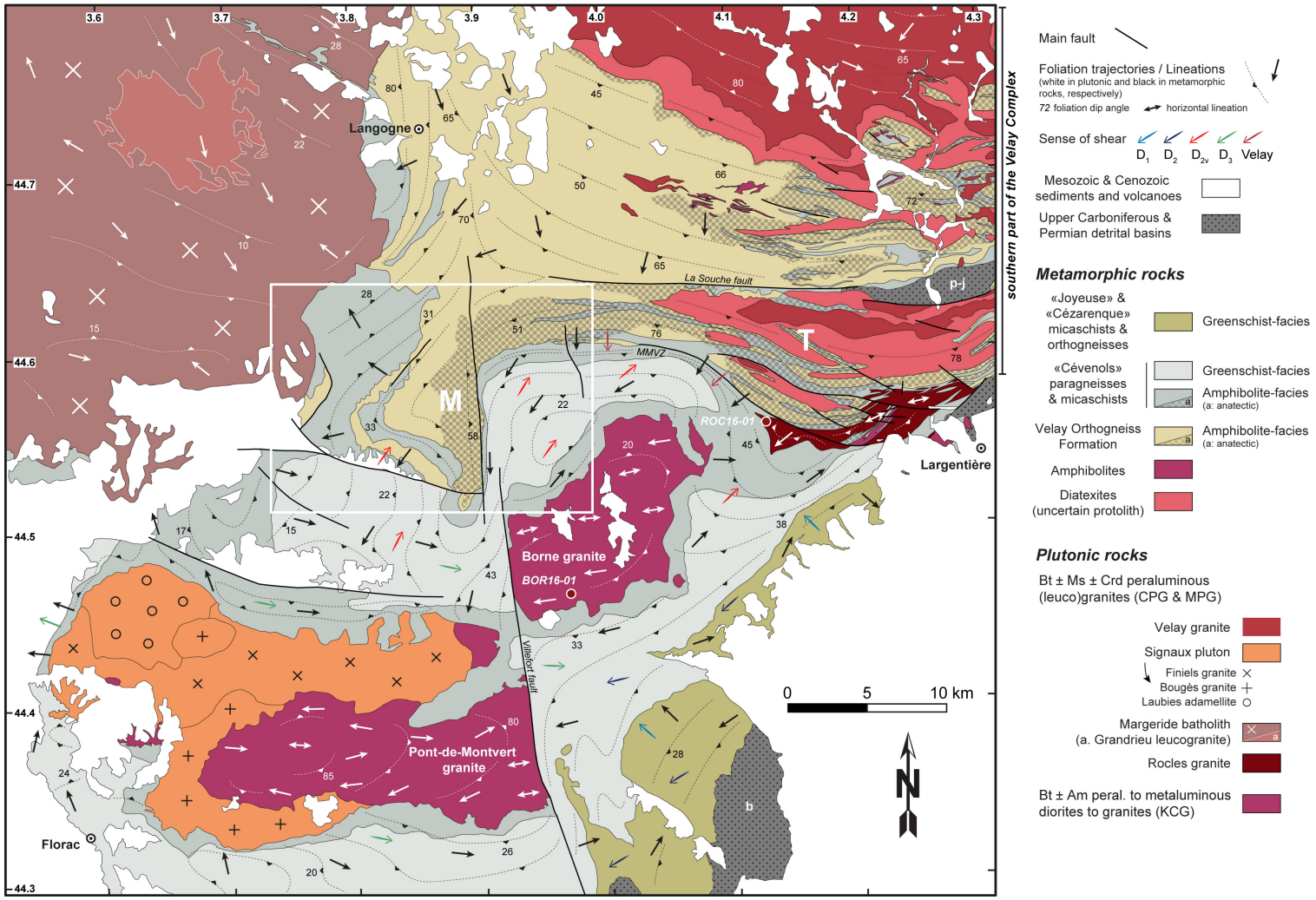

Figure 6.2: Geological map at scale 1/290000 outlining the situation of the study area. Lithological contours, foliation trajectories, main regional lineations drawn based on our own field survey and the works of Alabouvette et al. (1988); Bambier et al. (1985a); Bouilhol (2004); Bouilhol et al. (2006); Briand et al. (1994); Choubert and Girod (1974a); Couturié (1974); Dallain et al. (1999); Dumas (2003); Faure et al. (1992); Faure (1995); Gèze et al. (1979; 1980); Négron (1979); Talbot et al. (2004; 2005); Rakib (1996); Viard (1981) and Weisbrod et al. (1974). Abbreviations: M, Masméjean dome; T, Tanargue dome; p-j, Prades–Jaujac basin; b, Bessèges basin.

Constituent metamorphic rocks of the southern part of the Velay Complex include (Weisbrod, 1970): Ediacaran paragneisses from the "Série Cévenole" and late-Ediacaran orthogneisses from the "Série Ardéchoise" which are part of the "Velay Orthogneiss Formation" (see section 2.1). Scarce amphibolites corresponding to meta-alkali basalts are locally observed (Bambier et al., 1985b; Pin and Marini, 1993).

The main regional S_n foliation is reworked by prominent NW-SE to E-W trending folds affecting all lithologies, with second-order asymmetric chevrons showing south-dipping to vertical long limbs and horizontal short limbs (Anthonioz, 1985; Macaudière et al., 1987; Marignac et al., 1980). Folding was synchronous with limited M_3 anatexis (Laumonier et al., 1991; Macaudière et al., 1992) at T $\sim$ 720°C and P = 0.5–0.6 GPa (Ait Malek et al., 1995; Barbey et al., 2015; Montel et al., 1992). M_3 migmatites are generally metatexites (Fig. 6.2) and anatexis has been dated between 331 ± 4 (U–Th–Pb EPMA age on monazite, Be Mezeme et al., 2005a, Fig. 6.3 and 6.4) and 315 ± 5 Ma (U–Pb ID–TIMS on monazite, Mougeot et al., 1997, Fig. 6.3 and 6.4).

A more intense M_4 melting event at T $\geq$ 800°C and P $\sim$ 0.4 GPa (Barbey et al., 2015; Montel et al., 1992) developed coevally to the intrusion of the Velay granite (Dupraz and Didier, 1988; Lagarde et al., 1990; Weisbrod, 1962), dated at 305.9 ± 1.7 Ma (LA–ICP–MS U–Pb age on monazite, Couzinié et al., 2014, Fig. 6.3 and 6.4) and 301 ± 5 Ma (ID–TIMS U–Pb age on monazite, Mougeot et al., 1997, Fig. 6.3 and 6.4). M_4 migmatites are mostly diatexites (Fig. 6.2).

The last increment of melting resulted in the intrusion of the so-called "late-migmatitic granites" between 307 ± 2 Ma (LA–ICP–MS U–Th–Pb age on monazite, Didier et al., 2013) and 304.6 ± 5.0 Ma (U–Pb zircon, recalculated from Couzinié et al., 2014, taking into account systematic errors) and thought to have been generated at T ~850°C and P = 0.4–0.6 GPa (Barbey et al., 2015; Montel et al., 1986). Given their overlapping emplacement ages, undistinguishable within errors, the main Velay phase and the "late-migmatitic granites" are grouped together in Fig. 6.2. Potassic diorites (locally called "vaugnerites") originating from melting of the orogenic mantle (see section 5.3) are commonly observed within the dome and yielded identical within error emplacement ages between 307.4 ± 3.9 and 305.8 ± 4.1 Ma (U–Pb zircon, Couzinié et al., 2014, and Laurent et al., 2017, taking into account systematic errors, Fig. 6.3 and 6.4).

Contact between the migmatite dome and the overlying Cévennes schists
The contact corresponds to a high-temperature mylonite (Fig. 6.2) referred to as "Metamorphic Mylonitic Vellave Zone" (MMVZ, Bouilhol et al., 2006). In the Bt–Sil zone, the deformation features: (i) a non-negligible pure shear component and (ii) stretching lineation perpendicular to the dome–schists contact with a top-to-the S sense of a shear (Bouilhol et al., 2006). According to these authors, this pattern would reflect the diapiric ascent of the migmatite dome piercing through its metasedimentary cover and accounts for the constriction of the And–Crd–Bt zone in the Cévennes schists (see below and Fig. 6.2). At the contact between migmatites and schists lies the Rocles syntectonic granite (Weisbrod et al., 1980) showing a well-defined ENE–WSW trending magnetic lineation (Be Mezeme et al., 2007) and for which a range of ages have been obtained, from 325 ± 5 Ma (U–Th–Pb EPMA dating of monazite, Be Mezeme et al., 2006) down to 302 ± 3 Ma (Rb–Sr whole-rock, Caen-Vachette et al., 1981).

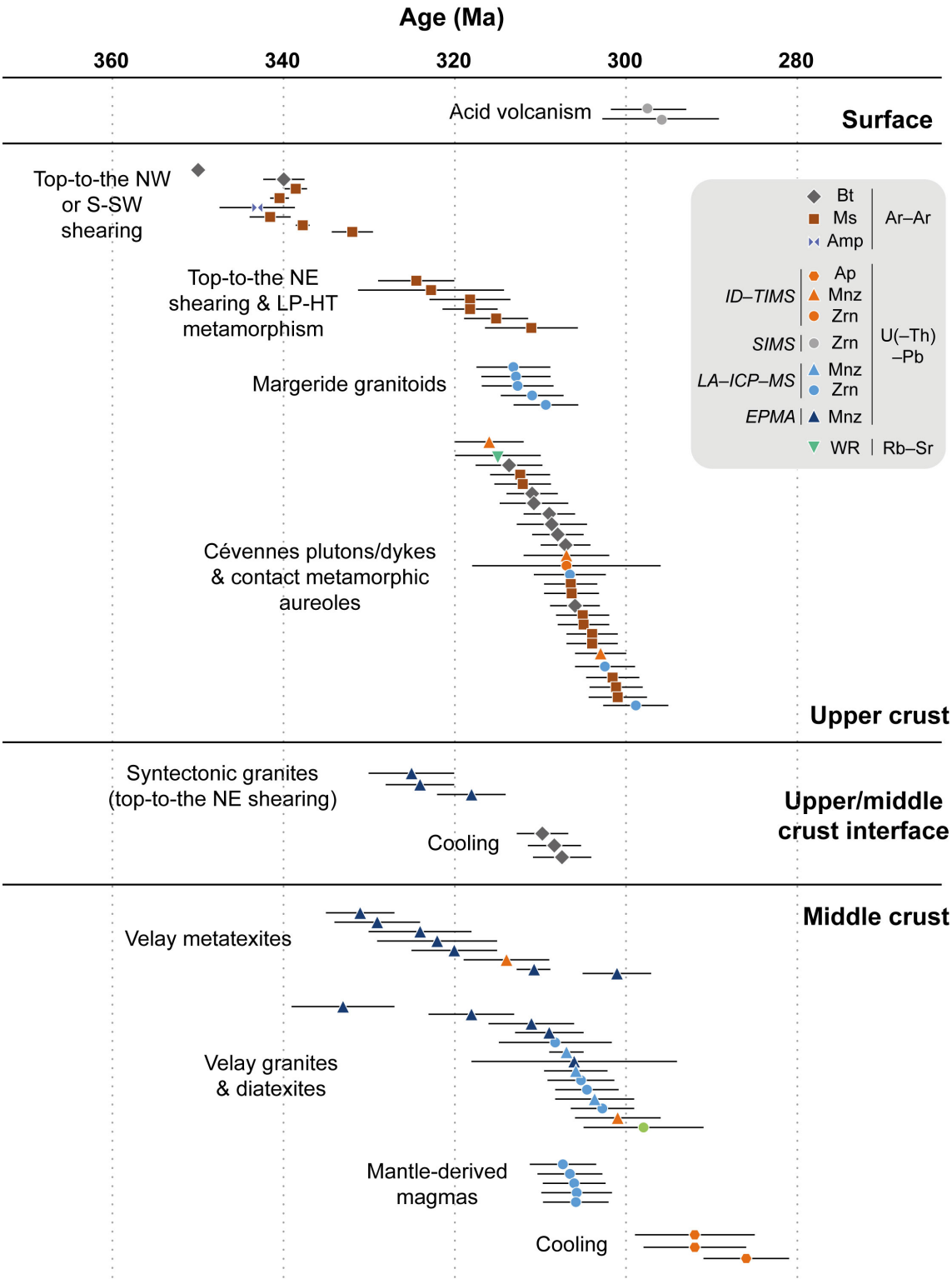

Figure 6.3: Summary of available geochronological constraints on tectonic, metamorphic and magmatic events in the upper and the middle crust and at the interface between them (namely the Mylonitic Metamorphic Vellave Zone of Bouilhol et al., 2006). Data from Be Mezeme et al. (2005a); Be Mezeme (2005b); Be Mezeme et al. (2006; 2007); Bouilhol et al. (2006); Bouilhol (2004); Brichau et al. (2007); Bruguier et al. (2003); Caron (1994); Cocherie et al. (2005); Chauvet et al. (2011); Couzinié et al. (2014); Didier et al. (2013); François (2009); Isnard (1996); Laurent et al. (2017); Mialhe (1980); Monié et al. (2000); Montel et al. (2002) and Mougeot et al. (1997).

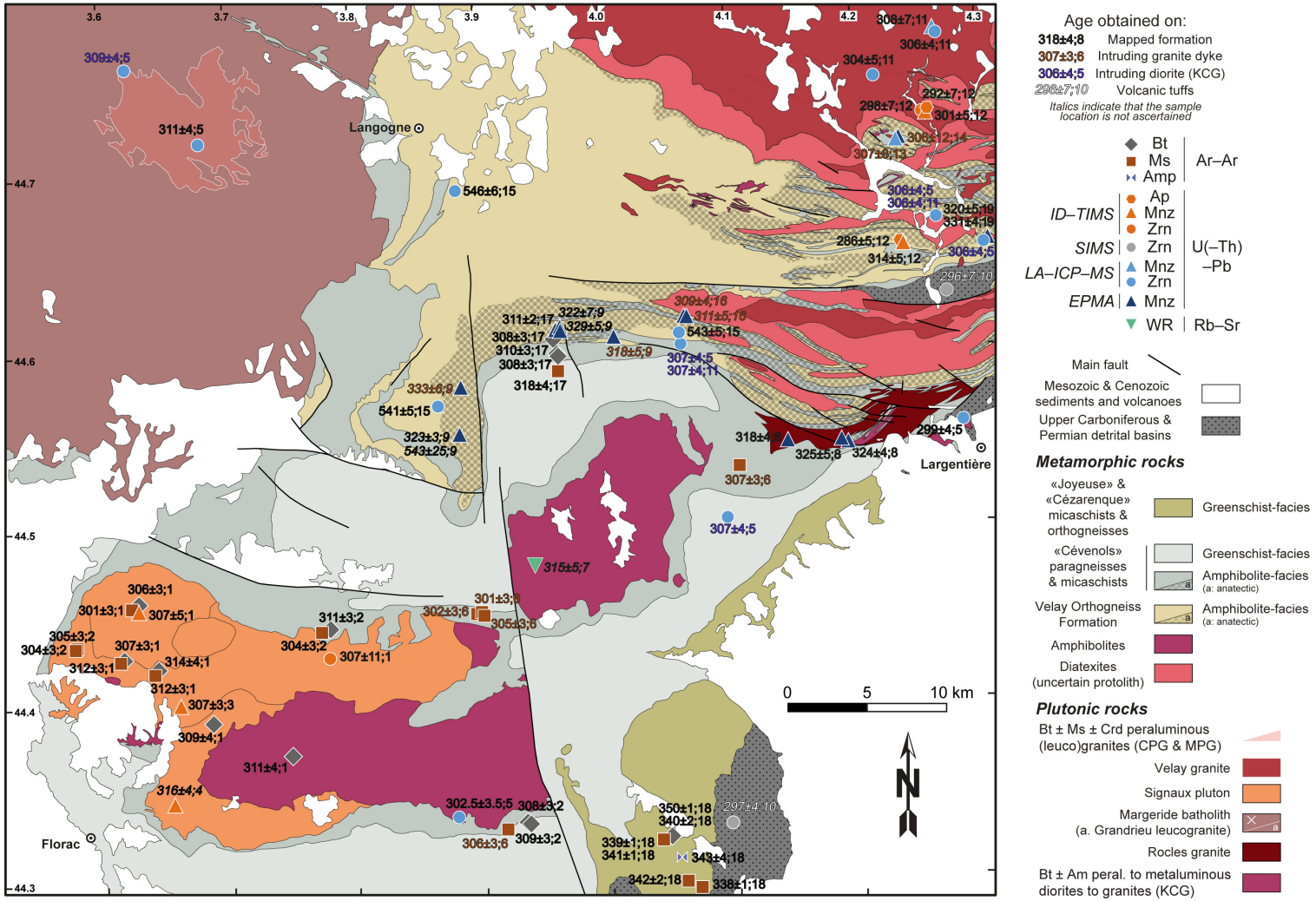

Figure 6.4: Geological map at scale 1/290000 identical to Fig. 6.2 onto which are reported available geochronological data. Each symbol refers to a specific dating technique as displayed Fig. 6.3. Data sources. 1:François (2009); 2: Monié et al. (2000); 3: Brichau et al. (2007); 4: Isnard (1996); 5: Laurent et al. (2017); 6: Chauvet et al. (2011); 7: Mialhe (1980); 8: Be Mezeme et al. (2007); 9: Be Mezeme et al. (2006); 10: Bruguier et al. (2003); 11: Couzinié et al. (2014); 12: Mougeot et al. (1997); 13: Didier et al. (2013); 14: Montel et al. (2002); 15: Couzinié et al. (2017); 16: Cocherie et al. (2005); 17: Bouilhol et al. (2006); 18: Costa (1990); 19: Be Mezeme et al. (2005a).

Timing of dome exhumation Top-to-the S shearing in the MMVZ has been dated at 310.7 ± 2 Ma and cooling at 307.5 ± 3.4 Ma (monazite EPMA U–Th–Pb and biotite Ar–Ar ages, respectively, Bouilhol et al., 2006, Fig. 6.3). Migmatites and granites are unconformably overlain by the Prades–Jaujac detrital basin and found within its basal conglomerate (Bouilhol et al., 2006). The zircon U–Pb age of 296 ± 6.8 Ma (SIMS, Bruguier et al., 2003, Fig. 6.3 and 6.4) obtained from bentonites indicate that high-grade rocks were already exposed at surface level by that time. This is consistent with the migmatites and granite U–Pb apatite cooling ages ranging between 292 ± 6 and 286 ± 5 Ma (Mougeot et al., 1997, Fig. 6.3 and 6.4).

6.1.2 The Cévennes schists

Lithologies The Cévennes schists are composed of two main litho-tectonic units. The "Joyeuse/Cézarenque" series are built up by greenschist-facies metasediments and calc-alkaline Bt-bearing augen gneisses (Crevola et al., 1983; Elmi et al., 1989) of unknown age. The "Cévenole" series comprise greenschist- to amphibolite-facies micaschists and quartzites corresponding to a metamorphosed Cambrian–Ordovician terrigenous sedimentary sequence (Faure et al., 2009).

Intruding granitoids The Cévennes schists are intruded by a set of igneous rocks:

- the Signaux batholith (Brichau et al., 2007), itself composed of the Laubies adamellite, the Finiels and Bougès granites. Those granitoids are peraluminous, show magmatic muscovite and/or cordierite (Guérangé-Lozes and Pellet, 1990; Sabourdy and Berthelay, 1977) and thus belong to the MPG/CPG types of Barbarin (1999), hence their crustal origin.
- the Pont-de-Monvert, Rabeyrals, Borne and Largentière plutons. All these granitoids are Kfs-porphyritic, contain mafic amphibole-bearing enclaves (Guérangé-Lozes and Pellet, 1990) and are intimately associated with vaugnerites (Couzinié et al., 2014) suggesting that they belong to the KCG type of Barbarin (1999). They would thus represent mafic magma differentiates (Laurent et al., 2017; Moyen et al., 2017a).
- plutonic to volcanic (lamprophyre and rhyolite) dykes. These rocks are locally widespread, for instance east of the Borne granite or south of the Mont-Lozère pluton (Alabouvette et al., 1988; Chauvet et al., 2011; Laurent et al., 2017; Weisbrod et al., 1974).

Structures Polyphase deformation affected the Cévennes schists. Early top-to-the W–NW thrusting (D_1, Table 6.1) generated kilometer-scale folds with a N–S to NE–SW axial planar foliation (Arthaud et al., 1969; Brouder, 1971). NW-SE trending stretching lineations with a top-to-the-NW sense of shear are described in the eastern Cévennes (Bouilhol et al., 2006). This event would have juxtaposed the "Joyeuse/Cézarenque" series over the "Cévenole" series (Barbey et al., 2015; Bouilhol et al., 2006). Both units were subsequently affected by top-to-the S–SW shearing (D_2) coeval with the development of E–W trending folds overturned to the South (Arnaud et al., 2004; Arthaud et al., 1969; Brouder, 1968; Faure et al., 1999; 2001; Lacassin and Van Den Driessche, 1982). Close to the Tanargue dome, the micaschists display a NE–SW trending stretching lineation but with a top-to-the NE sense of shear (Bouilhol et al., 2006; Faure et al., 2001) pinpointing an apparent transport of the metasediments over the Velay dome (D_2v). Intrusion of the Rocles granite would be coeval to this deformation phase (Be Mezeme et al., 2007). Finally, a late ductile deformation increment (D_3) featuring WNW–ESE trending lineations would have developed in an extensional context (Faure, 1995; Faure et al., 1999; 2001). Shear criteria indicate top-to-the-ESE and top-to-the WNW transport in the eastern and western Cévennes, respectively (Faure et al., 1999; 2001).

Name	Lineation direction	Sense of shear	Age
D_1	NW–SE	Top-to-the NW	$\geq$ 340 Ma
D_2	NE–SW to N–S	Top-to-the S–SW	320 $\leq$ X $\leq$ 340 Ma
D_{2v}	NE–SW	Top-to-the NE	*c.* 320 Ma
D_3	WNW–ESE	Top-to-the-ESE and WNW	$\leq$ 315 Ma

Table 6.1: Summary of available structural data in the Cévennes schists.

Structural studies were conducted on the Pont-de-Monvert and Borne plutons using conventional (Faure et al., 1992; Faure, 1995) and magnetic (AMS) methods together with gravimetry (Faure et al., 2001; Talbot et al., 2000; 2004). They identified a magma feeding zone west of the Pont-de-Montvert granite and showed that this pluton expanded eastwards in a regional E–W extensional context. The Borne pluton would rather be tabular and shows a ENE–WSW trending horizontal magmatic lineation (Fig. 6.2).

Because of their petrological similarities, the Borne and Pont-de-Montvert plutons have often been regarded as formerly being part of single batholith subsequently dismembered by the N–S trending Villefort fault (Fig. 6.2, Arthaud and Matte, 1975; Deroin et al., 1990; Lapadu-Hargues, 1947). Using both batholiths as passive markers, a lateral displacement of 12 km has been proposed (Deroin and Prost, 1993a; Deroin et al., 1993b; Lapadu-Hargues, 1947). Finally, E–W trending dextral to inverse faults (i.e. the Goulet and Orcières faults) were active in the Cenozoic (Briand et al., 1993).

Metamorphism and chronological constraints Caron (1994) investigated the "Joyeuse/Cézarenque" series and reported a set of biotite, muscovite and amphibole Ar–Ar ages that cluster around 340 Ma (Fig. 6.3 and 6.4). In this area, deformation during both the D_1 and D_2 events occurred under greenschist-facies conditions (Elmi et al., 1974). Given the closure temperatures of the analysed minerals, the date of c. 340 Ma may correspond either to the age of top-to-the NW shearing or top-to-the S–SW thrusting (Table 6.1).

Largely disputed are the temporal relationships between top-to-the S–SW thrusting and the regional metamorphism of the Cévennes schists. Arnaud and Burg (1993); Arnaud et al. (2004) and Faure et al. (1999; 2001) argued that both were coeval and regarded regional metamorphism as a prograde Barrowian sequence. In contrast, Rakib (1996) showed that mineral isograds actually cut across the main thrusts and that metamorphism post-dates D_2.

Figure 6.2 highlights that the And–Crd–Bt zones coalesce at the scale of the whole northern Cévennes, outlining a single amphibolite-facies domain wrapping around the Velay dome (Weisbrod, 1968) and intruding granites (Bouilhol et al., 2006). The latter developed thermal aureoles marked by the restoration of And and Crd blasts, indicating that intruded micaschists were part of the regional And–Crd–Bt zone (Briand et al., 1993). As a direct consequence of this, granite magmatism was coeval or postdated regional metamorphism. Available geochronological constraints on igneous rocks and their metamorphic aureoles (Fig. 6.3) argue for a protracted magmatic activity with emplacement of the Cévennes granitoids over a period of c. 15 Ma from 316 $\pm$ 4 (Ma intrusion of the Bougès granite, ID–TIMS U–Pb monazite age of Isnard, 1996) to 298.9 $\pm$ 3.8 Ma (intrusion of the Largentière granite, LA–ICP–MS U–Pb zircon age, recalculated from Laurent et al., 2017, Fig. 6.3 and 6.4).

In the vicinity of the Velay dome, top-to-the NE shearing (the D_{2v} event) has been dated in situ by Bouilhol et al. (2006) on syntectonic muscovite at c. 320 Ma (Fig. 6.3, Table 6.1). Following Rakib's interpretation, the muscovite ages of c. 320 Ma probably represent the age of the regional greenschist- to amphibolite-facies metamorphism, thus implying that the D_2 thrusting event is older than 320 Ma. The younger Ar–Ar biotite ages of 310–307 Ma obtained by Bouilhol et al. (2006) close to the dome would correspond

to cooling ages.

D_3 extensional deformation would have been coeval to the intrusion of the Pont-de-Montvert and Borne granites (Faure, 1995; Faure et al., 1999; 2001). Available ages for the former are inconsistent with a biotite Ar–Ar cooling age of 310.8 ± 4 Ma (François, 2009), statistically different and older than the zircon U–Pb date of 302.5 ± 3.5 Ma (LA–ICP–MS, recalculated from Laurent et al., 2017). Similarly, emplacement of the Borne granite is poorly constrained by a whole–rock Rb–Sr date of 315 ± 5 Ma Mialhe (1980). According to Bouilhol et al. (2006), the D_3 event postdated the intrusion of the Borne granite and led to the formation of the Bessèges coal basin (Fig. 6.2). Zircon U–Pb dating of bentonite in the latter yielded an age of 297.4 ± 4.4 Ma (Bruguier et al., 2003, Fig. 6.3 and 6.4) bracketing the age of D_3 between c. 315 and 300 Ma.

6.1.3 The Margeride pluton

The Margeride pluton is composed of several granitoid types (Couturié, 1977; Choubert and Girod, 1974b; Couturié and Geffroy, 1974; Lafon and Respaut, 1988):

- a largely dominant Bt-bearing, Kfs-porphyritic, peraluminous granite.
- potassic diorites ("vaugnerites") showing mingling and mixing textures with the main phase.
- muscovite-bearing leucogranites (i.e. the Grandrieu massif) cutting across the main phase.
- late microgranite, lamprophyre and rhyolite dykes.

Recent geochronological investigations (Laurent et al., 2017) yielded intrusion ages identical within uncertainties for the porphyritic phase, the vaugnerites and the leucogranites, between 313.2 ± 4.3 Ma and 309.4 ± 3.8 Ma (recalculated considering systematic errors). This batholith has also been the subject of structural studies using conventional and magnetic data together with gravimetric investigations (Feybesse et al., 1995; Laboue, 1982; Talbot et al., 2005). The nearly flat-lying magmatic foliation displayed by the porphyritic granites complies with an extensional setting while NW–SE trending magmatic lineations with top-to-the SE sense of shear point to SE–directed expansion during magma emplacement (Feybesse et al., 1995; Talbot et al., 2005).

6.1.4 The Masméjean dome

The Masméjean dome was first described by Lapadu-Hargues (1947) and subsequently investigated by Anthonioz (1987); Be Mezeme et al. (2006); Briand et al. (1993); Faure et al. (2001); Négron (1979) and Rakib (1996). The geological map presented Fig. 6.5 was drawn based on these works and our own field survey.

General overview and constituent lithologies The Masméjean dome is a triangular shaped antiform showing gently dipping southwestern and northwestern flanks that contrast with the steep eastern flank (Fig. 6.5). The dome is built up by an anatectic orthogneiss core mantled by an association of unmolten amphibolite-facies orthogneisses and metasediments. One orthogneiss sample has been dated section 2.1 and yielded a zircon U–Pb emplacement age of 541.4 ± 4.9 Ma (taking into account systematic errors, Fig. 6.3 and 6.4). Be Mezeme et al. (2006) obtained EPMA monazite ages of 323 ± 3 Ma and 543 ± 25 Ma from an anatectic orthogneiss which they interpret as reflecting the timing of partial melting and protolith emplacement, respectively. A single plurimetric amphibolite body was observed near the place known as Les Orts (Briand et al., 1993). Metasedimentary lithologies comprise paragneisses, micaschists and quartzites assumed to derive from a range of protoliths including greywackes, pelites and sandstones (Briand et al., 1993; Négron, 1979). The metasediments structurally overlay the orthogneisses or constitute metric to kilometric rafts embedded into them.

Our map differs from those of Briand et al. (1994) and Négron (1979) as it emphasizes the existence of hectometer-scale granite sills outlining the contact between migmatites and metasediments in the eastern flank of the antiform (Fig. 6.5). Those correspond to the "granulites de ségrégation" of Lapadu-Hargues (1947) and will be referred to as "Villefort granites" hereafter. Post-tectonic leucogranite, microgranite to rhyolite dykes are frequently observed in and out of the anatectic domain. Be Mezeme et al. (2006) reported an EPMA monazite age of 333 ± 6 Ma for a granite dyke but did not quote the exact GPS coordinates. Finally, Variscan igneous and metamorphic rocks are unconformably overlain by Lower Jurassic shallow marine limestones (Briand et al., 1993).

Relationships between the Masméjean dome and adjacent units Near Labasti-de-Puylaurent, the steep N–S foliation of the eastern flank of the Masméjean dome gradually rotates to an NE–SW and then E–W trend matching that displayed by the Tanargue migmatites (Briand et al., 1994; Lapadu-Hargues, 1947). The persistence of anatexis indicates that a petrological continuity exists between the Masméjean dome and the southern part of the Velay Complex (Be Mezeme et al., 2006).

To the South, the Masméjean dome is brought to contact with the Cévennes schists by the Goulet strike-slip to inverse Pyrenean fault (Briand et al., 1993). To the east, the contact is gradual yet locally dissected by the Villefort fault and notably features the above-mentioned granite sills. SW of Prévenchères, anatectic orthogneisses similar to those observed in the dome constitute the core of a kilometric antiform within the Cévennes schists (Briand et al., 1994; Négron, 1979; Rakib, 1996). Altogether, these observations suggest that the constitutive lithologies of the Masméjean dome were located structurally below the Cévennes schists.

Finally, the Margeride batholith is intrusive within amphibolite-facies metasediments from the northwestern flank of the dome and developed a limited contact metamorphic aureole (Briand et al., 1994).

6.2 Structural analysis and kinematic criteria

6.2.1 Observations from the dome mantle

This section summarizes the structural information gained in the course of two summer field campaigns (2015 and 2016) and the examination of *c.* 80 thin sections (most of them being spatially oriented). Fig. 6.6 presents interpretative cross-sections summarizing the available structural data on the Masméjean dome.

The southwestern flank of the dome

In this domain, the regional foliation S_n consistently trends ENE–SSW to NE–SW and gently dips to the SW. It gradually rotates east of Belvezet towards a N–S direction (Fig. 6.5). Intense deformation locally resulted in augen gneisses being converted into S–mylonites (Fig. 6.7a). Preservation of transposed symmetrical folds indicates that S_n reworks an older S_{n-1} foliation (Fig. 6.7b). Stretching lineations within S_n are marked by ellispoidal biotite aggegates and Kfs-blasts/clasts (in augen gneisses only) showing a strong preferential orientation in the YZ plane. Lineations generally plunge towards the SW–WSW with a maxima at N230 21° (Fig. 6.8a). Lineations in the orthogneisses located South of the Chassezac river and West of the Puylaurent dam show a slightly different orientation as they plunge to the SSE (Fig. 6.8a). Sections in the XZ plane consistently provide evidence for top-to-the NE–ENE shearing (Fig. 6.9). Shear criteria include C to C' shear bands, asymmetric drag folds and sigmoid mica "fishs".

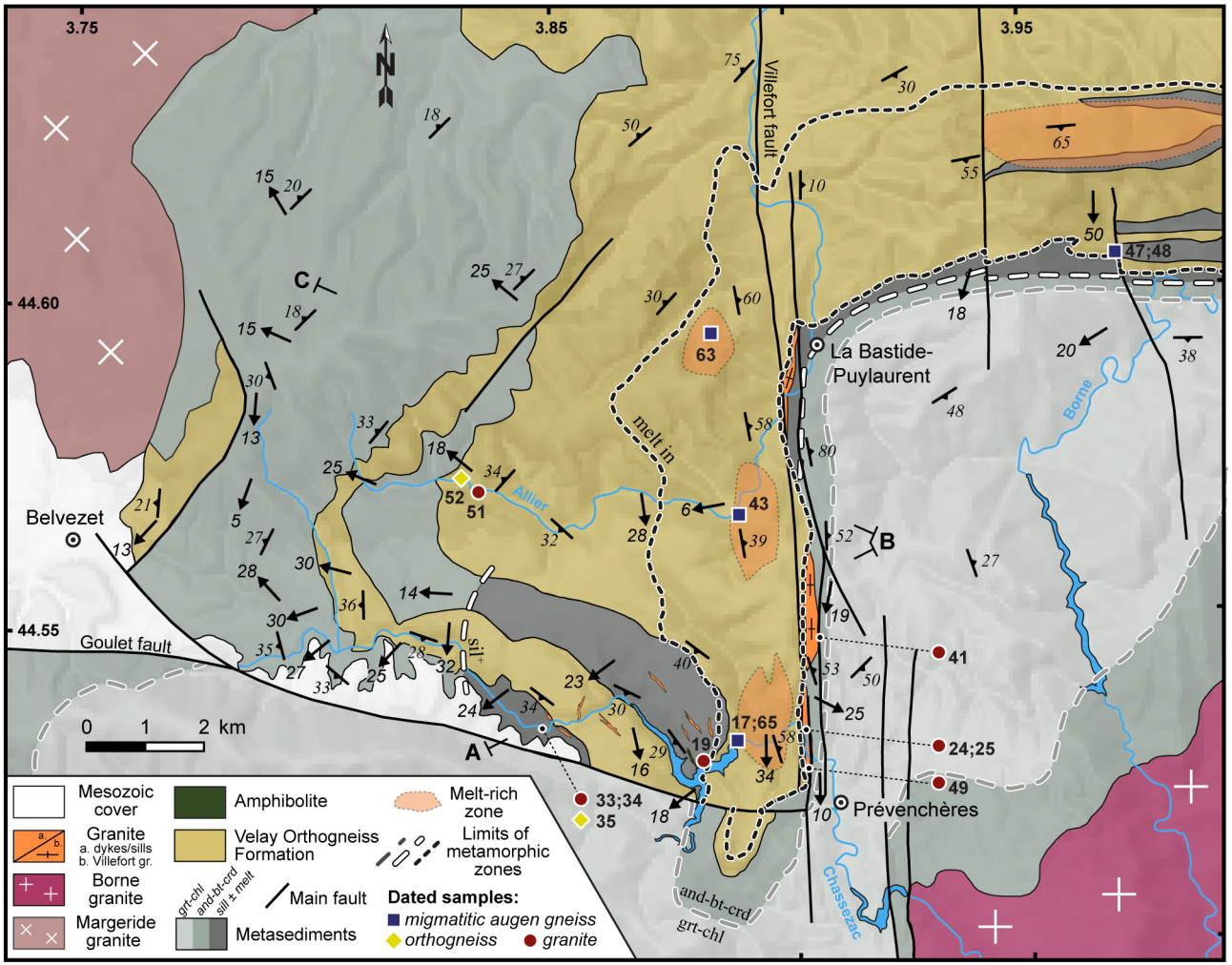

Figure 6.5: Geological map at scale 1/80,000 of the Masméjean dome. Drawn after our survey and the works of Briand et al. (1994); Négron (1979); Rakib (1996) and Weisbrod et al. (1974). A, B and C refer to the edges of the cross-sections Fig. 6.6.

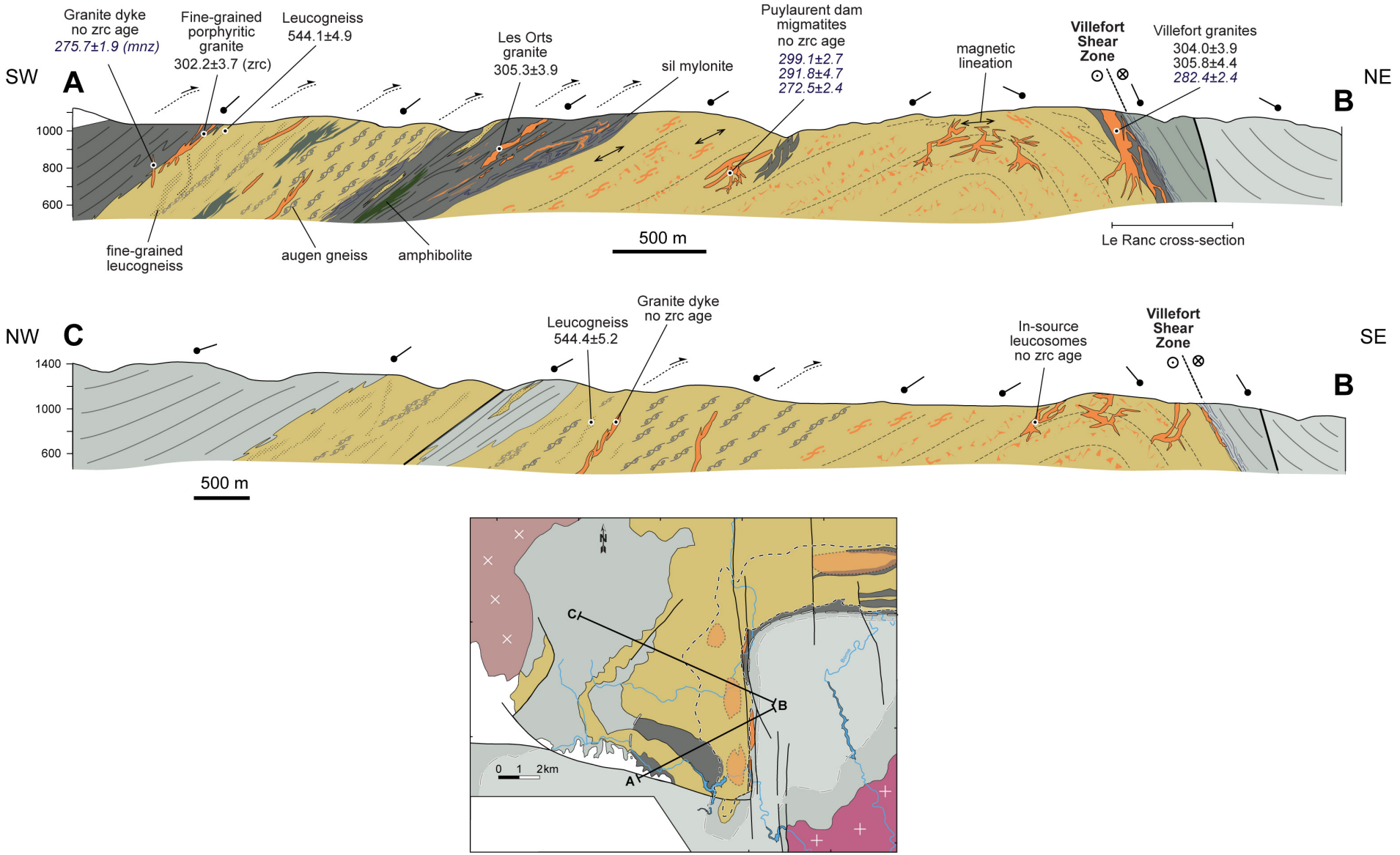

Figure 6.6: Cross-sections of the Masméjean dome. Same legend than Fig. 6.5.

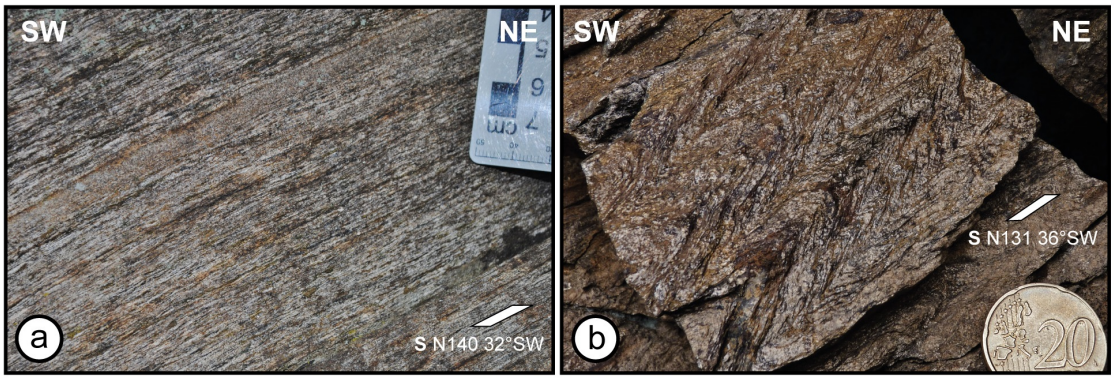

Figure 6.7: Zones of very intense ductile deformation. (a) Very fine-grained mylonitic orthogneiss grading into augen gneiss out of the shear zone, Bois du Pendu near the hamlet of L'Hermet (44.52625, 3.87397). (b) Symmetrical folds developed at the expense of an older S_{n-1} foliation and admitting S_n as axial plane, place known as Les Orts, shores of the Puylaurent dam (44.52805, 3.88016).

Unmolten rocks from southwestern flank have been intruded by several types of granitic magmas, forming dykes cutting across the foliation or sills concordant within it (Fig. 6.10d, e, f). Importantly, top-to-the NE–ENE shearing was coeval to post-dated granitic magmatism as documented by folded granite veinlets within metasediments (see Fig. 6.9c). Locally, S_n shows non-penetrative surface lineations associated with top-to-the SE shearing at the brittle-ductile transition (Fig. 6.10e).

The northwestern flank of the dome

In this domain, stretching lineations are very scarce and, when observed, gently plunge to the NW. Locally, a top-to-the SE sense of shear has been determined (Fig. 6.11). Local folds with vertical axial planes and gently NW-plunging hinges affected orthogneisses.

The eastern flank of the dome

The S_n foliation is N–S trending and steeply dipping towards the E (on average at 55°). Migmatites are overlain by quartz-rich paragneisses intruded by numerous granite sills, the "granulites de segregation" of Lapadu-Hargues (1947) (Fig. 6.10a,b,c). The And–Crd–Bt zone is notably narrow and its constituent lithologies (including a pluri-metric distinctive quartzite layer) pervasively affected by intense ductile deformation, locally resulting in S– and L–mylonites (Fig. 6.12a and b, respectively). Stretching lineations are

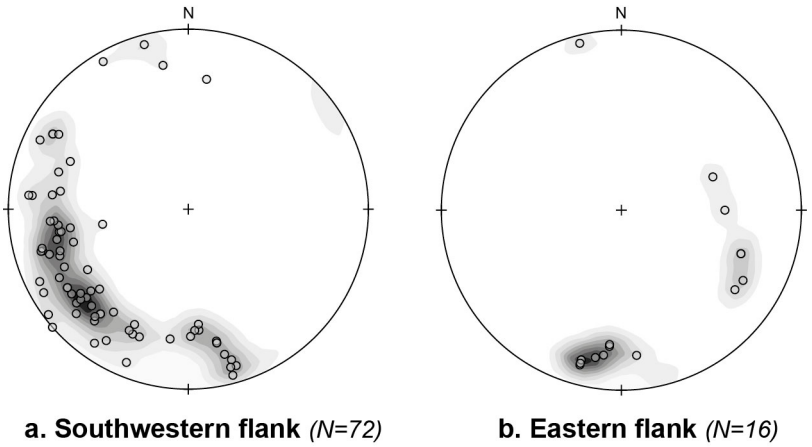

Figure 6.8: Stretching lineations observed in the mantle of the Masméjean dome. Plotted on Schmidt net (lower hemisphere) using the software OpenStereo (Grohmann and Campanha, 2010).

dominantly N–S trending and horizontal while a subordinate population gently plunges to the ESE (Fig. 6.8b). Left-lateral sense of shear is marked by asymmetric quartz aggregates and shear bands (Fig. 6.12c,d,e,f).

Most lithologies are affected by brittle deformation along N–S steeply dipping fracture and fault planes, related to the Villefort fault activity (Deroin et al., 1990; Deroin and Prost, 1993a; Lapadu-Hargues, 1947). Horizontal non penetrative lineations (striations) have been described by Deroin et al. (1990) and probably represent the latest increments of strike-slip deformation. The present-day differential altitude of the Triassic unconformity on both sides of the fault (200-300 m higher to the west) suggests a late normal movement where the footwall moved up to the west. This is supported by results of apatite fission track thermochronology documenting an inverse elevation–age profile across the fault (Barbarand et al., 2001).

Altogether, these observations indicate that the eastern flank of the Masméjean dome constitutes a wrench corridor marked by an early phase of ductile strike-slip deformation continued at brittle conditions during exhumation. Post-Variscan reactivation as a normal fault, most likely related to Pyrenean events, uplifted the western compartment including the Masméjean dome by *c.* 200 m. In the following, this structure will be referred to as "Villefort Shear Zone" (VSZ). The magnetic fabrics of the granite sills cartographically aligned along the VSZ are presented section 6.2.3.

6.2.2 Field observations and petrography of the core migmatites

The dome core typically features migmatites developed at the expense of orthogneisses (most often augen). Best exposures are found at the Puylaurent dam (where samples CHA-15-17 and 65 were collected, see Fig. 6.5). They dominantly consist in stromatic metatexites featuring: (i) 10 mm large in-situ leucosomes of granitic texture and composition with an assemblage Qz+Pg+Kfs±Bt±Ms±Sil; and (ii) narrow 1 to 2 mm large melanosomes consisting in Bt±Ms (Fig. 6.13a,b and 6.14). A second generation of muscovite formed during retrogression at the expense of sillimanite (when present, see Fig. 6.14a). Biotite was locally converted into chlorite at subsolidus conditions. Accessory phases include rutile, ilmenite, apatite and zircon.

In-situ leucosome distribution within fold hinges (Fig. 6.13d) presumably reflects the collection of anatectic liquids in low-strain domains during syn-anatectic deformation. The presence of larger, 10 cm thick concordant to discordant in-source leucosomes (in the sense of Sawyer, 2008, see Fig. 6.13a,b) is taken as evidence for melt mobility and coalescence, associated Bt- and Kfs-rich layers being regarded as residual domains. Granitic veins showing intricate and gradual transitions with their host metatexites are common (e.g. Fig. 6.13e,f) and would represent former melt percolation channels/pathways. Rafts of quartz-rich paragneiss resisters have been observed in several parts of the dome together with scarce intrusions of vaugnerites (Fig. 6.13d). The latter are intricately associated with Qz+Pg+Bt pegmatites, presumably corresponding to: (i) fractionated magmatic liquids derived from them (Montel and Weisbrod, 1986); or (ii) local melts from surrounding lithologies formed as a result of mafic magma intrusion.

Along the western and eastern limbs, the metatexite field foliation trajectories (when they can be reasonably mapped) tend to mimick that of the dome mantle (Fig. 6.2) and feature a similar asymmetry (steeply vs. gently dipping eastern/western flanks, respectively). In the dome core, the migmatite foliation turns horizontal and cascading folds admitting the foliation as axial plane have been observed. In contrast, linear fabrics were not identified.

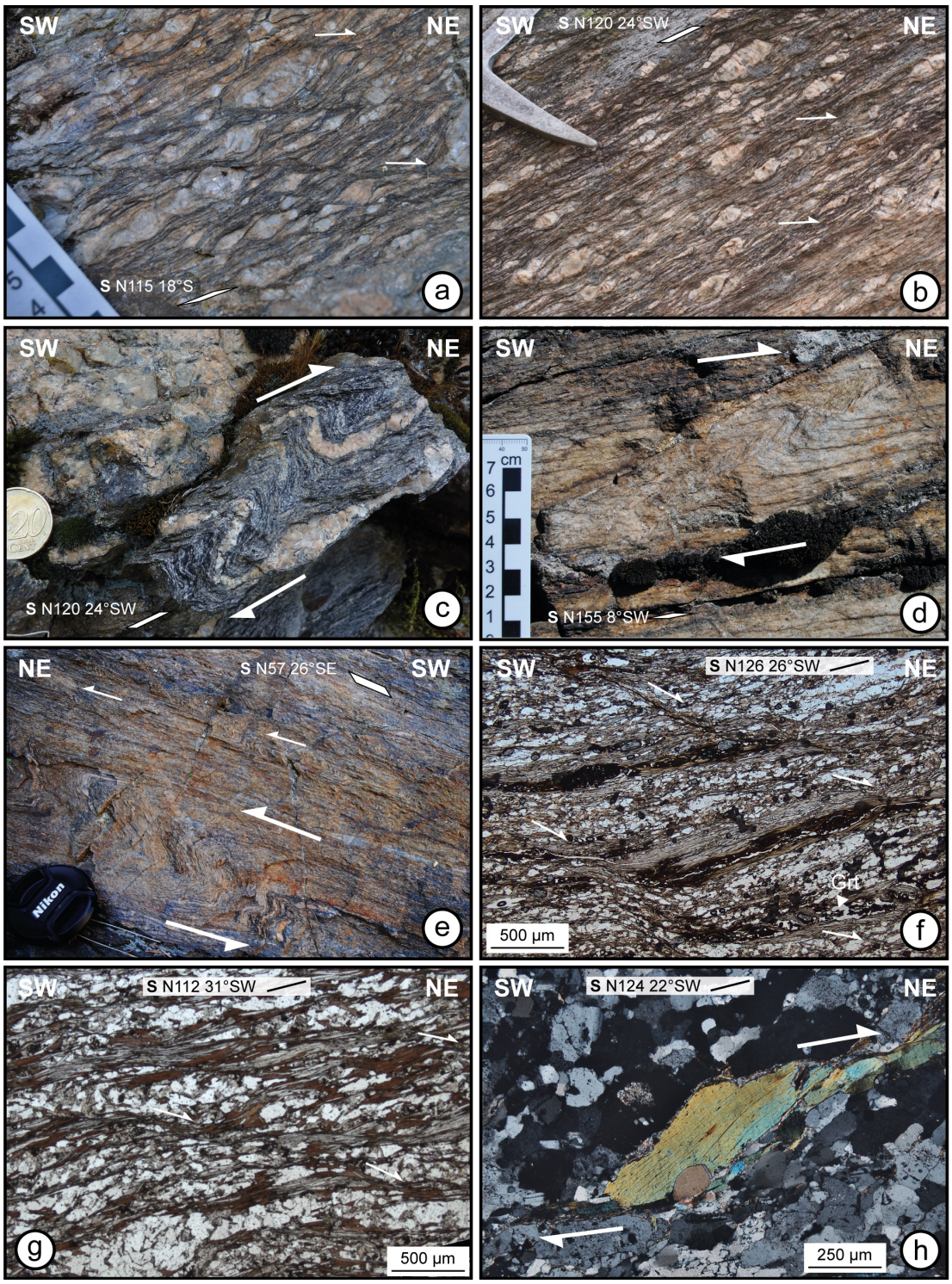

Figure 6.9: Evidence for regional top-to-the NE shearing. (a–b): Shear bands within mylonitic augen gneisses, Mirandol railway bridge (a: 44.54905, 3.81606) and Chassezac gully (b: 44.53744, 3.85751). (c): Drag folds developed at the expense of Sil-bearing paragneisses and granitic (presumably intrusive) layers indicating that top-to-the NE shearing was coeval or postdated granitic magmatism, Les Orts, shores of the Puylaurent dam (44.52889, 3.88019). (d) Drag folds affecting a leucogneiss pluri-metric layer within paragneisses, L'Hermet hamlet, shores of the Puylaurent dam, (44.52263, 3.87803). (e) Drag folds within Sil-bearing paragneisses from the Mylonitic Metamorphic Vellave Zone of Bouilhol et al. (2006), east of the Masméjean dome, Notre-Dame des Neiges abbey (44.60092,3.93683). (f) Plane-polarized-light photomicrograph of micaschists showing shear bands locally underlined by truncated garnet porphyroclasts, Mirandol hamlet (44.54613,3.81520). (g) Plane-polarized-light photomicrograph of a quartz-rich paragneiss affected by top-to-the NE shear bands, Chasseradès village, (44.55417, 3.82750). (h) Cross-polarized-light photomicrograph of a syntectonic mica fish in a leucogneiss, Mirandol hamlet (44.54613, 3.81520).

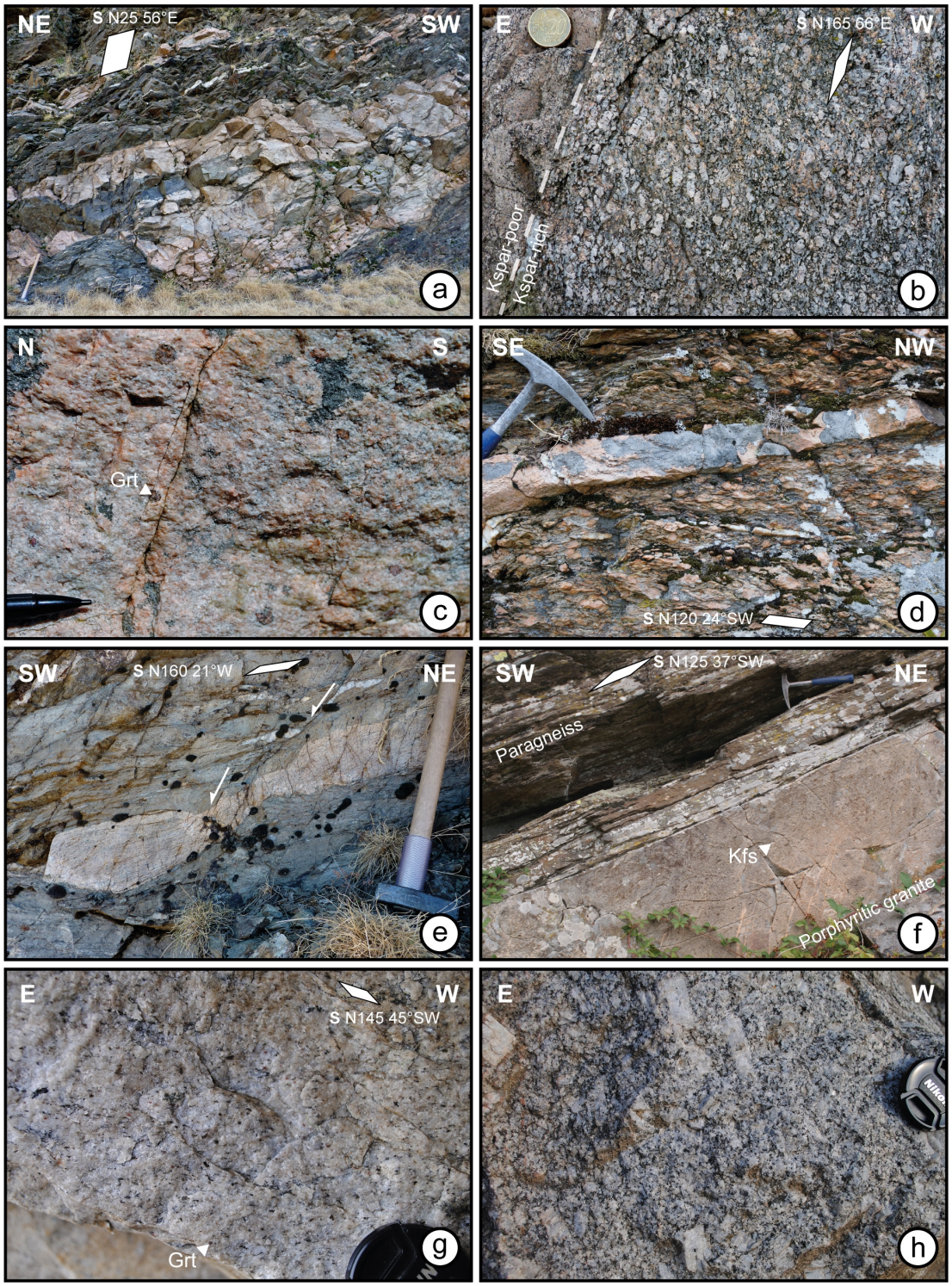

Figure 6.10: (a–c) Villefort granites, cropping out in the eastern flank of the Masmejean dome. (a) Set of steeply-deeping sills concordant in the foliation of Qz-rich paragneisses, Le Ranc hamlet, AMS site 8, dated sample CHA-15-25 (44.53152, 3.90263). (b) Magmatic layering with accumulation of macroscopically undeformed Kfs megacrysts, dated sample CHA-15-41, place known as Les Clous (44.54657, 3.90506). (c) Grt-bearing leucogranite, AMS site 10, Le Thort hamlet (44.55483, 3.90577). (d) Post-tectonic leucogranite dyke cutting across the foliation of the augen gneiss, Chassezac gully (44.53543, 3.85397). (e) Granite sill intrusive within Sil-bearing paragneisses and truncated by top-to-the S normal faults, dated sample CHA-15-19, place known as Les Orts, shores of the Puylaurent dam (44.52806, 3.88017). (f) Fine-grained Kfs-Bt-porphyritic granite sill concordant with the foliation of Sil-bearing paragneisses themselves embedded as a decametric rafts in augen gneisses, Chassezac gully (44.53522, 3.85039). (g) Grt-bearing facies of the Rocles syntectonic granite which magmatic foliation is underlined by Bt flakes, dated sample ROC-16-01, Le Travers hamlet (44.55534, 4.12841). (h) Kfs-porphyritic Borne granite, dated sample BOR-16-01, D51 road south of the Pied de Borne village (44.46468, 3.97477).

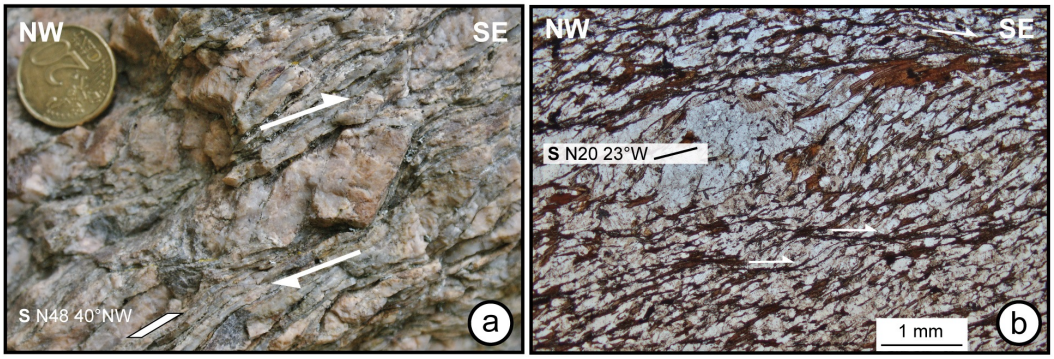

Figure 6.11: Evidence for top-to-the SE shearing in the northwestern flank of the Masméjean dome. (a) "Bookshelf" fragmented K–feldspar porphyroclast, place known as Majousseires (44.58474, 3.81716). (b) Shear bands within a quartz-rich biotite micaschist, place known as Majousseires (44.57436, 3.82279).

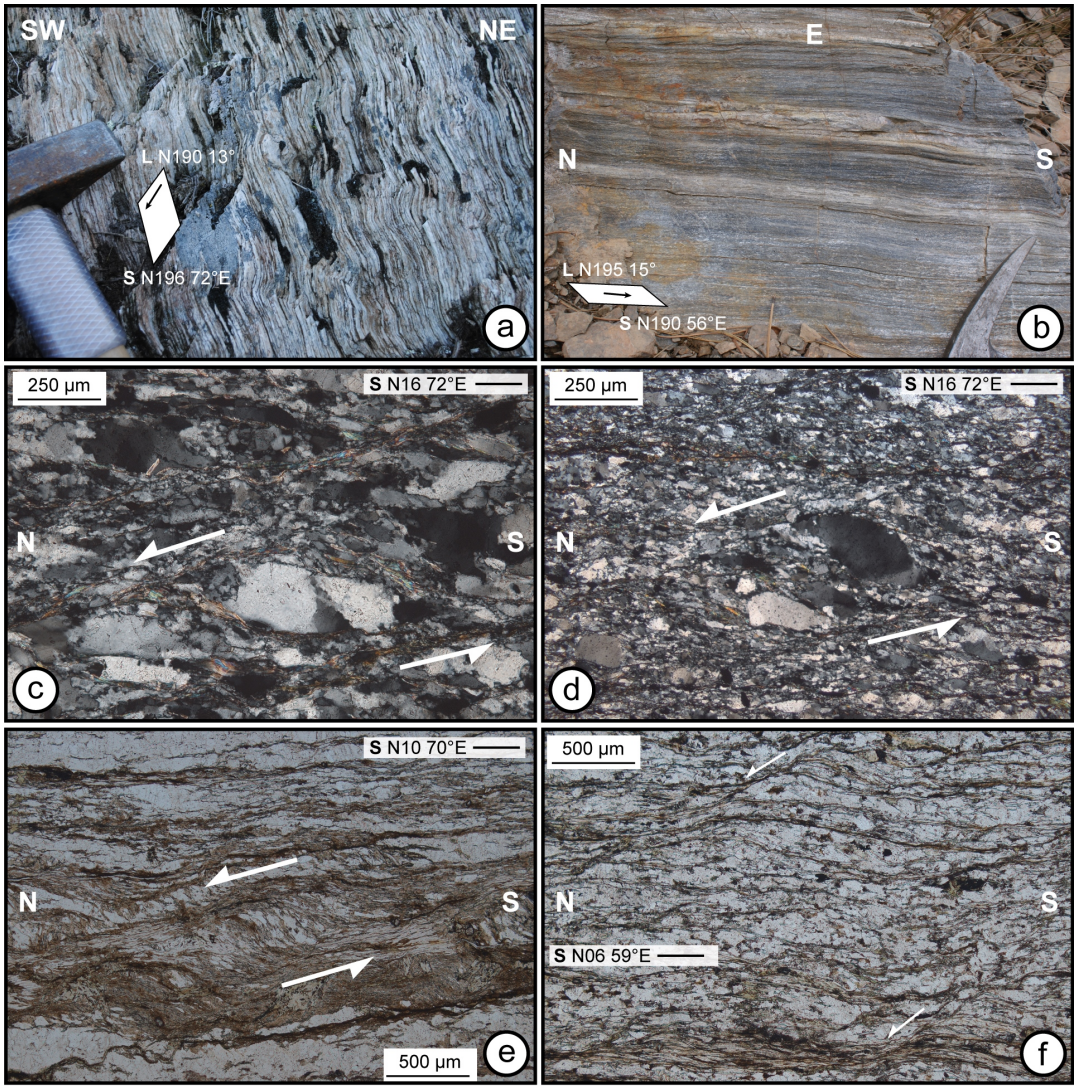

Figure 6.12: Ductile deformation along the Villefort shear zone. (a–b) Distinctive quartzite layer observed along the eastern limb of the Masméjean dome showing a nearly vertical foliation and horizontal mineral lineation marked by scarce Bt aggregates, Le Ranc (a: 44.53489, 3.90404) and La Molette (b: 44.54997, 3.90721) respectively. (c–d) Cross-polarized-light photomicrograph of a quartzite showing sigma-shaped quartz porphyroclasts deformed by shear bands oblique to the foliation and indicating sinistral displacement, Le Ranc hamlet (44.53500, 3.90415). (e–f) Plane-polarized-light photomicrograph of sinistral shear bands affecting (e) sigmoidal Qz–Bt aggregates in a quartzite, Le Ranc hamlet (44.52587, 3.90436) and (f) Qz-rich paragneisses, Prévenchères (44.52235, 3.90554).

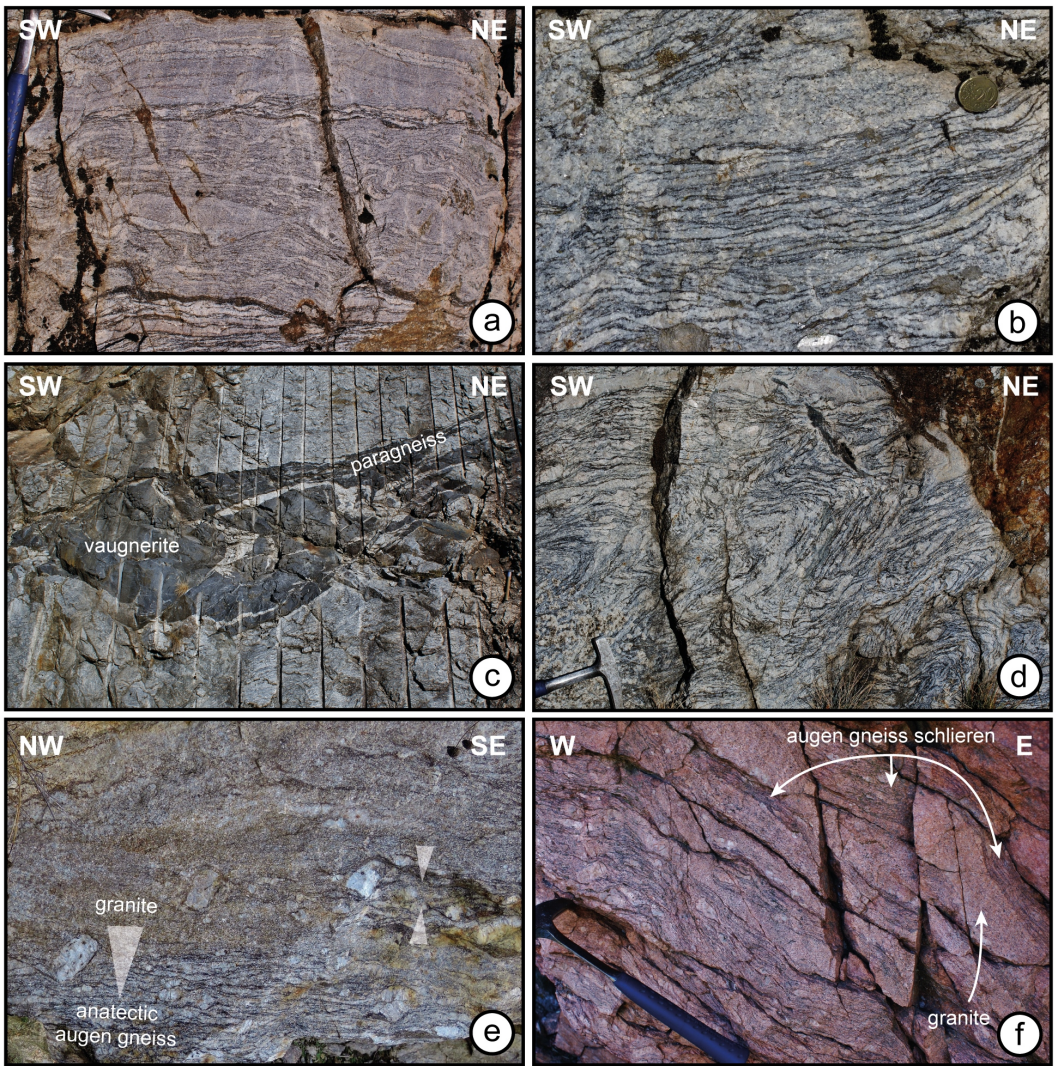

Figure 6.13: Typical migmatites from the Masméjean dome core, all developed at the expense of augen gneisses. (a) Metatexite with segregated neosome in the form of leucocratic quartzofeldspathic layers (leucosome), locally folded, and Bt–Kfs-rich melanocratic layers (melanosome). (b) Metatexite with both in-situ and in-source granitic leucosomes. (c) Qz-rich paragneiss resister within migmatites and rounded intrusion of K–rich diorite ("vaugnerite"). (d) Syn-anatectic folding of metatexite as evidenced by the leucosome distribution within fold hinges, presumably reflecting the collection of anatectic liquids in low-strain domains. (e–f) Intricate and gradual transitions between metatexites and granitic zones which contain rafts of anatectic augen gneisses and large Kfs prophyroclasts probably inherited from the latter. Such granitic zones are interpreted as melt percolation channels/pathways. Locations: (a–d) Puylaurent dam (44.53037, 3.88719); (e) Borne village (44.61738, 4.01109); (f) place known as Le Bouiol (44.51293, 3.88629).

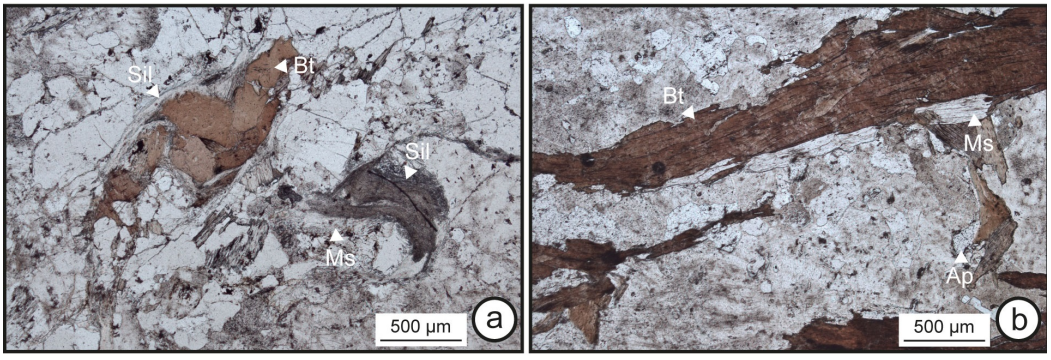

Figure 6.14: Plane-polarized light photomicrographs showing the mineral assemblages of the Masméjean dome migmatites. Mineral abbreviations after Whitney and Evans (2009).

6.2.3 AMS study of the dome core

Why AMS?

For the past 15 years, the study of gneiss domes has benefited from the spatial analysis of the anisotropy of magnetic susceptibility in migmatites (Bascou et al., 2013; Cavalcante et al., 2013; Charles et al., 2009; Ferré, 2003; Ferré et al., 2004; Kruckenberg et al., 2010; 2011; Parsons et al., 2016; Teyssier et al., 2005; Viegas et al., 2013). One of the reason for this lies in the fact that mineral and/or stretching lineations are very difficult to observe in migmatites. The ability to measure a magnetic lineation is thus highly informative as it allows to retrieve the transport/flow direction within the dome anatectic cores. Similarly, AMS studies have proven very successful in deciphering the internal fabrics of granite bodies, otherwise very challenging to image for lack of prominent tectonic markers.

Many studies since the 80's have shown that the magnetic fabrics of molten rocks depend on both the regional strain pattern and the internal buoyancy-driven magma dynamics (Benn et al., 1997; 2001; Bouchez and Gleizes, 1995; Gleizes et al., 1997; Guillet and Bouchez, 1983). In order to better constrain the strain pattern of the inner, anatectic part of the Masméjean dome, an AMS study has been conducted focusing on the core migmatites and the granite bodies cartographically aligned along the eastern flank of the dome.

Sampling and analytical methods

One hundred and two rock cores of 2.5 cm in diameter were collected at 11 sites with a gasoline-powered drill. Investigated rocks correspond to 6 metatexites and 5 Villefort granites (out of which 3 have been analysed for zircon and monazite U–Pb isotopes). Cores were oriented with a magnetic compass and subsequently cut in the lab to obtain specimens of standard size (2.2 cm in length; $N_{specimen} = 145$). Magnetic fabric measurements were performed at Saint-Etienne University using a AGICO MFK1 Kappabridge magnetic susceptometer (Agico, Brno). The revealed AMS ellipsoid is defined by the three principal axes K_1, K_2 and K_3 ($K_1 \geq K_2 \geq K_3$) mutually orthogonal. The parameters P' and T (Jelínek, 1981) were calculated to describe respectively the anisotropy and the shape of the fabric. Data retrieved from a group of specimen were processed using normalized tensor variability statistics (Hext, 1963; Jelínek, 1978). The results of all magnetic measurements are reported Table B18.

Magnetic mineralogy

Bulk magnetic susceptibilities (K_m) are very low (mostly $<150.10^{-6}$ SI in granites, $<100.10^{-6}$ SI in migmatites, see Fig. 6.15) and in the typical range of Al-rich crust-derived granites (Bouchez, 2000). Besides, there is no correlation between the degree of magnetic anisotropy P' and the bulk susceptibility (Fig. 6.16b). These features indicate that the magnetic susceptibility is controlled by paramagnetic minerals (Borradaile and Henry, 1997; Charles et al., 2009; Kruckenberg et al., 2010; Rochette et al., 1992). The lack of magnetite in our specimens has been confirmed by thermomagnetic K–T curves. Amongst paramagnetic minerals characterized by a high magnetic susceptibility (Borradaile and Henry, 1997), ilmenite was observed as (i) isolated grains in the specimen matrices; and, (ii) exsolutions within biotite/chlorite cleavage planes. Biotite is ubiquitously present in all specimens while garnet is particularly abundant in the Villefort granite sampled at site 10.

Magnetic fabrics

AMS parameters Rocks sampled at each site show low degrees of anisotropy (Fig. 6.16a), between 1.05 (0.5%) and 1.18 (1.8%) with an AMS ellipsoid shape being triaxial (T close to 0) in two Villefort granites (at site 5, dated sample CHA-15-41, and site 10)

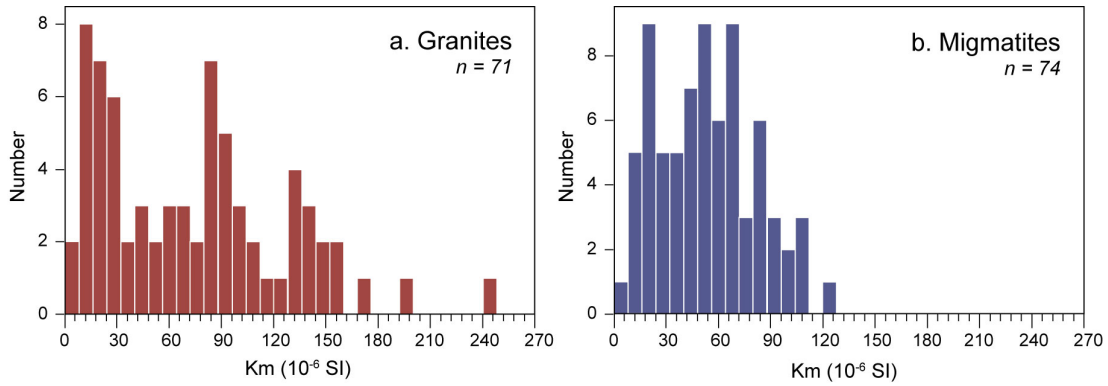

Figure 6.15: Histogram of bulk magnetic susceptibility for granite (a) and migmatite (b) specimens collected in the Masméjean dome.

and two migmatites (sites 3 and 7). The seven remaining sites feature an oblate ellipsoid. Strongest anisotropies (P' >1.13) are observed in two Villefort granites sampled near the hamlet of Le Ranc (sites 1 and 8, dated samples CHA-15-24 and CHA-15-25, respectively) and in two migmatites from the southwestern flank of the dome, near the contact zone with unmolten paragneisses (S3 and 4).

Structures in metatexites In metatexites, the magnetic foliation (which pole is defined by K_3, Fig. 6.17) pattern is consistent with that retrieved from field observations: (i) gently dipping towards the SW in the southwestern flank (S4 and 9) and the E–NE in the eastern flank (S6); (ii) sub-horizontal in the inner core (S3 and 11). Metatexites sampled along the western flank display a vertical NNW–trending foliation (S7). When clearly defined, magnetic lineations (direction of K_1) are horizontal, NNW-trending in the western flank (S7) and plunge to the W–SW in both the SW flank (S4 and 9) and the southern part of the inner core (S3).

Structures in granites Granites cropping out along the Villefort shear zone feature very contrasted AMS ellipsoids (Fig. 6.17). The three bodies sampled to the South on a transect along the Chassezac river show marked variations of the K_3 orientations from one to another (S1, 2 and 8). The magnetic foliation of the westernmost meter-scale body (S1) is N–S-trending and mimicks that of its host paragneiss, close to the contact with the metatexites. In contrast, granite sills S2 and S3 (out of which samples CHA-15-24 and CHA-15-25 were taken) show ENE–WSW to E–W-trending magnetic foliations even though the sills are concordant within the steeply dipping N–S foliation of the host paragneisses (see Fig. 6.10a). Granite body S5 (corresponding to dated sample CHA-15-41), collected further North, features vertical magmatic layering underlined by the accumulation of macroscopically undeformed Kfs megacrysts (see Fig. 6.10b). It shows a well-defined vertical magnetic foliation and a N–S horizontal magnetic lineation. Finally, the poorly anisotropic Grt-bearing granite S10 tends to show a vertical magnetic foliation and an E–W magnetic lineation.

Origin of the observed fabrics

Magnetic foliation poles are well-defined in all but one investigated site (S10). A the mineral scale, the <001> direction of biotite crystals corresponds to that of K_3 (Borradaile and Alford, 1987; Kruckenberg et al., 2010; Martín-Hernández and Hirt, 2003; Viegas et al., 2013; Zapletal, 1990). Therefore, since biotite is the most abundant paramagnetic mineral, the magnetic foliation would reflect the subparallel alignment of biotite crystals and thus the sample field foliation.

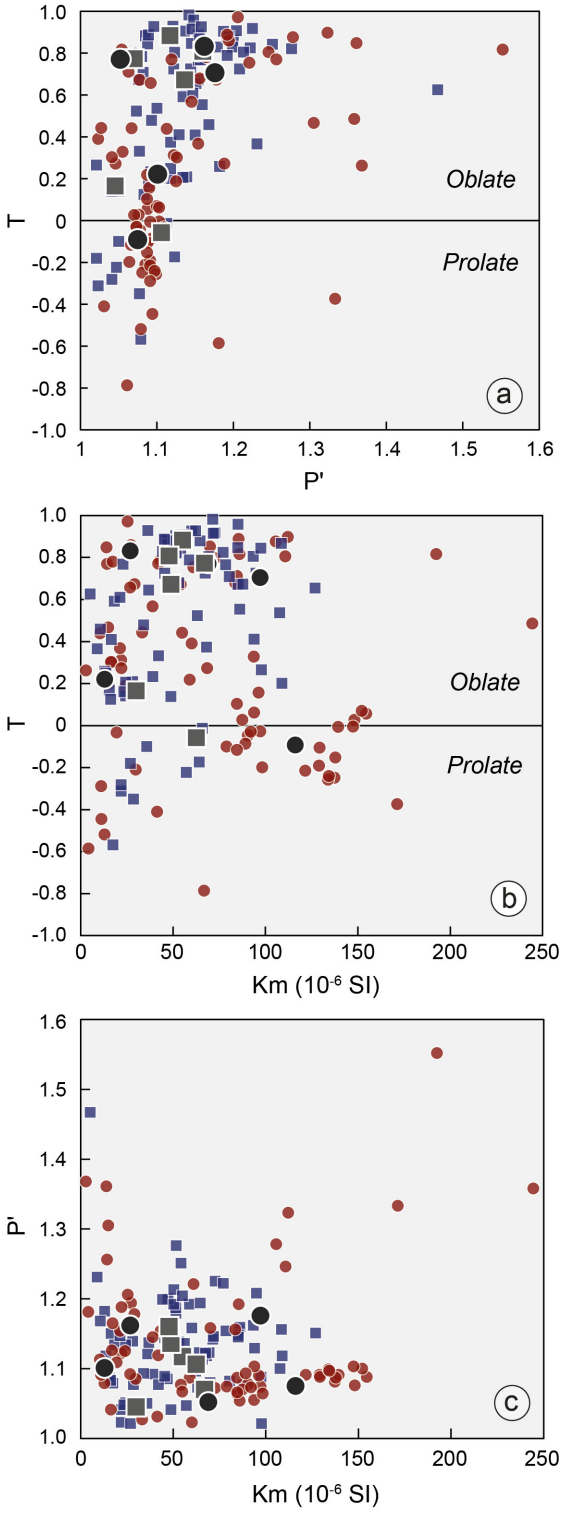

Figure 6.16: AMS scalar parameters for the Masméjean dome samples. Average values for each site correspond to the dark squares (migmatites) and circles (granites). (a) Shape parameter T (Jelínek, 1981) as a function of the total degree of magnetic anisotropy P'. (b) Shape parameter T versus bulk magnetic susceptibility K_m. (c) Total degree of magnetic anisotropy P' versus bulk magnetic susceptibility K_m.

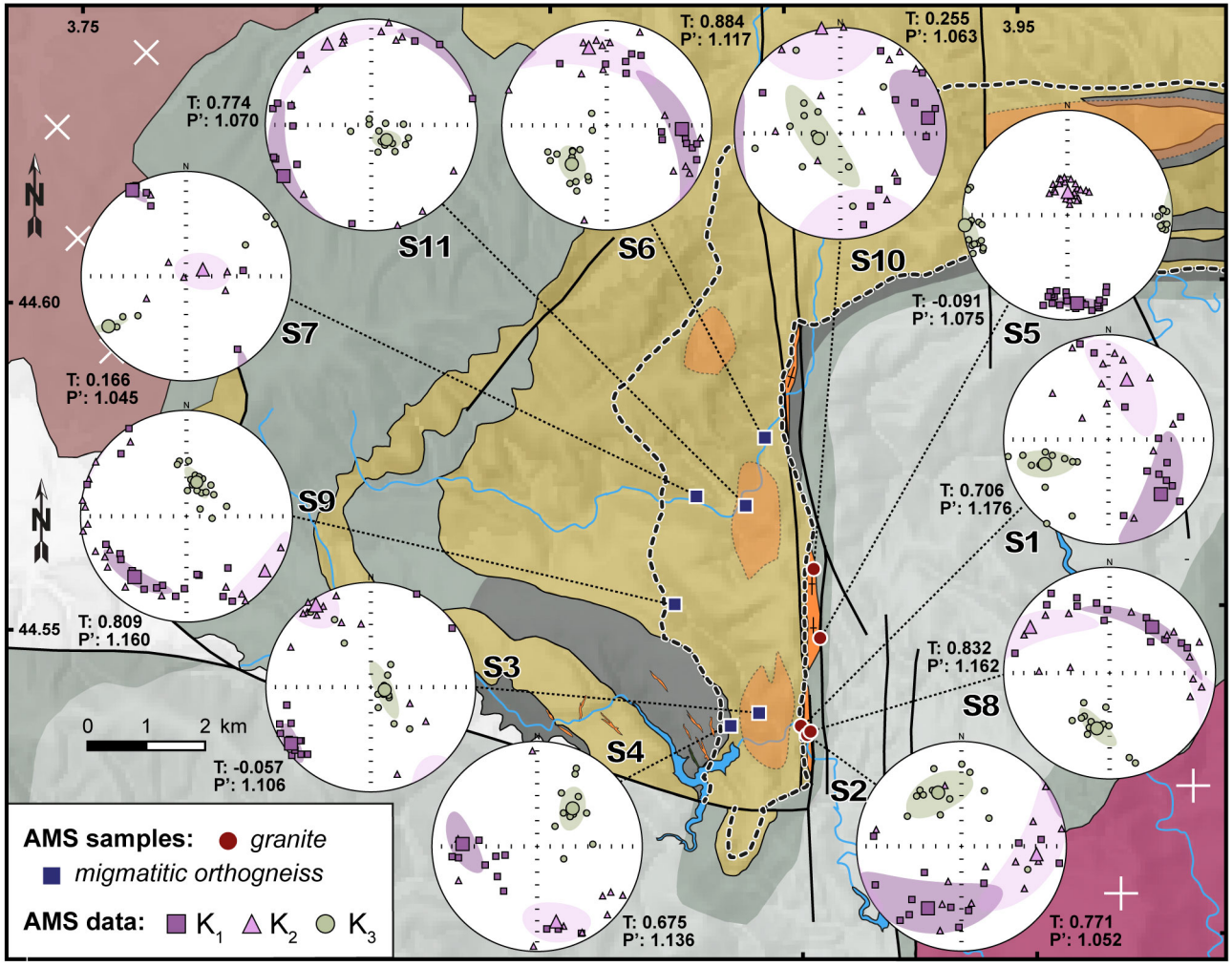

Figure 6.17: Projection of AMS data obtained for each sampling site of the Masméjean dome. AMS ellipsoid principal axes are projected onto lower hemisphere (equal area projection) and shown with 95% confidence ellipses. Same legend as Fig. 6.5. Full set of data presented Table B18.

In the absence of magnetite, the magnetic lineation may originate from: (i) preferred shape orientation of ilmenite grains (Bascou et al., 2002; Bolle et al., 2014; Borradaile and Henry, 1997) or (ii) the zone axis distribution of biotite crystals (Kruckenberg et al., 2010). To test the first hypothesis, thin sections were made in the K_1–K_2 plane of cores showing a well-defined magnetic lineation. They did not provide evidence for any preferred orientation of ilmenite crystals which are randomly oriented. Therefore, zone axis orientation of biotite crystals is preferred. In this frame, the concurrence of well-defined magnetic foliation and lineation, as observed in samples from sites 3, 4, 5, 7 and 9, would originate from the presence of an anastomosed network of biotite folia (Kruckenberg et al., 2010).

The low anisotropy of the AMS ellipsoid displayed by the granite from site 10 most likely originates from the local predominance of garnet over biotite. Indeed, garnet features elevated bulk magnetic susceptibilities, of the same order of magnitude than biotite, but characteristically low anisotropy degrees (Rochette et al., 1992). Consequently, the presence of garnet would substantially smoothen the anisotropic signal carried by biotite.

Interpretation

Migmatites In metatexites, the magnetic foliation and lineation would record the visco-plastic flow planes and direction of flow, respectively (Kruckenberg et al., 2010). Following this, the set of gently dipping magnetic lineations observed in the SW part of the dome (S4 and 9) may reflect the NE–E-directed upward flow of the migmatites, leading to dome exhumation. Horizontal lineation in the dome core (S3) possibly indicates non-coaxial flattening or could alternatively be "inherited" from an early exhumation stage along the SW flank. Importantly, the magnetic pattern observed in the northern part of the dome markedly differs from that of the southern and eastern parts as only scarce evidence for horizontal NNW–SSE-directed flow are preserved (S7). In the two remaining sites (S6 and 11), no preferred flow direction can be identified which supports a coaxial deformation regime. Consequently, the bulk of dome exhumation would have taken place in its southern part.

Villefort granites The vertical magnetic foliation displayed by granite S5 is consistent with the observed magmatic layering and suggests that the magnetic fabric reflects magmatic flow structures (Bouchez, 2000). This way, the flat-lying magnetic lineation would indicate syn-magmatic horizontal shearing and entail that S5 granite intrusion was coeval to wrenching along the Villefort Shear Zone. The magnetic foliations of granites S1, 2 and 8 are concordant to oblique with respect to that of the VSZ and these samples lack any magnetic lineation. It suggests that those bodies intruded and crystallized during a period of tectonic quiescence or after the end of the VSZ activity.

6.2.4 Conclusion

The dome is asymmetric in several respects: (i) field and magnetic foliations are gently vs. steeply dipping in its western and eastern parts, respectively; (ii) the And–Bt–Crd metamorphic zone is markedly narrower to the East, with the transition between migmatites and greenschist-facies rocks occurring in 100m; (iii) granite bodies are dominantly observed in its eastern flank. Such asymmetry is governed by ductile left-lateral shearing along the Villefort Shear Zone and entails that the latter controlled the dome shape and acted as a drain for anatectic liquids produced in the dome core.

AMS measurements performed on the core migmatites suggest that bulk flow and associated exhumation was focused in the southwestern part of the dome and mostly proceeded along shallow SW-dipping planes with a bulk transport towards the NE at an angle of *c.* 30°. In addition, foliation flattening and the presence of cascading folds attest

to vertical expansion, i.e. inflation of the dome core in line with buoyancy-driven flow (Brun and Van Den Driessche, 1994; Chen et al., 1990; Escuder Viruete et al., 2000).

Importantly, kinematic criteria indicate that the southwestern dome mantle was pervasively affected by top-to-the NE shearing resulting in the development of S–mylonites, notably at the paragneiss/orthogneiss interface. Structural observations thus point to an *apparent* thrusting of the mantle over the core. Similar relationships have been reported in the adjacent Tanargue dome (Bouilhol et al., 2006) and, at a regional scale, top-to-the NE shearing is attributed to the D_2v tectonic-metamorphic event, presumably as old as 320 Ma (Be Mezeme et al., 2007; Bouilhol et al., 2006).

A geochronological survey was conducted to address the timing of: (i) top-to-the NE shearing; (ii) wrenching along the Villefort Shear Zone; (iii) anatexis within the dome core; (iv) exhumation and brittle–ductile top-to-the S deformation. We targeted a range of igneous rocks, from orthogneisses to migmatites and granite dykes which relationships with respect to the main deformation phases were previously ascertained. The GPS coordinates of each sample can be found in Appendix Table B1.

6.3 U–Pb geochronology

6.3.1 Investigated samples

Orthogneisses

Two orthogneisses were selected in order to test whether they are affiliated to the late Ediacaran meta-granites of the Velay Orthogneiss Formation (section 2.1) or represent early Variscan pre-kinematic granitoids as proposed by Dupraz and Didier (1988). In any case, they predate the main deformation event responsible for the foliation development. **CHA-15-35** was taken near the hamlet of Le Couste 40 m east of the bridge over the Chassezac river (Fig. 6.5). It corresponds to the country-rock of granite dyke CHA-15-34 (see below). Sample **CHA-15-52** was collected at the place known as Majousseires on the path running along the left bank of the Allier river (Fig. 6.5).

Granites

Aligned along the Villefort Shear Zone Four granite bodies were sampled to bracket the timing of the Villefort Shear Zone activity. Specimen **CHA-15-24** was collected along the cliff below the hamlet of Le Ranc on the left bank of the Chassezac river (Fig. 6.5). It belongs to a large granite sill intruding the paragneisses and containing both paragneiss and orthogneiss enclaves (AMS site 2). **CHA-15-25** was sampled 200 m east to CHA-15-24. It corresponds to a meter-thick granite sill injected within quartz-rich paragneisses (AMS site 8, Fig. 6.10a). **CHA-15-49** was sampled near the village of Prévenchères at the place known as Le Mourio and was taken 800 m (at crow's flight) south of CHA-15-24 and 25, on the right bank of the Chassezac river. The granite is locally affected by brittle deformation related to the late activity of the Villefort fault. Specimen **CHA-15-41** was collected from a granite body at the place known as Les Clous (AMS site 5). The granite displays a magmatic fabric with a vertical foliation underlined by layers rich in centimetric K-feldspar crystals alternating with fine-grained leucocratic domains (Fig. 6.10b). Sub-solidus brittle deformation also affected the body and generated millimeter-scale cataclastic bands showing marked grain-size reduction and subsequent alteration.

Affected by late brittle–ductile top-to-the S deformation Specimen **CHA-15-19** was sampled along the trail running from the hamlet of Puylaurent to the place known as Les Orts abutting the shore of the Puylaurent dam (Fig. 6.5). It belongs to a meter-sized zoned granite sill with a pegmatitic upper part and a layered lower

part (from which the sample was taken). The whole sill experienced post-magmatic non-coaxial deformation at the brittle–ductile transition. Deformation along N110 shear planes shows an apparent top-to-the S displacement (Fig. 6.10e).

Post-tectonic dykes and sills Those were selected to bracket the end of the main deformation episode and basement cooling. Specimen **CHA-15-33** was sampled from a fine-grained porphyritic granite sill near the hamlet of Le Couste 20 m east of the bridge over the Chassezac river (Fig. 6.5). This granite displays a magmatic fabric defined by the planar orientation of millimetric K-feldspar and biotite flakes. **CHA-15-34** is a granite dyke collected 30 m east of sample CHA-15-33 (GPS coordinates: 3.84598, 44.53308). The dyke crosscuts the foliation of the surrounding orthogneisses (sample CHA-15-35) and is itself undeformed. **CHA-15-51** was taken from a granite dyke cropping out on the left bank of the Allier river at a place known as Majousseires (GPS coordinates: 3.83309, 44.57011). The granite is undeformed, cuts across augen gneisses and is clearly post-tectonic.

The Borne pluton Sample **BOR-16-01** is a Kfs-porphyritic, Bt-bearing granite representative of the main phase of the Borne batholith (Fig. 6.2). It was selected to address the temporal relationships between the Borne pluton and its presumed counterpart on the other side of the Villefort Shear Zone: the Pont-de-Montvert batholith, for which a zircon U–Pb emplacement age has recently been obtained by Laurent et al. (2017).

The Rocles pluton The current view of the Rocles granite being syntectonic with respect to the D_{2v} deformation (Fig. 6.2) partly relies on EPMA monazite ages (Be Mezeme et al., 2006; 2007). To ascertain the validity of those, sample **ROC-16-01** was collected at the hamlet of Le Travers. This specimen is a Grt- and Bt-bearing granite showing a magmatic foliation (Fig. 6.10g).

Migmatites

Several migmatites developed at the expense of meta-igneous rocks were selected to constrain the age of partial melting in the Masméjean dome and the adjacent Tanargue area (Fig. 6.5). Samples **CHA-15-47** and **CHA-15-48** were taken from the disused quarry at the western exit of Saint-Laurent-les-Bains and respectively correspond to a bulk metatexite and an in-source leucosome embedded within it. Specimen **CHA-15-43** is an in-source leucosome within flat-lying metatexites from the dome core. It was sampled on the cliff overhanging the railway at the Masméjean village. In-source leucosome **CHA-15-63** was collected at the place known as Charbonneire in the northern part of the dome. Specimens **CHA-15-17**, **CHA-15-65M** and **CHA-15-65L** were all sampled right below the Puylaurent dam and respectively correspond to a bulk metatexite, a melanosome and in-source leucosome.

6.3.2 Analytical techniques

Zircon grains were separated from the powdered rock samples at Saint-Etienne University using conventional techniques described in section 2.1, subsequently cast into epoxy mounts and polished down to an equatorial grain section. BSE and CL-imaging were performed at the Central Analytical Facility of Stellenbosch University (SUN, South Africa) using a Zeiss MERLIN SEM and at the Laboratoire Magmas et Volcans in Clermont-Ferrand (France) using a Jeol JSM-5910 SEM. Selected grains were dated by LA–ICP–MS in the course of two analytical sessions, one performed at GUF (2^{nd} and 3^{rd} of May, 2016) and the other one at ETH (12^{th} to 14^{th} of February, 2017). Information on the analytical methods are presented Appendix B.3.1 and B.3.3 while the results of standards

and samples measurements are provided in Tables B4–B6 and B7–B9, respectively. The comprehensive description of the U–Pb results for each sample is presented section B.3.4.

Monazites from samples CHA-15-34, CHA-15-48, CHA-15-65M and CHA-15-65L were extracted from the same powder fraction than zircon grains and similarly cast into epoxy mounts while those from CHA-15-17 and CHA-15-25 were identified on rock thin sections using a Zeiss MERLIN SEM-EDX. All grains were BSE-imaged at SUN using the same apparatus. Selected monazites were dated by the U–Pb LA–ICP–MS method at the Laboratoire Magmas et Volcans in Clermont-Ferrand (France). Analytical details are available sections B.5. The full set of data is provided Tables B15 and B16. All zircon Concordia or Intercept dates were calculated considering systematic errors as explained section 1.5.1.

6.3.3 Zircon textures, U–Pb dates and their interpretation

Orthogneisses

Zircon grains extracted from orthogneiss samples are euhedral to sub-euhedral, range in size from 80 to 400 μm, display aspect ratios between 1.4 and 3 and show well-developed pyramidal tips (Fig. 6.18a). Core–rims relationships are very common and typically feature CL-dark cores (most often unzoned and sometimes recrystallized) surrounded by rims showing magmatic oscillatory zoning. U–Pb dates retrieved from such rims and homogeneous grains exhibiting a similar zoning pattern are clustered and yield Condordia dates of 544.1 ± 4.9 Ma (MSWD$_{C+E}$=0.79) and 544.4 ± 5.2 Ma (MSWD$_{C+E}$=0.9) for CHA-15-35 and CHA-15-52, respectively (Fig. 6.19). Measured Th/U ratios are low (average value of 0.15). In both samples, few measurements yielded a range of younger, nearly discordant, ^{206}Pb/^{238}U dates down to 514 ± 7 Ma. Finally, analyses performed on zircon cores and additional core-free grains yielded concordant Paleo- and Neoproterozoic dates.

Importantly, identical zircon textures, Th/U ratios and U–Pb dates have been reported by Couzinié et al. (2017) on late Ediacaran meta-granites from the Velay Orthogneiss Formation. Following this, we interpret the Concordia dates obtained for each sample as the emplacement ages of their igneous protoliths. The range of younger ^{206}Pb/^{238}U dates would represent a recent Pb loss trend. Zircon domains showing older dates would correspond to source-inherited grains or xenocrysts incorporated from country-rocks during magma ascent. Consequently, both samples will be regarded as constituents of the Velay Orthogneiss Formation and not early Variscan granitic intrusions.

Villefort granites

Zircon grains show a broad range of sizes (60–350 μm) and aspect ratios (1.1–3.6). Core–rims relationships are observed in *c.* 50% of the imaged grains and two zircon types can be recognized. Most feature a CL-dark or bright occasionally zoned core, truncated by a new growth zone with distinct magmatic oscillatory zoning, similar to zircons extracted from orthogneisses. A second, scarce type correspond to zoned grains wrapped around by a poorly luminescent and porous rim (see zircon 6, Fig. 6.18b). Concordant ^{206}Pb/^{238}U dates obtained from cores and rims are exclusively pre-Variscan, dominantly Ediacaran. CL-dark rims are rich in common Pb and no concordant date was retrieved.

Most zircons devoid of core–rim relationships also yielded pre-Variscan (mostly Ediacaran) dates. Very few gave concordant Variscan U–Pb dates, often after a common Pb correction was performed (Fig. 6.18b). The Concordia dates of 305.8 ± 4.4 Ma (MSWD$_{C+E}$=1.5) and 304.0 ± 3.9 Ma (MSWD$_{C+E}$=1.4) are thus retained as the emplacement ages of the granites CHA-15-24 and CHA-15-41, respectively (Fig. 6.20a to d). One single concordant Variscan grain was analysed in sample CHA-15-49 and yielded an individual ^{206}Pb/^{238}U date of 305 ± 4 Ma, possibly corresponding to that of magma

intrusion. No concordant Variscan date was obtained for CHA-15-25. All zircon domains with pre-Variscan ages would correspond to xenocrysts or source-inherited grains.

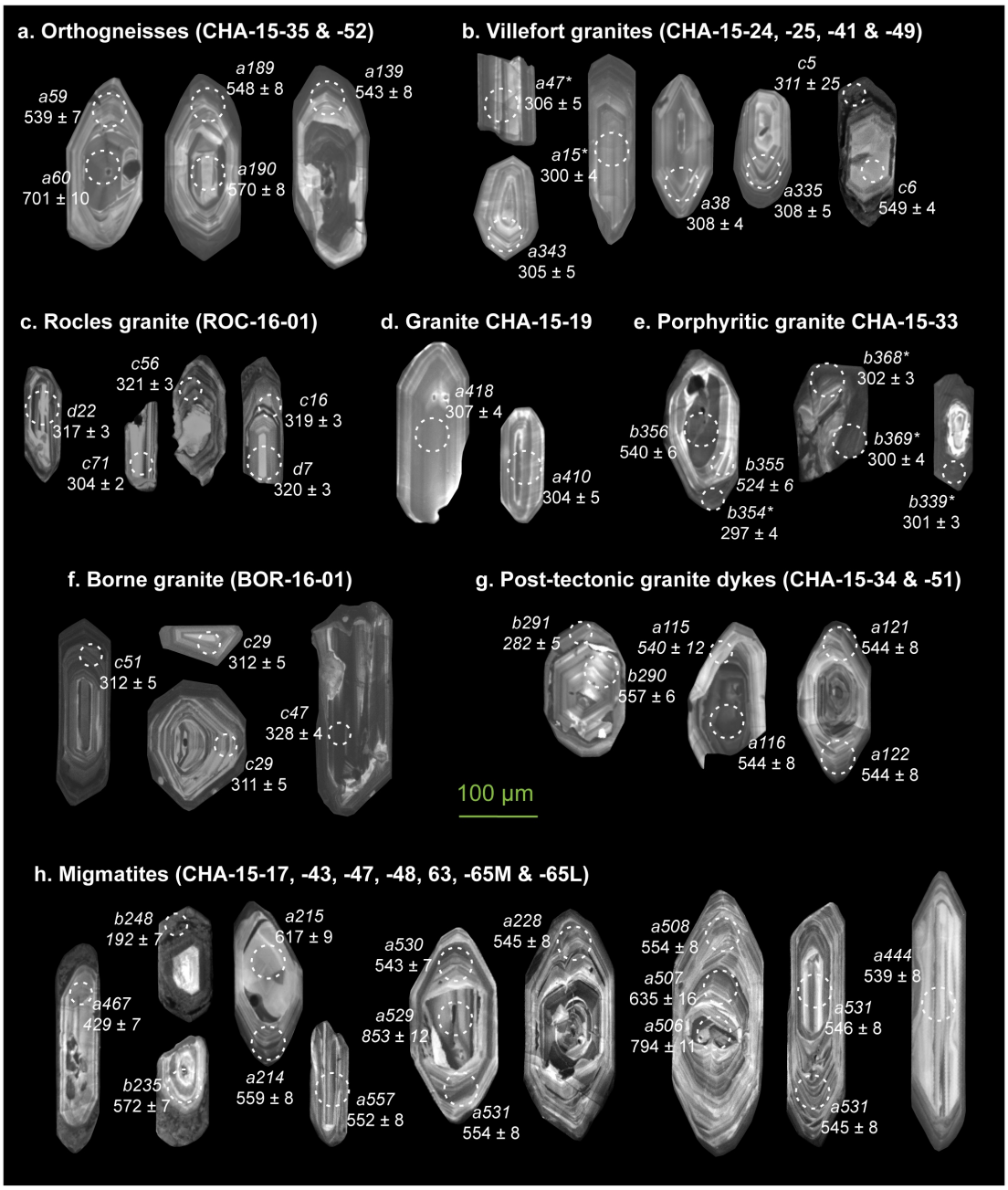

Figure 6.18: Representative cathodoluminescence images of zircon grains from dated samples. The locations of laser spots (white circles) are indicated along with the spot name (aXX, bXX, cXX, dXX; a and b refer to the sessions performed the 2^{nd} and 3^{rd} of May 2016 at GUF, respectively; c and d to the sessions performed the 12^{th} and 14^{th} of February 2017 at ETH, respectively). The corresponding $^{206}Pb/^{238}U$ dates are quoted with $\pm$ 2σ uncertainty, in Ma. All displayed analyses are concordant (except those in italic). Spot diameters are 20 and 30 μm.

The Rocles granite

Zircons from the Rocles granite are short (mostly <120 μm in length), show a large range of aspect ratios (from 1.2 to 8) and are often broken. Core–rim relationships are seldom observed. CL-images commonly reveal narrow to broad concentric zones and more complex convoluted zoning patterns (e.g. zircon 1, Fig. 6.18c). Many grains are CL-dark and metamictic. Most analyses trend along a mixing line between radiogenic

and common Pb compositions. The Concordia date of 319.8 ± 3.8 Ma ($MSWD_{C+E}$=1.5) calculated out of the seven concordant spots that anchor the trend is regarded as the best estimate of the emplacement age of the Rocles granite. The two younger $^{206}Pb/^{238}U$ dates of 312 ± 2 and 304 ± 2 Ma (Fig. 6.20e) would not correspond to any geological event and rather result from recent radiogenic Pb loss affecting the main, 320 Ma-old zircon population. Because of the weak curvature of the Concordia at Paleozoic times in the Tera-Wasserburg diagram, c. 320 Ma-old zircon having experienced limited Pb loss would still be concordant within uncertainty. Again, older dates would correspond to xenocrysts or source-inherited grains. The zircon U–Pb LA–ICP–MS emplacement age obtained in the course of this study is identical within error to the monazite "chemical" U–Th–Pb ages retrieved by Be Mezeme et al. (2007; 2006) which span between 325 ± 6 and 318 ± 4 Ma.

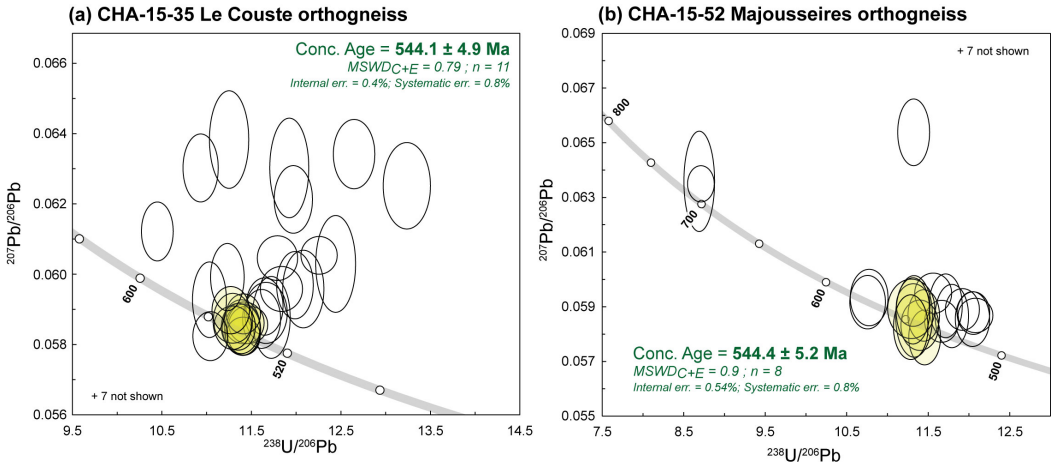

Figure 6.19: Tera-Wasserburg diagrams ($^{238}U/^{206}Pb$ vs. $^{207}Pb/^{206}Pb$) for zircon from the orthogneiss samples. Error ellipses and ages are displayed at 2σ level of uncertainty. Yellow ellipses are those considered for Concordia age calculations.

Les Orts granite sill sheared at the brittle–ductile transition

Zircon grains from this sample range in size from 100 to 300 μm and show aspect ratios between 2 and 6. They are generally euhedral even though some crystals are broken. Very few zircon cores have been observed (Fig. 6.18d) and oscillatory magmatic zoning is well-expressed in most grains. The emplacement age of the granite is given by the Concordia date of 305.3 ± 3.9 Ma ($MSWD_{C+E}$=0.6) calculated out of five concordant measurements (Fig. 6.20f). The older concordant $^{206}Pb/^{238}U$ date of 316 ± 4 Ma obtained on a single zircon core suggests that the latter represents a source-inherited crystal or a xenocryst.

Le Couste fine-grained porphyritic granite

Zircon crystals extracted from this sample are small (<120 μm) and generally show low aspect ratios (from 1.2 to 2.7). Many grains consist in a core wrapped around by a thin (<15 μm-large) CL-dark rim displaying faint oscillatory zoning (Fig. 6.18e). Analyses of the largest rims revealed high common Pb contents. The Pb_c corrected rim data cluster around the Concordia date of 302.2 ± 3.7 Ma ($MSWD_{C+E}$=1.6), taken as representative of that of magma intrusion (Fig. 6.21a). Older dates obtained on zircon cores and core-free grains would again be inherited from the protolith or country-rocks.

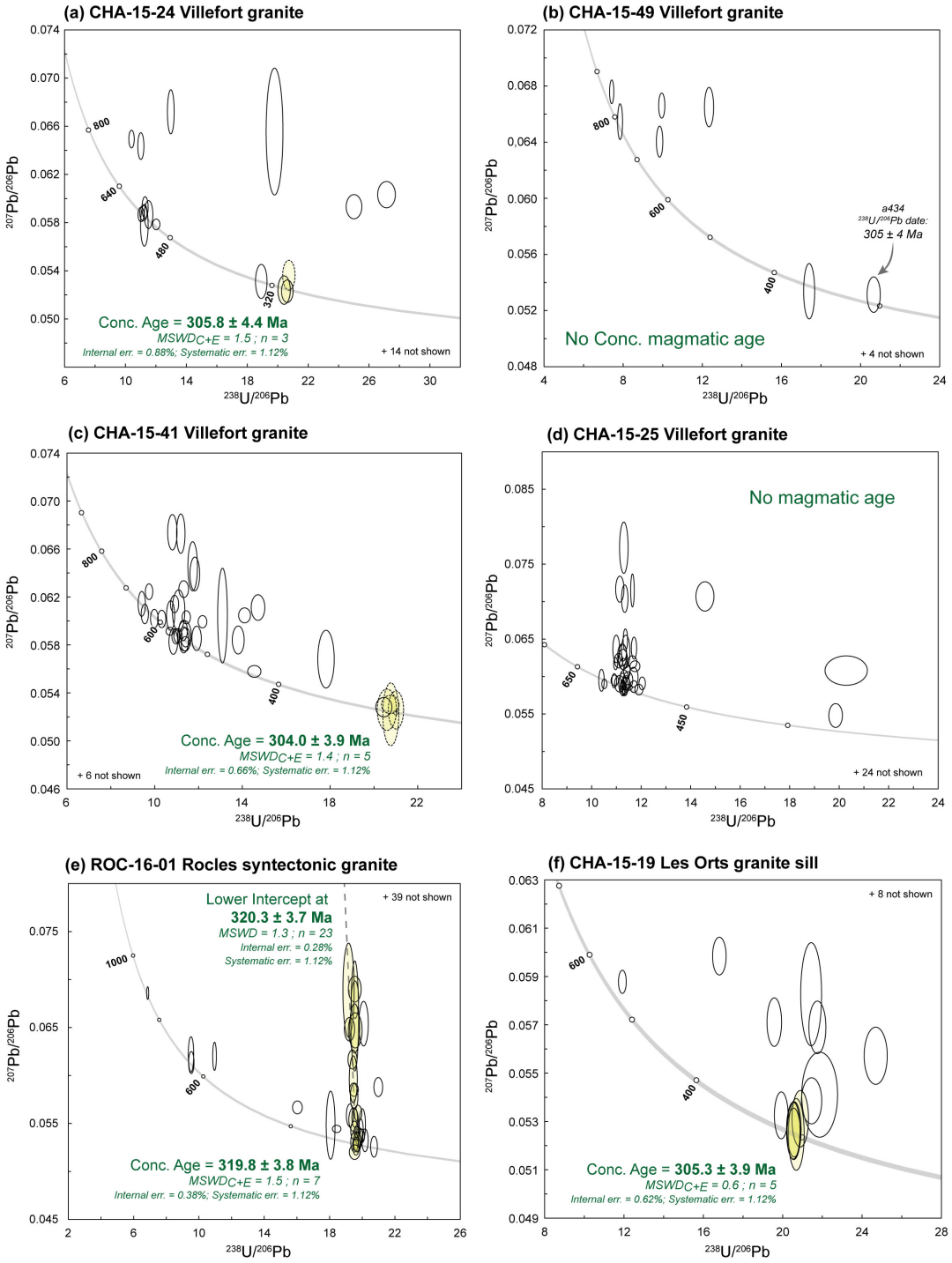

Figure 6.20: Tera-Wasserburg diagrams ($^{238}U/^{206}Pb$ vs. $^{207}Pb/^{206}Pb$) for zircon from: (a–d) the Villefort syntectonic granites; (e) the Rocles syntectonic granite, emplaced during the top-to-the NE shearing event; (f) the Les Orts granite, showing evidence for top-to-the S shearing at the brittle/ductile transition. Error ellipses and ages are displayed at 2σ level of uncertainty. Yellow ellipses are those considered for Concordia age calculations. Dotted ellipses are those for which a common Pb correction was performed.

The Borne batholith

Zircons from the Borne granite show a large range of sizes, from 80 to 350 μm and shapes (aspect ratios: 1 to 4). They often feature large, CL-dark, heavily recrystallized cores surrounded by rims commonly showing magmatic oscillatory zoning (Fig. 6.18f). Most analyses performed on such rims and core-free grains define a trend between radiogenic and common Pb compositions (Fig. 6.21a). Concordant measurements on this trend yield a Concordia date of 309.7 ± 3.6 Ma (MSWD$_{C+E}$=1.09), retained as the emplacement age of the Borne granite. It is within error identical to the whole-rock Rb–Sr age of Mialhe (1980). Spotted zircon cores (avoiding the recrystallized ones) gave a range of concordant ^{206}Pb/^{238}U dates from 549 ± 6 down to 316 ± 2 Ma regarded as inherited ages. One measurement performed on a rim yielded a younger concordant ^{206}Pb/^{238}U date of 297 ± 2 Ma that would result from limited Pb loss from the dominant population.

Post-tectonic granite dykes

Both dykes yielded very diverse zircon crystals with a range of shapes (aspect ratios between 1.1 and 3), sizes (60–300 μm) and core–rim relationships (large cores surrounded by thin CL-dark rims, core-free grains, cores surrounded by multiple growth zones). Not a single concordant Variscan date was obtained and all analysed grains are thus interpreted as being source-inherited or xenocrysts incorporated during magma ascent.

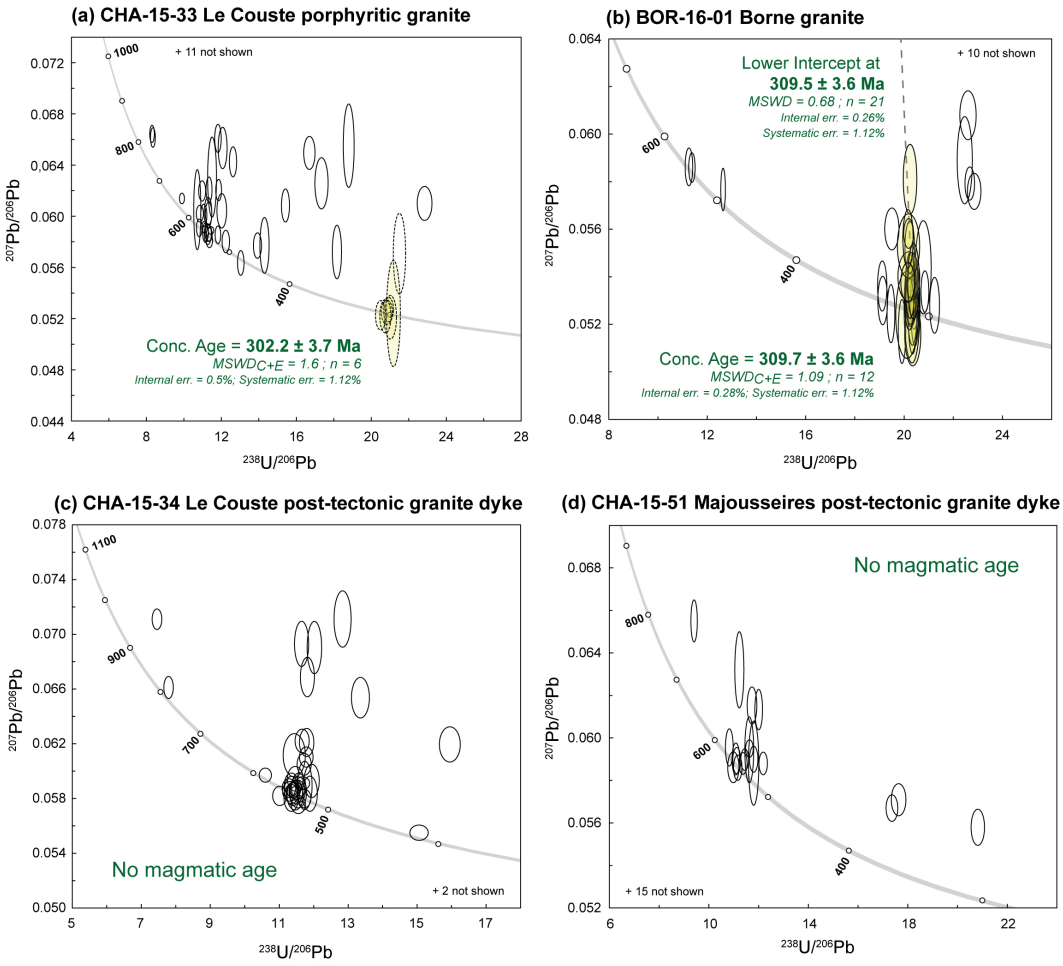

Figure 6.21: Tera-Wasserburg diagrams (^{238}U/^{206}Pb vs. ^{207}Pb/^{206}Pb) for zircon from samples of: (a) the Le Couste porphyritic granite sill; (b) the Borne porphyritic granite batholith; (c–d) post-tectonic granite dykes showing sharp intrusive contacts with their subsolidus country-rocks. Error ellipses and ages are displayed at 2σ level of uncertainty. Yellow ellipses are those considered for Concordia age calculations. Dotted ellipses are those for which a common Pb correction was performed.

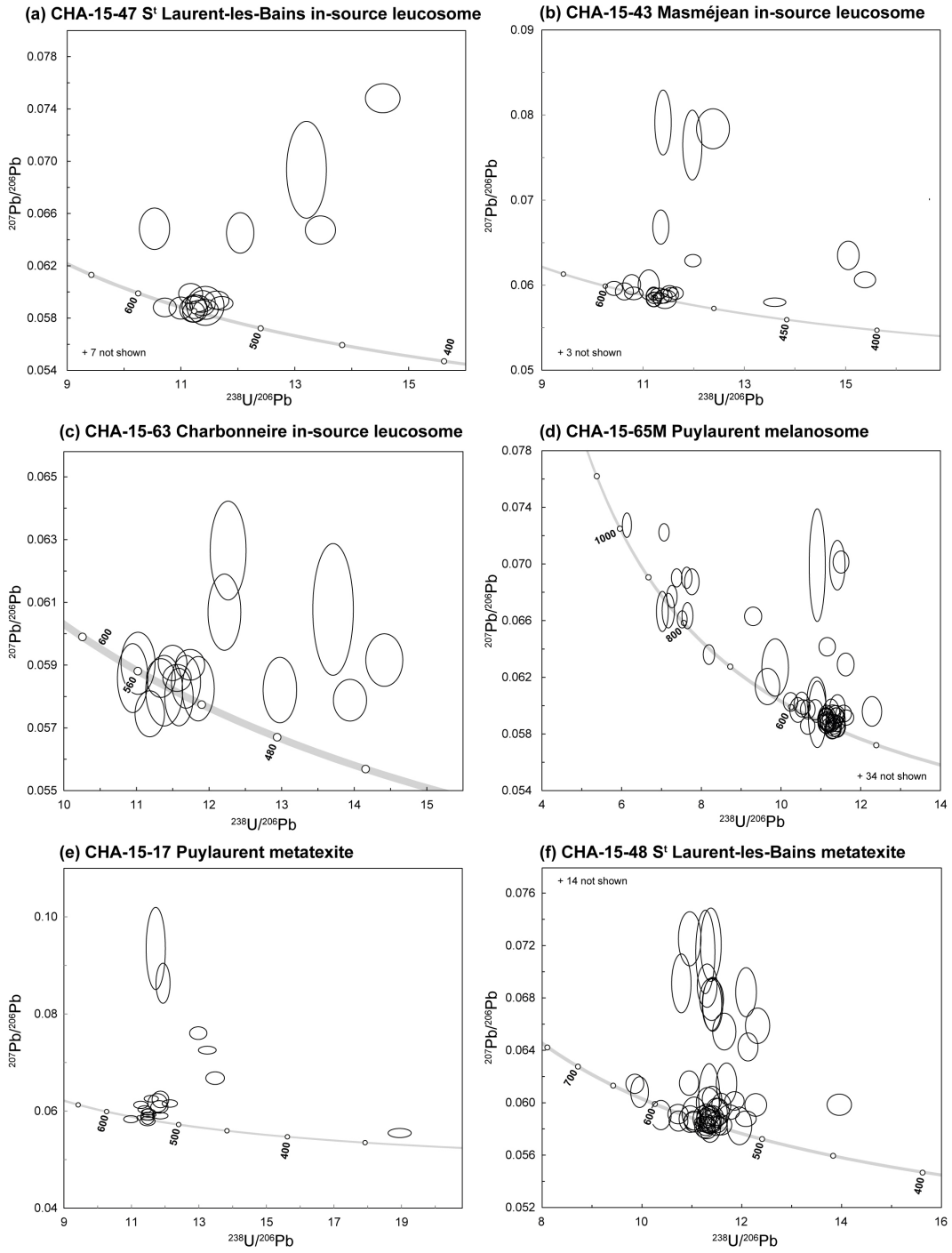

Figure 6.22: Tera-Wasserburg diagrams ($^{238}U/^{206}Pb$ vs. $^{207}Pb/^{206}Pb$) for zircon extracted from migmatite samples. Error ellipses and ages are displayed at 2σ level of uncertainty.

Migmatites

Zircon crystals extracted from the metatexites, in-source leucosomes and melanosome samples are very similar in sizes, shapes and internal textures to orthogneiss zircons. Faint differences are observed in metatexite CHA-15-17 which zircon grains tend to be more elongated (aspect ratios up to 5.5, see zircon 10, Fig. 6.18h) and commonly lack inherited cores. Besides, zircons are notably smaller in leucosome CHA-15-63 (<90 μm most often, see grain 5, Fig. 6.18h). Results of U–Pb dating are very consistent from a sample to another. Concordant $^{206}Pb/^{238}U$ dates obtained on core-free grains and rims cluster in the range 550–540 Ma (Fig. 6.22) and spotted zircon domains show low Th/U ratios (average value of 0.12). Cores and some core-free crystals yielded older, domi-

nantly Cryogenian–Ediacaran dates. The overall distribution of concordant $^{206}Pb/^{238}U$ dates remarkably mimicks that of orthogneisses from the Velay Orthogneiss Formation (Fig. 6.23). Altogether, this confirms that the migmatite protolith corresponds to the VOF orthogneisses. I did not attempt to calculate a multi-grain date for each sample (Concordia or Intercept) because such rocks likely behaved as a open-system during partial melting. This means that some zircon grains today retrieved in a migmatite sample may have been conveyed by mobile anatectic magmas and would not originate from the protolith.

Of striking importance is the lack of Variscan zircon record. Few grains extracted from in-source leucosomes CHA-15-43 and CHA-15-47 feature CL-dark porous metamictic rims wrapping around CL-bright zoned cores (zircon 1 to 3, Fig. 6.18h). The cores show dates similar to the other dominant grain population (i.e. between 650–540 Ma). Unfortunately, U–Pb compositions were only obtained for very few rims due to their complex matrix and the very high Pb_c contents. When available, rim analyses are highly discordant and show a scattered range of Permian to Jurassic $^{206}Pb/^{238}U$ dates, probably reflecting a combination of Pb loss and common Pb incorporation (Mezger and Krogstad, 1997). Those rims may have originally crystallized during anatexis or younger hydrothermal events but, in both cases, the age of the crystallization event(s) cannot be ascertained from the present dataset.

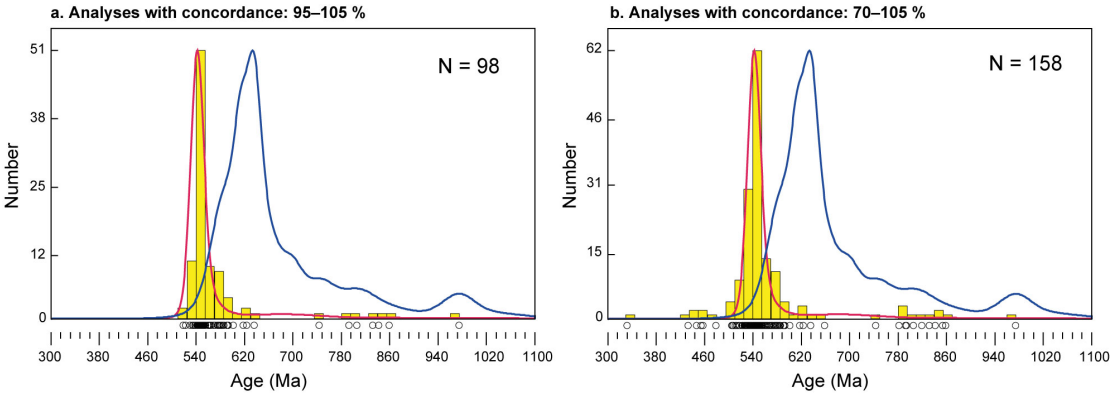

Figure 6.23: Histogram showing the $^{206}Pb/^{238}U$ dates of zircon grains analysed in migmatites from the southern part of the Velay Dome. Bin width is 15 Ma. Available zircon $^{206}Pb/^{238}U$ dates (concordance: 95–105%) for the Velay Orthogneiss Formation (in red, data from this chapter and Part 1, N=107) and regional metasediments (in blue, data from Chapter 2 and Chelle-Michou et al., 2017, N=445) represented as Kernel Density Estimates. The latter were calculated using the DensityPlotter program of Vermeesch (2012) with a bandwidth set at 15 Ma.

6.3.4 Monazite geochronology

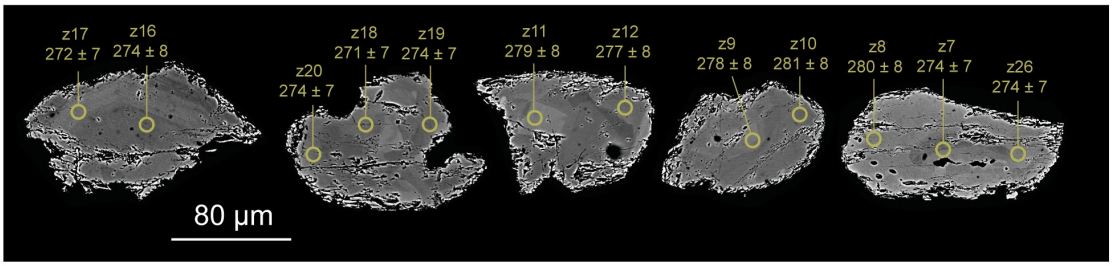

Figure 6.24: Representative back-scattered electron (BSE) images of monazite grains from granite dyke CHA-15-34. The locations of laser spots are indicated along with the spot name. The corresponding $^{206}Pb/^{238}U$ dates are quoted with $\pm 2\sigma$ uncertainty, in Ma. Spot diameter: 9 μm.

Textures and U–Pb results

Large (>60 μm) monazite grains were only observed in granite dyke CHA-15-34 and representative BSE images are displayed Fig. 6.24. For other samples, analysed grains were very small (often <20 μm) and no clear BSE zoning was identified.

Puylaurent migmatites Samples from the Puylaurent migmatite yielded contrasted results. Monazites from melanosome CHA-15-65M are all discordant and show scattered $^{206}Pb/^{238}U$ dates between 326 ± 9 and 294 ± 8 Ma (Fig. 6.25a). Several grains from in-source leucosome CHA-15-65L are also discordant but trend along a mixing line between radiogenic and common Pb compositions, with a lower intercept at 271.6 ± 3.2 Ma ($MSWD_{C+E}$=1.03). A similar $^{206}Pb/^{238}U$ weighted average date of 272.5 ± 2.4 Ma can be calculated out of the ten analyses (Fig. 6.25). Conversely, monazites from metatexite CHA-15-17 define an older $^{206}Pb/^{238}U$ weighted average date of 299.1 ± 2.7 Ma (excluding two measurements, one being highly discordant, Fig. 6.25c).

Saint-Laurent-les-Bains migmatite Few grains from a single sample were dated. Five analyses (one of them being concordant) define a mixing trend between radiogenic and common Pb compositions, which lower intercept yields a date of 291.8 ± 4.7 Ma. Two analyses performed on a grain show older discordant $^{206}Pb/^{238}U$ dates between 544 ± 15 and 518 ± 14 Ma (Fig. 6.25d).

Villefort granite CHA-15-25 Sixteen monazite grains have identical $^{206}Pb/^{238}U$ dates with a weighted average of 282.8 ± 2.2 Ma. Those define a mixing trend between radiogenic and common Pb with a lower intercept at 282.4 ± 2.4 Ma. Two discordant spots yielded older $^{206}Pb/^{238}U$ dates of 309 ± 10 and 359 ± 11 Ma (Fig. 6.25e).

Post-tectonic granite dyke CHA-15-34 BSE images of monazites from this sample reveal sector zoning (and possibly oscillatory concentric zoning in monazite 1, Fig. 6.24). All spotted domains show identical $^{206}Pb/^{238}U$ dates, even though 10 analyses out of 16 are discordant. A weighted average $^{206}Pb/^{238}U$ date of 275.7 ± 1.9 Ma can be calculated (Fig. 6.25f).

Interpretation of monazite dates

Migmatites A striking feature of the Puylaurent migmatites lies in the fact that samples taken less than 20 m away from each other yielded very different date patterns. Clearly, the Permian dates of *c.* 272 Ma retrieved from the leucosome cannot be regarded as the crystallization age of the melt fraction in the migmatite. Indeed, U–Pb apatite dating of Velay migmatites 20–30 km east of the study area yielded early Permian *c.* 290 Ma cooling ages. Furthermore, migmatite pebbles are found in the basal conglomerate of the Prades-Jaujac basin (Bouilhol et al., 2006), which infilling has been dated at 296.0 ± 6.8 Ma (zircon U–Pb SIMS on bentonite). Therefore, the date of 299.1 ± 2.7 Ma obtained on the metatexite more likely correspond to the migmatite crystallization age. Localized fluid circulation would have resulted in the resetting of leucosome CHA-15-65L monazites. Scattered $^{206}Pb/^{238}U$ dates in the metatexite may indicate successive monazite crystallization events, possibly in line with several melting episodes as suggested by Montel et al. (1992). Yet, as those dates are discordant they will not be further interpreted.

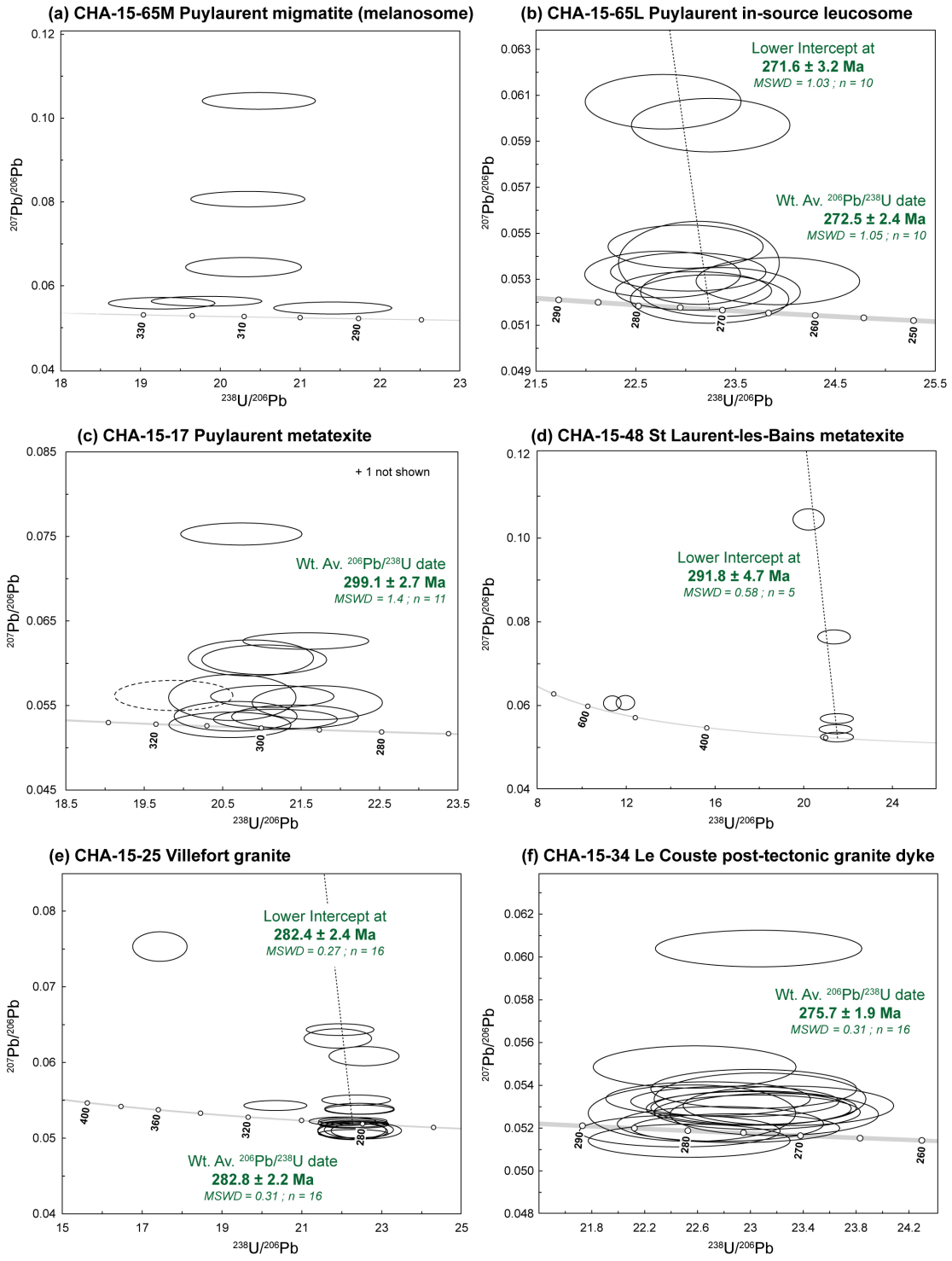

Figure 6.25: Tera-Wasserburg diagrams ($^{238}U/^{206}Pb$ vs. $^{207}Pb/^{206}Pb$) for monazite extracted from: (a–c) migmatites sampled at the Puylaurent dam; (d) a Saint-Laurent-les-Bains migmatite (see Bouilhol et al., 2006); (d) Villefort granite CHA-15-25; (e) post-tectonic granite dyke CHA-15-34. Zircon U–Pb dating did not yield any concordant Variscan date for all samples. Error ellipses and ages are displayed at 2σ level of uncertainty. Dotted ellipses were not considered for calculations.

The date of 291.8 ± 4.7 Ma obtained on the Saint-Laurent-les-Bains migmatite is difficult to interpret. It would most probably represent the age of an hydrothermal event, possibly related to the formation of the fluorite lodes and veins recognized nearby Saint-Laurent-les-Bains (Elmi et al., 1974; Weisbrod et al., 1974). The older monazite grain, showing late Ediacaran–early Cambrian $^{206}Pb/^{238}U$ dates, is regarded as inherited from the migmatite protolith i.e. the Velay Orthogneiss Formation. Similar inherited monazite grains in the Velay migmatites and granites have been described by Be Mezeme et al. (2006) and Didier et al. (2013).

Importantly, LA–ICP–MS monazite ages obtained in the course of this study are notably younger than the "chemical" U–Th–Pb ages reported by Bouilhol et al. (2006) and Be Mezeme et al. (2006) for both the Puylaurent and Saint-Laurent migmatites, spanning between 329 ± 5 and 310 ± 2 Ma. Those datasets were obtained following the procedure of Cocherie et al. (2005) and the statistical scheme developed by Cocherie and Albarede (2001) which efficiency has recently been challenged (Poujol et al., 2016). Besides, Poujol et al. (2016) and Trap et al. (2017) noticed that it tends to yield older ages than those obtained by LA–ICP–MS monazite dating. In our case study, most monazite analyses happened to be discordant, presumably as a result of common Pb incorporation. Therefore, the presence of non-radiogenic Pb in the monazite matrices, undetectable with a microprobe, would adequately explain the older ages retrieved by Bouilhol et al. (2006) and Be Mezeme et al. (2006) in the migmatites.

Villefort granite CHA-15-25 The weighted average $^{206}Pb/^{238}U$ date of 282.8 ± 2.2 Ma may correspond either to the crystallization age of the granite sill or the age of post-magmatic fluid circulation. The second possibility is supported by: (i) the location of the sample within the Villefort Shear Zone which activity continued under brittle conditions, likely to drain a range of deep to shallow crustal fluids; (ii) the very small size of monazite grains (mostly <20 μm in length), making them prone to recrystallization/resetting; (iii) the existence of crystals yielding older $^{206}Pb/^{238}U$ dates of 309 ± 10 and 359 ± 11 Ma, respectively, which may have escaped the localized fluid influx; (iv) field observations showing very intricate contacts between the granite and its host paragneiss (Fig. 6.10a), inconsistent with the granitic magma intruding an already cooled-down basement (see the U–Pb apatite cooling ages mentioned above). Therefore, the discordant date of 309 ± 10 Ma is retained as the age of magma crystallization while that of 359 ± 11 Ma, highly discordant, may be related to an early metamorphic event.

Granite dyke CHA-15-34 The $^{206}Pb/^{238}U$ date of 275.7 ± 1.9 Ma is regarded as the crystallization age of the granite dyke because of the typical oscillatory concentric zoning displayed by one monazite grain (see Fig. 6.24) and the lack of evidence for a pervasive fluid influx able to reset 80 μm-large grains. Interestingly, Be Mezeme et al. (2006) report crystallization ages between 333 ± 6 to 318 ± 5 Ma for several granite dykes in and around the Masméjean dome. Unfortunately, these authors did not quote the exact GPS coordinates so that the actual nature of the dated samples remains unclear and cannot be directly compared to our results. The obtained Permian age is identical to a whole-rock Rb–Sr age reported for the late Pont-de-Chervil granite, cropping out in the eastern part of the Velay dome (274 ± 7 Ma, Caen-Vachette et al., 1982).

6.3.5 Summary

Fig. 6.26 presents a summary of the geochronological data gained in the course of this study. The new age obtained on the Rocles granite confirms that regional D_{2v} top-to-the NE shearing is as old as *c.* 320 Ma. Following the conclusion of the AMS study, the *c.* 305 Ma emplacement ages of the Villefort granites indicate that the Villefort Shear Zone was active by that time. An identical age was retrieved for the granite sill CHA-15-19, pre-dating brittle-ductile top-to-the S shearing. The Borne granite yielded

a statistically older intrusion age than its presumed counterpart on the western side of the VSZ: the Pont-de-Montvert batholith (309.7 ± 3.6 vs. 302.5 ± 3.5 Ma, taking into account systematic errors). Emplacement of the fine-grained, porphyritic, granite sill CHA-15-33 at 302.8 ± 3.7 Ma entails that the Sil-zone of the Masméjean dome mantle had already significantly cooled down by that time. Metatexites from the dome core would have crystallized at *c.* 300 Ma, at the Carboniferous–Permian boundary. Permian ages mostly attest to fluid circulations but also to emplacement of late granite dykes.

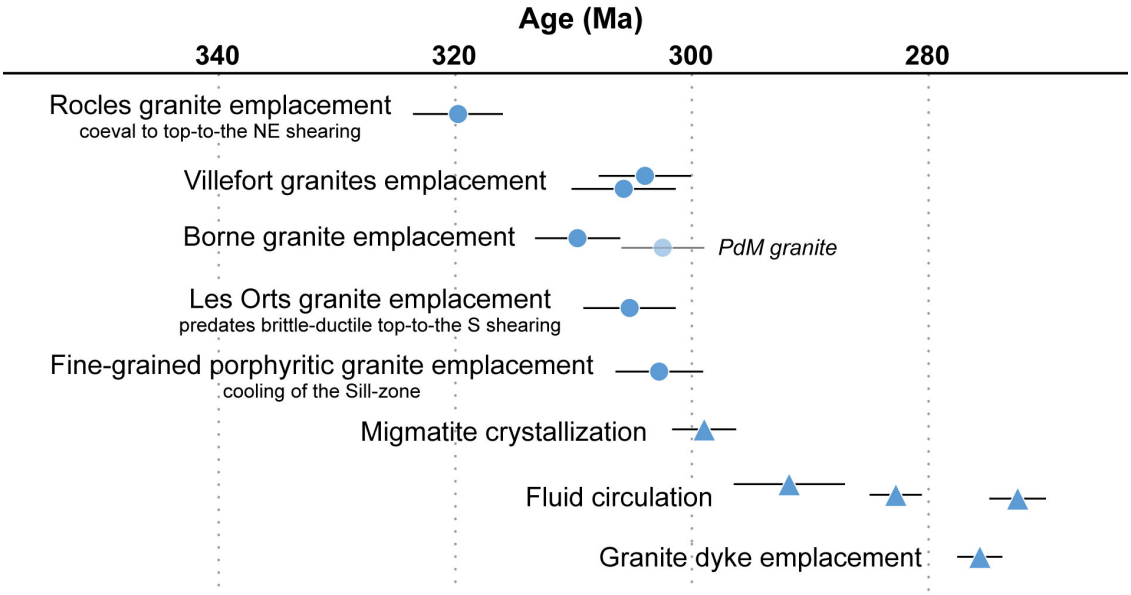

Figure 6.26: Summary of the zircon and monazite LA–ICP–MS U–Pb ages obtained in the course of this study. Same legend as Fig. 6.3. The emplacement age of the Pont-de-Montvert pluton is from Laurent et al. (2017).

6.4 Petrogenetic constraints on syn-doming crustal melting

The observation of in-source leucosomes and granite veins within the Masméjean migmatites attests to melt mobility and associated mass and heat transfer during doming. This section addresses the modes of melt production in the Masméjean dome and notably the linkage between migmatites and granites. For this purpose, a total of 25 new major and trace element whole-rock compositions were obtained for samples from the Masméjean dome and its close surroundings: 13 granites, 4 orthogneisses and 8 migmatites (3 bulk metatexites and 5 in source-leucosomes). Additional measurements on regional orthogneisses (N=20) from section 2.1 were added to the dataset (all analyses available in Appendix Table B1).

6.4.1 P–T conditions of anatexis in the migmatites

First-order thermodynamic modelling was performed to investigate the P–T conditions of melting in the dome core. Field observations (Fig. 6.13) and U–Pb zircon data (see previous section) indicate that augen gneisses from the Velay Orthogneiss Formation arguably constitute the protolith of the migmatites. Accordingly, a representative augen gneiss composition was chosen out of our database (SC-14-33) and pseudosections were calculated by Gibbs energy minimisation using PerpleX (Connolly, 2005) and the self-consistent thermodynamic dataset of Holland and Powell (1998) (updated version of 2004). The chemical system retained is Na_2O–CaO–K_2O–FeO–MgO–Al_2O_3–SiO_2–H_2O–TiO_2 (NCKFMASHT) i.e. all iron is ferrous and Mn not considered.

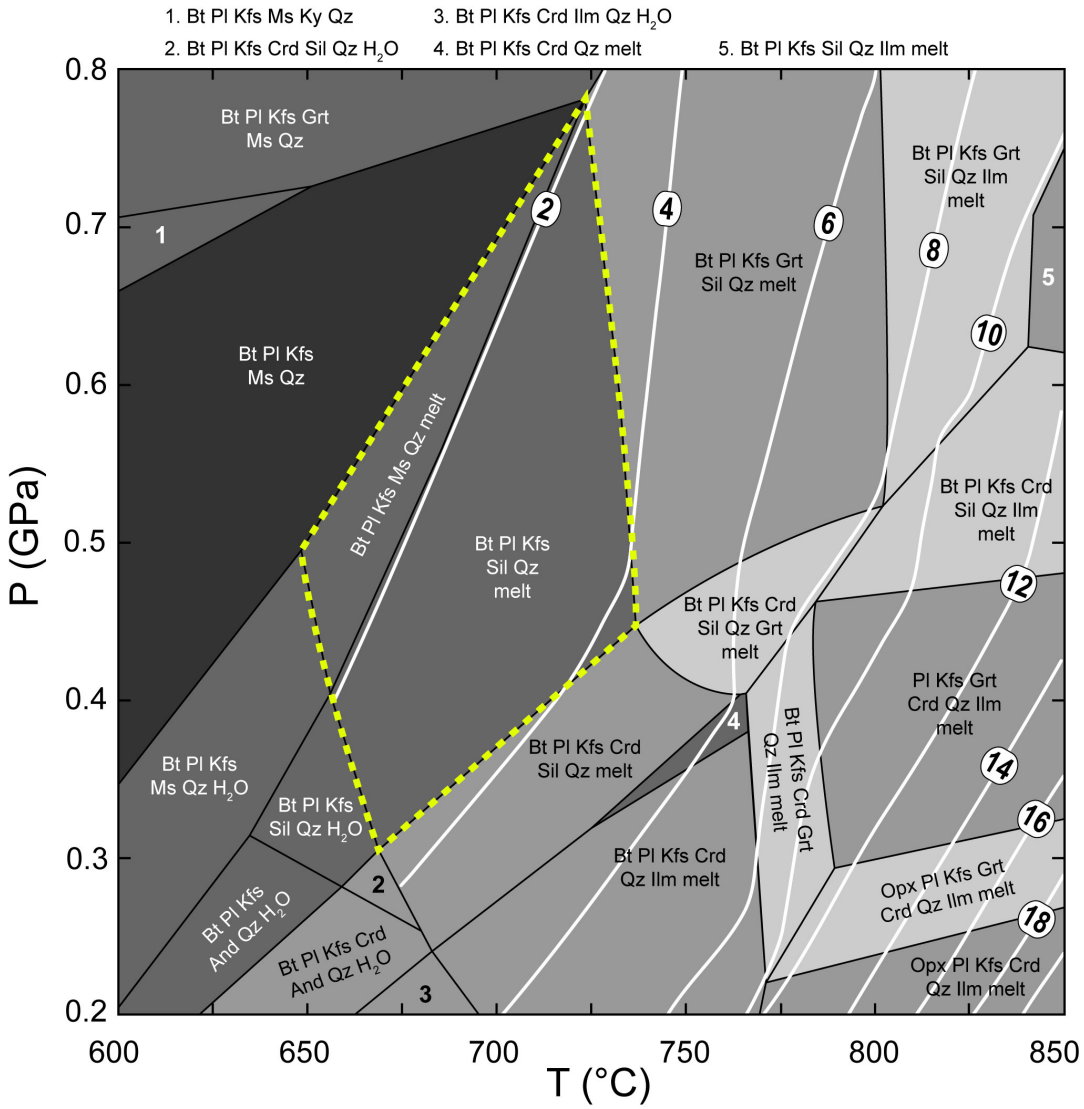

Figure 6.27: P–T pseudosection calculated using a representative augen gneiss composition. White lines are melt isopleths (with numbers indicating melt wt.%). Initial water content was adjusted to avoid subsolidus water oversaturation at 0.5 GPa. Mineral abbreviations after Whitney and Evans (2009).

The range of P–T conditions investigated is 0.2–0.8 GPa for 600–850 °C. Solutions models selected are: Bio(TCC) for biotite (Tajčmanová et al., 2009), Pl(h) and San for plagioclase and K-feldspar (Newton and Haselton, 1981), Mica(CHA1) for white mica (Auzanneau et al., 2009; Coggon and Holland, 2002), melt(HP) for anatectic melt (White et al., 2001), hCrd for cordierite and Opx(HP) for orthopyroxene (Powell and Holland, 1999), Gt(WPH) and Ilm(WPH) for garnet and ilmenite (White et al., 2000).

SC-14-33 composition was recast to anhydrous and the H_2O concentration subsequently adjusted to obtain a fully hydrated subsolidus system (maximal water content without subsolidus H_2O oversaturation) at 0.5 GPa. A T–X_{H_2O} pseudosection at this pressure (not shown) indicates that 0.53 wt.% H_2O in the bulk is necessary to reach full hydration. The retained chemical composition is displayed Table 6.2.

Sample	SiO_2	Al_2O_3	FeO	MgO	CaO	Na_2O	K_2O	TiO_2	H_2O
SC 14 33	72.56	14.90	2.02	0.40	0.76	3.12	5.52	0.19	0.53

Table 6.2: Chemical composition of the representative augen gneiss sample used for modelling.

Following petrographic observations (see section 6.2.2), the paragenesis inferred at

peak metamorphic conditions for the migmatites is: melt+Qz+Kfs+Pg+Bt±Sil±Ms ±Ilm±Ru+Ap+Zrc. The stability field of this mineral assemblage is bounded at low temperature by the solidus and at high temperature (and/or low pressure) by biotite-breakdown and associated appearance of garnet and/or cordierite (Fig. 6.27). As none of these minerals have been observed, we conclude that partial melting in the Masméjean dome took place at $0.75 < P < 0.3$ GPa and $650 < T < 730$ °C, consistent with the estimates of Dallain et al. (1999) and Montel et al. (1992).

Melt production would have occurred through water-present and muscovite dehydration-melting, generating sillimanite and K-feldspar as by-products (Clemens and Vielzeuf, 1987; Dallain et al., 1999; Patiño Douce and Harris, 1998; Thompson, 1982). Importantly, low melt productivity is expected at these P–T conditions with as little as 2–4 wt.% melt being produced.

6.4.2 Granite petrogenesis

Geochemistry and typology

Granites from the Masméjean dome are peraluminous (Fig. 6.28a) and define a trend between the felsic and highly peraluminous fields in the B–A diagram (Debon and Le Fort, 1983; Villaseca et al., 1998), indicative of an affinity to S–type granites (Clemens, 2003; Chappell and White, 1974; Villaseca et al., 1998). If they share similar major element compositions with meta-granites from the Velay Orthogneiss Formation, they distinctively show higher Nb/Y ratios (Fig. 6.28b). Metatexites mostly overlap in composition with unmolten orthogneisses apart for an enrichment in Nb, possibly related to biotite accumulation (Fig. 6.28d). In-source leucosomes are felsic peraluminous, Nb depleted and typically lack any Eu anomaly (Eu/Eu* close to 1).

Inherited zircon evidence for an orthogneiss source

Granites from the Masméjean dome and more generally from the southern border of the Velay dome contain abundant inherited/xenocrystic zircon grains (see Couzinié et al., 2014; Laurent et al., 2017, and this study). The distribution of $^{206}Pb/^{238}U$ dates measured on such grains is unimodal and features a marked peak at c. 545 Ma with few older (mostly Ediacaran–Cryogenian) and younger (Ordovician to Carboniferous) dates (Fig. 6.29).

Assuming that most xenocrysts were incorporated in the magma at source level, the perfect match between the granite inherited date distribution and that of the Velay Orthogneiss Formation indicates that the latter constitutes the source of most granite magmas emplaced in the Masméjean dome and its surroundings. Subordinate involvement of regional metasediments is supported by the presence of 560–680 Ma-old xenocrysts, even though *c.* 50% of those grains actually correspond to cores wrapped around by c. 545 Ma-old rims, suggesting they rather belonged to the source of the VOF meta-granites (see section 2.1). The origin of the three Ordovician zircon dates remains unknown as no rock of that age has been described in this region. Finally, Devonian–Carboniferous grains would have recorded early Variscan metamorphic/magmatic events affecting the local basement (Faure et al., 2009) before being incorporated in the magma at the origin of the Masméjean granites.

Low orthogneiss fertility: the X_{H2O} issue

The inherited zircon age pattern supports an orthogneiss source for regional granites. As those are spatially associated to the Masméjean and southern Velay migmatites, the genetic linkage between anatexites and granites must be addressed. Thermodynamic modelling shows that at peak metamorphic conditions, the melt productivity of augen gneisses at fully hydrated conditions is low (maximum of 4% wt.%). Such value is notably

lower than the liquid percolation threshold (LPT, 8 vol.% melt, Vigneresse et al., 1996) above which melt can escape its source and collect. Yet, field observations support the existence of former melt-enriched (in-source leucosome) and melt-depleted (biotite-rich melanosome) domains which clearly attest to efficient melt transfer and mobility in the Masméjean migmatites (Fig. 6.13a,b), potentially up to form Masméjean granite bodies.

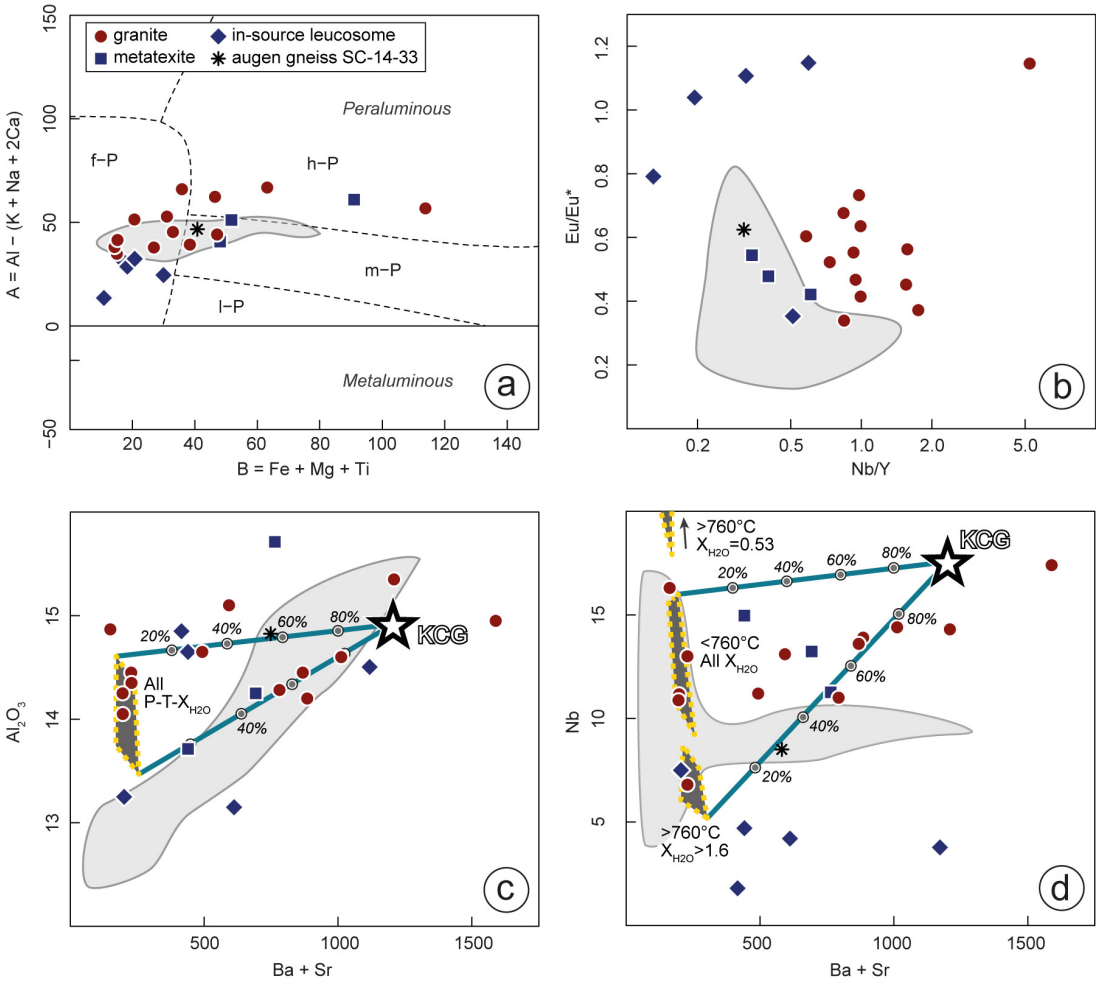

Figure 6.28: Geochemical characteristics of granites, metatexites, in-source leucosomes and basement orthogneisses from the Masméjean dome. (a) B–A diagram of Debon and Le Fort (1983) modified by Villaseca et al. (1998). (b) Eu/Eu* vs. Nb/Y plot. (c) Al_2O_3 vs. Ba + Sr plot, the dark field correspond to the modelled melt compositions. (d) Nb vs. Ba + Sr plot, the text right of each dark field indicates the specific T–X_{H2O} conditions. Same legend as Fig. 6.5 with additional symbols: blue diamonds and black asterisk, referring to in-source leucosomes and the representative augen gneiss sample SC-14-33 considered for thermodynamic modelling, respectively. Mixing trends are calculated between: (i) extremal model melt compositions and (ii) the average composition of K-rich calc-alkaline granites ("KCG" of Barbarin, 1999) from the French Massif Central, regarded as mantle-derived magma fractionates (Laurent et al., 2017; Moyen et al., 2017a). Data for KCGs (65–72 wt.% SiO_2) are from this study (sample BOR-16-01), Delfour et al. (1989); François (2009); Mialhe (1980); Sabourdy (1975), and personnal communications from B. Barbarin, M. Cuney and J.-F. Moyen. Number of analyses is 146 for Al_2O_3, 143 for Ba+Sr and 8 for Nb. The grey field depicts the compositional variability of orthogneisses from the Velay Orthogneiss Formation. X_{H2O} are quoted in wt.%.

Such inconsistency between field observations and the model predictions may have two origins. First, melt coalescence is a deformation-assisted process (Macaudière et al., 1992; McLellan, 1988; Sawyer, 2008) meaning that pure/simple shearing may be sufficient to expel liquids out of their solid matrix, even at (very) low melt fractions. An alternative view would be to consider that the "fully hydrated system" assumption is wrong and that anatexis was aqueous fluid-assisted (see Weinberg and Hasalová, 2015 and refer-

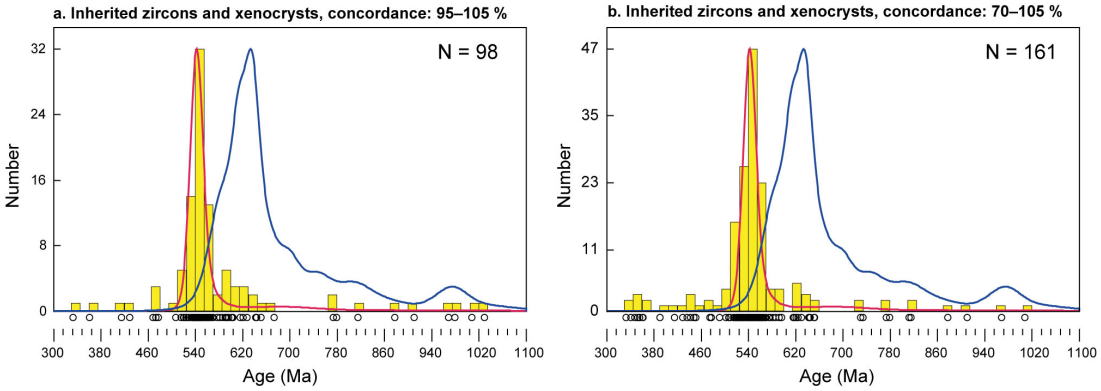

Figure 6.29: Histogram showing the $^{206}Pb/^{238}U$ dates of inherited zircon grains and xenocrysts from granites sampled in the southern part of the Velay Dome. Data from Couzinié et al. (2014) and this study. Bin width is 15 Ma. Available zircon $^{206}Pb/^{238}U$ dates (concordance: 95–105%) for the Velay Orthogneiss Formation (in red, data from this chapter and Part 1, N=107) and regional metasediments (in blue, data from Chapter 2 and Chelle-Michou et al., 2017, N=445) represented as Kernel Density Estimates. The latter were calculated using the DensityPlotter program of Vermeesch (2012) with a bandwidth set at 15 Ma.

ences therein). Elevated X_{H2O} in the bulk composition does not substantially affect the stability field of the main mineral assemblages but results in a dramatic increase of the melt productivity (Fig. 6.30). This partly stems from the overall "eutectic" composition of the orthogneiss source, with quartz and feldspars being dissolved in the melt phase via the reaction Qz + Kfs + Pl + H_2O = melt, only limited by water availability (Johannes and Holtz, 1996; Holtz and Johannes, 1991).

Increasing the H_2O content of the source orthogneiss may proceed via influx of: (i) meteoric water, percolating down to the middle crust (Wickham and Taylor Jr., 1985); (ii) metamorphic water, originating from the dehydration of deeper lithologies (Cartwright et al., 1995; Sawyer, 2010), (iii) magmatic water conveyed by uprising, hydrous melts (Weinberg and Hasalová, 2015). Evidence for case (i) are very scarce in the geological record (see review in Weinberg and Hasalová, 2015). In case (ii), release of aqueous fluids in the deep crust is likely to immediately promote partial melting so that H_2O would be transferred upsection dissolved in a melt phase (Sawyer, 2010) hence getting to case (iii).

Following Weinberg and Hasalová (2015), we envisage a situation where the intrusion of a water-rich magma creates a local water activity gradient in the middle crust. This promotes H_2O transfer from the melt to its country-rocks which would in turn initiate or enhance anatexis. Such model would adequately explain the apparent elevated melt volumes in migmatites, higher than predicted for subsolidus full hydration, and the spatial and temporal relationships between anatexis and granitic magmatism (see Fig. 6.13e,f).

Given the scarcity of mafic igneous rocks in the Masméjean dome, the intruding hydrous magmas were most likely of granite composition. Their inferred elevated H_2O contents suggests that they derive from the fractionation of a water-rich parental magma akin to vaugnerites (Parat et al., 2009). If our model is correct, granites from the Masméjean dome would intrinsically be of mixed origin: a fraction of their mass corresponds to collected, local anatectic liquids while the rest originates from fractionated mantle-derived magmas.

In order to test this hypothesis, we performed forward modelling to estimate the major and trace element compositions of anatectic liquids generated from orthogneiss melting for a range of P–T–X_{H2O} conditions and compared them to the natural granite compositions.

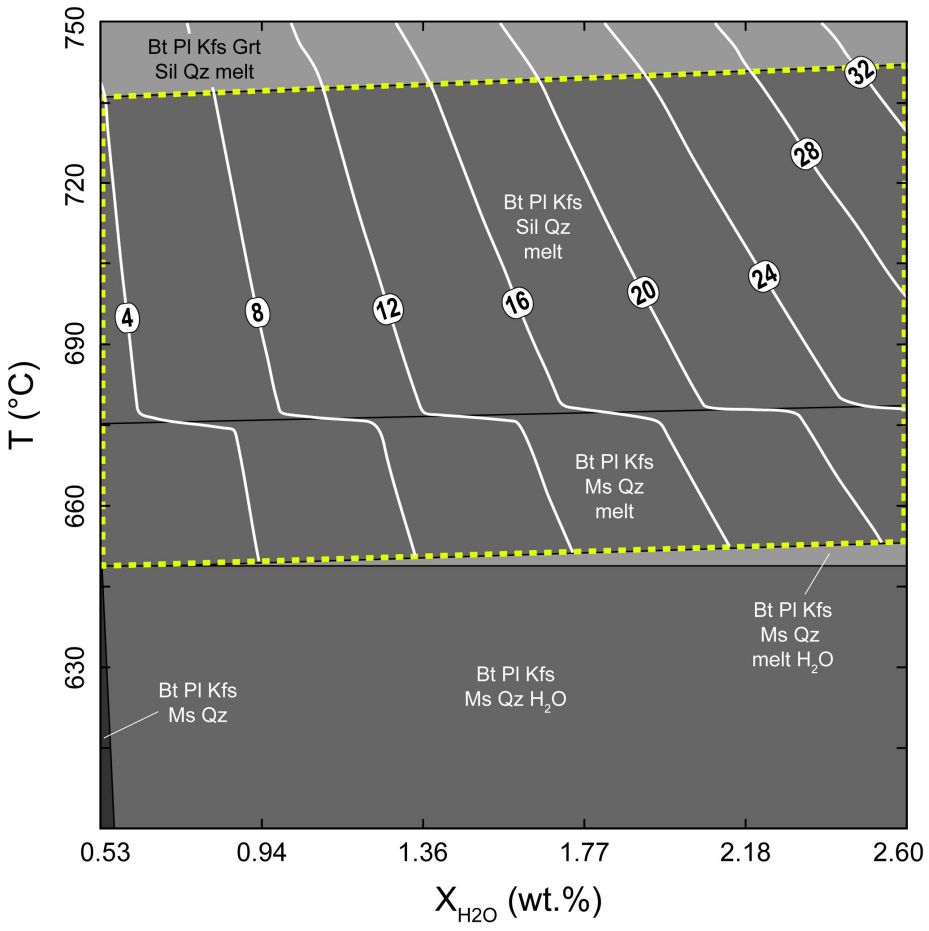

Figure 6.30: T–X_{H2O} pseudosection calculated using a representative augen gneiss composition. White lines are melt isopleths (with numbers indicating melt wt.%). For sake of clarity, isopleths were not drawn in the field Bt+Pl+Kfs+Ms+Qz+melt+H_2O. Mineral abbreviations after Whitney and Evans (2009).

Forward modelling of granite genesis

Phase proportions and melt compositions were calculated along three P-T paths consisting in isobaric heating from 680 to 800 °C at 0.4, 0.5 and 0.6 GPa, using the same representative augen gneiss composition as above (Table 6.2). Calculations were performed in closed-system, i.e. with no melt extraction (the melt is always in equilibrium with the solid residue). Three initial water contents were considered for the bulk starting composition: 0.53, 1.6 and 2.6 wt.% H_2O. Melt Ba, Sr and Nb contents were calculated at each step along the P–T path using: (i) the phase proportions retrieved from each step along the T–t path; and (ii) a set of partition coefficients for felsic systems compiled by Laurent (2012).

Results are depicted Fig. 6.28. First, four in-source leucosomes out of five show different chemical compositions than predicted by the model for anatectic melts. Their low Nb contents and elevated Eu/Eu* collectively suggest that they correspond to plagioclase-rich and biotite-poor cumulates. Five granite samples with low Ba + Sr would adequately correspond to pristine anatectic melts generated at T <760°C for a large range of X_{H2O} contents (from 0.53 to 2.6 wt.%) and T >760°C but elevated X_{H2O} (1.6 to 2.6 wt.%). Importantly, melting at high temperature under fully hydrated conditions (X_{H2O} = 0.53 wt.%) fails to reproduce natural composition has it generates melts with high Nb concentrations (Fig. 6.28d). In addition, the composition of 6 granites can be reasonably modelled as a mixture between local anatectic melts and 20–80% KCG magmas (Fig. 6.28c,d). Two samples are richer in Ba+Sr, possibly related to local K-feldspar accumulation.

To conclude, geochemical modelling supports a mixed origin for the Masméjean granites with a fraction corresponding to local pristine anatectic melts formed at T <730–760°C and the remaining being akin to KCG magmas. This way, elevated melt contents in metatexites most probably stem from the addition of external water, supplied by intruding mantle-derived KCG magmas.

6.4.3 Differential response to water ingress: role of inherited structures in controlling doming

The previous section illustrates how water diffusion from hydrous mantle-derived magmas would trigger substantial anatexis at moderate temperatures. In the case of the Masméjean dome, the dramatic effects of water ingress inherently stems from the unlimited availability of the cardinal minerals Qz+Pg+Kfs involved in the "eutectic" melting reaction (Holtz and Johannes, 1991; Johannes and Holtz, 1996). In other words, melting would have been markedly enhanced because of the *granitic* nature of the VOF protolith. The control exerted by the source composition and mineralogy on this phenomenon can be apprehended by comparing the melt productivities of ortho and paragneisses at 0.5 GPa when the water content increases due to interaction with KCG magmas.

Figure 6.31 shows that regional metagreywackes (reference material CEV, see Vielzeuf and Montel, 1994 and Montel and Vielzeuf, 1997) produce very limited amounts of melts below 720°C and are always less fertile than the VOF orthogneiss (twice as less on average) at elevated X_{H2O}. This feature simply reflects the absence of Kfs at subsolidus conditions (Montel and Vielzeuf, 1997; Vielzeuf and Montel, 1994), hampering substantial melt production by the "eutectic" melting reaction. In metagreywackes, Kfs is the limiting reactant and not H_2O as in the orthogneiss.

Importantly, these first-order calculations suggest that enhanced anatexis by water ingress is restricted to migmatites developed at the expense of meta-igneous lithologies, such as the VOF. This would adequately explain why the Masméjean dome is cored by orthogneisses. As anatexis and dome formation are intimately linked, both from a spatial and temporal point of view (Rey et al., 2009; Tirel et al., 2004; Whitney et al., 2004b), doming would only proceed in orthogneiss-dominated terrains.

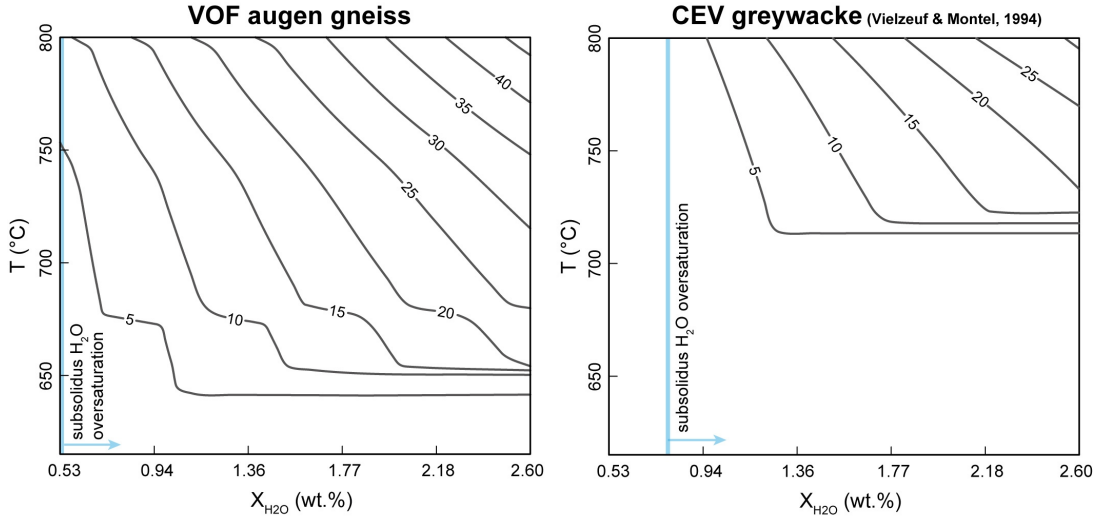

Figure 6.31: Comparison of respective melt productivities (in wt.%) for the Velay Orthogneiss Formation (augen gneiss sample SC-14-33) and a regional representative metagreywacke (CEV, Vielzeuf and Montel, 1994) with increasing water contents at a pressure of 0.5 GPa. Melt isopleths for the greywacke calculated using the same procedure as section 6.4.1.

6.5 Zircon behaviour during orthogneiss melting

A striking feature of the U–Pb zircon dataset is the comprehensive lack of Variscan grain in the migmatites. The same remark holds true for several granite bodies in and around the dome. This section addresses the origin of such scant Variscan zircon record.

6.5.1 Maximum Zr uptake in the melt fraction

In this section, we will consider that new zircon growth during anatexis exclusively results from the dissolution of pre-existing protolith zircon grains and re-precipitation of new grains (or overgrowths) from the melt phase (Watson, 1996). Zircon neoformation by Ostwald ripening (Nemchin et al., 2001) was not investigated. Experimental studies have determined the maximal amount of Zr that can be accommodated in a melt until it reaches zircon saturation, which depends on the temperature and melt chemistry (Boehnke et al., 2013; Watson and Harrison, 1983). Following this, it is possible to predict the maximal Zr content of felsic melts generated from the VOF orthogneisses in a range of P–T–$_{H2O}$ conditions. Figures 6.32 and 6.33 depict the maximal Zr content of melts produced from the same representative augen gneiss composition used in the modelling section 6.4. Such value strongly depends on the temperature of melting but little on the bulk water content of the protolith.

Assuming that all Zr in the orthogneiss is hosted in zircon, it becomes possible to calculate the proportion of the orthogneiss zircon budget that has to be dissolved in order to saturate the melt phase. The results are reported Fig. 6.34 and 6.35. Importantly, low and high bulk H_2O systems show contrasted behaviours. At low water content (Fig. 6.34), saturation of melt fractions >10 wt.% requires substantial zircon dissolution, up to 50 wt.% of the source zircon budget for only 20 wt.% melt in the migmatite. In contrast, at high H_2O content, saturation of elevated melt fractions can be reached through limited zircon dissolution. For instance, incorporation of 10 wt.% of the orthogneiss zircon pool can suffice to saturate a 24 wt.% melt fraction at 690°C.

Such differences arise from the fact that attaining substantial melt fractions at low H_2O content requires elevated temperature (Fig. 6.32) and is correlated to an increase in the melt M parameter (Boehnke et al., 2013; Miller et al., 2003). Both aspects result in higher maximal melt Zr content (Fig. 6.32) thus entailing extensive dissolution of the source budget. In contrast, there is little change in the M parameter value at elevated H_2O content because melt chemistry is buffered by the reaction Qz+Kfs+Pg+H_2O=melt (Holtz and Johannes, 1991; Johannes and Holtz, 1996). The maximal melt Zr content remains low (<90 ppm) and the melt phase can be saturated via limited dissolution of the zircon pool in the source.

To conclude, these results suggest that the amount of new magmatic zircon in a migmatite is a first-order estimate of the temperature of melting and the water content of the system.

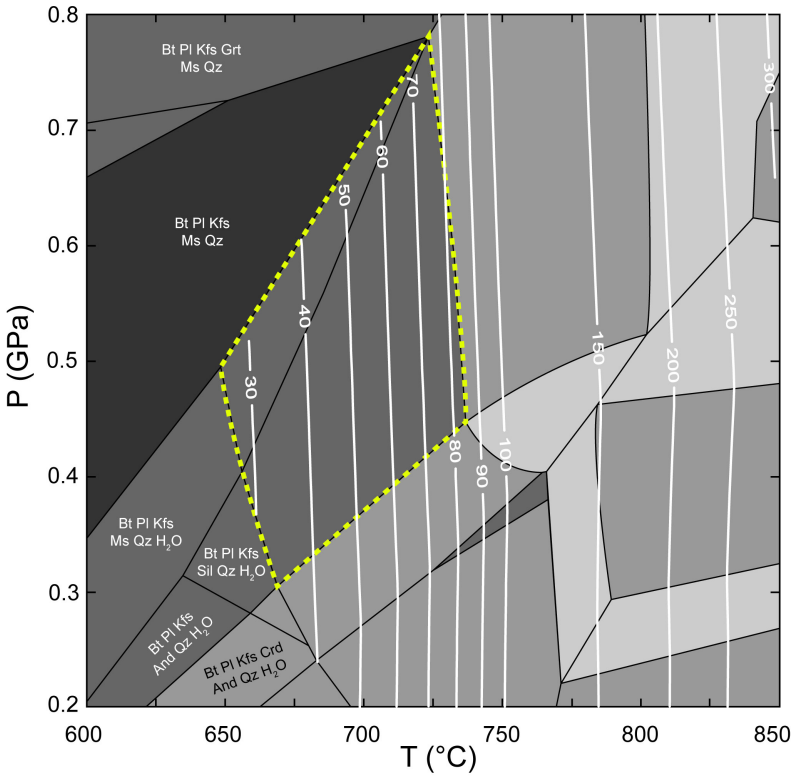

Figure 6.32: Calculated maximal Zr concentration (in ppm) in the melt phase for a fully hydrated (at 0.5 GPa) orthogneiss composition (SC-14-33). Based on the equation of Boehnke et al. (2013). The Zr concentration of the stoechiometric zircon was set at 497644 ppm.

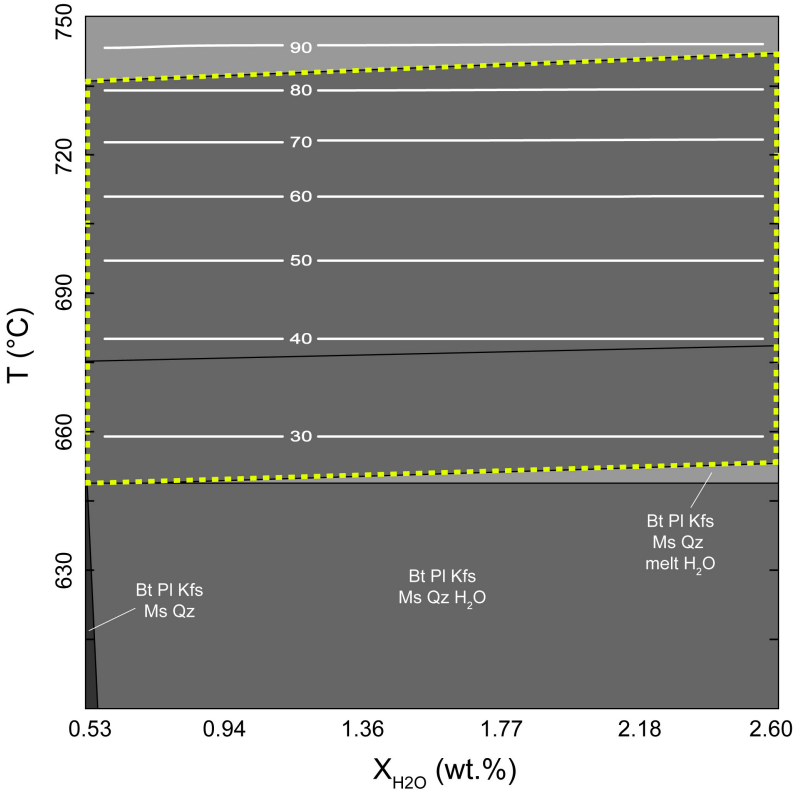

Figure 6.33: Calculated maximal Zr concentration (in ppm) in the melt phase, provided it is zircon saturated. Starting composition: orthogneiss SC-14-33. Based on the equation of Boehnke et al. (2013). The Zr concentration of the stoechiometric zircon was set at 497644 ppm. Pressure is 0.5 GPa.

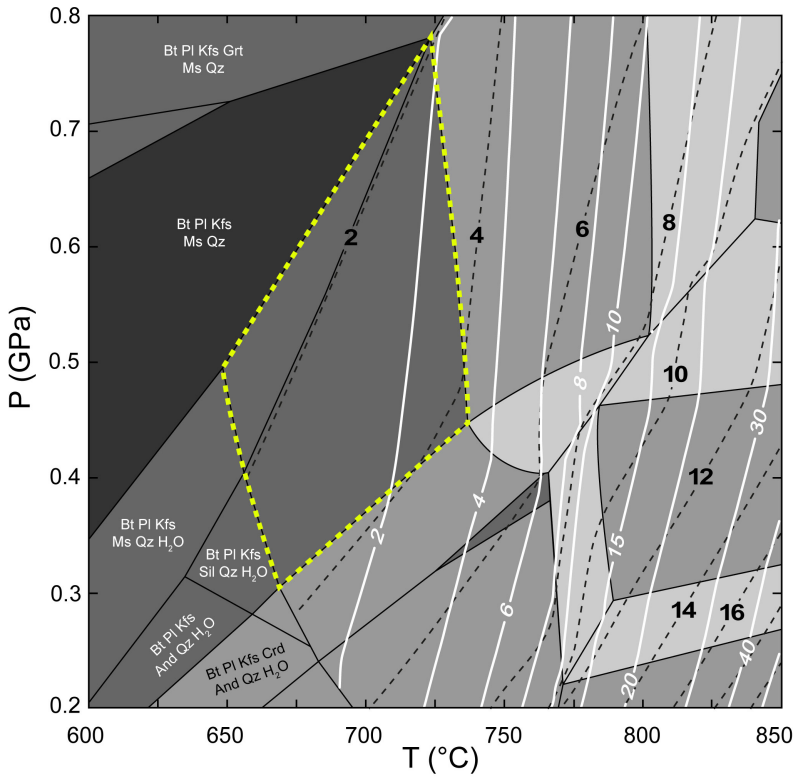

Figure 6.34: Calculated proportion (white lines, in wt.%) of the orthogneiss zircon budget to be dissolved in order to saturate the melt phase. The average Zr content of the protolith was set to 115 ppm for. Dotted lines and bold numbers are melt isopleths and melt contents in wt.%, respectively.

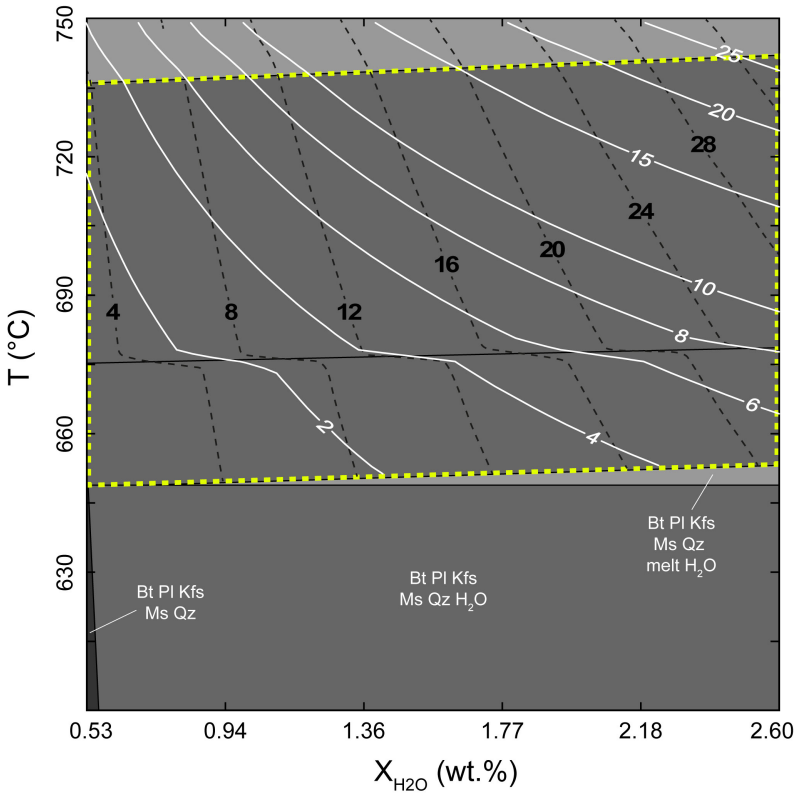

Figure 6.35: Calculated proportion (white lines, in wt.%) of the orthogneiss zircon budget to be dissolved in order to saturate the melt phase. The average Zr content of the protolith was set to 115 ppm for. Dotted lines and bold numbers are melt isopleths and melt contents in wt.%, respectively. Pressure is 0.5 GPa.

6.5.2 Additional complications

Calculations performed in the previous section considered an idealized and simplified case where the migmatite behaves as a closed-system, i.e. melt is retained within its source. Yet, melt loss events deplete or enrich the restite in Zr (depending on the melt Zr content vs. that of the protolith) which, in turn, affects further zircon dissolution in the residual melts (e.g. Kelsey et al., 2008; Yakymchuk and Brown, 2014).

Another range of parameters not investigated in our model are the kinetics effects as we assumed permanent melt–solid equilibrium. Importantly, the dissolution of zircon grains is controlled by the diffusion of Zr in the melt fraction (Watson, 1996). Therefore, rapid withdrawal of anatectic melts out of the source may result in a disequilibrium between melt and the solid residual matrix (Harris et al., 2000; Sawyer, 1991; Watt et al., 1996), hampering substantial zircon dissolution before melt extraction. However, disequilibrium melting might not always be the rule (e.g. Rubatto et al., 2001).

Finally, it was assumed that all zircon (and hence all Zr) from the protolith was part of the "reactive system", i.e. was not occluded in unreactive minerals during partial melting. Yet, biotite hosts notable amounts of zircon grains in metamorphic rocks (Clemens, 2003) meaning that, during melting at temperatures lower than that required for extensive biotite breakdown, part of the protolith zircon budget cannot physically interact with the melt and is in essence out of equilibrium (Bea and Montero, 1999; Skrzypek and Štípská, 2012).

6.5.3 Application to the Masméjean migmatites and granites

At melting conditions relevant for the Masméjean case study, i.e. T $<$ 730°C, saturation of the migmatite melt fraction would be achieved through limited zircon dissolution corresponding to *c.* 10 wt.% of the orthogneiss budget for a reasonable maximal melt content of 20 wt.%. Therefore, if the melt fraction crystallized in situ, one could expect *c.* 10 wt.% of the zircon grains (or grain domains) to have recorded the melting event. Such value is clearly a maximum estimate as it presumes a closed-system behaviour with full equilibration between melt and residue.

Following this, the lack of Variscan zircon in the Masméjean *metatexites* would result from the conjunction of: (i) low zircon solubility in the melt phase at the inferred P–T–X_{H2O} conditions of melting (Fig. 6.32 and 6.33), entailing that a *maximum* of only 10 wt.% of the grains would be magmatic and record anatexis; (ii) selective retention of zircon grains in biotite, as melting occurred at T $<$ 780°C (onset of biotite dehydration melting, Vielzeuf and Montel, 1994); (iii) kinetics effects, with the potentially short-lived evolution at elevated melt fractions preventing melt–residue equilibration; and, (iv) melt loss events, further hindering the probability to retrieve newly grown Variscan grains, critical for *melanosome* CHA-15-65M.

In the case of granitic magmas, the scarcity or even absence of Variscan zircon in some specimen suggests that the Zr content of the melt phase was insufficient to precipitate substantial amounts of new zircon. In this frame, it is most likely that the melts left their sources in a Zr-undersaturated state and did not further dissolve inherited grains or xenocrysts at emplacement levels, possibly because of fast cooling rates (Bindeman and Melnik, 2016; Watson, 1996).

Melt Zr-undersaturation would also adequately explain the absence of magmatic grains in the *in-source leucosomes*. Indeed, as geochemical data support a cumulative origin, crystallization of major minerals from the melt phase would have reduced the melt volume and thus entailed precipitation of new zircon if the melt had been saturated.

Consequently, a combination of several factors probably accounts for the scant zircon record of Variscan crustal melting. Importantly, the apparent Zr-undersaturation of crust-derived melts suggests that melt–residue equilibrium during anatexis was not achieved.

6.6 Formation of the Masméjean dome

6.6.1 Pre- to early-doming tectonic regime

Metamorphic rocks from the And–Crd–Bt and Grt–Chl zones record a regional pervasive top-to-the NE shearing event (D_{2v}) that is well documented in the southwestern flank of the Masméjean dome. New geochronological constraints on the Rocles syntectonic granite (Fig. 6.26), in conjunction with literature data (Be Mezeme et al., 2006; 2007; Bouilhol et al., 2006), indicate that top-to-the NE shearing probably lasted between 325–315 Ma. The end of this tectonic episode is bracketed by intrusion of the c. 315-310 Ma-old Margeride granite which occurred under NW–SE extension (Talbot et al., 2005).

At the regional scale, the N–S expansion of the main Velay granite would have caused doming and tilting of the originally flat-lying P_3 structures including the early Rocles granite (Be Mezeme et al., 2007; Burg and Vanderhaeghe, 1993; Lagarde and Dallain, 1994; Laumonier et al., 1991; Ledru et al., 2001; Marignac et al., 1980). Restoring the pre-doming geometry, top-to-the NE shearing would have affected a gently N-dipping foliation (Fig. 6.36a). Such situation markedly resembles that of the Pilat Shear Zone, described at the northern edge of the Velay Complex and presumably controlling its exhumation (Malavielle et al., 1990). Consequently, as originally suggested by Bouilhol et al. (2006), the pre-doming tectonic framework most probably consisted in extensional top-to-the NE shear zones affecting orthogneisses and overlying metasediments. Concomitant crustal melting is evidenced by the syntectonic emplacement of the Rocles peraluminous granite and the U–Pb ID–TIMS monazite date of 314 ± 5 Ma obtained on M_3 Velay migmatites by Mougeot et al. (1997).

6.6.2 Significance of the Villefort Shear Zone

Ductile vs. brittle activity

The existence of lateral displacement along the Villefort lineament has long been recognized (Lapadu-Hargues, 1947) and a total offset of 12 km estimated (Deroin and Prost, 1993a; Lapadu-Hargues, 1947; Talbot et al., 2004). According to Talbot et al. (2004), wrenching was Permian in age and dominantly occurred under brittle conditions.

Yet, a range of geochronological, structural and petrological observations argue against a substantial *brittle* offset. First, zircon U–Pb dating of two samples from the Pont-de-Montvert and Borne granites originally located c. 4 km away from each other (when the presumed offset is restored) yielded statistically different emplacement ages, thus questioning the existence of a unique batholith having behaved as a passive marker during wrenching. Second, foliation trajectories and the petrological continuity observed at the boundary between the Masméjean and Tanargue domes (near Saint-Laurent-les-Bains, Fig 6.2 and 6.5) cannot be reconciled with a 12 km, post-anatectic, brittle offset. Third, evidence for left-lateral ductile shearing (see section 6.2.1), syntectonic granite intrusion and the overall asymmetric shape of the Masméjean dome collectively demonstrate that the Villefort Shear Zone controlled the exhumation of the Masméjean migmatite dome on its eastern flank.

Consequently, we argue that left-lateral displacement dominantly took place under ductile conditions and initiated before *c.* 305 Ma, the intrusion age of the syntectonic Villefort granites (Fig. 6.36c). It is most likely that the Pont-de-Montvert and Borne plutons corresponded to different batholiths emplaced in a E–W to NE–SE extensional regime (Faure et al., 1992; Talbot et al., 2000; 2004) and which eastern and western terminations, respectively, were truncated by ductile and subsequent brittle (Deroin et al., 1990) deformation along the Villefort Shear Zone (Fig. 6.36c,d). In addition, apparent truncations may have been exacerbated by the subtractive effects of late normal faulting.

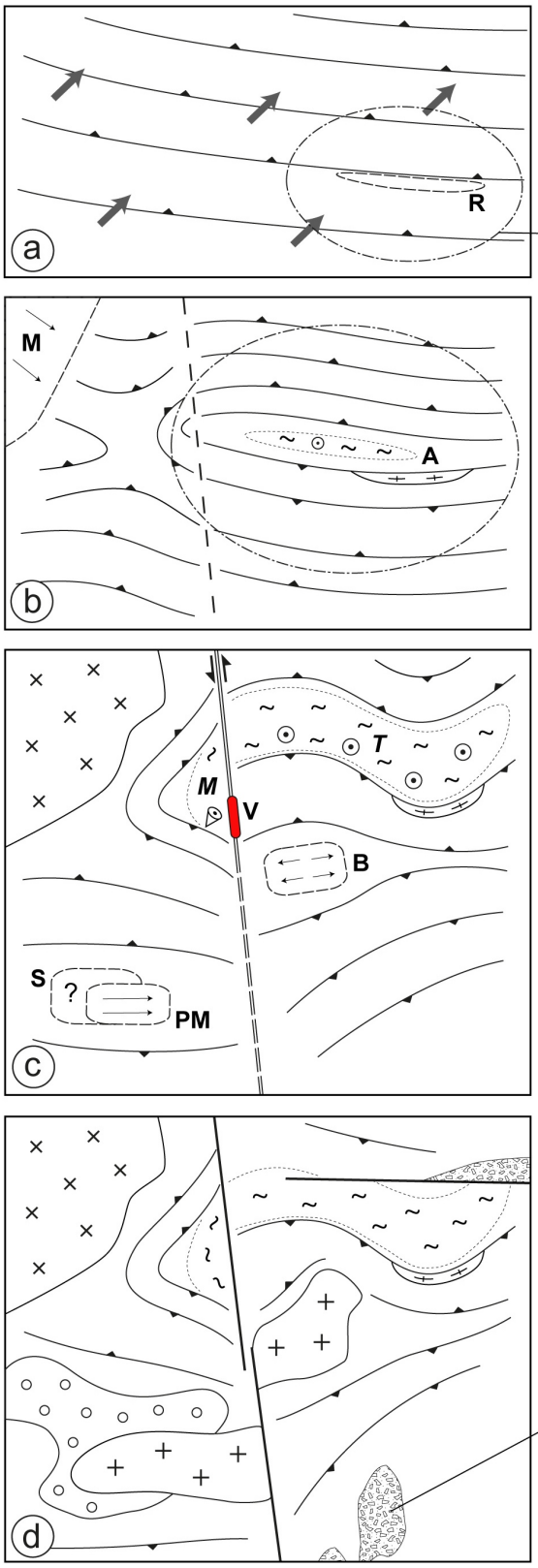

325-315 Ma

• Regional top-to-the NE extension affecting orthogneisses and overlying metasediments (shear bands, drag folds)
• Onset of anatexis at depth, intrusion of the syntectonic Rocles granite (R)

Extension of the partially molten crust layer at depth?

315-310 Ma

• The buoyant partially molten layer (**A**) pierces through its cover in an antiform (⊙indicates vertical extrusion)
• S-wards tilting of the Rocles granite and early top-to-the NE tectonic markers
• Emplacement of the Margeride granite (**M**) in an NW-SE extensional context
• Possible onset of the Villefort Shear Zone activity

310-300 Ma

• The Villefort Shear Zone isolates the Masméjean (***M***) and Tanargue (***T***) domes, coeval Villefort granites intrusion (**V**), activity confined to the middle crust?
• Vertical extrusion to the East, exhumation of the Masméjean dome to the West (🖈)
• Emplacement of the Cévenol granites (Borne **B**, Pont-de-Montvert **PM**, Signaux **S**) as individual plutons in a E-W to NE-SW upper crustal extensional context

300-275 Ma

• Regional cooling
• Onset of detrital sedimentation
• Fluid circulation
• Limited brittle deformation along the Villefort Shear Zone
• Late granite dyke injection

Detrital basin

Figure 6.36: Schematic maps illustrating the regional evolution of the study area between 325 and 275 Ma, with a particular emphasis on the formation of the Masméjean dome. To be related to Fig. 6.2.

Timing of initiation

The onset of the Villefort Shear Zone activity remains unclear. According to Prost and Becq-Giraudon (1989) and Lagarde et al. (1990), the VSZ extends further North and bounds the western part of the Velay Complex. In this area, Dupraz and Didier (1988) documented a set of syntectonic granites (the so-called "Chaise-Dieu" granites) emplaced during wrenching, presumably related to the VSZ activity. Laurent et al. (2017) obtained zircon and monazite U–Pb intrusion ages ranging between 318.3 ± 4.4 Ma and 314.5 ± 3.9 Ma (taking into account systematic errors). Consequently, the Villefort Shear Zone may have initiated as early as 320 Ma in the northern Velay and possibly propagated to the South at 315–310 Ma (Fig. 6.36b,c).

Isolating the Masméjean and Tanargue domes

Owing to the geometry of its foliation pattern, the western part of the Masméjean dome resembles the termination of a conical E–W trending antiform, akin to the Tanargue dome. Such geometry suggests an original connection between the two domes, besides supported by their petrological continuity. This way, both were most probably part of a single E–W trending antiformal structure in the core of which partially molten crust started being extruded at 315–310 Ma (Fig. 6.36b, Bouilhol et al., 2006). Left-lateral movements along the Villefort Shear Zone would have offset the western termination from the main part of the antiform (Fig. 6.36c) which evolved as the Masméjean and Tanargue domes, respectively.

Vertical strain partitioning in the crust?

In the time period 310–300 Ma, the middle crust was affected by strike-slip ductile shearing along the Villefort Shear Zone. In contrast, the internal structure of granitic plutons (Pont-de-Montvert and Borne, Fig. 6.36c) coevally emplaced at higher crustal levels rather recorded an E–W extensional context (Faure et al., 1992; Faure, 1995; Faure et al., 2001; Talbot et al., 2000; 2004). N–S wrenching is difficult to reconcile with synchronous E–W extension and points to a vertical strain partitioning within the crust section.

At mid-crustal level, the Villefort Shear Zone possibly acted as a transfer structure accommodating differential movements between the Velay Complex to the East, and the Margeride domain to the West. Such displacements would have taken place due to contrasted rheological behaviours of both crust segments. Experimental studies have demonstrated that the strength of a solid rock decreases by at least two orders of magnitude as soon as a small volume of melt is present in the matrix (Paquet et al., 1981; Rosenberg and Handy, 2005; Rushmer, 1996). As a matter of fact, by 310–300 Ma, the Margeride batholith was likely fully crystallized and its extraction left behind a stiff, dry residue. In contrast, anatexis was still ongoing in the Velay Complex by that time. Consequently, the Villefort Shear Zone possibly delineated the boundary between melt-rich and melt-depleted mid-crustal domains by the late Carboniferous. In this frame, the shear zone would have originally remained confined in the middle crust and lately propagated to the upper crust (Fig. 6.36d), probably at Permian times (Arthaud and Matte, 1975; Prost and Becq-Giraudon, 1989; Talbot et al., 2004).

6.6.3 Post-exhumation evolution

Timing of the Masméjean dome cooling is constrained by the respective ages of migmatite crystallization and fine-grained porphyritic granite intrusion, both occurring at *c.* 300 Ma (see section 6.3). The Permian evolution is marked by localized fluid circulations pinpointed by the recrystallization/resetting of monazite in the dome core and along the Villefort Shear Zone. Last increments of brittle deformation along the latter possibly

acted as a drain for a range of crustal fluids. Their origin is not ascertained but they may have been released by the crystallization of migmatites or deep magmas. Sedimentation in the Prades–Jaujac and Alès basins started in the early Permian (Bruguier et al., 2003) and the presence of migmatites in the basal conglomerates argues for fast denudation rates by the late Carboniferous/early Permian. Finally, the *c.* 275 Ma intrusion age of a granite dyke from the Masméjean dome suggests that high-temperature conditions and anatexis in the deep crust may have lasted until the middle Permian, as observed in other late-Variscan domains such as the Ivrea–Verbano zone (Klötzli et al., 2014 and references therein) or the Pyrénées (Denèle et al., 2012).

6.7 Conclusion

6.7.1 Middle-upper crust mechanical uncoupling during doming

Vertical extrusion of partially molten crust in the Masméjean dome is documented by the presence of cascading folds, the foliation flattening in the dome core and AMS measurements imaging a bulk flow along the southwestern dome flank towards the NE at an angle of *c.* 30° (see section 6.2.3). In this frame, normal top-to-the SW displacement of the dome mantle with respect to the core would be expected. Of critical importance is the comprehensive lack of tectonic evidence for such differential transport in the unmolten mantle. There, ductile meso- and micro-structures strictly relate to the early *c.* 320 M-old top-to-the NE shearing event. Only discrete top-to-the S brittle-ductile shear bands (see Fig. 6.10e) would record dome exhumation.

The observed situation demands a mechanical decoupling between the anatectic domain and the overlying unmolten lithologies. Here again the origin of such probably lies in the contrasted rheological properties of both materials, with the migmatites showing markedly lower strengths than subsolidus ortho/paragneisses. This way, the strain related to dome exhumation would have been localized within metatexites from the core–mantle interface, overlying unmolten lithologies acting as rigid passive blocks and remaining unaffected by the extrusion of the partially molten middle crust. Overall, such decoupling inherently stems from the presence of melt in the middle crust, which, as demonstrated above, partly results from a water influx from uprising deep magmas.

The picture drawn in the Masméjean area contrasts with that observed east of the Villefort Shear Zone, in the Tanargue dome. There, the Sil-Bt zone of the mantle is pervasively affected by top-to-the S shearing related to migmatites vertical extrusion (Bouilhol et al., 2006). Such different mechanical behaviour of the core–mantle interface compared to the Masméjean dome possibly stems from higher strain rates. Indeed, the steep migmatite foliation in the Tanargue area would testify for substantial vertical transport, larger than inferred for the Masméjean dome.

6.7.2 Respective roles of the regional strain field and the buoyancy-driven flow during doming

D_{2v} NE-SW extension, marked by the activation of top-to-the NE shear zones, pre-dated the formation of the Masméjean and Velay domes. This 325–315 Ma crustal thinning event was accompanied by early anatexis. A marked dynamic change took place at c. 315 Ma with the onset of partially molten crust vertical extrusion in the core of E–W trending antiforms. At that very same time, granite bodies emplaced in the upper crust record a general D_3 NW–SE to E–W extension, i.e. perpendicular to the migmatites flow direction. It comes from this that the regional D_{2v} event likely triggered the exhumation of the partially molten crust, but as soon as this process had been launched, the flow of the middle crust would have been mostly controlled by buoyancy and overall little affected by the upper crustal strain field. This is well evidenced in the Masméjean dome

where the migmatite core is mechanically decoupled with its overlying unmolten dome mantle.

The only external control on the Masméjean dome formation would correspond to the wrench corridor along its eastern flank, clearly acting as a boundary with the adjacent crustal domain, channelling dome exhumation and collecting anatectic liquids. Yet, the significance of this Villefort Shear Zone remains unclear as its late Carboniferous activity does not easily fit with a general E–W extensional context. This shear zone may have nucleated as a transfer fault, accommodating contrasted rheological behaviours on its western and eastern side. Indeed, to the West, intrusion of the Margeride granite, the largest batholith in France (Chantraine et al., 1996), likely drained large volumes of melt out of the middle crust, leaving behind a stiff residue. On the other hand, to the East, melt remained confined in the middle crust and ultimately led to doming.

In any case, the Masméjean dome and the southern part of the Velay Complex illustrate the dramatic rheological and tectonic effects of continental crust partial melting.

6.7.3 What controls the locus of doming during post-collisional extension

Following the conclusions of section 6.4, anatexis in the Masméjean dome would have occurred at moderate temperature (mostly <730–760°C) but still generated substantial amounts of melt due to water ingress from intruding mantle-derived granitic magmas (of KCG type). This viewpoint is corroborated by geochemical data indicating a mixed origin for the Masméjean granites with a fraction corresponding to local pristine anatectic melts and the remaining being akin to KCG magmas.

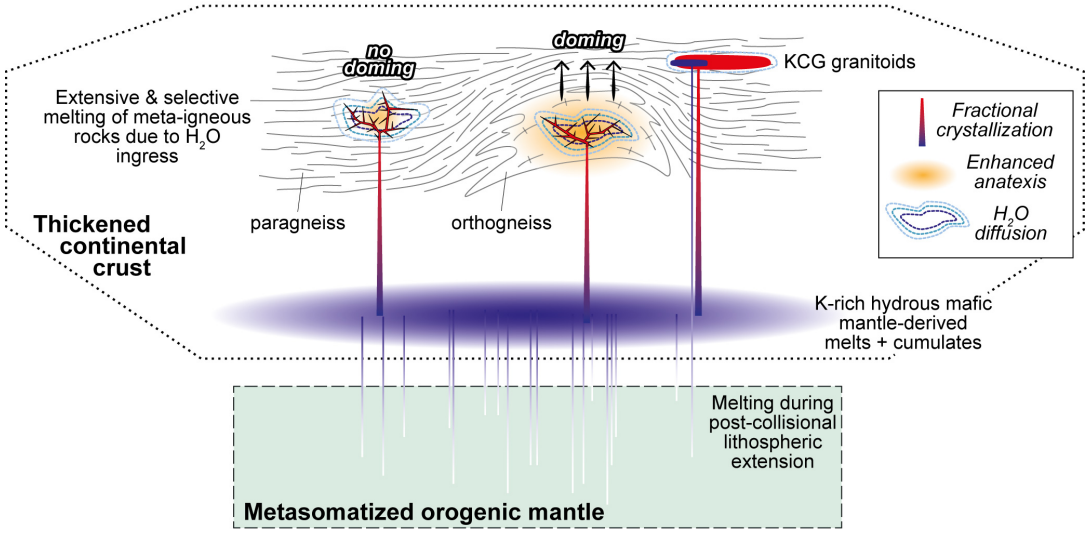

Figure 6.37: Conceptual sketch illustrating the role of mantle-derived magmas in ultimately controlling anatexis at mid-crustal levels. Lower crustal melting and associated peraluminous granite suites are not depicted.

Petrological constraints gained on the Masméjean dome formation hint a twofold control on the doming process (Fig. 6.37). The spatial distribution of hydrous magmas intrusions (originating from a metasomatized mantle source) delineates crustal zones with increased water contents. Such H_2O ingress promotes catastrophic melting in areas featuring substantial volumes of orthogneisses while leaving paragneiss-dominated domains unaffected. As partial melting and dome formation are intimately linked (Whitney et al., 2004a), the locus of doming during post-collisional evolution would depend on: (i) the pathways followed by mantle-derived magmas *en route* to the surface; and (ii) the pre-orogenic magmatic history of the crust segment, i.e. inherited structures and lithological heterogeneities.

This model is consistent with the geological record of doming worlwide. Indeed, gneiss domes are generally cored by anatectic meta-igneous rocks. For instance, the Dassu-Askole or Gurla Mandhata domes of the Himalayan Karakorum Metamorphic complex all feature anatectic orthogneiss cores and evidence for coeval mantle-derived magmatism (Murphy et al., 2002; Rolland et al., 2001). Other iconic cases include the Shuswap Metamorphic Complex in the Canadian Cordillera (Norlander et al., 2002; Parkinson, 1991), the Kesebir–Kardamos dome in Rhodope (Bonev et al., 2005) or the Aston–Bossost–Hospitalet domes in the Variscan Pyrénées (Denèle et al., 2014) to cite only a few.

Part III

General discussion

Chapter 7

The zircon U–Pb–Hf(–O) record of crust formation and reworking in the French Massif Central

7.1 Classical approaches to decipher crust evolution

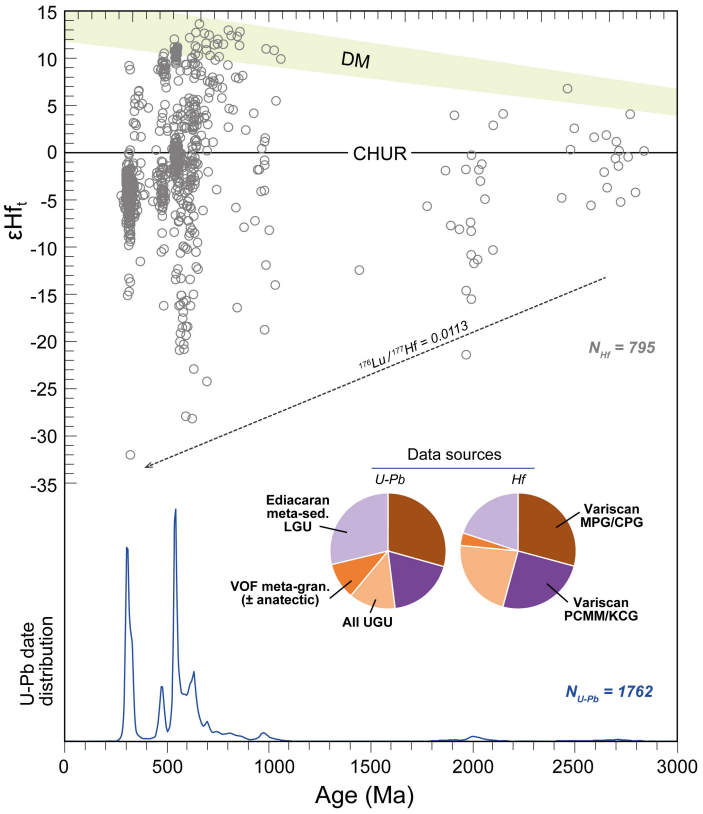

Figure 7.1: Summary of the coupled petrological and zircon U–Pb–Hf constraints obtained on the French Massif Central. Data from this work, Couzinié et al. (2014), Moyen et al. (2017a) and Chelle-Michou et al. (2017). The relative extent of the U–Pb date peaks has to be moderated with the uneven data sources. U–Pb date distribution is represented as a Kernel Density Estimate (KDE). Only 95–105% concordant ^{206}Pb/^{238}U (for dates < 1.2 Ga) and ^{207}Pb/^{206}Pb dates (for dates > 1.2 Ga) were considered. Plotted with the DensityPlotter program of Vermeesch (2012). The bandwidth was set to 12 Ma (the average 2σ error of individual analyses). The black dotted lines depicts the time-integrated ε_{Hf}(t) evolution of an upper crustal with a ^{176}Lu/^{177}Hf of 0.0113. The range for the Depleted Mantle reservoir is bracketed by the models of Naeraa et al. (2012) and Griffin et al. (2002).

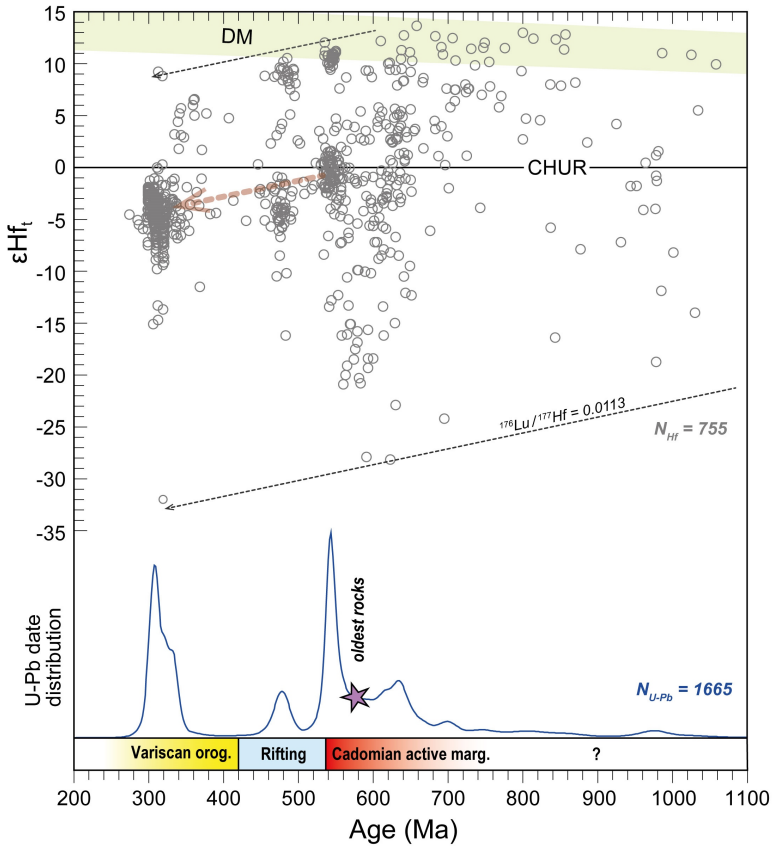

Figure 7.2: Summary of the coupled petrological and zircon U–Pb–Hf constraints obtained on the French Massif Central with en emphasis on the period 200–1100 Ma. Same legend as Fig. 7.1. The red dotted line highlights the linear ε_{Hf}(t)–time array connecting the Velay Orthogneiss Formation and the post-collisional Variscan granitoids with a slope corresponding to a ^{176}Lu/^{177}Hf of 0.01.

In this section, the evolution of the French Massif Central crust segment is reconstructed based on conventional zircon U–Pb–Hf methodologies. Our dataset is interrogated considering zircon data out of their petrological context, as if the grains were all detrital in origin. The limitations of such approach will be later discussed by confronting the results to the geological record of the French Massif Central.

7.1.1 Available dataset

Figures 7.1 and 7.2 present a summary of the zircon U–Pb–Hf data obtained by our group in the past 4 years. Importantly, a large range of rock types were targeted, covering at first-order all lithological components recognized so far in the French Massif Central.

7.1.2 U–Pb date distribution

The distribution of zircon U–Pb dates reflects the temporal succession of geological events that resulted in the formation of zircon grains. The most common situation is the crystallization of an intermediate to acid magma (Hoskin et al., 2000). Therefore, the U–Pb date distribution dominantly reflects the timing of magmatic episodes that affected a given crust segment.

Figure 7.3 shows that no matter the dataset considered (comprehensive set of data or only spots with available Hf isotope compositions) the same distribution is observed. Most dates range between 0.7 and 0.3 Ga defining two peaks at 0.3 and 0.6 Ga. This indicates that the FMC experienced substantial magmatic activity in the Neoproterozoic and Paleozoic. That being said, it is not possible to establish whether these magmatic

events built up the FMC crust or alternatively reworked pre-existing crustal lithologies. As a matter of fact, Paleoproterozoic and Archean zircon populations suggest the presence of older crustal components in the French Massif Central.

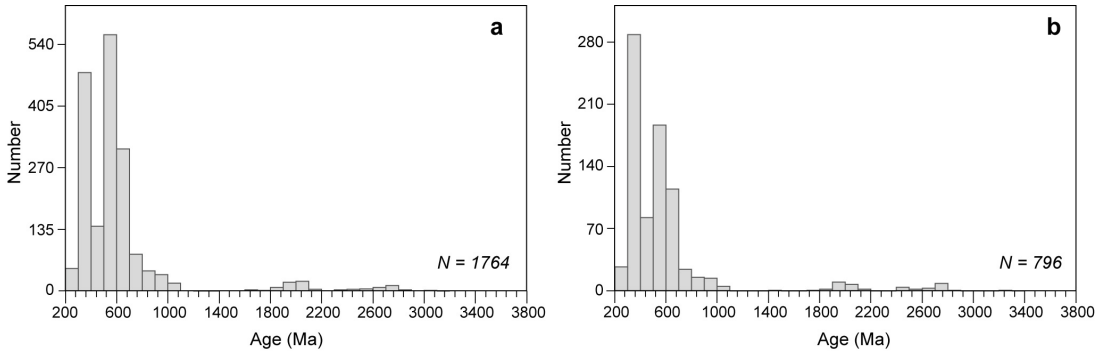

Figure 7.3: Histogram showing the distribution of zircon U–Pb dates in the French Massif Central. Are shown in (a) the full dataset and in (b) only the spots for which Hf isotope composition have also been measured. In both cases, only 95–105% concordant $^{206}Pb/^{238}U$ (for dates < 1.2 Ga) and $^{207}Pb/^{206}Pb$ dates (for dates > 1.2 Ga) were considered.

7.1.3 Hf model ages

A second approach to unravel the evolution of a crust segment relies on the calculation of Hf model ages (see Chapter 1 and references therein). Such procedure has been carried out using the available FMC dataset and the results are depicted Fig. 7.4. Clearly, model ages define an unimodal distribution with a major peak centred around 1.2 to 1.4 Ga depending on the composition of the Depleted Mantle reservoir retained for the calculations. A subordinate peak at 0.6 to 0.8 Ga may be identified. Finally, it must be stressed that a continuous range of model ages exists between 3.7 down to 0.4 Ga.

Zircon Hf model ages considered alone would indicate that the FMC crust is dominantly Mesoproterozoic in age with some components being as old as Paleoarchean.

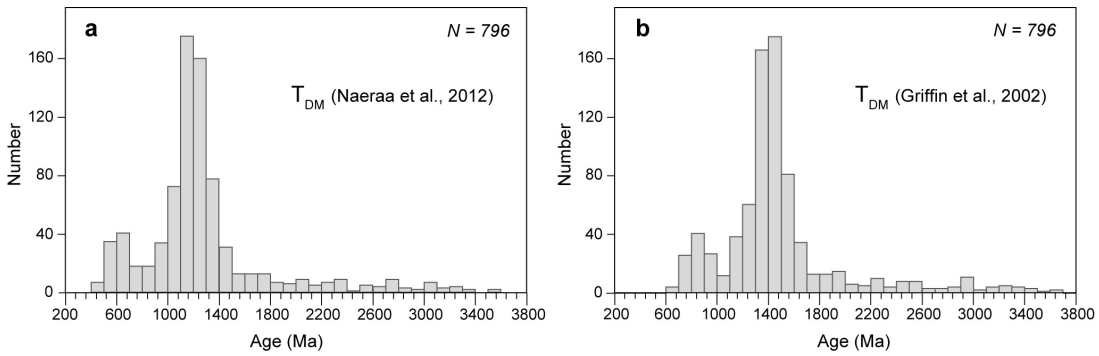

Figure 7.4: Histogram showing the distribution of zircon T_{DM} model ages in the French Massif Central. Calculated with a $^{176}Lu/^{177}Hf$ of 0.0113 and two Depleted Mantle reservoir compositions (a: Naeraa et al., 2012 and b: Griffin et al., 2002).

7.1.4 Integral growth curves

Integration of the above-mentioned age distributions yields crustal growth curves, i.e. the volume of the present-day crust that had already been extracted at a given time period. Such approach presumes incremental assembly of the crust and does not take into account the effects of crust destruction and recycling in the mantle.

Growth curves retrieved from zircon U–Pb data are very similar and indicate that 45 to 60% of the FMC crust formed between 0.8 and 0.5 Ga, that is, during the Cadomian

orogeny. Significant growth would have also taken place at Variscan times (25 to 45% of the crust being extracted between 0.4 to 0.2 Ga). Less than 5% of the crust would be Paleoproterozoic to Archean in age.

In contrast, T_{DM}-based curves point to a slow, continuous formation of the FMC crust since *c.* 3.3 Ga with a flare-up at 1.2–1.4 to 1.3–1.5 Ga (depending on the Depleted Mantle composition retained). New crust extraction continued till 0.6 Ga at a slower pace. Overall, more than 60% of the local crust would have formed during the Mesoproterozoic.

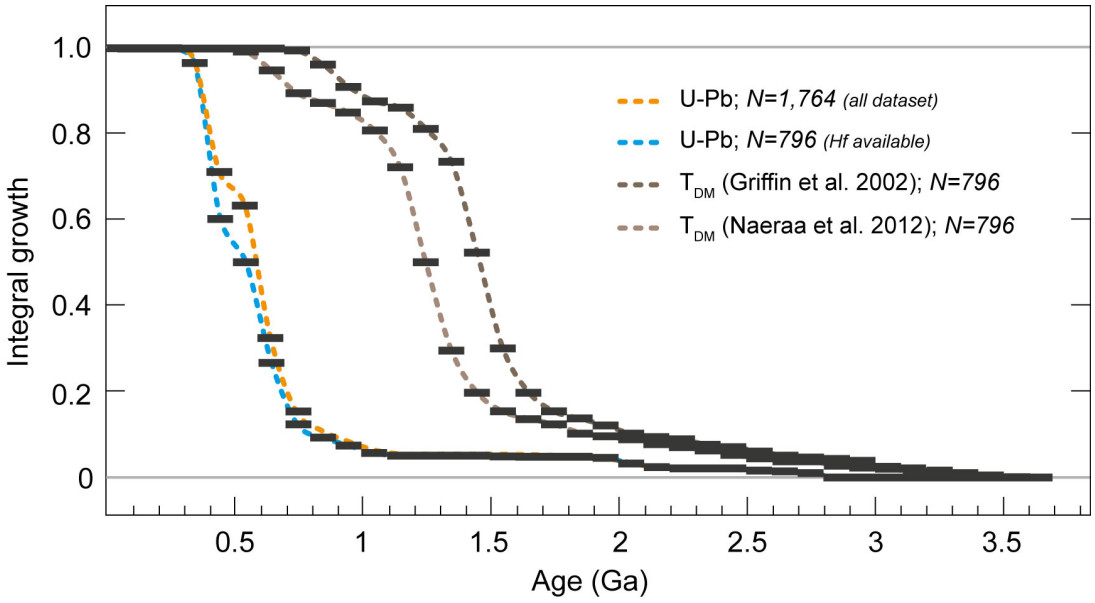

Figure 7.5: Integral growth curves of the French Massif Central crust obtained from the zircon U–Pb and T_{DM} date distributions.

7.1.5 Proportion of crust extracted from the Depleted Mantle at a given time

The Hf isotope dataset can be represented in a way that emphasizes the relative extent of new crust formation vs. crust reworking at a given time period. Following the approach of Belousova et al. (2010), Fig. 7.6 highlights that from a zircon Hf isotope perspective, extraction of new crust predominated over reworking between 3.7 and 0.7 Ga (with the exception of a major reworking event at 2.7–2.8 Ga). In contrast, the Cadomian and Variscan orogenies would have little contributed to the formation of new crust and magmas dominantly reworked pre-existing crustal lithologies.

7.1.6 ε_{Hf}(t)–time array

Figure 7.2 reveals the existence of a linear ε_{Hf}(t)–time array connecting late-Cadomian (*c.* 550 Ma-old) and Variscan zircon populations. The slope of this array corresponds to a $^{176}Lu/^{177}Hf$ of 0.01, typical of upper crustal lithologies (Taylor and McLennan, 1985). It suggests that magmas generated during the Variscan orogeny reworked a late Neoproterozoic crustal reservoir having a chondritic signature at *c.* 550 Ma.

7.2 Confrontation to the geological record and limitations of the methods

7.2.1 Inconsistencies with the geological record

U–Pb data support the formation of the French Massif Central crust in the Archean and Paleoproterozoic. However, there is no evidence for the existence of a pre-Neoproterozoic

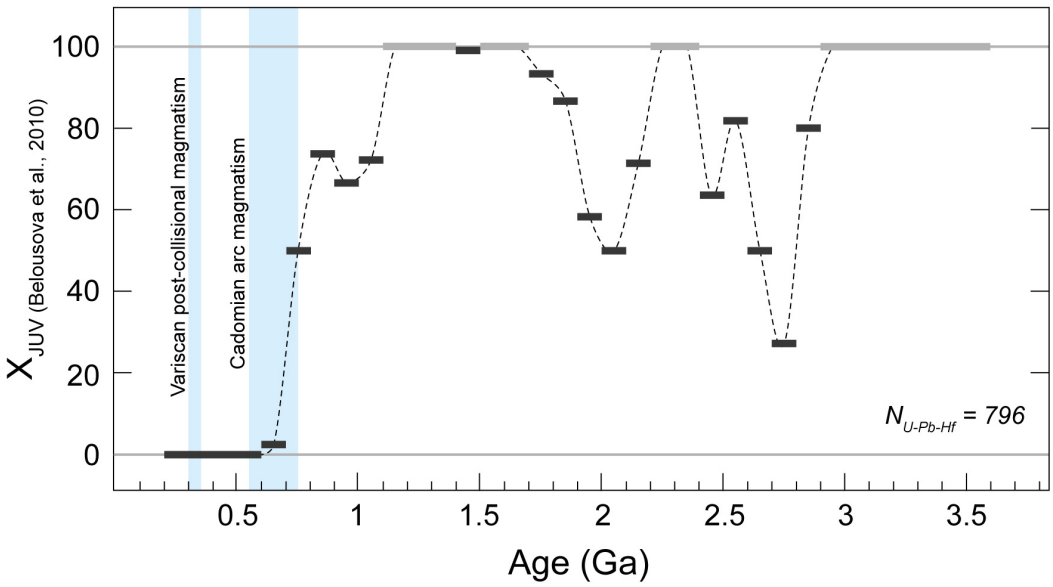

Figure 7.6: Relative extent of crust reworking vs. addition of materials extracted from the Depleted Mantle as a function of time. Calculated using the "juvenile proportion" algorithm proposed by Belousova et al. (2010) and T_{DM} calculated with the Depleted Mantle parameters of Griffin et al. (2002). Are superimposed periods of crust formation deduced from the examination of the geological record (see previous Chapters).

basement (Chelle-Michou et al., 2017; Roques et al., 1995), the oldest rocks so far identified corresponding to Ediacaran (meta)sediments.

Moreover, the information retrieved from zircon Hf isotopes would point to substantial crust formation during the Mesoproterozoic (see Fig. 7.4 and 7.5). This possibility must be discarded as a wealth of studies documented the extreme scarcity of Mesoproterozoic zircon grains in Cadomian terrains (including the French Massif Central, see review in Henderson et al., 2016), clearly arguing against any major crust forming episode of that age.

Besides, zircon Hf data processed conventionally would suggest that the Variscan orogeny is a period of strict crust reworking (see Fig. 7.6). Such result is at odds with the intrusion of mantle-derived magmas at the post-collisional stage (section 5.3), testifying for new additions to the crust volume. In fact, 5 to 10% of the FMC crust did formed at Variscan times (Moyen et al., 2017a).

To conclude, zircon U–Pb–Hf data considered alone erroneously point to substantial Mesoproterozoic FMC crust formation and do not account for Variscan crust production. The origin of these discrepancies can be addressed by examining the petrological context of the analysed grains.

7.2.2 Origin of the discrepancies

Misleading zircon U–Pb–Hf information simply result from a range of *mixing* processes, having taken place in a variety of environments.

Sedimentary mixing

Paleoproterozoic and Archean zircon grains (Fig. 7.3) are found as (i) detritus in Ediacaran (meta)sediments; and (ii) inherited crystals and xenocrysts in late Cadomian to Variscan crust-derived granites, most probably sourced in the former. Consequently, it is ambiguous to assess the origin of such grains. Indeed, they may originate from distal sources (see section 2.2) and this way should not be regarded as repositories of the

pre-Ediacaran history of the FMC crust segment.

In other words, the presence of pre-Neoproterozoic zircon grains in the FMC would originate from the mixing of a variety of detritus in the Ediacaran sedimentary basins and would not reflect the existence of an *in-situ* Paleoproterozoic to Archean crust in the FMC.

Mesoproterozoic model ages as a result of magma mixing

Ediacaran metasediments from the French Massif Central are typified by their very scattered detrital zircon Hf isotope compositions (up to 45 ε-unit, Fig. 7.1) observed within individual specimen (section 2.2). Such pattern is consistent with eroded Neoproterozoic magmatic rocks originating from melting of two sources: (i) the Depleted Mantle or materials extracted from this reservoir shortly prior to melting, as evidenced by zircon with highly radiogenic Hf isotope signature; (ii) old crustal remnants, most probably of Paleoproterozoic/Archean age, for grains with strongly non-radiogenic compositions. The whole range in between these endmembers, and notably the cluster between +5 and -5 ε-unit, most likely stem from mixing between magmas sourced in (i) and (ii) and thus of contrasted isotope compositions (Janoušek et al., 2004; Laumonier et al., 2014a;b; Wang et al., 2016).

This way, the Mesoproterozoic model ages displayed by detrital Neoproterozoic zircon do not reflect reworking of a Mesoproterozoic crustal reservoir but are instead mixed ages. Again, the involvement of an old, non-radiogenic Hf reservoir in the mixing model does not require the existence of a Paleoproterozoic/Archean crust in the French Massif Central as the mixing could have occurred in an adjacent terrain and the zircon grains subsequently transported to the FMC Ediacaran basins.

Mesoproterozoic model ages as a result of source mixing

A somewhat similar reasoning can be followed for crust-derived peraluminous granites from both the late Cadomian Velay Orthogneiss Formation and the Variscan post-collisional MPG/CPG suites. As they reworked the Ediacaran sediments, their source material was intrinsically heterogeneous in terms of zircon Hf isotope signature. Yet, both display tighter ranges of 3 and 7 ε-unit, respectively (Moyen et al., 2017a; Chelle-Michou et al., 2017; Couzinié et al., 2017).

The small-scale petrological processes at the origin of the zircon ε_{Hf}(t) homogenization have been detailed section 2.1 and encompass: (i) inherited zircon dissolution during melting and ascent due to Zr-undersaturated conditions, (ii) isotopic homogenization of the melt phase by advection and elemental/isotopic diffusion, followed by (iii) early saturation upon emplacement, preventing further dissolution of inherited grains. Those would have proceeded during both Cadomian and Variscan reworking events. In this case, the Mesoproterozoic Hf model ages displayed by magmatic zircon grains result from an averaging of the Hf isotope composition of the source material and are mixed in essence.

The consequences of crust recycling

Zircon grains crystallized in Variscan post-collisional mafic magmas (PCMM) and other granitoids from the KCG suite show subchondritic ε_{Hf}(t) despite the magma matter is dominantly of mantle origin (section 5.3). The reason for it lies in the the incorporation of 10–25% crustal crustal materials in the mantle source. Similar cases have been described in arc magmatic suites (Nebel et al., 2011; Roberts et al., 2013) further suggesting that the ε_{Hf}(t) is not a reliable repository of the proportion of crust- vs. mantle-derived components in a given magma.

In hybrid crust/mantle sources, the Hf budget is dominated by the recycled crustal component and the resulting magmas inherit a mixed, non-radiogenic Hf isotope signa-

ture (most of the Hf is provided by the crustal materials and the rest by the mantle). This feature explains why there is no Hf record of crust production at Variscan times (see Fig. 7.6). Besides, Mesoproterozoic Hf model ages displayed by magmatic zircons are here again the result of a mixing process and meaningless from a crust evolution perspective (section 5.3).

Significance of the linear ε_{Hf}(t)–time array

Inherited zircon grains in Variscan peraluminous granites (MPG/CPG) provide evidence for substantial reworking of the Velay Orthogneiss Formation (see sections 5.4 and 6.4). This way, the ε_{Hf}(t)–time array would simply reflect the remelting of the VOF crustal reservoir provided it had an average $^{176}Lu/^{177}Hf$ of 0.01 (further whole-rock isotopic measurements would clarify this point).

However, post-collisional mafic magmas (PCMM) and other granitoids from the KCG suite also plot within ε_{Hf}(t)–time array even though these rocks originate from melting of the mantle. Consequently, them matching the ε_{Hf}(t)–time array does not reflect inner crust reworking processes. Instead, it would result from: (i) the dominance of the crustal component over the Hf elemental budget in the hybrid mantle source; and (ii) the bulk Hf isotope signature of the inferred recycled crustal component being close to that of Ediacaran metasediments (section 5.3). Consequently, the PCMM/KCG case reassesses that care must be taken when interpreting ε_{Hf}(t)–time array solely in terms of closed-system crust reworking (Laurent and Zeh, 2015; Payne et al., 2016).

7.2.3 Additional methodological issues

On top of the flaws presented above, it must be stressed that a set of methodological issues create a range of biases in the zircon record, the importance of which must be kept in mind while reasoning on grains taken out of their petrological context.

A first problem inherently lies in the origin of the data considered. Large compilations as those commonly used to investigate crust evolution gather the results of studies originally conducted with a specific design. For instance, in the French Massif Central, around a half of the compiled data (Fig. 7.1) originate from studies that questioned the petrogenesis of Variscan post-collisional magmas (Couzinié et al., 2016; Laurent et al., 2017; Moyen et al., 2017a). This way, the human operator specifically targeted zircon rims, sometimes very narrow, with the aim to assess the timing of magma emplacement. Therefore, databases containing significant amounts of igneous zircon grains (in the sense that the analyses were performed with the aim to constrain the petrology of an igneous rock) are likely to be biased towards an over-representation of the most recent magmatic events.

When looking at detrital zircon data (from modern rivers or ancient sediments), the record of crust evolution is blurred by the inherently variable zircon fertility factor of each crustal lithology (Moecher and Samson, 2006; Dickinson, 2008). According to these authors, erosion of arc-related magmatic rocks will deliver 3.5 times less zircon grains than collisional igneous suites. It comes from this that the observed zircon proportions in the detrital record cannot be directly translated in terms of crust volumes. For instance the ratio between radiogenic vs. non-radiogenic grains has no potential to unravel the actual extent of new crust production vs. crust reworking at a given time period.

Finally, are only considered in the crust evolution models zircon grains yielding concordant U–Pb dates. Though, discordant grains do take part of the detrital zircon budget and originate as well from igneous precursors. Rejecting those entails that estimates are only retrieved from a partial set of data (Nemchin and Cawood, 2005) and bias the record towards an over-representation of mantle-derived rocks, more likely to yield concordant results than crust-derived collisional suites (sections 5.1 and 5.3).

7.3 Alternative formulations and ways forward

In the following, are address some questions surrounding the evolution of the French Massif Central crust segment. The underlying approach is to emphasize the efficiency of combining petrological information with zircon U–Pb–Hf data to unravel complex geological processes. Some of the discussed points are seen as future fields of investigation.

7.3.1 What is the proportion of young Neoproterozoic crust in the Ediacaran sedimentary basins of the Massif Central?

The Ediacaran (590–545 Ma) deposition of metasediments from the Lower Gneiss Unit stamps the formation of the earliest crustal rocks in the French Massif Central. Examination of the detrital zircon U–Pb–Hf signature indicates that the Ediacaran basins collected detritus from the adjacent Cadomian magmatic arc and a distal source, possibly the Saharan Metacraton (see section 2.2). From a crust evolution perspective, it is critical to establish the actual amount of young Neoproterozoic arc crust in the detritus that fed the Ediacaran basins. In other words, how much of the FMC earliest crust is Neoproterozoic in age?

As explained in the previous section, assessing the amount of young crust based on the proportion of Cadomian zircon grains showing radiogenic Hf isotope signatures is not relevant due to sampling biases (low zircon fertility of arc rocks, tendency to show concordant U–Pb dates). Besides, such approach would not take into account zircon grains having non DM-like, mixed Hf isotope signatures, even though part of their parental magma mass do represent new Neoproterozoic additions to the crust volume.

As an alternative, the (meta)granites from the Velay Orthogneiss Formation may provide another probe of the actual amount of Neoproterozoic detritus in the Ediacaran basins. Following the conclusions of section 2.1, the (meta)granites originate from melting of the Ediacaran metasediments and their chondritic Hf isotope signature would result from dissolution of detrital zircon grains during melting and Hf isotope homogenization during ascent. If true, this model hints that the VOF averages the Hf isotope composition of its Ediacaran sedimentary source.

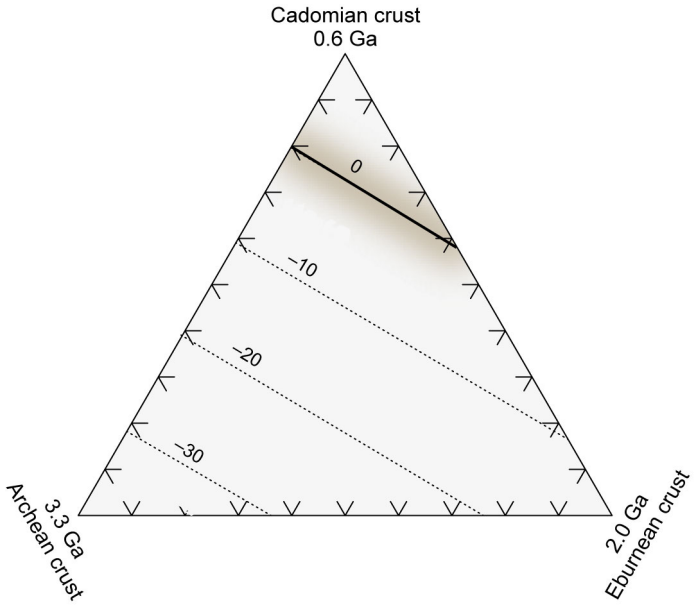

Figure 7.7: Triangular diagram showing ε_{Hf}(545 Ma) of a virtual sedimentary material as a function of the relative proportion of Archean, Eburnean (Paleoproterozoic) and Cadomian crust in the latter, assuming identical Hf concentrations in the three end-members. The highlighted value of zero corresponds to the composition of the crustal material required to explain the zircon Hf isotope signature of the Velay Orthogneiss Formation.

As highlighted section 7.2.2, the Ediacaran detritus can be seen as a mixture between a young Neoproterozoic crust and old crustal materials (Paleoproterozoic and older). Given the paleo-location of the FMC along the northern Gondwana margin, it is reasonable to consider that such materials consist in Eburnean (*c.* 2.0 Ga-old) and Neoarchean (*c.* 3.3 Ga-old) crusts (see Altumi et al., 2013; Nance and Murphy, 1994 and references therein). In this frame, the proportions of each component in the source of the VOF (meta)granites may be retrieved from their chondritic signature. The latter demands that 60–80 % of the Ediacaran detritus in the FMC corresponds to young Neoproterozoic crust (Fig. 7.7). Consequently, even though the genuine mantle-derived Cadomian igneous rocks have not been fully preserved, their erosion products substantially fed the late Ediacaran back-arc basins of the FMC and became *de facto* long-term additions to the continental crust volume.

The main limitation of this approach lies in the extent to which the source of the VOF is representative of the whole Ediacaran sedimentary sequence. By analogy with the shale geochemical model of Taylor and McLennan (1985), it has been proposed that peraluminous granites overall yield a bulk estimate of the continental crust composition (Allègre and Ben Othman, 1980), even though such view has been challenged in the early 90's (e.g. Turpin et al., 1990).

Lastly, several studies considered that a scatter in the zircon ε_{Hf}(t) at a given time period, as observed in the Ediacaran–Cryogenian record of the FMC, reflects the dominance of crust reworking processes (Dhuime et al., 2017; Kemp et al., 2006; Vervoort and Kemp, 2016). In contrast, this study shows that such situation may aswell attest to voluminous new crust production. Based on this Cadomian case, I suggest that the concomitant presence in the record of juvenile and isotopically evolved zircon grains may be taken as evidence for new crust production in an active margin developed at the edge of an old cratonic crust segment (the Gondwana in the present case).

7.3.2 Crust–mantle interactions during the Variscan collisional orogeny

Recent studies consider that the amount of continental crust being destroyed and recycled back in the mantle markedly increases during collisional events related to supercontinent assembly (Roberts, 2012; Stern and Scholl, 2010). One of the reason for it would be the subduction of continental crust units operating at the onset of collision (see Fig. 7.8a; Chopin, 2003; Guillot et al., 1997; Roecker, 1982). On the other hand, combined petrological and zircon U–Pb–Hf–O data suggest that a total of 5 to 10% of the FMC crust would have been newly formed by Variscan post-collisional magmatism (section 5.3). As a result, collisional orogens constitute sites of crust *recycling* and crust *formation* (see Fig. 7.8a). This section examines some underlying consequences of both phenomena taking place nearly coevally (at the scale of a collisional orogenic event).

There and back, the continental crust journey in the mantle

Post-collisional crust production is intimately associated with the remobilization of crustal lithologies that have been previously recycled, i.e. rendered back to the mantle (Campbell et al., 2014; Guo et al., 2014; Janoušek and Holub, 2007; Zhao et al., 2007; 2013). As post-collisional magmas systematically post-date by <50 Ma a subduction stage (section 5.3), they most probably re-incorporate to the crustal volume part of the matter that had been destroyed by continental subduction, shortly prior to collision (Fig. 7.8b).

A total of 15-38 wt.% of post-collisional magmas would actually correspond to atoms that were originally hosted in the continental crust (section 5.3). This way, the pathway followed by these atoms during continent–continent collision defines a short-lived crust/mantle geochemical cycle: crustal elements lost in the waning stages of subduction are stored in the mantle for <50 Ma and part of them return to the continental crust encapsulated within post-collisional magmas (PCMM/KCG). Such cycle is somehow sim-

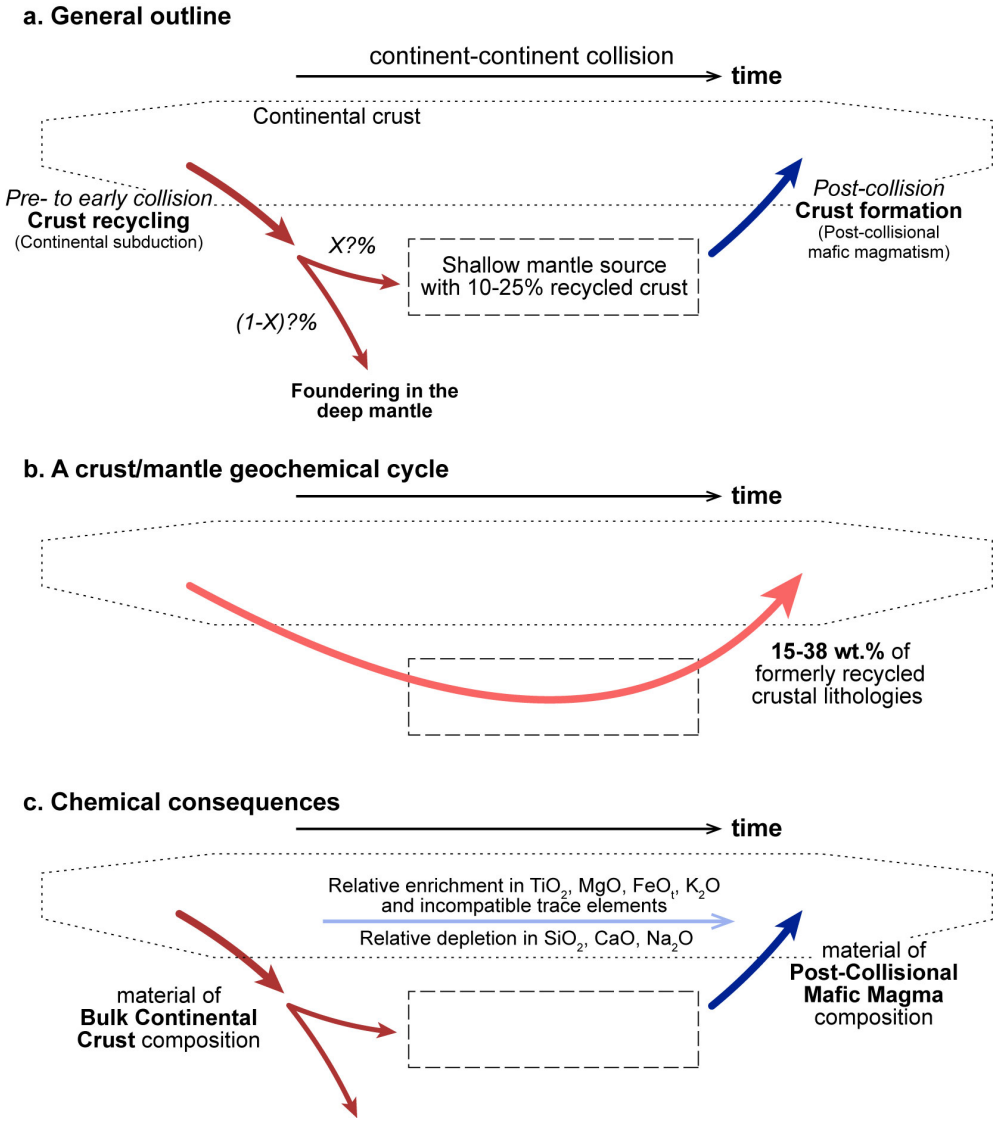

Figure 7.8: Summary of the observations and outcomes related to the evolution of the continental crust during collisional orogenic episodes. Delamination of the lower continental crust is not considered.

ilar in a shorter space and time scale with the well-documented case of long-term storage of oceanic to continental crust in the deep mantle and their subsequent re-mobilization in OIB basalts with EM flavour (Chauvel et al., 1992; Hofmann, 1997; Stracke et al., 2005; Stracke, 2012; Weaver, 1991; Willbold and Stracke, 2010).

It comes from this that since the onset of modern plate tectonics, presumably in the late Archean (Laurent et al., 2014), part of the continental crust volume would have been processed through this orogenic crust/mantle cycle and resided for a short time period in the mantle.

Consequences on the continental crust chemical composition

The materials recycled in the mantle during the pre- to early-collisional stage should have, on average, a composition akin to the Bulk Continental Crust because the whole crust section is presumably dragged down by subduction dynamics. On the other hand, new additions to the crust volume are mediated by post-collisional mafic magmas of peculiar chemical composition (section 5.3). Here is compared the incoming and outcoming chemical fluxes within the orogenic mantle in an attempt to qualitatively evaluate the crust/mantle mass transfers and address the impact of orogenies on the long-term chem-

ical evolution of the continental crust. The extent and consequences of orogenic lower crust delamination (Arndt and Goldstein, 1989; Lustrino, 2005) have not been considered in this discussion because this process remains poorly documented in the French Massif Central and can only be tackled in ancient orogenic systems via indirect arguments.

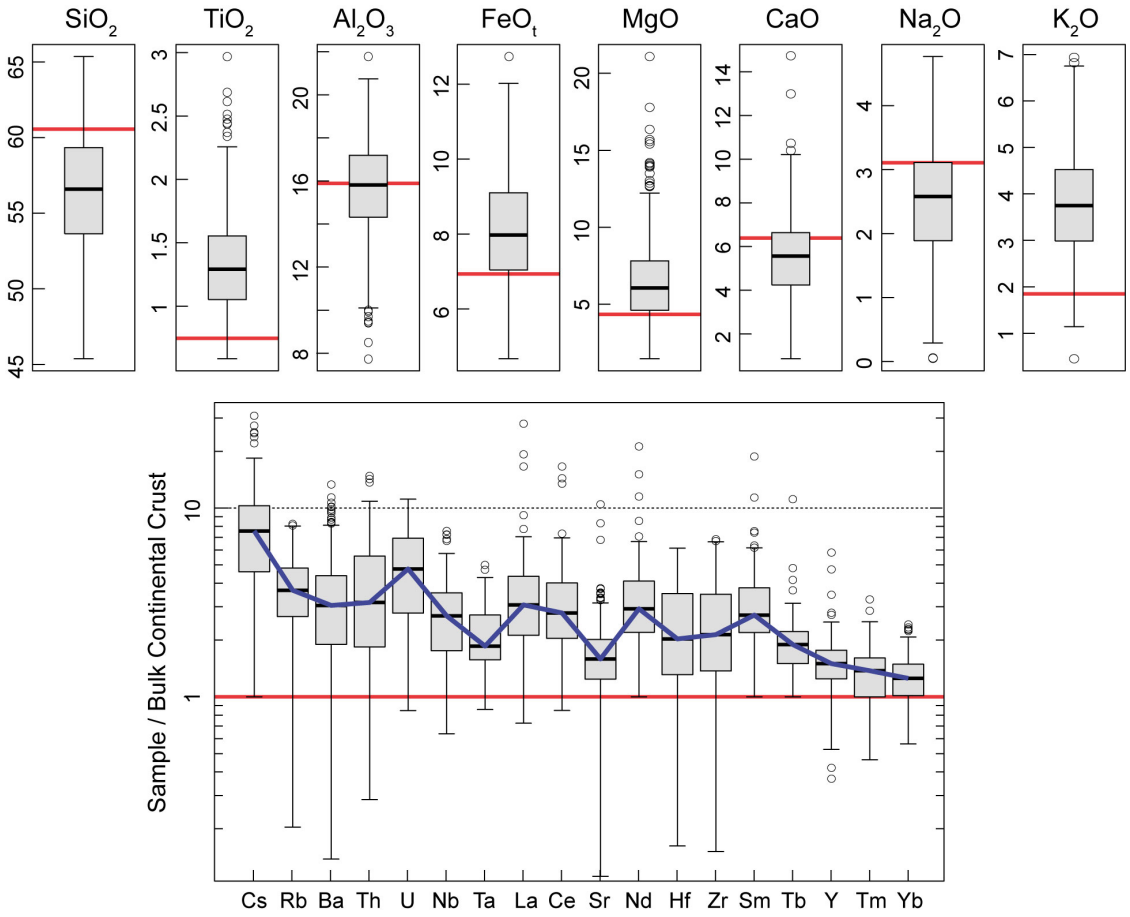

Figure 7.9: "Box-and-whiskers" plots for post-collisional mafic magmas from the French Massif Central, regarded as primary mantle melts (N=359 for majors, N=59 for traces). Data from Couzinié et al. (2016). The thick black line is the median, the sides of the rectangles 1^{st} and 3^{rd} quartiles, the horizontal lines the max/min values and the circles outliers. Red line denotes the composition of the Bulk Continental Crust (BCC) reservoir after Rudnick and Gao (2003). The multi-element diagram is normalized to this composition.

Based on the example of the French Massif Central, Fig. 7.9 shows that post-collisional mafic magmas (regarded as primary mantle melts) have lower median SiO_2, CaO and Na_2O contents than the bulk continental crust but higher TiO_2, FeO_t, MgO and K_2O. Therefore, the new orogenic additions to the crust volume are more basic, mafic and K-rich than the material lost and recycled in the mantle during continental subduction. From a trace element perspective, newly added materials are on average 2–3 times richer in incompatible elements than the bulk crust but overall display a similar pattern. This reflects the predominance of recycled crustal materials in the trace element budget of the enriched mantle source (section 5.3). All in all, collisional orogenic episodes would recycle in the mantle materials of (roughly) bulk crust composition and partly replace them by a more basic, mafic and K-rich component (Fig. 7.8c).

7.3.3 An overall limited record of crust reworking?

In the French Massif Central, examination of the zircon U–Pb date distribution of granites belonging to crust-derived peraluminous suites (MPG/CPG of Barbarin, 1999) reveals that as little as 32.6% (N=154/472) of the grains showing concordance between 95–

105% yielded Variscan dates and thus pinpointed the timing of magma emplacement (see Chapter 5 and 6, additional data from Couzinié et al., 2014, and Chelle-Michou et al., 2017). Such value is a maximum estimate because of the human operator tendency to target narrow zircon rims while analysing grains extracted from granites, in an attempt to better constrain the emplacement age (see section 7.2.3).

Interestingly, 30.1% (N=142/472) of the peraluminous granite zircon dates falls in the range 530–560 Ma and thus attests to reworking of meta-granites from the Velay Orthogneiss Formation. This proportion is even higher in the southern part of the Velay Complex and the Masméjean dome where some granites lack any grain of Variscan age. Similarly, migmatites developed at the expense of the VOF orthogneisses did not yield a single concordant Variscan date. The reasons for this have been discussed section 6.5 and lie in the low solubility of Zr in peraluminous melts and a range of kinetic factors. As a direct consequence, zircon extracted from Variscan crust-derived igneous rocks dominantly document pre-Variscan magmatic episodes.

From a crust evolution perspective, the Variscan case study suggests that igneous suites formed by pure crust reworking have a low potential to crystallize substantial amounts of magmatic zircon grains. This connects with the zircon fertility issue extensively discussed in Moecher and Samson (2006) and Dickinson (2008): peraluminous suites have low Zr contents, hence contain little zircon and on top of that only a third of them (in the Variscan case) are magmatic in origin. Consequently, the overall extent of the crust reworking record in large detrital zircon databases may be lower than currently thought. Nevertheless, it must be mentioned that in areas having experienced multiple reworking episodes (as the French Massif Central), the first reworking event (the late-Ediacaran VOF meta-granites) may still be substantially documented because affiliated zircon grains would also be encountered in igneous rocks formed during subsequent, younger crust reworking episodes (the Variscan peraluminous granites).

7.3.4 Further directions

The discussion conducted in this chapter outlines the extent to which the zircon U–Pb–Hf(–O) record of crust evolution may be ambiguous and challenging to interpret. The main reason for it lies in the fact that a given pattern may originate from a non-unique set of geological scenarios. Most accurate results are likely to be obtained when the petrological context of investigated zircon grains is fully assessed and provide guidance in interpreting the zircon record of crust evolution.

One possible way to fully explore the potential of zircon U–Pb–Hf data would be to independently document the detrital (modern or ancient) and igneous zircon records. This way, coupled petrological/age/isotopic information retrieved from igneous rocks could provide acute guidance to interpret the detrital zircon data, in essence more representative of the history of a given crust segment (see Dhuime et al., 2017, and references therein).

Therefore, a promising approach to constrain crust evolution on a global scale would be to: (i) reconstruct the evolutionary path of individual crust segments following the above-mentioned methodology; (ii) assemble all these pieces of information into a global model of continental crust evolution, pinpointing periods of major new crust production and documenting the associated mechanisms.

Appendix A

Supplementary materials of published articles

A.1 Laurent et al., 2017

Are presented in the following:

- the Supplementary Text which includes additional figures;
- Supplementary Table S1: Results of LA–SF–ICPMS U–Pb analyses of standard zircons GJ-1, Plešovice, OG-1 and BB;
- Supplementary Table S2: Results of LA–SF–ICPMS U–Pb analyses of zircons from granitoids and vaugnerites of the Eastern French Massif Central.

Supplementary material
to the article :

"Protracted, coeval crust- and mantle melting during Variscan late-orogenic evolution: zircon U-Pb dating in the eastern French Massif Central"

Oscar Laurent, Simon Couzinié, Armin Zeh, Olivier Vanderhaeghe, Jean-François Moyen, Arnaud Villaros, Véronique Gardien, Cyril Chelle-Michou*

***Corresponding author: olaurent@ulg.ac.be or oscarlaurent86@gmail.com ; Tel.:(+32)43662250**

1. Analytical techniques

U–Pb isotopic analyses were carried out at Goethe Universität Frankfrut (GUF) by laser ablation using a Resolution M-50 (Resonetics) 193 nm ArF excimer laser system attached to ThermoFinnigan Element 2 sector field ICPMS. We applied the same methods as in Zeh and Gerdes (2012); a detailed description of these analytical techniques is available as Supplementary Mate

For zircon analyses we used a repetition rate of 5.5 Hz, and laser spot-sizes of 28, 33, 40 and 50 µm for measurements of unknowns, and 40 µm for zircon reference materials GJ-1, Plešovice, OG-1 and BB. Unknown monazite grains were analyzed with a repetition rate of 4 Hz, a spot size of 12 µm and reference monazite (Moacir, Manangoutry and an in-house standard WM) with a spot size of 33 µm. Resulting fluence was ~2.5 to 3 $J \cdot cm^{-2}$. Sample surface was cleaned directly before each analysis by three pre-ablation pulses. Ablation was performed in a two-volume ablation cell (Laurin Technic, Australia) characterized by a very quick response time (<1 s until maximum signal strength is reached) and wash-out delay (<3 s to get <1% of maximum signal strength). It was fluxed during ablation with carrier gas consisting of a ~0.6 L min^{-1} He stream, mixed directly after the ablation cell with make-up gas consisting of ~0.07 L min^{-1} N_2 and 0.68 L min^{-1} Ar prior introduction into the plasma of the SF-ICP-MS. All gases had a purity of 99.999% and no homogenizer was used while mixing the gases, to prevent smoothing of the signal and thus be able to detect significant variations of the $^{207}Pb/^{206}Pb$ and $^{238}U/^{206}Pb$ ratios during measurements, possibly revealing the sequential sampling of different age domains within single zircon grains. Signal was tuned for maximum sensitivity for Pb and U while keeping low the production of oxides ($^{254}UO/^{238}U \leq 0.5\%$). The obtained sensitivity on zircon standard GJ-1 for ^{238}U and a 33 µm spot size varies from ~5000 cps·ppm^{-1} (session #1) to ~8000 cps·ppm^{-1} (session #2), at 5.5 Hz and ~3 $J \cdot cm^{-2}$.

Data were acquired using time resolved-peak jumping, the detector being set to analogue mode for ^{232}Th and ^{238}U and counting mode for ^{204}(Hg+Pb), ^{206}Pb, ^{207}Pb and ^{208}Pb. A total of 356 mass scans were acquired over ~41 s measurement (20 s of background measurement followed by 21 s of sample ablation) and integrated to 89 ratios (4 mass scans per integration, time resolution = 0.46 s). Those ratios were subsequently corrected offline for background signal, common Pb, instrumental mass discrimination and Pb/U fractionation (both laser-induced during individual measurements, and over the day) using an in-house MS Excel© spreadsheet (Gerdes and Zeh, 2006, 2009).

A common-Pb correction was carried out when necessary: for each ratio of an individual measurement, ^{204}Pb was estimated by subtracting the average background signal on mass 204, which mostly results from ^{204}Hg in the carrier gas (~500 cps), to the measured intensity. Composition of common Pb (i.e. $^{206}Pb/^{204}Pb$ and $^{207}Pb/^{204}Pb$ ratios) was determined using a model Pb composition (Stacey and Kramers, 1975) at the age of the sample, independently estimated using analyses devoid of common Pb. The inter-elemental fractionation ($^{206}Pb/^{238}U$) during the 21 s of sample ablation was corrected for each analysis by applying a linear regression through all measured ratios, excluding the outliers (±2σ), and considering that the intercept with the y-axis represents the 'true' ratio. Elemental fractionation over the analytical session, as well as instrumental mass discrimination, were corrected by normalization to the $^{206}Pb/^{238}U$ (0.0982) and $^{207}Pb/^{206}Pb$ (0.061) ratios of reference zircon GJ-1 (Jackson et al., 2004), using standard bracketing. Elemental concentrations in U and Pb were calculated using raw signal (in cps) of ^{238}U and ^{206}Pb for each spot, corrected from the analytical drift over the session (monitored using GJ-1), normalized to the recommended values of the GJ-1 zircon standard (U = 280.1 ppm; Pb = 25.5 ppm) and applying a spot size-dependent correction. Th/U ratio was determined for each spot using the mass fractionation-corrected $^{232}Th/^{238}U$ ratio, normalized to the recommended value of the GJ-1 zircon standard (Th/U = 0.0296).

Data from secondary standards were processed as unknowns to check the accuracy of the corrections. Our results (see Table S1, supplementary material) are all within error of the recommended TIMS values of the standard zircons Plešovice (weighted mean $^{206}Pb/^{238}U$ age = 337.13 ± 0.37 Ma; Sláma et al., 2008), OG-1 (weighted mean $^{206}Pb/^{206}Pb$ age = 3465.4 ± 0.6 Ma; Stern et al., 2009), and BB (DEGO: weighted mean $^{206}Pb/^{238}U$ age = 560 ± 0.8 Ma; Santos et al., in press), and the standard monazites Moacir (mean $^{207}Pb/^{235}U$ age = 504.3 ± 0.2 Ma, Gasquet et al., 2010), Manangoutry (mean $^{206}Pb/^{238}U$ age = 554.8 ± 3.8 Ma; Horstwood et al., 2003), and the in-house standard WM (mean $^{206}Pb/^{238}U$ age = 1027 ± 2 Ma; Axel Gerdes, GUF, personal communication).

The quoted uncertainties for each individual analysis are (i) for the $^{206}Pb/^{238}U$ ratio, the quadratic addition of the within-run precision (2σ) with the external reproducibility of standard zircon GJ-1 during the corresponding analytical session (0.5 to 1.5%, 2 sigma; see Table S1, supplementary material); and (ii) for the $^{207}Pb/^{206}Pb$ ratio, a ^{207}Pb signal-dependent uncertainty propagation, as described by Gerdes and Zeh (2009). The $^{207}Pb/^{235}U$ ratio was calculated using the corrected $^{206}Pb/^{238}U$ and $^{207}Pb/^{206}Pb$ ratios and assuming a natural $^{238}U/^{235}U$ of 137.88, and its uncertainty was obtained by quadratic addition of propagated errors on both ratios. Age calculations and data plotting were performed using the Isoplot toolkit (Ludwig, 2008) v.4.15 for MS Excel©. The complete dataset is available as supplementary material (Table S2).

2. Detailed results of zircon and monazite U-Pb analyses

2.1. CPG

➡ **Sample CHZ** (Fig. S1)

CHZ is from the Chalmazel granite, a plurikilometric screen of porphyritic biotite granite enclosed within the Velay granite at its northernmost margin. Four concordant spots from zircon cores yielded Ordovician to Neoproterozoic dates (410–625 Ma) and a highly discordant one (a99) has a Paleoproterozoic $^{207}Pb/^{206}Pb$ date of 2387 ± 7 Ma. The main population of analyses (n = 17), obtained from zircon rims or grains devoid of any core, define a Discordia with $^{206}Pb/^{238}U$ dates ranging between 275 and 332 Ma; the seven equivalent analyses with the highest $^{206}Pb/^{238}U$ ratios yield a Concordia date of 332.0 ± 2.0 Ma.

➡ **Sample OL-13-06** (Fig. S1)

OL-13-06 is a porphyritic biotite granite, representing the dominant phase of the large (>3000 km^2) Margeride batholith. The 33 analyses define a Discordia with an upper intercept at 321 ± 11 Ma (Fig. 4b); many spots have $^{206}Pb/^{238}U$ dates lower than 300 Ma (down to 31 Ma) and are generally characterized by large amounts of common Pb (between 1 and 10% and up to 40–60%). The eight analyses with the highest $^{206}Pb/^{238}U$ ratios define a Concordia date of 312.9 ± 2.0 Ma.

➡ **Sample OL-13-11** (Fig. S1)

OL-13-11 is from the Almance granite, a small laccolith flanking the western margin of the Velay dome (Feybesse et al., 1995). It contains zircon cores and xenocrysts from which 15 analyses yield early Carboniferous to Paleoproterozoic dates; 7 of them are >90% concordant and have early Carboniferous (~345 Ma; n = 3), Ordovician (a140 at ~475 Ma), late Neoproterozoic (550–580 Ma; n = 2) and Paleoproterozoic (a151 at ~2060 Ma) dates. Zircon rims and core-free grains are characterized by huge amounts of common Pb (between 2 and 52%) and highly variable 206Pb/238U dates dates ranging from 33 to 325 Ma (Figs. 4c and 4e) and highly variable $^{206}Pb/^{238}U$ dates dates ranging from 85 to 317 Ma. They define a Discordia with an upper intercept of 315 ± 48 Ma (n = 15) and the five analyses with the highest $^{206}Pb/^{238}U$ ratios, including two spots with <5% of common Pb, yield a Concordia date of 314.5 ± 1.7 Ma. Eight monazite grains showing typically magmatic, oscillatory zoning (Fig. S8) were also analyzed and yield a Concordia date of 315.4 ± 0.9 Ma.

➡ **Sample OL-13-14** (Fig. S1)

OL-13-14 is a sample of the Chaise-Dieu intrusion, which consists of biotite-bearing, porphyritic to even-grained granites and granodiorites (Feybesse et al., 1995) at the western margin of the Velay dome. This samples contains many xenocrysts and zircons with cores, representing more than half of the dataset. Most of them are >90% concordant (n = 21 out of 28 analyses). The main populations are represented by zircons having Cambrian (535–545 Ma; n = 9), late Neoproterozoic (550–590 Ma; n = 8), middle Neoproterozoic (660–780 Ma; n = 4), Ordovician (450 – 480Ma; n = 3) and discordant Neoarchean dates ($^{207}Pb/^{206}Pb$ dates ~2430 Ma;

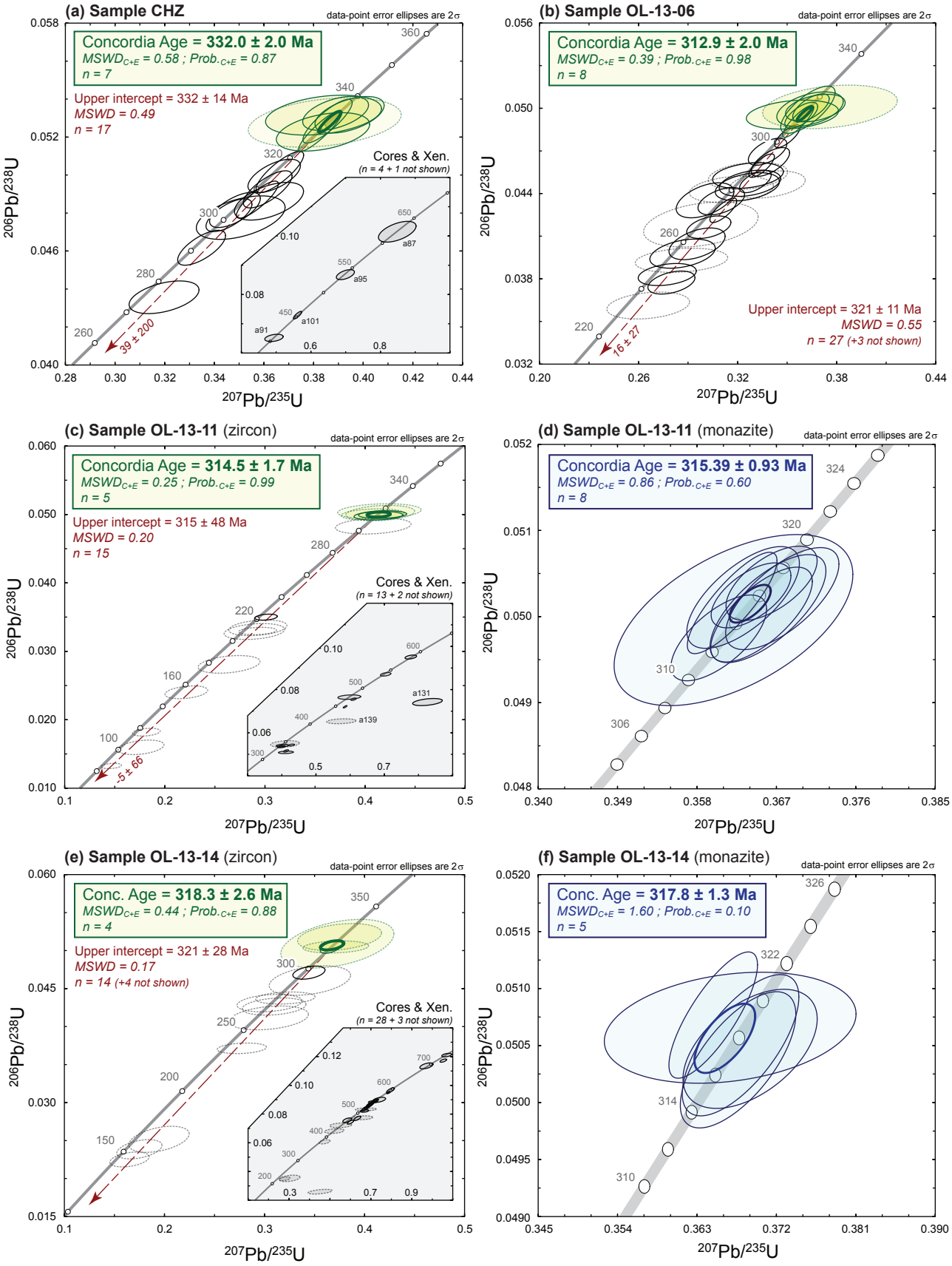

Figure S1: U-Pb Concordia diagrams (^{206}Pb/^{238}U vs. ^{207}Pb/^{235}U) for zircon (a, b, c, e) and monazite (d, f – in blue) analyses from samples of CPG from the eastern FMC. Insets in the bottom right of some diagrams represent close-ups to the analyses from zircon cores or xenocrysts ("Xen."), reported as shaded ellipses. Green ellipses are the oldest, equivalent concordant analyses from zircon rims or crystals devoid of any core (excluding outliers), used for the calculation of the Concordia Age. The dashed ellipses represent analyses with >5% of common ^{204}Pb (though used for age calculation). The dashed red lines are regressions through all the data from zircon rims or crystals devoid of any core; the arrow and numbers in italics point to the lower intercept of the Discordia. All ages are quoted to 2σ level of uncertainty.

n = 3). The zircon rims and core-free grains are characterized by extremely high common Pb contents, most often between 20 and 78%) and highly variable $^{206}Pb/^{238}U$ dates ranging from 33 to 325 Ma. They define a Discordia with an upper intercept of 321 ± 28 Ma (n = 18) and the four analyses with the highest $^{206}Pb/^{238}U$ ratios, including one with only ~1% common Pb and concordant at 318 Ma, yield a Concordia date of 318.3 ± 2.6 Ma. This date is identical to that obtained from 5 monazite grains (317.8 ± 1.3 Ma) from this sample, which are characterized by either well-developed, concentric oscillatory zoning or sector zoning (Fig. S8).

➡ **Sample OL-13-21** (Fig. S2)
OL-13-21 represents an equigranular variety of the Saint-Dier granite pluton, in the northwest of the study area (Livradois domain). Among the 26 analyses carried out on zircons from this sample, 7 are from zircon cores or xenocrysts and provide dates ranging from Devonian (~365 Ma; n = 1), Cambrian-Neoproterozoic (515–565 Ma; n = 3) to Mesoproterozoic (1000–1500 Ma; n = 3, including concordant analyze a227 at 1444 ± 22 Ma). Analyses from rims or crystals without cores (n = 19) have Carboniferous $^{206}Pb/^{238}U$ dates between 300 and 343 Ma and lie along a Discordia with an upper intercept at 336 ± 11 Ma, identical to the Concordia date of 336.9 ± 1.8 Ma calculated using the eleven equivalent spots with the highest $^{206}Pb/^{238}U$ ratios.

➡ **Sample TN-10** (Fig. S2)
TN-10 is from from a plurimetric enclave of K-feldspar porphyritic, biotite-bearing granite within the Velay granite at the eastern margin of the latter, close to Colombier-le-Vieux. This sample contains a limited amount of zircon cores, that with the exception of two concordant spots having respectively Cambrian (a191, $^{206}Pb/^{238}U$ date = 539 ± 4 Ma) and Mesoproterozoic (a172, $^{207}Pb/^{206}U$ date = 1025 ± 16 Ma) dates, are dominantly Neoproterozoic (645–970 Ma; n = 4). A total of 27 spots from zircon-free cores are scattered along a Discordia with an upper intercept at 320 ± 12 Ma, the five analyses with the highest $^{206}Pb/^{238}U$ ratios providing an identical Concordia date of 321.9 ± 1.3 Ma.

➡ **Sample TN-19** (Fig. S2)
TN-19 is the most representative facies of the porphyritic, biotite-bearing Tournon laccolith and was collected at the type locality in Tournon-sur-Rhône. It contains abundant zircon cores and xenocrysts, from which the analyses yield Ordovician to Neoproterozoic dates (470–770 Ma; n = 17). The main populations are Ordovician (~480 Ma; n = 5) and late Neoproterozoic (580 – 670 Ma; n = 7). Analyses from zircon rims or devoid of any core yield $^{206}Pb/^{238}U$ dates ranging between 261 and 325 Ma (n = 14), corresponding to a well-defined Discordia (MSWD = 0.15) with an upper intercept of 321 ± 6 Ma. The latter is identical to the Concordia date of 321.1 ± 1.1 Ma calculated using the six equivalent analyses with the highest $^{206}Pb/^{238}U$ ratios.

➡ **Sample TOU-01** (Fig. S2)
TOU-01 is a sample of K-felspar porphyritic, biotite-bearing granite from the Dunières laccolith that flanks the Velay granite at its easternmost margin. It contains only a few zircon cores having generally discordant U-Pb dates, only one (a54) showing a concordant Cambrian date ($^{206}Pb/^{238}U$ date = 541 ± 10 Ma). The others show a range of $^{207}Pb/^{206}Pb$ dates from late Cambrian to Neoarchean (490–2550 Ma; n = 7). Core-free zircons and rims show $^{206}Pb/^{238}U$ dates ranging from 270 to 327 Ma (n = 22), defining a Discordia trend with an upper intercept at 326 ± 11 Ma. The eleven spots with the highest, equivalent $^{206}Pb/^{238}U$ ratios define a Concordia date of 322.2 ± 1.5 Ma.

➡ **Sample PRC-57** (Fig. S2)
PRC-57 is representative of the main facies of the Velay cordierite- and biotite-bearing granite. It was collected in the central part of the dome, at the Pont-Rouge quarry. The zircon population from this sample is very heterogeneous; most grains have core-rim relationships or are obvious xenocrysts (broken edges cross-cutting the exiting zonation). A total of 21 analyses from those zircons yielded Devonian to Neoproterozoic dates, with several clusters at ~370 Ma (n = 4), ~470 Ma (n = 2), 530–580 Ma (n = 9) and 600–670 Ma (n = 3). Older dates (n = 3) include early Neoproterozoic to nearly Archean ages (concordant analyses a77 at ~840 Ma and a76 at ~2450 Ma). From zircon rims or devoid of any cores, 11 spots were obtained and have Permian to Carboniferous $^{206}Pb/^{238}U$ dates in the range 289–339 Ma, defining a Discordia with an upper intercept at 344 ± 19 Ma. Besides 4 analyses with high common Pb (4–10%) and one discordant spot (a80), those analyses define a Concordia date of 335.2 ± 1.2 Ma. On the other hand, 10 analyses of monazites from the same sample, showing either patchy or concentring zoning in BSE images (Fig. SX), yield a Concordia date of 302.8 ± 1.3 Ma.

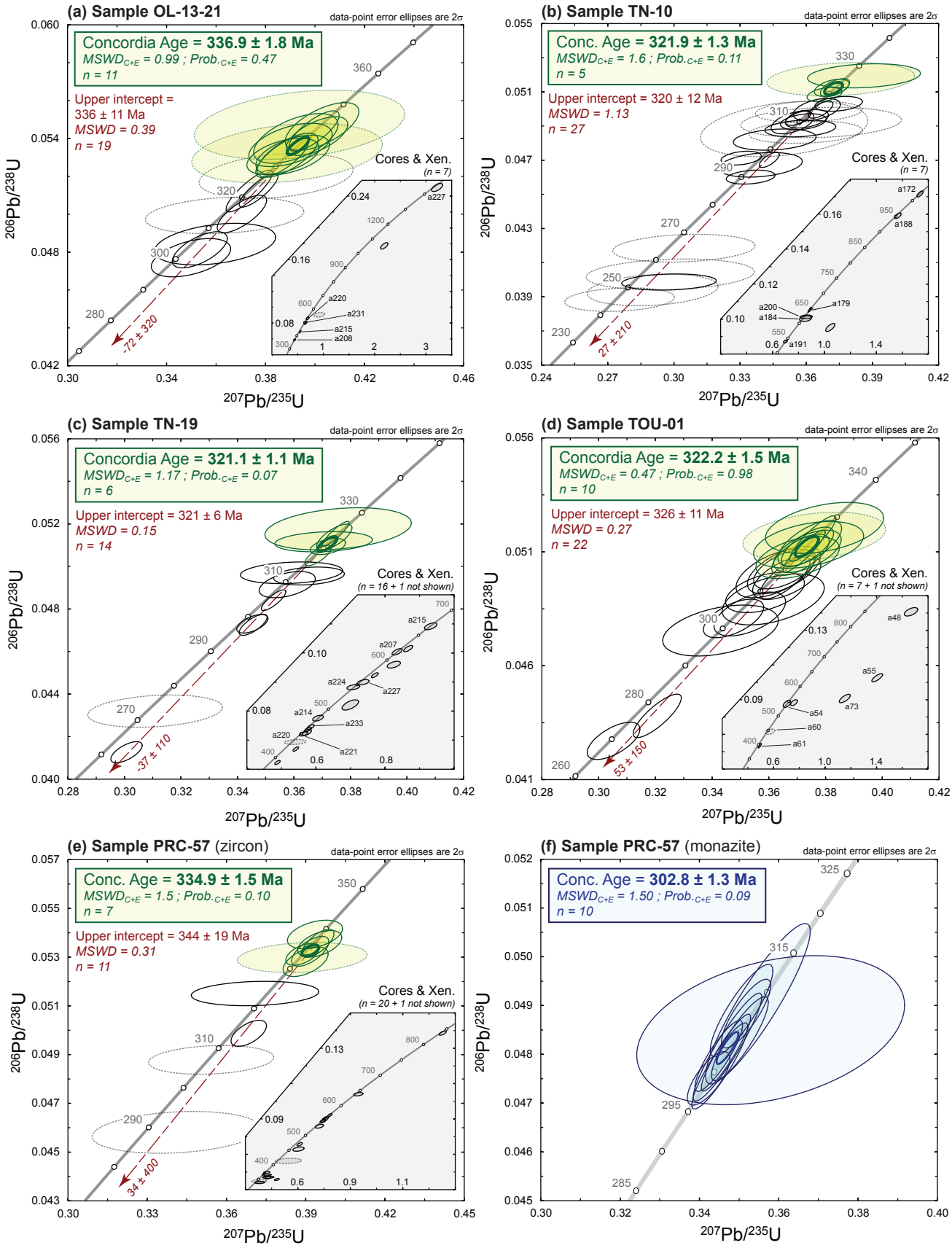

Figure S2: U-Pb Concordia diagrams (^{206}Pb/^{238}U vs. ^{207}Pb/^{235}U) for zircon (a–e) and monazite (f – in blue) analyses from samples of CPG from the eastern FMC. Insets in the bottom right of some diagrams represent close-ups to the analyses from zircon cores or xenocrysts ("Xen."), reported as shaded ellipses. Green ellipses are the oldest, equivalent concordant analyses from zircon rims or crystals devoid of any core (excluding outliers), used for the calculation of the Concordia Age. The dashed ellipses represent analyses with >5% of common ^{204}Pb (though used for age calculation). The dashed red lines are regressions through all the data from zircon rims or crystals devoid of any core; the arrow and numbers in italics point to the lower intercept of the Discordia. All ages are quoted to 2σ level of uncertainty.

2.2. MPG

➡ **Sample HER** (Fig. S3)
HER is a coarse-grained muscovite-bearing and slightly deformed leucogranite collected from the Hermitage pluton, at the northwestern limit of the Velay complex. This granite displays C–S structures related to syn-tectonic emplacement along a crustal-scale D_3 shear zone (Barbarin, 1983). Seven analyses from zircon cores and xenocrysts yielded Silurian to Neoproterozoic dates between 400 and 850 Ma (n = 6) and one Archean date (concordant spot a245 at 2591 ± 17 Ma). For zircons rims and core-free crystals, the $^{206}Pb/^{238}U$ dates are scattered between 206 and 327 Ma, defining a Discordia with an upper intercept of 323 ± 7 Ma (n = 20) which is identical to the Concordia date of 325.7 ± 1.3 Ma calculated using the five analyses with the highest, equivalent $^{206}Pb/^{238}U$ ratios.

➡ **Sample OL-13-08** (Fig. S3)
OL-13-08 is an equigranular muscovite-bearing leucogranite collected from the Grandrieu granite body, associated with the Margeride CPG batholith. According to field relationships, the Grandrieu granite is younger than the latter (Lafon and Respaut, 1988; Ledru et al., 2001). A large majority of zircon analyses from this sample are from xenocrysts and zircon cores (n = 25 out of 38). Those yielded several dates clusters: Devonian (360–380 Ma; n = 2), Ordovician (~480 Ma; n = 2), early Cambrian to late Neoproterozoic (530–580 Ma, most being concordant at 550–560 Ma; n = 13) and early Neoproterozoic to Neoarchean (840–2560 Ma; n = 6), including concordant spots at ~840 Ma (a121), ~955 Ma (a116), ~1850 Ma (a118) and ~2560 Ma (a117). Regarding zircon rims and grains without cores, 13 analyses have $^{206}Pb/^{238}U$ dates between 158 and 313 Ma, defining a Discordia with an upper intercept of 314 ± 10 Ma. An identical Concordia date of 311.0 ± 1.1 Ma was calculated from the six analyses with the highest and identical $^{206}Pb/^{238}U$ ratios, excluding two older outliers from the same grain (a108 and a109) having $^{206}Pb/^{238}U$ dates of 321–324 Ma and perhaps representing a xenocryst. The Concordia date from zircon is slightly older, yet overlaps with a Concordia date of 309.3 ± 1.2 Ma obtained from six monazite analyses in this sample, showing weak to sector zoning (Fig. SX).

➡ **Sample OL-13-09** (Fig. S3)
OL-13-09 is a medium-grained biotite- and muscovite-bearing granite from the Saint-Christophe d'Allier pluton, intrusive at the southwestern margin of the Velay dome and supposedly associated to the Margeride batholith (Feybesse et al., 1995). Most zircon analyses from those samples are from xenocrysts and zircon cores (n = 19 out of 25). Those yielded dates ranging from Devonian (a38, $^{206}Pb/^{238}U$ date of 391 ± 7 Ma), Ordovician (~490 Ma; n = 2), Cambrian (n = 10, including 9 analyses yielding a Concordia date of 534.8 ± 3.9 Ma) to late Neoproterozoic (550–570 Ma; n = 5), plus one middle Neoproterozoic spot (a32, $^{206}Pb/^{238}U$ date of 664 ± 12 Ma). Zircon grains devoid of any cores, or that are not xenocryrsts, are scarce: only 6 analyses were obtained from them. In spite of significant amounts of common Pb (0.25–21%), all are concordant, equivalent and define a Concordia date of 312.7 ± 2.3 Ma.

2.3. KCG

➡ **Sample OL-13-24** (Fig. S4)
OL-13-24 is a dark amphibole- and biotite-bearing quartz-diorite from the Gumières massif, a pluri-kilometric enclave in the Velay granite (Barbarin et al., 2012). Among the 32 analyses performed on zircons from this sample, 27 are within-error equivalent and define a Concordia date at 321.2 ± 1.2 Ma, while only 5 spots display slightly younger, significantly different $^{206}Pb/^{238}U$ dates (300–315 Ma).

➡ **Sample PRC-56** (Fig. S4)
PRC-56 represents an enclave of porphyritic, biotite- and amphibole-bearing granodiorite of KCG affinity within the Velay granite (sample PRC-57; see § 2.1) at the Pont-Rouge quarry. With the exception of 5 outliers having either significantly younger (n= 3) or older (n = 2) $^{206}Pb/^{238}U$ dates, all zircon spots from this sample are equivalent and define a Concordia date at 332.1 ± 0.7 Ma (n = 26).

➡ **Sample SJV** (Fig. S4)
SJV is a porphyritic biotite- and amphibole-bearing granodiorite that represents the main facies of the Saint-Julien-la-Vêtre pluton, at the northernmost edge of the Velay complex (Forez Mountains). Out of 28 analyses

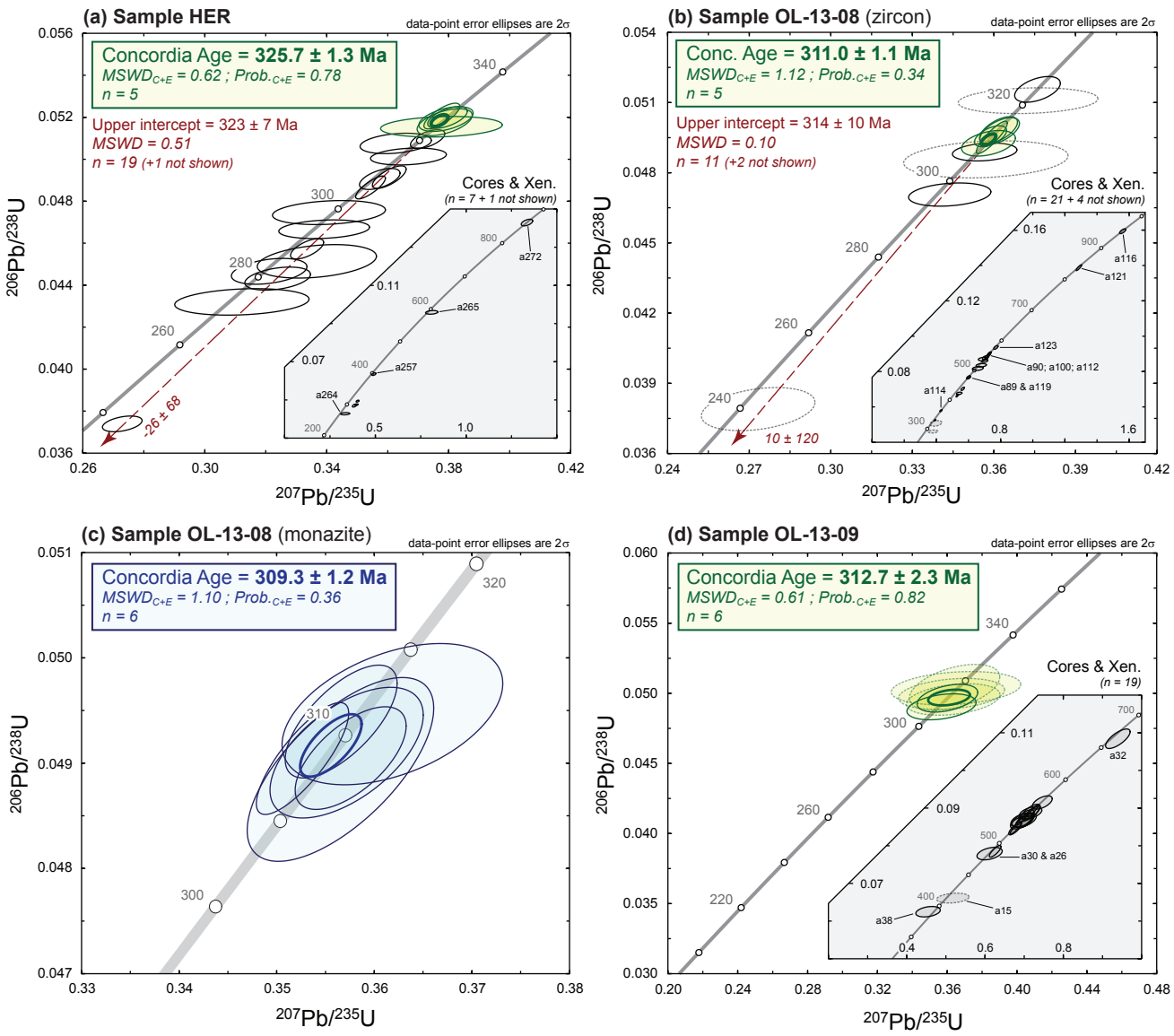

Figure S3: U-Pb Concordia diagrams (^{206}Pb/^{238}U vs. ^{207}Pb/^{235}U) for zircon (a, b, d) and monazite (c – in blue) analyses from samples of MPG from the eastern FMC. Insets in the bottom right of some diagrams represent close-ups to the analyses from zircon cores or xenocrysts ("Xen."), reported as shaded ellipses s. Green ellipses are the oldest, equivalent concordant analyses from zircon rims or crystals devoid of any core (excluding outliers), used for the calculation of the Concordia Age. The dashed ellipses represent analyses with >5% of common ^{204}Pb (though used for age calculation). The dashed red lines are regressions through all the data from zircon rims or crystals devoid of any core; the arrow and numbers in italics point to the lower intercept of the Discordia. All ages are quoted to 2σ level of uncertainty.

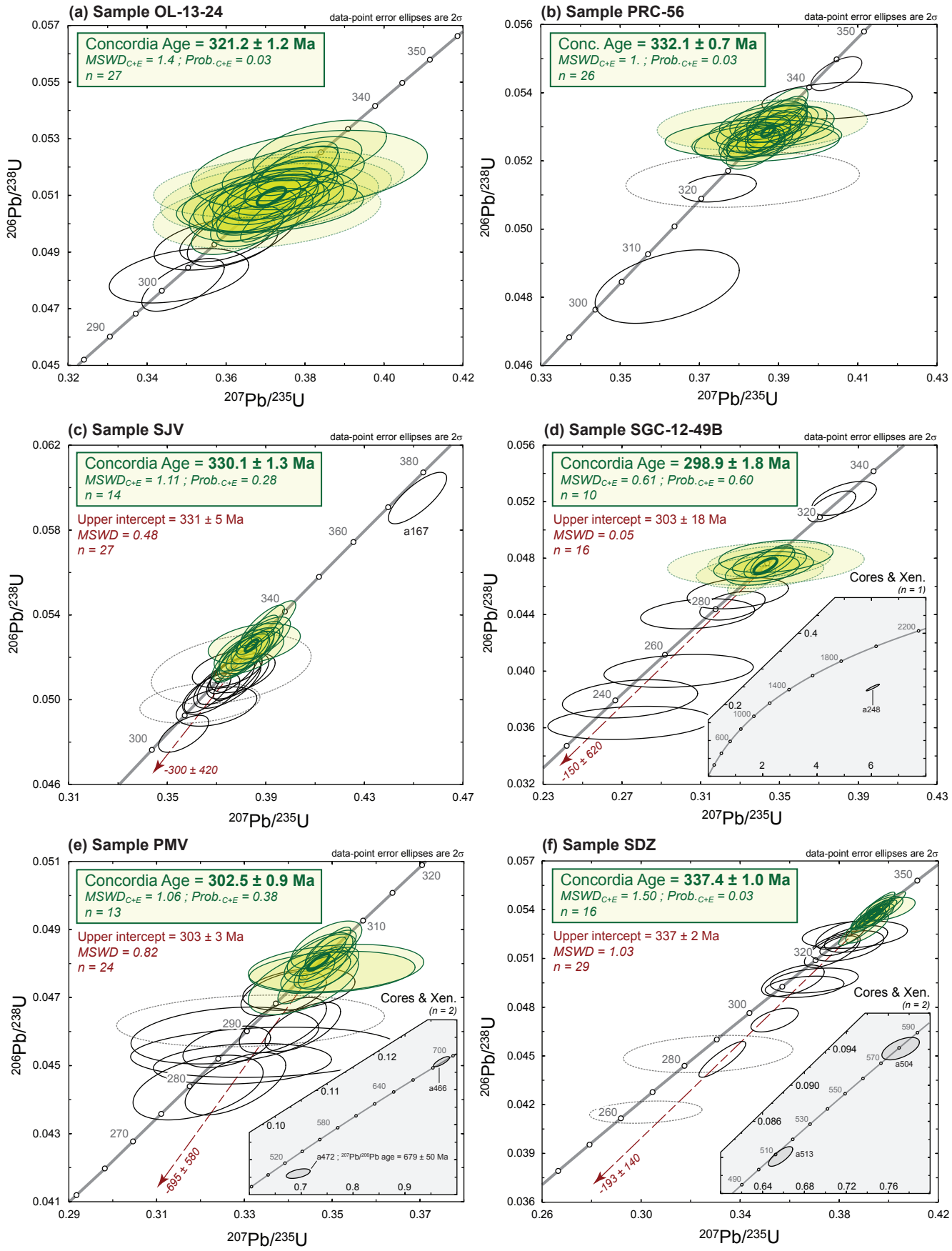

Figure S4: U-Pb Concordia diagrams (^{206}Pb/^{238}U vs. ^{207}Pb/^{235}U) for zircon analyses from samples of KCG from the eastern FMC. Insets in the bottom right of some diagrams represent close-ups to the analyses from zircon cores or xenocrysts ("Xen."), reported as shaded ellipses. Green ellipses are the oldest, equivalent concordant analyses from zircon rims or crystals devoid of any core (excluding outliers), used for the calculation of the Concordia Age. The dashed ellipses represent analyses with >5% of common ^{204}Pb (though used for age calculation). The dashed red lines are regressions through all the data from zircon rims or crystals devoid of any core; the arrow and numbers in italics point to the lower intercept of the Discordia. All ages are quoted to 2σ level of uncertainty.

performed on zircons from this sample, one spot (a167) yielded a sub-concordant, Devonian date at ~375 Ma, whereas the rest show Carboniferous $^{206}Pb/^{238}U$ dates between 305 and 337 Ma (n = 27), defining a Discordia with an upper intercept of 331 ± 5 Ma. Among those, the analyses with the highest, within-error equivalent $^{206}Pb/^{238}U$ ratios yield a Concordia date of 330.1 ± 1.3 Ma (n = 14).

➡ **Sample SGC-12-49B** (Fig. S4)
SGC-12-49B is a sample of K-feldspar porphyritic, biotite-bearing granite from the Largentière massif, in the Cévennes area, at an outcrop characterized by extensive magma mingling between the granite and vaugnerites. This sampl was already dated by Couzinié et al. (2014) but with limited confidence, owing to large uncertainties (304.1 ± 6.3 Ma). Apart from one spot from a single zircon core (a248) recording a highly discordant Neoarchean date ($^{207}Pb/^{206}Pb$ date of 2622 ± 18 Ma) and two outliers with $^{206}Pb/^{238}U$ dates of ~325 Ma, the main population of analyses (n = 16) is characterized by moderate to high proportions of common Pb (1–10%, and up to 15–18%) and shows Triassic to late Carboniferous $^{206}Pb/^{238}U$ dates (230–303 Ma). These analyses define a Discordia with an upper intercept of 303 ± 18 Ma. Among those, a Concordia date of 298.9 ± 1.8 Ma was calculated from the ten analyses with the highest, equivalent $^{206}Pb/^{238}U$ ratios.

➡ **Sample PMV** (Fig. S4)
PMV was collected from the southern edge of the Pont-de-Montvert pluton (W of Vialas), a large intrusion belonging to the Mont-Lozère complex, which also includes several MPG plutons (Bougès, Finiels and Laubies granites) and intrusive in the PAU (Cévennes schists) south of the Velay complex. Analyses from two zircon cores yielded two concordant (a466) to strongly discordant (a472) Neoproterozoic dates of ~680 Ma. Besides those, most zircon analyses are from grains devoid of any core (n = 24) and show a tight range of Permian to late Carboniferous $^{206}Pb/^{238}U$ dates (280–306 Ma). This dominant population plots along a Discordia with an upper intercept of 303 ± 3 Ma, identical to the Concordia date of 302.5 ± 0.9 Ma calculated using the 13 analyses with the highest, identical $^{206}Pb/^{238}U$ ratios.

➡ **Sample SDZ** (Fig. S4)
SDZ represents the KCG intrusions in the Lyonnais moutains, at the northwest of the study area. This sample was specifically collected from an equigranular, medim-grained biotite granite variety of the Salt-en-Donzy pluton near Cottance. Two zircon analyses from this sample are from small, rounded cores and yielded nearly concordant, Cambrian (a513; $^{207}Pb/^{206}Pb$ date = 532 ± 21 Ma) to Neoproterozoic (a504, $^{207}Pb/^{206}Pb$ date = 580 ± 6 Ma) dates. Apart from those, the main population of core-free zircons show scattered $^{206}Pb/^{238}U$ dates between 260 and 340 Ma, defining a Discordia with an upper intercept of 337 ± 2 Ma (n = 29). Nonetheless, most analyses are sub-concordant and clustered around 330–340 Ma, and among those, the 16 equivalent analyses with the highest $^{206}Pb/^{238}U$ provide a Concordia date of 337.4 ± 1.0 Ma.

2.4. Vaugnerites

➡ **Sample 533-1** (Fig. S5)
533-1 was collected from hectometric-scale vaugnerite intrusions in migmatitic orthogneisses belonging to the LGU, a few kilometers SE of Lamastre (eastern part of the Velay dome). Zircons from this samples show a tight range of $^{206}Pb/^{238}U$ dates between 296 and 308 Ma, defining a Discordia trend with an upper intercept of 321 ± 33 Ma (n = 16). Out of them, only 4 show significantly lower $^{206}Pb/^{238}U$ dates than a main population of identical spots from which a Concordia date of 307.8 ± 1.6 Ma (n = 12) was obtained.

➡ **Sample 533-2** (Fig. S5)
533-2 was sampled from a similar vaugnerite intrusion as 533-1. The zircon analyses from this sample show $^{206}Pb/^{238}U$ dates scattered between 288 and 311 Ma, plotting along a Discordia line with an upper intercept of 310 ± 6 Ma (n = 27). A Concordia date of 307.3 ± 1.3 Ma was calculated using the spots with the highest, identical $^{206}Pb/^{238}U$ ratios (n = 18).

➡ **Sample LR-31** (Fig. S5)
LR-31 belongs to a suite of gabbros and amphibole-bearing quartz diorites described by Vitel et al. (2000) in the inner part of the Velay granite, which show conspicuous mingling features with the latter (lobate contacts, intricate shapes) pointing to co-magmatism. Besides three outliers with $^{206}Pb/^{238}U$ dates below 292 Ma, all

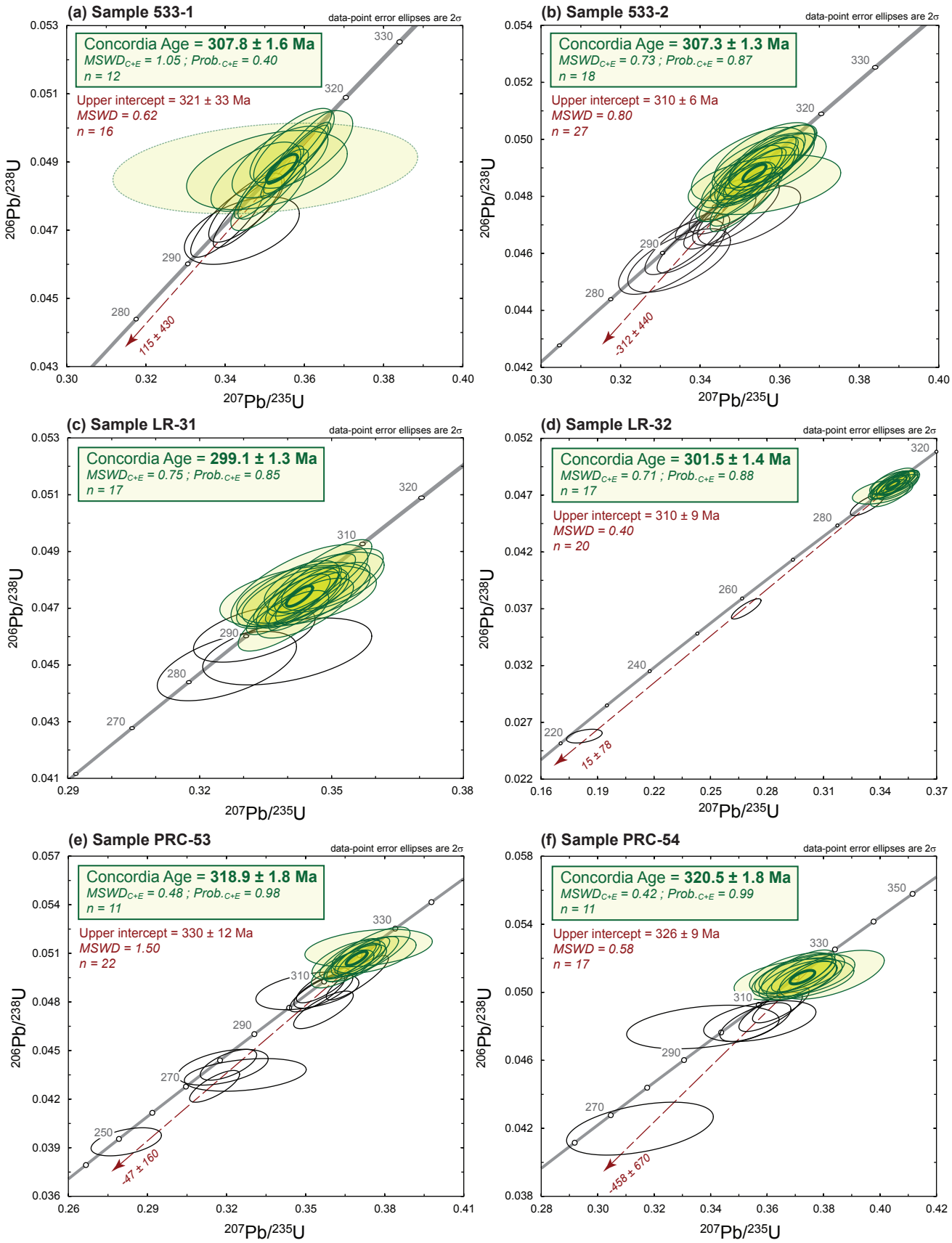

Figure S5: U-Pb Concordia diagrams (^{206}Pb/^{238}U vs. ^{207}Pb/^{235}U) for zircon analyses from samples of vaugnerites from the eastern FMC. Green ellipses are the oldest, equivalent concordant analyses from zircon rims or crystals devoid of any core (excluding outliers), used for the calculation of the Concordia Age. The dashed ellipses represent analyses with >5% of common ^{204}Pb (though used for age calculation). The dashed red lines are regressions through all the data from zircon rims or crystals devoid of any core; the arrow and numbers in italics point to the lower intercept of the Discordia. All ages are quoted to 2σ level of uncertainty.

zircon analyses from this sample are identical within error and yield a Concordia date of 299.1 ± 1.3 Ma (n = 17).

➡ **Sample LR-32** (Fig. S5)
LR-32 belongs to the same suite as LR-31. Apart from three zircon analyses with discordant, Jurassic to Permian $^{206}Pb/^{238}U$ dates (164–291 Ma), all analyses from this sample show very homogeneous and identical $^{206}Pb/^{238}U$ ratios corresponding to a Concordia date of 301.5 ± 1.4 Ma (n = 17).

➡ **Sample PRC-53** (Fig. S5)
PRC-53 was sampled at the Pont-Rouge quarry, roughly in the center of the Velay dome and ~10 km to the North of the site where LR-31 and LR-32 were collected. Together with PRC-54, these are quartz-syenites with distinctive richness in SiO_2 (60–62 wt.%) combined with very high K_2O contents (>6 wt.%) that make them unique among other vaugnerite occurrences throughout the Massif Central (unpublished data from S. Couzinié). They crop out as decametric-scale enclaves in the Velay granite (represented by sample PRC-56, see section 4.2) suggesting they represent dismembered fragments of earlier intrusions. Zircon analyses from sample PRC-53 are characterized by Permian to Carboniferous $^{206}Pb/^{238}U$ dates ranging from 249 to 323 Ma. Those analyses define a Discordia trend with an upper intercepts of 330 ± 12 Ma (n = 22). Among them, the analyses the highest, equivalent $^{206}Pb/^{238}U$ ratios correspond to a Concordia date of 318.9 ± 1.8 Ma (n = 11).

➡ **Sample PRC-54** (Fig. S5)
Like PRC-53, PRC-54 was sampled from a quartz-syenite enclave within the Velay granite at the Pont-Rouge quarry. Zircon analyses from this sample are also characterized by Permian to Carboniferous $^{206}Pb/^{238}U$ dates comprised between 265 and 321 Ma (n = 17) and a Discordia trend with an upper intercepts at 326 ± 9 Ma. Nonetheless, most analyses show within-error equivalent $^{206}Pb/^{238}U$ ratios that correspond to a Concordia date of 320.5 ± 1.8 Ma (n = 11).

➡ **Sample SC-13-02A** (Fig. S6)
In the composite Margeride granitic batholith (represented by sample OL-13-06, see § 2.1), vaugnerites occur as swarms of meter- to hectometer-sized enclaves. They outline a 20-km long NE-SW axis that extends out of the pluton in its easternmost part (Couturié, 1977). Although locally sharp, the contacts between vaugnerite and granite are most often intricate, rounded and irregular with lobate interfaces. Moreover, large K-feldspar xenocrysts of granitic origin are commonly observed in vaugnerites (Sabatier, 1991). Both lines of evidence support that mingling between both magmas took place. SC-13-02A is a SiO_2-rich vaugnerite from the Margeride batholith, from which only few zircons were extracted. They show a restricted range of Carboniferous $^{206}Pb/^{238}U$ dates (300–317 Ma), and a Concordia date of 313.2 ± 2.5 Ma (n = 5) was calculated excluding the two outliers with the lowest $^{206}Pb/^{238}U$ ratios (a124 and a128).

➡ **Sample SC-13-05** (Fig. S6)
SC-13-05 was also collected in a vaugnerite enclave within the Margeride batholith. In contrast with SC-13-02A, it has high MgO and low SiO_2 contents. Zircon analyses from this sample show $^{206}Pb/^{238}U$ dates ranging from 279 to 313 Ma and define a Discordia with an upper intercept at 311 ± 3 Ma (n = 18). A Concordia date of 309.4 ± 1.5 Ma was obtained from the analyses with the highest, identical $^{206}Pb/^{238}U$ ratios (n = 12).

➡ **Sample SC-13-09** (Fig. S6)
SC-13-09 was sampled near Pubellier, at the western edge of the Velay dome, and belongs to a small stock of pyroxene- and amphibole-bearing syenodiorite (Ledru et al., 1994) intrusive in the LGU orthogneisses. With the exception of few analyses with relatively high common Pb contents (1–8%) and showing $^{206}Pb/^{238}U$ dates of 294 to 303 Ma (n = 5), as well as one outlier (spot a271) displaying a $^{206}Pb/^{238}U$ date of 336 Ma (Fig. 9c), all zircon analyses are concordant and identical within error, corresponding to a Concordia date of 309.7 ± 1.2 Ma (n = 21).

➡ **Sample SC-13-14** (Fig. S6)
SC-13-14 is a very SiO_2-poor (<45 wt.%) vaugnerite collected from the Lyonnais area, close to Marcenod at the SW edge of the Soucieu granite. It is typical of vaugnerite occurrences North of the Velay dome, which intruded the UGU gneisses as small bodies along dextral NE-SW shear zones (Lardeaux and Dufour, 1987) and are coeval with a suite of syn-kinematic granites. From this sample, four analyses were obtained from zircon cores: analyses a22 and a32 display concordant, Devonian $^{206}Pb/^{238}U$ dates at 381 ± 10 Ma and 397 ± 8

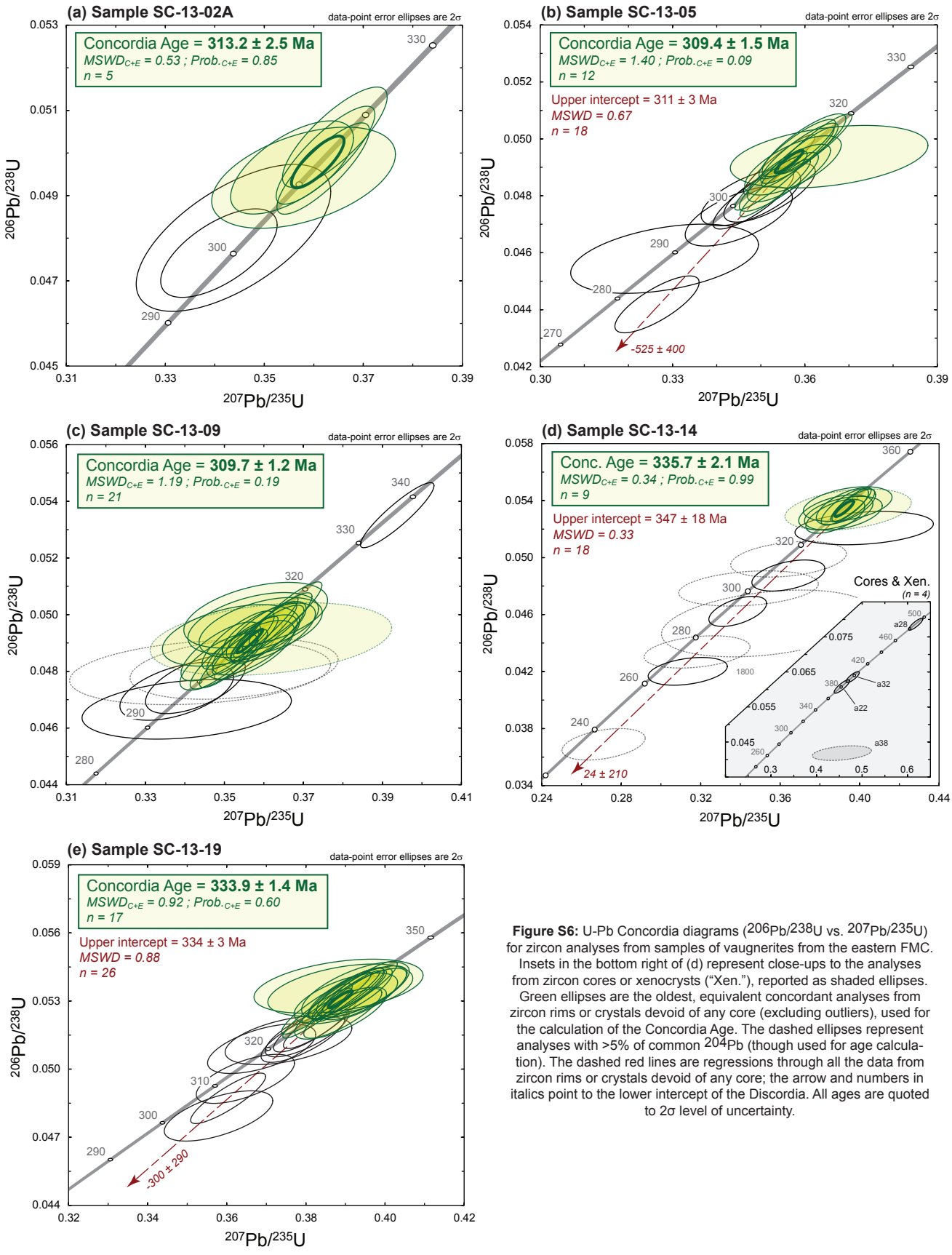

Figure S6: U-Pb Concordia diagrams (^{206}Pb/^{238}U vs. ^{207}Pb/^{235}U) for zircon analyses from samples of vaugnerites from the eastern FMC. Insets in the bottom right of (d) represent close-ups to the analyses from zircon cores or xenocrysts ("Xen."), reported as shaded ellipses. Green ellipses are the oldest, equivalent concordant analyses from zircon rims or crystals devoid of any core (excluding outliers), used for the calculation of the Concordia Age. The dashed ellipses represent analyses with >5% of common ^{204}Pb (though used for age calculation). The dashed red lines are regressions through all the data from zircon rims or crystals devoid of any core; the arrow and numbers in italics point to the lower intercept of the Discordia. All ages are quoted to 2σ level of uncertainty.

Ma respectively, whereas another concordant spot (a28) shows an Ordovician $^{206}Pb/^{238}U$ date of 488 ± 8 Ma. Analysis a38 is largely discordant and is characterized by an enormous amount of common Pb (~33%) such that its (poorly constrained) $^{207}Pb/^{206}Pb$ date of 1172 ± 216 Ma is probably meaningless. The analyses from zircons devoid of cores show $^{206}Pb/^{238}U$ dates scattered between 234 and 338 Ma, defining a Discordia with an upper intercept of 347 ± 18 Ma (n = 18). The analyses with the highest, within-error identical $^{206}Pb/^{238}U$ ratios yield a Concordia date of 335.7 ± 2.1 Ma (n = 9).

➡ **Sample SC-13-19** (Fig. S6)
SC-13-19 was collected in the Chassagny quarry in the Lyonnais area, where interactions between mafic and felsic magmas (corresponding to the associated granites) are well-exposed. Zircon analyses from this sample all show Carboniferous $^{206}Pb/^{238}U$ dates ranging from 302 to 337 Ma, plotting along a Discordia with an upper intercept of 334 ± 3 Ma (n = 26). A Concordia date of 333.9 ± 1.4 Ma was obtained using the equivalent analyses with the highest $^{206}Pb/^{238}U$ ratios (n = 17).

➡ **Sample SGC-12-13** (Fig. S7)
SGC-12-13 is a coarse-grained lamprophyre dyke crosscutting the low-grade Cevennes schists of the PAU, south of the Velay dome. It was collected close to Saint-Jean-de-Pourcharesse, 10 km to the East of the contact between the latter and the Borne KCG pluton. Out of nine zircon analyses, six have $^{206}Pb/^{238}U$ ratios that are identical within error and define a Concordia date of 306.6 ± 2.4 Ma. One spot (a12) displays a slightly older $^{206}Pb/^{238}U$ date of 322 ± 6 Ma, and may correspond to a xenocryst (darker CL luminescence). Two other outliers show significantly younger (Permian) $^{206}Pb/^{238}U$ dates.

➡ **Sample SGC-12-26** (Fig. S7)
SGC-12-26 was sampled from a decameter-sized, rounded vaugnerite enclave in migmatitic paragneisses at the southern edge of the Velay complex, along the Pont-de-Bayzan road cut (see Fig. 2b in Couzinié et al. 2014). Out of 24 zircon analyses from this sample, most have $^{206}Pb/^{238}U$ ratios that are identical within error and define a Concordia date of 306.1 ± 1.3 Ma (n = 20), whereas the other spots display slightly younger $^{206}Pb/^{238}U$ dates down to 290 Ma.

➡ **Sample SGC-12-39** (Fig. S7)
SGC-12-39 was collected in a vaugnerite sill intrusive in migmatitic paragneisses East of Loubaresse, at the southermost edge of the Velay dome. Apart from two outliers with Permian $^{206}Pb/^{238}U$ dates (a254 and a255), all zircon analyses from this sample are identical within error and define a late Carboniferous, Concordia date of 306.6 ± 1.6 Ma (n = 12).

➡ **Sample SGC-12-42** (Fig. S7)
SGC-12-42 represents a rounded, meter-sized vaugnerite enclave within migmatitic paragneisses near Meyras, at the southern limit of the Velay dome. Zircon analyses show a restricted range of $^{206}Pb/^{238}U$ dates between 293 and 310 Ma (n = 16). The equivalent analyses with the highest $^{206}Pb/^{238}U$ ratios yield a Concordia date of 305.9 ± 1.7 Ma (n = 11).

3. References

Barbarin, B., 1983. Les granites carbonifères du Forez septentrional (Massif Central Français). Typologie et relations entre les différents massifs. - Thèse 3e cycle, Université Clermont-Ferrand, 199 p.

Barbarin, B., Gerbe, M.-C., Vitel, G., Gonord, H., Couette, F., Lebret, P., 2012. Notice explicative, Carte géologique de la France (1/50 000e), feuille Firminy (nr. 744). Orléans, Bureau de Recherches Géologiques et Minières, 129 pp.

Couturié, J.-P., 1977, Le massif granitique de la Margeride (M.C.F.). Etude pétrographique, géochimique et structurale. Exemple de différenciation par gravité dans les roches granitiques. Evolution régionale de la croûte au cours de l'orogène hercynien. [Thèse de 3ème cycle: Clermont-Ferrand, 335 p.

Couzinié, S., Moyen, J. F., Villaros, A., Paquette, J. L., Scarrow, J. H., and Marignac, C., 2014. Temporal relationships between Mg-K mafic magmatism and catastrophic melting of the Variscan crust in the southern part of Velay Complex (Massif Central, France): Journal of GEOsciences, p. 69-86.

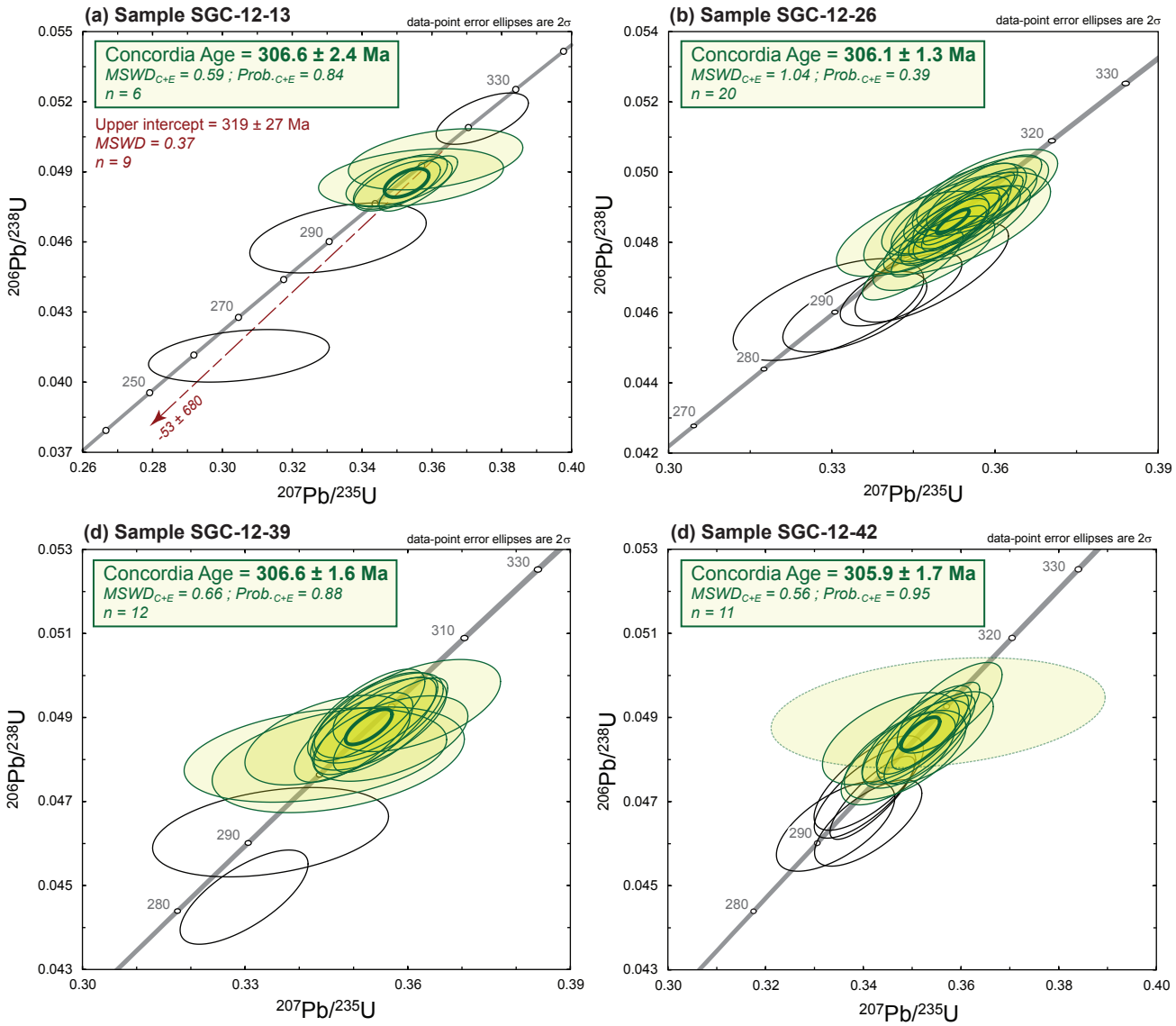

Figure S7: U-Pb Concordia diagrams ($^{206}Pb/^{238}U$ vs. $^{207}Pb/^{235}U$) for zircon analyses from samples of vaugnerites from the eastern FMC. Green ellipses are the oldest, equivalent concordant analyses from zircon rims or crystals devoid of any core (excluding outliers), used for the calculation of the Concordia Age. The dashed ellipses represent analyses with >5% of common ^{204}Pb (though used for age calculation). The dashed red lines are regressions through all the data from zircon rims or crystals devoid of any core; the arrow and numbers in italics point to the lower intercept of the Discordia. All ages are quoted to 2σ level of uncertainty.

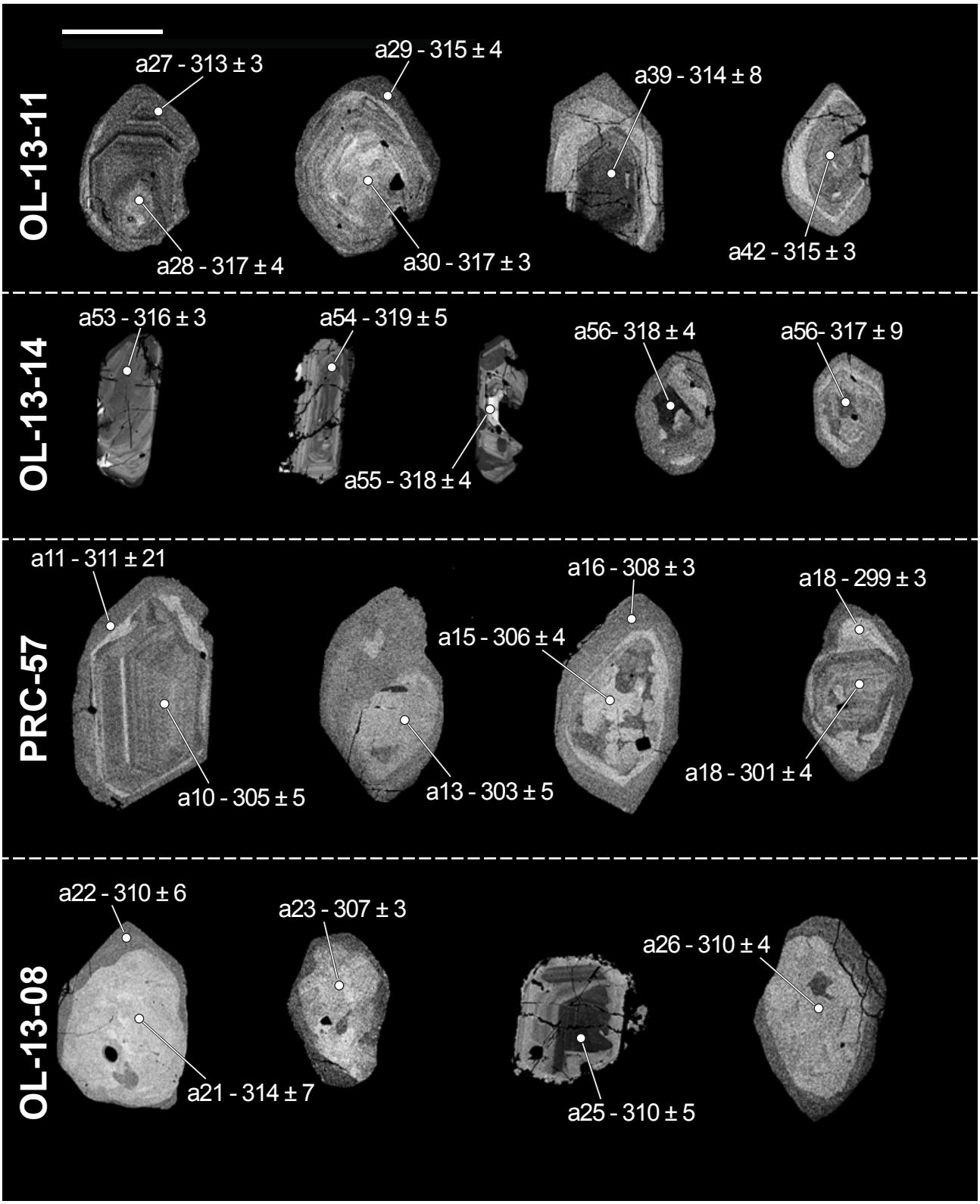

Figure S8: Selected back-scattered electron (BSE) images of representative monazite grains from the four samples of CPG and MPG for which this mineral has been analyzed. Analytical spots are indicated (white circles) as well as the corresponding analysis label and $^{206}Pb/^{238}U$ age (with 2σ uncertainty) in Ma. The scale bar is 100 µm.

Feybesse, J.-L., Couturié, J.-P., Ledru, P., Johan, V., 1995. Les granites de la Margeride, de Chambon le Château et de St Christophe: des laccolites synchrones des derniers stades de l'épaississement varisque. Géologie de la France 1, 27–45.

Gasquet, D., Bertrand, J.-M., Paquette, J.-L., Lehmann, J., Ratzov, G., De Ascenção Guedes, R., Tiepolo, M., Boullier, A.-M., Scaillet, S., Nomade, S., 2010. Miocene to Messinian deformation and hydrothermal activity in a pre-Alpine basement massif of the French western Alps: new U-Th-Pb and argon ages from the Lauzière massif. Bulletin de la Société Géologique de France 181(3), 227–241.

Gerdes, A., Zeh, A., 2006. Combined U–Pb and Hf isotope LA-(MC)ICP-MS analyses of detrital zircons: comparison with SHRIMP and new constraints for the provenance and age of an Armorican metasediment in Central Germany. Earth and Planetary Science Letters 249, 47–61.

Gerdes, A., Zeh, A., 2009. Zircon formation versus zircon alteration–new insights from combined U–Pb and Lu–Hf in situ LA-ICP-MS analyses, and consequences for the interpretation of Archean zircon from the Central Zone of the Limpopo Belt. Chemical Geology 261, 230–243.

Horstwood, M.S.A., Foster, G.L., Parrish, R.R., Noble, S.R., Nowell, G.M., 2003. Common-Pb corrected *in situ* U–Pb accessory mineral geochronology by LA-MC-ICP-MS. Journal of Analytical Atomic Spectrometry 18(8), 837–846.

Jackson, S.E., Pearson, N.J., Griffin, W.L., Belousova, E.A., 2004. The application of laser ablation-inductively coupled plasma-mass spectrometry to in situ U–Pb zircon geochronology 211, 47–69.

Lardeaux, J. M., and Dufour, E., 1987, Champs de déformation superposés dans la chaîne varisque. Exemple de la zone nord des Monts du Lyonnais (Massif Central français): Comptes Rendus de l'Académie des Sciences, Paris, v. 305, p. 61-64.

Ledru, P., Vitel, G., Marchand, J., Maurin, G., Mercier, F., Turland, M., Etlicher, B., Dautria, J. M., and Liotard, J. M., 1994, Notice explicative, Carte géol. France (1/50 000), feuille Craponne-sur-Arzon (767): BRGM.

Ludwig, K.R., 2008. Isoplot 3.70, A Geochronological Toolkit for Microsoft Excel. Berkeley Geochronology Central Special Publication No. 4, 76 pp.

Sabatier, H., 1991. Vaugnerites: special lamprophyre-derived mafic enclaves in some Hercynian granites from Western and Central Europe. In: Didier, J., and Barbarin, B. (eds.): Enclaves and Granite Petrology, Elsevier, Amsterdam, pp. 63-81.

Santos, M.M., Lana, C., Scholz, R., Buick, I., Kamo, S.L., Gerdes, A., Condon, D.J., Corfu, F., Tohver, E., Storey, C.D., Basei, M.A.S., Krambrock, K., Fantini, C., in press. BB zircon – A new Sri Lankan reference material for U-Pb and Hf isotopic laser ablation ICP-MS analysis.

Sláma, J., Kosler, J., Condon, D.J., Crowely, J.L., Gerdes, A., Hanchar, J.M., Horstwood, M.S.A., Morris, G.A., Nasdala, L., Norberg, N., Schaltegger, U., Schoene, B., Tubrett, M.N., Whitehouse, M.J., 2008. Plesovice zircon- a new natural reference material for U-Pb and Hf isotopic microanalysis. Chemical Geology 249 (1–2), 1–35.

Stacey, J., Kramers, J.D., 1975. Approximation of terrestrial lead isotope evolution by a two-stage model. Earth and Planetary Science Letters 26, 207–221.

Stern, R.A., Bodorkos, S., Kamo, S.L., Hickman, A.H., Corfu, F., 2009. Measurement of SIMS Instrumental Mass Fractionation of Pb Isotopes During Zircon Dating. Geostandards and Geoanalytical Research 33(2), 145–168.

Vitel, G., Garcia, D., Turland, M., Gonord, H., Etlicher, B., and Chafchafi, A., 2000, Notice explicative, Carte géol. France (1/50 000), feuille Monistrol-sur-Loire (768): BRGM.

Zeh, A., Gerdes, A., 2012. U–Pb and Hf isotope record of detrital zircons from gold-bearing sediments of the PietersburgGreenstone belt (South Africa) – is there a common provenance with the Witwatersrand Basin? Precambrian Research 204–205, 46–56.

Laurent et al., 2017. Supplementary Table S1:
Results of LA-SF-ICPMS U–Pb analyses of standard zircons GJ-1, Plesoviče, OG-1 and BB.

	^{207}Pb[a] (cps)	U[b] (ppm)	Pb[b] (ppm)	Th/U[b]	$^{206}Pb_c$[c] (%)	$^{206}Pb/^{238}U$[d]	±2σ (%)	$^{207}Pb/^{235}U$[e]	±2σ (%)	$^{207}Pb/^{206}Pb$[d]	±2σ (%)	ρ[f]	$^{206}Pb/^{238}U$	±2σ (Ma)	$^{207}Pb/^{235}U$	±2σ (Ma)	$^{207}Pb/^{206}Pb$	±2σ (Ma)	conc.[g] (%)
GJ-1																			
Session #1 (April 9th, 2014)																			
GJ1-01	8230	268	24.2	0.02	b.d.	0.0973	1.6	0.8131	3.2	0.06059	2.7	0.50	599	9	604	15	625	59	99
GJ1-02	8997	273	24.7	0.02	b.d.	0.0972	1.6	0.8267	3.2	0.06168	2.8	0.49	598	9	612	15	663	59	98
GJ1-03	9044	283	26.0	0.02	b.d.	0.0989	1.5	0.8227	3.0	0.06033	2.6	0.50	608	9	610	14	615	56	100
GJ1-04	9650	300	27.5	0.02	b.d.	0.0987	1.5	0.8394	3.1	0.06167	2.7	0.47	607	8	619	14	663	58	98
GJ1-05	9245	289	26.4	0.02	b.d.	0.0983	1.4	0.8241	3.1	0.06080	2.7	0.46	604	8	610	14	632	58	99
GJ1-06	8693	270	24.7	0.02	b.d.	0.0982	1.6	0.8322	3.1	0.06145	2.7	0.50	604	9	615	15	655	58	98
GJ1-07	8352	270	24.9	0.02	b.d.	0.0995	1.5	0.8368	3.1	0.06100	2.7	0.50	611	9	617	14	639	57	99
GJ1-08	8452	287	26.2	0.02	b.d.	0.0984	1.6	0.8196	3.1	0.06039	2.6	0.51	605	9	608	14	617	57	100
GJ1-09	8714	290	26.3	0.02	b.d.	0.0977	1.6	0.8152	3.2	0.06052	2.8	0.49	601	9	605	15	622	60	99
GJ1-10	8664	290	26.5	0.02	b.d.	0.0984	1.5	0.8327	3.2	0.06136	2.8	0.48	605	9	615	15	652	60	98
GJ1-11	8128	280	25.7	0.02	b.d.	0.0988	1.5	0.8414	3.2	0.06175	2.8	0.48	607	9	620	15	666	60	98
GJ1-12	7735	261	23.8	0.02	b.d.	0.0985	1.5	0.8303	3.0	0.06116	2.7	0.49	605	9	614	14	645	57	99
GJ1-13	7855	276	24.9	0.02	b.d.	0.0972	1.5	0.8052	3.0	0.06007	2.6	0.49	598	9	600	14	606	57	100
GJ1-14	8197	290	26.3	0.02	b.d.	0.0977	1.4	0.8155	3.1	0.06051	2.7	0.47	601	8	606	14	622	58	99
GJ1-15	7727	287	26.1	0.02	b.d.	0.0978	1.5	0.8149	3.1	0.06043	2.7	0.50	602	9	605	14	619	58	99
GJ1-16	7259	266	24.3	0.02	b.d.	0.0985	1.5	0.8354	3.2	0.06152	2.8	0.46	605	8	617	15	658	61	98
GJ1-17	6822	263	23.8	0.02	b.d.	0.0974	1.5	0.8059	3.2	0.06000	2.9	0.46	599	8	600	15	604	62	100
GJ1-18	7564	281	25.6	0.02	b.d.	0.0979	1.5	0.8382	3.1	0.06207	2.7	0.49	602	9	618	15	676	58	97
GJ1-19	8020	292	26.9	0.02	b.d.	0.0988	1.4	0.8329	3.1	0.06114	2.8	0.46	607	8	615	15	644	60	99
GJ1-20	8022	294	26.7	0.02	b.d.	0.0977	1.4	0.8327	3.0	0.06180	2.7	0.47	601	8	615	14	667	57	98
GJ1-21	7762	281	25.8	0.02	b.d.	0.0983	1.4	0.8290	3.0	0.06117	2.7	0.47	604	8	613	14	645	58	99
GJ1-22	7196	270	24.9	0.02	b.d.	0.0990	1.3	0.8377	2.9	0.06138	2.6	0.46	608	8	618	14	653	55	98
Average (n=22)		**280**	**25.6**	**0.022**		**0.0982**		**0.8264**		**0.0610**			**604**		**612**		**640**		
2 S.D. ext. (abs.)		**22**	**2.1**	**0.001**		**0.0013**		**0.0219**		**0.0012**			**7**		**12**		**43**		
2 S.D. ext. (%)						**1.3**		**2.6**		**2.0**			**Conc. Age = 604.9 ± 2.2 Ma**						
													($MSWD_{C+E}$ = 1.3 ; P_{C+E} = 0.11)						
Session #2 (August 13th, 2014)																			
GJ1-01	20230	283	25.8	0.02	b.d.	0.0979	0.8	0.812	1.8	0.06016	1.6	0.45	602	5	604	8	609	34	100
GJ1-02	19635	280	25.5	0.02	b.d.	0.0983	0.8	0.8160	1.7	0.06018	1.5	0.46	605	5	606	8	610	33	100
GJ1-03	19229	275	25.1	0.02	b.d.	0.0984	0.7	0.8148	1.8	0.06006	1.6	0.40	605	4	605	8	606	36	100
GJ1-04	19139	283	25.8	0.02	b.d.	0.0984	0.7	0.8143	1.6	0.06005	1.5	0.46	605	4	605	7	605	32	100
GJ1-05	19237	279	25.3	0.02	b.d.	0.0977	0.8	0.8087	1.7	0.06002	1.5	0.48	601	5	602	8	604	33	100
GJ1-06	18660	282	25.7	0.02	b.d.	0.0983	0.7	0.8153	1.6	0.06013	1.5	0.42	605	4	605	7	608	32	100
GJ1-07	18249	279	25.4	0.02	b.d.	0.0986	0.8	0.8174	1.6	0.06010	1.4	0.52	606	5	607	7	607	30	100
GJ1-08	18556	278	25.2	0.02	b.d.	0.0978	0.9	0.8099	1.7	0.06008	1.5	0.50	601	5	602	8	606	33	100
GJ1-09	18499	281	25.5	0.02	b.d.	0.0981	0.8	0.8119	1.7	0.06000	1.5	0.47	603	4	603	8	603	32	100
GJ1-10	18006	279	25.3	0.02	b.d.	0.0980	0.8	0.8113	1.8	0.06006	1.6	0.43	603	4	603	8	606	34	100
GJ1-11	18939	280	25.6	0.02	b.d.	0.0985	0.7	0.8157	1.7	0.06005	1.5	0.43	606	4	606	8	605	33	100
GJ1-12	18781	276	25.1	0.02	b.d.	0.0982	0.8	0.8125	1.7	0.05999	1.5	0.49	604	5	604	8	603	33	100
GJ1-13	18858	281	25.6	0.02	b.d.	0.0983	0.9	0.8151	1.7	0.06012	1.5	0.50	605	5	605	8	608	32	100
GJ1-14	18207	278	25.3	0.02	b.d.	0.0983	0.8	0.8135	1.7	0.06005	1.5	0.45	604	4	604	8	605	33	100
GJ1-15	19458	283	25.7	0.02	b.d.	0.0980	0.8	0.8107	1.6	0.06003	1.4	0.48	602	5	603	8	605	31	100
GJ1-16	18889	280	25.5	0.02	b.d.	0.0982	0.7	0.8132	1.6	0.06006	1.5	0.44	604	4	604	8	606	32	100
GJ1-17	18570	282	25.7	0.02	b.d.	0.0983	0.8	0.8144	1.7	0.06008	1.5	0.47	605	5	605	8	606	33	100
GJ1-18	19087	279	25.4	0.02	b.d.	0.0983	0.9	0.8111	1.7	0.05986	1.4	0.51	604	5	603	8	598	31	100
GJ1-19	18609	282	25.6	0.02	b.d.	0.0981	0.8	0.8115	1.9	0.06000	1.7	0.41	603	4	603	8	604	37	100
GJ1-20	18754	277	25.1	0.02	b.d.	0.0980	0.8	0.8116	1.7	0.06009	1.5	0.47	602	5	603	8	607	33	100
Average (n=20)		**280**	**25.4**	**0.024**		**0.0982**		**0.8131**		**0.0601**			**604**		**604**		**606**		
2 S.D. ext. (abs.)		**5**	**0.5**	**0.001**		**0.0005**		**0.0046**		**0.0001**			**3**		**3**		**5**		
2 S.D. ext. (%)						**0.5**		**0.6**		**0.2**			**Conc. Age = 603.9 ± 2.2 Ma**						
													($MSWD_{C+E}$ = 0.2 ; P_{C+E} = 0.99)						
Plesoviče																			
Session #1 (April 9th, 2014)																			
Pleso-01	10145	639	32.4	0.09	0.08	0.0538	1.8	0.3948	3.6	0.05318	3.1	0.51	338	6	338	10	336	71	100
Pleso-02	10120	644	33.0	0.09	0.31	0.0542	1.6	0.3982	2.5	0.05324	2.0	0.62	341	5	340	7	339	45	100
Pleso-03	8649	545	29.4	0.09	0.09	0.0551	1.7	0.4033	3.0	0.05312	2.5	0.55	346	6	344	9	334	58	103
Pleso-04	8488	573	29.2	0.09	0.20	0.0541	1.7	0.3962	3.0	0.05316	2.5	0.55	339	6	339	9	335	57	101
Pleso-05	7991	532	26.8	0.09	0.26	0.0532	1.9	0.3893	3.9	0.05308	3.4	0.49	334	6	334	11	332	77	101
Pleso-06	8023	529	30.2	0.09	0.30	0.0543	1.8	0.3984	4.1	0.05318	3.7	0.43	341	6	341	12	336	85	101
Pleso-07	7443	526	26.6	0.09	0.15	0.0535	1.5	0.3920	3.5	0.05316	3.2	0.42	336	5	336	10	336	73	100
Pleso-08	7827	564	28.5	0.09	0.36	0.0535	1.6	0.3929	4.1	0.05326	3.8	0.39	336	5	336	12	340	86	99
Pleso-09	7838	556	28.4	0.10	0.23	0.0535	1.5	0.3911	3.2	0.05302	2.8	0.48	336	5	335	9	330	64	102
Pleso-10	8936	645	33.2	0.10	0.22	0.0543	1.7	0.3975	3.2	0.05310	2.7	0.52	341	6	340	9	333	62	102
Pleso-11	9987	619	32.5	0.09	1.57	0.0538	1.7	0.3942	5.2	0.05312	4.9	0.33	338	6	337	15	334	110	101

Laurent et al., 2017. Supplementary Table S1 (continued):
Results of LA-SF-ICPMS U–Pb analyses of standard zircons GJ-1, Plesoviče, OG-1 and BB.

	^{207}Pb[a] (cps)	U[b] (ppm)	Pb[b] (ppm)	Th[b] U	^{206}Pbc[c] (%)	^{206}Pb[d] / ^{238}U	±2σ (%)	^{207}Pb[e] / ^{235}U	±2σ (%)	^{207}Pb[d] / ^{206}Pb	±2σ (%)	ρ[f]	^{206}Pb / ^{238}U	±2σ (Ma)	^{207}Pb / ^{235}U	±2σ (Ma)	^{207}Pb / ^{206}Pb	±2σ (Ma)	conc.[g] (%)
Average (n=11)		**579**	**30.0**	**0.094**		**0.0539**		**0.3953**		**0.0531**			**408**		**408**		**407**		
2 S.D. ext. (abs.)		**97**	**4.9**	**0.006**		**0.0011**		**0.0080**		**0.0001**			**324**		**325**		**326**		
2 S.D. ext. (%)						**2.0**		**2.0**		**0.3**			**Conc. Age = 338.6 ± 1.7 Ma**						
													(MSWD$_{C+E}$ = 0.66 ; P$_{C+E}$ = 0.87)						
Session #2 (August 13th, 2014)																			
Plešo01	22823	660	33.8	0.13	0.03	0.0542	0.8	0.3984	1.2	0.05328	0.8	0.71	340	3	341	3	341	19	100
Plešo02	22637	671	34.1	0.12	0.04	0.0540	1.0	0.3957	1.2	0.05316	0.7	0.79	339	3	338	3	336	17	101
Plešo03	22698	680	34.7	0.13	0.12	0.0541	0.9	0.3967	1.2	0.05323	0.7	0.78	339	3	339	3	338	17	100
Plešo04	22042	682	35.0	0.12	0.03	0.0544	0.9	0.3993	1.2	0.05321	0.7	0.82	342	3	341	3	338	15	101
Plešo05	22378	710	36.1	0.12	0.06	0.0539	1.0	0.3956	1.2	0.05321	0.7	0.81	339	3	338	3	338	16	100
Plešo06	23064	706	36.3	0.13	0.01	0.0546	0.9	0.4012	1.2	0.05326	0.8	0.74	343	3	343	3	340	18	101
Plešo07	23103	726	37.2	0.12	0.08	0.0543	1.0	0.3993	1.3	0.05334	0.9	0.74	341	3	341	4	343	19	99
Plešo09	22936	709	36.3	0.13	0.02	0.0543	0.8	0.3981	1.2	0.05322	0.8	0.69	341	3	340	3	338	19	101
Plešo10	22603	736	37.4	0.12	0.05	0.0540	0.8	0.3963	1.1	0.05320	0.8	0.73	339	3	339	3	337	17	101
Plešo11	23206	693	35.2	0.13	0.03	0.0539	0.9	0.3964	1.1	0.05329	0.6	0.85	339	3	339	3	341	13	99
Plešo12	23312	686	35.1	0.13	0.05	0.0544	0.8	0.3998	1.2	0.05333	0.8	0.73	341	3	341	3	343	18	100
Plešo13	22770	683	34.7	0.12	0.03	0.0540	0.9	0.3962	1.2	0.05323	0.7	0.78	339	3	339	3	339	16	100
Plešo14	22501	676	34.6	0.12	0.05	0.0544	0.8	0.3988	1.1	0.05322	0.8	0.67	341	3	341	3	338	19	101
Plešo15	22758	675	34.3	0.13	0.04	0.0539	1.0	0.3955	1.3	0.05322	0.8	0.76	338	3	338	4	338	19	100
Plešo16	22291	674	34.5	0.12	0.06	0.0543	1.0	0.3990	1.3	0.05330	0.8	0.80	341	3	341	4	341	17	100
Plešo17	29486	839	43.7	0.19	0.10	0.0543	0.9	0.3992	1.2	0.05328	0.8	0.73	341	3	341	4	341	19	100
Plešo18	26278	774	40.1	0.18	0.04	0.0543	0.9	0.3988	1.2	0.05328	0.7	0.77	341	3	341	3	341	17	100
Average (n=17)		**705**	**36.1**	**0.132**		**0.0542**		**0.3979**		**0.0533**			**339**		**339**		**339**		
2 S.D. ext. (abs.)		**89**	**5.0**	**0.040**		**0.0004**		**0.0035**		**0.0001**			**8**		**8**		**7**		
2 S.D. ext. (%)						**0.8**		**0.9**		**0.2**			**Conc. Age = 340.2 ± 0.8 Ma**						
													(MSWD$_{C+E}$ = 0.39 ; P$_{C+E}$ = 0.99)						
OG-1																			
Session #1 (April 9th, 2014)																			
OG1-01	221594	164	162.6	0.66	0.70	0.7127	2.1	29.130	2.3	0.29640	1.0	0.89	3469	56	3458	23	3452	16	100
OG1-02	144020	150	147.1	0.93	0.70	0.7115	1.8	29.270	1.8	0.29830	0.4	0.97	3464	48	3462	18	3462	7	100
OG1-03	128196	143	132.4	0.65	1.08	0.7105	2.2	28.910	2.3	0.29510	0.7	0.96	3460	59	3450	23	3445	10	100
OG1-04	123805	134	119.6	0.48	b.d.	0.7121	1.8	29.250	1.8	0.29790	0.5	0.97	3466	48	3462	18	3459	7	100
OG1-05	194964	180	180.5	0.94	0.87	0.7109	2.0	28.965	2.0	0.29551	0.4	0.98	3462	53	3452	20	3447	7	100
OG1-07	83721	93	85.3	0.72	2.41	0.7102	1.8	29.150	1.8	0.29760	0.5	0.96	3459	48	3458	18	3458	8	100
OG1-08	72584	82	77.0	0.82	0.08	0.7075	1.8	29.120	1.8	0.29840	0.5	0.96	3449	47	3457	18	3462	7	100
OG1-09	135953	155	140.1	0.59	0.25	0.7127	1.8	29.290	1.8	0.29800	0.4	0.98	3469	48	3463	18	3460	6	100
OG1-10	132368	129	129.5	0.92	0.05	0.7125	1.8	29.210	2.0	0.29730	0.8	0.91	3468	49	3460	20	3456	13	100
Average (n=9)		**137**	**130.5**	**0.746**		**0.7112**		**29.144**		**0.2972**			**3463**		**3458**		**3456**		
2 S.D. ext. (abs.)		**64**	**66.8**	**0.332**		**0.0033**		**0.2650**		**0.0024**			**13**		**9**		**13**		
2 S.D. ext. (%)						**0.5**		**0.9**		**0.8**			**Conc. Age = 3458 ± 7 Ma**						
													(MSWD$_{C+E}$ = 1.3 ; P$_{C+E}$ = 0.17)						
Session #2 (August 13th, 2014)																			
OG1-01	294755	109	110.1	1.20	1.65	0.7105	1.0	29.267	1.2	0.29876	0.7	0.83	3463	12	3460	27	3464	10	100
OG1-02	526578	195	197.2	1.39	0.59	0.7105	0.7	29.212	0.9	0.29819	0.5	0.85	3461	9	3460	20	3461	7	100
OG1-03	288100	108	117.4	1.62	1.33	0.7114	1.4	29.347	1.5	0.29917	0.6	0.91	3465	15	3464	37	3466	10	100
OG1-04	89588.9	41	36.9	0.59	0.14	0.7174	1.3	29.502	1.4	0.29827	0.6	0.91	3470	14	3486	35	3461	9	101
OG1-06	151415	65	62.3	1.11	b.d.	0.7085	1.2	29.184	1.3	0.29875	0.4	0.95	3460	13	3453	33	3464	6	100
OG1-07	185387	65	67.3	1.26	1.58	0.7120	1.4	29.130	1.5	0.29674	0.7	0.89	3458	15	3466	36	3453	11	100
OG1-08	111215	37	37.4	1.34	1.30	0.7079	1.3	29.217	1.5	0.29933	0.6	0.91	3461	14	3451	36	3467	9	100
OG1-09	129496	52	52.1	1.07	1.56	0.7136	1.9	29.433	2.0	0.29915	0.8	0.92	3468	20	3472	51	3466	13	100
OG1-10	112791	47	41.9	0.63	0.35	0.7087	1.5	29.210	1.6	0.29894	0.5	0.95	3461	16	3453	40	3465	8	100
OG1-11	209092	107	102.2	0.96	1.31	0.7119	1.5	29.343	1.6	0.29893	0.6	0.94	3465	16	3466	41	3465	9	100
Average (n=10)		**82**	**82.5**	**1.116**		**0.7112**		**29.285**		**0.2986**			**3463**		**3463**		**3463**		
2 S.D. ext. (abs.)		**97**	**100.7**	**0.646**		**0.0056**		**0.2369**		**0.0015**			**8**		**21**		**8**		
2 S.D. ext. (%)						**0.8**		**0.8**		**0.5**			**Conc. Age = 3463 ± 6 Ma**						
													(MSWD$_{C+E}$ = 0.44 ; P$_{C+E}$ = 0.98)						
BB																			
Session #1 (April 9th, 2014)																			
Degeo-01	18079	601	53.3	0.16	b.d.	0.0917	1.7	0.7447	2.1	0.05889	1.3	0.80	565	9	566	9	563	27	100
Degeo-02	18031	609	54.6	0.16	b.d.	0.0928	1.6	0.7568	2.4	0.05913	1.8	0.67	572	10	572	9	572	38	100
Degeo-03	17521	596	53.9	0.16	0.06	0.0937	1.7	0.7647	2.2	0.05920	1.5	0.75	577	10	577	9	575	32	100
Degeo-04	16787	596	53.0	0.16	b.d.	0.0922	1.5	0.7512	1.7	0.05911	0.8	0.89	569	7	568	8	571	17	99
Degeo-05	15704	570	50.6	0.16	0.05	0.0921	1.6	0.7494	2.1	0.05903	1.5	0.73	568	9	568	9	568	32	100
Degeo-06	15051	577	51.5	0.15	b.d.	0.0926	1.6	0.7541	1.9	0.05909	0.9	0.87	571	8	571	9	570	20	100
Degeo-07	14959	570	50.4	0.16	0.02	0.0916	1.5	0.7448	2.3	0.05897	1.7	0.67	565	10	565	8	566	37	100
Degeo-08	14648	566	50.0	0.17	b.d.	0.0915	1.5	0.7448	1.8	0.05903	1.0	0.85	565	8	564	8	568	21	99
Degeo-09	14207	563	50.1	0.16	b.d.	0.0922	1.5	0.7507	1.7	0.05908	0.9	0.86	569	7	568	8	570	19	100

Laurent et al., 2017. Supplementary Table S1 (continued):
Results of LA-SF-ICPMS U–Pb analyses of standard zircons GJ-1, Plesoviče, OG-1 and BB.

	^{207}Pb[a] (cps)	U[b] (ppm)	Pb[b] (ppm)	Th[b] U	^{206}Pbc[c] (%)	$^{206}Pb/^{238}U$[d]	±2σ (%)	$^{207}Pb/^{235}U$[e]	±2σ (%)	$^{207}Pb/^{206}Pb$[d]	±2σ (%)	ρ[f]	$^{206}Pb/^{238}U$	±2σ (Ma)	$^{207}Pb/^{235}U$	±2σ (Ma)	$^{207}Pb/^{206}Pb$	±2σ (Ma)	conc.[g] (%)
Degeo-10	14377	552	49.6	0.16	0.01	0.0928	1.5	0.7570	2.1	0.05916	1.4	0.72	572	9	572	8	573	31	100
Degeo-11	14544	573	51.3	0.16	b.d.	0.0927	1.6	0.7555	2.5	0.05912	2.0	0.62	571	11	571	9	571	43	100
Average (n=11)		**579**	**51.7**	**0.159**		**0.0923**		**0.7522**		**0.0591**			**569**		**569**		**570**		
2 S.D. ext. (abs.)		**36**	**3.5**	**0.007**		**0.0013**		**0.0125**		**0.0002**			**7**		**8**		**7**		
2 S.D. ext. (%)						**1.4**		**1.7**		**0.3**			**Conc. Age = 569.3 ± 2.5 Ma**						
													(MSWD$_{C+E}$ = 0.39 ; P$_{C+E}$ = 0.99)						

$^{206}Pb/^{238}U$ error is the quadratic addition of the within run precision (2σ) and the external reproducibility (2σ ext.) of the reference zircon GJ-1

$^{207}Pb/^{206}Pb$ uncertainty is calculated using ^{207}Pb signal dependent error propagation following Gerdes & Zeh (2009)

$^{207}Pb/^{235}U$ error is the quadratic addition of the $^{207}Pb/^{206}Pb$ and $^{206}Pb/^{238}U$ uncertainties

(a) Within-run background-corrected mean ^{207}Pb signal in cps (counts per second).

(b) U and Pb contents (in ppm) and Th/U ratios were calculated relative to GJ-1 reference zircon (U = 280 ppm; Pb = 25.5 ppm).

(c) Percentage of the common Pb on the ^{206}Pb (b.d. = below dectection limit) calculated using the interference- and background-corrected ^{204}Pb signal and common Pb model composition of Stacey & Kramers (1975).

(d) Corrected for background, within-run Pb/U fractionation (in case of $^{206}Pb/^{238}U$) and common Pb, and subsequently normalized to GJ-1 (ID-TIMS value/measured value).

(e) $^{207}Pb/^{235}U = {}^{207}Pb/^{206}Pb/(^{238}U/^{206}Pb*1/137.88)$

(f) ρ (rho) is the correlation coefficient between errors of $^{206}Pb/^{238}U$ and $^{207}Pb/^{235}U$.

(g) Degree of concordance = ($^{206}Pb/^{238}U$ age / $^{207}Pb/^{206}Pb$ age) × 100

Laurent et al., 2016. Supplementary Table S2:
Results of LA-SF-ICPMS U–Pb analyses of zircons from granitoids and vaugnerites of the Eastern French Massif Central.

	^{207}Pb[a] (cps)	U[b] (ppm)	Pb[b] (ppm)	Th[b]/U	^{206}Pbc[c] (%)	$^{206}Pb/^{238}U$[d]	±2σ (%)	$^{207}Pb/^{235}U$[e]	±2σ (%)	$^{207}Pb/^{206}Pb$[d]	±2σ (%)	ρ[f]	$^{206}Pb/^{238}U$	±2σ (Ma)	$^{207}Pb/^{235}U$	±2σ (Ma)	$^{207}Pb/^{206}Pb$	±2σ (Ma)	conc.[g] (%)
Granitoids																			
CHZ																			
Session #1 (April 9th, 2014)																			
a78	21589	1375	289.4	0.91	0.18	0.0528	1.8	0.3856	2.1	0.05293	1.1	0.85	332	6	331	6	326	25	102
a79	35429	2350	569.9	1.58	b.d.	0.0523	1.7	0.3827	1.9	0.05305	0.8	0.90	329	5	329	5	331	18	99
a80	67049	3232	709.8	1.39	1.30	0.0532	1.4	0.3889	2.8	0.05297	2.4	0.49	334	4	334	8	327	55	102
a82	11302	708	161.7	1.48	0.43	0.0532	1.5	0.3945	2.9	0.05381	2.5	0.51	334	5	338	8	363	56	92
a83	88527	4154	880.0	0.74	3.64	0.0532	1.6	0.3840	5.0	0.05240	4.7	0.32	334	5	330	14	303	106	110
a84	39364	2805	475.8	0.44	0.73	0.0479	1.5	0.3459	2.2	0.05239	1.6	0.67	302	4	302	6	303	37	100
a85	32384	911	200.8	0.58	8.34	0.0528	2.0	0.3845	6.5	0.05285	6.2	0.31	331	7	330	19	322	142	103
a86	23058	1543	252.4	0.28	0.92	0.0482	1.6	0.3483	2.4	0.05245	1.8	0.65	303	5	303	6	305	41	99
a87	40005	556	208.2	0.21	4.81	0.1014	2.9	0.8484	5.2	0.06066	4.4	0.55	623	17	624	25	627	94	99
a88	15521	1108	267.5	1.86	b.d.	0.0492	1.6	0.3615	2.2	0.05324	1.5	0.73	310	5	313	6	339	34	91
a89	8910	689	27.0	0.93	0.04	0.0500	1.4	0.3661	2.4	0.05315	1.9	0.61	314	4	317	6	335	42	94
a91	247927	8905	421.2	0.43	3.95	0.0652	1.6	0.4938	4.4	0.05495	4.1	0.35	407	6	407	15	410	91	99
a92	10515	745	62.9	1.07	0.53	0.0486	1.7	0.3601	3.2	0.05371	2.7	0.53	306	5	312	9	359	61	85
a93	26595	1853	167.2	1.43	0.30	0.0487	1.6	0.3573	1.9	0.05321	1.0	0.85	307	5	310	5	338	23	91
a94	38005	1569	59.6	0.31	3.03	0.0523	1.6	0.3838	4.0	0.05325	3.7	0.39	328	5	330	11	339	83	97
a95	20519	555	160.7	0.11	2.09	0.0868	1.6	0.6992	3.0	0.05844	2.6	0.53	536	8	538	13	546	56	98
a96	32949	2216	403.4	0.56	0.27	0.0502	1.8	0.3664	2.1	0.05298	1.2	0.83	315	5	317	6	328	27	96
a97	67341	3270	711.4	1.45	1.39	0.0462	1.6	0.3368	2.3	0.05291	1.7	0.70	291	5	295	6	325	38	90
a98	31208	1691	259.5	0.36	3.35	0.0478	2.0	0.3506	4.2	0.05325	3.7	0.47	301	6	305	11	339	83	89
a99	217754	1286	866.0	0.30	0.14	0.1809	2.4	3.8324	2.4	0.15366	0.4	0.98	1072	23	1600	20	2387	7	45
a100	75903	4345	644.2	0.15	2.33	0.0436	1.6	0.3197	3.6	0.05323	3.2	0.45	275	4	282	9	339	73	81
a101	15899	741	178.6	0.29	0.06	0.0729	1.5	0.5615	1.8	0.05583	1.0	0.83	454	6	452	6	446	22	102
HER																			
Session #2 (August 13th, 2014)																			
a245	101734	102	58.9	0.75	b.d.	0.4947	0.8	11.999	1.0	0.17593	0.6	0.79	2591	17	2604	9	2615	10	99
a246	20973	620	50.2	2.84	0.64	0.0508	0.8	0.3626	2.6	0.05182	2.5	0.30	319	2	314	7	277	58	115
a247	15138	472	28.5	1.59	0.61	0.0447	1.1	0.3211	3.2	0.05215	2.9	0.36	282	3	283	8	292	67	96
a248	13916	445	26.6	1.23	b.d.	0.0491	0.9	0.3605	1.3	0.05320	0.9	0.71	309	3	313	3	337	20	92
a249	83250	2323	113.6	0.06	0.72	0.0520	0.8	0.3796	1.4	0.05295	1.1	0.58	327	3	327	4	327	26	100
a250	5720	190	9.4	0.42	b.d.	0.0491	0.8	0.3574	1.5	0.05283	1.3	0.55	309	3	310	4	322	29	96
a251	17363	609	29.2	0.55	0.51	0.0451	1.4	0.3368	4.7	0.05411	4.5	0.30	285	4	295	12	376	102	76
a253	24601	539	25.9	0.23	2.78	0.0467	0.8	0.3392	3.6	0.05271	3.5	0.22	294	2	297	9	316	80	93
a254	7860	244	12.5	0.63	0.00	0.0475	0.8	0.3953	1.8	0.06036	1.6	0.43	299	2	338	5	617	35	49
a255	43239	1746	65.8	0.64	0.81	0.0324	1.4	0.2382	2.2	0.05329	1.8	0.61	206	3	217	4	341	40	60
a256	36135	851	53.5	1.27	1.76	0.0501	0.7	0.3655	2.8	0.05288	2.7	0.24	315	2	316	8	324	61	97
a257	30756	544	36.2	0.41	0.65	0.0636	0.9	0.4915	2.0	0.05609	1.7	0.47	397	4	406	7	456	38	87
a258	102320	3233	155.8	0.02	0.40	0.0521	1.0	0.3777	1.3	0.05263	0.8	0.76	327	3	325	4	313	19	105
a259	33620	608	35.5	0.71	3.87	0.0515	0.8	0.3776	4.3	0.05313	4.2	0.18	324	2	325	12	334	96	97
a260	11192	365	18.9	0.66	0.50	0.0471	1.4	0.3849	2.5	0.05932	2.1	0.55	296	4	331	7	579	45	51
a261	57890	1336	59.6	0.18	1.85	0.0443	1.0	0.3239	2.7	0.05301	2.5	0.37	280	3	285	7	329	57	85
a262	207029	7292	260.0	0.05	1.22	0.0374	0.8	0.2729	1.9	0.05294	1.8	0.42	237	2	245	4	326	40	73
a263	16903	519	25.6	0.22	0.14	0.0510	0.7	0.3731	1.2	0.05310	1.0	0.58	320	2	322	3	333	23	96
a264	12380	304	17.2	1.26	3.00	0.0428	1.1	0.3335	6.2	0.05651	6.1	0.18	270	3	292	16	473	134	57
a265	23899	286	28.6	0.36	1.78	0.0959	0.8	0.8105	3.4	0.06131	3.3	0.24	590	5	603	16	650	71	91
a267	198243	6273	273.8	0.13	0.55	0.0457	0.9	0.3335	1.3	0.05290	1.0	0.65	288	2	292	3	324	23	89
a268	122957	3735	179.6	0.39	0.24	0.0487	0.9	0.3544	1.1	0.05282	0.7	0.81	306	3	308	3	321	15	95
a269	7107	214	13.6	1.47	b.d.	0.0494	0.8	0.4020	1.6	0.05903	1.4	0.51	311	3	343	5	568	31	55
a270	22163	658	34.4	0.40	0.16	0.0518	1.0	0.3787	1.9	0.05306	1.7	0.52	325	3	326	5	331	38	98
a271	69886	1405	78.2	0.80	3.76	0.0475	1.0	0.3453	4.4	0.05277	4.3	0.22	299	3	301	11	319	97	94
a272	51563	397	57.2	0.28	0.74	0.1429	1.0	1.3354	1.9	0.06777	1.7	0.51	861	8	861	11	862	34	100
a273	11701	314	16.3	0.93	1.65	0.0432	1.2	0.3122	5.8	0.05240	5.6	0.21	273	3	276	14	303	129	90
a274	15460	436	23.4	0.44	0.63	0.0519	0.9	0.3791	1.9	0.05296	1.7	0.48	326	3	326	5	327	38	100
OL-13-06																			
Session #1 (April 9th, 2014)																			
a234	8476	682	30.4	0.39	0.29	0.0428	1.6	0.3114	2.1	0.05274	1.4	0.77	270	4	275	5	318	31	85
a235	33179	2312	120.3	0.56	1.28	0.0469	1.7	0.3391	2.8	0.05240	2.3	0.59	296	5	297	7	303	52	98
a236	8943	471	24.6	0.24	3.10	0.0500	1.6	0.3671	4.0	0.05324	3.7	0.39	315	5	318	11	339	84	93
a237	116707	2866	104.1	0.22	37.11	0.0183	6.0	0.1314	13.9	0.05213	12.6	0.43	117	7	125	17	291	287	40
a243	10925	704	32.0	0.41	2.55	0.0416	1.6	0.3025	3.6	0.05271	3.3	0.43	263	4	268	9	316	74	83
a244	411736	9091	369.8	0.25	41.96	0.0202	4.7	0.1458	12.9	0.05225	12.0	0.37	129	6	138	17	297	273	44
a245	30134	1475	63.5	0.28	4.11	0.0383	1.7	0.2793	5.1	0.05289	4.9	0.32	242	4	250	11	324	111	75
a246	15226	381	23.9	0.89	12.88	0.0418	3.1	0.3017	9.4	0.05231	8.9	0.33	264	8	268	22	299	203	88

Laurent et al., 2016. Supplementary Table S2 (continued):
Results of LA-SF-ICPMS U–Pb analyses of zircons from granitoids and vaugnerites of the Eastern French Massif Central.

	^{207}Pb[a] (cps)	U[b] (ppm)	Pb[b] (ppm)	Th/U[b]	^{206}Pbc[c] (%)	$^{206}Pb/^{238}U$[d]	±2σ (%)	$^{207}Pb/^{235}U$[e]	±2σ (%)	$^{207}Pb/^{206}Pb$[d]	±2σ (%)	ρ[f]	$^{206}Pb/^{238}U$	±2σ (Ma)	$^{207}Pb/^{235}U$	±2σ (Ma)	$^{207}Pb/^{206}Pb$	±2σ (Ma)	conc.[g] (%)
a247	19192	1277	67.0	0.38	1.38	0.0499	2.7	0.3626	3.7	0.05270	2.5	0.73	314	8	314	10	316	58	99
a248	37600	2095	92.8	0.47	3.22	0.0377	1.8	0.2799	4.2	0.05380	3.8	0.42	239	4	251	9	363	85	66
a249	41753	1531	66.9	0.08	13.34	0.0361	2.1	0.2610	7.8	0.05241	7.5	0.27	229	5	235	17	303	172	75
a250	9648	805	38.8	0.38	0.58	0.0462	1.8	0.3399	2.8	0.05333	2.1	0.64	291	5	297	7	343	48	85
a251	6595	541	25.9	0.23	0.14	0.0491	1.9	0.3567	2.2	0.05272	1.1	0.86	309	6	310	6	317	25	98
a252	12622	694	35.2	0.50	3.53	0.0447	1.7	0.3275	4.6	0.05311	4.3	0.36	282	5	288	12	333	98	85
a253	15146	540	29.0	0.37	8.03	0.0443	1.7	0.3162	6.6	0.05179	6.3	0.26	279	5	279	16	276	145	101
a254	34792	1364	71.8	0.32	6.02	0.0445	1.8	0.3259	4.9	0.05314	4.5	0.37	281	5	286	12	335	103	84
a255	4164	305	14.9	0.52	0.41	0.0446	1.8	0.3360	5.6	0.05459	5.3	0.31	282	5	294	14	395	119	71
a256	15171	933	45.9	0.58	2.16	0.0435	1.8	0.3101	3.7	0.05176	3.2	0.49	274	5	274	9	275	74	100
a257	8421	483	28.2	0.42	2.99	0.0496	1.7	0.3532	6.5	0.05170	6.2	0.26	312	5	307	17	272	142	115
a258	6600	500	26.1	0.40	0.72	0.0448	1.4	0.3307	2.4	0.05349	1.9	0.60	283	4	290	6	350	43	81
a259	13672	796	41.0	0.19	3.29	0.0499	2.0	0.3639	4.5	0.05285	4.1	0.44	314	6	315	12	322	92	98
a260	13360	564	29.6	0.37	6.25	0.0452	1.7	0.3263	6.0	0.05230	5.8	0.29	285	5	287	15	299	131	96
a261	307437	8298	190.6	0.05	61.23	0.0049	9.1	0.0332	14.5	0.04938	11.3	0.63	31	3	33	5	166	263	19
a262	7184	355	19.4	1.00	1.60	0.0405	2.3	0.2954	4.7	0.05296	4.1	0.48	256	6	263	11	327	94	78
a263	39557	1660	79.1	0.33	8.55	0.0393	1.8	0.2860	8.0	0.05278	7.8	0.22	249	4	255	18	319	177	78
a264	26277	1993	103.6	0.51	0.18	0.0480	1.4	0.3502	1.8	0.05287	1.2	0.76	302	4	305	5	323	26	94
a265	6709	285	15.3	0.47	4.93	0.0453	1.6	0.3263	5.4	0.05228	5.1	0.30	285	5	287	13	298	117	96
a266	27205	864	51.3	0.19	8.52	0.0501	2.5	0.3760	8.9	0.05443	8.5	0.28	315	8	324	25	389	191	81
a267	25426	1861	96.1	0.41	0.80	0.0495	1.5	0.3586	2.3	0.05253	1.7	0.66	311	5	311	6	309	39	101
a268	5821	443	23.0	0.50	0.79	0.0500	1.6	0.3644	2.5	0.05283	1.9	0.64	315	5	316	7	321	43	98
a269	8086	649	28.6	0.16	0.13	0.0460	1.5	0.3346	1.9	0.05279	1.2	0.78	290	4	293	5	320	27	91
a270	9080	577	30.6	0.78	2.28	0.0435	2.3	0.3003	4.8	0.05004	4.2	0.49	275	6	267	11	197	97	140
a271	14648	797	37.1	0.44	3.64	0.0398	2.1	0.2915	5.5	0.05317	5.1	0.38	251	5	260	13	336	116	75
OL-13-08																			
Session #2 (August 13th, 2014)																			
a86	132723	2706	168.1	0.06	0.42	0.0664	0.9	0.5301	1.2	0.05791	0.8	0.78	414	4	432	4	526	17	79
a87	24139	756	21.9	0.28	4.53	0.0248	3.6	0.1793	6.3	0.05250	5.1	0.58	158	6	167	10	307	117	51
a88	9127	223	15.6	0.30	b.d.	0.0702	1.1	0.5640	1.6	0.05824	1.2	0.67	438	4	454	6	539	25	81
a89	8012	173	13.1	0.33	0.02	0.0766	0.9	0.6001	1.6	0.05681	1.4	0.52	476	4	477	6	484	31	98
a90	17051	290	26.2	0.37	b.d.	0.0901	0.8	0.7290	1.1	0.05869	0.8	0.67	556	4	556	5	556	18	100
a91	20271	259	21.8	0.20	2.70	0.0836	1.0	0.6793	3.9	0.05896	3.7	0.25	517	5	526	16	566	81	91
a92	75314	1854	87.8	0.04	2.05	0.0491	0.6	0.3559	2.7	0.05261	2.6	0.23	309	2	309	7	312	60	99
a93	17613	352	19.0	0.59	5.42	0.0461	1.5	0.3796	6.6	0.05970	6.4	0.23	291	4	327	18	593	138	49
a94	12135	156	13.9	0.35	0.73	0.0871	0.9	0.6894	3.4	0.05743	3.3	0.27	538	5	532	14	508	71	106
a95	32420	1223	55.9	0.05	0.02	0.0495	1.1	0.3592	1.3	0.05262	0.6	0.88	312	3	312	3	313	14	100
a96	9751	195	13.4	0.33	1.22	0.0677	0.8	0.5423	2.6	0.05812	2.4	0.32	422	3	440	9	534	53	79
a97	14311	540	26.2	0.26	0.00	0.0498	0.9	0.3617	1.6	0.05265	1.3	0.60	313	3	313	4	314	29	100
a98	109557	2565	119.4	0.04	2.94	0.0472	0.9	0.3416	3.6	0.05254	3.5	0.24	297	2	298	9	309	80	96
a99	83214	1626	95.9	0.90	1.21	0.0493	0.9	0.3580	2.3	0.05271	2.1	0.40	310	3	311	6	316	47	98
a100	12600	208	18.4	0.32	0.08	0.0891	0.9	0.7217	1.4	0.05877	1.1	0.65	550	5	552	6	559	23	98
a106	68329	271	66.2	0.62	0.38	0.2194	1.4	3.1122	1.7	0.10289	1.0	0.83	1279	17	1436	13	1677	18	76
a107	122168	1381	113.9	0.04	3.95	0.0817	1.1	0.6578	4.2	0.05837	4.1	0.26	506	5	513	17	544	89	93
a108	8780	297	15.2	0.34	0.03	0.0516	0.9	0.3760	1.8	0.05289	1.6	0.48	324	3	324	5	324	36	100
a109	120114	2561	145.4	0.51	5.11	0.0511	0.9	0.3726	5.6	0.05290	5.6	0.16	321	3	322	16	325	126	99
a110	61608	1225	51.9	0.39	5.28	0.0379	2.0	0.2740	6.2	0.05245	5.9	0.32	240	5	246	14	305	135	79
a111	57111	1297	44.7	0.14	16.71	0.0305	2.4	0.2238	12.0	0.05322	11.7	0.20	194	5	205	22	338	266	57
a112	14039	241	20.8	0.25	0.02	0.0882	0.9	0.7140	1.3	0.05870	0.9	0.70	545	5	547	6	556	20	98
a113	71625	196	60.9	0.76	0.08	0.2581	0.8	4.2217	1.1	0.11864	0.7	0.76	1480	11	1678	9	1936	13	76
a114	17360	490	33.1	1.04	0.11	0.0579	0.8	0.4283	1.3	0.05367	1.1	0.57	363	3	362	4	357	25	102
a115	18221	304	25.9	0.10	0.07	0.0902	0.9	0.7314	1.2	0.05880	0.8	0.75	557	5	557	5	560	17	100
a116	68943	542	92.4	0.61	0.07	0.1594	0.7	1.5596	1.0	0.07098	0.7	0.69	953	6	954	6	957	15	100
a117	731345	880	437.1	0.48	b.d.	0.4569	0.6	10.724	0.7	0.17022	0.3	0.92	2426	12	2499	6	2560	4	95
a118	16700	41	17.8	1.66	0.05	0.3322	1.0	5.1603	1.3	0.11265	0.8	0.77	1849	16	1846	11	1843	15	100
a119	19706	424	31.2	0.19	0.01	0.0768	0.9	0.6006	1.3	0.05671	1.0	0.69	477	4	478	5	480	22	99
a120	55645	1741	91.8	0.41	b.d.	0.0525	0.6	0.3914	1.0	0.05411	0.7	0.67	330	2	335	3	376	16	88
a121	70588	674	91.4	0.22	0.03	0.1387	1.0	1.2871	1.1	0.06729	0.5	0.89	837	8	840	6	847	11	99
a122	31090	984	46.1	0.08	0.44	0.0498	0.9	0.3621	1.6	0.05276	1.3	0.57	313	3	314	4	318	30	98
a123	11769	181	18.7	0.75	0.05	0.0936	0.9	0.7703	1.5	0.05966	1.1	0.64	577	5	580	6	591	24	98
a124	85846	2625	120.9	0.04	0.57	0.0496	0.7	0.3588	1.3	0.05250	1.1	0.55	312	2	311	4	307	26	101
a125	52574	501	30.7	0.07	10.68	0.0507	2.5	0.3963	7.7	0.05671	7.2	0.33	319	8	339	22	480	160	66
a126	22164	337	27.9	0.08	1.33	0.0860	0.8	0.7021	2.1	0.05919	2.0	0.37	532	4	540	9	574	43	93
a127	36726	583	33.3	0.75	7.65	0.0486	1.3	0.3570	6.9	0.05331	6.8	0.19	306	4	310	19	342	154	89
a128	160789	2602	216.2	0.02	1.48	0.0879	1.0	0.7054	2.1	0.05822	1.9	0.47	543	5	542	9	538	41	101

Laurent et al., 2016. Supplementary Table S2 (continued):
Results of LA-SF-ICPMS U–Pb analyses of zircons from granitoids and vaugnerites of the Eastern French Massif Central.

	^{207}Pb[a] (cps)	U[b] (ppm)	Pb[b] (ppm)	Th/U[b]	^{206}Pbc[c] (%)	$^{206}Pb/^{238}U$[d]	±2σ (%)	$^{207}Pb/^{235}U$[e]	±2σ (%)	$^{207}Pb/^{206}Pb$[d]	±2σ (%)	ρ[f]	$^{206}Pb/^{238}U$	±2σ (Ma)	$^{207}Pb/^{235}U$	±2σ (Ma)	$^{207}Pb/^{206}Pb$	±2σ (Ma)	conc.[g] (%)
OL-13-09																			
Session #1 (April 9th, 2014)																			
a06	6229	424	15.2	0.31	0.25	0.0496	1.6	0.3601	3.9	0.05260	3.6	0.41	312	5	312	11	312	82	100
a07	5941	215	62.8	0.16	0.16	0.0868	1.8	0.7001	3.6	0.05847	3.1	0.50	537	9	539	15	547	68	98
a08	11689	387	134.5	0.54	0.17	0.0915	1.6	0.7462	2.8	0.05915	2.3	0.56	564	8	566	12	572	50	99
a09	32399	864	261.3	0.16	2.01	0.0869	1.8	0.6958	3.5	0.05809	3.0	0.50	537	9	536	15	533	66	101
a10	75497	2225	651.4	0.04	1.35	0.0880	1.5	0.7056	2.3	0.05816	1.8	0.64	544	8	542	10	536	39	101
a11	125517	3193	967.4	0.04	2.58	0.0888	1.4	0.7165	3.3	0.05854	2.9	0.44	548	7	549	14	550	64	100
a12	17135	583	163.5	0.09	0.50	0.0846	1.6	0.6773	2.0	0.05808	1.2	0.80	523	8	525	8	533	27	98
a13	94422	3157	862.5	0.02	0.30	0.0848	1.5	0.6789	1.7	0.05807	0.8	0.90	525	8	526	7	532	16	99
a15	29835	738	222.2	0.73	5.00	0.0661	1.6	0.5178	6.5	0.05680	6.3	0.25	413	6	424	23	484	140	85
a16	34535	1245	239.1	0.21	6.54	0.0496	1.8	0.3634	6.0	0.05319	5.7	0.31	312	6	315	16	337	130	93
a17	58537	1167	298.6	0.76	10.93	0.0500	1.8	0.3625	6.9	0.05263	6.6	0.26	314	6	314	19	313	150	100
a18	87595	4274	771.3	0.23	3.76	0.0490	1.5	0.3567	4.5	0.05276	4.3	0.34	309	5	310	12	319	97	97
a19	8290	307	91.4	0.16	0.15	0.0888	1.8	0.7204	2.2	0.05884	1.3	0.80	548	9	551	10	561	29	98
a20	79090	2095	649.0	0.23	1.98	0.0862	1.6	0.6912	3.1	0.05817	2.7	0.51	533	8	533	13	536	58	99
a21	51266	1846	516.4	0.04	0.19	0.0870	1.4	0.6946	1.5	0.05790	0.6	0.92	538	7	536	6	526	13	102
a22	28606	873	254.0	0.08	1.32	0.0867	1.7	0.6994	2.5	0.05851	1.8	0.68	536	9	538	10	549	39	98
a24	207338	784	437.6	0.17	20.91	0.0504	2.7	0.3642	5.8	0.05240	5.2	0.46	317	8	315	16	303	118	105
a26	19363	772	198.3	0.09	0.31	0.0785	1.6	0.6259	1.9	0.05781	1.1	0.82	487	7	494	8	523	25	93
a28	31144	1104	322.5	0.14	1.26	0.0864	1.5	0.6997	2.5	0.05875	2.0	0.59	534	8	539	11	558	44	96
a30	64226	1806	484.1	0.08	3.51	0.0779	1.7	0.6117	4.3	0.05693	3.9	0.40	484	8	485	17	489	87	99
a31	99800	3444	988.6	0.05	0.31	0.0892	1.5	0.7222	1.6	0.05870	0.6	0.94	551	8	552	7	556	12	99
a32	15163	378	151.6	0.43	0.74	0.1084	1.9	0.9392	2.7	0.06283	1.9	0.71	664	12	672	14	702	41	94
a38	19889	599	143.1	0.32	4.94	0.0625	1.8	0.4545	5.6	0.05275	5.3	0.32	391	7	380	18	318	121	123
a39	9761	280	89.2	0.36	0.83	0.0889	1.9	0.7166	2.8	0.05844	2.0	0.69	549	10	549	12	546	44	101
a40	60484	1221	308.9	0.75	10.91	0.0504	1.9	0.3650	8.3	0.05257	8.1	0.23	317	6	316	23	310	184	102
OL-13-11																			
Session #2 (August 13th, 2014)																			
a129	58162	1001	53.0	0.19	5.38	0.0498	1.0	0.3634	5.5	0.05290	5.4	0.19	313	3	315	15	325	122	97
a130	128489	1147	76.8	0.59	14.45	0.0483	2.0	0.3581	8.6	0.05376	8.4	0.23	304	6	311	23	361	189	84
a131	8341	165	13.6	0.64	b.d.	0.0742	1.8	0.8263	4.3	0.08073	3.9	0.42	462	8	612	20	1215	77	38
a132	303874	6040	153.2	0.23	18.82	0.0182	2.5	0.1316	8.6	0.05247	8.2	0.30	116	3	126	10	306	186	38
a133	21177	582	32.8	0.45	0.69	0.0543	0.6	0.4287	1.6	0.05724	1.5	0.39	341	2	362	5	501	33	68
a134	144076	529	101.4	0.13	0.70	0.1898	0.9	2.9639	1.1	0.11328	0.7	0.80	1120	9	1398	9	1853	12	60
a135	15341	391	22.8	0.62	1.04	0.0536	0.7	0.3985	2.3	0.05397	2.2	0.32	336	2	341	7	370	49	91
a136	207569	1868	90.1	0.50	31.73	0.0281	3.7	0.2158	11.7	0.05570	11.1	0.32	179	7	198	21	441	247	41
a137	16868	396	21.9	0.51	1.81	0.0509	0.9	0.4120	4.3	0.05867	4.2	0.21	320	3	350	13	555	93	58
a138	120401	1459	68.9	0.37	20.48	0.0334	2.8	0.2429	9.8	0.05269	9.3	0.29	212	6	221	20	316	213	67
a139	28659	313	22.7	0.24	5.87	0.0653	1.4	0.5742	6.1	0.06374	5.9	0.23	408	6	461	23	733	126	56
a140	65007	870	75.2	0.57	3.83	0.0765	1.1	0.5975	4.6	0.05664	4.4	0.24	475	5	476	18	477	98	100
a141	56605	1188	88.0	0.44	b.d.	0.0720	0.6	0.5852	0.8	0.05892	0.5	0.81	448	3	468	3	564	10	79
a142	19207	133	11.4	1.36	15.93	0.0502	1.8	0.3652	7.7	0.05276	7.5	0.24	316	6	316	21	318	170	99
a143	13265	290	20.9	0.17	0.00	0.0755	0.6	0.6100	1.1	0.05856	0.9	0.57	469	3	484	4	551	19	85
a144	12741	283	15.3	0.61	2.81	0.0500	0.9	0.3674	5.3	0.05331	5.3	0.17	314	3	318	15	342	119	92
a150	24602	486	27.0	0.20	3.15	0.0541	0.8	0.4022	3.7	0.05396	3.6	0.23	339	3	343	11	370	82	92
a151	86435	181	78.6	0.84	b.d.	0.3732	1.1	6.5956	1.3	0.12819	0.8	0.82	2044	19	2059	12	2073	13	99
a152	15728	243	20.4	0.12	0.88	0.0871	0.8	0.7039	1.8	0.05863	1.6	0.43	538	4	541	7	553	35	97
a153	162191	1134	71.0	0.88	23.10	0.0329	2.9	0.2362	10.5	0.05208	10.1	0.28	209	6	215	21	289	230	72
a154	5163	80	9.9	1.66	0.11	0.0951	0.8	0.7774	1.8	0.05930	1.6	0.45	586	4	584	8	578	35	101
a155	92870	1618	68.5	0.41	7.54	0.0330	1.3	0.2426	6.4	0.05337	6.2	0.21	209	3	221	13	345	141	61
a156	217355	3843	83.5	0.26	19.72	0.0132	2.4	0.0964	8.7	0.05280	8.3	0.27	85	2	93	8	320	190	26
a157	102226	875	65.6	0.54	16.74	0.0548	2.2	0.4092	8.4	0.05412	8.1	0.27	344	7	348	25	376	182	92
a158	51654	853	53.1	0.96	8.00	0.0500	1.3	0.3575	7.2	0.05186	7.1	0.19	315	4	310	19	279	162	113
a159	479324	2660	135.0	0.24	51.78	0.0160	5.4	0.1198	15.7	0.05441	14.7	0.35	102	6	115	17	388	330	26
a160	21952	637	22.9	0.22	2.70	0.0350	1.0	0.2511	3.6	0.05205	3.5	0.28	222	2	227	7	288	80	77
a161	25211	305	18.9	0.43	13.23	0.0505	1.8	0.3643	9.4	0.05236	9.2	0.19	317	6	315	26	301	209	105
a162	21734	641	35.5	0.62	0.42	0.0516	0.9	0.4126	1.5	0.05801	1.2	0.59	324	3	351	4	530	26	61
a163	51125	380	17.6	0.07	26.35	0.0240	3.2	0.1763	9.9	0.05326	9.4	0.32	153	5	165	15	340	212	45
OL-13-14																			
Session #1 (April 9th, 2014)																			
a108	60112.4	1436	331.7	0.08	7.18	0.0607	1.9	0.4739	4.6	0.05665	4.2	0.42	380	7	394	15	478	92	79
a109	312949	4032	904.3	0.06	31.34	0.0461	3.4	0.3405	9.8	0.05361	9.1	0.35	290	10	298	25	355	206	82
a110	13263	509	134.8	0.50	b.d.	0.0743	1.5	0.6000	2.1	0.05853	1.5	0.71	462	7	477	8	550	33	84
a111	30021	1149	304.9	0.07	0.05	0.0857	1.4	0.6902	1.7	0.05840	0.9	0.85	530	7	533	7	545	20	97
a112	19306	1554	216.1	0.22	1.55	0.0471	1.5	0.3444	3.8	0.05303	3.5	0.39	297	4	300	10	330	80	90

Laurent et al., 2016. Supplementary Table S2 (continued):
Results of LA-SF-ICPMS U–Pb analyses of zircons from granitoids and vaugnerites of the Eastern French Massif Central.

	^{207}Pb[a] (cps)	U[b] (ppm)	Pb[b] (ppm)	Th/U[b]	^{206}Pbc[c] (%)	$^{206}Pb/^{238}U$[d]	±2σ (%)	$^{207}Pb/^{235}U$[e]	±2σ (%)	$^{207}Pb/^{206}Pb$[d]	±2σ (%)	ρ[f]	$^{206}Pb/^{238}U$	±2σ (Ma)	$^{207}Pb/^{235}U$	±2σ (Ma)	$^{207}Pb/^{206}Pb$	±2σ (Ma)	conc.[g] (%)
a113	32467	631	172.9	0.08	11.52	0.0722	1.9	0.5526	7.9	0.05553	7.7	0.23	449	8	447	29	433	172	104
a114	124530	1860	359.2	0.22	31.10	0.0509	5.1	0.3680	12.5	0.05243	11.4	0.41	320	16	318	35	304	261	105
a115	150794	2768	419.4	0.04	36.94	0.0239	4.3	0.1749	10.6	0.05319	9.6	0.41	152	7	164	16	337	218	45
a116	118973	396	527.5	0.64	0.10	0.3410	1.9	7.4500	1.9	0.15846	0.3	0.98	1891	31	2167	17	2439	6	78
a117	9819	334	108.7	0.34	0.13	0.0965	1.5	0.7957	2.0	0.05978	1.3	0.75	594	8	594	9	596	29	100
a118	70216	1544	241.0	0.23	45.11	0.0259	5.1	0.4517	10.7	0.12630	9.4	0.48	165	8	378	34	2047	166	8
a120	8122	300	82.1	0.11	0.35	0.0870	1.7	0.6980	2.2	0.05820	1.4	0.78	538	9	538	9	537	30	100
a121	15993	660	160.0	0.20	1.25	0.0757	1.7	0.5842	3.0	0.05594	2.5	0.57	471	8	467	11	450	55	105
a122	6839	242	67.0	0.13	0.13	0.0878	1.5	0.7061	1.9	0.05831	1.2	0.77	543	8	542	8	541	26	100
a123	31758	709	176.6	0.13	7.59	0.0682	1.9	0.5213	7.5	0.05545	7.2	0.26	425	8	426	26	431	161	99
a124	14377	519	150.8	0.29	0.29	0.0872	1.6	0.7012	1.9	0.05835	1.0	0.84	539	8	540	8	543	22	99
a125	444834	3784	954.6	0.06	52.28	0.0252	5.6	0.1851	13.3	0.05334	12.1	0.42	160	9	172	21	343	274	47
a126	618828	10120	1133.4	0.10	78.46	0.0051	8.1	0.0430	14.7	0.06078	12.2	0.55	33	3	43	6	631	263	5
a127	27372	1005	265.2	0.08	0.23	0.0850	1.5	0.6815	1.7	0.05817	0.8	0.88	526	8	528	7	536	17	98
a128	28546	737	240.5	0.39	1.97	0.0899	1.6	0.7407	3.4	0.05972	3.0	0.46	555	8	563	15	594	66	94
a129	272602	2283	692.7	0.26	48.48	0.0352	5.2	0.3027	13.8	0.06230	12.7	0.38	223	11	269	33	685	272	33
a130	1007391	8985	1799.9	0.10	75.45	0.0080	8.0	0.0643	14.1	0.05853	11.6	0.57	51	4	63	9	550	254	9
a131	41003	1429	374.0	0.05	0.98	0.0839	1.8	0.6726	2.3	0.05817	1.4	0.79	519	9	522	9	536	31	97
a132	877003	8624	1610.4	0.10	77.18	0.0087	7.9	0.0706	13.6	0.05877	11.1	0.58	56	4	69	9	559	242	10
a133	21784	899	221.3	0.12	0.70	0.0770	1.6	0.6336	2.3	0.05969	1.6	0.72	478	8	498	9	592	34	81
a134	45603	1265	194.2	0.17	11.95	0.0350	2.9	0.2787	7.8	0.05782	7.2	0.38	222	6	250	17	523	158	42
a135	1009967	10394	1779.8	0.09	77.97	0.0059	8.5	0.0475	14.5	0.05821	11.7	0.59	38	3	47	7	538	255	7
a136	10475	420	112.0	0.07	0.28	0.0863	1.8	0.6940	2.3	0.05831	1.4	0.80	534	9	535	9	542	30	99
a137	23120	619	262.5	0.64	0.93	0.1136	1.5	0.9714	2.7	0.06204	2.3	0.55	693	10	689	14	675	49	103
Session #2 (August 13th, 2014)																			
a275	11205	194	17.4	0.76	0.75	0.0822	0.9	0.6684	2.5	0.05899	2.4	0.35	509	4	520	10	567	52	90
a276	42242	380	33.9	0.24	6.04	0.0833	1.0	0.6751	6.2	0.05877	6.1	0.16	516	5	524	26	559	133	92
a278	14296	156	21.7	1.04	0.04	0.1172	0.8	1.0538	1.2	0.06520	1.0	0.63	715	5	731	7	781	20	92
a279	29020	40	18.3	0.94	b.d.	0.3720	1.1	8.0851	1.3	0.15762	0.8	0.81	2039	19	2241	12	2430	13	84
a280	55475	103	44.9	1.51	b.d.	0.3298	1.1	7.1295	1.3	0.15679	0.8	0.81	1837	17	2128	12	2421	13	76
a281	20192	313	31.2	0.84	0.74	0.0885	0.8	0.7098	2.5	0.05817	2.4	0.32	547	4	545	11	536	53	102
a287	23328	369	32.9	0.09	0.04	0.0949	0.6	0.7854	0.9	0.06002	0.7	0.70	584	4	589	4	604	14	97
a288	177320	839	66.7	0.55	28.18	0.0411	3.1	0.3043	10.6	0.05365	10.1	0.29	260	8	270	25	356	229	73
a291	176216	1276	81.8	0.25	19.07	0.0431	2.2	0.3119	8.5	0.05249	8.2	0.25	272	6	276	21	307	188	89
a292	77660	1030	49.1	0.30	12.00	0.0371	1.5	0.2736	7.3	0.05344	7.2	0.21	235	4	246	16	347	163	68
a293	288541	1761	87.3	0.06	31.77	0.0225	3.6	0.1651	9.7	0.05320	9.1	0.36	143	5	155	14	337	206	43
a294	48717	705	40.5	0.28	9.32	0.0505	1.3	0.3712	7.2	0.05334	7.1	0.18	317	4	321	20	343	161	92
a295	257214	3406	174.6	0.08	12.30	0.0438	1.5	0.3208	7.6	0.05317	7.4	0.20	276	4	283	19	336	168	82
a296	149611	1180	74.2	0.32	18.92	0.0426	2.2	0.3096	8.4	0.05267	8.1	0.26	269	6	274	20	314	185	86
a297	49681	744	62.6	0.06	0.59	0.0895	0.8	0.7231	1.5	0.05857	1.3	0.55	553	4	553	7	551	28	100
a300	194946	1072	80.6	0.04	15.25	0.0518	2.8	0.3750	9.1	0.05252	8.7	0.30	325	9	323	26	308	198	106
a301	52899	857	71.0	0.04	0.13	0.0893	0.8	0.7191	1.3	0.05840	0.9	0.66	551	4	550	5	545	21	101
a302	4731	53	6.7	0.59	0.04	0.1211	0.8	1.0704	1.8	0.06413	1.7	0.44	737	6	739	10	746	35	99
a303	105046	2357	132.1	0.60	1.24	0.0505	1.2	0.3675	2.3	0.05276	1.9	0.53	318	4	318	6	318	44	100
a304	186366	1295	124.6	0.37	8.89	0.0774	1.5	0.6583	6.2	0.06168	6.0	0.24	481	7	514	25	663	129	72
OL-13-21																			
Session #1 (April 9th, 2014)																			
a208	25973	1258	73.1	0.08	1.55	0.0588	1.8	0.4366	3.5	0.05386	3.0	0.52	368	7	368	11	365	67	101
a209	94826	745	109.5	0.25	20.64	0.0905	2.7	0.9251	9.0	0.07414	8.5	0.30	558	14	665	45	1045	172	53
a210	50150	2276	115.8	0.06	6.29	0.0499	1.6	0.3661	7.1	0.05316	7.0	0.22	314	5	317	20	336	158	94
a211	35328	2918	133.3	0.06	1.78	0.0477	1.7	0.3499	3.7	0.05319	3.3	0.46	300	5	305	10	337	75	89
a212	141261	8848	468.9	0.12	1.72	0.0540	2.0	0.3922	3.6	0.05268	2.9	0.56	339	7	336	10	315	67	108
a213	55960	3598	192.2	0.17	0.62	0.0544	1.6	0.3996	2.1	0.05328	1.3	0.77	341	5	341	6	341	30	100
a214	48793	3065	161.1	0.17	0.99	0.0531	1.8	0.3889	2.6	0.05310	1.9	0.69	334	6	334	7	333	42	100
a215	14902	728	50.0	0.26	0.25	0.0690	1.8	0.5480	2.2	0.05763	1.2	0.83	430	8	444	8	516	27	83
a216	84786	4802	262.8	0.23	1.44	0.0541	1.5	0.4008	2.5	0.05370	2.0	0.61	340	5	342	7	359	45	95
a217	204546	14729	715.8	0.08	0.65	0.0512	1.8	0.3734	2.0	0.05287	1.0	0.86	322	6	322	6	323	24	100
a218	52703	2819	168.6	0.65	1.83	0.0531	1.5	0.3870	3.1	0.05291	2.7	0.48	333	5	332	9	325	61	103
a219	28541	284	56.3	0.44	2.18	0.1773	1.9	2.1854	2.7	0.08939	2.0	0.69	1052	18	1176	19	1412	38	75
a220	13100	510	43.3	0.36	0.77	0.0802	2.0	0.6511	3.5	0.05888	2.8	0.59	497	10	509	14	563	61	88
a221	53089	1556	93.9	0.15	9.07	0.0520	1.9	0.3817	6.7	0.05321	6.4	0.28	327	6	328	19	338	145	97
a222	22163	1335	63.6	0.18	1.04	0.0481	1.6	0.3534	2.6	0.05327	2.0	0.63	303	5	307	7	340	45	89
a223	162839	2242	195.2	0.49	19.72	0.0547	2.7	0.3937	8.8	0.05218	8.4	0.31	343	9	337	26	293	192	117
a224	72533	3603	190.4	0.06	2.48	0.0537	1.7	0.3901	3.5	0.05272	3.1	0.49	337	6	334	10	317	70	106
a225	110208	6097	377.8	0.71	1.94	0.0531	1.6	0.3910	3.1	0.05337	2.7	0.52	334	5	335	9	345	60	97
a226	8202	592	30.9	0.36	0.13	0.0513	1.4	0.3772	1.7	0.05336	0.9	0.84	322	4	325	5	344	21	94
a227	35106	254	75.8	0.76	2.40	0.2510	1.7	3.2149	2.7	0.09290	2.2	0.61	1444	22	1461	21	1486	41	97

Laurent et al., 2016. Supplementary Table S2 (continued):
Results of LA-SF-ICPMS U–Pb analyses of zircons from granitoids and vaugnerites of the Eastern French Massif Central.

	^{207}Pb[a] (cps)	U[b] (ppm)	Pb[b] (ppm)	Th/U[b]	^{206}Pbc[c] (%)	$^{206}Pb/^{238}U$[d]	±2σ (%)	$^{207}Pb/^{235}U$[e]	±2σ (%)	$^{207}Pb/^{206}Pb$[d]	±2σ (%)	ρ[f]	$^{206}Pb/^{238}U$	±2σ (Ma)	$^{207}Pb/^{235}U$	±2σ (Ma)	$^{207}Pb/^{206}Pb$	±2σ (Ma)	conc.[g] (%)
a228	25716	1417	82.0	0.28	1.02	0.0546	1.9	0.4028	3.0	0.05347	2.4	0.62	343	6	344	9	349	53	98
a229	18194	755	43.3	0.52	4.57	0.0484	1.9	0.3596	5.6	0.05386	5.2	0.33	305	6	312	15	365	118	83
a230	59460	3876	212.4	0.36	0.73	0.0530	1.7	0.3867	2.3	0.05288	1.5	0.75	333	5	332	6	324	34	103
a231	49350	1543	141.5	0.36	2.00	0.0860	1.7	0.6922	3.3	0.05839	2.8	0.52	532	9	534	14	544	61	98
a232	81630	5253	259.5	0.23	0.62	0.0500	1.6	0.3705	2.2	0.05372	1.5	0.73	315	5	320	6	359	34	88
a233	158821	3338	225.2	0.05	14.04	0.0532	2.4	0.3887	8.1	0.05297	7.7	0.30	334	8	333	23	327	175	102
OL-13-24																			
Session #1 (April 9th, 2014)																			
a171	13614	819	142.8	0.42	0.76	0.0502	1.7	0.3690	2.9	0.05330	2.3	0.58	316	5	319	8	341	53	93
a172	25806	1557	270.5	0.31	1.21	0.0511	1.8	0.3724	3.5	0.05285	3.0	0.53	321	6	321	10	323	67	100
a173	31595	1754	336.1	0.75	1.62	0.0507	1.6	0.3695	3.4	0.05284	3.0	0.47	319	5	319	9	322	68	99
a174	11370	705	114.4	0.26	0.64	0.0497	1.9	0.3644	3.2	0.05320	2.5	0.61	313	6	315	9	337	57	93
a175	65424	2242	487.4	0.82	6.22	0.0504	2.0	0.3691	6.4	0.05317	6.1	0.31	317	6	319	18	336	137	94
a176	45346	1968	347.0	0.19	4.53	0.0507	1.5	0.3699	5.2	0.05290	5.0	0.28	319	5	320	14	324	114	98
a177	29214	1758	326.8	0.78	0.83	0.0495	1.4	0.3618	2.7	0.05300	2.3	0.52	312	4	314	7	329	53	95
a178	12217	827	155.8	0.72	0.63	0.0513	1.5	0.3739	3.0	0.05291	2.5	0.52	322	5	323	8	325	57	99
a179	72217	3509	637.1	0.31	3.08	0.0518	1.5	0.3770	3.9	0.05282	3.6	0.39	325	5	325	11	321	82	101
a180	39183	1526	289.8	0.35	6.50	0.0509	1.9	0.3710	6.1	0.05284	5.8	0.32	320	6	320	17	322	131	99
a181	37278	2656	591.0	1.43	b.d.	0.0510	1.5	0.3725	2.0	0.05294	1.4	0.74	321	5	322	6	326	31	98
a182	13284	881	150.7	0.42	0.49	0.0507	1.7	0.3699	3.0	0.05295	2.4	0.58	319	5	320	8	327	55	98
a183	90814	3715	680.4	0.21	6.74	0.0516	1.5	0.3765	5.9	0.05296	5.7	0.26	324	5	324	17	327	129	99
a184	28452	1491	285.0	0.58	3.03	0.0508	1.8	0.3711	4.9	0.05296	4.5	0.36	320	6	320	14	327	103	98
a185	34271	2703	469.7	0.47	0.03	0.0503	1.5	0.3720	1.8	0.05365	1.0	0.84	316	5	321	5	356	23	89
a186	17569	1187	225.9	0.78	0.39	0.0503	1.5	0.3677	2.2	0.05306	1.7	0.66	316	5	318	6	331	38	95
a187	10532	682	124.1	0.68	0.50	0.0507	1.7	0.3708	4.2	0.05302	3.8	0.40	319	5	320	12	330	87	97
a188	33495	2399	424.6	0.43	1.05	0.0517	1.7	0.3767	2.6	0.05290	1.9	0.67	325	5	325	7	324	44	100
a189	6618	485	91.3	0.65	b.d.	0.0521	1.5	0.3805	3.0	0.05295	2.6	0.50	327	5	327	8	327	59	100
a190	6809	529	101.2	0.78	b.d.	0.0505	1.8	0.3684	3.9	0.05290	3.5	0.46	318	6	318	11	325	79	98
a191	69652	4627	784.0	0.24	0.99	0.0515	1.4	0.3744	2.2	0.05274	1.7	0.64	324	4	323	6	318	38	102
a192	5898	420	85.5	0.94	0.37	0.0511	1.5	0.3728	3.7	0.05288	3.4	0.39	321	5	322	10	324	78	99
a193	13057	778	141.3	0.72	1.10	0.0493	1.5	0.3575	3.6	0.05254	3.2	0.43	310	5	310	10	309	74	100
a199	41316	2818	101.9	0.45	0.63	0.0519	1.5	0.3786	2.2	0.05289	1.6	0.68	326	5	326	6	324	37	101
a200	6303	286	21.1	0.63	2.16	0.0482	1.6	0.3481	4.1	0.05241	3.8	0.39	303	5	303	11	303	87	100
a201	23402	1536	110.0	0.35	0.94	0.0510	1.4	0.3711	2.7	0.05279	2.3	0.53	321	4	320	7	320	52	100
a202	4417	315	10.4	0.23	0.52	0.0506	1.6	0.3683	2.4	0.05277	1.8	0.66	318	5	318	6	319	40	100
a203	4364	295	54.3	0.49	b.d.	0.0519	2.2	0.3811	6.4	0.05326	6.0	0.34	326	7	328	18	340	136	96
a204	13133	978	167.9	0.53	0.49	0.0478	1.6	0.3491	2.4	0.05292	1.9	0.65	301	5	304	6	325	42	93
a205	14768	545	116.6	0.71	5.31	0.0513	1.7	0.3740	6.6	0.05288	6.4	0.26	322	5	323	18	324	144	100
a206	6976	477	86.6	0.46	0.26	0.0526	1.7	0.3837	3.6	0.05292	3.2	0.46	330	5	330	10	325	73	102
a207	19169	1093	107.4	0.26	1.13	0.0498	1.4	0.3629	2.6	0.05288	2.2	0.54	313	4	314	7	324	50	97
PMV																			
Session #2 (August 13th, 2014)																			
a433	42475	888	41.9	0.16	1.59	0.0479	1.2	0.3509	4.7	0.05316	4.5	0.26	301	4	305	12	336	102	90
a436	5232	134	7.0	0.89	b.d.	0.0475	1.6	0.3434	3.0	0.05249	2.5	0.55	299	5	300	8	307	57	97
a437	59939	1566	71.9	0.17	0.20	0.0481	1.1	0.3478	1.3	0.05239	0.7	0.85	303	3	303	3	303	15	100
a444	23304	809	35.8	0.26	0.30	0.0451	1.1	0.3295	5.0	0.05305	4.9	0.22	284	3	289	13	331	111	86
a445	5288	144	7.7	0.97	0.52	0.0461	1.3	0.3433	2.0	0.05396	1.6	0.62	291	4	300	5	369	36	79
a446	6115	182	8.8	0.59	b.d.	0.0456	1.1	0.3260	2.5	0.05190	2.3	0.44	287	3	286	6	281	52	102
a448	67709	941	48.8	0.21	6.00	0.0463	1.3	0.3314	7.5	0.05190	7.4	0.18	292	4	291	19	281	169	104
a451	13888	608	27.5	0.13	0.30	0.0479	1.0	0.3492	1.6	0.05291	1.2	0.65	301	3	304	4	325	28	93
a452	46511	837	45.4	0.77	3.33	0.0459	1.5	0.3255	5.4	0.05146	5.2	0.28	289	4	286	13	261	118	111
a453	53220	1394	65.7	0.27	0.47	0.0471	1.1	0.3389	2.3	0.05218	2.0	0.49	297	3	296	6	293	47	101
a454	4732	140	7.0	0.53	b.d.	0.0477	1.0	0.3462	1.9	0.05261	1.6	0.55	301	3	302	5	312	36	96
a456	6616	189	9.7	1.10	b.d.	0.0444	1.8	0.3194	3.8	0.05223	3.4	0.46	280	5	281	9	296	77	95
a458	26439	749	33.5	0.12	b.d.	0.0475	1.2	0.3441	1.5	0.05253	1.0	0.77	299	3	300	4	309	22	97
a459	38406	1281	73.2	1.18	b.d.	0.0485	1.0	0.3490	1.2	0.05223	0.7	0.85	305	3	304	3	296	15	103
a460	7034	192	10.0	0.94	4.41	0.0454	1.3	0.3347	7.5	0.05348	7.4	0.18	286	4	293	19	349	166	82
a462	6169	198	9.9	0.67	b.d.	0.0462	1.4	0.3388	2.4	0.05320	1.9	0.60	291	4	296	6	337	43	86
a465	4446	131	6.5	0.55	2.40	0.0477	1.0	0.3500	4.4	0.05316	4.3	0.24	301	3	305	12	336	97	90
a466	53714	564	63.3	0.33	0.42	0.1130	1.0	0.9703	1.3	0.06225	0.8	0.80	690	7	689	7	683	17	101
a467	19181	580	26.5	0.13	0.11	0.0484	0.9	0.3497	1.4	0.05237	1.0	0.70	305	3	304	4	302	22	101
a468	18149	487	25.0	1.04	0.36	0.0445	1.7	0.3280	2.9	0.05349	2.3	0.59	280	5	288	7	350	52	80
a470	5435	151	8.6	1.23	1.53	0.0472	1.1	0.3424	3.0	0.05257	2.9	0.35	298	3	299	8	310	65	96
a471	6291	163	9.8	1.45	b.d.	0.0483	1.1	0.3472	1.8	0.05217	1.4	0.61	304	3	303	5	293	32	104
a472	16094	205	20.6	1.21	1.31	0.0810	1.4	0.6943	2.7	0.06215	2.3	0.51	502	7	535	11	679	50	74
a473	11748	372	19.3	0.75	b.d.	0.0479	1.0	0.3474	1.4	0.05263	1.0	0.72	302	3	303	4	313	23	96

Laurent et al., 2016. Supplementary Table S2 (continued):
Results of LA-SF-ICPMS U–Pb analyses of zircons from granitoids and vaugnerites of the Eastern French Massif Central.

	^{207}Pb[a] (cps)	U[b] (ppm)	Pb[b] (ppm)	Th/U[b]	^{206}Pbc[c] (%)	$^{206}Pb/^{238}U$[d]	±2σ (%)	$^{207}Pb/^{235}U$[e]	±2σ (%)	$^{207}Pb/^{206}Pb$[d]	±2σ (%)	ρ[f]	$^{206}Pb/^{238}U$	±2σ (Ma)	$^{207}Pb/^{235}U$	±2σ (Ma)	$^{207}Pb/^{206}Pb$	±2σ (Ma)	conc.[g] (%)
a474	6427	169	9.9	1.25	0.49	0.0482	1.2	0.3473	1.9	0.05230	1.5	0.63	303	4	303	5	299	34	101
a475	4990	142	8.1	1.16	0.25	0.0486	1.2	0.3487	1.9	0.05209	1.5	0.62	306	4	304	5	289	34	106
PRC-56																			
Session #2 (August 13th, 2014)																			
a08	26600	451	27.0	0.52	4.57	0.0527	0.8	0.3836	4.7	0.05283	4.7	0.18	331	3	330	13	322	106	103
a09	8022	160	10.1	0.93	2.90	0.0526	0.9	0.3863	3.9	0.05329	3.8	0.22	330	3	332	11	341	87	97
a10	12516	356	19.1	0.41	0.39	0.0529	0.9	0.3849	2.2	0.05280	2.0	0.42	332	3	331	6	320	46	104
a11	21855	667	35.7	0.37	b.d.	0.0534	0.7	0.3918	1.1	0.05317	0.8	0.66	336	2	336	3	336	18	100
a12	5817	160	8.9	0.56	0.24	0.0524	0.9	0.3842	1.6	0.05323	1.3	0.59	329	3	330	4	339	29	97
a13	5581	162	9.1	0.58	0.30	0.0532	0.9	0.3874	2.0	0.05282	1.8	0.43	334	3	332	6	321	42	104
a14	30098	688	40.4	0.65	1.90	0.0531	0.8	0.3895	3.0	0.05322	2.9	0.28	333	3	334	9	338	66	99
a15	5448	165	9.1	0.53	0.19	0.0530	0.8	0.3947	1.5	0.05399	1.3	0.55	333	3	338	4	371	29	90
a16	9910	292	17.3	0.89	0.02	0.0529	0.8	0.3891	1.5	0.05334	1.2	0.55	332	3	334	4	343	28	97
a17	7127	205	11.1	0.56	0.24	0.0512	0.7	0.3756	2.1	0.05321	2.0	0.31	322	2	324	6	338	45	95
a18	19935	612	37.8	1.47	0.32	0.0483	1.8	0.3611	4.1	0.05420	3.7	0.44	304	5	313	11	380	83	80
a19	9964	282	16.4	0.74	0.37	0.0525	0.8	0.3827	1.6	0.05283	1.5	0.47	330	2	329	5	322	33	103
a20	9369	263	15.1	0.66	0.81	0.0531	0.8	0.3881	1.9	0.05303	1.7	0.43	333	3	333	5	330	39	101
a21	15143	358	19.6	0.30	2.41	0.0529	0.7	0.3882	3.3	0.05327	3.2	0.22	332	2	333	9	340	73	98
a22	5459	168	9.2	0.50	0.17	0.0529	1.0	0.3900	1.8	0.05347	1.5	0.55	332	3	334	5	349	33	95
a23	6079	188	10.0	0.37	b.d.	0.0528	0.8	0.3863	1.4	0.05308	1.2	0.59	332	3	332	4	332	26	100
a24	10640	283	15.9	0.60	0.40	0.0526	0.7	0.3887	1.5	0.05358	1.3	0.48	331	2	333	4	353	29	94
a25	7371	228	13.1	0.74	0.13	0.0528	0.8	0.3851	1.7	0.05294	1.5	0.48	331	3	331	5	326	33	102
a26	16718	430	23.7	0.47	1.15	0.0526	0.9	0.3812	2.6	0.05258	2.5	0.33	330	3	328	7	311	57	106
a27	12522	364	21.8	0.95	0.03	0.0526	0.8	0.3830	1.3	0.05280	1.1	0.60	331	3	329	4	320	24	103
a28	21116	475	30.1	0.94	2.26	0.0538	0.8	0.4039	3.8	0.05448	3.7	0.21	338	3	345	11	391	84	86
a29	22705	436	26.9	0.76	5.53	0.0514	1.3	0.3809	6.3	0.05370	6.2	0.20	323	4	328	18	359	140	90
a30	6035	186	10.5	0.65	b.d.	0.0526	0.8	0.3842	1.5	0.05303	1.3	0.51	330	2	330	4	330	30	100
a31	14016	216	12.9	0.35	5.79	0.0530	1.1	0.3859	5.6	0.05276	5.5	0.20	333	4	331	16	318	125	105
a32	12117	348	20.7	0.72	0.20	0.0546	0.9	0.4065	1.5	0.05402	1.3	0.58	343	3	346	5	372	28	92
a38	10023	301	16.2	0.41	0.06	0.0533	0.8	0.3904	1.4	0.05312	1.2	0.55	335	3	335	4	334	27	100
a39	6148	188	11.8	1.21	0.07	0.0523	0.8	0.3835	1.7	0.05313	1.6	0.44	329	2	330	5	335	35	98
a40	8054	248	13.7	0.57	0.03	0.0525	0.7	0.3832	1.5	0.05291	1.3	0.46	330	2	329	4	325	30	102
a41	5875	179	10.7	0.85	0.16	0.0532	0.7	0.3910	1.9	0.05332	1.8	0.37	334	2	335	5	342	40	98
a42	14621	431	24.5	0.63	0.05	0.0535	0.9	0.3910	1.3	0.05297	1.0	0.69	336	3	335	4	328	22	103
a43	5560	180	10.3	0.68	0.07	0.0531	0.9	0.3897	1.6	0.05320	1.3	0.55	334	3	334	5	337	30	99
PRC-57																			
Session #2 (August 13th, 2014)																			
a44	11228	355	19.9	0.60	b.d.	0.0531	0.7	0.3887	1.3	0.05308	1.1	0.52	334	2	333	4	332	25	100
a45	12384	205	17.0	0.08	0.06	0.0887	0.8	0.7176	1.4	0.05868	1.2	0.57	548	4	549	6	555	25	99
a46	12189	341	22.3	1.03	b.d.	0.0567	0.9	0.4571	2.7	0.05844	2.5	0.34	356	3	382	9	546	55	65
a47	51183	552	41.2	0.88	9.13	0.0549	1.4	0.4161	6.9	0.05502	6.7	0.20	344	5	353	21	413	151	83
a48	20442	566	39.2	1.10	b.d.	0.0592	0.8	0.4406	1.1	0.05400	0.8	0.71	371	3	371	3	371	17	100
a49	11886	201	17.6	0.30	b.d.	0.0896	1.5	0.7291	1.9	0.05900	1.2	0.79	553	8	556	8	567	25	98
a50	32899	491	43.9	0.45	0.93	0.0859	1.0	0.7024	2.3	0.05932	2.1	0.44	531	5	540	10	579	45	92
a52	18096	499	34.9	1.16	b.d.	0.0586	0.7	0.4360	1.1	0.05392	0.8	0.68	367	3	367	3	368	18	100
a53	16455	430	29.0	1.00	0.05	0.0583	0.7	0.4659	1.2	0.05800	0.9	0.60	365	3	388	4	530	21	69
a55	10493	239	18.1	0.32	b.d.	0.0756	1.1	0.6087	1.7	0.05837	1.3	0.62	470	5	483	6	544	29	86
a56	92436	1079	58.3	0.04	9.88	0.0458	1.5	0.3441	7.6	0.05448	7.4	0.20	289	4	300	20	391	167	74
a57	6708	128	8.3	1.03	4.31	0.0515	0.8	0.3812	5.2	0.05367	5.1	0.15	324	3	328	15	357	115	91
a58	9176	158	10.0	0.74	5.05	0.0530	1.0	0.3887	5.2	0.05320	5.1	0.18	333	3	333	15	337	115	99
a59	12964	405	23.3	0.71	0.05	0.0532	0.9	0.3917	1.5	0.05336	1.1	0.64	334	3	336	4	344	26	97
a60	18839	439	30.4	0.97	0.94	0.0597	0.9	0.4513	2.7	0.05484	2.5	0.34	374	3	378	8	406	56	92
a61	21341	271	31.4	0.77	0.49	0.1040	0.8	0.8883	2.0	0.06195	1.9	0.37	638	5	645	10	672	40	95
a62	12273	202	19.4	0.53	b.d.	0.0921	0.8	0.7521	1.2	0.05921	0.8	0.71	568	5	569	5	575	18	99
a63	13489	286	17.0	0.55	1.47	0.0540	1.0	0.4186	4.5	0.05619	4.4	0.21	339	3	355	14	460	98	74
a64	42521	632	46.9	1.17	4.96	0.0570	0.9	0.4589	4.8	0.05836	4.7	0.19	358	3	383	16	543	103	66
a65	6434	209	12.0	0.70	0.01	0.0528	0.9	0.3899	1.8	0.05355	1.5	0.53	332	3	334	5	352	34	94
a66	25432	160	14.8	0.48	11.83	0.0662	1.8	0.5543	9.2	0.06070	9.0	0.20	413	7	448	34	629	194	66
a72	19959	341	29.0	0.11	b.d.	0.0902	0.9	0.7276	1.2	0.05847	0.8	0.73	557	5	555	5	547	18	102
a73	15840	391	24.6	0.79	0.62	0.0557	0.8	0.4994	1.9	0.06503	1.7	0.45	349	3	411	6	775	35	45
a74	21309	498	34.7	1.09	1.00	0.0577	0.7	0.4488	2.0	0.05639	1.8	0.36	362	2	376	6	468	41	77
a75	40444	687	36.3	0.15	6.05	0.0488	1.0	0.3542	5.5	0.05266	5.4	0.18	307	3	308	15	314	122	98
a76	88853	112	69.4	1.70	0.06	0.4606	0.8	10.221	1.0	0.16093	0.6	0.81	2442	16	2455	9	2465	10	99
a77	11654	115	18.4	0.98	0.05	0.1386	0.7	1.2897	1.1	0.06751	0.8	0.65	837	6	841	6	853	17	98
a78	17212	524	30.2	0.67	b.d.	0.0536	0.9	0.3946	1.3	0.05343	0.9	0.70	336	3	338	4	347	20	97
a80	8335	280	19.4	1.96	b.d.	0.0499	0.9	0.3660	1.5	0.05322	1.2	0.58	314	3	317	4	338	28	93

Laurent et al., 2016. Supplementary Table S2 (continued):
Results of LA-SF-ICPMS U–Pb analyses of zircons from granitoids and vaugnerites of the Eastern French Massif Central.

	^{207}Pb[a] (cps)	U[b] (ppm)	Pb[b] (ppm)	Th/U[b]	^{206}Pbc[c] (%)	$^{206}Pb/^{238}U$[d]	±2σ (%)	$^{207}Pb/^{235}U$[e]	±2σ (%)	$^{207}Pb/^{206}Pb$[d]	±2σ (%)	ρ[f]	$^{206}Pb/^{238}U$	±2σ (Ma)	$^{207}Pb/^{235}U$	±2σ (Ma)	$^{207}Pb/^{206}Pb$	±2σ (Ma)	conc.[g] (%)
a81	6690	199	11.4	0.65	0.13	0.0535	0.8	0.3953	1.7	0.05354	1.5	0.48	336	3	338	5	352	34	96
a83	24097	660	35.3	0.24	1.03	0.0539	0.9	0.3935	2.2	0.05292	2.0	0.41	339	3	337	6	325	45	104
a84	18834	298	21.6	0.10	1.41	0.0729	1.4	0.6030	3.6	0.05998	3.4	0.37	454	6	479	14	603	73	75
SDZ																			
Session #2 (August 13th, 2014)																			
a476	57616	1440	77.7	0.33	0.15	0.0544	1.1	0.4008	1.2	0.05345	0.6	0.89	341	4	342	4	348	13	98
a477	118329	3130	171.6	0.45	b.d.	0.0540	0.9	0.3947	1.0	0.05303	0.4	0.93	339	3	338	3	330	9	103
a478	38084	1016	51.1	0.11	b.d.	0.0536	1.0	0.3921	1.2	0.05308	0.5	0.89	336	3	336	3	332	12	101
a480	40714	916	46.8	0.18	b.d.	0.0534	0.9	0.3933	1.1	0.05341	0.6	0.83	335	3	337	3	346	14	97
a481	69828	1848	115.3	1.18	0.81	0.0518	1.5	0.3832	3.2	0.05368	2.8	0.47	325	5	329	9	358	63	91
a482	114057	3032	166.0	0.47	b.d.	0.0537	1.3	0.3940	1.4	0.05316	0.5	0.93	337	4	337	4	336	12	100
a483	68928	1734	91.7	0.37	0.74	0.0515	1.6	0.3772	2.4	0.05315	1.8	0.67	324	5	325	7	335	41	97
a484	60861	1433	68.9	0.14	1.19	0.0493	1.1	0.3660	3.5	0.05390	3.4	0.31	310	3	317	10	367	76	85
a485	108644	1630	96.4	1.85	8.76	0.0451	2.1	0.3271	8.5	0.05258	8.3	0.24	284	6	287	22	311	189	92
a486	23288	552	29.4	0.32	b.d.	0.0538	1.2	0.3966	1.4	0.05346	0.7	0.87	338	4	339	4	348	15	97
a487	81501	2095	106.7	0.15	b.d.	0.0537	1.5	0.3940	1.5	0.05319	0.4	0.96	337	5	337	4	337	9	100
a488	48936	1268	64.6	0.20	0.30	0.0524	1.3	0.3806	2.1	0.05265	1.7	0.62	329	4	327	6	314	38	105
a490	9819	235	13.0	0.51	b.d.	0.0536	1.1	0.3945	1.6	0.05336	1.1	0.72	337	4	338	5	344	24	98
a491	60722	1537	79.3	0.22	b.d.	0.0529	1.4	0.3913	1.8	0.05369	1.1	0.77	332	5	335	5	358	26	93
a492	39230	950	49.2	0.18	b.d.	0.0543	0.9	0.3968	1.2	0.05300	0.7	0.79	341	3	339	3	329	17	104
a493	33496	806	37.1	0.23	0.49	0.0472	1.3	0.3539	2.2	0.05437	1.8	0.57	297	4	308	6	386	41	77
a499	88067	1423	66.1	0.33	6.15	0.0415	1.3	0.3019	6.1	0.05271	6.0	0.22	262	3	268	15	316	136	83
a500	18632	452	26.2	0.68	b.d.	0.0540	1.7	0.3936	1.8	0.05290	0.7	0.92	339	6	337	5	324	16	104
a501	16480	446	24.4	0.41	0.50	0.0540	1.2	0.3971	1.8	0.05330	1.3	0.66	339	4	340	5	341	30	99
a502	31157	810	40.2	0.13	1.05	0.0522	1.3	0.3868	2.7	0.05374	2.4	0.48	328	4	332	8	360	53	91
a503	44836	1138	56.3	0.29	0.83	0.0496	1.6	0.3613	2.9	0.05280	2.4	0.56	312	5	313	8	320	54	98
a504	5661	73	7.6	0.85	b.d.	0.0941	1.1	0.7719	1.9	0.05951	1.6	0.57	580	6	581	8	586	34	99
a505	65233	1427	74.0	0.13	2.48	0.0525	1.3	0.3863	4.5	0.05340	4.3	0.29	330	4	332	13	346	97	95
a506	65980	1773	89.8	0.23	0.11	0.0518	1.0	0.3799	1.7	0.05321	1.3	0.58	325	3	327	5	338	31	96
a507	35760	861	43.7	0.16	b.d.	0.0534	0.9	0.3899	1.1	0.05298	0.6	0.86	335	3	334	3	328	13	102
a508	62642	1553	83.9	0.46	b.d.	0.0533	1.1	0.3912	1.4	0.05323	0.8	0.83	335	4	335	4	338	17	99
a509	83198	1691	92.8	0.72	1.92	0.0496	1.3	0.3700	3.9	0.05405	3.7	0.32	312	4	320	11	373	83	84
a510	27667	617	29.7	0.49	0.46	0.0448	2.0	0.3328	2.3	0.05389	1.2	0.87	282	6	292	6	367	26	77
a512	90754	1951	115.5	0.72	0.52	0.0541	1.0	0.4009	2.0	0.05378	1.7	0.53	339	3	342	6	362	38	94
a513	14773	218	18.8	0.62	b.d.	0.0821	1.1	0.6572	1.4	0.05805	0.9	0.75	509	5	513	6	532	21	96
a514	26533	745	38.0	0.18	0.16	0.0531	1.9	0.3901	2.2	0.05332	0.9	0.90	333	6	334	6	342	21	97
SGC-12-49B																			
Session #1 (April 9th, 2014)																			
a228	4173	353	18.2	0.49	2.25	0.0481	1.9	0.3482	6.8	0.05248	6.5	0.29	303	6	303	18	306	149	99
a229	2620	231	12.2	0.58	2.27	0.0479	1.8	0.3461	2.5	0.05243	1.8	0.71	302	5	302	7	304	41	99
a230	7585	664	36.0	0.77	0.08	0.0477	1.8	0.3449	4.4	0.05249	4.1	0.41	300	5	301	12	307	93	98
a231	12131	813	42.6	0.67	15.46	0.0478	1.9	0.3447	7.4	0.05236	7.1	0.26	301	6	301	19	317	163	95
a232	5720	449	24.7	0.83	9.46	0.0474	1.8	0.3419	6.1	0.05230	5.8	0.30	299	5	299	16	299	132	100
a233	1854	172	9.2	0.70	4.26	0.0477	1.9	0.3449	3.1	0.05244	2.4	0.62	300	6	301	8	305	55	99
a234	28288	954	59.0	1.30	0.42	0.0363	2.6	0.2710	12.5	0.05408	12.3	0.21	230	6	243	28	375	276	61
a235	9405	320	17.2	0.48	1.17	0.0400	2.4	0.3004	10.3	0.05445	10.0	0.23	253	6	267	24	390	225	65
a236	3788	266	15.1	0.71	6.76	0.0476	2.6	0.3431	11.9	0.05228	11.6	0.22	300	8	300	31	314	265	96
a237	6840	589	30.2	0.57	17.72	0.0464	1.9	0.3358	3.0	0.05248	2.3	0.63	292	5	294	8	306	53	95
a243	8867	720	34.1	0.22	4.88	0.0471	1.8	0.3413	4.5	0.05251	4.1	0.41	297	5	298	12	308	94	97
a244	9228	568	28.1	0.34	1.84	0.0441	2.0	0.3173	7.5	0.05223	7.2	0.26	278	5	280	18	296	164	94
a245	46792	1221	71.3	0.56	1.36	0.0380	2.9	0.2741	10.2	0.05225	9.8	0.28	241	7	246	23	312	224	77
a246	7499	491	24.7	0.42	b.d.	0.0455	2.0	0.3288	6.4	0.05239	6.1	0.31	287	6	289	16	303	138	95
a247	10574	848	41.2	0.47	1.70	0.0447	1.9	0.3235	4.2	0.05249	3.8	0.44	282	5	285	10	307	86	92
a248	236076	864	254.2	0.12	0.37	0.2482	3.0	6.0460	3.2	0.17660	1.1	0.94	1429	39	1982	28	2622	18	55
a249	4007	354	20.0	0.66	1.26	0.0522	1.9	0.3828	3.5	0.05315	3.0	0.54	328	6	329	10	335	67	98
a251	3096	270	15.2	0.54	1.06	0.0517	1.7	0.3765	2.6	0.05287	2.0	0.65	325	5	324	7	323	45	101
a252	5076	377	19.2	0.41	1.34	0.0470	2.0	0.3401	7.8	0.05249	7.5	0.26	296	6	297	20	323	171	92
SJV																			
Session #1 (April 9th, 2014)																			
a138	6988	504	86.8	0.45	0.02	0.0497	1.5	0.3700	3.6	0.05401	3.3	0.42	313	5	320	10	371	74	84
a139	6792	457	77.9	0.55	0.20	0.0484	1.5	0.3566	2.3	0.05344	1.8	0.63	305	4	310	6	348	41	88
a140	101299	3787	805.1	0.85	5.61	0.0498	1.6	0.3632	5.5	0.05285	5.3	0.29	314	5	315	15	322	119	97
a141	7282	479	16.7	0.21	0.39	0.0524	1.6	0.3858	2.1	0.05340	1.4	0.75	329	5	331	6	346	31	95
a142	4270	303	11.2	0.55	0.24	0.0519	1.6	0.3782	2.2	0.05284	1.5	0.75	326	5	326	6	322	33	101
a143	24833	495	47.2	0.35	12.77	0.0514	2.6	0.3760	7.0	0.05300	6.5	0.37	323	8	324	20	329	148	98

Laurent et al., 2016. Supplementary Table S2 (continued):
Results of LA-SF-ICPMS U–Pb analyses of zircons from granitoids and vaugnerites of the Eastern French Massif Central.

	^{207}Pb[a] (cps)	U[b] (ppm)	Pb[b] (ppm)	Th/U[b]	^{206}Pbc[c] (%)	$^{206}Pb/^{238}U$[d]	±2σ (%)	$^{207}Pb/^{235}U$[e]	±2σ (%)	$^{207}Pb/^{206}Pb$[d]	±2σ (%)	ρ[f]	$^{206}Pb/^{238}U$	±2σ (Ma)	$^{207}Pb/^{235}U$	±2σ (Ma)	$^{207}Pb/^{206}Pb$	±2σ (Ma)	conc.[g] (%)
a144	6194	405	28.3	0.31	0.69	0.0508	1.9	0.3724	3.0	0.05318	2.3	0.64	319	6	321	8	336	52	95
a145	21591	1533	58.8	0.68	0.03	0.0517	1.4	0.3776	1.9	0.05294	1.2	0.75	325	4	325	5	326	28	100
a151	90436	6912	1175.0	0.23	0.52	0.0531	1.4	0.3866	1.8	0.05284	1.1	0.80	333	5	332	5	322	24	103
a152	10488	753	141.0	0.52	0.10	0.0537	1.5	0.3932	1.9	0.05312	1.1	0.80	337	5	337	5	334	25	101
a153	4472	306	52.8	0.42	0.17	0.0511	1.7	0.3786	2.7	0.05372	2.1	0.63	321	5	326	8	359	48	89
a154	4429	318	55.4	0.44	0.22	0.0510	1.7	0.3786	2.1	0.05383	1.3	0.78	321	5	326	6	364	30	88
a155	31918	1988	369.7	0.63	0.80	0.0509	1.8	0.3738	2.5	0.05330	1.8	0.69	320	5	322	7	342	42	94
a156	7507	508	87.0	0.44	0.35	0.0503	1.5	0.3663	2.1	0.05279	1.5	0.73	317	5	317	6	320	33	99
a157	17208	1174	220.1	0.63	0.06	0.0513	1.7	0.3771	2.2	0.05326	1.5	0.75	323	5	325	6	340	34	95
a158	28423	1743	340.3	0.71	0.77	0.0527	1.5	0.3864	2.2	0.05318	1.6	0.69	331	5	332	6	337	37	98
a159	11799	878	171.8	0.87	0.06	0.0522	1.5	0.3842	2.8	0.05335	2.3	0.55	328	5	330	8	344	53	95
a160	6155	434	76.8	0.34	0.43	0.0529	1.5	0.3889	2.3	0.05331	1.7	0.66	332	5	334	7	342	39	97
a161	10603	729	123.9	0.37	0.27	0.0503	1.6	0.3678	2.6	0.05306	2.0	0.61	316	5	318	7	331	46	95
a162	5645	440	78.3	0.45	0.13	0.0523	1.5	0.3835	2.1	0.05320	1.5	0.70	329	5	330	6	337	33	97
a163	13671	931	166.3	0.44	0.78	0.0515	1.4	0.3756	3.1	0.05288	2.8	0.44	324	4	324	9	324	63	100
a164	5417	378	67.0	0.43	0.21	0.0520	1.7	0.3810	2.3	0.05309	1.5	0.73	327	5	328	6	333	35	98
a165	40817	1877	351.6	0.36	3.25	0.0526	1.5	0.3853	4.0	0.05308	3.7	0.37	331	5	331	11	332	83	100
a166	5180	389	67.4	0.42	0.20	0.0522	1.8	0.3823	2.4	0.05307	1.6	0.75	328	6	329	7	332	36	99
a167	17651	1002	198.9	0.33	0.05	0.0595	1.7	0.4516	2.1	0.05503	1.3	0.78	373	6	378	7	414	30	90
a168	22417	1570	279.6	0.41	0.19	0.0535	1.5	0.3885	1.9	0.05272	1.1	0.81	336	5	333	5	317	25	106
a169	22252	1442	258.4	0.44	0.66	0.0523	1.5	0.3801	2.4	0.05268	1.8	0.64	329	5	327	7	315	42	104
a170	9067	631	109.7	0.40	b.d.	0.0513	1.5	0.3806	2.8	0.05385	2.4	0.52	322	5	327	8	365	54	88
TN-10																			
Session #2 (August 13th, 2014)																			
a164	26473	812	44.8	0.78	0.19	0.0500	0.8	0.3666	1.2	0.05322	0.9	0.66	314	3	317	3	338	21	93
a165	15973	337	19.9	0.70	3.08	0.0519	1.1	0.3862	5.4	0.05393	5.3	0.20	326	4	332	15	368	119	89
a166	35824	840	50.5	1.09	1.16	0.0500	1.1	0.3648	2.4	0.05295	2.1	0.44	314	3	316	7	326	49	96
a167	269546	1280	116.4	1.24	24.35	0.0488	2.7	0.3500	8.9	0.05199	8.4	0.31	307	8	305	24	285	193	108
a168	51367	1635	72.4	0.10	0.16	0.0470	0.8	0.3432	1.1	0.05295	0.8	0.71	296	2	300	3	327	17	91
a169	59832	645	47.9	1.19	10.13	0.0517	1.5	0.3756	7.3	0.05265	7.1	0.21	325	5	324	20	314	162	104
a171	45683	1387	68.5	0.30	0.57	0.0495	0.7	0.3563	1.3	0.05223	1.1	0.56	311	2	309	3	296	25	105
a172	25752	179	32.2	0.52	b.d.	0.1716	0.8	1.7364	1.2	0.07341	0.8	0.72	1021	8	1022	7	1025	16	100
a173	51443	1217	66.8	0.66	0.94	0.0492	1.1	0.3538	2.2	0.05215	1.9	0.49	310	3	308	6	292	45	106
a174	70965	843	54.0	0.76	12.45	0.0492	1.5	0.3602	8.3	0.05309	8.1	0.18	310	4	312	22	332	184	93
a175	43034	1276	65.3	0.34	0.48	0.0512	0.8	0.3730	1.5	0.05280	1.2	0.58	322	3	322	4	320	27	101
a176	49571	974	48.5	0.13	4.06	0.0482	1.1	0.3508	4.4	0.05278	4.2	0.24	303	3	305	12	319	96	95
a177	21899	627	39.3	1.40	1.01	0.0494	0.9	0.3603	2.2	0.05287	2.0	0.40	311	3	312	6	323	46	96
a179	38572	540	54.9	0.20	b.d.	0.1051	0.9	0.8860	1.1	0.06112	0.7	0.79	644	5	644	5	643	15	100
a180	39112	1085	63.4	1.08	1.27	0.0492	0.8	0.3587	2.4	0.05282	2.2	0.33	310	2	311	6	321	51	96
a182	11107	99	11.4	0.65	0.01	0.0952	2.0	1.0450	2.8	0.07961	2.0	0.71	586	11	726	15	1187	39	49
a183	200007	1768	99.1	0.42	16.52	0.0394	1.9	0.2903	8.4	0.05345	8.1	0.23	249	5	259	19	348	184	72
a184	7099	135	13.9	0.49	1.42	0.1002	1.3	0.8545	4.5	0.06184	4.3	0.29	616	8	627	21	668	91	92
a185	9431	309	17.2	0.76	b.d.	0.0512	0.8	0.3715	1.7	0.05259	1.5	0.46	322	3	321	5	311	35	104
a186	46738	1551	74.8	0.37	0.82	0.0471	0.7	0.3305	2.3	0.05087	2.1	0.31	297	2	290	6	235	50	126
a187	20865	630	36.3	0.97	0.52	0.0503	0.7	0.3747	2.4	0.05403	2.2	0.30	316	2	323	7	372	50	85
a188	21172	163	25.9	0.29	0.05	0.1591	0.8	1.5658	1.3	0.07138	1.0	0.64	952	7	957	8	968	20	98
a189	31269	1126	54.7	0.86	4.21	0.0399	1.0	0.2868	6.1	0.05218	6.0	0.16	252	2	256	14	293	138	86
a190	40365	1218	79.0	1.58	0.60	0.0508	0.7	0.3683	1.8	0.05254	1.6	0.38	320	2	318	5	309	37	103
a191	47060	753	66.0	0.34	0.95	0.0871	0.8	0.6990	1.8	0.05817	1.6	0.47	539	4	538	7	536	34	100
a192	25219	439	26.3	1.15	5.17	0.0486	1.1	0.3597	5.9	0.05364	5.8	0.19	306	3	312	16	356	130	86
a198	50121	801	42.9	0.16	5.85	0.0498	1.0	0.3611	5.5	0.05255	5.4	0.19	314	3	313	15	309	122	101
a199	72018	1186	52.6	0.19	9.07	0.0388	1.4	0.2848	7.1	0.05319	7.0	0.20	246	3	254	16	337	158	73
a200	14991	120	13.9	0.49	4.77	0.1012	0.9	0.8584	4.5	0.06149	4.4	0.20	622	5	629	21	656	94	95
a201	88638	2305	110.7	0.37	1.91	0.0460	0.7	0.3348	2.7	0.05278	2.6	0.27	290	2	293	7	319	59	91
a202	72125	1088	62.3	0.64	4.40	0.0467	1.3	0.3393	4.5	0.05266	4.4	0.28	294	4	297	12	314	99	94
a204	41410	412	23.9	0.61	13.71	0.0403	1.8	0.2983	10.4	0.05368	10.3	0.18	255	5	265	25	357	232	71
a205	45452	1033	59.0	0.85	2.71	0.0489	0.8	0.3573	3.7	0.05305	3.6	0.22	307	2	310	10	331	81	93
a206	70961	740	44.1	0.60	12.95	0.0418	1.6	0.3118	8.5	0.05405	8.3	0.19	264	4	276	21	373	187	71
TN-19																			
Session #2 (August 13th, 2014)																			
a207	20807	283	30.8	0.69	0.21	0.1004	0.9	0.8351	1.4	0.06033	1.1	0.62	617	5	616	7	615	24	100
a208	24428	827	45.0	1.02	0.07	0.0473	0.9	0.3455	1.2	0.05303	0.8	0.73	298	2	301	3	330	18	90
a209	37542	1097	56.4	0.40	0.15	0.0509	0.6	0.3720	1.4	0.05297	1.2	0.44	320	2	321	4	327	28	98
a210	12716	258	18.8	0.38	b.d.	0.0726	0.9	0.5768	1.4	0.05766	1.0	0.67	452	4	462	5	517	22	87
a211	66323	1757	78.3	0.12	5.37	0.0432	1.4	0.3177	6.1	0.05333	6.0	0.23	273	4	280	15	343	135	79
a212	20485	464	30.5	0.38	b.d.	0.0669	0.9	0.5415	1.2	0.05867	0.8	0.73	418	4	439	4	555	18	75

Laurent et al., 2016. Supplementary Table S2 (continued):
Results of LA-SF-ICPMS U–Pb analyses of zircons from granitoids and vaugnerites of the Eastern French Massif Central.

	^{207}Pb[a] (cps)	U[b] (ppm)	Pb[b] (ppm)	Th/U[b]	^{206}Pbc[c] (%)	$^{206}Pb/^{238}U$[d]	±2σ (%)	$^{207}Pb/^{235}U$[e]	±2σ (%)	$^{207}Pb/^{206}Pb$[d]	±2σ (%)	ρ[f]	$^{206}Pb/^{238}U$	±2σ (Ma)	$^{207}Pb/^{235}U$	±2σ (Ma)	$^{207}Pb/^{206}Pb$	±2σ (Ma)	conc.[g] (%)
a213	69311	2396	95.9	0.20	0.25	0.0413	1.0	0.3007	1.5	0.05285	1.1	0.65	261	3	267	4	322	26	81
a214	51486	820	69.9	0.87	0.85	0.0776	1.1	0.6060	2.1	0.05666	1.8	0.51	482	5	481	8	478	40	101
a215	76036	850	92.0	0.30	0.80	0.1092	0.9	0.9321	1.6	0.06192	1.3	0.56	668	6	669	8	671	28	100
a216	53742	1748	86.8	1.21	b.d.	0.0514	1.0	0.3743	1.4	0.05283	1.0	0.71	323	3	323	4	322	22	100
a217	33318	613	37.2	0.72	3.00	0.0512	0.8	0.3705	3.8	0.05252	3.7	0.20	322	2	320	10	308	85	104
a218	3419	47	5.3	1.02	b.d.	0.0960	1.0	0.8254	1.9	0.06238	1.6	0.52	591	6	611	9	687	35	86
a219	6143	127	9.4	0.47	b.d.	0.0721	1.2	0.5743	1.8	0.05778	1.4	0.63	449	5	461	7	522	32	86
a220	17657	211	15.7	0.21	5.04	0.0694	1.0	0.5397	4.8	0.05643	4.7	0.21	432	4	438	17	469	104	92
a221	11186	235	17.0	0.35	0.26	0.0721	0.8	0.5637	1.7	0.05667	1.5	0.47	449	4	454	6	479	33	94
a222	34145	518	47.7	0.49	0.04	0.0923	0.7	0.7704	1.0	0.06051	0.7	0.72	569	4	580	5	622	16	92
a223	3880	128	7.3	1.03	0.19	0.0491	1.0	0.3576	2.3	0.05277	2.0	0.45	309	3	310	6	319	46	97
a224	16561	251	21.6	0.25	0.29	0.0882	0.8	0.7083	2.1	0.05823	2.0	0.37	545	4	544	9	538	44	101
a225	19582	639	32.0	0.59	0.19	0.0473	0.8	0.3453	1.3	0.05294	1.1	0.58	298	2	301	3	326	24	91
a226	31171	534	33.1	0.96	3.96	0.0518	1.6	0.3756	5.6	0.05263	5.4	0.28	325	5	324	16	313	123	104
a227	21932	350	36.3	1.02	0.15	0.0899	0.8	0.7369	1.9	0.05942	1.7	0.44	555	4	561	8	583	37	95
a228	30417	710	41.9	0.93	2.78	0.0497	0.8	0.3603	4.1	0.05257	4.0	0.20	313	3	312	11	310	91	101
a229	3970	64	6.6	1.22	b.d.	0.0821	1.8	0.6994	2.8	0.06177	2.2	0.63	509	9	538	12	666	47	76
a230	18386	457	26.9	0.09	b.d.	0.0623	0.9	0.4886	1.3	0.05686	1.0	0.70	390	3	404	4	486	21	80
a231	48973	1108	55.0	0.17	1.80	0.0496	0.7	0.3608	2.8	0.05280	2.8	0.24	312	2	313	8	320	63	97
a232	28938	920	49.9	0.70	0.05	0.0505	0.8	0.3685	1.0	0.05291	0.7	0.75	318	2	319	3	325	16	98
a233	17393	357	25.2	0.13	0.10	0.0746	0.9	0.5847	1.4	0.05688	1.1	0.62	464	4	467	5	487	25	95
a234	11443	182	11.5	0.36	0.77	0.0600	1.6	0.5366	3.6	0.06481	3.3	0.43	376	6	436	13	768	68	49
a242	30216	398	41.5	0.46	b.d.	0.1015	0.9	0.8670	1.2	0.06195	0.9	0.71	623	5	634	6	672	18	93
a243	54234	1739	86.6	0.24	b.d.	0.0515	0.9	0.3748	1.0	0.05274	0.5	0.90	324	3	323	3	318	10	102
a244	27490	928	48.3	0.69	b.d.	0.0484	0.8	0.3528	1.0	0.05285	0.6	0.82	305	2	307	3	322	13	95
TOU-01																			
Session #1 (April 9th, 2014)																			
a41	21817	1309	223.6	0.16	1.19	0.0514	1.6	0.3744	2.4	0.05286	1.9	0.65	323	5	323	7	323	42	100
a42	26422	1148	238.9	0.63	3.70	0.0513	1.6	0.3740	4.2	0.05287	3.9	0.38	323	5	323	12	323	89	100
a43	27851	1691	296.3	0.29	0.82	0.0509	1.5	0.3712	2.2	0.05292	1.7	0.66	320	5	321	6	325	38	98
a44	23042	1401	245.3	0.42	1.29	0.0481	1.4	0.3504	2.5	0.05286	2.0	0.58	303	4	305	7	323	46	94
a45	41263	1859	333.9	0.23	3.53	0.0475	1.9	0.3441	4.8	0.05249	4.4	0.40	299	6	300	13	307	101	98
a47	33889	2057	80.1	0.67	0.63	0.0502	1.7	0.3656	3.1	0.05283	2.5	0.57	316	5	316	8	321	58	98
a48	139822	1593	163.6	0.22	1.87	0.1407	1.4	1.6673	2.5	0.08595	2.1	0.55	849	11	996	16	1337	41	63
a49	18111	1066	79.4	0.37	1.30	0.0502	1.7	0.3653	2.9	0.05278	2.3	0.59	316	5	316	8	319	53	99
a50	12398	856	60.2	0.21	0.03	0.0512	1.4	0.3736	2.0	0.05291	1.5	0.69	322	4	322	6	325	33	99
a51	32661	2014	70.0	0.19	1.51	0.0507	1.5	0.3702	3.2	0.05290	2.9	0.46	319	5	320	9	325	66	98
a52	30438	1939	320.3	0.11	1.18	0.0502	1.4	0.3656	2.4	0.05278	2.0	0.58	316	4	316	7	319	45	99
a53	134778	396	628.5	0.74	0.36	0.3762	1.9	8.7952	2.0	0.16958	0.6	0.96	2058	34	2317	19	2553	10	81
a54	33192	961	415.0	1.57	1.48	0.0876	1.9	0.7033	3.4	0.05825	2.8	0.57	541	10	541	14	539	61	100
a55	57948	1123	400.2	0.16	0.00	0.1027	1.9	1.4049	2.4	0.09925	1.6	0.77	630	11	891	15	1610	29	39
a56	57029	1704	330.0	0.12	7.16	0.0517	1.7	0.3760	5.5	0.05278	5.2	0.31	325	5	324	15	319	118	102
a57	25528	679	230.7	0.46	0.75	0.0883	1.6	0.7585	2.8	0.06233	2.3	0.57	545	8	573	12	685	49	80
a58	27240	1861	304.2	0.12	0.16	0.0510	1.5	0.3725	1.6	0.05294	0.7	0.90	321	5	321	4	326	16	98
a59	20652	1222	243.3	0.89	1.72	0.0492	1.5	0.3587	3.2	0.05285	2.8	0.46	310	4	311	9	322	64	96
a60	83678	1992	571.8	0.41	6.28	0.0709	1.8	0.5734	5.4	0.05869	5.1	0.33	441	8	460	20	556	112	79
a61	32902	1707	359.0	0.20	0.24	0.0632	1.7	0.4968	2.1	0.05699	1.2	0.82	395	6	410	7	491	26	80
a62	19741	1455	209.4	0.15	0.32	0.0438	1.8	0.3207	2.2	0.05310	1.2	0.82	276	5	282	5	333	28	83
a63	38800	3142	512.5	0.60	0.98	0.0427	1.6	0.3053	2.5	0.05185	1.9	0.63	270	4	270	6	279	44	97
a65	12794	828	153.0	0.57	0.46	0.0500	1.6	0.3663	2.7	0.05313	2.2	0.58	315	5	317	7	334	49	94
a66	23889	1470	271.4	0.65	0.88	0.0483	1.6	0.3533	2.9	0.05309	2.4	0.56	304	5	307	8	332	55	91
a72	27846	1580	294.8	0.52	1.07	0.0510	1.5	0.3736	2.6	0.05311	2.1	0.57	321	5	322	7	334	48	96
a73	126298	2014	650.6	0.24	2.27	0.0907	2.2	1.1530	3.1	0.09222	2.1	0.72	560	12	779	17	1472	40	38
a74	22408	1557	247.0	0.05	0.03	0.0516	1.6	0.3755	1.8	0.05280	0.8	0.89	324	5	324	5	320	18	101
a75	15261	728	141.2	0.40	3.58	0.0520	1.8	0.3796	4.5	0.05290	4.1	0.39	327	6	327	13	325	94	101
a76	18896	1275	228.0	0.49	0.34	0.0500	1.5	0.3657	2.0	0.05305	1.3	0.76	314	5	316	5	331	29	95
a77	24980	1284	225.3	0.28	3.04	0.0491	1.9	0.3576	4.1	0.05287	3.7	0.45	309	6	310	11	323	83	96
Vaugnerites																			
533-1																			
Session #1 (April 9th, 2014)																			
a107	57895	1559	103.7	0.55	12.48	0.0488	2.2	0.3501	9.0	0.05203	8.7	0.25	307	7	305	24	287	199	107
a108	14077	1195	61.2	0.48	b.d.	0.0484	1.8	0.3511	2.0	0.05260	1.0	0.88	305	5	306	5	312	22	98
a109	29037	2440	128.0	0.54	b.d.	0.0490	1.8	0.3575	1.9	0.05291	0.8	0.92	308	5	310	5	325	18	95
a110	17155	1386	69.7	0.40	0.26	0.0484	1.7	0.3521	2.1	0.05282	1.1	0.84	304	5	306	5	321	25	95
a111	30618	1880	103.0	0.79	3.37	0.0488	1.9	0.3506	4.7	0.05214	4.3	0.41	307	6	305	13	291	98	105

Laurent et al., 2016. Supplementary Table S2 (continued):
Results of LA-SF-ICPMS U–Pb analyses of zircons from granitoids and vaugnerites of the Eastern French Massif Central.

	^{207}Pb[a] (cps)	U[b] (ppm)	Pb[b] (ppm)	Th/U[b]	^{206}Pbc[c] (%)	$^{206}Pb/^{238}U$[d]	±2σ (%)	$^{207}Pb/^{235}U$[e]	±2σ (%)	$^{207}Pb/^{206}Pb$[d]	±2σ (%)	ρ[f]	$^{206}Pb/^{238}U$	±2σ (Ma)	$^{207}Pb/^{235}U$	±2σ (Ma)	$^{207}Pb/^{206}Pb$	±2σ (Ma)	conc.[g] (%)
a112	24922	1782	96.2	0.73	1.38	0.0470	1.7	0.3442	3.4	0.05313	3.0	0.50	296	5	300	9	334	68	89
a113	22275	1739	90.9	0.52	0.79	0.0486	1.7	0.3478	2.7	0.05193	2.0	0.64	306	5	303	7	282	47	108
a114	16182	1392	75.7	0.73	b.d.	0.0477	1.7	0.3454	2.3	0.05256	1.4	0.77	300	5	301	6	310	33	97
a115	16363	1320	62.6	0.23	0.28	0.0480	1.7	0.3509	2.2	0.05303	1.4	0.77	302	5	305	6	330	32	92
a116	38754	3302	166.9	0.38	b.d.	0.0494	1.8	0.3587	1.9	0.05266	0.6	0.94	311	5	311	5	314	14	99
a117	12164	1071	49.8	0.21	b.d.	0.0475	1.8	0.3457	2.0	0.05276	1.0	0.86	299	5	301	5	319	24	94
a118	27160	2002	104.1	0.45	0.65	0.0495	1.8	0.3569	2.4	0.05231	1.6	0.74	311	5	310	7	299	38	104
a119	30644	2656	138.7	0.48	b.d.	0.0491	1.7	0.3582	1.9	0.05289	0.8	0.90	309	5	311	5	324	19	95
a120	28415	2123	113.6	0.53	1.05	0.0490	1.8	0.3539	2.8	0.05238	2.2	0.63	308	5	308	7	302	50	102
a121	32750	2474	130.2	0.44	0.98	0.0494	1.9	0.3597	2.8	0.05284	2.1	0.66	311	6	312	8	322	48	96
a122	29394	2628	138.8	0.59	0.28	0.0473	1.8	0.3405	2.2	0.05226	1.3	0.82	298	5	298	6	297	29	100
533-2																			
Session #1 (April 9th, 2014)																			
a345	7401	707	38.4	0.86	0.04	0.0463	1.8	0.3368	2.2	0.05272	1.3	0.82	292	5	295	6	317	29	92
a346	5693	534	31.3	0.99	b.d.	0.0490	1.8	0.3552	2.2	0.05261	1.2	0.84	308	5	309	6	312	27	99
a347	10212	491	25.7	0.56	0.72	0.0457	2.0	0.3347	3.2	0.05306	2.4	0.63	288	6	293	8	331	55	87
a348	13589	1232	63.2	0.52	0.25	0.0481	1.7	0.3489	2.2	0.05256	1.3	0.81	303	5	304	6	310	29	98
a349	3555	321	17.4	0.69	0.03	0.0488	1.8	0.3537	2.6	0.05256	1.8	0.71	307	5	307	7	310	41	99
a350	2750	260	13.3	0.41	b.d.	0.0494	1.9	0.3562	2.9	0.05225	2.2	0.66	311	6	309	8	296	50	105
a351	3854	374	20.3	0.83	b.d.	0.0464	1.9	0.3358	2.4	0.05251	1.5	0.80	292	5	294	6	308	33	95
a352	11578	976	53.9	0.69	0.67	0.0491	1.8	0.3574	3.3	0.05276	2.7	0.56	309	6	310	9	319	62	97
a353	10307	989	55.4	0.93	b.d.	0.0475	1.8	0.3428	2.0	0.05231	0.9	0.89	299	5	299	5	299	21	100
a354	5745	534	30.5	0.94	b.d.	0.0480	1.8	0.3517	2.1	0.05316	1.2	0.82	302	5	306	6	335	27	90
a355	2821	264	14.4	0.79	0.03	0.0489	1.9	0.3549	2.6	0.05262	1.7	0.75	308	6	308	7	312	39	99
a356	4679	446	22.3	0.42	0.28	0.0477	1.8	0.3476	2.4	0.05281	1.6	0.75	301	5	303	6	321	37	94
a357	1738	165	8.4	0.48	b.d.	0.0491	2.1	0.3521	3.3	0.05198	2.5	0.65	309	6	306	9	284	58	109
a358	7302	661	38.3	1.06	0.32	0.0472	1.7	0.3450	2.1	0.05295	1.3	0.79	298	5	301	6	327	30	91
a359	3229	306	17.0	0.83	b.d.	0.0482	1.8	0.3490	2.4	0.05255	1.5	0.75	303	5	304	6	309	35	98
a360	7018	556	32.2	0.96	0.72	0.0484	1.8	0.3562	4.4	0.05337	4.0	0.40	305	5	309	12	344	91	88
a361	10410	917	53.8	0.97	0.06	0.0487	1.7	0.3541	2.3	0.05274	1.5	0.76	307	5	308	6	317	33	97
a362	8926	825	48.7	1.04	b.d.	0.0486	1.7	0.3529	2.0	0.05262	1.0	0.86	306	5	307	5	312	23	98
a363	5634	534	30.5	0.90	b.d.	0.0487	1.8	0.3505	2.4	0.05220	1.5	0.78	307	5	305	6	294	34	104
a364	5709	478	27.0	0.86	0.19	0.0473	1.8	0.3523	3.0	0.05401	2.4	0.61	298	5	306	8	371	54	80
a365	6966	646	34.4	0.58	b.d.	0.0491	1.8	0.3545	2.2	0.05239	1.3	0.81	309	5	308	6	303	30	102
a366	2327	218	10.8	0.29	0.19	0.0494	1.9	0.3583	2.5	0.05265	1.7	0.75	311	6	311	7	314	38	99
a367	4251	410	22.4	0.74	0.20	0.0491	1.9	0.3574	2.6	0.05283	1.8	0.72	309	6	310	7	321	41	96
a368	1802	169	8.7	0.58	1.56	0.0459	2.3	0.3329	3.3	0.05256	2.3	0.71	290	7	292	8	310	53	93
a369	2696	247	13.1	0.61	b.d.	0.0494	1.8	0.3582	2.5	0.05257	1.7	0.72	311	5	311	7	310	39	100
a370	3523	334	18.1	0.80	1.30	0.0475	1.9	0.3486	2.6	0.05327	1.7	0.76	299	6	304	7	340	37	88
a371	9369	879	52.6	1.16	0.61	0.0478	1.8	0.3513	2.0	0.05331	1.0	0.86	301	5	306	5	342	23	88
LR-31																			
Session #1 (April 9th, 2014)																			
a318	7363	698	41.7	1.18	b.d.	0.0475	1.8	0.3436	2.1	0.05248	1.1	0.85	299	5	300	5	306	25	98
a319	9823	992	55.6	0.96	b.d.	0.0472	1.8	0.3445	2.1	0.05289	1.1	0.84	298	5	301	6	324	26	92
a321	4544	452	25.6	0.98	b.d.	0.0471	1.8	0.3402	2.3	0.05234	1.3	0.81	297	5	297	6	300	31	99
a322	3256	324	15.7	0.37	b.d.	0.0475	2.0	0.3401	2.8	0.05192	2.0	0.71	299	6	297	7	282	45	106
a323	4645	448	26.1	1.05	b.d.	0.0479	1.8	0.3462	2.2	0.05243	1.3	0.81	302	5	302	6	304	29	99
a324	3220	314	18.6	0.93	b.d.	0.0481	2.3	0.3473	2.8	0.05240	1.6	0.82	303	7	303	7	303	36	100
a325	4429	423	24.5	0.83	0.63	0.0475	1.8	0.3436	3.6	0.05242	3.1	0.51	299	5	300	9	304	71	99
a326	4695	457	25.3	0.95	0.09	0.0475	1.9	0.3480	2.5	0.05311	1.7	0.75	299	6	303	7	334	38	90
a327	5569	539	30.9	1.08	0.50	0.0466	1.9	0.3390	2.5	0.05282	1.6	0.75	293	5	296	6	321	37	91
a333	1978	210	10.1	0.45	b.d.	0.0478	2.5	0.3427	3.7	0.05204	2.7	0.68	301	7	299	10	287	62	105
a334	2259	211	11.4	0.87	b.d.	0.0450	2.2	0.3262	4.0	0.05262	3.3	0.56	283	6	287	10	312	75	91
a335	5230	499	29.2	1.09	0.53	0.0474	1.8	0.3418	2.9	0.05228	2.3	0.61	299	5	299	8	298	53	100
a336	5820	568	33.2	1.11	b.d.	0.0473	1.7	0.3426	2.3	0.05254	1.5	0.75	298	5	299	6	309	35	96
a337	4036	390	21.6	0.93	0.03	0.0470	1.8	0.3440	2.6	0.05308	1.9	0.70	296	5	300	7	332	42	89
a338	5340	505	29.1	1.17	b.d.	0.0462	1.8	0.3338	3.4	0.05239	2.9	0.52	291	5	292	9	303	66	96
a340	4412	427	24.4	1.02	b.d.	0.0474	1.7	0.3419	2.3	0.05232	1.5	0.76	299	5	299	6	299	34	100
a341	5052	453	25.4	0.88	0.18	0.0474	1.9	0.3424	4.2	0.05236	3.8	0.44	299	5	299	11	301	87	99
a342	4243	384	23.0	1.07	0.19	0.0479	1.8	0.3483	3.2	0.05274	2.6	0.57	302	5	303	8	318	60	95
a343	3853	378	30.9	3.26	b.d.	0.0455	2.1	0.3399	4.6	0.05421	4.1	0.46	287	6	297	12	380	92	75
a344	3384	329	19.0	1.03	b.d.	0.0480	1.9	0.3502	2.7	0.05290	2.0	0.69	302	5	305	7	325	45	93
LR-32																			
Session #1 (April 9th, 2014)																			
a207	6189	587	33.3	1.19	b.d.	0.0370	2.0	0.2690	2.4	0.05274	1.3	0.83	234	5	242	5	318	31	74

Laurent et al., 2016. Supplementary Table S2 (continued):
Results of LA-SF-ICPMS U–Pb analyses of zircons from granitoids and vaugnerites of the Eastern French Massif Central.

	^{207}Pb[a] (cps)	U[b] (ppm)	Pb[b] (ppm)	Th/U[b]	^{206}Pbc[c] (%)	$^{206}Pb/^{238}U$[d]	±2σ (%)	$^{207}Pb/^{235}U$[e]	±2σ (%)	$^{207}Pb/^{206}Pb$[d]	±2σ (%)	ρ[f]	$^{206}Pb/^{238}U$	±2σ (Ma)	$^{207}Pb/^{235}U$	±2σ (Ma)	$^{207}Pb/^{206}Pb$	±2σ (Ma)	conc.[g] (%)
a208	6868	628	35.7	0.84	b.d.	0.0462	1.7	0.3332	2.2	0.05235	1.4	0.77	291	5	292	6	301	32	97
a209	8516	778	54.5	1.81	0.32	0.0481	1.8	0.3473	3.0	0.05239	2.4	0.61	303	5	303	8	303	55	100
a210	7624	730	32.9	0.14	b.d.	0.0481	1.8	0.3506	2.1	0.05285	1.1	0.86	303	5	305	6	322	25	94
a211	3108	299	17.0	0.97	b.d.	0.0482	1.9	0.3468	2.7	0.05212	1.9	0.71	304	6	302	7	291	44	104
a212	5063	492	28.4	1.03	0.22	0.0473	1.9	0.3413	3.8	0.05234	3.3	0.49	298	5	298	10	300	76	99
a213	7330	686	41.8	1.15	0.39	0.0482	1.8	0.3506	2.3	0.05281	1.5	0.76	303	5	305	6	321	34	95
a214	8596	820	50.6	1.26	b.d.	0.0481	1.7	0.3460	2.2	0.05217	1.4	0.79	303	5	302	6	293	31	103
a215	6604	634	34.6	0.77	b.d.	0.0480	1.8	0.3492	2.2	0.05271	1.3	0.82	302	5	304	6	317	29	96
a216	2999	289	16.1	0.86	b.d.	0.0477	1.8	0.3451	2.5	0.05244	1.7	0.73	301	5	301	6	305	38	99
a217	8849	858	53.4	1.30	b.d.	0.0481	1.7	0.3483	2.4	0.05254	1.6	0.73	303	5	303	6	309	37	98
a218	2600	240	13.8	0.97	0.04	0.0478	1.8	0.3454	2.5	0.05243	1.7	0.74	301	5	301	7	304	39	99
a219	6605	614	36.1	1.10	0.71	0.0470	1.8	0.3453	2.5	0.05327	1.7	0.72	296	5	301	6	340	39	87
a220	4126	400	23.5	1.11	b.d.	0.0477	1.9	0.3440	2.4	0.05233	1.6	0.76	300	5	300	6	300	36	100
a221	8711	826	40.4	0.41	0.02	0.0477	1.7	0.3448	2.1	0.05244	1.3	0.80	300	5	301	6	305	29	99
a222	11994	1115	57.8	0.58	b.d.	0.0481	1.7	0.3463	2.0	0.05221	1.0	0.88	303	5	302	5	295	22	103
a224	17123	1950	56.0	0.89	2.02	0.0258	1.9	0.1830	4.2	0.05148	3.8	0.45	164	3	171	7	262	87	63
a225	3398	318	18.3	0.98	b.d.	0.0477	1.9	0.3493	2.6	0.05311	1.7	0.74	300	6	304	7	333	39	90
a226	2595	243	13.4	0.78	0.13	0.0479	2.1	0.3483	3.0	0.05274	2.1	0.71	302	6	303	8	317	47	95
PRC-53																			
Session #1 (April 9th, 2014)																			
a78	5675	443	25.6	0.77	0.76	0.0511	2.4	0.3747	3.3	0.05317	2.2	0.75	321	8	323	9	336	49	96
a79	11609	950	39.0	0.39	1.13	0.0394	1.8	0.2819	3.9	0.05194	3.4	0.46	249	4	252	9	283	78	88
a80	3856	311	17.3	0.61	b.d.	0.0509	1.8	0.3715	2.3	0.05297	1.4	0.79	320	6	321	6	328	32	98
a81	5966	477	26.9	0.69	0.14	0.0506	2.0	0.3663	3.1	0.05249	2.4	0.63	318	6	317	8	307	55	104
a82	4533	353	18.7	0.63	0.01	0.0485	1.9	0.3544	2.4	0.05297	1.5	0.79	305	6	308	6	327	34	93
a84	8829	624	30.5	0.63	1.68	0.0435	1.9	0.3271	5.8	0.05454	5.5	0.33	274	5	287	15	394	122	70
a85	4791	352	21.1	0.93	0.09	0.0500	1.9	0.3641	2.7	0.05277	1.9	0.72	315	6	315	7	319	42	99
a86	3599	301	15.8	0.58	0.14	0.0475	2.0	0.3568	2.6	0.05446	1.7	0.77	299	6	310	7	390	37	77
a87	6051	547	28.0	0.97	b.d.	0.0428	1.9	0.3155	2.5	0.05347	1.6	0.76	270	5	278	6	349	36	77
a88	3543	303	16.1	0.60	0.01	0.0490	1.8	0.3566	2.3	0.05275	1.5	0.78	309	5	310	6	318	33	97
a89	4503	376	19.0	0.75	0.34	0.0441	1.8	0.3207	2.7	0.05272	2.1	0.64	278	5	282	7	317	47	88
a90	7515	654	30.7	0.18	0.61	0.0508	2.0	0.3737	2.5	0.05334	1.6	0.78	319	6	322	7	343	36	93
a91	6556	518	28.8	0.63	0.49	0.0487	1.9	0.3507	4.6	0.05225	4.1	0.43	306	6	305	12	296	94	103
a92	3173	268	15.5	0.73	b.d.	0.0507	2.0	0.3668	2.6	0.05248	1.6	0.77	319	6	317	7	306	37	104
a93	3535	296	16.2	0.52	b.d.	0.0509	1.8	0.3760	3.5	0.05356	2.9	0.53	320	6	324	10	353	66	91
a94	7462	953	42.6	0.52	0.85	0.0440	2.1	0.3205	4.4	0.05286	3.9	0.47	277	6	282	11	323	88	86
a96	4928	402	23.7	0.80	b.d.	0.0513	1.8	0.3739	5.3	0.05283	5.0	0.35	323	6	323	15	322	112	100
a97	2851	226	12.1	0.47	0.04	0.0504	1.9	0.3679	2.4	0.05291	1.5	0.79	317	6	318	7	325	33	98
a98	6141	489	28.5	0.82	b.d.	0.0505	1.8	0.3674	2.1	0.05272	1.1	0.85	318	5	318	6	317	25	100
a99	5441	476	27.6	0.68	0.08	0.0495	2.3	0.3696	2.6	0.05416	1.3	0.87	311	7	319	7	378	29	82
a100	4783	397	23.2	0.82	0.45	0.0504	1.8	0.3688	2.6	0.05308	1.9	0.70	317	6	319	7	332	43	95
a101	5287	458	26.4	0.87	0.62	0.0487	1.8	0.3567	2.6	0.05313	1.8	0.71	307	5	310	7	334	41	92
PRC-54																			
Session #1 (April 9th, 2014)																			
a153	4884	411	22.6	0.57	b.d.	0.0507	1.8	0.3723	2.8	0.05328	2.1	0.66	319	6	321	8	341	47	94
a154	3328	274	15.1	0.58	1.67	0.0483	2.0	0.3574	4.5	0.05367	4.1	0.45	304	6	310	12	357	92	85
a157	3596	315	17.7	0.52	0.54	0.0512	2.1	0.3710	2.9	0.05256	2.0	0.72	322	6	320	8	310	45	104
a158	4619	397	22.9	0.75	0.60	0.0507	1.9	0.3708	3.0	0.05304	2.4	0.62	319	6	320	8	330	54	96
a159	3791	304	18.0	0.83	0.06	0.0511	1.8	0.3724	2.4	0.05281	1.6	0.75	321	6	321	7	321	36	100
a162	5057	444	21.1	0.17	b.d.	0.0489	1.9	0.3613	2.5	0.05363	1.6	0.76	307	6	313	7	356	37	86
a164	5449	467	27.3	0.82	0.32	0.0508	1.8	0.3739	2.3	0.05335	1.3	0.81	320	6	323	6	344	30	93
a165	7208	598	35.4	0.79	b.d.	0.0511	1.9	0.3723	3.3	0.05282	2.8	0.56	321	6	321	9	321	63	100
a166	4973	398	21.3	0.29	0.85	0.0510	2.3	0.3830	4.0	0.05442	3.2	0.58	321	7	329	11	389	72	83
a167	4541	365	19.7	0.42	0.40	0.0480	2.2	0.3373	6.5	0.05100	6.2	0.33	302	6	295	17	241	142	125
a168	2897	278	16.5	0.62	b.d.	0.0510	2.0	0.3734	3.9	0.05311	3.3	0.51	321	6	322	11	333	76	96
a169	3747	298	17.0	0.55	0.94	0.0511	1.9	0.3691	3.4	0.05235	2.8	0.57	321	6	319	9	301	64	107
a170	8110	469	28.9	0.86	1.21	0.0420	3.0	0.3150	6.7	0.05441	6.0	0.45	265	8	278	17	388	135	68
a171	4704	380	22.4	0.84	b.d.	0.0494	1.7	0.3649	2.3	0.05354	1.4	0.77	311	5	316	6	352	32	88
a173	6004	465	27.4	0.81	0.15	0.0509	1.9	0.3706	3.5	0.05286	3.0	0.54	320	6	320	10	323	67	99
a174	6642	425	24.9	0.72	1.55	0.0508	1.9	0.3695	4.7	0.05280	4.3	0.42	319	6	319	13	320	97	100
a175	3776	331	17.9	0.66	0.80	0.0484	1.9	0.3559	2.9	0.05329	2.2	0.67	305	6	309	8	341	49	89
SC-13-02A																			
Session #1 (April 9th, 2014)																			
a123	16281	1162	55.4	0.11	1.15	0.0497	1.8	0.3556	2.9	0.05193	2.2	0.63	312	5	309	8	283	51	111
a124	10583	580	33.9	0.40	1.52	0.0481	2.9	0.3438	4.7	0.05185	3.6	0.63	303	9	300	12	279	83	109

Laurent et al., 2016. Supplementary Table S2 (continued):
Results of LA-SF-ICPMS U–Pb analyses of zircons from granitoids and vaugnerites of the Eastern French Massif Central.

	^{207}Pb[a] (cps)	U[b] (ppm)	Pb[b] (ppm)	Th/U[b]	^{206}Pbc[c] (%)	$^{206}Pb/^{238}U$[d]	±2σ (%)	$^{207}Pb/^{235}U$[e]	±2σ (%)	$^{207}Pb/^{206}Pb$[d]	±2σ (%)	ρ[f]	$^{206}Pb/^{238}U$	±2σ (Ma)	$^{207}Pb/^{235}U$	±2σ (Ma)	$^{207}Pb/^{206}Pb$	±2σ (Ma)	conc.[g] (%)
a125	4151	348	16.9	0.29	0.83	0.0494	2.0	0.3579	4.2	0.05253	3.8	0.46	311	6	311	11	309	86	101
a126	37697	2917	138.1	0.08	0.64	0.0499	1.9	0.3624	2.2	0.05262	1.2	0.84	314	6	314	6	312	28	101
a127	28741	2367	112.3	0.15	b.d.	0.0496	1.8	0.3619	2.1	0.05288	1.2	0.84	312	5	314	6	324	26	96
a128	23592	1639	80.6	0.23	1.06	0.0476	1.8	0.3408	2.8	0.05188	2.2	0.63	300	5	298	7	280	50	107
a129	3761	293	16.7	0.28	b.d.	0.0504	1.9	0.3642	2.4	0.05245	1.4	0.80	317	6	315	6	305	32	104
SC-13-05																			
Session #1 (April 9th, 2014)																			
a130	22671	1914	90.0	0.10	0.06	0.0491	1.7	0.3542	1.9	0.05231	0.7	0.93	309	5	308	5	299	16	103
a131	18683	1681	76.2	0.72	b.d.	0.0494	1.7	0.3584	1.9	0.05267	0.7	0.93	311	5	311	5	314	16	99
a132	28199	2219	109.9	0.45	0.87	0.0491	1.7	0.3573	2.5	0.05281	1.8	0.69	309	5	310	7	321	41	96
a133	22021	1874	91.7	0.15	0.21	0.0495	1.7	0.3588	2.0	0.05257	1.0	0.87	311	5	311	5	310	22	100
a134	26155	2259	106.7	0.19	0.11	0.0485	1.7	0.3541	2.1	0.05297	1.1	0.84	305	5	308	6	327	25	93
a135	22772	1959	101.0	0.44	0.15	0.0498	1.8	0.3598	2.2	0.05242	1.2	0.84	313	6	312	6	304	27	103
a136	21383	1842	82.6	0.23	b.d.	0.0488	1.7	0.3564	2.2	0.05297	1.3	0.78	307	5	310	6	327	30	94
a137	27083	2416	119.1	0.34	0.05	0.0485	1.7	0.3523	1.9	0.05265	0.8	0.91	305	5	306	5	314	18	97
a138	47211	3167	165.9	0.39	4.32	0.0458	2.2	0.3282	5.3	0.05198	4.8	0.41	289	6	288	13	285	111	101
a139	31903	2622	127.3	0.27	0.78	0.0482	1.7	0.3516	2.4	0.05293	1.7	0.72	303	5	306	6	326	38	93
a140	19685	1685	78.3	0.08	b.d.	0.0498	1.7	0.3623	1.9	0.05274	0.8	0.91	313	5	314	5	318	18	99
a141	8310	752	45.7	1.19	b.d.	0.0480	1.8	0.3483	2.1	0.05258	1.2	0.83	303	5	303	6	311	27	97
a142	3600	356	18.9	1.04	b.d.	0.0442	1.8	0.3265	2.4	0.05359	1.5	0.77	279	5	287	6	354	34	79
a143	22951	1928	89.5	0.14	b.d.	0.0483	1.7	0.3533	1.8	0.05308	0.7	0.92	304	5	307	5	332	16	92
a144	18048	1610	73.4	0.42	b.d.	0.0496	1.7	0.3583	2.0	0.05235	1.0	0.87	312	5	311	5	301	22	104
a145	34254	2651	135.1	0.45	1.22	0.0480	1.7	0.3478	2.6	0.05256	2.0	0.65	302	5	303	7	310	46	98
a151	26236	2054	97.4	0.22	1.22	0.0474	1.8	0.3450	2.9	0.05285	2.2	0.63	298	5	301	8	322	51	93
a152	42315	2190	113.4	0.28	4.27	0.0494	1.8	0.3655	5.0	0.05369	4.7	0.36	311	6	316	14	358	105	87
SC-13-09																			
Session #1 (April 9th, 2014)																			
a269	11009	517	30.4	0.58	5.03	0.0491	2.1	0.3618	6.9	0.05340	6.6	0.31	309	6	314	19	346	149	89
a270	8640	800	44.0	0.75	b.d.	0.0484	1.7	0.3500	2.0	0.05245	1.1	0.86	305	5	305	5	305	24	100
a271	25541	2206	139.3	0.92	b.d.	0.0535	1.8	0.3937	1.9	0.05337	0.8	0.91	336	6	337	6	344	18	98
a272	20722	1925	110.6	0.89	0.51	0.0489	1.8	0.3577	2.5	0.05302	1.7	0.72	308	5	311	7	329	39	93
a273	13647	963	54.7	0.75	1.84	0.0497	1.8	0.3573	3.8	0.05215	3.3	0.47	313	5	310	10	292	76	107
a274	13872	1252	63.8	0.37	b.d.	0.0500	1.8	0.3655	2.1	0.05299	0.9	0.90	315	6	316	6	328	21	96
a275	6187	594	32.2	0.73	b.d.	0.0491	1.7	0.3535	2.1	0.05221	1.2	0.81	309	5	307	6	295	28	105
a276	19657	1832	104.8	0.84	b.d.	0.0494	1.7	0.3599	1.9	0.05284	0.9	0.89	311	5	312	5	322	19	97
a277	5741	473	27.3	0.62	1.06	0.0500	1.9	0.3579	4.2	0.05194	3.7	0.46	314	6	311	11	283	85	111
a278	18506	1014	58.3	0.70	4.83	0.0467	1.8	0.3400	6.4	0.05284	6.1	0.29	294	5	297	17	322	138	91
a279	8961	670	37.2	0.61	1.76	0.0493	1.8	0.3517	4.0	0.05177	3.6	0.45	310	5	306	11	275	83	113
a280	23926	1965	110.2	0.80	1.24	0.0475	1.8	0.3427	3.0	0.05228	2.4	0.59	299	5	299	8	298	56	101
a281	12209	1077	56.7	0.51	0.35	0.0494	1.7	0.3606	2.3	0.05291	1.5	0.75	311	5	313	6	325	34	96
a282	30891	1245	69.3	0.20	7.69	0.0480	1.9	0.3466	7.8	0.05241	7.5	0.25	302	6	302	21	303	172	99
a288	27883	1287	70.5	0.28	5.73	0.0481	1.8	0.3507	6.1	0.05290	5.9	0.30	303	5	305	16	325	133	93
a289	14414	1113	61.4	0.73	1.32	0.0473	1.8	0.3379	3.5	0.05183	3.0	0.51	298	5	296	9	278	69	107
a290	18639	1734	95.5	0.72	b.d.	0.0489	1.7	0.3553	1.9	0.05267	0.9	0.89	308	5	309	5	315	19	98
a291	12801	1201	69.5	0.95	b.d.	0.0485	1.7	0.3523	2.0	0.05273	1.0	0.87	305	5	306	5	317	22	96
a292	13709	1197	66.2	0.74	0.39	0.0487	1.7	0.3491	2.4	0.05199	1.6	0.74	307	5	304	6	285	36	108
a293	29892	2138	121.6	0.72	2.01	0.0495	1.7	0.3592	3.5	0.05258	3.1	0.49	312	5	312	9	311	70	100
a294	14567	1366	75.9	0.74	0.02	0.0487	1.7	0.3561	2.0	0.05301	0.9	0.88	307	5	309	5	329	21	93
a295	16905	1557	86.9	0.74	b.d.	0.0497	1.7	0.3634	2.0	0.05301	1.0	0.88	313	5	315	5	329	22	95
a296	23928	2103	133.4	1.25	0.81	0.0494	1.7	0.3612	2.7	0.05307	2.0	0.65	311	5	313	7	332	46	94
a297	38073	3563	189.2	0.58	b.d.	0.0495	1.7	0.3605	1.8	0.05277	0.6	0.94	312	5	313	5	319	14	98
a298	20911	1861	109.8	0.93	0.58	0.0488	1.7	0.3566	2.5	0.05304	1.9	0.68	307	5	310	7	331	42	93
a299	26664	2440	147.8	1.08	0.10	0.0493	1.7	0.3609	2.1	0.05310	1.2	0.82	310	5	313	6	333	27	93
a300	18573	1551	90.9	0.94	0.55	0.0483	1.7	0.3486	2.3	0.05231	1.6	0.73	304	5	304	6	299	36	102
SC-13-14																			
Session #1 (April 9th, 2014)																			
a15	29463	1321	63.2	0.96	5.61	0.0369	2.4	0.2711	6.3	0.05330	5.8	0.39	234	6	244	14	341	132	68
a16	14880	727	49.2	0.62	1.89	0.0538	1.8	0.3940	4.6	0.05316	4.2	0.40	338	6	337	13	335	96	101
a17	10208	641	33.3	0.58	1.25	0.0462	1.9	0.3386	3.5	0.05313	3.0	0.53	291	5	296	9	334	67	87
a18	21318	884	50.5	0.43	5.92	0.0499	2.0	0.3642	6.5	0.05295	6.2	0.31	314	6	315	18	327	141	96
a19	21296	774	48.4	0.92	6.83	0.0478	2.1	0.3546	8.1	0.05377	7.8	0.26	301	6	308	22	377	176	80
a20	6659	415	22.9	0.25	0.57	0.0531	1.8	0.3918	4.1	0.05350	3.7	0.45	334	6	336	12	350	83	95
a21	40077	2456	137.2	0.43	1.47	0.0529	1.8	0.3878	3.1	0.05316	2.5	0.59	332	6	333	9	336	57	99
a22	20803	1167	70.4	0.13	0.21	0.0608	2.6	0.4556	3.0	0.05430	1.6	0.85	381	10	381	10	383	37	99
a23	11046	571	29.5	0.66	2.30	0.0420	1.9	0.3046	5.3	0.05257	5.0	0.35	265	5	270	13	310	114	85

Laurent et al., 2016. Supplementary Table S2 (continued):
Results of LA-SF-ICPMS U–Pb analyses of zircons from granitoids and vaugnerites of the Eastern French Massif Central.

	^{207}Pb[a] (cps)	U[b] (ppm)	Pb[b] (ppm)	Th/U[b]	^{206}Pbc[c] (%)	$^{206}Pb/^{238}U$[d]	±2σ (%)	$^{207}Pb/^{235}U$[e]	±2σ (%)	$^{207}Pb/^{206}Pb$[d]	±2σ (%)	ρ[f]	$^{206}Pb/^{238}U$	±2σ (Ma)	$^{207}Pb/^{235}U$	±2σ (Ma)	$^{207}Pb/^{206}Pb$	±2σ (Ma)	conc.[g] (%)
a24	18836	858	46.3	0.72	5.58	0.0434	2.1	0.3182	6.8	0.05320	6.5	0.31	274	6	281	17	337	147	81
a25	16733	1178	61.7	0.17	0.24	0.0537	1.7	0.3968	2.2	0.05364	1.4	0.79	337	6	339	6	356	30	95
a26	12879	652	40.8	0.73	2.32	0.0532	1.9	0.3880	3.9	0.05292	3.4	0.48	334	6	333	11	325	78	103
a27	27562	984	66.4	0.80	7.43	0.0534	2.2	0.3942	6.6	0.05358	6.2	0.34	335	7	337	19	353	140	95
a28	8975	410	33.4	0.38	0.01	0.0786	1.8	0.6178	2.0	0.05698	1.0	0.86	488	8	488	8	491	23	99
a29	10672	661	35.2	0.18	0.18	0.0536	2.0	0.3931	3.1	0.05319	2.4	0.63	337	6	337	9	337	55	100
a30	4659	310	15.9	0.12	0.51	0.0535	1.9	0.3926	2.5	0.05317	1.5	0.78	336	6	336	7	336	35	100
a31	20997	1488	80.7	0.24	0.10	0.0537	1.8	0.3956	2.1	0.05342	1.1	0.86	337	6	338	6	347	24	97
a32	16355	974	62.0	0.23	0.03	0.0635	2.0	0.4793	2.5	0.05472	1.4	0.81	397	8	398	8	401	32	99
a38	52115	533	47.5	0.27	32.68	0.0418	4.1	0.4556	11.6	0.07900	10.9	0.35	264	11	381	38	1172	216	23
a39	61518	687	60.6	0.95	29.92	0.0454	4.2	0.3576	13.1	0.05715	12.4	0.32	286	12	310	36	497	273	58
a40	10117	617	32.0	0.34	1.02	0.0487	1.8	0.3641	4.1	0.05418	3.7	0.44	307	5	315	11	379	83	81
a41	8258	486	26.1	0.46	2.10	0.0522	1.8	0.4023	7.1	0.05589	6.8	0.26	328	6	343	21	448	152	73
SC-13-19																			
Session #1 (April 9th, 2014)																			
a176	5309	453	24.5	0.67	1.36	0.0479	1.9	0.3579	3.1	0.05415	2.5	0.60	302	6	311	8	377	56	80
a177	35612	2634	171.8	0.99	0.59	0.0533	1.7	0.3947	2.2	0.05369	1.4	0.78	335	6	338	6	358	32	93
a178	37941	2126	141.8	0.95	2.83	0.0535	1.8	0.3887	3.9	0.05272	3.4	0.46	336	6	333	11	317	78	106
a179	31432	2599	168.4	1.02	b.d.	0.0533	1.7	0.3906	1.9	0.05313	0.8	0.91	335	6	335	5	335	18	100
a180	16104	1161	67.4	0.68	1.02	0.0509	1.8	0.3688	3.0	0.05255	2.5	0.58	320	5	319	8	310	56	103
a181	19954	1602	97.1	0.74	b.d.	0.0533	1.8	0.3912	2.2	0.05320	1.3	0.80	335	6	335	6	337	30	99
a182	30264	2291	141.0	0.87	0.66	0.0516	1.7	0.3803	2.3	0.05342	1.5	0.76	325	5	327	6	347	34	94
a183	11566	943	53.9	0.61	b.d.	0.0520	1.7	0.3815	2.1	0.05322	1.1	0.84	327	6	328	6	338	26	97
a184	31644	2455	145.3	0.75	0.28	0.0525	1.8	0.3888	2.4	0.05374	1.7	0.73	330	6	333	7	360	37	91
a185	27725	2229	124.0	0.65	b.d.	0.0487	1.9	0.3603	2.1	0.05365	1.1	0.87	307	6	312	6	356	24	86
a186	16884	1314	80.6	0.69	0.42	0.0535	1.9	0.3925	2.8	0.05325	2.1	0.68	336	6	336	8	339	47	99
a187	23450	1955	121.2	0.83	b.d.	0.0532	1.7	0.3878	1.8	0.05292	0.7	0.93	334	6	333	5	325	15	103
a188	25727	2143	142.7	1.14	0.14	0.0532	1.7	0.3914	1.9	0.05334	0.7	0.92	334	6	335	5	343	16	97
a189	16040	1100	63.5	0.75	0.69	0.0496	1.8	0.3647	2.8	0.05336	2.1	0.64	312	5	316	8	344	48	91
a190	20338	1556	95.8	0.77	0.24	0.0533	1.7	0.3903	2.0	0.05307	1.0	0.85	335	6	335	6	332	24	101
a191	9495	806	40.2	0.16	b.d.	0.0514	1.7	0.3793	2.3	0.05352	1.5	0.76	323	5	326	6	351	33	92
a192	16904	1431	85.7	0.74	b.d.	0.0527	1.7	0.3828	1.9	0.05273	0.8	0.90	331	6	329	5	317	19	104
a193	34950	2920	197.7	1.21	b.d.	0.0532	1.7	0.3901	1.8	0.05316	0.6	0.95	334	6	334	5	336	13	100
a199	23191	1840	104.8	0.55	0.30	0.0531	1.7	0.3901	2.7	0.05326	2.1	0.63	334	6	334	8	340	48	98
a200	35658	1971	129.8	0.81	3.24	0.0537	1.8	0.3883	4.5	0.05248	4.1	0.40	337	6	333	13	306	94	110
a201	17406	1401	84.6	0.69	0.08	0.0536	1.7	0.3937	2.0	0.05326	0.9	0.89	337	6	337	6	340	20	99
a202	20551	1764	105.5	0.76	0.08	0.0522	1.7	0.3832	2.0	0.05323	0.9	0.88	328	5	329	6	339	21	97
a203	24667	1575	92.0	0.59	2.21	0.0513	1.7	0.3756	3.5	0.05312	3.0	0.49	322	5	324	10	334	69	96
a204	25955	2104	130.1	0.86	0.08	0.0525	1.7	0.3893	2.1	0.05383	1.2	0.82	330	5	334	6	364	26	91
a205	50789	4586	257.7	0.53	0.23	0.0525	1.7	0.3829	1.9	0.05292	0.7	0.92	330	6	329	5	326	16	101
a206	22131	1707	99.5	0.57	0.18	0.0534	1.7	0.3942	2.4	0.05351	1.6	0.72	336	6	337	7	350	37	96
SGC-12-13																			
Session #1 (April 9th, 2014)																			
a06	2173	157	8.5	0.61	b.d.	0.0486	2.0	0.3510	3.1	0.05241	2.4	0.63	306	6	305	8	303	55	101
a07	7516	433	27.6	0.90	1.46	0.0495	2.2	0.3611	5.7	0.05287	5.2	0.38	312	7	313	15	323	119	96
a08	4627	300	14.1	0.49	2.35	0.0411	2.2	0.3047	6.9	0.05374	6.6	0.32	260	6	270	17	360	148	72
a09	7449	615	34.0	0.73	0.28	0.0486	1.8	0.3506	3.5	0.05233	3.1	0.51	306	5	305	9	300	70	102
a10	6330	704	36.4	0.67	0.85	0.0462	2.6	0.3331	6.2	0.05233	5.6	0.43	291	8	292	16	300	128	97
a11	3988	265	15.3	0.62	0.63	0.0487	2.1	0.3540	6.1	0.05268	5.7	0.34	307	6	308	16	315	131	97
a12	16544	1078	62.9	0.66	0.83	0.0513	1.7	0.3744	2.9	0.05296	2.3	0.61	322	6	323	8	327	52	99
a13	21730	1540	79.7	0.47	0.76	0.0484	1.8	0.3501	2.9	0.05245	2.2	0.63	305	5	305	8	305	51	100
a14	4422	328	19.8	0.83	b.d.	0.0485	2.0	0.3561	2.6	0.05326	1.6	0.77	305	6	309	7	340	37	90
SGC-12-26																			
Session #1 (April 9th, 2014)																			
a372	7438	728	43.8	1.17	b.d.	0.0480	1.7	0.3497	2.0	0.05280	1.1	0.84	302	5	304	5	320	25	94
a373	2778	263	14.7	0.89	0.54	0.0460	2.0	0.3342	3.2	0.05267	2.5	0.63	290	6	293	8	315	57	92
a374	2177	201	10.7	0.59	b.d.	0.0489	2.2	0.3525	3.1	0.05223	2.2	0.71	308	7	307	8	296	50	104
a375	1368	129	7.2	0.80	b.d.	0.0485	2.5	0.3530	4.0	0.05275	3.1	0.62	306	7	307	11	318	71	96
a376	3408	322	17.0	0.55	0.07	0.0491	1.9	0.3537	2.4	0.05222	1.5	0.77	309	6	307	6	295	35	105
a378	6613	618	34.4	0.79	0.20	0.0488	1.8	0.3558	2.1	0.05285	1.1	0.85	307	5	309	6	322	26	95
a379	1657	148	7.5	0.32	0.21	0.0495	1.9	0.3585	3.0	0.05255	2.2	0.65	311	6	311	8	309	51	101
a380	4414	425	23.3	0.82	0.44	0.0477	1.8	0.3488	2.6	0.05304	1.9	0.69	300	5	304	7	331	43	91
a381	1050	90	4.3	0.36	b.d.	0.0461	2.6	0.3294	4.3	0.05183	3.5	0.59	290	7	289	11	278	80	104
a382	4158	336	18.4	0.72	b.d.	0.0486	1.8	0.3544	2.4	0.05294	1.6	0.75	306	5	308	6	326	36	94
a388	6784	533	29.1	0.74	b.d.	0.0485	1.8	0.3515	2.2	0.05256	1.2	0.82	305	5	306	6	310	28	98

Laurent et al., 2016. Supplementary Table S2 (continued):
Results of LA-SF-ICPMS U–Pb analyses of zircons from granitoids and vaugnerites of the Eastern French Massif Central.

	^{207}Pb[a] (cps)	U[b] (ppm)	Pb[b] (ppm)	Th/U[b]	^{206}Pbc[c] (%)	$^{206}Pb/^{238}U$[d]	±2σ (%)	$^{207}Pb/^{235}U$[e]	±2σ (%)	$^{207}Pb/^{206}Pb$[d]	±2σ (%)	ρ[f]	$^{206}Pb/^{238}U$	±2σ (Ma)	$^{207}Pb/^{235}U$	±2σ (Ma)	$^{207}Pb/^{206}Pb$	±2σ (Ma)	conc.[g] (%)
a389	3718	266	14.5	0.72	0.07	0.0485	1.8	0.3515	2.5	0.05259	1.7	0.73	305	5	306	7	311	40	98
a390	4714	335	19.7	1.13	0.04	0.0474	1.7	0.3449	2.2	0.05281	1.4	0.79	298	5	301	6	321	31	93
a391	12266	814	51.3	1.29	b.d.	0.0490	1.7	0.3552	1.9	0.05261	0.9	0.89	308	5	309	5	312	20	99
a392	4088	251	13.1	0.60	0.38	0.0485	1.8	0.3557	2.5	0.05315	1.7	0.73	306	5	309	7	335	38	91
a393	3231	192	10.2	0.73	b.d.	0.0467	1.8	0.3427	2.7	0.05319	1.9	0.68	294	5	299	7	337	44	87
a394	1687	93	4.9	0.51	b.d.	0.0493	1.9	0.3573	2.9	0.05256	2.2	0.66	310	6	310	8	310	49	100
a395	6898	375	21.7	1.05	b.d.	0.0484	1.7	0.3520	2.1	0.05277	1.3	0.81	305	5	306	6	319	28	96
a396	1975	101	4.7	0.19	0.07	0.0482	2.1	0.3449	3.3	0.05185	2.6	0.62	304	6	301	9	279	60	109
a397	5103	249	14.1	0.88	0.04	0.0482	1.8	0.3492	2.3	0.05255	1.4	0.78	303	5	304	6	309	32	98
a398	2501	116	5.9	0.50	0.01	0.0490	1.9	0.3563	2.6	0.05277	1.8	0.73	308	6	309	7	319	40	97
a399	4639	211	11.5	0.65	0.38	0.0494	1.8	0.3580	2.4	0.05256	1.6	0.74	311	5	311	6	310	37	100
a400	1869	78	4.0	0.49	b.d.	0.0472	2.4	0.3484	3.3	0.05352	2.2	0.74	297	7	304	9	351	50	85
a401	3006	127	7.0	0.78	0.17	0.0488	1.8	0.3520	2.6	0.05233	1.8	0.72	307	6	306	7	300	40	102
SGC-12-39																			
Session #1 (April 9th, 2014)																			
a254	5399	432	30.6	1.82	b.d.	0.0463	1.9	0.3347	5.3	0.05245	5.0	0.35	292	5	293	14	305	113	96
a255	3499	311	21.0	1.52	0.88	0.0447	2.0	0.3298	2.9	0.05348	2.1	0.70	282	6	289	7	349	47	81
a256	3132	331	21.2	1.36	0.07	0.0485	1.8	0.3452	3.6	0.05166	3.1	0.50	305	5	301	9	270	71	113
a257	3526	336	20.2	1.08	b.d.	0.0491	1.8	0.3524	2.5	0.05209	1.7	0.73	309	5	306	7	289	39	107
a258	4042	363	19.4	0.58	0.02	0.0490	1.8	0.3545	2.8	0.05249	2.1	0.64	308	5	308	7	307	48	100
a259	5015	481	32.9	1.67	0.03	0.0488	1.9	0.3540	2.6	0.05261	1.7	0.75	307	6	308	7	312	39	98
a260	9069	814	43.6	0.63	0.32	0.0485	1.7	0.3568	3.3	0.05335	2.8	0.52	305	5	310	9	344	63	89
a261	3638	346	22.9	1.34	0.07	0.0491	1.7	0.3542	2.6	0.05236	2.0	0.65	309	5	308	7	301	46	103
a262	4199	396	21.0	0.62	0.02	0.0485	1.8	0.3500	2.5	0.05231	1.8	0.71	305	5	305	7	299	41	102
a263	6428	499	36.8	1.81	b.d.	0.0493	1.8	0.3617	3.5	0.05322	3.0	0.52	310	6	313	9	338	67	92
a264	4575	433	25.7	0.99	b.d.	0.0488	1.9	0.3568	2.4	0.05301	1.5	0.78	307	6	310	6	329	34	93
a265	3325	237	15.1	1.32	3.96	0.0479	2.1	0.3463	5.5	0.05249	5.1	0.39	301	6	302	14	314	115	96
a266	7339	432	24.5	0.56	3.39	0.0481	1.9	0.3430	5.8	0.05171	5.4	0.33	303	6	299	15	273	125	111
a267	4846	430	26.2	1.11	b.d.	0.0489	1.8	0.3546	2.9	0.05265	2.2	0.64	307	6	308	8	314	51	98
SGC-12-42																			
Session #1 (April 9th, 2014)																			
a302	2768	271	13.5	0.42	b.d.	0.0472	1.8	0.3403	2.5	0.05230	1.7	0.74	297	5	297	6	298	38	100
a303	9186	261	17.2	0.47	12.57	0.0491	2.2	0.3553	7.9	0.05247	7.6	0.28	309	7	309	21	306	172	101
a304	2881	269	14.3	0.57	0.07	0.0485	1.9	0.3506	2.5	0.05240	1.7	0.74	305	6	305	7	303	39	101
a305	3768	362	18.2	0.41	0.01	0.0487	1.8	0.3524	2.3	0.05248	1.4	0.78	307	5	307	6	306	32	100
a306	10865	1062	66.4	1.28	b.d.	0.0488	1.7	0.3548	2.1	0.05273	1.1	0.84	307	5	308	6	317	26	97
a307	2810	269	13.1	0.45	b.d.	0.0465	1.8	0.3410	2.6	0.05320	1.9	0.69	293	5	298	7	337	43	87
a308	7511	718	39.0	0.72	b.d.	0.0485	1.8	0.3536	2.1	0.05290	1.2	0.82	305	5	307	6	324	28	94
a309	4457	421	21.1	0.49	b.d.	0.0471	1.7	0.3419	2.1	0.05265	1.2	0.83	297	5	299	5	314	27	95
a310	2707	250	12.3	0.40	b.d.	0.0474	1.9	0.3411	2.7	0.05215	1.9	0.72	299	6	298	7	292	42	102
a311	3064	300	15.5	0.54	b.d.	0.0485	1.8	0.3547	2.7	0.05302	2.0	0.67	305	6	308	7	330	46	93
a312	3476	322	16.9	0.60	0.01	0.0481	1.8	0.3486	2.9	0.05255	2.3	0.62	303	5	304	8	309	52	98
a313	2893	271	12.6	0.16	0.06	0.0484	1.8	0.3509	2.6	0.05262	1.9	0.68	304	5	305	7	312	43	97
a314	2794	271	12.6	0.16	b.d.	0.0485	1.8	0.3456	3.3	0.05169	2.7	0.56	305	6	301	9	272	63	112
a315	3557	355	15.5	0.09	0.99	0.0464	1.9	0.3343	3.0	0.05224	2.3	0.64	292	5	293	8	296	52	99
a316	4969	486	26.2	0.63	b.d.	0.0492	1.8	0.3577	2.5	0.05269	1.7	0.73	310	5	310	7	315	38	98
a317	2963	280	12.6	0.08	0.08	0.0480	1.9	0.3472	2.8	0.05243	2.0	0.68	302	6	303	7	304	46	99

$^{206}Pb/^{238}U$ error is the quadratic addition of the within run precision (2σ) and the external reproducibility (2σ ext.) of the reference zircon GJ-1

$^{207}Pb/^{206}Pb$ uncertainty is calculated using ^{207}Pb signal dependent error propagation following Gerdes & Zeh (2009)

$^{207}Pb/^{235}U$ error is the quadratic addition of the $^{207}Pb/^{206}Pb$ and $^{206}Pb/^{238}U$ uncertainties

(a) Within-run background-corrected mean ^{207}Pb signal in cps (counts per second).

(b) U and Pb contents (in ppm) and Th/U ratios were calculated relative to GJ-1 reference zircon (U = 280 ppm; Pb = 25.5 ppm).

(c) Percentage of the common Pb on the ^{206}Pb (b.d. = below dectection limit) calculated using the interference- and background-corrected ^{204}Pb signal and common Pb model composition of Stacey & Kramers (1975).

(d) Corrected for background, within-run Pb/U fractionation (in case of $^{206}Pb/^{238}U$) and common Pb, and subsequently normalized to GJ-1 (ID-TIMS value/measured value).

(e) $^{207}Pb/^{235}U = {}^{207}Pb/^{206}Pb/(^{238}U/^{206}Pb*1/137.88)$

(f) ρ (rho) is the correlation coefficient between errors of $^{206}Pb/^{238}U$ and $^{207}Pb/^{235}U$.

(g) Degree of concordance = $(^{206}Pb/^{238}U$ age / $^{207}Pb/^{206}Pb$ age) × 100

A.2 Couzinié et al., 2016

Are reported:

- the Supplementary Text with additional references;
- Supplementary Table 1: Whole-rock geochemical data for samples newly analyzed in the scope of this study;
- Supplementary Table 2: In situ LA–MC–ICP–MS Lu–Hf isotope data for zircon standards analyzed in this study;
- Supplementary Table 3: In situ LA–MC–ICP–MS Lu–Hf isotope data for zircon in PCMM samples from the eastern FMC;
- Supplementary Table 4: Zircon in situ SHRIMP O isotope data for standards during the analytical runs;
- Supplementary Table 5: Zircon in situ SHRIMP O isotope data for samples.

Compilations of whole-rock geochemical data and zircon Hf–O isotope compositions for other PCMM suites (Supplementary Tables 6 to 8) can be found online at https://doi.org/10.1016/j.epsl.2016

Supplementary material
to the article :

"Post-collisional magmatism: crustal growth not identified by zircon Hf-O isotopes"

Simon Couzinié, Oscar Laurent, Jean-François Moyen, Armin Zeh, Pierre Bouilhol, Arnaud Villaros*

*Corresponding author: simon.couzinie@univ-st-etienne.fr or simon.couzinie@ens-lyon.org

Whole-rock geochemistry

Samples were sawed at Saint-Etienne University and a *c.* 500 g fragment of each sample was sent to *ALS Global* for whole-rock chemical composition measurements. We chose the "Complete Characterization Package" which combines ICP-AES and ICP-MS analyses for major and trace elements, respectively. More information about analytical routines used by this company can be found at http://www.alsglobal.com/. Repeated analyses of standards MRGeo08, OGGeo08, NCSZC73007, SY-4, GBM908-10, GBM908-5 and GEOMS-03 were obtained during the analytical session.

Analyses on the standards were reproducible to < 1.6% for major elements, < 5.8% for trace elements (except Cr, V and Zr) and consistent within uncertainty with the expected values for these standards. Duplicate measurements of ten samples show external reproducibility better than 1.8% (RSD) for major elements (except CaO at 3.3%) and generally better than 9% (RSD) for trace elements, except for Sn, Ta, W, Se, Te, Lu and Cr. Thirty-two blanks display measured values typically under detection limits for all major and trace elements.

Results for the investigated samples are presented in Table S1.

These new measurements were added to a database gathering analyses of post-collisional mafic magmas from the Eastern French Massif Central (Agranier, 2001; Aït Malek, 1997; Ait Malek et al., 1995; Barbarin et al., 2012; Batias, 1979; Bellanger, 1980; Couturié, 1977; Downes et al., 1997; El Mouraouah, 1986; Ledru et al., 1994; Michon, 1979; Montel, 1988; Négron, 1979; Sabatier, 1978, 1984, 1991; Vitel et al., 2000; Williamson, 1991).

Zircon extraction and imaging

Samples weighing 5–10 kg were reduced using jaw and disc mills and sieved to <500 µm. Zircons were concentrated using conventional methods (Wilfley table, heavy liquids). After being hand-picked under a binocular microscope, 20 to 40 zircons per sample (only 13 for SC13-02A) were cast in epoxy mounts and subsequently polished to expose their interiors. Internal structures of zircon grains were documented in four steps: (i) transmitted light optical imaging; (ii) reflected light optical imaging; (iii) cathodoluminescence imaging (Fig. A6); (iv) low magnification SE-SEM imaging to assemble a navigation map. The last two steps were performed on a ZEISS EVO-150 SEM at the University of Granada (Spain).

Zircon U-Pb dating procedures

U–Pb isotopic analyses were carried out at Goethe Universität Frankfrut (GUF) by laser ablation using a Resolution M-50 (Resonetics) 193 nm ArF excimer laser system attached to a ThermoFinnigan Element 2 sector field ICPMS. We used a repetition rate of 5.5 Hz, laser spot-sizes of 28 or 33µm for measurements of unknowns, and 40 µm for zircon reference materials GJ-1, Plešovice, OG-1 and BB. Resulting fluence was ~2.5 to 3 J·cm–2. The sample surface was cleaned directly before each analysis by three pre-ablation pulses. Ablation was performed in a two-volume ablation cell (Laurin Technic, Australia) characterized by a very quick response time

(<1 s until maximum signal strength is reached) and wash-out delay (<3 s to get <1% of maximum signal strength). It was fluxed during ablation with a carrier gas consisting of a ~0.6 L min^{-1} He stream, mixed directly after the ablation cell with make-up gas consisting of ~0.07 L min^{-1} N_2 and 0.68 L min^{-1} Ar prior to introduction into the plasma of the SF-ICP-MS. All gases had a purity of 99.999% and no homogenizer was used while mixing the gases, to prevent smoothing of the signal and thus be able to detect significant variations of the $^{207}Pb/^{206}Pb$ and $^{238}U/^{206}Pb$ ratios during measurements, possibly revealing the sequential sampling of different age domains within single zircon grains. The signal was tuned for maximum sensitivity for Pb and U while keeping low the production of oxides ($^{254}UO/^{238}U \leq 0.5\%$). The obtained sensitivity on zircon standard GJ-1 for ^{238}U and a 33 μm spot size was about ~5000 cps·ppm^{-1} at 5.5 Hz and ~3 J·cm^{-2}.

Data were acquired using time resolved-peak jumping, the detector being set to analogue mode for ^{232}Th and ^{238}U and counting mode for ^{204}(Hg+Pb), ^{206}Pb, ^{207}Pb and ^{208}Pb. A total of 356 mass scans were acquired over ~41 s measurement (20 s of background measurement followed by 21 s of sample ablation) and integrated to 89 ratios (4 mass scans per integration, time resolution = 0.46 s). These ratios were subsequently corrected offline for background signal, common Pb, instrumental mass discrimination and Pb/U fractionation (both laser-induced during individual measurements, and over the day) using an in-house MS Excel© spreadsheet (Gerdes and Zeh, 2006, 2009).

A common-Pb correction was carried out when necessary: for each ratio of an individual measurement, ^{204}Pb was estimated by subtracting the average background signal on mass 204, which mostly results from ^{204}Hg in the carrier gas (~500 cps), to the measured intensity. Composition of common Pb (i.e. $^{206}Pb/^{204}Pb$ and $^{207}Pb/^{204}Pb$ ratios) was determined using a model Pb composition (Stacey and Kramers, 1975) at the age of the sample, independently estimated using analyses devoid of common Pb. The inter-elemental fractionation ($^{206}Pb/^{238}U$) during the 21

s of sample ablation was corrected for each analysis by applying a linear regression through all measured ratios, excluding the outliers (±2σ), and considering that the intercept with the y-axis represents the 'true' ratio. Elemental fractionation over the analytical session, as well as instrumental mass discrimination, were corrected by normalization to the $^{206}Pb/^{238}U$ (0.0982) and $^{207}Pb/^{206}Pb$ (0.061) ratios of reference zircon GJ-1 (Jackson et al., 2004), using standard bracketing. Elemental concentrations in U and Pb were calculated using raw signal (in cps) of ^{238}U and ^{206}Pb for each spot, corrected from the analytical drift over the session (monitored using GJ-1), normalized to the recommended values of the GJ-1 zircon standard (U = 280.1 ppm; Pb = 25.5 ppm) and applying a spot size-dependent correction. Th/U ratio was determined for each spot using the mass fractionation-corrected $^{232}Th/^{238}U$ ratio, normalized to the recommended value of the GJ-1 zircon standard (Th/U = 0.0296). Data from secondary standards were processed as unknowns to check the accuracy of the corrections. Our results are all within error of the recommended TIMS values of the standard zircons Plešovice (weighted mean $^{206}Pb/^{238}U$ age = 337.13 ± 0.37 Ma; Sláma et al. (2008), OG-1 (weighted mean $^{207}Pb/^{206}Pb$ age = 3465.4 ± 0.6 Ma; Stern et al. (2009)), and BB (DEGO: weighted mean $^{206}Pb/^{238}U$ age = 560 ± 0.8 Ma; Santos et al. (submitted)).

The quoted uncertainties for each individual analysis are (i) for the $^{206}Pb/^{238}U$ ratio, the quadratic addition of the within-run precision (2σ) with the external reproducibility of standard zircon GJ-1 during the corresponding analytical session (0.5 to 1.5%, 2 sigma); and (ii) for the $^{207}Pb/^{206}Pb$ ratio, a ^{207}Pb signal-dependent uncertainty propagation, as described by Gerdes and Zeh (2009).

The $^{207}Pb/^{235}U$ ratio was calculated using the corrected $^{206}Pb/^{238}U$ and $^{207}Pb/^{206}Pb$ ratios and assuming a natural $^{238}U/^{235}U$ of 137.88, and its uncertainty was obtained by quadratic addition of propagated errors on both ratios. Age calculations and data plotting were performed using the Isoplot toolkit (Ludwig, 2008) v.4.15 for MS Excel©.

Zircon Lu–Hf isotopes

Zircon Lu-Hf analyses for standards and samples are displayed Tables S2 and S3 respectively. Measurements were performed on magmatic zircons at GUF, using a Thermo-Finnigan Neptune multicollector ICP-MS attached to a Resolution M-50 193 nm Ar–F excimer laser ablation system, equipped with a two-volume Laurin Technic ablation cell. The latter is fluxed by high-purity, He carrier gas (~0.6 $L \cdot min^{-1}$) and is characterized by rapid response time (< 3 s to get maximum signal strength) and wash-out delay (<5 s to get <1% of maximum signal strength). Laser spots with diameters of 33 µm were drilled (Fig. 5) with repetition rates of 5.5 Hz and an energy density of ~6 $J \cdot cm^{-2}$. Make-up gas consisting of high-purity Ar (~0.75 $L \cdot min^{-1}$) and N_2 (~0.07 $L \cdot min^{-1}$) was admixed to the carrier gas to improve sensitivity. Post-ablation homogenization is performed by fluxing the gases through a Resolution Instruments Squid® tubing. Data were acquired using multi-collector static mode, during 58 s of measurement characterized by 1.052 s integration time (55 baseline-corrected ratios). ^{172}Yb, ^{173}Yb and ^{175}Lu masses were monitored to allow the correction of isobaric interferences (^{176}Yb and ^{176}Lu on ^{176}Hf). Instrumental mass bias for Yb isotopes (calculation of β^{Yb}) was monitored for each measurement using an exponential law, and corrected to the natural ratio $^{172}Yb/^{173}Yb = 1.35351$. Mass fractionation of Lu isotopes was assumed identical to that of Yb isotopes ($\beta^{Lu} = \beta^{Yb}$). The isobaric interferences were subsequently corrected to mass bias-corrected $^{176}Yb/^{173}Yb = 0.79502$ and $^{176}Lu/^{175}Lu = 0.02656$ (see Gerdes and Zeh (2006)). Mass bias for Hf isotopes (β^{Hf}) was determined using an exponential law and normalized to $^{179}Hf/^{177}Hf = 0.7325$. Accuracy and external reproducibility of the method were controlled by repeated analyses of reference zircon standards GJ-1 (Jackson et al., 2004; Morel et al., 2008), Plešovice (Sláma et al., 2008), Degeo (in-house) and 91500 (Wiedenbeck et al., 2004). The quoted uncertainties on $^{176}Hf/^{177}Hf$ ratios and $\varepsilon Hf_{(t)}$ are quadratic additions of within-run precision of each

measurement with the external reproducibility (2 S.D.) of the reference zircon standard GJ-1 (~70 ppm, see data table). Data reduction was carried out using an in-house MS Excel© spreadsheet (Gerdes and Zeh, 2006, 2009).

Calculations of initial $^{176}Hf/^{177}Hf$ ratios were performed using the individual $^{176}Lu/^{177}Hf$ ratio of each measurement, a decay constant of $\lambda_{176Lu} = 1.867 \times 10^{-11}$ (Scherer et al., 2001; Söderlund et al., 2004) and the emplacement age obtained by U-Pb zircon dating. For the calculation of the $\varepsilon Hf_{(t)}$, parameters of the chondritic uniform reservoir (CHUR) recommended by Bouvier et al. (2008) were used ($^{176}Lu/^{177}Hf = 0.0336$; $^{176}Hf/^{177}Hf = 0.282785$). Two-step depleted mantle (DM) Hf model ages (T_{DM2}^{C}) were calculated using a DM model considering linear regression from present-day depleted mantle as recommended by Griffin et al. (2002), i.e. $^{176}Lu/^{177}Hf = 0.0384$ and $^{176}Hf/^{177}Hf = 0.28325$, and an average $^{176}Lu/^{177}Hf$ of 0.0113 for the crustal reservoir.

Zircon O isotopes

Oxygen isotopes were analyzed with the IBERSIMS SHRIMP IIe/mc ion microprobe using multi collector mode following the method described by Ickert et al. (2008). Zircons were cast in "megamounts", i.e., 35 mm epoxy discs fixed in front of the mount holder so that no metallic parts or surface discontinuities faced the secondary ions extraction plate. The mount was coated with a 12 nm thick gold layer. The primary beam consisted of a 15 kV and 3 to 3.5 nA Cs ion beam focused to produce a 17x20 µm elliptical spot on the sample. The electric charge of the non-conductive zircons caused by the primary beam was neutralised with an electron beam that impacted the sample in a ≈200 µm diameter spot concentric with the Cs beam. The source slit was fixed at 150 µm and the secondary ^{18}O and ^{16}O were simultaneous measured in static mode using two Faraday cups with entry slits of 300 µm. The sample was pre-sputtered for 180 s prior to analyses. During the last 90 s of the pre-sputtering time the secondary beam and the electron beam

were steered to obtain the maximum signal on the Faraday cups. The measurement consisted in two sets of six scans, each scan was 10 s. The mass fractionation caused by Earth's magnetic field was compensated with Hemholtz coils operated at -309 mA. This eliminated the mass fractionation related to the horizontal steering of the secondary beam. Electron-induced secondary-ion emission (EISI) was measured for 10 s at the beginning of each scan and at the end of the measurement and subtracted accordingly. Data reduction was done using the POXI software developed by Peter Lanc and Peter Holden at the ANU. The zircon standard TEMORA-2 ($\delta^{18}O = 8.2 \pm 0.3$ ‰, Black et al., 2004|) was measured several times at the beginning of the session and after every four unknowns, and crosschecked against the 91500 zircon standard ($\delta^{18}O = 9.86 \pm 0.11$ ‰, Wiedenbeck et al., 2004); ten to fifteen replicates of which were measured as unknowns interspersed with these.

References

Agranier, A., 2001. Un exemple de magmatisme ultrapotassique syn-orogénique : les lamprophyres du Massif Central français. Master thesis, Clermont-Ferrand University, p. 51.

Aït Malek, H., 1997. Pétrologie, géochimie et géochronologie U-Pb d'associations acide-basiques: exemples du SE du Velay (Massif Central français) et de l'Anti-Atlas occidental (Maroc). PhD thesis, Nancy University, p. 297.

Ait Malek, H., Gasquet, D., Marignac, C., Bertrand, J.-M., 1995. Des xénolites à corindon dans une vaugnérite de l'Ardèche (Massif Central français) : implications pour le métamorphisme ardéchois. Comptes Rendus de l'Académie des Sciences, Paris 321, 959-966.

Barbarin, B., Gerbe, M.-C., Vitel, G., Gonord, H., Couette, F., Lebret, P., 2012. Notice explicative, Carte géol. France (1/50 000), feuille Firminy (744). BRGM, Orléans, p. 129.

Batias, P., 1979. Le massif de granite de Tournon-Saint-Cierges (Massif Central français). PhD thesis, Lyon University, p. 174.

Bellanger, D., 1980. Vaugnérites et roches associées des Cévennes Médianes : quelques aspects pétrologiques et géochimiques. PhD thesis, Lyon University, p. 180.

Black, L. P., Kamo, S. L., Allen, C. M., Davis, D. W., Aleinikoff, J. N., Valley, J. W., Mundil, R., Campbell, I. H., Korsch, R. J., Williams, I. S., and Foudoulis, C., 2004, Improved $^{206}Pb/^{238}U$ microprobe geochronology by the monitoring of a trace-element-related matrix effect; SHRIMP, ID–TIMS, ELA–ICP–MS and oxygen isotope documentation for a series of zircon standards: Chemical Geology, v. 205, no. 1-2, p. 115-140.

Bouvier, A., Vervoort, J.D., Patchett, P.J., 2008. The Lu–Hf and Sm–Nd isotopic composition of CHUR: Constraints from unequilibrated chondrites and implications for the bulk composition of terrestrial planets. Earth and Planetary Science Letters 273, 48-57.

Couturié, J.-P., 1977. Le massif granitique de la Margeride (M.C.F.). Etude pétrographique, géochimique et structurale. Exemple de différenciation par gravité dans les roches granitiques. Evolution régionale de la croûte au cours de l'orogène hercynien. PhD thesis, Clermont-Ferrand University, p. 335.

Downes, H., Shaw, A., Williamson, B.J., Thirlwall, M.F., 1997. Sr, Nd and Pb isotopic evidence for the lower crustal origin of Hercynian granodiorites and monzogranites, Massif Central, France. Chemical Geology 136, 99-122.

El Mouraouah, A., 1986. Palingenèse du granite du Velay autour de la diorite du Peyron (Burzetn Ardèche, MCF), approche pétrographique et géochimique de la genèse des granites tardimigmatitiques. PhD thesis, Clermont-Ferrand University, p. 183.

Gerdes, A., Zeh, A., 2006. Combined U–Pb and Hf isotope LA-(MC-)ICP-MS analyses of detrital zircons: Comparison with SHRIMP and new constraints for the provenance and age of an Armorican metasediment in Central Germany. Earth and Planetary Science Letters 249, 47-61.

Gerdes, A., Zeh, A., 2009. Zircon formation versus zircon alteration — New insights from combined U–Pb and Lu–Hf in-situ LA-ICP-MS analyses, and consequences for the interpretation of Archean zircon from the Central Zone of the Limpopo Belt. Chemical Geology 261, 230-243.

Griffin, W.L., Wang, X., Jackson, S.E., Pearson, N.J., O'Reilly, S.Y., Xu, X.-S., Zhou, X., 2002. Zircon chemistry and magma mixing, SE China: In-situ analysis of Hf isotopes, Tonglu and Pingtan igneous complexes. Lithos 61, 237-269.

Ickert, R., Hiess, J., Williams, I., Holden, P., Ireland, T., Lanc, P., Schram, N., Foster, J., and Clement, S., 2008, Determining high precision, in situ, oxygen isotope ratios with a SHRIMP II: Analyses of MPI-DING silicate-glass reference materials and zircon from contrasting granites: Chemical Geology, v. 257, no. 1-2, p. 114-128.

Jackson, S.E., Pearson, N.J., Griffin, W.L., Belousova, E.A., 2004. The application of laser ablation-inductively coupled plasma-mass spectrometry to in situ U–Pb zircon geochronology. Chemical Geology 211, 47-69.

Ledru, P., Vitel, G., Marchand, J., Maurin, G., Mercier, F., Turland, M., Etlicher, B., Dautria, J.M., Liotard, J.M., 1994. Notice explicative, Carte géol. France (1/50 000), feuille Craponne-sur-Arzon (767). BRGM, Orléans, p. 74.

Ludwig, K.R., 2008. A Geochronological Toolkit for Microsoft Excel, Berkeley Geochronology Central Special Publication, p. 76.

Michon, G., 1979. Typologie des vaugnérites des Monts du Lyonnais et du Haut-Vivarais, Massif Central Français. PhD thesis, Lyon University, p. 330.

Montel, J.M., 1988. Première découverte d'une vaugnérite à orthopyroxène : pétrographie, géochimie et conséquences pour la genèse des vaugnérites. Comptes Rendus de l'Académie des Sciences, Paris 306, 985-990.

Morel, M.L.A., Nebel, O., Nebel-Jacobsen, Y.J., Miller, J.S., Vroon, P.Z., 2008. Hafnium isotope characterization of the GJ-1 zircon reference material by solution and laser-ablation MC-ICPMS. Chemical Geology 255, 231-235.

Négron, J., 1979. Pétrologie et géochimie des formations quartzofeldspathiques de la série mésozonale du Chassezac (Lozère, Massif Central français). PhD thesis, Lyon University, p. 175.

Sabatier, H., 1978. Remarques préliminaires sur quelques vaugnérites du Massif central. Comptes Rendus de l'Académie des Sciences, Paris 286, 9-12.

Sabatier, H., 1984. Vaugnérites et granites magnésiens dans le Massif central français: une association particulière de roches grenues acides et basiques. Etude pétrographique. Paris VI University, p. 606.

Sabatier, H., 1991. Vaugnerites: special lamprophyre derived mafic enclaves in some Hercynian granites from Western and Central Europe., in: Didier, J., Barbarin, B. (Eds.), Enclaves and Grantie Petrology. Elsevier, Amsterdam, pp. 63-81.

Santos, M.M., Lana, C., Scholz, R., Buick, I., Kamo, S.L., Gerdes, A., Condon, D.J., Corfu, F., Tohver, E., Storey, C., Basei, M., Krambrock, K., Fantini, C., submitted. BB zircon – A new Sri Lankan reference material for U-Pb and Hf isotopic laser ablation ICP-MS analysis. Geostandards and Geoanalytical Research

Scherer, E.E., Münker, C., Mezger, K., 2001. Calibration of the Lutetium-Hafnium Clock. Science 293, 683-687.

Sláma, J., Košler, J., Condon, D.J., Crowley, J.L., Gerdes, A., Hanchar, J.M., Horstwood, M.S.A., Morris, G.A., Nasdala, L., Norberg, N., Schaltegger, U., Schoene, B., Tubrett, M.N., Whitehouse,

M.J., 2008. Plešovice zircon — A new natural reference material for U–Pb and Hf isotopic microanalysis. Chemical Geology 249, 1-35.

Söderlund, U., Patchett, P.J., Vervoort, J.D., Isachsen, C.E., 2004. The 176Lu decay constant determined by Lu–Hf and U–Pb isotope systematics of Precambrian mafic intrusions. Earth and Planetary Science Letters 219, 311-324.

Stacey, J.S., Kramers, J.D., 1975. Approximation of Terrestrial Lead Isotope Evolution by a 2-Stage Model. Earth and Planetary Science Letters 26, 207-221.

Stern, R.A., Bodorkos, S., Kamo, S.L., Hickman, A.H., Corfu, F., 2009. Measurement of SIMS Instrumental Mass Fractionation of Pb Isotopes during Zircon Dating. Geostandards and Geoanalytical Research 33, 145-168.

Vitel, G., Garcia, D., Turland, M., Gonord, H., Etlicher, B., Chafchafi, A., 2000. Notice explicative, Carte géol. France (1/50 000), feuille Monistrol-sur-Loire (768). BRGM, Orléans, p. 99.

Wiedenbeck, M., Hanchar, J.M., Peck, W.H., Sylvester, P., Valley, J., Whitehouse, M., Kronz, A., Morishita, Y., Nasdala, L., 2004. Further Characterisation of the 91500 Zircon Crystal. Geostandards and Geoanalytical Research 28, 9-39.

Williamson, B.J., 1991. The petrology of the Velay granite complex, Massif Central France. PhD thesis, London University, p. 272.

Couzinié et al., 2016. Supp. Table 1: Whole-rock geochemical data for samples newly analyzed in the scope of this study

Sample	LR33a	LR33b	LR34	D2-1	PRC51	PRC55	SC-13-10	SGC 12 015B	SGC 12 015D
Ref ALS	LR13221482	LR13221482	LR13221482	LR13221482	LR13221482	LR13221482	LR13221482	LR13221482	LR13221482
Long	4.113827	4.113827	4.113827	4.34499	4.101357	4.101357	3.65903	4.22173	4.22173
Lat	45.28477	45.28477	45.28477	44.58553	45.32981	45.32981	45.22445	44.75042	44.75042
Locality	La Roche	La Roche	La Roche	Lamastre	Pont-Rouge quarry	Pont-Rouge quarry	Pubellier	Peyron	Peyron
Type	vaugnerite	vaugnerite	vaugnerite	vaugnerite	syenite	syenite	vaugnerite	vaugnerite	vaugnerite
Details	fine-grained, HAS	coarse-grained, HAS	HAS	sample courtesy of V. Gardien	fine-grained, LAS	LAS	light facies	fine-grained, loose	fine-grained vgn. + equigranular gr., loose
SiO_2	55.40	55.50	61.70	47.70	61.40	62.10	60.20	52.50	52.40
Al_2O_3	19.55	18.10	17.55	10.95	14.30	16.20	16.10	17.05	17.05
Fe_2O_3	6.82	7.17	5.93	10.40	5.03	5.55	5.51	9.30	9.29
CaO	4.21	4.06	3.83	8.98	2.59	1.76	4.75	5.80	5.80
MgO	3.08	4.01	2.16	12.95	5.25	2.87	4.54	5.56	5.58
Na_2O	3.53	3.30	3.96	1.16	2.10	3.35	2.70	2.58	2.56
K_2O	2.54	3.12	2.58	4.68	5.15	4.47	4.86	2.57	2.53
Cr_2O_3	0.01	0.01	<0.01	0.12	0.03	0.01	0.02	0.01	0.01
TiO_2	1.32	0.99	1.18	1.96	1.32	1.33	0.93	1.80	1.78
MnO	0.06	0.08	0.05	0.13	0.07	0.07	0.08	0.12	0.13
P_2O_5	0.34	0.43	0.34	0.51	1.14	0.69	0.47	0.55	0.54
SrO	0.12	0.07	0.07	0.04	0.08	0.05	0.08	0.06	0.06
BaO	0.11	0.10	0.13	0.40	0.33	0.18	0.21	0.11	0.10
C	0.15	0.12	0.02	0.07	0.03	0.02	<0.01	0.03	0.03
S	0.07	0.10	0.01	0.39	0.02	0.02	0.02	0.09	0.09
Ba	1135	975	1200	3820	3060	1815	1915	1075	993
Ce	74.7	66.3	114.5	50.6	218.0	266.0	164.0	91.9	91.7
Cr	50	110	10	930	240	80	120	140	140
Cs	8.72	11.75	7.21	4.34	16.40	8.29	13.40	7.91	8.24
Dy	4.41	2.76	5.23	4.29	4.83	5.71	3.96	7.63	6.61
Er	2.11	2.05	2.51	1.81	2.02	2.51	1.86	3.99	4.29
Eu	2.05	1.84	1.51	1.61	2.67	2.27	2.55	2.10	1.93
Ga	27.2	23.7	25.5	14.4	25.4	28.2	21.0	20.6	22.5
Gd	5.26	5.06	6.72	5.13	9.87	9.47	7.71	8.98	9.33
Hf	5.9	5.3	11.0	2.8	22.7	15.8	7.7	7.7	7.5
Ho	0.81	0.71	0.87	0.78	0.72	0.92	0.71	1.35	1.43
La	36.8	32.5	60.6	23.2	96.5	126.5	88.6	43.3	47.6
Lu	0.23	0.17	0.24	0.33	0.17	0.20	0.29	0.54	0.53
Nb	12.1	10.6	15.8	9.7	60.5	32.3	17.1	23.6	22.6
Nd	35.4	33.3	44.4	27.5	100.5	111.5	68.7	46.2	43.9
Pr	8.68	7.88	12.55	6.26	26.30	31.20	18.50	11.20	10.50
Rb	147.0	185.5	171.5	210.0	284.0	227.0	200.0	97.5	95.6
Sm	7.26	6.04	8.75	6.15	18.85	18.65	10.50	9.27	9.65
Sn	4	3	3	2	8	2	9	2	3
Sr	775.0	648.0	582.0	306.0	681.0	419.0	680.0	479.0	473.0
Ta	0.7	1.0	1.2	0.7	3.5	1.5	2.1	1.4	1.6
Tb	0.71	0.64	1.00	0.74	1.21	1.19	0.95	1.33	1.11
Th	5.04	5.24	13.75	5.98	45.90	42.40	28.70	8.70	8.48
Tl	0.7	0.7	1.1	0.6	1.4	0.9	1.0	0.6	<0.5
Tm	0.31	0.25	0.31	0.26	0.24	0.29	0.22	0.63	0.56
U	1.39	1.16	2.59	1.26	10.20	7.25	13.60	1.97	1.54
V	133	125	85	360	62	85	106	146	141
W	<1	<1	<1	3	<1	1	1	2	15
Y	17.9	15.5	24.1	21	21.7	23.4	20.2	36.2	35.9
Yb	1.50	1.33	2.17	1.83	1.44	1.58	1.86	3.43	3.39
Zr	260	189	412	99	875	577	295	310	308
As	0.2	0.2	1.8	0.6	1.1	1.4	<0.1	3.4	2.2
Bi	0.04	0.04	0.03	0.04	0.14	0.04	0.16	0.11	0.09
Hg	<0.005	<0.005	0.005	<0.005	<0.005	<0.005	<0.005	<0.005	<0.005
Sb	<0.05	<0.05	<0.05	<0.05	<0.05	<0.05	<0.05	0.05	<0.05
Se	0.6	0.4	0.8	0.7	0.9	0.6	0.3	0.4	0.7
Te	<0.01	0.02	<0.01	<0.01	<0.01	<0.01	<0.01	<0.01	<0.01
LOI	2.62	1.99	1.11	1.88	1.15	1.74	1.12	2.23	2.14
Total	99.71	98.93	100.59	101.86	99.94	100.37	101.57	100.24	99.97
Ag	<0.5	<0.5	<0.5	<0.5	<0.5	<0.5	<0.5	<0.5	<0.5
Cd	<0.5	<0.5	<0.5	<0.5	<0.5	<0.5	<0.5	<0.5	<0.5
Co	20	23	12	49	16	14	19	30	30
Cu	16	26	10	44	10	8	50	24	19
Li	30	30	20	40	30	60	50	50	50
Mo	<1	<1	<1	1	<1	2	1	1	1
Ni	26	54	8	193	130	16	59	48	45
Pb	14	12	17	6	47	41	39	11	10
Sc	21	13	15	38	11	13	12	19	20
Zn	78	85	112	77	84	111	61	106	91
Ge									
In									
Re									

Couzinié et al., 2016. Supp. Table 1 (cont.): Whole-rock geochemical data for samples newly analyzed in the scope of this study

Sample	SGC 12 017	SGC 12 019	SGC 12 035A	SGC 12 035B	SGC 12 038A	SGC 12 041B	SGC 12 046	SGC 12 054B	SGC 12 060
Ref ALS	LR13221482	LR13221482	LR13221482	LR13221482	LR13221482	LR13221482	LR13221482	LR13221482	LR13221482
Long	4.22375	4.23872	4.30583	4.30583	4.0701	4.27347	4.28713	4.34852	4.07357
Lat	44.74817	44.74693	44.65670	44.65670	44.60028	44.67322	44.55378	44.69622	44.67992
Locality	Peyron	Burzet	Pont-de-Bayzan	Pont-de-Bayzan	Loubaresse	Meyras	Largentiere	Chadenet	Pei Plot
Type	vaugnerite	vaugnerite	vaugnerite	vaugnerite	vaugnerite	vaugnerite	vaugnerite	vaugnerite	vaugnerite
Details	coarse-grained vgn.	enclave within Velay granite	intermediate rim of the sill	core of the sill	intermediate facies	intermediate facies	medium-grained, darkest facies, Kfs blasts	at the contact with the "late-migmatitic" granite	medium-grained, spotted-facies, folded
SiO_2	50.50	55.40	56.80	55.70	59.60	53.40	56.40	60.60	58.70
Al_2O_3	16.50	17.75	18.05	18.10	16.75	17.95	15.45	16.05	16.90
Fe_2O_3	9.17	8.12	7.85	8.04	5.31	8.80	7.00	8.45	6.40
CaO	6.13	3.39	4.09	4.06	3.00	4.80	4.25	3.78	4.18
MgO	5.55	4.62	3.18	3.50	3.08	4.95	4.60	2.60	4.18
Na_2O	3.31	1.76	1.94	1.46	3.65	2.39	2.16	3.56	2.24
K_2O	2.69	3.66	3.70	4.32	3.27	3.66	4.20	2.42	3.61
Cr_2O_3	0.02	0.01	<0.01	<0.01	0.01	0.01	0.01	<0.01	0.02
TiO_2	1.60	1.96	1.48	1.45	1.55	1.94	0.92	1.78	1.44
MnO	0.12	0.11	0.09	0.10	0.07	0.10	0.10	0.12	0.10
P_2O_5	0.46	0.59	0.54	0.52	0.59	0.51	0.53	0.49	0.73
SrO	0.07	0.05	0.06	0.08	0.08	0.05	0.07	0.03	0.05
BaO	0.09	0.08	0.16	0.19	0.12	0.13	0.14	0.06	0.16
C	<0.01	<0.01	0.07	0.10	<0.01	<0.01	0.02	<0.01	<0.01
S	0.06	0.01	0.07	0.05	0.02	0.02	0.07	0.04	0.03
Ba	877	817	1560	1935	1155	1320	1405	548	1580
Ce	88.5	93.9	100.5	96.1	177.0	153.0	71.7	86.5	145.0
Cr	150	100	10	10	70	110	140	30	140
Cs	3.26	14.40	10.95	13.50	10.70	12.70	15.25	5.67	22.60
Dy	6.67	5.61	6.16	6.57	5.93	6.90	4.68	8.38	6.27
Er	3.71	2.56	3.87	3.12	2.40	3.01	2.72	5.04	2.66
Eu	1.76	2.60	2.00	1.97	2.51	2.43	1.36	1.79	2.23
Ga	20.2	22.0	23.5	28.3	27.2	28.5	18.0	23.2	22.1
Gd	7.74	9.36	9.43	7.53	9.37	9.94	5.88	9.23	8.94
Hf	6.1	7.3	8.0	8.3	13.2	11.7	5.1	6.8	14.2
Ho	1.20	1.05	1.13	1.12	0.98	1.21	0.87	1.61	0.86
La	42.5	46.3	49.5	48.1	86.8	73.9	35.1	42.1	76.6
Lu	0.54	0.32	0.39	0.46	0.30	0.31	0.45	0.59	0.28
Nb	23.2	29.2	18.4	18.5	32.8	24.7	13.2	19.7	28.6
Nd	42.7	50.1	48.6	48.6	78.8	82.1	35.0	42.9	75.2
Pr	9.95	12.15	11.80	12.35	20.20	19.95	9.04	10.40	19.20
Rb	81.2	164.0	181.0	219.0	218.0	175.0	148.5	159.0	300.0
Sm	9.17	10.40	9.11	9.24	12.85	12.65	7.29	9.49	12.30
Sn	3	4	5	5	4	5	4	3	12
Sr	526.0	381.0	451.0	486.0	515.0	395.0	522.0	268.0	435.0
Ta	1.1	1.1	1.5	1.2	1.9	2.1	1.1	1.4	1.9
Tb	1.05	1.20	1.01	1.07	1.15	1.26	0.91	1.36	1.19
Th	8.48	8.40	13.90	12.45	20.00	16.15	14.35	12.55	23.60
Tl	<0.5	0.8	0.8	0.8	1.0	0.6	0.9	0.6	1.6
Tm	0.57	0.35	0.50	0.54	0.41	0.42	0.39	0.70	0.41
U	1.28	2.14	3.52	2.80	2.99	3.15	4.09	4.00	5.45
V	139	91	121	128	62	121	155	142	142
W	2	6	1	2	1	1	1	4	2
Y	31.7	26.8	29.6	31.7	26	32.3	27.4	42.4	24.8
Yb	3.06	2.13	3.04	2.52	2.18	2.64	2.32	3.80	2.27
Zr	282	284	313	312	543	427	212	281	537
As	6.5	6.7	1.3	1.7	2.3	1.4	2.2	2.3	1.8
Bi	0.05	0.22	0.16	0.14	0.15	0.2	0.07	0.09	0.32
Hg	<0.005	<0.005	<0.005	0.005	0.006	0.006	<0.005	<0.005	<0.005
Sb	<0.05	<0.05	0.13	0.08	0.05	0.05	0.09	0.07	0.05
Se	0.7	1.3	1.4	1.3	0.8	0.6	0.6	1.1	1.1
Te	0.01	<0.01	<0.01	0.01	0.01	<0.01	<0.01	0.01	<0.01
LOI	1.8	3.66	2.31	2.53	1.65	2.08	2.2	1.63	1.44
Total	98.01	101.16	100.25	100.05	98.73	100.77	98.03	101.57	100.15
Ag	<0.5	<0.5	<0.5	<0.5	<0.5	<0.5	<0.5	<0.5	<0.5
Cd	<0.5	<0.5	<0.5	<0.5	<0.5	<0.5	<0.5	<0.5	<0.5
Co	29	26	19	18	16	27	20	18	17
Cu	15	15	8	6	8	9	13	15	38
Li	40	100	100	100	90	60	80	70	110
Mo	1	1	1	<1	<1	<1	1	<1	<1
Ni	48	57	2	3	37	17	19	4	17
Pb	8	13	15	22	16	10	22	14	2
Sc	20	13	13	13	9	20	21	22	18
Zn	95	97	93	93	77	95	84	95	76
Ge									
In									
Re									

Couzinié et al., 2016. Supp. Table 1 (cont.): Whole-rock geochemical data for samples newly analyzed in the scope of this study

Sample	SGC 12 061	SGC 12 010A	SGC 12 010B	SGC 12 011A	SGC 12 011B	SGC 12 012	SC-13-02b	SC-13-06	SC-13-07
Ref ALS	LR13221482	LR13221482	LR13221482	LR13221482	LR13221482	LR13221482	LR13221482	LR13221482	LR13221482
Long	4.07418	4.05583	4.05583	4.08857	4.08857	4.08857	3.47373	3.79974	3.79974
Lat	44.68115	44.50997	44.50997	44.49843	44.49843	44.49818	44.68734	44.82754	44.82754
Locality	Pei Plot	La Borne	La Borne	La Borne	La Borne	La Borne	Moulin de Linas	Jagonzac	Jagonzac
Type	vaugnerite	lamprophyre	lamprophyre	lamprophyre	lamprophyre	lamprophyre	vaugnerite	vaugnerite	vaugnerite
Details	equigranular	dyke	dyke	dyke	dyke	dyke	fine-grained	coarse-grained	dark, fine-grained
SiO_2	57.80	55.70	53.50	54.70	55.10	56.50	62.00	52.30	55.50
Al_2O_3	17.30	12.90	14.15	14.45	12.90	16.00	12.45	15.30	18.00
Fe_2O_3	6.09	6.75	8.65	6.79	6.36	7.45	7.42	7.30	7.53
CaO	4.47	5.77	5.37	5.49	4.27	3.37	3.27	7.32	6.47
MgO	2.54	7.01	8.47	6.28	9.04	5.34	8.00	6.42	3.79
Na_2O	2.59	2.17	1.16	2.16	1.66	2.46	1.50	2.57	3.75
K_2O	5.41	5.31	4.87	5.79	6.32	3.93	4.00	4.48	3.43
Cr_2O_3	<0.01	0.06	0.07	0.05	0.06	0.02	0.06	0.03	<0.01
TiO_2	1.14	1.05	1.20	1.40	1.25	1.06	0.98	1.37	1.06
MnO	0.08	0.22	0.14	0.10	0.08	0.10	0.13	0.11	0.11
P_2O_5	0.56	0.78	0.91	1.01	0.97	0.66	0.32	0.90	0.51
SrO	0.07	0.08	0.07	0.09	0.08	0.10	0.01	0.10	0.12
BaO	0.17	0.34	0.29	0.31	0.37	0.29	0.07	0.38	0.22
C	0.01	0.02	0.02	0.03	0.02	0.02	0.03	<0.01	0.02
S	0.02	0.01	0.02	0.15	0.02	0.15	0.02	0.03	0.09
Ba	1710	3240	2510	3000	3570	2740	573	3420	2020
Ce	125.5	185.0	219.0	145.5	202.0	146.5	37.0	136.0	165.0
Cr	30	520	590	390	500	220	430	220	<10
Cs	7.01	2.97	61.60	15.80	19.45	47.60	28.00	10.80	12.60
Dy	6.21	8.38	8.14	7.14	7.66	7.50	4.39	6.15	5.84
Er	3.12	2.80	3.29	2.89	3.32	3.62	2.30	3.26	2.89
Eu	2.09	3.94	3.99	3.18	3.55	2.95	0.63	3.46	2.93
Ga	24.9	17.1	21.0	18.5	18.9	22.0	23.1	21.2	22.9
Gd	9.00	15.15	15.75	11.25	14.15	10.30	5.23	10.20	9.65
Hf	12.6	16.1	17.4	14.3	12.9	13.7	1.6	5.2	6.9
Ho	1.10	1.37	1.22	1.17	1.39	1.10	0.94	1.02	1.08
La	63.1	94.1	88.6	70.8	104.0	69.8	16.5	64.8	88.6
Lu	0.47	0.36	0.36	0.49	0.37	0.45	0.31	0.37	0.34
Nb	20.5	23.4	24.9	37.7	28.6	30.3	10.3	20.3	15.4
Nd	63.8	133.0	122.5	78.5	130.0	74.4	25.8	73.7	74.9
Pr	16.35	29.20	28.40	18.50	30.40	18.35	5.35	18.70	19.85
Rb	211.0	136.5	312.0	179.5	235.0	253.0	319.0	205.0	148.5
Sm	10.65	24.10	22.70	14.75	24.70	15.30	6.82	13.80	14.80
Sn	5	30	66	74	50	75	9	12	6
Sr	590.0	654.0	543.0	756.0	682.0	802.0	168.5	961.0	1045.0
Ta	1.6	1.3	1.1	1.1	1.2	1.2	1.0	1.5	1.4
Tb	1.25	1.88	1.72	1.31	1.68	1.36	0.71	1.40	1.20
Th	22.90	76.50	82.90	31.40	59.40	51.60	3.66	27.70	32.60
Tl	0.6	0.7	1.8	0.9	0.9	1.9	1.6	1.7	1.0
Tm	0.30	0.44	0.35	0.46	0.39	0.49	0.26	0.41	0.44
U	4.63	9.72	10.15	7.10	11.60	10.60	3.78	7.39	6.91
V	73	136	140	158	116	103	127	182	172
W	1	12	346	5	2	34	8	5	1
Y	28.4	39.1	31.8	33.6	40.3	33.5	22	31.2	29.1
Yb	2.67	1.93	2.13	2.38	2.02	2.63	2.11	2.63	2.55
Zr	459	532	528	577	498	509	49	231	275
As	0.2	202	>250	204	222	>250	7.9	<0.1	0.7
Bi	0.12	1.3	1.46	0.63	0.6	0.16	0.81	0.13	0.25
Hg	<0.005	0.007	0.06	0.011	0.006	0.014	<0.005	<0.005	<0.005
Sb	<0.05	0.39	0.27	0.8	1.02	1.03	<0.05	<0.05	<0.05
Se	0.7	0.7	1	0.9	1.1	1.1	0.8	0.4	0.3
Te	<0.01	0.02	0.04	0.02	0.01	0.01	<0.01	<0.01	<0.01
LOI	1.68	2.2	2.73	1.51	2.52	1.84	1.71	1.33	1.27
Total	99.9	100.34	101.58	100.13	100.98	99.12	101.92	99.91	101.76
Ag	<0.5	<0.5	<0.5	<0.5	<0.5	<0.5	<0.5	<0.5	<0.5
Cd	<0.5	0.8	<0.5	<0.5	<0.5	<0.5	<0.5	<0.5	<0.5
Co	12	26	32	25	28	23	30	24	17
Cu	3	1	1	9	2	47	15	13	15
Li	50	40	110	50	40	50	140	70	70
Mo	<1	<1	<1	1	<1	2	<1	<1	<1
Ni	3	151	154	35	212	85	130	49	2
Pb	24	42	24	65	61	26	7	40	37
Sc	14	20	23	22	16	18	18	20	14
Zn	83	190	205	126	83	194	99	79	75
Ge									
In									
Re									

Couzinié et al., 2016. Supp. Table 1 (cont.): Whole-rock geochemical data for samples newly analyzed in the scope of this study

Sample	533-1	533-2	LR31	LR32	PRC53	PRC54	SC-13-09	SGC 12 026	SGC 12 039
Ref ALS	LR13221482	LR13221482	LR13221482	LR13221482	LR13221482	LR13221482	LR13221482	LR13221482	LR13221482
Long	4.37411	4.37411	4.113827	4.113827	4.101357	4.101357	3.65911	4.30658	4.07053
Lat	44.58249	44.58249	45.28477	45.28477	45.32981	45.32981	45.22474	44.65778	44.60045
Locality	Lamastre	Lamastre	La Roche	La Roche	Pont-Rouge quarry	Pont-Rouge quarry	Pubellier	Pont-de-Bayzan	Loubaresse
Type	vaugnerite	vaugnerite	vaugnerite	vaugnerite	syenite	syenite	vaugnerite	vaugnerite	vaugnerite
Details	sample courtesy of V. Gardien	sample courtesy of V. Gardien	Bt-clusters, HAS	Bt-clusters, HAS	LAS	LAS	dark facies	rounded enclave	coarse-granied, dark facies
SiO_2	56.40	50.50	52.80	49.90	60.00	61.80	57.70	50.60	57.60
Al_2O_3	11.45	9.25	15.05	14.75	15.95	15.90	13.25	13.45	14.70
Fe_2O_3	5.96	9.27	6.65	7.95	5.60	5.32	6.80	8.27	6.13
CaO	6.12	9.83	6.26	5.36	2.09	2.29	3.46	6.81	4.11
MgO	7.80	13.25	9.51	9.10	3.14	2.81	8.38	7.73	5.74
Na_2O	2.00	1.45	2.41	2.24	2.06	2.27	2.30	1.51	2.96
K_2O	4.16	2.93	1.77	2.44	6.69	6.38	4.21	5.71	3.42
Cr_2O_3	0.07	0.13	0.08	0.08	0.01	0.01	0.06	0.04	0.03
TiO_2	1.06	0.92	0.70	1.13	1.46	1.30	0.72	1.51	1.36
MnO	0.08	0.14	0.10	0.11	0.07	0.07	0.10	0.11	0.09
P_2O_5	0.60	0.60	0.35	0.37	0.75	0.65	0.32	1.22	0.68
SrO	0.03	0.04	0.08	0.07	0.06	0.06	0.08	0.06	0.10
BaO	0.18	0.18	0.06	0.08	0.23	0.20	0.15	0.46	0.19
C	0.02	0.06	0.26	0.29	0.02	0.02	0.01	0.26	0.02
S	0.12	0.23	0.06	0.07	0.04	0.04	0.08	0.05	0.04
Ba	1780	1580	597	746	2250	1890	1475	4490	1430
Ce	36.4	53.3	64.7	81.6	223.0	252.0	123.0	77.2	177.5
Cr	560	910	640	570	90	90	460	310	180
Cs	8.43	2.36	20.40	16.35	18.90	16.65	15.70	13.30	5.94
Dy	3.48	4.18	4.07	5.47	5.22	6.02	3.41	7.40	4.20
Er	1.56	2.08	2.01	3.43	2.50	2.24	1.49	3.89	1.75
Eu	1.35	1.49	1.24	1.76	3.07	2.77	1.75	2.04	2.31
Ga	16.5	12.2	18.1	17.5	27.9	27.3	18.9	17.8	20.4
Gd	4.23	5.94	4.77	6.11	8.64	9.66	6.28	8.25	8.52
Hf	1.9	4.0	2.9	4.3	15.6	15.0	6.3	5.0	10.2
Ho	0.64	0.85	0.67	1.05	0.86	0.96	0.48	1.23	0.62
La	14.5	24.5	34.7	41.3	103.0	122.0	61.7	33.8	91.5
Lu	0.15	0.23	0.28	0.42	0.27	0.32	0.27	0.49	0.24
Nb	14.3	9.0	9.6	14.1	36.8	36.6	15.2	14.0	23.4
Nd	20.2	27.8	26.6	38.7	105.0	106.0	51.4	41.9	77.5
Pr	4.84	6.57	7.69	10.20	27.00	28.70	14.10	9.71	20.80
Rb	232.0	95.7	89.7	105.0	305.0	303.0	180.0	173.0	138.5
Sm	6.07	6.16	5.45	7.51	17.95	16.65	8.83	8.22	12.95
Sn	19	3	2	2	10	8	6	4	6
Sr	250.0	345.0	641.0	570.0	503.0	522.0	485.0	490.0	577.0
Ta	2.0	0.7	0.6	1.1	2.3	2.3	1.4	1.1	1.0
Tb	0.62	0.81	0.69	1.11	1.14	1.09	0.72	1.13	0.92
Th	4.25	6.19	8.18	8.06	40.10	50.90	25.40	6.24	23.00
Tl	0.9	0.5	<0.5	0.7	1.7	1.4	1.4	0.8	0.5
Tm	0.13	0.19	0.23	0.45	0.30	0.28	0.17	0.53	0.27
U	4.06	1.37	4.41	4.09	7.56	7.53	5.80	2.64	3.01
V	212	175	139	192	90	75	122	237	73
W	6	<1	2	<1	<1	1	6	7	1
Y	16.7	18.7	17.7	24.4	21.8	25.1	17.1	33.1	18.6
Yb	1.07	1.64	1.40	2.80	1.63	1.83	1.72	3.57	1.18
Zr	76	156	98	149	641	559	259	187	437
As	0.8	0.4	2.1	2.4	2.7	0.6	0.3	3.8	3.2
Bi	0.15	0.08	0.06	0.05	0.15	0.21	0.19	0.21	0.12
Hg	<0.005	<0.005	<0.005	<0.005	<0.005	0.008	<0.005	<0.005	<0.005
Sb	<0.05	<0.05	<0.05	<0.05	<0.05	<0.05	<0.05	0.15	<0.05
Se	0.4	0.2	<0.2	0.4	0.9	0.9	0.6	0.6	0.6
Te	<0.01	<0.01	0.01	0.01	<0.01	0.01	<0.01	<0.01	<0.01
LOI	1.12	1.88	4.45	4.41	1.46	1.28	1.45	2.41	0.99
Total	97.03	100.37	100.27	97.99	99.57	100.34	98.98	99.89	98.1
Ag	<0.5	<0.5	<0.5	<0.5	<0.5	<0.5	<0.5	<0.5	<0.5
Cd	1.5	<0.5	<0.5	0.5	<0.5	<0.5	<0.5	<0.5	<0.5
Co	27	46	46	44	16	14	31	25	21
Cu	41	36	34	34	16	17	30	11	10
Li	60	30	40	50	30	30	50	50	50
Mo	<1	1	<1	1	<1	<1	1	1	1
Ni	23	61	232	200	17	16	207	6	136
Pb	10	13	9	9	42	45	43	20	8
Sc	26	36	25	29	13	13	15	31	13
Zn	82	76	82	93	94	100	73	83	84
Ge									
In									
Re									

Couzinié et al., 2016. Supp. Table 1 (cont.): Whole-rock geochemical data for samples newly analyzed in the scope of this study

Sample	SGC 12 042	SGC 12 013	SC-13-02a	SC-13-05
Ref ALS	LR13221482	LR13221482	LR13221482	LR13221482
Long	4.27383	4.08863	3.47373	3.63152
Lat	44.67262	44.49668	44.68734	44.76482
Locality	Meyras	La Borne	Moulin de Linas	L'Aldeyres
Type	vaugnerite	lamprophyre	vaugnerite	vaugnerite
Details	rounded body	medium-grained dyke	coarse-grained	coarse-grained
SiO_2	51.00	50.20	58.90	50.80
Al_2O_3	17.80	13.00	13.15	12.70
Fe_2O_3	8.96	8.22	6.75	10.20
CaO	5.26	4.95	4.90	6.54
MgO	5.20	11.45	6.88	12.60
Na_2O	1.41	1.41	2.33	2.14
K_2O	4.88	4.51	3.00	3.19
Cr_2O_3	0.01	0.08	0.05	0.08
TiO_2	1.94	1.10	0.90	0.97
MnO	0.10	0.12	0.09	0.14
P_2O_5	0.56	0.67	0.28	0.36
SrO	0.06	0.05	0.02	0.04
BaO	0.14	0.20	0.07	0.16
C	0.14	0.32	0.02	0.01
S	0.08	0.02	0.05	0.12
Ba	1365	1915	631	1375
Ce	152.0	97.4	72.7	75.0
Cr	100	730	360	590
Cs	14.65	30.60	15.45	9.20
Dy	7.30	4.92	4.39	4.03
Er	3.36	2.60	2.41	1.84
Eu	2.56	2.24	1.67	1.87
Ga	29.0	18.1	17.5	16.1
Gd	10.00	7.71	5.71	6.79
Hf	13.7	8.1	6.4	5.4
Ho	1.17	0.94	0.73	0.65
La	67.6	43.6	33.6	35.8
Lu	0.42	0.37	0.36	0.25
Nb	28.6	17.4	11.5	13.2
Nd	80.7	55.1	37.2	39.7
Pr	19.60	13.15	9.11	9.71
Rb	210.0	199.5	194.0	139.5
Sm	12.85	10.30	8.00	8.40
Sn	4	6	9	4
Sr	421.0	406.0	302.0	413.0
Ta	2.1	1.0	1.4	1.1
Tb	1.40	0.92	0.85	0.81
Th	17.95	24.60	16.75	16.15
Tl	0.7	1.2	0.8	1.7
Tm	0.56	0.36	0.26	0.19
U	2.77	5.61	6.18	4.93
V	117	150	102	135
W	1	2	4	3
Y	31.4	23.8	23.7	19.8
Yb	2.68	2.30	2.14	1.55
Zr	529	330	222	185
As	0.8	57.6	4.3	2.6
Bi	0.12	0.17	0.09	0.25
Hg	<0.005	0.007	<0.005	0.009
Sb	0.05	2.1	0.06	<0.05
Se	0.5	0.6	0.6	0.3
Te	<0.01	0.01	<0.01	<0.01
LOI	2.46	3.65	1.26	1.82
Total	99.78	99.61	98.58	101.74
Ag	<0.5	<0.5	<0.5	<0.5
Cd	<0.5	<0.5	<0.5	0.6
Co	27	40	28	52
Cu	19	17	32	43
Li	90	70	90	30
Mo	1	1	<1	1
Ni	16	254	110	152
Pb	9	23	12	22
Sc	19	21	14	20
Zn	105	92	69	91
Ge				
In				
Re				

Couzinié et al., 2016. Supp. Table 2: In *situ* LA-MC-ICPMS Lu-Hf isotope data for zircon standards analyzed in this study

	$^{176}Yb/^{177}Hf$ [a]	±2s	$^{176}Lu/^{177}Hf$ [a]	±2s	$^{178}Hf/^{177}Hf$	$^{180}Hf/^{177}Hf$	Sig_{Hf} [b] (V)	$^{176}Hf/^{177}Hf$	±2s	$^{176}Hf/^{177}Hf_{(t)}$	eHf(t) [c]	±2s	T_{DM2} [d] (Ga)
GJ1-1	0.0089	1	0.00029	0	1.46714	1.88665	9	0.282006	24	0.282003	-14.2	0.8	2.25
GJ1-2	0.0088	1	0.00029	0	1.46718	1.88677	9	0.281989	27	0.281986	-14.8	1.0	2.28
GJ1-3	0.0101	1	0.00033	0	1.46713	1.88660	9	0.282007	29	0.282004	-14.1	1.0	2.25
GJ1-4	0.0081	0	0.00028	0	1.46711	1.88673	9	0.281992	29	0.281989	-14.7	1.0	2.27
GJ1-5	0.0077	0	0.00026	0	1.46714	1.88662	13	0.282016	24	0.282013	-13.8	0.9	2.23
GJ1-6	0.0071	0	0.00025	0	1.46715	1.88682	12	0.281994	25	0.281991	-14.6	0.9	2.27
GJ1-7	0.0077	0	0.00026	0	1.46713	1.88678	13	0.281996	25	0.281993	-14.5	0.9	2.27
GJ1-8	0.0080	0	0.00026	0	1.46716	1.88671	13	0.281995	24	0.281992	-14.5	0.9	2.27
GJ1-9	0.0082	1	0.00026	0	1.46714	1.88665	14	0.282006	24	0.282003	-14.2	0.8	2.25
GJ1-10	0.0080	1	0.00026	0	1.46718	1.88664	13	0.282010	25	0.282007	-14.0	0.9	2.24
GJ1-11	0.0072	0	0.00024	0	1.46716	1.88687	12	0.281982	24	0.281980	-15.0	0.8	2.29
GJ1-12	0.0079	0	0.00025	0	1.46714	1.88679	12	0.281996	25	0.281993	-14.5	0.9	2.27
GJ1-13	0.0081	1	0.00026	0	1.46714	1.88679	11	0.281988	25	0.281985	-14.8	0.9	2.28
GJ1-14	0.0078	0	0.00025	0	1.46714	1.88673	11	0.282000	27	0.281997	-14.4	1.0	2.26
GJ1-15	0.0075	1	0.00024	0	1.46711	1.88679	10	0.282002	26	0.282000	-14.3	0.9	2.25
GJ1-16	0.0074	0	0.00024	0	1.46720	1.88675	10	0.281997	28	0.281994	-14.5	1.0	2.26
GJ1-17	0.0082	1	0.00026	0	1.46715	1.88661	15	0.282002	23	0.281999	-14.3	0.8	2.25
GJ1-18	0.0082	1	0.00026	0	1.46715	1.88676	15	0.282002	24	0.281999	-14.3	0.9	2.25
GJ1-19	0.0074	0	0.00025	0	1.46710	1.88678	13	0.282014	24	0.282011	-13.9	0.9	2.23
GJ1-20	0.0074	1	0.00024	0	1.46712	1.88668	14	0.282006	25	0.282003	-14.1	0.9	2.25
GJ1-21	0.0076	1	0.00024	0	1.46713	1.88669	14	0.282015	24	0.282012	-13.8	0.9	2.23
GJ1-22	0.0078	0	0.00025	0	1.46709	1.88670	14	0.281983	25	0.281980	-15.0	0.9	2.29
Average (n=22)	**0.0080**		**0.00026**		**1.46714**	**1.88672**		**0.282000**			**-14.4**		
2 S.D. ext.	**0.0013**		**0.00004**		**0.00005**	**0.00015**		**0.000020**			**0.7**		
91500-1	0.0100	0	0.00034	0	1.46722	1.88678	7	0.282292	26	0.282285	6.2	0.9	1.50
91500-2	0.0108	0	0.00036	0	1.46720	1.88673	7	0.282319	31	0.282312	7.1	1.1	1.44
91500-3	0.0115	1	0.00038	0	1.46712	1.88653	7	0.282301	29	0.282293	6.5	1.0	1.48
91500-4	0.0098	1	0.00032	0	1.46716	1.88670	12	0.282300	25	0.282294	6.5	0.9	1.48
91500-5	0.0103	1	0.00033	0	1.46715	1.88672	12	0.282272	24	0.282266	5.5	0.9	1.53
91500-6	0.0047	1	0.00016	0	1.46716	1.88674	10	0.282291	27	0.282288	6.3	0.9	1.49
91500-7	0.0098	1	0.00032	0	1.46715	1.88668	10	0.282286	27	0.282279	6.0	1.0	1.51
91500-8	0.0085	0	0.00028	0	1.46713	1.88680	9	0.282287	27	0.282281	6.1	1.0	1.50
91500-9	0.0093	1	0.00031	0	1.46711	1.88670	9	0.282287	26	0.282281	6.0	0.9	1.51
91500-10	0.0046	0	0.00015	0	1.46715	1.88664	13	0.282287	26	0.282283	6.1	0.9	1.50
91500-11	0.0046	0	0.00015	0	1.46710	1.88653	12	0.282293	27	0.282290	6.4	0.9	1.49
91500-12	0.0081	0	0.00027	0	1.46713	1.88665	13	0.282301	25	0.282296	6.6	0.9	1.48
91500-13	0.0082	1	0.00026	0	1.46712	1.88660	13	0.282320	26	0.282314	7.2	0.9	1.44
Average (n=13)	**0.0085**		**0.00028**		**1.46715**	**1.88668**		**0.282295**			**6.4**		
2 S.D. ext.	**0.0048**		**0.00015**		**0.00007**	**0.00017**		**0.000027**			**0.9**		
Pleso1	0.0048	1	0.00013	0	1.46715	1.88681	12	0.282480	27	0.282480	-3.3	1.0	1.44
Pleso2	0.0060	1	0.00014	0	1.46714	1.88674	12	0.282474	25	0.282473	-3.5	0.9	1.46
Pleso3	0.0074	0	0.00017	0	1.46720	1.88674	13	0.282466	25	0.282465	-3.8	0.9	1.47
Pleso4	0.0067	1	0.00015	0	1.46715	1.88679	21	0.282465	24	0.282464	-3.9	0.9	1.47
Pleso5	0.0051	1	0.00012	0	1.46715	1.88667	22	0.282468	23	0.282468	-3.7	0.8	1.47
Pleso7	0.0037	1	0.00009	0	1.46712	1.88669	17	0.282475	23	0.282475	-3.5	0.8	1.45
Pleso8	0.0046	2	0.00010	0	1.46715	1.88684	16	0.282464	25	0.282464	-3.9	0.9	1.48
Pleso9	0.0061	2	0.00014	0	1.46715	1.88667	15	0.282466	23	0.282466	-3.8	0.8	1.47
Pleso10	0.0066	2	0.00014	0	1.46713	1.88670	23	0.282466	22	0.282466	-3.8	0.8	1.47
Pleso11	0.0048	1	0.00012	0	1.46711	1.88666	23	0.282480	23	0.282479	-3.3	0.8	1.44
Pleso12	0.0044	0	0.00011	0	1.46711	1.88672	22	0.282474	25	0.282473	-3.5	0.9	1.46
Pleso13	0.0043	0	0.00009	0	1.46714	1.88670	21	0.282482	23	0.282482	-3.2	0.8	1.44
Pleso14	0.0044	0	0.00009	0	1.46715	1.88678	22	0.282477	24	0.282476	-3.4	0.8	1.45
Average (n=13)	**0.0053**		**0.00012**		**1.46714**	**1.88673**		**0.282472**			**-3.6**		
2 S.D. ext.	**0.0022**		**0.00005**		**0.00005**	**0.00012**		**0.000013**			**0.5**		
DEGEO1	0.0063	0	0.00018	0	1.46722	1.88670	7	0.281739	31	0.281737	-24.4	1.1	2.77
DEGEO2	0.0064	0	0.00018	0	1.46720	1.88685	7	0.281724	28	0.281722	-24.9	1.0	2.80
DEGEO3	0.0065	0	0.00018	0	1.46715	1.88679	8	0.281722	29	0.281720	-25.0	1.0	2.80
DEGEO4	0.0065	1	0.00017	0	1.46716	1.88670	12	0.281732	25	0.281730	-24.7	0.9	2.78
DEGEO5	0.0062	1	0.00017	0	1.46718	1.88668	12	0.281727	28	0.281725	-24.8	1.0	2.79
DEGEO6	0.0062	1	0.00017	0	1.46716	1.88676	10	0.281707	31	0.281706	-25.5	1.1	2.83
DEGEO7	0.0063	1	0.00017	0	1.46712	1.88665	10	0.281735	27	0.281734	-24.5	1.0	2.78
DEGEO8	0.0063	1	0.00017	0	1.46716	1.88677	9	0.281706	30	0.281705	-25.6	1.1	2.83
DEGEO9	0.0062	1	0.00017	0	1.46712	1.88664	9	0.281702	26	0.281700	-25.7	0.9	2.84
DEGEO12	0.0064	1	0.00017	0	1.46712	1.88668	13	0.281710	26	0.281708	-25.5	0.9	2.83
DEGEO13	0.0061	1	0.00017	0	1.46713	1.88673	13	0.281728	25	0.281726	-24.8	0.9	2.79
Average (n=11)	**0.0063**		**0.00017**		**1.46716**	**1.88672**		**0.281721**			**-25.1**		
2 S.D. ext.	**0.0003**		**0.00001**		**0.00007**	**0.00013**		**0.000026**			**0.9**		

Couzinié et al., 2016. Supp. Tab. 2 (cont.): In *situ* LA-MC-ICPMS Lu-Hf isotope data for zircon standards analyzed in this study

(a) $^{176}Yb/^{177}Hf = (^{176}Yb/^{173}Yb)_{true} \times (^{173}Yb/^{177}Hf)_{meas} \times (M_{173(Yb)}/M_{177(Hf)})^{b(Hf)}$, $b(Hf) = \ln(^{179}Hf/^{177}Hf_{true} / {}^{179}Hf/^{177}Hf_{measured}) / \ln (M_{179(Hf)}/M_{177(Hf)})$,
M=mass of respective isotope. The $^{176}Lu/^{177}Hf$ were calculated in a similar way by using the $^{175}Lu/^{177}Hf$ and b(Yb).

(b) Mean Hf signal in volt.

(c) Initial $^{176}Hf/^{177}Hf$ and eHf calculated using the apparent Pb-Pb age determined by LA-ICP-MS dating (see column f), and the CHUR parameters:
$^{176}Lu/^{177}Hf = 0.0336$, and $^{176}Hf/^{177}Hf = 0.282785$ (Bouvier *et al*., 2008).

(d) two stage model age in billion years using the measured $^{176}Lu/^{177}Lu$ of each spot (first stage = age of zircon),

a value of 0.0113 for the average continental crust (second stage),
and a juvenile crust (NC) $^{176}Lu/^{177}Lu$ and $^{176}Hf/^{177}Hf$ of 0.0384 and 0.28314, respectively.

Couzinié et al., 2016. Supp. Tab. 3: *In situ* LA-MC-ICPMS Lu-Hf isotope data for zircon in PCMM samples from the eastern FMC

	$^{176}Yb/^{177}Hf$ [a]	±2s	$^{176}Lu/^{177}Hf$ [a]	±2s	$^{178}Hf/^{177}Hf$	$^{180}Hf/^{177}Hf$	Sig_{Hf} [b] (V)	$^{176}Hf/^{177}Hf$	±2s	$^{176}Hf/^{177}Hf_{(t)}$	eHf(t) [c]	±2s	T_{DM2} [d] (Ga)
Monzodiorite SC-13-05													
a131	0.0282	45	0.00086	13	1.46714	1.88661	13	0.282454	34	0.282449	-4.9	1.2	1.51
a133	0.0228	50	0.00075	15	1.46709	1.88622	7	0.282362	32	0.282358	-8.2	1.1	1.69
a134	0.0264	55	0.00081	15	1.46699	1.88612	7	0.282414	37	0.282409	-6.4	1.3	1.59
a135	0.0267	57	0.00081	17	1.46704	1.88599	8	0.282389	41	0.282384	-7.2	1.5	1.64
a136	0.0266	64	0.00085	18	1.46702	1.88556	8	0.282372	41	0.282367	-7.9	1.5	1.67
a140	0.0248	29	0.00077	9	1.46704	1.88626	7	0.282430	34	0.282426	-5.8	1.2	1.56
a143	0.0171	43	0.00059	12	1.46708	1.88641	7	0.282430	34	0.282426	-5.8	1.2	1.56
a144	0.0356	62	0.00107	18	1.46713	1.88669	13	0.282491	32	0.282485	-3.7	1.1	1.45
a138	0.0095	13	0.00032	4	1.46710	1.88610	8	0.282397	36	0.282395	-6.9	1.3	1.62
a130	0.0252	49	0.00078	13	1.46699	1.88570	7	0.282427	37	0.282422	-5.9	1.3	1.57
a130-SC1305-NoUPb-1	0.0220	59	0.00067	16	1.46700	1.88550	8	0.282341	63	0.282338	-8.9	2.2	1.73
a130-SC1305-NoUPb-2	0.0247	24	0.00082	7	1.46704	1.88636	7	0.282421	32	0.282416	-6.1	1.1	1.58
a130-SC1305-NoUPb-3	0.0383	45	0.00115	13	1.46699	1.88636	7	0.282436	37	0.282429	-5.6	1.3	1.55
a130-SC1305-NoUPb-4	0.0270	68	0.00083	20	1.46713	1.88652	8	0.282438	31	0.282433	-5.5	1.1	1.54
Mean (n=14)	0.0254		0.00079		1.46706	1.88617				**0.282410**	**-6.3**		**1.59**
±2σ (ext.)	0.0139		0.00039		0.00011	0.00075				**0.000077**	**2.7**		
Qz Monzodiorite SC-13-02A													
a123	0.0358	9	0.00113	2	1.46710	1.88653	10	0.282391	32	0.282384	-7.3	1.1	1.64
a125	0.0376	18	0.00120	5	1.46707	1.88656	9	0.282352	36	0.282345	-8.7	1.3	1.72
a126	0.0712	52	0.00212	15	1.46719	1.88697	10	0.282483	36	0.282471	-4.2	1.3	1.47
a127	0.0584	27	0.00183	7	1.46712	1.88671	16	0.282439	28	0.282429	-5.7	1.0	1.55
a127-SC1302A-NoUPb-1	0.0222	24	0.00058	6	1.46711	1.88667	21	0.282439	49	0.282436	-5.4	1.7	1.54
a127-SC1302A-NoUPb-2	0.0265	7	0.00079	2	1.46711	1.88652	15	0.282426	29	0.282421	-5.9	1.0	1.57
Mean (n=6)	0.0420		0.00128		1.46712	1.88666				**0.282414**	**-6.2**		**1.58**
±2σ (ext.)	0.0380		0.00119		0.00008	0.00034				**0.000088**	**3.1**		
Qz Syenite PRC-53													
a79	0.0243	22	0.00072	6	1.46721	1.88665	11	0.282471	39	0.282467	-4.2	1.4	1.48
a84	0.0147	10	0.00044	2	1.46707	1.88615	14	0.282394	31	0.282391	-6.8	1.1	1.62
a84-prc53-NoUPb-1	0.0189	12	0.00056	4	1.46712	1.88644	12	0.282452	27	0.282448	-4.8	1.0	1.51
a84-prc53-NoUPb-2	0.0150	11	0.00044	3	1.46713	1.88655	14	0.282462	33	0.282459	-4.4	1.2	1.49
a84-prc53-NoUPb-3	0.0157	9	0.00049	3	1.46710	1.88636	15	0.282404	32	0.282402	-6.5	1.1	1.60
a84-prc53-NoUPb-4	0.0220	13	0.00064	4	1.46712	1.88645	14	0.282443	28	0.282439	-5.1	1.0	1.53
a84-prc53-NoUPb-5	0.0159	7	0.00048	2	1.46714	1.88650	11	0.282410	24	0.282407	-6.3	0.8	1.59
a84-prc53-NoUPb-6	0.0172	16	0.00045	4	1.46708	1.88648	14	0.282483	28	0.282480	-3.7	1.0	1.45
a85	0.0126	20	0.00038	6	1.46704	1.88612	6	0.282355	35	0.282353	-8.2	1.3	1.70
a86	0.0170	8	0.00052	3	1.46706	1.88606	6	0.282377	37	0.282374	-7.4	1.3	1.66
a87	0.0149	14	0.00042	3	1.46696	1.88565	9	0.282322	32	0.282319	-9.4	1.1	1.76
a90	0.0111	16	0.00035	5	1.46703	1.88598	15	0.282339	32	0.282337	-8.7	1.1	1.73
a92	0.0118	9	0.00037	3	1.46713	1.88664	13	0.282419	28	0.282417	-5.9	1.0	1.57
a94	0.0220	10	0.00064	4	1.46703	1.88601	13	0.282442	32	0.282438	-5.2	1.1	1.53
a96	0.0142	7	0.00045	2	1.46708	1.88648	11	0.282425	27	0.282422	-5.7	1.0	1.56
a97	0.0132	7	0.00039	2	1.46713	1.88654	12	0.282439	31	0.282436	-5.2	1.1	1.54
a100	0.0145	16	0.00045	5	1.46709	1.88630	14	0.282385	32	0.282382	-7.2	1.1	1.64
a101	0.0193	19	0.00058	5	1.46718	1.88668	10	0.282469	30	0.282466	-4.2	1.1	1.48

Couzinié et al., 2016. Supp. Tab. 3 (cont.): *In situ* LA-MC-ICPMS Lu-Hf isotope data for zircon in PCMM samples from the eastern FMC

	$^{176}Yb/^{177}Hf$ [a]	±2s	$^{176}Lu/^{177}Hf$ [a]	±2s	$^{178}Hf/^{177}Hf$	$^{180}Hf/^{177}Hf$	Sig_{Hf} [b] (V)	$^{176}Hf/^{177}Hf$	±2s	$^{176}Hf/^{177}Hf_{(t)}$	eHf(t) [c]	±2s	T_{DM2} [d] (Ga)
Mean (n=18)	0.0163		0.00049		1.46709	1.88634				**0.282413**	**-6.1**		**1.58**
±2σ (ext.)	0.0074		0.00021		0.00012	0.00056				**0.000093**	**3.3**		
Qz Monzonite PRC-54													
a153	0.0228	15	0.00069	4	1.46705	1.88626	6	0.282433	37	0.282429	-5.5	1.3	1.55
a155	0.0206	11	0.00061	3	1.46698	1.88620	6	0.282394	41	0.282390	-6.9	1.4	1.63
a156	0.0127	12	0.00039	4	1.46711	1.88630	11	0.282411	35	0.282408	-6.2	1.2	1.59
a158	0.0223	18	0.00068	5	1.46717	1.88661	11	0.282469	35	0.282465	-4.2	1.2	1.48
a159	0.0144	16	0.00045	5	1.46715	1.88663	10	0.282411	25	0.282409	-6.2	0.9	1.59
a161	0.0131	19	0.00040	6	1.46700	1.88601	6	0.282379	30	0.282377	-7.3	1.0	1.65
a162	0.0137	15	0.00043	4	1.46703	1.88581	6	0.282371	38	0.282368	-7.6	1.3	1.67
a167	0.0167	13	0.00052	4	1.46706	1.88625	10	0.282413	29	0.282410	-6.2	1.0	1.59
a168	0.0198	14	0.00059	4	1.46710	1.88650	11	0.282421	32	0.282417	-5.9	1.1	1.57
a169	0.0150	14	0.00046	4	1.46705	1.88613	12	0.282382	30	0.282380	-7.2	1.0	1.64
a172	0.0169	6	0.00052	2	1.46703	1.88599	7	0.282344	37	0.282341	-8.6	1.3	1.72
a174	0.0160	21	0.00049	6	1.46713	1.88648	7	0.282423	41	0.282420	-5.8	1.4	1.57
a174-PRC54-NoUPb-1	0.0161	17	0.00048	5	1.46710	1.88623	13	0.282381	35	0.282378	-7.3	1.2	1.65
a174-PRC54-NoUPb-3	0.0207	15	0.00061	4	1.46698	1.88574	12	0.282329	30	0.282325	-9.2	1.1	1.75
a174-PRC54-NoUPb-4	0.0180	13	0.00053	4	1.46710	1.88636	11	0.282408	26	0.282405	-6.3	0.9	1.60
Mean (n=15)	0.0173		0.00052		1.46707	1.88623				**0.282395**	**-6.7**		**1.62**
±2σ (ext.)	0.0066		0.00019		0.00012	0.00053				**0.000070**	**2.5**		
Diorite LR-32													
a208	0.0562	99	0.00189	32	1.46715	1.88678	7	0.282533	29	0.282523	-2.6	1.0	1.38
a210	0.0096	11	0.00041	4	1.46714	1.88663	7	0.282507	29	0.282505	-3.2	1.0	1.41
a211	0.0874	27	0.00299	9	1.46707	1.88668	7	0.282576	28	0.282559	-1.3	1.0	1.31
a212	0.0583	58	0.00198	20	1.46710	1.88632	10	0.282494	28	0.282483	-4.0	1.0	1.45
a214	0.0746	17	0.00247	5	1.46702	1.88619	9	0.282492	35	0.282478	-4.2	1.2	1.46
a215	0.0769	18	0.00230	9	1.46717	1.88673	8	0.282549	27	0.282536	-2.1	1.0	1.35
a217	0.0272	52	0.00095	17	1.46709	1.88637	9	0.282501	30	0.282495	-3.5	1.0	1.43
a218	0.0234	39	0.00080	12	1.46707	1.88642	9	0.282485	28	0.282481	-4.1	1.0	1.46
a219	0.0788	18	0.00271	6	1.46716	1.88669	7	0.282555	29	0.282539	-2.0	1.0	1.34
a220	0.0458	35	0.00158	11	1.46701	1.88629	4	0.282487	33	0.282478	-4.2	1.2	1.46
a221	0.0258	24	0.00096	9	1.46707	1.88631	4	0.282512	44	0.282507	-3.1	1.6	1.41
a223	0.1707	242	0.00401	51	1.46698	1.88634	9	0.282539	52	0.282516	-2.8	1.8	1.39
a226	0.0199	33	0.00076	11	1.46713	1.88644	8	0.282510	30	0.282506	-3.2	1.1	1.41
a227	0.0757	36	0.00256	13	1.46701	1.88603	5	0.282524	43	0.282509	-3.0	1.5	1.40
a227-LR32-NoUPb-1	0.0992	23	0.00323	9	1.46703	1.88596	5	0.282491	44	0.282473	-4.3	1.6	1.47
Mean (n=15)	0.0620		0.00197		1.46708	1.88641				**0.282506**	**-3.2**		**1.41**
±2σ (ext.)	0.0820		0.00211		0.00012	0.00050				**0.000051**	**1.8**		
Qz Diorite LR-31													
a318	0.0261	61	0.00089	19	1.46715	1.88662	13	0.282512	32	0.282507	-3.2	1.1	1.41
a319	0.0882	144	0.00270	40	1.46713	1.88652	12	0.282557	30	0.282541	-2.0	1.1	1.34
a319-LR31-NoUPb-1	0.0230	31	0.00067	8	1.46710	1.88651	16	0.282507	29	0.282503	-3.3	1.0	1.42
a321	0.0626	49	0.00207	14	1.46709	1.88672	10	0.282532	30	0.282521	-2.7	1.1	1.38
a322	0.0190	5	0.00076	2	1.46716	1.88680	6	0.282529	30	0.282524	-2.6	1.0	1.37
a323	0.0573	37	0.00194	12	1.46710	1.88657	12	0.282542	25	0.282531	-2.3	0.9	1.36

Couzinié et al., 2016. Supp. Tab. 3 (cont.): *In situ* LA-MC-ICPMS Lu-Hf isotope data for zircon in PCMM samples from the eastern FMC

	$^{176}Yb/^{177}Hf$ [a]	±2s	$^{176}Lu/^{177}Hf$ [a]	±2s	$^{178}Hf/^{177}Hf$	$^{180}Hf/^{177}Hf$	Sig_{Hf} [b] (V)	$^{176}Hf/^{177}Hf$	±2s	$^{176}Hf/^{177}Hf_{(t)}$	eHf(t) [c]	±2s	T_{DM2} [d] (Ga)
a325	0.0500	58	0.00172	18	1.46713	1.88668	13	0.282543	27	0.282533	-2.3	1.0	1.36
a326	0.0301	49	0.00105	16	1.46710	1.88650	13	0.282518	25	0.282512	-3.0	0.9	1.40
a334	0.0263	7	0.00093	3	1.46715	1.88670	11	0.282538	26	0.282533	-2.3	0.9	1.36
a335	0.0412	45	0.00142	14	1.46717	1.88678	11	0.282551	24	0.282543	-1.9	0.9	1.34
a337	0.0448	26	0.00152	9	1.46713	1.88646	14	0.282520	25	0.282511	-3.0	0.9	1.40
a338	0.0422	66	0.00140	21	1.46709	1.88642	14	0.282516	30	0.282508	-3.1	1.1	1.41
a339	0.0180	14	0.00063	4	1.46717	1.88680	12	0.282539	30	0.282535	-2.2	1.1	1.35
a339-LR31-NoUPb-1	0.0430	25	0.00141	8	1.46716	1.88673	13	0.282537	27	0.282529	-2.4	0.9	1.36
a339-LR31-NoUPb-2	0.0472	55	0.00154	14	1.46708	1.88646	13	0.282471	32	0.282462	-4.8	1.1	1.49
a343	0.0469	54	0.00145	12	1.46716	1.88672	11	0.282546	32	0.282538	-2.1	1.1	1.35
Mean (n=16)	0.0416		0.00138		1.46713	1.88662				**0.282521**	**-2.7**		**1.38**
±2σ (ext.)	0.0366		0.00112		0.00006	0.00026				**0.000041**	**1.4**		
Qz Monzodiorite SC-13-09													
a270	0.0383	48	0.00118	13	1.46712	1.88693	16	0.282497	25	0.282490	-3.5	0.9	1.44
a271	0.0529	72	0.00161	20	1.46719	1.88692	14	0.282492	32	0.282482	-3.2	1.1	1.44
a273	0.0403	32	0.00121	9	1.46714	1.88691	15	0.282510	27	0.282503	-3.1	0.9	1.41
a277	0.0331	24	0.00099	7	1.46711	1.88679	14	0.282505	26	0.282499	-3.2	0.9	1.42
a278	0.0256	22	0.00075	6	1.46719	1.88697	17	0.282473	27	0.282468	-4.3	1.0	1.48
a279	0.0358	24	0.00107	7	1.46711	1.88652	14	0.282467	24	0.282461	-4.6	0.9	1.49
a281	0.0393	27	0.00113	8	1.46716	1.88687	20	0.282488	24	0.282482	-3.8	0.9	1.45
a281-sc13-09-NoUPb-1	0.0609	74	0.00178	21	1.46720	1.88669	14	0.282512	26	0.282502	-3.1	0.9	1.41
a288	0.0418	37	0.00126	10	1.46713	1.88658	18	0.282483	28	0.282475	-4.1	1.0	1.46
a290	0.0389	21	0.00113	6	1.46709	1.88652	18	0.282474	24	0.282467	-4.4	0.9	1.48
a292	0.0249	22	0.00075	6	1.46715	1.88693	21	0.282507	23	0.282503	-3.1	0.8	1.41
a294	0.0448	38	0.00131	10	1.46710	1.88661	16	0.282466	26	0.282458	-4.7	0.9	1.50
a295	0.0571	18	0.00165	5	1.46713	1.88674	18	0.282502	25	0.282493	-3.4	0.9	1.43
a298	0.0529	27	0.00155	7	1.46717	1.88662	14	0.282515	25	0.282506	-3.0	0.9	1.41
a299	0.0323	73	0.00096	20	1.46718	1.88672	24	0.282464	30	0.282459	-4.6	1.1	1.50
a300	0.0549	16	0.00160	4	1.46712	1.88670	15	0.282488	24	0.282478	-3.9	0.8	1.46
Mean (n=16)	0.0421		0.00124		1.46714	1.88675				**0.282483**	**-3.8**		**1.45**
±2σ (ext.)	0.0219		0.00063		0.00007	0.00031				**0.000034**	**1.2**		
Qz Monzodiorite SGC-12-39													
a255	0.0323	28	0.00096	8	1.46715	1.88678	14	0.282493	27	0.282488	-3.7	0.9	1.44
a255-sgc12-39-NoUPb-1	0.0361	26	0.00106	8	1.46721	1.88698	14	0.282526	27	0.282520	-2.6	1.0	1.38
a255-sgc12-39-NoUPb-2	0.0098	9	0.00034	2	1.46714	1.88671	15	0.282473	27	0.282471	-4.3	0.9	1.47
a255-sgc12-39-NoUPb-3	0.0206	30	0.00063	9	1.46715	1.88674	15	0.282478	27	0.282474	-4.2	0.9	1.47
a255-sgc12-39-NoUPb-4	0.0136	10	0.00043	3	1.46715	1.88667	17	0.282461	26	0.282459	-4.7	0.9	1.50
a255-sgc12-39-NoUPb-5	0.0158	24	0.00047	6	1.46714	1.88677	16	0.282481	25	0.282478	-4.0	0.9	1.46
a256	0.0153	26	0.00052	8	1.46711	1.88636	6	0.282437	39	0.282434	-5.6	1.4	1.55
a257	0.0217	18	0.00067	5	1.46715	1.88680	14	0.282501	26	0.282498	-3.3	0.9	1.42
a259	0.0286	13	0.00087	4	1.46711	1.88675	13	0.282515	24	0.282510	-2.9	0.8	1.40
a260	0.0358	58	0.00106	16	1.46712	1.88674	16	0.282474	30	0.282468	-4.4	1.1	1.48
a261	0.0210	34	0.00060	10	1.46713	1.88677	21	0.282494	27	0.282491	-3.6	1.0	1.44
a262	0.0117	10	0.00039	3	1.46716	1.88678	16	0.282485	26	0.282483	-3.8	0.9	1.45
a263	0.0432	24	0.00126	7	1.46717	1.88669	15	0.282504	25	0.282497	-3.4	0.9	1.42
a265	0.0227	45	0.00069	12	1.46714	1.88672	15	0.282499	25	0.282496	-3.4	0.9	1.43

Couzinié et al., 2016. Supp. Tab. 3 (cont.): *In situ* LA-MC-ICPMS Lu-Hf isotope data for zircon in PCMM samples from the eastern FMC

	$^{176}Yb/^{177}Hf$ [a]	±2s	$^{176}Lu/^{177}Hf$ [a]	±2s	$^{178}Hf/^{177}Hf$	$^{180}Hf/^{177}Hf$	Sig_{Hf} [b] (V)	$^{176}Hf/^{177}Hf$	±2s	$^{176}Hf/^{177}Hf_{(t)}$	eHf(t) [c]	±2s	T_{DM2} [d] (Ga)
a266	0.0148	36	0.00048	10	1.46716	1.88674	16	0.282496	23	0.282493	-3.5	0.8	1.43
a267	0.0460	56	0.00131	15	1.46715	1.88685	16	0.282514	28	0.282507	-3.0	1.0	1.40
Mean (n=16)	0.0243		0.00073		1.46715	1.88674				**0.282485**	**-3.8**		**1.45**
±2σ (ext.)	0.0228		0.00063		0.00005	0.00025				**0.000042**	**1.5**		
Monzodiorite SGC-12-42													
a301	0.0562	12	0.00172	3	1.46716	1.88669	13	0.282511	26	0.282501	-3.2	0.9	1.42
a303	0.0382	40	0.00118	12	1.46716	1.88683	14	0.282486	31	0.282479	-4.0	1.1	1.46
a304	0.0245	18	0.00075	6	1.46715	1.88670	16	0.282455	23	0.282451	-5.0	0.8	1.51
a305	0.0137	18	0.00042	5	1.46714	1.88668	20	0.282445	27	0.282443	-5.3	1.0	1.53
a306	0.0583	85	0.00176	23	1.46713	1.88670	13	0.282490	25	0.282480	-4.0	0.9	1.46
a309	0.0205	29	0.00063	8	1.46714	1.88663	18	0.282458	26	0.282454	-4.9	0.9	1.51
a311	0.0318	16	0.00097	5	1.46714	1.88679	14	0.282462	24	0.282456	-4.8	0.8	1.50
a313	0.0176	18	0.00057	5	1.46710	1.88674	15	0.282452	24	0.282448	-5.1	0.9	1.52
a313-sgc12-42-NoUPb-1	0.0085	12	0.00029	4	1.46715	1.88679	17	0.282451	26	0.282450	-5.1	0.9	1.52
a313-sgc12-42-NoUPb-3	0.0154	5	0.00049	2	1.46714	1.88664	13	0.282474	25	0.282472	-4.3	0.9	1.47
a313-sgc12-42-NoUPb-4	0.0123	29	0.00041	8	1.46713	1.88679	17	0.282459	23	0.282457	-4.8	0.8	1.50
a313-sgc12-42-NoUPb-5	0.0297	17	0.00090	5	1.46713	1.88667	16	0.282446	26	0.282441	-5.4	0.9	1.53
a315	0.0211	41	0.00068	13	1.46715	1.88661	14	0.282455	24	0.282451	-5.0	0.9	1.51
a317	0.0150	16	0.00049	5	1.46718	1.88679	18	0.282474	25	0.282471	-4.3	0.9	1.47
Mean (n=14)	0.0259		0.00080		1.46714	1.88672				**0.282461**	**-4.7**		**1.49**
±2σ (ext.)	0.0312		0.00093		0.00004	0.00014				**0.000034**	**1.2**		
Monzodiorite SGC-12-26													
a373	0.0432	58	0.00150	19	1.46716	1.88661	12	0.282505	26	0.282496	-3.4	0.9	1.43
a375	0.0222	39	0.00079	12	1.46718	1.88674	12	0.282487	27	0.282483	-3.9	0.9	1.45
a377	0.0359	79	0.00121	25	1.46715	1.88669	13	0.282500	28	0.282493	-3.5	1.0	1.43
a378	0.1035	58	0.00339	19	1.46716	1.88676	12	0.282541	26	0.282522	-2.5	0.9	1.38
a379	0.0227	35	0.00077	11	1.46712	1.88680	12	0.282516	27	0.282512	-2.9	1.0	1.40
a380	0.0709	17	0.00235	5	1.46715	1.88667	12	0.282538	27	0.282525	-2.4	0.9	1.37
a381	0.0179	15	0.00074	4	1.46708	1.88678	11	0.282489	26	0.282485	-3.8	0.9	1.45
a388	0.0591	44	0.00201	15	1.46709	1.88663	13	0.282518	26	0.282507	-3.0	0.9	1.41
a390	0.0346	61	0.00119	18	1.46715	1.88657	13	0.282503	25	0.282496	-3.4	0.9	1.43
a392	0.0340	27	0.00123	9	1.46714	1.88668	12	0.282488	25	0.282481	-3.9	0.9	1.45
a395	0.0475	16	0.00161	4	1.46714	1.88681	11	0.282516	27	0.282507	-3.0	1.0	1.40
a396	0.0111	12	0.00048	4	1.46713	1.88673	12	0.282511	26	0.282509	-3.0	0.9	1.40
a397	0.0850	47	0.00281	14	1.46716	1.88680	11	0.282554	31	0.282538	-1.9	1.1	1.34
a398	0.0451	59	0.00154	20	1.46713	1.88677	13	0.282507	25	0.282498	-3.4	0.9	1.42
a400	0.0418	48	0.00144	16	1.46714	1.88662	13	0.282494	27	0.282485	-3.8	1.0	1.45
Mean (n=15)	0.0450		0.00154		1.46714	1.88671				**0.282502**	**-3.2**		**1.41**
±2σ (ext.)	0.0511		0.00162		0.00005	0.00015				**0.000034**	**1.2**		
Diorite 533 - 2													
a345	0.0438	22	0.00142	7	1.46709	1.88645	14	0.282509	31	0.282501	-3.2	1.1	1.42
a346	0.0461	34	0.00154	9	1.46717	1.88673	11	0.282546	27	0.282537	-1.9	1.0	1.35
a347	0.0214	9	0.00074	3	1.46717	1.88681	13	0.282511	28	0.282507	-3.0	1.0	1.40
a348	0.0294	16	0.00107	5	1.46715	1.88678	13	0.282513	26	0.282506	-3.0	0.9	1.41
a351	0.0292	34	0.00095	11	1.46717	1.88670	11	0.282522	26	0.282516	-2.7	0.9	1.39

Couzinié et al., 2016. Supp. Tab. 3 (cont.): *In situ* LA-MC-ICPMS Lu-Hf isotope data for zircon in PCMM samples from the eastern FMC

	$^{176}Yb/^{177}Hf$ [a]	±2s	$^{176}Lu/^{177}Hf$ [a]	±2s	$^{178}Hf/^{177}Hf$	$^{180}Hf/^{177}Hf$	Sig_{Hf} [b] (V)	$^{176}Hf/^{177}Hf$	±2s	$^{176}Hf/^{177}Hf_{(t)}$	eHf(t) [c]	±2s	T_{DM2} [d] (Ga)
a353	0.0411	18	0.00138	5	1.46719	1.88665	12	0.282519	27	0.282511	-2.9	0.9	1.40
a354	0.0522	36	0.00169	11	1.46718	1.88676	11	0.282571	26	0.282562	-1.1	0.9	1.30
a358	0.0494	28	0.00162	7	1.46712	1.88657	13	0.282504	27	0.282494	-3.5	0.9	1.43
a360	0.0570	49	0.00184	14	1.46717	1.88687	10	0.282550	28	0.282540	-1.8	1.0	1.34
a361	0.0325	45	0.00107	14	1.46711	1.88670	13	0.282524	24	0.282518	-2.6	0.8	1.38
a363	0.0357	15	0.00119	3	1.46710	1.88655	14	0.282523	25	0.282516	-2.7	0.9	1.39
a364	0.0380	33	0.00121	9	1.46710	1.88677	14	0.282529	27	0.282522	-2.5	0.9	1.38
a365	0.0269	25	0.00090	8	1.46710	1.88665	11	0.282485	26	0.282480	-4.0	0.9	1.46
a366	0.0136	12	0.00053	3	1.46716	1.88679	11	0.282504	27	0.282501	-3.2	1.0	1.42
a367	0.0514	30	0.00166	10	1.46712	1.88665	11	0.282543	27	0.282533	-2.1	1.0	1.35
Mean (n=15)	0.0379		0.00125		1.46714	1.88670				**0.282516**	**-2.7**		**1.39**
±2σ (ext.)	0.0248		0.00076		0.00007	0.00022				**0.000041**	**1.4**		
Qz Monzodiorite 533 - 1													
a107	0.0597	65	0.00191	20	1.46709	1.88650	12	0.282521	28	0.282510	-2.9	1.0	1.40
a110	0.0325	66	0.00105	21	1.46717	1.88662	13	0.282501	36	0.282495	-3.4	1.3	1.43
a112	0.0535	75	0.00165	22	1.46712	1.88649	14	0.282507	34	0.282497	-3.3	1.2	1.42
a113	0.0673	60	0.00215	18	1.46705	1.88649	10	0.282496	29	0.282483	-3.8	1.0	1.45
a115	0.0366	25	0.00127	9	1.46708	1.88632	12	0.282467	28	0.282459	-4.7	1.0	1.50
a116	0.0888	96	0.00272	28	1.46698	1.88586	10	0.282490	35	0.282474	-4.2	1.2	1.47
a117	0.0391	71	0.00125	22	1.46715	1.88635	12	0.282458	27	0.282451	-5.0	0.9	1.51
a118	0.0339	36	0.00109	11	1.46711	1.88637	12	0.282471	30	0.282465	-4.5	1.0	1.49
a119	0.0528	189	0.00158	55	1.46717	1.88687	11	0.282507	26	0.282498	-3.3	0.9	1.42
a119b	0.0846	143	0.00258	44	1.46710	1.88633	13	0.282482	31	0.282467	-4.4	1.1	1.48
a122	0.0492	64	0.00156	18	1.46704	1.88639	12	0.282446	30	0.282437	-5.4	1.1	1.54
Mean (n=11)	0.0544		0.00171		1.46710	1.88642				**0.282476**	**-4.1**		**1.46**
±2σ (ext.)	0.0389		0.00114		0.00011	0.00049				**0.000045**	**1.6**		

(a) $^{176}Yb/^{177}Hf = (^{176}Yb/^{173}Yb)_{true} \times (^{173}Yb/^{177}Hf)_{meas} \times (M_{173(Yb)}/M_{177(Hf)})^{b(Hf)}$, $b(Hf) = \ln(^{179}Hf/^{177}Hf_{true} / {}^{179}Hf/^{177}Hf_{measured}) / \ln(M_{179(Hf)}/M_{177(Hf)})$, M=mass of respective isotope. The $^{176}Lu/^{177}Hf$ were calculated in a similar way by using the $^{175}Lu/^{177}Hf$ and b(Yb).

(b) Mean Hf signal in volt.

(c) Initial $^{176}Hf/^{177}Hf$ and eHf calculated using an emplacement age of 311 Ma and the CHUR parameters:

$^{176}Lu/^{177}Hf = 0.0336$, and $^{176}Hf/^{177}Hf = 0.282785$ (Bouvier *et al*., 2008).

(d) two stage model age in billion years using the measured $^{176}Lu/^{177}Lu$ of each spot (first stage = age of zircon), a value of 0.0113 for the average continental crust (second stage), and a juvenile crust (NC) $^{176}Lu/^{177}Lu$ and $^{176}Hf/^{177}Hf$ of 0.0384 and 0.28325, respectively.

Couzinié et al., 2016. Supplementary Table 4:

Zircon in situ SHRIMP O isotope data for standards during the analytical runs

Cross-checking standard, Zircon 91500, delta 18O = 9.86 ± 0.11 ‰ Wiedenbeck et al., 2004

Session 1

spot ID	$\delta^{18}O$ ‰	error (1σ)	$^{18}O/^{16}O$	error (1σ)
91500-1	9.92	0.12	0.00202508	0.00002460
91500-2	9.57	0.06	0.00202438	0.00001239
91500-3	9.76	0.08	0.00202478	0.00001714
91500-4	9.85	0.09	0.00202494	0.00001892
91500-5	9.77	0.07	0.00202479	0.00001534
91500-6	9.81	0.06	0.00202487	0.00001323
91500-7	10.09	0.10	0.00202542	0.00002094
91500-8	9.54	0.09	0.00202432	0.00001994
91500-9	9.81	0.07	0.00202487	0.00001515
91500-10	9.99	0.07	0.00202523	0.00001499
91500-11	10.30	0.07	0.00202585	0.00001388
91500-12	9.42	0.13	0.00202410	0.00002860
statistics on 91500	**mean=**	**9.82**	**std dev=**	**0.24**

Calibration standard TEMORA 2, measured every 4 unknowns; calibration value delta 18O = 8.2 ‰, standard deviation = 0.39; measured on 42 spots in 23 grains

Session 2

spot ID	$\delta^{18}O$ ‰	error (1σ)	$^{18}O/^{16}O$	error (1σ)
91500-1	9.73	0.10	0.00202471	0.00002158
91500-2	9.94	0.15	0.00202512	0.00002979
91500-3	9.75	0.11	0.00202475	0.00002369
91500-4	9.60	0.13	0.00202445	0.00002709
91500-5	9.93	0.15	0.00202511	0.00002969
91500-6	10.17	0.12	0.00202559	0.00002473
91500-7	9.71	0.15	0.00202468	0.00003178
91500-8	9.72	0.13	0.00202470	0.00002723
91500-9	10.46	0.15	0.00202618	0.00002850
91500-10	10.01	0.09	0.00202527	0.00001820
91500-11	9.78	0.11	0.00202482	0.00002271
91500-12	9.69	0.10	0.00202462	0.00002105
91500-13	9.90	0.10	0.00202505	0.00002051
91500-14	9.95	0.08	0.00202514	0.00001713
statistics on 91500	**mean=**	**9.84**	**std dev=**	**0.23**

Calibration standard TEMORA 2, measured every 4 unknowns; calibration value delta 18O = 8.2 ‰, standard deviation = 0.38; measured on 28 spots in 20 grains

Session 3

spot ID	$\delta^{18}O$ ‰	error (1σ)	$^{18}O/^{16}O$	error (1σ)
91500-1	9.91	0.11	0.00202507	0.00002206
91500-2	9.60	0.12	0.00202445	0.00002435
91500-3	9.96	0.13	0.00202517	0.00002568
91500-4	10.02	0.08	0.00202529	0.00001540
91500-5	10.06	0.07	0.00202538	0.00001396
91500-6	10.16	0.10	0.00202558	0.00002009
91500-7	9.19	0.11	0.00202363	0.00002359
91500-8	9.86	0.07	0.00202497	0.00001410
91500-9	9.73	0.08	0.00202471	0.00001756
91500-10	9.72	0.09	0.00202469	0.00001957
statistics on 91500	**mean=**	**9.89**	**std dev=**	**0.28**

Calibration standard TEMORA 2, measured every 4 unknowns; calibration value delta 18O = 8.2 ‰, standard deviation = 0.41; measured on 20 spots in 20 grains

Couzinié et al., 2016. Supplementary Table 5:

Zircon in situ SHRIMP O isotope data for samples

	$\delta^{18}O$ ‰	error (1σ)	$^{18}O/^{16}O$	error (1σ)
Session 1				
Qz Monzodiorite 533 - 2				
1.1	6.95	0.10	0.00201913	0.00002953
3.1	7.31	0.12	0.00201985	0.00003337
4.1	7.45	0.10	0.00202014	0.00002690
5.1	7.46	0.11	0.00202015	0.00002993
6.1	7.62	0.11	0.00202048	0.00002847
7.1	7.30	0.10	0.00201983	0.00002793
9.1	8.37	0.10	0.00202199	0.00002327
10.1	8.51	0.11	0.00202227	0.00002573
10.2	8.42	0.08	0.00202208	0.00002031
11.1	8.23	0.11	0.00202171	0.00002780
14.1	8.38	0.12	0.00202200	0.00002793
15.1	7.76	0.10	0.00202076	0.00002732
16.1	8.50	0.11	0.00202224	0.00002610
17.1	7.81	0.10	0.00202085	0.00002502
18.1	7.64	0.12	0.00202053	0.00003199
19.1	7.95	0.09	0.00202113	0.00002377
Mean (n=16)	**7.85**			
±2σ (ext.)	**1.00**			
Qz Diorite LR-31				
3.1	7.73	0.09	0.00202070	0.00002391
4.1	7.75	0.10	0.00202074	0.00002629
5.1	7.57	0.12	0.00202039	0.00003092
7.1	8.69	0.11	0.00202262	0.00002449
9.1	8.01	0.10	0.00202126	0.00002436
10.1	8.07	0.11	0.00202139	0.00002769
11.1	7.92	0.10	0.00202107	0.00002568
12.1	8.08	0.09	0.00202140	0.00002353
13.1	7.45	0.10	0.00202015	0.00002598
14.1	7.39	0.11	0.00202001	0.00002988
15.1	7.31	0.09	0.00201985	0.00002518
Mean (n=11)	**7.81**			
±2σ (ext.)	**0.80**			
Qz Monzodiorite SC-13-09				
1.1	7.81	0.13	0.00202087	0.00003430
2.1	7.81	0.10	0.00202086	0.00002698
3.1	8.39	0.12	0.00202203	0.00002935
4.1	8.91	0.08	0.00202307	0.00001867
6.1	8.32	0.11	0.00202189	0.00002662
7.1	8.05	0.09	0.00202135	0.00002191
8.1	8.11	0.09	0.00202147	0.00002171
9.1	8.25	0.09	0.00202173	0.00002174
10.1	7.75	0.10	0.00202074	0.00002642
12.1	8.08	0.11	0.00202141	0.00002674
13.1	8.00	0.12	0.00202124	0.00002977
14.1	7.92	0.10	0.00202107	0.00002549
15.1	8.09	0.11	0.00202142	0.00002765
16.1	8.01	0.09	0.00202125	0.00002199
18.1	8.03	0.11	0.00202129	0.00002743
Mean (n=15)	**8.10**			
±2σ (ext.)	**0.58**			
Monzodiorite SGC-12-42				
1.1	7.67	0.11	0.00202057	0.00002796
2.1	8.22	0.11	0.00202168	0.00002695
3.1	6.41	0.09	0.00201806	0.00002971
4.1	6.87	0.10	0.00201898	0.00003041
5.1	7.15	0.10	0.00201953	0.00002862
5.2	7.02	0.09	0.00201928	0.00002585
7.1	8.04	0.11	0.00202131	0.00002669
8.1	7.80	0.11	0.00202085	0.00002768
9.1	7.18	0.11	0.00201960	0.00003039
10.1	6.89	0.12	0.00201901	0.00003500
11.1	7.27	0.10	0.00201978	0.00002823

	$\delta^{18}O$ ‰	error (1σ)	$^{18}O/^{16}O$	error (1σ)
Monzodiorite SGC-12-42				
12.1	8.24	0.11	0.00202172	0.00002673
13.1	8.13	0.09	0.00202151	0.00002179
14.1	7.67	0.10	0.00202058	0.00002528
15.1	6.69	0.13	0.00201862	0.00003877
16.1	7.59	0.08	0.00202041	0.00002124
Mean (n=16)	**7.43**			
±2σ (ext.)	**1.15**			
Session 2				
Qz Syenite PRC-53				
1.1	8.02	0.16	0.00202128	0.00003925
2.1	8.58	0.14	0.00202241	0.00003258
3.1	7.82	0.15	0.00202088	0.00003899
4.1	8.13	0.18	0.00202149	0.00004497
5.1	7.92	0.13	0.00202108	0.00003339
6.1	8.04	0.14	0.00202132	0.00003405
7.1	7.98	0.15	0.00202121	0.00003769
8.1	7.83	0.14	0.00202089	0.00003641
9.1	7.76	0.16	0.00202076	0.00004097
10.1	8.80	0.13	0.00202284	0.00002944
11.1	7.69	0.14	0.00202063	0.00003761
12.1	8.30	0.13	0.00202184	0.00003149
13.1	8.08	0.13	0.00202141	0.00003306
14.1	8.92	0.13	0.00202309	0.00002984
16.1	9.23	0.15	0.00202370	0.00003288
17.1	7.94	0.12	0.00202111	0.00002942
18.1	8.13	0.13	0.00202149	0.00003239
19.1	8.80	0.14	0.00202285	0.00003183
20.1	8.34	0.14	0.00202192	0.00003450
21.1	7.92	0.13	0.00202107	0.00003229
Mean (n=20)	**8.21**			
±2σ (ext.)	**0.87**			
Qz Monzonite PRC-54				
1.1	9.59	0.10	0.00202444	0.00002205
2.1	9.39	0.14	0.00202404	0.00003012
3.1	8.41	0.13	0.00202206	0.00003211
3.2	7.99	0.14	0.00202121	0.00003653
4.1	7.73	0.12	0.00202071	0.00003092
5.1	7.78	0.15	0.00202080	0.00004019
6.1	7.37	0.14	0.00201997	0.00003842
7.1	6.86	0.13	0.00201896	0.00003736
8.1	8.25	0.13	0.00202175	0.00003146
9.1	8.54	0.14	0.00202232	0.00003348
10.1	7.28	0.12	0.00201979	0.00003417
11.1	7.41	0.10	0.00202006	0.00002702
13.1	8.44	0.09	0.00202212	0.00002040
14.1	8.21	0.11	0.00202166	0.00002765
15.1	9.28	0.12	0.00202381	0.00002610
16.1	7.97	0.12	0.00202119	0.00003013
17.1	9.97	0.12	0.00202520	0.00002535
Mean (n=17)	**8.26**			
±2σ (ext.)	**1.75**			
Qz Monzodiorite 533 - 1				
1.1	8.11	0.14	0.00202146	0.00003541
2.1	8.80	0.13	0.00202285	0.00002888
3.1	8.43	0.18	0.00202211	0.00004311
4.1	7.75	0.14	0.00202075	0.00003696
5.1	7.72	0.15	0.00202067	0.00003997
7.1	8.21	0.09	0.00202166	0.00002231
8.1	7.94	0.11	0.00202112	0.00002892
9.1	7.62	0.12	0.00202048	0.00003208
11.1	8.37	0.16	0.00202197	0.00003809
12.1	7.68	0.16	0.00202061	0.00004301
13.1	7.81	0.14	0.00202086	0.00003732

Couzinié et al., 2016. Supplementary Table 5 (continued):

Zircon in situ SHRIMP O isotope data for samples

	$\delta^{18}O$ ‰	error (1σ)	$^{18}O/^{16}O$	error (1σ)
Qz Monzodiorite 533 - 1				
14.1	6.87	0.14	0.00201898	0.00003987
15.1	6.62	0.11	0.00201848	0.00003355
Mean (n=13)	**7.84**			
±2σ (ext.)	**1.19**			
Session 3				
Monzodiorite SGC-12-26				
1.1	6.46	0.10	0.00201815	0.00003044
2.1	6.85	0.12	0.00201893	0.00003444
3.1	6.92	0.11	0.00201908	0.00003203
4.1	6.93	0.11	0.00201909	0.00003322
5.1	7.05	0.11	0.00201933	0.00003269
6.1	8.01	0.10	0.00202126	0.00002625
7.1	7.20	0.10	0.00201965	0.00002933
8.1	7.68	0.10	0.00202060	0.00002640
9.1	7.84	0.10	0.00202092	0.00002566
10.1	7.72	0.10	0.00202068	0.00002695
11.1	7.57	0.16	0.00202037	0.00004284
12.1	7.46	0.12	0.00202017	0.00003296
13.1	7.25	0.09	0.00201973	0.00002540
14.1	6.39	0.16	0.00201801	0.00005138
15.1	7.57	0.07	0.00202039	0.00001931
16.1	7.37	0.08	0.00201997	0.00002172
17.1	7.86	0.07	0.00202097	0.00001714
18.1	7.62	0.09	0.00202048	0.00002295
19.1	8.02	0.11	0.00202128	0.00002712
20.1	7.04	0.08	0.00201931	0.00002311
21.1	7.54	0.08	0.00202031	0.00002116
22.1	6.84	0.09	0.00201891	0.00002669
23.1	7.20	0.09	0.00201964	0.00002491
Mean (n=23)	**7.32**			
±2σ (ext.)	**0.92**			

A.3 Couzinié et al., 2017

Are presented:

- the Supplementary Text;
- the Supplementary Figures;
- Supplementary Table 1: New whole-rock major and trace elements data obtained on the Velay Orthogneiss Formation;
- Supplementary Table 3: Operating conditions for the LA–ICP–MS equipment;
- Supplementary Table 4: Results of LA–ICP–MS U–Pb analyses of the Plešovice zircon standard;
- Supplementary Table 5: Results of LA–ICP–MS U–Pb analyses of zircons from the Velay Orthogneiss Formation;
- Supplementary Table 6: In situ LA–MC–ICP–MS Lu–Hf isotope data for zircon standards analyzed in this study;
- Supplementary Table 7: In situ LA–MC–ICP–MS Lu–Hf isotope data for zircon grains from augen gneisses
- Supplementary Table 8: Set of partition coefficients retained in the modelling section 5.2.2.

Available whole-rock major and trace elements data on the Velay Orthogneiss Formation from the litterature (Supplementary Table 2) are not presented here but can be found online at https://doi.org/10.1016/j.lithos.2017.06.001.

Supplementary material
to the article :
"Cadomian S-type granites as basement rocks of the Variscan belt (Massif Central, France): implications for the crustal evolution of the north Gondwana margin"

Simon Couzinié, Oscar Laurent, Marc Poujol, Michaël Mintrone, Cyril Chelle-Michou, Jean-François Moyen, Pierre Bouilhol, Adrien Vezinet, Linda Marko

*Corresponding author: simon.couzinie@univ-st-etienne.fr or simon.couzinie@ens-lyon.org

Whole-rock geochemistry procedures

Samples were sawed at Saint-Etienne University and a *c.* 500 g (for leucogneisses) to 2000 g (for augen gneisses) fragment of each sample was sent to *ALS Global* firm for whole-rock chemical composition measurements. We chose the "Complete Characterization Package" which combines ICP-AES and ICP-MS analyses for major and trace elements, respectively. More information about analytical routines used by this company can be found at http://www.alsglobal.com/. Repeated analyses of standards SY-4, GRE-3, OREAS-121 and AMIS0304 were realized during the analytical session.

Analyses of the standards were reproducible to < 1.7% for most major elements (except K_2O 2.4%, MgO 6.4% and P_2O_5 4.6%), < 7.9% for trace elements (except Cr 25%, V 12.5%, and Ba 10.9%) and consistent within uncertainty with the expected values. Duplicate measurements of four samples show external reproducibility better than 1.1% (RSD) for major elements (except P_2O_5 at 4.6%) and generally better than 5.4% (RSD) for trace elements except for Tl, Tm, Lu, Hf and V. Fifteen blanks display measured values typically under detection limits for all major and trace elements.

Results for the investigated samples are presented in Table S1.

References quoted in the field description of the VOF (section 2.2)

Lochon, P., 1985. Les métaleucogranites du Haut Vivarais et leur environnement : évolution et implications géodynamiques. Lyon, p. 236.

Mergoil-Daniel, J., 1970. Les feldspaths potassiques dans les roches métamorphiques du Massif Central français. Clermont-Ferrand, p. 304.

Négron, J., 1979. Pétrologie et géochimie des formations quartzofeldspathiques de la série mésozonale du Chassezac (Lozère, Massif Central français). Lyon, p. 175.

R'Kha Chaham, K., 1989. Etude pétrologique et structurale de l'ensemble orthogneissique de l'arc de Fix (Massif Central français). Clermont-Ferrand, p. 162.

Serrano, J.-J., 1979. Gisement et pétrologie des faciès anatectiques et granitiques du substratum de la série métamorphique du Pilat (Haute-Loire, Massif Central français). Lyon, p. 254.

Tardy de Montravel, C., 1971. Les gneiss oeillés du Massif du Pilat et leurs feldspaths alcalins. Lyon, p. 73.

Weisbrod, A., 1970. Pétrologie du socle métamorphique des Cévennes médianes (Massif Central français) : reconstitution sédimentologique et approche thermodynamique du métamorphisme. Nancy, p. 381.

References of experimental studies listed in Table 2

Bogaerts, M., Scaillet, B., Auwera, J.V., 2006. Phase Equilibria of the Lyngdal Granodiorite (Norway): Implications for the Origin of Metaluminous Ferroan Granitoids. Journal of Petrology 47, 2405-2431.

Holtz, F., Johannes, W., 1991. Genesis of peraluminous granites I. Experimental investigation of melt compositions at 3 and 5 kb and various H2O activities. Journal of Petrology 32, 935-958.

Montel, J.M., Vielzeuf, D., 1997. Partial melting of metagreywackes, Part II. Compositions of minerals and melts. Contributions to Mineralogy and Petrology 128, 176-196.

Patiño Douce, A.E., Beard, A.D., 1995. Dehydration-melting of biotite gneiss and quartz amphibolite from 3 to 15 kbar. Journal of Petrology 36, 707-738.

Patiño Douce, A.E., Harris, N., 1998. Experimental constraints on Himalayan anatexis. Journal of Petrology 39, 690-710.

Patiño Douce, A.E., Johnston, A.D., 1991. Phase equilibria and melt productivity in the pelitic system: implications for the origin of peraluminous granitoids and aluminous granulites. Contributions to Mineralogy and Petrology 107, 202-218.

Pickering, J.M., Johnston, A.D., 1998. Fluid-absent melting behavior of a two-mica metapelite: experimental constraints on the origin of the Black Hills granite. Journal of Petrology 29, 1787-1804.

Skjerlie, K.P., Johnston, A.D., 1996. Vapour-absent melting from 10 to 20 kbar of crustal rocks that contain multiple hydrous phases: implications for anatexis in the deep to very deep continental crust and active continental margins. Journal of Petrology 37, 661-691.

Stevens, G., 1995. Compositional controls on partial melting in high-grade metapelites, Department of Earth Sciences. Manchester, p. 243.

Vielzeuf, D., Holloway, J.R., 1988. Experimental determination of the fluid-absent melting relations in the pelitic system. Contributions to Mineralogy and Petrology 98, 257-276.

Watkins, J.M., Clemens, J.D., Treloar, P.J., 2007. Archaean TTGs as sources of younger granitic magmas: melting of sodic metatonalites at 0.6-1.2 GPa. Contributions to Mineralogy and Petrology 154, 91-110.

Supporting information for the geochronological data compilation (Figure 14)

Abbreviations: AC, Aire de Côte; AF, Arc de Fix; Ap, Apié; Au, Aubazine; Ba, Bassurels; Ce, Ceaulmont; Ch, Chateauneuf; Cp, Caplongue; CV, Clair-Vive; Di, Dinan; He, Héric; La, Lanneau;

LB, La Bessenoits; Lv, Lévézou; Ma, Marvejols; MC, Moulin du Chambon; Me, Meuzac; M^{t}M, Mont Mars; Mr, Merle; Mu, Mulatet; Pa, Palanges; Pe; Peyrolles; Pi, Picades; Ps, Plaisance: PL, Pont de Larn; Pt, Pilat; Po, Plouer; Pm, Pomayrols; PV, Port de Vaurs; RA, Roche L'Abeille; Rd, Rodez; Re, Réquista; Ro, Rouergue; Ru, Ruynes; Sa, Sauviat; SS, Saut-du-Saumont; Se, Sériès; S^{t}E, St Eutrope; So, Somail; S^{t}A, St André-la-Côte; S^{t}Ay, St Alyre, St Malo; S^{t}Y, St Yrieix; Th, Thaurion; Tr, Tournon; Tu, Tulle; Vr, Veronzac; Yz, Yzeron.

References: (1) Lévêque (1985); (2) Alabouvette et al. (1989); (3) Defaut et al. (1991); (4) Lasserre et al. (1980); (5) Lafon (1984); (6) This study; (7) Lescuyer and Cocherie (1992); (8) Caen-Vachette (1979); (9) Be Mezeme et al. (2006); (10) Padel et al. (this volume); (11) Pin and Lancelot (1978); (12) Bernard-Griffiths (1975); (13) Mathonnat (1983); (14) Mougeot et al. (1997); (15) Ducrot et al. (1979); (16) Melleton et al. (2010); (17) Alexandrov et al. (2001); (18) Maurel et al. (2003); (19) Delbos et al. (1964-1965); (20) Duthou et al. (1984); (21) Duthou (1977); (22) Caron (1994); (23) Duthou et al. (1981); (24) Gebauer et al. (1981); (25) Lafon (1986); (26) Faure et al. (2009a); (27) Pin and Lancelot (1982); (28) Chelle-Michou et al. (2017); (29) Paquette et al. (1995); (30) Marchand and Lancelot in Forestier et al. (1979); (31) Dufour (1982); (32) Berger et al. (2010); (33) Cocherie et al. (2005); (34) Lotout et al. (2016); (35) Feybesse et al. (1995); (36) Monier et al. (1980); (37) Alexandre (2007); (38) Pitra et al. (2012); (39) Roger et al. (2015).

Alabouvette, B., Burg, J.-P., Lefavrais-Raymond, A., Leyreloup, A.F., Delor, C., 1989. Notice explicative, Carte géol. France (1/50 000), feuille Rodez (884), Orléans, p. 47.

Alexandre, P., 2007. U–Pb zircon SIMS ages from the French Massif Central and implication for the pre-Variscan tectonic evolution in Western Europe. Comptes Rendus Geoscience 339, 613-621.

Alexandrov, P., Floc'h, J.-P., Cuney, M., Cheilletz, A., 2001. Ion microprobe dating of zircons from the Upper Gneiss Unit (South Limousin, Massif Central, France). Comptes Rendus de l'Académie des Sciences, Paris 332, 625-632.

Be Mezeme, E., Cocherie, A., Faure, M., Legendre, O., Rossi, P., 2006. Electron microprobe monazite geochronology of magmatic events: Examples from Variscan migmatites and granitoids, Massif Central, France. Lithos 87, 276-288.

Berger, J., Féménias, O., Ohnenstetter, D., Bruguier, O., Plissart, G., Mercier, J.-C.C., Demaiffe, D., 2010. New occurrence of UHP eclogites in Limousin (French Massif Central): Age, tectonic setting and fluid–rock interactions. Lithos 118, 365-382.

Bernard-Griffiths, J., 1975. Essai sur la signification des âges au strontium dans une série métamorphique, le bas Limousin : Massif central français. Clermont-Ferrand, p. 243.

Caen-Vachette, M., 1979. Age cambrien des rhyolites transformées en leptynites dans la série métamorphique du Pilat (Massif Central français). Comptes Rendus de l'Académie des Sciences, Paris 289, 997-1000.

Caron, C., 1994. Les minéralisations Pb-Zn associées au Paléozoique inférieur d'Europe méridionale. Traçage isotropique Pb-Pb des gites de l'Iglesiente (SW Sardaigne) et des Cévennes et évolution du socle encaissant par la géochronologie U-Pb, 40Ar-39Ar et K-Ar. Montpellier, p. 288.

Chelle-Michou, C., Laurent, O., Moyen, J.-F., Block, S., Paquette, J.-L., Couzinié, S., Gardien, V., Vanderhaeghe, O., Villaros, A., Zeh, A., 2017. Pre-Cadomian to late-Variscan odyssey of the eastern Massif Central, France: Formation of the West European crust in a nutshell. Gondwana Research 46, 170-190.Cocherie, A., Baudin, T., Autran, A., Guerrot, C., Fanning, C.M., Laumonier, B., 2005. U-Pb zircon (ID-TIMS and SHRIMP) evidence for the early Ordovician

intrusion of metagranites in the late Proterozoic Canaveilles Group of the Pyrenees and te Montagne Noire (France). Bulletin de la Société Géologique de France 176, 269-282.

Defaut, B., Burg, J.-P., Leyreloup, A.F., Romney, F., Fuchs, Y., Alabouvette, B., Lefavrais-Raymond, A., 1990. Notice explicative, Carte géol. France (1/50 000), feuille Séverac-le-Château (885), Orléans, p. 58.

Delbos, L., Lasserre, M., Roques, M., 1964-1965. Géochronologie et rétromorphose dans la série cristallophyllienne du Rouerue (Massif central français). Sci. Terre, Nancy 10, 329-342.

Ducrot, J., Lancelot, J., Reille, J.-L., 1979. Dating in the Montagne Noire of a remnant of a major phase of crustal thinning characteristic of Prevariscan Europe. Bulletin de la Société Géologique de France 21, 501-505.

Dufour, E., 1982. Pétrologie et géochimie des formations orthométamorphiques acides des Monts du Lyonnais (Massif central, France). Lyon, p. 241.

Duthou, J.-L., 1977. Chronologie Rb-Sr et géochimie des granitoïdes d'un segment de la chaîne Varisque, relations avec le métamorphisme : le Nord Limousin, Massif Central français. Clermont-Ferrand, p. 294.

Duthou, J.-L., Cantagrel, J.-M., Didier, J., Vialette, Y., 1984. Palaeozoic granitoids from te French Massif Central: age and origin studied by 87Rb-87Sr system. Physics of the Earth and Planetary Interiors 35, 131-144.

Duthou, J.-L., Piboule, M., Gay, M., Dufour, E., 1981. Datations radiométriques Rb-Sr sur les orthogranulites des Monts du Lyonnais (Massif Central français). Comptes Rendus de l'Académie des Sciences, Paris 292, 749-752.

Faure, M., Brouder, P., Thierry, J., Alabouvette, B., Cocherie, A., Bouchot, V., 2009. Notice explicative, Carte géol. France (1/50 000), feuille Saint-André-de-Valborgne (911). BRGM, Orléans, p. 138.

Feybesse, J.-L., Lardeaux, J.M., Tegyey, M., Peterlongo, J.-M., Kerrien, Y., Lemière, B., Maurin, G., Mercier, F., Thiéblemont, D., 1995. Notice explicative, Carte géol. France (1/50 000), feuille Saint-Symphorien-sur-Coise (721). BRGM, Orléans, p. 110.

Forestier, F.-H., al., 1979. Granulites, éclogites, péridotites en France, Livret guide d'excursion, Sciences de la Terre, Nancy, pp. 61-103.

Gebauer, D., Bernard-Griffiths, J., Grünenfelder, M., 1981. U-Pb zircon and monazite dating of a mafic-ultramafic complex and its country rocks. Contributions to Mineralogy and Petrology 76, 292-300.

Lafon, J.M., 1984. The “Granodiorite de Caplongue”, a new evidence for Cambrian magmatism in Eastern Rouergue. Comptes Rendus de l'Académie des Sciences, Paris 298, 595-600.

Lafon, J.M., 1986. Géochronologie U–Pb appliquée à deux segments du Massif Central français. Le Rouergue oriental et le Limousin central. Montpellier, p. 1152.

Lasserre, M., Tempier, P., Philibert, J., 1980. Géochronologie Rb/Sr d'une intrusion cambrienne de la région de Saint-Flour (Massif Central français). Comptes Rendus de l'Académie des Sciences, Paris 291, 737-740.

Lescuyer, J.-L., Cocherie, A., 1992. Single-zircon dating of the Sériès meta-dacites: evidence for a Late Proterozoic age of the "X Schists" from Montagne Noire (Southern French Massif Central). Comptes Rendus de l'Académie des Sciences, Paris 314, 1071-1077.

Lévêque, M.-H., 1985. Evidence of Precambrian basement within the French “Massif Central”: the “Palanges” orthogneiss (Aveyron). Comptes Rendus de l'Académie des Sciences, Paris 300, 277-282.

Lotout, C., Pitra, P., Poujol, M., Van Den Driessche, J., 2016. Ordovician magmatism in the Lévézou massif (French Massif Central): tectonic and geodynamic implications. International Journal of Earth Sciences 106, 501-515.

Mathonnat, M., 1983. La série métamorphique du Cézallier (Massif Central français). Clermont-Ferrand, p. 208.

Maurel, O., Monié, P., Respaut, J.-P., Leyreloup, A.F., Maluski, H., 2003. Pre-metamorphic 40Ar/39Ar and U–Pb ages in HP metagranitoids from the Hercynian belt (France). Chemical Geology 193, 195-214.

Melleton, J., Cocherie, A., Faure, M., Rossi, P., 2010. Precambrian protoliths and Early Paleozoic magmatism in the French Massif Central: U–Pb data and the North Gondwana connection in the west European Variscan belt. Gondwana Research 17, 13-25.

Monier, G., Labernadière, H., Duthou, J.-L., 1980. The granitoids of Southern Millevaches ; first cartographic and petrographic results ; mean chemical composition ; proposition of a chronology of emplacement. Bulletin de la Société Géologique de France 7, 447-454.

Mougeot, R., Respaut, J.P., Ledru, P., Marignac, C., 1997. U-Pb chronology on accessory minerals of the Velay anatectic dome (French Massif Central). European Journal of Mineralogy 9, 141-156.

Padel, M., Alvaro, J.J., Clausen, S., Guillot, F., Poujol, M., Chichorro, M., Monceret, E., Pereira, F., Vizcaïno, D., submitted. U–Pb laser ablation ICP-MS zircon dating across the Ediacaran–Cambrian transition of the Montagne Noire, southern France. Submitted at Comptes Rendus Geoscience.

Paquette, J.L., Monchoux, P., Couturier, M., 1995. Geochemical and isotopic study of a norite-eclogite transition in the European Variscan belt: Implications for U-Pb zircon systematics in metabasic rocks. Geochimica et Cosmochimica Acta 59, 1611-1622.

Pin, C., Lancelot, J., 1978. Un exemple de magmatisme cambrien dans le Massif Central : les métadiorites quartziques intrusives dans la série du Lot. Bulletin de la Société Géologique de France 7, 203-208.

Pin, C., Lancelot, J., 1982. U-Pb Dating of an Early Paleozoic Bimodal Magmatism in the French Massif Central and of Its Further Metamorphic Evolution. Contributions to Mineralogy and Petrology 79, 1-12.

Pitra, P., Poujol, M., Van Den Driessche, J., Poilvet, J.-C., Paquette, J.-L., 2012. Early Permian extensional shearing of an Ordovician granite: The Saint-Eutrope "C/S-like" orthogneiss (Montagne Noire, French Massif Central). Comptes Rendus Geoscience 344, 377-384.

Roger, F., Teyssier, C., Respaut, J.-P., Rey, P.F., Jolivet, M., Whitney, D.L., Paquette, J.-L., Brunel, M., 2015. Timing of formation and exhumation of the Montagne Noire double dome, French Massif Central. Tectonophysics 640-641, 53-69.

Supplementary figures

to the article : "Cadomian S-type granites as basement rocks of the Variscan belt (Massif Central, France): implications for the crustal evolution of the north Gondwana margin"

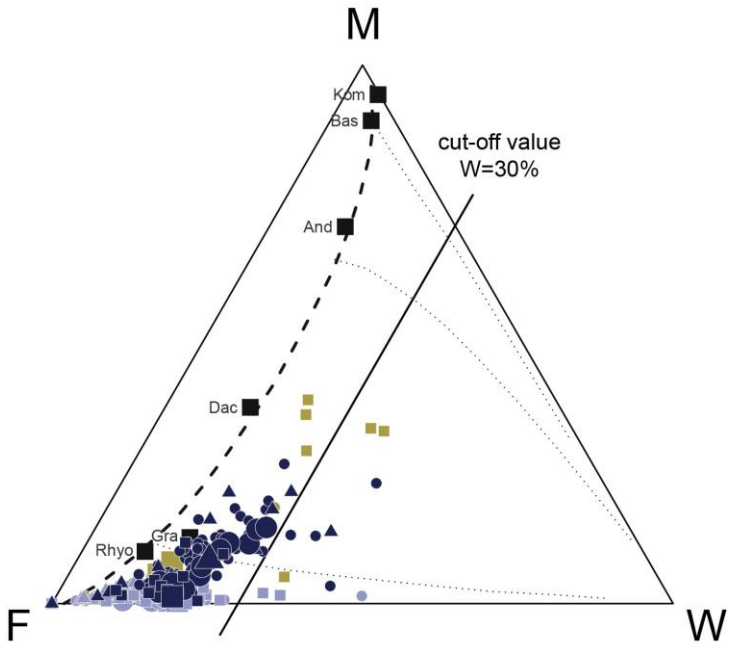

Figure S1: MFW plot (Ohta and Arai, 2007) for the VOF samples retained for geochemical interpretations. Meta-igneous rocks experienced limited LILE mobility. Large symbols represent newly obtained geochemical data. Same legend as Fig. 6.

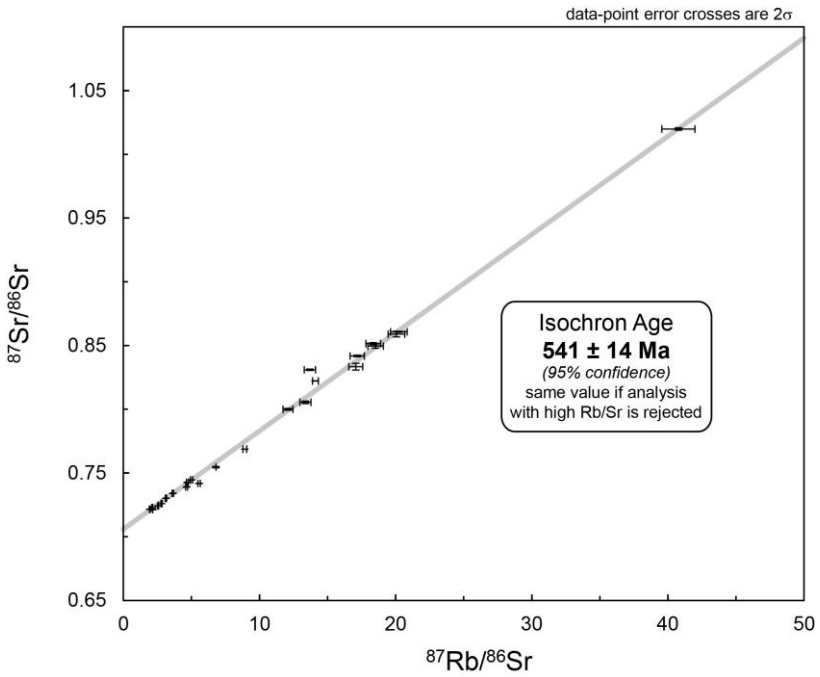

Figure S2: Rb-Sr isochron for samples of augen gneisses and leucogneisses from the VOF. Data from the literature (Caen-Vachette, 1979; R'Kha Chaham et al., 1990). The isochron age of 541 ± 14 Ma (N=22, calculated with the Isoplot program using the robust regression mode) argues for limited mobility of LILE (here Rb and Sr) during amphibolite-facies metamorphism.

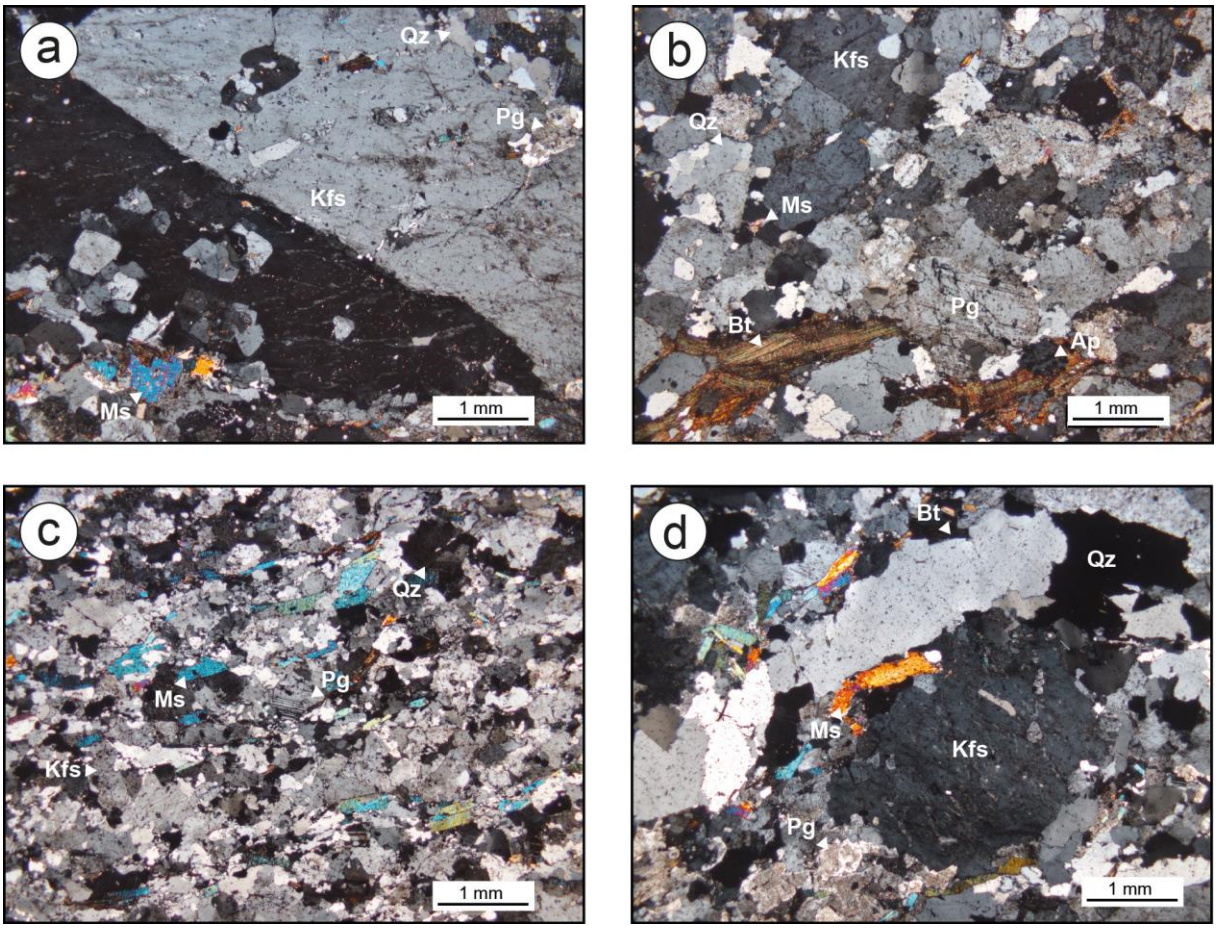

Figure S3: Photomicrographs showing the mineral assemblages of the dated samples: (a-b) augen gneisses MM06 and MM11, respectively; (c-d) leucogneisses MM09 and MM10, respectively.

Couzinié et al., 2017. Supplementary Table 1: New whole-rock major and trace elements data obtained on the Velay Orthogneiss Formation.

Sample	MM06	MM09	MM10	MM11	MM12	OSZ	PG3	SC14 06	SC14 07	SC14 08	SC14 09	SC14 10	SC14 11	SC14 12	SC14 13
Area	Arc de Fix	Arc de Fix	Arc de Fix	Arc de Fix	Pilat	Pilat	Pilat	Vivarais	Vivarais	Vivarais	Vivarais	Vivarais	Vivarais	Vivarais	Vivarais
Lat. N	44.98811	44.69490	44.56838	44.60534	45.41075	45.41724	45.41059	45.02800	45.02800	45.03204	45.03204	45.07805	45.12503	45.12458	45.22961
Long. E	3.68093	3.88376	3.87095	4.07040	4.53991	4.53230	4.53977	4.49277	4.49277	4.49436	4.49436	4.44173	4.54082	4.54009	4.40612
Type	Augen gneiss	Leucogneiss	Leucogneiss	Augen gneiss	Leucogneiss	Augen gneiss	Leucogneiss	Banded gneiss	Augen gneiss	Banded gneiss	Banded gneiss	Banded gneiss	Leucogneiss	Banded gneiss	Augen gneiss
Code	AUGEN	LEPT	LEPT	AUGEN	LEPT	AUGEN	LEPT	OG	AUGEN	OG	OG	OG	LEPT	OG	AUGEN
SiO_2	73.3	76.5	75.1	71.3	74.8	69.9	74.2	77.4	77.2	73.7	72	76.5	77	77.1	76.1
Al_2O_3	13.1	12.9	13.15	14.8	12.65	14.55	12.8	12.25	11.9	14.5	14.5	12.8	12.8	12.3	13.5
Fe_2O_3	1.76	1.93	1.68	3.08	2.01	2.73	2.05	2.06	1.83	2.1	2.65	2.25	1.69	2.19	1.82
MnO	0.02	0.03	0.02	0.04	0.03	0.03	0.02	0.02	0.02	0.03	0.04	0.02	0.02	0.02	0.03
MgO	0.21	0.11	0.09	0.84	0.22	0.67	0.26	0.18	0.15	0.44	0.52	0.19	0.08	0.18	0.08
CaO	0.56	0.32	0.42	1.08	0.53	1.02	0.56	0.49	0.43	0.99	1.18	0.59	0.39	0.48	0.42
Na_2O	2.85	2.39	3.01	2.79	2.87	3.05	3.05	2.87	2.38	3.91	4.27	2.67	2.68	2.54	3.44
K_2O	5	5.42	4.93	4.36	4.55	5.02	4.79	4.67	5.48	4.24	3.96	5.49	5.56	4.86	4.26
TiO_2	0.18	0.04	0.06	0.37	0.12	0.3	0.13	0.13	0.11	0.23	0.27	0.14	0.07	0.12	0.07
P_2O_5	0.19	0.2	0.27	0.23	0.25	0.24	0.29	0.19	0.21	0.27	0.31	0.24	0.26	0.24	0.35
LOI	0.79	0.55	0.79	1.39	0.85	0.89	0.69	0.53	0.42	0.57	0.51	0.59	0.67	0.66	0.87
Ag	<0.5	<0.5	0.8	<0.5	<0.5	<0.5	<0.5	<0.5	0.5	0.5	0.5	0.5	<0.5	<0.5	<0.5
As	3.5	1.3	42.6	1.9	2.6	5.3	1.8	0.5	0.4	0.7	0.4	0.4	0.6	4.7	3.1
Ba	356	39.6	78.9	689	116	698	164	91.6	74.9	417	642	173	35.6	97.1	26.5
Bi	0.24	0.24	1.75	0.54	0.63	0.07	0.95	0.08	0.06	0.13	0.27	0.12	0.08	0.42	0.35
Cd	<0.5	<0.5	<0.5	<0.5	<0.5	<0.5	<0.5	<0.5	<0.5	<0.5	<0.5	<0.5	<0.5	<0.5	<0.5
Ce	34.2	10.8	10.9	54.3	17.7	57.6	25.9	19.3	17.1	51.8	64.3	27.2	7.3	20	9
Co	2	1	1	5	2	3	1	<1	1	2	4	2	<1	1	1
Cr	10	20	10	20	10	20	<10	10	20	10	20	10	10	10	10
Cs	4.93	3.92	5.01	13.45	5.15	12.8	6.68	3.26	2.6	4.56	5.88	4.34	4.99	5.51	7.55
Cu	3	2	10	7	2	4	5	3	2	<1	2	6	1	3	3
Dy	4.2	1.82	2.88	5.54	3.22	4.8	3.42	4.14	3.56	2.48	2.99	5.38	2	4.18	2.39
Er	2	0.92	1.51	3.19	1.4	3.44	1.46	2.26	1.99	0.82	1.32	3.13	0.89	1.97	0.91
Eu	0.56	0.15	0.13	0.94	0.26	0.84	0.36	0.16	0.17	0.57	0.88	0.29	0.09	0.18	0.14
Ga	16.2	21	21.7	17.9	18.7	20.1	18.4	17.5	16.9	22.9	21.2	18.7	20.5	20.3	25.4
Gd	3.93	1.19	1.71	5.84	2.52	6.31	3.09	2.68	2.31	3.38	4.12	3.65	1.23	2.93	1.82
Hf	3.6	2	2.6	4.6	2.9	3.8	2.8	2.7	2.8	3.9	5.6	3.6	2.1	2.8	2.6
Hg	<0.005	<0.005	0.02	0.006	0.01	<0.005	<0.005	0.007	<0.005	<0.005	0.016	0.01	0.006	0.011	<0.005
Ho	0.77	0.35	0.47	1.07	0.54	1.19	0.61	0.79	0.64	0.33	0.52	0.99	0.33	0.75	0.34
In	0.046	0.009	0.04	0.07	0.047			0.093	0.081	0.115	0.088	0.059	0.103	0.108	0.054
La	15.7	5.6	4.5	25.8	7.9	27.3	11.1	9	7.7	25.6	32.2	12.1	3.4	8.9	3.9
Li	30	10	20	60	60	60	50	40	30	70	60	40	50	70	70
Lu	0.21	0.09	0.14	0.38	0.11	0.42	0.15	0.2	0.17	0.07	0.16	0.35	0.08	0.19	0.08
Nb	7.9	4	10.6	9.3	10.9	10.7	11.1	11.2	8	11.1	13.9	10	11.7	13.6	15.3
Nd	15.5	4.4	5.1	27.2	8.2	25.3	11.3	8.3	7.8	22.7	28.8	12.7	3.3	9.6	4.3
Ni	3	<1	1	11	2	4	1	<1	1	4	3	2	2	1	2
Pb	25	19	20	20	18	24	20	19	18	30	38	19	10	18	10
Pr	4.02	1.18	1.36	6.47	2.05	6.64	2.87	2.26	2.14	5.87	7.22	3.13	0.83	2.28	1.15
Rb	170.5	213	251	151.5	237	167	260	241	254	281	278	244	282	293	322
Re	<0.001	<0.001	<0.001	<0.001	0.001			<0.001	<0.001	<0.001	<0.001	<0.001	<0.001	<0.001	<0.001
Sb	0.05	<0.05	1.4	0.05	<0.05	<0.05	<0.05	<0.05	<0.05	<0.05	<0.05	<0.05	<0.05	<0.05	<0.05
Sc	2	1	3	5	2	4	2	2	2	3	4	2	2	2	2
Se	0.6	<0.2	<0.2	0.9	0.6	<0.2	0.3	0.3	0.3	0.3	0.2	<0.2	0.5	0.6	0.4
Sm	4.35	1.23	1.49	5.66	2.32	6.01	3.05	2.4	2.37	4.59	5.78	3.36	1.08	2.43	1.71
Sn	4	6	9	6	7	8	9	6	5	8	16	5	6	6	7
Sr	64.5	17.2	19.7	110.5	28.6	125	38.6	22.2	24.1	134.5	187.5	36.6	11.4	26.1	10.2
Ta	0.8	0.7	1.5	1	1.3	1.2	1.5	0.7	0.6	1	1.9	0.7	1	1.3	1.8
Tb	0.7	0.27	0.4	0.87	0.48	1.06	0.64	0.54	0.49	0.49	0.59	0.75	0.28	0.56	0.39
Te	<0.01	<0.01	<0.01	<0.01	<0.01	<0.01	0.01	<0.01	<0.01	<0.01	<0.01	<0.01	<0.01	<0.01	<0.01
Th	8.53	4.16	4.58	10.2	6.09	11	7.02	7.7	6.31	15.2	21.4	9.15	5.28	8.22	4.37
Tl	0.9	1.1	1.6	0.7	1.1	0.6	1	1.2	1.1	1.3	1.5	1.1	1.4	1.1	1.4
Tm	0.3	0.13	0.19	0.43	0.2	0.5	0.23	0.33	0.25	0.1	0.18	0.46	0.11	0.26	0.14
U	3.2	2.29	10.4	3.03	8.44	2.31	6.69	4.81	4.96	5.89	6.37	4.22	7.3	7.92	14
V	12	<5	<5	30	7	28	9	7	6	10	16	8	<5	6	<5
W	1	4	4	2	1	<1	<1	1	<1	2	2	1	1	2	1
Y	23.5	11.2	15.4	31	18	27.9	20.4	24.1	22	10.2	14.3	31	12.1	23.4	11.8
Yb	1.86	0.79	1.3	2.97	1	2.59	0.78	1.76	1.62	0.52	1.32	2.68	0.73	1.5	0.73
Zn	58	46	33	33	41	63	54	59	45	74	73	48	46	70	73
Zr	117	49	51	170	80	142	82	80	75	132	176	101	43	81	54

Couzinié et al., 2017. Supplementary Table 1 (continued): New whole-rock major and trace elements data obtained on the Velay Orthogneiss Formation.

Sample	SC14 14	SC14 16	SC14 21	SC14 22	SC14 25	SC14 27	SC14 28	SC14 30	SC14 31	SC14 32	SC14 33	SC14 34	SC14 35	SC14 37	SC14 38
Area	Vivarais	Vivarais	Vivarais	Vivarais	Arc de Fix	Arc de Fix	Arc de Fix	Arc de Fix	Arc de Fix	Arc de Fix	Arc de Fix	Arc de Fix	Arc de Fix	Arc de Fix	Arc de Fix
Lat. N	45.20891	45.29857	45.40639	45.30632	45.26191	45.20795	44.98793	44.95867	44.94692	44.76386	44.76386	44.69490	44.69490	44.56838	44.53111
Long. E	4.49379	4.64510	4.65522	4.65525	3.65904	3.61540	3.68103	3.70022	3.68603	3.88516	3.88516	3.88376	3.88376	3.87095	3.88741
Type	Banded gneiss	Leucogneiss	Banded gneiss	Augen gneiss	Augen gneiss	Augen gneiss	Augen gneiss	Augen gneiss	Augen gneiss	Leucogneiss	Augen gneiss	Leucogneiss	Augen gneiss	Augen gneiss	Augen gneiss
Code	OG	LEPT	OG	LEPT	AUGEN	AUGEN	AUGEN	AUGEN	AUGEN	LEPT	AUGEN	LEPT	AUGEN	AUGEN	AUGEN
SiO_2	77.5	76.9	76.9	77.6	72.7	73.7	73.6	71.6	72.8	75.4	72.8	75.6	75.2	70.8	71.4
Al_2O_3	12.2	13.05	12.45	12.45	13.7	13.9	13.75	14.6	13.45	12.5	14.95	12.95	13.5	14.1	13.85
Fe_2O_3	1.8	1.77	1.68	1.42	2.02	2.49	2.03	3.18	2.61	2.17	2.25	1.72	2	2.61	3.61
MnO	0.03	0.02	0.02	0.02	0.03	0.03	0.03	0.04	0.03	0.02	0.03	0.03	0.02	0.03	0.05
MgO	0.13	0.07	0.13	0.13	0.35	0.46	0.26	0.81	0.51	0.19	0.4	0.11	0.23	0.58	0.97
CaO	0.42	0.41	0.44	0.38	0.71	0.74	0.53	1.18	0.91	0.35	0.76	0.38	0.55	0.45	1.16
Na_2O	2.86	3.38	2.89	2.56	3	3.08	3.08	3.2	2.79	1.88	3.13	2.59	3.06	2.7	2.9
K_2O	4.42	4.6	4.57	4.65	4.68	4.81	5.02	4.27	4.69	6.65	5.54	5.64	4.91	5.53	4.27
TiO_2	0.09	0.06	0.11	0.11	0.18	0.24	0.19	0.35	0.26	0.13	0.19	0.04	0.13	0.29	0.39
P_2O_5	0.21	0.35	0.23	0.22	0.14	0.22	0.21	0.25	0.2	0.25	0.24	0.2	0.22	0.26	0.2
LOI	0.75	0.56	0.87	1.45	1	0.84	0.94	1.06	0.75	0.56	0.83	0.5	0.66	1.27	1.05
Ag	<0.5	<0.5	<0.5	0.5	<0.5	<0.5	<0.5	0.5	0.5	0.5	0.5	0.6	<0.5	0.5	<0.5
As	0.2	6.9	0.8	1	2	4.1	2.5	1.5	1.1	0.4	2.3	5.5	1.9	6.6	0.9
Ba	37.8	19.7	105	54.1	444	454	365	704	539	92.8	576	104	297	667	413
Bi	0.11	0.94	0.12	0.15	0.84	0.14	1.69	0.42	0.19	0.08	0.31	0.18	2.15	0.3	0.08
Cd	<0.5	<0.5	<0.5	<0.5	<0.5	<0.5	<0.5	<0.5	<0.5	<0.5	<0.5	<0.5	<0.5	<0.5	<0.5
Ce	13.7	8.3	18.4	13.7	45.1	48.6	37.2	55.8	49.3	27.9	36.3	13	20.3	48.8	44.4
Co	1	1	<1	1	2	3	2	4	4	2	3	1	2	3	6
Cr	20	20	10	10	10	20	20	20	20	10	20	10	20	20	40
Cs	5.16	13.1	3.33	3.36	5.71	11.55	10.7	7.53	6.2	3.53	6.2	5.08	7.27	8.53	13.85
Cu	1	2	<1	<1	6	4	5	4	5	3	4	3	1	2	<1
Dy	2.9	1.98	3.59	2.37	6.61	6.08	3.88	7.38	6.04	6.57	5	3.04	3.18	6.12	5.34
Er	1.59	0.81	1.87	1.13	4.5	3.27	1.74	3.45	4.06	3.49	2.75	1.87	1.68	3.77	2.72
Eu	0.18	0.05	0.22	0.1	0.57	0.72	0.57	1.03	0.89	0.29	0.82	0.22	0.35	0.82	0.95
Ga	18.1	25.6	19.8	21.9	17	17	18.5	18.6	17.4	13.8	18.8	19	22.2	19.2	21.2
Gd	2.1	1.17	2.61	1.48	4.89	5.21	3.97	7.6	5.01	4.64	3.9	1.6	2.15	5.22	5.39
Hf	2	2.2	3.1	3	3.9	4.6	3.3	5.8	4.4	5.2	3.6	2.1	2.3	3.8	4.2
Hg	<0.005	0.005	0.01	<0.005	0.006	0.01	0.02	<0.005	<0.005	0.008	<0.005	<0.005	0.006	0.017	0.006
Ho	0.53	0.36	0.63	0.35	1.28	1.06	0.63	1.3	1.12	1.26	0.95	0.57	0.55	1.23	0.99
In	0.066	0.033	0.027	0.047	0.041	0.051	0.023	0.047	0.033	0.042	0.02	0.022	0.028	0.04	0.044
La	6.4	3.6	8.7	6.8	21.2	22.5	17.6	25.4	22.9	12.1	17.1	6.2	11.1	26.2	24.4
Li	60	120	30	30	40	80	50	70	40	30	50	30	30	30	90
Lu	0.16	0.06	0.16	0.1	0.48	0.37	0.13	0.42	0.46	0.23	0.27	0.19	0.13	0.5	0.4
Nb	10.3	21.3	12	16.4	10.2	9.4	9.3	10.5	7.9	8.1	8.4	3.9	9.5	9.9	13.5
Nd	6.4	3.7	8.8	6.1	20.7	23.4	17	29.6	23.2	12.5	16.4	5.4	10.3	25.8	24.9
Ni	3	2	2	1	4	4	4	7	6	2	4	1	2	6	12
Pb	11	8	9	6	32	24	32	27	24	30	26	19	19	30	16
Pr	1.63	1.02	2.18	1.58	5.5	5.7	4.4	6.88	5.84	3.17	4.22	1.52	2.98	6.8	6.2
Rb	261	546	267	283	148	176	207	140.5	137.5	224	184	224	217	211	229
Re	<0.001	<0.001	<0.001	<0.001	<0.001	0.001	<0.001	<0.001	<0.001	<0.001	<0.001	<0.001	<0.001	<0.001	<0.001
Sb	<0.05	<0.05	<0.05	<0.05	0.05	<0.05	0.08	0.09	<0.05	<0.05	<0.05	<0.05	<0.05	0.74	<0.05
Sc	2	3	2	3	3	3	2	4	4	2	3	2	2	4	6
Se	<0.2	<0.2	<0.2	0.2	0.4	<0.2	<0.2	<0.2	0.6	0.3	0.3	0.3	<0.2	0.4	<0.2
Sm	1.85	1.06	2.24	1.52	5.57	5.58	3.84	6.93	5.19	3.54	4.22	1.61	2.29	6.14	4.99
Sn	5	26	7	8	6	5	7	4	3	4	6	5	6	7	7
Sr	15.9	23.2	22.3	19.5	83.5	93.1	60.3	125	100	38	87.4	34.4	45.7	98.1	101
Ta	1	3.2	1.3	1.6	0.9	0.9	1	0.8	0.7	0.7	1.1	0.7	1.1	1.2	1.4
Tb	0.37	0.25	0.54	0.33	0.88	0.87	0.67	1.26	0.88	0.96	0.78	0.38	0.41	0.98	0.75
Te	<0.01	<0.01	<0.01	<0.01	<0.01	0.01	0.01	0.01	0.01	0.01	<0.01	<0.01	0.01	0.01	<0.01
Th	5.41	5.33	8.88	8.25	10.4	10.9	8.62	10.2	10.7	9.86	7.99	4.25	6.63	8.93	10.5
Tl	1.4	2.3	1.1	1.2	0.7	0.7	1	0.6	0.5	1.1	0.7	0.9	0.9	1	1.2
Tm	0.21	0.12	0.24	0.16	0.6	0.45	0.2	0.42	0.61	0.42	0.35	0.25	0.2	0.56	0.38
U	2.8	12.65	8.54	3.86	4.85	3.03	4.03	2.7	2.11	3.47	4.25	3.83	4.53	5.02	3.87
V	7	<5	5	5	13	15	12	26	20	<5	13	<5	6	18	40
W	<1	9	2	2	1	1	2	1	1	1	3	4	4	2	5
Y	16.2	11	20.6	13.1	39.1	31.3	19.4	39	35.2	40.6	26.9	18.6	18.1	39.7	28.8
Yb	1.34	0.63	1.55	0.91	3.71	2.84	1.27	3.07	3.56	2.29	2.46	1.77	1.12	3.46	2.3
Zn	37	53	51	32	41	42	51	50	48	40	35	32	45	46	66
Zr	48	49	83	79	143	163	111	234	156	155	117	59	63	138	151

Couzinié et al., 2017. Supplementary Table 1 (continued): New whole-rock major and trace elements data obtained on the Velay Orthogneiss Formation.

Sample	SC14 42	SC14 45	SC14 47	SC14 48	SC14 49
Area	Arc de Fix	Arc de Fix	Arc de Fix	Arc de Fix	Arc de Fix
Lat. N	44.61961	44.61692	44.60534	44.55854	44.55854
Long. E	4.00833	4.01186	4.07040	4.19263	4.19263
Type	Leucogneiss	Augen gneiss	Augen gneiss	Leucogneiss	Leucogneiss
Code	LEPT	AUGEN	AUGEN	LEPT	LEPT
SiO_2	78	69.9	69.4	77.3	77.4
Al_2O_3	12.95	14.25	15.5	12.55	12.7
Fe_2O_3	1.38	3.41	2.99	2.14	1.97
MnO	0.01	0.05	0.04	0.05	0.04
MgO	0.35	1.14	0.8	0.15	0.17
CaO	0.51	1.16	1.23	0.36	0.4
Na_2O	3.94	2.98	2.93	3.2	3.04
K_2O	2.97	4.63	5.43	4.86	4.54
TiO_2	0.09	0.45	0.35	0.07	0.08
P_2O_5	0.24	0.24	0.24	0.2	0.22
LOI	0.65	1.05	0.93	0.19	0.3
Ag	<0.5	<0.5	<0.5	<0.5	<0.5
As	0.2	1.5	6.6	0.4	0.4
Ba	104	773	1140	233	178.5
Bi	0.1	0.22	0.13	0.11	0.12
Cd	<0.5	<0.5	<0.5	<0.5	<0.5
Ce	12.3	53.1	40.7	10.4	10.7
Co	1	6	4	1	1
Cr	10	40	10	10	<10
Cs	6.35	10.7	9.93	3.22	5.36
Cu	<1	6	2	1	<1
Dy	3.02	5.68	5.85	3.17	2.63
Er	1.64	4.11	3.54	1.99	1.76
Eu	0.19	0.97	1.27	0.13	0.13
Ga	23	20.2	21.1	19.8	21.8
Gd	2	5.57	4.82	1.53	1.57
Hf	2.2	4.9	5	1.6	2.2
Hg	0.015	<0.005	0.005	0.009	0.006
Ho	0.57	1.09	1.16	0.66	0.58
In	0.042	0.024	0.046	0.069	0.062
La	6.9	28.9	22.2	4.9	5.4
Li	50	60	60	40	40
Lu	0.15	0.6	0.53	0.34	0.24
Nb	11.4	13.1	9.5	7.7	8.1
Nd	6.2	32	23.1	5.2	4.6
Ni	3	9	7	<1	<1
Pb	6	27	27	19	10
Pr	1.86	8.11	6.06	1.35	1.26
Rb	121	156.5	160	307	305
Re	<0.001	<0.001	<0.001	<0.001	<0.001
Sb	<0.05	<0.05	<0.05	<0.05	<0.05
Sc	3	7	5	3	3
Se	0.3	0.7	<0.2	<0.2	<0.2
Sm	2.04	6.33	4.67	1.64	1.85
Sn	5	8	7	14	10
Sr	77.8	164	141	62	33.7
Ta	1.1	1.3	0.8	1	1
Tb	0.36	0.76	0.86	0.39	0.34
Te	<0.01	<0.01	<0.01	<0.01	<0.01
Th	5.48	11.2	9.25	5.83	4.68
Tl	0.5	0.5	0.7	1.3	1.4
Tm	0.23	0.52	0.57	0.38	0.28
U	6.48	3.89	3.17	7.15	9.25
V	<5	45	23	<5	<5
W	1	2	2	1	1
Y	17.8	36.1	33	20.5	15.6
Yb	1.49	3.52	3.58	2.39	1.89
Zn	14	59	50	46	36
Zr	56	180	171	45	58

Couzinié et al., 2017. Supplementary Table 3: Operating conditions for the LA-ICP-MS equipment

Laboratory & Sample Preparation	
Laboratory name	Géosciences Rennes, UMR CNRS 6118, Rennes, France
Sample type/mineral	zircon
Sample preparation	Conventional mineral separation, 1 inch resin mount, 1mm polish to finish
Imaging	(BSE) imaging using a Jeol JSM-6400 SEM at the Ecole des Mines de St Etienne (France) (CL) imaging using a Jeol JSM-5910 SEM at the Laboratoire Magmas et Volcans (Clermont-Ferrand, France)
Laser ablation system	
Make, Model & type	ESI NWR193UC, Excimer
Ablation cell	ESI NWR TwoVol2
Laser wavelength	193 nm
Pulse width	< 5 ns
Fluence	8.8 J/cm^{-2}
Repetition rate	3 Hz
Spot size	20 - 35 µm
Sampling mode / pattern	Single spot
Carrier gas	100% He, Ar make-up gas and N_2 (3 ml/mn) combined using in-house smoothing device
Background collection	20 seconds
Ablation duration	60 seconds
Wash-out delay	15 seconds
Cell carrier gas flow (He)	0.75 l/min
ICP-MS Instrument	
Make, Model & type	Agilent 7700x, Q-ICP-MS
Sample introduction	Via conventional tubing
RF power	1350W
Sampler, skimmer cones	Ni
Extraction lenses	X type
Make-up gas flow (Ar)	0.85 l/min
Detection system	Single collector secondary electron multiplier
Data acquisition protocol	Time-resolved analysis
Scanning mode	Peak hopping, one point per peak
Detector mode	Pulse counting, dead time correction applied, and analog mode when signal intensity > ≈ 10^6 cps
Masses measured	^{204}(Hg + Pb), ^{206}Pb, ^{207}Pb, ^{208}Pb, ^{232}Th, ^{238}U
Integration time per peak	10-30 ms
Sensitivity / Efficiency	20000 cps/ppm Pb (50µm, 10Hz)
Data Processing	
Gas blank	20 seconds on-peak
Calibration strategy	GJ1 zircon standard used as primary reference material, 91500 used as secondary reference material (quality control)
Reference Material info	GJ1 (Jackson et al., 2004) Plešovice (Slama et al., 2008)
Data processing package used	GLITTER ® (van Achterbergh et al., 2001)
Quality control / Validation	Plešovice: concordia age = 337.0 ± 1.0 Ma (N=20; MSWD$_{C+E}$=0.21)

Couzinié et al., 2017. Supplementary Table 4: Results of LA-ICPMS U–Pb analyses of the Plešovice zircon standard

	Pb[a] (ppm)	U[a] (ppm)	Th[a]/U	$^{207}Pb/^{235}U$	±2σ	$^{206}Pb/^{238}U$	±2σ	ρ[d]	$^{207}Pb/^{206}Pb$	±2σ (Ma)	$^{206}Pb/^{238}U$	±2σ (Ma)	$^{207}Pb/^{235}U$	±2σ (Ma)	conc.[e] (%)	label[f]
Plešovice																
Session #1 (May 11th, 2015)																
4110515	29	604	0.08	0.373	0.009	0.0506	0.0012	0.96	350.3	48.7	318.4	7.5	322.2	7.0	91	Concordant
17110515	26	520	0.08	0.395	0.010	0.0537	0.0013	0.93	345.7	51.4	337.0	8.0	338.1	7.6	97	Concordant
31110515	27	549	0.08	0.392	0.011	0.0536	0.0013	0.90	331.0	53.3	336.8	8.1	336.1	7.9	102	Concordant
41110515	29	577	0.08	0.395	0.011	0.0538	0.0013	0.91	340.1	52.3	337.6	8.2	337.9	7.9	99	Concordant
Session #2 (May 12th, 2015)																
5120515a	31	624	0.09	0.393	0.011	0.0538	0.0014	0.91	327.8	52.1	337.7	8.4	336.4	7.9	103	Concordant
17120515a	34	669	0.10	0.393	0.010	0.0537	0.0014	0.96	329.7	48.5	337.5	8.3	336.4	7.5	102	Concordant
30120515a	32	628	0.10	0.389	0.011	0.0538	0.0014	0.87	304.2	57.0	337.7	8.3	333.4	8.3	111	Concordant
41120515a	30	588	0.10	0.393	0.012	0.0537	0.0014	0.86	328.9	58.6	337.3	8.3	336.2	8.5	103	Concordant
4120515b	32	641	0.09	0.393	0.010	0.0535	0.0013	0.95	341.3	49.9	336.0	8.2	336.7	7.6	98	Concordant
17120515b	31	637	0.09	0.386	0.011	0.0517	0.0013	0.92	375.1	52.5	325.1	8.0	331.3	7.8	87	Concordant
31120515b	33	669	0.10	0.394	0.011	0.0536	0.0014	0.94	344.2	51.2	336.3	8.3	337.2	7.8	98	Concordant
41120515b	32	646	0.09	0.388	0.012	0.0536	0.0014	0.81	306.5	63.5	336.7	8.4	332.9	9.0	110	Concordant
4120515c	31	618	0.09	0.392	0.011	0.0538	0.0013	0.92	323.8	51.8	337.7	8.1	335.9	7.7	104	Concordant
17120515c	31	622	0.09	0.388	0.011	0.0536	0.0013	0.86	311.0	57.0	336.3	8.0	333.1	8.0	108	Concordant
30120515c	30	583	0.09	0.392	0.011	0.0537	0.0013	0.87	327.8	56.0	337.4	7.9	336.2	7.9	103	Concordant
41120515c	32	617	0.10	0.395	0.012	0.0536	0.0013	0.82	345.3	60.5	336.6	7.8	337.7	8.4	97	Concordant
Session #3 (May 13th, 2015)																
4130515	14	281	0.09	0.397	0.023	0.0533	0.0025	0.80	372.6	61.3	334.9	7.6	339.6	8.4	90	Concordant
18130515	16	325	0.09	0.391	0.023	0.0537	0.0025	0.78	323.3	63.6	337.1	7.6	335.3	8.6	104	Concordant
Session #4 (October 19th, 2015)																
4191015	44	853	0.12	0.394	0.009	0.0542	0.0012	0.93	319.9	50.4	340.1	7.3	337.5	6.9	106	Concordant
17191015	36	718	0.11	0.395	0.010	0.0535	0.0012	0.90	349.5	51.7	336.1	7.2	337.8	7.1	96	Concordant
30191015	36	710	0.11	0.391	0.010	0.0538	0.0012	0.87	316.0	53.9	337.6	7.3	334.8	7.2	107	Concordant
41191015	36	719	0.11	0.395	0.010	0.0537	0.0012	0.84	344.0	55.8	337.0	7.3	337.9	7.5	98	Concordant

(a) U and Pb contents (in ppm) and Th/U ratios were calculated relative to GJ-1 reference zircon (U = 280 ppm; Pb = 25.5 ppm).

(b) $^{207}Pb/^{235}U = {}^{207}Pb/^{206}Pb/(^{238}U/^{206}Pb*1/137.88)$

(c) Corrected for background, within-run Pb/U fractionation and subsequently normalized to GJ-1 (ID-TIMS value/measured value).

(d) ρ (rho) is the correlation coefficient between errors of $^{206}Pb/^{238}U$ and $^{207}Pb/^{235}U$.

(e) Degree of concordance = ($^{206}Pb/^{238}U$ age / $^{207}Pb/^{206}Pb$ age) × 100

(f) The label "concordant" vs. "discordant" for each spot was attributed based on the position of the error ellipse with respect to the Concordia curve. If the ellipse intersects the Concordia, then the spot is "concordant".

Couzinié et al., 2017. Supplementary Table 5: Results of LA-ICPMS U–Pb analyses of zircons from the Velay Orthogneiss Formation

	Pb[a] (ppm)	U[a] (ppm)	Th[a]/U	$^{207}Pb/^{235}U$[b]	±2σ	$^{206}Pb/^{238}U$[c]	±2σ	ρ[d]	$^{207}Pb/^{206}Pb$	±2σ (Ma)	$^{206}Pb/^{238}U$	±2σ (Ma)	$^{207}Pb/^{235}U$	±2σ (Ma)	conc.[e] (%)	label[f]
Arc-de-Fix augen gneiss MM06 - S[t] Privat-d'Allier																
Session #1 (May 11th, 2015)																
z1*	17	205	0.08	0.712	0.019	0.0879	0.0021	0.93	558.9	49.0	542.8	12.6	545.9	11.0	97	Concordant
z2*	57	698	0.05	0.697	0.017	0.0865	0.0021	0.97	545.9	46.1	534.7	12.4	536.8	10.4	98	Concordant
z3	24	206	0.46	0.928	0.024	0.1079	0.0026	0.94	688.1	47.2	660.3	15.2	666.6	12.6	96	Concordant
z4*	17	198	0.09	0.701	0.018	0.0881	0.0021	0.94	519.6	49.5	544.3	12.6	539.6	10.9	105	Concordant
z5*	30	363	0.05	0.703	0.018	0.0876	0.0021	0.95	535.2	48.4	541.5	12.6	540.4	10.6	101	Concordant
z6*	24	290	0.06	0.709	0.018	0.0873	0.0021	0.94	563.7	48.2	539.5	12.5	544.1	10.9	96	Concordant
z7b	77	949	0.03	0.721	0.018	0.0864	0.0021	0.97	622.9	45.3	534.0	12.4	551.1	10.6	86	Normally Discordant
z8	16	192	0.12	0.789	0.021	0.0879	0.0021	0.92	777.7	48.3	542.9	12.7	590.4	11.9	70	Normally Discordant
z9*	52	644	0.06	0.711	0.018	0.0871	0.0021	0.97	576.3	46.0	538.1	12.5	545.4	10.6	93	Concordant
z10	50	634	0.06	0.718	0.018	0.0831	0.0020	0.96	696.9	45.3	514.5	12.0	549.3	10.7	74	Normally Discordant
z11*	20	237	0.11	0.705	0.019	0.0878	0.0021	0.93	538.6	50.4	542.3	12.7	541.6	11.0	101	Concordant
z12*	36	446	0.04	0.701	0.018	0.0867	0.0021	0.94	554.3	47.9	536.2	12.6	539.6	10.8	97	Concordant
z13*	18	214	0.14	0.708	0.019	0.0876	0.0021	0.93	554.5	49.1	541.3	12.7	543.8	11.1	98	Concordant
z14*	15	179	0.10	0.711	0.019	0.0878	0.0022	0.92	555.8	49.7	542.5	12.8	545.0	11.2	98	Concordant
z15*	15	179	0.14	0.707	0.019	0.0875	0.0022	0.91	550.8	50.7	540.9	12.8	542.8	11.4	98	Concordant
z16*	12	150	0.10	0.716	0.020	0.0880	0.0022	0.89	568.1	52.1	543.5	12.8	548.2	11.7	96	Concordant
z18a*	14	163	0.15	0.707	0.021	0.0877	0.0022	0.85	547.0	56.3	542.0	12.9	542.9	12.3	99	Concordant
z18b*	11	126	0.15	0.717	0.020	0.0880	0.0022	0.89	570.8	52.0	543.8	12.9	549.0	11.7	95	Concordant
z19	19	145	0.58	1.036	0.028	0.1184	0.0029	0.92	723.5	48.7	721.4	16.9	721.8	13.9	100	Concordant
z20	91	1214	0.03	0.664	0.017	0.0822	0.0020	0.95	551.5	48.0	509.1	12.1	516.9	10.6	92	Normally Discordant
z21a*	76	949	0.02	0.704	0.018	0.0875	0.0022	0.95	543.3	47.6	540.4	12.8	540.9	11.0	99	Concordant
z21b	11	125	0.33	0.720	0.023	0.0867	0.0022	0.80	612.1	60.7	535.8	13.0	550.6	13.4	88	Normally Discordant
z22	12	127	0.61	0.797	0.024	0.0882	0.0022	0.84	793.2	55.2	544.7	13.1	595.3	13.5	69	Normally Discordant
z23	30	364	0.05	0.733	0.020	0.0907	0.0023	0.92	553.3	49.9	559.7	13.4	558.4	11.6	101	Concordant
z24*	9	107	0.27	0.711	0.021	0.0880	0.0022	0.85	553.4	56.6	543.8	13.1	545.6	12.5	98	Concordant
z25	15	164	0.64	0.788	0.022	0.0878	0.0022	0.89	778.6	50.5	542.4	13.0	590.1	12.6	70	Normally Discordant
Arc-de-Fix augen gneiss MM11 - Col de Meyrand																
Session #2 (May 12th, 2015)																
z26*	34	428	0.05	0.703	0.018	0.0872	0.0022	0.96	549.3	46.4	538.7	13.1	540.7	11.0	98	Concordant
z27*	17	209	0.08	0.712	0.019	0.0875	0.0022	0.94	567.4	48.0	541.0	13.2	546.0	11.4	95	Concordant
z29*	14	170	0.18	0.708	0.019	0.0884	0.0022	0.93	534.0	50.1	546.0	13.3	543.7	11.4	102	Concordant

Couzinié et al., 2017. Supplementary Table 5 (continued): Results of LA-ICPMS U–Pb analyses of zircons from the Velay Orthogneiss Formation

	Pb^a (ppm)	U^a (ppm)	$\frac{Th^a}{U}$	$\frac{^{207}Pb^b}{^{235}U}$	±2σ	$\frac{^{206}Pb^c}{^{238}U}$	±2σ	ρ[d]	$\frac{^{207}Pb}{^{206}Pb}$	±2σ (Ma)	$\frac{^{206}Pb}{^{238}U}$	±2σ (Ma)	$\frac{^{207}Pb}{^{235}U}$	±2σ (Ma)	conc.[e] (%)	label[f]
z30	16	164	0.33	0.764	0.021	0.0943	0.0024	0.93	558.3	49.8	580.7	14.1	576.1	12.1	104	Concordant
z31	49	202	0.44	3.821	0.098	0.2085	0.0053	0.98	2137.3	36.2	1220.7	28.1	1597.1	20.7	57	Normally Discordant
z32*	32	385	0.08	0.711	0.019	0.0884	0.0022	0.97	543.3	46.4	545.8	13.2	545.2	11.0	100	Concordant
z33	139	744	0.36	1.913	0.049	0.1819	0.0046	0.99	1102.9	41.0	1077.1	25.0	1085.6	17.1	98	Concordant
z34*	27	333	0.06	0.716	0.019	0.0881	0.0022	0.96	564.4	46.7	544.5	13.2	548.3	11.1	96	Concordant
z35*	24	287	0.09	0.719	0.019	0.0881	0.0022	0.95	573.9	47.1	544.2	13.2	549.9	11.2	95	Normally Discordant
z36*	47	572	0.04	0.713	0.018	0.0881	0.0022	0.97	555.9	45.9	544.3	13.2	546.5	11.0	98	Concordant
z37*	24	290	0.12	0.700	0.019	0.0870	0.0022	0.95	544.5	48.0	537.6	13.0	538.9	11.1	99	Concordant
z38	11	127	0.16	0.780	0.021	0.0889	0.0023	0.92	727.7	49.0	549.3	13.3	585.2	12.2	75	Normally Discordant
z39*	18	216	0.06	0.705	0.019	0.0877	0.0022	0.94	541.5	50.1	541.7	13.1	541.8	11.3	100	Concordant
z40*	44	546	0.04	0.697	0.018	0.0865	0.0022	0.96	545.4	46.8	535.1	12.9	537.0	10.9	98	Concordant
z41*	14	167	0.21	0.714	0.020	0.0876	0.0022	0.92	571.1	50.2	541.4	13.1	547.0	11.6	95	Concordant
z42*	18	222	0.12	0.709	0.019	0.0875	0.0022	0.93	561.5	48.9	540.5	13.1	544.4	11.4	96	Concordant
z43a*	19	231	0.05	0.718	0.019	0.0885	0.0022	0.94	561.8	48.0	546.3	13.2	549.3	11.3	97	Concordant
z43b	26	224	0.32	0.998	0.026	0.1150	0.0029	0.96	706.5	46.4	701.5	16.7	702.6	13.4	99	Concordant
z44	22	191	1.43	0.707	0.019	0.0864	0.0022	0.92	581.3	49.9	534.2	12.9	543.1	11.5	92	Normally Discordant
z45*	12	148	0.12	0.706	0.019	0.0880	0.0022	0.91	535.7	52.3	543.6	13.2	542.2	11.6	101	Concordant
z46	49	423	0.10	1.122	0.029	0.1203	0.0030	0.97	858.1	44.4	732.0	17.4	763.8	14.0	85	Normally Discordant
z47	5	33	0.20	1.353	0.041	0.1432	0.0036	0.83	885.7	55.8	862.6	20.6	869.0	17.9	97	Concordant
z48	18	129	0.47	1.182	0.032	0.1301	0.0033	0.93	802.8	47.7	788.3	18.7	792.0	14.9	98	Concordant
z49	130	1665	0.04	0.687	0.018	0.0842	0.0021	0.98	574.1	46.0	521.0	12.5	530.9	10.6	91	Normally Discordant
z50	34	449	0.06	0.639	0.017	0.0811	0.0020	0.95	497.6	49.0	502.6	12.1	501.8	10.4	101	Concordant
z51	9	109	0.19	0.767	0.022	0.0860	0.0022	0.90	762.9	50.9	532.1	12.9	577.9	12.4	70	Normally Discordant
z52*	27	330	0.07	0.708	0.019	0.0879	0.0022	0.94	543.6	48.7	543.3	13.1	543.3	11.2	100	Concordant
z53*	18	220	0.11	0.707	0.019	0.0873	0.0022	0.93	560.0	50.2	539.3	13.0	543.3	11.5	96	Concordant
Leucogneiss MM10 - Labastide-Puylaurent																
Session #2 (May 12th, 2015)																
z82*	31	385	0.06	0.710	0.019	0.0877	0.0022	0.93	556.3	49.4	541.9	12.8	544.6	11.2	97	Concordant
z83	31	298	0.27	0.898	0.024	0.1056	0.0026	0.92	663.5	48.8	646.9	15.1	650.6	12.8	97	Concordant
z84	19	116	1.25	1.199	0.035	0.1299	0.0032	0.85	836.1	53.6	787.4	18.3	800.1	16.1	94	Normally Discordant
z85	16	178	0.30	0.738	0.021	0.0908	0.0022	0.86	563.2	55.2	560.5	13.2	561.0	12.4	100	Concordant
z86*	14	170	0.23	0.716	0.021	0.0876	0.0022	0.83	576.7	57.5	541.2	12.8	548.0	12.6	94	Concordant
z87*	38	477	0.06	0.708	0.019	0.0877	0.0021	0.93	552.9	49.0	541.7	12.7	543.8	11.1	98	Concordant

Couzinié et al., 2017. Supplementary Table 5 (continued): Results of LA-ICPMS U–Pb analyses of zircons from the Velay Orthogneiss Formation

	Pb[a] (ppm)	U[a] (ppm)	Th[a]/U	$^{207}Pb/^{235}U$	±2σ	$^{206}Pb/^{238}U$	±2σ	ρ[d]	$^{207}Pb/^{206}Pb$	±2σ (Ma)	$^{206}Pb/^{238}U$	±2σ (Ma)	$^{207}Pb/^{235}U$	±2σ (Ma)	conc.[e] (%)	label[f]
z88	16	166	0.93	0.928	0.026	0.0908	0.0022	0.88	1045.9	49.3	560.3	13.2	666.8	13.6	54	Normally Discordant
z89*	17	201	0.15	0.710	0.020	0.0874	0.0021	0.86	565.3	55.7	540.1	12.7	544.9	12.1	96	Concordant
z90	27	272	0.55	0.759	0.021	0.0924	0.0023	0.90	588.2	51.5	569.4	13.3	573.1	11.9	97	Concordant
z92	58	835	0.05	0.612	0.016	0.0750	0.0018	0.94	572.0	48.4	466.5	10.9	484.7	10.0	82	Normally Discordant
z93	11	149	0.12	0.646	0.019	0.0805	0.0020	0.82	538.9	59.4	498.9	11.7	506.2	11.8	93	Concordant
z94	20	247	0.31	0.642	0.018	0.0798	0.0019	0.87	545.7	53.7	494.7	11.6	503.8	11.1	91	Normally Discordant
z95	42	649	0.29	0.618	0.017	0.0669	0.0016	0.89	837.2	49.8	417.3	9.8	488.3	10.5	50	Normally Discordant
z96	73	1044	0.18	0.634	0.016	0.0741	0.0018	0.93	676.6	47.8	460.9	10.7	498.8	10.2	68	Normally Discordant
z97*	14	166	0.11	0.705	0.022	0.0875	0.0021	0.78	545.3	62.9	540.9	12.7	541.7	13.2	99	Concordant
z98*	10	106	0.38	0.705	0.023	0.0874	0.0021	0.76	548.9	64.6	540.0	12.7	541.6	13.5	98	Concordant
z99	31	443	0.10	0.607	0.017	0.0738	0.0018	0.84	591.5	55.4	459.2	10.7	481.8	11.0	78	Normally Discordant
z100	28	271	0.56	0.798	0.023	0.0965	0.0023	0.86	604.3	54.5	593.8	13.7	595.9	12.7	98	Concordant
z101	61	386	0.22	2.082	0.055	0.1523	0.0037	0.91	1608.2	43.6	914.1	20.5	1143.0	18.2	57	Normally Discordant
z102	57	357	0.21	3.229	0.086	0.1509	0.0036	0.90	2404.4	40.0	906.0	20.3	1464.2	20.6	38	Normally Discordant
z103	16	200	0.15	0.663	0.019	0.0813	0.0020	0.84	574.1	56.5	503.6	11.7	516.4	11.6	88	Normally Discordant
z104	15	189	0.08	0.675	0.020	0.0817	0.0020	0.83	602.6	56.9	506.2	11.7	524.0	11.9	84	Normally Discordant
z105	52	304	0.58	1.500	0.041	0.1537	0.0037	0.87	951.6	50.3	921.7	20.6	930.5	16.7	97	Concordant
z106	27	346	0.07	0.650	0.018	0.0811	0.0019	0.85	534.7	56.4	502.5	11.6	508.3	11.2	94	Concordant
z107	31	460	0.21	0.653	0.018	0.0692	0.0017	0.87	884.6	51.5	431.1	10.0	510.5	11.1	49	Normally Discordant
z108	47	641	0.06	0.622	0.017	0.0777	0.0019	0.88	532.7	54.5	482.4	11.1	491.3	10.6	91	Normally Discordant
z109	14	207	0.46	0.483	0.015	0.0619	0.0015	0.79	473.2	62.6	387.3	9.0	399.9	10.1	82	Normally Discordant
z110	25	340	0.08	0.626	0.018	0.0780	0.0019	0.84	538.0	57.7	484.4	11.1	493.9	11.1	90	Normally Discordant
Session #3 (May 13th, 2015)																
z129	17	219	0.17	0.642	0.018	0.0788	0.0018	0.82	570.1	56.6	489.2	10.9	503.6	11.2	86	Normally Discordant
z130	45	184	2.48	1.463	0.039	0.1483	0.0034	0.86	972.9	50.2	891.6	19.3	915.2	16.2	92	Normally Discordant
z131	33	314	0.39	0.843	0.023	0.0993	0.0023	0.85	658.7	53.6	610.3	13.5	620.6	12.6	93	Normally Discordant
z133	87	1328	0.31	0.596	0.015	0.0683	0.0016	0.91	718.5	48.2	426.2	9.5	475.0	9.5	59	Normally Discordant
z134*	20	232	0.29	0.710	0.020	0.0875	0.0020	0.83	560.0	55.8	540.9	12.0	544.6	11.7	97	Concordant
z135	23	290	0.11	0.691	0.019	0.0819	0.0019	0.84	647.7	54.5	507.3	11.3	533.5	11.4	78	Normally Discordant
z136	28	242	0.58	0.911	0.026	0.1074	0.0025	0.82	657.7	56.2	657.8	14.5	657.7	13.7	100	Concordant
z137	87	667	0.16	1.254	0.033	0.1332	0.0031	0.88	878.3	49.4	805.8	17.5	825.3	14.8	92	Normally Discordant
z138	55	733	2.90	0.926	0.028	0.0573	0.0014	0.79	1914.3	51.2	359.1	8.3	665.4	14.7	19	Normally Discordant
z139*	26	315	0.08	0.704	0.020	0.0872	0.0020	0.81	549.1	58.3	539.2	12.0	541.1	12.0	98	Concordant

Couzinié et al., 2017. Supplementary Table 5 (continued): Results of LA-ICPMS U–Pb analyses of zircons from the Velay Orthogneiss Formation

	Pb[a] (ppm)	U[a] (ppm)	Th[a]/U	$^{207}Pb/^{235}U$	±2σ	$^{206}Pb/^{238}U$	±2σ	ρ[d]	$^{207}Pb/^{206}Pb$	±2σ (Ma)	$^{206}Pb/^{238}U$	±2σ (Ma)	$^{207}Pb/^{235}U$	±2σ (Ma)	conc.[e] (%)	label[f]
z140*	43	525	0.06	0.719	0.020	0.0874	0.0020	0.83	593.7	55.9	540.0	12.0	550.3	11.9	91	Normally Discordant
Session #4 (October 19th, 2015)																
z82a*	40	483	0.07	0.703	0.018	0.0880	0.0019	0.88	528.4	52.4	543.4	11.5	540.6	10.5	103	Concordant
z83a*	15	171	0.27	0.701	0.019	0.0877	0.0020	0.81	530.8	58.5	541.7	11.6	539.7	11.6	102	Concordant
z84a	20	204	0.25	0.819	0.021	0.0983	0.0022	0.85	620.4	53.3	604.2	12.8	607.6	12.0	97	Concordant
z86a*	29	349	0.10	0.708	0.018	0.0875	0.0019	0.89	554.1	51.2	540.8	11.5	543.3	10.5	98	Concordant
z89a	20	260	0.10	0.664	0.017	0.0825	0.0018	0.86	544.6	52.4	511.0	10.9	517.1	10.3	94	Concordant
z89b*	24	290	0.13	0.699	0.018	0.0875	0.0019	0.85	528.1	54.7	540.4	11.5	538.1	10.9	102	Concordant
z90a	48	541	0.23	0.741	0.018	0.0911	0.0020	0.93	566.5	47.8	561.9	11.9	562.8	10.2	99	Concordant
z90b*	45	561	0.05	0.707	0.017	0.0870	0.0019	0.93	564.5	48.1	537.8	11.4	542.9	10.0	95	Concordant
z90c*	33	401	0.08	0.707	0.017	0.0877	0.0019	0.91	546.2	49.3	542.0	11.5	542.7	10.2	99	Concordant
z92a	85	1076	0.07	0.693	0.017	0.0846	0.0019	0.89	581.7	50.1	523.4	11.1	534.4	10.3	90	Normally Discordant
z92b*	30	360	0.11	0.746	0.019	0.0881	0.0020	0.86	652.9	52.4	544.5	11.6	565.9	11.2	83	Normally Discordant
z93a*	17	196	0.20	0.703	0.019	0.0878	0.0019	0.82	534.0	57.3	542.4	11.6	540.8	11.4	102	Concordant
z93b*	17	202	0.15	0.706	0.019	0.0878	0.0020	0.82	539.8	57.7	542.6	11.6	542.2	11.4	101	Concordant
z97a*	19	226	0.14	0.701	0.018	0.0880	0.0019	0.85	520.8	53.8	544.0	11.5	539.5	10.8	104	Concordant
z97b	33	425	0.06	0.681	0.018	0.0828	0.0018	0.87	593.2	51.7	512.7	10.9	527.6	10.6	86	Normally Discordant
z97c*	15	183	0.11	0.703	0.019	0.0874	0.0019	0.83	541.3	57.0	540.4	11.5	540.6	11.3	100	Concordant
z98a*	24	293	0.10	0.713	0.021	0.0872	0.0020	0.77	578.0	60.5	538.9	11.6	546.4	12.3	93	Concordant
z100a*	58	721	0.03	0.702	0.017	0.0872	0.0019	0.93	544.7	48.2	538.9	11.4	540.0	10.0	99	Concordant
z100b	38	487	0.07	0.686	0.017	0.0838	0.0019	0.89	581.3	50.4	518.7	11.0	530.4	10.3	89	Normally Discordant
z101a*	15	181	0.14	0.695	0.019	0.0873	0.0019	0.82	522.5	56.8	539.3	11.5	536.1	11.3	103	Concordant
z101b*	16	180	0.42	0.701	0.020	0.0880	0.0020	0.79	521.4	59.1	543.4	11.6	539.2	11.8	104	Concordant
z103a*	24	291	0.09	0.706	0.019	0.0874	0.0019	0.83	550.3	55.2	540.2	11.5	542.1	11.2	98	Concordant
z106b*	58	709	0.06	0.705	0.018	0.0877	0.0019	0.87	541.5	53.4	541.9	11.5	541.9	10.6	100	Concordant
z109a	28	352	0.11	0.696	0.019	0.0842	0.0019	0.82	599.9	56.4	521.3	11.1	536.1	11.4	87	Normally Discordant
z136a	29	393	0.06	0.638	0.016	0.0790	0.0017	0.87	551.2	51.7	490.3	10.4	501.2	10.0	89	Normally Discordant
z136b*	33	403	0.09	0.724	0.018	0.0874	0.0019	0.88	608.2	50.9	539.8	11.4	553.1	10.7	89	Normally Discordant
Leucogneiss MM09 - Langogne																
Session #2 (May 12th, 2015)																
z54	49	632	0.14	0.722	0.018	0.0812	0.0020	0.97	757.9	44.3	503.4	12.1	552.0	10.9	66	Normally Discordant
z55*	22	257	0.12	0.715	0.019	0.0893	0.0022	0.94	531.0	49.8	551.5	13.2	547.6	11.3	104	Concordant

Couzinié et al., 2017. Supplementary Table 5 (continued): Results of LA-ICPMS U–Pb analyses of zircons from the Velay Orthogneiss Formation

	Pb[a] (ppm)	U[a] (ppm)	Th[a]/U	$^{207}Pb/^{235}U$	±2σ	$^{206}Pb/^{238}U$	±2σ	ρ[d]	$^{207}Pb/^{206}Pb$	±2σ (Ma)	$^{206}Pb/^{238}U$	±2σ (Ma)	$^{207}Pb/^{235}U$	±2σ (Ma)	conc.[e] (%)	label[f]
z56*	15	174	0.09	0.713	0.019	0.0895	0.0022	0.93	522.6	50.2	552.5	13.2	546.7	11.4	106	Concordant
z57	27	252	0.09	1.031	0.027	0.1124	0.0028	0.95	824.1	45.4	686.7	16.3	719.7	13.5	83	Normally Discordant
z58	96	1264	0.04	0.683	0.017	0.0813	0.0020	0.98	634.7	44.4	504.1	12.1	528.3	10.4	79	Normally Discordant
z59	186	2451	0.02	0.666	0.017	0.0823	0.0021	0.99	554.8	44.9	509.9	12.2	518.2	10.2	92	Normally Discordant
z60	244	3178	0.02	0.674	0.017	0.0835	0.0021	0.99	551.7	44.8	516.7	12.4	523.1	10.3	94	Normally Discordant
z62*	111	1370	0.05	0.726	0.018	0.0874	0.0022	0.98	611.4	44.8	540.2	12.9	554.0	10.9	88	Normally Discordant
z63	70	307	0.13	3.342	0.086	0.2295	0.0057	0.97	1725.5	38.7	1331.8	30.1	1491.0	20.1	77	Normally Discordant
z64	16	232	0.11	0.607	0.016	0.0743	0.0019	0.93	576.1	48.9	462.0	11.2	481.5	10.3	80	Normally Discordant
z65	21	245	0.13	0.785	0.021	0.0874	0.0022	0.92	778.2	48.5	540.2	13.0	588.2	12.2	69	Normally Discordant
z66*	36	453	0.03	0.707	0.019	0.0869	0.0022	0.96	567.3	47.1	537.1	12.9	542.9	11.0	95	Normally Discordant
z67*	28	332	0.12	0.712	0.019	0.0886	0.0022	0.94	539.7	49.5	547.1	13.2	545.8	11.2	101	Concordant
z68	11	122	0.19	0.803	0.023	0.0884	0.0022	0.89	803.0	51.0	546.3	13.2	598.7	12.9	68	Normally Discordant
z69	45	612	0.07	0.661	0.017	0.0796	0.0020	0.96	613.4	46.6	493.7	11.9	515.5	10.6	80	Normally Discordant
z70	31	420	0.39	0.698	0.018	0.0766	0.0019	0.95	810.8	45.6	475.8	11.5	537.9	11.0	59	Normally Discordant
z71*	31	385	0.08	0.704	0.019	0.0873	0.0022	0.95	547.5	48.2	539.6	13.0	541.0	11.2	99	Concordant
z74	20	266	0.19	0.702	0.020	0.0800	0.0020	0.90	729.6	50.0	496.2	12.1	540.0	11.7	68	Normally Discordant
z75*	19	224	0.25	0.721	0.020	0.0891	0.0023	0.92	555.8	50.4	550.1	13.3	551.1	11.7	99	Concordant
z76	23	292	0.08	0.706	0.020	0.0830	0.0021	0.88	663.3	52.3	514.0	12.5	542.2	12.0	77	Normally Discordant
z77*	42	534	0.07	0.695	0.019	0.0858	0.0022	0.93	558.4	48.7	530.4	12.9	535.6	11.2	95	Concordant
z78*	77	959	0.03	0.710	0.019	0.0878	0.0022	0.95	555.5	47.8	542.2	13.1	544.7	11.2	98	Concordant
z79	32	369	0.13	0.732	0.020	0.0907	0.0023	0.93	550.1	49.4	559.9	13.6	557.9	11.7	102	Concordant
z80	30	363	0.69	0.807	0.022	0.0861	0.0022	0.93	868.9	47.0	532.5	12.9	601.0	12.4	61	Normally Discordant
z81	84	444	0.31	2.606	0.070	0.1772	0.0045	0.95	1744.0	40.3	1051.4	24.5	1302.4	19.6	60	Normally Discordant

(a) U and Pb contents (in ppm) and Th/U ratios were calculated relative to GJ-1 reference zircon (U = 280 ppm; Pb = 25.5 ppm).

(b) $^{207}Pb/^{235}U = {}^{207}Pb/^{206}Pb/(^{238}U/^{206}Pb*1/137.88)$

(c) Corrected for background, within-run Pb/U fractionation and subsequently normalized to GJ-1 (ID-TIMS value/measured value).

(d) ρ (rho) is the correlation coefficient between errors of $^{206}Pb/^{238}U$ and $^{207}Pb/^{235}U$.

(e) Degree of concordance = ($^{206}Pb/^{238}U$ age / $^{207}Pb/^{206}Pb$ age) × 100

(f) The label “concordant” vs. “discordant” for each spot was attributed based on the position of the error ellipse with respect to the Concordia curve. If the ellipse intersects the Concordia, then the spot is “concordant”.

* analyses retained for calculation of Concordia date

Couzinié et al., 2017. Supplementary Table 6: In situ LA-MC-ICPMS Lu-Hf isotope data for zircon standards analyzed in this study

	Spot size (μm)	$^{176}Yb/^{177}Hf$ [a]	±2σ (abs.)	$^{176}Lu/^{177}Hf$ [a]	±2σ (abs.)	$^{178}Hf/^{177}Hf$	±2σ (abs.)	$^{180}Hf/^{177}Hf$	±2σ (abs.)	Sig_{Hf} [b] (V)	$^{176}Hf/^{177}Hf$	±2σ [c] (abs.)	$^{176}Hf/^{177}Hf_{(t)}$ [e]	$\varepsilon Hf_{(t)}$ [e]	±2σ [c] (abs.)	T_{DM2} [f] (Ga)	Age [g] (Ma)
GJ-1 (08/02/2016)																	
GJ1-12Jcm-40_1	40	0.0080	0.0006	0.00026	0.00002	1.46718	0.00004	1.88680	0.00014	15	**0.281993**	0.000029	0.281990	-14.7	1.0	2.19	601
GJ1-12Jcm-40_2	40	0.0075	0.0006	0.00025	0.00002	1.46722	0.00003	1.88686	0.00008	16	**0.282000**	0.000024	0.281998	-14.5	0.9	2.18	601
GJ1-12Jcm-40_3	40	0.0074	0.0006	0.00025	0.00002	1.46717	0.00004	1.88652	0.00012	11	**0.282025**	0.000027	0.282022	-13.6	1.0	2.13	601
GJ1-12Jcm-40_4	40	0.0074	0.0006	0.00025	0.00002	1.46726	0.00004	1.88637	0.00011	11	**0.282002**	0.000031	0.281999	-14.4	1.1	2.17	601
GJ1-12Jcm-40_5	40	0.0074	0.0006	0.00025	0.00002	1.46726	0.00005	1.88653	0.00011	10	**0.281996**	0.000030	0.281993	-14.6	1.0	2.19	601
GJ1-12Jcm-40_6	40	0.0073	0.0006	0.00025	0.00001	1.46722	0.00005	1.88657	0.00011	10	**0.282018**	0.000031	0.282015	-13.8	1.1	2.14	601
GJ1-12Jcm-40_7	40	0.0074	0.0006	0.00025	0.00001	1.46725	0.00005	1.88638	0.00012	9	**0.282004**	0.000029	0.282001	-14.3	1.0	2.17	601
GJ1-12Jcm-40_8	40	0.0073	0.0006	0.00025	0.00001	1.46729	0.00005	1.88632	0.00011	8	**0.282027**	0.000032	0.282024	-13.5	1.1	2.13	601
GJ1-12Jcm-40_9	40	0.0073	0.0006	0.00024	0.00001	1.46727	0.00005	1.88650	0.00012	9	**0.282011**	0.000026	0.282009	-14.1	0.9	2.16	601
GJ1-12Jcm-40_10	40	0.0075	0.0006	0.00025	0.00001	1.46733	0.00006	1.88640	0.00014	9	**0.282007**	0.000030	0.282004	-14.2	1.1	2.16	601
GJ1-12Jcm-40_11	40	0.0071	0.0006	0.00024	0.00001	1.46721	0.00007	1.88644	0.00012	8	**0.282013**	0.000028	0.282010	-14.0	1.0	2.15	601
GJ1-12Jcm-40_12	40	0.0071	0.0006	0.00024	0.00001	1.46729	0.00005	1.88653	0.00013	8	**0.281992**	0.000032	0.281990	-14.7	1.1	2.19	601
GJ1-12Jcm-40_13	40	0.0074	0.0006	0.00024	0.00001	1.46722	0.00006	1.88630	0.00021	6	**0.282014**	0.000030	0.282012	-14.0	1.1	2.15	601
GJ1-12Jcm-40_14	40	0.0072	0.0006	0.00024	0.00001	1.46731	0.00004	1.88657	0.00017	7	**0.282010**	0.000031	0.282007	-14.1	1.1	2.16	601
GJ1-12Jcm-40_15	40	0.0070	0.0006	0.00024	0.00001	1.46728	0.00005	1.88657	0.00014	8	**0.282013**	0.000029	0.282011	-14.0	1.0	2.15	601
GJ1-12Jcm-40_16	40	0.0070	0.0006	0.00024	0.00001	1.46722	0.00006	1.88645	0.00012	7	**0.282007**	0.000029	0.282005	-14.2	1.0	2.16	601
GJ1-12Jcm-40_17	40	0.0071	0.0006	0.00024	0.00001	1.46723	0.00007	1.88649	0.00012	7	**0.282009**	0.000030	0.282006	-14.2	1.1	2.16	601
Average		**0.0073**		**0.00024**		**1.46725**		**1.88651**			0.282008		**0.282006**	**-14.2**			
2 S.E. (abs.)		**0.0005**		**0.00001**		**0.00009**		**0.00030**			0.000020		**0.000020**	**0.7**			
2 S.E. (%)		**7**		**6**		**0.006**		**0.02**			0.0070		**0.0070**				
Plešovice																	
Pleso-12Jcm-40_1	40	0.0256	0.0026	0.00048	0.00004	1.46720	0.00004	1.88668	0.00010	13	**0.282482**	0.000026	0.282479	-3.3	0.9	1.35	338
Pleso-12Jcm-40_2	40	0.0110	0.0009	0.00024	0.00001	1.46724	0.00004	1.88666	0.00013	13	**0.282480**	0.000026	0.282479	-3.3	0.9	1.35	338
Pleso-12Jcm-40_3	40	0.0062	0.0005	0.00013	0.00001	1.46723	0.00003	1.88671	0.00010	15	**0.282476**	0.000028	0.282475	-3.4	1.0	1.36	338
Pleso-12Jcm-40_4	40	0.0063	0.0005	0.00013	0.00001	1.46723	0.00004	1.88669	0.00014	13	**0.282471**	0.000025	0.282470	-3.6	0.9	1.37	338
Pleso-12Jcm-40_5	40	0.0068	0.0005	0.00014	0.00001	1.46726	0.00004	1.88642	0.00009	13	**0.282475**	0.000023	0.282474	-3.5	0.8	1.36	338
Pleso-12Jcm-40_6	40	0.0066	0.0005	0.00013	0.00001	1.46728	0.00004	1.88639	0.00009	14	**0.282491**	0.000025	0.282490	-2.9	0.9	1.33	338
Pleso-12Jcm-40_7	40	0.0067	0.0005	0.00014	0.00001	1.46722	0.00004	1.88658	0.00009	13	**0.282480**	0.000025	0.282479	-3.3	0.9	1.35	338
Pleso-12Jcm-40_8	40	0.0062	0.0005	0.00013	0.00001	1.46725	0.00004	1.88635	0.00010	11	**0.282485**	0.000026	0.282485	-3.1	0.9	1.34	338
Pleso-12Jcm-40_9	40	0.0068	0.0005	0.00014	0.00001	1.46722	0.00006	1.88650	0.00013	11	**0.282484**	0.000027	0.282483	-3.1	1.0	1.34	338
Pleso-12Jcm-40_10	40	0.0063	0.0005	0.00013	0.00001	1.46726	0.00006	1.88655	0.00010	11	**0.282467**	0.000025	0.282466	-3.8	0.9	1.38	338
Pleso-12Jcm-40_11	40	0.0063	0.0005	0.00013	0.00001	1.46727	0.00006	1.88650	0.00016	11	**0.282477**	0.000034	0.282476	-3.4	1.2	1.36	338
Pleso-12Jcm-40_12	40	0.0067	0.0005	0.00014	0.00001	1.46724	0.00005	1.88646	0.00012	10	**0.282476**	0.000029	0.282475	-3.4	1.0	1.36	338
Average		**0.0085**		**0.00017**		**1.46724**		**1.88654**			0.282479		**0.282478**	**-3.4**			
2 S.E. (abs.)		**0.0111**		**0.00020**		**0.00005**		**0.00025**			0.000013		**0.000013**	**0.5**			
2 S.E. (%)		**131**		**117**		**0.003**		**0.01**			0.0046		**0.0046**				

Couzinié et al., 2017. Supplementary Table 6 (continued): In situ LA-MC-ICPMS Lu-Hf isotope data for zircon standards analyzed in this study

	Spot size	^{176}Yb [a]	±2σ	^{176}Lu [a]	±2σ	^{178}Hf	±2σ	^{180}Hf	±2σ	Sig_{Hf} [b]	**^{176}Hf**	±2σ [c]	^{176}Hf [e]	$\varepsilon Hf_{(t)}$ [e]	±2σ [c]	T_{DM2} [f]	Age [g]
	(μm)	^{177}Hf	(abs.)	^{177}Hf	(abs.)	^{177}Hf	(abs.)	^{177}Hf	(abs.)	(V)	**^{177}Hf**	(abs.)	$^{177}Hf_{(t)}$		(abs.)	(Ga)	(Ma)
Temora																	
TM-12Jcm-40_1	40	0.0150	0.0012	0.00051	0.00003	1.46724	0.00004	1.88668	0.00012	12	**0.282679**	0.000027	0.282675	5.4	1.0	0.94	419
TM-12Jcm-40_2	40	0.0132	0.0012	0.00045	0.00004	1.46733	0.00004	1.88654	0.00010	10	**0.282683**	0.000026	0.282679	5.6	0.9	0.93	419
TM-12Jcm-40_3	40	0.0132	0.0012	0.00045	0.00004	1.46733	0.00004	1.88656	0.00009	10	**0.282673**	0.000026	0.282670	5.3	0.9	0.95	419
TM-12Jcm-40_4	40	0.0211	0.0017	0.00077	0.00005	1.46727	0.00007	1.88670	0.00012	10	**0.282690**	0.000028	0.282684	5.8	1.0	0.92	419
TM-12Jcm-40_5	40	0.0193	0.0018	0.00063	0.00005	1.46732	0.00006	1.88631	0.00013	10	**0.282681**	0.000035	0.282676	5.5	1.2	0.93	419
TM-12Jcm-40_6	40	0.0447	0.0037	0.00136	0.00008	1.46733	0.00005	1.88632	0.00020	9	**0.282695**	0.000027	0.282684	5.8	1.0	0.92	419
TM-12Jcm-40_7	40	0.0348	0.0028	0.00108	0.00006	1.46725	0.00005	1.88647	0.00013	9	**0.282694**	0.000036	0.282686	5.8	1.3	0.92	419
TM-12Jcm-40_8	40	0.0232	0.0019	0.00076	0.00005	1.46731	0.00006	1.88626	0.00017	9	**0.282680**	0.000034	0.282674	5.4	1.2	0.94	419
TM-12Jcm-40_9	40	0.0371	0.0030	0.00122	0.00007	1.46723	0.00006	1.88664	0.00012	7	**0.282694**	0.000033	0.282685	5.8	1.2	0.92	419
TM-12Jcm-40_10	40	0.0353	0.0029	0.00113	0.00007	1.46736	0.00007	1.88629	0.00017	7	**0.282683**	0.000038	0.282674	5.4	1.3	0.94	419
TM-12Jcm-40_11	40	0.0144	0.0014	0.00050	0.00004	1.46722	0.00006	1.88650	0.00014	8	**0.282678**	0.000033	0.282674	5.4	1.2	0.94	419
TM-12Jcm-40_12	40	0.0385	0.0032	0.00132	0.00008	1.46722	0.00006	1.88632	0.00016	7	**0.282687**	0.000030	0.282677	5.5	1.1	0.93	419
Average		**0.0258**		**0.00085**		**1.46728**		**1.88646**			**0.282685**		**0.282678**	**5.6**			
2 S.E. (abs.)		**0.0230**		**0.00071**		**0.00010**		**0.00032**			**0.000014**		**0.000011**	**0.4**			
2 S.E. (%)		**89**		**84**		**0.007**		**0.02**			**0.0051**		**0.0037**				

(a) $^{176}Yb/^{177}Hf = (^{176}Yb/^{173}Yb)_{true} \times (^{173}Yb/^{177}Hf)_{meas} \times (M_{173(Yb)}/M_{177(Hf)})^{b(Hf)}$, $b(Hf) = \ln(^{179}Hf/^{177}Hf_{true} / {}^{179}Hf/^{177}Hf_{measured}) / \ln(M_{179(Hf)}/M_{177(Hf)})$, M=mass of respective isotope. The 176Lu/177Hf were calculated in a similar way by using the 175Lu/177Hf and b(Yb).

(b) Mean Hf signal in volt.

(c) Initial $^{176}Hf/^{177}Hf$ and eHf calculated using the apparent Pb-Pb age determined by LA-ICP-MS dating (see column f), and the CHUR parameters: $^{176}Lu/^{177}Hf = 0.0336$, and $^{176}Hf/^{177}Hf = 0.282785$ (Bouvier *et al* ., 2008).

(d) two stage model age in billion years using the measured $^{176}Lu/^{177}Lu$ of each spot (first stage = age of zircon), a value of 0.0113 for the average continental crust (second stage), and a juvenile crust (NC) $^{176}Lu/^{177}Lu$ and $^{176}Hf/^{177}Hf$ of 0.0384 and 0.28314, respectively.

Couzinié et al., 2017. Supplementary Table 7: In situ LA-MC-ICPMS Lu-Hf isotope data for zircon grains from augen gneisses

	^{176}Yb / ^{177}Hf [a]	±2σ (abs.)	^{176}Lu / ^{177}Hf [a]	±2σ (abs.)	^{178}Hf / ^{177}Hf	±2σ (abs.)	^{180}Hf / ^{177}Hf	±2σ (abs.)	Sig_{Hf} [b] (V)	^{176}Hf / ^{177}Hf	±2σ (abs.)	Apparent age (Ma)	±2σ (Ma)	Conc. (%)	^{176}Hf / $^{177}Hf_{App}$ [c]	$\varepsilon Hf_{(t)}$ [c]	±2σ (abs.)	^{176}Hf / $^{177}Hf_{(t\ int)}$ [d]	$\varepsilon Hf_{(t)}$ [d]	±2σ (abs.)	T_{DM2} [e] (Ga)	T_{DM2} [f] (Ga)
Sample MM06 (St. Privat augen orthogneiss)																						
MM06-40-1	0.0548	0.0046	0.00167	0.00011	1.46719	0.00005	1.88677	0.00017	11	0.282438	0.000032	543	6	99	0.282421	-0.8	1.1	0.282421	-0.8	1.1	1.40	1.19
MM06-4Hz-40-6	0.0607	0.0053	0.00190	0.00013	1.46721	0.00007	1.88647	0.00013	7	0.282506	0.000037	540	6	99	0.282486	1.5	1.3	0.282486	1.5	1.3	1.27	1.06
MM06-4Hz-40-15	0.0989	0.0087	0.00315	0.00022	1.46723	0.00009	1.88627	0.00017	7	0.282498	0.000027	541	6	100	0.282466	0.8	0.9	0.282466	0.8	0.9	1.31	1.10
MM06-4Hz-40-16	0.0659	0.0056	0.00176	0.00012	1.46720	0.00005	1.88670	0.00014	9	0.282423	0.000030	544	6	99	0.282405	-1.3	1.1	0.282405	-1.4	1.1	1.43	1.22
MM06-4Hz-40-18	0.0735	0.0059	0.00227	0.00014	1.46730	0.00004	1.88678	0.00016	7	0.282508	0.000041	544	6	99	0.282485	1.5	1.5	0.282485	1.5	1.5	1.28	1.06
MM06-4Hz-40-24	0.0724	0.0070	0.00223	0.00018	1.46721	0.00005	1.88663	0.00015	7	0.282510	0.000036	544	7	100	0.282487	1.6	1.3	0.282487	1.6	1.3	1.27	1.05
MM06-4Hz-60-2	0.0455	0.0038	0.00095	0.00006	1.46718	0.00004	1.88667	0.00011	17	0.282405	0.000024	535	6	100	0.282395	-1.9	0.9	0.282395	-1.7	0.9	1.45	1.24
MM06-4Hz-60-4	0.0887	0.0073	0.00268	0.00017	1.46707	0.00005	1.88708	0.00019	14	0.282429	0.000034	544	6	101	0.282402	-1.4	1.2	0.282402	-1.5	1.2	1.44	1.23
MM06-4Hz-60-9	0.0403	0.0032	0.00078	0.00005	1.46717	0.00005	1.88685	0.00016	17	0.282384	0.000023	538	6	99	0.282376	-2.5	0.8	0.282376	-2.4	0.8	1.49	1.28
MM06-4Hz-60-11	0.0428	0.0037	0.00128	0.00008	1.46710	0.00008	1.88711	0.00018	12	0.282500	0.000025	542	6	100	0.282487	1.5	0.9	0.282487	1.5	0.9	1.27	1.05
MM06-4Hz-60-12	0.0566	0.0046	0.00140	0.00009	1.46715	0.00004	1.88689	0.00011	16	0.282406	0.000026	536	6	99	0.282392	-1.9	0.9	0.282392	-1.8	0.9	1.46	1.25
MM06-4Hz-60-13	0.0724	0.0059	0.00213	0.00013	1.46715	0.00003	1.88691	0.00007	15	0.282467	0.000026	541	6	100	0.282445	0.1	0.9	0.282445	0.1	0.9	1.35	1.14
MM06-4Hz-60-14	0.0751	0.0061	0.00225	0.00014	1.46720	0.00004	1.88692	0.00011	15	0.282467	0.000029	543	6	100	0.282444	0.0	1.0	0.282444	0.0	1.0	1.36	1.14
																	Avg	**0.282438**	**-0.2**		**1.37**	**1.15**
																	2 SD	**0.000083**	**2.9**			
Sample MM11 (Col de Meyrand augen orthogneiss)																						
MM11-4Hz-60-26	0.0657	0.0053	0.00201	0.00012	1.46710	0.00004	1.88689	0.00011	14	**0.282457**	0.000033	539	7	100	0.282437	-0.3	1.2	0.282437	-0.2	1.2	1.37	1.16
MM11-4Hz-60-27	0.0705	0.0057	0.00221	0.00013	1.46712	0.00004	1.88698	0.00014	15	**0.282451**	0.000029	541	7	99	0.282429	-0.5	1.0	0.282429	-0.5	1.0	1.39	1.17
MM11-4Hz-60-29a	0.0412	0.0037	0.00130	0.00009	1.46716	0.00004	1.88685	0.00012	15	**0.282468**	0.000026	546	7	100	0.282454	0.5	0.9	0.282454	0.4	0.9	1.34	1.12
MM11-4Hz-60-29b	0.0633	0.0053	0.00195	0.00012	1.46716	0.00004	1.88685	0.00009	15	**0.282457**	0.000025	546	7	100	0.282437	-0.1	0.9	0.282438	-0.2	0.9	1.37	1.15
MM11-4Hz-60-34	0.0867	0.0070	0.00259	0.00016	1.46716	0.00004	1.88674	0.00010	17	**0.282441**	0.000026	545	7	99	0.282415	-0.9	0.9	0.282415	-1.0	0.9	1.41	1.20
MM11-4Hz-60-34b	0.0668	0.0054	0.00208	0.00013	1.46720	0.00003	1.88663	0.00010	17	**0.282483**	0.000025	545	7	99	0.282462	0.7	0.9	0.282462	0.7	0.9	1.32	1.11
MM11-4Hz-60-35	0.0680	0.0055	0.00209	0.00013	1.46719	0.00005	1.88691	0.00011	14	**0.282439**	0.000027	544	7	99	0.282417	-0.9	1.0	0.282417	-0.9	1.0	1.41	1.19
MM11-4Hz-60-37	0.0686	0.0055	0.00211	0.00013	1.46711	0.00005	1.88667	0.00013	15	**0.282453**	0.000031	538	7	100	0.282432	-0.5	1.1	0.282432	-0.4	1.1	1.38	1.17
MM11-4Hz-60-39	0.0746	0.0060	0.00228	0.00014	1.46719	0.00004	1.88680	0.00012	15	**0.282430**	0.000027	542	7	100	0.282407	-1.3	1.0	0.282407	-1.3	1.0	1.43	1.22
MM11-4Hz-60-41	0.0447	0.0036	0.00141	0.00008	1.46717	0.00006	1.88684	0.00018	14	**0.282454**	0.000026	541	7	99	0.282440	-0.1	0.9	0.282440	-0.1	0.9	1.37	1.15
MM11-4Hz-60-42	0.0552	0.0045	0.00173	0.00011	1.46719	0.00004	1.88684	0.00009	15	**0.282472**	0.000025	541	7	99	0.282454	0.4	0.9	0.282454	0.4	0.9	1.34	1.12
MM11-4Hz-60-44a	0.0682	0.0056	0.00208	0.00013	1.46711	0.00004	1.88695	0.00013	14	**0.282455**	0.000026	534	6	98	0.282434	-0.5	0.9	0.282434	-0.3	0.9	1.38	1.16

Couzinié et al., 2017. Supplementary Table 7: In situ LA-MC-ICPMS Lu-Hf isotope data for zircon grains from augen gneisses

	^{176}Yb / ^{177}Hf	±2σ (abs.)	^{176}Lu / ^{177}Hf	±2σ (abs.)	^{178}Hf / ^{177}Hf	±2σ (abs.)	^{180}Hf / ^{177}Hf	±2σ (abs.)	Sig_{Hf} (V)	^{176}Hf / ^{177}Hf	±2σ (abs.)	Apparent age (Ma)	±2σ (Ma)	Conc. (%)	^{176}Hf / $^{177}Hf_{App}$	$\varepsilon Hf_{(t)}$	±2σ (abs.)	^{176}Hf / $^{177}Hf_{(t\ int)}$	$\varepsilon Hf_{(t)}$	±2σ (abs.)	T_{DM2} (Ga)	T_{DM2} (Ga)
MM11-4Hz-60-44b	0.0719	0.0061	0.00216	0.00014	1.46722	0.00003	1.88686	0.00012	14	**0.282481**	0.000029	534	6	98	0.282459	0.4	1.0	0.282459	0.6	1.0	1.33	1.11
MM11-4Hz-60-45	0.0700	0.0056	0.00219	0.00013	1.46727	0.00004	1.88666	0.00009	16	**0.282459**	0.000025	544	7	100	0.282437	-0.2	0.9	0.282437	-0.2	0.9	1.37	1.16
																	Avg	**0.282437**	**-0.2**		**1.37**	**1.16**
																	2 SD	**0.000033**	**1.2**			

(a) $^{176}Yb/^{177}Hf = (^{176}Yb/^{173}Yb)_{true} \times (^{173}Yb/^{177}Hf)_{meas} \times (M_{173(Yb)}/M_{177(Hf)})^{b(Hf)}$, $b(Hf) = \ln(^{179}Hf/^{177}Hf_{true} / {}^{179}Hf/^{177}Hf_{measured}) / \ln (M_{179(Hf)}/M_{177(Hf)})$, M=mass of respective isotope. The $^{176}Lu/^{177}Hf$ were calculated in a similar way by using the $^{175}Lu/^{177}Hf$ and b(Yb).

(b) Mean Hf signal in volt.

(c) Initial $^{176}Hf/^{177}Hf$ and eHf calculated using the apparent age of each zircon domain spotted and the CHUR parameters:

$^{176}Lu/^{177}Hf = 0.0336$, and $^{176}Hf/^{177}Hf = 0.282785$ (Bouvier *et al*., 2008).

(d) Initial $^{176}Hf/^{177}Hf$ and eHf calculated using the emplacement age of each sample and the CHUR parameters:

$^{176}Lu/^{177}Hf = 0.0336$, and $^{176}Hf/^{177}Hf = 0.282785$ (Bouvier *et al*., 2008).

(e) two stage model age in billion years using the measured $^{176}Lu/^{177}Lu$ of each spot (first stage = age of zircon), a value of 0.0113 for the average continental crust (second stage), and a juvenile crust (NC) $^{176}Lu/^{177}Lu$ and $^{176}Hf/^{177}Hf$ of 0.0384 and 0.28325, respectively (Griffin et al., 2002).

(f) two stage model age in billion years using the measured $^{176}Lu/^{177}Lu$ of each spot (first stage = age of zircon), a value of 0.0113 for the average continental crust (second stage), and a juvenile crust (NC) $^{176}Lu/^{177}Lu$ and $^{176}Hf/^{177}Hf$ of 0.0375 and 0.28312, respectively (Naeraa et al., 2012).

Couzinié et al., 2017. Supplementary Table 8: Set of partition coefficients retained in the modelling section 5.2.2.

Element	Mineral	Kd	Reference
Ba	Biotite	10.15	Ewart & Griffin 1994
	K-Feldspar	6.65	-
	Plagioclase	0.76	-
Nb	Biotite	1.30	Montel 1996
	ilmenite	51.8	Ewart & Griffin 1994
	K-Feldspar	0.06	-
	Plagioclase	0.07	-
Sr	Biotite	0.45	Nash et Crecraft 1985
	K-Feldspar	4.18	Ewart & Griffin 1994
	Plagioclase	7.96	-

References

Ewart, A., and Griffin, W. L., 1994, Application of proton-microprobe data to trace-element partitioning in volcanic rocks: Chemical Geology, v. 117, p. 251-284.

Montel, J. M., 1996, Géochimie de la fusion de la croûte continentale: Thèse d'état, Nancy, 105 p.

Nash, W. P., and Crecraft, H. R., 1985, Partition coefficients for trace elements in silicic magmas: Geochimica et Cosmochimica Acta, v. 49, p. 2309-2322.

Appendix B

Full dataset

B.1 Whole-rock geochemical data

In this section are reported the whole-rock geochemical analyses conducted on:

- amphibolite samples from the Lower Gneiss Unit (see section 2.3)
- amphibolite samples from the Upper Gneiss Unit (see section 3.3)
- amphibole-bearing gneisses sampled at the Riverie quarry (see section 3.5)
- metasediments investigated for detrital zircon U–Pb–Hf isotope compositions
- a range of crustal lithologies (metasediments, orthogneisses, granites) from the Masméjean dome and surrounding areas.

The dataset is available as Table B1. Analytical details on the sample preparation procedure together with an estimate of the accuracy and reproducibility of the analyses are given in the supplementary materials of Couzinié et al. (2016) and Couzinié et al. (2017), see section A.3 and A.2.

Table B1: Whole-rock major and trace element compositions obtained on lithologies from the UGU/LGU

Sample	MG01	MG02	MG04	MG05	MG06	RV-1	RV-2	MM01	MM02
Ref ALS	LR17005608	LR17005608	LR17005608	LR17005608	LR17005608	LR16016981	LR16016981	LR15096747	LR15096747
Long	4.57860	4.57769	4.57820	4.58819	4.58827	4.58827	4.58827	4.43565	4.51147
Lat	45.59175	45.59077	45.59086	45.59650	45.59646	45.59646	45.59646	45.08400	45.07050
Locality	Riverie	Riverie	Riverie	Riverie	Riverie	Riverie	Riverie	Rochepaule	Fromentoux
Type	amphibolite	amphibolite	amphibolite	amphibolite	amphibolite	tonalite	tonalite	amphibolite	amphibolite
Details									layered
SiO_2	49.30	52.90	48.60	51.90	51.40	68.40	65.50	45.90	43.80
Al_2O_3	17.30	15.55	17.10	15.65	14.95	15.20	15.55	15.40	13.40
Fe_2O_3	7.62	10.85	7.55	8.86	12.20	4.33	5.47	13.45	12.70
CaO	14.05	8.10	12.65	8.64	7.39	4.50	3.77	10.95	14.45
MgO	8.49	4.17	9.55	7.50	4.97	2.13	2.84	3.60	7.62
Na_2O	2.19	4.11	2.06	4.04	4.32	5.08	4.96	3.46	1.77
K_2O	0.30	0.59	0.62	0.87	0.81	0.40	0.57	1.01	0.61
Cr_2O_3	0.04	0.01	0.07	0.04	<0,01	0.01	<0,01	0.02	0.07
TiO_2	0.39	1.82	0.28	1.30	2.36	0.37	0.40	2.72	2.56
MnO	0.13	0.14	0.13	0.17	0.21	0.08	0.07	0.15	0.17
P_2O_5	0.02	0.26	0.02	0.13	0.28	0.04	0.06	0.90	0.52
SrO	0.03	0.02	0.02	0.01	0.02	0.02	0.03	0.12	0.15
BaO	<0,01	0.01	0.02	0.04	0.02	0.02	0.03	0.05	0.01
C	0.02	0.02	0.06	0.01	0.05	0.02	0.12	0.01	0.02
S	0.16	0.06	0.02	<0,01	0.07	0.11	<0,01	0.10	0.55
Ba	42	87.7	159	323	198	222	244	415	48.6
Ce	1.8	27.5	1.6	14.7	23.9	19.9	16.8	98.7	84.7
Cr	330	70	550	270	30	20	10	120	490
Cs	5.50	0.35	23.20	0.76	1.12	0.26	1.18	1.27	0.64
Dy	1.38	6.00	0.95	4.30	7.04	2.33	1.62	6.45	5.49
Er	1.06	3.99	0.69	2.94	4.17	1.53	1.10	2.90	2.55
Eu	0.45	1.58	0.33	1.16	1.80	0.66	0.57	3.19	2.43
Ga	15.3	25.2	14.8	17.1	23.6	14.5	15.9	23.4	23.9
Gd	1.23	6.40	0.90	4.47	7.14	2.44	1.69	9.26	7.06
Hf	0.4	4.4	0.3	2.6	4.0	3.5	3.5	7.5	5.9
Ho	0.31	1.36	0.28	0.97	1.41	0.50	0.33	1.09	0.88
La	0.9	11.3	1.2	6.4	9.8	8.3	8.0	43.0	40.9
Lu	0.10	0.55	0.08	0.37	0.59	0.27	0.20	0.31	0.26
Nb	0.2	6.3	0.2	3.8	4.4	2.3	1.9	58.2	48.4
Nd	2.0	19.3	1.4	10.6	19.1	10.8	9.2	55.6	42.4
Pr	0.28	4.02	0.30	2.23	3.85	2.41	2.06	12.65	9.57
Rb	7.7	7.9	20.1	16.4	17.6	7.9	13.9	13.8	8.2
Sm	0.88	5.38	0.54	3.40	5.28	2.71	1.99	11.10	8.33
Sn	<1	1	2	1	1	2	1	4	29
Sr	277.0	293.0	208.0	192.0	249.0	250.0	287.0	968.0	1450.0
Ta	<0,1	0.4	<0,1	0.2	0.1	0.3	0.4	3.8	3.5
Tb	0.25	1.07	0.16	0.74	1.11	0.36	0.23	1.15	1.01
Th	0.18	1.03	0.05	0.84	1.21	0.74	1.14	5.28	5.68
Tl	<0,5	<0,5	<0,5	<0,5	<0,5	<0,5	<0,5	<0,5	<0,5
Tm	0.15	0.58	0.10	0.39	0.63	0.24	0.16	0.37	0.33
U	0.07	0.74	0.06	0.56	0.65	0.38	0.55	1.64	1.49
V	215	234	177	227	362	78	113	105	226
W	<1	<1	<1	1	1	<1	<1	1	1
Y	8.3	37.8	6.6	24.2	40.6	14.9	9.9	28.7	25.6
Yb	0.94	3.35	0.70	2.51	4.37	1.66	1.18	2.12	1.94
Zr	12	189	12	99	193	134	107	327	255
As	5.2	0.2	3.1	<0,1	0.3	0.3	<0,1	1.5	67.2
Bi	0.08	0.02	0.06	0.02	0.01	0.02	0.01	0.14	5.62
Hg	<0,005	<0,005	0.006	<0,005	<0,005	<0,005	<0,005	0.007	<0,005
Sb	0.18	0.07	0.15	0.13	0.15	<0,05	0.73	0.07	0.06
Se	0.3	0.2	0.2	0.2	0.7	0.2	0.4	0.6	1.2
Te	0.01	0.01	0.01	0.01	0.01	<0,01	<0,01	<0,01	0.04
LOI	1.07	0.47	1.39	1.01	1.23	0.51	2.25	0.41	1.42
Total	100.93	99	100.06	100.16	100.16	101.09	101.5	98.14	99.25
Ag	<0,5	<0,5	<0,5	<0,5	<0,5	<0,5	<0,5	0.9	1
Cd	<0,5	0.6	<0,5	0.7	0.6	<0,5	<0,5	<0,5	0.8
Co	36	29	45	36	35	13	14	36	68
Cu	53	29	10	1	20	25	2	33	144
Li	<10	<10	10	<10	<10	10	30	10	<10
Mo	<1	1	<1	<1	<1	<1	<1	<1	<1
Ni	63	16	119	53	5	13	10	69	286
Pb	3	2	9	<2	<2	2	<2	2	6
Sc	44	25	39	35	31	10	14	12	21
Zn	36	103	50	81	73	33	46	144	123
Ge	<5	<5	<5	<5	<5	<5	<5	<5	<5
In	0.007	0.024	0.009	0.013	0.018	0.007	0.019	0.049	0.111
Re	<0,001	0.001	<0,001	<0,001	0.001	<0,001	<0,001	0.001	0.001

Table B1 (continued): Whole-rock major and trace element compositions obtained on lithologies from the LGU

Sample	MM03	MM04	PIL-16-01	SEN-16-01	PdB-16-01a	PdB-16-01b	ROC-16-01	CHA-16-02	BOR-16-01
Ref ALS	LR15096747	LR15096747	LR17005608	LR17005608	LR17005608	LR17005608	LR17005608	LR17005608	LR17005608
Long	4.51147	4.51147	4.41651	3.60390	4.30584	4.30584	4.07712	3.79093	3.58485
Lat	45.07050	45.07050	45.40051	45.16402	44.65707	44.65707	44.33320	44.54597	44.27880
Locality	Fromentoux	Fromentoux	Saint-Etienne	Jax	Pont-de-Bavzan	Pont-de-Bavzan	Le Travers	Chasseradès	Pied de Borne
Type	amphibolite	amphibolite	metasediment	metasediment	paragneiss	paragneiss	granite	metasediment	granite
Details							Ms-Bt-Gt syntectonic granite		Porphyroid granite
SiO_2	45.10	46.60	87.50	77.70	67.00	59.60	75.30	72.70	69.50
Al_2O_3	13.25	13.40	7.20	12.75	14.30	17.45	14.80	13.70	13.80
Fe_2O_3	12.90	13.85	1.63	2.46	6.63	8.22	1.37	3.54	2.89
CaO	16.95	9.97	0.45	1.35	2.18	1.35	0.47	0.31	1.70
MgO	4.93	5.73	0.58	0.81	2.56	3.41	0.11	1.44	1.47
Na_2O	2.43	3.63	2.06	2.53	2.79	2.41	4.64	0.02	2.66
K_2O	0.36	0.55	0.87	1.75	2.62	4.35	3.77	5.37	5.01
Cr_2O_3	0.06	0.02	<0,01	0.01	0.02	0.01	<0,01	0.01	0.01
TiO_2	1.75	3.36	0.37	0.54	1.14	0.95	0.04	0.54	0.38
MnO	0.20	0.15	0.01	0.06	0.09	0.07	0.06	0.05	0.06
P_2O_5	0.19	0.33	0.06	0.14	0.27	0.26	0.27	0.14	0.22
SrO	0.10	0.06	0.01	0.02	0.03	0.02	<0,01	<0,01	0.03
BaO	0.01	0.01	0.02	0.04	0.06	0.09	<0,01	0.10	0.07
C	0.04	0.01	0.02	0.03	0.01	<0,01	0.01	0.04	0.01
S	0.16	0.32	<0,01	<0,01	0.08	0.01	<0,01	<0,01	<0,01
Ba	53	127	205	341	525	885	26.1	922	629
Ce	24.7	43.2	73.6	81.4	66.3	77.8	7.0	53.7	61.7
Cr	390	120	20	40	110	110	10	60	60
Cs	1.62	0.31	1.28	1.58	10.05	16.45	9.25	12.55	16.55
Dy	3.39	5.85	3.43	5.56	5.39	6.15	0.84	3.87	3.43
Er	1.92	2.83	2.00	3.11	3.28	3.84	0.48	2.15	2.12
Eu	1.22	2.00	0.92	1.41	1.49	1.21	0.09	0.38	0.83
Ga	17.9	20.3	7.6	14.5	18.8	27.8	25.7	15.8	18.3
Gd	4.18	6.30	4.16	6.43	5.79	6.90	0.64	4.31	4.21
Hf	2.7	4.5	7.9	7.5	8.4	5.5	1.6	6.1	4.8
Ho	0.63	0.97	0.62	1.08	1.17	1.30	0.13	0.80	0.72
La	11.1	19.6	35.4	39.8	33.7	38.3	3.8	28.0	32.2
Lu	0.20	0.26	0.28	0.42	0.47	0.49	0.07	0.34	0.30
Nb	13.9	26.6	8.4	10.2	13.2	14.4	16.2	9.0	17.2
Nd	14.7	25.8	27.5	33.5	31.7	37.3	2.7	24.9	25.7
Pr	3.19	5.70	8.08	9.42	8.32	10.10	0.74	6.51	7.28
Rb	9.9	5.7	30.9	56.3	105.5	205.0	395.0	200.0	266.0
Sm	3.96	7.01	5.20	6.77	6.81	8.43	0.82	5.10	5.58
Sn	38	2	1	2	3	4	17	1	14
Sr	817.0	548.0	88.6	212.0	277.0	244.0	15.9	27.4	297.0
Ta	1.0	1.8	0.7	0.8	0.8	0.9	2.5	0.6	2.4
Tb	0.63	0.93	0.62	0.92	0.95	1.05	0.15	0.64	0.64
Th	1.60	2.63	15.45	12.80	8.98	9.38	2.85	9.01	25.20
Tl	<0,5	<0,5	<0,5	<0,5	0.6	0.9	2.2	0.9	1.1
Tm	0.25	0.35	0.29	0.45	0.47	0.53	0.09	0.33	0.30
U	0.59	0.66	3.47	2.57	2.51	2.69	8.57	3.21	8.26
V	201	326	21	45	131	163	<5	97	42
W	2	<1	2	1	1	2	1	3	1
Y	16.9	25.7	17.8	27.9	29.7	38.2	4.8	21.4	21
Yb	1.44	2.04	1.71	2.82	2.96	3.39	0.58	2.12	2.16
Zr	104	179	320	288	314	241	30	232	190
As	11.6	2.3	0.7	17	<0,1	0.9	3.5	0.4	1.3
Bi	6.5	0.26	0.12	0.19	0.27	0.25	2.97	0.22	1.01
Hg	0.008	0.009	<0,005	<0,005	<0,005	<0,005	<0,005	<0,005	<0,005
Sb	0.09	0.06	<0,05	<0,05	0.08	0.13	0.06	0.08	<0,05
Se	0.2	1	0.6	0.3	0.5	0.9	<0,2	0.6	0.6
Te	0.02	<0,01	<0,01	0.03	0.06	0.04	0.02	0.03	0.01
LOI	1.41	0.74	0.7	1.46	1.15	2.51	0.47	3.01	0.67
Total	99.64	98.4	101.46	101.62	100.84	100.7	101.3	100.93	98.47
Ag	0.8	0.9	<0,5	<0,5	<0,5	<0,5	<0,5	0.7	<0,5
Cd	0.9	0.5	<0,5	<0,5	<0,5	<0,5	<0,5	<0,5	<0,5
Co	56	55	2	4	14	17	<1	7	5
Cu	145	126	5	9	30	32	2	56	2
Li	10	<10	10	10	60	90	50	210	100
Mo	<1	<1	<1	<1	<1	<1	<1	<1	<1
Ni	240	54	9	7	29	53	<1	19	9
Pb	9	<2	12	75	15	21	33	6	37
Sc	20	28	3	5	14	18	2	8	7
Zn	183	134	24	127	83	180	63	43	46
Ge	<5	<5	<5	<5	<5	<5	<5	<5	<5
In	0.045	0.035	0.009	0.013	0.069	0.082	0.011	0.026	0.042
Re	0.001	0.002	0.001	<0,001	<0,001	<0,001	<0,001	<0,001	<0,001

Table B1 (continued): Whole-rock major and trace element compositions obtained on the Masméjean dome area

Sample	CHA-15-05	CHA-15-07	CHA-15-17	CHA-15-19	CHA-15-24	CHA-15-29	CHA-15-33	CHA-15-34	CHA-15-25
Ref ALS	LR16016981	LR16016981	LR16016981	LR16016981	LR16016981	LR16016981	LR16016981	LR16016981	LR16016981
Long	3.88036	3.86111	3.88742	3.88017	3.90175	3.87859	3.84491	3.84598	3.90264
Lat	44.52902	44.53889	44.53103	44.52806	44.53318	44.51265	44.53368	44.53308	44.53148
Locality	Les Orts	L'Adrech	Barrage de Puvlaurent	Les Orts	Le Ranc	Piéchelapie	Le Couste	Le Couste	Le Ranc
Type	granite	granite	augen gneiss	granite	granite	granite	granite	granite	granite
Details		"4-Vios type"	metatexite				"4-Vios type"		
SiO_2	71.30	66.00	69.60	73.00	74.30	73.60	71.40	75.00	72.60
Al_2O_3	14.20	14.95	15.70	14.45	14.35	14.05	14.65	14.25	14.45
Fe_2O_3	2.41	3.75	2.47	1.59	0.92	0.90	1.83	1.01	1.49
CaO	0.29	1.40	0.99	0.43	0.45	0.45	0.78	0.44	0.62
MgO	0.53	2.37	0.56	0.38	0.13	0.10	0.53	0.07	0.27
Na_2O	2.85	1.78	4.05	2.81	3.68	4.15	2.99	4.22	3.49
K_2O	6.22	6.08	4.78	5.87	4.96	4.10	5.83	4.37	5.22
Cr_2O_3	0.01	0.02	<0,01	<0,01	<0,01	<0,01	0.01	<0,01	<0,01
TiO_2	0.30	0.64	0.26	0.15	0.05	0.03	0.19	0.05	0.12
MnO	0.02	0.06	0.03	0.02	0.01	0.02	0.03	0.02	0.02
P_2O_5	0.20	0.56	0.27	0.30	0.19	0.26	0.30	0.22	0.33
SrO	<0,01	0.03	<0,01	<0,01	<0,01	<0,01	<0,01	<0,01	<0,01
BaO	0.09	0.14	0.08	0.08	0.02	0.02	0.04	0.02	0.02
C	0.02	0.03	0.01	0.01	0.01	0.01	0.01	0.01	0.02
S	0.01	<0,01	0.01	0.01	0.02	0.02	0.01	<0,01	0.01
Ba	773	1310	668	733	167.5	161	390	158.5	167.5
Ce	78.9	55.1	51.4	32.9	7.0	9.3	37.8	9.6	18.3
Cr	20	100	10	<10	<10	10	20	<10	<10
Cs	3.83	14.65	9.21	5.94	5.10	7.19	12.15	9.28	5.14
Dy	3.74	3.37	5.84	2.88	0.23	1.00	2.33	1.27	2.97
Er	1.96	1.59	3.45	1.41	0.08	0.57	1.02	0.50	1.30
Eu	0.86	1.11	0.93	0.61	0.15	0.09	0.47	0.20	0.25
Ga	15.2	17.8	19.4	16.3	18.3	19.3	22.7	19.3	22.5
Gd	4.46	4.23	5.00	2.61	0.38	0.76	2.73	1.00	2.26
Hf	5.9	4.8	4.6	3.2	0.8	1.6	3.1	1.0	1.5
Ho	0.67	0.56	1.19	0.51	0.04	0.20	0.42	0.21	0.50
La	37.9	30.0	24.6	16.7	4.5	5.2	20.2	5.1	8.7
Lu	0.23	0.18	0.37	0.16	0.02	0.07	0.12	0.06	0.13
Nb	13.9	17.4	11.2	13.6	6.8	11.2	11.2	11.0	13.0
Nd	32.6	26.9	23.7	13.6	2.6	3.8	17.0	3.9	8.3
Pr	8.73	6.39	5.84	3.43	0.72	1.05	4.47	1.01	2.15
Rb	171.5	221.0	186.5	174.0	190.0	202.0	284.0	235.0	203.0
Sm	5.68	5.07	5.48	2.91	0.42	0.72	3.46	1.18	2.23
Sn	10	12	6	4	5	13	15	13	7
Sr	112.0	279.0	96.2	135.5	60.2	36.6	103.0	37.0	61.3
Ta	1.1	4.2	1.0	1.2	0.6	3.0	1.5	4.3	1.0
Tb	0.69	0.57	0.86	0.47	0.03	0.12	0.43	0.21	0.43
Th	18.35	13.50	10.10	8.06	2.99	2.52	9.41	3.04	3.66
Tl	1.1	1.2	0.8	1.0	0.8	0.9	1.2	1.3	0.8
Tm	0.25	0.22	0.46	0.20	0.03	0.08	0.12	0.07	0.18
U	8.28	7.62	2.82	6.06	18.75	2.64	6.60	2.91	9.96
V	12	62	19	11	<5	6	16	<5	<5
W	1	1	2	1	<1	3	5	3	3
Y	18.9	17.8	32.8	16.2	1.3	6.4	11.9	7	15.4
Yb	1.41	1.25	2.87	1.25	0.11	0.63	0.91	0.48	1.03
Zr	194	152	145	81	14	30	89	20	34
As	10.6	7.3	2.4	1.2	0.9	0.5	1.7	0.4	0.8
Bi	0.11	0.4	0.04	2.94	6.59	1.66	0.65	1	2.61
Hg	<0,005	<0,005	<0,005	0.006	<0,005	<0,005	<0,005	<0,005	<0,005
Sb	0.11	0.1	0.13	<0,05	<0,05	0.06	<0,05	<0,05	<0,05
Se	0.5	0.7	0.8	0.4	<0,2	0.2	0.2	0.3	0.4
Te	<0,01	<0,01	<0,01	0.04	<0,01	0.02	<0,01	<0,01	0.02
LOI	0.96	1.92	0.91	1.01	0.61	0.69	0.71	0.61	0.7
Total	99.38	99.7	99.7	100.09	99.67	98.37	99.29	100.28	99.33
Ag	<0,5	<0,5	<0,5	0.5	<0,5	<0,5	<0,5	<0,5	<0,5
Cd	<0,5	<0,5	<0,5	<0,5	<0,5	<0,5	<0,5	<0,5	<0,5
Co	2	8	3	1	<1	<1	3	<1	1
Cu	15	7	2	7	6	6	2	1	3
Li	30	110	60	40	30	20	70	30	40
Mo	<1	<1	<1	<1	<1	<1	<1	<1	<1
Ni	4	19	4	1	<1	1	4	1	<1
Pb	29	40	22	23	30	10	29	16	19
Sc	4	10	3	3	1	2	4	2	6
Zn	34	121	49	15	19	8	45	12	23
Ge	<5	<5	<5	<5	<5	<5	<5	<5	<5
In	0.032	0.045	0.035	0.012	0.011	0.006	0.023	0.009	0.017
Re	<0,001	<0,001	0.001	0.001	<0,001	<0,001	<0,001	<0,001	<0,001

Table B1 (continued): Whole-rock major and trace element compositions obtained on the Masméjean dome area

Sample	CHA-15-35	CHA-15-36	CHA-15-41	CHA-15-43	CHA-15-44	CHA-15-47	CHA-15-48	CHA-15-49	CHA-15-51
Ref ALS	LR16016981	LR16016981	LR16016981	LR16016981	LR16016981	LR16016981	LR16016981	LR16016981	LR16016981
Long	3.84598	3.84611	3.90506	3.87934	3.80854	3.96989	3.96989	3.90300	3.83309
Lat	44.53308	44.53295	44.54657	44.56799	44.54674	44.60493	44.60493	44.52644	44.57011
Locality	Le Couste	Le Couste	les Clous-Maurines	Masmejean	Mirandol	St-Laurent-les-Bains	St-Laurent-les-Bains	Le Mourio	Majousseires
Type	leucogneiss	leucogneiss	granite	migmatite	leucogneiss	migmatite	augen gneiss	granite	granite
Details				in source leucosome		in source leucosome	metatexite		
SiO_2	75.20	77.30	69.30	75.10	78.60	76.30	70.60	71.90	73.80
Al_2O_3	12.45	13.25	15.35	13.25	12.40	13.15	14.25	14.60	14.85
Fe_2O_3	1.37	1.35	2.67	1.02	1.23	1.19	2.57	2.11	1.30
CaO	0.40	0.46	0.55	0.31	0.36	0.45	0.74	0.41	0.45
MgO	0.10	0.09	0.96	0.14	0.09	0.19	0.64	0.67	0.14
Na_2O	2.91	3.06	2.75	2.61	3.08	2.57	2.72	2.93	3.60
K_2O	4.52	4.77	5.93	6.27	4.29	5.96	5.40	5.41	5.07
Cr_2O_3	<0,01	<0,01	<0,01	<0,01	<0,01	<0,01	0.01	0.01	<0,01
TiO_2	0.09	0.09	0.47	0.06	0.06	0.09	0.29	0.27	0.07
MnO	0.02	0.02	0.03	0.01	0.02	0.01	0.03	0.02	0.03
P_2O_5	0.29	0.35	0.29	0.26	0.36	0.13	0.28	0.27	0.34
SrO	<0,01	<0,01	0.02	<0,01	<0,01	<0,01	<0,01	0.01	<0,01
BaO	0.01	0.02	0.10	0.02	0.01	0.06	0.07	0.08	0.01
C	0.01	0.01	<0,01	0.01	0.01	0.01	<0,01	0.01	0.01
S	0.01	<0,01	<0,01	<0,01	0.01	0.01	0.02	<0,01	<0,01
Ba	102	181.5	945	147	64.5	526	604	798	128
Ce	11.9	13.3	68.3	10.3	6.9	16.0	58.1	64.4	8.0
Cr	<10	<10	20	<10	<10	<10	20	20	<10
Cs	8.76	19.05	6.59	6.58	12.30	5.92	15.05	6.59	6.73
Dy	2.41	2.72	2.69	2.59	1.91	3.27	5.49	2.92	1.98
Er	0.92	1.08	1.32	1.48	0.82	2.48	3.30	1.56	0.93
Eu	0.14	0.20	1.03	0.17	0.10	0.60	0.85	0.73	0.20
Ga	17.9	20.9	21.2	15.8	21.0	12.8	19.4	18.8	22.3
Gd	1.54	1.80	4.08	1.68	1.05	1.77	5.11	3.44	1.44
Hf	1.9	2.3	6.3	2.4	2.5	1.9	5.0	4.1	0.8
Ho	0.41	0.46	0.49	0.46	0.32	0.71	1.13	0.51	0.30
La	5.3	5.7	39.7	4.9	3.1	7.8	27.2	32.4	3.9
Lu	0.07	0.12	0.16	0.19	0.08	0.31	0.37	0.18	0.10
Nb	12.2	15.4	14.3	7.5	16.7	4.2	13.2	14.4	16.3
Nd	5.1	5.8	33.5	4.9	3.5	6.7	26.1	27.7	3.7
Pr	1.37	1.52	8.51	1.25	0.80	1.67	6.56	7.16	1.07
Rb	261.0	331.0	222.0	216.0	362.0	179.5	229.0	207.0	255.0
Sm	1.50	1.73	6.02	1.29	0.89	1.76	5.84	4.74	1.27
Sn	8	11	6	6	14	5	6	7	18
Sr	20.2	30.0	264.0	54.2	11.5	85.8	88.8	214.0	34.4
Ta	14.5	2.5	1.7	0.6	3.5	0.6	1.0	2.8	2.9
Tb	0.33	0.42	0.53	0.34	0.23	0.34	0.90	0.49	0.26
Th	4.80	5.41	26.90	4.12	3.61	3.74	11.00	22.60	1.80
Tl	1.0	1.7	1.1	1.1	1.4	0.8	1.2	1.0	0.8
Tm	0.13	0.14	0.16	0.20	0.11	0.33	0.44	0.20	0.12
U	8.91	6.17	5.92	6.37	23.20	3.87	4.54	4.15	3.85
V	<5	6	33	5	<5	5	23	24	<5
W	4	5	2	1	12	1	2	3	5
Y	12.2	15.5	14.4	14.7	11.1	21.6	32.9	15.6	10.5
Yb	0.69	0.86	1.13	1.37	0.64	2.16	2.78	1.47	0.89
Zr	37	43	228	42	39	42	162	146	17
As	1.3	1.4	7.8	13.4	1.2	1	2.3	1.4	2
Bi	0.8	0.1	0.14	0.31	3.24	0.1	0.21	0.05	4.78
Hg	0.01	<0,005	<0,005	<0,005	0.005	<0,005	<0,005	<0,005	<0,005
Sb	0.05	0.19	0.11	0.14	0.12	<0,05	0.12	<0,05	<0,05
Se	0.6	0.7	0.6	0.4	0.4	<0,2	0.7	0.5	0.4
Te	<0,01	<0,01	<0,01	<0,01	0.01	<0,01	<0,01	<0,01	<0,01
LOI	0.65	0.67	1.61	0.7	0.76	0.46	0.97	1.54	0.84
Total	98.01	101.43	100.03	99.75	101.26	100.56	98.57	100.23	100.5
Ag	<0,5	<0,5	<0,5	<0,5	<0,5	<0,5	<0,5	<0,5	<0,5
Cd	<0,5	<0,5	<0,5	<0,5	<0,5	<0,5	<0,5	<0,5	<0,5
Co	<1	<1	2	<1	<1	1	2	3	<1
Cu	3	12	3	3	3	1	9	5	2
Li	60	70	60	20	50	40	70	30	30
Mo	<1	<1	<1	<1	<1	<1	<1	<1	<1
Ni	<1	1	6	<1	<1	1	5	6	<1
Pb	15	118	33	35	6	25	23	23	20
Sc	2	2	5	2	2	1	4	4	3
Zn	25	33	39	10	30	16	62	21	18
Ge	<5	<5	<5	<5	<5	<5	<5	<5	<5
In	0.024	0.023	0.02	0.016	0.013	0.018	0.055	0.007	0.012
Re	<0,001	<0,001	<0,001	<0,001	<0,001	<0,001	<0,001	0.001	<0,001

Table B1 (continued): Whole-rock major and trace element compositions obtained on the Masméjean dome area

Sample	CHA-15-52	CHA-15-59	CHA-15-63	CHA-15-65L	CHA-15-65M	SC14 40	SC14 46
Ref ALS	LR16016981	LR16016981	LR16016981	LR16016981	LR16016981	LR15096747	LR15096747
Long	3.82921	3.87213	3.88324	3.88742	3.88742	3.90157	4.01186
Lat	44.57224	44.60196	44.59365	44.53103	44.53103	44.53354	44.61692
Locality	Majousseires	la Soucheire	Charbonneire	Barrage de Puylaurent	Barrage de Puylaurent	Chassezac vallev	Borne
Type	leucogneiss	granite	migmatite	migmatite	augen gneiss	granite	leucosome
Details			in source leucosome	in source leucosome	metatexite	concordant vein within paragneiss	in situ leucosome in orthogneiss
SiO_2	76.00	72.60	72.60	73.70	71.00	74.00	74.00
Al_2O_3	12.90	15.10	14.85	14.65	13.70	14.25	14.50
Fe_2O_3	1.91	1.90	0.70	1.03	4.12	1.79	1.39
CaO	0.42	0.64	0.52	0.44	0.43	0.53	1.72
MgO	0.13	0.37	0.07	0.18	1.38	0.34	0.45
Na_2O	3.01	3.07	3.25	3.59	2.60	2.78	3.38
K_2O	4.88	5.10	7.27	5.99	5.14	5.90	4.23
Cr_2O_3	<0,01	<0,01	<0,01	<0,01	0.01	<0,01	<0,01
TiO_2	0.12	0.23	0.03	0.07	0.41	0.17	0.11
MnO	0.03	0.03	0.02	0.02	0.05	0.02	0.03
P_2O_5	0.29	0.26	0.49	0.21	0.18	0.18	0.17
SrO	<0,01	0.01	<0,01	<0,01	<0,01	0.01	0.03
BaO	0.01	0.05	0.04	0.04	0.04	0.07	0.09
C	0.01	0.01	0.01	0.01	0.01	0.03	<0,01
S	<0,01	<0,01	<0,01	<0,01	<0,01	0.01	<0,01
Ba	62.1	467	352	361	375	674	857
Ce	15.9	77.8	7.0	10.4	55.7	31.9	31.4
Cr	<10	<10	<10	<10	20	10	10
Cs	4.14	7.62	5.15	5.38	14.75	7.32	4.79
Dy	4.51	2.46	2.03	1.42	4.55	3.18	2.26
Er	2.83	1.00	1.22	0.75	2.54	1.54	1.04
Eu	0.10	0.67	0.40	0.44	0.66	0.63	0.97
Ga	19.6	20.5	14.5	14.2	19.1	21.6	17.9
Gd	2.63	4.26	1.73	1.22	4.48	3.45	2.60
Hf	3.4	4.2	1.4	1.2	4.3	3.0	2.2
Ho	0.99	0.47	0.43	0.25	0.86	0.63	0.34
La	7.3	41.8	3.0	5.3	26.3	17.4	19.7
Lu	0.29	0.14	0.17	0.09	0.29	0.24	0.12
Nb	15.3	13.1	1.8	4.7	14.9	11.0	3.7
Nd	7.8	31.0	4.1	5.2	24.7	15.4	15.8
Pr	1.95	8.13	0.86	1.22	6.04	4.83	4.36
Rb	229.0	212.0	263.0	207.0	265.0	193.0	111.5
Sm	2.42	5.73	1.38	1.13	5.23	2.95	2.76
Sn	7	11	8	5	11	6	4
Sr	21.6	126.0	63.4	78.7	66.6	119.5	286.0
Ta	2.4	1.6	1.5	0.9	1.4	1.3	0.4
Tb	0.63	0.53	0.31	0.23	0.72	0.45	0.33
Th	8.40	21.20	0.87	2.42	10.65	8.16	8.01
Tl	1.1	0.9	1.0	0.8	1.1	0.7	<0,5
Tm	0.38	0.14	0.20	0.11	0.36	0.23	0.15
U	3.01	5.93	5.70	2.57	4.80	6.44	2.46
V	5	10	<5	6	38	<5	9
W	5	3	<1	1	2	1	1
Y	29.5	13.2	13.9	7.9	24.5	18.9	11.5
Yb	2.49	0.97	1.19	0.67	2.01	1.33	1.07
Zr	78	140	18	19	140	96	60
As	2.6	1.9	11.8	0.5	1.9	0.4	1.7
Bi	0.8	1.08	2.07	0.2	0.13	0.76	0.11
Hg	<0,005	<0,005	<0,005	<0,005	<0,005	<0,005	0.005
Sb	<0,05	<0,05	0.36	<0,05	<0,05	<0,05	<0,05
Se	0.8	0.4	0.6	<0,2	0.3	<0,2	<0,2
Te	<0,01	<0,01	<0,01	<0,01	<0,01	<0,01	0.03
LOI	0.68	1.21	0.3	0.63	1.01	0.85	0.53
Total	100.38	100.57	100.14	100.55	100.07	100.89	100.63
Ag	<0,5	<0,5	<0,5	<0,5	<0,5	<0,5	<0,5
Cd	<0,5	<0,5	<0,5	<0,5	<0,5	<0,5	<0,5
Co	1	1	<1	1	5	1	3
Cu	5	1	12	1	1	4	4
Li	30	60	20	20	130	20	30
Mo	<1	<1	<1	<1	<1	<1	<1
Ni	<1	1	<1	<1	12	<1	6
Pb	21	24	52	35	28	39	31
Sc	2	3	1	1	7	3	2
Zn	21	47	29	19	107	37	14
Ge	<5	<5	<5	<5	<5	<5	<5
In	0.041	0.018	0.049	0.014	0.07	0.031	0.024
Re	<0,001	<0,001	<0,001	<0,001	<0,001	<0,001	<0,001

B.2 Mineral chemistry

B.2.1 Analytical details

Mineral major element compositions were obtained using a Zeiss EVO MA15 Scanning Electron Microscope at the Central Analytical Facility (CAF) of Stellenbosch University, South Africa. Mineral compositions were quantified by EDX (Energy Dispersive X-ray) analysis using an Oxford Instruments® X-Max 20 mm^2 detector and the Oxford INCA software. Beam conditions were 20 kV accelerating voltage, 1.5 nA probe current, a working distance of 8.5 mm and a specimen beam current of 20 nA. Analyses were quantified using natural mineral standards.

B.2.2 Data tables

Mineral compositions obtained in the course of this study are reported in the following tables:

- Table B2: Mineral compositions of the RV-1 and RV-2 amphibole-bearing gneisses from the Upper Gneiss Unit, Riverie quarry, see section 3.5.
- Table B3: Mineral compositions of the biotite-bearing granite RV-3, Riverie quarry, see section 5.2.

Table B2: Mineral compositions of Riverie meta-tonalite samples RV-1 and RV-2

	RV1 - Amphiboles												
	S 1	S 2	S 3	S 4	S 5	S 6	S 7	S 8	S 9	S 10	S 11	S 12	S 13
SiO_2	46.43	46.12	45.61	47.48	44.43	46.62	46.41	44.03	43.83	47.46	47.82	44.98	46.33
TiO_2	0.86	0.94	1.04	0.97	1.09	0.85	0.86	1.10	1.21	0.88	0.80	1.02	0.85
Al_2O_3	8.51	8.67	9.53	7.58	10.06	8.79	8.39	9.68	9.83	7.81	7.69	9.53	7.97
FeO	15.15	14.76	15.05	13.85	15.73	14.71	14.81	15.64	15.33	14.58	14.95	15.95	14.00
MnO	0.55	0.58	0.46	0.53	0.56	0.53	0.58	0.49	0.46	0.59	0.60	0.49	0.44
MgO	13.33	13.44	13.04	13.71	12.23	13.09	13.32	12.23	11.84	13.61	13.66	12.47	13.17
CaO	10.80	11.30	11.42	11.55	11.39	10.94	11.22	11.10	11.45	11.47	11.34	11.12	11.87
Na_2O	1.58	1.39	1.52	1.24	1.64	1.58	1.46	1.74	1.48	1.29	1.43	1.80	1.04
K_2O	0.38	0.28	0.43	0.34	0.45	0.31	0.33	0.43	0.45	0.28	0.36	0.38	0.28
Total	97.59	97.50	98.10	97.24	97.58	97.41	97.37	96.44	95.89	97.97	98.65	97.74	95.94
No. Ox	23	23	23	23	23	23	23	23	23	23	23	23	23
Si	6.70	6.67	6.59	6.89	6.49	6.74	6.73	6.51	6.53	6.83	6.84	6.55	6.84
Al iv	1.30	1.33	1.41	1.11	1.51	1.26	1.27	1.49	1.47	1.17	1.16	1.45	1.16
Al vi	0.14	0.14	0.21	0.18	0.23	0.24	0.16	0.19	0.26	0.16	0.14	0.18	0.22
Ti	0.09	0.10	0.11	0.11	0.12	0.09	0.09	0.12	0.14	0.10	0.09	0.11	0.09
Fe3+	1.12	1.04	0.94	0.71	0.93	0.94	0.96	0.97	0.76	0.87	0.91	1.00	0.64
Fe2+	0.71	0.75	0.87	0.97	0.99	0.84	0.83	0.97	1.15	0.88	0.88	0.94	1.08
Mn	0.07	0.07	0.06	0.06	0.07	0.06	0.07	0.06	0.06	0.07	0.07	0.06	0.06
Mg	2.87	2.90	2.81	2.96	2.66	2.82	2.88	2.69	2.63	2.92	2.91	2.71	2.90
Ca	1.67	1.75	1.77	1.80	1.78	1.70	1.74	1.76	1.83	1.77	1.74	1.73	1.88
Na	0.44	0.39	0.43	0.35	0.46	0.44	0.41	0.50	0.43	0.36	0.40	0.51	0.30
K	0.07	0.05	0.08	0.06	0.08	0.06	0.06	0.08	0.09	0.05	0.06	0.07	0.05
OH*	2.00	2.00	2.00	2.00	2.00	2.00	2.00	2.00	2.00	2.00	2.00	2.00	2.00
Total	17.18	17.19	17.27	17.21	17.33	17.20	17.22	17.34	17.34	17.18	17.20	17.31	17.23

	RV2 - Amphiboles												
	S 14	S 2	S 3	S 4	S 5	S 6	S 7	S 8	S 9	S 10	S 11	S 13	S 14
SiO_2	46.62	46.04	47.27	47.57	46.23	47.51	45.68	49.02	46.78	46.54	47.22	49.23	46.74
TiO_2	0.90	0.76	0.72	0.57	0.81	0.53	0.70	0.56	0.71	0.72	0.66	0.55	0.76
Al_2O_3	8.23	9.49	8.22	8.40	9.75	8.28	9.48	6.96	8.79	9.19	8.61	6.95	9.04
FeO	15.31	16.35	15.98	15.42	16.76	15.97	16.47	15.17	16.51	16.50	16.38	15.51	16.98
MnO	0.56	0.50	0.57	0.38	0.48	0.42	0.39	0.47	0.63	0.42	0.46	0.48	0.47
MgO	13.77	12.04	13.08	13.00	11.96	12.88	12.22	13.91	12.50	12.30	12.72	13.96	12.17
CaO	10.35	11.39	11.10	11.72	11.54	11.90	11.68	11.47	11.01	11.45	11.06	11.29	11.25
Na_2O	1.35	1.34	1.44	1.03	1.47	1.04	1.33	0.89	1.54	1.45	1.54	1.10	1.37
K_2O	0.37	0.38	0.36	0.42	0.56	0.41	0.47	0.30	0.41	0.42	0.45	0.26	0.46
Total	97.44	98.29	98.74	98.51	99.57	98.93	98.42	98.74	98.88	99.00	99.10	99.34	99.24
No. Ox	23	23	23	23	23	23	23	23	23	23	23	23	23
Si	6.67	6.66	6.76	6.83	6.63	6.82	6.62	6.97	6.71	6.69	6.75	6.95	6.70
Al iv	1.33	1.34	1.24	1.17	1.37	1.18	1.38	1.03	1.29	1.31	1.25	1.05	1.30
Al vi	0.06	0.28	0.15	0.26	0.28	0.22	0.24	0.13	0.19	0.25	0.20	0.11	0.23
Ti	0.10	0.08	0.08	0.06	0.09	0.06	0.08	0.06	0.08	0.08	0.07	0.06	0.08
Fe3+	1.45	0.91	1.06	0.81	0.85	0.82	0.90	0.99	1.06	0.89	1.01	1.05	0.99
Fe2+	0.38	1.06	0.85	1.04	1.16	1.09	1.10	0.81	0.92	1.09	0.95	0.78	1.05
Mn	0.07	0.06	0.07	0.05	0.06	0.05	0.05	0.06	0.08	0.05	0.06	0.06	0.06
Mg	2.94	2.60	2.79	2.78	2.56	2.76	2.64	2.95	2.67	2.64	2.71	2.94	2.60
Ca	1.59	1.77	1.70	1.80	1.77	1.83	1.81	1.75	1.69	1.76	1.69	1.71	1.73
Na	0.37	0.38	0.40	0.29	0.41	0.29	0.37	0.24	0.43	0.40	0.43	0.30	0.38
K	0.07	0.07	0.07	0.08	0.10	0.07	0.09	0.05	0.07	0.08	0.08	0.05	0.08
OH*	2.00	2.00	2.00	2.00	2.00	2.00	2.00	2.00	2.00	2.00	2.00	2.00	2.00
Total	17.03	17.21	17.17	17.17	17.28	17.19	17.28	17.04	17.19	17.25	17.20	17.06	17.19

Table B2 (cont.): Mineral compositions of Riverie meta-tonalite samples RV-1 and RV-2

	RV1 - Biotites															
	S 3	S 4	S 6	S 7	S 8	S 9	S 10	S 11	S 12	S 13	S 14	S 15	S 16	S 17	S 18	S 19
SiO_2	35.58	35.46	36.00	35.51	35.05	36.36	37.67	36.75	37.17	36.91	37.06	37.47	37.09	37.20	37.21	35.53
TiO_2	2.80	2.59	2.90	2.94	2.88	3.06	2.99	2.92	3.64	3.27	3.42	3.33	3.09	3.48	3.41	2.43
Al_2O_3	14.16	14.40	14.01	14.33	14.34	14.47	14.54	14.79	14.25	14.52	14.18	14.49	14.62	14.46	14.74	15.03
FeO	19.79	19.62	17.39	17.47	18.64	18.18	17.38	17.52	17.42	17.50	17.96	17.64	17.26	17.52	17.51	19.25
MnO	0.17	0.24	0.15	0.18	0.16	0.13	0.23	0.21	0.14	0.15	0.20	0.00	0.00	0.00	0.23	0.24
MgO	11.83	11.92	12.73	13.03	13.56	13.37	13.32	13.60	12.63	12.84	12.99	12.94	12.96	12.79	12.94	13.23
CaO	0.21	0.13	0.00	0.00	0.16	0.13	0.13	0.12	0.00	0.00	0.00	0.00	0.00	0.00	0.00	0.00
Na_2O	0.00	0.19	0.19	0.22	0.00	0.00	0.19	0.23	0.00	0.24	0.27	0.00	0.00	0.00	0.29	0.00
K_2O	7.87	7.67	8.71	7.91	6.61	8.03	9.14	8.30	9.29	9.30	9.16	9.27	9.13	9.25	8.99	7.08
Total	92.40	92.21	92.07	91.60	91.39	93.72	95.61	94.43	94.54	94.74	95.25	95.14	94.16	94.70	95.32	92.79
No. Ox	22	22	22	22	22	22	22	22	22	22	22	22	22	22	22	22
Si	5.59	5.58	5.64	5.57	5.50	5.58	5.67	5.58	5.66	5.62	5.62	5.66	5.66	5.65	5.62	5.51
Al iv	2.41	2.42	2.36	2.43	2.50	2.42	2.33	2.42	2.34	2.38	2.38	2.34	2.34	2.35	2.38	2.49
Al vi	0.21	0.25	0.22	0.22	0.16	0.19	0.24	0.23	0.22	0.23	0.16	0.25	0.29	0.24	0.24	0.26
Ti	0.33	0.31	0.34	0.35	0.34	0.35	0.34	0.33	0.42	0.37	0.39	0.38	0.35	0.40	0.39	0.28
Fe3+	0.00	0.00	0.00	0.00	0.00	0.00	0.00	0.00	0.00	0.00	0.00	0.00	0.00	0.00	0.00	0.00
Fe2+	2.60	2.58	2.28	2.29	2.45	2.33	2.19	2.23	2.22	2.23	2.28	2.23	2.20	2.23	2.21	2.50
Mn	0.02	0.03	0.02	0.02	0.02	0.02	0.03	0.03	0.02	0.02	0.03	0.00	0.00	0.00	0.03	0.03
Mg	2.77	2.80	2.97	3.05	3.18	3.06	2.99	3.08	2.87	2.92	2.94	2.92	2.95	2.90	2.91	3.06
Ca	0.04	0.02	0.00	0.00	0.03	0.02	0.02	0.02	0.00	0.00	0.00	0.00	0.00	0.00	0.00	0.00
Na	0.00	0.06	0.06	0.07	0.00	0.00	0.06	0.07	0.00	0.07	0.08	0.00	0.00	0.00	0.08	0.00
K	1.58	1.54	1.74	1.58	1.32	1.57	1.75	1.61	1.81	1.81	1.77	1.79	1.78	1.79	1.73	1.40
OH*	2.00	2.00	2.00	2.00	2.00	2.00	2.00	2.00	2.00	2.00	2.00	2.00	2.00	2.00	2.00	2.00
Total	19.55	19.58	19.63	19.58	19.49	19.55	19.61	19.59	19.55	19.64	19.64	19.56	19.56	19.55	19.59	19.53

Table B2 (cont.): Mineral compositions of Riverie meta-tonalite samples RV-1 and RV-2

	RV1 - Plagioclase													RV2 - Plagioclase									
	S 1	S 2	S 3	S 4	S 5	S 6	S 7	S 8	S 9	S 10	S 11	S 12	S 13	S 1	S 2	S 3	S 4	S 5	S 6	S 7	S 8	S 9	S 10
SiO_2	61.50	62.43	62.53	62.51	62.21	62.18	62.32	62.12	62.63	62.17	62.16	62.57	62.24	62.12	62.59	62.02	62.54	62.00	61.85	62.23	62.12	62.04	62.48
TiO_2	0.00	0.00	0.00	0.00	0.00	0.00	0.00	0.00	0.00	0.00	0.00	0.00	0.00	0.00	0.00	0.00	0.00	0.00	0.00	0.00	0.00	0.00	0.00
Al_2O_3	23.35	23.75	24.09	23.69	23.69	23.54	24.19	23.71	23.84	24.15	23.98	23.93	23.78	23.23	23.95	23.60	23.70	24.25	24.15	23.72	23.63	23.77	23.40
FeO	0.18	0.00	0.14	0.00	0.14	0.00	0.00	0.14	0.00	0.13	0.00	0.17	0.00	0.00	0.19	0.17	0.17	0.16	0.00	0.22	0.00	0.23	0.00
CaO	5.07	5.38	5.44	5.21	5.35	5.07	5.49	5.18	5.31	5.53	5.33	5.41	5.57	5.28	5.70	5.78	5.58	5.96	5.84	5.64	5.54	5.59	5.65
Na_2O	8.52	8.44	8.54	8.78	8.28	8.64	8.81	8.78	8.70	8.48	8.70	8.96	8.40	8.80	8.79	8.60	8.58	8.59	8.65	8.38	8.78	8.60	8.64
K_2O	0.25	0.23	0.21	0.11	0.25	0.22	0.16	0.19	0.14	0.16	0.22	0.22	0.22	0.15	0.18	0.24	0.22	0.18	0.22	0.32	0.11	0.25	0.30
Total	98.88	100.23	100.94	100.30	99.92	99.65	100.96	100.13	100.63	100.62	100.38	101.27	100.22	99.58	101.40	100.42	100.79	101.14	100.72	100.51	100.17	100.48	100.62
Si	2.76	2.76	2.75	2.76	2.76	2.76	2.74	2.75	2.76	2.74	2.75	2.75	2.75	2.77	2.75	2.75	2.76	2.73	2.73	2.75	2.75	2.75	2.76
Ti	0.00	0.00	0.00	0.00	0.00	0.00	0.00	0.00	0.00	0.00	0.00	0.00	0.00	0.00	0.00	0.00	0.00	0.00	0.00	0.00	0.00	0.00	0.00
Al	1.23	1.24	1.25	1.23	1.24	1.23	1.25	1.24	1.24	1.26	1.25	1.24	1.24	1.22	1.24	1.23	1.23	1.26	1.26	1.24	1.23	1.24	1.22
Fe(ii)	0.01	0.00	0.01	0.00	0.01	0.00	0.00	0.01	0.00	0.00	0.00	0.01	0.00	0.00	0.01	0.01	0.01	0.01	0.00	0.01	0.00	0.01	0.00
Ca	0.24	0.25	0.26	0.25	0.25	0.24	0.26	0.25	0.25	0.26	0.25	0.25	0.26	0.25	0.27	0.27	0.26	0.28	0.28	0.27	0.26	0.27	0.27
Na	0.74	0.72	0.73	0.75	0.71	0.75	0.75	0.75	0.74	0.72	0.75	0.76	0.72	0.76	0.75	0.74	0.73	0.73	0.74	0.72	0.75	0.74	0.74
K	0.01	0.01	0.01	0.01	0.01	0.01	0.01	0.01	0.01	0.01	0.01	0.01	0.01	0.01	0.01	0.01	0.01	0.01	0.01	0.02	0.01	0.01	0.02
Total	5.00	4.99	5.00	5.00	4.98	5.00	5.01	5.01	5.00	5.00	5.01	5.02	4.99	5.01	5.01	5.01	5.00	5.01	5.02	5.00	5.01	5.01	5.01
An	24.39	25.71	25.73	24.52	25.92	24.19	25.40	24.33	25.02	26.24	24.99	24.73	26.47	24.71	26.10	26.74	26.11	27.43	26.85	26.60	25.69	26.07	26.12
Ab	74.16	72.99	73.11	74.85	72.61	74.56	73.73	74.61	74.21	72.85	73.78	74.08	72.28	74.47	72.89	71.94	72.67	71.59	71.93	71.59	73.68	72.52	72.23
Or	1.44	1.29	1.16	0.63	1.47	1.24	0.86	1.06	0.77	0.91	1.23	1.19	1.25	0.82	1.00	1.32	1.22	0.97	1.22	1.81	0.62	1.40	1.65

Table B3: Mineral compositions of Riverie granite sample RV-3

Biotite

	S 2	S 3	S 4	S 5	S 6	S 7	S 8	S 9	S 10	S 11	S 12	S 13	S 14	S 15	S 16	S 17	S 18
SiO_2	36.50	36.53	36.55	36.72	36.70	36.33	35.81	36.37	34.73	35.31	35.81	36.21	36.24	36.13	36.57	35.77	36.34
TiO_2	3.60	3.32	3.22	3.10	3.61	3.15	2.90	2.95	2.94	3.19	3.69	3.14	3.43	3.06	3.18	3.29	3.89
Al_2O_3	14.08	14.25	14.55	14.29	14.18	14.18	14.13	14.53	14.17	13.94	14.51	14.14	14.49	14.26	14.49	14.36	14.27
FeO	17.93	18.73	17.24	18.10	17.63	17.68	19.75	18.59	18.83	18.35	19.37	19.46	19.35	19.43	18.43	18.52	17.90
MnO	0.00	0.00	0.00	0.00	0.00	0.00	0.13	0.00	0.00	0.00	0.00	0.00	0.00	0.00	0.00	0.18	0.14
MgO	11.94	12.00	12.24	12.35	12.29	12.14	11.38	12.32	10.96	11.63	10.79	11.07	10.91	11.23	11.66	11.80	11.44
CaO	0.18	0.00	0.00	0.00	0.00	0.00	0.12	0.00	0.00	0.17	0.00	0.00	0.12	0.00	0.13	0.12	0.00
Na_2O	0.00	0.00	0.00	0.22	0.00	0.00	0.00	0.20	0.21	0.00	0.20	0.00	0.00	0.00	0.00	0.00	0.00
K_2O	8.87	8.76	8.95	8.64	8.85	8.83	8.31	8.43	8.79	8.40	8.63	8.85	8.84	8.71	8.86	8.29	9.10
Total	93.11	93.58	92.75	93.42	93.25	92.32	92.54	93.40	90.65	91.00	92.99	92.87	93.38	92.82	93.32	92.34	93.09
Ox.	22.00	22.00	22.00	22.00	22.00	22.00	22.00	22.00	22.00	22.00	22.00	22.00	22.00	22.00	22.00	22.00	22.00
Si	5.66	5.64	5.66	5.66	5.66	5.67	5.63	5.62	5.58	5.62	5.60	5.67	5.64	5.65	5.66	5.60	5.64
Al iv	2.34	2.36	2.34	2.34	2.34	2.33	2.37	2.38	2.42	2.38	2.40	2.33	2.36	2.35	2.34	2.40	2.36
Al vi	0.23	0.24	0.32	0.26	0.24	0.28	0.25	0.27	0.27	0.23	0.27	0.28	0.29	0.28	0.30	0.25	0.25
Ti	0.42	0.39	0.37	0.36	0.42	0.37	0.34	0.34	0.36	0.38	0.43	0.37	0.40	0.36	0.37	0.39	0.45
Cr	0.00	0.00	0.00	0.00	0.00	0.00	0.00	0.00	0.00	0.00	0.00	0.00	0.00	0.00	0.00	0.00	0.00
Fe	2.32	2.42	2.23	2.33	2.28	2.31	2.60	2.40	2.53	2.44	2.53	2.55	2.52	2.54	2.39	2.42	2.32
Mn	0.00	0.00	0.00	0.00	0.00	0.00	0.02	0.00	0.00	0.00	0.00	0.00	0.00	0.00	0.00	0.02	0.02
Mg	2.76	2.76	2.83	2.84	2.83	2.82	2.67	2.84	2.63	2.76	2.51	2.58	2.53	2.62	2.69	2.75	2.65
Ca	0.03	0.00	0.00	0.00	0.00	0.00	0.02	0.00	0.00	0.03	0.00	0.00	0.02	0.00	0.02	0.02	0.00
Na	0.00	0.00	0.00	0.07	0.00	0.00	0.00	0.06	0.07	0.00	0.06	0.00	0.00	0.00	0.00	0.00	0.00
K	1.75	1.73	1.77	1.70	1.74	1.76	1.67	1.66	1.80	1.71	1.72	1.77	1.75	1.74	1.75	1.66	1.80
OH*	2.00	2.00	2.00	2.00	2.00	2.00	2.00	2.00	2.00	2.00	2.00	2.00	2.00	2.00	2.00	2.00	2.00
Total	19.51	19.54	19.52	19.56	19.50	19.54	19.55	19.57	19.65	19.55	19.53	19.54	19.51	19.54	19.52	19.52	19.50

Plagioclase

	S 2	S 3	S 4	S 5	S 6	S 7	S 8	S 9	S 10	S 11	S 12
SiO_2	62.62	62.59	62.79	62.39	62.41	62.62	62.57	62.71	62.41	62.67	62.59
TiO_2	0.00	0.00	0.00	0.12	0.00	0.00	0.00	0.00	0.00	0.00	0.00
Al_2O_3	23.92	24.05	24.20	23.65	23.94	23.77	24.03	23.88	23.80	23.91	23.70
FeO	0.14	0.00	0.00	0.00	0.00	0.00	0.16	0.00	0.00	0.00	0.00
CaO	5.34	5.40	5.23	5.39	5.23	5.20	5.32	5.29	5.21	5.22	5.19
Na_2O	8.64	8.48	8.38	8.42	8.52	8.39	8.45	8.72	8.75	8.66	8.84
K_2O	0.28	0.17	0.28	0.21	0.24	0.26	0.20	0.26	0.23	0.16	0.19
Total	100.93	100.69	100.87	100.17	100.34	100.24	100.73	100.85	100.40	100.63	100.51
Si	2.75	2.75	2.76	2.76	2.76	2.77	2.75	2.76	2.76	2.76	2.76
Ti	0.00	0.00	0.00	0.00	0.00	0.00	0.00	0.00	0.00	0.00	0.00
Al	1.24	1.25	1.25	1.23	1.25	1.24	1.25	1.24	1.24	1.24	1.23
Fe(ii)	0.01	0.00	0.00	0.00	0.00	0.00	0.01	0.00	0.00	0.00	0.00
Ca	0.25	0.25	0.25	0.26	0.25	0.25	0.25	0.25	0.25	0.25	0.25
Na	0.74	0.72	0.71	0.72	0.73	0.72	0.72	0.74	0.75	0.74	0.76
K	0.02	0.01	0.02	0.01	0.01	0.01	0.01	0.01	0.01	0.01	0.01
Total	5.00	4.99	4.98	4.99	4.99	4.98	4.99	5.00	5.00	4.99	5.01
An	25.06	25.76	25.23	25.81	25.00	25.14	25.50	24.73	24.43	24.78	24.22
Ab	73.36	73.29	73.19	73.02	73.64	73.38	73.35	73.82	74.30	74.33	74.73
Or	1.58	0.96	1.58	1.17	1.36	1.48	1.14	1.45	1.27	0.89	1.05

B.3 Zircon U–Pb isotope measurements

This section presents the analytical procedures and results of U–Pb dating sessions which have not been the subject of publication. The reader can find the analytical notes and comprehensive dataset of published results in the Supplementary materials of the articles (see section A).

B.3.1 Analytical details on the GUF session

Zircon U–Pb isotopic analyses were carried out at Goethe Universität Frankfrut (GUF) by laser ablation using a Resolution M-50 (Resonetics) 193 nm ArF excimer laser system attached to ThermoFinnigan Element 2 sector field ICP–MS. We applied the same methods as in Zeh and Gerdes (2012).

We used a repetition rate of 5.5 Hz, and laser spot-sizes of 20 and 30 μm for measurements of unknowns, and zircon reference materials GJ-1, Plešovice and BB-16. Resulting fluence was ~2.5 to 3 J.cm^{-2}. Sample surface was cleaned directly before each analysis by three pre-ablation pulses. Ablation was performed in a two-volume ablation cell (Laurin Technic, Australia) characterized by a very quick response time (<1 s until maximum signal strength is reached) and wash-out delay (<3 s to get <1% of maximum signal strength). It was fluxed during ablation with carrier gas consisting of a ~0.6 L.min^{-1} He stream, mixed directly after the ablation cell with make-up gas consisting of ~0.07 L.min^{-1} N_2 and 0.68 L.min^{-1} Ar prior introduction into the plasma of the SF–ICP–MS. All gases had a purity of 99.999% and no homogenizer was used while mixing the gases, to prevent smoothing of the signal and thus be able to detect significant variations of the ^{207}Pb/^{206}Pb and ^{238}U/^{206}Pb ratios during measurements, possibly revealing the sequential sampling of different age domains within single zircon grains. Signal was tuned for maximum sensitivity for Pb and U while keeping low the production of oxides (^{254}UO/^{238}U $\leq$ 0.5%). The obtained sensitivity on zircon standard GJ-1 for ^{238}U and a 30 µm spot size is close to 10000 cps.ppm^{-1} at 5.5 Hz and 3 J.cm^{-2}.

Data were acquired using time resolved-peak jumping, the detector being set to analogue mode for ^{232}Th and ^{238}U and counting mode for ^{204}(Hg+Pb), ^{206}Pb, ^{207}Pb and ^{208}Pb. A total of 356 mass scans were acquired over ≈41 s measurement (20 s of background measurement followed by 21 s of sample ablation) and integrated to 89 ratios (4 mass scans per integration, time resolution = 0.46 s). Those ratios were subsequently corrected offline for background signal, common Pb, instrumental mass discrimination and Pb/U fractionation (both laser-induced during individual measurements, and over the day) using an in-house MS Excel® spreadsheet (Gerdes and Zeh, 2006; 2009).

A large number of analyses in our dataset shows moderate to high common Pb (Pb_c) contents. Correcting isotopic compositions from Pb_c is not straightforward for three main reasons. First, there is a clear uncertainty on the age at which Pb_c was incorporated in the zircon structure. This is particularly true for inherited zircon grains (zircon cores, xenocrysts). Indeed, their Pb_c might be as old as the grain itself (incorporated during crystallization) or subsequently added, for instance via interaction with metamorphic fluids. Moreover, considering that the age of Pb_c incorporation is given by the ^{206}Pb/^{238}U date does not account for the potential effect of Pb loss and resulting discordance which are likely to occur in polymetamorphic environments such as the Variscan FMC. Such a guestimate is not satisfactory as it might result in artificially young concordant ^{206}Pb/^{238}U dates. Finally, the Pb_c correction itself reduces the precision of the analytical data because of: (i) the use of a *model* Pb_c composition (Stacey and Kramers, 1975); (ii) the interference at mass 204 between ^{204}Hg (originating from the gas carrier) and ^{204}Pb leading to a larger uncertainty on the Pb_c-corrected ^{207}Pb/^{206}Pb ratios. As a consequence of this, inherently discordant Pb_c-corrected analyses would be labelled concordant because of their large error ellipse that would overlap with the Concordia curve.

Aware of all the above-mentioned caveats and in an attempt to hamper the yield of meaningless, Pb_c-corrected concordant dates, we decided to restrict the use of a Pb_c correction to zircons grains: (i) extracted from granite samples, for which a late Carboniferous to early Permian intrusion age can be expected given the regional geological context (see Laurent et al., 2017 and references therein), (ii) showing $^{206}Pb/^{238}U$ dates close to that of concordant, Pb_c-free zircon from the same sample. The methodology applied is as follows.

For each ratio of an individual measurement, ^{204}Pb was estimated by subtracting the average background signal on mass 204, which mostly results from ^{204}Hg in the carrier gas (≈500 cps), to the measured intensity. Composition of common Pb (i.e. $^{206}Pb/^{204}Pb$ and $^{207}Pb/^{204}Pb$ ratios) was determined using a model Pb composition (Stacey and Kramers, 1975) at the age of 305 Ma. The inter-elemental fractionation $^{206}Pb/^{238}U$ during the 21 s of sample ablation was corrected for each analysis by applying a linear regression through all measured ratios, excluding the outliers ($\pm 2\sigma$), and considering that the intercept with the y-axis represents the "true" ratio. Elemental fractionation over the analytical session, as well as instrumental mass discrimination, were corrected by normalization to the $^{206}Pb/^{238}U$ (0.0982) and $^{207}Pb/^{206}Pb$ (0.061) ratios of reference zircon GJ-1 (Jackson et al., 2004), using standard bracketing. Elemental concentrations in U and Pb were calculated using raw signal (in cps) of ^{238}U and ^{206}Pb for each spot, corrected from the analytical drift over the session (monitored using GJ-1), normalized to the recommended values of the GJ-1 zircon standard (U = 280.1 ppm; Pb = 25.5 ppm) and applying a spot size-dependent correction. Th/U ratio was determined for each spot using the mass fractionation-corrected $^{232}Th/^{238}U$ ratio, normalized to the recommended value of the GJ-1 zircon standard (Th/U = 0.0296).

Data from secondary standards were processed as unknowns to check the accuracy of the corrections (Fig. B.1). Our results are within error of the recommended TIMS values for the standard zircon BB-16 (weighted mean $^{206}Pb/^{238}U = 560 \pm 0.8$ Ma; Santos et al., in press). For Plešovice, our in-situ measurements outline two statistically distinct Concordia ages of c. 343 and c. 336 Ma (see Fig. B.1), the latter being identical within error to the TIMS weighted mean $^{206}Pb/^{238}U$ age of 337.13 ± 0.37 Ma reported by Sláma et al. (2008a). The c. 343 Ma-old population may reflect the presence of older, inherited zircon domains within the Plešovice grains.

The quoted uncertainties for each individual analysis are (i) for the $^{206}Pb/^{238}U$ ratio, the quadratic addition of the within-run precision (2σ) with the external reproducibility of standard zircon GJ-1 during the corresponding analytical session (0.5 to 1.5%, 2σ); and (ii) for the $^{207}Pb/^{206}Pb$ ratio, a ^{207}Pb signal-dependent uncertainty propagation, as described by Gerdes and Zeh (2009). The $^{207}Pb/^{235}U$ ratio was calculated using the $^{206}Pb/^{238}U$ and $^{207}Pb/^{206}Pb$ ratios and assuming a natural $^{238}U/^{235}U$ of 137.88, and its uncertainty was obtained by quadratic addition of propagated errors on both ratios. Age calculations and data plotting were performed using the Isoplot/Ex v.4.15 (Ludwig, 2008) for MS Excel®.

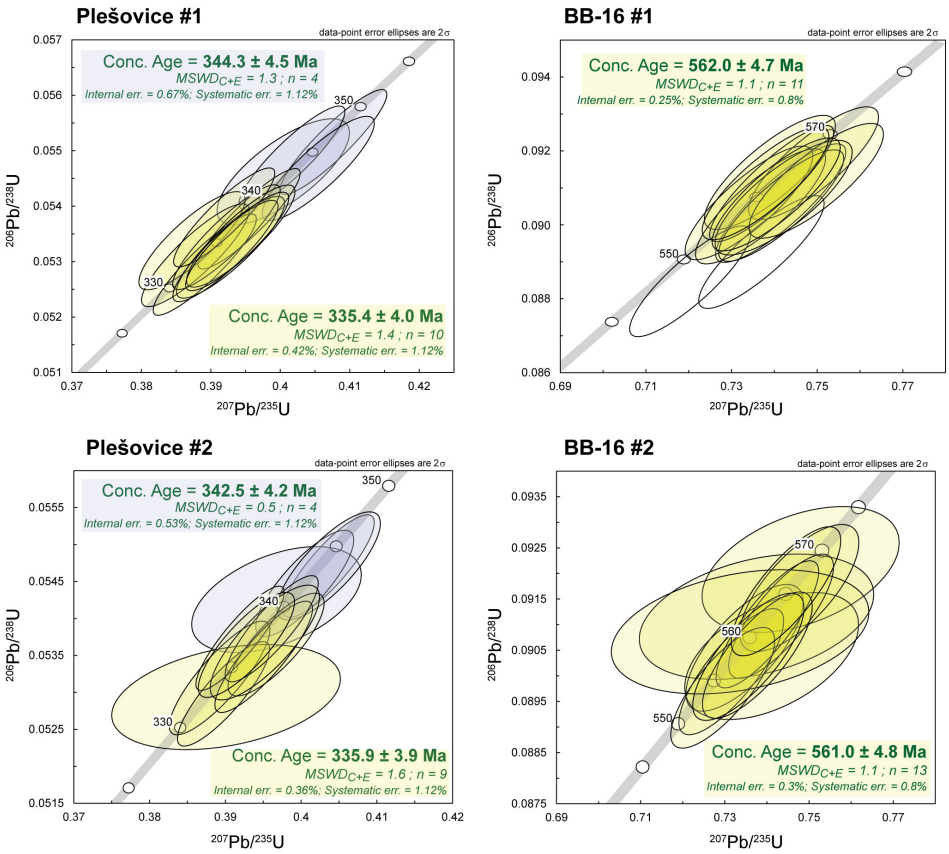

Figure B.1: Wetherill diagrams (^{206}Pb/^{238}U vs. ^{207}Pb/^{235}U) for secondary zircon standards Plešovice and BB-16 analysed during the two analytical sessions conducted at GUF. Error ellipses and ages are displayed at 2σ level of uncertainty. Yellow and blue ellipses are those considered for Concordia age calculations.

B.3.2 Analytical details on the SUN session

U-Pb data were obtained at the Central Analytical Facility, Stellenbosch University, and were acquired by laser ablation – single collector – magnetic sector field – inductively coupled plasma–mass spectrometry (LA–SF–ICP–MS) employing a Thermo Finnigan Element 2 mass spectrometer coupled to a Resonetics Resolution S155 excimer laser ablation system. The methods employed for analysis are described in detail by Frei and Gerdes (2009). Data processing was performed using an in-house MS Excel® spreadsheet (Gerdes and Zeh, 2006). The GJ-1 zircon reference material (Jackson et al., 2004) was used as primary standard. For quality control, the 91500 (Wiedenbeck et al., 1995; 2004), Temora (Black et al., 2003; 2004) and Plešovice (Sláma et al., 2008a) zircon reference materials were analysed, and the results were in agreement with the published ID–TIMS ages (Fig. B.2). The calculation of dates, as well as plotting of Tera-Wasserburg diagram were performed using Isoplot/Ex v.4.15 (Ludwig, 2008) for MS Excel®.

B.3.3 Analytical details on the ETH session

Zircon U–Pb isotopic analyses were carried out at ETH Zürich, Switzerland by laser ablation – inductively coupled plasma – sector field – mass spectrometry (LA–ICP–SF–MS) using a RESOlution M-50 (Resonetics/ASI) 193 nm ArF excimer laser system attached to a ThermoFinnigan Element XR mass spectrometer.

We used a laser repetition rate of 5 Hz, a spot size of 20 or 30 μm and a laser output energy of 80 to 100 mJ, corresponding to an energy density on sample of *c.* 2.0 to 2.5

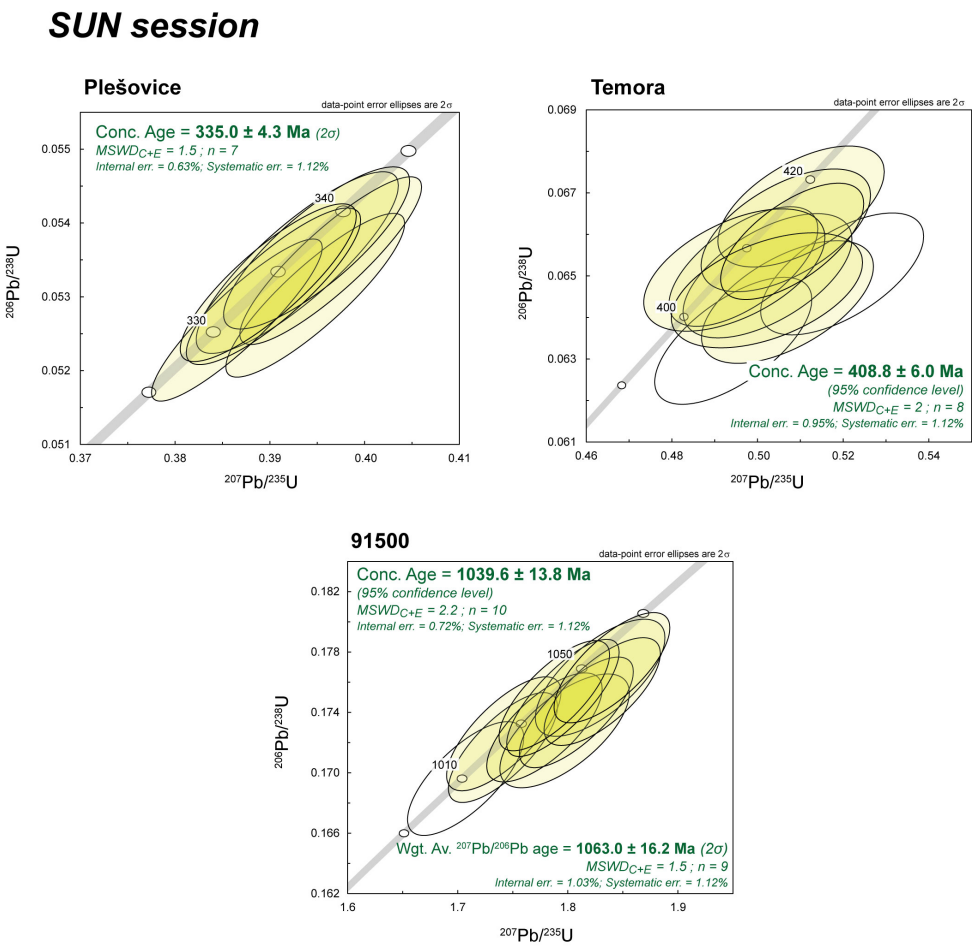

Figure B.2: Wetherill diagrams (^{206}Pb/^{238}U vs. ^{207}Pb/^{235}U) for secondary zircon standards Plešovice, Temora and 91500 analysed during the analytical sessions conducted at SUN. Error ellipses and ages are displayed at 2σ level of uncertainty. Yellow ellipses are those considered for Concordia age calculations.

J.cm^{-2}. The sample surface was cleaned immediately before each analysis by three pre-ablation pulses. Ablation was performed in a Laurin Technic S-155 dual-volume ablation cell fluxed with carrier gas consisting of *c.* 0.7 L.min^{-1} He (5.0 grade), mixed directly after the ablation cell with sample gas consisting of *c.* 1 L.min^{-1} Ar (6.0 grade) prior to introduction into the plasma of the ICP–SF–MS. We used Ni X-cones specifically dedicated to zircon U–Pb geochronology. The signal was tuned for maximum sensitivity for Th and U while keeping low the production of oxides (the resulting ^{248}ThO^{+}/^{232}Th^{+} ratio was $\leq$0.25%). The obtained sensitivities on zircon reference material GJ-1 for ^{238}U and ^{232}Th were 7000 to 9000 cps.ppm^{-1} at 30 μm spot size, 5 Hz and *c.* 2 J.cm^{-2}. The intensities for the following isotopes were acquired using time resolved-peak jumping (between brackets are the dwell times in ms) and triple detector mode: ^{202}Hg (10), ^{204}(Hg+Pb) (20), ^{206}Pb (100), ^{207}Pb (100), ^{208}Pb (10), ^{232}Th (10), ^{235}U (10), ^{238}U (20) (total sweep time of 0.29 s). A total of 165 mass scans were acquired over *c.* 50 s measurement (20 s of background measurement followed by 30 s of sample ablation).

The resulting intensities were subsequently processed offline with the Igor Pro Iolite v2.5 software (Hellstrom et al., 2008), using the VizualAge data reduction scheme (Petrus and Kamber, 2012). Background-subtracted intensities were used to calculate isotope ratios, which were corrected for downhole Pb/U and Pb/Th fractionation (after Paton et al., 2010), instrumental mass discrimination and drift through the analytical session by standard bracketing against zircon reference material GJ-1 (using isotope ratios recommended by Horstwood et al., 2016). No common Pb correction was carried

out. Elemental concentrations in U, Th and Pb were calculated using average intensities (in cps) of ^{238}U, ^{232}Th and ^{208}Pb for each spot and sensitivities calculated from the GJ-1 zircon standard, after correction of sensitivity drift over the session. The quoted uncertainties for each individual analysis correspond to the internal (2 S.E.) statistical error and propagated uncertainty based on the scatter of the primary reference material (see Paton et al., 2010).

Data from secondary zircon reference materials were processed as unknowns to check the accuracy of the corrections (Fig. B.3 and B.4. The obtained U-Pb dates are close to the reference ages determined by TIMS for the zircon reference materials Plešovice (Sláma et al., 2008a), 91500 (Wiedenbeck et al., 1995; 2004) and Temora (Black et al., 2003). Age calculations and data plotting were performed using the Isoplot toolkit (Ludwig, 2008) v.4.15 for MS Excel®.

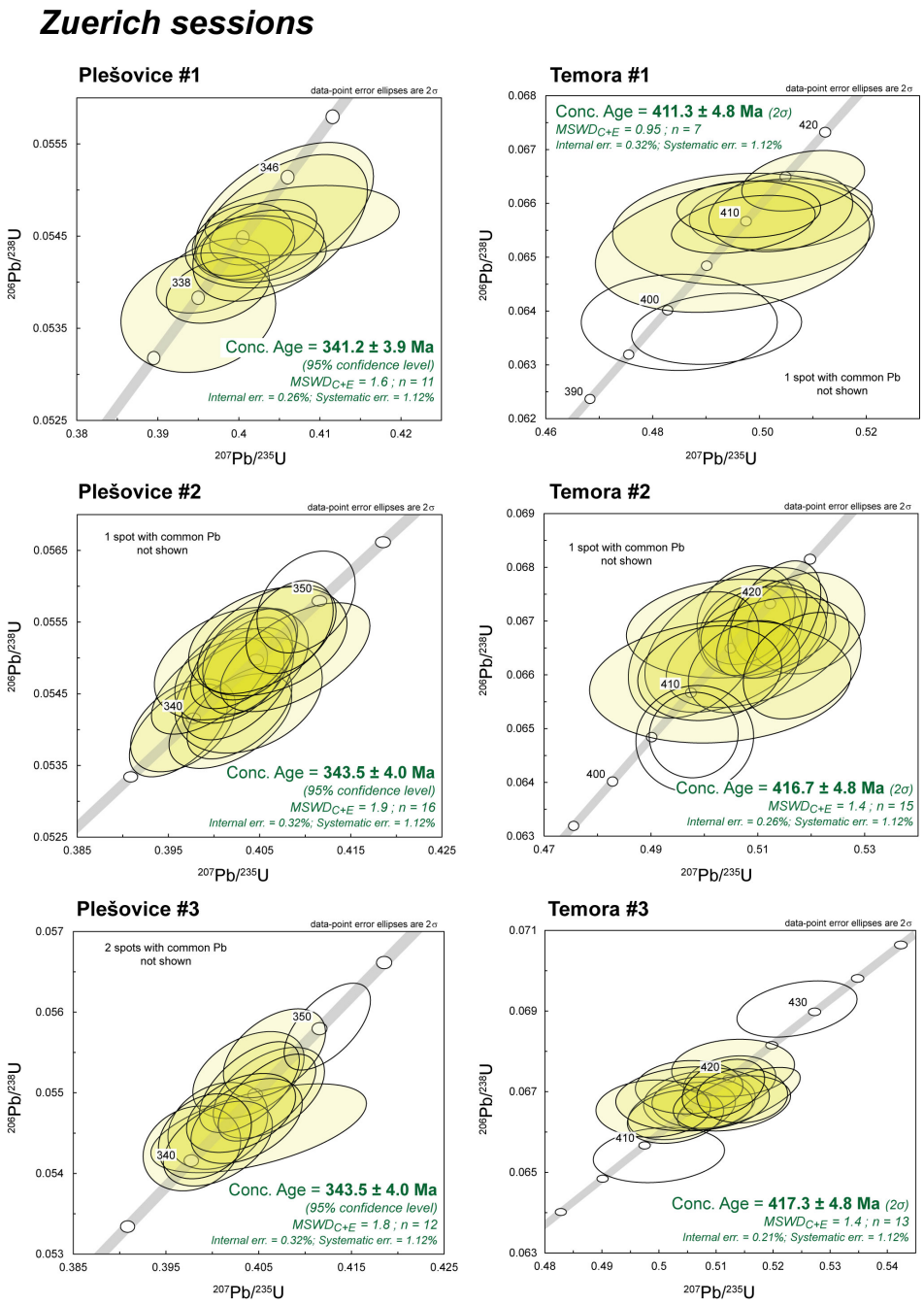

Figure B.3: Wetherill diagrams ($^{206}Pb/^{238}U$ vs. $^{207}Pb/^{235}U$) for secondary zircon standards Plešovice and Temora analysed during the three analytical sessions at ETH Zuerich. Error ellipses and ages are displayed at 2σ level of uncertainty. Yellow ellipses are those considered for Concordia age calculations.

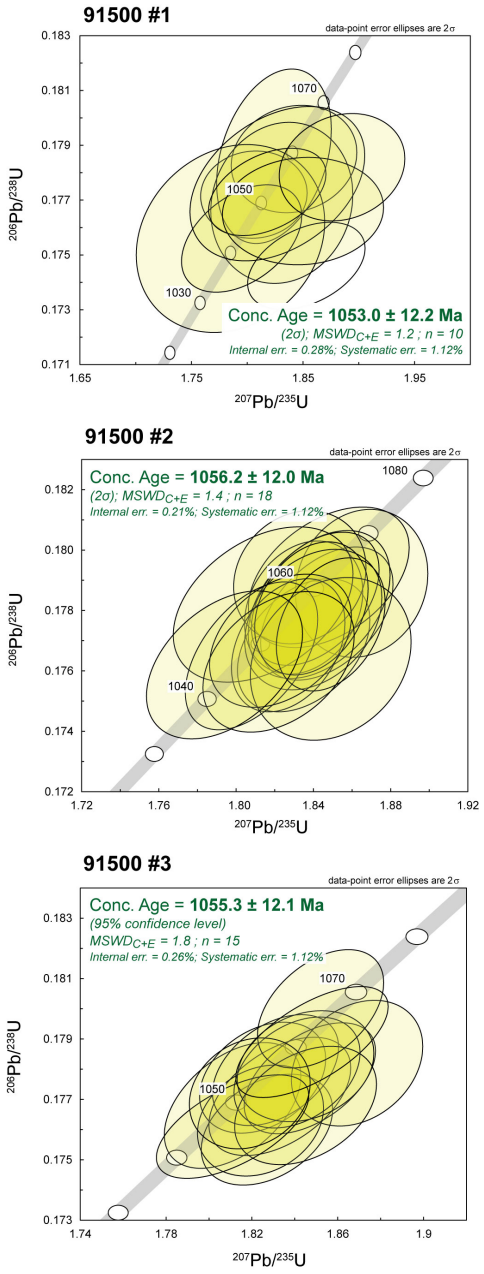

Figure B.4: Wetherill diagrams (^{206}Pb/^{238}U vs. ^{207}Pb/^{235}U) for secondary zircon standard 91500 analysed during the three analytical sessions at ETH Zuerich. Error ellipses and ages are displayed at 2σ level of uncertainty. Yellow ellipses are those considered for Concordia age calculations.

B.3.4 Zircon U–Pb results of Chapter 6

Orthogneisses

CHA-15-35 Forty-two measurements were conducted on 30 zircon grains. Eight analyses revealed high estimated common Pb contents (>1.2%) and will not be examined further because the calculated discordant dates can be interpreted as a combination of Pb loss and incorporation of Pb_c without any possibility to discriminate between both. Seventeen zircon spots are discordant (concordance <93%) with $^{206}Pb/^{238}U$ dates ranging from 469 ± 7 Ma (a163) to 589 ± 8 Ma and $^{207}Pb/^{206}Pb$ dates from 547 ± 20 Ma (a192) to 736 ± 38 Ma (a144). Estimated common Pb concentrations in the spotted zircon domains are low to moderate (up to 0.9%). Seventeen measurements performed on zircon rims and core-free grains yielded concordant $^{206}Pb/^{238}U$ dates out of which eleven are statistically equivalent and allow calculation of a Concordia date of 544.1 ± 4.9 Ma (MSWD of concordance+equivalence=0.79). Three analyses conducted on two zircon cores and one zircon rim yielded older $^{206}Pb/^{238}U$ dates of 559 ± 8 (a161 and a166) and 570 ± 8 Ma (a190), respectively. Three spots drilled on zircon rims and core-free grains gave younger$^{206}Pb/^{238}U$ dates than the main population ranging from 532 ± 8 Ma (a178) to 528 ± 7 Ma (a184) but all three are nearly discordant.

CHA-15-52 Twenty-eight spots were drilled on 23 grains. Five analyses showed substantial amounts of Pb_c (>1.2%) and were not considered further. Two analyses of zircon cores yielded slightly discordant (concordance: c. 92%) $^{207}Pb/^{206}Pb$ dates of 2481 ± 8 Ma (a73) and 2486 ± 7 Ma (a83). Two measurements yielded identical concordant $^{206}Pb/^{238}U$ dates of 702 ± 12 Ma (a79, homogeneous grain) and 701 ± 10 Ma (a60, core). One measurement performed on a zircon rim (a72) has a moderate Pb_c content (c. 0.8%) and a discordant (concordance: 69%) $^{207}Pb/^{206}Pb$ date of 787 ± 32 Ma. The 18 remaining analyses displayed negligible to low estimated Pb_c concentrations (<0.4%). Ten spots drilled on a core and a rim gave concordant $^{206}Pb/^{238}U$ dates of 573 ± 9 Ma (a82) and 572 ± 10 Ma (a58). Eight measurements performed on cores, rims and homogeneous grains yielded statistically equivalent $^{206}Pb/^{238}U$ dates out of which a Concordia date of 544.4 ± 5.2 Ma ($MSWD_{C+E}$=0.9) can be calculated. The eight last spots are all discordant with $^{207}Pb/^{206}Pb$ dates ranging from 585 ± 22 Ma (a85) down to 547 ± 23 Ma (a87).

Granites

CHA-15-24 Thirty spots were drilled on 26 zircons grains which often appear homogeneous in CL-images and seldom show core-rim relationships. Sixteen spots are markedly discordant and have large amounts of common Pb (often >3%). Two spots with negligible amounts of Pb_c yielded discordant $^{207}Pb/^{206}Pb$ dates of 753 ± 30 (a346, homogenous zircon) and 772 ± 20 (a345, zircon core) Ma respectively. Two more discordant (concordance: c. 40%) analyses performed on homogeneous zircons showed moderate amounts of Pb_c (from 0.6 to 1.2%) and yielded $^{207}Pb/^{206}Pb$ dates of 615 ± 32 (a317) and 579 ± 30 Ma (a355). Five measurements conducted on a zircon core, three rims and an homogeneous zircon yielded similar $^{206}Pb/^{238}U$ dates ranging from 560 ± 8 Ma (a359) down to 537 ± 10 Ma (a326). Two analyses conducted on homogeneous zircon grains show concordant $^{206}Pb/^{238}U$ dates of 515 ± 8 (a322) and 332 ± 5 Ma (a336) respectively. Finally, a zircon rim and a homogeneous zircon, both devoid of Pb_c produced equivalent $^{206}Pb/^{238}U$ dates of 308 ± 5 (a335) and 305 ± 5 (a343) Ma respectively. Common-lead corrected (see introductory section for the method) rim analysis a344 shows a similar $^{206}Pb/^{238}U$ date of 304 ± 5 Ma. A Concordia date of 305.8 ± 4.4 Ma can be calculated out of these 3 measurements with a MSWD of concordance+equivalence equal to 1.5.

CHA-15-49 Eleven analyses were performed on 9 grains. Zircon from this sample are almost always homogeneous and very few cores can be observed. The proportion of grains with high aspect ratios (>5) is higher than in other samples. Three measurements display very high estimated Pb_c contents (>7%) and are markedly discordant. They will not be considered further. Four analyses gave concordant $^{206}Pb/^{238}U$ dates: 776 ± 10 Ma (core, a453), 815 ± 9 Ma (homogeneous grain, a457), 360 ± 5 Ma (homogeneous grain, a444) and 305 ± 4 Ma (homogeneous grain, a434). The four remaining spots yielded discordant results. Two rims have $^{206}Pb/^{238}U$ dates of c. 600 Ma, one core a $^{206}Pb/^{238}U$ date of c. 500 Ma and a homogeneous grain a $^{207}Pb/^{206}Pb$ date of 1934 ± 8 Ma.

CHA-15-41 Forty-two spots were drilled on 34 zircon grains. Most grains are core-free and display narrow oscillatory zoning patterns in CL but some have broader alternating bands (up to 10 μm large). Few grains with clear core-rim relationships are also present in the investigated collection. Five analyses have high Pb_c contents (>1.4%) and will not be considered further. One measurement performed on a core-free zircon yielded a concordant $^{206}Pb/^{238}U$ date of 1008 ± 13 Ma (a48). Seventeen spots drilled on zircon rims, cores and core-free crystals show low to moderate amounts of Pb_c (mostly <0.6% but sometimes up to 1.1%) and are discordant (concordance <94%). Their $^{207}Pb/^{206}Pb$ dates range from 484 ± 76 Ma (a29) to 850 ± 37 Ma (a17). Thirteen measurements on zircon rims and core-free grains display concordant $^{206}Pb/^{238}U$ dates between 542 ± 7 Ma (a45) and 652 ± 10 Ma (a40). One spot on a homogeneous grain (a25) gives a younger concordant $^{206}Pb/^{238}U$ date of 429 ± 7 Ma. Five analyses yielded $^{206}Pb/^{238}U$ dates of c. 300 Ma and a Pb_c correction was applied to 4 of them. The five are statistically equivalent and a Concordia date of 304.0 ± 3.9 Ma can be calculated ($MSWD_{C+E}$=1.4).

CHA-15-25 Twenty analyses were conducted on 17 grains, all but one from the first population at GUF. Forty-two spots were drilled at ETH on 32 grains. Both datasets will be described concomitantly (see discussion on their equivalence in the introductory section). Spot names will be referred to as faXX and zaYY for those performed at GUF and ETH, respectively. Twenty-nine measurements are highly discordant (concordance <58%) and will not be discussed further. Fourteen spots yielded concordant $^{206}Pb/^{238}U$ dates ranging from 592 ± 5 Ma (za27) down to 520 ± 6 Ma (fa412). Seventeen analyses gave similar yet discordant $^{206}Pb/^{238}U$ dates, from 563 ± 3 Ma (za42) down to 514 ± 4 Ma (za36). Finally, one measurement performed on a zircon core yielded an older concordant $^{206}Pb/^{238}U$ date of 910 ± 10 Ma (fa422).

CHA-15-19 Twenty-two analyses were performed on 22 grains. They all display characteristic oscillatory zoning on CL images and are almost always devoid of inherited cores. Nine spots revealed substantial amounts of Pb_c (>1%) in the zircon structure and will not be described and interpreted further. Seven analyses performed on homogeneous zircon and zircon rims with low Pb_c contents (<0.7%) are discordant (concordance: 54–93%). Five have $^{206}Pb/^{238}U$ dates ranging from 321 ± 5 (a406) down to 256 ± 5 Ma (a408) and $^{207}Pb/^{206}Pb$ dates ranging from 540 ± 65 (a412) down to 365 ± 33 Ma (a421). One spot drilled on zircon rim (a411) yielded a $^{207}Pb/^{206}Pb$ date of 559 ± 15 Ma and another one (a415) an older $^{207}Pb/^{206}Pb$ date of 598 ± 23 Ma. Amongst the concordant spots, analysis a403 show a $^{206}Pb/^{238}U$ date of 316 ± 4 Ma. The five remaining are statistically equivalent and allow the calculation of a Concordia date of 305.3 ± 3.9 Ma ($MSWD_{C+E}$=0.6).

CHA-15-33 Fifty-three analyses were conducted on 44 grains. Zircon are notably small in this sample (often <100 μm in length). Oscillatory zoning was almost always observed together with frequent core–rim relationships. Twelve analyses are markedly

discordant, show elevated Pb_c contents (often >3%) and will not be discussed further. Twelve measurements performed on homogeneous grains, rims and cores gave concordant $^{206}Pb/^{238}U$ dates ranging from 621 ± 7 (a317) down to 476 ± 5 Ma (a351) with a cluster at c. 540 Ma. One spot yielded an older concordant $^{206}Pb/^{238}U$ date of 968 ± 11 Ma. Twenty analyses are discordant (concordance: 52–93%) and show a wide range of $^{206}Pb/^{238}U$ dates between 733 ± 8 (a366) and 345 ± 4 Ma (a393). Six common lead corrected analyses, performed on 5 zircon rims and a homogeneous grain are statistically equivalent and a Concordia date of 302.2 ± 3.7 Ma ($MSWD_{C+E}$=1.6) can be calculated out of them. Two spots also performed on zircon rims yielded younger $^{206}Pb/^{238}U$ dates of 293 ± 4 (a327) and 276 ± 4 Ma (a382) but are both discordant, even after the Pc_c correction applied to spot a327.

CHA-15-34 Thirty-eight spots were drilled on 28 grains. Spot a110 (core-free grain) revealed very high Pb_c contents (>3.1%) and will not be considered further. Seven analyses show moderate to elevated concentrations in Pb_c (from 0.7 to 1.4%) and are all discordant with $^{207}Pb/^{206}Pb$ dates ranging from 961 ± 48 Ma (a91) to 578 ± 37 Ma (a127) and $^{206}Pb/^{238}U$ dates from 392 ± 6 Ma (a109) to 531 ± 7 Ma (a98). One analysis of a zircon rim (a130) is slightly discordant (concordance = 93%) and has a $^{207}Pb/^{206}Pb$ date of 1948 ± 7 Ma. Measurements performed on zircon core a100 yielded a subconcordant $^{206}Pb/^{238}U$ date of 778 ± 11 Ma. Spot a120 is discordant (concordance = 84%) and has a $^{207}Pb/^{206}Pb$ date of 964 ± 18 Ma.

CHA-15-51 Thirty-four spots were drilled on 26 grains. All zircon grains display oscillatory zoning and some core–rim relationships have been observed. Fifteen measurements yielded discordant $^{206}Pb/^{238}U$ dates (concordance: 7–73%), feature moderate to very high common Pb contents (from 0.3 up to 20%) and will not be discussed further. Eight analyses performed on homogeneous grains, a core and a rim are concordant and show $^{206}Pb/^{238}U$ dates ranging from 570 ± 6 (a273) down to 524 ± 7 Ma (a275). Seven measurements gave discordant (concordance: 77–92%) $^{206}Pb/^{238}U$ dates in the same range from 550 ± 7 Ma (a302) down to 508 ± 6 Ma (a308). One spot performed on a zircon core (a296) is discordant, shows an older $^{206}Pb/^{238}U$ date of 651 ± 7 Ma and a $^{207}Pb/^{206}Pb$ date of 791 ± 26 Ma.

BOR-16-01 Forty-six spots were drilled on cores, rims and homogeneous grains. Ten analyses are markedly discordant (concordance < 44%) and will not be considered further. Twelve concordant measurements yielded $^{206}Pb/^{238}U$ dates identical within error and a statistically acceptable Concordia date of 309.7 ± 3.6 Ma can be calculated out of them ($MSWD_{C+E}$=1.09). Nine additional measurements show similar yet discordant $^{206}Pb/^{238}U$ dates and define a trend between common and radiogenic Pb compositions. This trend intercepts the Concordia curve at 309.5 ± 3.6 Ma. Seven analyses yielded older concordant $^{206}Pb/^{238}U$ dates ranging from 549 ± 6 Ma down to 316 ± 2 Ma. One spot gave a younger concordant $^{206}Pb/^{238}U$ date of 297 ± 2 Ma. The rest of the data is discordant.

ROC-16-01 Thirty-eight measurements are notably discordant (concordance < 37%) and will not be further commented on. Three concordant spots performed on cores show Proterozoic $^{206}Pb/^{238}U$ dates ranging from 877 ± 6 Ma to 643 ± 9 Ma. One grain domain has a discordant $^{207}Pb/^{206}Pb$ date of 3437 ± 90 Ma. Twenty-three measurements trend along a mixing line between radiogenic and common Pb composition, with a lower intercept at 320.3 ± 3.7 Ma. Considering only the concordant analyses belonging to the trend, a Concordia date of 319.8 ± 3.8 Ma ($MSWD_{C+E}$=1.5) can be calculated. Two measurements yielded younger $^{206}Pb/^{238}U$ dates of 312 ± 2 (a8) and 304 ± 2 Ma (a71), respectively. The rest of the data is discordant.

Migmatites

CHA-15-43 (in-source leucosome) Out of the 27 analyses, 3 are highly discordant (concordance <20%) and will not be examined further. Eleven measurements performed on core-free grains and zircon rims yielded discordant $^{206}Pb/^{238}U$ dates ranging from 555 ± 8 (a259) down to 406 ± 4 Ma (a232). The 13 remaining spots showed concordant results.

CHA-15-63 A total of 30 analyses were conducted on 28 zircons. Most of the zircons do not show core-rim relationships. Thirteen spots have elevated Pb_c contents (from 1.5 to 11.2%) and notably discordant dates (mostly between 15 and 60% concordance), they won't be considered further. So will the overconcordant spot a279 be. Eight analyses performed on zircon rims and core-free grains showed low to moderate Pb_c contents (<0.7%) and yielded discordant $^{207}Pb/^{206}Pb$ dates (concordance <94%) ranging from 768 ± 70 Ma (a309) to 567 ± 15 Ma (a310). One spot has a younger $^{207}Pb/^{206}Pb$ date of 538 ± 32 Ma. Core-free grains, cores and rims all gave $^{206}Pb/^{238}U$ dates between 590 ± 7 (a266) and 535 ± 6 Ma (a243) with a clear cluster in the period 550–540 Ma.

CHA-15-47 Twenty-five spots were drilled on 23 zircons grains. Zircons usually show core-rim relationships (most often dark cores surrounded by righter rims) buts some grains are core-free. Nine analyzed zircon domains contained substantial amount of Pbc (>1.2%, up to 24%) and won't be described further. Six analyses of zircon rims and core-free zircons are discordant (60% < concordance < 92%) and have low Pb_c contents (below detection limit to 0.4%). $^{207}Pb/^{206}Pb$ dates show two clusters: (i) between 572 ± 16 Ma (a457) and 599 ± 23 Ma (a483); (ii) between 759 ± 41 Ma (a479) and 769 ± 42 Ma (a470). Two spots yielded concordant $^{206}Pb/^{238}U$ dates of 561 ± 8 Ma (rim a461) and 575 ± 8 Ma (spot a475, core-free zircon). Ten Concordant spots yielded $^{206}Pb/^{238}U$ dates clustering between 575 ± 8 (a475) and 540 ± 8 Ma (a458).

CHA-15-48 Sixty-six analyses were performed on 56 zircon grains. Twenty-four measurements performed on zircons with our without core-rim relationships yielded $^{206}Pb/^{238}U$ dates between 589 ± 8 Ma and 415 ± 8 Ma but revealed significant amounts of common Pb (> 0.6%) resulting in a marked discordance (concordance < 68%). Only the 13 analyses with less than 2% Pb_c will be further considered together with the 42 ones with Pb_c < 0.6%. Two zircon cores have discordant late Archean to early Paleoproterozoic $^{207}Pb/^{206}Pb$ dates of respectively 2519 ± 6 Ma (a248) and 2437 ± 29 Ma (a223). One spot (a219) yielded a discordant $^{207}Pb/^{206}Pb$ date of 1973 ± 16 Ma. Four spots performed on zircon cores devoid of common Pb yielded concordant to sub-concordant $^{206}Pb/^{238}U$ dates between 623 ± 9 Ma (a227) and 575 ± 9 Ma (a274). Five analyses conducted on core-free zircons and zircon rims yielded concordant 238U/206Pb dates ranging from 559 ± 9 Ma (a214) to 574 ± 8 Ma (a218). Twenty-five measurements performed on cores, rims or core-free grains are discordant (concordance <93%). Among them, 12 have low Pb_c contents (<0.5%), show concordance between 75% and 93% and $^{207}Pb/^{206}Pb$ dates between 559 ± 18 Ma (a265) and 657 ± 27 Ma (a235). The 13 remaining have Pbc >0.5% with concordance mostly between 55% and 68% and older $^{207}Pb/^{206}Pb$ dates. Eighteen analyses yielded concordant $^{206}Pb/^{238}U$ dates ranging from 551 ± 7 Ma (a276) to 518 ± 8 Ma (a224).

CHA-15-17 Twenty-one spots were drilled on 21 grains, only on zircon rims and core-free crystals apart from spot a423 which corresponds to a core. Five analyses bear substantial amounts of Pb_c (>1.1%) and will not be further discussed. Eleven analyses are discordant (concordance: 76 to 93%), show subordinate to moderate amounts of Pb_c (below detection limit to 0.9%) out of which 10 $^{206}Pb/^{238}U$ dates between 548 ± 8 Ma (a429) and 510 ± 7 Ma (a432) and $^{207}Pb/^{206}Pb$ dates ranging from 569 ± 20 Ma

(a424) to 693 ± 19 Ma (a450). Spot a452 has younger $^{206}Pb/^{238}U$ and $^{207}Pb/^{206}Pb$ dates of respectively 332 ± 5 Ma and 432 ± 31 Ma. Four core-free crystals have identical concordant $^{206}Pb/^{238}U$ dates of 539–538 ± 7–8 Ma. One zircon core yielded an older date of 562 ± 9 Ma (a423).

CHA-15-65L Twenty-first spots were drilled on 18 zircons grains. Not a single concordant measurement was obtained for this sample. All zircon domains showed very high common Pb content and are highly discordant (concordance <23%). The 3 least discordant analyses (conc.: 67–93%) have $^{206}Pb/^{238}U$ dates between 547 ± 8 (a388) and 511 ± 9 Ma (a374).

CHA-15-65M A total of 85 measurements were performed, out of which 33 were markedly discordant and not considered further. Two zircon cores have discordant $^{207}Pb/^{206}Pb$ dates of 1557 ± 21 Ma (conc.: 95%, a525) and 1773 ± 12 Ma (conc.: 82%, a509). Nineteen other spots were discordant. Those performed on zircon cores show a range of $^{206}Pb/^{238}U$ dates spanning between 853 ± 12 (a529) and 566 ± 10 Ma (a584). Discordant rims and core-free grains have younger $^{206}Pb/^{238}U$ dates, from 565 ± 8 (a513) down to 505 ± 8 Ma (a484). A range of cores, rims and core-free grains yielded concordant $^{206}Pb/^{238}U$ dates between 974 ± 14 (a490) and 542 ± 8 Ma (a493) once again clustering around 555–545 Ma.

B.3.5 Data tables

In the following are reported the measurements of zircon standards for each session:

- Table B4: Results of LA–ICP–MS U–Pb analyses of zircon standards performed during the sessions at GUF, 2nd and 3rd of May, 2016;
- Table B5: Results of LA–ICP–MS U–Pb analyses of zircon standards performed during the session at SUN, 26th of October, 2016;
- Table B6: Results of LA–ICP–MS U–Pb analyses of zircon standards performed during the sessions at ETH Zürich, 12 to 14th of February, 2017.

Analyses of zircon grains from investigated samples can be found in the following tables:

- Table B7: Results of LA–ICP–MS zircon U–Pb analyses performed during the sessions at GUF, 2nd and 3rd of May, 2016;
- Table B8: Results of LA–ICP–MS zircon U–Pb analyses performed during the session at SUN, 26th of October, 2016;
- Table B9: Results of LA–ICP–MS zircon U–Pb analyses performed during the sessions at ETH Zürich, 12 to 14th of February, 2017.

Table B3: Results of LA-ICP-MS U–Pb analyses of zircon standards performed during the sessions at GUF, 2nd and 3rd of May, 2016

grain	^{207}Pb[a] (cps)	U[b] (ppm)	Pb[b] (ppm)	Th[b]/U	^{206}Pbc[c] (%)	$^{206}Pb/^{238}U$[d]	±2σ (%)	$^{207}Pb/^{235}U$[d]	±2σ (%)	$^{207}Pb/^{206}Pb$[d]	±2σ (%)	rho[e]	$^{206}Pb/^{238}U$	±2σ (Ma)	$^{207}Pb/^{235}U$	±2σ (Ma)	$^{207}Pb/^{206}Pb$	±2σ (Ma)	conc.[f] (%)
Seq.1																			
Pleso-01	35868	16433	854	0.18	0.07	0.05462	1.4	0.4004	1.9	0.05317	1.3	0.74	343	5	342	6	336	30	102
Pleso-02	36752	17580	922	0.18	0.01	0.05516	1.4	0.4077	1.5	0.05360	0.6	0.91	346	5	347	5	354	15	98
Pleso-03	32918	16568	864	0.18	0.00	0.05488	1.4	0.4017	1.6	0.05309	0.7	0.89	344	5	343	5	333	16	104
Pleso-04	32844	17053	867	0.18	b.d.	0.05344	1.4	0.3922	1.6	0.05323	0.7	0.90	336	5	336	5	339	16	99
Pleso-05	32105	17287	884	0.18	b.d.	0.05380	1.4	0.3919	1.5	0.05284	0.7	0.89	338	4	336	4	322	16	105
Pleso-06	29247	15678	818	0.19	b.d.	0.05468	1.4	0.4055	1.6	0.05378	0.8	0.87	343	5	346	5	362	18	95
Pleso-07	28914	16278	834	0.19	0.00	0.05377	1.4	0.3955	1.5	0.05335	0.6	0.91	338	5	338	4	344	15	98
Pleso-08	27534	16446	835	0.18	0.00	0.05338	1.4	0.3873	1.6	0.05263	0.9	0.84	335	4	332	5	313	20	107
Pleso-09	27940	16927	856	0.18	0.00	0.05311	1.4	0.3878	1.6	0.05295	0.8	0.87	334	5	333	5	327	18	102
Pleso-10	28760	17792	897	0.18	b.d.	0.05295	1.4	0.3891	1.6	0.05330	0.7	0.90	333	5	334	4	342	15	97
Pleso-11	27316	17250	875	0.18	0.00	0.05326	1.4	0.3928	1.6	0.05350	0.8	0.87	334	5	336	5	350	18	96
Pleso-12	27316	17248	878	0.18	0.00	0.05346	1.4	0.3943	1.6	0.05350	0.8	0.87	336	5	338	5	350	18	96
Pleso-13	24378	15912	806	0.18	b.d.	0.05319	1.4	0.3921	1.6	0.05347	0.7	0.89	334	5	336	5	349	16	96
Pleso-14	27660	17529	891	0.18	0.00	0.05337	1.4	0.3938	1.5	0.05352	0.7	0.88	335	4	337	4	351	16	96
BB16-1	21488	5433	486	0.31	b.d.	0.09059	1.4	0.7415	1.7	0.05937	0.8	0.86	559	8	563	7	581	18	96
BB16-2	18605	5106	450	0.32	0.02	0.08926	1.4	0.7370	1.6	0.05988	0.8	0.86	551	7	561	7	599	18	92
BB16-3	15540	5166	464	0.31	0.00	0.09142	1.4	0.7390	1.7	0.05863	1.0	0.81	564	7	562	7	553	21	102
BB16-4	14731	5471	491	0.28	0.01	0.09167	1.4	0.7492	1.7	0.05927	0.9	0.82	565	7	568	7	577	21	98
BB16-5	19335	5004	447	0.32	0.10	0.09059	1.4	0.7341	1.7	0.05877	0.9	0.83	559	7	559	7	559	20	100
BB16-6	19147	5239	457	0.31	0.02	0.08847	1.4	0.7204	1.6	0.05905	0.8	0.86	546	7	551	7	569	18	96
BB16-7	17506	5087	454	0.32	0.02	0.09050	1.4	0.7368	1.7	0.05905	0.9	0.83	558	8	561	7	569	20	98
BB16-8	18202	5608	502	0.30	0.11	0.09112	1.4	0.7394	1.6	0.05885	0.8	0.88	562	8	562	7	562	17	100
BB16-9	17249	5210	465	0.32	0.00	0.09052	1.4	0.7416	1.6	0.05942	0.9	0.85	559	7	563	7	583	19	96
BB16-10	16662	5166	465	0.32	0.00	0.09119	1.4	0.7498	1.7	0.05963	1.0	0.81	563	8	568	7	590	22	95
BB16-11	15400	5189	464	0.31	0.00	0.09074	1.4	0.7422	1.8	0.05932	1.1	0.79	560	7	564	8	579	23	97
BB16-12	15617	5202	466	0.32	b.d.	0.09082	1.4	0.7404	1.7	0.05913	0.9	0.83	560	7	563	7	572	20	98
BB16-13	12574	4289	385	0.31	b.d.	0.09112	1.4	0.7380	1.6	0.05874	0.9	0.83	562	7	561	7	557	20	101
Seq.2																			
Pleso-01	41966	21077	1096	0.18	0.14	0.05471	1.0	0.4036	1.2	0.05351	0.6	0.85	343	3	344	4	350	15	98
Pleso-02	40803	18094	947	0.20	0.71	0.05426	1.1	0.3968	2.3	0.05304	2.0	0.47	341	4	339	7	330	46	103
Pleso-03	36733	19273	985	0.19	0.10	0.05373	1.1	0.3919	1.2	0.05290	0.6	0.88	337	4	336	3	325	13	104
Pleso-04	37351	19504	1010	0.20	0.14	0.05448	1.1	0.4005	1.3	0.05332	0.8	0.82	342	4	342	4	342	17	100
Pleso-05	35210	18668	954	0.20	b.d.	0.05364	1.1	0.3928	1.3	0.05311	0.8	0.82	337	4	336	4	333	17	101
Pleso-06	34759	18762	977	0.20	0.19	0.05471	1.1	0.4036	1.4	0.05351	0.8	0.79	343	4	344	4	350	19	98
Pleso-07	34602	19160	982	0.20	b.d.	0.05386	1.1	0.3961	1.3	0.05334	0.6	0.86	338	4	339	4	343	15	99
Pleso-08	32719	18352	930	0.20	b.d.	0.05319	1.2	0.3892	1.4	0.05307	0.7	0.85	334	4	334	4	332	17	101
Pleso-09	33495	18896	953	0.20	b.d.	0.05298	1.1	0.3898	1.3	0.05336	0.7	0.85	333	4	334	4	344	15	97
Pleso-10	30845	17070	874	0.21	b.d.	0.05365	1.1	0.3967	1.3	0.05363	0.8	0.81	337	3	339	4	356	17	95
Pleso-11	27316	17055	801	0.20	0.00	0.04931	1.1	0.3640	1.4	0.05354	0.8	0.82	310	3	315	4	352	18	88
Pleso-12	29334	16937	867	0.21	0.26	0.05367	1.2	0.3952	1.5	0.05340	0.9	0.79	337	4	338	4	346	21	97
Pleso-13	35935	17731	911	0.20	1.65	0.05294	1.1	0.3901	3.2	0.05345	3.0	0.35	333	4	334	9	348	67	96
Pleso-14	33275	19651	1001	0.20	b.d.	0.05348	1.2	0.3951	1.3	0.05358	0.7	0.86	336	4	338	4	353	15	95
BB16-1	22924	5769	524	0.34	0.07	0.09208	1.1	0.7480	2.6	0.05892	2.3	0.43	568	6	567	11	564	50	101
BB16-2	19468	5318	478	0.35	0.29	0.09116	1.1	0.7375	3.1	0.05868	2.9	0.36	562	6	561	13	555	63	101
BB16-3	17271	5089	455	0.35	0.18	0.09055	1.1	0.7347	1.5	0.05884	1.1	0.72	559	6	559	7	561	23	100

Table B3 (cont.): Results of LA-ICP-MS U–Pb analyses of zircon standards performed during the sessions at GUF, 2nd and 3rd of May, 2016

grain	^{207}Pb[a] (cps)	U[b] (ppm)	Pb[b] (ppm)	Th[b]/U	^{206}Pbc[c] (%)	$^{206}Pb/^{238}U$[d]	±2σ (%)	$^{207}Pb/^{235}U$[d]	±2σ (%)	$^{207}Pb/^{206}Pb$[d]	±2σ (%)	rho[e]	$^{206}Pb/^{238}U$	±2σ (Ma)	$^{207}Pb/^{235}U$	±2σ (Ma)	$^{207}Pb/^{206}Pb$	±2σ (Ma)	conc.[f] (%)
Seq.2																			
BB16-4	18041	5421	492	0.45	b.d.	0.09039	1.1	0.7411	2.3	0.05947	2.0	0.49	558	6	563	10	584	43	95
BB16-5	20108	5355	485	0.35	b.d.	0.09172	1.1	0.7477	1.5	0.05912	1.1	0.72	566	6	567	7	572	23	99
BB16-6	20313	5574	501	0.34	b.d.	0.09116	1.1	0.7434	1.4	0.05914	0.8	0.79	562	6	564	6	572	18	98
BB16-7	20668	5886	523	0.35	0.15	0.09008	1.1	0.7315	1.4	0.05890	0.8	0.80	556	6	557	6	563	18	99
BB16-8	19610	5637	506	0.35	0.01	0.09101	1.1	0.7401	1.3	0.05898	0.8	0.83	561	6	562	6	566	16	99
BB16-9	19025	5573	494	0.35	0.18	0.08977	1.1	0.7295	1.4	0.05894	0.9	0.78	554	6	556	6	565	19	98
BB16-10	19577	5695	510	0.36	0.40	0.09086	1.1	0.7336	3.4	0.05856	3.2	0.32	561	6	559	15	551	70	102
BB16-11	18476	5593	498	0.35	b.d.	0.09040	1.1	0.7377	1.4	0.05918	0.9	0.77	558	6	561	6	574	20	97
BB16-12	18840	5670	506	0.36	0.16	0.09037	1.1	0.7356	1.5	0.05903	0.9	0.76	558	6	560	6	568	21	98
BB16-13	18033	5700	515	0.35	b.d.	0.09165	1.1	0.7445	1.4	0.05891	0.9	0.79	565	6	565	6	564	19	100

Spot size = 30µm; depth of crater ~20µm. $^{206}Pb/^{238}U$ error is the quadratic additions of the within run precision (2 SE) and the external reproducibility (2 SD) of the reference zircon.

$^{207}Pb/^{206}Pb$ error propagation (^{207}Pb signal dependent) following Gerdes & Zeh (2009). $^{207}Pb/^{235}U$ error is the quadratic addition of the $^{207}Pb/^{206}Pb$ and $^{206}Pb/^{238}U$ uncertainty.

[a]Within run background-corrected mean ^{207}Pb signal in cps (counts per second).

[b] U and Pb content and Th/U ratio were calculated relative to GJ-1 reference zircon.

[c] percentage of the common Pb on the ^{206}Pb. b.d. = below dectection limit.

[d] corrected for background, within-run Pb/U fractionation (in case of $^{206}Pb/^{238}U$) and subsequently normalised to GJ-1 (ID-TIMS value/measured value);

$^{207}Pb/^{235}U$ calculated using $^{207}Pb/^{206}Pb/(^{238}U/^{206}Pb*1/137.88)$

[e] rho is the $^{206}Pb/^{238}U/^{207}Pb/^{235}U$ error correlation coefficient.

[f] degree of concordance = $^{206}Pb/^{238}U$ age / $^{207}Pb/^{206}Pb$ age x 100

Table B4: Results of LA-ICP-MS U–Pb analyses of zircon standards performed during the sessions at SUN, 26th of October, 2016

grain	^{207}Pb[a] (cps)	U[b] (ppm)	Pb[b] (ppm)	Th[b]/U	$^{207}Pb/^{235}U$[c]	±2σ (%)	$^{206}Pb/^{238}U$[c]	±2σ (%)	rho[d]	$^{207}Pb/^{206}Pb$	±2σ (%)	$^{206}Pb/^{238}U$	±2σ (Ma)	$^{207}Pb/^{235}U$	±2σ (Ma)	$^{207}Pb/^{206}Pb$	±2σ (Ma)	conc.[e] (%)
Pleso-01	17897	10779	544	0.10	0.3929	2.2	0.05346	1.9	0.85	0.05330	1.2	336	6	336	6	342	27	98
Pleso-02	22796	14328	727	0.13	0.3948	2.0	0.05302	1.7	0.88	0.05400	0.9	333	6	338	6	371	21	90
Pleso-03	24306	15222	780	0.14	0.3964	2.0	0.05349	1.7	0.88	0.05375	0.9	336	6	339	6	361	21	93
Pleso-04	22114	14300	721	0.14	0.3865	1.9	0.05269	1.7	0.89	0.05321	0.9	331	5	332	5	338	19	98
Pleso-05	25249	16424	844	0.14	0.3949	2.0	0.05366	1.7	0.82	0.05338	1.2	337	5	338	6	345	26	98
Pleso-06	23618	16106	819	0.14	0.3904	1.9	0.05314	1.6	0.85	0.05328	1.0	334	5	335	6	341	23	98
Pleso-07	25368	17175	874	0.14	0.3898	1.9	0.05319	1.6	0.84	0.05315	1.0	334	5	334	6	335	24	100
91500-1	6452	865	155	0.33	1.7418	2.4	0.17258	1.8	0.73	0.07320	1.7	1026	17	1024	16	1019	34	101
91500-2	6473	883	155	0.33	1.7072	2.5	0.16962	1.8	0.72	0.07300	1.8	1010	17	1011	16	1014	36	100
91500-3	6637	896	164	0.33	1.8293	2.6	0.17629	1.8	0.68	0.07526	1.9	1047	17	1056	17	1075	39	97
91500-4	6844	933	168	0.34	1.8077	2.3	0.17400	1.7	0.74	0.07535	1.6	1034	16	1048	15	1078	32	96
91500-5	6813	926	166	0.34	1.7970	2.7	0.17278	1.8	0.67	0.07543	2.0	1027	17	1044	18	1080	40	95
91500-6	6839	969	174	0.33	1.7787	2.4	0.17301	1.7	0.71	0.07457	1.7	1029	16	1038	16	1057	34	97
91500-7	7476	1055	192	0.34	1.8312	2.4	0.17538	1.7	0.71	0.07573	1.7	1042	16	1057	16	1088	33	96
91500-8	7139	1043	188	0.32	1.7955	2.3	0.17496	1.8	0.78	0.07443	1.5	1039	17	1044	15	1053	29	99
91500-9	7268	1064	193	0.33	1.7877	2.3	0.17510	1.7	0.74	0.07404	1.5	1040	16	1041	15	1043	31	100
91500-10	7359	1066	195	0.33	1.8400	2.3	0.17696	1.7	0.72	0.07541	1.6	1050	16	1060	15	1080	32	97
91500-11	7148	1070	189	0.33	1.7410	2.3	0.17167	1.7	0.74	0.07355	1.6	1021	16	1024	15	1029	31	99
Temora2-1	2248	1059	73	0.46	0.5070	3.2	0.06437	1.9	0.58	0.05712	2.6	402	7	416	11	496	58	81
Temora2-2	2736	1269	89	0.47	0.5198	3.0	0.06505	1.8	0.62	0.05795	2.4	406	7	425	10	528	52	77
Temora2-3	3193	1587	107	0.44	0.4943	3.0	0.06344	2.0	0.65	0.05652	2.3	396	8	408	10	473	51	84
Temora2-4	2900	1432	99	0.46	0.5023	3.2	0.06500	1.9	0.59	0.05605	2.6	406	7	413	11	454	58	89
Temora2-5	3020	1548	107	0.45	0.4967	2.9	0.06523	1.8	0.63	0.05523	2.2	407	7	409	10	422	50	97
Temora2-6	3007	1535	109	0.45	0.5102	3.1	0.06667	1.8	0.57	0.05550	2.5	416	7	419	11	432	57	96
Temora2-7	3425	1814	126	0.44	0.5066	3.2	0.06610	1.8	0.57	0.05559	2.6	413	7	416	11	436	58	95
Temora2-8	3267	1776	122	0.43	0.4946	3.5	0.06514	1.8	0.53	0.05506	3.0	407	7	408	12	415	66	98
Temora2-9	3162	1629	111	0.42	0.5022	3.6	0.06465	1.7	0.48	0.05633	3.2	404	7	413	12	466	70	87
Temora2-10	3470	1859	129	0.43	0.5081	2.7	0.06583	1.7	0.65	0.05598	2.0	411	7	417	9	451	45	91

Spot size = 30µm; depth of crater ~20µm. $^{206}Pb/^{238}U$ error is the quadratic additions of the within run precision (2 SE) and the external reproducibility (2 SD) of the reference zircon. $^{207}Pb/^{206}Pb$ error propagation (^{207}Pb signal dependent) following Gerdes & Zeh (2009). $^{207}Pb/^{235}U$ error is the quadratic addition of the $^{207}Pb/^{206}Pb$ and $^{206}Pb/^{238}U$ uncertainty.

[a] Within run background-corrected mean ^{207}Pb signal in cps (counts per second).

[b] U and Pb content and Th/U ratio were calculated relative to GJ-1 reference zircon.

[c] corrected for background, within-run Pb/U fractionation (in case of $^{206}Pb/^{238}U$) and subsequently normalised to GJ-1 (ID-TIMS value/measured value);

$^{207}Pb/^{235}U$ calculated using $^{207}Pb/^{206}Pb/(^{238}U/^{206}Pb*1/137.88)$

[d] rho is the $^{206}Pb/^{238}U/^{207}Pb/^{235}U$ error correlation coefficient.

[e] degree of concordance = $^{206}Pb/^{238}U$ age / $^{207}Pb/^{206}Pb$ age x 100

Table B5: Results of LA-ICP-MS U–Pb analyses of zircon standards performed during the sessions at ETH Zürich, 12 to 14th of February, 2017

grain	^{207}Pb[a] (cps)	U[b] (ppm)	Pb[b] (ppm)	Th[b]/U	$^{207}Pb/^{235}U$[c]	±2σ (abs)	$^{206}Pb/^{238}U$[c]	±2σ (abs)	rho[d]	$^{207}Pb/^{206}Pb$[c]	±2σ (abs)	$^{206}Pb/^{238}U$	±2σ (Ma)	$^{207}Pb/^{235}U$	±2σ (Ma)	$^{207}Pb/^{206}Pb$	±2σ (Ma)	conc.[e] (%)
Seq.1																		
Z_Plesovice_1	7570	1047	495	0.12	0.4056	0.0090	0.05477	0.00061	0.51	0.05383	0.00089	344	4	346	7	370	40	93
Z_Plesovice_2	9080	1154	778	0.16	0.3968	0.0057	0.05407	0.00033	0.41	0.05350	0.00069	339	2	339	4	351	28	97
Z_Plesovice_3	4350	578	238	0.10	0.4078	0.0098	0.05467	0.00031	0.24	0.05430	0.00130	343	2	347	7	379	52	91
Z_Plesovice_4	7600	880	644	0.15	0.4030	0.0054	0.05454	0.00029	0.37	0.05335	0.00063	342	2	344	4	344	27	100
Z_Plesovice_5	7110	842	494	0.13	0.4008	0.0050	0.05436	0.00027	0.26	0.05321	0.00062	341	2	342	4	338	27	101
Z_Plesovice_6	6980	962	403	0.11	0.3950	0.0078	0.05367	0.00053	0.15	0.05350	0.00120	337	3	338	6	347	50	97
Z_Plesovice_7	5090	605	267	0.11	0.3974	0.0052	0.05391	0.00029	0.33	0.05351	0.00066	339	2	340	4	350	27	97
Z_Plesovice_8	7710	903	730	0.17	0.4005	0.0051	0.05446	0.00032	0.27	0.05351	0.00064	342	2	342	4	354	27	97
Z_Plesovice_9	5260	624	294	0.11	0.4021	0.0071	0.05433	0.00032	0.07	0.05368	0.00095	341	2	343	5	355	39	96
Z_Plesovice_10	8510	1097	709	0.15	0.4029	0.0062	0.05439	0.00032	0.23	0.05394	0.00080	341	2	344	4	365	34	94
Z_Plesovice_11	8570	1187	661	0.14	0.4051	0.0088	0.05459	0.00065	0.51	0.05400	0.00110	343	4	345	6	368	46	93
Z_Temora2_1	1293	120	361	0.56	0.5040	0.0140	0.06580	0.00054	0.16	0.05590	0.00160	411	3	416	10	439	63	94
Z_Temora2_2	1206	118	203	0.34	0.4920	0.0130	0.06367	0.00054	0.19	0.05610	0.00140	398	3	407	9	442	58	90
Z_Temora2_3	1389	159	248	0.36	0.4970	0.0200	0.06552	0.00085	0.09	0.05440	0.00210	409	5	409	13	395	80	104
Z_Temora2_4	772	83	110	0.28	0.4950	0.0210	0.06520	0.00100	0.26	0.05530	0.00230	407	6	408	14	405	91	101
Z_Temora2_5	1081	102	214	0.40	0.5040	0.0110	0.06585	0.00061	0.21	0.05570	0.00130	412	4	414	8	437	53	94
Z_Temora2_6	1125	105	337	0.57	0.5330	0.0200	0.06199	0.00072	0.12	0.06230	0.00240	388	4	434	13	661	80	59
Z_Temora2_7	961	97	284	0.57	0.4850	0.0150	0.06379	0.00073	0.00	0.05490	0.00180	399	4	400	10	400	73	100
Z_Temora2_8	2720	273	800	0.57	0.5082	0.0094	0.06642	0.00046	0.33	0.05516	0.00094	415	3	417	6	425	39	98
Z_Temora2_9	2410	234	699	0.57	0.4970	0.0110	0.06561	0.00044	0.35	0.05520	0.00120	410	3	410	8	409	48	100
Z_Temora2_10	2150	202	608	0.54	0.4980	0.0110	0.06589	0.00043	0.05	0.05480	0.00120	411	3	411	7	403	48	102
Z_91500_1	1862	50	212	0.34	1.8420	0.0460	0.17850	0.00160	0.12	0.07450	0.00190	1059	9	1059	17	1044	53	101
Z_91500_2	2096	53	298	0.41	1.8060	0.0390	0.17720	0.00130	0.04	0.07390	0.00160	1052	7	1046	14	1028	43	102
Z_91500_3	2051	50	300	0.40	1.8240	0.0420	0.17860	0.00260	0.31	0.07370	0.00180	1059	14	1053	15	1031	50	103
Z_91500_4	2629	77	383	0.39	1.8310	0.0520	0.17690	0.00240	0.10	0.07460	0.00200	1050	13	1055	19	1076	55	98
Z_91500_5	2500	82	356	0.40	1.7850	0.0690	0.17560	0.00280	0.18	0.07450	0.00290	1043	15	1039	25	1068	83	98
Z_91500_6	2272	65	325	0.39	1.7950	0.0440	0.17560	0.00160	0.43	0.07390	0.00170	1043	9	1047	16	1036	44	101
Z_91500_7	2499	76	353	0.40	1.8270	0.0640	0.17760	0.00230	0.37	0.07500	0.00240	1054	13	1058	21	1073	62	98
Z_91500_8	2121	58	285	0.38	1.8180	0.0430	0.17730	0.00130	0.41	0.07450	0.00160	1052	7	1052	16	1052	42	100
Z_91500_9	1944	50	268	0.36	1.8530	0.0430	0.17460	0.00130	0.40	0.07680	0.00160	1037	7	1063	15	1106	42	94
Z_91500_10	1896	50	233	0.35	1.8500	0.0590	0.17660	0.00160	0.07	0.07520	0.00250	1048	9	1064	21	1089	62	96
Z_91500_11	1579	41	180	0.32	1.8850	0.0460	0.17820	0.00160	0.16	0.07740	0.00190	1057	9	1075	17	1123	49	94
Seq.2																		
Z_Plesovice_1	11870	561	263	0.10	0.4058	0.0062	0.05526	0.00062	0.51	0.05312	0.00064	347	4	346	5	344	26	101
Z_Plesovice_2	11710	555	280	0.11	0.4019	0.0069	0.05492	0.00064	0.37	0.05292	0.00076	345	4	343	5	329	35	105
Z_Plesovice_3	12070	595	277	0.11	0.4101	0.0044	0.05578	0.00058	0.35	0.05333	0.00046	350	4	349	3	345	19	101
Z_Plesovice_4	11510	534	265	0.11	0.4089	0.0067	0.05501	0.00062	0.57	0.05384	0.00066	345	4	348	5	367	26	94
Z_Plesovice_5	12190	611	286	0.11	0.4083	0.0039	0.05543	0.00053	0.35	0.05352	0.00043	348	3	348	3	351	18	99
Z_Plesovice_6	11590	551	266	0.11	0.4026	0.0050	0.05464	0.00064	0.49	0.05334	0.00059	343	4	344	4	341	25	101
Z_Plesovice_7	11250	526	260	0.10	0.4059	0.0071	0.05523	0.00062	0.33	0.05324	0.00077	347	4	346	5	337	33	103
Z_Plesovice_8	12200	585	283	0.11	0.4033	0.0048	0.05499	0.00057	0.55	0.05333	0.00044	345	4	344	4	341	19	101
Z_Plesovice_9	12230	612	282	0.11	0.4037	0.0040	0.05489	0.00055	0.43	0.05335	0.00043	345	3	344	3	344	19	100
Z_Plesovice_10	12190	609	281	0.11	0.4039	0.0042	0.05505	0.00052	0.36	0.05337	0.00044	345	3	344	3	345	19	100
Z_Plesovice_11	11270	542	267	0.11	0.4028	0.0047	0.05424	0.00053	0.54	0.05387	0.00045	341	3	344	3	364	19	94
Z_Plesovice_12	11940	580	292	0.11	0.4017	0.0049	0.05475	0.00054	0.35	0.05308	0.00050	344	3	343	4	330	21	104
Z_Plesovice_13	12570	647	297	0.11	0.3995	0.0052	0.05461	0.00055	0.62	0.05317	0.00054	343	3	341	4	340	23	101

grain	^{207}Pb[a] (cps)	U[b] (ppm)	Pb[b] (ppm)	Th[b] / U	^{207}Pb[c] / ^{235}U	±2σ (abs)	^{206}Pb[c] / ^{238}U	±2σ (abs)	rho[d]	^{207}Pb[c] / ^{206}Pb	±2σ (abs)	^{206}Pb / ^{238}U	±2σ (Ma)	^{207}Pb / ^{235}U	±2σ (Ma)	^{207}Pb / ^{206}Pb	±2σ (Ma)	conc.[e] (%)
Seq.2																		
Z_Plesovice_14	12080	577	344	0.10	0.4241	0.0053	0.05442	0.00053	0.55	0.05676	0.00050	342	3	359	4	482	19	71
Z_Plesovice_15	12550	695	299	0.10	0.4038	0.0066	0.05448	0.00066	0.29	0.05390	0.00100	342	4	344	5	361	44	95
Z_Plesovice_16	11920	623	273	0.10	0.3966	0.0047	0.05406	0.00053	0.43	0.05320	0.00050	339	3	339	3	335	21	101
Z_Plesovice_17	11570	583	277	0.10	0.3961	0.0044	0.05399	0.00053	0.55	0.05326	0.00045	339	3	339	3	342	19	99
Z_Plesovice_18	12550	635	290	0.11	0.4018	0.0055	0.05412	0.00054	0.50	0.05410	0.00058	340	3	343	4	373	24	91
Z_Temora2_1	8170	329	1273	0.73	0.5116	0.0055	0.06696	0.00065	0.11	0.05541	0.00056	418	4	420	4	427	23	98
Z_Temora2_2	3755	154	252	0.34	0.5078	0.0075	0.06711	0.00075	0.23	0.05478	0.00071	419	5	418	5	410	29	102
Z_Temora2_3	8030	320	1051	0.60	0.5075	0.0070	0.06682	0.00068	0.21	0.05483	0.00069	417	4	417	5	404	28	103
Z_Temora2_4	4261	158	354	0.40	0.5190	0.0090	0.06696	0.00077	0.17	0.05592	0.00098	418	5	425	6	457	39	91
Z_Temora2_5	5210	230	734	0.63	0.5060	0.0140	0.06665	0.00110	0.46	0.05540	0.00140	416	6	416	10	423	54	98
Z_Temora2_6	2155	81	248	0.56	0.5050	0.0160	0.06686	0.00075	0.14	0.05510	0.00170	417	5	415	11	436	70	96
Z_Temora2_7	2850	98	324	0.54	0.6540	0.0260	0.06728	0.00100	0.32	0.07030	0.00260	420	6	510	16	942	83	45
Z_Temora2_8	3837	156	467	0.57	0.4980	0.0068	0.06488	0.00065	0.03	0.05551	0.00070	405	4	411	4	437	30	93
Z_Temora2_9	2730	105	259	0.42	0.5111	0.0096	0.06679	0.00070	0.18	0.05580	0.00100	417	4	420	6	441	40	95
Z_Temora2_10	3064	113	327	0.53	0.5100	0.0140	0.06642	0.00084	0.43	0.05640	0.00150	415	5	419	9	462	58	90
Z_Temora2_11	4049	176	479	0.54	0.4980	0.0100	0.06637	0.00096	0.35	0.05500	0.00120	414	6	411	7	408	48	102
Z_Temora2_12	12350	509	1428	0.55	0.5131	0.0071	0.06703	0.00089	0.45	0.05555	0.00065	418	5	420	5	432	26	97
Z_Temora2_13	14130	563	1694	0.56	0.5107	0.0069	0.06688	0.00073	0.58	0.05497	0.00050	417	4	419	5	410	21	102
Z_Temora2_14	2365	96	195	0.36	0.5074	0.0085	0.06615	0.00070	0.32	0.05592	0.00084	413	4	417	6	452	33	91
Z_Temora2_15	1538	67	157	0.43	0.5030	0.0200	0.06587	0.00093	0.14	0.05530	0.00210	411	6	413	13	406	84	101
Z_Temora2_16	4750	183	732	0.71	0.4982	0.0090	0.06481	0.00081	0.05	0.05540	0.00110	405	5	410	6	421	46	96
Z_Temora2_17	2140	85	173	0.36	0.5010	0.0110	0.06603	0.00072	0.16	0.05520	0.00120	412	4	412	7	413	48	100
Z_Temora2_18	3900	144	265	0.31	0.5183	0.0090	0.06617	0.00081	0.32	0.05687	0.00097	413	5	424	6	488	37	85
Z_91500_1	7220	75	458	0.41	1.8650	0.0280	0.17890	0.00200	0.13	0.07560	0.00110	1061	11	1068	10	1081	30	98
Z_91500_2	6960	75	435	0.41	1.8350	0.0280	0.17685	0.00180	0.38	0.07520	0.00092	1050	10	1057	10	1073	25	98
Z_91500_3	7450	82	465	0.41	1.8470	0.0280	0.17790	0.00180	0.44	0.07554	0.00094	1055	10	1064	10	1080	25	98
Z_91500_4	7810	91	491	0.41	1.8480	0.0340	0.17910	0.00190	0.42	0.07470	0.00100	1062	10	1064	12	1060	28	100
Z_91500_5	7410	82	472	0.41	1.8350	0.0250	0.17810	0.00180	0.24	0.07480	0.00093	1056	10	1057	9	1060	25	100
Z_91500_6	7560	84	464	0.41	1.8430	0.0300	0.17820	0.00200	0.40	0.07520	0.00110	1057	11	1062	11	1070	30	99
Z_91500_7	7470	85	468	0.41	1.8330	0.0280	0.17910	0.00180	0.14	0.07450	0.00110	1062	10	1057	10	1057	27	100
Z_91500_8	7170	77	456	0.41	1.8410	0.0270	0.17839	0.00180	0.43	0.07478	0.00091	1058	10	1060	10	1062	24	100
Z_91500_9	6190	65	411	0.42	1.8140	0.0380	0.17820	0.00210	0.39	0.07350	0.00110	1057	12	1050	14	1025	31	103
Z_91500_10	7410	86	457	0.41	1.8400	0.0290	0.17770	0.00190	0.31	0.07546	0.00088	1054	10	1059	10	1089	26	97
Z_91500_11	6870	76	430	0.41	1.8270	0.0240	0.17685	0.00180	0.34	0.07515	0.00081	1050	10	1056	8	1070	22	98
Z_91500_12	7000	80	452	0.41	1.8080	0.0280	0.17650	0.00200	0.50	0.07390	0.00095	1048	11	1048	10	1040	25	101
Z_91500_13	7430	86	464	0.41	1.8490	0.0340	0.17640	0.00220	0.21	0.07570	0.00130	1047	12	1062	12	1090	34	96
Z_91500_14	6930	75	440	0.41	1.8390	0.0240	0.17807	0.00180	0.30	0.07492	0.00086	1056	10	1060	9	1066	23	99
Z_91500_15	6560	71	413	0.41	1.8230	0.0300	0.17700	0.00180	0.37	0.07430	0.00110	1050	10	1053	11	1054	29	100
Z_91500_16	6880	74	446	0.41	1.8490	0.0230	0.17754	0.00180	0.33	0.07571	0.00085	1054	10	1063	8	1087	23	97
Z_91500_17	6260	66	391	0.41	1.8220	0.0320	0.17630	0.00190	0.37	0.07490	0.00120	1047	10	1057	10	1061	31	99
Z_91500_18	6060	64	394	0.41	1.7940	0.0330	0.17620	0.00200	0.42	0.07400	0.00120	1046	11	1043	12	1045	30	100
Seq.3																		
Z_Plesovice_1	12220	622	320	0.11	0.4039	0.0049	0.05522	0.00044	0.40	0.05311	0.00048	347	3	344	4	330	21	105
Z_Plesovice_2	13650	833	338	0.11	0.4050	0.0095	0.05456	0.00045	0.56	0.05440	0.00130	343	3	345	7	396	45	86
Z_Plesovice_3	15530	707	636	0.12	0.4831	0.0059	0.05670	0.00045	0.54	0.05326	0.00053	356	3	400	4	666	20	53
Z_Plesovice_4	9230	489	228	0.10	0.4006	0.0044	0.05459	0.00044	0.25	0.05382	0.00048	343	3	342	3	337	23	102
Z_Plesovice_5	17440	1031	687	0.17	0.4061	0.0049	0.05500	0.00046	0.47	0.05339	0.00048	345	3	346	4	361	21	96
Z_Plesovice_6	11650	666	298	0.11	0.4067	0.0045	0.05549	0.00045	0.46	0.05366	0.00050	348	3	346	3	350	21	99

grain	^{207}Pb[a] (cps)	U[b] (ppm)	Pb[b] (ppm)	Th[b]/U	$^{207}Pb/^{235}U$[c]	±2σ (abs)	$^{206}Pb/^{238}U$[c]	±2σ (abs)	rho[d]	$^{207}Pb/^{206}Pb$[c]	±2σ (abs)	$^{206}Pb/^{238}U$	±2σ (Ma)	$^{207}Pb/^{235}U$	±2σ (Ma)	$^{207}Pb/^{206}Pb$	±2σ (Ma)	conc.[e] (%)
Seq.3																		
Z_Plesovice_7	17800	1052	675	0.16	0.4124	0.0038	0.05582	0.00044	0.60	0.05340	0.00042	350	3	351	3	355	15	99
Z_Plesovice_8	8080	429	200	0.11	0.3978	0.0043	0.05431	0.00043	0.19	0.05327	0.00052	341	3	341	3	365	22	93
Z_Plesovice_9	20040	1263	766	0.16	0.4040	0.0044	0.05507	0.00046	0.59	0.05351	0.00041	346	3	344	3	354	18	98
Z_Plesovice_10	11650	711	295	0.11	0.4006	0.0048	0.05437	0.00043	0.44	0.05341	0.00052	341	3	343	4	337	22	101
Z_Plesovice_11	17890	1124	744	0.17	0.4059	0.0043	0.05494	0.00044	0.63	0.05354	0.00054	345	3	346	3	349	18	99
Z_Plesovice_12	13190	778	546	0.16	0.4037	0.0049	0.05465	0.00043	0.43	0.05320	0.00043	343	3	344	4	346	22	99
Z_Plesovice_13	15090	828	622	0.13	0.4615	0.0064	0.05629	0.00045	0.44	0.05356	0.00036	353	3	386	4	572	30	62
Z_Plesovice_14	9040	563	226	0.10	0.4031	0.0048	0.05475	0.00040	0.41	0.06177	0.00059	344	3	344	4	349	22	98
Z_Plesovice_15	11920	723	307	0.11	0.3992	0.0041	0.05446	0.00043	0.28	0.05920	0.00086	342	3	341	3	335	17	102
Z_Temora2_1	3350	145	392	0.52	0.5071	0.0080	0.06677	0.00060	0.13	0.05520	0.00110	417	4	416	5	417	35	100
Z_Temora2_2	3380	156	437	0.59	0.5040	0.0077	0.06652	0.00058	0.34	0.05535	0.00085	415	4	414	6	409	34	101
Z_Temora2_3	5940	250	959	0.70	0.5124	0.0066	0.06724	0.00053	0.23	0.05502	0.00083	420	3	421	4	437	25	96
Z_Temora2_4	3092	141	241	0.34	0.5130	0.0088	0.06759	0.00058	0.11	0.05510	0.00084	422	4	420	6	419	36	101
Z_Temora2_5	6000	276	791	0.57	0.5076	0.0072	0.06673	0.00052	0.02	0.05542	0.00061	416	3	417	5	425	30	98
Z_Temora2_6	4372	202	379	0.37	0.5029	0.0069	0.06638	0.00054	0.24	0.05520	0.00088	414	3	414	5	397	27	104
Z_Temora2_7	3104	149	436	0.58	0.5140	0.0088	0.06683	0.00063	0.67	0.05529	0.00074	417	4	421	6	446	42	93
Z_Temora2_8	4030	192	528	0.56	0.5053	0.0077	0.06711	0.00054	0.05	0.05462	0.00067	419	3	416	5	399	35	105
Z_Temora2_9	3320	149	263	0.30	0.4990	0.0082	0.06658	0.00058	0.06	0.05610	0.00100	416	4	411	6	389	34	107
Z_Temora2_10	3570	160	462	0.55	0.5242	0.0086	0.06905	0.00057	0.35	0.05454	0.00086	430	3	428	6	424	35	102
Z_Temora2_11	3894	175	285	0.30	0.5128	0.0084	0.06671	0.00056	0.28	0.05460	0.00084	416	3	420	6	419	34	99
Z_Temora2_12	2710	126	285	0.42	0.5000	0.0094	0.06543	0.00056	0.17	0.05523	0.00085	409	3	411	6	415	42	98
Z_Temora2_13	2110	104	250	0.47	0.5059	0.0110	0.06682	0.00065	0.09	0.05490	0.00110	417	4	417	7	405	46	103
Z_Temora2_14	4528	204	745	0.71	0.5146	0.0065	0.06690	0.00055	0.05	0.05610	0.00068	418	3	421	4	450	26	93
Z_Temora2_15	11360	541	1560	0.56	0.5113	0.0059	0.06708	0.00059	0.34	0.05493	0.00051	419	4	419	4	406	21	103
Z_91500_1	6240	73	422	0.41	1.8110	0.0260	0.17680	0.00170	0.47	0.07520	0.00086	1049	9	1050	9	1054	26	100
Z_91500_2	6680	84	446	0.40	1.8250	0.0240	0.17772	0.00150	0.34	0.07490	0.00100	1055	8	1054	9	1055	23	100
Z_91500_3	6200	71	409	0.41	1.8270	0.0250	0.17600	0.00150	0.36	0.07472	0.00091	1045	8	1056	9	1070	23	98
Z_91500_4	6730	83	437	0.41	1.8330	0.0270	0.17710	0.00160	0.48	0.07450	0.00098	1051	9	1057	10	1070	25	98
Z_91500_5	6080	75	405	0.41	1.8310	0.0240	0.17797	0.00150	0.41	0.07573	0.00097	1056	8	1057	9	1070	24	99
Z_91500_6	5670	67	373	0.40	1.8470	0.0250	0.17770	0.00150	0.49	0.07500	0.00095	1054	8	1062	9	1076	20	98
Z_91500_7	6510	86	422	0.41	1.8690	0.0250	0.17820	0.00170	0.27	0.07440	0.00081	1057	9	1070	9	1100	25	96
Z_91500_8	5960	77	412	0.41	1.8240	0.0240	0.17630	0.00150	0.23	0.07539	0.00078	1047	8	1054	9	1061	25	99
Z_91500_9	6010	78	406	0.41	1.8410	0.0240	0.17789	0.00150	0.36	0.07440	0.00084	1055	8	1061	9	1064	22	99
Z_91500_10	6110	79	417	0.41	1.8450	0.0260	0.17810	0.00150	0.23	0.07483	0.00083	1057	9	1061	9	1082	26	98
Z_91500_11	6270	81	441	0.41	1.8450	0.0270	0.17680	0.00160	0.36	0.07494	0.00090	1050	9	1063	9	1084	25	97
Z_91500_12	6630	90	471	0.41	1.8520	0.0240	0.18000	0.00160	0.44	0.07553	0.00095	1067	9	1067	9	1065	23	100
Z_91500_13	6640	95	474	0.41	1.8110	0.0290	0.17610	0.00140	0.60	0.07620	0.00096	1046	8	1048	10	1068	28	98
Z_91500_14	6310	85	443	0.41	1.8190	0.0230	0.17720	0.00150	0.19	0.07460	0.00086	1052	8	1052	8	1049	22	100
Z_91500_15	6910	103	474	0.41	1.8480	0.0290	0.17890	0.00150	0.64	0.07630	0.00092	1061	8	1062	10	1099	24	97

Spot size = 20µm (for seq. 1) and 30µm (for seq. 2 & 3)

[a] Within run background-corrected mean ^{207}Pb signal in cps (counts per second).

[b] U and Pb content and Th/U ratio were calculated relative to GJ-1 reference zircon.

[c] corrected for background, within-run Pb/U fractionation (in case of $^{206}Pb/^{238}U$) and subsequently normalised to GJ-1 (ID-TIMS value/measured value); $^{207}Pb/^{235}U$ obtained from signal measured on masses 207 and 235

[d] rho is the $^{206}Pb/^{238}U/^{207}Pb/^{235}U$ error correlation coefficient.

[e] degree of concordance = $^{206}Pb/^{238}U$ age / $^{207}Pb/^{206}Pb$ age x 100

Table B7: Results of LA-ICP-MS zircon U–Pb analyses performed during the sessions at GUF, 2nd and 3rd of May, 2016

grain	^{207}Pb[a] (cps)	U[b] (ppm)	Pb[b] (ppm)	Th[b]/U	^{206}Pbc[c] (%)	$^{206}Pb/^{238}U$[d]	±2s (%)	$^{207}Pb/^{235}U$[d]	±2s (%)	$^{207}Pb/^{206}Pb$[d]	±2s (%)	rho[e]	$^{206}Pb/^{238}U$	±2s (Ma)	$^{207}Pb/^{235}U$	±2s (Ma)	$^{207}Pb/^{206}Pb$	±2s (Ma)	conc.[f] (%)	Grain zone[g]
Seq.1																				
CHA15-41 La Molette syntectonic granite																				
a06	18840	4831	401	0.23	0.82	0.08452	1.5	0.7449	2.4	0.06392	1.8	0.65	523	8	565	10	739	38	71	h
a07*	30714	13703	691	0.45	0.47	0.04815	1.4	0.3467	4.3	0.05222	4.1	0.33	303	4	302	11	295	94	103	h
a08	13623	3524	311	0.19	0.59	0.09217	1.5	0.7405	2.1	0.05827	1.5	0.71	568	8	563	9	540	32	105	h
a09*	44311	21491	1054	0.31	0.11	0.04821	1.6	0.3525	2.0	0.05303	1.2	0.80	303	5	307	5	330	26	92	h
a10	24983	6439	547	0.10	0.09	0.09036	1.4	0.7321	1.6	0.05876	0.8	0.86	558	7	558	7	558	18	100	r
a11	37098	8168	1043	0.48	0.23	0.10263	1.4	0.8835	1.7	0.06244	0.9	0.86	630	9	643	8	689	18	91	c
a12	31240	12228	785	0.06	0.24	0.06797	1.7	0.5727	2.2	0.06112	1.4	0.77	424	7	460	8	643	31	66	r
a13	77668	19817	1815	0.38	0.23	0.09169	1.4	0.7763	1.7	0.06141	1.0	0.82	566	8	583	8	654	21	87	c
a15*	24069	10885	581	0.67	0.67	0.04761	1.4	0.3451	2.8	0.05258	2.5	0.48	300	4	301	7	311	56	97	h
a16	16202	4120	404	0.57	0.21	0.09323	1.4	0.7771	2.2	0.06046	1.7	0.65	575	8	584	10	620	36	93	h
a17	57023	13049	1446	0.15	0.89	0.09254	1.6	0.8599	2.4	0.06739	1.8	0.67	571	9	630	11	850	37	67	h
a18	15513	3526	347	0.71	1.07	0.08936	1.4	0.8289	2.4	0.06728	2.0	0.58	552	7	613	11	846	42	65	h
a19	22983	10171	446	0.34	2.58	0.04348	2.6	0.4333	4.6	0.07227	3.8	0.57	274	7	366	14	994	77	28	r
a20	111848	32859	2450	0.22	0.56	0.07637	1.4	0.6365	5.5	0.06045	5.3	0.25	474	6	500	22	620	115	77	h
a21	59428	17459	1272	0.33	0.60	0.07240	1.6	0.5831	2.3	0.05841	1.6	0.70	451	7	466	9	545	36	83	h
a23	22201	5786	494	0.10	0.11	0.09114	1.4	0.7380	1.7	0.05873	0.9	0.84	562	7	561	7	557	19	101	r
a24	143511	48213	1890	0.05	1.43	0.03706	3.3	0.3573	4.1	0.06993	2.4	0.81	235	8	310	11	926	49	25	r
a25	35864	11980	796	0.22	0.06	0.06875	1.7	0.5289	1.8	0.05579	0.7	0.92	429	7	431	7	444	16	97	h
a26	24884	2801	526	0.84	0.11	0.16922	1.4	1.7213	1.6	0.07378	0.7	0.88	1008	13	1017	10	1035	15	97	h
a27	3949	1076	90	0.14	b.d.	0.08801	2.2	0.7131	2.8	0.05876	1.8	0.79	544	12	547	12	558	38	97	h
a28	21878	9852	521	0.51	2.93	0.04613	1.5	0.4658	4.9	0.07323	4.7	0.30	291	4	388	16	1020	95	28	h
a29	5199	3234	171	0.16	0.27	0.05613	1.7	0.4397	3.9	0.05681	3.5	0.44	352	6	370	12	484	76	73	r2
a30	9569	2421	201	0.09	0.17	0.08852	1.4	0.7225	1.8	0.05920	1.2	0.77	547	7	552	8	574	25	95	r1
a31	30591	7491	570	0.12	1.85	0.07716	1.6	0.7624	3.1	0.07166	2.7	0.52	479	7	575	14	976	55	49	r
a32	58283	17902	1368	0.05	0.22	0.08210	1.3	0.6784	1.5	0.05994	0.7	0.89	509	7	526	6	601	15	85	r
a38	8604	4556	232	0.58	b.d.	0.04889	1.5	0.3560	1.9	0.05281	1.3	0.76	308	4	309	5	321	28	96	h
a39	49798	16211	1438	0.45	0.14	0.08740	1.4	0.7267	1.6	0.06030	0.7	0.88	540	7	555	7	615	16	88	h
a40	8839	1852	184	0.08	b.d.	0.10626	1.4	0.9000	2.0	0.06143	1.4	0.72	651	9	652	10	654	30	100	h
a41	6954	1925	169	0.38	b.d.	0.08830	1.6	0.7113	2.2	0.05842	1.5	0.72	545	8	546	9	546	33	100	h
a42	79124	21403	1844	0.24	0.54	0.08831	1.6	0.7629	1.8	0.06265	0.9	0.87	546	8	576	8	696	20	78	r
a43	25639	6487	611	0.74	0.20	0.08524	1.5	0.7587	3.0	0.06456	2.6	0.50	527	8	573	13	760	55	69	h
a45	31987	8719	717	0.10	0.24	0.08773	1.4	0.7027	1.6	0.05809	0.9	0.85	542	7	540	7	533	19	102	r
a46	4361	1090	111	0.95	0.93	0.09016	2.1	0.7566	3.1	0.06087	2.3	0.67	556	11	572	14	635	50	88	c
a47*	33565	15549	863	0.02	1.02	0.04857	1.7	0.3522	3.2	0.05259	2.7	0.55	306	5	306	8	311	61	98	h
a48	25930	9014	519	0.44	4.02	0.04487	1.5	0.5418	4.7	0.08757	4.5	0.32	283	4	440	17	1373	86	21	h
a50	11806	4661	329	0.38	0.05	0.07093	1.6	0.5913	1.8	0.06046	0.8	0.88	442	7	472	7	620	18	71	h
a51	21343	4278	573	1.00	b.d.	0.10471	1.4	0.8746	1.8	0.06058	1.1	0.78	642	9	638	8	624	24	103	h
a52	19687	5526	457	0.12	0.07	0.08768	1.5	0.7088	1.9	0.05863	1.1	0.80	542	8	544	8	554	25	98	h
a53	58891	15607	1470	0.44	b.d.	0.09351	1.3	0.7625	1.4	0.05914	0.5	0.95	576	7	575	6	572	10	101	h
a54	11345	2708	291	0.72	0.20	0.10014	1.4	0.8312	1.8	0.06020	1.0	0.81	615	8	614	8	611	23	101	h
a55	10254	3102	248	0.15	0.06	0.08395	1.5	0.6777	2.0	0.05855	1.4	0.72	520	7	525	8	550	31	94	r
a56	12915	3133	362	1.19	b.d.	0.09689	1.5	0.8038	1.8	0.06017	1.0	0.83	596	8	599	8	610	21	98	c

Table B7 (continued): Results of LA-ICP-MS zircon U–Pb analyses performed during the sessions at GUF, 2nd and 3rd of May, 2016

grain	^{207}Pb[a] (cps)	U[b] (ppm)	Pb[b] (ppm)	Th[b] / U	^{206}Pbc[c] (%)	^{206}Pb[d] / ^{238}U	±2s (%)	^{207}Pb[d] / ^{235}U	±2s (%)	^{207}Pb[d] / ^{206}Pb	±2s (%)	rho[e]	^{206}Pb / ^{238}U	±2s (Ma)	^{207}Pb / ^{235}U	±2s (Ma)	^{207}Pb / ^{206}Pb	±2s (Ma)	conc.[f] (%)	Grain zone[g]
CHA15-52 Majousseires leucogneiss																				
a57	23077	5302	415	0.52	2.74	0.07686	1.5	0.8684	3.7	0.08195	3.4	0.42	477	7	635	18	1244	66	38	h
a58	16257	4487	399	0.21	b.d.	0.09280	1.8	0.7593	2.3	0.05934	1.4	0.78	572	10	574	10	579	31	99	c
a59	9911	2792	234	0.21	b.d.	0.08729	1.4	0.6966	2.0	0.05788	1.4	0.70	539	7	537	8	525	31	103	r
a60	17872	3660	470	0.90	b.d.	0.11480	1.5	1.0050	1.8	0.06350	0.9	0.87	701	10	706	9	725	18	97	c
a61	18509	4794	379	0.11	0.06	0.08390	1.4	0.6813	1.8	0.05890	1.1	0.80	519	7	528	7	563	23	92	r
a62	45866	10121	844	0.11	2.12	0.08445	1.4	0.8808	3.6	0.07565	3.3	0.40	523	7	641	17	1086	66	48	h
a63	4437	926	78	0.17	b.d.	0.08829	1.6	0.7140	2.6	0.05865	2.1	0.62	545	9	547	11	554	45	98	h
a64	15563	4191	351	0.14	b.d.	0.08837	1.5	0.7197	1.8	0.05906	1.1	0.81	546	8	550	8	569	23	96	h
a65	12656	3682	347	0.93	0.10	0.08482	1.4	0.6860	2.1	0.05866	1.6	0.66	525	7	530	9	555	35	95	h
a66	18115	5198	420	0.13	0.28	0.08537	1.4	0.6949	2.1	0.05903	1.6	0.66	528	7	536	9	568	35	93	h
a72	36935	9250	795	0.30	0.78	0.08833	1.4	0.7963	2.1	0.06538	1.5	0.68	546	7	595	9	787	32	69	r
a73	105355	2180	1103	0.97	b.d.	0.42018	1.4	9.4085	1.5	0.16240	0.5	0.95	2261	27	2379	14	2481	8	91	c
a74	14048	3744	312	0.15	0.45	0.08775	1.7	0.7056	2.1	0.05832	1.3	0.79	542	9	542	9	542	28	100	c
a75	31068	8804	685	0.09	b.d.	0.08304	1.4	0.6703	2.0	0.05855	1.4	0.71	514	7	521	8	550	31	93	r
a76	6515	1144	99	0.27	b.d.	0.08861	1.5	0.7117	2.3	0.05825	1.7	0.68	547	8	546	10	539	36	101	r2
a77	4430	847	71	0.15	b.d.	0.08856	2.1	0.7195	2.6	0.05892	1.5	0.81	547	11	550	11	564	33	97	r1
a78	13523	3770	312	0.14	0.07	0.08738	1.4	0.7070	1.9	0.05868	1.3	0.73	540	7	543	8	555	29	97	h
a79	5311	1155	137	0.55	b.d.	0.11507	1.8	1.0088	2.9	0.06359	2.4	0.60	702	12	708	15	728	50	96	h
a80	29764	8796	678	0.06	0.24	0.08296	1.4	0.6722	1.7	0.05877	1.1	0.78	514	7	522	7	558	24	92	r
a81	45968	11911	922	0.23	1.76	0.07906	1.4	0.7877	2.8	0.07226	2.4	0.51	490	7	590	12	993	48	49	r
a82	8008	2211	200	0.26	b.d.	0.09297	1.7	0.7584	2.1	0.05917	1.4	0.78	573	9	573	9	573	29	100	r
a83	148451	3296	1668	0.94	b.d.	0.42700	1.4	9.5926	1.4	0.16293	0.4	0.95	2292	27	2396	13	2486	7	92	c
a84	7352	1365	117	0.23	0.32	0.08839	1.5	0.7172	2.2	0.05885	1.7	0.66	546	8	549	10	562	37	97	r
a85	25785	6784	560	0.14	0.33	0.08650	1.6	0.7095	1.9	0.05949	1.0	0.84	535	8	544	8	585	22	91	h
a86	27532	6791	564	0.09	1.22	0.08624	1.4	0.7915	2.6	0.06656	2.2	0.54	533	7	592	12	824	46	65	h
a87	15786	4630	377	0.15	0.00	0.08573	1.5	0.6911	1.8	0.05847	1.1	0.81	530	7	533	8	547	23	97	r
a88	63623	8831	820	0.13	7.42	0.08267	1.8	1.2528	9.4	0.10991	9.2	0.19	512	9	825	55	1798	168	28	h
a89	19125	6132	475	0.08	b.d.	0.08278	1.4	0.6698	1.7	0.05868	0.9	0.85	513	7	521	7	555	19	92	h
CHA15-34 Le Couste granite dyke																				
a90	52236	13104	1063	0.07	1.19	0.08462	1.4	0.7803	2.3	0.06688	1.8	0.62	524	7	586	10	834	37	63	r
a91	11157	2937	239	0.38	1.38	0.07790	1.6	0.7638	2.8	0.07112	2.4	0.56	484	7	576	13	961	48	50	c
a93	9501	2731	231	0.25	b.d.	0.08724	1.7	0.7002	2.2	0.05821	1.5	0.75	539	9	539	9	538	32	100	h
a94	42447	13294	945	0.07	1.03	0.07488	1.6	0.6749	2.4	0.06537	1.9	0.65	465	7	524	10	786	39	59	r
a95	7204	2130	180	0.28	b.d.	0.08647	1.5	0.7008	2.1	0.05878	1.5	0.70	535	8	539	9	559	33	96	c
a96	13222	3317	283	0.26	0.06	0.08772	1.4	0.7056	1.8	0.05834	1.2	0.76	542	7	542	8	542	26	100	h
a98	32288	7706	642	0.09	1.16	0.08584	1.4	0.8202	2.4	0.06930	1.9	0.59	531	7	608	11	908	40	58	h
a99	47787	14020	1110	0.03	0.12	0.08559	1.4	0.6977	1.5	0.05912	0.7	0.91	529	7	537	6	571	14	93	r
a100	15636	2587	417	1.57	b.d.	0.12834	1.4	1.1699	1.7	0.06612	1.0	0.82	778	11	787	10	810	21	96	c
a101	24081	10234	666	0.23	b.d.	0.06642	1.4	0.5083	1.7	0.05550	0.8	0.87	415	6	417	6	433	18	96	h
a107	15833	4551	379	0.12	0.07	0.08839	1.6	0.7132	1.8	0.05852	1.0	0.84	546	8	547	8	549	22	99	r
a109	18493	7184	431	0.43	1.01	0.06270	1.6	0.5356	2.3	0.06195	1.7	0.68	392	6	436	8	673	36	58	h
a110	34533	7455	596	0.13	3.14	0.07769	1.9	0.9146	4.5	0.08539	4.0	0.43	482	9	660	22	1324	78	36	h
a111	15587	4688	374	0.09	0.01	0.08519	1.5	0.6925	2.9	0.05896	2.4	0.52	527	8	534	12	566	53	93	h
a112	15269	4319	361	0.12	b.d.	0.08863	1.4	0.7181	1.7	0.05877	0.9	0.83	547	7	550	7	558	21	98	h
a113	23855	7651	630	0.14	b.d.	0.08698	1.4	0.7005	1.5	0.05841	0.7	0.90	538	7	539	6	545	15	99	r
a114	40061	10438	1097	0.77	0.00	0.09436	1.4	0.7768	1.5	0.05971	0.7	0.89	581	8	584	7	593	15	98	h

Table B7 (continued): Results of LA-ICP-MS zircon U–Pb analyses performed during the sessions at GUF, 2nd and 3rd of May, 2016

grain	^{207}Pb[a] (cps)	U[b] (ppm)	Pb[b] (ppm)	Th[b] / U	$^{206}Pb_c$[c] (%)	^{206}Pb[d] / ^{238}U	±2s (%)	^{207}Pb[d] / ^{235}U	±2s (%)	^{207}Pb[d] / ^{206}Pb	±2s (%)	rho[e]	^{206}Pb / ^{238}U	±2s (Ma)	^{207}Pb / ^{235}U	±2s (Ma)	^{207}Pb / ^{206}Pb	±2s (Ma)	conc.[f] (%)	Grain zone[g]
a115	4183	654	56	0.24	b.d.	0.08744	2.3	0.7373	3.1	0.06116	2.1	0.74	540	12	561	14	645	45	84	r
a116	14357	4349	368	0.17	0.05	0.08813	1.5	0.7055	2.1	0.05806	1.4	0.73	544	8	542	9	532	31	102	c
a117	11233	3262	259	0.13	0.56	0.08410	1.5	0.6766	2.3	0.05835	1.8	0.64	521	7	525	10	543	39	96	r
a119	5656	1673	146	0.42	0.04	0.08661	1.8	0.6981	2.4	0.05846	1.6	0.75	535	9	538	10	547	35	98	r
a120	27599	3885	580	0.77	0.18	0.13412	1.5	1.3174	1.8	0.07124	0.9	0.87	811	12	853	10	964	18	84	c
a121	9635	2853	242	0.22	0.34	0.08803	1.5	0.7115	2.0	0.05862	1.4	0.73	544	8	546	9	553	31	98	r
a122	11245	3307	279	0.20	b.d.	0.08809	1.5	0.7167	1.9	0.05901	1.2	0.78	544	8	549	8	567	26	96	r
a123	9893	2793	234	0.26	0.30	0.08477	1.5	0.7258	2.0	0.06210	1.4	0.73	525	7	554	9	677	29	77	h
a124	17136	4988	407	0.12	0.21	0.08672	1.5	0.7012	1.8	0.05864	1.0	0.83	536	8	539	8	554	22	97	h
a125	24809	7386	597	0.10	0.03	0.08655	1.5	0.6870	1.8	0.05757	0.9	0.84	535	8	531	7	513	21	104	r
a126	21197	6371	509	0.09	0.31	0.08530	1.4	0.6823	1.7	0.05801	1.0	0.82	528	7	528	7	530	21	100	r
a127	8585	2505	203	0.21	0.74	0.08374	1.5	0.6845	2.3	0.05929	1.7	0.67	518	8	529	9	578	37	90	h
a128	7275	2013	165	0.11	0.09	0.08721	1.6	0.7148	2.1	0.05945	1.2	0.80	539	8	548	9	583	27	92	h
a129	27331	8088	663	0.10	0.12	0.08757	1.4	0.7076	1.6	0.05860	0.8	0.87	541	7	543	7	552	18	98	r
a130	174783	6589	2181	0.26	0.07	0.32382	1.4	5.3330	1.4	0.11944	0.4	0.97	1808	22	1874	12	1948	7	93	r
a132	15504	4504	386	0.14	b.d.	0.09078	1.5	0.7284	1.8	0.05819	1.0	0.84	560	8	556	8	537	22	104	r
a133	21486	5500	447	0.14	1.30	0.08319	1.4	0.7918	2.7	0.06903	2.3	0.53	515	7	592	12	900	47	57	r
a134	10127	2978	249	0.19	0.07	0.08708	1.4	0.7023	1.9	0.05849	1.2	0.75	538	7	540	8	548	27	98	r
a135	21320	6384	519	0.16	0.18	0.08485	1.4	0.7140	1.7	0.06103	1.0	0.81	525	7	547	7	640	21	82	r
a136	51775	14595	1176	0.07	0.44	0.08572	1.4	0.7353	1.8	0.06221	1.1	0.78	530	7	560	8	681	24	78	r
a137	40230	11764	942	0.08	0.28	0.08530	1.4	0.7116	1.8	0.06050	1.1	0.80	528	7	546	8	622	23	85	r
CHA15-35 Le Couste leucogneiss																				
a138	18152	5430	426	0.14	0.31	0.08278	1.6	0.6800	2.2	0.05958	1.5	0.72	513	8	527	9	588	33	87	h
a139	30627	9564	786	0.10	0.22	0.08783	1.5	0.7085	1.9	0.05851	1.1	0.82	543	8	544	8	549	23	99	r
a140	81841	24611	1926	0.10	0.57	0.08355	1.5	0.7157	1.9	0.06213	1.3	0.76	517	7	548	8	679	27	76	h
a141	21684	5780	522	0.67	0.57	0.08387	1.5	0.7288	2.4	0.06302	1.8	0.63	519	7	556	10	709	39	73	h
a142	21053	6358	480	0.16	0.35	0.07907	1.5	0.6914	2.0	0.06342	1.3	0.76	491	7	534	8	722	27	68	r
a144	56499	16042	1343	0.09	0.65	0.08888	1.6	0.7823	2.4	0.06383	1.8	0.67	549	8	587	11	736	38	75	r
a145	23299	6060	512	0.11	1.15	0.08750	1.5	0.7999	2.4	0.06631	1.9	0.62	541	8	597	11	816	39	66	r
a151	28332	12371	581	0.40	1.74	0.04696	1.9	0.4572	3.4	0.07061	2.8	0.56	296	6	382	11	946	58	31	r2
a152	14739	3542	291	0.26	1.96	0.08026	1.5	0.8816	3.3	0.07966	2.9	0.47	498	7	642	16	1189	58	42	r1
a153	17139	5182	430	0.14	0.11	0.08772	1.4	0.7066	1.8	0.05842	1.0	0.82	542	7	543	7	546	22	99	r
a155	11970	3744	308	0.20	b.d.	0.08574	1.7	0.6963	2.1	0.05890	1.2	0.81	530	8	537	9	563	26	94	r
a156	31308	9355	767	0.10	0.02	0.08757	1.6	0.7078	1.8	0.05862	0.8	0.89	541	8	543	8	553	18	98	h
a158	22393	6878	567	0.09	0.16	0.08807	1.4	0.7105	1.7	0.05851	0.9	0.83	544	7	545	7	549	20	99	r
a160	78858	30567	1637	0.15	2.59	0.05364	1.6	0.5933	3.5	0.08023	3.1	0.45	337	5	473	13	1203	62	28	r
a161	18589	5323	465	0.24	0.14	0.09057	1.4	0.7273	1.7	0.05824	1.0	0.83	559	8	555	7	539	21	104	c
a163	22870	7271	520	0.13	0.94	0.07555	1.6	0.6512	2.3	0.06252	1.6	0.71	469	7	509	9	692	34	68	r
a164	20002	5559	460	0.05	0.33	0.08903	1.4	0.7356	1.9	0.05992	1.3	0.72	550	7	560	8	601	28	92	r
a165	20170	6212	467	0.29	1.80	0.07624	2.0	0.7429	3.9	0.07067	3.3	0.51	474	9	564	17	948	68	50	h
a166	21807	6655	566	0.09	0.24	0.09065	1.4	0.7409	2.0	0.05928	1.5	0.69	559	8	563	9	577	32	97	r
a167	23271	7546	569	0.10	0.55	0.08037	1.5	0.6682	2.4	0.06029	1.9	0.62	498	7	520	10	614	40	81	h
a168	76868	21921	1732	0.04	0.27	0.08481	1.6	0.7070	1.8	0.06046	0.9	0.88	525	8	543	8	620	19	85	r
a169	36210	11210	742	0.33	2.28	0.06639	1.7	0.7144	3.3	0.07804	2.9	0.51	414	7	547	14	1148	57	36	r
a170	13420	4877	245	0.62	3.40	0.04771	2.2	0.5660	4.7	0.08605	4.1	0.47	300	6	455	17	1339	80	22	h
a171	25080	8008	661	0.12	0.16	0.08763	1.4	0.7114	1.6	0.05887	0.8	0.87	542	7	546	7	562	17	96	r
a175	44163	13899	1099	0.14	0.07	0.08449	1.6	0.6941	1.8	0.05958	0.9	0.88	523	8	535	8	588	19	89	r

Table B7 (continued): Results of LA-ICP-MS zircon U–Pb analyses performed during the sessions at GUF, 2nd and 3rd of May, 2016

grain	^{207}Pb[a] (cps)	U[b] (ppm)	Pb[b] (ppm)	$\frac{Th}{U}$[b]	^{206}Pbc[c] (%)	$\frac{^{206}Pb}{^{238}U}$[d]	±2s (%)	$\frac{^{207}Pb}{^{235}U}$[d]	±2s (%)	$\frac{^{207}Pb}{^{206}Pb}$[d]	±2s (%)	rho[e]	$\frac{^{206}Pb}{^{238}U}$	±2s (Ma)	$\frac{^{207}Pb}{^{235}U}$	±2s (Ma)	$\frac{^{207}Pb}{^{206}Pb}$	±2s (Ma)	conc.[f] (%)	Grain zone[g]
a176	22257	6010	531	0.20	0.52	0.09147	1.5	0.7948	1.9	0.06302	1.3	0.76	564	8	594	9	709	27	80	c
a177	30467	9564	742	0.13	0.23	0.08342	1.4	0.6866	1.9	0.05969	1.3	0.73	517	7	531	8	592	28	87	h
a178	12426	3802	311	0.16	0.19	0.08610	1.5	0.6972	1.9	0.05873	1.2	0.79	532	8	537	8	557	25	96	h
a179	16756	4881	408	0.12	0.25	0.08856	1.6	0.7163	1.9	0.05866	1.1	0.82	547	8	548	8	554	24	99	r
a180	40337	12849	1041	0.06	0.18	0.08722	1.6	0.7043	1.7	0.05856	0.7	0.90	539	8	541	7	551	16	98	r
a181	40662	12130	1000	0.07	0.22	0.08856	1.5	0.7151	1.7	0.05857	0.7	0.90	547	8	548	7	551	16	99	r
a182	15967	4304	411	0.38	0.46	0.09570	1.4	0.8078	1.8	0.06122	1.1	0.78	589	8	601	8	647	24	91	c
a183	61675	19324	1481	0.14	0.21	0.08159	1.4	0.6810	1.5	0.06054	0.7	0.88	506	7	527	6	623	16	81	h
a184	10985	3398	273	0.12	0.55	0.08531	1.5	0.6913	2.2	0.05877	1.6	0.67	528	7	534	9	559	35	94	r
a185	60950	13574	1132	0.37	2.77	0.08263	1.4	0.9453	3.8	0.08297	3.5	0.38	512	7	676	19	1268	68	40	r
a186	23519	7259	596	0.09	0.02	0.08768	1.4	0.7040	1.6	0.05824	0.8	0.88	542	7	541	7	539	17	101	r
a187	17153	5216	421	0.11	0.48	0.08586	1.5	0.6994	1.8	0.05908	1.1	0.79	531	7	538	8	570	25	93	h
a188	12768	4097	340	0.14	b.d.	0.08762	1.4	0.7059	1.7	0.05843	1.0	0.80	541	7	542	7	546	22	99	r
a189	13671	4017	338	0.15	0.02	0.08874	1.5	0.7216	1.8	0.05898	0.9	0.85	548	8	552	8	566	20	97	r
a190	19485	5825	504	0.09	0.04	0.09251	1.4	0.7470	1.7	0.05857	0.8	0.86	570	8	566	7	551	18	104	c
a191	33646	7479	605	0.08	0.04	0.08664	1.5	0.7069	1.7	0.05918	0.8	0.89	536	8	543	7	574	17	93	c
a192	35657	16043	1210	0.03	b.d.	0.08178	1.4	0.6591	1.7	0.05846	0.9	0.85	507	7	514	7	547	20	93	r
CHA15-48 St Laurent-les-Bains migmatite																				
a200	8574	2600	245	0.71	0.17	0.08674	1.5	0.7091	2.1	0.05929	1.4	0.74	536	8	544	9	578	31	93	c
a201	39053	9664	817	0.08	1.21	0.08770	1.4	0.8160	2.8	0.06748	2.4	0.50	542	7	606	13	853	50	64	r
a202	47315	12244	961	0.16	2.26	0.07992	1.6	0.8085	5.2	0.07337	4.9	0.31	496	8	602	24	1024	99	48	h
a203	17520	5331	445	0.15	0.25	0.08807	1.5	0.7124	2.1	0.05867	1.4	0.73	544	8	546	9	555	31	98	c
a204	11279	3476	287	0.10	b.d.	0.08786	1.5	0.7101	1.9	0.05862	1.2	0.79	543	8	545	8	553	26	98	r
a205	8502	1786	159	0.42	b.d.	0.08834	1.7	0.7309	2.3	0.06001	1.6	0.73	546	9	557	10	604	34	90	h
a206	10338	3151	273	0.36	0.47	0.08703	1.6	0.7108	2.2	0.05924	1.5	0.71	538	8	545	9	576	33	93	r
a207	12811	4182	321	0.09	0.39	0.08144	1.5	0.6718	1.9	0.05983	1.2	0.78	505	7	522	8	597	26	84	r
a208	12564	2594	216	0.19	7.08	0.07373	1.8	1.1365	7.2	0.11179	7.0	0.25	459	8	771	40	1829	126	25	r2
a209	90580	19075	1601	0.05	3.25	0.08215	1.4	0.9753	3.9	0.08610	3.6	0.36	509	7	691	20	1341	70	38	r1
a210	21720	6825	568	0.11	b.d.	0.08851	1.4	0.7059	1.6	0.05784	0.8	0.85	547	7	542	7	524	18	104	r
a211	55868	14607	1223	0.05	1.28	0.08758	1.4	0.8153	2.9	0.06752	2.5	0.50	541	7	605	13	854	52	63	r1
a212	38068	11852	942	0.07	0.23	0.08507	1.4	0.6953	1.6	0.05927	0.8	0.87	526	7	536	7	577	17	91	r2
a213	9199	2903	262	0.56	b.d.	0.08705	1.5	0.7020	1.9	0.05849	1.1	0.81	538	8	540	8	548	24	98	h
a214	15858	4777	410	0.16	0.53	0.09052	1.5	0.7310	1.9	0.05857	1.1	0.80	559	8	557	8	551	25	101	r
a215	6018	1603	206	1.72	b.d.	0.10047	1.5	0.8424	2.1	0.06081	1.6	0.68	617	9	620	10	633	34	98	c
a216	20999	5298	458	0.11	1.96	0.08787	1.5	0.8731	3.5	0.07206	3.2	0.42	543	8	637	17	988	65	55	r
a217	18868	4508	460	0.71	1.10	0.09268	1.5	0.8832	3.0	0.06911	2.7	0.48	571	8	643	15	902	55	63	c
a218	10443	3246	289	0.20	b.d.	0.09318	1.4	0.7529	1.8	0.05860	1.1	0.80	574	8	570	8	552	23	104	r
a219	68413	2991	1074	1.64	0.38	0.25689	1.7	4.2910	2.0	0.12114	0.9	0.89	1474	23	1692	16	1973	16	75	c
a220	19537	5964	506	0.09	b.d.	0.09060	1.5	0.7320	1.8	0.05860	0.9	0.84	559	8	558	8	552	21	101	r2
a221	8605	2459	206	0.17	0.61	0.08584	1.6	0.7744	2.4	0.06543	1.8	0.68	531	8	582	11	788	37	67	r1
a222	35223	10958	908	0.07	b.d.	0.08891	1.4	0.7176	1.5	0.05853	0.6	0.92	549	7	549	7	550	13	100	r
a223	209814	4730	2439	1.02	0.07	0.42565	1.4	9.7486	1.4	0.16611	0.3	0.97	2286	27	2411	13	2519	6	91	c
a224	10527	3404	282	0.33	0.46	0.08366	1.7	0.6717	2.6	0.05823	2.0	0.64	518	8	522	11	539	44	96	h
a225	26249	9307	720	0.08	0.67	0.08119	1.6	0.7374	2.3	0.06587	1.7	0.69	503	8	561	10	802	35	63	r
a226	10676	3319	280	0.22	b.d.	0.08760	1.6	0.7104	2.1	0.05881	1.3	0.76	541	8	545	9	560	29	97	c
a227	17246	4461	447	0.31	0.19	0.10144	1.5	0.8594	1.8	0.06145	1.0	0.84	623	9	630	8	655	21	95	c
a228	30689	9565	789	0.09	b.d.	0.08825	1.4	0.7085	1.6	0.05823	0.8	0.89	545	8	544	7	538	16	101	r

Table B7 (continued): Results of LA-ICP-MS zircon U–Pb analyses performed during the sessions at GUF, 2nd and 3rd of May, 2016

grain	^{207}Pb[a] (cps)	U[b] (ppm)	Pb[b] (ppm)	Th[b]/U	^{206}Pbc[c] (%)	$^{206}Pb/^{238}U$[d]	±2s (%)	$^{207}Pb/^{235}U$[d]	±2s (%)	$^{207}Pb/^{206}Pb$[d]	±2s (%)	rho[e]	$^{206}Pb/^{238}U$	±2s (Ma)	$^{207}Pb/^{235}U$	±2s (Ma)	$^{207}Pb/^{206}Pb$	±2s (Ma)	conc.[f] (%)	Grain zone[g]
a229	19854	5263	456	0.13	1.25	0.08845	1.4	0.8407	2.4	0.06894	2.0	0.59	546	8	620	11	897	40	61	r
a231	44686	8162	753	0.07	5.71	0.08400	1.6	1.2953	6.3	0.11184	6.1	0.26	520	8	844	37	1830	111	28	r
a232	39063	7973	841	0.53	2.51	0.09562	1.5	1.0509	3.6	0.07971	3.3	0.41	589	8	729	19	1190	66	49	r
a233	22206	6607	535	0.09	0.93	0.08551	1.4	0.7245	2.5	0.06145	2.1	0.56	529	7	553	11	655	45	81	h
a234	53727	12783	1134	0.04	1.73	0.09125	1.7	0.9124	2.9	0.07251	2.3	0.59	563	9	658	14	1000	47	56	h
a235	22912	6504	562	0.11	0.41	0.09137	1.4	0.7747	1.9	0.06150	1.2	0.76	564	8	582	8	657	27	86	h
a237	20946	6330	529	0.11	b.d.	0.08813	1.5	0.7349	3.7	0.06048	3.4	0.41	544	8	559	16	621	73	88	h
a243	8352	2615	228	0.26	b.d.	0.08855	1.4	0.7181	2.1	0.05881	1.5	0.69	547	8	550	9	560	33	98	h
a244	14916	4732	393	0.10	0.10	0.08855	1.4	0.7181	1.8	0.05882	1.1	0.79	547	7	550	7	560	23	98	r
a245	47426	15600	1229	0.03	0.30	0.08436	1.3	0.6995	1.6	0.06014	1.0	0.81	522	7	539	7	609	21	86	r
a246	9636	2968	271	0.58	b.d.	0.08693	1.5	0.6977	1.8	0.05821	1.0	0.83	537	8	537	7	538	22	100	c
a247	11195	3019	261	0.18	0.78	0.08775	1.7	0.8214	2.6	0.06790	1.9	0.66	542	9	609	12	865	40	63	c
a248	249663	7786	2705	0.44	0.35	0.31633	2.0	6.9002	2.6	0.15821	1.7	0.75	1772	30	2099	23	2437	29	73	c
a249	21793	7079	572	0.08	0.33	0.08628	1.3	0.7115	1.8	0.05981	1.2	0.73	533	7	546	8	597	27	89	r
a250	18438	7095	638	0.49	b.d.	0.08809	1.4	0.7169	1.8	0.05903	1.1	0.80	544	7	549	8	568	23	96	r
a251	10865	4056	341	0.14	0.01	0.08881	1.5	0.7121	1.9	0.05815	1.2	0.78	549	8	546	8	535	26	102	c
a254	13534	4342	355	0.15	0.32	0.08627	1.5	0.6935	1.8	0.05830	1.1	0.81	533	8	535	8	541	23	99	r
a255	13855	4498	383	0.11	0.25	0.09053	1.8	0.7387	2.5	0.05918	1.7	0.72	559	10	562	11	574	38	97	h
a256	41795	8287	732	0.13	4.52	0.08300	1.6	1.0943	6.2	0.09563	6.0	0.26	514	8	751	34	1540	113	33	c
a258	15397	4381	379	0.15	0.29	0.09118	1.7	0.7386	2.2	0.05875	1.4	0.76	563	9	562	9	558	31	101	h
a259	5955	1773	170	0.35	b.d.	0.09634	1.6	0.7845	2.2	0.05906	1.5	0.72	593	9	588	10	569	34	104	c
a260	42387	12763	1015	0.05	1.46	0.08274	1.4	0.7807	2.6	0.06844	2.2	0.53	512	7	586	12	882	46	58	r
a261	29215	7453	648	0.09	1.42	0.08873	1.4	0.8749	3.9	0.07151	3.6	0.36	548	7	638	19	972	74	56	c
a262	36942	11020	865	0.07	0.76	0.08248	1.4	0.7307	1.9	0.06426	1.4	0.71	511	7	557	8	750	29	68	c
a263	23111	5327	398	0.14	5.21	0.06946	1.8	0.9228	5.6	0.09636	5.3	0.31	433	7	664	28	1555	100	28	r
a264	17855	6853	463	0.07	0.32	0.07167	1.4	0.5914	1.8	0.05985	1.1	0.79	446	6	472	7	598	24	75	h
a265	28345	9333	721	0.07	b.d.	0.08276	1.4	0.6707	1.6	0.05877	0.8	0.86	513	7	521	7	559	18	92	r
a267	57799	9542	770	0.05	9.73	0.06649	2.1	1.2777	8.2	0.13936	7.9	0.25	415	8	836	48	2219	137	19	r
a268	10940	3389	293	0.27	0.07	0.08866	1.4	0.7128	1.8	0.05831	1.1	0.78	548	7	546	8	542	25	101	h
a269	27587	7727	588	0.06	4.22	0.07491	1.5	0.8675	5.4	0.08399	5.2	0.28	466	7	634	26	1292	101	36	h
a270	54866	9799	881	0.08	5.68	0.08232	1.5	1.1649	6.9	0.10263	6.8	0.22	510	7	784	39	1672	125	30	h
a271	14558	4075	314	0.23	2.75	0.07429	1.5	0.7881	4.0	0.07694	3.7	0.38	462	7	590	18	1120	74	41	h
a273	7028	2497	209	0.15	b.d.	0.08801	1.6	0.7064	2.3	0.05821	1.7	0.67	544	8	543	10	538	38	101	r
a274	14059	4401	384	0.09	b.d.	0.09325	1.6	0.7603	1.9	0.05913	1.0	0.83	575	9	574	8	572	22	100	c
a275	12978	4196	349	0.14	0.25	0.08783	1.4	0.7065	1.7	0.05834	0.9	0.84	543	8	543	7	543	20	100	r
a276	12517	4012	344	0.20	b.d.	0.08920	1.4	0.7229	1.9	0.05877	1.4	0.71	551	7	552	8	559	30	99	c
a277	11720	3613	301	0.13	0.50	0.08769	1.4	0.7289	1.9	0.06029	1.3	0.73	542	7	556	8	614	28	88	r
CHA15-63 Charbonneire in-source leucosome																				
a278	14726	5010	388	0.10	b.d.	0.08189	1.5	0.6852	2.2	0.06069	1.6	0.68	507	7	530	9	628	35	81	h
a279	12323	4033	340	0.12	0.26	0.08942	1.5	0.7083	1.8	0.05745	1.0	0.82	552	8	544	8	509	23	109	h
a280	15035	6961	453	0.06	b.d.	0.06937	1.4	0.5659	1.8	0.05916	1.2	0.78	432	6	455	7	573	25	75	h
a281	38373	7749	644	0.03	6.19	0.07705	1.7	1.1129	6.2	0.10476	6.0	0.27	478	8	760	34	1710	110	28	r
a282	17787	3831	354	0.09	2.54	0.09251	1.6	0.9807	5.0	0.07689	4.7	0.31	570	9	694	25	1118	95	51	r
a288	16628	4124	390	0.29	1.63	0.09263	1.5	0.9388	4.3	0.07351	4.1	0.35	571	8	672	22	1028	82	56	h
a289	20860	6965	555	0.06	0.13	0.08560	1.4	0.6900	1.8	0.05847	1.2	0.77	529	7	533	8	547	26	97	h
a290	13536	7204	374	0.04	2.50	0.05393	2.1	0.5515	8.5	0.07417	8.3	0.25	339	7	446	31	1046	167	32	h
a291	42552	14737	1183	0.06	b.d.	0.08651	1.4	0.6989	1.5	0.05859	0.6	0.92	535	7	538	6	552	13	97	h

Table B7 (continued): Results of LA-ICP-MS zircon U–Pb analyses performed during the sessions at GUF, 2nd and 3rd of May, 2016

grain	^{207}Pb[a] (cps)	U[b] (ppm)	Pb[b] (ppm)	$\frac{Th}{U}$[b]	^{206}Pbc[c] (%)	$\frac{^{206}Pb}{^{238}U}$[d]	±2s (%)	$\frac{^{207}Pb}{^{235}U}$[d]	±2s (%)	$\frac{^{207}Pb}{^{206}Pb}$[d]	±2s (%)	rho[e]	$\frac{^{206}Pb}{^{238}U}$	±2s (Ma)	$\frac{^{207}Pb}{^{235}U}$	±2s (Ma)	$\frac{^{207}Pb}{^{206}Pb}$	±2s (Ma)	conc.[f] (%)	Grain zone[g]
a292	14323	4527	389	0.12	0.40	0.09134	1.6	0.7379	2.2	0.05859	1.5	0.71	563	8	561	9	552	33	102	h
a294	43276	5401	555	0.12	11.21	0.08077	1.9	1.6730	7.0	0.15022	6.8	0.27	501	9	998	46	2348	116	21	r
a295	16405	4167	369	0.13	1.48	0.08997	1.7	0.8653	3.0	0.06975	2.5	0.55	555	9	633	14	921	52	60	r
a296	36937	8418	710	0.08	4.08	0.08090	1.6	1.0234	5.8	0.09175	5.6	0.28	501	8	716	30	1462	106	34	h
a297	13793	4356	355	0.13	0.35	0.08632	1.4	0.6901	1.9	0.05798	1.3	0.73	534	7	533	8	529	28	101	c
a298	21891	7573	592	0.05	0.06	0.08438	1.5	0.6777	2.1	0.05825	1.4	0.73	522	8	525	9	539	31	97	r
a299	23305	7776	535	0.06	1.63	0.07295	1.7	0.6113	3.3	0.06077	2.8	0.51	454	7	484	13	631	61	72	h
a301	58549	10314	833	0.16	10.42	0.06579	2.0	1.3769	7.4	0.15179	7.1	0.27	411	8	879	45	2366	122	17	r
a302	35743	12079	931	0.07	0.67	0.08154	1.6	0.7044	2.6	0.06265	2.1	0.63	505	8	541	11	696	44	73	r
a303	92623	23966	1553	0.02	6.20	0.05729	1.6	1.0009	6.8	0.12671	6.6	0.23	359	6	704	35	2053	117	17	r
a304	15186	5325	388	0.10	0.63	0.07707	1.5	0.6185	2.1	0.05821	1.5	0.70	479	7	489	8	538	32	89	h
a305	37355	11488	950	0.09	0.25	0.08820	1.4	0.7125	1.7	0.05859	0.9	0.86	545	7	546	7	552	19	99	r
a306	151947	58414	2831	0.03	7.55	0.04455	1.7	0.6846	7.2	0.11145	7.0	0.23	281	5	530	30	1823	128	15	h
a308	65188	20891	1337	0.04	3.86	0.06467	1.8	0.6753	7.6	0.07573	7.4	0.23	404	7	524	32	1088	148	37	h
a309	15247	3583	271	0.13	b.d.	0.07715	1.9	0.6894	3.8	0.06481	3.3	0.50	479	9	532	16	768	70	62	h
a310	36541	13221	1048	0.06	b.d.	0.08518	1.4	0.6931	1.5	0.05901	0.7	0.90	527	7	535	6	567	15	93	r
a312	21370	10410	694	0.04	0.07	0.07173	1.3	0.5724	1.6	0.05788	0.9	0.82	447	6	460	6	525	21	85	h
a313	22249	7339	598	0.09	b.d.	0.08697	1.4	0.7084	1.6	0.05907	0.8	0.87	538	7	544	7	570	17	94	r
a314	31900	7137	580	0.05	0.08	0.08786	1.8	0.7048	2.4	0.05819	1.6	0.76	543	10	542	10	537	35	101	h
a315	42444	19401	850	0.03	2.30	0.04441	2.3	0.4507	3.9	0.07360	3.2	0.58	280	6	378	12	1030	64	27	h
a316	8806	2848	257	0.36	b.d.	0.09073	1.7	0.7388	2.2	0.05906	1.4	0.79	560	9	562	10	569	30	98	h
CHA15-24 Le Ranc syntectonic granite																				
a317	32182	28333	998	0.12	0.60	0.03683	1.8	0.3064	2.3	0.06033	1.5	0.76	233	4	271	5	615	32	38	h
a318	8192	2754	231	0.11	b.d.	0.08898	1.8	0.7089	3.1	0.05779	2.5	0.60	549	10	544	13	522	54	105	r
a320	107994	64847	2229	0.07	3.37	0.03392	2.5	0.3580	6.7	0.07653	6.2	0.37	215	5	311	18	1109	124	19	h
a321	137272	65982	3434	0.04	2.99	0.05319	1.7	0.5616	4.8	0.07658	4.5	0.36	334	6	453	18	1110	89	30	h
a322	40553	14646	1125	0.03	0.13	0.08320	1.6	0.6637	1.8	0.05786	0.6	0.93	515	8	517	7	524	14	98	r
a323	26682	8487	708	0.07	0.19	0.08949	1.7	0.7255	1.9	0.05880	0.9	0.89	553	9	554	8	560	20	99	h
a325	126617	16152	965	0.29	37.07	0.02533	6.3	1.2312	11.9	0.35247	10.1	0.53	161	10	815	69	3718	154	4	h
a326	9412	2946	255	0.35	b.d.	0.08684	2.0	0.7025	2.6	0.05867	1.6	0.78	537	10	540	11	555	35	97	c
a333	9486	3117	263	0.16	b.d.	0.08860	1.5	0.7238	1.9	0.05925	1.2	0.76	547	8	553	8	576	27	95	r
a334	4938	2833	154	0.58	2.42	0.05052	2.3	0.4587	6.9	0.06584	6.5	0.33	318	7	383	22	801	137	40	r
a335 c	5545	3546	186	0.74	b.d.	0.04897	1.6	0.3538	2.5	0.05240	1.8	0.66	308	5	308	7	303	42	102	r
a336	12166	7646	417	0.60	0.32	0.05285	1.6	0.3871	2.7	0.05312	2.2	0.60	332	5	332	8	334	49	99	r
a337	141152	42273	3107	0.02	3.38	0.06528	2.2	0.7634	4.5	0.08482	3.9	0.49	408	9	576	20	1311	77	31	r1
a338	255667	134297	3810	0.03	10.67	0.02375	2.3	0.4470	7.6	0.13651	7.2	0.30	151	3	375	24	2183	126	7	r2
a339	20734	4683	262	0.28	6.82	0.04303	2.9	0.6935	8.1	0.11689	7.5	0.36	272	8	535	34	1909	135	14	c
a341	42598	7804	247	0.01	11.32	0.02123	12.0	0.4217	18.6	0.14405	14.2	0.64	135	16	357	58	2276	245	6	r
a343 c	5194	3462	180	0.73	b.d.	0.04847	1.5	0.3496	2.1	0.05231	1.5	0.72	305	5	304	6	299	33	102	h
a344* c	108859	55713	2523	0.02	1.08	0.04823	1.6	0.3567	2.5	0.05364	1.9	0.65	304	5	310	7	356	43	85	r
a345	147577	40195	3773	0.21	0.41	0.09619	1.4	0.8612	1.7	0.06494	0.9	0.83	592	8	631	8	772	20	77	c
a346	13877	4240	376	0.25	0.02	0.09084	1.5	0.8061	2.1	0.06436	1.4	0.73	561	8	600	9	753	30	74	h
a347	108306	72715	1612	0.08	6.15	0.01964	3.2	0.2744	6.7	0.10133	5.9	0.48	125	4	246	15	1649	109	8	h
a350	68125	18690	636	0.01	8.86	0.02868	2.0	0.5017	7.2	0.12689	6.9	0.28	182	4	413	25	2055	122	9	r
a351	17079	5205	427	0.46	1.25	0.07706	1.4	0.7140	2.6	0.06720	2.2	0.53	479	6	547	11	844	46	57	c
a353	111608	93376	1563	0.02	4.71	0.01531	3.2	0.1938	6.0	0.09181	5.0	0.54	98	3	180	10	1463	96	7	h
a354	70057	6733	597	0.73	31.79	0.04239	2.5	1.8594	5.0	0.31810	4.3	0.51	268	7	1067	33	3561	66	8	h

Table B7 (continued): Results of LA-ICP-MS zircon U–Pb analyses performed during the sessions at GUF, 2nd and 3rd of May, 2016

grain	^{207}Pb[a] (cps)	U[b] (ppm)	Pb[b] (ppm)	Th[b]/U	^{206}Pbc[c] (%)	$^{206}Pb/^{238}U$[d]	±2s (%)	$^{207}Pb/^{235}U$[d]	±2s (%)	$^{207}Pb/^{206}Pb$[d]	±2s (%)	rho[e]	$^{206}Pb/^{238}U$	±2s (Ma)	$^{207}Pb/^{235}U$	±2s (Ma)	$^{207}Pb/^{206}Pb$	±2s (Ma)	conc.[f] (%)	Grain zone[g]
a355	75675	61724	2335	0.05	1.27	0.03998	1.7	0.3270	2.2	0.05932	1.4	0.77	253	4	287	5	579	30	44	h
a357	9784	2315	196	0.28	4.51	0.07561	2.0	0.9550	4.5	0.09161	4.1	0.44	470	9	681	23	1459	77	32	r
a358	18258	7870	283	0.08	2.22	0.03391	5.0	0.3948	6.7	0.08445	4.5	0.74	215	11	338	19	1303	87	16	h
a359	27094	8718	742	0.10	0.02	0.09075	1.5	0.7342	1.7	0.05868	0.8	0.87	560	8	559	7	555	18	101	r
a361	39222	16323	769	0.42	3.91	0.04358	1.7	0.5318	2.2	0.08851	1.3	0.79	275	5	433	8	1394	25	20	h
CHA15-65L Puylaurent migmatite leucosome																				
a363	362332	19280	2489	0.05	24.25	0.05169	3.7	2.5334	45.3	0.35549	45.2	0.08	325	12	1282	399	3731	687	9	h
a365	334706	7417	2129	0.40	38.46	0.08734	4.5	5.9091	10.0	0.49070	9.0	0.45	540	23	1963	91	4214	132	13	r
a367	101372	5955	881	0.25	24.07	0.08325	2.9	2.8327	9.3	0.24678	8.8	0.31	515	15	1364	72	3164	140	16	r
a368	1070974	24898	5928	0.27	67.07	0.05351	7.1	4.4092	12.4	0.59757	10.1	0.58	336	23	1714	108	4502	147	7	c
a369	239527	22994	2087	0.02	18.48	0.05086	2.5	1.8337	9.9	0.26151	9.6	0.25	320	8	1058	67	3256	151	10	r
a371	1028382	7914	4759	0.05	73.53	0.06895	4.1	6.2750	4.7	0.66006	2.2	0.88	430	17	2015	42	4646	32	9	r
a372	473476	2154	1516	0.31	71.13	0.10069	5.3	8.9371	6.1	0.64372	2.9	0.88	618	31	2332	57	4610	42	13	r2
a373	15641	5370	432	0.10	b.d.	0.08574	1.4	0.6976	1.7	0.05902	1.0	0.80	530	7	537	7	568	23	93	r1
a374	15131	4859	385	0.11	0.95	0.08256	1.8	0.7352	3.9	0.06459	3.5	0.46	511	9	560	17	761	73	67	c
a376	225326	22806	1894	0.18	34.02	0.04232	2.1	1.8549	4.2	0.31790	3.6	0.50	267	6	1065	28	3560	56	8	h
a377	97583	9065	1040	0.05	15.14	0.08214	1.8	1.9925	4.3	0.17592	3.9	0.42	509	9	1113	29	2615	65	19	h
a378	193767	10122	1572	0.09	38.34	0.07548	2.4	3.4829	4.3	0.33465	3.6	0.55	469	11	1523	35	3639	55	13	r
a379	63299	13773	1086	0.04	7.41	0.07072	1.6	1.1301	6.4	0.11589	6.2	0.26	441	7	768	35	1894	111	23	r
a380	119556	5659	974	0.13	29.72	0.08380	3.6	3.8208	9.9	0.33068	9.3	0.36	519	18	1597	83	3620	142	14	h
a382	81696	23320	1009	0.00	14.49	0.03275	2.5	0.7556	11.0	0.16734	10.7	0.23	208	5	571	49	2531	180	8	r
a388	19180	6302	534	0.19	0.13	0.08851	1.6	0.7280	1.8	0.05965	0.8	0.90	547	8	555	8	591	17	93	c
a390	204065	1312	675	0.55	66.32	0.08127	9.8	6.6405	14.1	0.59260	10.1	0.69	504	47	2065	132	4490	147	11	r2
a391	183440	2584	1004	0.36	59.16	0.08876	6.7	6.6843	11.9	0.54618	9.8	0.57	548	35	2071	111	4371	143	13	r1
a392	993795	5557	4577	0.63	74.84	0.08427	9.3	8.0271	13.7	0.69085	10.1	0.68	522	47	2234	132	4712	145	11	h
a393	64841	6372	762	0.08	0.55	0.08666	1.4	2.1774	18.3	0.18223	18.3	0.08	536	7	1174	136	2673	303	20	h
a397	261300	8840	1823	0.08	39.75	0.08116	1.7	4.3914	4.0	0.39245	3.6	0.43	503	8	1711	34	3880	55	13	r
CHA15-19 Les Orts boudinaged granite																				
a398	11014	5698	323	1.51	2.27	0.04440	1.5	0.4359	2.2	0.07119	1.6	0.69	280	4	367	7	963	33	29	h
a399	5624	3937	211	1.19	0.70	0.04574	3.4	0.3412	4.3	0.05411	2.7	0.79	288	10	298	11	376	60	77	h
a400	17985	11867	498	0.45	3.65	0.03772	1.8	0.3969	3.9	0.07631	3.5	0.45	239	4	339	11	1103	69	22	h
a401	6468	4485	238	0.83	0.48	0.04860	1.4	0.3530	2.3	0.05267	1.8	0.62	306	4	307	6	315	40	97	h
a402	6364	4127	223	1.21	1.35	0.04598	1.6	0.3607	2.2	0.05690	1.6	0.72	290	5	313	6	488	34	59	h
a403	6916	4461	244	0.79	0.45	0.05019	1.4	0.3685	2.1	0.05325	1.5	0.69	316	4	319	6	340	34	93	h
a404	4832	3408	188	1.07	0.52	0.04788	1.6	0.3506	2.4	0.05311	1.8	0.67	302	5	305	6	334	41	90	h
a405	7869	4382	231	0.85	2.21	0.04532	1.5	0.4456	2.1	0.07132	1.4	0.74	286	4	374	7	967	28	30	h
a406	6246	4148	246	1.03	b.d.	0.05109	1.5	0.4023	2.1	0.05711	1.4	0.73	321	5	343	6	496	32	65	h
a408	11014	7757	327	0.47	0.24	0.04051	1.9	0.3112	2.6	0.05572	1.7	0.74	256	5	275	6	441	39	58	h
a409	15660	5366	297	0.90	7.70	0.04415	1.7	0.6797	5.3	0.11166	5.0	0.32	278	5	527	22	1827	91	15	r
a410	6264	4380	252	1.29	0.10	0.04834	1.6	0.3497	2.8	0.05246	2.3	0.56	304	5	304	7	306	53	100	h
a411	29763	10190	804	0.11	0.29	0.08390	1.3	0.6800	1.5	0.05878	0.7	0.90	519	7	527	6	559	15	93	r
a412	9623	6456	305	0.41	0.70	0.04666	2.0	0.3748	3.6	0.05827	3.0	0.56	294	6	323	10	540	65	54	h
a414	16899	8179	367	0.01	2.98	0.03797	1.9	0.3576	3.2	0.06831	2.5	0.60	240	5	310	9	878	52	27	h
a415	49707	24904	1383	0.03	0.62	0.05950	1.7	0.4910	2.0	0.05985	1.1	0.84	373	6	406	7	598	23	62	r
a416	5698	3994	232	1.30	b.d.	0.04866	1.4	0.3521	2.1	0.05249	1.7	0.63	306	4	306	6	307	38	100	h
a417	41196	15660	1075	0.08	1.01	0.07162	1.7	0.6456	2.2	0.06538	1.5	0.76	446	7	506	9	786	30	57	r

Table B7 (continued): Results of LA-ICP-MS zircon U–Pb analyses performed during the sessions at GUF, 2nd and 3rd of May, 2016

grain	^{207}Pb[a] (cps)	U[b] (ppm)	Pb[b] (ppm)	$\frac{Th}{U}$[b]	^{206}Pbc[c] (%)	$\frac{^{206}Pb}{^{238}U}$[d]	±2s (%)	$\frac{^{207}Pb}{^{235}U}$[d]	±2s (%)	$\frac{^{207}Pb}{^{206}Pb}$[d]	±2s (%)	rho[e]	$\frac{^{206}Pb}{^{238}U}$	±2s (Ma)	$\frac{^{207}Pb}{^{235}U}$	±2s (Ma)	$\frac{^{207}Pb}{^{206}Pb}$	±2s (Ma)	conc.[f] (%)	Grain zone[g]
a418	7251	5088	302	1.40	b.d.	0.04870	1.4	0.3533	2.3	0.05262	1.8	0.60	307	4	307	6	313	42	98	h
a419	38682	11374	564	0.58	10.19	0.03750	2.0	0.6510	2.5	0.12591	1.4	0.82	237	5	509	10	2042	25	12	h
a420	8705	5964	233	1.07	2.12	0.03270	2.0	0.3156	3.1	0.07001	2.4	0.64	207	4	279	8	929	50	22	h
a421	5362	3489	185	0.97	b.d.	0.04661	2.0	0.3461	2.4	0.05385	1.4	0.80	294	6	302	6	365	33	80	h
CHA15-17 Puylaurent migmatite mesosome																				
a423	12328	4103	359	0.21	b.d.	0.09102	1.6	0.7320	1.9	0.05833	1.0	0.84	562	9	558	8	542	22	104	c
a424	20805	7602	605	0.11	b.d.	0.08432	1.6	0.6864	1.8	0.05904	0.9	0.86	522	8	531	7	569	20	92	r
a425	22256	7747	624	0.12	0.76	0.08492	2.0	0.7222	3.2	0.06168	2.5	0.62	525	10	552	14	663	54	79	h
a426	14369	5078	407	0.10	0.68	0.08432	1.7	0.7253	2.8	0.06239	2.2	0.61	522	9	554	12	687	48	76	h
a427	17025	5887	481	0.10	b.d.	0.08709	1.4	0.7071	2.7	0.05889	2.2	0.53	538	7	543	11	563	49	96	h
a428	23078	7632	628	0.08	0.44	0.08776	1.4	0.7302	1.8	0.06035	1.0	0.82	542	8	557	8	616	21	88	h
a429	15957	5238	442	0.12	0.54	0.08868	1.5	0.7493	1.8	0.06128	1.0	0.83	548	8	568	8	649	21	84	h
a432	22883	8369	651	0.08	0.68	0.08239	1.5	0.6993	1.8	0.06156	1.0	0.83	510	7	538	8	659	22	77	h
a433	42618	12498	1011	0.04	0.20	0.08694	1.4	0.7168	1.7	0.05980	0.9	0.86	537	7	549	7	596	19	90	h
a434	11971	4819	385	0.10	0.06	0.08453	1.8	0.7093	2.5	0.06085	1.7	0.72	523	9	544	10	634	37	83	h
a435	27756	9417	769	0.09	0.15	0.08711	1.4	0.7052	1.7	0.05872	0.8	0.87	538	7	542	7	557	18	97	h
a436	29813	9474	720	0.06	2.11	0.07703	1.6	0.8077	2.1	0.07605	1.4	0.76	478	7	601	10	1096	28	44	h
a438	77666	18099	1546	0.04	3.37	0.08377	1.4	0.9972	4.2	0.08633	3.9	0.34	519	7	702	21	1346	75	39	h
a444	7594	3035	266	0.43	b.d.	0.08712	1.6	0.6959	2.1	0.05793	1.4	0.76	539	8	536	9	527	30	102	h
a446	13040	4442	367	0.15	b.d.	0.08713	1.4	0.7082	1.8	0.05895	1.1	0.78	539	7	544	8	565	25	95	h
a447	19528	4197	383	0.13	5.10	0.08531	2.0	1.0997	7.7	0.09349	7.4	0.26	528	10	753	42	1498	140	35	h
a448	38696	13819	1116	0.05	0.01	0.08674	1.4	0.7080	1.6	0.05919	0.7	0.91	536	7	544	7	574	14	93	h
a449	107525	34127	2498	0.03	1.81	0.07548	1.6	0.7550	1.9	0.07255	0.9	0.87	469	7	571	8	1001	18	47	r
a450	18138	6215	507	0.07	0.92	0.08629	1.5	0.7442	1.7	0.06255	0.9	0.86	534	8	565	8	693	19	77	r
a451	10152	3977	292	0.17	1.09	0.07418	1.7	0.6830	2.3	0.06678	1.6	0.72	461	7	529	10	831	33	56	h
a452	48466	39751	1941	0.02	0.56	0.05278	1.5	0.4037	2.0	0.05548	1.4	0.73	332	5	344	6	432	31	77	h
CHA15-47 St Laurent-les-Bains in-source leucosome																				
a454	228800	38666	2025	0.03	23.88	0.02972	1.8	1.0456	7.3	0.25517	7.1	0.25	189	3	727	39	3217	111	6	r
a455	3824	1283	121	0.74	b.d.	0.08750	2.3	0.7110	3.1	0.05894	2.1	0.75	541	12	545	13	565	45	96	h
a456	98844	19095	1635	0.04	7.28	0.07605	1.7	1.2310	3.5	0.11740	3.1	0.48	472	8	815	20	1917	55	25	r
a457	27661	9717	773	0.07	b.d.	0.08535	1.4	0.6958	1.5	0.05913	0.7	0.89	528	7	536	6	572	16	92	r
a458	11204	3779	312	0.12	0.17	0.08745	1.6	0.7074	1.9	0.05867	1.1	0.83	540	8	543	8	555	23	97	c
a459	20497	7101	574	0.09	0.17	0.08600	1.5	0.7040	1.8	0.05937	1.0	0.84	532	8	541	8	581	21	92	h
a460	13235	3044	222	0.04	1.20	0.07573	2.2	0.7241	4.9	0.06935	4.4	0.44	471	10	553	21	909	90	52	h
a461	9604	3295	284	0.15	0.08	0.09094	1.5	0.7369	1.9	0.05877	1.2	0.80	561	8	561	8	559	26	100	r
a462	7677	2693	245	0.53	b.d.	0.08788	1.6	0.7167	2.1	0.05915	1.3	0.77	543	8	549	9	573	29	95	h
a464	35732	18562	881	0.01	1.57	0.04922	1.5	0.5020	9.7	0.07397	9.6	0.16	310	5	413	34	1041	194	30	r
a465	49458	17279	1410	0.05	b.d.	0.08812	1.4	0.7158	1.5	0.05891	0.6	0.91	544	7	548	7	564	14	97	r
a466	22110	8039	589	0.25	0.09	0.07435	1.6	0.6637	2.1	0.06474	1.4	0.76	462	7	517	9	766	29	60	h
a467	25367	8726	592	0.04	2.48	0.06876	1.7	0.7093	2.1	0.07482	1.2	0.82	429	7	544	9	1064	24	40	c
a469	205129	104771	3052	0.05	10.72	0.02470	8.1	0.4546	9.2	0.13348	4.3	0.88	157	13	380	30	2144	76	7	r
a470	6871	1914	173	0.09	0.38	0.09492	2.1	0.8485	2.9	0.06484	2.0	0.72	585	12	624	13	769	42	76	r
a471	74315	5098	1033	0.09	4.03	0.18693	1.7	3.6661	2.0	0.14224	1.1	0.84	1105	17	1564	16	2255	19	49	r
a473	147710	7150	950	0.35	19.94	0.04704	1.5	2.3379	7.2	0.36044	7.0	0.21	296	4	1224	52	3752	107	8	h
a475	15523	5049	446	0.14	b.d.	0.09331	1.5	0.7568	1.8	0.05882	1.0	0.84	575	8	572	8	560	22	103	h
a476	176165	20961	1716	0.34	18.83	0.05031	2.2	1.5712	3.7	0.22652	3.0	0.60	316	7	959	23	3028	47	10	r

Table B7 (continued): Results of LA-ICP-MS zircon U–Pb analyses performed during the sessions at GUF, 2nd and 3rd of May, 2016

grain	^{207}Pb[a] (cps)	U[b] (ppm)	Pb[b] (ppm)	Th[b] / U	^{206}Pbc[c] (%)	^{206}Pb[d] / ^{238}U	±2s (%)	^{207}Pb[d] / ^{235}U	±2s (%)	^{207}Pb[d] / ^{206}Pb	±2s (%)	rho[e]	^{206}Pb / ^{238}U	±2s (Ma)	^{207}Pb / ^{235}U	±2s (Ma)	^{207}Pb / ^{206}Pb	±2s (Ma)	conc.[f] (%)	Grain zone[g]
a477	17624	5744	482	0.13	b.d.	0.08862	1.5	0.7223	1.8	0.05912	0.9	0.87	547	8	552	7	571	19	96	h
a479	27048	9861	774	0.04	0.07	0.08305	1.6	0.7388	2.6	0.06452	2.0	0.64	514	8	562	11	759	41	68	h
a480	6442	2227	226	1.05	b.d.	0.08909	1.8	0.7208	2.3	0.05867	1.4	0.79	550	9	551	10	555	30	99	h
a481	9559	3312	282	0.18	0.32	0.08902	1.6	0.7226	2.0	0.05887	1.3	0.78	550	8	552	9	562	27	98	h
a482	19287	6697	554	0.06	0.07	0.08911	1.4	0.7187	1.8	0.05849	1.1	0.79	550	7	550	8	548	24	100	r
a483	13093	4433	442	0.89	b.d.	0.08952	1.5	0.7390	1.9	0.05987	1.1	0.82	553	8	562	8	599	23	92	h
CHA15-65M Puylaurent migmatite mesosome																				
a484	14132	6121	462	0.04	b.d.	0.08141	1.6	0.6689	2.2	0.05959	1.4	0.75	505	8	520	9	589	31	86	r
a485	32268	6558	1171	0.70	b.d.	0.13296	1.4	1.2116	1.5	0.06609	0.8	0.87	805	10	806	9	809	16	99	c
a486	71190	15299	2215	0.00	1.40	0.11603	1.4	1.2139	3.6	0.07587	3.4	0.38	708	9	807	20	1092	67	65	c
a487	19416	6434	560	0.06	b.d.	0.09372	1.4	0.7570	1.6	0.05858	0.8	0.85	578	8	572	7	552	19	105	r
a488	51467	14611	1233	0.07	1.47	0.08691	1.4	0.8405	1.7	0.07014	0.9	0.84	537	7	619	8	932	19	58	h
a489	16711	5590	468	0.11	0.01	0.08914	1.4	0.7240	1.7	0.05891	1.0	0.82	550	7	553	7	564	21	98	h
a490	27767	4123	829	1.40	0.45	0.16304	1.5	1.6352	1.8	0.07274	1.0	0.84	974	14	984	11	1007	20	97	c
a491	27197	9411	769	0.12	0.12	0.08642	1.4	0.7082	1.6	0.05944	0.8	0.86	534	7	544	7	583	18	92	r
a492	21558	7296	612	0.08	0.24	0.08981	1.4	0.7339	1.6	0.05927	0.8	0.86	554	7	559	7	577	18	96	h
a493	9954	3389	286	0.21	b.d.	0.08766	1.5	0.7074	1.9	0.05853	1.1	0.82	542	8	543	8	550	23	99	h
a499	13779	4619	394	0.14	b.d.	0.08993	1.4	0.7291	1.8	0.05880	1.0	0.81	555	8	556	8	560	22	99	h
a500	26424	6843	541	0.14	3.42	0.07613	1.6	0.8783	2.5	0.08367	1.9	0.64	473	7	640	12	1285	37	37	h
a501	12049	4215	354	0.18	b.d.	0.08777	1.6	0.7140	1.9	0.05900	1.2	0.80	542	8	547	8	567	25	96	h
a502	10937	3585	343	0.38	0.24	0.09595	1.6	0.7897	2.0	0.05969	1.2	0.79	591	9	591	9	592	26	100	h
a504	78627	8571	1160	0.79	11.72	0.09285	1.6	2.0613	3.6	0.16102	3.2	0.44	572	9	1136	25	2466	54	23	c
a505	63380	9164	876	0.09	9.03	0.07700	1.8	1.5392	4.9	0.14497	4.5	0.37	478	8	946	30	2287	78	21	r
a506	24818	4526	608	0.42	0.13	0.13100	1.4	1.2467	1.7	0.06902	0.9	0.84	794	11	822	9	899	18	88	c
a507	4752	1303	129	0.15	b.d.	0.10351	2.6	0.8756	3.1	0.06135	1.7	0.84	635	16	639	15	652	37	97	r1
a508	10771	3652	310	0.12	b.d.	0.08977	1.5	0.7292	1.9	0.05891	1.2	0.76	554	8	556	8	564	27	98	r2
a509	92731	6144	1548	0.14	b.d.	0.25391	1.6	3.7966	1.7	0.10845	0.6	0.93	1459	21	1592	14	1773	12	82	c
a510	31365	4981	490	0.12	9.72	0.08311	1.5	1.4904	11.6	0.13006	11.5	0.13	515	8	926	73	2099	202	25	r
a511	22479	3066	457	0.82	5.18	0.11821	1.6	1.7994	2.5	0.11040	2.0	0.62	720	11	1045	17	1806	36	40	c
a512	20822	7264	598	0.09	0.30	0.08774	1.4	0.7163	1.6	0.05921	0.9	0.85	542	7	548	7	575	19	94	r
a513	15951	4610	442	0.44	1.85	0.09167	1.5	0.8837	4.9	0.06992	4.6	0.31	565	8	643	24	926	96	61	h
a515	37052	4141	747	0.84	4.31	0.14622	1.8	2.1216	2.0	0.10524	0.9	0.90	880	15	1156	14	1718	16	51	c
a516	26694	9266	766	0.08	b.d.	0.08849	1.5	0.7264	1.6	0.05953	0.7	0.90	547	8	554	7	587	15	93	r
a517	108129	10245	1475	0.28	20.35	0.09785	1.8	3.0345	3.1	0.22492	2.5	0.57	602	10	1416	24	3016	40	20	c
a518	17978	6026	499	0.11	b.d.	0.08759	1.4	0.7232	1.8	0.05989	1.2	0.75	541	7	553	8	599	26	90	r
a519	13360	2775	456	1.56	b.d.	0.13068	1.5	1.1955	1.9	0.06635	1.1	0.79	792	11	799	10	817	24	97	c
a520	6333	1220	207	1.27	b.d.	0.13942	1.8	1.2824	2.3	0.06671	1.5	0.76	841	14	838	13	829	31	102	r2
a521	6698	1259	222	1.40	0.75	0.14238	1.7	1.3084	2.5	0.06665	1.7	0.71	858	14	849	14	827	36	104	r1
a522	28891	5898	594	0.13	2.39	0.09907	1.7	1.0961	2.1	0.08025	1.3	0.78	609	10	751	11	1203	26	51	c
a523	30047	4655	418	0.15	1.99	0.08858	1.5	0.9283	2.3	0.07600	1.7	0.67	547	8	667	11	1095	34	50	r1
a524	22581	3676	359	0.10	8.24	0.08336	1.7	1.4789	8.3	0.12866	8.1	0.21	516	8	922	51	2080	142	25	r2
a525	41560	2041	687	1.67	b.d.	0.25828	1.4	3.4358	1.8	0.09648	1.1	0.78	1481	19	1513	14	1557	21	95	c
a527	11488	2297	303	0.38	0.36	0.12882	1.9	1.2210	2.2	0.06874	1.1	0.87	781	14	810	12	891	22	88	c
a528	18547	6133	536	0.08	0.03	0.09369	1.4	0.7716	1.7	0.05973	0.9	0.84	577	8	581	8	594	20	97	r
a529	33046	3863	547	0.27	0.50	0.14155	1.5	1.4099	1.7	0.07224	0.7	0.91	853	12	893	10	993	14	86	c
a530	19862	6862	563	0.08	b.d.	0.08784	1.4	0.7166	1.7	0.05916	0.9	0.82	543	7	549	7	573	21	95	r
a531	9755	3229	270	0.06	b.d.	0.08970	1.6	0.7311	2.0	0.05911	1.3	0.78	554	8	557	9	571	27	97	r

Table B7 (continued): Results of LA-ICP-MS zircon U–Pb analyses performed during the sessions at GUF, 2nd and 3rd of May, 2016

grain	^{207}Pb[a] (cps)	U[b] (ppm)	Pb[b] (ppm)	Th[b] / U	^{206}Pbc[c] (%)	^{206}Pb[d] / ^{238}U	±2s (%)	^{207}Pb[d] / ^{235}U	±2s (%)	^{207}Pb[d] / ^{206}Pb	±2s (%)	rho[e]	^{206}Pb / ^{238}U	±2s (Ma)	^{207}Pb / ^{235}U	±2s (Ma)	^{207}Pb / ^{206}Pb	±2s (Ma)	conc.[f] (%)	Grain zone[g]
a532	14546	5093	421	0.08	0.13	0.08860	1.4	0.7121	1.7	0.05829	0.9	0.84	547	7	546	7	541	20	101	h
a534	79531	11667	930	0.02	39.20	0.05467	2.7	1.3860	21.2	0.18388	21.0	0.13	343	9	883	133	2688	347	13	r
a535	19244	6574	534	0.08	1.04	0.08603	1.5	0.7462	1.8	0.06290	1.0	0.82	532	8	566	8	705	22	75	h
a536	38708	13806	1122	0.13	b.d.	0.08600	1.4	0.7014	1.6	0.05915	0.7	0.88	532	7	540	7	573	16	93	h
a537	49420	7274	767	0.13	7.91	0.08881	1.4	1.5738	3.0	0.12852	2.7	0.46	549	7	960	19	2078	47	26	r
a538	219517	12345	3136	0.12	2.23	0.24101	1.5	4.3375	2.2	0.13053	1.7	0.66	1392	18	1701	19	2105	30	66	c
a539	22886	7996	668	0.09	b.d.	0.08933	1.4	0.7244	1.7	0.05882	0.9	0.85	552	8	553	7	560	19	98	r
a540	18959	5025	530	0.22	0.08	0.10751	1.9	0.9829	2.1	0.06630	0.8	0.92	658	12	695	10	816	17	81	c
a541	19529	6842	570	0.12	0.35	0.08842	1.4	0.7106	1.7	0.05829	0.9	0.86	546	8	545	7	541	19	101	r
a542	22490	7862	654	0.12	0.19	0.08826	1.5	0.7163	1.7	0.05887	0.7	0.91	545	8	549	7	562	15	97	c
a543	36752	2133	648	0.97	2.28	0.25257	1.4	4.3782	1.8	0.12572	1.1	0.79	1452	18	1708	15	2039	19	71	c
a544	45305	11348	972	0.12	2.37	0.08432	1.6	0.9376	1.8	0.08065	0.8	0.90	522	8	672	9	1213	15	43	r
a545	5066	934	86	0.41	5.13	0.08076	2.4	1.2994	4.2	0.11668	3.5	0.58	501	12	845	25	1906	62	26	r
a547	40775	12784	1044	0.05	0.10	0.08787	1.6	0.7193	1.8	0.05937	0.9	0.88	543	8	550	8	581	19	94	r
a548	45685	13841	1177	0.08	1.40	0.08761	1.4	0.8446	2.5	0.06992	2.0	0.56	541	7	622	12	926	42	58	r
a554	59959	12340	1246	0.42	5.17	0.08703	1.5	1.1898	2.6	0.09915	2.2	0.56	538	8	796	15	1608	41	33	c
a555	19104	6765	567	0.15	0.14	0.08827	1.4	0.7138	1.6	0.05864	0.9	0.83	545	7	547	7	554	20	98	r
a556	17310	6165	509	0.12	0.11	0.08770	1.4	0.7078	1.8	0.05853	1.1	0.80	542	7	543	7	550	23	99	c
a557	25352	8913	749	0.11	0.06	0.08934	1.5	0.7238	1.7	0.05875	0.9	0.86	552	8	553	7	558	19	99	h
a558	29835	6767	617	0.11	4.50	0.08711	1.5	1.1021	5.6	0.09176	5.4	0.27	538	8	754	31	1462	103	37	h
a559	5632	1410	137	0.10	0.15	0.10148	2.8	0.8772	3.8	0.06269	2.6	0.72	623	16	639	18	698	56	89	c
a560	19202	6004	513	0.04	b.d.	0.09211	1.4	0.7583	1.7	0.05971	1.0	0.82	568	8	573	7	593	21	96	r1
a561	15596	4749	420	0.05	b.d.	0.09505	1.5	0.7874	1.9	0.06008	1.2	0.78	585	8	590	9	606	26	97	r1
a562	8961	2876	241	0.08	0.05	0.08882	1.6	0.7262	2.3	0.05929	1.6	0.70	549	8	554	10	578	35	95	r2
a563	36772	11629	1183	0.69	0.10	0.09477	1.4	0.7827	1.6	0.05990	0.7	0.90	584	8	587	7	600	15	97	c
a564	24281	8500	728	0.22	0.02	0.08895	1.5	0.7191	1.6	0.05864	0.7	0.90	549	8	550	7	554	16	99	h
a565	23073	2780	394	0.18	b.d.	0.14266	1.6	1.8286	2.2	0.09296	1.5	0.73	860	13	1056	14	1487	28	58	c
a566	13481	4614	395	0.18	0.22	0.08950	1.4	0.7267	1.7	0.05889	1.0	0.83	553	8	555	7	563	21	98	r
a567	48862	2571	708	0.67	0.32	0.24048	1.7	4.7531	1.8	0.14335	0.7	0.93	1389	21	1777	15	2268	12	61	c
a568	45243	5543	718	0.16	1.10	0.12017	1.6	1.8537	1.9	0.11187	1.1	0.81	732	11	1065	13	1830	20	40	r1
a569	25574	3724	358	0.07	5.66	0.08427	1.7	1.3428	4.1	0.11556	3.7	0.43	522	9	864	24	1889	67	28	r2
a570	26557	8045	684	0.04	0.61	0.09028	1.4	0.7985	1.6	0.06415	0.8	0.88	557	8	596	7	747	16	75	r3
a571	14430	2849	440	0.93	b.d.	0.13771	1.5	1.2853	1.8	0.06770	1.0	0.84	832	11	839	10	859	20	97	c
a572	9548	1552	210	1.33	5.64	0.09910	1.7	1.4768	3.0	0.10809	2.5	0.55	609	10	921	18	1767	46	34	c
a573	13178	4654	383	0.07	0.04	0.08833	1.4	0.7122	1.7	0.05847	0.9	0.84	546	7	546	7	548	20	100	r
a574	67433	3324	636	0.17	0.70	0.18648	1.7	2.9808	1.9	0.11593	0.9	0.87	1102	17	1403	15	1894	17	58	c
a575	45545	2654	481	0.25	1.55	0.16815	1.7	2.7009	2.4	0.11650	1.6	0.74	1002	16	1329	18	1903	29	53	r1
a576	6248	1321	118	0.13	0.24	0.09438	1.5	0.7742	2.7	0.05949	2.3	0.55	581	8	582	12	585	49	99	r2
a577	37009	6957	943	0.28	b.d.	0.13545	1.5	1.2890	1.7	0.06902	0.8	0.89	819	11	841	10	899	16	91	c
a579	155113	11801	1733	0.26	25.78	0.08800	2.0	3.3238	2.7	0.27394	1.8	0.73	544	10	1487	21	3329	29	16	h
a580	23170	5583	708	0.56	b.d.	0.12207	1.4	1.0705	1.7	0.06360	0.9	0.85	742	10	739	9	728	19	102	c
a581	19385	5980	553	0.13	0.33	0.09764	1.5	0.8113	1.7	0.06026	0.9	0.85	601	8	603	8	613	19	98	r1
a582	16362	4916	412	0.10	2.34	0.08472	1.4	0.8634	3.1	0.07392	2.7	0.46	524	7	632	15	1039	55	50	r2
a583	33615	9277	784	0.11	1.92	0.08492	1.4	0.8880	3.1	0.07584	2.7	0.47	525	7	645	15	1091	54	48	r
a584	9984	2313	203	0.12	0.76	0.09183	1.8	0.7650	2.8	0.06042	2.2	0.63	566	10	577	12	619	47	92	c
RV-1 Riverie meta-tonalite																				
a585	8430	2826	204	0.19	0.51	0.07213	1.7	0.6911	2.1	0.06949	1.3	0.80	449	7	533	9	913	26	49	

Table B7 (continued): Results of LA-ICP-MS zircon U–Pb analyses performed during the sessions at GUF, 2nd and 3rd of May, 2016

grain	^{207}Pb[a] (cps)	U[b] (ppm)	Pb[b] (ppm)	Th[b] U	^{206}Pbc[c] (%)	^{206}Pb[d] / ^{238}U	±2s (%)	^{207}Pb[d] / ^{235}U	±2s (%)	^{207}Pb[d] / ^{206}Pb	±2s (%)	rho[e]	^{206}Pb / ^{238}U	±2s (Ma)	^{207}Pb / ^{235}U	±2s (Ma)	^{207}Pb / ^{206}Pb	±2s (Ma)	conc.[f] (%)	Grain zone[g]
a586	10989	3594	309	0.33	0.52	0.08485	1.4	0.7847	1.8	0.06707	1.2	0.78	525	7	588	8	840	24	63	
a587	5431	1877	158	0.24	0.80	0.08644	1.8	0.7115	2.2	0.05969	1.3	0.80	534	9	546	9	593	29	90	
a588	5922	2264	182	0.27	0.42	0.08220	1.9	0.6633	2.3	0.05852	1.2	0.85	509	9	517	9	549	26	93	
a589	9900	4484	281	0.11	0.83	0.06550	1.6	0.5542	1.9	0.06136	1.1	0.83	409	6	448	7	652	23	63	
a590	6832	2423	201	0.17	0.25	0.08686	1.6	0.7028	2.4	0.05869	1.7	0.68	537	8	540	10	556	38	97	
a595	6912	1986	171	0.26	b.d.	0.08865	1.8	0.7287	2.2	0.05962	1.3	0.80	548	9	556	9	590	29	93	
a596	4811	1127	95	0.18	b.d.	0.08795	2.2	0.7001	2.7	0.05774	1.6	0.81	543	11	539	11	520	35	105	
a598	9600	3426	288	0.17	0.31	0.08827	1.5	0.7162	1.9	0.05885	1.2	0.78	545	8	548	8	562	26	97	
Seq.2																				
RV-1 Riverie meta-tonalite																				
a06	9688	2655	222	0.18	b.d.	0.08766	1.1	0.7075	1.8	0.05854	1.4	0.63	542	6	543	8	550	31	99	
a08	18090	4995	426	0.25	b.d.	0.08814	1.2	0.7159	1.7	0.05891	1.3	0.68	545	6	548	7	564	28	97	
a09	6981	1930	166	0.29	b.d.	0.08847	1.3	0.7186	1.9	0.05891	1.4	0.67	547	7	550	8	564	31	97	
a10	25713	7190	622	0.45	0.12	0.08625	1.1	0.7012	1.3	0.05896	0.7	0.83	533	6	539	5	566	16	94	
a11	20421	6176	496	0.20	0.60	0.08348	1.1	0.6864	1.7	0.05963	1.3	0.67	517	6	531	7	590	27	88	
a12	24433	6250	491	0.14	0.30	0.08257	1.4	0.6855	1.9	0.06021	1.2	0.75	511	7	530	8	611	26	84	
a13	13206	3800	323	0.26	0.22	0.08766	1.3	0.7219	1.9	0.05973	1.3	0.72	542	7	552	8	594	28	91	
a14	53651	14479	901	0.16	3.07	0.05980	1.6	0.6609	7.8	0.08015	7.7	0.20	374	6	515	32	1201	151	31	
a15	14078	3741	330	0.38	0.11	0.08869	1.1	0.7250	1.5	0.05929	1.0	0.73	548	6	554	6	578	22	95	
a16	23141	6227	388	0.14	2.51	0.06080	1.4	0.6388	3.4	0.07619	3.1	0.40	381	5	502	14	1100	62	35	
a17	5766	1552	133	0.24	b.d.	0.08882	1.2	0.7193	1.9	0.05874	1.5	0.60	549	6	550	8	557	34	98	
a18	11666	3173	268	0.16	0.37	0.08893	1.1	0.7145	1.6	0.05827	1.2	0.67	549	6	547	7	540	26	102	
a19	26879	7211	636	0.43	0.34	0.08793	1.1	0.7199	1.5	0.05938	1.0	0.76	543	6	551	6	581	21	93	
a20	8492	2252	193	0.34	b.d.	0.08675	1.9	0.6913	2.3	0.05780	1.4	0.80	536	10	534	10	522	31	103	
a21	15679	4029	342	0.18	b.d.	0.08871	1.2	0.7193	1.5	0.05881	0.9	0.81	548	6	550	6	560	19	98	
a22	18932	4363	397	0.33	0.73	0.08880	1.3	0.8837	2.8	0.07218	2.5	0.45	548	7	643	14	991	51	55	
a23	12437	3210	271	0.20	0.13	0.08753	1.2	0.7460	2.1	0.06181	1.7	0.57	541	6	566	9	668	37	81	
a24	13707	3788	320	0.18	b.d.	0.08846	1.4	0.7163	2.2	0.05873	1.8	0.61	546	7	548	9	557	39	98	
a25	10735	3021	255	0.21	0.20	0.08822	1.1	0.7120	1.5	0.05853	1.0	0.73	545	6	546	6	550	23	99	
a26	20787	6006	425	0.52	1.34	0.06922	1.4	0.6544	2.5	0.06857	2.1	0.55	431	6	511	10	886	43	49	
a30	7549	2271	180	0.17	0.19	0.08321	1.2	0.6680	1.9	0.05822	1.5	0.62	515	6	519	8	538	32	96	
a31	12129	3529	300	0.23	0.08	0.08827	1.3	0.7193	1.9	0.05910	1.3	0.70	545	7	550	8	571	29	96	
a39	9017	2542	219	0.35	0.56	0.08744	1.2	0.7084	1.9	0.05876	1.5	0.60	540	6	544	8	558	34	97	
a40	11338	3210	276	0.30	0.05	0.08804	1.1	0.7132	1.6	0.05875	1.2	0.69	544	6	547	7	558	25	97	
a41	19538	5463	449	0.26	0.14	0.08474	1.1	0.6879	1.5	0.05888	1.0	0.75	524	6	532	6	562	21	93	
a42	6893	1945	165	0.24	0.17	0.08771	1.1	0.7159	1.9	0.05920	1.5	0.62	542	6	548	8	574	32	94	
a43	16084	4535	383	0.22	0.37	0.08791	1.1	0.7102	1.6	0.05859	1.2	0.67	543	6	545	7	552	26	98	
a44	15981	4483	379	0.28	b.d.	0.08661	1.1	0.7178	1.8	0.06011	1.4	0.61	535	6	549	8	607	31	88	
a45	12947	3444	284	0.33	0.02	0.08367	1.2	0.6817	2.1	0.05909	1.8	0.55	518	6	528	9	570	39	91	
a46	22829	6172	520	0.24	0.14	0.08721	1.2	0.7145	1.5	0.05942	0.9	0.82	539	6	547	6	583	19	93	
a47	12283	3383	296	0.44	0.37	0.08575	1.1	0.7361	1.8	0.06226	1.5	0.61	530	6	560	8	683	31	78	
RV-2 Riverie meta-tonalite																				
a48	25583	6386	548	0.35	b.d.	0.08671	1.2	0.7024	1.4	0.05875	0.8	0.83	536	6	540	6	558	17	96	
a49	23129	6639	560	0.30	0.13	0.08650	1.0	0.7019	1.3	0.05885	0.8	0.80	535	5	540	5	561	17	95	
a50	20688	6456	491	0.23	0.82	0.07800	1.1	0.7203	2.4	0.06697	2.1	0.48	484	5	551	10	837	43	58	

Table B7 (continued): Results of LA-ICP-MS zircon U–Pb analyses performed during the sessions at GUF, 2nd and 3rd of May, 2016

grain	^{207}Pb[a] (cps)	U[b] (ppm)	Pb[b] (ppm)	Th[b] / U	^{206}Pbc[c] (%)	^{206}Pb[d] / ^{238}U	±2s (%)	^{207}Pb[d] / ^{235}U	±2s (%)	^{207}Pb[d] / ^{206}Pb	±2s (%)	rho[e]	^{206}Pb / ^{238}U	±2s (Ma)	^{207}Pb / ^{235}U	±2s (Ma)	^{207}Pb / ^{206}Pb	±2s (Ma)	conc.[f] (%)	Grain zone[g]
a52	9945	2884	242	0.15	b.d.	0.08845	1.3	0.7166	1.7	0.05876	1.2	0.74	546	7	549	7	558	25	98	
a53	12588	3570	296	0.16	b.d.	0.08760	1.3	0.7100	1.6	0.05878	1.1	0.76	541	7	545	7	559	23	97	
a54	14985	6119	503	0.17	0.10	0.08675	1.1	0.6978	1.6	0.05834	1.2	0.68	536	6	537	7	543	25	99	
a55	8856	2546	213	0.15	b.d.	0.08831	1.3	0.7163	1.9	0.05882	1.3	0.72	546	7	548	8	561	29	97	
a56	9125	1713	143	0.35	b.d.	0.08398	1.3	0.6815	1.8	0.05885	1.3	0.72	520	6	528	7	562	27	93	
a57	9625	2758	235	0.20	0.15	0.08902	1.4	0.7256	2.0	0.05912	1.5	0.68	550	7	554	9	571	32	96	
a58	28610	7910	688	0.31	0.15	0.08861	1.2	0.7425	1.5	0.06078	0.8	0.82	547	6	564	6	631	18	87	
a59	21735	6533	537	0.25	b.d.	0.08519	1.2	0.6896	1.9	0.05871	1.4	0.67	527	6	533	8	556	30	95	
a60	17491	5636	392	0.37	0.31	0.07033	1.6	0.5948	2.1	0.06134	1.4	0.74	438	7	474	8	651	31	67	
a61	20187	5762	488	0.29	b.d.	0.08716	1.1	0.7050	1.4	0.05867	0.9	0.78	539	6	542	6	555	19	97	
a62	7942	2271	194	0.25	0.82	0.08874	1.4	0.7105	2.2	0.05807	1.7	0.64	548	7	545	9	532	36	103	
a63	16612	4685	399	0.22	0.03	0.08877	1.2	0.7183	1.5	0.05869	0.8	0.83	548	6	550	6	556	18	99	
a64	7247	2086	178	0.29	0.27	0.08795	1.2	0.7041	2.3	0.05806	1.9	0.53	543	6	541	10	532	42	102	
a65	41973	18749	990	0.02	0.11	0.05764	1.2	0.4285	1.4	0.05392	0.7	0.85	361	4	362	4	368	17	98	
a66	48222	14744	771	0.04	0.38	0.05638	1.3	0.4369	1.6	0.05620	1.0	0.78	354	4	368	5	460	22	77	
a72	17516	5068	435	0.25	b.d.	0.08880	1.2	0.7124	1.6	0.05819	1.1	0.74	548	6	546	7	537	23	102	
a73	18478	5346	442	0.20	b.d.	0.08649	1.1	0.6985	1.4	0.05857	0.9	0.77	535	5	538	6	551	19	97	
a74	10193	2954	245	0.17	0.48	0.08726	1.3	0.7060	2.0	0.05869	1.6	0.64	539	7	542	9	555	34	97	
a75	20755	6060	513	0.23	0.18	0.08812	1.2	0.7119	1.5	0.05859	0.9	0.79	544	6	546	6	552	19	99	
a76	17379	5120	440	0.34	0.19	0.08738	1.1	0.7001	1.5	0.05811	0.9	0.76	540	6	539	6	534	21	101	
a79	8186	2395	202	0.21	b.d.	0.08814	1.2	0.7185	1.9	0.05912	1.4	0.65	545	6	550	8	571	31	95	
a80	25436	7531	634	0.26	b.d.	0.08716	1.2	0.6972	1.4	0.05802	0.7	0.85	539	6	537	6	531	16	102	
a81	17242	4824	399	0.25	b.d.	0.08547	1.1	0.6878	1.3	0.05837	0.8	0.79	529	5	531	6	543	18	97	
a82	16995	5061	425	0.21	0.01	0.08761	1.2	0.7054	1.5	0.05840	1.0	0.77	541	6	542	6	545	21	99	
a83	11907	3319	284	0.30	0.34	0.08768	1.4	0.7059	1.9	0.05840	1.2	0.76	542	7	542	8	545	26	99	
a84	12669	3718	305	0.16	b.d.	0.08638	1.2	0.7084	1.5	0.05949	1.0	0.76	534	6	544	6	585	22	91	
a85	17119	4992	419	0.24	b.d.	0.08704	1.2	0.6986	1.5	0.05821	1.0	0.76	538	6	538	6	538	22	100	
a86	17862	4978	425	0.24	0.07	0.08812	1.3	0.7175	1.6	0.05905	0.9	0.81	544	7	549	7	569	20	96	
a88	15424	2921	249	0.20	0.48	0.08903	1.3	0.7186	1.8	0.05854	1.3	0.70	550	7	550	8	550	28	100	
a89	13516	5457	438	0.13	b.d.	0.08513	1.3	0.6858	1.8	0.05843	1.2	0.74	527	7	530	8	546	27	96	
CHA15-43 Masméjean migmatite																				
a228	46535	14060	1157	0.05	b.d.	0.08878	1.1	0.7185	1.3	0.05870	0.6	0.87	548	6	550	6	556	14	99	r
a230	21535	4886	434	0.19	2.54	0.08776	1.2	0.9574	4.1	0.07912	3.9	0.28	542	6	682	21	1175	78	46	r
a232	41042	15447	945	0.04	0.44	0.06500	1.1	0.5434	1.7	0.06063	1.3	0.66	406	4	441	6	626	27	65	h
a233	18030	5168	440	0.19	0.02	0.08921	1.1	0.7211	1.9	0.05863	1.6	0.57	551	6	551	8	553	35	100	h
a235	14229	2754	241	0.11	0.49	0.09280	1.3	0.7686	2.1	0.06007	1.6	0.64	572	7	579	9	606	34	94	c
a236	10048	2882	245	0.27	b.d.	0.08747	1.6	0.7040	2.2	0.05837	1.6	0.72	541	8	541	9	544	34	99	c
a237	17724	4887	411	0.26	0.29	0.08679	1.1	0.7091	1.4	0.05926	0.9	0.76	537	6	544	6	577	21	93	h
a243	18707	5516	451	0.13	0.24	0.08660	1.1	0.7032	1.6	0.05889	1.2	0.69	535	6	541	7	563	25	95	h
a244	24255	7501	620	0.10	0.14	0.08820	1.3	0.7107	1.6	0.05845	0.9	0.83	545	7	545	7	547	19	100	h
a245	45654	16236	1323	0.06	0.01	0.08767	1.2	0.7094	1.7	0.05868	1.1	0.73	542	6	544	7	555	25	98	r
a246	7616	2294	205	0.44	b.d.	0.08917	1.1	0.7170	1.6	0.05832	1.2	0.67	551	6	549	7	542	27	102	c
a248	50510	18890	578	0.09	2.85	0.03024	3.9	0.3299	8.1	0.07912	7.1	0.48	192	7	290	21	1175	140	16	r
a249	14776	4473	377	0.14	0.55	0.08915	1.1	0.7223	1.7	0.05876	1.3	0.66	550	6	552	7	558	28	99	r
a251	72298	23052	1801	0.05	0.52	0.08344	1.1	0.7234	1.5	0.06288	0.9	0.76	517	5	553	6	704	20	73	r
a252	22616	6310	538	0.18	0.21	0.08834	1.2	0.7193	1.5	0.05906	0.8	0.83	546	6	550	6	569	18	96	c
a253	46565	23545	920	0.14	4.67	0.03837	1.6	0.4477	7.8	0.08462	7.6	0.21	243	4	376	25	1307	148	19	r

Table B7 (continued): Results of LA-ICP-MS zircon U–Pb analyses performed during the sessions at GUF, 2nd and 3rd of May, 2016

grain	^{207}Pb[a] (cps)	U[b] (ppm)	Pb[b] (ppm)	Th[b]/U	^{206}Pbc[c] (%)	$^{206}Pb/^{238}U$[d]	±2s (%)	$^{207}Pb/^{235}U$[d]	±2s (%)	$^{207}Pb/^{206}Pb$[d]	±2s (%)	rho[e]	$^{206}Pb/^{238}U$	±2s (Ma)	$^{207}Pb/^{235}U$	±2s (Ma)	$^{207}Pb/^{206}Pb$	±2s (Ma)	conc.[f] (%)	Grain zone[g]
a254	26514	6080	510	0.82	2.23	0.08352	1.3	0.8806	4.6	0.07647	4.4	0.28	517	6	641	22	1107	88	47	r
a255	39350	16455	1128	0.06	0.01	0.07352	1.3	0.5879	1.5	0.05799	0.7	0.88	457	6	470	6	530	15	86	h
a256	40057	8115	715	0.10	0.26	0.09406	1.4	0.7686	1.9	0.05926	1.4	0.70	579	8	579	9	577	30	100	h
a257	49810	13815	1156	0.05	0.88	0.08810	1.1	0.8118	2.7	0.06683	2.5	0.42	544	6	603	12	832	51	65	h
a258	76463	24829	980	0.01	4.02	0.03929	1.8	0.4495	5.0	0.08297	4.6	0.37	248	4	377	16	1268	90	20	h
a259	7351	2042	174	0.12	b.d.	0.08999	1.5	0.7449	2.8	0.06003	2.4	0.54	555	8	565	12	605	52	92	r
a262	38083	5755	471	0.18	1.98	0.08077	2.1	0.8729	3.3	0.07838	2.5	0.66	501	10	637	16	1157	49	43	r1
a264	51744	15753	1259	0.09	0.06	0.08590	1.1	0.6994	1.5	0.05905	1.0	0.73	531	5	538	6	569	22	93	r2
a265	10767	3018	275	0.38	b.d.	0.09245	1.4	0.7525	1.7	0.05903	1.0	0.80	570	8	570	8	568	22	100	c
a266	14235	2402	215	0.07	b.d.	0.09590	1.3	0.7884	1.7	0.05962	1.1	0.76	590	7	590	8	590	25	100	r
a267	29014	11187	707	0.06	1.26	0.06642	1.2	0.5815	2.4	0.06350	2.2	0.47	415	5	465	9	725	46	57	r
CHA15-51 Majousseires granite dyke																				
a269	24028	8759	552	0.20	1.94	0.06316	1.4	0.6621	3.5	0.07603	3.2	0.39	395	5	516	14	1096	65	36	r
a272	241276	57389	2086	0.00	14.48	0.02128	1.8	0.7585	8.8	0.25855	8.6	0.21	136	2	573	39	3238	136	4	r
a273	17381	4990	442	0.22	b.d.	0.09240	1.2	0.7587	1.7	0.05955	1.2	0.70	570	6	573	7	587	26	97	h
a274	18181	5643	461	0.17	b.d.	0.08602	1.2	0.7050	2.5	0.05944	2.1	0.51	532	6	542	10	583	46	91	h
a275	10005	3146	254	0.18	1.01	0.08473	1.4	0.6871	3.1	0.05881	2.7	0.46	524	7	531	13	560	60	94	c
a276	30178	24419	412	0.10	5.31	0.01613	1.9	0.1960	6.0	0.08813	5.7	0.32	103	2	182	10	1385	110	7	r
a277	71915	8799	1274	0.59	0.28	0.13106	1.3	1.5920	1.4	0.08810	0.5	0.93	794	10	967	9	1385	10	57	c
a278	22026	4116	472	0.25	0.31	0.11499	1.9	1.2111	2.4	0.07639	1.6	0.76	702	12	806	14	1105	31	63	r
a279	48113	15134	1215	0.07	0.57	0.08522	1.4	0.7229	1.8	0.06153	1.2	0.76	527	7	552	8	658	25	80	h
a280	78163	18462	1231	0.20	6.06	0.06040	1.5	0.9039	5.6	0.10853	5.4	0.27	378	5	654	27	1775	99	21	c
a281	12185	4691	193	0.06	0.70	0.04314	4.6	0.3616	5.1	0.06078	2.2	0.90	272	12	313	14	632	47	43	r
a282	182960	174877	3832	0.00	6.27	0.02044	2.4	0.2910	6.2	0.10328	5.7	0.39	130	3	259	14	1684	105	8	r
a290	9896	2965	286	0.78	0.19	0.09021	1.1	0.7340	1.5	0.05901	1.0	0.73	557	6	559	7	568	23	98	c
a291	13204	3095	151	0.11	4.36	0.04477	1.9	0.6084	4.8	0.09855	4.4	0.40	282	5	483	19	1597	82	18	r
a292	31068	8404	623	0.40	2.39	0.07337	1.3	0.8067	3.3	0.07974	3.1	0.38	456	6	601	15	1190	60	38	h
a293	36947	11211	955	0.10	0.11	0.09103	1.7	0.7358	2.0	0.05862	1.0	0.86	562	9	560	8	553	22	102	r
a294	128282	40834	3168	0.03	0.53	0.08331	1.1	0.7045	1.6	0.06134	1.3	0.64	516	5	541	7	651	27	79	h
a295	36940	11298	906	0.07	b.d.	0.08598	1.1	0.7053	1.2	0.05950	0.6	0.88	532	6	542	5	585	12	91	h
a296	39608	9181	1131	1.10	0.54	0.10632	1.1	0.9603	1.7	0.06551	1.2	0.67	651	7	683	8	791	26	82	c
a297	37703	13014	924	0.09	0.40	0.07293	1.1	0.7213	4.5	0.07173	4.4	0.25	454	5	551	19	978	89	46	r
a298	12605	3748	295	0.20	1.23	0.08086	1.3	0.6968	3.2	0.06250	2.9	0.40	501	6	537	13	691	62	73	r
a302	12965	3800	369	0.78	0.52	0.08908	1.3	0.7763	2.7	0.06321	2.3	0.50	550	7	583	12	715	49	77	r
a303	23288	7039	593	0.12	b.d.	0.08958	1.2	0.7238	1.5	0.05860	0.8	0.83	553	7	553	6	552	18	100	h
a304	32271	9044	690	0.21	1.15	0.07747	1.3	0.7318	2.3	0.06851	1.9	0.56	481	6	558	10	884	39	54	h
a305	31955	15099	802	0.02	0.30	0.05759	1.1	0.4503	1.4	0.05670	0.9	0.78	361	4	377	5	480	20	75	r
a306	196314	26501	1523	0.14	19.89	0.03417	3.8	1.0215	10.5	0.21682	9.8	0.36	217	8	715	56	2957	158	7	r
a308	44687	17278	1308	0.03	0.25	0.08206	1.1	0.6653	1.3	0.05880	0.7	0.84	508	6	518	5	560	16	91	h
a310	38162	13624	1080	0.08	0.01	0.08473	1.2	0.6893	1.4	0.05900	0.9	0.81	524	6	532	6	567	19	92	r
a311	36215	11280	921	0.08	b.d.	0.08740	1.1	0.7108	1.3	0.05898	0.7	0.84	540	6	545	6	566	15	95	r
a312	28634	8508	704	0.12	0.10	0.08791	1.2	0.7128	1.4	0.05880	0.7	0.86	543	6	546	6	560	15	97	h
a313	159538	57361	3273	0.05	1.63	0.05875	1.9	0.5733	3.3	0.07077	2.7	0.57	368	7	460	12	951	55	39	h
a314	52407	27463	1238	0.10	0.34	0.04804	1.1	0.3696	1.6	0.05580	1.2	0.65	302	3	319	4	444	28	68	h
a315	23136	6876	584	0.14	0.22	0.08992	1.2	0.7307	1.5	0.05894	0.9	0.81	555	6	557	6	565	19	98	r
a316	58106	26880	1408	0.03	b.d.	0.05672	1.4	0.4465	1.7	0.05709	1.1	0.78	356	5	375	5	495	24	72	r

Table B7 (continued): Results of LA-ICP-MS zircon U–Pb analyses performed during the sessions at GUF, 2nd and 3rd of May, 2016

grain	^{207}Pb[a] (cps)	U[b] (ppm)	Pb[b] (ppm)	Th[b] / U	^{206}Pbc[c] (%)	^{206}Pb[d] / ^{238}U	±2s (%)	^{207}Pb[d] / ^{235}U	±2s (%)	^{207}Pb[d] / ^{206}Pb	±2s (%)	rho[e]	^{206}Pb / ^{238}U	±2s (Ma)	^{207}Pb / ^{235}U	±2s (Ma)	^{207}Pb / ^{206}Pb	±2s (Ma)	conc.[f] (%)	Grain zone[g]
CHA15-33 Le Couste syntectonic porphyritic granite																				
a317	55309	14344	1704	0.14	0.07	0.10104	1.1	0.8553	1.2	0.06139	0.6	0.89	621	7	628	6	653	12	95	h
a318	39520	5602	955	0.66	0.15	0.16201	1.3	1.5975	1.5	0.07151	0.7	0.87	968	11	969	9	972	15	100	r
a322	73615	21318	1831	0.06	0.02	0.09215	1.4	0.7649	1.7	0.06021	0.9	0.85	568	8	577	7	611	19	93	r
a323	19001	5517	475	0.06	b.d.	0.09243	1.1	0.7530	1.5	0.05909	1.0	0.76	570	6	570	6	570	21	100	r
a324	19858	9703	590	0.04	0.20	0.06485	1.1	0.5440	2.1	0.06084	1.7	0.55	405	4	441	7	634	37	64	r
a325	9969	2584	222	0.31	b.d.	0.08691	1.7	0.7556	4.4	0.06305	4.1	0.38	537	9	571	19	710	86	76	h
a326	19280	5538	460	0.14	b.d.	0.08801	1.2	0.7049	1.4	0.05809	0.8	0.84	544	6	542	6	533	17	102	h
a327*	136580	56862	2632	0.01	3.97	0.04651	1.3	0.3660	4.7	0.05708	4.5	0.27	293	4	317	13	495	99	59	r
a335	23874	7195	612	0.14	b.d.	0.09009	1.1	0.7347	1.3	0.05915	0.6	0.88	556	6	559	6	573	14	97	r
a336	17603	7076	406	0.07	0.63	0.05989	1.5	0.5363	2.2	0.06495	1.6	0.67	375	5	436	8	773	34	49	r
a337	11487	3783	328	0.30	b.d.	0.08859	1.5	0.7364	2.2	0.06029	1.6	0.67	547	8	560	9	614	35	89	r
a338	13919	7261	421	0.75	1.91	0.05320	1.3	0.4806	4.3	0.06551	4.1	0.30	334	4	398	14	791	85	42	h
a339*	74504	55424	2448	0.02	0.40	0.04782	1.1	0.3476	1.8	0.05271	1.5	0.58	301	3	303	5	316	34	95	r
a341	17534	5188	434	0.15	b.d.	0.08838	1.3	0.7149	1.6	0.05867	0.9	0.83	546	7	548	7	555	19	98	r
a342	15467	4937	336	0.09	2.30	0.06990	1.3	0.6686	3.5	0.06938	3.2	0.38	436	6	520	14	910	66	48	r
a343	27023	7334	611	0.11	0.51	0.08868	1.4	0.7166	1.8	0.05861	1.1	0.78	548	7	549	8	552	24	99	r
a344	56812	15940	1255	0.07	1.62	0.08131	1.1	0.7928	2.5	0.07071	2.2	0.46	504	6	593	11	949	45	53	r
a345	32308	9655	775	0.12	0.58	0.08436	1.1	0.7216	1.5	0.06204	1.1	0.70	522	5	552	7	676	24	77	r
a346	19744	5494	434	0.17	1.56	0.07881	1.4	0.8101	2.8	0.07455	2.4	0.51	489	7	603	13	1056	48	46	r
a347	81035	12653	1168	0.10	9.75	0.07812	1.5	1.4759	7.0	0.13702	6.8	0.22	485	7	921	43	2190	118	22	r
a348	22890	7748	530	0.14	0.12	0.07180	1.3	0.5713	1.9	0.05771	1.4	0.67	447	5	459	7	519	31	86	r
a349*	31244	20070	952	0.32	0.17	0.04878	1.1	0.3514	2.1	0.05226	1.8	0.53	307	3	306	6	297	41	103	h
a350	14886	4664	390	0.13	0.17	0.08835	1.2	0.7335	1.7	0.06021	1.2	0.72	546	6	559	7	611	26	89	h
a351	11654	4436	319	0.11	0.38	0.07671	1.1	0.5960	1.8	0.05635	1.4	0.61	476	5	475	7	466	31	102	h
a352	61132	19230	1573	0.06	0.11	0.08806	1.1	0.7112	1.3	0.05858	0.7	0.84	544	6	545	6	551	16	99	r
a353	33228	10251	810	0.08	b.d.	0.08463	1.0	0.6832	1.4	0.05855	1.0	0.73	524	5	529	6	550	21	95	r
a354*	41934	9541	458	0.01	5.50	0.04721	1.4	0.3411	6.6	0.05241	6.5	0.22	297	4	298	17	303	148	98	r2
a355	64309	18350	1487	0.09	0.72	0.08462	1.2	0.7710	1.8	0.06608	1.4	0.66	524	6	580	8	809	28	65	r1
a356	88734	26999	2194	0.06	b.d.	0.08737	1.1	0.7094	1.2	0.05889	0.4	0.93	540	6	544	5	563	9	96	c
a359	21127	4511	588	0.73	b.d.	0.11981	1.3	1.0928	1.6	0.06615	0.9	0.80	729	9	750	8	811	20	90	c
a360	45264	14850	1170	0.06	1.00	0.08286	1.6	0.7465	2.6	0.06534	2.0	0.62	513	8	566	11	785	42	65	h
a363	22373	6707	567	0.13	0.27	0.08968	1.1	0.7261	1.5	0.05872	1.1	0.73	554	6	554	7	557	23	99	r
a364*	28877	12692	569	0.02	0.51	0.04818	1.2	0.3467	2.4	0.05219	2.0	0.50	303	3	302	6	294	47	103	r
a365	9017	1174	105	0.23	3.77	0.08034	1.9	1.1480	5.0	0.10364	4.7	0.37	498	9	776	28	1690	86	29	c
a366	28924	5801	739	0.68	0.18	0.12047	1.2	1.1035	1.5	0.06644	0.8	0.82	733	8	755	8	820	17	89	r1
a367	10369	2552	210	0.27	b.d.	0.08172	1.3	0.6538	1.8	0.05803	1.2	0.73	506	6	511	7	531	27	95	r2
a368*	65015	43491	1963	0.10	0.52	0.04801	1.2	0.3475	1.9	0.05250	1.5	0.62	302	3	303	5	307	34	98	r
a369*	37121	27835	1258	0.08	1.37	0.04757	1.3	0.3418	3.0	0.05211	2.7	0.43	300	4	299	8	290	61	103	r
a371	9605	1562	90	0.10	0.80	0.05766	1.7	0.4975	3.1	0.06258	2.6	0.54	361	6	410	11	694	56	52	c
a372	95639	29785	2226	0.04	0.60	0.07923	1.2	0.7019	1.9	0.06426	1.5	0.64	491	6	540	8	750	32	66	h
a373	34996	10710	828	0.04	0.41	0.08318	1.8	0.6930	2.5	0.06043	1.8	0.69	515	9	535	11	619	39	83	h
a376	25678	7447	638	0.08	0.34	0.09112	1.4	0.7786	1.7	0.06198	1.0	0.80	562	7	585	8	673	22	83	h
a379	107875	27508	1809	0.18	4.56	0.06234	1.3	0.8283	5.4	0.09636	5.2	0.25	390	5	613	25	1555	98	25	h
a381	77204	8841	966	0.08	13.73	0.08479	1.8	1.9400	7.8	0.16595	7.6	0.24	525	9	1095	54	2517	128	21	h
a382	37847	14184	587	0.08	0.89	0.04377	1.4	0.3682	2.3	0.06100	1.8	0.62	276	4	318	6	639	38	43	r
a389	12817	2037	152	0.06	5.27	0.07045	1.5	0.9454	6.0	0.09733	5.8	0.25	439	6	676	30	1574	109	28	h
a391	3694	719	64	0.13	2.44	0.09332	1.4	0.7787	4.5	0.06052	4.2	0.32	575	8	585	20	622	91	92	r

Table B7 (continued): Results of LA-ICP-MS zircon U–Pb analyses performed during the sessions at GUF, 2nd and 3rd of May, 2016

grain	^{207}Pb[a] (cps)	U[b] (ppm)	Pb[b] (ppm)	Th[b]/U	^{206}Pbc[c] (%)	$^{206}Pb/^{238}U$[d]	±2s (%)	$^{207}Pb/^{235}U$[d]	±2s (%)	$^{207}Pb/^{206}Pb$[d]	±2s (%)	rho[e]	$^{206}Pb/^{238}U$	±2s (Ma)	$^{207}Pb/^{235}U$	±2s (Ma)	$^{207}Pb/^{206}Pb$	±2s (Ma)	conc.[f] (%)	Grain zone[g]
a393	14341	5187	278	0.15	0.14	0.05504	1.1	0.4342	3.2	0.05721	3.0	0.35	345	4	366	10	500	66	69	r
a394	32663	13469	910	0.23	b.d.	0.06992	1.4	0.5565	3.4	0.05773	3.1	0.41	436	6	449	12	519	68	84	h
a395	130844	69002	2319	0.02	3.75	0.03277	1.5	0.3829	5.1	0.08474	4.8	0.30	208	3	329	14	1310	94	16	r2
a396	15082	4453	540	2.29	0.27	0.08816	1.1	0.7546	1.7	0.06208	1.3	0.66	545	6	571	8	677	28	80	r1
a398	7713	2343	206	0.26	0.35	0.09041	1.2	0.7488	1.7	0.06007	1.2	0.72	558	7	568	7	606	26	92	c
a399	24999	5098	453	0.08	3.85	0.08503	1.2	1.1052	4.9	0.09427	4.7	0.25	526	6	756	26	1513	89	35	r
CHA15-25 Le Ranc syntectonic granite																				
a402	301032	143560	5180	0.01	3.58	0.03541	1.4	0.3939	4.3	0.08068	4.1	0.33	224	3	337	13	1214	81	18	r
a404	67536	17834	1430	0.04	0.33	0.08511	1.4	0.7202	1.7	0.06138	1.0	0.82	527	7	551	7	652	21	81	h
a405	68381	34955	1459	0.00	2.35	0.04285	2.3	0.4229	5.1	0.07158	4.5	0.45	270	6	358	15	974	92	28	r
a407	22044	6822	567	0.15	0.07	0.08790	1.3	0.7157	1.7	0.05905	1.2	0.73	543	7	548	7	569	26	95	h
a408	17102	5061	460	0.41	b.d.	0.09146	1.1	0.7502	1.5	0.05948	1.0	0.75	564	6	568	7	585	21	96	h
a409	9708	2827	233	0.03	1.46	0.08791	1.2	0.7677	3.1	0.06333	2.8	0.40	543	6	578	14	719	60	75	h
a411	20441	12245	668	0.03	0.97	0.05878	1.3	0.4209	4.6	0.05193	4.4	0.28	368	5	357	14	282	101	131	h
a412	26200	8761	691	0.12	b.d.	0.08397	1.1	0.6746	1.5	0.05826	1.0	0.75	520	6	524	6	540	22	96	h
a413	66076	16127	1413	0.08	1.45	0.08979	1.2	0.8873	2.3	0.07167	2.0	0.53	554	7	645	11	977	40	57	h
a415	42078	12769	1039	0.08	b.d.	0.08720	1.3	0.7041	1.4	0.05856	0.6	0.91	539	7	541	6	551	12	98	h
a416	14562	4129	357	0.16	0.13	0.09016	1.2	0.7724	1.8	0.06213	1.3	0.69	557	7	581	8	679	28	82	r
a418	370749	38397	3552	0.03	15.05	0.06457	3.2	1.5990	8.3	0.17961	7.6	0.39	403	12	970	53	2649	127	15	c
a419	73317	14438	773	0.04	5.39	0.04460	2.7	0.7015	5.6	0.11408	4.9	0.48	281	7	540	24	1865	88	15	r
a420	41327	12131	1014	0.09	0.47	0.08868	1.1	0.7542	1.5	0.06169	1.0	0.75	548	6	571	6	663	21	83	c
a421	10342	2895	243	0.29	b.d.	0.08554	1.3	0.7067	2.2	0.05992	1.8	0.58	529	7	543	9	601	39	88	r
a422	24826	3808	569	0.31	0.12	0.15162	1.2	1.4683	1.4	0.07024	0.8	0.83	910	10	917	9	935	16	97	c
a423	41471	13484	1073	0.08	b.d.	0.08541	1.1	0.6907	1.6	0.05865	1.1	0.70	528	6	533	6	554	24	95	r
a424	15728	4579	393	0.18	0.84	0.08902	1.3	0.7717	2.3	0.06287	1.9	0.57	550	7	581	10	704	41	78	h
a425	28280	10216	515	0.09	1.39	0.05049	1.6	0.4909	2.6	0.07051	2.1	0.61	318	5	405	9	943	42	34	h
a428	78213	32846	1444	0.03	0.55	0.04501	1.5	0.4216	2.6	0.06792	2.2	0.58	284	4	357	8	866	45	33	c
a429	81284	51054	1835	0.00	3.45	0.03729	1.4	0.3794	5.0	0.07380	4.8	0.28	236	3	327	14	1036	97	23	r
CHA15-49 Le Mourio syntectonic granite																				
a432	37958	17346	760	0.42	4.21	0.03944	1.5	0.4911	7.0	0.09031	6.8	0.21	249	4	406	24	1432	131	17	h
a434	13876	8543	413	0.45	0.42	0.04839	1.3	0.3546	2.4	0.05314	1.9	0.56	305	4	308	6	335	44	91	h
a444	31791	14044	769	0.27	0.63	0.05746	1.3	0.4229	3.3	0.05338	3.0	0.40	360	5	358	10	345	68	104	h
a447	101961	6009	573	0.17	39.61	0.04155	6.8	2.7698	24.8	0.48353	23.8	0.28	262	18	1347	204	4192	352	6	h
a450	20475	5065	613	1.47	0.38	0.10048	1.3	0.9228	1.7	0.06661	1.1	0.76	617	8	664	8	825	23	75	r1
a451	13321	2163	213	0.54	0.71	0.10158	1.3	0.8969	2.0	0.06404	1.4	0.69	624	8	650	9	743	30	84	r2
a452	139735	6404	2392	1.13	0.17	0.26862	1.7	4.3907	1.8	0.11855	0.5	0.96	1534	23	1711	15	1934	8	79	h
a453	10037	1982	271	0.77	0.55	0.12745	1.3	1.1504	2.1	0.06546	1.6	0.64	773	10	777	11	789	33	98	c
a454	28581	6737	332	0.06	6.13	0.04570	2.6	0.6450	8.1	0.10235	7.7	0.32	288	7	505	33	1667	142	17	r
a455	94628	28494	2438	0.00	0.90	0.08102	1.5	0.7428	2.3	0.06650	1.7	0.66	502	7	564	10	822	36	61	c
a457	18727	3457	465	0.31	b.d.	0.13471	1.2	1.2554	1.6	0.06759	1.0	0.76	815	9	826	9	856	21	95	h

Table B7 (continued): Results of LA-ICP-MS zircon U–Pb analyses performed during the sessions at GUF, 2nd and 3rd of May, 2016

Spot size = 20 and 30µm; depth of crater ~20µm. $^{206}Pb/^{238}U$ error is the quadratic additions of the within run precision (2 SE)

and the external reproducibility (2 SD) of the reference zircon.

$^{207}Pb/^{206}Pb$ error propagation (^{207}Pb signal dependent) following Gerdes & Zeh (2009). $^{207}Pb/^{235}U$ error is the quadratic addition of the $^{207}Pb/^{206}Pb$ and $^{206}Pb/^{238}U$ uncertainty.

[a]Within run background-corrected mean ^{207}Pb signal in cps (counts per second).

[b] U and Pb content and Th/U ratio were calculated relative to GJ-1 reference zircon.

[c] percentage of the common Pb on the ^{206}Pb. b.d. = below dectection limit.

[d] corrected for background, within-run Pb/U fractionation (in case of $^{206}Pb/^{238}U$), common Pb using Stacy and Kramers (1975) model Pb composition (specified by a *,

see text for discussion) and subsequently normalised to GJ-1 (ID-TIMS value/measured value); $^{207}Pb/^{235}U$ calculated using $^{207}Pb/^{206}Pb/(^{238}U/^{206}Pb*1/137.88)$

[e] rho is the $^{206}Pb/^{238}U/^{207}Pb/^{235}U$ error correlation coefficient.

[f] degree of concordance = $^{206}Pb/^{238}U$ age / $^{207}Pb/^{206}Pb$ age x 100

[g] Zone of the grain on which the analysis was performed. C: core; r(1 or 2): rim (internal or external corona); h: grain devoid of core-rim relationship.

Table B8: Results of LA-ICP-MS zircon U–Pb analyses performed during the session at SUN, 26th of October, 2016

grain	$^{207}Pb^{a}$ (cps)	U^{b} (ppm)	Pb^{b} (ppm)	$\frac{Th^{b}}{U}$	$\frac{^{206}Pb^{a}}{^{238}U}$	±2σ (%)	$\frac{^{207}Pb^{a}}{^{235}U}$	±2σ (%)	$\frac{^{207}Pb^{a}}{^{206}Pb}$	±2σ (%)	rho[e]	$\frac{^{206}Pb}{^{238}U}$	±2σ (Ma)	$\frac{^{207}Pb}{^{235}U}$	±2σ (Ma)	$\frac{^{207}Pb}{^{206}Pb}$	±2σ (Ma)	conc.[f] (%)
RV-3 Riverie biotite granite																		
b133	9547	5346	270	0.05	0.05322	1.9	0.43795	2.7	0.05968	2.0	0.69	334	6	369	8	592	43	56
b134	17491	10619	577	0.28	0.05386	1.7	0.39825	1.9	0.05363	0.8	0.89	338	6	340	5	356	19	95
b135	21528	12899	642	0.03	0.05179	1.7	0.48040	3.8	0.06727	3.4	0.46	326	6	398	13	846	71	38
b136	30319	18140	993	0.32	0.05318	1.8	0.40612	2.2	0.05539	1.3	0.82	334	6	346	7	428	28	78
b137	34427	12520	652	0.30	0.04984	2.3	0.46997	6.3	0.06839	5.9	0.36	314	7	391	21	880	121	36
b140	32621	13748	794	0.38	0.05452	1.8	0.46328	6.0	0.06163	5.7	0.31	342	6	387	19	661	122	52
b141	27023	10112	545	0.04	0.05016	2.1	0.67139	20.8	0.09708	20.7	0.10	315	6	522	89	1569	388	20
b142	18185	7554	385	0.07	0.04739	2.4	0.61713	7.9	0.09445	7.5	0.30	298	7	488	31	1517	142	20
b143	11500	4770	232	0.04	0.04415	2.2	0.67102	21.7	0.11023	21.6	0.10	278	6	521	93	1803	393	15
b144	26509	16532	828	0.15	0.05127	1.8	0.40072	2.4	0.05669	1.5	0.77	322	6	342	7	479	33	67
b145	35042	16000	755	0.07	0.04497	1.7	0.50418	2.3	0.08132	1.6	0.74	284	5	415	8	1229	31	23
b146	16647	9957	493	0.03	0.05283	1.9	0.41763	2.4	0.05734	1.4	0.79	332	6	354	7	505	31	66
b147	18089	11390	580	0.03	0.05409	1.9	0.44179	2.5	0.05924	1.7	0.75	340	6	372	8	576	36	59
b148	32796	20805	1052	0.13	0.05284	1.9	0.39738	2.4	0.05455	1.5	0.79	332	6	340	7	394	34	84
b149	25554	12004	714	0.49	0.05170	1.8	0.51814	2.3	0.07269	1.4	0.80	325	6	424	8	1005	28	32
b151	35034	24038	1128	0.08	0.04954	2.1	0.37016	2.2	0.05419	0.9	0.92	312	6	320	6	379	19	82
b158	27184	18222	863	0.08	0.04800	1.8	0.48788	2.3	0.07371	1.5	0.77	302	5	403	8	1034	30	29
b159	26522	15845	761	0.07	0.05043	2.2	0.40872	3.3	0.05878	2.5	0.67	317	7	348	10	559	54	57
b160	11551	5050	302	0.08	0.06263	2.6	0.50215	3.0	0.05815	1.5	0.87	392	10	413	10	535	32	73
b161	31200	18439	868	0.06	0.04958	1.9	0.38801	2.6	0.05675	1.8	0.74	312	6	333	7	482	39	65
b162	72383	43491	2201	0.04	0.05441	1.9	0.41133	2.0	0.05483	0.8	0.92	342	6	350	6	405	18	84
b163	51294	37384	1851	0.03	0.05363	1.7	0.39755	1.9	0.05376	0.8	0.90	337	6	340	5	361	18	93
b164	65853	41061	2227	0.37	0.05008	2.0	0.41461	2.4	0.06004	1.3	0.84	315	6	352	7	605	27	52
b165	46084	22763	1273	0.35	0.05383	2.1	0.41053	2.6	0.05531	1.6	0.79	338	7	349	8	425	36	80
b166	26224	16582	821	0.20	0.05033	2.1	0.39778	2.4	0.05732	1.2	0.86	317	6	340	7	504	27	63
b167	21739	14501	708	0.20	0.04932	1.7	0.36667	2.4	0.05392	1.7	0.70	310	5	317	7	368	39	84
b168	23900	12411	644	0.03	0.05386	2.0	0.49141	3.3	0.06617	2.6	0.62	338	7	406	11	812	54	42
b169	24605	10394	524	0.07	0.05345	1.9	0.40502	2.3	0.05496	1.3	0.82	336	6	345	7	411	29	82
b171	16701	11324	548	0.25	0.04814	2.1	0.36794	2.6	0.05543	1.4	0.83	303	6	318	7	430	31	71
b174	30654	22394	1122	0.14	0.05181	1.9	0.40307	2.1	0.05643	1.0	0.87	326	6	344	6	469	23	69
b175	53276	30263	1526	0.04	0.05198	1.9	0.47370	2.3	0.06610	1.3	0.82	327	6	394	8	809	28	40
b176	27421	16353	812	0.08	0.05065	1.7	0.45860	2.5	0.06566	1.8	0.69	319	5	383	8	796	38	40
b177	67155	49422	1970	0.08	0.04128	2.1	0.33793	2.3	0.05938	1.1	0.88	261	5	296	6	581	24	45
b178	21227	12864	633	0.10	0.05129	1.7	0.41470	2.3	0.05864	1.5	0.75	322	5	352	7	554	33	58
b179	28950	16928	851	0.07	0.05274	1.8	0.42438	2.1	0.05835	1.1	0.84	331	6	359	6	543	24	61
b180	30017	18535	901	0.12	0.05049	2.4	0.38720	2.7	0.05562	1.2	0.90	318	7	332	8	437	26	73
b181	43885	21811	1044	0.07	0.04750	1.9	0.48952	2.7	0.07475	1.9	0.72	299	6	405	9	1062	38	28
b182	22867	7214	419	0.08	0.05330	2.0	0.64497	4.5	0.08777	4.0	0.46	335	7	505	18	1377	77	24
b183	15901	8369	413	0.09	0.05174	1.9	0.40435	3.0	0.05668	2.4	0.61	325	6	345	9	479	53	68
b184	11243	5084	265	0.05	0.05207	1.8	0.51151	7.0	0.07125	6.7	0.26	327	6	419	24	964	137	34
b185	21559	8955	656	0.24	0.07262	1.7	0.61222	2.2	0.06114	1.4	0.78	452	7	485	8	644	29	70
b186	20081	9821	565	0.10	0.05982	1.8	0.46361	2.0	0.05621	1.0	0.87	375	6	387	6	461	22	81
b187	37241	18463	910	0.06	0.05028	1.8	0.46096	3.1	0.06649	2.5	0.59	316	6	385	10	822	52	38
b188	19084	15813	776	0.06	0.05161	2.0	0.44532	2.8	0.06258	1.9	0.72	324	6	374	9	694	41	47
b191	24835	21106	1051	0.03	0.05398	1.8	0.40150	2.1	0.05395	1.0	0.87	339	6	343	6	369	23	92
b192	10549	4862	259	0.10	0.05199	2.1	0.53418	3.1	0.07452	2.3	0.67	327	7	435	11	1056	46	31

Table B8 (cont.): Results of LA-ICP-MS zircon U–Pb analyses performed during the session at SUN, 26th of October, 2016

grain	^{207}Pb[a] (cps)	U[b] (ppm)	Pb[b] (ppm)	Th[b]/U	^{206}Pb[d]/^{238}U	±2σ (%)	^{207}Pb[d]/^{235}U	±2σ (%)	^{207}Pb[d]/^{206}Pb	±2σ (%)	rho[e]	^{206}Pb/^{238}U	±2σ (Ma)	^{207}Pb/^{235}U	±2σ (Ma)	^{207}Pb/^{206}Pb	±2σ (Ma)	conc.[f] (%)
b193	14110	8071	385	0.06	0.05059	1.9	0.40846	2.3	0.05856	1.4	0.81	318	6	348	7	551	30	58
b194	111082	77519	3801	0.03	0.05323	1.9	0.39008	2.0	0.05315	0.5	0.96	334	6	334	6	335	12	100
b195	10084	6195	343	0.07	0.05868	1.8	0.45569	2.9	0.05632	2.3	0.62	368	6	381	9	465	50	79
b196	18257	10403	542	0.12	0.05369	2.2	0.43829	2.7	0.05921	1.6	0.80	337	7	369	8	575	35	59
b197	25485	14224	695	0.08	0.05150	1.9	0.42028	2.3	0.05919	1.3	0.81	324	6	356	7	574	29	56
b198	36718	20512	987	0.04	0.04926	1.8	0.45842	2.2	0.06750	1.3	0.81	310	5	383	7	853	26	36
b199	12502	7521	380	0.04	0.05352	1.8	0.43336	2.4	0.05872	1.6	0.74	336	6	366	7	557	35	60

Spot size = 30µm; depth of crater ~20µm. $^{206}Pb/^{238}U$ error is the quadratic additions of the within run precision (2 SE) and the external reproducibility (2 SD) of the reference zircon.

$^{207}Pb/^{206}Pb$ error propagation (^{207}Pb signal dependent) following Gerdes & Zeh (2009). $^{207}Pb/^{235}U$ error is the quadratic addition of the $^{207}Pb/^{206}Pb$ and $^{206}Pb/^{238}U$ uncertainty.

[a]Within run background-corrected mean ^{207}Pb signal in cps (counts per second).

[b] U and Pb content and Th/U ratio were calculated relative to GJ-1 reference zircon.

[c] corrected for background, within-run Pb/U fractionation (in case of $^{206}Pb/^{238}U$) and subsequently normalised to GJ-1 (ID-TIMS value/measured value);

$^{207}Pb/^{235}U$ calculated using $^{207}Pb/^{206}Pb/(^{238}U/^{206}Pb*1/137.88)$

[d] rho is the $^{206}Pb/^{238}U/^{207}Pb/^{235}U$ error correlation coefficient.

[e] degree of concordance = $^{206}Pb/^{238}U$ age / $^{207}Pb/^{206}Pb$ age x 100

Table B9: Results of LA-ICP-MS zircon U–Pb analyses performed during the sessions at ETH Zürich, 12 to 14th of February, 2017

grain	^{207}Pb[a] (cps)	U[b] (ppm)	Pb[b] (ppm)	Th[b]/U	$^{207}Pb/^{235}U$[c]	±2σ (abs)	$^{206}Pb/^{238}U$[c]	±2σ (abs)	rho[d]	$^{207}Pb/^{206}Pb$[c]	±2σ (abs)	$^{207}Pb/^{235}U$ (Ma)	±2σ	$^{206}Pb/^{238}U$ (Ma)	±2σ	$^{207}Pb/^{206}Pb$ (Ma)	±2σ	conc.[e] (%)
Seq. 1																		
BOR-16-01 Borne porphyritic granite																		
BOR16_01_1	1065	136	310	0.55	0.3570	0.0110	0.04917	0.00043	0.12	0.05320	0.00170	310	9	309	3	315	71	98
BOR16_01_2	3170	309	928	0.63	0.4890	0.0210	0.04956	0.00050	0.48	0.07190	0.00280	406	14	312	3	965	81	32
BOR16_01_3	19400	1313	5780	0.64	0.7119	0.0093	0.08789	0.00082	0.76	0.05859	0.00051	546	5	543	5	551	19	99
BOR16_01_4	1543	233	497	0.57	0.3580	0.0110	0.04812	0.00061	0.27	0.05440	0.00160	310	8	303	4	382	64	79
BOR16_01_5	11670	1528	2504	0.39	0.3701	0.0086	0.04952	0.00089	0.74	0.05401	0.00085	319	6	312	6	365	35	85
BOR16_01_6	33900	4940	5110	0.22	0.3245	0.0074	0.03324	0.00063	0.92	0.07054	0.00069	286	6	211	4	942	20	22
BOR16_01_7	4310	704	449	0.19	0.3590	0.0110	0.04970	0.00092	0.47	0.05240	0.00150	311	8	313	6	299	62	105
BOR16_01_8	8490	1312	1008	0.21	0.3646	0.0080	0.04940	0.00038	0.27	0.05360	0.00110	316	6	311	2	359	47	87
BOR16_01_9	2650	352	1160	0.83	0.3599	0.0064	0.04947	0.00036	0.22	0.05285	0.00089	312	5	311	2	320	39	97
BOR16_01_11	26340	3510	2540	0.17	0.3954	0.0063	0.05127	0.00062	0.68	0.05601	0.00072	338	5	322	4	455	28	71
BOR16_01_12	3340	398	707	0.39	0.3591	0.0090	0.05021	0.00031	0.28	0.05170	0.00110	311	7	316	2	265	51	119
BOR16_01_14	10630	670	2850	0.49	0.9100	0.1000	0.05300	0.00100	0.92	0.12000	0.01100	629	52	333	6	1750	170	19
BOR16_01_15	2509	321	773	0.57	0.3800	0.0085	0.04960	0.00042	0.35	0.05560	0.00100	327	6	312	3	430	43	73
BOR16_01_17	6960	650	2035	0.56	0.5760	0.0170	0.05005	0.00041	0.21	0.08310	0.00240	462	11	315	3	1276	54	25
BOR16_01_19	6450	495	620	0.20	0.6242	0.0077	0.07909	0.00048	0.27	0.05767	0.00073	492	5	491	3	520	28	94
BOR16_01_20	7500	1040	3490	0.90	0.3627	0.0094	0.04451	0.00050	0.25	0.05890	0.00150	315	7	281	3	554	56	51
BOR16_01_21	2717	383	1023	0.71	0.3543	0.0078	0.04915	0.00033	0.26	0.05210	0.00110	308	6	309	2	281	50	110
BOR16_01_22	43000	6880	7020	0.28	0.3454	0.0058	0.04376	0.00043	0.84	0.05759	0.00062	301	4	276	3	513	23	54
BOR16_01_23	3166	502	1058	0.60	0.3541	0.0088	0.04891	0.00034	0.00	0.05280	0.00140	308	7	308	2	314	60	98
BOR16_01_24	4930	756	1564	0.57	0.3622	0.0082	0.04905	0.00046	0.05	0.05380	0.00130	314	6	309	3	368	52	84
BOR16_01_25	14300	950	302	0.05	0.7193	0.0110	0.08884	0.00099	0.71	0.05862	0.00065	551	6	549	6	550	24	100
BOR16_01_26	1820	256	642	0.65	0.3507	0.0083	0.04913	0.00065	0.34	0.05160	0.00110	305	6	309	4	273	46	113
BOR16_01_27	9740	1154	1025	0.20	0.3633	0.0060	0.04931	0.00045	0.24	0.05305	0.00093	315	5	310	3	328	40	95
BOR16_01_28	24950	3330	2460	0.15	0.3515	0.0042	0.04411	0.00031	0.61	0.05792	0.00057	306	3	278	2	525	22	53
BOR16_01_29	2951	391	1449	0.94	0.3587	0.0067	0.04900	0.00033	0.19	0.05295	0.00094	311	5	308	2	324	41	95
BOR16_01_30	30400	4500	1670	0.09	0.3749	0.0068	0.04955	0.00091	0.60	0.05530	0.00110	323	5	312	6	422	43	74
BOR16_01_31	29500	3670	13500	0.87	0.3814	0.0044	0.04954	0.00040	0.65	0.05582	0.00051	328	3	312	3	444	20	70
BOR16_01_32	7090	1040	1341	0.35	0.3528	0.0049	0.04797	0.00030	0.44	0.05338	0.00071	307	4	302	2	342	30	88
BOR16_01_33	17800	2520	1860	0.18	0.3677	0.0053	0.04962	0.00057	0.57	0.05376	0.00068	318	4	312	4	362	28	86
BOR16_01_35	7040	832	4510	1.18	0.3685	0.0051	0.04935	0.00036	0.37	0.05407	0.00079	319	4	311	2	371	33	84
BOR16_01_37	4200	610	1821	0.84	0.3622	0.0064	0.04920	0.00035	0.12	0.05356	0.00097	314	5	310	2	348	41	89
BOR16_01_38	19350	2230	2490	0.13	0.5140	0.0360	0.05222	0.00054	0.64	0.07080	0.00430	420	24	328	3	930	120	35
BOR16_01_39	3455	416	1161	0.61	0.3862	0.0065	0.05232	0.00042	0.28	0.05361	0.00086	332	5	329	3	356	35	92
BOR16_01_40	2599	371	728	0.51	0.3428	0.0059	0.04708	0.00036	0.26	0.05280	0.00096	299	5	297	2	312	41	95
BOR16_01_41	59200	8520	5340	0.12	0.3726	0.0071	0.04425	0.00053	0.79	0.06079	0.00084	322	5	279	3	630	30	44
BOR16_01_42	50900	3589	13400	0.52	0.8050	0.0750	0.05359	0.00085	0.24	0.10920	0.00970	597	42	337	5	1760	160	19
BOR16_01_43	39640	4080	3830	0.06	0.5033	0.0085	0.05055	0.00032	0.05	0.07260	0.00130	414	6	318	2	997	36	32
BOR16_01_44	3000	390	1266	0.74	0.3715	0.0072	0.05137	0.00034	0.13	0.05245	0.00100	321	5	323	2	297	43	109
BOR16_01_45	58600	4090	13930	0.39	0.6950	0.0130	0.05147	0.00072	0.39	0.09800	0.00200	537	8	324	4	1596	35	20
BOR16_01_46	1977	257	745	0.63	0.3966	0.0092	0.04940	0.00055	0.42	0.05810	0.00120	340	7	311	3	529	46	59
BOR16_01_47	16110	2280	10030	1.13	0.3819	0.0059	0.05227	0.00044	0.35	0.05300	0.00083	328	4	328	3	326	35	101
BOR16_01_48	37060	1987	2367	0.06	0.8666	0.0094	0.09251	0.00055	0.64	0.06799	0.00061	634	5	570	3	869	19	66
BOR16_01_49	2490	294	1450	1.09	0.3540	0.0120	0.04920	0.00064	0.22	0.05270	0.00190	310	10	310	4	305	79	102
BOR16_01_50	3440	463	1181	0.60	0.3774	0.0070	0.04943	0.00039	0.44	0.05523	0.00090	325	5	311	2	421	37	74
BOR16_01_51	4190	586	1411	0.63	0.3602	0.0060	0.04934	0.00040	0.40	0.05297	0.00079	312	5	310	3	327	34	95
BOR16_01_52	27900	5150	4790	0.31	0.2838	0.0041	0.03378	0.00036	0.79	0.06130	0.00061	254	3	214	2	649	21	33

Table B9 (continued): Results of LA-ICP-MS zircon U–Pb analyses performed during the sessions at ETH Zürich, 12 to 14th of February, 2017

grain	^{207}Pb[a] (cps)	U[b] (ppm)	Pb[b] (ppm)	Th[b]/U	$^{207}Pb/^{235}U$[c]	±2σ (abs)	$^{206}Pb/^{238}U$[c]	±2σ (abs)	rho[d]	$^{207}Pb/^{206}Pb$[c]	±2σ (abs)	$^{207}Pb/^{235}U$	±2σ (Ma)	$^{206}Pb/^{238}U$	±2σ (Ma)	$^{207}Pb/^{206}Pb$	±2σ (Ma)	conc.[e] (%)
CHA-15-25 Le Ranc syntectonic granite																		
CHA15_25_1	9030	475	837	0.09	0.9260	0.0360	0.08850	0.00110	0.19	0.07720	0.00280	662	19	547	6	1092	72	50
CHA15_25_2	7660	465	308	0.08	0.7140	0.0130	0.08777	0.00087	0.59	0.05901	0.00090	547	8	542	5	565	33	96
CHA15_25_3	7930	535	470	0.09	0.8010	0.0170	0.09097	0.00093	0.57	0.06370	0.00150	597	10	561	6	726	48	77
CHA15_25_4	75860	6970	7250	0.02	0.6110	0.0140	0.05281	0.00047	0.75	0.08510	0.00130	484	9	332	3	1318	30	25
CHA15_25_5	82700	8600	7600	0.01	0.6500	0.1200	0.04950	0.00410	0.94	0.09240	0.00900	501	68	311	25	1440	180	22
CHA15_25_6	3690	255	189	0.11	0.7210	0.0110	0.08882	0.00069	0.37	0.05851	0.00089	551	7	549	4	551	34	100
CHA15_25_7	188000	29300	3950	0.01	0.2910	0.0120	0.03720	0.00150	0.91	0.05656	0.00078	259	9	236	9	481	29	49
CHA15_25_8	10220	668	328	0.07	0.7480	0.0120	0.09164	0.00068	0.47	0.05944	0.00078	567	7	565	4	583	29	97
CHA15_25_9	27400	820	5300	0.07	1.3480	0.0920	0.05820	0.00100	0.35	0.17300	0.01500	864	39	365	6	2640	160	14
CHA15_25_10	148000	8140	27100	0.00	0.9330	0.0460	0.03767	0.00041	0.41	0.17930	0.00810	664	24	238	3	2612	73	9
CHA15_25_11	4750	322	569	0.22	0.7350	0.0150	0.08990	0.00130	0.67	0.05904	0.00090	559	9	555	8	563	33	99
CHA15_25_12	3001	337	780	0.50	0.3800	0.0120	0.05036	0.00057	0.49	0.05480	0.00130	329	9	317	4	400	51	79
CHA15_25_13	133000	9520	24900	0.14	0.7540	0.0180	0.03314	0.00029	0.54	0.16580	0.00370	570	11	210	2	2518	39	8
CHA15_25_14	18900	1294	1520	0.07	0.6670	0.0260	0.06860	0.00140	0.95	0.07070	0.00160	517	15	427	8	939	44	46
CHA15_25_15	16200	1158	555	0.04	0.7520	0.0150	0.08539	0.00064	0.24	0.06380	0.00120	569	9	528	4	730	40	72
CHA15_25_16	662000	32700	113000	0.05	0.9830	0.0650	0.05230	0.00170	0.56	0.13600	0.00730	693	33	328	11	2164	99	15
CHA15_25_17	27420	2247	765	0.05	0.7020	0.0120	0.08720	0.00120	0.51	0.05954	0.00091	540	7	539	7	586	33	92
CHA15_25_18	36900	2850	968	0.02	0.7410	0.0130	0.08590	0.00110	0.83	0.06193	0.00069	563	7	531	6	671	24	79
CHA15_25_19	21500	1380	725	0.04	0.7690	0.0200	0.08880	0.00120	0.68	0.06230	0.00110	578	12	548	7	676	38	81
CHA15_25_20	119000	4260	21030	0.08	1.5280	0.0730	0.07050	0.00130	0.52	0.15950	0.00600	939	29	439	8	2455	61	18
CHA15_25_21	28500	1630	1720	0.03	0.8510	0.0230	0.08585	0.00043	0.64	0.07150	0.00180	624	13	531	3	960	54	55
CHA15_25_22	11020	705	520	0.05	0.7770	0.0150	0.08884	0.00095	0.53	0.06318	0.00093	583	8	549	6	711	31	77
CHA15_25_23	4580	202	944	0.26	1.1090	0.0560	0.09750	0.00190	0.89	0.08320	0.00280	751	25	599	11	1247	62	48
CHA15_25_24	571000	67000	26000	0.02	0.4230	0.0130	0.04930	0.00170	0.69	0.06080	0.00160	360	10	310	10	636	58	49
CHA15_25_25	129000	6640	26420	0.06	1.1930	0.0520	0.04140	0.00120	0.51	0.21100	0.00790	797	24	261	8	2912	60	9
CHA15_25_26	102000	10900	8650	0.01	0.4580	0.0350	0.04060	0.00260	0.59	0.07990	0.00460	378	25	256	16	1190	120	22
CHA15_25_27	8180	566	2340	0.64	0.7920	0.0150	0.09618	0.00083	0.42	0.05950	0.00120	592	9	592	5	595	41	99
CHA15_25_28	43300	2560	4390	0.03	0.8170	0.0170	0.06780	0.00140	0.49	0.08730	0.00210	608	10	423	8	1358	47	31
CHA15_25_29	58500	3450	6860	0.07	0.8330	0.0240	0.06290	0.00260	0.60	0.09650	0.00350	616	13	393	16	1555	72	25
CHA15_25_30	22800	1357	3750	0.32	0.7840	0.0150	0.08801	0.00056	0.39	0.06490	0.00120	588	9	544	3	762	38	71
CHA15_25_31	49100	3770	800	0.19	0.7314	0.0084	0.08841	0.00100	0.47	0.06000	0.00070	557	5	546	6	603	25	91
CHA15_25_33	15380	945	333	0.05	0.7103	0.0090	0.08826	0.00054	0.46	0.05837	0.00066	545	5	545	3	542	25	101
CHA15_25_35	4480	333	360	0.16	0.7250	0.0160	0.08894	0.00093	0.30	0.05900	0.00120	555	9	549	6	562	46	98
CHA15_25_36	39600	3110	468	0.02	0.6796	0.0096	0.08305	0.00073	0.61	0.05909	0.00070	526	6	514	4	573	27	90
CHA15_25_37	21200	1480	392	0.04	0.7759	0.0092	0.09512	0.00077	0.47	0.05902	0.00052	583	5	586	5	567	19	103
CHA15_25_38	18800	1287	538	0.04	0.7320	0.0120	0.08754	0.00085	0.64	0.06076	0.00079	557	7	541	5	629	28	86
CHA15_25_39	48400	2825	3130	0.05	0.8530	0.0230	0.08821	0.00083	0.78	0.07040	0.00150	626	13	545	5	932	43	58
CHA15_25_40	4640	281	375	0.16	0.7170	0.0120	0.08820	0.00087	0.33	0.05861	0.00096	549	7	545	5	557	34	98
CHA15_25_41	130000	3540	24700	0.05	1.8860	0.0430	0.07750	0.00110	0.53	0.17570	0.00310	1075	15	481	7	2611	29	18
CHA15_25_42	16300	1040	681	0.07	0.7736	0.0092	0.09119	0.00054	0.39	0.06173	0.00067	582	5	563	3	665	23	85
CHA15_25_43	11200	339	1530	0.05	1.5060	0.0310	0.10330	0.00190	0.15	0.10550	0.00300	931	13	633	11	1705	55	37
CHA15_25_44	50300	1940	9340	0.05	1.5900	0.1800	0.05920	0.00130	0.92	0.19100	0.01800	936	74	371	8	2640	170	14
MM-03 Vivarais amphibolite																		
MM03_1	1127	133	59	0.07	0.3600	0.0240	0.04870	0.00110	0.08	0.05380	0.00360	311	18	307	7	340	150	90
MM03_2	1059	131	63	0.11	0.3590	0.0120	0.04887	0.00053	0.08	0.05310	0.00170	311	9	308	3	319	73	96

Table B9 (continued): Results of LA-ICP-MS zircon U–Pb analyses performed during the sessions at ETH Zürich, 12 to 14th of February, 2017

grain	^{207}Pb[a] (cps)	U[b] (ppm)	Pb[b] (ppm)	Th[b]/U	$^{207}Pb/^{235}U$[c]	±2σ (abs)	$^{206}Pb/^{238}U$[c]	±2σ (abs)	rho[d]	$^{207}Pb/^{206}Pb$[c]	±2σ (abs)	$^{207}Pb/^{235}U$	±2σ (Ma)	$^{206}Pb/^{238}U$	±2σ (Ma)	$^{207}Pb/^{206}Pb$	±2σ (Ma)	conc.[e] (%)
MM03_4	839	107	9	0.02	0.3640	0.0120	0.05051	0.00045	0.20	0.05280	0.00170	316	9	318	3	303	71	105
MM03_5	421	39	59	0.14	0.6120	0.0840	0.05170	0.00130	0.11	0.08600	0.01100	477	51	325	8	1230	240	26
MM03_6	1155	157	39	0.07	0.3636	0.0094	0.04883	0.00040	0.09	0.05380	0.00150	315	7	307	2	366	59	84
MM03_7	1376	170	47	0.06	0.3650	0.0120	0.04987	0.00036	0.03	0.05330	0.00170	316	9	314	2	337	68	93
MM03_8	12730	1133	4440	0.61	0.4975	0.0098	0.06167	0.00058	0.49	0.05832	0.00086	411	6	386	4	547	34	71
MM03_9	407	52	4	0.01	0.3760	0.0160	0.04931	0.00052	0.05	0.05550	0.00230	325	12	311	3	433	91	72
MM03_10	487	14	107	0.28	1.7300	0.1500	0.06340	0.00170	0.11	0.20100	0.01700	1022	56	396	11	2810	140	14
MM03_11	739	84	104	0.22	0.4430	0.0260	0.05142	0.00085	0.20	0.06320	0.00320	375	17	323	5	719	96	45
MM03_12	8660	893	3440	0.48	0.4370	0.0068	0.05700	0.00036	0.41	0.05575	0.00077	368	5	357	2	443	30	81
MM03_13	6284	420	3663	1.25	0.7320	0.0170	0.08710	0.00170	0.84	0.06141	0.00077	557	10	538	10	650	27	83
MM03_14	1163	156	26	0.04	0.3660	0.0110	0.04882	0.00044	0.23	0.05490	0.00150	318	8	307	3	395	61	78
MM03_15	16620	1758	17100	1.90	0.5540	0.0230	0.06970	0.00170	0.72	0.05850	0.00170	447	15	434	10	543	63	80
MM03_16	11760	1401	6190	0.69	0.4730	0.0110	0.06034	0.00067	0.80	0.05668	0.00090	393	8	378	4	477	35	79
MM03_17	11560	1021	8000	1.16	0.4956	0.0086	0.06166	0.00062	0.56	0.05864	0.00086	409	6	386	4	550	32	70
MM03_19	2181	268	221	0.13	0.4470	0.0160	0.04897	0.00056	0.18	0.06680	0.00250	375	11	308	3	816	79	38
MM03_20	1427	190	45	0.06	0.3530	0.0085	0.04895	0.00038	0.40	0.05230	0.00110	307	6	308	2	287	48	107
MM03_21	17300	1690	10300	1.04	0.6200	0.0210	0.07560	0.00280	0.90	0.06020	0.00110	489	13	470	17	610	38	77
MM03_22	11310	1188	3010	0.45	0.4430	0.0130	0.05531	0.00046	0.31	0.05800	0.00160	373	9	347	3	526	59	66
MM03_23	416	58	6	0.02	0.3560	0.0150	0.04834	0.00065	0.04	0.05300	0.00220	308	12	304	4	325	91	94
MM03_24	317	45	9	0.02	0.3740	0.0190	0.05011	0.00080	0.22	0.05440	0.00250	322	14	315	5	390	110	81
MM03_25	1759	43	375	0.19	1.9240	0.0740	0.06458	0.00100	0.58	0.21490	0.00660	1083	26	403	6	2926	50	14
MM03_26	831	45	149	0.04	0.8640	0.0500	0.04898	0.00096	0.50	0.12610	0.00630	626	27	308	6	2011	95	15
ROC-16-01 Rocles syntectonic granite																		
ROC16-01 - 2	6500	829	2070	0.42	0.3692	0.0065	0.05120	0.00069	0.74	0.05201	0.00062	319	5	322	4	282	28	114
ROC16-01 - 5	7950	437	4770	1.26	0.9080	0.0280	0.10510	0.00150	0.66	0.06220	0.00150	656	15	644	9	692	46	93
ROC16-01 - 8	2221	290	553	0.46	0.3621	0.0070	0.04958	0.00039	0.25	0.05324	0.00097	314	5	312	2	334	42	93
ROC16-01 - 10	25000	2430	2610	0.04	0.6070	0.0280	0.05539	0.00090	0.80	0.08040	0.00250	481	18	348	6	1202	61	29
ROC16-01 - 11	17500	2198	1230	0.04	0.4620	0.0360	0.05117	0.00050	0.36	0.06620	0.00470	384	25	322	3	780	150	41
ROC16-01 - 12	20500	2800	802	0.03	0.3870	0.0070	0.04766	0.00050	0.88	0.05879	0.00081	332	5	300	3	557	30	54
ROC16-01 - 13	22150	2430	1810	0.07	0.4679	0.0093	0.05203	0.00070	0.56	0.06482	0.00100	391	7	327	4	770	35	42
ROC16-01 - 14	38300	2190	5860	0.06	0.7640	0.0280	0.05580	0.00250	0.46	0.10190	0.00430	575	16	350	15	1644	83	21
ROC16-01 - 15	60800	2166	12180	0.08	1.4170	0.0360	0.05666	0.00071	0.70	0.18420	0.00370	895	15	355	4	2687	32	13
ROC16-01 - 16	3670	480	978	0.49	0.3699	0.0068	0.05078	0.00050	0.49	0.05303	0.00082	319	5	319	3	328	34	97
ROC16-01 - 17	30810	1489	6140	0.07	1.1120	0.0160	0.04512	0.00031	0.46	0.17930	0.00250	759	8	285	2	2645	23	11
ROC16-01 - 19	21760	3148	14320	1.34	0.3974	0.0075	0.05196	0.00048	0.48	0.05584	0.00097	340	6	327	3	444	39	74
ROC16-01 - 20	6840	865	1620	0.38	0.4114	0.0095	0.05127	0.00050	0.75	0.05780	0.00110	350	7	322	3	513	41	63
ROC16-01 - 26	38710	4313	511	0.03	0.3738	0.0057	0.05122	0.00049	0.58	0.05306	0.00085	322	4	322	3	330	37	98
ROC16-01 - 32	16600	816	5420	0.92	1.0760	0.0930	0.05713	0.00043	0.55	0.13300	0.01000	736	44	358	3	2140	150	17
ROC16-01 - 33	12200	712	3920	0.81	0.9910	0.0970	0.05443	0.00076	0.81	0.13200	0.01200	695	47	342	5	2110	140	16
ROC16-01 - 34	26170	2791	1997	0.03	0.4639	0.0079	0.04642	0.00046	0.49	0.07232	0.00100	388	5	293	3	993	29	29
ROC16-01 - 35	8850	1232	680	0.11	0.4190	0.0170	0.05141	0.00053	0.57	0.05960	0.00200	355	12	323	3	585	73	55
ROC16-01 - 36	4790	594	461	0.12	0.3670	0.0180	0.04280	0.00032	0.05	0.06270	0.00320	316	13	270	2	660	110	41
ROC16-01 - 37	4570	617	522	0.18	0.3754	0.0067	0.05021	0.00030	0.32	0.05426	0.00098	324	5	316	2	375	40	84
ROC16-01 - 38	151000	6580	28300	0.04	1.1690	0.0270	0.05002	0.00055	0.55	0.17040	0.00340	785	12	315	3	2557	32	12
ROC16-01 - 41	8710	1208	944	0.18	0.3895	0.0085	0.05137	0.00062	0.61	0.05540	0.00100	334	6	323	4	424	42	76
ROC16-01 - 42	96000	2900	21600	0.14	1.4740	0.0650	0.04510	0.00066	0.23	0.24700	0.01200	914	26	284	4	3124	77	9
ROC16-01 - 43	33200	2104	4300	0.04	0.7050	0.0300	0.05401	0.00077	0.58	0.09390	0.00340	543	17	339	5	1489	66	23

Table B9 (continued): Results of LA-ICP-MS zircon U–Pb analyses performed during the sessions at ETH Zürich, 12 to 14th of February, 2017

grain	^{207}Pb[a] (cps)	U[b] (ppm)	Pb[b] (ppm)	Th[b]/U	$^{207}Pb/^{235}U$[c]	±2σ (abs)	$^{206}Pb/^{238}U$[c]	±2σ (abs)	rho[d]	$^{207}Pb/^{206}Pb$[c]	±2σ (abs)	$^{207}Pb/^{235}U$	±2σ (Ma)	$^{206}Pb/^{238}U$	±2σ (Ma)	$^{207}Pb/^{206}Pb$	±2σ (Ma)	conc.[e] (%)
ROC16-01 - 47	22900	771	6430	0.70	1.4000	0.0460	0.06115	0.00053	0.53	0.16560	0.00500	898	17	383	3	2513	50	15
ROC16-01 - 49	9790	1305	4420	0.86	0.3917	0.0064	0.05119	0.00037	0.24	0.05561	0.00082	336	4	322	2	445	36	72
ROC16-01 - 51	11730	1384	1610	0.19	0.4460	0.0110	0.04979	0.00058	0.03	0.06540	0.00190	375	8	313	4	786	61	40
ROC16-01 - 53	5320	312	6110	2.39	0.7820	0.0160	0.09128	0.00078	0.22	0.06200	0.00120	586	9	563	5	672	41	84
ROC16-01 - 56	5970	819	398	0.12	0.3716	0.0054	0.05099	0.00040	0.48	0.05254	0.00069	321	4	321	3	312	30	103
ROC16-01 - 58	13990	900	2293	0.06	0.6750	0.0110	0.04234	0.00028	0.27	0.11590	0.00180	523	7	267	2	1891	28	14
ROC16-01 - 60	77900	13150	1906	0.02	0.3184	0.0060	0.04169	0.00081	0.93	0.05608	0.00048	281	5	263	5	455	19	58
ROC16-01 - 61	5850	789	2240	0.63	0.3814	0.0072	0.05121	0.00050	0.58	0.05424	0.00082	328	5	322	3	377	34	85
ROC16-01 - 62	76000	1041	18700	0.41	3.0200	0.2400	0.06161	0.00097	0.69	0.35500	0.02500	1384	61	385	6	3640	110	11
ROC16-01 - 64	8570	643	1365	0.23	0.5690	0.0120	0.05485	0.00067	0.59	0.07630	0.00150	460	8	344	4	1098	39	31
ROC16-01 - 67	22640	1108	6230	0.41	1.0080	0.0340	0.03074	0.00029	0.16	0.23730	0.00790	705	17	195	2	3101	53	6
ROC16-01 - 68	52300	5370	6560	0.03	0.5020	0.0190	0.04190	0.00130	0.92	0.08810	0.00140	415	13	265	8	1383	31	19
ROC16-01 - 71	3534	485	1219	0.59	0.3500	0.0064	0.04826	0.00039	0.35	0.05257	0.00089	305	5	304	2	316	37	96
ROC16-01 - 73	82000	2660	17400	0.13	1.5700	0.1200	0.05176	0.00069	0.79	0.21700	0.01500	935	50	325	4	2900	120	11
ROC16-01 - 74	59800	3180	12000	0.09	0.9290	0.0450	0.03091	0.00082	0.50	0.21530	0.00640	662	24	196	5	2930	49	7
ROC16-01 - 75	22000	432	6120	0.77	2.2780	0.0990	0.06779	0.00059	0.51	0.24240	0.00950	1198	32	423	4	3114	66	14
ROC16-01 - 76	111000	6070	20000	0.01	0.8620	0.0450	0.03890	0.00120	0.25	0.16080	0.00820	625	25	246	7	2469	81	10
ROC16-01 - 78	40000	2221	7950	0.04	0.9900	0.0310	0.04004	0.00059	0.63	0.17930	0.00430	698	16	253	4	2644	39	10
ROC16-01 - 80	85000	9480	6550	0.05	0.4866	0.0082	0.05117	0.00084	0.75	0.06900	0.00110	403	6	322	5	902	33	36
ROC16-01 - 81	49900	6530	3060	0.04	0.4570	0.0130	0.05110	0.00090	0.47	0.06470	0.00150	382	9	321	6	763	50	42
ROC16-01 - 82	98000	9940	13900	0.01	0.4200	0.0400	0.03089	0.00051	0.59	0.10080	0.00980	349	27	196	3	1480	150	13
ROC16-01 - 83	35000	1180	6700	0.00	35.0000	11.0000	0.72000	0.23000	0.99	0.30400	0.01600	2440	390	2670	740	3437	90	78
ROC16-01 - 84	2800	146	870	0.66	0.8900	0.0200	0.10490	0.00150	0.71	0.06135	0.00094	645	11	643	9	650	34	99
ROC16-01 - 85	14510	1455	1489	0.06	0.5019	0.0087	0.04844	0.00030	0.34	0.07590	0.00130	413	6	305	2	1089	33	28
ROC16-01 - 86	69000	2340	16400	0.00	18.1000	4.4000	0.25300	0.06000	0.99	0.47600	0.01200	2300	290	1350	300	4159	35	32
ROC16-01 - 87	91500	3850	18200	0.08	1.3410	0.0650	0.05140	0.00130	0.60	0.18720	0.00630	862	28	323	8	2713	53	12
Seq. 2																		
PdB-16-01 Pont-de-Bayzan metasediment																		
PDB16_1	66600	1274	2020	0.17	1.1260	0.0170	0.12780	0.00150	0.73	0.06421	0.00063	766	8	775	9	748	21	104
PDB16_2	35470	561	1367	0.23	1.1920	0.0270	0.13390	0.00210	0.81	0.06436	0.00073	796	13	810	12	753	24	108
PDB16_3	70000	1316	2066	0.18	1.0850	0.0110	0.12300	0.00140	0.77	0.06388	0.00033	746	5	748	8	737	11	101
PDB16_4	3021	51	243	0.43	1.1680	0.0350	0.11858	0.00140	0.55	0.07210	0.00210	786	17	722	8	972	56	74
PDB16_5	69400	198	892	0.18	7.1460	0.0670	0.33030	0.00340	0.65	0.15705	0.00090	2129	8	1840	16	2424	10	76
PDB16_6	152500	352	5150	0.45	8.2990	0.0710	0.38720	0.00390	0.53	0.15517	0.00089	2264	8	2110	18	2403	10	88
PDB16_7	4148	88	746	0.94	0.9670	0.0140	0.11356	0.00120	0.34	0.06170	0.00080	687	7	693	7	666	28	104
PDB16_8	185000	639	1579	0.10	5.9350	0.0760	0.35710	0.00440	0.81	0.12067	0.00071	1966	11	1968	21	1966	10	100
PDB16_9	11150	249	1970	0.88	0.8989	0.0110	0.10616	0.00120	0.35	0.06152	0.00064	652	6	650	7	655	22	99
PDB16_10	25200	342	2000	0.48	1.4910	0.0140	0.15500	0.00170	0.63	0.06962	0.00045	927	6	929	9	918	13	101
PDB16_11	12320	282	1888	0.78	0.8738	0.0098	0.10390	0.00100	0.88	0.06096	0.00054	637	5	637	6	636	19	100
PDB16_12	6370	178	1133	0.90	0.8020	0.0180	0.09650	0.00160	0.59	0.06120	0.00120	598	10	594	9	644	43	92
PDB16_13	13110	299	1778	0.70	0.9160	0.0150	0.10719	0.00110	0.30	0.06188	0.00090	660	8	656	6	667	31	98
PDB16_14	119000	1345	29400	2.50	1.8400	0.1300	0.10520	0.00120	0.63	0.12790	0.00850	1058	47	645	7	2020	120	32
PDB16_15	4280	70	470	0.59	1.2100	0.0200	0.13209	0.00140	0.34	0.06666	0.00091	806	9	800	8	831	29	96
PDB16_16	10980	272	1329	0.60	0.8078	0.0096	0.09797	0.00100	0.59	0.06007	0.00054	602	5	603	6	604	19	100
PDB16_17	2371	58	383	0.85	0.8470	0.0160	0.10093	0.00110	0.21	0.06080	0.00110	624	8	620	6	638	39	97
PDB16_18	2331	40	125	0.27	1.1490	0.0220	0.12746	0.00140	0.27	0.06550	0.00120	778	10	773	8	781	37	99

Table B9 (continued): Results of LA-ICP-MS zircon U–Pb analyses performed during the sessions at ETH Zürich, 12 to 14th of February, 2017

grain	^{207}Pb[a] (cps)	U[b] (ppm)	Pb[b] (ppm)	Th[b]/U	$^{207}Pb/^{235}U$[c]	±2σ (abs)	$^{206}Pb/^{238}U$[c]	±2σ (abs)	rho[d]	$^{207}Pb/^{206}Pb$[c]	±2σ (abs)	$^{207}Pb/^{235}U$	±2σ (Ma)	$^{206}Pb/^{238}U$	±2σ (Ma)	$^{207}Pb/^{206}Pb$	±2σ (Ma)	conc.[e] (%)
PDB16_19	18960	337	1590	0.44	1.2030	0.0150	0.13283	0.00140	0.68	0.06619	0.00053	802	7	804	8	811	17	99
PDB16_20	20110	502	3012	0.76	0.8790	0.0150	0.10497	0.00120	0.65	0.06055	0.00053	640	8	643	7	623	19	103
PDB16_21	8160	182	953	0.58	0.9980	0.0210	0.11580	0.00160	0.41	0.06300	0.00130	702	11	706	9	706	43	100
PDB16_22	3590	92	360	0.50	0.8360	0.0170	0.10075	0.00110	0.47	0.06030	0.00110	618	10	619	6	621	38	100
PDB16_23	33280	561	3090	0.53	1.3120	0.0300	0.13460	0.00160	0.53	0.07100	0.00130	851	13	814	9	953	36	85
PDB16_24	3430	64	352	0.56	1.0860	0.0180	0.12285	0.00130	0.23	0.06440	0.00100	746	9	747	8	752	34	99
PDB16_25	9720	174	773	0.44	1.0900	0.0130	0.12272	0.00130	0.44	0.06461	0.00063	748	6	746	8	764	21	98
PDB16_26	132000	2641	5140	0.21	1.0990	0.0160	0.12368	0.00140	0.57	0.06479	0.00072	753	8	752	8	766	24	98
PDB16_27	5590	110	595	0.56	1.0860	0.0240	0.12330	0.00150	0.22	0.06390	0.00140	748	11	750	9	739	45	101
PDB16_28	2458	51	213	0.44	0.9290	0.0180	0.10640	0.00120	0.15	0.06330	0.00120	667	10	652	7	713	40	91
PDB16_29	7050	138	632	0.47	0.9890	0.0140	0.11254	0.00110	0.36	0.06353	0.00084	699	8	688	7	727	29	95
PDB16_30	15190	304	1115	0.40	1.0140	0.0120	0.11689	0.00120	0.53	0.06279	0.00056	711	6	713	7	699	19	102
PDB16_31	11880	166	1028	0.51	1.4320	0.0150	0.14846	0.00150	0.45	0.07036	0.00064	902	6	892	9	940	19	95
PDB16_32	23810	294	1475	0.33	1.6200	0.0190	0.16930	0.00190	0.76	0.06943	0.00040	979	8	1008	11	912	12	111
PDB16_33	11940	306	2395	1.03	0.8540	0.0110	0.10188	0.00130	0.35	0.06124	0.00058	628	6	625	7	652	23	96
PDB16_34	4170	90	415	0.56	1.0040	0.0180	0.11551	0.00130	0.18	0.06340	0.00110	706	9	705	7	716	37	98
PDB16_35	50000	1150	3910	0.40	0.9290	0.0150	0.10575	0.00120	0.67	0.06396	0.00067	667	8	648	7	742	23	87
PDB16_36	34000	671	4360	0.69	0.9920	0.0130	0.11490	0.00120	0.50	0.06238	0.00064	700	7	701	7	686	22	102
PDB16_37	3845	75	384	0.55	1.0950	0.0240	0.12310	0.00160	0.47	0.06460	0.00120	750	12	748	9	764	41	98
PDB16_38	16050	300	1417	0.49	1.1820	0.0270	0.12990	0.00180	0.65	0.06630	0.00110	792	13	787	10	820	32	96
PDB16_39	42100	641	3760	0.47	1.3310	0.0340	0.12627	0.00130	0.17	0.07610	0.00180	857	15	767	7	1089	48	70
PDB16_40	3660	75	514	0.75	1.0210	0.0190	0.11686	0.00130	0.14	0.06340	0.00100	715	9	712	8	729	35	98
PDB16_41	2826	43	328	0.64	1.3230	0.0250	0.14220	0.00170	0.22	0.06710	0.00120	856	11	857	10	842	38	102
PDB16_42	15810	419	2440	0.77	0.8010	0.0120	0.09697	0.00100	0.38	0.06018	0.00075	597	7	597	6	608	27	98
PDB16_43	40350	489	3470	0.54	1.6230	0.0140	0.16324	0.00160	0.59	0.07215	0.00041	980	6	975	9	989	12	99
PDB16_44	45860	636	3645	0.44	1.4820	0.0220	0.15040	0.00170	0.72	0.07139	0.00068	922	9	903	9	966	19	93
PDB16_45	36800	883	2781	0.41	0.9000	0.0120	0.10650	0.00120	0.58	0.06140	0.00057	652	6	652	7	652	20	100
PDB16_46	43700	781	4020	0.52	1.1087	0.0097	0.12523	0.00120	0.30	0.06404	0.00043	758	5	761	7	744	15	102
PDB16_47	12500	304	624	0.28	0.9180	0.0170	0.10889	0.00130	0.64	0.06135	0.00089	661	9	666	8	649	31	103
PDB16_48	18650	457	2113	0.60	0.8065	0.0100	0.09645	0.00099	0.45	0.06084	0.00061	600	6	594	6	632	22	94
PDB16_49	98800	1269	8770	0.56	1.5930	0.0210	0.14970	0.00160	0.81	0.07704	0.00053	967	8	899	9	1124	14	80
PDB16_50	43800	674	2741	0.38	1.3700	0.0150	0.14456	0.00150	0.86	0.06890	0.00046	876	6	870	8	895	14	97
PDB16_51	6540	155	446	0.36	0.8140	0.0150	0.09641	0.00100	0.45	0.06112	0.00090	606	9	593	6	640	32	93
PDB16_52	30430	673	2879	0.52	0.9019	0.0081	0.10692	0.00100	0.50	0.06117	0.00039	653	4	655	6	644	14	102
PDB16_53	11690	281	2336	1.07	0.8820	0.0120	0.10543	0.00130	0.45	0.06102	0.00070	642	7	646	7	643	24	100
PDB16_54	29800	659	2570	0.46	1.0450	0.0200	0.12020	0.00240	0.48	0.06380	0.00120	726	10	731	14	735	41	99
PDB16_55	2061	41	372	0.97	0.9950	0.0210	0.11514	0.00130	0.12	0.06310	0.00130	702	10	703	8	710	43	99
PDB16_56	21460	349	1990	0.53	1.3680	0.0490	0.12930	0.00190	0.61	0.07720	0.00230	874	21	784	11	1123	57	70
PDB16_57	102000	203	3590	0.55	10.0660	0.1100	0.46160	0.00570	0.92	0.15815	0.00075	2440	10	2446	25	2437	8	100
PDB16_58	72200	1620	27900	2.58	0.8980	0.0140	0.09436	0.00096	0.20	0.06880	0.00110	651	8	581	6	891	32	65
PDB16_59	16800	405	1572	0.48	0.8559	0.0100	0.10211	0.00110	0.39	0.06103	0.00065	629	6	627	6	642	23	98
PDB16_60	62950	1693	7820	0.65	0.8580	0.0170	0.10270	0.00150	0.58	0.06130	0.00100	629	10	631	9	648	36	97
PDB16_61	34600	925	2911	0.75	0.8260	0.0280	0.08590	0.00480	0.94	0.07090	0.00210	609	16	530	29	939	60	56
PDB16_62	12270	208	945	0.42	1.1810	0.0160	0.12760	0.00150	0.45	0.06678	0.00078	792	8	774	9	830	25	93
PDB16_63	1994	41	272	0.72	0.9800	0.0210	0.11319	0.00120	0.01	0.06300	0.00140	693	11	691	7	701	47	99
PDB16_64	34800	962	2090	0.31	0.8240	0.0120	0.09848	0.00120	0.78	0.06124	0.00063	610	7	606	7	647	22	94
PDB16_65	15160	251	3375	1.43	1.2520	0.0600	0.10178	0.00110	0.17	0.08900	0.00420	819	27	625	7	1380	89	45
PDB16_66	26200	692	1817	0.34	0.8121	0.0099	0.09789	0.00100	0.61	0.06014	0.00052	604	6	602	6	607	19	99

Table B9 (continued): Results of LA-ICP-MS zircon U–Pb analyses performed during the sessions at ETH Zürich, 12 to 14th of February, 2017

grain	^{207}Pb[a] (cps)	U[b] (ppm)	Pb[b] (ppm)	Th[b]/U	$^{207}Pb/^{235}U$[c]	±2σ (abs)	$^{206}Pb/^{238}U$[c]	±2σ (abs)	rho[d]	$^{207}Pb/^{206}Pb$[c]	±2σ (abs)	$^{207}Pb/^{235}U$	±2σ (Ma)	$^{206}Pb/^{238}U$	±2σ (Ma)	$^{207}Pb/^{206}Pb$	±2σ (Ma)	conc.[e] (%)
PDB16_67	15030	407	784	0.25	0.8110	0.0150	0.09675	0.00100	0.24	0.06092	0.00097	603	8	595	6	634	34	94
PDB16_68	15840	303	2023	0.70	1.1420	0.0180	0.12797	0.00150	0.45	0.06554	0.00099	773	8	776	8	789	31	98
PDB16_69	26850	350	4770	1.07	1.7010	0.0340	0.16960	0.00290	0.66	0.07330	0.00100	1009	13	1010	16	1021	28	99
PDB16_70	6520	145	505	0.39	0.9060	0.0130	0.10435	0.00120	0.40	0.06301	0.00079	655	7	640	7	711	26	90
PDB16_71	9620	163	607	0.35	1.2310	0.0210	0.13451	0.00150	0.47	0.06670	0.00100	816	9	814	8	822	31	99
PDB16_72	38200	702	4720	0.64	1.0790	0.0160	0.11460	0.00180	0.31	0.06860	0.00100	743	8	699	11	886	31	79
PDB16_73	18500	318	737	0.22	1.2160	0.0150	0.13450	0.00180	0.67	0.06617	0.00054	807	7	813	10	813	16	100
PDB16_74	5210	119	479	0.45	0.8640	0.0130	0.10141	0.00110	0.55	0.06200	0.00077	633	7	623	7	669	27	93
PDB16_75	8400	114	2116	1.60	1.5940	0.0230	0.15960	0.00170	0.40	0.07312	0.00095	968	9	954	10	1021	25	93
PDB16_76	8280	164	630	0.41	1.0510	0.0150	0.11962	0.00140	0.24	0.06383	0.00095	729	8	728	8	732	31	100
PDB16_77	112800	2363	7530	0.37	1.0343	0.0094	0.11971	0.00120	0.62	0.06304	0.00034	721	5	729	7	709	11	103
PDB16_78	19530	483	1290	0.34	0.8222	0.0099	0.09925	0.00100	0.72	0.06009	0.00045	609	6	610	6	605	16	101
PDB16_79	17450	371	2078	0.62	0.9375	0.0100	0.10894	0.00100	0.22	0.06206	0.00054	671	5	667	6	675	19	99
PDB16_80	39940	957	3020	0.40	0.8636	0.0091	0.10289	0.00110	0.54	0.06118	0.00048	632	5	631	6	644	17	98
PDB16_81	32330	853	2080	0.33	0.8110	0.0099	0.09760	0.00120	0.50	0.06058	0.00053	603	6	600	7	623	19	96
PDB16_82	619000	1236	4890	0.12	10.1140	0.0890	0.45600	0.00430	0.76	0.16099	0.00069	2445	8	2422	19	2466	7	98
PDB16_83	23420	354	1676	0.40	1.2580	0.0200	0.13750	0.00200	0.76	0.06688	0.00066	829	10	831	12	833	20	100
PDB16_84	12330	217	1180	0.53	1.2790	0.0230	0.13870	0.00180	0.41	0.06694	0.00096	836	10	837	10	835	30	100
PDB16_85	5913	110	494	0.43	1.0730	0.0140	0.12100	0.00130	0.36	0.06415	0.00076	740	7	736	7	746	25	99
PDB16_86	15420	428	1617	0.52	0.8270	0.0160	0.10040	0.00160	0.75	0.06054	0.00075	612	9	617	10	622	27	99
PDB16_87	26660	590	1520	0.29	0.9480	0.0120	0.11010	0.00150	0.54	0.06200	0.00060	677	6	673	9	673	21	100
PDB16_88	32380	681	4954	0.83	0.9605	0.0089	0.11236	0.00110	0.43	0.06204	0.00045	683	5	686	6	676	15	102
PDB16_89	9220	218	2540	1.41	0.8080	0.0170	0.09721	0.00110	0.13	0.06010	0.00110	601	9	598	6	615	44	97
PDB16_90	73000	1005	9000	0.72	1.5930	0.0220	0.16380	0.00200	0.30	0.07059	0.00087	967	9	978	11	944	25	104
PDB16_91	8740	207	688	0.41	0.8160	0.0140	0.09799	0.00110	0.41	0.05994	0.00088	605	8	603	6	604	33	100
PDB16_92	15210	419	1137	0.37	0.7840	0.0110	0.09587	0.00110	0.40	0.05927	0.00073	588	7	590	6	575	27	103
PDB16_93	21270	235	1170	0.24	1.7980	0.0360	0.17650	0.00360	0.89	0.07361	0.00056	1043	13	1047	20	1029	15	102
PDB16_94	64580	956	5000	0.49	1.5250	0.0200	0.15910	0.00180	0.57	0.07030	0.00100	943	8	952	10	937	29	102
PDB16_95	5940	126	406	0.35	0.9310	0.0150	0.10922	0.00110	0.28	0.06171	0.00085	669	8	668	6	663	30	101
PDB16_96	132900	243	7000	0.85	11.1300	0.0940	0.46790	0.00440	0.61	0.17237	0.00078	2534	8	2474	19	2581	8	96
PDB16_97	23640	527	3630	0.82	0.8542	0.0091	0.10250	0.00120	0.63	0.06062	0.00050	627	5	629	7	624	18	101
PDB16_98	28600	718	1730	0.33	0.8202	0.0079	0.09864	0.00099	0.61	0.06002	0.00036	608	4	607	6	605	13	100
PDB16_99	22570	465	2888	0.69	0.9801	0.0100	0.11328	0.00130	0.74	0.06289	0.00041	694	5	692	8	703	14	98
PDB16_100	26410	501	1000	0.20	1.1073	0.0120	0.12434	0.00120	0.38	0.06477	0.00050	757	6	756	7	772	16	98
PDB16_101	26420	503	2165	0.46	1.1050	0.0120	0.12256	0.00140	0.55	0.06532	0.00051	756	6	745	8	786	16	95
PDB16_102	3284	53	220	0.37	1.1800	0.0280	0.13183	0.00140	0.29	0.06490	0.00140	790	13	798	8	771	46	104
PDB16_103	22540	428	2691	0.70	1.0890	0.0160	0.12225	0.00140	0.65	0.06448	0.00062	748	8	744	8	756	20	98
PDB16_104	49200	659	7800	0.94	1.4810	0.0270	0.13093	0.00130	0.05	0.08180	0.00140	924	11	793	7	1240	35	64
PDB16_105	17300	323	1990	0.63	1.0413	0.0110	0.11875	0.00120	0.52	0.06343	0.00048	724	6	723	7	722	16	100
PDB16_106	4950	100	330	0.36	0.9910	0.0140	0.11404	0.00120	0.16	0.06301	0.00083	700	7	696	7	704	28	99
PDB16_107	10630	203	540	0.27	1.0400	0.0130	0.11893	0.00130	0.50	0.06341	0.00062	724	6	724	7	722	21	100
PDB16_108	24130	529	6020	1.23	0.8649	0.0110	0.10372	0.00120	0.60	0.06068	0.00056	633	6	636	7	627	20	101
PDB16_109	9180	210	1991	1.16	0.9250	0.0160	0.10882	0.00130	0.55	0.06185	0.00085	664	8	666	8	676	30	98
PDB16_110	2723	48	204	0.43	1.1270	0.0220	0.12553	0.00140	0.51	0.06500	0.00120	765	11	762	8	776	37	98
PDB16_111	55000	595	1216	0.15	1.9150	0.0340	0.18430	0.00330	0.93	0.07517	0.00048	1085	12	1090	18	1072	13	102
PDB16_112	4350	117	420	0.48	0.7940	0.0160	0.09615	0.00110	0.32	0.06010	0.00120	594	9	592	6	609	43	97
PDB16_113	19400	403	1699	0.48	1.0250	0.0150	0.11794	0.00140	0.38	0.06245	0.00080	716	8	719	8	697	27	103
PDB16_114	4490	87	501	0.42	1.0140	0.0250	0.11140	0.00170	0.77	0.06640	0.00100	710	12	681	10	826	31	82

Table B9 (continued): Results of LA-ICP-MS zircon U–Pb analyses performed during the sessions at ETH Zürich, 12 to 14th of February, 2017

grain	^{207}Pb[a] (cps)	U[b] (ppm)	Pb[b] (ppm)	Th[b]/U	$^{207}Pb/^{235}U$[c]	±2σ (abs)	$^{206}Pb/^{238}U$[c]	±2σ (abs)	rho[d]	$^{207}Pb/^{206}Pb$[c]	±2σ (abs)	$^{207}Pb/^{235}U$	±2σ (Ma)	$^{206}Pb/^{238}U$	±2σ (Ma)	$^{207}Pb/^{206}Pb$	±2σ (Ma)	conc.[e] (%)
PDB16_115	31900	432	4320	0.76	1.4800	0.0310	0.14250	0.00200	0.65	0.07560	0.00110	921	13	859	11	1084	31	79
PDB16_116	3930	85	645	0.87	0.9780	0.0310	0.11330	0.00150	0.04	0.06380	0.00270	691	16	692	9	731	78	95
PDB16_117	12870	289	1147	0.45	0.8970	0.0130	0.10410	0.00100	0.41	0.06258	0.00075	650	7	638	6	690	25	93
PDB16_118	50600	624	5630	0.72	1.6550	0.0250	0.16384	0.00170	0.41	0.07310	0.00084	991	9	978	10	1015	23	96
PDB16_119	9780	214	680	0.37	0.9064	0.0094	0.10260	0.00100	0.44	0.06412	0.00050	655	5	630	6	748	16	84
PDB16_120	5000	110	701	0.77	0.9000	0.0120	0.10620	0.00120	0.35	0.06121	0.00074	651	7	651	7	650	25	100
PDB16_121	3157	77	229	0.37	0.8950	0.0200	0.10630	0.00130	0.14	0.06080	0.00150	649	11	651	8	624	52	104
PDB16_122	9520	221	742	0.39	0.8792	0.0110	0.10450	0.00120	0.44	0.06117	0.00067	640	6	641	7	646	23	99
PDB16_123	5050	114	716	0.73	0.9160	0.0140	0.10747	0.00110	0.27	0.06223	0.00087	661	7	658	6	682	29	96
PDB16_124	2340	42	226	0.51	1.0890	0.0210	0.12328	0.00140	0.45	0.06370	0.00110	749	11	749	8	731	38	103
PDB16_125	17280	427	365	0.11	0.8197	0.0082	0.09850	0.00092	0.44	0.06038	0.00044	608	5	606	5	618	16	98
PDB16_126	6900	141	504	0.38	0.9920	0.0120	0.11432	0.00120	0.32	0.06284	0.00060	699	6	698	7	703	20	99
PDB16_127	10710	222	1414	0.70	0.9840	0.0130	0.11360	0.00120	0.42	0.06282	0.00069	696	6	694	7	709	23	98
PDB16_128	10770	244	3360	1.40	0.8530	0.0160	0.10240	0.00180	0.76	0.06086	0.00073	626	9	630	11	639	24	99
PDB16_129	17800	297	3000	0.97	1.1657	0.0110	0.12954	0.00130	0.57	0.06498	0.00048	785	5	785	8	776	15	101
PDB16_130	9110	131	1279	0.87	1.3250	0.0260	0.14190	0.00230	0.64	0.06780	0.00110	856	11	855	13	861	35	99
PDB16_131	7790	189	1570	1.03	0.8240	0.0099	0.09918	0.00100	0.26	0.06019	0.00061	610	6	610	6	607	22	100
PDB16_132	84600	1612	9820	0.60	1.0460	0.0140	0.11206	0.00120	0.48	0.06744	0.00060	727	7	685	7	850	18	81
PDB16_133	21000	338	2470	0.60	1.2500	0.0190	0.13590	0.00170	0.81	0.06666	0.00056	823	9	821	10	828	18	99
PDB16_134	24190	416	2543	0.58	1.1630	0.0130	0.12963	0.00130	0.82	0.06521	0.00046	784	6	786	7	782	14	100
PDB16_135	28900	46	1721	1.04	12.6900	0.1300	0.51170	0.00560	0.56	0.17970	0.00120	2656	9	2663	24	2649	11	101
PDB16_136	9810	221	647	0.35	0.8716	0.0110	0.10506	0.00110	0.50	0.06000	0.00058	636	6	644	7	609	22	106
PDB16_137	16840	289	1136	0.37	1.1090	0.0150	0.12426	0.00140	0.41	0.06454	0.00071	757	7	755	8	758	23	100
PDB16_138	3997	90	240	0.32	0.8430	0.0190	0.10121	0.00130	0.43	0.06020	0.00110	620	10	622	8	607	40	102
PDB16_139	7282	144	358	0.27	0.9990	0.0130	0.11553	0.00120	0.38	0.06257	0.00062	705	6	705	7	694	22	102
PDB16_140	24170	566	776	0.17	0.8871	0.0093	0.10575	0.00110	0.31	0.06050	0.00052	645	5	648	7	620	19	105
PDB16_141	27450	621	988	0.18	0.9024	0.0110	0.10617	0.00110	0.60	0.06225	0.00049	653	6	650	7	681	17	96
PDB16_142	17230	352	1235	0.37	0.9985	0.0093	0.11529	0.00110	0.23	0.06281	0.00048	703	5	703	6	702	17	100
PDB16_143	4970	124	1250	1.24	0.7810	0.0120	0.09518	0.00094	0.39	0.05933	0.00080	586	7	586	6	575	30	102
PDB16_144	409600	948	19170	0.73	9.6230	0.1000	0.42920	0.00480	0.48	0.16412	0.00097	2399	10	2302	22	2498	10	92
PDB16_145	33770	579	2907	0.47	1.2470	0.0180	0.13580	0.00160	0.51	0.06657	0.00074	822	8	821	9	823	23	100
PDB16_146	17960	293	1274	0.39	1.2540	0.0170	0.13244	0.00140	0.65	0.06875	0.00062	825	8	802	8	893	19	90
PDB16_147	3670	58	391	0.59	1.2850	0.0230	0.13670	0.00170	0.36	0.06810	0.00120	839	10	826	10	869	36	95
PDB16_148	70100	1720	8790	1.08	0.8320	0.0160	0.09420	0.00200	0.93	0.06373	0.00044	615	9	580	12	737	14	79
PDB16_149	52300	1110	6282	0.65	0.9436	0.0084	0.11030	0.00110	0.70	0.06191	0.00034	675	4	674	6	672	12	100
PDB16_150	37210	759	8480	1.16	0.9912	0.0110	0.11469	0.00120	0.63	0.06289	0.00049	699	6	700	7	703	16	100
PDB16_151	24590	612	6462	1.36	0.8273	0.0095	0.09974	0.00110	0.52	0.06048	0.00049	612	5	613	7	620	17	99
PDB16_152	93120	2286	4174	0.24	0.8806	0.0110	0.10224	0.00120	0.90	0.06269	0.00052	641	6	628	7	697	18	90
PDB16_153	17130	373	1832	0.56	0.9077	0.0093	0.10663	0.00100	0.60	0.06156	0.00042	656	5	653	6	662	14	99
PDB16_154	24660	311	4110	1.04	1.5940	0.0160	0.16195	0.00160	0.65	0.07164	0.00048	968	7	968	9	974	14	99
PDB16_155	6030	143	880	0.75	0.8940	0.0150	0.10560	0.00140	0.28	0.06160	0.00110	649	8	647	8	661	40	98
PDB16_156	4730	115	693	0.77	0.9170	0.0230	0.10706	0.00130	0.73	0.06310	0.00120	660	12	656	8	709	40	92
PDB16_157	25460	574	5420	1.17	0.9540	0.0180	0.11020	0.00170	0.75	0.06298	0.00071	681	9	674	10	706	24	95
PDB16_158	11020	245	1159	0.53	0.8980	0.0140	0.10004	0.00130	0.81	0.06513	0.00063	650	8	615	8	776	20	79
PDB16_159	75900	299	2144	0.24	5.1190	0.0760	0.29140	0.00400	0.93	0.12677	0.00066	1838	13	1648	20	2053	9	80
PDB16_160	99400	2559	3720	0.21	0.8236	0.0079	0.09876	0.00093	0.31	0.06058	0.00044	610	4	607	6	623	16	97
PDB16_161	51600	224	2729	0.56	4.3460	0.0530	0.27140	0.00280	0.64	0.11600	0.00110	1702	10	1548	14	1897	16	82
PDB16_162	25880	666	1510	0.30	0.8530	0.0140	0.10099	0.00120	0.45	0.06108	0.00069	626	7	620	7	646	26	96

Table B9 (continued): Results of LA-ICP-MS zircon U–Pb analyses performed during the sessions at ETH Zürich, 12 to 14th of February, 2017

grain	^{207}Pb[a] (cps)	U[b] (ppm)	Pb[b] (ppm)	Th[b]/U	$^{207}Pb/^{235}U$[c]	±2σ (abs)	$^{206}Pb/^{238}U$[c]	±2σ (abs)	rho[d]	$^{207}Pb/^{206}Pb$[c]	±2σ (abs)	$^{207}Pb/^{235}U$ (Ma)	±2σ	$^{206}Pb/^{238}U$ (Ma)	±2σ	$^{207}Pb/^{206}Pb$ (Ma)	±2σ	conc.[e] (%)
PDB16_163	2900	61	309	0.52	0.9190	0.0200	0.10660	0.00140	0.26	0.06260	0.00130	663	11	653	8	693	46	94
PDB16_164	7170	154	1226	0.89	0.9370	0.0140	0.10917	0.00110	0.36	0.06223	0.00070	671	7	668	7	679	24	98
PDB16_165	59100	1423	4150	0.37	0.8690	0.0110	0.10345	0.00120	0.65	0.06118	0.00048	636	6	635	7	645	17	98
PDB16_166	29000	608	3782	0.71	0.9930	0.0120	0.11447	0.00130	0.73	0.06310	0.00048	700	6	699	8	710	16	98
PDB16_167	73800	285	12060	1.65	5.0500	0.0460	0.32040	0.00320	0.63	0.11410	0.00068	1827	8	1792	16	1866	11	96
PDB16_168	59000	1455	5031	0.45	0.8196	0.0080	0.09478	0.00096	0.53	0.06249	0.00041	608	5	584	6	692	14	84
PDB16_169	12140	275	930	0.40	0.8857	0.0100	0.10487	0.00099	0.36	0.06136	0.00055	644	6	643	6	652	20	99
PDB16_170	7980	148	607	0.40	1.0430	0.0170	0.12268	0.00130	0.54	0.06180	0.00077	726	8	746	8	664	27	112
PDB16_171	17950	332	1845	0.54	1.0770	0.0140	0.11807	0.00130	0.87	0.06585	0.00067	742	7	719	8	800	21	90
PDB16_172	83900	2184	6270	0.40	0.8810	0.0130	0.10462	0.00130	0.58	0.06140	0.00060	641	7	641	7	662	27	97
PDB16_173	49400	797	5240	0.69	1.2670	0.0140	0.12720	0.00180	0.76	0.07230	0.00049	831	6	772	10	995	14	78
PDB16_174	15140	257	679	0.22	1.1190	0.0190	0.12500	0.00150	0.53	0.06471	0.00088	762	9	759	9	763	29	100
PDB16_175	28500	424	2775	0.57	1.3445	0.0120	0.14387	0.00140	0.51	0.06777	0.00045	865	5	867	8	860	14	101
PDB16_176	10960	226	1395	0.63	0.9890	0.0150	0.11148	0.00130	0.55	0.06421	0.00070	698	8	681	8	745	23	91
PDB16_177	4380	75	522	0.64	1.2010	0.0180	0.13267	0.00150	0.82	0.06586	0.00079	801	9	803	9	805	25	100
PDB16_178	23400	474	3870	0.79	0.9340	0.0360	0.10210	0.00200	0.82	0.06810	0.00170	669	19	627	12	861	51	73
PDB16_179	1558	37	107	0.37	0.8600	0.0240	0.10153	0.00120	0.17	0.06110	0.00150	629	13	623	7	630	54	99
PDB16_180	22390	341	1495	0.40	1.4310	0.0260	0.15080	0.00170	0.45	0.06900	0.00100	902	11	905	9	895	31	101
PDB16_181	10070	218	1357	0.70	0.9550	0.0110	0.11121	0.00130	0.63	0.06228	0.00053	681	6	680	7	683	18	100
PDB16_182	10640	233	1407	0.68	0.8700	0.0140	0.10449	0.00110	0.08	0.06032	0.00099	635	8	641	6	612	35	105
PDB16_183	27600	350	6820	1.22	1.5810	0.0390	0.14590	0.00270	0.90	0.07876	0.00095	964	16	878	15	1165	24	75
PDB16_184	5230	121	1060	1.01	0.8590	0.0130	0.10261	0.00100	0.24	0.06074	0.00079	630	7	630	6	629	29	100
PDB16_185	186200	333	4330	0.37	10.6400	0.1500	0.43960	0.00610	0.75	0.17630	0.00170	2492	13	2348	27	2618	16	90
PDB16_186	12090	318	1570	0.64	0.7640	0.0140	0.09003	0.00097	0.61	0.06146	0.00089	576	8	556	6	657	29	85
PDB16_187	18700	367	1769	0.52	1.0230	0.0130	0.12064	0.00130	0.75	0.06150	0.00045	716	7	734	8	655	16	112
PDB16_188	27160	671	4660	0.88	0.8065	0.0096	0.09422	0.00090	0.47	0.06222	0.00059	600	5	581	5	682	20	85
PDB16_189	7040	293	306	0.13	0.4819	0.0064	0.06205	0.00067	0.46	0.05645	0.00055	399	4	388	4	467	22	83
PDB16_190	21710	465	762	0.18	1.0220	0.0160	0.11599	0.00120	0.46	0.06400	0.00077	716	8	707	7	740	25	96
PDB16_191	546900	1055	17800	0.47	9.8200	0.1500	0.41790	0.00600	0.86	0.17040	0.00130	2418	14	2251	27	2566	12	88
PDB16_192	17220	273	1896	0.64	1.2500	0.0130	0.13294	0.00140	0.56	0.06810	0.00055	824	6	805	8	874	16	92
PDB16_193	38810	708	2704	0.36	1.0560	0.0140	0.11957	0.00140	0.69	0.06393	0.00055	731	7	728	8	744	17	98
PDB16_194	3240	65	736	1.25	1.0050	0.0220	0.11238	0.00130	0.43	0.06470	0.00120	708	11	687	7	761	39	90
PDB16_195	16370	396	1992	0.62	0.8419	0.0082	0.10099	0.00098	0.55	0.06037	0.00041	620	5	620	6	619	15	100
PDB16_196	8370	210	791	0.46	0.8430	0.0130	0.10071	0.00100	0.36	0.06067	0.00080	620	7	619	6	625	29	99
PDB16_197	17170	399	3365	0.99	0.8771	0.0086	0.10443	0.00100	0.46	0.06108	0.00043	640	5	640	6	641	15	100
PDB16_198	11840	242	1449	0.64	0.9170	0.0190	0.10770	0.00160	0.54	0.06233	0.00094	660	10	659	9	684	32	96
PDB16_199	17250	357	1471	0.47	1.0560	0.0160	0.12004	0.00140	0.54	0.06429	0.00073	732	8	731	8	750	24	97
PDB16_200	23210	355	1723	0.42	1.4210	0.0230	0.14820	0.00180	0.47	0.06990	0.00100	898	10	891	10	923	30	97
PIL-16-01 Pilat metasediment																		
PIL16_1	10590	244	4450	1.82	0.8525	0.0110	0.10184	0.00110	0.58	0.06103	0.00059	626	6	625	7	644	21	97
PIL16_2	43400	781	4930	0.60	1.0560	0.0270	0.09964	0.00130	0.06	0.07690	0.00200	732	13	613	8	1114	53	55
PIL16_3	9260	166	986	0.62	1.1350	0.0190	0.12690	0.00160	0.66	0.06515	0.00090	772	10	770	9	776	29	99
PIL16_4	6160	106	561	0.49	1.2150	0.0270	0.13320	0.00250	0.80	0.06602	0.00081	807	12	806	14	812	27	99
PIL16_5	25490	662	1918	0.38	0.7573	0.0090	0.09260	0.00110	0.43	0.05964	0.00064	572	5	571	7	589	23	97
PIL16_6	38500	79	2190	0.81	9.2300	0.1800	0.44410	0.00590	0.70	0.15080	0.00200	2361	18	2369	27	2354	23	101
PIL16_7	4310	104	1287	1.56	0.8220	0.0150	0.09991	0.00120	0.44	0.05990	0.00100	610	8	614	7	608	36	101
PIL16_8	134500	163	5630	0.84	15.3900	0.1700	0.53740	0.00620	0.63	0.20780	0.00200	2839	10	2772	26	2888	16	96

Table B9 (continued): Results of LA-ICP-MS zircon U–Pb analyses performed during the sessions at ETH Zürich, 12 to 14th of February, 2017

grain	^{207}Pb[a] (cps)	U[b] (ppm)	Pb[b] (ppm)	Th[b]/U	$^{207}Pb/^{235}U$[c]	±2σ (abs)	$^{206}Pb/^{238}U$[c]	±2σ (abs)	rho[d]	$^{207}Pb/^{206}Pb$[c]	±2σ (abs)	$^{207}Pb/^{235}U$	±2σ (Ma)	$^{206}Pb/^{238}U$	±2σ (Ma)	$^{207}Pb/^{206}Pb$	±2σ (Ma)	conc.[e] (%)
PIL16_9	1970	47	200	0.51	0.8600	0.0170	0.10230	0.00140	0.33	0.06070	0.00120	631	9	629	8	638	44	99
PIL16_10	185400	585	7650	0.53	6.8090	0.1000	0.36070	0.00500	0.81	0.13730	0.00140	2086	13	1985	23	2192	17	91
PIL16_11	15840	344	1109	0.36	0.8889	0.0110	0.10365	0.00100	0.43	0.06200	0.00064	646	6	636	6	672	22	95
PIL16_12	10350	243	1397	0.68	0.8492	0.0100	0.10163	0.00100	0.27	0.06043	0.00060	625	6	624	6	616	21	101
PIL16_13	7670	80	1079	0.92	1.8470	0.0280	0.17889	0.00180	0.11	0.07480	0.00100	1062	10	1061	10	1064	28	100
PIL16_14	55130	204	6400	1.23	5.3120	0.0570	0.33610	0.00380	0.79	0.11444	0.00062	1870	9	1868	18	1871	10	100
PIL16_15	27160	618	1384	0.26	0.8721	0.0090	0.10392	0.00100	0.50	0.06070	0.00043	638	5	637	6	627	15	102
PIL16_16	5240	127	1140	1.02	0.8040	0.0120	0.09781	0.00110	0.16	0.05947	0.00079	599	7	602	6	587	29	102
PIL16_17	8530	198	1317	0.79	0.8670	0.0120	0.10307	0.00100	0.27	0.06085	0.00071	634	6	632	6	633	25	100
PIL16_18	38800	61	896	0.43	14.0900	0.2700	0.53200	0.00720	0.75	0.19260	0.00210	2755	18	2750	31	2763	18	100
PIL16_19	1403	39	136	0.44	0.7520	0.0230	0.09137	0.00110	0.30	0.05890	0.00170	568	14	564	7	573	58	98
PIL16_20	21430	592	1254	0.29	0.8060	0.0220	0.09299	0.00130	0.37	0.06290	0.00150	603	13	573	8	703	50	82
PIL16_21	18930	419	4310	1.19	0.9450	0.0200	0.09906	0.00110	0.19	0.06900	0.00140	675	10	609	7	907	42	67
PIL16_22	10170	252	3350	1.71	0.8252	0.0110	0.09961	0.00110	0.51	0.06015	0.00062	611	6	612	7	606	22	101
PIL16_23	68100	239	2174	0.33	5.3500	0.1400	0.31410	0.00550	0.89	0.12390	0.00160	1875	22	1761	27	2012	23	88
PIL16_24	162200	305	223	0.02	10.5100	0.1500	0.42040	0.00620	0.83	0.18040	0.00140	2480	13	2262	28	2657	13	85
PIL16_25	1750	39	479	1.64	0.8910	0.0260	0.09003	0.00110	0.39	0.07190	0.00190	645	14	556	6	981	51	57
PIL16_26	6510	171	1095	0.88	0.8280	0.0210	0.09712	0.00110	0.68	0.06180	0.00130	612	12	598	6	663	45	90
PIL16_28	30900	876	5690	0.96	0.7963	0.0110	0.09562	0.00120	0.48	0.06047	0.00068	595	6	589	7	620	24	95
PIL16_29	9490	158	1907	1.18	1.2610	0.0200	0.13624	0.00140	0.48	0.06716	0.00091	829	9	823	8	845	27	97
PIL16_30	10080	212	1226	0.61	0.9310	0.0140	0.10879	0.00120	0.71	0.06217	0.00059	668	8	666	7	677	20	98
PIL16_31	90300	1160	11240	0.76	1.5910	0.0980	0.10030	0.00130	0.54	0.11400	0.00640	950	40	616	8	1780	120	35
PIL16_32	514400	1209	6490	0.18	9.0980	0.1100	0.41090	0.00410	0.59	0.16090	0.00140	2348	11	2219	19	2464	15	90
PIL16_33	284000	502	9640	0.56	11.9200	0.1200	0.49700	0.00550	0.66	0.17390	0.00120	2598	10	2601	23	2596	11	100
PIL16_34	10980	241	1537	0.73	0.8900	0.0140	0.10624	0.00130	0.67	0.06065	0.00071	646	8	651	7	624	25	104
PIL16_35	27340	94	4424	1.79	6.0630	0.0900	0.36080	0.00390	0.52	0.12240	0.00160	1987	13	1986	18	1989	23	100
PIL16_36	22540	590	2271	0.51	0.7843	0.0082	0.09536	0.00100	0.42	0.05954	0.00056	588	5	587	6	594	21	99
PIL16_37	65100	1978	2960	0.22	0.7730	0.0120	0.09210	0.00170	0.76	0.06113	0.00074	581	7	568	10	643	26	88
PIL16_38	841	21	180	1.12	0.8340	0.0290	0.09320	0.00150	0.40	0.06610	0.00240	617	17	575	9	838	67	69
PIL16_39	9160	224	758	0.44	0.8680	0.0110	0.10391	0.00110	0.31	0.06077	0.00087	634	6	637	6	627	31	102
PIL16_42	45700	644	3820	0.29	1.3970	0.0430	0.09694	0.00110	0.56	0.10500	0.00290	887	19	596	7	1697	50	35
PIL16_43	3800	94	254	0.31	0.7790	0.0180	0.09441	0.00120	0.33	0.06000	0.00130	584	10	582	7	595	47	98
PIL16_44	9150	152	949	0.55	1.1700	0.0170	0.12911	0.00150	0.82	0.06570	0.00083	786	8	783	9	794	27	99
PIL16_45	6420	159	449	0.35	0.8140	0.0120	0.09764	0.00120	0.58	0.06032	0.00065	604	7	601	7	614	23	98
PIL16_46	66800	185	2521	0.35	6.9670	0.0740	0.36990	0.00370	0.71	0.13613	0.00090	2108	9	2029	17	2178	12	93
PIL16_47	2287	34	499	1.50	1.3800	0.0660	0.10010	0.00120	0.05	0.09990	0.00490	886	27	615	7	1617	89	38
PIL16_48	14810	359	2653	0.90	0.8111	0.0095	0.09751	0.00099	0.46	0.06013	0.00054	603	5	600	6	606	19	99
PIL16_49	17820	225	4450	1.68	1.5430	0.0760	0.10750	0.00150	0.87	0.10380	0.00410	946	31	658	9	1674	76	39
PIL16_50	12340	248	1413	0.60	1.0040	0.0330	0.10107	0.00120	0.81	0.07160	0.00180	703	17	621	7	963	54	64
PIL16_51	26100	592	3810	0.78	0.8894	0.0110	0.10153	0.00098	0.42	0.06328	0.00054	646	6	623	6	715	18	87
PIL16_52	34300	353	4930	0.81	2.1700	0.1000	0.11202	0.00120	0.80	0.13990	0.00590	1159	34	684	7	2197	74	31
PIL16_53	29200	331	3280	0.71	1.7480	0.0180	0.17288	0.00180	0.60	0.07296	0.00051	1027	7	1028	10	1012	14	102
PIL16_54	5820	157	495	0.40	0.7390	0.0150	0.08625	0.00100	0.62	0.06242	0.00094	563	9	533	6	683	33	78
PIL16_55	55400	1299	3473	0.32	0.9070	0.0130	0.10542	0.00120	0.59	0.06270	0.00057	656	7	646	7	697	19	93
PIL16_56	183000	270	4230	0.40	13.0500	0.1500	0.48680	0.00550	0.65	0.19450	0.00150	2683	11	2557	24	2780	13	92
PIL16_57	7450	102	878	0.75	1.6310	0.0400	0.16320	0.00210	0.42	0.07260	0.00150	981	15	974	11	1008	45	97
PIL16_58	361000	1365	575	0.01	5.9240	0.0600	0.35690	0.00500	0.69	0.12130	0.00130	1965	9	1967	24	1975	20	100
PIL16_59	20810	625	1359	0.31	0.7290	0.0110	0.08976	0.00096	0.47	0.05916	0.00079	556	7	554	6	572	29	97

Table B9 (continued): Results of LA-ICP-MS zircon U–Pb analyses performed during the sessions at ETH Zürich, 12 to 14th of February, 2017

grain	^{207}Pb[a] (cps)	U[b] (ppm)	Pb[b] (ppm)	Th[b]/U	$^{207}Pb/^{235}U$[c]	±2σ (abs)	$^{206}Pb/^{238}U$[c]	±2σ (abs)	rho[d]	$^{207}Pb/^{206}Pb$[c]	±2σ (abs)	$^{207}Pb/^{235}U$	±2σ (Ma)	$^{206}Pb/^{238}U$	±2σ (Ma)	$^{207}Pb/^{206}Pb$	±2σ (Ma)	conc.[e] (%)
PIL16_61	4550	63	639	0.81	1.4530	0.0390	0.10812	0.00130	0.61	0.09700	0.00220	912	16	662	7	1572	40	42
PIL16_62	6610	150	414	0.32	0.8961	0.0110	0.10582	0.00100	0.06	0.06158	0.00069	650	6	648	6	662	24	98
PIL16_63	5550	126	349	0.33	0.8830	0.0140	0.10414	0.00110	0.74	0.06123	0.00084	642	8	639	6	646	30	99
PIL16_64	89300	1539	9450	0.48	1.1280	0.0310	0.09750	0.00170	0.38	0.08440	0.00220	765	14	599	10	1307	51	46
PIL16_65	42580	61	2052	0.71	13.4400	0.1500	0.49680	0.00490	0.47	0.19630	0.00160	2711	11	2600	21	2795	14	93
PIL16_66	9270	215	487	0.27	0.8609	0.0110	0.10059	0.00100	0.10	0.06211	0.00075	630	6	618	6	677	26	91
PIL16_67	182400	678	3988	0.25	5.5810	0.0580	0.33020	0.00350	0.83	0.12261	0.00063	1913	9	1840	17	1994	9	92
PIL16_68	9260	220	598	0.33	0.8421	0.0095	0.10119	0.00099	0.26	0.06037	0.00057	620	5	621	6	617	20	101
PIL16_69	4830	121	1300	1.34	0.8150	0.0170	0.09436	0.00100	0.15	0.06270	0.00130	605	10	581	6	707	45	82
PIL16_70	763000	1569	8010	0.39	9.7900	0.1500	0.40280	0.00660	0.95	0.17600	0.00077	2415	14	2181	30	2615	7	83
PIL16_71	9520	196	1913	1.06	0.9480	0.0160	0.08260	0.00140	0.66	0.08280	0.00110	677	8	513	8	1262	25	41
PIL16_72	44700	962	922	0.07	0.9420	0.0200	0.10170	0.00220	0.76	0.06770	0.00098	673	10	624	13	861	30	72
PIL16_73	3600	87	689	1.01	0.8340	0.0180	0.09304	0.00110	0.43	0.06510	0.00130	615	10	574	7	778	40	74
PIL16_74	13510	356	1143	0.41	0.7731	0.0100	0.09263	0.00096	0.40	0.06066	0.00066	581	6	571	6	625	24	91
PIL16_75	37700	268	1320	0.19	2.9900	0.2700	0.20000	0.01300	1.00	0.10500	0.00340	1356	76	1170	71	1707	62	69
PIL16_76	25800	682	188	0.02	0.7609	0.0070	0.09285	0.00092	0.59	0.05953	0.00039	574	4	572	5	587	14	98
PIL16_77	1305	36	262	0.98	0.7690	0.0250	0.09320	0.00160	0.15	0.06090	0.00210	578	15	574	10	618	74	93
PIL16_78	52320	1416	4190	0.40	0.7968	0.0092	0.09584	0.00110	0.97	0.06035	0.00058	595	5	590	6	615	21	96
PIL16_79	23790	511	1228	0.26	0.8932	0.0087	0.10454	0.00110	0.38	0.06165	0.00049	648	5	641	6	661	17	97
PIL16_80	17810	339	1850	0.53	1.0380	0.0220	0.10511	0.00130	0.30	0.07190	0.00150	722	11	644	7	984	42	65
PIL16_81	29180	709	312	0.04	0.8638	0.0100	0.10080	0.00100	0.32	0.06190	0.00061	632	6	619	6	669	21	93
PIL16_82	80100	1606	2920	0.11	0.9980	0.0150	0.10248	0.00120	0.76	0.07022	0.00067	702	8	629	7	932	20	67
PIL16_83	18200	59	2390	1.36	6.1180	0.0810	0.36190	0.00440	0.59	0.12270	0.00110	1992	12	1991	21	1994	15	100
PIL16_84	7020	182	539	0.38	0.7330	0.0140	0.08980	0.00130	0.38	0.05920	0.00100	558	8	555	8	573	37	97
PIL16_85	38800	886	3410	0.45	0.9580	0.0270	0.10410	0.00130	0.48	0.06670	0.00140	682	14	638	8	827	42	77
PIL16_86	87700	1542	4990	0.32	1.1390	0.0160	0.10807	0.00100	0.33	0.07656	0.00091	771	8	662	6	1111	24	60
PIL16_87	30350	41	2083	1.31	14.3700	0.2100	0.53540	0.00720	0.79	0.19340	0.00170	2774	14	2764	30	2773	14	100
PIL16_88	4900	122	573	0.62	0.8430	0.0150	0.09855	0.00110	0.21	0.06230	0.00100	621	8	606	6	681	34	89
PIL16_89	42700	975	3880	0.48	0.8504	0.0096	0.09855	0.00100	0.51	0.06250	0.00050	625	5	606	6	692	17	88
PIL16_90	15500	196	1395	0.57	1.6590	0.0250	0.16434	0.00170	0.43	0.07352	0.00086	993	9	981	9	1026	24	96
PIL16_91	146800	512	13400	0.96	5.5900	0.0550	0.34630	0.00360	0.70	0.11695	0.00073	1914	9	1917	17	1910	11	100
PIL16_92	48200	1377	1677	0.17	0.7860	0.0098	0.09527	0.00120	0.42	0.06051	0.00066	589	6	587	7	621	23	94
PIL16_93	18700	516	2960	0.83	0.7550	0.0140	0.09198	0.00120	0.27	0.05995	0.00079	571	8	567	7	601	29	94
PIL16_94	35000	764	2780	0.39	0.8882	0.0098	0.10495	0.00100	0.54	0.06138	0.00051	645	5	643	6	651	18	99
PIL16_95	30540	663	10230	1.80	0.8759	0.0110	0.10359	0.00110	0.55	0.06115	0.00055	639	6	635	7	644	19	99
PIL16_96	24770	537	2619	0.56	0.8984	0.0110	0.10412	0.00110	0.49	0.06262	0.00057	651	6	639	6	693	19	92
PIL16_97	41800	879	4150	0.52	1.0050	0.0120	0.10100	0.00110	0.35	0.07228	0.00071	706	6	620	6	993	20	62
PIL16_98	20610	261	2611	0.78	1.7580	0.0260	0.17230	0.00200	0.27	0.07450	0.00100	1030	10	1025	11	1052	27	97
PIL16_99	20200	342	231	0.02	1.1400	0.0170	0.12280	0.00170	0.79	0.06770	0.00057	772	8	747	10	858	17	87
PIL16_100	20000	453	1687	0.43	0.8966	0.0088	0.10557	0.00110	0.38	0.06175	0.00048	650	5	647	6	664	17	97
PIL16_101	75700	1236	10000	0.92	1.2010	0.0430	0.08378	0.00110	0.15	0.10480	0.00400	800	20	519	7	1685	69	31
PIL16_102	78200	117	3710	0.68	12.5200	0.1400	0.50390	0.00570	0.74	0.18040	0.00150	2644	11	2630	24	2656	14	99
PIL16_103	15220	366	680	0.23	0.8293	0.0089	0.09985	0.00098	0.36	0.06032	0.00050	613	5	614	6	615	17	100
PIL16_104	23050	551	2310	0.54	0.8741	0.0110	0.10359	0.00110	0.49	0.06128	0.00057	638	6	635	7	647	20	98
PIL16_105	32300	77	1487	0.64	8.4230	0.1100	0.40310	0.00430	0.59	0.15140	0.00160	2277	12	2183	20	2361	18	92
PIL16_106	4997	85	930	1.14	1.2040	0.0430	0.09724	0.00100	0.34	0.09010	0.00310	799	19	598	6	1423	65	42
PIL16_107	142800	702	3420	0.30	4.0860	0.0380	0.27450	0.00280	0.70	0.10820	0.00056	1651	8	1564	14	1769	10	88
PIL16_108	2257	46	392	0.91	0.9990	0.0200	0.11441	0.00120	0.23	0.06310	0.00110	705	10	698	7	715	39	98

Table B9 (continued): Results of LA-ICP-MS zircon U–Pb analyses performed during the sessions at ETH Zürich, 12 to 14th of February, 2017

grain	^{207}Pb[a] (cps)	U[b] (ppm)	Pb[b] (ppm)	Th[b]/U	$^{207}Pb/^{235}U$[c]	±2σ (abs)	$^{206}Pb/^{238}U$[c]	±2σ (abs)	rho[d]	$^{207}Pb/^{206}Pb$[c]	±2σ (abs)	$^{207}Pb/^{235}U$	±2σ (Ma)	$^{206}Pb/^{238}U$	±2σ (Ma)	$^{207}Pb/^{206}Pb$	±2σ (Ma)	conc.[e] (%)
PIL16_109	4210	35	494	0.92	2.5820	0.0850	0.08560	0.00130	0.45	0.22120	0.00670	1294	24	530	8	2986	49	18
PIL16_110	1159	30	353	1.50	0.7770	0.0170	0.09524	0.00110	0.13	0.05940	0.00130	584	10	586	7	571	49	103
PIL16_111	11110	256	2580	1.19	0.8350	0.0110	0.09951	0.00100	0.16	0.06104	0.00074	616	6	612	6	638	26	96
PIL16_112	4982	128	521	0.54	0.7913	0.0100	0.09575	0.00098	0.24	0.05982	0.00068	592	6	590	6	596	24	99
PIL16_113	21900	274	2171	0.61	1.6410	0.0170	0.16506	0.00170	0.48	0.07204	0.00055	987	7	985	9	990	16	99
PIL16_114	1166	30	292	1.23	0.7760	0.0220	0.09353	0.00120	0.37	0.05960	0.00160	583	13	576	7	597	62	97
PIL16_115	21810	568	1244	0.30	0.8220	0.0110	0.09907	0.00110	0.43	0.06035	0.00061	609	6	609	6	614	22	99
PIL16_116	11370	314	261	0.11	0.6846	0.0088	0.08504	0.00083	0.15	0.05841	0.00070	529	5	526	5	548	27	96
PIL16_117	61900	1698	4710	0.35	0.6930	0.0150	0.07870	0.00160	0.94	0.06389	0.00048	534	9	488	10	740	16	66
PIL16_118	81500	334	1726	0.21	4.7000	0.1200	0.31410	0.00720	0.94	0.10860	0.00100	1765	21	1760	35	1776	18	99
PIL16_119	8860	234	962	0.55	0.8650	0.0370	0.10470	0.00200	0.46	0.06040	0.00230	632	20	642	12	610	83	105
PIL16_120	78300	979	1325	0.06	1.4920	0.0290	0.14580	0.00280	0.82	0.07475	0.00091	930	13	877	16	1061	25	83
PIL16_121	22400	526	4677	1.09	0.8755	0.0097	0.10359	0.00110	0.35	0.06131	0.00056	639	5	635	6	651	19	98
PIL16_122	31080	765	2659	0.45	0.8873	0.0096	0.10479	0.00110	0.48	0.06143	0.00046	645	5	642	7	654	16	98
PIL16_123	10810	267	3007	1.38	0.8230	0.0120	0.09874	0.00100	0.23	0.06037	0.00074	610	7	607	6	618	27	98
PIL16_124	95900	265	3630	0.36	6.9600	0.1300	0.36430	0.00610	0.86	0.14090	0.00160	2106	17	2002	29	2237	19	89
PIL16_125	27260	749	3510	0.67	0.7237	0.0070	0.08913	0.00088	0.37	0.05873	0.00043	553	4	550	5	556	16	99
PIL16_126	192000	557	15200	0.83	6.8300	0.1200	0.37980	0.00460	0.77	0.13030	0.00130	2089	15	2075	22	2101	17	99
PIL16_127	58800	1408	5140	0.38	0.9350	0.0190	0.08407	0.00100	0.17	0.08040	0.00160	670	10	520	6	1204	38	43
PIL16_128	132200	170	5300	0.64	14.7500	0.1900	0.51290	0.00570	0.68	0.20850	0.00160	2799	12	2669	24	2894	12	92
PIL16_129	6510	180	2425	1.90	0.7870	0.0190	0.09410	0.00130	0.06	0.06070	0.00140	589	11	580	8	626	52	93
PIL16_130	95500	2320	1126	0.06	0.8720	0.0120	0.10387	0.00130	0.85	0.06094	0.00040	637	6	637	7	636	14	100
PIL16_131	11840	323	1808	0.77	0.7679	0.0099	0.09330	0.00096	0.42	0.06008	0.00066	579	6	575	6	604	24	95
PIL16_132	228300	738	5390	0.28	6.2110	0.0820	0.35830	0.00370	0.83	0.12575	0.00089	2005	12	1974	18	2038	12	97
PIL16_133	49100	952	5410	0.62	1.1250	0.0270	0.10252	0.00120	0.40	0.07950	0.00160	765	13	629	7	1181	39	53
PIL16_134	14130	358	2630	0.97	0.8760	0.0130	0.10398	0.00120	0.30	0.06208	0.00079	639	7	638	7	676	27	94
PIL16_135	21500	547	1186	0.27	0.7880	0.0140	0.08961	0.00120	0.82	0.06375	0.00062	590	8	553	7	733	21	75
PIL16_136	6850	160	767	0.57	0.9110	0.0140	0.10581	0.00110	0.39	0.06231	0.00079	657	8	648	6	686	28	95
PIL16_137	11400	252	7910	3.42	0.9158	0.0093	0.10498	0.00110	0.40	0.06313	0.00050	660	5	644	6	713	17	90
PIL16_138	7480	170	875	0.58	0.8470	0.0180	0.10066	0.00130	0.26	0.06100	0.00100	622	10	618	8	634	36	98
PIL16_139	16860	247	3260	1.14	1.3730	0.0130	0.14546	0.00150	0.39	0.06856	0.00052	877	6	876	8	886	16	99
PIL16_140	7880	188	1358	0.91	0.8140	0.0130	0.09753	0.00100	0.39	0.06058	0.00078	605	7	600	6	629	29	95
PIL16_141	139200	326	2400	0.22	8.7190	0.1000	0.40370	0.00480	0.89	0.15635	0.00081	2309	11	2186	22	2417	9	90
PIL16_142	4620	106	339	0.38	0.9340	0.0210	0.11195	0.00130	0.62	0.06110	0.00100	669	11	684	8	638	37	107
PIL16_143	4740	91	556	0.62	0.9880	0.0280	0.10791	0.00130	0.76	0.06690	0.00160	700	15	661	8	852	49	78
PIL16_144	8070	222	1518	0.91	0.7247	0.0100	0.08961	0.00092	0.29	0.05867	0.00069	553	6	553	6	562	25	98
PIL16_145	4540	117	542	0.57	0.7570	0.0130	0.09179	0.00093	0.26	0.05966	0.00088	572	7	566	6	591	33	96
PIL16_146	11520	214	2580	1.32	1.0110	0.0160	0.09849	0.00120	0.25	0.07420	0.00110	709	8	606	7	1042	30	58
PIL16_147	19670	473	1796	0.45	0.8071	0.0087	0.09805	0.00098	0.36	0.05979	0.00052	601	5	603	6	595	19	101
PIL16_148	2892	70	355	0.64	0.8820	0.0220	0.10430	0.00140	0.35	0.06210	0.00150	643	11	640	8	671	49	95
PIL16_149	161200	236	7300	0.78	13.0330	0.1200	0.51330	0.00510	0.53	0.18460	0.00120	2682	9	2671	22	2694	11	99
PIL16_150	182200	652	688	0.02	5.3110	0.0880	0.30660	0.00340	0.82	0.12560	0.00130	1870	14	1724	17	2037	19	85
PIL16_151	41000	1130	2140	0.27	0.7637	0.0073	0.09309	0.00093	0.55	0.05947	0.00037	576	4	574	6	587	14	98
PIL16_152	40250	184	838	0.21	4.2930	0.0490	0.26600	0.00270	0.61	0.11637	0.00089	1691	9	1521	14	1902	14	80
PIL16_153	22570	560	1918	0.43	0.7974	0.0080	0.09609	0.00093	0.53	0.06010	0.00044	595	5	591	6	607	16	97
PIL16_154	10900	283	1744	0.81	0.8304	0.0100	0.09925	0.00110	0.34	0.06088	0.00064	614	6	610	6	633	23	96
PIL16_155	2263	50	240	0.51	0.9130	0.0180	0.10730	0.00120	0.22	0.06150	0.00120	659	10	657	7	661	41	99
PIL16_156	9270	225	1850	1.06	0.8350	0.0120	0.09900	0.00120	0.57	0.06053	0.00077	616	7	609	7	623	28	98

Table B9 (continued): Results of LA-ICP-MS zircon U–Pb analyses performed during the sessions at ETH Zürich, 12 to 14th of February, 2017

grain	^{207}Pb[a] (cps)	U[b] (ppm)	Pb[b] (ppm)	Th[b]/U	$^{207}Pb/^{235}U$[c]	±2σ (abs)	$^{206}Pb/^{238}U$[c]	±2σ (abs)	rho[d]	$^{207}Pb/^{206}Pb$[c]	±2σ (abs)	$^{207}Pb/^{235}U$	±2σ (Ma)	$^{206}Pb/^{238}U$	±2σ (Ma)	$^{207}Pb/^{206}Pb$	±2σ (Ma)	conc.[e] (%)
PIL16_157	1519	33	168	0.57	0.9070	0.0190	0.10519	0.00130	0.09	0.06170	0.00120	654	10	645	8	679	43	95
PIL16_158	1039	25	223	1.12	0.8180	0.0240	0.09888	0.00120	0.06	0.06000	0.00180	609	13	608	7	613	61	99
PIL16_159	23520	524	725	0.17	0.8953	0.0093	0.10560	0.00110	0.70	0.06137	0.00040	649	5	647	6	651	14	99
PIL16_160	729	18	436	3.27	0.8000	0.0280	0.09250	0.00130	0.14	0.06250	0.00220	595	16	570	8	688	69	83
PIL16_161	13070	373	1390	0.50	0.7438	0.0092	0.08752	0.00110	0.57	0.06163	0.00056	565	5	541	6	660	20	82
PIL16_162	94600	284	9290	1.06	6.4670	0.0800	0.35920	0.00410	0.60	0.12940	0.00130	2041	11	1978	19	2093	16	95
PIL16_163	28830	124	3391	1.18	4.9090	0.0570	0.30740	0.00370	0.42	0.11580	0.00120	1803	10	1728	18	1892	19	91
PIL16_164	10270	273	829	0.40	0.7435	0.0100	0.09120	0.00088	0.43	0.05931	0.00067	564	6	563	5	575	25	98
PIL16_165	13690	316	1174	0.45	0.8800	0.0120	0.10446	0.00130	0.77	0.06113	0.00046	641	6	640	8	642	16	100
PIL16_166	27200	85	2020	0.83	7.3500	0.2000	0.39540	0.00890	0.98	0.13400	0.00150	2123	37	2136	47	2149	20	99
PIL16_167	13580	290	313	0.05	0.9350	0.0180	0.09979	0.00100	0.68	0.06790	0.00100	669	9	613	6	864	30	71
PIL16_168	9200	220	1412	0.77	0.8412	0.0100	0.10091	0.00100	0.31	0.06059	0.00061	620	6	620	6	622	22	100
PIL16_169	45200	735	6210	0.77	1.2660	0.0690	0.10021	0.00130	0.72	0.09120	0.00430	821	31	616	7	1393	92	44
PIL16_170	6160	149	551	0.45	0.8300	0.0120	0.09942	0.00099	0.33	0.06051	0.00074	613	7	611	6	621	26	98
PIL16_171	5720	94	326	0.34	1.2330	0.0190	0.13392	0.00140	0.21	0.06691	0.00095	816	8	811	8	832	29	97
PIL16_172	10160	272	1048	0.52	0.8420	0.0280	0.09870	0.00140	0.08	0.06290	0.00190	620	15	607	8	699	64	87
PIL16_173	26500	671	1989	0.39	0.7576	0.0085	0.09209	0.00093	0.50	0.05980	0.00049	573	5	568	6	595	18	95
PIL16_174	21500	490	1778	0.32	0.8972	0.0110	0.07775	0.00089	0.42	0.08378	0.00079	651	5	483	5	1286	18	38
PIL16_175	50870	1271	2297	0.23	0.7774	0.0100	0.09428	0.00099	0.74	0.06002	0.00059	584	6	581	6	603	21	96
PIL16_176	57710	1423	8300	0.79	0.8674	0.0110	0.09983	0.00110	0.67	0.06312	0.00054	634	6	613	6	711	18	86
PIL16_177	12540	230	1860	0.66	1.1300	0.0310	0.09705	0.00110	0.47	0.08290	0.00180	766	14	597	7	1279	45	47
PIL16_178	11900	310	1934	0.84	0.7760	0.0120	0.09422	0.00100	0.54	0.05968	0.00073	583	7	580	6	590	26	98
PIL16_179	6640	197	826	0.53	0.6630	0.0190	0.07470	0.00150	0.75	0.06458	0.00098	515	12	464	9	754	32	62
PIL16_180	15040	409	1449	0.45	0.7375	0.0090	0.08546	0.00089	0.61	0.06272	0.00052	561	5	529	5	699	18	76
PIL16_181	19860	212	2380	0.68	1.7630	0.0580	0.09848	0.00110	0.84	0.12970	0.00360	1028	20	606	7	2087	47	29
PIL16_182	10310	257	599	0.29	0.8041	0.0083	0.09693	0.00096	0.32	0.06025	0.00047	599	5	596	6	611	17	98
PIL16_183	4310	103	617	0.66	0.8470	0.0140	0.10096	0.00120	0.42	0.06107	0.00090	623	8	620	7	635	32	98
PIL16_184	16050	321	1799	0.62	0.9399	0.0110	0.11033	0.00120	0.30	0.06229	0.00066	673	6	675	7	687	24	98
PIL16_185	14620	365	2259	0.79	0.8280	0.0220	0.09438	0.00120	0.80	0.06330	0.00110	611	12	581	7	717	37	81
PIL16_186	9360	149	1230	0.61	1.2600	0.1200	0.07960	0.00400	0.76	0.11650	0.00530	807	46	493	24	1871	70	26
PIL16_187	14570	362	2330	0.83	0.8111	0.0090	0.09740	0.00095	0.48	0.06037	0.00047	604	5	599	6	615	17	97
PIL16_188	15490	426	229	0.07	0.7384	0.0082	0.08863	0.00089	0.49	0.06037	0.00049	562	5	547	5	617	18	89
PIL16_189	3740	97	551	0.75	0.7900	0.0140	0.09225	0.00110	0.39	0.06172	0.00094	591	8	569	7	667	33	85
PIL16_190	7591	179	1764	1.20	0.8580	0.0130	0.10220	0.00140	0.70	0.06086	0.00062	628	7	627	8	631	22	99
PIL16_191	3572	87	533	0.76	0.8330	0.0130	0.10027	0.00110	0.29	0.06037	0.00080	615	7	616	7	619	29	99
PIL16_192	8260	151	1541	1.09	1.0360	0.0140	0.11358	0.00120	0.20	0.06635	0.00094	722	7	694	7	815	29	85
PIL16_193	17880	430	1191	0.34	0.8329	0.0097	0.09980	0.00095	0.40	0.06057	0.00055	615	5	614	6	624	19	98
PIL16_194	5410	136	707	0.65	0.8090	0.0120	0.09831	0.00110	0.57	0.05970	0.00069	602	7	605	7	590	25	102
PIL16_195	5420	166	298	0.27	0.7490	0.0170	0.09070	0.00140	0.11	0.06140	0.00180	568	10	560	8	648	61	86
PIL16_196	8830	197	920	0.53	0.8741	0.0110	0.10364	0.00100	0.37	0.06105	0.00063	638	6	636	6	641	22	99
PIL16_197	13700	54	796	0.60	4.8190	0.0580	0.31130	0.00350	0.38	0.11230	0.00110	1788	10	1749	17	1838	18	95
PIL16_198	25500	456	2000	0.42	1.1392	0.0110	0.12697	0.00130	0.53	0.06492	0.00042	772	5	771	7	771	14	100
PIL16_199	303000	1316	4570	0.11	4.4540	0.0810	0.25820	0.00380	0.86	0.12530	0.00100	1722	15	1481	19	2032	15	73
PIL16_200	5280	136	986	0.96	0.7460	0.0130	0.09040	0.00100	0.14	0.06020	0.00100	566	7	558	6	606	37	92
PIL16_201	30600	500	3330	0.58	1.3230	0.0620	0.09990	0.00140	0.13	0.09540	0.00440	848	28	614	8	1504	92	41
PIL16_202	8900	224	825	0.45	0.7710	0.0150	0.09065	0.00097	0.41	0.06170	0.00100	580	9	559	6	658	36	85
PIL16_203	5770	147	1296	1.13	0.8870	0.0240	0.10136	0.00130	0.27	0.06450	0.00180	644	13	622	8	750	58	83
PIL16_204	21430	523	586	0.14	0.8716	0.0100	0.10305	0.00110	0.57	0.06116	0.00051	636	6	632	7	644	18	98

Table B9 (continued): Results of LA-ICP-MS zircon U–Pb analyses performed during the sessions at ETH Zürich, 12 to 14th of February, 2017

grain	^{207}Pb[a] (cps)	U[b] (ppm)	Pb[b] (ppm)	Th[b]/U	$^{207}Pb/^{235}U$[c]	±2σ (abs)	$^{206}Pb/^{238}U$[c]	±2σ (abs)	rho[d]	$^{207}Pb/^{206}Pb$[c]	±2σ (abs)	$^{207}Pb/^{235}U$	±2σ (Ma)	$^{206}Pb/^{238}U$	±2σ (Ma)	$^{207}Pb/^{206}Pb$	±2σ (Ma)	conc.[e] (%)
PIL16_205	14320	371	3390	1.20	0.7780	0.0140	0.08965	0.00130	0.84	0.06298	0.00057	585	8	553	8	710	20	78
PIL16_206	45400	1194	3000	0.33	0.8141	0.0087	0.09797	0.00110	0.36	0.06049	0.00051	605	5	603	7	620	18	97
PIL16_207	12130	141	608	0.31	1.7350	0.0260	0.16770	0.00180	0.35	0.07514	0.00091	1024	9	999	10	1070	24	93
PIL16_208	9130	235	662	0.36	0.7495	0.0100	0.08844	0.00097	0.39	0.06132	0.00074	568	6	546	6	647	26	84
PIL16_209	13340	160	2508	1.15	1.5740	0.0260	0.16010	0.00190	0.92	0.07107	0.00096	960	10	957	11	958	28	100
PIL16_210	12120	316	738	0.29	0.7970	0.0140	0.09393	0.00110	0.52	0.06146	0.00089	595	8	579	6	653	31	89
PIL16_211	17160	249	580	0.16	1.3300	0.0150	0.12882	0.00140	0.62	0.07473	0.00059	860	6	781	8	1065	17	73
PIL16_212	9810	242	1218	0.58	0.8570	0.0160	0.09600	0.00140	0.37	0.06550	0.00110	628	9	591	8	796	33	74
PIL16_213	6600	113	285	0.16	1.1610	0.0490	0.10670	0.00260	0.84	0.07990	0.00220	786	24	653	15	1195	55	55
PIL16_214	4100	119	519	0.63	0.7490	0.0170	0.09178	0.00110	0.26	0.05920	0.00130	569	9	566	6	569	48	99
PIL16_215	81600	313	4920	0.63	5.0050	0.0490	0.30150	0.00320	0.63	0.12018	0.00077	1820	8	1699	16	1958	12	87
PIL16_216	13960	319	1681	0.62	0.8656	0.0100	0.09957	0.00098	0.30	0.06297	0.00064	633	6	612	6	709	21	86
Seq. 3																		
MM-03 Vivarais amphibolite																		
MM03_1	16430	585	3480	0.76	0.6460	0.0650	0.07014	0.00098	0.69	0.06750	0.00610	506	35	437	6	851	130	51
MM03_2	31810	1214	9420	1.06	0.6230	0.0090	0.07640	0.00130	0.74	0.05896	0.00130	492	6	475	8	564	43	84
MM03_3	19050	803	5640	1.08	0.5906	0.0098	0.07373	0.00080	0.78	0.05822	0.00051	471	6	459	5	541	19	85
MM03_4	22460	1106	14290	2.50	0.5299	0.0064	0.06676	0.00068	0.60	0.05771	0.00044	432	4	417	4	517	16	81
MM03_5	32300	1300	11080	1.33	0.5990	0.0110	0.07470	0.00140	0.90	0.05814	0.00038	476	7	465	9	534	14	87
MM03_6	14130	650	5220	1.28	0.5181	0.0066	0.06683	0.00073	0.64	0.05689	0.00057	424	4	417	4	484	22	86
MM03_7	19460	1059	4220	0.60	0.4713	0.0052	0.06095	0.00050	0.45	0.05593	0.00067	392	4	381	3	448	25	85
MM03_8	20530	1025	5760	0.59	0.4740	0.0100	0.06170	0.00076	0.88	0.05583	0.00061	394	7	386	5	444	23	87
MM03_9	25740	1328	10200	1.43	0.4734	0.0054	0.05839	0.00051	0.65	0.05873	0.00044	393	4	366	3	556	16	66
MM03_10	6200	247	3050	1.91	0.6450	0.0230	0.08000	0.00220	0.39	0.05740	0.00140	505	15	496	13	516	53	96
MM03_11	20800	1040	4540	0.76	0.4720	0.0100	0.05808	0.00076	0.49	0.05940	0.00081	393	7	364	5	577	28	63
MM03_12	61000	2150	28500	3.51	0.7080	0.0510	0.05981	0.00086	0.86	0.08560	0.00530	530	23	374	5	1242	92	30
MM03_13	44660	1744	4037	0.33	0.5999	0.0067	0.06735	0.00057	0.08	0.06473	0.00088	477	4	420	4	767	28	55
MM03_15	2882	199	44	0.06	0.3593	0.0062	0.04921	0.00043	0.03	0.05260	0.00087	312	5	310	3	305	37	102
ROC-16-01 Rocles syntectonic granite																		
ROC16_1	20710	1167	1011	0.19	0.4182	0.0220	0.05536	0.00068	0.45	0.05482	0.00290	355	14	347	4	404	90	86
ROC16_2	16180	861	1864	0.43	0.4130	0.0068	0.05131	0.00058	0.78	0.05852	0.00057	351	5	323	4	547	21	59
ROC16_3	7680	491	909	0.48	0.3681	0.0050	0.05013	0.00040	0.30	0.05369	0.00060	318	4	315	3	354	25	89
ROC16_4	11530	666	1480	0.53	0.3932	0.0063	0.05066	0.00049	0.63	0.05606	0.00069	337	5	319	3	451	27	71
ROC16_5	80000	2520	5350	0.03	0.7470	0.0600	0.04891	0.00210	0.33	0.11060	0.00420	564	30	308	13	1811	69	17
ROC16_6	17570	1153	508	0.11	0.3742	0.0046	0.05080	0.00042	0.39	0.05411	0.00046	323	3	320	3	374	18	86
ROC16_7	6250	366	709	0.46	0.3724	0.0047	0.05091	0.00048	0.34	0.05283	0.00061	321	3	320	3	327	27	98
ROC16_8	87500	5020	1080	0.04	0.4082	0.0043	0.05425	0.00063	0.83	0.05443	0.00031	348	3	341	4	388	13	88
ROC16_9	117000	1494	12700	0.35	1.7600	0.1600	0.06620	0.00200	0.99	0.18700	0.01200	998	60	413	12	2640	110	16
ROC16_10	49800	1282	7090	0.78	0.8320	0.0510	0.05652	0.00075	0.94	0.10750	0.00550	613	27	354	5	1760	90	20
ROC16_11	150000	1703	16800	0.57	1.9100	0.1300	0.06570	0.00140	0.91	0.21100	0.01100	1076	46	410	8	2859	91	14
ROC16_12	7110	469	845	0.47	0.3727	0.0065	0.05077	0.00048	0.15	0.05310	0.00085	322	5	319	3	338	34	94
ROC16_13	25910	889	3485	0.54	0.6930	0.0300	0.05333	0.00054	0.47	0.09400	0.00380	531	18	335	3	1467	81	23
ROC16_14	842000	2200	93000	0.37	7.6600	0.4600	0.12380	0.00520	0.95	0.44600	0.01200	2167	57	751	30	4058	43	19
ROC16_15	14000	645	2750	0.92	0.4950	0.0310	0.05219	0.00077	0.68	0.06890	0.00400	404	20	328	5	860	120	38
ROC16_16	9330	512	837	0.36	0.4367	0.0076	0.05154	0.00060	0.43	0.06166	0.00081	368	6	324	4	659	29	49

Table B9 (continued): Results of LA-ICP-MS zircon U–Pb analyses performed during the sessions at ETH Zürich, 12 to 14th of February, 2017

grain	^{207}Pb[a] (cps)	U[b] (ppm)	Pb[b] (ppm)	Th[b]/U	$^{207}Pb/^{235}U$[c]	±2σ (abs)	$^{206}Pb/^{238}U$[c]	±2σ (abs)	rho[d]	$^{207}Pb/^{206}Pb$[c]	±2σ (abs)	$^{207}Pb/^{235}U$ (Ma)	±2σ	$^{206}Pb/^{238}U$ (Ma)	±2σ	$^{207}Pb/^{206}Pb$ (Ma)	±2σ	conc.[e] (%)
ROC16_18	54500	724	6480	0.48	1.7020	0.0340	0.09251	0.00100	0.24	0.13360	0.00260	1008	13	570	6	2138	34	27
ROC16_20	30300	752	3780	0.44	0.8650	0.0320	0.05235	0.00054	0.16	0.12150	0.00490	633	18	329	3	1939	73	17
ROC16_21	59000	829	5600	0.12	1.6300	5.9000	0.06580	0.07200	0.96	0.17100	0.04100	930	330	410	330	2510	190	16
ROC16_22	7180	445	1208	0.69	0.3699	0.0064	0.05044	0.00045	0.58	0.05355	0.00081	319	5	317	3	350	35	91
ROC16_23	11840	558	1494	0.52	0.4600	0.0120	0.05119	0.00065	0.54	0.06490	0.00210	383	8	322	4	750	65	43
ROC16_24	13520	586	475	0.14	0.4840	0.0064	0.06238	0.00095	0.42	0.05667	0.00055	401	4	390	6	481	21	81
ROC16_25	25090	1491	1283	0.20	0.3818	0.0100	0.04998	0.00039	0.50	0.05482	0.00140	328	7	314	2	403	48	78
ROC16_27	14560	234	1340	0.49	1.3740	0.0150	0.14572	0.00110	0.49	0.06859	0.00054	878	6	877	6	889	17	99
ROC16_28	22770	1130	1064	0.10	0.4780	0.0093	0.05114	0.00048	0.14	0.06790	0.00160	396	6	322	3	868	42	37
ROC16_29	16030	402	2241	0.71	0.9450	0.0340	0.04945	0.00050	0.29	0.13870	0.00470	675	19	311	3	2212	72	14
ROC16_30	10900	380	1330	0.44	0.6170	0.0490	0.04993	0.00069	0.26	0.08950	0.00600	487	25	314	4	1412	100	22
SEN-16-01 Senouire meta-sediments																		
SEN16_1	5450	98	606	0.59	1.2030	0.0170	0.13210	0.00110	0.33	0.06625	0.00090	802	8	800	6	813	27	98
SEN16_2	15930	352	2864	0.86	0.9220	0.0110	0.10929	0.00100	0.18	0.06144	0.00053	664	6	669	6	657	19	102
SEN16_3	55420	1537	4628	0.41	0.8201	0.0084	0.09926	0.00110	0.78	0.06004	0.00039	608	5	610	7	604	14	101
SEN16_4	19530	471	1919	0.49	0.8590	0.0120	0.10121	0.00089	0.74	0.06160	0.00053	629	7	622	5	659	18	94
SEN16_5	65500	583	6210	0.84	2.6450	0.0400	0.16790	0.00210	0.70	0.11500	0.00077	1313	12	1000	12	1879	13	53
SEN16_6	36080	220	1556	0.34	3.9560	0.0570	0.28150	0.00380	0.67	0.10380	0.00066	1625	13	1599	19	1692	12	95
SEN16_7	117500	2869	5800	0.19	0.9520	0.0370	0.10810	0.00130	0.76	0.06445	0.00250	679	18	662	8	755	66	88
SEN16_8	18740	239	3046	0.94	1.6890	0.0160	0.16860	0.00140	0.44	0.07250	0.00049	1004	6	1005	8	998	14	101
SEN16_9	24030	682	3860	0.80	0.8490	0.0091	0.10213	0.00092	0.44	0.06150	0.00048	624	5	627	5	654	16	96
SEN16_10	2850	77	1538	2.55	0.7530	0.0150	0.09251	0.00099	0.31	0.06010	0.00096	569	9	570	6	606	35	94
SEN16_11	213500	840	5580	0.27	5.5540	0.0700	0.34470	0.00380	0.92	0.11718	0.00057	1908	11	1909	18	1914	9	100
SEN16_12	14510	200	2962	1.21	1.6540	0.0200	0.16370	0.00140	0.61	0.07360	0.00064	993	8	977	8	1029	18	95
SEN16_13	18010	278	980	0.27	1.3550	0.0180	0.14410	0.00160	0.68	0.06824	0.00053	871	8	868	9	875	16	99
SEN16_14	11760	340	2942	1.19	0.8240	0.0260	0.09989	0.00089	0.16	0.06010	0.00180	610	14	614	5	604	53	102
SEN16_15	19550	99	2057	0.93	4.6760	0.0690	0.31370	0.00400	0.90	0.10750	0.00088	1762	14	1775	20	1756	15	101
SEN16_17	185000	1126	20900	0.70	3.3200	0.1700	0.08710	0.00270	0.73	0.27660	0.00980	1487	48	539	16	3346	64	16
SEN16_18	25080	393	5810	1.67	1.3760	0.0450	0.09515	0.00110	0.33	0.10530	0.00300	878	19	586	6	1713	54	34
SEN16_19	17410	412	4604	1.29	0.8570	0.0130	0.10184	0.00085	0.41	0.06152	0.00065	628	7	625	5	656	21	95
SEN16_21	6240	120	618	0.46	1.1730	0.0180	0.13030	0.00180	0.54	0.06566	0.00081	788	9	790	10	801	25	99
SEN16_22	8100	199	1486	0.87	0.8730	0.0130	0.10040	0.00100	0.52	0.06391	0.00082	637	7	617	6	740	28	83
SEN16_23	3473	92	749	1.02	0.7710	0.0150	0.09452	0.00086	0.54	0.05880	0.00110	580	9	582	5	570	40	102
SEN16_24	26390	625	218	0.08	0.9860	0.0120	0.11244	0.00100	0.79	0.06366	0.00039	697	6	687	6	730	13	94
SEN16_25	3860	115	730	0.87	0.8010	0.0150	0.09670	0.00120	0.08	0.06080	0.00110	597	9	595	7	634	38	94
SEN16_26	80900	128	4210	0.74	13.2400	0.1900	0.51190	0.00570	0.77	0.18620	0.00150	2697	14	2665	25	2708	14	98
SEN16_27	6690	202	2502	1.80	0.7760	0.0230	0.09344	0.00100	0.26	0.06050	0.00180	583	12	576	6	619	56	93
SEN16_28	9070	235	1177	0.62	0.7960	0.0100	0.09581	0.00083	0.42	0.06090	0.00057	595	6	590	5	632	21	93
SEN16_29	12840	189	2418	1.13	1.6280	0.0200	0.16370	0.00150	0.37	0.07267	0.00068	981	8	977	8	1003	19	97
SEN16_30	27430	739	7480	1.33	0.8660	0.0140	0.10264	0.00130	0.58	0.06189	0.00044	633	8	630	8	669	16	94
SEN16_31	15100	286	2680	0.94	1.2300	0.0160	0.13580	0.00120	0.51	0.06636	0.00064	814	7	821	7	820	20	100
SEN16_32	22200	509	2810	0.59	1.0280	0.0210	0.11370	0.00150	0.67	0.06579	0.00069	717	11	694	9	796	23	87
SEN16_34	13720	396	2189	0.75	0.8190	0.0150	0.09872	0.00098	0.42	0.06056	0.00077	608	8	608	6	626	25	97
SEN16_35	99100	291	6630	0.77	7.2620	0.0680	0.38840	0.00300	0.69	0.13623	0.00078	2145	9	2115	14	2179	10	97
SEN16_36	23060	592	5122	1.10	0.9060	0.0130	0.10735	0.00180	0.56	0.06138	0.00057	655	7	659	11	655	19	101
SEN16_37	4780	107	1218	1.35	1.0490	0.0190	0.10225	0.00130	0.01	0.07500	0.00160	730	9	628	8	1079	42	58
SEN16_38	14870	353	2104	0.70	0.8520	0.0160	0.10186	0.00087	0.56	0.06159	0.00084	626	8	625	5	658	27	95

Table B9 (continued): Results of LA-ICP-MS zircon U–Pb analyses performed during the sessions at ETH Zürich, 12 to 14th of February, 2017

grain	^{207}Pb[a] (cps)	U[b] (ppm)	Pb[b] (ppm)	Th[b] U	$\frac{^{207}Pb^c}{^{235}U}$	±2σ (abs)	$\frac{^{206}Pb^c}{^{238}U}$	±2σ (abs)	rho[d]	$\frac{^{207}Pb^c}{^{206}Pb}$	±2σ (abs)	$\frac{^{207}Pb}{^{235}U}$	±2σ (Ma)	$\frac{^{206}Pb}{^{238}U}$	±2σ (Ma)	$\frac{^{207}Pb}{^{206}Pb}$	±2σ (Ma)	conc.[e] (%)
SEN16_39	32380	410	2635	0.45	1.6090	0.0180	0.16440	0.00150	0.75	0.07176	0.00050	973	7	981	8	978	14	100
SEN16_40	13450	331	3770	1.33	0.8440	0.0140	0.10052	0.00140	0.67	0.06094	0.00046	622	7	618	8	643	16	96
SEN16_41	23720	620	4050	1.08	0.8464	0.0100	0.09188	0.00083	0.63	0.06708	0.00050	623	6	567	5	839	15	68
SEN16_42	157400	1209	16800	0.78	2.7400	0.1300	0.08000	0.00130	0.48	0.25100	0.01000	1327	33	496	8	3170	64	16
SEN16_43	12090	303	1950	0.79	0.8793	0.0100	0.10461	0.00083	0.44	0.06092	0.00057	640	5	641	5	639	21	100
SEN16_44	20430	360	865	0.17	1.2400	0.0150	0.12794	0.00120	0.75	0.07019	0.00054	819	7	776	7	932	16	83
SEN16_45	3960	104	1458	1.76	0.7800	0.0470	0.09464	0.00110	0.36	0.06040	0.00280	585	24	583	6	623	79	94
SEN16_46	16090	432	2910	0.85	0.8272	0.0085	0.10030	0.00080	0.58	0.06013	0.00046	612	5	616	5	608	16	101
SEN16_47	12200	329	3092	1.19	0.8060	0.0120	0.09669	0.00089	0.68	0.06034	0.00063	601	7	595	5	616	22	97
SEN16_48	12960	234	542	0.19	1.3270	0.0250	0.14190	0.00230	0.63	0.06790	0.00049	857	12	856	13	863	16	99
SEN16_49	194900	353	8100	0.72	13.3900	0.1500	0.51120	0.00440	0.64	0.19220	0.00120	2707	11	2661	19	2760	10	96
SEN16_50	34330	725	1912	0.28	1.0790	0.0110	0.12250	0.00096	0.54	0.06402	0.00044	743	6	745	6	744	15	100
SEN16_51	27090	537	1940	0.32	1.1001	0.0110	0.12345	0.00100	0.57	0.06474	0.00046	753	5	750	6	764	15	98
SEN16_52	2370	71	963	1.89	0.7510	0.0160	0.09150	0.00088	0.40	0.05940	0.00120	568	10	564	5	574	44	98
SEN16_53	17760	208	4050	1.36	1.7630	0.0410	0.17220	0.00290	0.76	0.07470	0.00085	1031	16	1026	16	1062	22	97
SEN16_54	20500	256	1880	0.54	1.7370	0.0370	0.17280	0.00390	0.94	0.07364	0.00051	1023	14	1027	21	1030	14	100
SEN16_55	36870	842	6224	0.90	1.0300	0.0140	0.10920	0.00120	0.34	0.06840	0.00110	718	7	668	7	876	31	76
SEN16_56	13750	346	3400	1.20	0.8840	0.0110	0.10515	0.00100	0.62	0.06080	0.00056	643	6	645	6	635	20	101
SEN16_57	15880	439	1180	0.31	0.7906	0.0093	0.09558	0.00071	0.45	0.06026	0.00058	592	5	589	4	612	21	96
SEN16_58	9760	233	1640	0.78	0.9260	0.0110	0.10837	0.00089	0.47	0.06206	0.00063	665	6	663	5	673	22	99
SEN16_59	74400	115	4910	1.26	16.4500	0.2200	0.56900	0.00720	0.68	0.21520	0.00110	2903	14	2902	31	2944	8	99
SEN16_60	232500	615	7160	0.48	9.0000	0.2000	0.41750	0.00680	0.82	0.15700	0.00130	2337	23	2249	32	2423	15	93
SEN16_61	28210	675	2116	0.35	0.9790	0.0190	0.10561	0.00087	0.48	0.06743	0.00140	693	9	647	5	849	39	76
SEN16_62	15660	275	956	0.33	1.3540	0.0150	0.14440	0.00130	0.44	0.06853	0.00051	869	6	869	8	883	16	98
SEN16_64	34050	776	6750	0.97	0.9030	0.0800	0.10858	0.00130	0.71	0.06079	0.00410	653	27	665	8	630	82	105
SEN16_65	6670	191	1266	0.87	0.7728	0.0110	0.09387	0.00077	0.33	0.05995	0.00070	581	6	578	5	601	25	96
SEN16_66	52110	1248	8667	0.83	0.9311	0.0084	0.10957	0.00093	0.67	0.06193	0.00036	668	4	670	5	672	12	100
SEN16_67	94300	354	3340	0.46	5.8900	0.0550	0.29400	0.00250	0.78	0.14570	0.00066	1960	8	1663	12	2297	8	72
SEN16_68	135000	207	2780	0.26	13.9900	0.2300	0.53260	0.00690	0.69	0.19000	0.00150	2750	16	2752	29	2741	13	100
SEN16_69	4110	73	397	0.43	1.2420	0.0280	0.11030	0.00170	0.32	0.08150	0.00180	821	13	674	10	1221	43	55
SEN16_70	24430	512	1848	0.33	1.0200	0.0110	0.11365	0.00100	0.58	0.06510	0.00044	714	6	694	6	781	14	89
SEN16_71	6390	159	456	0.34	0.8430	0.0100	0.10037	0.00080	0.22	0.06110	0.00073	620	6	617	5	638	25	97
SEN16_72	87100	312	732	0.07	6.3000	0.0620	0.36790	0.00310	0.51	0.12390	0.00085	2018	8	2020	15	2013	12	100
SEN16_73	11020	249	178	0.08	1.0120	0.0130	0.11620	0.00098	0.53	0.06324	0.00057	710	7	709	6	720	20	98
SEN16_74	7510	137	1585	1.12	1.1840	0.0160	0.13147	0.00120	0.39	0.06515	0.00077	794	8	796	7	775	25	103
SEN16_75	90100	309	2980	0.38	6.7200	0.1700	0.37960	0.00740	0.62	0.12860	0.00110	2076	25	2074	35	2083	16	100
SEN16_76	16770	377	2076	0.59	0.9180	0.0110	0.10900	0.00099	0.67	0.06195	0.00052	663	6	667	6	671	18	99
SEN16_77	27480	651	5750	1.06	0.8760	0.0140	0.10398	0.00083	0.42	0.06162	0.00068	639	7	638	5	659	23	97
SEN16_78	19860	522	9030	2.08	0.8180	0.0230	0.09802	0.00081	0.45	0.06069	0.00160	607	12	603	5	639	49	94
SEN16_79	5192	143	2330	2.05	0.7910	0.0130	0.09554	0.00090	0.28	0.05999	0.00091	592	7	588	5	601	33	98
SEN16_80	17750	464	4460	1.18	0.8397	0.0086	0.10162	0.00086	0.64	0.05950	0.00043	619	5	624	5	587	15	106
SEN16_81	16440	440	3850	1.13	0.7940	0.0099	0.09690	0.00096	0.57	0.05958	0.00046	593	6	596	6	587	16	102
SEN16_82	212200	682	5150	0.28	6.8800	0.0660	0.39030	0.00350	0.77	0.12710	0.00060	2096	9	2124	16	2058	8	103
SEN16_83	301200	1296	1576	0.06	5.7700	0.2000	0.34550	0.01200	0.53	0.12230	0.00077	1941	36	1913	63	1990	11	96
SEN16_84	104300	470	5660	0.57	5.1900	0.1400	0.27520	0.00630	0.97	0.13717	0.00086	1848	23	1566	32	2191	11	71
SEN16_85	18730	554	7180	1.93	0.7620	0.0110	0.08800	0.00160	0.82	0.06369	0.00058	577	6	543	9	729	20	75
SEN16_86	19830	649	5570	1.45	0.7330	0.0100	0.08110	0.00140	0.53	0.06600	0.00062	558	6	503	8	804	20	63
SEN16_88	802	2	95	1.37	11.3000	2.7000	0.14690	0.03000	0.50	0.55800	0.02600	2553	110	882	140	4384	66	20

Table B9 (continued): Results of LA-ICP-MS zircon U–Pb analyses performed during the sessions at ETH Zürich, 12 to 14th of February, 2017

grain	^{207}Pb[a] (cps)	U[b] (ppm)	Pb[b] (ppm)	Th[b]/U	$^{207}Pb/^{235}U$[c]	±2σ (abs)	$^{206}Pb/^{238}U$[c]	±2σ (abs)	rho[d]	$^{207}Pb/^{206}Pb$[c]	±2σ (abs)	$^{207}Pb/^{235}U$	±2σ (Ma)	$^{206}Pb/^{238}U$	±2σ (Ma)	$^{207}Pb/^{206}Pb$	±2σ (Ma)	conc.[e] (%)
CHA-16-02 Cévennes meta-sediments																		
CHA16_1	13810	388	2309	0.78	0.8510	0.0160	0.09511	0.00250	0.67	0.06511	0.00320	625	9	586	15	776	80	75
CHA16_2	5930	153	721	0.59	0.8670	0.0130	0.10296	0.00088	0.34	0.06079	0.00082	634	7	632	5	642	27	98
CHA16_3	21990	58	787	0.40	7.8600	0.2800	0.41660	0.01300	0.84	0.13920	0.00094	2213	27	2245	57	2216	12	101
CHA16_4	15390	383	1822	0.62	0.9600	0.0140	0.10733	0.00200	0.20	0.06482	0.00110	683	7	657	12	766	34	86
CHA16_5	22360	642	7490	1.60	0.8790	0.0170	0.10440	0.00120	0.61	0.06128	0.00074	640	9	640	7	648	24	99
CHA16_6	420200	530	14090	0.68	18.7400	0.1700	0.59370	0.00470	0.72	0.22920	0.00120	3028	9	3004	19	3046	8	99
CHA16_7	26980	844	1406	0.24	0.7870	0.0100	0.09423	0.00091	0.79	0.06038	0.00048	589	6	581	5	616	17	94
CHA16_8	10370	309	904	0.40	0.7680	0.0120	0.09381	0.00082	0.45	0.05987	0.00074	578	7	578	5	605	27	96
CHA16_9	36700	859	3530	0.43	0.9790	0.0180	0.09110	0.00120	0.29	0.07850	0.00160	692	9	562	7	1154	42	49
CHA16_10	13400	179	1805	0.75	1.5770	0.0200	0.16150	0.00140	0.63	0.07152	0.00058	961	8	965	8	970	17	99
CHA16_11	7820	213	934	0.55	0.8720	0.0130	0.10387	0.00120	0.47	0.06031	0.00071	636	7	637	7	615	26	104
CHA16_12	11820	45	792	0.69	6.0690	0.0680	0.35930	0.00320	0.43	0.12230	0.00100	1985	10	1979	15	1988	15	100
CHA16_13	19250	71	1693	0.86	6.1980	0.0590	0.36440	0.00320	0.61	0.12334	0.00074	2004	8	2003	15	2004	11	100
CHA16_15	21600	607	3300	0.72	0.8648	0.0091	0.10379	0.00092	0.30	0.06045	0.00048	633	5	637	6	618	17	103
CHA16_16	18490	472	2229	0.56	0.9360	0.0130	0.10987	0.00110	0.67	0.06140	0.00061	671	7	672	6	658	21	102
CHA16_17	9470	249	300	0.14	0.8910	0.0110	0.10565	0.00100	0.46	0.06080	0.00060	647	6	648	6	629	21	103
CHA16_18	37790	72	1215	0.47	11.3700	0.1600	0.48570	0.00550	0.69	0.16900	0.00180	2554	16	2552	24	2547	21	100
CHA16_19	13950	368	3713	1.15	0.8342	0.0093	0.09993	0.00095	0.66	0.06095	0.00052	616	5	614	6	636	19	97
CHA16_20	8920	281	366	0.17	0.8350	0.0170	0.09550	0.00210	0.69	0.06410	0.00130	616	9	588	12	739	33	80
CHA16_21	184900	712	2280	0.13	5.8020	0.0830	0.34240	0.00290	0.70	0.12250	0.00074	1946	11	1898	14	1992	11	95
CHA16_22	3245	86	572	0.82	0.8740	0.0170	0.10382	0.00110	0.43	0.06086	0.00095	638	9	637	6	643	35	99
CHA16_23	12730	326	1844	0.65	0.8542	0.0100	0.10186	0.00100	0.35	0.06068	0.00057	627	6	625	6	625	20	100
CHA16_24	3820	86	314	0.37	0.9860	0.0170	0.11470	0.00120	0.29	0.06210	0.00100	697	9	700	7	676	35	104
CHA16_25	10300	254	1193	0.55	0.9257	0.0097	0.10819	0.00091	0.26	0.06209	0.00048	666	5	662	5	678	17	98
CHA16_26	7090	200	768	0.55	0.8180	0.0110	0.08902	0.00069	0.42	0.06637	0.00078	608	6	550	4	817	24	67
CHA16_27	68330	949	1702	0.15	1.5990	0.0210	0.15840	0.00190	0.53	0.07250	0.00048	970	9	948	11	1000	13	95
CHA16_28	14010	402	1956	0.61	0.8810	0.0120	0.08359	0.00190	0.47	0.07750	0.00160	641	6	518	11	1131	49	46
CHA16_29	5760	160	736	0.59	0.8740	0.0400	0.10361	0.00140	0.38	0.06136	0.00210	639	21	636	8	653	63	97
CHA16_30	25230	646	668	0.12	0.8608	0.0120	0.10115	0.00097	0.65	0.06169	0.00054	630	6	621	6	662	18	94
CHA16_31	39640	971	4610	0.57	0.9680	0.0093	0.11240	0.00091	0.66	0.06225	0.00039	687	5	687	5	682	13	101
CHA16_32	12470	312	1796	0.66	0.8570	0.0110	0.10250	0.00120	0.68	0.06120	0.00055	630	6	629	7	644	19	98
CHA16_33	6460	159	1106	0.78	0.9420	0.0180	0.11020	0.00180	0.72	0.06198	0.00063	673	10	674	10	671	22	100
CHA16_34	5920	171	362	0.28	0.7510	0.0087	0.09208	0.00081	0.22	0.05943	0.00064	569	5	568	5	578	24	98
CHA16_35	23680	646	2587	0.50	0.8293	0.0100	0.10042	0.00084	0.26	0.05984	0.00047	613	6	617	5	597	17	103
CHA16_37	40800	698	6090	0.94	1.2610	0.0210	0.10038	0.00110	0.76	0.09070	0.00160	827	9	617	7	1436	34	43
CHA16_38	15320	388	1540	0.47	0.8540	0.0097	0.10193	0.00082	0.51	0.06099	0.00052	627	5	626	5	636	18	98
CHA16_39	5810	155	214	0.17	0.8810	0.0120	0.10471	0.00094	0.30	0.06121	0.00072	641	7	642	6	646	25	99
CHA16_40	1731	48	248	0.70	0.8600	0.0180	0.10284	0.00110	0.05	0.06090	0.00140	631	10	631	6	634	45	100
CHA16_41	37860	1047	1864	0.23	0.9210	0.0110	0.10780	0.00091	0.63	0.06250	0.00047	663	6	660	5	690	16	96
CHA16_42	19550	545	5316	1.28	0.7800	0.0110	0.09504	0.00097	0.42	0.05952	0.00052	585	6	585	6	583	19	100
CHA16_43	4820	60	670	0.87	2.0300	0.0290	0.19010	0.00280	0.43	0.07870	0.00076	1125	10	1122	15	1160	20	97
CHA16_44	4690	125	632	0.62	0.8380	0.0110	0.10011	0.00082	0.28	0.06088	0.00069	618	6	615	5	636	25	97
CHA16_47	3904	103	605	0.73	0.8870	0.0130	0.10288	0.00090	0.08	0.06246	0.00095	644	7	631	5	683	32	92
CHA16_48	11280	363	1314	0.53	0.7501	0.0078	0.09185	0.00084	0.54	0.05946	0.00048	568	5	566	5	582	18	97
CHA16_49	13140	367	1132	0.40	0.8710	0.0110	0.10366	0.00095	0.42	0.06152	0.00061	636	6	636	6	659	21	96
CHA16_50	23820	104	1770	0.71	5.2640	0.0530	0.33470	0.00270	0.62	0.11412	0.00072	1864	8	1861	13	1866	11	100
CHA16_51	6150	165	978	0.74	0.9000	0.0120	0.10710	0.00097	0.12	0.06084	0.00084	652	7	656	6	630	29	104

Table B9 (continued): Results of LA-ICP-MS zircon U–Pb analyses performed during the sessions at ETH Zürich, 12 to 14th of February, 2017

grain	^{207}Pb[a] (cps)	U[b] (ppm)	Pb[b] (ppm)	Th[b]/U	$^{207}Pb/^{235}U$[c]	±2σ (abs)	$^{206}Pb/^{238}U$[c]	±2σ (abs)	rho[d]	$^{207}Pb/^{206}Pb$[c]	±2σ (abs)	$^{207}Pb/^{235}U$ (Ma)	±2σ	$^{206}Pb/^{238}U$ (Ma)	±2σ	$^{207}Pb/^{206}Pb$ (Ma)	±2σ	conc.[e] (%)
CHA16_52	67200	104	1373	0.37	15.6900	0.1800	0.55410	0.00450	0.38	0.20390	0.00190	2858	11	2842	19	2856	15	100
CHA16_53	7510	220	754	0.47	0.7770	0.0110	0.09473	0.00090	0.58	0.05918	0.00063	584	6	583	5	573	22	102
CHA16_54	23200	630	2100	0.44	0.9230	0.0300	0.10800	0.00170	0.64	0.06185	0.00150	664	15	661	10	668	45	99
CHA16_55	9620	251	795	0.39	0.8920	0.0100	0.10616	0.00097	0.37	0.06109	0.00061	647	6	650	6	640	21	102
CHA16_56	14510	406	1371	0.44	0.8750	0.0110	0.10494	0.00089	0.54	0.06082	0.00058	639	6	643	5	629	21	102
CHA16_57	25800	775	3700	0.70	0.8900	0.0120	0.10540	0.00093	0.81	0.06240	0.00084	646	6	646	5	685	25	94
CHA16_59	21600	89	1477	0.75	6.0800	0.0710	0.35990	0.00370	0.74	0.12300	0.00110	1986	11	1981	18	1999	16	99
CHA16_60	29220	889	2941	0.48	0.8420	0.0250	0.09340	0.00340	0.71	0.06678	0.00150	620	15	576	21	830	40	69
CHA16_61	27400	713	5510	0.97	0.9070	0.0095	0.10670	0.00120	0.54	0.06136	0.00071	655	5	654	7	657	24	99
CHA16_62	4950	128	621	0.62	0.8790	0.0120	0.10474	0.00098	0.38	0.06090	0.00080	641	7	642	6	634	28	101
CHA16_63	31100	818	3480	0.54	0.8957	0.0084	0.10642	0.00080	0.54	0.06111	0.00038	650	5	652	5	642	13	102
CHA16_64	13010	359	1174	0.40	0.8373	0.0100	0.10014	0.00093	0.61	0.06062	0.00054	617	6	615	5	627	19	98
CHA16_65	307000	1330	1820	0.06	6.2900	0.0490	0.37080	0.00290	0.68	0.12460	0.00057	2016	7	2033	14	2022	8	101
CHA16_66	32920	1098	6360	1.11	0.7650	0.0310	0.07300	0.00081	0.52	0.07680	0.00410	577	16	454	5	1115	76	41
CHA16_68	17770	483	3330	0.76	0.8625	0.0170	0.10323	0.00098	0.14	0.06051	0.00120	633	9	633	6	623	37	102
CHA16_69	29000	810	5910	0.94	0.8770	0.0140	0.10440	0.00110	0.80	0.06137	0.00058	640	7	640	7	655	20	98
CHA16_70	4109	102	692	0.79	0.9350	0.0160	0.10858	0.00100	0.04	0.06270	0.00099	670	8	665	6	691	33	96
CHA16_71	5240	144	751	0.67	0.8720	0.0120	0.10289	0.00083	0.14	0.06132	0.00081	637	7	631	5	652	28	97
CHA16_73	3218	85	498	0.72	0.8240	0.0230	0.09746	0.00110	0.54	0.06180	0.00120	610	12	600	6	675	38	89
CHA16_74	3660	100	466	0.61	0.8420	0.0120	0.09768	0.00097	0.30	0.06249	0.00069	620	7	601	6	687	25	87
CHA16_75	16550	464	1812	0.52	0.8761	0.0098	0.10288	0.00081	0.47	0.06177	0.00052	639	5	631	5	668	18	95
CHA16_76	14430	202	1480	0.59	1.6670	0.0250	0.16670	0.00240	0.82	0.07222	0.00054	996	10	994	13	991	15	100
CHA16_77	41900	844	3308	0.42	1.2550	0.0140	0.13610	0.00150	0.61	0.06782	0.00079	826	6	823	9	862	23	95
CHA16_78	957	28	527	2.62	0.7950	0.0250	0.09524	0.00110	0.04	0.06050	0.00210	593	14	586	6	600	72	98
CHA16_79	14760	384	637	0.19	0.8792	0.0090	0.10341	0.00090	0.41	0.06169	0.00055	640	5	634	5	661	19	96
CHA16_80	3640	93	698	0.96	0.9330	0.0180	0.10884	0.00092	0.33	0.06210	0.00110	669	10	666	5	673	40	99
CHA16_81	3944	109	681	0.77	0.8280	0.0130	0.09926	0.00089	0.30	0.06075	0.00089	613	7	610	5	624	31	98
CHA16_82	15210	463	1490	0.44	0.7630	0.0092	0.09280	0.00084	0.54	0.05959	0.00050	576	5	572	5	589	18	97
CHA16_83	14900	377	1838	0.59	0.8879	0.0079	0.10579	0.00080	0.38	0.06107	0.00045	646	4	648	5	640	16	101
CHA16_84	10100	289	1080	0.51	0.8225	0.0096	0.09942	0.00120	0.53	0.06023	0.00059	609	5	611	7	614	21	99
CHA16_85	14930	409	4621	1.55	0.7970	0.0082	0.09564	0.00088	0.43	0.06135	0.00043	595	5	589	5	650	15	91
CHA16_86	35200	200	2310	0.56	4.1110	0.0390	0.29370	0.00250	0.62	0.10151	0.00068	1656	8	1660	12	1651	12	101
CHA16_87	11640	329	1790	0.64	0.7660	0.0100	0.09370	0.00099	0.48	0.05980	0.00060	577	6	578	6	604	22	96
CHA16_89	22340	577	2612	0.54	0.8510	0.0083	0.10179	0.00087	0.56	0.06058	0.00057	625	5	625	5	629	20	99
CHA16_90	22820	332	1029	0.24	1.6690	0.0210	0.16597	0.00160	0.49	0.07256	0.00064	996	8	990	9	1000	17	99
CHA16_91	27800	715	4170	0.71	0.9238	0.0093	0.10859	0.00110	0.60	0.06150	0.00045	664	5	665	6	655	16	101
CHA16_92	9240	202	1400	0.71	1.1120	0.0300	0.12350	0.00380	0.45	0.06445	0.00079	759	15	751	22	755	24	99
CHA16_93	15950	383	667	0.21	1.0510	0.0100	0.11932	0.00089	0.42	0.06383	0.00047	729	5	727	5	735	16	99
CHA16_94	12270	284	1769	0.71	0.9560	0.0110	0.11152	0.00120	0.51	0.06208	0.00051	681	5	682	7	676	17	101
CHA16_95	33300	898	2460	0.33	0.8637	0.0110	0.09195	0.00081	0.24	0.06789	0.00066	633	6	567	5	865	20	66
CHA16_96	3408	99	454	0.62	0.8730	0.0140	0.10351	0.00093	0.12	0.06170	0.00100	638	8	635	5	655	36	97
CHA16_97	4750	140	1187	1.16	0.7710	0.0120	0.09378	0.00076	0.17	0.05963	0.00078	580	7	578	5	585	28	99
CHA16_98	15370	467	2540	0.65	0.7928	0.0110	0.08420	0.00140	0.26	0.06870	0.00120	592	6	521	9	890	35	59
CHA16_99	28750	597	4540	0.90	1.1290	0.0120	0.08090	0.00120	0.16	0.10070	0.00170	767	6	502	7	1639	31	31
CHA16_100	1984	57	326	0.74	0.8000	0.0160	0.09651	0.00095	0.16	0.05990	0.00110	596	9	594	6	604	39	98
CHA16_101	28050	902	3730	0.67	0.8040	0.0130	0.08921	0.00150	0.55	0.06504	0.00069	599	8	551	9	774	22	71
CHA16_102	14270	403	3270	1.12	0.8770	0.0120	0.09623	0.00130	0.29	0.06625	0.00058	639	6	592	8	811	18	73
CHA16_103	4860	148	686	0.63	0.8330	0.0140	0.10000	0.00110	0.18	0.06020	0.00085	615	8	615	6	608	29	101

Table B9 (continued): Results of LA-ICP-MS zircon U–Pb analyses performed during the sessions at ETH Zürich, 12 to 14th of February, 2017

grain	^{207}Pb[a] (cps)	U[b] (ppm)	Pb[b] (ppm)	Th[b]/U	$^{207}Pb/^{235}U$[c]	±2σ (abs)	$^{206}Pb/^{238}U$[c]	±2σ (abs)	rho[d]	$^{207}Pb/^{206}Pb$[c]	±2σ (abs)	$^{207}Pb/^{235}U$	±2σ (Ma)	$^{206}Pb/^{238}U$	±2σ (Ma)	$^{207}Pb/^{206}Pb$	±2σ (Ma)	conc.[e] (%)
CHA16_104	9190	254	884	0.44	0.8222	0.0091	0.09853	0.00088	0.37	0.06027	0.00057	609	5	606	5	611	21	99
CHA16_105	19280	372	2368	0.64	1.3270	0.0160	0.13983	0.00140	0.55	0.06810	0.00059	857	7	844	8	876	18	96
CHA16_106	15530	415	699	0.20	0.8120	0.0140	0.09641	0.00100	0.79	0.06166	0.00130	604	8	593	6	660	39	90
CHA16_107	37970	157	10770	2.98	6.3200	0.2800	0.36560	0.01500	0.67	0.12640	0.00110	2021	61	2008	77	2055	16	98
CHA16_108	20260	563	5230	1.19	0.8880	0.0097	0.10498	0.00100	0.43	0.06098	0.00042	646	5	644	6	646	14	100
CHA16_109	15640	514	4470	1.32	0.7920	0.0098	0.09607	0.00140	0.52	0.05985	0.00150	592	5	591	8	596	46	99
CHA16_110	3788	110	519	0.63	0.8500	0.0120	0.10132	0.00094	0.28	0.06040	0.00072	624	7	622	6	614	25	101
CHA16_111	3392	87	918	1.29	0.8550	0.0130	0.10130	0.00084	0.25	0.06180	0.00091	629	7	622	5	661	32	94
CHA16_112	15030	412	1708	0.52	0.8541	0.0084	0.10178	0.00080	0.25	0.06085	0.00053	627	5	625	5	634	19	99
CHA16_113	71600	169	5840	1.22	9.7300	0.0920	0.38120	0.00330	0.77	0.18490	0.00093	2409	9	2082	15	2697	8	77
CHA16_114	13020	374	891	0.33	0.8333	0.0087	0.09794	0.00079	0.36	0.06175	0.00049	615	5	602	5	664	17	91
CHA16_115	13550	361	1388	0.49	0.8920	0.0100	0.10540	0.00095	0.45	0.06107	0.00053	647	6	646	6	640	19	101
CHA16_116	4044	110	656	0.80	0.8730	0.0150	0.10105	0.00090	0.35	0.06280	0.00110	637	8	621	5	698	36	89
CHA16_117	4180	97	431	0.52	1.0450	0.0170	0.11632	0.00110	0.09	0.06460	0.00087	726	9	709	7	756	28	94
CHA16_118	6120	162	1320	0.96	0.8770	0.0120	0.10343	0.00089	0.33	0.06121	0.00077	639	7	635	5	642	27	99
CHA16_119	17180	455	2903	0.84	0.8380	0.0096	0.10052	0.00079	0.20	0.06078	0.00060	619	5	618	5	628	21	98
CHA16_121	19640	489	5960	1.35	0.8940	0.0095	0.10576	0.00094	0.30	0.06134	0.00065	649	5	648	6	650	21	100
CHA16_122	15390	509	1791	0.53	0.7620	0.0110	0.09270	0.00075	0.49	0.05984	0.00074	575	6	572	4	595	26	96
CHA16_123	2696	73	243	0.41	0.8750	0.0160	0.10412	0.00098	0.33	0.06097	0.00092	642	9	639	6	643	36	99
CHA16_124	5000	143	678	0.63	0.8470	0.0150	0.10152	0.00120	0.47	0.06068	0.00088	623	8	623	7	626	31	100
CHA16_125	13110	299	930	0.34	0.9880	0.0140	0.11393	0.00170	0.38	0.06286	0.00066	699	7	696	10	701	21	99
CHA16_126	15860	490	1541	0.41	0.8420	0.0110	0.08909	0.00190	0.35	0.06730	0.00200	620	6	550	11	856	53	64
CHA16_127	5160	158	960	0.82	0.7520	0.0095	0.09154	0.00073	0.25	0.05956	0.00068	570	6	565	4	584	24	97
CHA16_128	32640	466	727	0.12	1.6530	0.0140	0.16533	0.00130	0.46	0.07228	0.00041	992	6	986	7	994	11	99
CHA16_129	3290	93	422	0.56	0.8270	0.0160	0.09931	0.00098	0.23	0.05980	0.00110	611	9	610	6	603	40	101
CHA16_130	21140	608	3347	0.74	0.7690	0.0096	0.09155	0.00082	0.37	0.06130	0.00049	579	5	565	5	658	17	86
CHA16_131	110200	654	8720	0.72	3.9950	0.0510	0.24990	0.00310	0.61	0.11494	0.00061	1633	10	1438	16	1878	10	77
CHA16_132	7620	154	1059	0.68	1.1140	0.0180	0.09839	0.00160	0.49	0.08260	0.00220	760	8	605	9	1256	47	48
CHA16_133	34900	875	5090	0.71	0.9420	0.0170	0.10047	0.00100	0.48	0.06748	0.00092	673	9	617	6	851	27	73
CHA16_134	9980	274	554	0.25	0.8250	0.0098	0.09855	0.00090	0.33	0.06082	0.00060	611	6	606	5	630	21	96
CHA16_135	12170	386	3125	1.15	0.7830	0.0092	0.09403	0.00082	0.33	0.06010	0.00058	587	5	579	5	604	21	96
CHA16_136	61600	1070	4770	0.22	1.4450	0.0430	0.11250	0.00410	0.94	0.09200	0.00098	904	18	686	24	1465	21	47
CHA16_137	4820	117	1018	1.02	1.0090	0.0170	0.11480	0.00098	0.49	0.06364	0.00086	709	8	701	6	731	29	96
CHA16_138	3860	94	675	0.88	0.9650	0.0180	0.11248	0.00120	0.59	0.06128	0.00091	688	9	687	7	647	32	106
CHA16_139	20080	575	4270	1.00	0.8435	0.0081	0.09561	0.00073	0.03	0.06361	0.00043	621	4	589	4	727	14	81
CHA16_140	4790	124	491	0.48	0.8900	0.0120	0.10448	0.00087	0.26	0.06092	0.00080	646	7	641	5	631	29	102
CHA16_141	22300	656	3710	0.78	0.8780	0.0100	0.10327	0.00100	0.18	0.06162	0.00049	640	6	634	6	659	17	96
CHA16_142	64870	127	2970	0.72	13.2600	0.1100	0.50830	0.00380	0.68	0.18730	0.00110	2697	8	2649	16	2718	10	97
CHA16_143	15520	449	791	0.23	0.8700	0.0130	0.09981	0.00170	0.49	0.06323	0.00069	635	8	613	10	720	22	85
CHA16_144	15470	310	4520	1.52	1.2320	0.0180	0.13217	0.00140	0.41	0.06752	0.00056	816	9	800	8	852	17	94
CHA16_145	25580	568	2512	0.53	1.0070	0.0110	0.10460	0.00110	0.59	0.07008	0.00043	707	5	641	6	930	13	69
CHA16_146	3150	95	1015	1.48	0.8140	0.0150	0.09748	0.00082	0.30	0.06053	0.00100	605	9	600	5	624	37	96
CHA16_147	6622	178	819	0.59	0.8790	0.0110	0.10366	0.00083	0.39	0.06122	0.00068	640	6	636	5	644	24	99
CHA16_148	15700	446	2430	0.63	0.8410	0.0140	0.08320	0.00140	0.76	0.07251	0.00073	620	8	515	8	998	20	52
CHA16_149	1956	54	128	0.29	0.8560	0.0230	0.09260	0.00120	0.58	0.06720	0.00140	628	12	571	7	838	44	68
CHA16_150	6470	157	1112	0.80	1.0280	0.0180	0.11407	0.00110	0.88	0.06461	0.00130	718	9	696	6	763	39	91
CHA16_151	23260	601	1722	0.33	0.8740	0.0110	0.10104	0.00110	0.56	0.06277	0.00071	638	6	621	6	699	23	89
CHA16_152	88100	297	7790	1.15	7.2600	0.1600	0.32930	0.00730	0.76	0.15670	0.00090	2143	20	1835	35	2420	10	76

Table B9 (continued): Results of LA-ICP-MS zircon U–Pb analyses performed during the sessions at ETH Zürich, 12 to 14th of February, 2017

grain	^{207}Pb[a] (cps)	U[b] (ppm)	Pb[b] (ppm)	Th[b]/U	$^{207}Pb/^{235}U$[c]	±2σ (abs)	$^{206}Pb/^{238}U$[c]	±2σ (abs)	rho[d]	$^{207}Pb/^{206}Pb$[c]	±2σ (abs)	$^{207}Pb/^{235}U$	±2σ (Ma)	$^{206}Pb/^{238}U$	±2σ (Ma)	$^{207}Pb/^{206}Pb$	±2σ (Ma)	conc.[e] (%)
CHA16_153	22570	563	977	0.16	0.9070	0.0310	0.10230	0.00120	0.62	0.06429	0.00280	655	15	628	7	756	72	83
CHA16_154	20700	632	979	0.21	0.8760	0.0220	0.10370	0.00140	0.78	0.06178	0.00290	638	11	636	9	665	78	96
CHA16_155	10240	315	1256	0.55	0.8050	0.0110	0.09330	0.00077	0.31	0.06183	0.00073	600	6	575	5	666	24	86
CHA16_156	4750	115	567	0.54	0.9560	0.0150	0.11170	0.00120	0.32	0.06180	0.00090	681	8	683	7	666	31	103
CHA16_157	4200	88	667	0.79	1.1480	0.0180	0.12699	0.00110	0.35	0.06536	0.00083	778	8	771	6	789	28	98
CHA16_158	21990	568	1369	0.30	0.8720	0.0084	0.10318	0.00084	0.47	0.06150	0.00043	636	5	633	5	656	16	96
CHA16_159	23040	797	1657	0.38	0.7770	0.0150	0.09330	0.00096	0.46	0.06110	0.00110	584	8	575	6	641	34	90
CHA16_160	10370	312	3324	1.42	0.7590	0.0092	0.09006	0.00074	0.36	0.06080	0.00058	573	5	556	4	636	20	87
CHA16_161	5910	172	2230	1.67	0.8660	0.0110	0.10258	0.00091	0.14	0.06110	0.00078	634	6	630	5	642	28	98
CHA16_162	14240	353	1584	0.55	0.9780	0.0130	0.11270	0.00130	0.72	0.06286	0.00056	692	7	689	7	704	19	98
CHA16_163	205000	676	10110	0.58	6.9840	0.0810	0.37860	0.00340	0.69	0.13390	0.00086	2109	10	2070	16	2149	12	96
CHA16_164	59300	215	3520	0.75	6.6150	0.0630	0.35860	0.00290	0.67	0.13303	0.00074	2061	8	1975	14	2138	10	92
CHA16_165	13000	402	2580	0.92	0.8770	0.0170	0.10293	0.00110	0.36	0.06170	0.00130	639	9	632	6	660	40	96
CHA16_166	6040	157	265	0.20	1.0390	0.0210	0.11740	0.00100	0.71	0.06470	0.00100	723	10	716	6	760	31	94
CHA16_167	9080	268	622	0.31	0.8470	0.0100	0.10036	0.00084	0.61	0.06083	0.00052	623	6	617	5	634	18	97
CHA16_168	39000	71	1450	0.58	12.8500	0.3600	0.51310	0.01100	0.75	0.17920	0.00200	2668	30	2674	48	2645	18	101
CHA16_169	2062	42	275	0.63	1.1980	0.0280	0.13330	0.00150	0.07	0.06500	0.00140	798	13	807	9	768	48	105
CHA16_170	7370	232	883	0.54	0.7731	0.0094	0.09423	0.00074	0.31	0.05977	0.00065	581	5	581	4	592	24	98
CHA16_171	64900	125	2650	0.64	11.8700	0.7700	0.44680	0.02400	0.62	0.19210	0.00490	2594	90	2381	120	2760	52	86
CHA16_172	3930	101	664	0.78	0.8790	0.0180	0.10218	0.00520	0.43	0.06340	0.00430	646	10	627	31	732	110	86
CHA16_174	11650	202	1856	0.85	1.3060	0.0160	0.14070	0.00120	0.26	0.06761	0.00064	848	7	849	7	861	19	99
CHA16_175	5100	68	376	0.44	1.8370	0.0290	0.17830	0.00160	0.44	0.07474	0.00098	1058	10	1058	9	1057	27	100
CHA16_176	8260	240	918	0.51	0.8246	0.0097	0.09911	0.00083	0.09	0.06007	0.00074	610	5	609	5	608	28	100
CHA16_177	15250	523	3580	1.15	0.7810	0.0076	0.09232	0.00075	0.51	0.06124	0.00041	586	4	569	4	647	14	88
CHA16_178	31040	491	4695	0.83	1.5930	0.0150	0.16138	0.00120	0.59	0.07168	0.00047	967	6	964	7	978	13	99
CHA16_179	11010	328	935	0.39	0.8257	0.0092	0.09896	0.00077	0.39	0.06062	0.00053	611	5	608	5	626	18	97
CHA16_180	44600	1383	5790	0.58	0.8680	0.0660	0.10437	0.00086	0.28	0.06066	0.00460	634	30	640	5	645	110	99
CHA16_181	63030	124	3141	0.76	13.1200	0.1300	0.50990	0.00440	0.59	0.18550	0.00100	2688	10	2656	19	2705	9	98
CHA16_182	3401	90	497	0.67	0.9380	0.0150	0.11037	0.00100	0.09	0.06130	0.00094	672	8	675	6	652	33	104
CHA16_183	8440	252	1985	1.08	0.8086	0.0098	0.09778	0.00081	0.15	0.06008	0.00067	601	6	601	5	603	24	100
CHA16_184	3055	44	791	1.43	1.6060	0.0290	0.16250	0.00150	0.36	0.07180	0.00130	974	12	970	9	980	36	99
CHA16_185	3639	99	623	0.81	0.9080	0.0170	0.09677	0.00085	0.23	0.06810	0.00130	656	9	595	5	864	38	69
CHA16_186	226100	592	7670	0.41	9.3130	0.1100	0.44520	0.00430	0.91	0.15207	0.00077	2368	11	2374	19	2370	9	100
CHA16_187	30700	901	1239	0.12	0.8571	0.0096	0.08520	0.00077	0.31	0.07319	0.00076	629	5	527	5	1022	20	52
CHA16_188	11890	402	860	0.32	0.7462	0.0079	0.09147	0.00070	0.33	0.05904	0.00051	566	5	564	4	574	19	98
CHA16_189	12420	357	2700	1.01	0.8600	0.0097	0.10258	0.00083	0.30	0.06070	0.00055	630	5	630	5	631	19	100
CHA16_190	32690	801	1646	0.24	0.9970	0.0087	0.11545	0.00084	0.44	0.06230	0.00039	702	4	704	5	683	13	103
CHA16_191	880	28	309	1.60	0.7970	0.0240	0.09631	0.00120	0.06	0.06040	0.00180	595	14	593	7	640	61	93
CHA16_192	1483	45	577	1.77	0.7930	0.0210	0.09607	0.00120	0.34	0.06020	0.00160	593	12	591	7	599	60	99
CHA16_193	22200	493	3510	0.78	1.1180	0.0400	0.09350	0.00460	0.69	0.09350	0.00470	760	19	575	27	1456	88	39
CHA16_194	27200	840	1310	0.15	0.8550	0.0100	0.10329	0.00094	0.60	0.06027	0.00050	627	6	634	6	611	18	104
CHA16_195	37200	653	4010	0.56	1.5160	0.0310	0.15430	0.00260	0.49	0.07097	0.00051	937	13	925	15	960	15	96
CHA16_196	7310	234	1704	1.03	0.7798	0.0098	0.09483	0.00076	0.85	0.05990	0.00066	585	6	584	5	599	24	97
CHA16_197	25640	775	2392	0.41	0.8249	0.0150	0.09991	0.00082	0.51	0.05970	0.00110	611	9	614	5	595	37	103
CHA16_198	16520	527	605	0.17	0.7570	0.0078	0.09269	0.00075	0.44	0.05922	0.00050	573	5	571	4	573	18	100
CHA16_199	10600	156	1841	0.93	1.5730	0.0300	0.15530	0.00500	0.59	0.07478	0.00240	959	12	931	29	1062	57	88
CHA16_200	12760	251	1501	0.59	1.2380	0.0120	0.13514	0.00110	0.36	0.06642	0.00058	818	6	817	6	825	19	99
CHA16_201	3510	111	630	0.82	0.7820	0.0130	0.09498	0.00095	0.45	0.06014	0.00080	587	8	585	6	614	30	95

Table B9 (continued): Results of LA-ICP-MS zircon U–Pb analyses performed during the sessions at ETH Zürich, 12 to 14th of February, 2017

grain	^{207}Pb[a] (cps)	U[b] (ppm)	Pb[b] (ppm)	Th[b]/U	$^{207}Pb/^{235}U$[c]	±2σ (abs)	$^{206}Pb/^{238}U$[c]	±2σ (abs)	rho[d]	$^{207}Pb/^{206}Pb$[c]	±2σ (abs)	$^{207}Pb/^{235}U$	±2σ (Ma)	$^{206}Pb/^{238}U$	±2σ (Ma)	$^{207}Pb/^{206}Pb$	±2σ (Ma)	conc.[e] (%)
CHA16_202	6210	166	817	0.63	1.0010	0.0140	0.11570	0.00099	0.41	0.06350	0.00070	704	7	706	6	723	23	98
CHA16_203	11000	310	1730	0.74	0.8660	0.0100	0.10360	0.00099	0.53	0.06099	0.00065	633	6	636	6	636	23	100
CHA16_204	28460	458	5980	1.54	1.4300	0.0590	0.08940	0.00098	0.72	0.11620	0.00520	901	25	552	6	1906	82	29
CHA16_205	8260	255	2250	1.33	0.8610	0.0130	0.10295	0.00130	0.42	0.06090	0.00064	631	7	632	7	637	23	99
CHA16_206	46740	1287	3960	0.38	0.9210	0.0150	0.10211	0.00120	0.37	0.06549	0.00068	663	8	627	7	786	21	80
CHA16_207	7940	236	954	0.54	0.8370	0.0120	0.10057	0.00092	0.45	0.06015	0.00063	618	7	618	5	625	23	99
CHA16_208	15090	430	3165	0.92	0.8020	0.0190	0.09455	0.00360	0.60	0.06196	0.00160	598	11	582	21	671	49	87

Spot size = 20µm (for seq. 1) and 30µm (for seq. 2 & 3)

[a]Within run background-corrected mean ^{207}Pb signal in cps (counts per second).

[b] U and Pb content and Th/U ratio were calculated relative to GJ-1 reference zircon.

[c] corrected for background, within-run Pb/U fractionation (in case of $^{206}Pb/^{238}U$) and subsequently normalised to GJ-1 (ID-TIMS value/measured value); $^{207}Pb/^{235}U$ obtained from signal measured on masses 207 and 235

[d] rho is the $^{206}Pb/^{238}U/^{207}Pb/^{235}U$ error correlation coefficient.

[e] degree of concordance = $^{206}Pb/^{238}U$ age / $^{207}Pb/^{206}Pb$ age x 100

B.4 Zircon Hf isotope compositions

B.4.1 Analytical details on the GUF session

The analytical procedure is exactly the same as followed by Couzinié et al. (2017) and the reader is referred to section A.3.

B.4.2 Analytical details on the LMV session

The procedure followed in the course of this analytical session has been published in Moyen et al. (2017b). Hafnium isotope measurements were performed with a Thermo Scientific Neptune Plus multi-collector ICP–MS coupled to the Resonetics M50E 193nm laser excimer system. The MC–ICP–MS is equipped with 9 Faraday cups and amplifiers with 10^{11} Ω. Data were collected in static mode (^{171}Yb, ^{173}Yb, ^{174}Hf, ^{175}Lu, ^{176}Hf-Yb-Lu, ^{177Hf}, ^{178Hf}, ^{179Hf}). The overall operating conditions and instrument settings are reported in Table B12. Each LA–MC–ICP–MS analysis consisted of 20 s of gas background data followed by 40 s of ablation. With an integration time of 1 s, each analysis typically produced 36-40 isotopic ratios. Mass bias effects on Hf were corrected using an exponential law and a true value for ^{179}Hf/^{177}Hf of 0.7325 (Patchett and Tatsumoto, 1980; Patchett et al., 1981). Data were reduced in the following order and based upon user-selected background and sample integration intervals. Firstly, the mean signal intensity of the 20-second gas background was subtracted from the signal acquired during the laser firing onto the sample. These corrected signal intensities were taken further during data reduction. β_{Yb} was determined using the ^{173}Yb/^{171}Yb measured during each zircon analysis and the ref ^{173}Yb/^{171}Yb of 1.132685 (Chu et al., 2002; Fischer et al., 2011), following the equation :

$$\beta_{Yb} = \frac{\ln \frac{^{173}Yb/^{171}Yb_{ref}}{^{173}Yb/^{171}Yb_{meas}}}{\ln \frac{M176}{M171}} \tag{B.1}$$

The ^{176}Yb isobaric interference on ^{176}Hf was then determined using ^{176}Yb/^{173}Yb of 0.79618 and the ^{176}Lu isobaric interference on ^{176}Hf was determined using the measured interference-free ^{175}Lu mass assuming that $\beta_{Lu} = \beta_{Yb}$, and using the ref $^{176Lu}/^{175Lu}$ of 0.02655 (Vervoort et al., 2004).

$$^{176}Yb_{calculated} = ^{173}Yb_{measured} \times \left(\frac{^{176}Yb}{^{173}Yb}\right)_{ref} \times \left(\frac{M173}{M176}\right)^{\beta(Yb)} \tag{B.2}$$

$$^{176}Lu_{calculated} = ^{175}Lu_{measured} \times \left(\frac{^{176}Lu}{^{175}Lu}\right)_{ref} \times \left(\frac{M175}{M176}\right)^{\beta(Yb)} \tag{B.3}$$

Both determined ^{176}Lu and ^{176}Yb signals were subtracted from the total 176 signal intensity and the calculated ^{176}Hf signal were used to determine the mass biais using the true ^{179}Hf/^{177}Hf ratio of 0.7325 (Patchett and Tatsumoto, 1980), following the equation :

$$\beta_{Hf} = \frac{\ln \frac{^{179}Hf/^{177}Hf_{ref}}{^{179}Hf/^{177}Hf_{meas}}}{\ln \frac{M179}{M177}} \tag{B.4}$$

Finally the interference corrected ^{176}Hf/^{177}Hf is evaluated according to the following equation:

$$\left(\frac{^{176}Hf}{^{177}Hf}\right)_{corrected} = \left(\frac{^{176}(Hf+Yb+Lu)_{meas} - ^{176}Yb_{calc} - ^{176}Lu_{calc}}{^{177}Hf_{meas}}\right) \times \left(\frac{M176}{M177}\right)^{\beta(Hf)} \quad \text{(B.5)}$$

The $^{176}Hf/^{177}Hf$ for all samples were corrected for mass bias using β_{Hf}. Outlier rejection of the Hf isotopic ratio for each analysis were performed using a two-standard deviation criterion.

Table B10: Operating conditions and instrument settings for Hf analyses

Laser ablation system	
Make, Model & type	Resonetics/M-50E 193nm, Excimer
Ablation cell & volume	Laurin Cell ® two volumes cell, Laurin Technic Ltd., volume ca. 1cm³
Laser wavelength	193 nm
Pulse width	< 4 ns
Fluence	3.6 J.cm-2
Repetition rate	6 Hz
spot size	40-47 um
Sampling mode / pattern	Single spot
Background collection	30 secs
Helium gas flow rate	0.67-0.70 L.min-1
Nitrogen gas flow rate	0.0045 L.min-1
Ablation duration	60 secs
Wash-out delay	30 secs
ICP-MS Instrument	
Instrument	Neptune
RF power	1200 W
Cool gas flow	14 L.min-1
Auxiliary gas	0.66 L.min-1
Sample gas	0.86 L.min-1
Scan mode	Static
Scanned masses (L4 to H3)	171 (L4), 173 (L3), 174 (L2), 175 (L1)
	176 (C), 177 (H1), 178 (H2), 179 (H3)
Mass resolution	300
Number of scans	70
Ablation time	40 s
background	20 s
Integration time	1 s

B.4.3 Data tables

This section provides the results of zircon LA–MC–ICP–MS Lu–Hf isotope measurements. The data are reported in the following tables:

- **Table B11:** In situ LA-MC-ICP-MS Lu-Hf isotope data for zircon standards analyzed at GUF, 1st of August, 2016;
- **Table B12:** results for amphibole-bearing gneisses sampled at the Riverie quarry, see section 3.5.
- **Table B13:** results of analyses conducted on zircon standards during the analytical session performed at LMV.
- **Table B14:** results of analyses conducted on zircon grains from investigated samples during the analytical session performed at LMV.

Table B11: In situ LA-MC-ICP-MS Lu-Hf isotope data for zircon standards analysed at GUF, 1st of August, 2016

	Spot size (µm)	$^{176}Yb/^{177}Hf$ [a]	±2σ (abs.)	$^{176}Lu/^{177}Hf$ [a]	±2σ (abs.)	$^{178}Hf/^{177}Hf$	±2σ (abs.)	$^{180}Hf/^{177}Hf$	±2σ (abs.)	Sig_{Hf} [b] (V)	$^{176}Hf/^{177}Hf$	±2σ (abs.)	$^{176}Hf/^{177}Hf_{(t)}$ [c]	$\varepsilon Hf_{(t)}$ [c]	±2σ (abs.)	T_{DM2} [e] (Ga)	Age (Ma)
GJ-1																	
Session #1 (08/01/2016)																	
GJ1-40-12Jcm_1	40	0.0084	0.0007	0.00025	0.00003	1.46720	0.00005	1.88668	0.00010	11	**0.281977**	0.000033	0.281974	-15.3	1.2	2.22	601
GJ1-40-12Jcm_2	40	0.0080	0.0006	0.00027	0.00002	1.46725	0.00004	1.88639	0.00015	8	**0.282005**	0.000031	0.282002	-14.3	1.1	2.17	601
GJ1-40-12Jcm_3	40	0.0080	0.0006	0.00026	0.00002	1.46723	0.00007	1.88633	0.00016	8	**0.282014**	0.000029	0.282011	-14.0	1.0	2.15	601
GJ1-40-12Jcm_4	40	0.0080	0.0006	0.00027	0.00002	1.46722	0.00006	1.88630	0.00012	9	**0.282027**	0.000033	0.282024	-13.5	1.2	2.13	601
GJ1-40-12Jcm_5	40	0.0076	0.0006	0.00026	0.00002	1.46727	0.00006	1.88650	0.00019	7	**0.282001**	0.000034	0.281998	-14.4	1.2	2.18	601
GJ1-40-12Jcm_6	40	0.0076	0.0006	0.00026	0.00002	1.46725	0.00006	1.88663	0.00017	8	**0.282016**	0.000033	0.282013	-13.9	1.2	2.15	601
GJ1-40-12Jcm_7	40	0.0078	0.0006	0.00026	0.00002	1.46724	0.00007	1.88635	0.00014	7	**0.282020**	0.000030	0.282017	-13.8	1.0	2.14	601
GJ1-40-12Jcm_8	40	0.0078	0.0006	0.00025	0.00002	1.46727	0.00004	1.88626	0.00013	8	**0.282026**	0.000029	0.282023	-13.6	1.0	2.13	601
GJ1-40-12Jcm_9	40	0.0078	0.0006	0.00025	0.00001	1.46729	0.00006	1.88630	0.00014	8	**0.282021**	0.000033	0.282018	-13.7	1.2	2.14	601
GJ1-40-12Jcm_10	40	0.0078	0.0006	0.00025	0.00002	1.46734	0.00006	1.88652	0.00014	8	**0.282021**	0.000032	0.282018	-13.7	1.1	2.14	601
GJ1-40-12Jcm_11	40	0.0078	0.0006	0.00025	0.00002	1.46729	0.00005	1.88632	0.00012	8	**0.282013**	0.000036	0.282010	-14.0	1.3	2.15	601
GJ1-40-12Jcm_12	40	0.0076	0.0006	0.00025	0.00002	1.46718	0.00006	1.88642	0.00011	8	**0.282005**	0.000040	0.282002	-14.3	1.4	2.17	601
GJ1-40-12Jcm_13	40	0.0077	0.0006	0.00025	0.00001	1.46727	0.00005	1.88655	0.00015	7	**0.282023**	0.000034	0.282020	-13.7	1.2	2.13	601
GJ1-40-12Jcm_14	40	0.0074	0.0006	0.00025	0.00001	1.46729	0.00006	1.88618	0.00011	8	**0.282027**	0.000030	0.282024	-13.5	1.1	2.13	601
GJ1-40-12Jcm_15	40	0.0072	0.0006	0.00025	0.00001	1.46729	0.00005	1.88626	0.00013	8	**0.282021**	0.000033	0.282018	-13.7	1.2	2.14	601
GJ1-40-12Jcm_16	40	0.0074	0.0006	0.00025	0.00001	1.46720	0.00005	1.88627	0.00014	7	**0.282013**	0.000031	0.282010	-14.0	1.1	2.15	601
GJ1-40-12Jcm_17	40	0.0073	0.0006	0.00025	0.00001	1.46729	0.00006	1.88623	0.00012	7	**0.282016**	0.000036	0.282014	-13.9	1.3	2.15	601
GJ1-40-12Jcm_18	40	0.0073	0.0006	0.00024	0.00001	1.46723	0.00005	1.88613	0.00015	7	**0.282029**	0.000037	0.282026	-13.5	1.3	2.12	601
GJ1-40-12Jcm_19	40	0.0073	0.0006	0.00024	0.00001	1.46732	0.00006	1.88638	0.00013	6	**0.282027**	0.000033	0.282025	-13.5	1.2	2.12	601
GJ1-40-12Jcm_20	40	0.0072	0.0006	0.00024	0.00001	1.46722	0.00006	1.88643	0.00014	6	**0.281989**	0.000034	0.281987	-14.8	1.2	2.20	601
GJ1-60-12Jcm_1	60	0.0074	0.0006	0.00024	0.00001	1.46724	0.00004	1.88649	0.00010	14	**0.282020**	0.000027	0.282017	-13.8	0.9	2.14	601
GJ1-60-12Jcm_2	60	0.0074	0.0006	0.00024	0.00001	1.46721	0.00004	1.88661	0.00008	15	**0.282005**	0.000026	0.282003	-14.3	0.9	2.17	601
Average		**0.0076**		**0.00025**		**1.46725**		**1.88639**			0.282014		**0.282012**	**-14.0**			
2 S.E. (abs.)		**0.0006**		**0.00002**		**0.00008**		**0.00030**			**0.000026**		**0.000026**	**0.9**			
2 S.E. (%)		**8**		**7**		**0.006**		**0.02**			**0.0093**		**0.0093**				
Plešovice																	
Session #1 (08/01/2016)																	
Pleso-40-12Jcm_1	40	0.0066	0.0005	0.00014	0.00001	1.46722	0.00006	1.88643	0.00012	10	**0.282472**	0.000031	0.282471	-3.6	1.1	1.37	338
Pleso-40-12Jcm_2	40	0.0071	0.0006	0.00015	0.00001	1.46723	0.00004	1.88653	0.00011	11	**0.282483**	0.000031	0.282482	-3.2	1.1	1.35	338
Pleso-40-12Jcm_3	40	0.0072	0.0006	0.00015	0.00001	1.46728	0.00006	1.88646	0.00012	11	**0.282474**	0.000032	0.282473	-3.5	1.1	1.36	338
Pleso-40-12Jcm_4	40	0.0071	0.0006	0.00014	0.00001	1.46727	0.00004	1.88662	0.00009	12	**0.282470**	0.000029	0.282469	-3.7	1.0	1.37	338
Pleso-40-12Jcm_5	40	0.0070	0.0006	0.00014	0.00001	1.46726	0.00004	1.88652	0.00011	12	**0.282484**	0.000028	0.282483	-3.2	1.0	1.34	338
Pleso-40-12Jcm_6	40	0.0070	0.0006	0.00014	0.00001	1.46727	0.00005	1.88655	0.00011	12	**0.282480**	0.000030	0.282479	-3.3	1.0	1.35	338
Pleso-40-12Jcm_7	40	0.0068	0.0005	0.00014	0.00001	1.46724	0.00005	1.88644	0.00013	11	**0.282478**	0.000029	0.282477	-3.4	1.0	1.36	338
Pleso-40-12Jcm_8	40	0.0069	0.0006	0.00014	0.00001	1.46721	0.00005	1.88652	0.00012	11	**0.282485**	0.000028	0.282484	-3.1	1.0	1.34	338
Pleso-40-12Jcm_9	40	0.0063	0.0005	0.00013	0.00001	1.46721	0.00005	1.88632	0.00011	10	**0.282486**	0.000032	0.282485	-3.1	1.1	1.34	338
Pleso-40-12Jcm_1	40	0.0064	0.0005	0.00012	0.00002	1.46722	0.00005	1.88652	0.00009	10	**0.282472**	0.000028	0.282471	-3.6	1.0	1.37	338
Pleso-40-12Jcm_1	40	0.0069	0.0005	0.00014	0.00001	1.46722	0.00004	1.88625	0.00010	10	**0.282478**	0.000028	0.282477	-3.4	1.0	1.36	338
Pleso-40-12Jcm_1	40	0.0067	0.0006	0.00014	0.00001	1.46728	0.00005	1.88643	0.00012	10	**0.282483**	0.000030	0.282482	-3.2	1.1	1.35	338
Pleso-40-12Jcm_1	40	0.0067	0.0005	0.00014	0.00001	1.46725	0.00006	1.88637	0.00012	10	**0.282473**	0.000027	0.282472	-3.5	1.0	1.36	338
Pleso-40-12Jcm_1	40	0.0063	0.0005	0.00013	0.00001	1.46726	0.00004	1.88640	0.00010	11	**0.282487**	0.000031	0.282486	-3.1	1.1	1.34	338

Table B11 (continued): In situ LA-MC-ICP-MS Lu-Hf isotope data for zircon standards analysed at LMV, 7th of June, 2017

	Spot size (µm)	$^{176}Yb/^{177}Hf$ [a]	±2σ (abs.)	$^{176}Lu/^{177}Hf$ [a]	±2σ (abs.)	$^{178}Hf/^{177}Hf$	±2σ (abs.)	$^{180}Hf/^{177}Hf$	±2σ (abs.)	Sig_{Hf} [b] (V)	$^{176}Hf/^{177}Hf$	±2σ (abs.)	$^{176}Hf/^{177}Hf_{(t)}$ [c]	$\varepsilon Hf_{(t)}$ [c]	±2σ (abs.)	T_{DM2} [e] (Ga)	Age (Ma)
Plešovice																	
Average		**0.0068**		**0.00014**		**1.46724**		**1.88645**			**0.282479**		**0.282478**	**-3.3**			
2 S.E. (abs.)		**0.0006**		**0.00002**		**0.00005**		**0.00020**			**0.000012**		**0.000012**	**0.4**			
2 S.E. (%)		**9**		**12**		**0.004**		**0.01**			**0.0041**		**0.0041**				
Temora																	
Session #1 (08/01/2016)																	
TM-40-12Jcm_1	40	0.0190	0.0027	0.00066	0.00008	1.46746	0.00013	1.88586	0.00043	9	**0.282710**	0.000046	0.282705	6.5	1.6	0.88	419
TM-40-12Jcm_2	40	0.0391	0.0033	0.00130	0.00008	1.46717	0.00004	1.88639	0.00012	9	**0.282692**	0.000034	0.282682	5.7	1.2	0.92	419
TM-40-12Jcm_3	40	0.0408	0.0034	0.00130	0.00008	1.46726	0.00005	1.88636	0.00014	9	**0.282688**	0.000031	0.282678	5.5	1.1	0.93	419
TM-40-12Jcm_4	40	0.0416	0.0041	0.00128	0.00010	1.46719	0.00004	1.88649	0.00013	9	**0.282695**	0.000030	0.282685	5.8	1.1	0.92	419
TM-40-12Jcm_5	40	0.0282	0.0025	0.00093	0.00006	1.46727	0.00007	1.88642	0.00016	9	**0.282684**	0.000030	0.282677	5.5	1.0	0.93	419
TM-40-12Jcm_6	40	0.0240	0.0019	0.00078	0.00005	1.46733	0.00008	1.88626	0.00024	9	**0.282715**	0.000040	0.282709	6.6	1.4	0.87	419
TM-40-12Jcm_7	40	0.0190	0.0015	0.00066	0.00004	1.46727	0.00007	1.88633	0.00013	7	**0.282702**	0.000034	0.282697	6.2	1.2	0.89	419
TM-40-12Jcm_8	40	0.0196	0.0017	0.00061	0.00004	1.46731	0.00006	1.88632	0.00014	8	**0.282695**	0.000031	0.282690	6.0	1.1	0.91	419
TM-40-12Jcm_9	40	0.0190	0.0015	0.00066	0.00004	1.46725	0.00007	1.88631	0.00012	7	**0.282696**	0.000030	0.282691	6.0	1.1	0.91	419
TM-40-12Jcm_10	40	0.0152	0.0013	0.00053	0.00004	1.46723	0.00004	1.88623	0.00011	8	**0.282682**	0.000033	0.282678	5.6	1.2	0.93	419
TM-40-12Jcm_11	40	0.0161	0.0014	0.00055	0.00004	1.46728	0.00007	1.88632	0.00016	7	**0.282682**	0.000036	0.282678	5.5	1.3	0.93	419
TM-40-12Jcm_12	40	0.0249	0.0021	0.00090	0.00006	1.46738	0.00010	1.88620	0.00027	8	**0.282701**	0.000041	0.282694	6.1	1.4	0.90	419
Average		**0.0255**		**0.00085**		**1.46728**		**1.88629**			**0.282695**		**0.282689**	**5.9**			
2 S.E. (abs.)		**0.0195**		**0.00059**		**0.00016**		**0.00031**			**0.000021**		**0.000022**	**0.8**			
2 S.E. (%)		**76**		**70**		**0.011**		**0.02**			**0.0075**		**0.0078**				

(a) $^{176}Yb/^{177}Hf = (^{176}Yb/^{173}Yb)_{true} \times (^{173}Yb/^{177}Hf)_{meas} \times (M_{173(Yb)}/M_{177(Hf)})^{b(Hf)}$, $b(Hf) = \ln(^{179}Hf/^{177}Hf_{true} / {}^{179}Hf/^{177}Hf_{measured}) / \ln (M_{179(Hf)}/M_{177(Hf)})$, M=mass of respective isotope. The $^{176}Lu/^{177}Hf$ were calculated in a similar way by using the 175Lu/177Hf and b(Yb).

(b) Mean Hf signal in volt.

(c) Initial $^{176}Hf/^{177}Hf$ and eHf calculated using the apparent Pb-Pb age determined by LA-ICP-MS dating (see column f), and the CHUR parameters: $^{176}Lu/^{177}Hf = 0.0336$, and $^{176}Hf/^{177}Hf = 0.282785$ (Bouvier *et al* ., 2008).

(d) two stage model age in billion years using the measured $^{176}Lu/^{177}Lu$ of each spot (first stage = age of zircon), a value of 0.0113 for the average continental crust (second stage), and a juvenile crust (NC) $^{176}Lu/^{177}Lu$ and $^{176}Hf/^{177}Hf$ of 0.0384 and 0.28314, respectively.

Table B12: In situ LA-MC-ICP-MS Lu-Hf isotope data for zircon grains from amphibole-bearing gneisses analyzed at GUF, 1st of August, 2016

	$^{176}Yb/^{177}Hf$ [a]	±2σ (abs.)	$^{176}Lu/^{177}Hf$ [a]	±2σ (abs.)	$^{178}Hf/^{177}Hf$	±2σ (abs.)	$^{180}Hf/^{177}Hf$	±2σ (abs.)	Sig_{Hf} [b] (V)	$^{176}Hf/^{177}Hf$	±2σ (abs.)	Apparent age (Ma)	±2σ (Ma)	Conc. (%)	$^{176}Hf/^{177}Hf_{App}$ [c]	$\varepsilon Hf_{(app)}$ [c]	±2σ (abs.)	Intrusion age (Ma)	±2σ (Ma)	$^{176}Hf/^{177}Hf_{(t\ int)}$ [d]	$\varepsilon Hf_{(t)}$ [d]	±2σ (abs.)	DM $_{Griffin}$ [e]	DM $_{Naeraa}$ [f]
Sample RV-1																								
RV1-40-12a-a0	0.0271	0.0023	0.00092	0.00006	1.46719	0.00007	1.88641	0.00019	6	0.282759	0.000041	547	7	97	0.282749	11.0	1.5	546	5	0.282749	10.9	1.5	0.76	0.52
RV1-40-16a-a1	0.0145	0.0013	0.00053	0.00003	1.46716	0.00006	1.88662	0.00017	6	0.282757	0.000035	549	6	102	0.282752	11.1	1.2	546	5	0.282752	11.0	1.2	0.75	0.51
RV1-40-20a-a2	0.0201	0.0023	0.00076	0.00008	1.46737	0.00014	1.88620	0.00051	6	0.282748	0.000056	546	7	98	0.282740	10.6	2.0	546	5	0.282740	10.6	2.0	0.78	0.54
RV1-40-23a-a2	0.0287	0.0024	0.00100	0.00006	1.46717	0.00007	1.88623	0.00021	6	0.282755	0.000045	545	6	99	0.282744	10.7	1.6	546	5	0.282744	10.7	1.6	0.77	0.53
RV1-40-28a-a3	0.0232	0.0020	0.00089	0.00006	1.46716	0.00005	1.88674	0.00014	7	0.282750	0.000035	547	7	96	0.282741	10.6	1.2	546	5	0.282741	10.6	1.2	0.77	0.54
RV1-40-28b-a3	0.0343	0.0032	0.00117	0.00009	1.46723	0.00007	1.88682	0.00015	7	0.282761	0.000036	540	6	97	0.282749	10.8	1.3	546	5	0.282749	10.9	1.3	0.76	0.52
RV1-40-30a-a4	0.0237	0.0019	0.00092	0.00006	1.46705	0.00007	1.88675	0.00018	5	0.282749	0.000046	544	6	97	0.282740	10.6	1.6	546	5	0.282740	10.6	1.6	0.78	0.54
RV1-40-30b-a4	0.0231	0.0019	0.00085	0.00005	1.46724	0.00012	1.88677	0.00034	6	0.282742	0.000041	542	6	94	0.282733	10.3	1.5	546	5	0.282733	10.4	1.5	0.79	0.55
RV1-40-33a-a4	0.0282	0.0026	0.00104	0.00007	1.46712	0.00011	1.88693	0.00024	6	0.282719	0.000042	543	6	98	0.282709	9.4	1.5	546	5	0.282709	9.5	1.5	0.84	0.60
RV1-40-3a	0.0230	0.0022	0.00089	0.00007	1.46748	0.00016	1.88524	0.00061	6	0.282740	0.000049	*546*	*5*		0.282731	10.3	1.7	546	5	0.282731	10.3	1.7	0.79	0.56
RV1-40-46a	0.0148	0.0012	0.00055	0.00003	1.46724	0.00006	1.88646	0.00018	5	0.282736	0.000045	*546*	*5*		0.282730	10.2	1.6	546	5	0.282730	10.2	1.6	0.80	0.56
RV1-40-46b	0.0366	0.0032	0.00126	0.00009	1.46723	0.00007	1.88644	0.00011	7	0.282760	0.000040	*546*	*5*		0.282748	10.9	1.4	546	5	0.282748	10.9	1.4	0.76	0.52
RV1-40-47a-a6	0.0156	0.0013	0.00062	0.00004	1.46726	0.00004	1.88673	0.00013	9	0.282721	0.000032	542	6	99	0.282715	9.6	1.1	546	5	0.282715	9.7	1.1	0.83	0.59
RV1-40-8a-a08	0.0203	0.0016	0.00078	0.00005	1.46712	0.00009	1.88664	0.00024	7	0.282737	0.000038	545	6	97	0.282729	10.2	1.3	546	5	0.282729	10.2	1.3	0.80	0.56
																			Avg	0.282736	10.5			
																			2 SE	0.000026	0.9			
Sample RV-2																								
RV2-40-49a-a4	0.0285	0.0025	0.00115	0.00008	1.46732	0.00007	1.88595	0.00017	6	0.282775	0.000041	536	6	96	0.282764	11.2	1.4	544	5	0.282763	11.4	1.4	0.73	0.49
RV2-40-49b-a4	0.0352	0.0029	0.00127	0.00008	1.46722	0.00006	1.88659	0.00013	9	0.282765	0.000033	535	5	95	0.282752	10.8	1.2	544	5	0.282752	11.0	1.2	0.75	0.51
RV2-40-50a-a5	0.0315	0.0035	0.00121	0.00011	1.46704	0.00006	1.88662	0.00012	7	0.282730	0.000033	546	7	98	0.282717	9.8	1.2	544	5	0.282717	9.7	1.2	0.82	0.58
RV2-40-51a-a5	0.0231	0.0030	0.00093	0.00011	1.46713	0.00009	1.88693	0.00022	8	0.282732	0.000035	541	7	97	0.282723	9.9	1.2	544	5	0.282723	9.9	1.2	0.81	0.57
RV2-40-52a-a5	0.0175	0.0015	0.00071	0.00005	1.46729	0.00006	1.88631	0.00018	8	0.282745	0.000036	546	7	98	0.282738	10.5	1.3	544	5	0.282738	10.5	1.3	0.78	0.54
RV2-40-53a-a5	0.0265	0.0022	0.00101	0.00006	1.46712	0.00009	1.88715	0.00018	9	0.282742	0.000040	520	6	93	0.282732	9.7	1.4	544	5	0.282732	10.3	1.4	0.79	0.55
RV2-40-54a-a5	0.0139	0.0012	0.00053	0.00003	1.46718	0.00012	1.88658	0.00045	8	0.282760	0.000051	550	7	96	0.282755	11.2	1.8	544	5	0.282755	11.1	1.8	0.75	0.51
RV2-40-58a-a6	0.0264	0.0022	0.00105	0.00007	1.46717	0.00006	1.88634	0.00014	7	0.282756	0.000032	548	6	99	0.282745	10.8	1.1	544	5	0.282745	10.7	1.1	0.77	0.53
RV2-40-58b-a6	0.0398	0.0045	0.00141	0.00013	1.46723	0.00007	1.88642	0.00016	8	0.282764	0.000038	539	6	97	0.282749	10.8	1.3	544	5	0.282749	10.9	1.3	0.76	0.52
RV2-40-59a-a6	0.0307	0.0027	0.00107	0.00007	1.46717	0.00006	1.88628	0.00012	6	0.282751	0.000034	361	4	98	0.282744	6.6	1.2	544	5	0.282740	10.5	1.2	0.78	0.54
RV2-40-60a-a7	0.0332	0.0033	0.00131	0.00010	1.46725	0.00007	1.88673	0.00013	7	0.282747	0.000031	548	6	102	0.282733	10.4	1.1	544	5	0.282733	10.3	1.1	0.79	0.55
RV2-40-60b-a7	0.0270	0.0033	0.00103	0.00010	1.46734	0.00007	1.88630	0.00020	7	0.282798	0.000044	535	5	97	0.282788	12.0	1.5	544	5	0.282787	12.2	1.5	0.68	0.44
RV2-40-61a-a7	0.0209	0.0017	0.00084	0.00005	1.46713	0.00006	1.88672	0.00020	7	0.282738	0.000032	539	7	97	0.282730	10.1	1.1	544	5	0.282730	10.2	1.1	0.80	0.56
RV2-40-63a-a8	0.0188	0.0016	0.00074	0.00005	1.46723	0.00005	1.88654	0.00014	8	0.282759	0.000032	550	7	100	0.282751	11.1	1.1	544	5	0.282751	10.9	1.1	0.75	0.52
RV2-40-66a-a8	0.0264	0.0023	0.00093	0.00012	1.46717	0.00009	1.88638	0.00018	8	0.282737	0.000049	541	6	99	0.282728	10.1	1.7	544	5	0.282728	10.1	1.7	0.80	0.56
RV2-40-72a-a7	0.0376	0.0031	0.00144	0.00009	1.46723	0.00007	1.88660	0.00015	8	0.282748	0.000034	544	6	99	0.282734	10.3	1.2	544	5	0.282734	10.3	1.2	0.79	0.55
RV2-40-75a-a8	0.0249	0.0025	0.00098	0.00008	1.46720	0.00008	1.88663	0.00019	8	0.282761	0.000037	544	6	99	0.282751	10.9	1.3	544	5	0.282751	10.9	1.3	0.76	0.52
																			Avg	0.282743	10.7			
																			2 SE	0.000034	1.2			

Table B12 (continued): In situ LA-MC-ICP-MS Lu-Hf isotope data for zircon grains from amphibole-bearing gneisses analyzed at GUF, 1st of August, 2016

(a) $^{176}Yb/^{177}Hf = (^{176}Yb/^{173}Yb)_{true} \times (^{173}Yb/^{177}Hf)_{meas} \times (M_{173(Yb)}/M_{177(Hf)})^{b(Hf)}$, $b(Hf) = \ln(^{179}Hf/^{177}Hf_{true} / {}^{179}Hf/^{177}Hf_{measured}) / \ln (M_{179(Hf)}/M_{177(Hf)})$, M=mass of respective isotope. The $^{176}Lu/^{177}Hf$ were calculated in a similar way by using the $^{175}Lu/^{177}Hf$ and b(Yb).

(b) Mean Hf signal in volt.

(c) Initial $^{176}Hf/^{177}Hf$ and eHf calculated using the apparent age of each zircon and the CHUR parameters:

$^{176}Lu/^{177}Hf = 0.0336$, and $^{176}Hf/^{177}Hf = 0.282785$ (Bouvier *et al*., 2008).

(d) Initial $^{176}Hf/^{177}Hf$ and eHf calculated using the emplacement age of each sample and the CHUR parameters:

$^{176}Lu/^{177}Hf = 0.0336$, and $^{176}Hf/^{177}Hf = 0.282785$ (Bouvier *et al*., 2008).

(e) two stage model age in billion years using the measured $^{176}Lu/^{177}Lu$ of each spot (first stage = age of zircon), a value of 0.0113 for the average continental crust (second stage), and a juvenile crust (NC) $^{176}Lu/^{177}Lu$ and $^{176}Hf/^{177}Hf$ of 0.0384 and 0.28325, respectively (Griffin et al., 2002).

(f) two stage model age in billion years using the measured $^{176}Lu/^{177}Lu$ of each spot (first stage = age of zircon), a value of 0.0113 for the average continental crust (second stage), and a juvenile crust (NC) $^{176}Lu/^{177}Lu$ and $^{176}Hf/^{177}Hf$ of 0.0375 and 0.28312, respectively (Naeraa et al., 2012).

Table B13: In situ LA-MC-ICP-MS Lu-Hf isotope data for zircon standards analyzed at LMV, 7th of June, 2017

	$^{176}Hf/^{177}Hf$	2 SE	$^{178}Hf/^{177}Hf$	2 SE	$^{176}Lu/^{177}Hf$	2 SE	$^{176}Yb/^{177}Hf$	2 SE
91500 #1	0.282334	0.000027	1.467228	0.000042	0.000452	0.000001	0.01608	0.00012
91500 #2	0.282389	0.000024	1.467314	0.000043	0.000446	0.000001	0.01569	0.00010
91500 #3	0.282313	0.000026	1.467234	0.000042	0.000430	0.000000	0.01525	0.00011
91500 #4	0.282347	0.000024	1.467268	0.000047	0.000438	0.000000	0.01525	0.00007
91500 #5	0.282350	0.000032	1.467270	0.000043	0.000419	0.000001	0.01409	0.00010
91500 #6	0.282320	0.000029	1.467182	0.000055	0.000407	0.000001	0.01347	0.00009
91500 #7	0.282342	0.000025	1.467329	0.000038	0.000395	0.000001	0.01291	0.00010
91500 #8	0.282331	0.000029	1.467330	0.000050	0.000382	0.000001	0.01226	0.00007
91500 #9	0.282293	0.000026	1.467260	0.000054	0.000382	0.000001	0.01227	0.00011
91500 #10	0.282325	0.000029	1.467216	0.000054	0.000371	0.000000	0.01168	0.00007
91500 #11	0.282306	0.000021	1.467216	0.000048	0.000360	0.000000	0.01145	0.00010
91500 #12	0.282325	0.000030	1.467302	0.000052	0.000373	0.000000	0.01164	0.00007
91500 #13	0.282338	0.000028	1.467250	0.000042	0.000364	0.000000	0.01130	0.00007
91500 #14	0.282331	0.000029	1.467265	0.000055	0.000354	0.000000	0.01114	0.00011
91500 #15	0.282354	0.000028	1.467265	0.000040	0.000359	0.000000	0.01101	0.00006
91500 #16	0.282334	0.000022	1.467272	0.000044	0.000293	0.000000	0.00910	0.00009
91500 #17	0.282312	0.000022	1.467296	0.000054	0.000337	0.000000	0.01028	0.00005
91500 #18	0.282322	0.000020	1.467269	0.000046	0.000300	0.000000	0.00932	0.00009
91500 #19	0.282340	0.000028	1.467248	0.000044	0.000350	0.000000	0.01065	0.00005
Average	**0.282328**							
2SD	**0.000033**							
Reference: 0.282308 ± 0.000006, Blichert-Toft (2008)								
GJ-1 #1	0.282096	0.000022	1.467246	0.000040	0.000322	0.000000	0.01119	0.00011
GJ-1 #2	0.282161	0.000046	1.467245	0.000048	0.000362	0.000001	0.01450	0.00020
GJ-1 #3	0.282107	0.000023	1.467256	0.000027	0.000324	0.000000	0.01152	0.00012
GJ-1 #4	0.282077	0.000023	1.467313	0.000042	0.0003189	0.0000003	0.01150	0.00012
GJ-1 #5	0.282051	0.000023	1.467195	0.000032	0.0002949	0.0000004	0.00980	0.00009
GJ-1 #6	0.282065	0.000020	1.467300	0.000038	0.0002849	0.0000003	0.00931	0.00009
GJ-1 #7	0.282079	0.000023	1.467294	0.000048	0.0002797	0.0000002	0.00899	0.00009
GJ-1 #8	0.282041	0.000023	1.467281	0.000039	0.0002718	0.0000003	0.00858	0.00008
GJ-1 #9	0.282023	0.000027	1.467283	0.000040	0.0002666	0.0000002	0.00840	0.00008
GJ-1 #10	0.282020	0.000020	1.467220	0.000047	0.0002635	0.0000003	0.00834	0.00008

Table B13 (continued): In situ LA-MC-ICP-MS Lu-Hf isotope data for zircon standards analyzed at LMV, 7th of June, 2017

	$^{176}Hf/^{177}Hf$	2 SE	$^{178}Hf/^{177}Hf$	2 SE	$^{176}Lu/^{177}Hf$	2 SE	$^{176}Yb/^{177}Hf$	2 SE
GJ-1 #11	0.282007	0.000028	1.467217	0.000034	0.0002636	0.0000003	0.00826	0.00009
GJ-1 #12	0.282006	0.000023	1.467256	0.000033	0.0002632	0.0000002	0.00823	0.00009
GJ-1 #13	0.282016	0.000017	1.467227	0.000038	0.0002626	0.0000004	0.00819	0.00008
GJ-1 #14	0.282038	0.000021	1.467310	0.000047	0.0002623	0.0000003	0.00806	0.00007
GJ-1 #15	0.282040	0.000027	1.467349	0.000029	0.000256	0.000000	0.00782	0.00006
GJ-1 #16	0.282016	0.000022	1.467230	0.000030	0.0002527	0.0000002	0.00773	0.00008
GJ-1 #17	0.282052	0.000021	1.467271	0.000031	0.0002545	0.0000003	0.00782	0.00009
GJ-1 #18	0.282037	0.000017	1.467281	0.000037	0.0002517	0.0000003	0.00772	0.00008
GJ-1 #19	0.282056	0.000025	1.467320	0.000039	0.0002535	0.0000003	0.00776	0.00009
Average	**0.282036**							
2SD	**0.000043**							

Reference: 0.282000 ± 0.000005, Morel et al. (2008)

Mud Tank #1	0.282537	0.000019	1.467309	0.000033	0.0000303	0.0000001	0.00116	0.00001
Mud Tank #2	0.282524	0.000017	1.467250	0.000029	0.0000302	0.0000001	0.00115	0.00001
Mud Tank #3	0.282533	0.000016	1.467293	0.000038	0.0000285	0.0000001	0.00108	0.00001
Mud Tank #4	0.282543	0.000016	1.467255	0.000038	0.0000299	0.0000001	0.00113	0.00001
Mud Tank #5	0.282570	0.000018	1.467280	0.000043	0.0000285	0.0000001	0.00103	0.00001
Mud Tank #6	0.282524	0.000020	1.467262	0.000046	0.000027	0.000000	0.00098	0.00001
Mud Tank #7	0.282503	0.000018	1.467244	0.000041	0.000028	0.000000	0.00098	0.00001
Mud Tank #8	0.282540	0.000019	1.467285	0.000041	0.000027	0.000000	0.00094	0.00001
Mud Tank #9	0.282547	0.000018	1.467259	0.000039	0.000029	0.000000	0.00099	0.00001
Mud Tank #1	0.282526	0.000015	1.467301	0.000039	0.000027	0.000000	0.00092	0.00001
Mud Tank #1	0.282516	0.000020	1.467256	0.000031	0.000024	0.000000	0.00083	0.00001
Mud Tank #1	0.282522	0.000020	1.467307	0.000035	0.000033	0.000000	0.00114	0.00001
Mud Tank #1	0.282496	0.000015	1.467201	0.000038	0.000024	0.000000	0.00082	0.00001
Mud Tank #1	0.282551	0.000017	1.467266	0.000039	0.000032	0.000000	0.00108	0.00001
Mud Tank #1	0.282518	0.000023	1.467298	0.000035	0.000025	0.000000	0.00086	0.00001
Mud Tank #1	0.282552	0.000018	1.467306	0.000029	0.000026	0.000000	0.00089	0.00001
Mud Tank #1	0.282535	0.000016	1.467367	0.000032	0.000026	0.000000	0.00088	0.00001
Mud Tank #1	0.282526	0.000017	1.467283	0.000027	0.000022	0.000000	0.00074	0.00001
Mud Tank #1	0.282564	0.000019	1.467334	0.000101	0.000023	0.000000	0.00079	0.00001
Average	**0.282533**							
2SD	**0.000042**							

Reference: 0.282507 ± 0.000003, Woodhead and Hergt (2005)

Table B14: In situ LA-MC-ICP-MS Lu-Hf isotope data for zircon grains from meta-sediments analysed at LMV, 7th of June, 2017

Spot	$^{176}Hf/^{177}Hf$	2 SE	$^{178}Hf/^{177}Hf$	2 SE	$^{176}Lu/^{177}Hf$	2 SE	$^{176}Yb/^{177}Hf$	2 SE	Age	2σ	$^{176}Hf/^{177}Hf(T)$	$\varepsilon_{Hf}(T)$	2σ
E-CHA16 #1-94	0.282497	0.000025	1.467257	0.000042	0.001248	0.000056	0.03874	0.00177	682	7	0.282481	4.5	0.9
E-CHA16 #2-93	0.282549	0.000016	1.467242	0.000050	0.000600	0.000001	0.01910	0.00009	727	5	0.282541	7.6	0.5
E-CHA16 #3-96	0.282544	0.000027	1.467274	0.000050	0.001249	0.000036	0.03836	0.00169	635	5	0.282529	5.1	1.0
E-CHA16 #4-97	0.282387	0.000027	1.467272	0.000038	0.000851	0.000056	0.02613	0.00201	578	8	0.282378	-1.5	0.9
E-CHA16 #5-100	0.282680	0.000019	1.467303	0.000041	0.000496	0.000019	0.01659	0.00060	594	6	0.282674	9.3	0.7
E-CHA16 #6-105	0.282630	0.000025	1.467271	0.000043	0.001916	0.000023	0.06561	0.00115	844	8	0.282600	12.3	0.9
E-CHA16 #7-104	0.282525	0.000023	1.467291	0.000033	0.001080	0.000039	0.03393	0.00172	606	5	0.282513	3.9	0.8
E-CHA16 #8-a109	0.282330	0.000027	1.467285	0.000037	0.001569	0.000038	0.05026	0.00128	597	8	0.282313	-3.4	1.0
E-CHA16 #9-110	0.282691	0.000029	1.467246	0.000046	0.001145	0.000005	0.03571	0.00044	622	6	0.282678	10.1	1.0
E-CHA16 #10-209	0.282504	0.000026	1.467245	0.000053	0.002318	0.000072	0.06799	0.00230	644	6	0.282476	3.4	0.9
E-CHA16 #11-111	0.282516	0.000032	1.467230	0.000039	0.001392	0.000048	0.04545	0.00144	622	5	0.282499	3.8	1.1
E-CHA16 #12-118	0.282474	0.000024	1.467282	0.000035	0.001154	0.000029	0.03270	0.00057	635	5	0.282461	2.7	0.8
E-CHA16 #13-123	0.282525	0.000020	1.467278	0.000034	0.000434	0.000015	0.01186	0.00036	639	6	0.282520	4.9	0.7
E-CHA16 #14-124	0.282484	0.000024	1.467253	0.000040	0.001460	0.000059	0.04633	0.00200	623	7	0.282467	2.7	0.8
E-CHA16 #15-127	0.281981	0.000019	1.467269	0.000039	0.000629	0.000016	0.02085	0.00054	565	4	0.281974	-16.1	0.7
E-CHA16 #16-128	0.282503	0.000027	1.467286	0.000049	0.001684	0.000028	0.05377	0.00074	986	7	0.282472	11.0	1.0
E-CHA16 #17-129	0.282369	0.000020	1.467249	0.000035	0.000967	0.000041	0.02984	0.00146	610	6	0.282358	-1.5	0.7
E-CHA16 #18-135	0.281955	0.000027	1.467281	0.000039	0.000964	0.000022	0.03016	0.00069	579	5	0.281944	-16.9	1.0
E-CHA16 #19-137	0.282304	0.000023	1.467293	0.000041	0.001378	0.000018	0.04108	0.00131	701	6	0.282286	-2.0	0.8
E-CHA16 #20-140	0.282635	0.000032	1.467237	0.000040	0.001464	0.000072	0.04406	0.00202	641	5	0.282617	8.4	1.1
E-CHA16 #21-142	0.281099	0.000023	1.467259	0.000033	0.001071	0.000010	0.03495	0.00013	2718	10	0.281044	0.2	0.8
E-CHA16 #22-146	0.282387	0.000019	1.467237	0.000054	0.000551	0.000003	0.01759	0.00016	600	5	0.282381	-0.9	0.7
E-CHA16 #23-154	0.282298	0.000023	1.467260	0.000033	0.000654	0.000025	0.02193	0.00106	636	9	0.282290	-3.3	0.8
E-CHA16 #24-156	0.282729	0.000024	1.467325	0.000028	0.001346	0.000061	0.03734	0.00180	683	7	0.282711	12.7	0.8
E-CHA16 #25-157	0.282503	0.000023	1.467288	0.000037	0.000738	0.000022	0.01996	0.00050	771	6	0.282492	6.9	0.8
E-CHA16 #26-163	0.281579	0.000022	1.467227	0.000045	0.001278	0.000111	0.04326	0.00460	2149	12	0.281527	4.1	0.8
E-CHA16 #27-165	0.282543	0.000030	1.467309	0.000050	0.001114	0.000034	0.03397	0.00109	632	6	0.282530	5.1	1.1
E-CHA16 #28-167	0.282522	0.000020	1.467278	0.000027	0.000714	0.000019	0.02107	0.00076	617	5	0.282513	4.2	0.7
E-CHA16 #29-168	0.281055	0.000021	1.467277	0.000035	0.000521	0.000012	0.01694	0.00045	2645	18	0.281029	-2.0	0.7
E-CHA16 #30-175	0.282408	0.000019	1.467292	0.000035	0.000632	0.000049	0.01652	0.00119	1058	9	0.282396	9.9	0.7
E-CHA16 #31-176	0.282548	0.000025	1.467300	0.000037	0.000691	0.000008	0.01971	0.00024	609	5	0.282540	4.9	0.9
E-CHA16 #32-179	0.282269	0.000020	1.467262	0.000036	0.000314	0.000001	0.01088	0.00003	608	5	0.282266	-4.8	0.7
E-CHA16 #33-178	0.282225	0.000035	1.467281	0.000043	0.002006	0.000113	0.06568	0.00400	964	7	0.282188	0.5	1.2
E-CHA16 #34-180	0.282635	0.000020	1.467273	0.000041	0.001556	0.000049	0.04766	0.00185	640	5	0.282616	8.3	0.7
E-CHA16 #35-181	0.281142	0.000018	1.467284	0.000039	0.001198	0.000008	0.03927	0.00060	2705	9	0.281080	1.2	0.6

Table B14 (continued): In situ LA-MC-ICP-MS Lu-Hf isotope data for zircon grains from meta-sediments analysed at LMV, 7th of June, 2017

Spot	$^{176}Hf/^{177}Hf$	2 SE	$^{178}Hf/^{177}Hf$	2 SE	$^{176}Lu/^{177}Hf$	2 SE	$^{176}Yb/^{177}Hf$	2 SE	Age	2σ	$^{176}Hf/^{177}Hf(T)$	$\varepsilon_{Hf}(T)$	2σ
E-CHA16 #36-183	0.282269	0.000016	1.467282	0.000028	0.000731	0.000003	0.02099	0.00025	601	5	0.282261	-5.1	0.6
E-CHA16 #37-189	0.282490	0.000022	1.467237	0.000040	0.001957	0.000078	0.06197	0.00266	630	5	0.282467	2.8	0.8
E-CHA16 #38-192	0.282338	0.000015	1.467272	0.000038	0.000342	0.000005	0.01146	0.00014	591	7	0.282335	-2.8	0.5
E-CHA16 #39-198	0.282511	0.000019	1.467270	0.000040	0.000729	0.000026	0.02523	0.00080	571	4	0.282503	2.8	0.7
E-CHA16 #40-195	0.282337	0.000020	1.467266	0.000042	0.001076	0.000045	0.03230	0.00133	925	15	0.282319	4.2	0.7
E-CHA16 #41-203	0.282386	0.000021	1.467295	0.000047	0.001403	0.000078	0.04263	0.00223	636	6	0.282369	-0.5	0.8
E-CHA16 #42-207	0.282382	0.000021	1.467276	0.000045	0.000948	0.000035	0.02806	0.00103	618	5	0.282371	-0.9	0.7
H-PdB16 #1-199	0.282662	0.000021	1.467269	0.000049	0.001101	0.000015	0.03608	0.00045	731	8	0.282647	11.4	0.8
H-PdB16 #2-7	0.282676	0.000028	1.467253	0.000031	0.001571	0.000051	0.05068	0.00188	693	7	0.282655	10.9	1.0
H-PdB16 #3-8	0.281612	0.000026	1.467196	0.000046	0.003527	0.000073	0.10743	0.00125	1966	10	0.281481	-1.8	0.9
H-PdB16 #4-9	0.282651	0.000018	1.467246	0.000031	0.001278	0.000017	0.04350	0.00082	650	7	0.282635	9.2	0.6
H-PdB16 #5-11	0.282690	0.000022	1.467284	0.000029	0.000912	0.000034	0.02894	0.00146	637	6	0.282679	10.5	0.8
H-PdB16 #6-15	0.282672	0.000027	1.467281	0.000029	0.001727	0.000158	0.05327	0.00492	800	8	0.282646	13.0	1.0
H-PdB16 #7-19	0.282425	0.000027	1.467255	0.000034	0.000974	0.000028	0.02930	0.00087	804	8	0.282410	4.7	0.9
H-PdB16 #8-20	0.282052	0.000018	1.467255	0.000035	0.001131	0.000023	0.03744	0.00040	643	7	0.282038	-12.1	0.6
H-PdB16 #9-21	0.282709	0.000022	1.467252	0.000035	0.001316	0.000090	0.04310	0.00278	706	9	0.282692	12.5	0.8
H-PdB16 #10-24	0.282649	0.000021	1.467261	0.000043	0.000719	0.000023	0.02251	0.00057	747	8	0.282639	11.5	0.7
H-PdB16 #11-41	0.282617	0.000023	1.467273	0.000025	0.000750	0.000030	0.02373	0.00121	857	10	0.282605	12.8	0.8
H-PdB16 #12-45	0.282674	0.000019	1.467273	0.000041	0.000858	0.000032	0.02650	0.00106	652	7	0.282664	10.3	0.7
H-PdB16 #13-57	0.281114	0.000019	1.467226	0.000042	0.000557	0.000006	0.01839	0.00018	2437	8	0.281088	-4.8	0.7
H-PdB16 #14-50	0.282487	0.000022	1.467246	0.000044	0.001282	0.000038	0.03401	0.00089	870	8	0.282466	8.2	0.8
H-PdB16 #15-63	0.282696	0.000024	1.467265	0.000031	0.001487	0.000063	0.04107	0.00187	691	7	0.282677	11.6	0.9
H-PdB16 #16-68	0.282642	0.000023	1.467235	0.000048	0.001517	0.000040	0.04256	0.00088	776	8	0.282620	11.5	0.8
H-PdB16 #17-81	0.282660	0.000040	1.467256	0.000038	0.002500	0.000135	0.08423	0.00427	814	8	0.282622	12.4	1.4
H-PdB16 #18-85	0.282613	0.000023	1.467238	0.000038	0.001054	0.000014	0.03241	0.00054	736	7	0.282598	9.8	0.8
H-PdB16 #19-90	0.282237	0.000031	1.467290	0.000036	0.0019890	0.0000430	0.06447	0.00165	978	11	0.282200	1.2	1.1
H-PdB16 #20-92	0.282686	0.000018	1.467228	0.000041	0.0008300	0.0000196	0.02348	0.00049	590	6	0.282677	9.3	0.6
H-PdB16 #21-94	0.282154	0.000018	1.467212	0.000043	0.0011679	0.0000397	0.03794	0.00089	952	10	0.282133	-1.8	0.6
H-PdB16 #22-96	0.280993	0.000016	1.467258	0.000035	0.0004329	0.0000020	0.01375	0.00015	2581	8	0.280972	-5.6	0.6
H-PdB16 #23-98	0.282582	0.000017	1.467225	0.000030	0.0014609	0.0000531	0.04989	0.00171	607	6	0.282566	5.8	0.6
H-PdB16 #24-100	0.282550	0.000021	1.467195	0.000033	0.0015456	0.0000120	0.04222	0.00042	756	7	0.282528	7.8	0.7
H-PdB16 #25-102	0.282560	0.000026	1.467274	0.000040	0.0010991	0.0000041	0.03152	0.00036	798	8	0.282543	9.3	0.9
H-PdB16 #26-105	0.282580	0.000023	1.467215	0.000043	0.0019133	0.0000357	0.06161	0.00174	723	7	0.282554	8.0	0.8
H-PdB16 #27-106	0.282362	0.000025	1.467241	0.000042	0.0007310	0.0000165	0.02474	0.00045	696	7	0.282353	0.2	0.9

Table B16 (continued): In situ LA-MC-ICP-MS Lu-Hf isotope data for zircon grains from meta-sediments analysed at LMV, 7th of June, 2017

Spot	$^{176}Hf/^{177}Hf$	2 SE	$^{178}Hf/^{177}Hf$	2 SE	$^{176}Lu/^{177}Hf$	2 SE	$^{176}Yb/^{177}Hf$	2 SE	Age	2σ	$^{176}Hf/^{177}Hf(T)$	$\varepsilon_{Hf}(T)$	2σ
H-PdB16 #28-107	0.282542	0.000021	1.467178	0.000036	0.0006679	0.0000084	0.02163	0.00051	724	7	0.282533	7.3	0.7
H-PdB16 #29-195	0.282699	0.000020	1.467166	0.000041	0.0018612	0.0000078	0.06197	0.00063	620	6	0.282677	10.0	0.7
H-PdB16 #30-117	0.282663	0.000024	1.467254	0.000032	0.0010600	0.0000086	0.03452	0.00033	638	6	0.282651	9.5	0.8
H-PdB16 #31-118	0.281675	0.000032	1.467290	0.000043	0.0020242	0.0000335	0.05693	0.00084	978	10	0.281638	-18.7	1.1
H-PdB16 #32-120	0.282044	0.000037	1.467238	0.000043	0.0014341	0.0001316	0.04371	0.00407	651	7	0.282027	-12.3	1.3
H-PdB16 #33-122	0.282754	0.000025	1.467226	0.000039	0.0011027	0.0000115	0.03206	0.00052	641	7	0.282741	12.7	0.9
H-PdB16 #34-124	0.282661	0.000028	1.467268	0.000042	0.0006746	0.0000503	0.01708	0.00129	749	8	0.282651	12.0	1.0
H-PdB16 #35-125	0.282530	0.000019	1.467259	0.000039	0.0001590	0.0000067	0.00658	0.00015	606	5	0.282528	4.4	0.7
H-PdB16 #36-128	0.282662	0.000031	1.467282	0.000034	0.0008056	0.0000881	0.02679	0.00295	630	11	0.282653	9.4	1.1
H-PdB16 #37-130	0.282583	0.000022	1.467224	0.000045	0.0010455	0.0000342	0.03344	0.00127	855	13	0.282566	11.4	0.8
H-PdB16 #38-131	0.282763	0.000031	1.467223	0.000035	0.0016061	0.0000199	0.05046	0.00028	610	6	0.282745	12.2	1.1
H-PdB16 #39-138	0.282670	0.000021	1.467237	0.000058	0.0009571	0.0000921	0.02915	0.00292	622	8	0.282659	9.4	0.7
H-PdB16 #40-137	0.282627	0.000032	1.467264	0.000036	0.0021801	0.0000650	0.07757	0.00299	755	8	0.282596	10.2	1.1
H-PdB16 #41-123	0.282773	0.000028	1.467243	0.000043	0.0014087	0.0000497	0.04128	0.00143	658	6	0.282756	13.7	1.0
H-PdB16 #42-144	0.281309	0.000021	1.467312	0.000040	0.0011122	0.0000414	0.03237	0.00112	2498	10	0.281256	2.6	0.7
H-PdB16 #43-167	0.281590	0.000024	1.467248	0.000036	0.001356	0.000113	0.04325	0.00332	1866	11	0.281542	-1.9	0.9
H-PIL16 #1-9	0.282559	0.000030	1.467184	0.000034	0.000943	0.000041	0.03089	0.00119	629	8	0.282548	5.6	1.1
H-PIL16 #2-18	0.281028	0.000021	1.467232	0.000040	0.000602	0.000022	0.02144	0.00083	2763	18	0.280996	-0.4	0.7
H-PIL16 #3-19	0.282686	0.000039	1.467157	0.000053	0.001075	0.000111	0.03696	0.00376	564	7	0.282675	8.7	1.4
H-PIL16 #4-22	0.282320	0.000027	1.467298	0.000033	0.000918	0.000014	0.03309	0.00076	612	7	0.282310	-3.2	1.0
H-PIL16 #5-15	0.282514	0.000022	1.467230	0.000061	0.001418	0.000034	0.05078	0.00130	637	6	0.282497	4.0	0.8
H-PIL16 #6-17	0.282622	0.000028	1.467272	0.000037	0.000995	0.000039	0.03460	0.00159	632	6	0.282610	7.9	1.0
H-PIL16 #7-30	0.282611	0.000029	1.467230	0.000035	0.001170	0.000025	0.03649	0.00077	666	7	0.282597	8.2	1.0
H-PIL16 #8-29	0.282405	0.000024	1.467252	0.000042	0.000754	0.000018	0.02392	0.00072	823	8	0.282394	4.6	0.8
H-PIL16 #9-34	0.282323	0.000021	1.467234	0.000029	0.001196	0.000035	0.03843	0.00140	651	7	0.282309	-2.3	0.7
H-PIL16 #10-33	0.281218	0.000022	1.467211	0.000026	0.001073	0.000028	0.03504	0.00117	2596	11	0.281164	1.6	0.8
H-PIL16 #11-35	0.281318	0.000022	1.467292	0.000036	0.000279	0.000001	0.01107	0.00012	1989	23	0.281308	-7.4	0.8
H-PIL16 #12-36	0.282314	0.000024	1.467244	0.000049	0.001597	0.000037	0.05577	0.00149	587	6	0.282296	-4.2	0.8
H-PIL16 #13-39	0.282549	0.000027	1.467248	0.000037	0.001110	0.000094	0.03262	0.00278	637	6	0.282536	5.4	0.9
H-PIL16 #14-48	0.282260	0.000022	1.467209	0.000044	0.001102	0.000036	0.03622	0.00117	600	6	0.282248	-5.6	0.8
H-PIL16 #15-79	0.282092	0.000024	1.467309	0.000034	0.000694	0.000040	0.02248	0.00125	641	6	0.282084	-10.5	0.8
H-PIL16 #16-84	0.282664	0.000027	1.467254	0.000043	0.001318	0.000080	0.04360	0.00236	555	8	0.282651	7.6	0.9
H-PIL16 #17-87	0.281195	0.000023	1.467265	0.000042	0.001480	0.000012	0.04679	0.00063	2773	14	0.281116	4.1	0.8
H-PIL16 #18-83	0.281543	0.000030	1.467243	0.000046	0.001004	0.000032	0.03413	0.00126	1994	15	0.281505	-0.2	1.1

Table B16 (continued): In situ LA-MC-ICP-MS Lu-Hf isotope data for zircon grains from meta-sediments analysed at LMV, 7th of June, 2017

Spot	$^{176}Hf/^{177}Hf$	2 SE	$^{178}Hf/^{177}Hf$	2 SE	$^{176}Lu/^{177}Hf$	2 SE	$^{176}Yb/^{177}Hf$	2 SE	Age	2σ	$^{176}Hf/^{177}Hf(T)$	$\varepsilon_{Hf}(T)$	2σ
H-PIL16 #19-91	0.281744	0.000027	1.467255	0.000038	0.001809	0.000048	0.06404	0.00230	1910	11	0.281678	4.0	0.9
H-PIL16 #20-90	0.282231	0.000019	1.467278	0.000031	0.001215	0.000006	0.03918	0.00022	981	9	0.282208	1.6	0.7
H-PIL16 #21-94	0.282367	0.000018	1.467297	0.000030	0.001477	0.000071	0.04866	0.00227	643	6	0.282350	-1.1	0.6
H-PIL16 #22-98	0.282479	0.000030	1.467235	0.000044	0.001889	0.000019	0.06895	0.00060	1025	11	0.282443	10.8	1.1
H-PIL16 #23-102	0.281176	0.000027	1.467293	0.000043	0.000869	0.000035	0.02919	0.00139	2656	14	0.281131	1.9	1.0
H-PIL16 #24-103	0.282309	0.000017	1.467331	0.000029	0.000712	0.000097	0.02263	0.00327	614	6	0.282300	-3.5	0.6
H-PIL16 #25-104	0.282505	0.000018	1.467257	0.000042	0.001024	0.000011	0.02959	0.00066	635	7	0.282493	3.8	0.6
H-PIL16 #26-11	0.282575	0.000034	1.467242	0.000043	0.002058	0.000045	0.06995	0.00117	612	6	0.282552	5.4	1.2
H-PIL16 #27-110	0.282385	0.000023	1.467323	0.000041	0.000554	0.000004	0.01690	0.00009	586	7	0.282379	-1.3	0.8
H-PIL16 #28-112	0.282397	0.000022	1.467257	0.000045	0.000730	0.000011	0.02538	0.00025	590	6	0.282389	-0.9	0.8
H-PIL16 #29-113	0.281848	0.000022	1.467215	0.000050	0.001183	0.000091	0.03884	0.00340	985	9	0.281827	-11.9	0.8
H-PIL16 #30-114	0.282395	0.000032	1.467276	0.000046	0.000981	0.000024	0.03390	0.00116	576	6	0.282384	-1.3	1.1
H-PIL16 #31-118	0.281524	0.000023	1.467299	0.000034	0.000869	0.000006	0.02608	0.00024	1776	18	0.281494	-5.7	0.8
H-PIL16 #32-122	0.282414	0.000025	1.467245	0.000047	0.000992	0.000017	0.03421	0.00053	642	7	0.282402	0.8	0.9
H-PIL16 #33-125	0.282593	0.000026	1.467226	0.000039	0.002166	0.000073	0.07536	0.00293	550	5	0.282571	4.7	0.9
H-PIL16 #34-130	0.282314	0.000021	1.467259	0.000036	0.001165	0.000015	0.03651	0.00065	637	7	0.282300	-3.0	0.8
H-PIL16 #35-126	0.281566	0.000027	1.467237	0.000050	0.001051	0.000042	0.03079	0.00113	2101	17	0.281524	2.9	1.0

B.5 Monazite U–Pb isotope measurements

B.5.1 Analytical details on the LMV session

U–Pb isotopic data were obtained using the laser ablation inductively coupled plasma mass spectrometry (LA–ICP–MS) unit maintained at the Laboratoire Magmas and Volcans, Clermont-Ferrand, France, from monazite grains separated from rock powders as well as grains identified in standard petrographic thin sections. The analyses involved ablation with a Resonetics M-50 Excimer laser system operating at a wavelength of 193 nm (Müller et al., 2009). Spot diameter of 9 μm was associated with repetition rates of 3 Hz and a fluence of 2.9 J/cm^{-2}. The ablated material was carried into helium and then mixed with nitrogen and argon before injection into the plasma source of a Thermo Element XR Sector Field high-resolution ICP–MS. The analytical method for isotope dating with LA-ICPMS is similar to that reported in Paquette and Tiepolo (2007), Hurai et al. (2010) and Paquette et al. (2014). Data are corrected for the U–Pb fractionation occurring during laser sampling and for instrumental mass bias by standard bracketing with repeated measurements of the Trebilcock monazite (Tomascak et al., 1996; Kohn and Vervoort, 2008). Reproducibility and age uncertainty of reference material are propagated by quadratic addition (Horstwood et al., 2003). Repeated analyses of the Itambé monazite treated as unknowns independently controlled the reproducibility and accuracy of corrections. Data reduction was carried out using the GLITTER® software package from Macquarie Research Ltd. (Van Achterbergh et al., 2001; Jackson et al., 2004). Calculated ratios were exported and concordia ages and diagrams were generated using Isoplot/Ex v. 4.15 software package for MS Excel® (Ludwig, 2008). U–Th–Pb concentrations were calibrated relative to the certified contents of these elements in the Itambé monazite (Gasquet et al., 2010). The methodology is summarized Table B15.

Results of LA–ICP–MS U–Pb dating of the Itambé monazite reference material are displayed Table B16. The obtained weighted average $^{207}Pb/^{235}U$ age of 507.8 ± 3.8 Ma (Fig. B.5), overlapping within error with the ID–TIMS literature value (Gasquet et al., 2010).

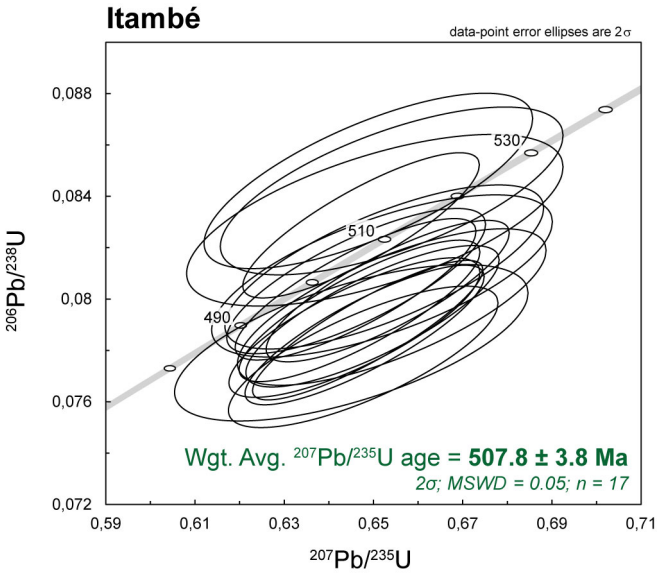

Figure B.5: Wetherill diagram ($^{206}Pb/^{238}U$ vs. $^{207}Pb/^{235}U$) for secondary monazite standards Itambé analysed during the analytical sessions conducted at LMV. Error ellipses and ages are displayed at 2σ level of uncertainty.

B.5.2 Data tables

This section provides the analytical conditions and results of monazite LA–ICP–MS U–Pb isotope measurements reported in the following tables:

- **Table B15:** Summary of experimental conditions for LA–ICP–MS analyses conducted at LMV;
- **Table B16:** Results of LA–ICP–MS U–Pb analyses of monazite standard Itambé, performed at LMV, 15th of November, 2016;
- **Table B17:** Results of LA–ICP–MS U–Pb analyses of monazite from investigated samples, performed at LMV, 15th of November, 2016;

B.6 AMS measurements

Table B18 presents the results of AMS measurements performed at Saint-Etienne University (see section 6.2.3 for analytical details).

Table B15. Summary of experimental conditions for LA-ICPMS analyses conducted at LMV

Laboratory & Sample Preparation	
Laboratory name	Laboratoire Magmas & Volcans, Clermont-Ferrand, France
Sample type/mineral	Monazite
Sample preparation	Polished thin sections, polished 1-inch resin mounts, 0.25 µm polish to finish
Imaging	BSE with a Zeiss MERLIN SEM at Stellenbosch university
Laser ablation system	
Model & type	Resonetics/M-50E, ATL AtlexExcimer
Ablation cell & volume	Laurin Cell ® two volumes cell, Laurin Technic Ltd., volume ca. 1-2 cm^3
Laser wavelength	193 nm
Pulse width	<4 ns
Fluence	2.9 $J.cm^{-2}$
Repetition rate	3 Hz
Spot size	9 µm
Sampling mode / pattern	Single spot
Carrier gas	100% He, Ar make-up gas and N_2 combined using the Squid® device from RESOlution Instruments.
Background collection	30 secs
Ablation duration	60 secs
Wash-out delay	30 secs
Cell carrier gas flow	0.7 l/min
ICP-MS Instrument	
Make, Model & type	Thermo Element XR single collector sector field ICP-MS
Sample introduction	Via conventional tubing
RF power	1300W
Make-up gas flow	0.95 l/min Ar
Detection system	Single collector secondary electron multiplier
Masses measured	204, 206, 207, 208, 232, 238
Integration time per peak	10 ms
Total integration time per reading	130 ms (should represent the time resolution of the data)
Sensitivity / Efficiency	150 000 cps/ppm U and Th (3µm.s line, 47µm, 10 Hz, 9 $J.cm^{-2}$ on NIST 612 reference material)
Dead time	35 ns
Data Processing	
Gas blank	30 second on-peak
Calibration strategy	Monazite: Trebilcock as primary reference material and Itambé as secondary reference material.
Reference Material info	Itambé monazite (Gasquet et al. 2010) Trebilcock monazite (Tomascak et al. 1996, Kohn and Vervoort 2008)
Data processing package / Correction for LIEF	GLITTER ® (van Achterbergh et al. 2001)
Mass discrimination	Monazite: standard-sample bracketing with $^{207}Pb/^{206}Pb$ and $^{206}Pb/^{238}U$ normalized to Trebilcock
Common-Pb correction, composition and uncertainty	No common-Pb correction.
Uncertainty level & propagation	Ages are quoted at 2σ absolute, propagation is by quadratic addition according to Horstwood et al. (2003). Reproducibility and age uncertainty of reference material are propagated.
Quality control	Itambé: weighted average $^{207}Pb/^{235}U$ age = 507.8±3.8 (2σ)

Table B16: Results of LA-ICP-MS U–Pb analyses of monazite standard Itambé, performed at LMV, 15th of November, 2016

grain	$^{207}Pb^{d}/^{235}U$	±2σ (abs.)	$^{206}Pb^{d}/^{238}U$	±2σ (abs.)	rho[e]	$^{206}Pb/^{238}U$	±2σ (Ma)	$^{207}Pb/^{235}U$	±2σ (Ma)
z5 151116a	0.6469	0.0221	0.07954	0.00225	0.83	493	13	507	14
z6 151116a	0.6480	0.0219	0.07860	0.00222	0.84	488	13	507	14
z27 151116a	0.6477	0.0247	0.07775	0.00225	0.76	483	13	507	15
z28 151116a	0.6461	0.0237	0.08070	0.00231	0.78	500	14	506	15
z5 151116b	0.6487	0.0211	0.07879	0.00222	0.87	489	13	508	13
z6 151116b	0.6472	0.0217	0.08287	0.00231	0.83	513	14	507	13
z41 151116b	0.6532	0.0223	0.08031	0.00225	0.82	498	13	510	14
z42 151116b	0.6460	0.0221	0.08038	0.00225	0.82	498	13	506	14
z51 151116b	0.6498	0.0232	0.07933	0.00225	0.79	492	13	508	14
z52 151116b	0.6457	0.0230	0.07889	0.00222	0.79	489	13	506	14
z5 151116c	0.6450	0.0324	0.07830	0.00249	0.63	486	15	505	20
z6 151116c	0.6541	0.0283	0.07969	0.00249	0.72	494	15	511	17
z33 151116c	0.6541	0.0314	0.08421	0.00267	0.66	521	16	511	19
z34 151116c	0.6519	0.0312	0.08090	0.00258	0.67	501	15	510	19
z5 151116d	0.6524	0.0292	0.08125	0.00261	0.72	504	16	510	18
z6 151116d	0.6503	0.0345	0.08307	0.00273	0.62	514	16	509	21
z32 151116d	0.6489	0.0301	0.08460	0.00279	0.71	524	17	508	19
							Avg.	**508**	
							2 S.D	**4**	

Table B17: Results of LA-ICP-MS U–Pb analyses of monazite samples, performed at LMV, 15th of Nov. 2016

An.#	Pb (ppm)	Th (ppm)	U (ppm)	Th/U	$^{207}Pb^{d}/^{235}U$	±2s (abs.)	$^{206}Pb^{d}/^{238}U$	±2s (abs.)	rho[e]	$^{206}Pb/^{238}U$	±2s (Ma)
CHA-15-17 Puylaurent migmatite (thin section)											
z8	1110	47578	11818	4.0	0.40053	0.01320	0.04638	0.00141	0.92	292	9
z9	959	60887	2719	22.4	0.95350	0.03255	0.05049	0.00156	0.91	318	10
z10	1076	68441	5933	11.5	0.35149	0.01515	0.04607	0.00144	0.73	290	9
z11	387	2263	8446	0.3	0.34548	0.01290	0.04668	0.00144	0.83	294	9
z19	828	37713	7463	5.1	0.50057	0.01683	0.04822	0.00147	0.91	304	9
z20	975	61573	4522	13.6	0.36589	0.01311	0.04732	0.00144	0.85	298	9
z21	551	30686	3586	8.6	0.35848	0.01467	0.04839	0.00150	0.76	305	9
z22	1479	96715	5389	17.9	0.39610	0.01542	0.04755	0.00147	0.79	300	9
z27	355	20131	2416	8.3	0.37407	0.01911	0.04849	0.00156	0.63	305	10
z28	311	17611	1885	9.3	0.38977	0.01575	0.05031	0.00156	0.77	316	10
z29	1192	70517	6411	11.0	0.34752	0.01233	0.04723	0.00144	0.86	298	9
z31	544	26498	4447	6.0	0.35296	0.01365	0.04856	0.00150	0.80	306	9
z32	1174	78400	3355	23.4	0.40076	0.01701	0.04794	0.00150	0.74	302	9
CHA-15-65M Puylaurent migmatite (melanosome; mount)											
z7	790	39380	5660	7.0	0.35221	0.01248	0.04671	0.00132	0.80	294	8
z8	752	40458	4092	9.9	0.43788	0.01803	0.04928	0.00144	0.71	310	9
z9	858	36991	6232	5.9	0.39953	0.01389	0.0519	0.00147	0.81	326	9
z10	2969	183749	11883	15.5	0.54676	0.01869	0.04915	0.00141	0.84	309	9
z11	2068	86578	18230	4.7	0.70091	0.02265	0.04882	0.00138	0.87	307	9
z13	2064	103432	13876	7.5	0.39153	0.01299	0.05043	0.00144	0.86	317	9
CHA-15-65L Puylaurent migmatite (leucosome; mount)											
z29	5217	157142	82307	1.9	0.31930	0.00972	0.04343	0.00120	0.91	274	7
z31	4996	155471	77270	2.0	0.31362	0.00960	0.04333	0.00120	0.90	274	7
z35	2869	171846	18554	9.3	0.30971	0.01008	0.04283	0.00120	0.86	270	7
z37	6326	214940	89458	2.4	0.32625	0.01011	0.04348	0.00120	0.89	274	8
z38	6428	184560	106368	1.7	0.30934	0.01002	0.04303	0.00120	0.86	272	7
z40	2956	168017	24118	7.0	0.30500	0.00981	0.0418	0.00117	0.87	264	7
z45	2341	135593	17266	7.9	0.32016	0.01266	0.04323	0.00123	0.72	273	8
z46	3686	130991	49283	2.7	0.36763	0.01185	0.04391	0.00123	0.87	277	8
z47	4406	150764	61713	2.4	0.32221	0.01032	0.04392	0.00123	0.87	277	8
z49	5289	162277	85236	1.9	0.35405	0.01137	0.04301	0.00120	0.87	271	7
CHA15-48 St Laurent-les-Bains migmatite (mount)											
z16	2149	112215	16847	6.7	0.33645	0.01128	0.04651	0.00132	0.85	293	8
z17	2597	116652	27169	4.3	0.36486	0.01203	0.04652	0.00132	0.86	293	8
z18	3503	110801	49928	2.2	0.34956	0.01143	0.04665	0.00132	0.87	294	8
z21	2202	79052	26030	3.0	0.49296	0.01647	0.0468	0.00132	0.84	295	8
z22	1179	55436	8443	6.6	0.71224	0.02475	0.04945	0.00141	0.82	311	9
z23	2030	78773	3081	25.6	0.69964	0.02580	0.08362	0.00240	0.78	518	14
z24	2034	76324	2857	26.7	0.73418	0.02745	0.08796	0.00252	0.77	544	15
CHA-15-34 Le Couste post-tectonic granite dyke (mount)											
z7	1970	88799	22118	4.0	0.31710	0.00957	0.04343	0.00120	0.92	274	7
z8	3491	146268	41607	3.5	0.31453	0.00954	0.04437	0.00123	0.91	280	8
z9	1762	86566	16666	5.2	0.32446	0.00987	0.04409	0.00123	0.92	278	8
z10	2604	110055	31064	3.5	0.31828	0.00954	0.04451	0.00123	0.92	281	8
z11	2247	139908	12568	11.1	0.33500	0.01053	0.04429	0.00123	0.88	279	8
z12	2421	132827	20303	6.5	0.31603	0.00972	0.04391	0.00123	0.91	277	8
z15	1199	71231	8350	8.5	0.32212	0.01128	0.04433	0.00126	0.81	280	8
z16	2188	135902	13345	10.2	0.31888	0.01083	0.04334	0.00123	0.84	274	8
z17	2177	130765	15244	8.6	0.31312	0.00993	0.04314	0.00120	0.88	272	7
z18	1930	108366	15448	7.0	0.31405	0.00984	0.04294	0.00120	0.89	271	7
z19	2665	119409	30918	3.9	0.31548	0.00957	0.04338	0.00120	0.91	274	7
z20	3421	176094	43661	4.0	0.36106	0.01083	0.04336	0.00120	0.92	274	7
z21	3760	100697	63548	1.6	0.31741	0.00957	0.0435	0.00120	0.91	275	7
z22	3939	120085	61747	1.9	0.31324	0.00942	0.04369	0.00123	0.94	276	8
z25	4909	142513	79359	1.8	0.32084	0.00969	0.0437	0.00123	0.93	276	8
z26	2883	139622	28965	4.8	0.32237	0.00996	0.04343	0.00120	0.89	274	7
CHA-15-25 Le Ranc granite sill (thin section)											
z7	2550	61771	44490	1.4	0.32003	0.01032	0.04484	0.00141	0.98	283	9
z8	3195	88029	52047	1.7	0.32360	0.01044	0.04489	0.00141	0.97	283	9
z10	2055	91963	8262	11.1	0.32714	0.01056	0.04542	0.00141	0.96	286	9
z11	656	65435	2032	32.2	0.40401	0.01338	0.04554	0.00144	0.95	287	9
z15	1129	194609	818	238.0	0.31092	0.01128	0.04422	0.00141	0.88	279	9
z16	1146	195348	810	241.2	0.31634	0.01152	0.04494	0.00141	0.86	283	9
z17	107	8327	222	37.6	0.59525	0.02280	0.05732	0.00183	0.83	359	11
z18	1968	115713	7416	15.6	0.32014	0.01041	0.0448	0.00141	0.97	283	9
z19	1154	72337	4199	17.2	0.33938	0.01122	0.04472	0.00141	0.95	282	9

Table B17 (cont.): Results of LA-ICP-MS U–Pb analyses of monazite samples, LMV, 15th of Nov. 2016

An.#	Pb (ppm)	Th (ppm)	U (ppm)	Th/U	$^{207}Pb^{d}/^{235}U$	±2s (abs.)	$^{206}Pb^{d}/^{238}U$	±2s (abs.)	rho[e]	$^{206}Pb/^{238}U$	±2s (Ma)
CHA-15-25 Le Ranc granite sill (thin section)											
z20	652	46193	2013	22.9	0.39773	0.01416	0.04566	0.00144	0.89	288	9
z21	914	177045	1255	141.1	0.37184	0.01341	0.04433	0.00141	0.88	280	9
z22	1709	137860	5423	25.4	0.33027	0.01089	0.04455	0.00141	0.96	281	9
z25	1049	244978	630	389.1	0.31421	0.01131	0.04459	0.00141	0.88	281	9
z26	1041	242900	623	389.7	0.31518	0.01155	0.0449	0.00144	0.88	283	9
z27	1097	80477	3105	25.9	0.36824	0.01224	0.04917	0.00156	0.95	309	10
z28	2450	217215	7276	29.9	0.31298	0.01041	0.04486	0.00144	0.97	283	9
z29	1642	143151	4921	29.1	0.33113	0.01107	0.04456	0.00141	0.95	281	9
z30	3540	101452	56474	1.8	0.32177	0.01071	0.04488	0.00144	0.96	283	9

Table B18: Results of AMS measurements performed at Saint-Etienne University

Specimen	Km (.10^{-6} SI)	L	F	P	P'	T	U	K_1dec	K_1inc	K_2dec	K_2inc	K_3dec	K_3inc
Site 1 Le Ranc (44.533778, 3,900976)													
15CVE04A	112.1	1.013	1.266	1.282	1.323	0.898	0.885	111.5	39.8	4.2	19.7	254.2	43.7
15CVE05A	29.8	1.05	1.033	1.085	1.085	-0.209	-0.229	88.5	50.6	308.8	32	205.4	20.3
15CVE06A	171.3	1.213	1.092	1.325	1.333	-0.373	-0.433	126	25.9	307.7	64.1	216.3	0.7
15CVE07A	22.0	1.04	1.077	1.12	1.122	0.313	0.287	129.1	50.8	355.7	29.3	251.5	23.6
15CVE08A	247.7	1.079	1.245	1.343	1.358	0.486	0.429	72.5	28.7	338.2	7.9	234.4	60.1
15CVE08B	43.2	1.014	1.124	1.139	1.154	0.788	0.775	343.4	5.3	77.4	37.1	246.4	52.4
15CVE09A	42.0	1.012	1.095	1.108	1.119	0.771	0.76	125.2	32.9	352.7	46.3	233	25.3
15CVE10A	27.3	1.011	1.159	1.172	1.194	0.86	0.849	26.7	61.5	162.3	21.2	259.6	18.1
15CVE11A	192.4	1.037	1.435	1.488	1.552	0.817	0.782	168.7	26.8	357	62.9	260.4	3.3
15CVE12A	61.1	1.023	1.174	1.201	1.221	0.754	0.734	130.9	10.9	34.4	30.7	238.3	57
15CVE13A	105.6	1.014	1.228	1.244	1.278	0.877	0.864	350.6	17.3	105.4	53.4	249.8	31.1
15CVE13B	110.8	1.02	1.198	1.221	1.246	0.806	0.789	124.6	41.2	10.6	24.9	258.8	38.6
Site 2 Le Ranc (44.53317, 3.901795)													
15CVE14A	59.0	1.033	1.052	1.086	1.087	0.219	0.199	276.6	16.7	170.3	43	22.4	42.3
15CVE15A	83.6	1.022	1.12	1.145	1.156	0.679	0.661	219.6	9.1	124.8	27.9	326.1	60.4
15CVE16A	54.1	1.011	1.06	1.072	1.077	0.672	0.662	99.8	5.9	199.9	59.7	6.5	29.6
15CVE17A	70.0	1.01	1.129	1.14	1.158	0.853	0.844	86.7	44.5	194	16.8	299.1	40.7
15VCE18A	93.7	1.018	1.035	1.054	1.055	0.329	0.317	148.7	56.1	55.2	2.4	323.5	33.8
15CVE19A	84.6	1.008	1.05	1.059	1.063	0.712	0.705	234.7	54.3	102	26	0.2	22.7
15CVE20A	68.5	1.016	1.029	1.046	1.046	0.273	0.262	189.9	40.6	71.8	28.8	318.3	35.9
15CVE21A	41.4	1.021	1.009	1.03	1.031	-0.41	-0.416	181.8	23.7	280.2	18.5	44.4	59.2
15CVE21B	66.8	1.05	1.006	1.056	1.061	-0.786	-0.791	222.9	31.2	344.5	40.8	109.3	33.5
15CVE22A	54.9	1.018	1.046	1.065	1.067	0.442	0.429	245.9	10.9	131.8	64.7	340.4	22.5
15CVE22B	72.7	1.006	1.059	1.065	1.072	0.797	0.791	217.3	19	107.2	45	323.4	38.9
15CVE23A	86.0	1.004	1.044	1.049	1.054	0.817	0.813	85.1	24.7	198	40.2	332.6	39.7
15CVE24A	60.1	1.007	1.015	1.022	1.023	0.391	0.386	173.7	38.2	80.8	3.7	346.1	51.6
Site 3 Combe Serre (44.535566, 3.891003)													
15CVE25A	8.9	1.067	1.149	1.226	1.231	0.366	0.321	26.2	1	295.9	16.3	119.8	73.7
15CVE26A	28.2	1.053	1.081	1.138	1.139	0.209	0.178	257.9	19.2	163.3	13	41.3	66.5
15CVE27A	28.6	1.05	1.024	1.075	1.077	-0.349	-0.365	245.6	17.7	351.1	40	137.2	44.7
15CVE27B	13.0	1.063	1.11	1.18	1.182	0.259	0.22	54	4.8	322.6	16.2	160	73.1
15CVE28A	24.3	1.021	1.029	1.051	1.051	0.141	0.129	248	7	339	8.7	119.7	78.8
15CVE29A	68.2	1.035	1.078	1.115	1.118	0.374	0.351	229.2	0.5	319.2	7.9	135.3	82.1
15CVE30A	108.9	1.045	1.069	1.117	1.118	0.202	0.175	223.2	13.1	122.9	37.6	329	49.4
15CVE30B	126.9	1.023	1.115	1.141	1.151	0.655	0.636	242.8	3.5	335.2	33.8	147.6	55.9
15CVE31B	65.8	1.056	1.054	1.113	1.113	-0.013	-0.04	230.2	6.6	104.9	78.7	321.3	9.1
15CVE31A	86.1	1.032	1.115	1.15	1.159	0.555	0.53	232.4	17.3	114.3	56.4	331.8	27.8
15CVE32A	64.2	1.07	1.049	1.122	1.123	-0.173	-0.201	233	16	323.1	0.4	54.5	73.9
15CVE33A	95.0	1.024	1.162	1.191	1.208	0.725	0.704	226.1	8.4	317	6.1	82.5	79.6
15CVE33B	93.9	1.035	1.087	1.125	1.129	0.411	0.386	237.3	8.4	329.2	12.5	114.3	74.8
Site 4 Puylaurent (44.533841, 3.885268)													
15CVE34B	69.4	1.01	1.099	1.111	1.123	0.804	0.795	165.7	19.8	268.2	31.1	48.4	51.9
15CVE34A	71.4	1.001	1.121	1.122	1.142	0.982	0.981	173.3	22	274.5	25.6	47.9	55.1
15CVE35A	13.6	1.042	1.071	1.117	1.118	0.249	0.223	263.1	19.7	357.1	11.1	114.9	67.2
15CVE36A	10.7	1.041	1.116	1.162	1.168	0.459	0.429	153	7.9	245.8	19.2	41.6	69.1
15CVE37A	93.3	1.013	1.131	1.146	1.162	0.806	0.794	254.8	64.2	122.6	18	26.6	17.8
15CVE38B	16.5	1.041	1.1	1.145	1.15	0.41	0.382	276.1	43.8	182	4.2	87.7	45.9
15CVE38A	18.3	1.025	1.099	1.126	1.134	0.592	0.572	250.4	46.5	152.7	7.2	56	42.6
15CVE39A	5.2	1.07	1.34	1.433	1.467	0.626	0.57	261.8	25.4	161.9	20	38.2	56.7
15CVE40A	85.2	1.003	1.125	1.128	1.148	0.958	0.956	232.8	50.8	134.7	6.5	39.5	38.4
15CVE41A	85.1	1.009	1.119	1.129	1.145	0.847	0.839	216.8	45.9	120.3	6.2	24.4	43.4
15CVE42A	67.5	1.015	1.096	1.112	1.122	0.725	0.712	256.6	56.9	127.8	22.2	27.7	23.2
Site 5 Les Clous (44.546591, 3.905026)													
15CVE43A	154.5	1.041	1.046	1.088	1.088	0.057	0.036	161	7.2	39.1	76.6	252.5	11.2
15CVE43B	137.3	1.049	1.029	1.08	1.081	-0.248	-0.266	165.6	6.7	12.9	82.5	256	3.4
15CVE44A	148.1	1.036	1.038	1.076	1.076	0.028	0.01	174.9	11.5	34.4	75.2	266.8	9.1
15CVE45A	152.1	1.045	1.052	1.1	1.1	0.07	0.047	172.8	15.6	18.1	72.8	264.8	7
15CVE46A	147.5	1.05	1.05	1.103	1.103	-0.004	-0.028	170.6	16.1	38.4	66.8	265.4	16.3
15CVE46B	139.3	1.045	1.044	1.091	1.091	-0.006	-0.028	168.7	13.9	44.8	66	263.6	19.1
15CVE47A	97.3	1.037	1.035	1.074	1.074	-0.027	-0.044	189.2	22.4	345.2	65.7	95.5	8.9
15CVE47B	98.3	1.038	1.025	1.064	1.064	-0.198	-0.212	181	27.4	346.6	61.9	87.9	6
15CVE48A	96.3	1.037	1.051	1.09	1.09	0.157	0.136	191.2	24	355.4	65.2	98.5	6
15CVE48B	93.9	1.047	1.054	1.103	1.103	0.063	0.039	188.1	28	355.2	61.4	95.2	5.4
15CVE48C	84.5	1.038	1.047	1.086	1.087	0.104	0.084	192.7	25.7	349.3	62.3	98.1	9.6
15CVE49A	90.5	1.04	1.037	1.078	1.078	-0.046	-0.064	180.7	23.1	334	64.5	86.3	10.2
15CVE49B	89.2	1.049	1.041	1.093	1.093	-0.086	-0.108	180.3	19.1	331.9	68.5	87	9.5
15CVE50B	87.4	1.033	1.035	1.07	1.07	0.027	0.01	184.9	15	318.4	68.8	90.8	14.7

Table B18 (cont.): Results of AMS measurements performed at Saint-Etienne University

Specimen	Km (.10^{-6} SI)	L	F	P	P'	T	U	K_1dec	K_1inc	K_2dec	K_2inc	K_3dec	K_3inc
15CVE50A	92.1	1.037	1.035	1.073	1.073	-0.029	-0.047	189.8	15.5	331.1	70.4	96.5	11.7
15CVE51B	78.9	1.04	1.033	1.074	1.074	-0.099	-0.117	195	11.8	35.9	77.4	285.9	4.4
15CVE51A	84.6	1.036	1.029	1.066	1.066	-0.116	-0.132	193.3	21.1	21.1	68.7	284.3	2.7
15CVE52B	129.0	1.053	1.036	1.091	1.091	-0.19	-0.211	157.2	11	354	78.5	247.9	3.2
15CVE52A	129.3	1.048	1.039	1.088	1.088	-0.105	-0.125	161.5	9.5	10.4	79.1	252.4	5.1
15CVE55A	137.8	1.049	1.036	1.087	1.087	-0.152	-0.172	151.5	23.1	5.5	62.8	247.4	13.6
15CVE55B	121.6	1.054	1.034	1.09	1.091	-0.215	-0.235	153.5	18.7	14.9	65.8	248.6	14.9
15CVE56A	133.9	1.06	1.035	1.098	1.099	-0.257	-0.279	161	12	15.1	75.6	252.7	7.8
15CVE56B	134.3	1.059	1.036	1.096	1.097	-0.24	-0.262	159.4	14.4	28.4	68.6	253.5	15.4
Site 6 Puech Redon (44.577817, 3.895382)													
15CVE57A	45.4	1.017	1.113	1.133	1.144	0.725	0.71	322.7	26.8	81.4	43.5	212.3	34.6
15CVE58A	85.2	1.022	1.118	1.143	1.154	0.672	0.653	20.4	46	289.2	1.1	198.2	44
15CVE59A	45.7	1.007	1.128	1.136	1.154	0.886	0.879	26.1	26.5	120.6	9	227.8	61.7
15CVE60B	51.6	1.013	1.145	1.16	1.179	0.829	0.817	99.7	24.9	356.8	25.7	227.4	52.8
15CVE60A	53.1	1.019	1.106	1.127	1.138	0.68	0.663	19.3	28.5	118.1	15.8	233.7	56.7
15CVE60B	51.4	1.007	1.156	1.164	1.187	0.905	0.898	102.8	23.1	2.3	23.2	232.4	56.3
15CVE61A	56.1	1.005	1.113	1.119	1.136	0.906	0.9	96.7	46.4	343.9	20.3	237.9	36.6
15CVE62A	36.3	1.004	1.102	1.106	1.121	0.929	0.926	16.5	36.6	125.1	23.3	240	44.3
15CVE62B	36.9	1.022	1.104	1.128	1.137	0.646	0.628	104.5	44.6	352.9	20.5	245.7	38.4
15CVE63A	46.8	1.004	1.071	1.075	1.085	0.883	0.879	104.7	16.7	356.2	46.6	208.6	38.6
15CVE64A	47.2	1.011	1.164	1.177	1.2	0.862	0.851	358.9	41.2	98.4	10.7	200.1	46.8
15CVE65A	78.5	1.015	1.123	1.14	1.154	0.766	0.753	95.5	27.8	333.3	45.3	204.5	31.8
15CVE66A	57.2	1.028	1.018	1.047	1.047	-0.223	-0.234	111	9	19.8	7.5	250.6	78.2
15CVE67A	80.5	1.011	1.065	1.076	1.082	0.709	0.7	101.6	13.4	193.2	6.5	308.7	75
Site 7 Masméjean (44.568143, 3.878975)													
15CVE69A	39.1	1.034	1.055	1.091	1.092	0.234	0.213	329.6	0.7	223.3	87.6	59.6	2.3
15CVE70A	21.9	1.015	1.008	1.023	1.023	-0.312	-0.317	84.3	44.4	336.2	17.6	230.6	40.3
15CVE71B	34.1	1.023	1.065	1.089	1.093	0.479	0.462	333.5	25.9	111.4	56.8	233.7	19.2
15CVE71A	35.8	1.027	1.022	1.05	1.05	-0.099	-0.111	334.6	12.8	85.6	57.6	237.3	29.2
15CVE72A	27.0	1.013	1.009	1.021	1.021	-0.18	-0.185	331.1	1.5	239.1	53.8	62.2	36.2
15CVE73A	22.0	1.026	1.014	1.041	1.041	-0.281	-0.29	144.9	15.8	305.6	73.3	53.4	5.2
Site 8 Le Ranc (44.531518, 3.90263)													
17CVE01A	14.3	1.024	1.203	1.232	1.256	0.77	0.748	52.7	49.7	270.4	33.9	166.9	19.2
17CVE02A	14.0	1.021	1.291	1.319	1.361	0.848	0.827	33.6	37.2	293.4	13.2	187.3	49.8
17CVE03A	14.9	1.071	1.208	1.293	1.305	0.467	0.416	58.8	38.8	311.5	20.3	200.4	44.2
17CVE04A	85.4	1.009	1.159	1.169	1.192	0.889	0.88	357.9	39.8	107.1	21.5	218.2	42.4
17CVE05A	25.5	1.002	1.175	1.178	1.206	0.972	0.97	281.9	9.7	20	39.6	180.7	48.7
17CVE05B	29.1	1.025	1.136	1.165	1.178	0.674	0.652	71.9	23.9	325.1	33.2	190.4	47.1
17CVE06C	22.1	1.064	1.115	1.186	1.188	0.273	0.233	317.4	13.3	57.3	35.9	210.4	50.9
17CVE06B	21.3	1.045	1.1	1.15	1.154	0.368	0.337	323.8	7.4	58	29.4	221.1	59.5
17CVE06A	24.1	1.049	1.072	1.124	1.125	0.188	0.16	336.5	23.4	71.7	11.7	186.2	63.5
17CVE07A	26.8	1.014	1.071	1.086	1.092	0.658	0.647	354.1	48.6	99.3	13	199.9	38.5
17CVE07B	17.3	1.015	1.132	1.15	1.165	0.781	0.768	334.1	30.5	79.4	24.1	200.9	49.4
17CVE08A	38.9	1.028	1.107	1.138	1.145	0.568	0.546	349.5	33.1	94.8	22	212	48.5
Site 9 Les Gouttes (44.548959, 3.868486)													
17CVE10A	54.2	1.016	1.204	1.223	1.251	0.843	0.828	199.1	31.5	290.2	1.9	23.4	58.4
17CVE10B	72.8	1.007	1.187	1.196	1.225	0.918	0.911	202.5	27.6	109.1	6.5	6.9	61.5
17CVE10C	77.1	1.016	1.179	1.198	1.222	0.825	0.811	181.6	32.1	274.6	4.7	12	57.5
17CVE11B	17.4	1.058	1.016	1.075	1.079	-0.567	-0.579	224.8	28.1	322.5	14.1	76.1	58
17CVE11A	15.5	1.036	1.051	1.089	1.089	0.169	0.149	210	21.3	300.4	0.9	32.7	68.7
17CVE12B	44.2	1.014	1.161	1.178	1.199	0.829	0.816	187.7	24.7	278.1	1	10.4	65.3
17CVE12A	50.3	1.017	1.171	1.191	1.213	0.805	0.789	155.5	17.8	248.2	8.3	2.2	70.2
17CVE13A	24.3	1.051	1.078	1.133	1.134	0.207	0.177	240.5	28.7	145.1	9.8	38.1	59.3
17CVE13B	22.9	1.015	1.125	1.143	1.157	0.769	0.756	236.6	26.8	145.6	2	51.7	63.1
17CVE13C	21.3	1.026	1.11	1.138	1.147	0.61	0.589	168.1	42.6	264.7	7.1	2.3	46.6
17CVE14A	71.8	1.005	1.123	1.128	1.146	0.915	0.909	313.7	15.6	220.3	11.8	94.8	70.3
17CVE15B	60.0	1.005	1.133	1.138	1.158	0.926	0.921	326.8	1.1	236.5	11.7	61.9	78.2
17CVE15A	50.3	1.01	1.159	1.17	1.192	0.879	0.87	151.7	9.7	245.6	21.6	39	66.1
17CVE16A	58.8	1.017	1.154	1.174	1.192	0.789	0.774	250.7	20.6	151.3	23.5	17.5	57.9
17CVE16B	55.0	1.008	1.17	1.179	1.204	0.907	0.9	287.7	1.7	197.1	21.3	22.2	68.7
17CVE17A	51.7	1.02	1.222	1.246	1.276	0.822	0.804	169.7	43.5	261.2	1.5	352.7	46.4
17CVE17B	64.7	1.01	1.16	1.171	1.194	0.879	0.87	141.4	37.4	242.8	14.5	350	48.9

Table B18 (cont.): Results of AMS measurements performed at Saint-Etienne University

Specimen	Km (.10^{-6} SI)	L	F	P	P'	T	U	K_1dec	K_1inc	K_2dec	K_2inc	K_3dec	K_3inc
Site 10 Le Thort (44.555368, 3.905332)													
17CVE18A	4.2	1.133	1.033	1.171	1.181	-0.585	-0.61	67.7	25	218.4	61.9	332	12.1
17CVE18B	15.1	1.041	1.062	1.105	1.106	0.201	0.177	53.5	4.2	145.4	23.5	314.1	66.1
17CVE20B	2.9	1.121	1.216	1.363	1.368	0.263	0.19	297.6	18.4	34	18.5	165.8	63.4
17CVE21B	19.5	1.055	1.051	1.109	1.109	-0.032	-0.058	145.6	35.8	50	7.6	309.8	53.2
17CVE22A	16.9	1.042	1.079	1.124	1.126	0.302	0.275	130.1	30.4	36.5	6.2	296.2	58.8
17CVE23A	33.2	1.007	1.019	1.026	1.027	0.443	0.438	157.4	26.5	270.8	38.7	42.8	39.9
17CVE24A	10.4	1.03	1.078	1.11	1.113	0.439	0.418	92.1	20	1.8	0.9	269.4	70
17CVE25B	11.3	1.065	1.025	1.091	1.094	-0.445	-0.462	75.3	8.2	332.1	57.9	170.2	30.8
17CVE25C	12.9	1.057	1.018	1.075	1.079	-0.518	-0.531	58.7	38.9	324.6	5	228.6	50.6
17CVE25A	16.5	1.014	1.026	1.041	1.041	0.303	0.294	26	14.3	126.7	36.1	278.1	50.3
17CVE26A	11.1	1.057	1.031	1.09	1.091	-0.288	-0.308	165.8	12	45.9	66.9	260.1	19.4
Site 11 Masméjean railway (44.565239, 3.887277)													
17CVE27A	87.7	1.011	1.059	1.07	1.076	0.674	0.665	191	5.5	283.5	24.1	88.9	65.2
17CVE28A	42.1	1.025	1.05	1.076	1.077	0.332	0.315	250.4	4.7	342	18	146.2	71.3
17CVE29A	107.7	1.021	1.072	1.095	1.1	0.537	0.52	279.4	6.5	9.8	3.6	128.7	82.6
17CVE30A	70.0	1.008	1.065	1.073	1.08	0.784	0.778	283.4	23.2	19.6	14.2	138.4	62.4
17CVE30B	97.5	1.006	1.073	1.079	1.088	0.844	0.839	283	10.1	16.5	18.8	166.1	68.4
17CVE31A	108.6	1.009	1.128	1.138	1.156	0.868	0.86	251.7	3.3	342.5	14.4	148.9	75.2
17CVE32B	45.4	1.004	1.074	1.078	1.089	0.887	0.883	40.3	0.4	310.2	21.6	131.4	68.4
17CVE32C	62.2	1.003	1.081	1.084	1.096	0.928	0.925	269.2	26.9	6.2	13.5	120.1	59.4
17CVE32A	63.2	1.016	1.053	1.07	1.073	0.524	0.512	242	21.7	340.4	20.2	109.3	59.6
17CVE33A	23.4	1.02	1.027	1.047	1.048	0.161	0.15	75.5	1.4	165.5	0.9	286.2	88.3
17CVE33B	16.3	1.036	1.046	1.083	1.083	0.125	0.105	27.4	11.8	119.8	11.4	252.7	73.4
17CVE34B	97.8	1.007	1.013	1.02	1.021	0.266	0.262	314.7	7	223.7	8.5	83.7	79
17CVE34A	48.8	1.017	1.023	1.041	1.041	0.139	0.129	239.8	0.9	149.7	4.8	340.9	85.1

Bibliography

Abati, J., Aghzer, A. M., Gerdes, A., and Ennih, N. (2010). Detrital zircon ages of Neoproterozoic sequences of the Moroccan Anti-Atlas belt. *Precambrian Research 181*(1-4), 115–128.

Abati, J., Aghzer, A. M., Gerdes, A., and Ennih, N. (2012). Insights on the crustal evolution of the West African Craton from Hf isotopes in detrital zircons from the Anti-Atlas belt. *Precambrian Research 212-213*, 263–274.

Abati, J., Gerdes, A., Fernandez Suarez, J., Arenas, R., Whitehouse, M. J., and Diez Fernandez, R. (2009). Magmatism and early-Variscan continental subduction in the northern Gondwana margin recorded in zircons from the basal units of Galicia, NW Spain. *Geological Society of America Bulletin 122*(1-2), 219–235.

Abdelsalam, M. G., Liégeois, J.-P., and Stern, R. J. (2002). The Saharan Metacraton. *Journal of African Earth Sciences 34*(3-4), 119–136.

Adam, J., Green, T. H., and Sie, S. H. (1993). Proton microprobe determined partitioning of Rb, Sr, Ba, Y, Zr, Nb and Ta between experimentally produced amphiboles and silicate melts with variable F content. *Chemical Geology 109*, 29–49.

Ait Malek, H., Gasquet, D., Marignac, C., and Bertrand, J.-M. (1995). Des xénolites à corindon dans une vaugnérite de l'Ardèche (Massif Central français) : implications pour le métamorphisme ardéchois. *Comptes Rendus de l'Académie des Sciences, Paris 321*, 959–966.

Alabouvette, B., Arthaud, F., Bodeur, Y., Barthes, J.-P., Paloc, H., and Aubague, M. (1988). *Notice explicative, Carte géol. France (1/50 000), feuille Le Vigan (937)*. Orléans: BRGM.

Alabouvette, B., Burg, J.-P., Lefavrais-Raymond, A., Leyreloup, A. F., and Delor, C. (1989). *Notice explicative, Carte géol. France (1/50 000), feuille Rodez (884)*. Orléans: BRGM.

Alabouvette, B., Pellet, J., Brouder, P., Rabinovitch, M., Roger, G., Van Moort, J. C., Fernandez, A., Girard, F., Sabourdy, G., Mialhe, J., and Vialette, Y. (1988). *Carte géol. France (1/50 000), feuille Génolhac (887)*. Orléans: BRGM.

Albarede, F. (1998). The growth of continental crust. *Tectonophysics 296*, 1–14.

Alexandre, P. (2007). U–Pb zircon SIMS ages from the French Massif Central and implication for the pre-Variscan tectonic evolution in Western Europe. *Comptes Rendus Geoscience 339*(9), 613–621.

Allègre, C. J. and Ben Othman, D. (1980). Nd–Sr isotopic relationship in granitoid rocks and continental crust development: a chemical approach to orogenesis. *Nature 286*, 335–342.

Alsac, C., Cabanis, B., Guerange-Lozes, J., and Béziat, D. (1987). Magmatic characteristics of Ordovician basic volcanism in the Saint-Salvi-de-Carcavès nappe (Tarn, Aveyron, France). *Comptes Rendus de l'Académie des Sciences, Paris 305*, 1199–1205.

Altumi, M. M., Elicki, O., Linnemann, U., Hofmann, M., Sagawe, A., and Gärtner, A. (2013). U–Pb LA–ICP–MS detrital zircon ages from the Cambrian of Al Qarqaf Arch, central-western Libya: Provenance of the West Gondwanan sand sea at the dawn of the early Palaeozoic. *Journal of African Earth Sciences 79*, 74–97.

Amelin, Y., Lee, D.-C., Halliday, A. N., and Pidgeon, R. T. (1999). Nature of the Earth's earliest crust from hafnium isotopes in single detrital zircons. *Nature 399*, 252–255.

Anderson, A. T. (1982). Parental basalts in subduction zones: Implications for continental evolution. *Journal of Geophysical Research: Solid Earth 87*(B8), 7047–7060.

Annen, C., Blundy, J. D., and J., S. R. S. (2006). The genesis of intermediate and silicic magmas in deep crustal hot zones. *Journal of Petrology 47*(3), 505–539.

Annen, C. and Sparks, R. S. J. (2002). Effects of repetitive emplacement of basaltic intrusions on thermal evolution and melt generation in the crust. *Earth and Planetary Science Letters 203*, 937–955.

Anthonioz, P.-M. (1985). Analyse tectonique du socle de l'Ardèche (Massif Central français). Une lecture nouvelle d'un segment de la chaîne hercynienne. *Comptes Rendus de l'Académie des Sciences, Paris 300*, 699–702.

Anthonioz, P.-M. (1987). Intérêt de l'analyse des déformations dans l'encaissant d'un granite pour interpréter la mise en place de la masse plutonique et ses relations avec le contexte : les cas du "dôme diapirique" hercynien du Velay (Massif Central français). *Comptes Rendus de l'Académie des Sciences, Paris 304*, 1015–1018.

Appleby, S. K., Gillespie, M. R., Graham, C. M., Hinton, R. W., Oliver, G. J. H., and Kelly, N. M. (2009). Do S-type granites commonly sample infracrustal sources? New results from an integrated O, U–Pb and Hf isotope study of zircon. *Contributions to Mineralogy and Petrology 160*(1), 115–132.

Arculus, R. J. (1999). Origins of the Continental Crust. *Journal & Proceedings of the Royal Society of New South Wales 132*, 83–110.

Arnaud, F., Boullier, A. M., and Burg, J. P. (2004). Shear structures and microstructures in micaschists: the Variscan Cévennes duplex (French Massif Central). *Journal of Structural Geology 26*(5), 855–868.

Arnaud, F. and Burg, J.-P. (1993). Microstructures des mylonites schisteuses : cartographie des chevauchements varisques dans les Cévennes et détermination de leur cinématique. *Comptes Rendus de l'Académie des Sciences, Paris 317*, 1441–1447.

Arndt, N. T. and Goldstein, S. L. (1987). Use and abuse of crust-formation ages. *Geology 15*, 893–895.

Arndt, N. T. and Goldstein, S. L. (1989). An open boundary between lower continental crust and mantle: its role in crust formation and crustal recycling. *Tectonophysics 161*, 201–212.

Arthaud, F., Mattauer, M., and Matte, P. (1969). La direction des plis couchés penniques de la phase majeure hercynienne est subméridienne dans les Cévennes méridionales. *Comptes Rendus de l'Académie des Sciences, Paris 269*, 556–559.

Arthaud, F. and Matte, P. (1975). Les décrochements tardi-hercyniens du Sud-Ouest de l'Europe. Géométrie et essai de reconstitution des conditions de la déformation. *Tectonophysics 25*, 139–171.

Arthaud, F. and Matte, P. (1977). Late Paleozoic strike-slip faulting in southern Europe and northern Africa: Result of a right-lateral shear zone between the Appalachians and the Urals. *Geological Society of America Bulletin 88*(9), 1305.

Austrheim, H. (1986-1987). Eclogitization of lower crustal granulites by fluid migration through shear zones. *Earth and Planetary Science Letters 81*, 221–232.

Auvray, B., Peucat, J.-J., and Brun, J.-P. (1992). Discussion on tectonothermal chronology of early Cadomian arc development in Guernsey and Sark, Channel Islands. *Journal of the Geological Society, London 149*, 683–686.

Auzanneau, E., Schmidt, M. W., Vielzeuf, D., and D Connolly, J. A. (2009). Titanium in phengite: a geobarometer for high temperature eclogites. *Contributions to Mineralogy and Petrology 159*(1), 1–24.

Avigad, D., Gerdes, A., Morag, N., and Bechstädt, T. (2012). Coupled U–Pb–Hf of detrital zircons of Cambrian sandstones from Morocco and Sardinia: Implications for provenance and Precambrian crustal evolution of North Africa. *Gondwana Research 21*(2-3), 690–703.

Avigad, D., Kolodner, K., McWilliams, M., Persing, H., and Weissbrod, T. (2003). Origin of northern Gondwana Cambrian sandstone revealed by detrital zircon SHRIMP dating. *Geology 31*(3), 227.

Avigad, D., Weissbrod, T., Gerdes, A., Zlatkin, O., Ireland, T. R., and Morag, N. (2015). The detrital zircon U–Pb–Hf fingerprint of the northern Arabian–Nubian Shield as reflected by a Late Ediacaran arkosic wedge (Zenifim Formation; subsurface Israel). *Precambrian Research 266*, 1–11.

Ayers, J. C. and Watson, E. B. (1991). Solubility of apatite, monazite, zircon, and rutile in supercritical fluids with implications for subduction zone geochemistry. *Philosophical Transactions of the Royal Society of London 335*, 365–375.

Ballouard, C. (2016). *Origine, évolution et exhumation des leucogranites peralumineux de la chaîne hercynienne armoricaine : implication sur la métallogénie de l'uranium*. PhD thesis.

Ballèvre, M., Bosse, V., Ducassou, C., and Pitra, P. (2009). Palaeozoic history of the Armorican Massif: Models for the tectonic evolution of the suture zones. *Comptes Rendus Geoscience 341*(2-3), 174–201.

Ballèvre, M., Fourcade, S., Capdevila, R., Peucat, J. J., Cocherie, A., and Fanning, C. M. (2012). Geochronology and geochemistry of Ordovician felsic volcanism in the Southern Armorican Massif (Variscan belt, France): Implications for the breakup of Gondwana. *Gondwana Research 21*(4), 1019–1036.

Ballèvre, M., Le Goff, E., and Hébert, R. (2001). The tectonothermal evolution of the Cadomian belt of northern Brittany, France: a Neoproterozoic volcanic arc. *Tectonophysics 331*, 19–43.

Ballèvre, M., Martinez Catalan, J. R., Lopez-Carmona, A., Pitra, P., Abati, J., Fernandez, R. D., Ducassou, C., Arenas, R., Bosse, V., Castineiras, P., Fernandez-Suarez, J., Gomez Barreiro, J., Paquette, J. L., Peucat, J. J., Poujol, M., Ruffet, G., and Sanchez Martinez, S. (2014). Correlation of the nappe stack in the Ibero-Armorican arc across the Bay of Biscay: a joint French-Spanish project. *Geological Society, London, Special Publications 405*(1), 77–113.

Bambier, A., Berger, E.-T., Mergoil, J., Valadas, B., Veyret, Y., and Weisbrod, A. (1985a). *Carte géol. France (1/50 000), feuille Le Bleymard (863)*. Orléans: BRGM.

Bambier, A., Berger, E.-T., Mergoil, J., Valadas, B., Veyret, Y., and Weisbrod, A. (1985b). *Notice explicative, Carte géol. France (1/50 000), feuille Burzet (840)*. Orléans: BRGM.

Barbarand, J., Lucazeau, F., Pagel, M., and Séranne, M. (2001). Burial and exhumation history of south-eastern Massif Central (France) constrained by apatite fission-track thermochronology. *Tectonophysics 335*, 275–290.

Barbarin, B. (1999). A review of the relationships between granitoid types, their origins and their geodynamic environments. *Lithos 46*, 605–626.

Barbey, P., Villaros, A., Marignac, C., and Montel, J. M. (2015). Multiphase melting, magma emplacement and P-T-time path in late-collisional context: the Velay example (Massif Central, France). *Bulletin de la Société Géologique de France 186*(2-3), 93–116.

Bard, J.-P. and Loueyit, J. (1978). Sur l'origine des gneiss oeillés de l'Espinouse dans la zone axiale de la Montagne Noire (Massif Central) : conséquences tectoniques. *Bulletin de la Société Géologique de*

France 20(5), 751–772.

Barker, F., Farmer, G. L., Ayuso, R. A., Plafker, G., and Lull, J. S. (1992). The 50 Ma granodiorite of the Eastern Gulf of Alaska: melting in an accretionary prism in the forearc. *Journal of Geophysical Research 64*(B5), 6757–6778.

Barraud, J., Gardien, V., Allemand, P., and Grandjean, P. (2004). Analogue models of melt-flow networks in folding migmatites. *Journal of Structural Geology 26*(2), 307–324.

Barrientos, X. and Selverstone, J. (1993). Infiltration vs. thermal overprinting of epidote blueschists, Ile de Groix, France. *Geology 21*(1), 69.

Bascou, J., Henry, B., Ménot, R.-P., Funaki, M., and Barruol, G. (2013). Contribution of AMS measurements in understanding the migmatitic terrains of Pointe Géologie, Terre Adélie (East-Antarctica). *Tectonophysics 603*, 123–135.

Bascou, J., Raposo, M. I. B., Vauchez, A., and Egydio-Silva, M. (2002). Titanohematite lattice-preferred orientation and magnetic anisotropy in high-temperature mylonites. *Earth and Planetary Science Letters 198*, 77–92.

Be Mezeme, E. (2005b). *Contribution de la géochronologie U-Th-Pb sur monazite à la compréhension de la fusion crustale dans la chaîne Varisque française et implication géodynamique*. PhD thesis.

Be Mezeme, E., Cocherie, A., Faure, M., Legendre, O., and Rossi, P. (2006). Electron microprobe monazite geochronology of magmatic events: Examples from Variscan migmatites and granitoids, Massif Central, France. *Lithos 87*(3-4), 276–288.

Be Mezeme, E., Faure, M., Chen, Y., Cocherie, A., and Talbot, J. Y. (2007). Structural, AMS and geochronological study of a laccolith emplaced during Late Variscan orogenic extension: the Rocles pluton (SE French Massif Central). *International Journal of Earth Sciences 96*(2), 215–228.

Be Mezeme, E., Faure, M., Cocherie, A., and Chen, Y. (2005a). In situ chemical dating of tectonothermal events in the French Variscan Belt. *Terra Nova 17*(5), 420–426.

Bea, F. and Montero, P. (1999). Behavior of accessory phases and redistribution of Zr, REE, Y, Th, and U during metamorphism and partial melting of metapelites in the lower crust: An example from the Kinzigite Formation of Ivrea-Verbano, NW Italy. *Geochimica et Cosmochimica Acta 63*(7/8), 1133–1153.

Beard, J. S. and Lofgren, G. E. (1991). Dehydration melting and water-saturated melting of basaltic and andesitic greenstones and amphibolites at 1, 3 and 6.9 kb. *Journal of Petrology 32*(2), 365–401.

Becq-Giraudon, J. F., Montenat, C., and Van Den Driessche, J. (1996). Hercynian high-altitude phenomena in the French Massif Central: tectonic implications. *Palaeogeography, Palaeoclimatology, Palaeoecology 122*, 227–241.

Bellot, J.-P. and Roig, J.-Y. (2007). Episodic exhumation of HP rocks inferred from structural data and P-T paths from the southwestern Massif Central (Variscan belt, France). *Journal of Structural Geology 29*(9), 1538–1557.

Belousova, E. A., Griffin, W. L., and O'Reilly, S. Y. (2006). Zircon crystal morphology, trace element signatures and Hf isotope composition as a tool for petrogenetic modelling: Examples From Eastern Australian granitoids. *Journal of Petrology 47*(2), 329–353.

Belousova, E. A., Kostitsyn, Y. A., Griffin, W. L., Begg, G. C., O'Reilly, S. Y., and Pearson, N. J. (2010). The growth of the continental crust: Constraints from zircon Hf-isotope data. *Lithos 119*(3-4), 457–466.

Belousova, E. A., Reid, A. J., Griffin, W. L., and O'Reilly, S. Y. (2009). Rejuvenation vs. recycling of Archean crust in the Gawler Craton, South Australia: Evidence from U–Pb and Hf isotopes in detrital zircon. *Lithos 113*(3-4), 570–582.

Benn, K., Horne, R. J., Kontak, D. J., Pignotta, G. S., and Evans, N. G. (1997). Syn-Acadian emplacement model for the South Mountain batholith, Meguma terrane, Nova Scotia: Magnetic fabric and structural analyses. *GSA Bulletin 109*(10), 1279–1293.

Benn, K., Paterson, S. R., Lund, S. P., Pignotta, G. S., and Kruse, S. (2001). Magmatic fabrics in batholiths as markers of regional strains and plate kinematics: Example of the Cretaceous Mt. Stuart batholith. *Physics and Chemistry of the Earth 26*(4-5), 343–354.

Berger, J., Féménias, O., Ohnenstetter, D., Bruguier, O., Plissart, G., Mercier, J.-C. C., and Demaiffe, D. (2010a). New occurrence of UHP eclogites in Limousin (French Massif Central): Age, tectonic setting and fluid–rock interactions. *Lithos 118*(3-4), 365–382.

Berger, J., Féménias, O., Ohnenstetter, D., Plissart, G., and Mercier, J. C. C. (2010b). Origin and tectonic significance of corundum-kyanite-sapphirine amphibolites from the Variscan French Massif Central. *Journal of Metamorphic Geology 28*(3), 341–360.

Bernard-Griffiths, J. (1975). *Essai sur la signification des âges au strontium dans une série métamorphique, le bas Limousin : Massif central français*. PhD thesis.

Bernard-Griffiths, J., Gebauer, D., Grünenfelder, M., and Piboule, M. (1985). The tonalite belt of Limousin (French Central Massif) : U-Pb zircon ages and tectonic implications. *Bulletin de la Société Géologique de France 1*(4), 523–529.

Bindeman, I. N. and Melnik, O. E. (2016). Zircon survival, rebirth and recycling during crustal melting, magma crystallization, and mixing based on numerical modelling. *Journal of Petrology 57*(3), 437–460.

Binon, M. and Pin, C. (1989). A Rb-Sr and U-Pb isotopic study of two granite massifs from Montagne

bourbonnaise (NE Massif central, France). *Bulletin de la Société Géologique de France 8*(4), 695–703.

Biot, M. A. and Odé, H. (1965). Theory of gravity instability with variable overburden and compaction. *Geophysics 30*, 213–227.

Birch, F. (1954). Heat from radioactivity. In H. Faul (Ed.), *Nuclear Geology*. New York: Wiley and Sons.

Black, L. P., Kamo, S. L., Allen, C. M., Aleinikoff, J. N., Davis, D. W., Korsch, R. J., and Foudoulis, C. (2003). TEMORA 1: a new zircon standard for phanerozoic U–Pb geochronology. *Chemical Geology 2003*, 155–170.

Black, L. P., Kamo, S. L., Allen, C. M., Davis, D. W., Aleinikoff, J. N., Valley, J. W., Mundil, R., Campbell, I. H., Korsch, R. J., Williams, I. S., and Foudoulis, C. (2004). Improved $^{206}Pb/^{238}U$ microprobe geochronology by the monitoring of a trace-element-related matrix effect; SHRIMP, ID–TIMS, ELA–ICP–MS and oxygen isotope documentation for a series of zircon standards. *Chemical Geology 205*(1-2), 115–140.

Blanc, D. (1981). *Les roches basiques et ultrabasiques des Monts du Lyonnais. Etude pétrographique, minéralogique et géochimique*. PhD thesis.

Blatter, D. L., Sisson, T. W., and Hankins, W. B. (2013). Crystallization of oxidized, moderately hydrous arc basalt at mid- to lower-crustal pressures: implications for andesite genesis. *Contributions to Mineralogy and Petrology 166*(3), 861–886.

Blichert-Toft, J. (2008). The Hf isotopic composition of zircon reference material 91500. *Chemical Geology 253*, 252–527.

Block, S., Baratoux, L., Zeh, A., Laurent, O., Bruguier, O., Jessell, M., Ailleres, L., Sagna, R., Parra-Avila, L. A., and Bosch, D. (2016). Paleoproterozoic juvenile crust formation and stabilisation in the south-eastern West African Craton (Ghana); New insights from U–Pb–Hf zircon data and geochemistry. *Precambrian Research 287*, 1–30.

Bodinier, J. L. (1983). Etude géochimique du massif basique et ultrabasique de Najac (Aveyron). Conséquences géotectoniques. *Bulletin de la Société Géologique de France 25*(2), 185–193.

Bodinier, J. L., Burg, J.-P., Leyreloup, A. F., and Vidal, H. (1988). Reliques d'un bassin d'arrière-arc subducté, puis obducté dans la région de Marvejols (Massif central). *Bulletin de la Société Géologique de France 4*(1), 21–33.

Boehnke, P., Watson, E. B., Trail, D., Harrison, T. M., and Schmitt, A. K. (2013). Zircon saturation re-revisited. *Chemical Geology 351*, 324–334.

Boekhout, F., Roberts, N. M. W., Gerdes, A., and Schaltegger, U. (2015). A Hf-isotope perspective on continent formation in the south Peruvian Andes. *Geological Society, London, Special Publications 389*(1), 305–321.

Bolle, O., Charlier, B., Bascou, J., Diot, H., and McEnroe, S. A. (2014). Anisotropy of magnetic susceptibility versus lattice- and shape-preferred orientation in the Lac Tio hemo-ilmenite ore body (Grenville province, Quebec). *Tectonophysics 629*, 87–108.

Bonev, N., Burg, J.-P., and Ivanov, Z. (2005). Mesozoic–Tertiary structural evolution of an extensional gneiss dome–the Kesebir–Kardamos dome, eastern Rhodope (Bulgaria–Greece). *International Journal of Earth Sciences 95*(2), 318–340.

Borradaile, G. and Alford, C. (1987). Relationship between magnetic susceptibility and strain in laboratory experiments. *Tectonophysics 133*, 121–135.

Borradaile, G. J. and Henry, B. (1997). Tectonic applications of magnetic susceptibility and its anisotropy. *Earth-Science Reviews 42*, 49–93.

Bouchardon, J.-L. (1987). Evaluation des conditions de Pression-Température du "top" métamorphique des éclogites du Lévézou (Rouergue, Massif Central français). *Comptes Rendus de l'Académie des Sciences, Paris 305*, 271–275.

Bouchardon, J.-L. (1989). Témoins de cisaillements syn-éclogitisation : les éclogites blastomylonitiques à clastes d'omphacite du Lévézou (Rouergue, Massif Central français). *Comptes Rendus de l'Académie des Sciences, Paris 309*, 69–72.

Bouchez, J. L. (2000). Anisotropie de susceptibilité magnétique et fabrique des granites. *Comptes Rendus de l'Académie des Sciences, Paris 330*, 1–14.

Bouchez, J. L. and Gleizes, G. (1995). Two-stage deformation of the Mont-Louis-Andorra granite pluton (Variscan Pyrenees) inferred from magnetic susceptibility anisotropy. *Journal of the Geological Society, London 152*, 669–679.

Bouhallier, H., Chardon, D., and Choukroune, P. (1995). Strain patterns in Archaean dome-and-basin structures: The Dharwar craton (Karnataka, South India). *Earth and Planetary Science Letters 135*, 57–75.

Bouilhol, P. (2004). *La Zone Mylonitique Métamorphique Vellave (ZMMV) : une mylonite en cisaillement pur qui signe la mise en place du dôme du Velay sur sa bordure Sud*. M.Sc. thesis.

Bouilhol, P., Jagoutz, O., Hanchar, J. M., and Dudas, F. O. (2013). Dating the India–Eurasia collision through arc magmatic records. *Earth and Planetary Science Letters 366*, 163–175.

Bouilhol, P., Leyreloup, A. F., Delor, C., Vauchez, A., and Monié, P. (2006). Relationships between lower and upper crust tectonic during doming: the mylonitic southern edge of the Velay metamorphic core complex (Cévennes-French Massif Central). *Geodinamica Acta 19*(3-4), 137–153.

Bouvier, A., Vervoort, J. D., and Patchett, P. J. (2008). The Lu–Hf and Sm–Nd isotopic composition

of CHUR: Constraints from unequilibrated chondrites and implications for the bulk composition of terrestrial planets. *Earth and Planetary Science Letters 273*(1-2), 48–57.

Bowring, S. A. and Williams, I. S. (1999). Priscoan (4.00-4.03 Ga) orthogneisses from northwestern Canada. *Contributions to Mineralogy and Petrology 134*, 3–16.

Briand, B., Bouchardon, J.-L., Capiez, P., and Piboule, M. (2002). Felsic (A-type)–basic (plume-induced) Early Palaeozoic bimodal magmatism in the Maures Massif (southeastern France). *Geological Magazine 139*(03).

Briand, B., Bouchardon, J.-L., Ouali, H., Piboule, M., and Capiez, P. (1995). Geochemistry of bimodal amphibolite-felsic gneiss complexes from eastern Massif Central, France. *Geological Magazine 132*(3), 321–337.

Briand, B., Bouchardon, J.-L., Santallier, D., Piboule, M., Ouali, H., and Capiez, P. (1992). Alkaline affinity of the metabasites in the gneissic series surrounding the Velay migmatitic domain. *Géologie de la France 2*, 9–15.

Briand, B., Combémorel, R., Couturié, J.-P., Bérard, P., and Vautrelle, C. (1993). *Notice explicative, Carte géol. France (1/50 000), feuille Le Bleymard (863)*. Orléans: BRGM.

Briand, B., Négron, J., Viard, M., Combémorel, R., and Couturié, J.-P. (1994). *Carte géol. France (1/50 000), feuille Le Bleymard (863)*. Orléans: BRGM.

Briand, B. and Piboule, M. (1979). Les métabasites de la série de Marvejols (Massif central) : témoins d'un magmatisme tholéïtique d'arrière-arc cambro-ordovicien. *Bulletin du B.R.G.M. 2*, 131–171.

Briand, B., Piboule, M., and Bouchardon, J.-L. (1988). Diversité géochimique des métabasites des groupes leptyno-amphiboliques du Rouergue et de Marvejols (Massif central). Origine et implications. *Bulletin de la Société Géologique de France 4*(3), 489–498.

Briand, B., Piboule, M., Santallier, D., and Bouchardon, J.-L. (1991). Geochemistry and tectonic implications of two Ordovician bimodal igneous complexes, southern French Massif Central. *Journal of the Geological Society, London 148*, 959–971.

Brichau, S., Respaut, J.-P., and Monié, P. (2007). New age constraints on emplacement of the Cévenol granitoids, South French Massif Central. *International Journal of Earth Sciences 97*(4), 725–738.

Brouder, P. (1968). De la présence de nappes-plis de style pennique dans une série métamorphique hercynienne. *Comptes Rendus de l'Académie des Sciences, Paris 267*, 575–578.

Brouder, P. (1971). Les étapes de formation d'un édifice hercynien polyphasé : les Cévennes (Massif central, France). *Comptes Rendus de l'Académie des Sciences, Paris 273*, 27–29.

Brown, M. (1994). The generation, segregation, ascent and emplacement of granite magma: the migmatite-to-crustally-derived granite connection in thickened orogens. *Earth-Science Reviews 36*, 83–130.

Brown, M. (1995). The late-Precambrian geodynamic evolution of the Armorica segment of the Cadomian belt (France): Distortion of an active continental margin during south-west directed convergence and subduction of a bathymetric high. *Géologie de la France 3*, 3–22.

Brown, M. and D'Lemos, R. S. (1991). The Cadomian granites of Mancellia, northeast Armorican Massif of France: relationship to the St. Malo migmatite belt, petrogenesis and tectonic setting. *Precambrian Research 51*, 393–427.

Brown, M., Power, G. M., Topley, C. G., and D'Lemos, R. S. (1990). Cadomian magmatism in the North Armorican Massif. In R. S. D'Lemos, R. A. Strachan, and C. G. Topley (Eds.), *The Cadomian orogeny*, Volume 51, pp. 81–213. Geological Society Special Publication.

Bruguier, O., Becq-Giraudon, J. F., Champenois, M., Deloule, E., Ludden, J., and Mangin, D. (2003). Application of in situ zircon geochronology and accessory phase chemistry to constraining basin development during post-collisional extension: a case study from the French Massif Central. *Chemical Geology 201*(3-4), 319–336.

Brun, J. P. and Van Den Driessche, J. (1994). Extensional gneiss domes and detachement fault systems : structure and kinematics. *Bulletin de la Société Géologique de France 165*(6), 519–530.

Burg, J.-P. (1983). *Tectogénèse comparée de deux segments de chaîne de collision: Le Sud du Tibet (suture du Tsangpo); la chaîne hercynienne en Europe (sutures du Massif Central)*. Habilitation thesis.

Burg, J.-P., Davy, P., Nievergelt, P., Oberli, F., Seward, D., Diao, Z., and Meier, M. (1997). Exhumation during crustal folding in the Namche-Barwa syntaxis. *Terra Nova 9*, 53–56.

Burg, J.-P., Delor, C., Leyreloup, A. F., and Romney, F. (1989). Inverted metamorphic zonation and Variscan thrust tectonics in the Rouergue area (Massif Central, France): P-T-t record from mineral to regional scale. In J. S. Daly, J. Cliff, and B. W. D. Yardley (Eds.), *Evolution of Metamorphic Belts*, Volume 43 of *Geological Society Special Publications*, pp. 423–439.

Burg, J.-P., Kaus, B. J. P., and Podladchikov, Y. Y. (2004). Dome structures in collision orogens: Mechanical investigation of the gravity/compression interplay. In D. L. Whitney, C. Teyssier, and C. S. Siddoway (Eds.), *Gneiss domes in orogeny*, Volume 380, pp. 47–66. Geological Society of America Special Paper.

Burg, J.-P., Leyreloup, A. F., Marchand, J., and Matte, P. (1984). Inverted metamorphic zonation and large scale thrusting in the Variscan belt: An example in the French Massif central. *Journal of the Geological Society, London 14*, 47–61.

Burg, J.-P. and Matte, P. (1978). A cross section through the French Massif Central and the scope of

its Variscan geodynamic evolution. *Z. dt. geol. Ges. 129*, 429–460.

Burg, J.-P., Van Den Driessche, J., and Brun, J. P. (1994). Syn- to post-thickening extension in the Variscan Belt of Western Europe: Modes and structural consequences. *Géologie de la France 3*, 33–51.

Burg, J.-P. and Vanderhaeghe, O. (1993). Structures and way-up criteria in migmatites, with application to the Velay dome (French massif Central). *Journal of Structural Geology 15*(11), 1293–1301.

Béziat, D., Bruchon, I., Joron, J.-L., and Monchoux, P. (1992). Magmatic characteristics of Cambrian volcanites from the western Monts de Lacaune area (Montagne Noire, south Massif Central, France). *Comptes Rendus de l'Académie des Sciences, Paris 314*, 475–481.

Béziat, D., Joron, J.-L., and Monchoux, P. (1993). Spessartites in the Montagne Noire, France: mineralogical and geochemical data. *European Journal of Mineralogy 5*, 879–891.

Caen-Vachette, M. (1979). Age cambrien des rhyolites transformées en leptynites dans la série métamorphique du Pilat (Massif Central français). *Comptes Rendus de l'Académie des Sciences, Paris 289*, 997–1000.

Caen-Vachette, M., Couturié, J.-P., and Didier, J. (1982). Ages radiométriques des granites anatectiques et tardimigmatitique du Velay (Massif Central français). *Comptes Rendus de l'Académie des Sciences, Paris 294*, 135–138.

Caen-Vachette, M., Couturié, J.-P., and Fernandez, A. (1981). Age westphalien du granite de Rocles (Cévennes, Massif Central français). *Comptes Rendus de l'Académie des Sciences, Paris 293*, 957–960.

Caen-Vachette, M., Gay, M., Peterlongo, J.-M., Pitiot, P., and Vitel, G. (1984). Age radiométrique du granite syntectonique du Gouffre d'Enfer et du métamorphisme hercynien dans la série de basse pression du Pilat. *Comptes Rendus de l'Académie des Sciences, Paris 299*, 1201–1204.

Calvert, A. T., Gans, P. B., and Amato, J. M. (1999). Diapiric ascent and cooling of a sillimanite gneiss dome revealed by $^{40}Ar/^{39}Ar$ thermochronology: the Kigluaik Mountains, Seward Peninsula, Alaska. In U. Ring, M. T. Brandon, G. S. Lister, and S. D. Willet (Eds.), *Exhumation Processes: Normal Faulting, Ductile Flow and Erosion*, Volume 154, pp. 205–232. Geological Society, London, Special Publications.

Calvez, J. Y. and Vidal, P. (1978). Two billion years old relicts in the Hercynian Belt of Western Europe. *Contributions to Mineralogy and Petrology 65*, 395–399.

Campbell, I. H. and Allen, C. (2008). Formation of supercontinents linked to increases in atmospheric oxygen. *Nature Geoscience 1*, 554–558.

Campbell, I. H., Stepanov, A. S., Liang, H.-Y., Allen, C. M., Norman, M. D., Zhang, Y.-Q., and Xie, Y.-W. (2014). The origin of shoshonites: new insights from the Tertiary high-potassium intrusions of eastern Tibet. *Contributions to Mineralogy and Petrology 167*(3), 1–22.

Caron, C. (1994). *Les minéralisations Pb-Zn associées au Paléozoique inférieur d'Europe méridionale. Traçage isotropique Pb–Pb des gites de l'Iglesiente (SW Sardaigne) et des Cévennes et évolution du socle encaissant par la géochronologie U–Pb, ^{40}Ar–^{39}Ar et K–Ar*. PhD thesis.

Cartwright, I., Vry, J., and Sandiford, M. (1995). Changes in stable isotope ratios of metapeUtes and marbles during regional metamorphism, Mount Lofty Ranges, South Australia: implications for crustal scale fluid flow. *Contributions to Mineralogy and Petrology 120*, 292–310.

Cavalcante, G. C. G., Egydio-Silva, M., Vauchez, A., Camps, P., and Oliveira, E. (2013). Strain distribution across a partially molten middle crust: Insights from the AMS mapping of the Carlos Chagas Anatexite, Araçuaí belt (East Brazil). *Journal of Structural Geology 55*, 79–100.

Cawood, P. A., Hawkesworth, C. J., and Dhuime, B. (2013). The continental record and the generation of continental crust. *Geological Society of America Bulletin 125*(1-2), 14–32.

Cawood, P. A., Kröner, A., Collins, W. J., Kusky, T. M., Mooney, W. D., and Windley, B. F. (2009). Accretionary orogens through Earth history. *Geological Society, London, Special Publications 318*(1), 1–36.

Chantraine, J., Autran, A., and Cavelier, C. (1996). *Carte géologique de la France à l'échelle du millionième, 6ème édition*. Orléans: BRGM.

Chantraine, J., Egal, E., Thiéblemont, D., Le Goff, E., Guerrot, C., Ballèvre, M., and Guennoc, P. (2001). The Cadomian active margin (Northern Armorican Massif, France): a segment of the North Atlantic Panafrican belt. *Tectonophysics 331*, 1–18.

Chapman, D. S. (1986). Thermal gradients in the continental crust. In J. B. Dawson, D. A. Carswell, J. Hall, and K. H. Wedepohl (Eds.), *The Nature of the Lower Continental Crust*, Volume 24, pp. 63–70. Geological Society of London, Special Publication.

Chappell, B. W. and White, A. J. R. (1974). Two contrasting granite types. *Pacific Geology 8*, 173–174.

Chappell, B. W. and White, A. J. R. (2001). Two contrasting granite types: 25 years later. *Australian Journal of Earth Sciences 48*(4), 489–499.

Charles, N., Faure, M., and Chen, Y. (2009). The Montagne Noire migmatitic dome emplacement (French Massif Central): new insights from petrofabric and AMS studies. *Journal of Structural Geology 31*(11), 1423–1440.

Chauvel, C., Hofmann, A. W., and Vidal, P. (1992). HIMU–EM: The French Polynesian connection. *Earth and Planetary Science Letters 110*, 99–119.

Chauvet, A., Volland-Tuduri, N., Lerouge, C., Bouchot, V., Monié, P., Charonnat, X., and Faure, M. (2011). Geochronological and geochemical characterization of magmatic-hydrothermal events within the Southern Variscan external domain (Cévennes area, France). *International Journal of Earth*

Sciences 101(1), 69–86.

Chelle-Michou, C., Laurent, O., Moyen, J.-F., Block, S., Paquette, J.-L., Couzinié, S., Gardien, V., Vanderhaeghe, O., Villaros, A., and Zeh, A. (2017). Pre-Cadomian to late-Variscan odyssey of the eastern Massif Central, France: Formation of the West European crust in a nutshell. *Gondwana Research 46*, 170–190.

Chen, Z., Liu, Y., Hodges, K. V., Burchfiel, B. C., Royden, L. H., and Deng, C. (1990). The Kangmar Dome: A Metamorphic Core Complex in Southern Xizang (Tibet). *Science 250*, 1552–1556.

Chenevoy, M. (1971). *Notice explicative, Carte géol. France (1/50 000), feuille Saint-Etienne (745)*. Orléans: BRGM.

Chenevoy, M., Gay, M., and Lochon, P. (1986). Metamorphic alkali-basalts and leucogranites in the Western Vivarais series (French Central Massif): a record of two major tectonic events in paleozoic time. *Comptes Rendus de l'Académie des Sciences, Paris 303*, 725–730.

Chenevoy, M., Lochon, P., Masmejean, B., and Michon, G. (1995). *Notice explicative, Carte géol. France (1/50 000), feuille Saint-Agrève (793)*. Orléans: BRGM.

Chiron, J.-C. and Kerrien, Y. (1979). *Notice explicative, Carte géol. France (1/250 000), feuille Lyon (29)*. Orléans: BRGM.

Chopin, C. (2003). Ultrahigh-pressure metamorphism: tracing continental crust into the mantle. *Earth and Planetary Science Letters 212*(1-2), 1–14.

Choubert, B. and Girod, M. (1974a). *Carte géol. France (1/50 000), feuille Langogne (839)*. Orléans: BRGM.

Choubert, B. and Girod, M. (1974b). *Notice explicative, Carte géol. France (1/50 000), feuille Langogne (839)*. Orléans: BRGM.

Christensen, N. I. and Mooney, W. D. (1995). Seismic velocity structure and composition of the continental crust: A global view. *Journal of Geophysical Research: Solid Earth 100*(B6), 9761–9788.

Chu, N., Taylor, R. N., Chavagnac, V., Nesbitt, R. W., Boella, R. M., Milton, J. A., German, C. R., Bayon, G., and Burton, K. (2002). Hf isotope ratio analysis using multi-collector inductively coupled plasma mass spectrometry: an evaluation of isobaric interference corrections. *Journal of Analytical Atomic Spectrometry 17*, 1567–1574.

Chèvremont, P., Floc'h, J.-P., Ménillet, F., Stussi, J., Delbos, R., Sauret, B., Blès, J., Courbe, C., Vuaillat, D., and Gravelat, C. (1996). *Notice explicative, Carte géol. France (1/50 000), feuille Rochechouart (687)*. Orléans: BRGM.

Clark, C., Fitzsimons, I. C. W., Healy, D., and Harley, S. L. (2011). How Does the Continental Crust Get Really Hot? *Elements 7*(4), 235–240.

Clemens, J. D. (1990). The granulite - granite connexion. In D. Vielzeuf and P. Vidal (Eds.), *Granulites and Crustal Evolution*, pp. 25–36. Kluwer, Dordrecht.

Clemens, J. D. (2003). S-type granitic magmas—petrogenetic issues, models and evidence. *Earth-Science Reviews 61*(1-2), 1–18.

Clemens, J. D. and Stevens, G. (2012). What controls chemical variation in granitic magmas? *Lithos 134-135*, 317–329.

Clemens, J. D., Stevens, G., and Farina, F. (2011). The enigmatic sources of I-type granites: The peritectic connexion. *Lithos 126*(3-4), 174–181.

Clemens, J. D. and Vielzeuf, D. (1987). Constraints on melting and magma production in the crust. *Earth and Planetary Science Letters 86*, 287–306.

Clift, P. (2004). Controls on tectonic accretion versus erosion in subduction zones: Implications for the origin and recycling of the continental crust. *Reviews of Geophysics 42*(2).

Clift, P. D., Vannucchi, P., and Morgan, J. P. (2009). Crustal redistribution, crust–mantle recycling and Phanerozoic evolution of the continental crust. *Earth-Science Reviews 97*(1-4), 80–104.

Cocherie, A. and Albarede, F. (2001). An improved U–Th–Pb age calculation for electron microprobe dating of monazite. *Geochimica et Cosmochimica Acta 65*(24), 4509–4522.

Cocherie, A., Baudin, T., Autran, A., Guerrot, C., Fanning, C. M., and Laumonier, B. (2005). U–Pb zircon (ID–TIMS and SHRIMP) evidence for the early ordovician intrusion of metagranites in the late Proterozoic Canaveilles Group of the Pyrenees and te Montagne Noire (France). *Bulletin de la Société Géologique de France 176*(3), 269–282.

Cocherie, A., Be Mezeme, E., Legendre, O., Fanning, C. M., Faure, M., and Rossi, P. (2005). Electron-microprobe dating as a tool for determining the closure of Th–U–Pb systems in migmatitic monazites. *American Mineralogist 90*, 607–618.

Coffrant, D. and Piboule, M. (1971). Les éclogites et roches associées des massifs basiques de Saint-Joseph (monts du Lyonnais, Massif central français). *Bulletin de la Société Géologique de France 13*(3-4), 283–291.

Coggon, R. and Holland, T. J. B. (2002). Mixing properties of phengitic micas and revised garnet-phengite thermobarometers. *Journal of Metamorphic Geology 20*, 683–696.

Collins, W. J. (2002). Hot orogens, tectonic switching, and creation of continental crust. *Geology 30*(6), 535–538.

Collins, W. J. and Richards, S. W. (2008). Geodynamic significance of S-type granites in circum-Pacific orogens. *Geology 36*(7), 559.

Condamine, P. and Médard, E. (2014). Experimental melting of phlogopite-bearing mantle at 1 GPa:

Implications for potassic magmatism. *Earth and Planetary Science Letters 397*, 80–92.
Condie, K. C. (1998). Episodic continental growth and supercontinents: a mantle avalanche connection? *Earth and Planetary Science Letters 163*, 97–108.
Condie, K. C. (2004). Supercontinents and superplume events: distinguishing signals in the geologic record. *Physics of the Earth and Planetary Interiors 146*(1-2), 319–332.
Condie, K. C. (2014). Growth of continental crust: a balance between preservation and recycling. *Mineralogical Magazine 78*(3), 623–637.
Condie, K. C. and Aster, R. C. (2010). Episodic zircon age spectra of orogenic granitoids: The supercontinent connection and continental growth. *Precambrian Research 180*(3-4), 227–236.
Condie, K. C., Beyer, E., Belousova, E., Griffin, W. L., and O'Reilly, S. Y. (2005). U–Pb isotopic ages and Hf isotopic composition of single zircons: The search for juvenile Precambrian continental crust. *Precambrian Research 139*(1-2), 42–100.
Condie, K. C., Bickford, M. E., Aster, R. C., Belousova, E., and Scholl, D. W. (2011). Episodic zircon ages, Hf isotopic composition, and the preservation rate of continental crust. *Geological Society of America Bulletin 123*(5-6), 951–957.
Connolly, J. A. D. (2005). Computation of phase equilibria by linear programming: A tool for geodynamic modeling and its application to subduction zone decarbonation. *Earth and Planetary Science Letters 236*(1-2), 524–541.
Corfu, F., Hanchar, J. M., Hoskin, P. W. O., and Kinny, P. D. (2003). Atlas of Zircon Textures. *Reviews in Mineralogy and Geochemistry 53*, 469–500.
Costa, S. (1989). Age radiométrique ^{39}Ar-^{40}Ar du métamorphisme des séries du Lot et du charriage du groupe leptyno-amphibolique de Marvejols (M.C.F.). *Comptes Rendus de l'Académie des Sciences, Paris 309*, 561–567.
Costa, S. (1990). *De la collision continentale à l'extension tardiorogénique : 100 millions d'années d'histoire varisque dans le Massif central français. Une étude chronologique par la méthode ^{40}Ar–^{39}Ar.* PhD thesis.
Costa, S., Maluski, H., and Lardeaux, J. M. (1993). ^{40}Ar–^{39}Ar chronology of Variscan tectonometamorphic events in an exhumed crustal nappe: the Monts du Lyonnais complex (Massif Central, France). *Chemical Geology 105*, 339–359.
Couturié, J.-P. (1974). *Carte géol. France (1/50 000), feuille St-Chély-d'Apcher (838).* Orléans: BRGM.
Couturié, J.-P. (1977). *Le massif granitique de la Margeride (M.C.F.). Etude pétrographique, géochimique et structurale. Exemple de différenciation par gravité dans les roches granitiques. Evolution régionale de la croûte au cours de l'orogène hercynien.* PhD thesis.
Couturié, J.-P. and Geffroy, J. (1974). *Notice explicative, Carte géol. France (1/50 000), feuille St-Chély-d'Apcher (0838).* Orléans: BRGM.
Couzinié, S., Laurent, O., Moyen, J. F., Zeh, A., Bouilhol, P., and Villaros, A. (2016). Post-collisional magmatism: Crustal growth not identified by zircon Hf-O isotopes. *Earth and Planetary Science Letters 456*, 182–195.
Couzinié, S., Laurent, O., Poujol, M., Mintrone, M., Chelle-Michou, C., Moyen, J.-F., Bouilhol, P., Vezinet, A., and Marko, L. (2017). Cadomian S-type granites as basement rocks of the Variscan belt (Massif Central, France): Implications for the crustal evolution of the north Gondwana margin. *Lithos 286-287*, 16–34.
Couzinié, S., Moyen, J. F., Villaros, A., Paquette, J. L., Scarrow, J. H., and Marignac, C. (2014). Temporal relationships between Mg-K mafic magmatism and catastrophic melting of the Variscan crust in the southern part of Velay Complex (Massif Central, France). *Journal of GEOsciences*, 69–86.
Crevola, G., Boucarut, M., Magontier, J., and Collomb, P. (1983). Origine granitique des gneiss de la Cézarenque (Cévennes, Massif Central) : identification de plusieurs faciès plutoniques originels. *Comptes Rendus de l'Académie des Sciences, Paris 296*, 1519–1522.
Crook, K. A. W. (1980). Fore-arc evolution and continental growth: a general model. *Journal of Structural Geology 2*(3), 289–303.
Currie, C. A. and Hyndman, R. D. (2006). The thermal structure of subduction zone back arcs. *Journal of Geophysical Research 111*.
Dabard, M. P., Loi, A., and Peucat, J. J. (1996). Zircon typology combined with Sm-Nd whole-rock isotope analysis to study Brioverian sediments from the Armorican Massif. *Sedimentary Geology 101*, 243–260.
Dallain, C., Schulmann, K., and Ledru, P. (1999). Textural evolution in the transition from subsolidus annealing to melting process, Velay Dome, French Massif Central. *Journal of Metamorphic Geology 17*, 61–74.
Dallmeyer, R. D., D'Lemos, R. S., Strachan, R. A., and Mueller, P. A. (1991). Tectonothermal chronology of early Cadomian arc development in Guernsey and Sark, Channel Islands. *Journal of the Geological Society, London 148*, 691–702.
Davidson, J. P. and Arculus, R. (2006). The significance of Phanerozoic arc magmatism in generating continental crust. In M. Brown and T. Rushmer (Eds.), *Evolution and Differentiation of the Continental Crust*, pp. 135–172. Cambridge University Press.
Davoine, P. (1971). Sur la géochimie et l'évolution métamorphique des leptynites des monts du Lyon-

nais, comparaison avec des leptynites du mont Pilat (Massif central français). *Bulletin de la Société Géologique de France 12*(1), 42–59.

De La Roche, J., Leterrier, J., Grandclaude, P., and Marchal, M. (1980). A classification of volcanic and plutonic rocks using R1-R2 diagram and major-element analyses – Its relationships with current nomenclature. *Chemical Geology 29*, 183–210.

Debon, F. and Le Fort, P. (1983). A chemical-mineralogical classification of common plutonic rocks and associations. *Transactions of the Royal Society of Edinburgh 73*, 135–149.

Debon, F. and Lemmet, M. (1999). Evolution of Mg/Fe ratios in Late Variscan plutonic rocks from the External Crystalline Massifs of the Alps (France, Italy, Switzerland). *Journal of Petrology 40*(7), 1151–1185.

Defaut, B., Burg, J.-P., Leyreloup, A. F., Romney, F., Fuchs, Y., Alabouvette, B., and Lefavrais-Raymond, A. (1990). *Notice explicative, Carte géol. France (1/50 000), feuille Séverac-le-Château (885)*. Orléans: BRGM.

Delbos, L., Lasserre, M., and Roques, M. (1964-1965). Géochronologie et rétromorphose dans la série cristallophyllienne du Rouergue (Massif central français). *Sci. Terre, Nancy 10*(3-4), 329–342.

Delfour, J. (1989). Données lithostratigraphiques et géochimiques sur le Dévono-Dinantien de la partie sud du faisceau du Morvan (nord-est du Massif central français). *Géologie de la France 4*, 49–77.

Delfour, J., Dufour, E., Feybesse, J.-L., Johan, V., Kerrien, Y., Lardeaux, J. M., Lemière, B., Mouterde, R., and Tegyey, M. (1989). *Notice explicative, Carte géol. France (1/50 000), feuille Tarare (697)*. Orléans: BRGM.

Delor, C., Burg, J.-P., Guiraud, M., and Leyreloup, A. F. (1987). Les métapélites à phengite-chloritoïde-grenat-staurotide-disthène de la klippe de Najac-Carmaux : Nouveaux marqueurs d'un métamorphisme de haute pression varisque en Rouergue occidental. *Comptes Rendus de l'Académie des Sciences, Paris 305*, 589–595.

Delor, C., Leyreloup, A. F., Bodinier, J. L., and Burg, J.-P. (1986). Découverte d'éclogites à glaucophane dans la klippe de Najac (Massif Central, France) : nouveaux témoins océaniques d'un stade haute pression dans la chaîne de collision varisque. *Comptes Rendus de l'Académie des Sciences, Paris 302*(11), 739–744.

Demange, M. (2014). *Notice explicative, Carte géol. France (1/50 000), feuille Mazamet (1012)*. Orléans: BRGM.

Denis, E. and Dabard, M. P. (1988). Sandstone petrography and geochemistry of late Proterozoic sediments of the Armorican Massif (France) – A key to basin development during the Cadomian orogeny. *Precambrian Research 42*, 189–206.

Denèle, Y., Laumonier, B., Paquette, J. L., Olivier, P., Gleizes, G., and Barbey, P. (2014). Timing of granite emplacement, crustal flow and gneiss dome formation in the Variscan segment of the Pyrenees. *Geological Society, London, Special Publications 405*(1), 265–287.

Denèle, Y., Paquette, J.-L., Olivier, P., and Barbey, P. (2012). Permian granites in the Pyrenees: the Aya pluton (Basque Country). *Terra Nova 24*(2), 105–113.

Deroin, J.-P., Becq-Giraudon, J. F., and Prost, A. E. (1990). Fracturation tardi-hercynienne et détritisme associé : chronologie des évènements dans les massifs granitiques cévenols décrochés par la faille de Villefort (Mont Lozère et Borne, Massif Central, France). *Comptes Rendus de l'Académie des Sciences, Paris 311*, 865–871.

Deroin, J.-P., Girault, F., Rouzeau, O., and Scanvic, J.-Y. (1993b). Cartographie géologique en Velay : aspects méthodologiques de l'étude par télédétection et présentation des résultats. *Géologie de la France 1*, 3–13.

Deroin, J.-P. and Prost, A. E. (1993a). Déformation tardi-hercynienne du batholite de Villefort (Mont Lozère et Massif de la Borne). Ses rapports avec les sédiments permiens du Pont-de-Montvert (Cévennes, Sud-Est du Massif central). *Géologie de la France 2*, 23–30.

Dewey, J. F. and Burke, K. C. A. (1973). Tibetan, Variscan, and Precambrian basement reactivation: products of continental collision. *The Journal of Geology 81*(6), 683–692.

Díez Fernández, R., Catalán, J. R. M., Gerdes, A., Abati, J., Arenas, R., and Fernández-Suárez, J. (2010). U–Pb ages of detrital zircons from the Basal allochthonous units of NW Iberia: Provenance and paleoposition on the northern margin of Gondwana during the Neoproterozoic and Paleozoic. *Gondwana Research 18*(2-3), 385–399.

Díez Montes, A., Martínez Catalán, J. R., and Bellido Mulas, F. (2010). Role of the Ollo de Sapo massive felsic volcanism of NW Iberia in the Early Ordovician dynamics of northern Gondwana. *Gondwana Research 17*(2-3), 363–376.

Dhuime, B., Hawkesworth, C. J., Cawood, P. A., and Storey, C. D. (2012). A change in the geodynamics of continental growth 3 billion years ago. *Science 335*(6074), 1334–6.

Dhuime, B., Hawkesworth, C. J., Delavault, H., and Cawood, P. A. (2017). Continental growth seen through the sedimentary record. *Sedimentary Geology 357*, 16–32.

Dickinson, W. R. (2008). Impact of differential zircon fertility of granitoid basement rocks in North America on age populations of detrital zircons and implications for granite petrogenesis. *Earth and Planetary Science Letters 275*(1-2), 80–92.

Didier, A., Bosse, V., Boulvais, P., Bouloton, J., Paquette, J. L., Montel, J. M., and Devidal, J. L. (2013). Disturbance versus preservation of U–Th–Pb ages in monazite during fluid–rock interaction:

textural, chemical and isotopic in situ study in microgranites (Velay Dome, France). *Contributions to Mineralogy and Petrology 165*(6), 1051–1072.

Didier, J., Duthou, J.-L., and Lameyre, J. (1982). Mantle and crustal granites: genetic classification of orogenic granites and the nature of their enclaves. *Journal of Volcanology and Geothermal Research 14*, 125–132.

Dissler, E., Doré, F., Dupret, L., Gresselin, F., and Le Gall, J. (1988). Cadomian geodynamical evolution in the northeastern Armorican massif. *Bulletin de la Société Géologique de France 8*(4), 801–814.

D'Lemos, R. S. and Brown, M. (1993). Sm–Nd isotope characteristics of late Cadomian granite magmatism in northern France and the Channel Islands. *Geological Magazine 130*(6), 797–804.

D'Lemos, R. S., Strachan, R. A., and Topley, C. G. (1990). The Cadomian orogeny in the North Armorican Massif: a brief review. In R. S. D'Lemos, R. A. Strachan, and C. G. Topley (Eds.), *The Cadomian Orogeny*, Volume 51, pp. 3–12. Geological Society Special Publication.

Doublier, M. P., Potel, S., and Wemmer, K. (2006). Age and grade of metamorphism in the eastern Monts de Lacaune — Implications for the collisional accretion in Variscan externides (French Massif Central). *Geodinamica Acta 6*, 391–407.

Doublier, M. P., Potel, S., and Wemmer, K. (2015). The tectono-metamorphic evolution of the very low-grade hangingwall constrains two-stage gneiss dome formation in the Montagne Noire (Southern France). *Journal of Metamorphic Geology 33*(1), 71–89.

Downes, H. (1993). The nature of the lower continental crust of Europe: petrological and geochemical evidence from xenoliths. *Physics of the Earth and Planetary Interiors 79*, 195–218.

Downes, H., Bodinier, J. L., Dupuy, C., Leyreloup, A. F., and Dostal, J. (1989). Isotope and trace-element heterogeneities in high-grade basic metamorphic rocks of Marvejols: Tectonic implications for the Hercynian suture zone of the French Massif Central. *Lithos 24*, 37–54.

Downes, H. and Duthou, J.-L. (1988). Isotopic and trace-element arguments for the lower-crustal origin of hercynien granitoids and pre-hercynian orthogneisses, Massif Central (France). *Chemical Geology 68*, 291–308.

Downes, H., Reichow, M. K., Mason, P. R. D., Beard, A. D., and Thirlwall, M. F. (2003). Mantle domains in the lithosphere beneath the French Massif Central: trace element and isotopic evidence from mantle clinopyroxenes. *Chemical Geology 200*(1-2), 71–87.

Drost, K., Gerdes, A., Jeffries, T., Linnemann, U., and Storey, C. (2011). Provenance of Neoproterozoic and early Paleozoic siliciclastic rocks of the Teplá-Barrandian unit (Bohemian Massif): Evidence from U–Pb detrital zircon ages. *Gondwana Research 19*(1), 213–231.

Dubuisson, G., Hirn, A., Girardeau, J., Mercier, J.-C. C., and Veinante, J.-L. (1988). Multiple Variscan nappes in Limousin, western Massif Central, France: geophysical constraints to the geological model and geodynamic implications. *Tectonophysics 147*, 19–31.

Dubuisson, G., Mercier, J.-C. C., Girardeau, J., and Frison, J.-Y. (1989). Evidence for a lost ocean in Variscan terranes of the western Massif Central, France. *Nature 337*, 729–732.

Ducrot, J., Lancelot, J., and Marchand, J. (1983). Datation U-Pb sur zircons de l'éclogite de la Borie (Haut-Allier, France) et conséquences sur l'évolution ante-hercynienne de l'Europe occidentale. *Earth and Planetary Science Letters 62*, 385–394.

Ducrot, J., Lancelot, J., and Reille, J.-L. (1979). Datation en Montagne Noire d'un témoin d'une phase majeure d'amincissement crustal caractéristique de l'Europe prévarisque. *Bulletin de la Société Géologique de France 21*(4), 501–505.

Dufour, E. (1982). *Pétrologie et géochimie des formations orthométamorphiques acides des Monts du Lyonnais (Massif central, France)*. PhD thesis.

Dufour, E. (1985). Granulite facies metamorphism and retrogressive evolution of the Monts du Lyonnais metabasites (Massif Central, France). *Lithos 18*, 97–113.

Dufour, E., Lardeaux, J. M., and Coffrant, D. (1985). Eclogites et granulites dans les Monts du Lyonnais : une évolution métamorphique plurifaciale éohercynienne. *Comptes Rendus de l'Académie des Sciences, Paris 300*(4), 141–144.

Duguet, M. and Faure, M. (2004). Successive shearing tectonics during the Hercynian collisional evolution of the southwestern French Massif Central. *Bulletin de la Société Géologique de France 175*(1), 49–59.

Duguet, M., Le Breton, N., and Faure, M. (2007). P–T paths reconstruction of a collisional event: The example of the Thiviers-Payzac Unit in the Variscan French Massif Central. *Lithos 98*(1-4), 210–232.

Dumas, S. (2003). *Le métamorphisme régional des Cévennes occidentales (Massif Central français) : une conséquence de la mise en place du dôme anatectique vellave*. M.Sc. thesis.

Dupraz, J. and Didier, J. (1988). Le complexe anatectique du Velay (Massif central français) : structure d'ensemble et évolution géologique. *Géologie de la France 4*, 73–88.

Dupret, L., Dissler, E., Doré, F., Gresselin, F., and Le Gall, J. (1990). Cadomian geodynamic evolution of the northeastern Armorican Massif (Normandy and Maine). In R. S. D'Lemos, R. A. Strachan, and C. G. Topley (Eds.), *The Cadomian orogeny*, Volume 51, pp. 115–131. Geological Society Special Publication.

Duthou, J.-L. (1977). *Chronologie Rb-Sr et géochimie des granitoïdes d'un segment de la chaîne Varisque, relations avec le métamorphisme : le Nord Limousin, Massif Central français*. PhD thesis.

Duthou, J.-L., Cantagrel, J.-M., Didier, J., and Vialette, Y. (1984). Palaeozoic granitoids from te French Massif Central: age and origin studied by ^{87}Rb–^{87}Sr system. *Physics of the Earth and Planetary*

Interiors 35, 131–144.

Duthou, J.-L., Chenevoy, M., and Gay, M. (1994). Rb-Sr middle Devonian age of cordierite bearing migmatites from Lyonnais area (French Massif Central). *Comptes Rendus de l'Académie des Sciences, Paris 319*, 791–796.

Duthou, J.-L., Piboule, M., Gay, M., and Dufour, E. (1981). Datations radiométriques Rb-Sr sur les orthogranulites des Monts du Lyonnais (Massif Central français). *Comptes Rendus de l'Académie des Sciences, Paris 292*, 749–752.

Egal, E., Guennoc, P., Le Goff, E., Thiéblemont, D., Lebret, P., and Hallégouet, B. (1996). The Cadomian orogeny revisited in northern Brittany. In *Avalonian and Related Peri-Gondwanan Terranes of the Circum-North Atlantic*, Volume 304, pp. 218–318. Geological Society of America, Special Publication.

Egal, E., Hallegouët, B., Le Goff, E., Schroetter, J.-M., Mougin, B., Cocherie, A., Langouët, L., Monnier, J.-L., Théveniaut, H., Thiéblemont, D., and Thomas, E. (2011). *Notice explicative, Carte géol. France (1/50 000), feuille Dinan (245)*. Orléans: BRGM.

Eglinger, A., Thébaud, N., Zeh, A., Davis, J., Miller, J., Parra-Avila, L. A., Loucks, R., McCuaig, C., and Belousova, E. (2017). New insights into the crustal growth of the Paleoproterozoic margin of the Archean Kéména-Man domain, West African craton (Guinea): Implications for gold mineral system. *Precambrian Research 292*, 258–289.

Eiler, J. M. (2001). Oxygen isotope variations of basaltic lavas and upper mantle rocks. In J. Valley and D. R. Cole (Eds.), *Stable isotope geochemistry*, Volume 43, pp. 319–364. Washington D.C.: Mineralogical Society of America.

Elmi, S., Brouder, P., Berger, G., Gras, H., Busnardo, R., Bérard, P., and Vautrelle, C. (1989). *Notice explicative, Carte géol. France (1/50 000), feuille Bessèges (888)*. Orléans: BRGM.

Elmi, S., Feys, R., Samama, J. C., and Weisbrod, A. (1974). *Notice explicative, Carte géol. France (1/50 000), feuille Largentière (864)*. Orléans: BRGM.

Ennih, N. and Liégeois, J.-P. (2008). The boundaries of the West African craton, with special reference to the basement of the Moroccan metacratonic Anti-Atlas belt. In N. Ennih and J.-P. Liégeois (Eds.), *The Boundaries of the West African Craton*, Volume 297, pp. 1–17. Geological Society, London, Special Publications.

Escuder Viruete, J., Díaz de Neira, A., Hernáiz Huerta, P. P., Monthel, J., Senz, J. G., Joubert, M., Lopera, E., Ullrich, T., Friedman, R., and Mortensen, J. (2006). Magmatic relationships and ages of Caribbean Island arc tholeiites, boninites and related felsic rocks, Dominican Republic. *Lithos 90*(3-4), 161–186.

Escuder Viruete, J., Indares, A., and Arenas, R. (2000). P-T paths derived from garnet growth zoning in an extensional setting: an example from the Tormes Gneiss Dome (Iberian massif, Spain). *Journal of Petrology 41*(10), 1489–1515.

Farina, F., Stevens, G., Gerdes, A., and Frei, D. (2014). Small-scale Hf isotopic variability in the Peninsula pluton (South Africa): the processes that control inheritance of source 176Hf/177Hf diversity in S-type granites. *Contributions to Mineralogy and Petrology 168*.

Faryad, S. W., Jedlicka, R., and Collett, S. (2013). Eclogite facies rocks of the Monotonous unit, clue to Variscan suture in the Moldanubian Zone (Bohemian Massif). *Lithos 179*, 353–363.

Faryad, S. W. and Kachlík, V. (2013). New evidence of blueschist facies rocks and their geotectonic implication for Variscan suture(s) in the Bohemian Massif. *Journal of Metamorphic Geology 31*(1), 63–82.

Faure, M. (1995). Late orogenic carboniferous extensions in the Variscan French Massif Central. *Tectonics 14*(1), 132–153.

Faure, M., Brouder, P., Thierry, J., Alabouvette, B., Cocherie, A., and Bouchot, V. (2009). *Notice explicative, Carte géol. France (1/50 000), feuille Saint-André-de-Valborgne (911)*. Orléans: BRGM.

Faure, M., Charonnat, X., and Chauvet, A. (1999). Schéma structural et évolution tectonique du domaine para-autochtone cévenol de la chaîne hercynienne (Massif central français). *Comptes Rendus de l'Académie des Sciences, Paris 328*, 401–407.

Faure, M., Charonnat, X., Chauvet, A., Chen, Y., Talbot, J. Y., Martelet, G., Courrioux, G., Monié, P., and Milési, J.-P. (2001). Tectonic evolution of the Cévennes para-autochtonous domain of the Hercynian French Massif Central and its bearing on ore deposits formation. *Bulletin de la Société Géologique de France 172*(6), 687–696.

Faure, M., Cocherie, A., Be Mezeme, E., Charles, N., and Rossi, P. (2010). Middle Carboniferous crustal melting in the Variscan Belt: New insights from U–Th–Pb_{tot} monazite and U–Pb zircon ages of the Montagne Noire Axial Zone (southern French Massif Central). *Gondwana Research 18*(4), 653–673.

Faure, M., Lardeaux, J.-M., and Ledru, P. (2009). A review of the pre-Permian geology of the Variscan French Massif Central. *Comptes Rendus Geoscience 341*(2-3), 202–213.

Faure, M., Leloix, C., and Roig, J.-Y. (1997). L'évolution polycyclique de la chaîne hercynienne. *Bulletin de la Société Géologique de France 168*(6), 695–705.

Faure, M., Li, X.-H., and Lin, W. (2017). The northwest-directed "Bretonian phase" in the French Variscan Belt (Massif Central and Massif Armoricain): A consequence of the Early Carboniferous Gondwana–Laurussia collision. *Comptes Rendus Geoscience 349*(3), 126–136.

Faure, M., Pons, J., and Babinault, J.-F. (1992). Le pluton du Pont-de-Montvert : un granite syntectonique extravasé vers l'Est pendant le désépaississement crustal varisque du Massif Central français.

Comptes Rendus de l'Académie des Sciences, Paris 315, 201–208.

Fernandez-Suarez, J., Gutiérrez Alonso, G., and Jeffries, T. E. (2002). The importance of along-margin terrane transport in northern Gondwana: insights from detrital zircon parentage in Neoproterozoic rocks from Iberia and Brittany. *Earth and Planetary Science Letters 204*(1-2), 75–88.

Fernández-Suárez, J., Gutiérrez-Alonso, G., Jenner, G. A., and Tubrett, M. N. (2000). New ideas on the Proterozoic-Early Palaeozoic evolution of NW Iberia: insights from U–Pb detrital zircon ages. *Precambrian Research 102*, 185–206.

Ferré, E. C. (2003). Magnetic susceptibility anisotropy: A new petrofabric tool in migmatites. *Journal of Geophysical Research 108*(B2).

Ferré, E. C., Martín-Hernández, F., Teyssier, C., and Jackson, M. (2004). Paramagnetic and ferromagnetic anisotropy of magnetic susceptibility in migmatites: measurements in high and low fields and kinematic implications. *Geophysical Journal International 157*(3), 1119–1129.

Feybesse, J.-L., Couturié, J.-P., Ledru, P., and Johan, V. (1995). Les granites de la Margeride, de Chambon-le-Château et de Saint-Christophe-d'Allier (Massif central) : des laccolites synchrones des derniers stades de l'épaississement varisque. *Géologie de la France 1*, 27–45.

Feybesse, J.-L., Lardeaux, J. M., Tegyey, M., Peterlongo, J.-M., Kerrien, Y., Lemière, B., Maurin, G., Mercier, F., and Thiéblemont, D. (1995). *Notice explicative, Carte géol. France (1/50 000), feuille Saint-Symphorien-sur-Coise (721)*. Orléans: BRGM.

Fischer, C. M., Hanchar, J. M., Samson, S. D., Dhuime, B., Blichert-Toft, J., Vervoort, J., and Lam, R. (2011). Synthetic zircon doped with hafnium and rare earth elements: A reference material for in situ hafnium isotope analysis. *Chemical Geology 286*, 32–47.

Fisher, C. M., Vervoort, J. D., and DuFrane, S. A. (2014). Accurate Hf isotope determinations of complex zircons using the "laser ablation split stream" method. *Geochemistry, Geophysics, Geosystems 15*(1), 121–139.

Féménias, O., Coussaert, N., Bingen, B., Whitehouse, M., Mercier, J.-C. C., and Demaiffe, D. (2003). A Permian underplating event in late- to post-orogenic tectonic setting. Evidence from the mafic–ultramafic layered xenoliths from Beaunit (French Massif Central). *Chemical Geology 199*(3-4), 293–315.

Forestier, F.-H. (1961). Métamorphisme hercynien et antéhercynien dans le bassin du haut-Allier (Massif Central français). *Bulletin du service de la carte géologique de France 271*(59).

Forestier, F.-H. (1969). Découverte de niveaux d'amphibolites à pargasite, anorthite, corindon et saphirine dans les schistes cristallins de la vallée du Haut-Allier. Existence du faciès granulite dans le Massif Central Français. *Contributions to Mineralogy and Petrology 23*, 194–235.

Fournier-Vinas, C. and Debat, P. (1970). Présence de micro-organismes dans les terrains métamorphiques précambriens (schistes X) de l'Ouest de la Montagne Noire. *Bulletin de la Société Géologique de France 7*(2), 351–355.

Franke, W. (1989). Variscan plate tectonics in Central Europe - current ideas and open questions. *Tectonophysics 169*, 221–228.

Franke, W. (2000). The mid-European segment of the Variscides: tectonostratigraphic units, terrane boundaries and plate tectonic evolution. *Geological Society, London, Special Publications 179*(1), 35–61.

François, T. (2009). *Contraintes géochimiques et géochronologiques sur l'origine et la mise en place des granites du Mont Lozère*. M.Sc. thesis.

Frei, D. and Gerdes, A. (2009). Precise and accurate in situ U–Pb dating of zircon with high sample throughput by automated LA-SF-ICP-MS. *Chemical Geology 261*(3-4), 261–270.

Fujimaki, H. (1986). Partition coefficients of Hf, Zr, and REE between zircon, apatite, and liquid. *Contributions to Mineralogy and Petrology 94*, 42–45.

Gaetani, G. A. and Grove, T. L. (1998). The influence of water on melting of mantle peridotite. *Contributions to Mineralogy and Petrology 131*, 323–346.

Gao, S., Luo, T.-C., Zhang, B.-R., Zhang, H.-F., Han, Y.-W., Zhao, Z.-D., and Hu, Y.-K. (1998). Chemical composition of the continental crust as revealed by studies in East China. *Geochimica et Cosmochimica Acta 62*(11), 1959–1975.

Gardien, V. (1990). Reliques de grenat et de staurotide dans la série métamorphique de basse pression du Mont Pilat (Massif Central français) : témonis d'une évolution tectonométamorphique polyphasée. *Comptes Rendus de l'Académie des Sciences, Paris 310*, 233–240.

Gardien, V. (1993). High to medium pressure relics in the eastern Vivarais series (Eastern part of the French Massif central). *Comptes Rendus de l'Académie des Sciences, Paris 316*, 1247–1254.

Gardien, V. and Lardeaux, J. M. (1991). Découverte d'éclogites dans la synforme de Maclas : extension de l'unité supérieure des gneiss à l'Est du Massif Central. *Comptes Rendus de l'Académie des Sciences, Paris 312*, 61–68.

Gardien, V., Lardeaux, J. M., and Misseri, M. (1988). Les péridotites des Monts du Lyonnais (M.C.F.) : témoins privilégiés d'une subduction de lithosphère paléozoïque. *Comptes Rendus de l'Académie des Sciences, Paris 307*, 1967–1972.

Gardien, V., Teygey, M., Lardeaux, J. M., Misseri, M., and Dufour, E. (1990). Crust-mantle relationships in the French Variscan chain: the example of the Southern Monts du Lyonnais unit (eastern French Massif Central). *Journal of Metamorphic Geology 8*, 477–492.

Gardiner, N. J., Kirkland, C. L., and Van Kranendonk, M. J. (2016). The juvenile hafnium isotope signal as a record of supercontinent cycles. *Sci Rep 6*, 38503.

Garfunkel, Z. (2015). The relations between Gondwana and the adjacent peripheral Cadomian domain—constrains on the origin, history, and paleogeography of the peripheral domain. *Gondwana Research 28*, 1257–1281.

Gasquet, D., Bertrand, J.-M., Paquette, J. L., Lehmann, J., Ratzov, G., De Ascenção Guedes, R., Tiepolo, M., Boullier, A. M., Scaillet, S., and Nomade, S. (2010). Miocene to Messinian deformation and hydrothermal activity in a pre-Alpine basement massif of the French western Alps: new U–Th–Pb and argon ages from the Lauzière massif. *Bulletin de la Société Géologique de France 181*(3), 227–241.

Gay, M., Peterlongo, J.-M., and Caen-Vachette, M. (1981). Age radiométrique des granites en massifs allongés et en feuillets minces, syntectoniques dans les Monts du Lyonais (Massif Central français). *Comptes Rendus de l'Académie des Sciences, Paris 293*, 993–996.

Gébelin, A., Roger, F., and Brunel, M. (2009). Syntectonic crustal melting and high-grade metamorphism in a transpressional regime, Variscan Massif Central, France. *Tectonophysics 477*(3-4), 229–243.

Gebauer, D., Bernard-Griffiths, J., and Grünenfelder, M. (1981). U-Pb zircon and monazite dating of a mafic-ultramafic complex and its country rocks. *Contributions to Mineralogy and Petrology 76*, 292–300.

Gehrels, G. E., Valencia, V. A., and Ruiz, J. (2008). Enhanced precision, accuracy, efficiency, and spatial resolution of U-Pb ages by laser ablation-multicollector-inductively coupled plasma-mass spectrometry. *Geochemistry, Geophysics, Geosystems 9*(3).

Gerdes, A. and Zeh, A. (2006). Combined U–Pb and Hf isotope LA-(MC-)ICP-MS analyses of detrital zircons: Comparison with SHRIMP and new constraints for the provenance and age of an Armorican metasediment in Central Germany. *Earth and Planetary Science Letters 249*(1-2), 47–61.

Gerdes, A. and Zeh, A. (2009). Zircon formation versus zircon alteration — New insights from combined U–Pb and Lu–Hf in-situ LA-ICP-MS analyses, and consequences for the interpretation of Archean zircon from the Central Zone of the Limpopo Belt. *Chemical Geology 261*(3-4), 230–243.

Girardeau, J. (1986). *Ophiolites et chaines de collision: exemples des chaines Himalaya-Tibet et Hercyniennes. Etude petro-structurale des ophiolites et de leurs encaissants: interpretations géodynamiques.* Habilitation thesis.

Giraud, A., Marchand, J., Dupuy, C., and Dostal, J. (1984). Geochemistry of leptyno-amphibolite complex from Haut-Allier (French Massif Central). *Lithos 17*, 203–214.

Glazner, A. F. (2007). Thermal limitations on incorporation of wall rock into magma. *Geology 35*(4), 319.

Gleizes, G., Leblanc, D., and Bouchez, J. L. (1997). Variscan granites of the Pyrenees revisited: their role as syntectonic markers of the orogen. *Terra Nova 9*(38-41).

Godard, G. (1990). Découverte d'éclogites, de péridotites à spinelle et d'amphibolites à anorthite, spinelle et corindon dans le Morvan. *Comptes Rendus de l'Académie des Sciences, Paris 310*, 227–232.

Goodge, J. W. and Vervoort, J. D. (2006). Origin of Mesoproterozoic A-type granites in Laurentia: Hf isotope evidence. *Earth and Planetary Science Letters 243*(3-4), 711–731.

Gougeon, R., Néraudeau, D., Dabard, M.-P., Pierson-Wickmann, A.-C., Polette, F., Poujol, M., and Saint-Martin, J.-P. (2017). Trace Fossils from the Brioverian (Ediacaran–Fortunian) in Brittany (NW France). *Ichnos*, 1–14.

Graviou, P. and Auvray, B. (1990). Late Precambrian M-type granitoid genesis in the Cadomian belt of NW France. In R. S. D'Lemos, R. A. Strachan, and C. G. Topley (Eds.), *The Cadomian orogeny*, Volume 51, pp. 231–244. Geological Society Special Publication.

Griffin, W. L., Pearson, N. J., Belousova, E., Jackson, S. E., Van Achterbergh, E., O'Reilly, S. Y., and Shee, S. R. (2000). The Hf isotope composition of cratonic mantle: LAM-MC-ICPMS analysis of zircon megacrysts in kimberlites. *Geochimica et Cosmochimica Acta 64*(1), 133–147.

Griffin, W. L., Wang, X., Jackson, S. E., Pearson, N. J., O'Reilly, S. Y., Xu, X.-S., and Zhou, X. (2002). Zircon chemistry and magma mixing, SE China: In-situ analysis of Hf isotopes, Tonglu and Pingtan igneous complexes. *Lithos 61*, 237–269.

Grohmann, C. H. and Campanha, G. A. C. (2010). OpenStereo: open source, cross-platform software for structural geology analysis. *AGU 2010 Fall Meeting*.

Grove, T. L., Elkins-Tanton, L. T., Parman, S. W., Chatterjee, N., Muntener, O., and Gaetani, G. A. (2003). Fractional crystallization and mantle-melting controls on calc-alkaline differentiation trends. *Contributions to Mineralogy and Petrology 145*(5), 515–533.

Guerrot, C. and Peucat, J. J. (1990). U-Pb geochronology of the Upper Proterozoic Cadomian orogeny in the northern Armorican Massif, France. In R. S. D'Lemos, R. A. Strachan, and C. G. Topley (Eds.), *The Cadomian Orogeny*, Volume 51, pp. 13–26. Geological Society Special Publication.

Guillet, P. and Bouchez, J. L. (1983). Anisotropy of magnetic susceptibility and magmatic structures in the Guérande granite massif (France). *Tectonics 2*(5), 419–429.

Guillot, S., de Sigoyer, J., Lardeaux, J. M., and Mascle, G. (1997). Eclogitic metasediments from the Tso Morari area (Ladakh, Himalaya): evidence for continental subduction during India-Asia convergence. *Contributions to Mineralogy and Petrology 128*, 197–212.

Guillot, S. and Ménot, R.-P. (2009). Paleozoic evolution of the External Crystalline Massifs of the Western Alps. *Comptes Rendus Geoscience 341*(2-3), 253–265.

Guo, Z., Wilson, M., Zhang, L., Zhang, M., Cheng, Z., and Liu, J. (2014). The role of subduction channel mélanges and convergent subduction systems in the petrogenesis of post-collisional K-rich mafic magmatism in NW Tibet. *Lithos 198-199*, 184–201.

Guérangé-Lozes, J. and Burg, J.-P. (1990). Variscan nappes in the southwest of the Massif Central (1 : 250 000 geological and structural maps of Montpellier and Aurillac). *Géologie de la France 3-4*, 71–106.

Guérangé-Lozes, J. and Pellet, J. (1990). *Notice explicative, Carte géol. France (1/50 000), feuille Génolhac (887)*. Orléans: BRGM.

Gèze, B., Couturié, J.-P., and Briand, B. (1979). *Carte géol. France (1/50 000), feuille Mende (862)*. Orléans: BRGM.

Gèze, B., Pellet, J., and Paloc, H. (1980). *Carte géol. France (1/50 000), feuille Florac (886)*. Orléans: BRGM.

Hajná, J., Žák, J., and Dörr, W. (2017). Time scales and mechanisms of growth of active margins of Gondwana: A model based on detrital zircon ages from the Neoproterozoic to Cambrian Blovice accretionary complex, Bohemian Massif. *Gondwana Research 42*, 63–83.

Harris, N., Vance, D., and Ayres, M. (2000). From sediment to granite: timescales of anatexis in the upper crust. *Chemical Geology 162*, 155–167.

Harvey, J., Gannoun, A., Burton, K. W., Schiano, P., Rogers, N. W., and Alard, O. (2010). Unravelling the effects of melt depletion and secondary infiltration on mantle Re–Os isotopes beneath the French Massif Central. *Geochimica et Cosmochimica Acta 74*(1), 293–320.

Hawkesworth, C., Cawood, P., Kemp, T., Storey, C., and Dhuime, B. (2009). A matter of preservation. *Science 323*(5910), 49–50.

Hawkesworth, C. J., Dhuime, B., Pietranik, A. B., Cawood, P. A., Kemp, A. I. S., and Storey, C. D. (2010). The generation and evolution of the continental crust. *Journal of the Geological Society 167*(2), 229–248.

Hawkesworth, C. J. and Kemp, A. I. (2006). Evolution of the continental crust. *Nature 443*(7113), 811–7.

Hawkesworth, C. J. and Kemp, A. I. S. (2006a). The differentiation and rates of generation of the continental crust. *Chemical Geology 226*(3-4), 134–143.

Hawkesworth, C. J. and Kemp, A. I. S. (2006b). Using hafnium and oxygen isotopes in zircons to unravel the record of crustal evolution. *Chemical Geology 226*(3-4), 144–162.

Hellstrom, J. C., Paton, C., Woodhead, J. D., and Hergt, J. M. (2008). Iolite: Software for spatially resolved LA-(quad and MC) ICP-MS analysis. In P. J. Sylvester (Ed.), *Laser ablation ICP-MS in the Earth sciences: Current practices and outstanding issues*, pp. 343–348. Mineralogical Association of Canada.

Henderson, B. J., Collins, W. J., Murphy, J. B., Gutierrez-Alonso, G., and Hand, M. (2016). Gondwanan basement terranes of the Variscan–Appalachian orogen: Baltican, Saharan and West African hafnium isotopic fingerprints in Avalonia, Iberia and the Armorican Terranes. *Tectonophysics 681*, 278–304.

Hermann, J. and Rubatto, D. (2009). Accessory phase control on the trace element signature of sediment melts in subduction zones. *Chemical Geology 265*(3-4), 512–526.

Herron, M. M. (1988). Geochemical classification of terrigenous sands and shales from core and log data. *Journal of Sedimentary Petrology 58*(5), 820–829.

Hext, G. (1963). The estimation of second-order tensors, with related tests and designs. *Biometrika 50*, 353.

Hidalgo, S., Gerbe, M. C., Martin, H., Samaniego, P., and Bourdon, E. (2012). Role of crustal and slab components in the Northern Volcanic Zone of the Andes (Ecuador) constrained by Sr–Nd–O isotopes. *Lithos 132-133*, 180–192.

Hirata, T. and Nesbitt, R. W. (1995). U-Pb isotope geochronology of zircon: Evaluation of the laser probe-inductively coupled plasma mass spectrometry technique. *Geochimica et Cosmochimica Acta 59*(12), 2491–2500.

Hirose, K. (1997). Melting experiments on lherzolite KLB-1 under hydrous conditions and generation of high-magnesian andesitic melts. *Geology 25*(1), 42–44.

Hirose, K. and Kawamoto, T. (1995). Hydrous partial melting of lherzolite at 1 GPa: the effect of H_2O on the genesis of basaltic magmas. *Earth and Planetary Science Letters 133*, 463–473.

Hirschmann, M. M., Tenner, T., Aubaud, C., and Withers, A. C. (2009). Dehydration melting of nominally anhydrous mantle: The primacy of partitioning. *Physics of the Earth and Planetary Interiors 176*(1-2), 54–68.

Hofmann, A. W. (1997). Mantle geochemistry: the message from oceanic volcanism. *Nature 385*, 219–229.

Holbrook, W. S., Mooney, W. D., and Christensen, N. I. (1992). The seismic velocity structure of the deep continental crust. In D. M. Fountain, R. Arculus, and R. W. Kay (Eds.), *Continental Lower Crust*, pp. 1–44. Amsterdam: Elsevier.

Holland, T. J. B. and Powell, R. (1998). An internally consistent thermodynamic data set for phases of petrological interest. *Journal of Metamorphic Geology 16*, 309–343.

Holtz, F. and Johannes, W. (1991). Genesis of peraluminous granites I. Experimental investigation of melt compositions at 3 and 5 kb and various H_2O activities. *Journal of Petrology 32*(5), 935–958.

Horstwood, M. S. A., Foster, G. L., Parrish, R. R., Noble, S. R., and Nowell, G. M. (2003). Common-Pb corrected in situ U-Pb accessory mineral geochronology by LA-MC-ICP-MS. *Journal of Analytical Atomic Spectrometry 18*(8), 837–846.

Horstwood, M. S. A., Košler, J., Gehrels, G., Jackson, S. E., McLean, N. M., Paton, C., Pearson, N. J., Sircombe, K., Sylvester, P., Vermeesch, P., Bowring, J. F., Condon, D. J., and Schoene, B. (2016). Community-Derived Standards for LA-ICP-MS U-(Th-)Pb Geochronology - Uncertainty Propagation, Age Interpretation and Data Reporting. *Geostandards and Geoanalytical Research 40*(3), 311–332.

Hoskin, P. W. O. and Black, L. P. (2000). Metamorphic zircon formation by solid-state recrystallization of protolith igneous zircon. *Journal of Metamorphic Geology 18*, 423–439.

Hoskin, P. W. O., Kinny, P. D., Wyborn, D., and Chappell, B. W. (2000). Identifying accessory mineral saturation during differentiation in granitoid magmas: an integrated approach. *Journal of Petrology 41*(9), 1365–1396.

Hurai, V., Paquette, J. L., Huraiová, M., and Konečný, P. (2010). U–Th–Pb geochronology of zircon and monazite from syenite and pincinite xenoliths in Pliocene alkali basalts of the intra-Carpathian back-arc basin. *Journal of Volcanology and Geothermal Research 198*(3-4), 275–287.

Hurley, P. M. and Rand, J. R. (1969). Pre-drift continental nuclei. *Science 164*, 1229–1242.

Hutchison, R., Chambers, A. L., Paul, D. K., and Harris, P. G. (1975). Chemical variation among French ultramafic xenoliths – evidence for a heterogeneous upper mantle. *Mineralogical Magazine 40*, 153–170.

Iizuka, T., Horie, K., Komiya, T., Maruyama, S., Hirata, T., Hidaka, H., and Windley, B. F. (2006). 4.2 Ga zircon xenocryst in an Acasta gneiss from northwestern Canada: Evidence for early continental crust. *Geology 34*(4), 245.

Iizuka, T., Komiya, T., Rino, S., Maruyama, S., and Hirata, T. (2010). Detrital zircon evidence for Hf isotopic evolution of granitoid crust and continental growth. *Geochimica et Cosmochimica Acta 74*(8), 2450–2472.

Inglis, J. D., Samson, S. D., D'Lemos, R. S., and Hamilton, M. (2004). U–Pb geochronological constraints on the tectonothermal evolution of the Paleoproterozoic basement of Cadomia, La Hague, NW France. *Precambrian Research 134*(3-4), 293–315.

Innocent, C. (1993). *Contribution des isotopes à longue période à la connaissance de l'altération de la croûte continentale*. PhD thesis.

Innocent, C., Michard, A., Guerrot, C., and Hamelin, B. (2003). Datation U-Pb sur zircons à 548 Ma de leptynites des Maures centrales. Signification géodynamique des complexes leptyno-amphibolitiques de l'Europe varisque. *Bulletin de la Société Géologique de France 174*(6), 585–594.

Ishihara, S. (1977). The magnetite-series and ilmenite-series granitic rocks. *Mining Geology 27*, 293–305.

Isnard, H. (1996). *Datation par la méthode U–Pb sur monazites des granites du Mont Lozère et de l'Est de la Margeride (laccolites de Chambon-le- Château et de St-Christophe d'Allier): contribution à l'histoire post-tectonique du Massif Central Français*. M.Sc. thesis.

Jackson, S. E., Pearson, N. J., Griffin, W. L., and Belousova, E. A. (2004). The application of laser ablation-inductively coupled plasma-mass spectrometry to in situ U–Pb zircon geochronology. *Chemical Geology 211*(1-2), 47–69.

Jaffey, A. H., Flynn, K. F., Glendenin, L. E., Bentley, W. C., and Essling, A. M. (1971, Nov). Precision measurement of half-lives and specific activities of ^{235}U and ^{238}U. *Phys. Rev. C. 4*, 1889–1906.

Janoušek, V., Braithwaite, C. J. R., Bowes, D. R., and Gerdes, A. (2004). Magma-mixing in the genesis of Hercynian calc-alkaline granitoids: an integrated petrographic and geochemical study of the Sázava intrusion, Central Bohemian Pluton, Czech Republic. *Lithos 78*(1-2), 67–99.

Janoušek, V. and Holub, F. V. (2007). The causal link between HP-HT metamorphism ad ultrapotassic magmatism in collisional orogens: case study from the Moldanubian Zone of the Bohemian Massif. *Proceedings of the Geologists' Association 118*, 75–86.

Javier Álvaro, J., Colmenar, J., Monceret, E., Pouclet, A., and Vizcaïno, D. (2016). Late Ordovician (post-Sardic) rifting branches in the North Gondwanan Montagne Noire and Mouthoumet massifs of southern France. *Tectonophysics 681*, 111–123.

Jelínek, V. (1978). Statistical processing of anisotropy of magnetic susceptibility measured on groups of specimen. *Studia Geophysica et Geodaetica 22*, 50–62.

Jelínek, V. (1981). Characterization of the magnetic fabric of rocks. *Tectonophysics 79*, T63–T67.

Jégouzo, P., Peucat, J. J., and Audren, C. (1986). Caractérisation et signification géodynamique des orthogneiss calco-alcalins d'âge ordovicien de Bretagne méridionale. *Bulletin de la Société Géologique de France 2*(5), 839–848.

Johannes, W. and Holtz, F. (1996). *Petrogenesis and experimental petrology of granitic rocks*. Berlin Heidelberg New York: Springer.

Kay, R. W. and Mahlburg-Kay, S. (1991). Creation and destruction of the lower continental crust. *Geologische Rundschau 80*(2), 259–278.

Kelemen, P. B., Hanghoj, K., and Greene, A. R. (2003). One view of the geochemistry of subduction-related magmatic arcs, withan emphasis on primitive andesite and lower crust. In R. L. Rudnick (Ed.), *Treatise on Goechemistry*, Volume 3, pp. 593–659. Elsevier.

Kelsey, D. E., Clark, C., and Hand, M. (2008). Thermobarometric modelling of zircon and monazite growth in melt-bearing systems: examples using model metapelitic and metapsammitic granulites.

Journal of Metamorphic Geology 26(2), 199–212.
Kemp, A. I., Hawkesworth, C. J., Foster, G. L., Paterson, B. A., Woodhead, J. D., Hergt, J. M., Gray, C. M., and Whitehouse, M. J. (2007). Magmatic and crustal differentiation history of granitic rocks from Hf-O isotopes in zircon. *Science 315*(5814), 980–3.
Kemp, A. I., Hawkesworth, C. J., Paterson, B. A., and Kinny, P. D. (2006). Episodic growth of the Gondwana supercontinent from hafnium and oxygen isotopes in zircon. *Nature 439*(7076), 580–3.
Kemp, A. I. S., Foster, G. L., Scherstén, A., Whitehouse, M. J., Darling, J., and Storey, C. (2009). Concurrent Pb–Hf isotope analysis of zircon by laser ablation multi-collector ICP-MS, with implications for the crustal evolution of Greenland and the Himalayas. *Chemical Geology 261*(3-4), 244–260.
Kemp, A. I. S., Hawkesworth, C. J., Collins, W. J., Gray, C. M., Blevin, P. L., and EIMF (2009). Isotopic evidence for rapid continental growth in an extensional accretionary orogen: The Tasmanides, eastern Australia. *Earth and Planetary Science Letters 284*, 455–466.
Kemp, A. I. S., Hickman, A. H., Kirkland, C. L., and Vervoort, J. D. (2015). Hf isotopes in detrital and inherited zircons of the Pilbara Craton provide no evidence for Hadean continents. *Precambrian Research 261*, 112–126.
Kemp, A. I. S., Wormald, R. J., Whitehouse, M. J., and Price, R. C. (2005). Hf isotopes in zircon reveal contrasting sources and crystallization histories for alkaline to peralkaline granites of Temora, southeastern Australia. *Geology 33*(10), 797.
King, E. M., Valley, J. W., Davis, D. W., and Edwards, G. R. (1998). Oxygen isotope ratios of Archean plutonic zircons from granite–greenstone belts of the Superior Province: indicator of magmatic source. *Precambrian Research 92*, 365–387.
Kirkland, C. L., Smithies, R. H., Woodhouse, A. J., Howard, H. M., Wingate, M. T. D., Belousova, E. A., Cliff, J. B., Murphy, R. C., and Spaggiari, C. V. (2013). Constraints and deception in the isotopic record; the crustal evolution of the west Musgrave Province, central Australia. *Gondwana Research 23*(2), 759–781.
Klötzli, U. S., Sinigoi, S., Quick, J. E., Demarchi, G., Tassinari, C. C. G., Sato, K., and Günes, Z. (2014). Duration of igneous activity in the Sesia Magmatic System and implications for high-temperature metamorphism in the Ivrea–Verbano deep crust. *Lithos 206-207*, 19–33.
Kohn, M. J. and Vervoort, J. D. (2008). U-Th-Pb dating of monazite by single-collector ICP-MS: Pitfalls and potential. *Geochemistry, Geophysics, Geosystems 9*(4).
Kolodner, K., Avigad, D., McWilliams, M., Wooden, J. L., Weissbrod, T., and Feinstein, S. (2006). Provenance of north Gondwana Cambrian–Ordovician sandstone: U–Pb SHRIMP dating of detrital zircons from Israel and Jordan. *Geological Magazine 143*(03), 367.
Kramers, J. D., Kreissig, K., and Jones, M. Q. W. (2001). Crustal heat production and style of metamorphism: a comparison between two Archean high grade provinces in the Limpopo Belt, southern Africa. *Precambrian Research 112*, 149–163.
Kroner, U. and Romer, R. L. (2013). Two plates — Many subduction zones: The Variscan orogeny reconsidered. *Gondwana Research 24*(1), 298–329.
Kruckenberg, S. C., Ferré, E. C., Teyssier, C., Vanderhaeghe, O., Whitney, D. L., Seaton, N. C. A., and Skord, J. A. (2010). Viscoplastic flow in migmatites deduced from fabric anisotropy: An example from the Naxos dome, Greece. *Journal of Geophysical Research 115*(B9).
Kruckenberg, S. C., Vanderhaeghe, O., Ferré, E. C., Teyssier, C., and Whitney, D. L. (2011). Flow of partially molten crust and the internal dynamics of a migmatite dome, Naxos, Greece. *Tectonics 30*(3).
Küster, D., Liégeois, J.-P., Matukov, D., Sergeev, S., and Lucassen, F. (2008). Zircon geochronology and Sr, Nd, Pb isotope geochemistry of granitoids from Bayuda Desert and Sabaloka (Sudan): Evidence for a Bayudian event (920–900 Ma) preceding the Pan-African orogenic cycle (860–590 Ma) at the eastern boundary of the Saharan Metacraton. *Precambrian Research 164*(1-2), 16–39.
Laboue, M. (1982). *Etude structurale du massif de la Margeride*. PhD thesis.
Lacassin, R. and Van Den Driessche, J. (1982). Analyse de la déformation hercynienne majeure des gneiss de la Cézarenque (Cévennes, Massif-Central). *Comptes Rendus de l'Académie des Sciences, Paris 295*, 1027–1030.
Lafon, J. M. (1984). La granodiorite de Caplongue, nouveau témoin d'un magmatisme cambrien dans le Rouergue oriental. *Comptes Rendus de l'Académie des Sciences, Paris 298*(14), 595–600.
Lafon, J. M. (1986). *Géochronologie U–Pb appliquée à deux segments du Massif Central français. Le Rouergue oriental et le Limousin central*. PhD thesis.
Lafon, J. M. and Respaut, J.-P. (1988). Géochronologie U-Pb et leucogranites varisques : cas des massifs de Grandrieu (Lozère) et de la Porcherie (Limousin), Massif Central français. *Bull. Minéral. 111*, 225–237.
Lagarde, J.-L. and Dallain, C. (1994). Strain patterns within the late Variscan granitic dome of Velay, French Massif Central. *Journal of Structural Geology 16*(6), 839–852.
Lagarde, J.-L., Dallain, C., and Capdevila, R. (1990). Contexte tetonique de la fusion crustale post-collision dans la chaîne hercynienne : l'exemple du complexe anatectique du Velay (Massif central français). *Comptes Rendus de l'Académie des Sciences, Paris 311*, 477–484.
Lancaster, P. J., Storey, C. D., Hawkesworth, C. J., and Dhuime, B. (2011). Understanding the roles of crustal growth and preservation in the detrital zircon record. *Earth and Planetary Science Letters 305*(3-4), 405–412.

Lapadu-Hargues, P. (1947). Les massifs de la Margeride et du mont Lozère et leurs bordures. *Bull. Serv. Carte géol Fr. 46*(222), 420–432.

Lapierre, H., Basile, C., Berly, T., and Canard, E. (2008). Potassic late orogenic Stephanian volcanism in the Southwest French Massif central (Decazeville, Figeac, Lacapelle-Marival basins): an example for mantle metasomatism along strike-slip faults? *Bulletin de la Société Géologique de France 179*(5), 491–502.

Lardeaux, J. M., Ledru, P., Daniel, I., and Duchene, S. (2001). The Variscan French Massif Central – a new addition ot the ultra-high pressure metamorphic "club": exhumation porcesses and geodynamic consequences. *Tectonophysics 332*, 143–167.

Lardeaux, J. M., Reynard, B., and Dufour, E. (1989). Granulites à kornérupine et décompression post-orogénique des Monts du Lyonnais (M.C.F.). *Comptes Rendus de l'Académie des Sciences, Paris 308*, 1443–1449.

Lardeaux, J. M., Schulmann, K., Faure, M., Janousek, V., Lexa, O., Skrzypek, E., Edel, J. B., and Stipska, P. (2014). The Moldanubian Zone in the French Massif Central, Vosges/Schwarzwald and Bohemian Massif revisited: differences and similarities. *Geological Society, London, Special Publications 405*(1), 7–44.

Lasnier, B. (1968). Découverte de roches éclogitiques dans le groupe leptyno-amphibolique des monts du Lyonnais (Massif central français). *Bulletin de la Société Géologique de France 7*(10), 179–185.

Laumonier, B., Marignac, C., Cheilletz, A., and Macaudière, J. (1991). Relations entre tectoniques superposées, migmatisations et mise en place des granites sur l'exemple de la bordure sud du dôme du Velay (région de Laviolle, Ardèche, France). *Comptes Rendus de l'Académie des Sciences, Paris 313*, 937–944.

Laumonier, M., Scaillet, B., Arbaret, L., and Champallier, R. (2014b). Experimental simulation of magma mixing at high pressure. *Lithos 196-197*, 281–300.

Laumonier, M., Scaillet, B., Pichavant, M., Champallier, R., Andujar, J., and Arbaret, L. (2014a). On the conditions of magma mixing and its bearing on andesite production in the crust. *Nature 5*, 5607.

Laurent, O. (2012). *Les changements géodynamiques à la transition Archéen-Protérozoïque : étude des granitoïdes de la marge Nord du craton du Kaapvaal (Afrique du Sud)*. PhD thesis.

Laurent, O., Couzinié, S., Zeh, A., Vanderhaeghe, O., Moyen, J.-F., Villaros, A., Gardien, V., and Chelle-Michou, C. (2017). Protracted, coeval crust and mantle melting during Variscan late-orogenic evolution: U–Pb dating in the eastern French Massif Central. *International Journal of Earth Sciences 106*(2), 421–451.

Laurent, O., Doucelance, R., Martin, H., and Moyen, J.-F. (2013). Differentiation of the late-Archaean sanukitoid series and some implications for crustal growth: Insights from geochemical modelling on the Bulai pluton, Central Limpopo Belt, South Africa. *Precambrian Research 227*, 186–203.

Laurent, O., Martin, H., Moyen, J. F., and Doucelance, R. (2014). The diversity and evolution of late-Archean granitoids: Evidence for the onset of "modern-style" plate tectonics between 3.0 and 2.5 Ga. *Lithos 205*, 208–235.

Laurent, O. and Zeh, A. (2015). A linear Hf isotope-age array despite different granitoid sources and complex Archean geodynamics: Example from the Pietersburg block (South Africa). *Earth and Planetary Science Letters 430*, 326–338.

Leake, B. E., Wooley, A. R., Arps, C. E. S., Birch, W. D., Gilbert, M. C., Grice, J. D., Hawthorne, F. C., Kato, A., Kisch, H. J., Krivovichev, V. G., Linthout, K., Laird, J., Mandarino, J. A., Maresch, W. V., Nickel, E. H., Rock, N. M. S., Schumacher, J. C., Smith, D. C., Stephenson, N. C. N., Ungaretti, L., Whittaker, E. J., and Youzhi, G. (1997). Nomenclature of amphiboles: report of the subcommitee on amphiboles of the International Mineralogical Association, Commission on new minerals and mineral names. *The Canadian Mineralogist 35*, 219–246.

Ledru, P., Courrioux, G., Dallain, C., Lardeaux, J. M., Montel, J. M., Vanderhaeghe, O., and Vitel, G. (2001). The Velay dome (French Massif Central): melt generation and granite emplacement during orogenic evolution. *Tectonophysics 342*, 207–237.

Ledru, P., Lardeaux, J. M., Santallier, D., Autran, A., Quenardel, J.-M., Floc'h, J.-P., Lerouge, G., Maillet, N., Marchand, J., and Ploquin, A. (1989). Where are the nappes in the French Massif central? *Bulletin de la Société Géologique de France 8*(5), 605–618.

Ledru, P., Vitel, G., Marchand, J., Maurin, G., Mercier, F., Turland, M., Etlicher, B., Dautria, J. M., and Liotard, J. (1994). *Notice explicative, Carte géol. France (1/50 000), feuille Craponne-sur-Arzon (767)*. Orléans: BRGM.

Legendre, C., Briand, B., Thierry, J., Lebret, P., Joly, A., and Bertin, C. (2009). *Notice explicative, Carte géol. France (1/50 000), feuille Saint-Geniez-d'Olt (861)*. Orléans: BRGM.

Leloix, C., Faure, M., and Feybesse, J.-L. (1999). Hercynian polyphase tectonics in the northeast French Massif Central: the closure of the Brévenne Devonian–Dinantian rift. *International Journal of Earth Sciences 88*, 409–421.

Lenoir, X., Garrido, C. J., Bodinier, J. L., and Dautria, J. M. (2000). Contrasting lithospheric mantle domains beneath the Massif Central (France) revealed by geochemistry of peridotite xenoliths. *Earth and Planetary Science Letters 181*, 359–375.

Lescuyer, J.-L. and Cocherie, A. (1992). Single-zircon dating of the Sériès meta-dacites: evidence for a Late Proterozoic age of the "X Schists" from Montagne Noire (Southern French Massif Central).

Comptes Rendus de l'Académie des Sciences, Paris 314, 1071–1077.

Lescuyer, J.-L. and Giot, D. (1986). *Action concertée : les minéralisations Pb–Zn de Montagne Noire et leurs relations avec leux encaissant cambrien carbonaté sur quelques exemples du versant nord (La Rabasse, Brusque, Les Comtes) et du versant sud (Bibaud, Tête Rousse)*. Rapp. BRGM. 86 SGN 166 GEO.

Liew, T. C. and Hofmann, A. W. (1988). Precambrian crustal components, plutonic associations, plate environment of the Hercynian Fold Belt of central Europe: Indications from a Nd and Sr isotopic study. *Contributions to Mineralogy and Petrology 98*, 129–138.

Lin, W., Faure, M., Li, X.-h., Chu, Y., Ji, W., and Xue, Z. (2016). Detrital zircon age distribution from Devonian and Carboniferous sandstone in the Southern Variscan Fold-and-Thrust belt (Montagne Noire, French Massif Central), and their bearings on the Variscan belt evolution. *Tectonophysics 677-678*, 1–33.

Linnemann, U., Gehmlich, M., Tichomirowa, M., Buschmann, B., Nasdala, L., Jonas, P., Lützner, H., and Bombach, K. (2000). From Cadomian subduction to Early Palaeozoic rifting: The evolution of Saxo-Thuringia at the margin of Gondwana in the light of single zircon geochronology and basin development (Central European Variscides, Germany). In W. Franke, V. Haak, O. Oncken, and D. Tanner (Eds.), *Orogenic Processes: Quantification and Modelling in the Variscan Belt*, Volume 179, pp. 131–153. London, Geological Society, Special Publications.

Linnemann, U., Gerdes, A., Hofmann, M., and Marko, L. (2014). The Cadomian Orogen: Neoproterozoic to Early Cambrian crustal growth and orogenic zoning along the periphery of the West African Craton—Constraints from U–Pb zircon ages and Hf isotopes (Schwarzburg Antiform, Germany). *Precambrian Research 244*, 236–278.

Linnemann, U., Herbosch, A., Liégeois, J.-P., Pin, C., Gärtner, A., and Hofmann, M. (2012). The Cambrian to Devonian odyssey of the Brabant Massif within Avalonia: A review with new zircon ages, geochemistry, Sm–Nd isotopes, stratigraphy and palaeogeography. *Earth-Science Reviews 112*(3-4), 126–154.

Linnemann, U., McNaughton, N. J., Romer, R. L., Gehmlich, M., Drost, K., and Tonk, C. (2004). West African provenance for Saxo-Thuringia (Bohemian Massif): Did Armorica ever leave pre-Pangean Gondwana? U/Pb-SHRIMP zircon evidence and the Nd-isotopic record. *International Journal of Earth Sciences 93*(5), 683–705.

Linnemann, U., Ouzegane, K., Drareni, A., Hofmann, M., Becker, S., Gärtner, A., and Sagawe, A. (2011). Sands of West Gondwana: An archive of secular magmatism and plate interactions — A case study from the Cambro-Ordovician section of the Tassili Ouan Ahaggar (Algerian Sahara) using U–Pb–LA-ICP-MS detrital zircon ages. *Lithos 123*(1-4), 188–203.

Linnemann, U., Pereira, F., Jeffries, T. E., Drost, K., and Gerdes, A. (2008). The Cadomian Orogeny and the opening of the Rheic Ocean: The diacrony of geotectonic processes constrained by LA-ICP-MS U–Pb zircon dating (Ossa-Morena and Saxo-Thuringian Zones, Iberian and Bohemian Massifs). *Tectonophysics 461*(1-4), 21–43.

Lochon, P. (1985). *Les métaleucogranites du Haut Vivarais et leur environnement : évolution et implications géodynamiques*. PhD thesis.

Lotout, C., Pitra, P., Poujol, M., and Van Den Driessche, J. (2017). Ordovician magmatism in the Lévézou massif (French Massif Central): tectonic and geodynamic implications. *International Journal of Earth Sciences 106*(2), 501–515.

Lépine, J., Ben Ayad, M. A., and Béziat, D. (1988). Evidence for early Cambrian alkaline metabasites from the gold-bearing district of Salsigne (Montagne Noire, South Massif Central, France). *Comptes Rendus de l'Académie des Sciences, Paris 306*, 1087–1092.

Ludwig, K. R. (2008). *A Geochronological Toolkit for Microsoft Excel*, Volume 4 of *Berkeley Geochronology Central Special Publication*.

Lustrino, M. (2005). How the delamination and detachment of lower crust can influence basaltic magmatism. *Earth-Science Reviews 72*(1-2), 21–38.

Álvaro, J. J., Bauluz, B., Clausen, S., Devaere, L., Gil Imaz, A., Monceret, E., and Vizcaïno, D. (2014). Stratigraphic review of the Cambrian-Lower Ordovician volcanosedimentary complexes from the northern Montagne Noire. *Stratigraphy 11*(1), 83–96.

Álvaro, J. J., Courjault-Radé, P., Chauvel, J. J., Dabard, M. P., Debrenne, F., Feist, R., Pillola, G. L., Vennin, E., and Vizcaïno, D. (1998). Nouveau découpage stratigraphique des séries cambriennes des nappes de Pardailhan et du Minervois (versant sud de la Montagne Noire, France). *Géologie de la France 2*, 3–12.

Álvaro, J. J., Gonzalez-Gomez, C., and Vizcaïno, D. (2003). Paleogeographic patterns of the Cambrian–Ordovician transition in the southern Montagne Noire (France): preliminary results. *Bulletin de la Société Géologique de France 174*(3), 217–225.

Lévêque, M.-H. (1985). Mise en évidence d'un témoin d'un socle précambrien dans le Massif Central français : l'orthogneiss des Palanges (Aveyron). *Comptes Rendus de l'Académie des Sciences, Paris 300*(7), 277–282.

Macaudière, J., Barbey, P., Jabbori, J., and Marignac, C. (1992). Le stade initial de fusion dans le développement des dômes anatectiques : le dôme du Velay (Massif Central français). *Comptes Rendus de l'Académie des Sciences, Paris 315*, 1761–1767.

Macaudière, J., Marignac, C., and Weisbrod, A. (1987). Grandes nappes synschisteuses collisionnelles dans la catazone hercynienne des Cévennes médianes (Massif Central, France). *Comptes Rendus de l'Académie des Sciences, Paris 304*(19), 1195–1199.

Maierová, P., Schulmann, K., Lexa, O., Guillot, S., Štípská, P., Janoušek, V., and Čadek, O. (2016). European Variscan orogenic evolution as an analogue of Tibetan-Himalayan orogen: Insights from petrology and numerical modeling. *Tectonics 35*(7), 1760–1780.

Malavielle, J., Guihot, P., Costa, S., Lardeaux, J. M., and Gardien, V. (1990). Collapse of the thickened Variscan crust in the French Massif Central: Mont Pilat extensional shear zone and St. Etienne Late Carboniferous basin. *Tectonophysics 177*, 139–149.

Mallik, A., Nelson, J., and Dasgupta, R. (2015). Partial melting of fertile peridotite fluxed by hydrous rhyolitic melt at 2–3 GPa: implications for mantle wedge hybridization by sediment melt and generation of ultrapotassic magmas in convergent margins. *Contributions to Mineralogy and Petrology 169*(5), 1–24.

Maluski, H. and Monié, P. (1988). ^{40}Ar-^{39}Ar laser probe multi-dating inside signle biotites of a Variscan orthogneiss (Pinet, Massif Central, France). *Chemical Geology 73*, 245–263.

Marchesi, C., Garrido, C. J., Godard, M., Belley, F., and Ferré, E. (2009). Migration and accumulation of ultra-depleted subduction-related melts in the Massif du Sud ophiolite (New Caledonia). *Chemical Geology 266*(3-4), 171–186.

Marignac, C., Leroy, J., Macaudière, J., Pichavant, M., and Weisbrod, A. (1980). Evolution tectonométamorphique d'un segment de l'orogène hercynien : les Cévennes médianes, Massif Central français. *Comptes Rendus de l'Académie des Sciences, Paris 291*, 605–608.

Marini, F. (1987). Relictual clinopyroxenes in paleozoic metabasites from Albigeois: tracers of a distensive transitional-to-tholeiitic volcanism ("Schistes et Roches Vertes" formation, Tarn, probable ordovician age). *Comptes Rendus de l'Académie des Sciences, Paris 304*, 29–34.

Marini, F. (1988). The Sardinian phase and the Ordovician distension of the South Variscan realm as consequences of hotspot activity: a possible inference based on new data from the Albigeois metabasites. *Comptes Rendus de l'Académie des Sciences, Paris 306*, 443–450.

Marschall, H. R., Hawkesworth, C. J., Storey, C. D., Dhuime, B., Leat, P. T., Meyer, H. P., and Tamm-Buckle, S. (2010). The Annandagstoppane Granite, East Antarctica: Evidence for Archaean Intracrustal Recycling in the Kaapvaal-Grunehogna Craton from Zircon O and Hf Isotopes. *Journal of Petrology 51*(11), 2277–2301.

Martin, H., Smithies, R. H., Rapp, R., Moyen, J. F., and Champion, D. (2005). An overview of adakite, tonalite–trondhjemite–granodiorite (TTG), and sanukitoid: relationships and some implications for crustal evolution. *Lithos 79*(1-2), 1–24.

Martín-Hernández, F. and Hirt, A. M. (2003). The anisotropy of magnetic susceptibility in biotite, muscovite and chlorite single crystals. *Tectonophysics 367*(1-2), 13–28.

Martínez Catalán, J. R., Arenas, R., Abati, J., Martínez, S. S., García, F. D., Suárez, J. F., Cuadra, P. G., Castiñeiras, P., Barreiro, J. G., Montes, A. D., Clavijo, E. G., Pascual, F. J. R., Andonaegui, P., Jeffries, T. E., Alcock, J. E., Fernández, R. D., and Carmona, A. L. (2009). A rootless suture and the loss of the roots of a mountain chain: The Variscan belt of NW Iberia. *Comptes Rendus Geoscience 341*(2-3), 114–126.

Martínez Catalán, J. R., Arenas, R., García, F. D., Cuadra, P. G., Gómez-Barreiro, J., Abati, J., Castiñeiras, P., Fernández-Suárez, J., Martínez, S. S., Andonaegui, P., Clavijo, E. G., Montes, A. D., Pascual, F. J. R., and Aguado, B. V. (2007). Space and time in the tectonic evolution of the northwestern Iberian Massif: Implications for the Variscan belt. *200*, 403–423.

Mattauer, M., Brunel, M., and Matte, P. (1988). Failles normales ductiles et grands chevauchements. Une nouvelle analogie entre l'Himalaya et la chaîne hercynienne du Massif Central français. *Comptes Rendus de l'Académie des Sciences, Paris 306*, 671–676.

Matte, P. (1986a). La chaîne varisque parmi les chaînes paléozoïques péri atlantiques, modèle d'évolution et position des grands blocs continentaux au Permo-Carbonifère. *Bulletin de la Société Géologique de France 8*(2), 9–24.

Matte, P. (1986b). Tectonics and plate tectonics model for the Variscan belt of Europe. *Tectonophysics 126*, 329–374.

Matte, P. (1991). Accretionary history and crustal evolution of the Variscan belt in Western Europe. *Tectonophysics 196*, 309–337.

Matte, P. (2001). The Variscan collage and orogeny (480-290 Ma) and the tectonic definition of the Armorica microplate: a review. *Terra Nova 13*, 122–128.

Matte, P., Maluski, H., Rajlich, P., and Franke, W. (1990). Terrane boundaries in the Bohemian Massif: Result of large-scale Variscan shearing. *Tectonophysics 177*(1), 151 – 170. International IGCP Conference Project 233.

Maurel, O., Monié, P., Respaut, J.-P., Leyreloup, A. F., and Maluski, H. (2003). Pre-metamorphic ^{40}Ar/^{39}Ar and U–Pb ages in HP metagranitoids from the Hercynian belt (France). *Chemical Geology 193*, 195–214.

McLellan, E. L. (1988). Migmatite structures in the Central Gneiss Complex, Boca de Quadra, Alaska. *Journal of Metamorphic Geology 6*, 517–542.

Meinhold, G., Morton, A. C., and Avigad, D. (2013). New insights into peri-Gondwana paleogeography

and the Gondwana super-fan system from detrital zircon U–Pb ages. *Gondwana Research 23*(2), 661–665.

Meinhold, G., Morton, A. C., Fanning, C. M., Frei, D., Howard, J. P., Phillips, R. J., Strogen, D., and Whitham, A. G. (2011). Evidence from detrital zircons for recycling of Mesoproterozoic and Neoproterozoic crust recorded in Paleozoic and Mesozoic sandstones of southern Libya. *Earth and Planetary Science Letters 312*(1-2), 164–175.

Melleton, J., Cocherie, A., Faure, M., and Rossi, P. (2010). Precambrian protoliths and Early Paleozoic magmatism in the French Massif Central: U–Pb data and the North Gondwana connection in the west European Variscan belt. *Gondwana Research 17*(1), 13–25.

Mercier, L., Johan, V., Lardeaux, J. M., and Ledru, P. (1989). Découverte d'éclogites dans l'Artense (M.C.F.) Implications pour la définition des nappes à l'Est du Sillon Houiller. *Comptes Rendus de l'Académie des Sciences, Paris 308*, 315–320.

Metcalfe, R. V., Smith, E. I., Walker, J. D., Reed, R. C., and Gonzales, D. A. (1995). Isotopic disequilibrium among commingled hybrid magmas: evidence for a two-stage magma mixing-commingling process in the Mt. Perkins pluton, Arizona. *The Journal of Geology 103*, 509–527.

Mezger, K. and Krogstad, E. J. (1997). Interpretation of discordant U-Pb zircon ages: An evaluation. *Journal of Metamorphic Geology 15*, 127–140.

Mialhe, J. (1980). *Le massif granitique de la Borne (Cévennes). Etude pétrographique, géochimique, géochronologique et structurale.* Phd.

Michaut, C. and Jaupart, C. (2007). Secular cooling and thermal structure of continental lithosphere. *Earth and Planetary Science Letters 257*(1-2), 83–96.

Michon, G. (1979). *Typologie des vaugnérites des Monts du Lyonnais et du Haut-Vivarais, Massif Central Français.* PhD thesis.

Middlemost, E. A. K. (1994). Naming materials in the magma/igneous rock system. *Earth-Science Reviews 37*, 215–224.

Miller, B. V., Samson, S. D., and D'Lemos, R. S. (2001). U–Pb geochronological constraints on the timing of plutonism, volcanism, and sedimentation, Jersey, Channel Islands, UK. *Journal of the Geological Society, London 158*, 243–252.

Miller, C. F., McDowell, S. M., and Mapes, R. W. (2003). Hot and cold granites? Implications of zircon saturation temperatures and preservation of inheritance. *Geology 31*(6), 529–532.

Mintrone, M. (2016). *Constraining the duration of metamorphic events by modeling of phase equilibrium and diffusion in garnet. Example from the French Massif Central.* M.sc. thesis.

Müller, W., Shelley, M., Miller, P., and Broude, S. (2009). Initial performance metrics of a new custom-designed ArF excimer LA-ICPMS system coupled to a two-volume laser-ablation cell. *J. Anal. At. Spectrom. 24*(2), 209–214.

Ménard, G. and Molnar, P. (1988). Collapse of a Hercynian Tibetan Plateau into a late Palaeozoic European Basin and Range province. *Nature 334*, 235–237.

Ménot, R. P., Peucat, J. J., Scarenzi, D., and Piboule, M. (1988). 496 My age of plagiogranites in the Chamrousse ophiolite complex (external crystalline massifs in the French Alps): evidence of a Lower Paleozoic oceanization. *Earth and Planetary Science Letters 88*, 82–92.

Moecher, D. and Samson, S. (2006). Differential zircon fertility of source terranes and natural bias in the detrital zircon record: Implications for sedimentary provenance analysis. *Earth and Planetary Science Letters 247*(3-4), 252–266.

Molina, F. M. (1973). *Etude géologique des terrains cristallins de la région de St-Agrève (Ardèche).* PhD thesis.

Monié, P., Respaut, J. P., Brichau, S., Bouchot, V., Faure, M., and Roig, J.-Y. (2000). $^{40}Ar/^{39}Ar$ and U-Pb geochronology applied to Au-W-Sb metallogenesis in the Cévennes and Chataigneraie districts (southern Massif Central, France). In V. Bouchot and R. Moritz (Eds.), *A GEODE-GeoFrance 3D workshop on orogenic gold deposits in Europe with emphasis on the Variscides*, Volume 297 of *Doc BRGM Extended Abstr*, pp. 77–79.

Monier, G. (1980). *Pétrologie des granitoïdes du Sud-Millevaches (M.C.F.). Minéralogie, géochimie, géochronologie.* PhD thesis.

Montel, J. M., Bouloton, J., Veschambre, M., Pellier, C., and Ceret, K. (2002). Ages stéphaniens des microgranites du Velay (Massif central français). *Géologie de la France 1*, 15–20.

Montel, J. M., Marignac, C., Barbey, P., and Pichavant, M. (1992). Thermobarometry and granite genesis: the Hercynian low-P, high-T Velay anatectic dome (French Massif Central). *Journal of Metamorphic Geology 10*, 1–15.

Montel, J. M. and Vielzeuf, D. (1997). Partial melting of metagreywackes, Part II. Compositions of minerals and melts. *Contributions to Mineralogy and Petrology 128*, 176–196.

Montel, J. M., Weber, C., Barbey, P., and Pichavant, M. (1986). Thermo-barométrie du domaine anatectique du Velay (Massif Central, France) et conditions de génèse des granites tardi-migmatitiques. *Comptes Rendus de l'Académie des Sciences, Paris 302*, 647–652.

Montel, J. M. and Weisbrod, A. (1986). Characteristics and evolution of "vaugneritic magmas": an analytical and experimental approach, on the example of the Cévennes Médianes (French Massif Central). *Bull. Minéral. 109*, 575–587.

Mooney, W. D., Laske, G., and Masters, T. G. (1998). CRUST 5.1: A global crustal model at 5° × 5°.

Journal of Geophysical Research: Solid Earth 103(B1), 727–747.

Morag, N., Avigad, D., Gerdes, A., Belousova, E., and Harlavan, Y. (2011a). Detrital zircon Hf isotopic composition indicates long-distance transport of North Gondwana Cambrian-Ordovician sandstones. *Geology 39*(10), 955–958.

Morag, N., Avigad, D., Gerdes, A., Belousova, E., and Harlavan, Y. (2011b). Crustal evolution and recycling in the northern Arabian-Nubian Shield: New perspectives from zircon Lu–Hf and U–Pb systematics. *Precambrian Research 186*(1-4), 101–116.

Morag, N., Avigad, D., Gerdes, A., and Harlavan, Y. (2012). 1000–580 Ma crustal evolution in the northern Arabian-Nubian Shield revealed by U–Pb–Hf of detrital zircons from late Neoproterozoic sediments (Elat area, Israel). *Precambrian Research 208-211*, 197–212.

Morel, M. L. A., Nebel, O., Nebel-Jacobsen, Y. J., Miller, J. S., and Vroon, P. Z. (2008). Hafnium isotope characterization of the GJ-1 zircon reference material by solution and laser-ablation MC-ICPMS. *Chemical Geology 255*(1-2), 231–235.

Mougeot, R., Respaut, J. P., Ledru, P., and Marignac, C. (1997). U-Pb chronology on accessory minerals of the Velay anatectic dome (French Massif Central). *European Journal of Mineralogy 9*, 141–156.

Moyen, J. F., Laurent, O., Chelle-Michou, C., Couzinié, S., Vanderhaeghe, O., Zeh, A., Villaros, A., and Gardien, V. (2017a). Collision vs. subduction-related magmatism: Two contrasting ways of granite formation and implications for crustal growth. *Lithos 277*, 154–177.

Moyen, J. F., Paquette, J. L., Ionov, D. A., Gannoun, A., Korsakov, A. V., Golovin, A. V., and Moine, B. N. (2017b). Paleoproterozoic rejuvenation and replacement of Archaean lithosphere: Evidence from zircon U–Pb dating and Hf isotopes in crustal xenoliths at Udachnaya, Siberian craton. *Earth and Planetary Science Letters 457*, 149–159.

Murgulov, V., Beyer, E., Griffin, W. L., O'Reilly, S. Y., Walters, S. G., and Stephens, D. (2007). Crustal evolution in the Georgetown Inlier, North Queensland, Australia: a detrital zircon grain study. *Chemical Geology 245*(3-4), 198–218.

Murphy, J. B., Gutiérrez-Alonso, G., Fernández-Suárez, J., and Braid, J. A. (2008). Probing crustal and mantle lithosphere origin through Ordovician volcanic rocks along the Iberian passive margin of Gondwana. *Tectonophysics 461*(1-4), 166–180.

Murphy, M. A., Yin, A., Kapp, P., Harrison, T. M., Manning, C. E., Ryerson, F. J., Lin, D., and Jinghui, G. (2002). Structural evolution of the Gurla Mandhata detachment system, southwest Tibet: Implications for the eastward extent of the Karakoram fault system. *Geological Society of America Bulletin 114*(4), 428–447.

Naeraa, T., Schersten, A., Rosing, M. T., Kemp, A. I., Hoffmann, J. E., Kokfelt, T. F., and Whitehouse, M. J. (2012). Hafnium isotope evidence for a transition in the dynamics of continental growth 3.2 Gyr ago. *Nature 485*(7400), 627–30.

Nagy, E. A., Samson, S. D., and D'Lemos, R. S. (2002). U–Pb geochronological constraints on the timing of Brioverian sedimentation and regional deformation in the St. Brieuc region of the Neoproterozoic Cadomian orogen, northern France. *Precambrian Research 116*, 1–17.

Nance, R. D., Gutiérrez-Alonso, G., Keppie, J. D., Linnemann, U., Murphy, J. B., Quesada, C., Strachan, R. A., and Woodcock, N. H. (2010). Evolution of the Rheic Ocean. *Gondwana Research 17*(2-3), 194–222.

Nance, R. D. and Linnemann, U. (2008). The Rheic Ocean: Origin, Evolution, and Significance. *GSA Today 18*(12), 4.

Nance, R. D. and Murphy, J. B. (1994). Contrasting basement isotopic signatures and the palinspastic restoration of peripheral orogens: Example from the Neoproterozoic Avalonian-Cadomian belt. *Geology 22*, 617–620.

Nebel, O., Vroon, P. Z., van Westrenen, W., Iizuka, T., and Davies, G. R. (2011). The effect of sediment recycling in subduction zones on the Hf isotope character of new arc crust, Banda arc, Indonesia. *Earth and Planetary Science Letters 303*(3-4), 240–250.

Nemchin, A. A. and Cawood, P. A. (2005). Discordance of the U–Pb system in detrital zircons: Implication for provenance studies of sedimentary rocks. *Sedimentary Geology 182*(1-4), 143–162.

Nemchin, A. A., Giannini, L. M., Bodorkos, S., and Oliver, N. H. S. (2001). Ostwald ripening as a possible mechanism for zircon overgrowth formation during anatexis: Theoretical constraints, a numerical model, and its application to pelitic migmatites of the Tickalara Metamorphics, northwestern Australia. *Geochimica et Cosmochimica Acta 65*(2771-2787).

Newton, R. C. and Haselton, H. T. (1981). Thermodynamics of the garnet-plagioclase-Al_2SiO_5–quartz geobarometer. In R. C. Newton, A. Navrotsky, and B. J. Wood (Eds.), *Thermodynamics of minerals and melts*, pp. 131–147. New York: Springer.

Négron, J. (1979). *Pétrologie et géochimie des formations quartzofeldspathiques de la série mésozonale du Chassezac (Lozère, Massif Central français)*. PhD thesis.

Niu, Y., Zhao, Z., Zhu, D.-C., and Mo, X. (2013). Continental collision zones are primary sites for net continental crust growth — A testable hypothesis. *Earth-Science Reviews 127*, 96–110.

Norlander, B. H., Whitney, D. L., Teyssier, C., and Vanderhaeghe, O. (2002). Partial melting and decompression of the Thor-Odin dome, Shuswap metamorphic core complex, Canadian Cordillera. *Lithos 61*, 103–125.

O'Connor, J. T. (1965). A classification for Quartz-rich igneous rocks based on feldspar ratios. In *U.S.*

Geol. Survey Prof Paper 525-B, pp. B79–B84.

Ohta, T. and Arai, H. (2007). Statistical empirical index of chemical weathering in igneous rocks: A new tool for evaluating the degree of weathering. *Chemical Geology 240*(3-4), 280–297.

Orejana, D., Merino Martínez, E., Villaseca, C., and Andersen, T. (2015). Ediacaran–Cambrian paleogeography and geodynamic setting of the Central Iberian Zone: Constraints from coupled U–Pb–Hf isotopes of detrital zircons. *Precambrian Research 261*, 234–251.

Ouali, H. (1993). *Caractérisation géochimique des paléomagmatites de quelques unités lithotectoniques du Massif Central français : Implications géodynamiques.* PhD thesis.

Padel, M., Álvaro, J. J., Clausen, S., Guillot, F., Poujol, M., Chichorro, M., Monceret, r., Pereira, M. F., and Vizcaïno, D. (2017). U–Pb laser ablation ICP-MS zircon dating across the Ediacaran–Cambrian transition of the Montagne Noire, southern France. *Comptes Rendus Geoscience*.

Paquet, J., François, P., and Nédélec, A. (1981). Effect of partial melting on rock deformation: experimental and natural evidences on rocks of granitic compositions. *Tectonophysics 78*, 545–565.

Paquette, J. L., Monchoux, P., and Couturier, M. (1995). Geochemical and isotopic study of a norite-eclogite transition in the European Variscan belt: Implications for U-Pb zircon systematics in metabasic rocks. *Geochimica et Cosmochimica Acta 59*(8), 1611–1622.

Paquette, J.-L., Piro, J.-L., Devidal, J.-L., Bosse, V., Didier, A., Sanac, S., and Abdelnour, Y. (2014). Sensitivity enhancement in LA-ICP-MS by N_2 addition to carrier gas: Application to radiometric dating of U–Th–bearing minerals. *Agilent ICP-MS Journal 58*, 1–5.

Paquette, J. L. and Tiepolo, M. (2007). High resolution (5 μm) U–Th–Pb isotope dating of monazite with excimer laser ablation (ELA)-ICPMS. *Chemical Geology 240*(3-4), 222–237.

Parat, F., Holtz, F., René, M., and Almeev, R. (2009). Experimental constraints on ultrapotassic magmatism from the Bohemian Massif (durbachite series, Czech Republic). *Contributions to Mineralogy and Petrology 159*(3), 331–347.

Paris, F. and Robardet, M. (1990). Early Palaeozoic palaeobiogeography of the Variscan regions. *Tectonophysics 177*, 193–213.

Parkinson, D. (1991). Age and isotopic character of Early Proterozoic basement gneisses in the southern Monashee Complex, southeastern British Columbia. *Canadian Journal of Earth Sciences 28*, 1159–1168.

Parsons, A. J., Ferré, E. C., Law, R. D., Lloyd, G. E., Phillips, R. J., and Searle, M. P. (2016). Orogen-parallel deformation of the Himalayan midcrust: Insights from structural and magnetic fabric analyses of the Greater Himalayan Sequence, Annapurna-Dhaulagiri Himalaya, central Nepal. *Tectonics 35*(11), 2515–2537.

Patchett, P. J., Kuovo, O., Hedge, C. E., and Tatsumoto, M. (1981). Evolution of the continental crust and mantle heterogeneity: evidence from Hf isotopes. *Contributions to Mineralogy and Petrology 78*, 279–297.

Patchett, P. J. and Tatsumoto, M. (1980). Lu–Hf total-rock isochron for the eucrite meteorites. *Nature 288*, 571–574.

Patiño Douce, A. E. and Harris, N. (1998). Experimental constraints on Himalayan anatexis. *Journal of Petrology 39*(4), 690–710.

Paton, C., Woodhead, J. D., Hellstrom, J. C., Hergt, J. M., Greig, A., and Maas, R. (2010). Improved laser ablation U-Pb zircon geochronology through robust downhole fractionation correction. *Geochemistry, Geophysics, Geosystems 11*(3), 1–36.

Payne, J. L., McInerney, D. J., Barovich, K. M., Kirkland, C. L., Pearson, N. J., and Hand, M. (2016). Strengths and limitations of zircon Lu-Hf and O isotopes in modelling crustal growth. *Lithos 248-251*, 175–192.

Pearce, J. A. (1996). Trace element geochemistry of volcanic rocks: Applications for massive sulphide exploration. Short Course Notes, pp. 79–113. Geological Association of Canada.

Pearce, J. A. (2008). Geochemical fingerprinting of oceanic basalts with applications to ophiolite classification and the search for Archean oceanic crust. *Lithos 100*(1-4), 14–48.

Pearce, J. A. (2014). Immobile element fingerprinting of ophiolites. *Elements 10*, 101–108.

Pearce, J. A. and Peate, D. W. (1995). Tectonic implications of the composition of volcanic arc magmas. *Annual Review of Earth and Planetary Sciences 23*, 251–285.

Pecerillo, A. and Taylor, S. R. (1976). Geochemistry of Eocene calc-alkaline volcanic rocks from the Kastamonu area, Northern Turkey. *Contributions to Mineralogy and Petrology 58*, 63–81.

Peiffer, M.-T. (1985). Données nouvelles sur la ligne tonalitique du Limousin et les "diorites quartziques" qui la composent. *Comptes Rendus de l'Académie des Sciences, Paris 300*(8), 345–348.

Pereira, M. F., Linnemann, U., Hofmann, M., Chichorro, M., Solá, A. R., Medina, J., and Silva, J. B. (2012). The provenance of Late Ediacaran and Early Ordovician siliciclastic rocks in the Southwest Central Iberian Zone: Constraints from detrital zircon data on northern Gondwana margin evolution during the late Neoproterozoic. *Precambrian Research 192-195*, 166–189.

Peterlongo, J.-M. (1958). *Les terrains cristallins des Monts du Lyonnais (Massif central français)*, Volume 4 of *Annales de la Faculté des Sciences de Clermont*.

Petersson, A., Scherstén, A., Bingen, B., Gerdes, A., and Whitehouse, M. J. (2015). Mesoproterozoic continental growth: U–Pb–Hf–O zircon record in the Idefjorden Terrane, Sveconorwegian Orogen. *Precambrian Research 261*, 75–95.

Petersson, A., Scherstén, A., and Gerdes, A. (2017). Extensive reworking of Archaean crust within the Birimian terrane in Ghana as revealed by combined zircon U-Pb and Lu-Hf isotopes. *Geoscience Frontiers*.

Petersson, A., Scherstén, A., Kemp, A. I. S., Kristinsdóttir, B., Kalvig, P., and Anum, S. (2016). Zircon U–Pb–Hf evidence for subduction related crustal growth and reworking of Archaean crust within the Palaeoproterozoic Birimian terrane, West African Craton, SE Ghana. *Precambrian Research 275*, 286–309.

Petford, N. and Gallagher, K. (2001). Partial melting of the mafic (amphibolitic) lower crust by periodic influx of basaltic magma. *Earth and Planetary Science Letters 193*, 483–499.

Petrus, J. A. and Kamber, B. S. (2012). VizualAge: A novel approach to laser ablation ICP-MS U-Pb geochronology data reduction. *Geostandards and Geoanalytical Research 36*(3), 247–270.

Peucat, J. J. (1986). Behaviour of Rb-Sr whole-rock and U-Pb zircon systems during partial melting as shown in migmatitic gneisses from the Saint-Malo Massif, NE Brittany, France. *Journal of the Geological Society, London 143*, 875–886.

Pfeifer, L. S., Soreghan, G. S., Pochat, S., Van Den Driessche, J., and Thomson, S. N. (2016). Permian exhumation of the Montagne Noire core complex recorded in the Graissessac-Lodève Basin, France. *Basin Research*.

Piboule, M. (1977). Utilisation de l'analyse factorielle discriminante pour la reconnaissance de la nature des magmas parents des amphibolites. Application à quelques métabasites du Rouergue et du Limousin (Massif Central français). *Bulletin de la Société Géologique de France 19*(5), 1133–1143.

Piboule, M. (1979). *L'origine des amphibolites : approche géochimique et mathématique. Application aux amphibolites du Massif Central Français*. Habilitation thesis.

Piboule, M. and Briand, B. (1985). Geochemistry of eclogites and associated rocks of the southeastern area of the French Massif Central: origin of the protoliths. *Chemical Geology 50*, 189–199.

Pietranik, A., Słodczyk, E., Hawkesworth, C. J., Breitkreuz, C., Storey, C. D., Whitehouse, M., and Milke, R. (2013). Heterogeneous zircon cargo in voluminous late Paleozoic rhyolites: Hf, O isotope and Zr/Hf records of plutonic to volcanic magma evolution. *Journal of Petrology 54*(8), 1483–1501.

Pietranik, A. B., Hawkesworth, C. J., Storey, C. D., Kemp, A. I. S., Sircombe, K. N., Whitehouse, M. J., and Bleeker, W. (2008). Episodic, mafic crust formation from 4.5 to 2.8 Ga: New evidence from detrital zircons, Slave craton, Canada. *Geology 36*(11), 875.

Pin, C. (1979). *Géochronologie U–Pb et microtectonique des séries métamorphiques anté-stéphaniennes de l'Aubrac et de la région de Marvejols (Massif Central)*. PhD thesis.

Pin, C. and Carme, F. (1987). A Sm–Nd isotopic study of 500 Ma old oceanic crust in the Variscan belt of Western Europe: the Chamrousse ophiolite complex, Western Alps (France). *Contributions to Mineralogy and Petrology 96*, 406–413.

Pin, C. and Duthou, J.-L. (1990). Source of Hercynian granitoids from the French Massif Central: Inferences from Nd isotopes and consequences for crustal evolution. *Chemical Geology 83*, 281–296.

Pin, C. and Lancelot, J. (1978). Un exemple de magmatisme cambrien dans le Massif Central : les métadiorites quartziques intrusives dans la série du Lot. *Bulletin de la Société Géologique de France 7*(2), 203–208.

Pin, C. and Lancelot, J. (1982). U-Pb Dating of an Early Paleozoic Bimodal Magmatism in the French Massif Central and of Its Further Metamorphic Evolution. *Contributions to Mineralogy and Petrology 79*, 1–12.

Pin, C. and Marini, F. (1993). Early Ordovician continental break-up in Variscan Europe: Nd-Sr isotope and trace element evidence from bimodal igneous associations of the Southern Massif Central, France. *Lithos 29*, 177–196.

Pin, C. and Paquette, J. L. (1997). A mantle-derived bimodal suite in the Hercynian Belt: Nd isotope and trace element evidence for a subduction-related rift origin of the Late Devonian Brévenne metavolcanics, Massif Central (France). *Contributions to Mineralogy and Petrology 129*, 222–238.

Pin, C. and Paquette, J. L. (2002). Sr-Nd isotope and trace element evidence for a Late Devonian active margin in northern Massif Central (France). *Geodinamica Acta 15*, 63–77.

Pitra, P., Poujol, M., Van Den Driessche, J., Poilvet, J.-C., and Paquette, J.-L. (2012). Early Permian extensional shearing of an Ordovician granite: The Saint-Eutrope "C/S-like" orthogneiss (Montagne Noire, French Massif Central). *Comptes Rendus Geoscience 344*(8), 377–384.

Plank, T. (2005). Constraints from thorium/lanthanum on sediment recycling at subduction zones and the evolution of the continents. *Journal of Petrology 46*(5), 921–944.

Plank, T. and Langmuir, C. H. (1998). The chemical composition of subducting sediment and its conseqiences for the crust and mantle. *Chemical Geology 145*, 325–394.

Poilvet, J.-C., Poujol, M., Pitra, P., Van Den Driessche, J., and Paquette, J.-L. (2011). The Montalet granite, Montagne Noire, France: An Early Permian syn-extensional pluton as evidenced by new U-Th-Pb data on zircon and monazite. *Comptes Rendus Geoscience 343*(7), 454–461.

Pouclet, A., Álvaro, J. J., Bardintzeff, J.-M., Imaz, A. G., Monceret, E., and Vizcaïno, D. (in press). Cambrian–early Ordovician volcanism across the South Armorican and Occitan Domains of the Variscan Belt in France: Continental break-up and rifting of the northern Gondwana margin. *Geoscience Frontiers*.

Poujol, M., Pitra, P., Van Den Driessche, J., Tartèse, R., Ruffet, G., Paquette, J.-L., and Poilvet, J.-C.

(2016). Two-stage partial melting during the Variscan extensional tectonics (Montagne Noire, France). *International Journal of Earth Sciences 106*(2), 477–500.

Powell, R. and Holland, T. (1999). Relating formulations of the thermodynamics of mineral solid solutions: Activity modeling of pyroxenes, amphiboles, and micas. *American Mineralogist 84*, 1–14.

Power, G. M., Brewer, T. S., Brown, M., and Gibbons, W. (1990). Late Precambrian foliated plutonic complexes of the Channel Islands and La Hague: early Cadomian plutonism. In R. S. D'Lemos, R. A. Strachan, and C. G. Topley (Eds.), *The Cadomian orogeny*, Volume 51, pp. 215–229. Geological Society Special Publication.

Prost, A. E. and Becq-Giraudon, J. F. (1989). Evidence for mid-Permian compressive tectonics in Western Europe supported by a comparison with the Alleghanian geodynamic evolution. *Tectonophysics 169*, 333–340.

Rabu, D., Chantraine, J., Chauvel, J. J., Denis, E., Balé, P., and Bardy, P. (1990). The Brioverian (Upper Proterozoic) and the Cadomian orogeny in the Armorican Massif. In R. S. D'Lemos, R. A. Strachan, and C. G. Topley (Eds.), *The Cadomian Orogeny*, Volume 51, pp. 81–94. Geological Society Special Publication.

Rakib, A. (1996). *Le métamorphisme régional de basse pression des Cévennes occidentales: une conséquence directe de la mise en place du dôme thermique vellave (Massif central français)*. PhD thesis.

Rapp, R. P. and Watson, E. B. (1995). Dehydration melting of metabasalt at 8-32 kbar: implications for continental growth and crust-mantle recycling. *Journal of Petrology 36*(4), 891–931.

Ratajeski, K., Sisson, T. W., and Glazner, A. F. (2005). Experimental and geochemical evidence for derivation of the El Capitan Granite, California, by partial melting of hydrous gabbroic lower crust. *Contributions to Mineralogy and Petrology 149*(6), 713–734.

Rey, P., Burg, J.-P., and Casey, M. (1997). The Scandinavian Caledonides and their relationship to the Variscan belt. In J.-P. Burg and M. Ford (Eds.), *Orogeny Through Time*, Volume 121, pp. 179–200. Special Publications Geolological Society, London.

Rey, P., Vanderhaeghe, O., and Teyssier, C. (2001). Gravitational collapse of the continental crust: definition, regimes and modes. *Tectonophysics 342*, 435–449.

Rey, P. F., Teyssier, C., Kruckenberg, S. C., and Whitney, D. L. (2011). Viscous collision in channel explains double domes in metamorphic core complexes. *Geology 39*(4), 387–390.

Rey, P. F., Teyssier, C., and Whitney, D. L. (2009). The role of partial melting and extensional strain rates in the development of metamorphic core complexes. *Tectonophysics 477*(3-4), 135–144.

Rino, S., Komiya, T., Windley, B. F., Katayama, I., Motoki, A., and Hirata, T. (2004). Major episodic increases of continental crustal growth determined from zircon ages of river sands; implications for mantle overturns in the Early Precambrian. *Physics of the Earth and Planetary Interiors 146*, 369–394.

Robardet, M. (2003). The Armorica 'microplate': fact or fiction? Critical review of the concept and contradictory palaeobiogeographical data. *Palaeogeography, Palaeoclimatology, Palaeoecology 195*(1-2), 125–148.

Roberts, N. M. W. (2012). Increased loss of continental crust during supercontinent amalgamation. *Gondwana Research 21*(4), 994–1000.

Roberts, N. M. W., Slagstad, T., Parrish, R. R., Norry, M. J., Marker, M., and Horstwood, M. S. A. (2013). Sedimentary recycling in arc magmas: geochemical and U–Pb–Hf–O constraints on the Mesoproterozoic Suldal Arc, SW Norway. *Contributions to Mineralogy and Petrology 165*(3), 507–523.

Roberts, N. M. W. and Spencer, C. J. (2014). The zircon archive of continent formation through time. *Geological Society, London, Special Publications 389*(1), 197–225.

Rochette, P., Jackson, M., and Aubourg, C. (1992). Rock magnetism and the interpretation of anisotropy of magnetic susceptibility. *Reviews of Geophysics 30*, 209–226.

Roecker, S. W. (1982). Velocity structure of the Pamir-Indu Kush region: possible evidence of subducted crust. *Journal of Geophysical Research 87*, 945–959.

Roger, F., Respaut, J.-P., Brunel, M., Matte, P., and Paquette, J.-L. (2004). Première datation U–Pb des orthogneiss œillés de la zone axiale de la Montagne noire (Sud du Massif central) : nouveaux témoins du magmatisme ordovicien dans la chaîne Varisque. *Comptes Rendus Geoscience 336*(1), 19–28.

Roger, F., Teyssier, C., Respaut, J.-P., Rey, P. F., Jolivet, M., Whitney, D. L., Paquette, J.-L., and Brunel, M. (2015). Timing of formation and exhumation of the Montagne Noire double dome, French Massif Central. *Tectonophysics 640-641*, 53–69.

Rogers, J. J. W. and Santosh, M. (2003). Supercontinents in Earth History. *Gondwana Research 6*(3), 357–368.

Rolland, Y., Mahéo, G., Guillot, F., and Pecher, A. (2001). Tectono-metamorphic evolution of the Karakorum Metamorphic complex (Dassu-Askole area, NE Pakistan): exhumation of mid-crustal HT-MP gneisses in a convergent context. *Journal of Metamorphic Geology 19*, 717–737.

Roques, M., Pin, C., and Duthou, J.-L. (1995). Substratum antéhercynien et collision hercynienne dans le Massif central français. *Comptes Rendus de l'Académie des Sciences, Paris 320*, 817–821.

Rosenberg, C. L. and Handy, M. R. (2005). Experimental deformation of partially melted granite revisited: implications for the continental crust. *Journal of Metamorphic Geology 23*(1), 19–28.

Rossi, P., Cocherie, A., Fanning, C. M., and Deloule, E. (2006). Variscan to eo-Alpine events recorded

in European lower-crust zircons sampled from the French Massif Central and Corsica, France. *Lithos 87*(3-4), 235–260.

Rubatto, D. (2002). Zircon trace element geochemistry: partitioning with garnet and the link between U–Pb ages and metamorphism. *Chemical Geology 184*, 123–138.

Rubatto, D., Williams, I. S., and Buick, I. S. (2001). Zircon and monazite response to prograde metamorphism in the Reynolds range, central Australia. *Contributions to Mineralogy and Petrology 140*, 458–468.

Rudnick, R. L. (1995). Making continental crust. *Nature 378*, 571–578.

Rudnick, R. L. and Fountain, D. M. (1995). Nature and composition of the continental crust: a lower crustal perspective. *Reviews of Geophysics 33*(3), 267–309.

Rudnick, R. L. and Gao, S. (2003). Composition of the continental crust. In R. L. Rudnick (Ed.), *The Crust*, Treatise on Geochemistry, pp. 1–64. Oxford: Elsevier-Pergamon.

Rushmer, T. (1991). Partial melting of two amphibolites: contrasting experimental results under fluid-absent conditions. *Contributions to Mineralogy and Petrology 107*, 41–59.

Rushmer, T. (1996). Melt segregation in the lower crust: how have experiments helped us? *Earth and Environmental Science Transactions of the Royal Society of Edinburgh 87*(1-2), 73–83.

Rybach, L. (1976). Radioactive heat production in rocks and its relation to other petrophysical parameters. *Pageoph 114*, 309–317.

Sabatier, H. (1984). *Vaugnérites et granites magnésiens dans le Massif central français: une association particulière de roches grenues acides et basiques. Etude pétrographique.* PhD thesis.

Sabourdy, G. (1975). *Apport de la géochimie à la connaissance de la pétrogenèse des granitoïdes des Cévennes méridionales, Massif central français.* PhD thesis.

Sabourdy, G. and Berthelay, J.-C. (1977). Premiers résultats de l'étude géochimique des granites grenus à biotite et à deux micas du Mont Lozere (Massif Central français). *Comptes Rendus sommaires de la Société Géologique de France*, 133–136.

Samson, S. D. and D'Lemos, R. S. (1998). U–Pb geochronology and Sm–Nd isotopic composition of Proterozoic gneisses, Channel Islands, UK. *Journal of the Geological Society, London 155*, 609–618.

Samson, S. D., D'Lemos, R. S., Blichert-Toft, J., and Vervoort, J. (2003). U–Pb geochronology and Hf–Nd isotope compositions of the oldest Neoproterozoic crust within the Cadomian orogen: new evidence for a unique juvenile terrane. *Earth and Planetary Science Letters 208*(3-4), 165–180.

Samson, S. D., D'Lemos, R. S., Miller, B. V., and Hamilton, M. A. (2005). Neoproterozoic palaeogeography of the Cadomia and Avalon terranes: constraints from detrital zircon U-Pb ages. *Journal of the Geological Society 162*(1), 65–71.

Sandiford, M., Hand, M., and McLaren, S. (1998). High geothermal gradient metamorphism during thermal subsidence. *Earth and Planetary Science Letters 163*, 149–165.

Santallier, D., Briand, B., Ménot, R. P., and Piboule, M. (1988). Les complexes leptyno-amphioliques (C.L.A.) : revue critique et suggestions pour un meilleur emploi de ce terme. *Bulletin de la Société Géologique de France 8*(4), 3–12.

Santos, M. M., Lana, C., Scholz, R., Buick, I., Kamo, S. L., Gerdes, A., Condon, D. J., Corfu, F., Tohver, E., Storey, C., Basei, M., Krambrock, K., and Fantini, C. (in press). BB zircon – A new Sri Lankan reference material for U-Pb and Hf isotopic laser ablation ICP-MS analysis.

Sawyer, E. (1991). Disequilibrium melting and the rate of melt–residuum separation during migmatization of mafic rocks from the Grenville Front, Quebec. *Journal of Petrology 32*, 701–738.

Sawyer, E. W. (1994). Melt segregation in the continental crust. *Geology 22*, 1019–1022.

Sawyer, E. W. (2008). *Atlas of Migmatites.* NRC Research Press.

Sawyer, E. W. (2010). Migmatites formed by water-fluxed partial melting of a leucogranodiorite protolith: Microstructures in the residual rocks and source of the fluid. *Lithos 116*(3-4), 273–286.

Sawyer, E. W., Cesare, B., and Brown, M. (2011). When the Continental Crust Melts. *Elements 7*(4), 229–234.

Scholl, D. W. and Von Huene, R. (2009). Implications of estimated magmatic additions and recyling losses at the subduction zones of accretionary (non collisional) and collisional (suturing) orogens. In P. A. Cawood and A. Kröner (Eds.), *Earth Accretionary Systems in Space and Time*, Volume 318, pp. 105–125. Geological Society of London Special Publications.

Schulmann, K., Lexa, O., Janou ek, V., Lardeaux, J. M., and Edel, J. B. (2014). Anatomy of a diffuse cryptic suture zone: An example from the Bohemian Massif, European Variscides. *Geology 42*(4), 275–278.

Schulz, B. (2009). EMP-monazite age controls on P-T paths of garnet metapelites in the Variscan inverted metamorphic sequence of La Sioule, French Massif Central. *Bulletin de la Société Géologique de France 180*(3), 271–282.

Schulz, B. (2014). Early Carboniferous P-T path from the Upper Gneiss Unit of Haut-Allier (French Massif Central) - reconstructed by geothermobarometry and EMP-Th-U-Pb monazite dating. *Journal of Geosciences*, 327–349.

Schulz, B., Triboulet, C., Audren, C., and Feybesse, J.-L. (1996). Zoned garnets in metapelites and P-T-deformation path interpretation of the Variscan inverted metamorphic sequence of Haut-Allier, French Massif Central. *Z. dt. geol. Ges. 147*, 249–273.

Schulz, B., Triboulet, C., Audren, C., and Feybesse, J.-L. (2001). P-T paths from metapelite garnet

zonations, and crustal stacking in the Variscan inverted metamorphic sequence of La Sioule, French Massif Central. *Z. dt. geol. Ges. 152*, 1–25.

Sen, C. and Dunn, T. (1994). Dehydration melting of a basaltic composition amphibolite at 1.5 and 2.0 GPa: implications for the origin of adakites. *Contributions to Mineralogy and Petrology 117*, 394–409.

Seyler, M. (1986). *Magmatologie des séries volcaniques métamorphiques – L'exemple des métavolcanites cambro-ordoviciennes, en particulier alcalines, du socle provençal (France)*. PhD thesis.

Shaw, A., Downes, H., and Thirlwall, M. F. (1993). The quartz-diorites of Limousin: Elemental and isotopic evidence for Devono-Carboniferous subduction in the Hercynian belt of the French Massif Central. *Chemical Geology 107*, 1–18.

Shervais, J. W. (1982). Ti–V plots and the petrogenesis of modern and ophiolitic lavas. *Earth and Planetary Science Letters 59*, 101–118.

Simien, F., Mattauer, M., and Allègre, C. J. (1999). Nd isotopes in the stratigraphic record of the Montagne Noire (French Massif Central): No significant Paleozoic juvenile inputs, and pre-Hercynian paleogeography. *The Journal of Geology 107*, 87–97.

Sisson, T. W. (1994). Hornblende-melt trace-element partitioning measured by ion microprobe. *Chemical Geology 117*, 331–334.

Sisson, T. W., Ratajeski, K., Hankins, W. B., and Glazner, A. F. (2005). Voluminous granitic magmas from common basaltic sources. *Contributions to Mineralogy and Petrology 148*(6), 635–661.

Skrzypek, E. and Štípská, P. (2012). The origin of zircon and the significance of U–Pb ages in high-grade metamorphic rocks: a case study from the Variscan orogenic root (Vosges Mountains, NE France). *Contributions to Mineralogy and Petrology 164*, 935–957.

Sláma, J., Dunkley, D. J., Kachlík, V., and Kusiak, M. A. (2008b). Transition from island-arc to passive setting on the continental margin of Gondwana: U–Pb zircon dating of Neoproterozoic metaconglomerates from the SE margin of the Teplá–Barrandian Unit, Bohemian Massif. *Tectonophysics 461*(1-4), 44–59.

Sláma, J. and Žák, J. (2017). How far did the Cadomian "terranes" travel from Gondwana during early Palaeozoic? A critical reappraisal based on detrital zircon geochronology. *International Geology Review*, 1–20.

Sláma, J., Košler, J., Condon, D. J., Crowley, J. L., Gerdes, A., Hanchar, J. M., Horstwood, M. S. A., Morris, G. A., Nasdala, L., Norberg, N., Schaltegger, U., Schoene, B., Tubrett, M. N., and Whitehouse, M. J. (2008a). Plešovice zircon — A new natural reference material for U–Pb and Hf isotopic microanalysis. *Chemical Geology 249*(1-2), 1–35.

Soula, J.-C., Debat, P., Brusset, S., Bessière, G., Christophoul, F., and Déramond, J. (2001). Thrust-related, diapiric, and extensional doming in a frontal orogenic wedge: example of the Montagne Noire, Southern French Hercynian Belt. *Journal of Structural Geology 23*, 1677–1699.

Spandler, C., Mavrogenes, J., and Hermann, J. (2007). Experimental constraints on element mobility from subducted sediments using high-P synthetic fluid/melt inclusions. *Chemical Geology 239*(3-4), 228–249.

Spencer, C. J., Cawood, P. A., Hawkesworth, C. J., Prave, A. R., Roberts, N. M. W., Horstwood, M. S. A., and Whitehouse, M. J. (2015). Generation and preservation of continental crust in the Grenville Orogeny. *Geoscience Frontiers 6*(3), 357–372.

Spencer, C. J., Hawkesworth, C., Cawood, P. A., and Dhuime, B. (2013). Not all supercontinents are created equal: Gondwana-Rodinia case study. *Geology 41*(7), 795–798.

Stacey, J. S. and Kramers, J. D. (1975). Approximation of terrestrial lead isotope evolution by a 2-stage model. *Earth and Planetary Science Letters 26*(2), 207–221.

Stampfli, G. M., Hochard, C., Vérard, C., Wilhem, C., and vonRaumer, J. (2013). The formation of Pangea. *Tectonophysics 593*, 1–19.

Stern, C. R. (2011). Subduction erosion: Rates, mechanisms, and its role in arc magmatism and the evolution of the continental crust and mantle. *Gondwana Research 20*(2-3), 284–308.

Stern, R. A., Ali, K. A., Liégeois, J. P., Johnson, P. R., Kozdroj, W., and Kattan, F. H. (2010). Distribution and significance of pre-Neoproterozoic zircons in juvenile Neoproterozoic igneous rocks of the Arabian Nubian Shield. *American Journal of Science 310*, 791–811.

Stern, R. J. (2002). Crustal evolution in the East African Orogen: a neodymium isotopic perspective. *Journal of African Earth Sciences 34*(3-4), 109–117.

Stern, R. J. and Scholl, D. W. (2010). Yin and yang of continental crust creation and destruction by plate tectonic processes. *International Geology Review 52*(1), 1–31.

Strachan, R. A., D'Lemos, R. S., and Dallmeyer, R. D. (1996). Neoproterozoic evolution of an active plate margin: North Armorican Massif, France. In R. D. Nance and M. D. Thompson (Eds.), *Avalonian and Related Peri-Gondwanan Terranes of the Circum–North Atlantic*, Volume 304, pp. 319–332. Boulder, Colorado: Geological Society of America Special Paper.

Stracke, A. (2012). Earth's heterogeneous mantle: A product of convection-driven interaction between crust and mantle. *Chemical Geology 330-331*, 274–299.

Stracke, A., Hofmann, A. W., and Hart, S. R. (2005). FOZO, HIMU, and the rest of the mantle zoo. *Geochemistry, Geophysics, Geosystems 6*(5), n/a–n/a.

Sultan, M., Chamberlain, K. R., Bowring, S. A., and Arvidson, R. E. (1990). Geochronologic and isotopic evidence for involvement of pre-Pan-African crust in the Nubian Shield, Egypt. *Geology 18*, 761–764.

Sun, S. s. and McDonough, W. F. (1989). Chemical and isotopic systematics of oceanic basalts: implications for mantle composition and processes. *Geological Society, London, Special Publications 42*(1), 313–345.

Supply, P. (1981). *Géochronologie U–Pb et pétrologie des enclaves granulitiques de Bournac (Massif Central)*. M.Sc. thesis.

Tajčmanová, L., Connolly, J. A. D., and Cesare, B. (2009). A thermodynamic model for titanium and ferric iron solution in biotite. *Journal of Metamorphic Geology 27*(2), 153–165.

Talbot, J. Y., Chen, Y., Faure, M., and Lin, W. (2000). AMS study of the Pont-de-Montvert-Borne porphyritic granite pluton (French Massif Central) and its tectonic implications. *Geophysical Journal International 140*, 677–686.

Talbot, J.-Y., Faure, M., Chen, Y., and Martelet, G. (2005). Pull-apart emplacement of the Margeride granitic complex (French Massif Central). Implications for the late evolution of the Variscan orogen. *Journal of Structural Geology 27*(9), 1610–1629.

Talbot, J.-Y., Martelet, G., Courrioux, G., Chen, Y., and Faure, M. (2004). Emplacement in an extensional setting of the Mont Lozère–Borne granitic complex (SE France) inferred from comprehensive AMS, structural and gravity studies. *Journal of Structural Geology 26*(1), 11–28.

Tatsumi, Y., Hamilton, D. L., and Nesbitt, R. W. (1986). Chemical characteristics of fluid phase released from a subducted lithosphere and origin of arc magmas: evidence from high-pressure experiments and natural rocks. *Journal of Volcanology and Geothermal Research 29*, 293–309.

Taylor, S. R. (1977). Island arc models and the composition of the continental crust. In M. Talwani (Ed.), *Island Arcs, Deep Sea Trenches and Back-Arc Basins*, pp. 325–336. Washington DC: American Geophysical Union.

Taylor, S. R. and McLennan, S. M. (1985). *The Continental Crust: its Composition and Evolution*. Oxford: Blackwell.

Taylor, S. R. and McLennan, S. M. (1995). The geochemical evolution of the continental crust. *Reviews of Geophysics 33*(2), 241–265.

Teyssier, C., Ferré, E. C., Whitney, D. L., Norlander, B., Vanderhaeghe, O., and Parkinson, D. (2005). Flow of partially molten crust and origin of detachments during collapse of the Cordilleran Orogen. In D. Bruhn and L. Burlini (Eds.), *High-strain zones: structure and physical properties*, Volume 245, pp. 39–64. Geological Society, London, Special Publications.

Teyssier, C. and Whitney, D. L. (2002). Gneiss domes and orogeny. *Geology 30*(12), 1139–1142.

Thompson, A. B. (1982). Dehydration melting of pelitic rocks and the generation of H_2O-undersaturated granitic liquids. *American Journal of Science 282*, 1567–1595.

Tirel, C., Brun, J. P., and Burov, E. B. (2004). Thermomechanical modeling of extensional gneiss domes. In D. L. Whitney, C. Teyssier, and C. Siddoway (Eds.), *Gneiss domes in orogeny*, Volume 380, pp. 67–78. Geological Society of America Special Paper.

Tomascak, P. B., Krogstad, E. J., and Walker, R. J. (1996). U-Pb monazite geochronology of granitic rocks from Maine: Implications for late Paleozoic tectonics in the Northern Appalachian. *The Journal of Geology 104*, 185–195.

Štípská, P., Schulmann, K., and Höck, V. (2000). Complex metamorphic zonation of the Thaya dome: result of buckling and gravitational collapse of an imbricated nappe sequence. In J. Cosgrove and M. S. Ameen (Eds.), *Forced Folds and Fractures*, Volume 169, pp. 197–211. Geological Society, London, Special Publications.

Trap, P., Roger, F., Cenki-Tok, B., and Paquette, J. L. (2017). Timing and duration of partial melting and magmatism in the Variscan Montagne Noire gneiss dome (French Massif Central). *International Journal of Earth Sciences 106*(2), 453–476.

Turpin, L., Cuney, M., Friedrich, M., Bouchez, J. L., and Aubertin, M. (1990). Meta-igneous origin of Hercynian peraluminous granites in N.W. French Massif Central: implications for crustal history reconstructions. *Contributions to Mineralogy and Petrology 104*, 163–172.

Valley, J., Graham, C. M., Harte, B., Eiler, J. M., and Kinny, P. D. (1998). Ion microprobe analysis of oxygen, carbon, and hydrogen isotope ratios. In *Applications of Microanalytical Techniques to Understanding Mineralizing Processes*, Volume 7, pp. 73–98. Littleton: Society of Economic Geologists.

Valley, J. W. (2003). Oxygen isotopes in zircon. In J. M. Hanchar and P. W. O. Hoskin (Eds.), *Zircon*, Volume 53 of *Reviews in Mineralogy and Geochemistry*, pp. 343–385. Washington DC.

Valley, J. W., Lackey, J. S., Cavosie, A. J., Clechenko, C. C., Spicuzza, M. J., Basei, M. A. S., Bindeman, I. N., Ferreira, V. P., Sial, A. N., King, E. M., Peck, W. H., Sinha, A. K., and Wei, C. S. (2005). 4.4 billion years of crustal maturation: oxygen isotope ratios of magmatic zircon. *Contributions to Mineralogy and Petrology 150*(6), 561–580.

Valverde-Vaquero, P. and Dunning, G. R. (2000). New U–Pb ages for Early Ordovician magmatism in Central Spain. *Journal of the Geological Society, London 157*, 15–26.

Van Achterbergh, E., Ryan, C., Jackson, S. E., and Griffin, W. L. (2001). Data reduction software for LA-ICP-MS: appendix. In P. J. Sylvester (Ed.), *Laser Ablation-ICP-Mass Spectrometry in the Earth Sciences: Principles and Applications,*, Volume 29 of *Short Courses Series*, pp. 239–243. Ottawa, Ontario, Canada: Mineralog Assoc Canada (MAC).

Vanderhaeghe, O. (2009). Migmatites, granites and orogeny: Flow modes of partially-molten rocks and magmas associated with melt/solid segregation in orogenic belts. *Tectonophysics 477*(3-4), 119–134.

Vanderhaeghe, O., Gardien, V., Moyen, J. F., Gébelin, A., Laurent, O., Couzinié, S., Chelle-Michou, C., and Villaros, A. Flow of the partially molten Variscan orogenic crust from syn-orogenic exhumation of subducted continental crust to gravitational collapse along a convergent plate boundary marked by slab retreat. *24e Réunion des Sciences de la Terre, Pau.*.

Vanderhaeghe, O. and Teyssier, C. (2001). Crustal-scale rheological transitions during late-orogenic collapse. *Tectonophysics 335*, 211–228.

Vavra, G., Schmid, R., and Gebauer, D. (1999). Internal morphology, habit and U–Th–Pb microanalysis of amphibolite-to-granulite facies zircons: geochronology of the Ivrea Zone (Southern Alps). *Contributions to Mineralogy and Petrology 134*, 380–404.

Vermeesch, P. (2012). On the visualisation of detrital age distributions. *Chemical Geology 312-313*, 190–194.

Vervoort, J. D. and Kemp, A. I. S. (2016). Clarifying the zircon Hf isotope record of crust–mantle evolution. *Chemical Geology 425*, 65–75.

Vervoort, J. D., Patchett, P. J., Blichert-Toft, J., and Albarède, F. (1999). Relationships between Lu–Hf and Sm–Nd isotopic systems in the global sedimentary system. *Earth and Planetary Science Letters 168*, 79–99.

Vervoort, J. D., Patchett, P. J., Soderlund, U., and Baker, M. (2004). Isotopic composition of Yb and the determination of Lu concentrations and Lu/Hf by isotope dilution using MC-ICPMS. *Geochemistry, Geophysics, Geosystems 5*, 1–15.

Viard, M. (1981). *Lithostratigraphie et pétrologie des formations métamorphiques du versant nord du mont Lozère.* PhD thesis.

Viegas, L. G. F., Archanjo, C. J., and Vauchez, A. (2013). Fabrics of migmatites and the relationships between partial melting and deformation in high-grade transpressional shear zones: The Espinho Branco anatexite (Borborema Province, NE Brazil). *Journal of Structural Geology 48*, 45–56.

Vielzeuf, D., Clemens, J. D., Pin, C., and Moinet, E. (1990). Granites, granulites, and crustal differentiation. In D. Vielzeuf and P. Vidal (Eds.), *Granulites and Crustal evolution*, pp. 59–85. Kluwer, Dordrecht.

Vielzeuf, D. and Montel, J. M. (1994). Partial melting of metagreywackes. Part I. Fluid-absent experiments and phase relationships. *Contributions to Mineralogy and Petrology 117*, 375–393.

Vigneresse, J. L., Barbey, P., and Cuney, M. (1996). Rheological transitions during partial melting and crystallization with application to felsic magma segregation and transfer. *Journal of Petrology 37*(6), 1579–1600.

Villaros, A., Buick, I. S., and Stevens, G. (2012). Isotopic variations in S-type granites: an inheritance from a heterogeneous source? *Contributions to Mineralogy and Petrology 163*(2), 243–257.

Villaseca, C., Barbero, L., and Herreros, V. (1998). A re-examination of the typology of peraluminous granite types in intracontinental orogenic belts. *Transactions of the Royal Society of Edinburgh.*

Villaseca, C., Merino Martínez, E., Orejana, D., Andersen, T., and Belousova, E. (2016). Zircon Hf signatures from granitic orthogneisses of the Spanish Central System: Significance and sources of the Cambro-Ordovician magmatism in the Iberian Variscan Belt. *Gondwana Research 34*, 60–83.

Vitel, G. (1985). Granulite-facies-amphibolite facies transition in basic enclaves of the Velay granite (French Massif Central). *Comptes Rendus de l'Académie des Sciences, Paris 300*(9), 407–412.

Vitel, G. (1988). Le granite du Gouffre d'Enfer (Massif central français). Pétrologie d'un marqueur tectonique varisque. *Bulletin de la Société Géologique de France 8*, 907–915.

Vogel, T. A., Patino, L. C., Alvarado, G. E., and Gans, P. B. (2004). Silicic ignimbrites within the Costa Rican volcanic front: evidence for the formation of continental crust. *Earth and Planetary Science Letters 226*(1-2), 149–159.

Voice, P. J., Kowalewski, M., and Eriksson, K. A. (2011). Quantifying the timing and rate of crustal evolution: Global compilation of radiometrically dated detrital zircon grains. *The Journal of Geology 119*(2), 109–126.

Von Huene, R. and Lallemand, S. (1990). Tectonic erosion along the Japan and Peru convergent margins. *GSA Bulletin 102*, 704–720.

Wang, C. Y., Campbell, I. H., Stepanov, A. S., Allen, C. M., and Burtsev, I. N. (2011). Growth rate of the preserved continental crust: II. Constraints from Hf and O isotopes in detrital zircons from Greater Russian Rivers. *Geochimica et Cosmochimica Acta 75*(5), 1308–1345.

Wang, M., Nebel, O., and Wang, C. Y. (2016). The flaw in the crustal 'zircon archive': Mixed Hf isotope signatures record progressive contamination of late-stage liquid in mafic–ultramafic layered intrusions. *Journal of Petrology 57*(1), 27–52.

Watson, E. B. (1996). Dissolution, growth and survival of zircons during crustal fusion: kinetic principals, geological models and implications for isotopic inheritance. *Transactions of the Royal Society of Edinburgh 87*(1-2), 43–56.

Watson, E. B. and Harrison, T. M. (1983). Zircon saturation revisited: temperature and composition effects in a variety of crustal magma types. *Earth and Planetary Science Letters 64*, 295–304.

Watt, G. R., Burns, I. M., and Graham, G. A. (1996). Chemical characteristics of migmatites: Accessory phase distribution and evidence for fast melt segregation rates. *Contributions to Mineralogy and Petrology 125*, 100–111.

Weaver, B. L. (1991). The origin of ocean island basalt end-member compositions: trace element and

isotopic constraints. *Earth and Planetary Science Letters 104*, 381–397.
Wedepohl, K. H. (1995). The composition of the continental crust. *Geochimica et Cosmochimica Acta 59*, 1217–1232.
Weinberg, R. F. and Hasalová, P. (2015). Water-fluxed melting of the continental crust: A review. *Lithos 212-215*, 158–188.
Weinberg, R. F. and Podladchikov, Y. Y. (1994). Diapiric ascent of magmas through power law crust and mantle. *Journal of Geophysical Research 99*(B5), 9543–9559.
Weinberg, R. F. and Schmeling, H. (1992). Polydiapirs: multiwavelength gravity structures. *Journal of Structural Geology 14*(4), 425–436.
Weisbrod, A. (1962). Relations pétrogénétiques entre les migmatites oeilées et le granite du Velay (Massif central français). *Comptes Rendus de l'Académie des Sciences, Paris 254*, 3004–3006.
Weisbrod, A. (1968). Les conditions du métamorphisme dans les Cévennes médianes (Massif Central, France). *Comptes Rendus de l'Académie des Sciences, Paris 266*, 755–757.
Weisbrod, A. (1970). *Pétrologie du socle métamorphique des Cévennes médianes (Massif Central français) : reconstitution sédimentologique et approche thermodynamique du métamorphisme.* Habilitation thesis.
Weisbrod, A., Pichavant, M., Marignac, C., Macaudière, J., and Leroy, J. (1980). Relations structurales et chronologiques entre le magmatisme basique, les granitisations et l'évolution tectonométamorphique tardihercynienne dans les Cévennes Médianes, Massif Central Français. *Comptes Rendus de l'Académie des Sciences, Paris 291*, 665–668.
Weisbrod, A., Samama, J. C., Elmi, S., and Berger, E. (1974). *Carte géol. France (1/50 000), feuille Largentière (864).* Orléans: BRGM.
Whalen, J. B., Currie, K. L., and Chappell, B. W. (1987). A-type granites: geochemical characteristics, discrimination and petrogenesis. *Contributions to Mineralogy and Petrology 95*, 407–419.
White, R. W., Powell, R., and Holland, T. J. B. (2001). Calculation of partial melting equilibria in the system Na_2O-CaO-K_2O-FeO-MgO-Al_2O_3-SiO_2-H_2O (NCKFMASH). *Journal of Metamorphic Geology 19*, 139–153.
White, R. W., Powell, R., Holland, T. J. B., and Worley, B. A. (2000). The effect of TiO_2 and Fe_2O_3 on metapelitic assemblages at greenschist and amphibolite facies conditions: mineral equilibria calculations in the system K_2O–FeO–MgO–Al_2O_3–SiO_2–H_2O–TiO_2–Fe_2O_3. *Journal of Metamorphic Geology 18*, 497–511.
Whitney, D. L. and Evans, B. W. (2009). Abbreviations for names of rock-forming minerals. *American Mineralogist 95*(1), 185–187.
Whitney, D. L., Roger, F., Teyssier, C., Rey, P. F., and Respaut, J. P. (2015). Syn-collapse eclogite metamorphism and exhumation of deep crust in a migmatite dome: The P–T–t record of the youngest Variscan eclogite (Montagne Noire, French Massif Central). *Earth and Planetary Science Letters 430*, 224–234.
Whitney, D. L., Teyssier, C., and Fayon, A. K. (2004b). Isothermal decompression, partial melting and exhumation of deep continental crust. In J. Grocott, K. J. W. McCaffrey, G. K. Taylor, and B. Tikoff (Eds.), *Vertical coupling and decoupling in the lithosphere*, Volume 227, pp. 313–326. Geological Society, London, Special Publications.
Whitney, D. L., Teyssier, C., and Vanderhaeghe, O. (2004a). Gneiss domes and crustal flow. In D. L. Whitney, C. Teyssier, and C. S. Siddoway (Eds.), *Gneiss domes in orogeny*, Volume 380, pp. 15–34. Geological Society of America Special Paper.
Wickham, S. M. and Taylor Jr., H. P. (1985). Stable isotopic evidence for large-scale seawater infiltration in a regional metamorphic terrane; the Trois Seigneurs Massif, Pyrenees, France. *Contributions to Mineralogy and Petrology 91*, 122–137.
Wiedenbeck, M., Allé, P., Corfu, F., Griffin, W. L., Meier, M., Oberli, F., Von Quadt, A., Roddick, J. C., and Spiegel, W. (1995). Three natural zircon standards for U-Th-Pb, Lu-Hf, trace element and REE analyses. *Geostandards Newsletter 19*, 1–23.
Wiedenbeck, M., Hanchar, J. M., Peck, W. H., Sylvester, P., Valley, J., Whitehouse, M., Kronz, A., Morishita, Y., and Nasdala, L. (2004). Further characterisation of the 91500 zircon crystal. *Geostandards and Geoanalytical Research 28*(1), 9–39.
Wiederer, U., Königshof, P., Feist, R., Franke, W., and Doublier, M. P. (2002). Low-grade metamorphism in the Montagne Noire (S-France): Conodont Alteration Index (CAI) in Palaeozoic carbonates and implications for the exhumation of a hot metamorphic core complex. *Schweiz. Mineral. Petrog. Mitt. 82*, 393–407.
Willbold, M. and Stracke, A. (2010). Formation of enriched mantle components by recycling of upper and lower continental crust. *Chemical Geology 276*(3-4), 188–197.
Williamson, B. J., Downes, H., and Thirlwall, M. F. (1992). The relationship between crustal magmatic underplating and granite genesis: an example from the Velay granite complex, Massif Central, France. *Transactions of the Royal Society of Edinburgh 83*, 235–245.
Winchester, J. A. and Floyd, P. A. (1977). Geochemical discrimination of different magma series and their differenciation products using immobile elements. *Chemical Geology 20*, 325–343.
Wittig, N., Baker, J. A., and Downes, H. (2007). U–Th–Pb and Lu–Hf isotopic constraints on the evolution of sub-continental lithospheric mantle, French Massif Central. *Geochimica et Cosmochimica*

Acta 71(5), 1290–1311.

Woodhead, J., Hergt, J., Shelley, M., Eggins, S., and Kemp, R. (2004). Zircon Hf-isotope analysis with an excimer laser, depth profiling, ablation of complex geometries, and concomitant age estimation. *Chemical Geology 209*(1-2), 121–135.

Woodhead, J. D. and Hergt, J. M. (2005). A preliminary appraisal of seven natural zircon reference materials for in situ Hf isotope determination. *Geostandards and Geoanalytical Research 29*(2), 183–195.

Workman, R. K. and Hart, S. R. (2005). Major and trace element composition of the depleted MORB mantle (DMM). *Earth and Planetary Science Letters 231*(1-2), 53–72.

Yakymchuk, C. and Brown, M. (2014). Behaviour of zircon and monazite during crustal melting. *Journal of the Geological Society 171*(4), 465–479.

Yousif, I. A. (1980). *Les amphibolites de la série métamorphique de basse pression du Vivarais occidental et du Mont Pilat : étude lithostratigraphique, pétrographique et géochimique*. PhD thesis.

Zandt, G., Gilbert, H., Owens, T. J., Ducea, M., Saleeby, J., and Jones, C. H. (2004). Active foundering of a continental arc root beneath the southern Sierra Nevada in California. *Nature 431*, 41–46.

Zapletal, K. (1990). Low-field susceptibility anisotropy of some biotite crystals. *Physics of the Earth and Planetary Interiors 63*, 85–97.

Zeh, A. and Gerdes, A. (2010). Baltica- and Gondwana-derived sediments in the Mid-German Crystalline Rise (Central Europe): Implications for the closure of the Rheic ocean. *Gondwana Research 17*, 254–263.

Zeh, A. and Gerdes, A. (2012). U–Pb and Hf isotope record of detrital zircons from gold-bearing sediments of the Pietersburg Greenstone Belt (South Africa)—Is there a common provenance with the Witwatersrand Basin? *Precambrian Research 204-205*, 46–56.

Zeh, A., Gerdes, A., Klemd, R., and Barton, J. M. (2007). Archaean to Proterozoic Crustal Evolution in the Central Zone of the Limpopo Belt (South Africa-Botswana): Constraints from Combined U-Pb and Lu-Hf Isotope Analyses of Zircon. *Journal of Petrology 48*(8), 1605–1639.

Zeh, A., Gerdes, A., and Millonig, L. (2011). Hafnium isotope record of the Ancient Gneiss Complex, Swaziland, southern Africa: evidence for Archaean crust-mantle formation and crust reworking between 3.66 and 2.73 Ga. *Journal of the Geological Society 168*(4), 953–964.

Zeh, A., Stern, R. A., and Gerdes, A. (2014). The oldest zircons of Africa—Their U–Pb–Hf–O isotope and trace element systematics, and implications for Hadean to Archean crust–mantle evolution. *Precambrian Research 241*, 203–230.

Zeitler, P. K., Chamberlain, C. P., and Smith, H. A. (1993). Synchronous anatexis, metamorphism, and rapid denudation at Nanga Parbat (Pakistan Himalaya). *Geology 21*, 347–350.

Zhao, Z. F., Dai, L. Q., and Zheng, Y. F. (2013). Postcollisional mafic igneous rocks record crust-mantle interaction during continental deep subduction. *Sci Rep 3*, 3413.

Zhao, Z.-F., Zheng, Y.-F., Wei, C.-S., and Wu, Y.-B. (2007). Post-collisional granitoids from the Dabie orogen in China: Zircon U–Pb age, element and O isotope evidence for recycling of subducted continental crust. *Lithos 93*(3-4), 248–272.

Ziberna, L., Klemme, S., and Nimis, P. (2013). Garnet and spinel in fertile and depleted mantle: insights from thermodynamic modelling. *Contributions to Mineralogy and Petrology 166*, 411–421.

Zorpi, M. J., Coulon, C., Orsini, J. B., and Cocirta, C. (1989). Magma mingling, zoning and emplacement in calc-alkaline granitoid plutons. *Tectonophysics 157*, 315–329.

Zurbriggen, R. (2015). Ordovician orogeny in the Alps: a reappraisal. *International Journal of Earth Sciences 104*(2), 335–350.